

Lawrence Berkeley National Laboratory

Lawrence Berkeley National Laboratory

Title

MATERIALS AND MOLECULAR RESEARCH DIVISION ANNUAL REPORT 1979

Permalink

<https://escholarship.org/uc/item/8w27h6rr>

Author

Authors, Various

Publication Date

1980-03-01

MATERIALS AND MOLECULAR RESEARCH DIVISION

Annual Report 1979

March 1980

RECEIVED
LAWRENCE
BERKELEY LABORATORY
OCT 14 1980
LIBRARY AND
DOCUMENTS SECTION

TWO-WEEK LOAN COPY

*This is a Library Circulating Copy
which may be borrowed for two weeks.
For a personal retention copy, call
Tech. Info. Division, Ext. 6782.*

*Lawrence Berkeley Laboratory
University of California, Berkeley*

DISCLAIMER

This document was prepared as an account of work sponsored by the United States Government. While this document is believed to contain correct information, neither the United States Government nor any agency thereof, nor the Regents of the University of California, nor any of their employees, makes any warranty, express or implied, or assumes any legal responsibility for the accuracy, completeness, or usefulness of any information, apparatus, product, or process disclosed, or represents that its use would not infringe privately owned rights. Reference herein to any specific commercial product, process, or service by its trade name, trademark, manufacturer, or otherwise, does not necessarily constitute or imply its endorsement, recommendation, or favoring by the United States Government or any agency thereof, or the Regents of the University of California. The views and opinions of authors expressed herein do not necessarily state or reflect those of the United States Government or any agency thereof or the Regents of the University of California.

MATERIALS AND MOLECULAR
RESEARCH DIVISION

Annual Report 1979

March 1980

*Lawrence Berkeley Laboratory
University of California
Berkeley, California*

CONTENTS

| | |
|---|----|
| GENERAL INTRODUCTION | 1 |
| <i>David A. Shirley</i> | |
| I. MATERIALS SCIENCES | |
| A. Metallurgy and Ceramics | |
| 1. Structure of Materials | |
| a. Microstructure, Properties and Alloy Design: Inorganic Materials | |
| <i>Gareth Thomas, Investigator</i> | |
| Alloy Design: Medium Carbon Steels, "Qua-Tough Alloys" | |
| 1. Optimization of Fe/CrC Base Steels for Improved Mechanical Properties (For Structural Applications). | 7 |
| Low Carbon Dual Phase Steels | |
| 1. Metallurgical Factors Controlling Impact Properties of Dual-Phase (DP) Steels. . . | 9 |
| 2. Effects of Morphology on the Mechanical Properties of Dual Phase Fe/Si/C Steels. . | 12 |
| 3. Mechanical Properties and Microstructures of Dual Phase Steels Containing Silicon, Aluminum, and Molybdenum | 14 |
| 4. Design of Dual Phase Steels with Carbide Forming Elements | 15 |
| Phase Transitions | |
| 1. Morphology and Crystallography of Lath Martensites | 16 |
| 2. Determination of Local Hydrogen Concentration Using Cold Stage Electron Microscopy | 20 |
| Refractory Ceramics | |
| 1. The Crystallization of Oxynitride Glasses | 21 |
| 2. C and B in Sintered SiC | 21 |
| Analytical Microscopy | |
| 1. Development of Energy Loss Spectroscopy | 21 |
| Physical Properties and Microstructures of Alloys and Ceramics | |
| 1. Rare Earth-Cobalt Hard Magnets | 24 |
| 2. High Permeability Ni-Zn-Co Ferrites | 25 |
| 3. Higher Permeability (Mn,Zn) Ferrites | 26 |
| 4. Bubble Garnet Films | 28 |
| 5. Magnetic Properties of Plasma Deposited Iron-Iron Oxide Thin Films | 28 |
| Research Plans for Calendar Year 1980 | 29 |
| 1979 Publications and Reports | 30 |
| b. Atomic Resolution Microscopy | |
| <i>R. Gronsky and G. Thomas, Investigators</i> | |
| 1. Electron Microscopy of Spinodal Structures at High Resolution | 33 |
| 2. The Effect of Lens Aberrations on Lattice Images of Spinodally Decomposed Alloys | 34 |
| 3. Lattice Imaging of Modulated Structures | 35 |
| 4. Grain Boundary Precipitation in Aluminum Alloys: Effect of Boundary Structure . . | 36 |
| 5. Direct Imaging of Grain Boundaries | 37 |
| 6. The Structure of Ultra-Thin Oxide on Silicon | 38 |
| 7. High-Resolution Studies of G.P. Zone Formation in Au-Ni Alloys | 39 |
| Research Plans for Calendar Year 1980 | 39 |
| 1979 Publications and Reports | 40 |

| | | |
|----|--|----|
| c. | 1.5 MeV Electron Microscope | |
| | <i>K. H. Westmacott, Investigator</i> | |
| | 1. Progress Report of Facility Development | 41 |
| | 2. Phase Transformation in Interstitial Alloys | 41 |
| | 3. The Origin of Unusual Dislocation Structures in Ion-Thinned NiO Single Crystals | 43 |
| | 4. Plastic Deformation of MgO (Al ₂ O ₃) _{1.1} Spinel at 0.28 Tm | 44 |
| | Research Plans for Calendar Year 1980 | 46 |
| | 1979 Publications and Reports | 46 |
| 2. | Mechanical Properties | |
| a. | Theoretical Problems in Alloy Design | |
| | <i>J. W. Morris, Jr., Investigator</i> | |
| | Theoretical Studies | |
| | 1. Precipitation and Coarsening Reactions in Two-Dimensional Ising Lattices | 47 |
| | 2. The Elastic Energy Contribution to Solid State Phase Transformation | 47 |
| | 3. The Theory of Martensitic Transformations in an Idealized Elastic Solid | 48 |
| | 4. Tweed and Coarsening Reactions in Simple Elastic Solids | 50 |
| | 5. The Habit of a Tetragonal Precipitate in a Cubic Matrix: Analytical Results | 51 |
| | 6. Shape and Habit of Tetragonal Precipitates in Anisotropic Cubic Matrices: Particle Size and Shape Effects | 52 |
| | Fundamental Experimental Studies in Alloy Steels | |
| | 1. Research on the Composition of Austenite Precipitated During Intercritical Tempering in Fe-Ni Alloys | 52 |
| | 2. The Scavenging Effect of Retained Austenite in Low Carbon Fe-Ni Alloys | 53 |
| | 3. The Influence of Retained Austenite on the Toughness of Ferritic Cryogenic Steels | 54 |
| | Alloy Development Research in Ferritic Cryogenic Steels | |
| | 1. The Achievement of Cryogenic Toughness in Low Manganese Ferritic Steel | 56 |
| | 2. Metallurgical Interpretation of the QLT Treatment for Low Nickel Cryogenic Steels | 57 |
| | Welding Research | |
| | 1. A Review of the Development of Ferritic Consumable for the Welding of 9% Nickel Steel | 57 |
| | 2. A Study of Ferritic Weld Deposits in Fe-9Ni Steel | 58 |
| | 3. Weldability Studies on Grain-Refined Fe-12Ni-0.25Ti for Liquid Helium Use | 59 |
| | Superconductivity Research | |
| | 1. Monolithic Processing of V-Ga Superconductors | 59 |
| | 2. The Attainment of High Critical Temperatures in V-Ga Monolithic Wire Through Direct Precipitation | 59 |
| | Research Plans for Calendar Year 1980 | 60 |
| | 1979 Publications and Reports | 61 |
| b. | Structure-Property Relationships in Semiconductor Materials | |
| | <i>J. Washburn, Investigator</i> | |
| | 1. Cross Section Transmission Electron Microscopy as a Powerful New Technique for the Study of Defects in Thin Surface Layers | 63 |
| | 2. On the Interpretation of Channeled Rutherford Backscattering Yields from Multilayer Subsurface Damage | 65 |
| | 3. Laser and Electron-Beam Annealing Effects in Gallium Arsenide | 67 |
| | 4. Effect of Implantation Temperature on Ion-Implantation Damage in Silicon | 69 |
| | 5. A New Experimental Technique for Studying the Regrowth of Amorphous Layers in Semiconductors | 71 |
| | 6. A Model for Regrowth of Amorphous Silicon which Explains the Orientation Dependence of Regrowth Rate and the Nature of the Residual Defect Population | 73 |

| | | |
|--|--|-----|
| 7. | Ion Thinning and Electron Beam Damage in Cadmium Sulfide During Specimen Preparation and Transmission Electron Microscope Observation | 74 |
| 8. | Characteristics of Cds-Cu _x S and (Cd,Zn)S - Cu _x S Heterojunctions | 75 |
| 9. | On the Degradation of Spectral Selectivity of Black Chrome Solar Absorber Coatings During Short-Term High-Temperature Exposures | 77 |
| | Research Plans for Calendar Year 1980 | 78 |
| | 1979 Publications and Reports | 79 |
| c. Mechanical Properties of Ceramics | | |
| | <i>Anthony G. Evans, Investigator</i> | |
| | High Temperature Deformation and Failure | |
| 1. | Statistical Models of Failure | 82 |
| 2. | Creep Fracture Induced by Grain Boundary Sliding | 83 |
| 3. | The Effect of Cavitation on the Tensile Deformation Behavior of Alumina | 84 |
| 4. | Some Effects of Cavities on Creep in Ceramics | 84 |
| 5. | High Temperature Creep in Al ₂ O ₃ -SiO ₂ Ceramics | 86 |
| 6. | Internal Friction in Al ₂ O ₃ , SiO ₂ Materials | 86 |
| | Toughening Mechanisms in Ceramics | |
| 1. | Martensitic Toughening in Ceramics | 88 |
| 2. | Martensitic Transformation in Zirconia | 89 |
| 3. | Toughening in the Al ₂ O ₃ /ZrO ₂ System | 91 |
| | Research Plans for Calendar Year 1980 | 92 |
| | 1979 Publications and Reports | 92 |
| 3. Physical Properties | | |
| a. Superconductivity Effects--High Field Superconductivity | | |
| | <i>J. Wang and J. W. Morris, Jr., Investigators</i> | |
| 1. | An Investigation of the Effects of Particle Size on the Mechanical Properties of Porous and Tin-Infiltrated Niobium Rods Fabricated by a Thermoplastic-Powder Metallurgy Technique | 94 |
| 2. | High Field Current Carrying Capacity of Niobium-Tin Superconducting Wire Produced by the Infiltration Process | 95 |
| 3. | The Possibility of Eliminating the Tantalum Diffusion Barrier in Niobium-Tin Superconducting Wire Fabricated by the Infiltration Process | 96 |
| 4. | Scanning Auger Microscopy Study of the Role of Oxygen on the Fracture of Tin-Infiltrated Niobium Rod | 96 |
| | 1979 Publications and Reports | 97 |
| b. Interfaces and Ceramics Microstructures | | |
| | <i>J. A. Pask, Investigator</i> | |
| 1. | Wetting and Reactions in the Sodium Silicate/Iron System | 99 |
| 2. | Wetting and Adherence of Na-Borate Glass on Gold | 101 |
| 3. | Microstructure and Interface Studies in Thick Film Conductor Systems | 101 |
| 4. | Reaction and Bonding at ZnO Thin Film and Si Substrate Interfaces | 103 |
| 5. | Corrosion of Silicate Materials by Hydrogen Gas and HF Acid Solution | 103 |
| 6. | Corrosion and Mechanical Behavior Correlations with Composition and Microstructure of Aluminum Silicate Refractories | 105 |
| 7. | Sintering of Mullite-Containing Compositions | 106 |
| 8. | Thermodynamics and Mechanisms of Sintering | 107 |
| 9. | Sintering of MgO | 108 |
| 10. | Analysis and Kinetics of Solid State Reactions in PbO-ZrO ₂ System | 109 |
| | Research Plans for Calendar Year 1980 | 110 |
| | 1979 Publications and Reports | 111 |
| c. High Temperature Reactions | | |
| | <i>Alan W. Searcy, Investigator</i> | |
| 1. | Partial Molal Properties of CO ₂ in CaCO ₃ and the Solubility of CaO in CaO ₃ as a Function of Temperature | 112 |
| 2. | The Kinetics of Decomposition of CaCO ₃ at High CO ₂ Partial Pressures | 113 |

| | | |
|----|---|-----|
| 3. | The Influence of Self-Cooling on the Apparent Activation Enthalpy of Decomposition of CaCO_3 | 114 |
| 4. | Catalysis of the Decomposition of CaCO_3 and of the Sintering of CaO | 115 |
| 5. | The Kinetics of Reaction of CO_2 with Porous CaO Powders | 116 |
| 6. | Characterization of the Porous CaO Particles Formed by Decomposition of CaCO_3 and Ca(OH)_2 in Vacuum | 116 |
| 7. | Use of N_2 Adsorption Isotherms to Deduce Reactant-Product Orientation of Relationships in Vapor Phase Hydration of Sub-Micron Particles of CaO | 117 |
| | Research Plans for Calendar Year 1980 | 118 |
| | 1979 Publications and Reports | 119 |
| d. | Chemical Properties of Ceramic Alloys and Processing of Ceramic Materials <i>L. C. De Jonghe, Investigator</i> | |
| 1. | Gas Solid Reaction: Reduction of Oxides | 120 |
| 2. | Transient Liquid Phase Sintering of Ceramics | 121 |
| | Research Plans for Calendar Year 1980 | 122 |
| | 1979 Publications and Reports | 122 |
| e. | Structure and Electrical Properties of Composite Materials <i>Robert H. Bragg, Investigator</i> | |
| 1. | Electrical Conduction and Hall Effect in Glassy Carbon | 124 |
| 2. | Effect of Hydrostatic Pressure and Grinding on the Density and Pore Structure of Glassy Carbon | 126 |
| 3. | Correction for Compton Scattering in Glassy Carbon Diffraction Patterns | 129 |
| 4. | Short Term Heat Treatment of Glassy Carbon Samples | 129 |
| | Research Plans for Calendar Year 1980 | 131 |
| | 1979 Publications and Reports | 131 |
| f. | High Temperature Oxidation and Corrosion of Materials <i>David P. Whittle, Investigator</i> | |
| 1. | Equilibria in Gaseous Systems | 132 |
| 2. | Corrosion Mechanisms in Complex Environments of Low Oxidizing Potential | 134 |
| 3. | Hot Corrosion of Nickel-Base Alloys at Intermediate Temperatures | 136 |
| 4. | Corrosion by Solid Sulfatic Deposits | 137 |
| 5. | Adherence of Al_2O_3 Oxide Films | 138 |
| 6. | Oxidation Behavior of a Two-Phase Alloy: Fe - 44%Cu | 139 |
| 7. | Formation of Subscales of Varying Composition | 141 |
| | Research Plans for Calendar Year 1980 | 143 |
| | 1979 Publications and Reports | 144 |
| 4. | Engineering Materials | |
| a. | Erosion-Corrosion-Wear Program <i>Alan V. Levy, Investigator</i> | |
| | Erosion Behavior | |
| 1. | Erosion Mechanisms in Ductile Metals | 146 |
| 2. | Erosion of Thin Scales | 148 |
| 3. | Erosion Mechanisms in Brittle Solids | 149 |
| 4. | Effect of Particle Characteristics on Erosion of Ductile Metals | 150 |
| 5. | The Halo Effect in Jet Impingement Solid Particle Erosion Testing of Ductile Metals | 151 |
| | Corrosion Behavior | |
| 1. | Corrosion of Metals by Char | 152 |
| 2. | Catalytic Deactivation | 153 |
| | Two Phase Flow Behavior | |
| 1. | Gas-Particle Flow in the Entry Region of a Curved Pipe | 155 |
| 2. | Separation Effects in Gas-Particle Flows at High Reynolds Numbers | 156 |
| 3. | Aerodynamic Effects in the Erosion Process | 157 |
| 4. | Development of a Laser Test System for Two-Phase Flow Studies | 157 |

| | |
|--|-----|
| Research Plans for Calendar Year 1980 | 159 |
| 1979 Publications and Reports | 159 |
| b. In-Situ Investigations of Gas-Solid Reactions by Electron Microscopy <i>J. W. Evans and K. H. Westmacott, Investigators</i> | |
| 1. Early Stages of Reduction of Nickel Oxide Single Crystals: An Investigation by Transmission Electron Microscopy | 161 |
| Research Plans for Calendar Year 1980 | 162 |
| 1979 Publications and Reports | 162 |
| B. Solid State Physics | |
| 1. Experimental Solid-State Physics | |
| a. Far Infrared Spectroscopy <i>Paul L. Richards, Investigator</i> | |
| 1. Infrared Spectra of CO Chemisorbed on Ni | 164 |
| 2. Electrons on the Surface of Liquid Helium | 165 |
| 3. Superconducting Receivers for Millimeter Microwaves | 166 |
| 4. Grid Polarizers for Infrared Fourier Spectrometers | 167 |
| Research Plans for Calendar Year 1980 | 168 |
| 1979 Publications and Reports | 168 |
| b. Experimental Solid State Physics and Quantum Electronics <i>Y. Ron Shen, Investigator</i> | |
| 1. Surface Coherent Anti-Stokes Raman Spectroscopy | 170 |
| 2. Coherent Second Harmonic Generation by Counter-Propagating Surface Plasmons . . . | 172 |
| 3. Measurement of Refractive Indices and Study of Isotropic-Nematic Phase Transition by the Surface Plasmon Technique | 173 |
| 4. Polarization-Sensitive Coherent Anti-Stokes Raman Spectroscopy | 174 |
| 5. Dynamics of Resonant Strong Interaction of Light with Atoms and Molecules | 176 |
| 6. Multi-Photon Dissociation of Molecules | 177 |
| Research Plans for Calendar Year 1980 | 177 |
| 1979 Publications and Reports | 177 |
| c. Excited Quantum Fluids in Solids <i>Carson D. Jeffries, Investigator</i> | |
| 1. Lifetime and Diffusion of Free Excitons in Ge | 179 |
| 2. Experimental Limit on the Net Charge of Electron-Hole Drops in Ge | 182 |
| 3. The Metal-Insulator Transition in Uniformly Strained Ge | 183 |
| 4. Buildup of the Strain-Confined Electron-Hole Liquid | 185 |
| 5. Properties of the Electron-Hole Liquid in Ge and Si as a Function of Density . . . | 188 |
| Research Plans for Calendar Year 1980 | 189 |
| 1979 Publications and Reports | 190 |
| d. Superconductivity, Superconductivity Devices, and 1/f Noise <i>John Clarke, Investigator</i> | |
| 1. Magnetotellurics at a Geothermal Site | 191 |
| 2. All Nb Low Noise DC SQUID with 1 μm Tunnel Junctions | 193 |
| 3. Supercurrent-Induced Charge Imbalance in the Presence of a Thermal Gradient. . . . | 195 |
| 4. Calculations of Quasiparticle Branch Relaxation Rates in Superconductors | 196 |
| 5. Boundary Resistance of the Superconducting-Normal Interface | 197 |
| 6. Measurement of the Quasiparticle Charge Relaxation Rate in Al-Er Alloys | 199 |
| Research Plans for Calendar Year 1980 | 200 |
| 1979 Publications and Reports | 201 |
| 2. Theoretical Solid State Physics | |
| a. Theoretical Solid State Physics <i>Marvin L. Cohen, Investigator</i> | |
| 1. Pseudopotential Techniques and Electronic Properties of Solids | 203 |

| | |
|---|-----|
| 2. Solid Surfaces and Interfaces | 203 |
| 3. Superconductivity | 204 |
| Research Plans for Calendar Year 1980 | 204 |
| 1979 Publications and Reports | 204 |
| C. Materials Chemistry | |
| 1. Chemical Structure | |
| a. Low Temperature Properties of Materials | |
| <i>Norman E. Phillips, Investigator</i> | |
| 1. Use of a Microcomputer for On Line Calculations of Low Temperature Heat Capacity Data | 206 |
| 2. Low Temperature Heat Capacity of <u>AuGd</u> , a Weakly Interacting Spin Glass | 208 |
| Research Plans for Calendar Year 1980 | 209 |
| b. Electrochemical Processes | |
| <i>C. W. Tobias, Investigator</i> | |
| 1. Gas-Electrolyte-Electrode Interfaces--Primary Potential and Current Distribution Around a Bubble on an Electrode | 211 |
| 2. High Rate Electrolysis Processes--the Effect of Suspended Inert Particles on Limiting Currents to a Rotating Disk | 212 |
| 3. Research Leading to New Electrochemical Processes--Anodic Processes in Propylene Carbonate | 213 |
| Research Plans for Calendar Year 1980 | 214 |
| 1979 Publications and Reports | 214 |
| 2. High-Temperature and Surface Chemistry | |
| a. High-Temperature Chemistry | |
| <i>Leo Brewer, Investigator</i> | |
| 1. High-Temperature Solid-Electrolyte Electromotive Cell Measurements of Generalized-Lewis-Acid-Base Interactions in Binary Transition Metal Alloys | 216 |
| 2. High-Temperature Gaseous Equilibria Measurements of Generalized-Lewis-Acid-Base Interactions in Binary Transition Metal Alloys | 216 |
| 3. Critical Evaluation and Compilation of High-Temperature Thermodynamic Data | 216 |
| 4. Stabilities of Homonuclear Diatomic Molecules | 216 |
| 5. Ternary Phase Equilibria of A-B-X Systems with X+B, C, N, and O | 217 |
| Research Plans for Calendar Year 1980 | 217 |
| 1979 Publications and Reports | 217 |
| b. Chemistry and Materials Problems in Energy Production Technologies | |
| <i>D. R. Olander, Investigator</i> | |
| 1. Bubble Migration in Stress Gradients | 219 |
| 2. Solubility and Diffusion of Ruthenium in UO_2 | 219 |
| 3. Thermal Gradient Brine Inclusion Migration in Salt | 221 |
| 4. Investigation of the Iron-Chlorine Reaction by Modulated Molecular Beam Mass Spectrometry | 222 |
| 5. Oxygen Self-Diffusion in Hypostoichiometric Urania | 222 |
| 6. The Theory of Uranium Enrichment by the Gas Centrifuge | 224 |
| Research Plans for Calendar Year 1980 | 225 |
| 1979 Publications and Reports | 225 |
| c. Plasma Enhanced Deposition of Thin Films | |
| <i>D. W. Hess, Investigator</i> | |
| 1. Plasma-Enhanced Deposition of Iron/Iron Oxide Films | 226 |
| Research Plans for Calendar Year 1980 | 227 |
| 1979 Publications and Reports | 227 |

| | | |
|----|--|-----|
| d. | Electrochemical Phase Boundaries | |
| | <i>Rolf H. Muller, Investigator</i> | |
| | 1. Use of Film-Formation Models for the Interpretation of Ellipsometer Measurements | 228 |
| | 2. Conventions and Formulas for Using the Mueller-Stokes Calculus in Ellipsometry | 230 |
| | 3. Fourth International Conference on Ellipsometry | 230 |
| | 4. Interferometry of Mass-Transfer Boundary Layers | 230 |
| | Research Plans for Calendar Year 1980 | 231 |
| | 1979 Publications and Reports | 232 |
| e. | Solid State and Surface Reactions | |
| | <i>Gabor A. Somorjai, Investigator</i> | |
| | Surface Structure and Chemisorption by Low Energy Electron Diffraction | |
| | 1. Surface Structure Analysis of the Reconstructed (100) Crystal Faces of Iridium, Platinum and Gold | 233 |
| | 2. Measurement of the Leed Diffraction Beam Intensities from Chemisorbed CO on the Rh(111) Crystal Face | 233 |
| | 3. Low Energy Electron Diffraction Studies of the Surfaces of Molecular Crystals (Ice, Ammonia, Naphthalene, Benzene) | 233 |
| | 4. Leed Study of the Adsorption of Acetic Acid and Propionic Acid on Ag(111) | 233 |
| | 5. A Leed-AES Study of the Reconstructed Pt(110) Surface and the Effects of Oxygen Treatment | 234 |
| | 6. Leed, AES and Thermal Desorption Studies of the Oxidation of the Rh(111) Surface | 234 |
| | 7. Adsorbed Monolayers on Solid Surfaces | 234 |
| | 8. A New Microfacet Notation for High Miller Index Surfaces of Cubic Materials with Terrace, Step and Kink Structures | 234 |
| | 9. Surface Structures of Metallic Monolayers on Metal Crystal Surfaces | 234 |
| | 10. The Structure and Composition of Potassium Layers Deposited on Ni(111) Crystal Surfaces | 235 |
| | Electron Spectroscopy Studies of Solid Surfaces and Adsorbates | |
| | 1. The Chemisorption of Acetylene and Ethylene on Rh(111): A High Resolution Electron Energy Loss and Leed Study | 235 |
| | 2. Evidence of the Weakening of the CO Bond upon Coadsorption with Hydrocarbons | 235 |
| | 3. The Chemisorption of CO and CO ₂ on Rh(111) Studied by High Resolution Electron Energy Loss Spectroscopy | 235 |
| | Molecular Beam-Surface Interactions | |
| | 1. The Kinetics of Ammonia Decomposition on the (111) and Stepped Crystal Faces of Platinum | 236 |
| | 2. The Velocity and Angular Distributions of Products from the Platinum Surface Catalyzed Reactions of H, H ₂ and O ₂ | 236 |
| | Studies of Catalyzed Surface Reactions | |
| | 1. Correlations of Cyclohexene Reactions on Platinum Crystal Surfaces over Ten Orders of Magnitude Pressure Range: Variations of Structure Sensitivity, Rates and Reaction Probabilities | 236 |
| | 2. High Pressure Studies of Cyclohexane Dehydrogenation and Hydrogenolysis over Platinum Crystal Surfaces | 236 |
| | 3. The Structure and Reactivity of Ordered Platinum Structure and Monolayers Epitaxially Deposited on the Au(100) Crystal Face | 237 |
| | Research Plans for Calendar Year 1980 | 237 |
| | 1979 Publications and Reports | 237 |
| f. | Nuclear Magnetic Resonance | |
| | <i>Alexander Pines, Investigator</i> | |
| | 1. Selective Excitation of n-Quantum Transitions | 240 |
| | 2. Information Theory Treatment of Multiple-Quantum Coherence | 240 |
| | 3. Relaxation of Multiple Quantum Transitions | 241 |
| | 4. Analogy of Multiple-Quantum NMR to Isotopic Labeling | 242 |

| | |
|--|-----|
| 5. Statistical Configurations of Aliphatic Chains | 242 |
| 6. Correlation in the Motion of Coupled Methyl Groups | 243 |
| 7. Biphenyl Conformation in a Liquid Crystal Molecule | 243 |
| 8. Synthesis of Liquid and Solid Crystals | 244 |
| 9. Anisotropic Relaxation of Deuterated Hexamethylbenzene | 244 |
| 10. Spin-Lattice Relaxation of Reorienting or Tunneling Deuterated Methyl Groups | 244 |
| 11. Rotational Polarization of Solid Methyl Iodine | 245 |
| 12. Exchange of Rotational Polarization in Methyl Groups | 245 |
| 13. Viscosity Dependence of the Magnetic Isotope Effect | 246 |
| 14. Computer Programs for NMR and Conformational Analysis | 247 |
| Research Plans for Calendar Year 1980 | 247 |
| 1979 Publications and Reports | 248 |

II. CHEMICAL SCIENCES

A. Fundamental Interactions

1. Photochemical and Radiation Sciences

a. Photon-Assisted Surface Reactions, Materials and Mechanisms

Gabor A. Somorjai, Investigator

| | |
|---|-----|
| 1. Photocatalytic Hydrogen Production from Water over SrTiO ₃ Crystal Surfaces | 253 |
| 2. Electron Spectroscopy (XPS and UPS) Studies of the Adsorption of H ₂ , O ₂ , and H ₂ O on Reduced and Stoichiometric SrTiO ₃ | 253 |
| 3. High Temperature Photocatalytic Dissociation of H ₂ O on SrTiO ₃ and TiO ₂ | 253 |

| | |
|---|-----|
| Research Plans for Calendar Year 1980 | 253 |
| 1979 Publications and Reports | 253 |

b. Photochemistry of Materials in the Stratosphere

H. S. Johnston, Investigator

| | |
|---|-----|
| 1. Absolute Quantum Yields for Two Channels of Photolysis of NO ₃ Free Radical | 255 |
| 2. Rate Constant for the Reaction of O(³ P) with Nitrogen Dioxide | 257 |
| 3. Absolute Quantum Yields for Photolysis of Di-Nitrogen Pentoxide | 258 |
| 4. Isotope Effect on the Ultraviolet Absorption Spectrum of Nitrous Oxide | 259 |
| 5. Instantaneous Global Ozone Balance Including Observed Nitrogen Dioxide | 261 |
| 6. Thunderstorms as Possible Micrometeorological Sink for Stratospheric Water | 265 |
| 7. Development of Stable Electrical Waveform Sources for a Molecular Modulation | 266 |

| | |
|---|-----|
| Research Plans for Calendar Year 1980 | 266 |
| 1979 Publications and Reports | 267 |

2. Chemical Physics

a. Energy Transfer and Structural Studies of Molecules on Surfaces

C. B. Harris, Investigator

| | |
|--|-----|
| 1. Optical Spectroscopy of Chemisorbed Molecules on Ni(111) | 268 |
| 2. Raman Spectroscopy of Molecules Adsorbed on Ni(111) and Ag(111) | 269 |
| 3. The Dynamics of Energy Transfer from Photoexcited Molecules to Metal Surfaces. | 270 |
| 4. Low Level Light Signal Averaging Using an Optical Multichannel Analyzer (OMA). | 270 |
| 5. Investigations of Liquid Structure by Picosecond Laser Spectroscopy | 271 |
| 6. A Critical Test of Vibrational Dephasing Theories in Liquids Using Selective Coherent Picosecond Stokes Scattering | 272 |
| 7. A Critical Test of Vibrational Dephasing Theories in Solids Using Spontaneous Raman Scattering in an Isotopic Mixed Crystal | 273 |
| 8. Frequency Mixing through Self-Phase Modulation in Picosecond Pulses | 274 |

| | |
|---|-----|
| Research Plans for Calendar Year 1980 | 276 |
| 1979 Publications and Reports | 276 |

b. Molecular Beam Spectroscopy

John S. Winn, Investigator

| | |
|--|-----|
| 1. Analytical Potential Functions for Weakly-Bound Molecules | 278 |
| 2. Empirical Methods of Estimating Diatomic Binding Energies | 279 |
| 3. Dynamics of Chemiluminescent Chemi-Ionization | 279 |
| 4. Mechanism of Metal Carbonyl Dissociation by Metastable Rare Gases | 281 |

| | | |
|----|--|-----|
| 5. | Production and Chemistry of Metal Atoms and Metal Clusters by Molecular Beams Methods | 282 |
| 6. | Molecular Beam Electric Resonance Spectroscopy | 283 |
| | Research Plans for Calendar Year 1980 | 283 |
| | 1979 Publications and Reports | 284 |
| c. | Selective Photochemistry <i>C. Bradley Moore, Investigator</i> | |
| 1. | Pressure Broadening of Single Vibrational-Rotational Transitions of Acetylene at $v = 5$ | 285 |
| 2. | Analysis of the Fifth Overtone Spectrum of Propane | 287 |
| 3. | Vibration-Vibration Energy Transfer in Methane | 288 |
| | Research Plans for Calendar Year 1980 | 290 |
| | 1979 Publications and Reports | 290 |
| d. | Physical Chemistry with Emphasis on Thermodynamic Properties <i>Kenneth S. Pitzer, Investigator</i> | |
| 1. | Improved <i>Ab Initio</i> Effective Core Potentials for Molecular Calculations | 292 |
| 2. | Relativistic Effects on Molecular Properties: Au_2 , TlH , PbS , and $PbSe$ | 294 |
| 3. | Thermodynamic Properties of Electrolytes: From Dilute Solutions to Fused Salts | 297 |
| | Research Plans for Calendar Year 1980 | 299 |
| | 1979 Publications and Reports | 299 |
| e. | Chemical Dynamics Studies <i>Bruce H. Mahan, Investigator</i> | |
| 1. | Laser Induced Fluorescence Studies of Molecular Ions | 300 |
| 2. | Dynamics of $CO_2^+-D_2$ Collisions | 302 |
| 3. | Dynamics of N^+-H_2 Collisions | 303 |
| | Research Plans for Calendar Year 1980 | 304 |
| | 1979 Publications and Reports | 304 |
| f. | Theory of Low Energy Atomic and Molecular Collision Processes <i>William H. Miller, Investigator</i> | |
| 1. | Classical Model for the Electronic Degrees of Freedom in Non-Adiabatic Collision Processes | 305 |
| 2. | Effect of Tunneling on Unimolecular Rate Constants, with Application to Formaldehyde | 307 |
| 3. | Reaction Path Hamiltonian for Polyatomic Molecules | 308 |
| 4. | Unified Model for Diffractive and Inelastic Scattering of a Light Atom from a Solid Surface | 309 |
| 5. | On the Quantum Mechanical Implications of Classical Ergodicity | 311 |
| | Research Plans for Calendar Year 1980 | 311 |
| | 1979 Publications and Reports | 312 |
| g. | Photoelectron Spectroscopy <i>David A. Shirley, Investigator</i> | |
| | Solid-State and Surface Research | |
| 1. | Condensed Phase Photoelectron Asymmetry: A New Effect | 314 |
| 2. | Photoelectron Diffraction Studies of Carbon Monoxide Overlayers | 315 |
| 3. | Photoelectron Diffraction Measurements of Sulfur and Selenium Adsorbed on Ni(001) | 316 |
| 4. | High-Resolution Photoemission Study of the Copper (100) Surface State | 318 |
| 5. | Angle-Resolved Photoemission Determination of Λ -Line Valence Bands in Pt and Au Using Synchrotron Radiation | 319 |
| 6. | Investigation of the Valence-Band Structure Along Δ , Σ , and Σ' in Ag Using Angle-Resolved Photoemission | 321 |
| 7. | An Angle-Resolved Photoemission Determination of the Valence-Band Structure of Pt between Γ and X | 322 |
| 8. | Electronic Structure in GaAs/Ge from Angle-Resolved Photoemission | 323 |

Gas-Phase Research

1. Angular Distribution of Xe5s \rightarrow ϵ p Photoelectrons Near the Cooper Minimum 324
2. Resonance Photoelectron Spectroscopy: A New Method--The Photoelectron Spectra of Atomic Ba at Selected Autoionizing Resonances 325
3. Polarized Fluorescence from Photodissociation Fragments: A Study of ICN Photolysis Using Synchrotron Radiation 326
4. The Ejected Electron Spectra of Atomic Yb and Ba 327
5. Decay Dynamics of XeF* ($B^2\Sigma^+$ and $C^2\Pi_{3/2}$) States 328
6. The Photoelectron Angular Distributions of HBr and HI at $h\nu = 21.2\text{eV}$ 329

- Research Plans for Calendar Year 1980 330
- 1979 Publications and Reports 331

- h. Crossed Molecular Beams
Y. T. Lee, Investigator
 1. Competitive Decay of the Complex Formed in the Reaction $O(^3P) + C_6H_6$ and C_6D_6 . . . 333
 2. The Dynamics of the Reaction $O(^1D) + H_2 \rightarrow H_2O \rightarrow OH + H$ 335
 3. Primary Product Identification in the Reaction of Oxygen Atoms with Toluene. . . . 336
 4. Observation of CH_3O Product in the Crossed Beam Study of the $O(^1D_2) + CH_4$ Reaction 337
 5. Vibrational Predissociation Spectra of Weakly Bound Van Der Waals Complexes. . . . 338
 6. Vibrational Predissociation Spectra of Small Hydrogen Bonded Clusters 340
 7. State Selected Ion-Molecule Reactions: $H_2^+ + He$ and $H_2^+ + D_2$ 341
 8. Molecular Beam Studies of the Reaction Dynamics of $F + H_2, D_2$ 343
 9. Dynamics of the Reaction $Li + HF \rightarrow LiF + H$ 345
 10. Chemiluminescence Measurements for the Reactions of Fluorine Atoms with I_2, ICl and Br_2 346
 11. Elastic Scattering of HF with Xe 348
 12. Close-Coupling Study of Halogen (2P) + Rare Gas (1S) Scattering 349

 - Research Plans for Calendar Year 1980 351
 - 1979 Publications and Reports 351

- i. Potential Energy Surfaces for Chemical Reactions
Henry F. Schaefer III, Investigator
 1. Conformational Preferences and Electronic Structures of $Ni(C_2H_4)_2$ and $Ni(C_2H_4)_3$ 354
 2. 1,1-Dilithioethylene: A Ground State Triplet Olefin with Nearly Free Rotation about the Double Bond 356
 3. The Gas Phase Structures of Transitional Metal Dihydrides 358
 4. Sulfur Oxide: Low-Lying Bound Molecular Electronic States of SO 359
 5. Potential Energy Hypersurface for the Prototype $M + HF$ Reaction: $Li + HF \rightarrow LiF + H$ 361

 - Research Plans for Calendar Year 1980 363
 - 1979 Publications and Reports 363

3. Atomic Physics
 - a. Low Energy Atomic Physics
H. A. Shugart, Investigator
 1. Observation of Parity Nonconservation in the $6^2P_{1/2} - 7^2P_{1/2}$ Transition in Atomic Thallium 365
 2. New Experiments in Parity Non-Conservation 365
 3. Fluorescence of Laser Excited Trapped Li^+ Metastable Ions 366
 4. Hysteresis in Swept Frequency Fluorescent Response 370

 - Research Plans for Calendar Year 1980 371
 - 1979 Publications and Reports 371

 - b. Atomic Physics
R. Marrus, Investigator
 1. Radiative Decay of the $2^2P_{3/2,1/2}$ States in Lithiumlike Krypton ($Z=36$) and the $2s2p^2^3P_1$ State in Berylliumlike Krypton 373
 2. Charge Changing Cross Sections for Heavy Ions at Energies to 8.5 MeV/amu 373

| | |
|---|-----|
| Research Plans for Calendar Year 1980 | 377 |
| 1979 Publications and Reports | 377 |
| B. Processes and Techniques | |
| 1. Chemical Energy | |
| a. Formation of Oxyacids of Sulfur from SO ₂ | |
| <i>Robert E. Connick, Investigator</i> | |
| 1. The Dimerization of HSO ₃ ⁻ | 378 |
| 2. Experiments to Distinguish Between H-SO ₃ ⁻ and SO ₃ -H ⁻ | 378 |
| Research Plans for Calendar Year 1980 | 378 |
| 1979 Publications and Reports | 379 |
| b. Conversion of Coal to Clean Liquid and Gaseous Fuels | |
| <i>A. T. Bell, G. A. Somorjai, and K. P. C. Vollhardt, Investigators</i> | |
| 1. Carbon Monoxide Hydrogenation Over Clean and Oxidized Rhodium Crystal Surface: Correlations of Structure, Composition and Reactivity | 380 |
| 2. High Resolution Electron Energy Loss Spectroscopy (HREELS) Study of CO ₂ Dissociation on Rhodium Surfaces | 380 |
| 3. The Catalyzed Surface Reactions of CO and NO on Rhodium Crystal Surfaces, and ELS Study | 380 |
| 4. Supported Ruthenium Cluster Complexes as Catalysts for Fischer-Tropsch Synthesis | 380 |
| 5. Hydrogenolysis of Ether Linkages in Coal-Related Model Compounds Catalyzed by Nickel and Nickel Sulfide in the Presence and Absence of Zinc Chloride. | 380 |
| 6. Coal Liquefaction Using a Zinc Chloride Catalyst | 383 |
| 7. Biscarbyne Clusters of Cobalt as Potential Homogeneous Analogs of Fischer- Tropsch Intermediates | 384 |
| 8. Transition Metal Activation of Carbon-Carbon Bonds | 387 |
| 9. Polystyrene Supported Homogeneous Catalysts | 388 |
| Research Plans for Calendar Year 1980 | 389 |
| 1979 Publications and Reports | 389 |
| c. Synthetic and Physical Chemistry | |
| <i>William L. Jolly, Investigator</i> | |
| 1. A Study of the Bonding in Transition Metal Carbonyl Hydrides | 393 |
| 2. An XPS Study of the Relative π-Acceptor Abilities of the Nitrosyl and Carbonyl Ligands | 394 |
| 3. A Study of Charge Transfer in Back-Bonding to Carbonyl and Nitrosyl Groups | 395 |
| Research Plans for Calendar Year 1980 | 397 |
| 1979 Publications and Reports | 397 |
| d. Electrochemical Systems | |
| <i>John Newman, Investigator</i> | |
| 1. Anomalous Diffusion Coefficients and Bipolar Electrodes | 399 |
| 2. The Effect of Coal Char on the Corrosion of 304 Stainless Steel | 400 |
| 3. Characteristics of the Dropping Mercury Electrode Below the Limiting Current | 400 |
| 4. The Short Time Solution for the Concentration Step at the Surface of a Rotating Disk | 401 |
| 5. The Warburg Impedance in the Presence of Convective Flow | 401 |
| Research Plans for Calendar Year 1980 | 401 |
| 1979 Publications and Reports | 401 |
| e. Metal Cluster--Metal Surface Analogy | |
| <i>Earl L. Muetterties, Investigator</i> | |
| 1. Chemical and Structural Features of Chemisorbed Species on Metallic Surfaces | 402 |
| Research Plans for Calendar Year 1980 | 402 |
| 1979 Publications and Reports | 402 |

| | | |
|----|--|-----|
| f. | High-Energy Oxidizers and Localized-Electron Solids <i>Neil Bartlett, Investigator</i> | |
| 1. | Novel Graphite Salts of High Oxidizing Potential | 404 |
| 2. | Composition and Staging in the Graphite/AsF ₆ System and Its Relationship To Graphite/AsF ₅ | 404 |
| 3. | EXAFS Studies of Arsenic Fluorides, and Graphite Intercalated by AsF ₅ and AsF ₆ ⁻ | 407 |
| 4. | Electron Oxidation of Benzene and Coronene | 408 |
| 5. | The Exploitation of KrF ₂ and Its Salts in the Preparation of BrF ₆ and ClF ₆ ⁺ Salts | 409 |
| | Research Plans for Calendar Year 1980 | 410 |
| | 1979 Publications and Reports | 411 |
| g. | Transition Metal Catalyzed Conversion of CO, NO, H ₂ and Organic Molecules to Fuels and Petrochemicals <i>Robert G. Bergman, Investigator</i> | |
| 1. | Mechanism of the Reaction Between Organotransition Metal Alkyls and Hydrides. A Model for the Aldehyde-Forming Step in the Oxo Process | 413 |
| 2. | Conversion of Metal Alkyls into Alkanes by Hydrogenation | 414 |
| 3. | Reaction of a Metal Alkyl with Ethylene as a Model for Ziegler-Natta Polymerization. Evidence for the Olefin Insertion Mechanism | 415 |
| 4. | Reaction of a Bridged Binuclear Dialkylcobalt Complex with CO and Phosphines. Observation of Competing Inter- and Intramolecular Methyl Transfer | 417 |
| 5. | Reversible Metal-to-Metal Methyl Transfer in η ⁵ -Cyclopentadienyl- (Trimethylphosphine)Dimethylcobalt(III) | 419 |
| | Research Plans for Calendar Year 1980 | 422 |
| | 1979 Publications and Reports | 422 |
| 2. | Chemical Engineering Sciences | |
| a. | High-Pressure Phase Equilibria in Hydrocarbon-Water (Brine) Systems <i>John M. Prausnitz, Investigator</i> | |
| 1. | High-Pressure Phase Equilibria for Methane-Water (Brine) | 424 |
| 2. | Modifications of Generalized Van Der Waals Theory for Mixtures | 425 |
| 3. | Liquid-Liquid Phase Equilibria for Heavy Hydrocarbon-Water Systems | 425 |
| | Research Plans for Calendar Year 1980 | 426 |
| | 1979 Publications and Reports | 426 |

III. NUCLEAR SCIENCES

A. Low Energy Nuclear Sciences

1. Heavy Element Chemistry

a. Actinide Chemistry

*Norman M. Edelstein, Richard A. Andersen, Neil Bartlett, John G. Conway,
Kenneth Raymond, Glenn T. Seaborg, Andrew Streitwieser, Jr., David H. Templeton,
and Allan Zalkin, Investigators*

Specific Sequestering Agents for the Actinides

| | | |
|----|--|-----|
| 1. | Removal of ²³⁸ Pu(IV) from Mice by Sulfonated Tetrameric Catechoyl Amides | 431 |
| 2. | Crystal and Molecular Structures of Tetrakis (Catecholato)-Hafnate(IV) and -Cerate(IV). Further Evidence for a Ligand Field Effect in the Structure of Tetrakis(Catecholato)-Uranate(IV) | 435 |
| 3. | Free Metal and Free Ligand Concentrations Determined from Titrations Using Only a pH Electrode. Partial Derivatives in Equilibrium Studies | 437 |
| 4. | Stability Constants for Catechol Models of Enterobactin | 438 |

Synthetic and Structural Studies of Actinides and Other Compounds

| | | |
|----|---|-----|
| 1. | Cyclooctatetraeneactinide (IV) Bis-Borohydrides | 440 |
| 2. | Structure of Two Crystalline Forms of Cyclooctatetraenethorium(IV) Dichloride Bistetrahydrofuran | 440 |
| 3. | Hydrido[Tris(Hexamethyldisilylamido)]-Thorium(IV) and -Uranium(IV) | 442 |
| 4. | Hydrogen-Deuterium Exchange: Perdeutero-Hydrido-Tris(Hexamethyldisilyl) Amido-Thorium(IV) and -Uranium(IV) | 443 |
| 5. | Structure and Bonding of f- and d- Transition Metal Organometallic Compounds | 445 |

| | | |
|-----|---|-----|
| 6. | Towards the Synthesis of Heptavalent Neptunium Fluorides and Oxyfluorides | 447 |
| 7. | Structure of Tris(Urea)Dioxouranium(VI) Sulfate, $UO_2(OC(NH_2)_2)_3 SO_4$ | 448 |
| 8. | A Structure of Di- μ -Aquo-Bis(Dioxodinitrato-Uranium(VI))Dimidazole, [$UO_2(NO_3)_2 \cdot H_2O \cdot C_3H_4N_2$] $_2$, A Water-Bridged Dimer of Uranyl Nitrate | 449 |
| 9. | Imidazolium Tetrachlorodioxouranium(VI), [$C_3N_2H_5^+$] $_2 [UO_2Cl_4]^{-2}$ | 450 |
| 10. | Crystal and Molecular Structures of Decamethylmanganocene and Decamethyl- ferrocene. Static Jahn-Teller Distortion in a Metallocene | 451 |
| 11. | Anomalous Scattering by Cobalt and Chlorine of (+)-Tris(Ethylenediamine) Cobalt(III) Chloride (+)-Tartrate Pentahydrate and Its Crystal Structure | 453 |
| 12. | L $_3$ -Edge Anomalous Scattering of X-Rays by Praseodymium and Samarium | 454 |
| 13. | Polarized X-Ray Absorption and Double Refraction in Vanadyl Bisacetylacetonate | 455 |

Physical and Spectroscopic Studies

| | | |
|----|---|-----|
| 1. | NMR Studies of Uranocenes | 457 |
| 2. | Cyclic Voltammetry Studies of Substituted Cyclooctatetraenes | 460 |
| 3. | Synthesis and Characterization of Pa(IV), Np(IV), and Pu(IV) Borohydrides | 461 |
| 4. | Energy Level Analysis of $Np^{3+}:LaCl_3$ and $Np^{3+}:LaBr_3$ | 462 |
| 5. | A Quasi-Relativistic SCF X- α Study of Octahedral $5f^1$ Complexes | 465 |
| 6. | Identification of U $_{III}$ and U $_{IV}$ Lines | 468 |
| | Research Plans for Calendar Year 1980 | 469 |
| | 1979 Publications and Reports | 470 |

IV. FOSSIL ENERGY

a. Electrode Surface Chemistry

Phillip N. Ross, Investigator

| | | |
|----|---|-----|
| 1. | Structure Sensitivity in the Electrosorption of Hydrogen on Platinum | 475 |
| 2. | The Effect of Pt Structure and Carbon Chemistry on the Electrocatalytic Properties of Pt Supported on Carbon | 477 |
| | Research Plans for Calendar Year 1980 | 479 |
| | 1979 Publications and Reports | 479 |

b. Deuterium Analysis of Coal by NMR

A. Pines, Investigator

| | | |
|----|--|-----|
| 1. | Carbon-13 Analysis of Whole and Processed Coals | 480 |
| 2. | Double Quantum Powder Lineshapes | 480 |
| 3. | High Resolution Deuterium NMR by Magic Angle Sample Spinning | 481 |
| 4. | Double Quantum NMR in Rotating Samples | 481 |
| 5. | NMR Deuterium Cross-Polarization in Rotating Samples | 482 |
| 6. | Spin Diffusion and Relaxation in Magic Angle NMR | 482 |
| 7. | Synthesis of Deuterium Labeled Materials | 483 |
| 8. | High Field NMR Spectrometer | 483 |
| | Research Plans for Calendar Year 1980 | 483 |
| | 1979 Publications and Reports | 484 |

c. Coal Liquefaction Alloys Test Program

Alan V. Levy, Investigator

| | | |
|----|---|-----|
| 1. | Erosion Behavior of Metals in Coal Slurries | 486 |
| 2. | Erosion of Piping in a Slurry Loop | 487 |
| | Research Plans for Calendar Year 1980 | 488 |
| | 1979 Publications and Reports | 488 |

d. Oil Shale Retort Components

A. Levy and D. Whittle, Investigators

| | | |
|----|--|-----|
| 1. | Corrosion in Simulated In-Situ Oil Shale Retorts | 489 |
| | Research Plans for Calendar Year 1980 | 490 |
| | 1979 Publications and Reports | 490 |

| | |
|---|-----|
| e. Chemistry and Morphology of Coal Liquefaction <i>H. Heinemann, Investigator</i> | |
| 1. Generation and Chemistry of 1,4-Dehydrobenzene: Hydrogen Transfer to Reactive Aromatic Free Radical Sites | 491 |
| 2. Thermal Reactions of Tetralin: A Model for Hydrogen Transfer Processes Occurring During Coal Pyrolysis and Liquefaction | 492 |
| Research Plans for Calendar Year 1980 | 494 |

V. ADVANCED ISOTOPE SEPARATION TECHNOLOGY

| | |
|---|-----|
| a. Laser Isotope Separation <i>C. Bradley Moore, Investigator</i> | |
| 1. 3.3 μm Multiphoton Dissociation | 497 |
| 2. Single Rotational Level Lifetime of S_1 Formaldehyde: Electric Field Effects . . . | 498 |
| Research Plans for Calendar Year 1980 | 499 |
| 1979 Publications and Reports | 500 |
| b. Molecular Beam Laser Isotope Separation <i>Y. T. Lee and Y. R. Shen, Investigator</i> | |
| 1. Identification of Primary Products in Multiphoton Dissociation of CF_3CDCl_2 | 501 |
| 2. Molecular Elimination of Cl_2 in Multiphoton Dissociation of CF_2Cl_2 | 502 |
| 3. Competing Dissociation Channels in Multiphoton Dissociation of Ethyl Vinyl Ether | 504 |
| 4. Vibrational Predissociation Spectra of HF and Mixed HF-DF Clusters | 505 |
| Research Plans for Calendar Year 1980 | 506 |
| 1979 Publications and Reports | 507 |

VI. ENERGY STORAGE

| | |
|---|-----|
| a. Development of Electrochemical Synthesis and Energy Storage <i>James W. Evans, Rolf H. Muller, John Newman, Phillip N. Ross, and Charles W. Tobias, Investigators</i> | |
| Surface Morphology of Metals in Electrodeposition | |
| 1. Dynamic Modeling of Surface Profiles in Electrodeposition and Dissolution | 511 |
| Anodic Surface Layers on Battery Materials | |
| 1. Ellipsometry of Sulfate Films on Lead | 513 |
| Metal Couples in Non-Aqueous Solvents | |
| 1. Studies on the Electrochemical Behavior of Potassium in Propylene Carbonate. . . . | 515 |
| Analysis and Simulation of Electrochemical Systems | |
| 1. Mathematical Modeling of the Lithium/Iron Sulfide Battery | 516 |
| 2. Silicon Deposition on a Rotating Disk | 518 |
| 3. A Comparison Between Flow-Through and Flow-By Porous Electrodes for Redox Energy Storage | 518 |
| 4. Experimental Determination of Cupric Ion Diffusivities in $\text{CuSO}_4/\text{H}_2\text{SO}_4/\text{C}_3\text{H}_5(\text{OH})_3$ Solutions | 518 |
| Improvements in Efficiency of Aluminum Reduction Cells | |
| 1. Calculated Current Efficiencies for 185kA Aluminum Cells with Alternative Bus-Bar Arrangements | 518 |
| Engineering Analysis of Gas Evolution in Electrolysis | |
| 1. Gas Evolution in Forced Flow | 519 |

| | |
|---|-----|
| Research Plans for Calendar Year 1980 | 520 |
| 1979 Publications and Reports | 522 |

VII. OTHER PROJECTS

| | |
|--|-----|
| a. Solution Thermodynamics of Sulfites and Sulfite Oxidation Mechanisms <i>Leo Brewer and Robert Connick, Investigators</i> | |
| 1. Thermodynamic Properties of Multicomponent Aqueous Solutions of Alkali and Alkaline Earth Sulfites, Sulfates, and Halides | 527 |
| 2. Thermodynamic Properties of Solid Phases of the $\text{CaSO}_3\text{-CaSO}_4\text{-H}_2\text{O}$ System | 527 |
| 3. The Kinetics of Oxidation of Bisulfite Ion by Oxygen | 527 |
| Research Plans for Calendar Year 1980 | 528 |
| 1979 Publications and Reports | 528 |
| b. Process Chemical Parameters in Aqueous Sulfur Dioxide Removal by Lime/Limestone Scrubbers <i>Beat Meyer and Robert E. Connick, Investigators</i> | |
| 1. The Reaction of Ammonia with Sulfur Dioxide | 529 |
| 2. Raman Spectrometric Determinations of Aqueous Sulfur Oxyanion | 529 |
| 3. Chemistry of Aqueous Oxyacids of Sulfur | 529 |
| 4. Chemistry of Waste Sulfur Utilization | 530 |
| Research Plans for Calendar Year 1980 | 530 |
| 1979 Publications and Reports | 530 |
| c. Coal Liquefaction Research <i>Heinz Heinemann, Investigator</i> | |
| 1. Catalytic Cracking of n-Hexadecane | 532 |
| 2. Fixed Bed and Suspension Bed Fischer-Tropsch Reaction | 533 |
| Research Plans for Calendar Year 1980 | 533 |
| 1979 Publications and Reports | 533 |
| d. Thermodynamic Properties of Chemical Species in Nuclear Waste <i>N. Edelstein, S. D. Brown, and R. J. Silva, Investigators</i> | |
| 1. Theoretical Studies of Metal Complexation at Stationary Electrodes | 534 |
| 2. Evaluation of Metal Complexation Kinetics and Thermodynamics at the Hanging Mercury Drop Electrode | 535 |
| Research Plans for Calendar Year 1980 | 536 |
| 1979 Publications and Reports | 536 |
| e. High Strength Austenitic Alloys for Generator Retaining Rings <i>J. W. Morris, Jr. and G. Thomas, Investigators</i> | |
| 1. Precipitations Hardening in Fe-Ni Base Austenitic Alloys | 537 |
| Research Plans for Calendar Year 1980 | 537 |
| 1979 Publications and Reports | 537 |
| f. Oxygen Reduction in Concentrated Phosphoric Acid by Carbon-Supported Pt Alloy Electrocatalysts <i>Phillip N. Ross, Investigator</i> | |
| 1. Oxygen Reduction in Concentrated Phosphoric Acid by Carbon-Supported Pt Alloy Catalysts | 539 |
| Research Plans for Calendar Year 1980 | 540 |
| g. Substructure and Properties of Sodium Beta Alumina Solid Electrolytes <i>L. C. De Jonghe, Investigator</i> | |
| 1. Breakdown Studies | 541 |
| 2. Local Electrode Current Densities | 542 |
| Research Plans for Calendar Year 1980 | 543 |
| 1979 Publications and Reports | 543 |

VIII. APPENDICES

 A. MMRD Staff 1979 547

 B. List of Seminars 556

GENERAL INTRODUCTION

Calendar year 1979 was another good year for the Materials and Molecular Research Division, characterized by further consolidation of programs, some program growth, and intensive planning for the future Chemical and Materials Science Laboratory Building Project. At the end of 1979 there were affiliated with MMRD 37 faculty senior scientists, 8 staff senior scientists, 12 associated faculty, 35 staff scientists, 112 postdoctorals and other scientific personnel, 334 graduate students, and 120 technical, administrative, and clerical support staff for a total of 658. At this writing (February, 1980) the FY 1980 operating budget of MMRD is \$13 million. This represents an increase of \$2 million from a FY 1979 base of \$11 million. It is notable that half of this increase is in the Basic Energy Sciences, which went up from \$9 million to \$10 million, while the other half is in Energy Technology areas both within and outside the DOE, which increased from \$1.6 million to \$2.7 million. All in all, a total of 12 new programs have been added, at a total operating level of \$1.4 million. It is particularly gratifying that, for the first time, our Fossil Energy program exceeds \$1 million in operating funds. During calendar 1979, 201 journal articles were published by members of MMRD, and 46 Ph.D and 13 M.S. degrees were awarded to MMRD students.

Three new MMRD activities can be singled out for special comment. Their unifying theme is their building on expertise already available in MMRD to establish a program for which the whole exceeds the sum of the parts. Each of these activities thereby brings to bear in areas of energy technological relevance the skills of outstanding investigators, including graduate students, who are affiliated with MMRD. In these activities we have thereby been able to combine the organizational infrastructure often found in national laboratories with the intellectual firepower of an outstanding graduate university. The three activities are:

- *The Chemical and Materials Sciences Laboratory.* This project has at last been funded in FY 1980. It will culminate in the construction of a laboratory building adjacent to Building 62 and comparable in size. This building will be specially equipped with several state-of-the-art instruments for research in surface science and catalysis. It will also house laboratories and instrumentation for the Atomic Resolution Microscope facility, while the microscope itself will be installed in a tower adjacent to Building 72.
- *Coal Chemistry and Morphology.* This program is jointly sponsored by the Department of Energy's Fossil Energy Division and the Chemical Sciences Division of Basic Energy Sciences under the principal investigatorship of Heinz Heinemann. A number of components of this

program are directed by MMRD investigators, including Robert Bergman, Peter Vollhardt, Alan Levy, Gabor Somorjai, James Evans, and Alex Bell. This program represents a new approach in that it involves collaboration between basic and applied sponsoring offices in DOE. It could serve as a prototype for other programs in which the talents of basic researchers are focused on problems of specific interest in energy technologies.

- *Development of Electrochemical Synthesis and Energy Storage.* This program, funded by DOE's Division of Energy Storage Systems, includes investigators from LBL's Energy and Environment Division as well as MMRD. Investigators involved in it include Charles Tobias, Rolf Muller, John Newman, James Evans, Lutgard De Jonghe, and Philip Ross; De Jonghe and Ross also play administrative roles in the program. In addition to research at LBL, this program monitors projects in a number of other institutions. Professor Elton Cairns, who is an electrochemist in addition to being head of the Energy and Environment Division, is in charge of this program.

There have been several changes at the principal investigator level. John H. Clark joined MMRD in the Fall of 1979. John (a student of C. B. Moore) received his Ph.D. at Berkeley and spent two years at Los Alamos as an Oppenheimer Fellow. He will initiate a research program in picosecond laser chemistry. Professor Moshe Rosen is visiting MMRD from Israel. He is directing the superconducting program formerly directed by Milton Pickus.

Finally, I must report with great regret the death of Professor Mitchel Shen on August 7, 1979. Professor Shen had just joined MMRD and initiated a very promising program in polymer synthesis. His death is a great loss to the University.

Two conferences were organized by MMRD scientists in 1979:

- The conference on Corrosion/Erosion of Coal Conversion Materials was held January 24-26, 1979 at the Marina Marriott Inn, in Berkeley. It was organized by Mr. Alan Levy, and co-sponsored by MMRD together with the National Association of Corrosion Engineers.
- The Fourth International Conference on Ellipsometry was held in the Building 50 Auditorium August 20-22, 1979. It was organized by Dr. Rolf Muller and sponsored jointly by MMRD and the Army Research Office.

Our Annual Program Review was held on February 11 and 12, 1980. The Review Committee, J. S. Waugh, Massachusetts Institute of Technology (Chairman); R. L. Coble, Massachusetts Institute of Technology;

M. E. Fine, Northwestern University; S. Liu, Iowa State University; J. Wiedersich, Argonne National Laboratory; and J. T. Yates, Jr., National Bureau of Standards, attended the presentation sessions, reviewed the draft Annual Report contributions in this publication, talked with our investigators and observed their posters displayed in Building 62.

As always, a substantial number of honors and awards befell MMRD scientists in 1979. A selected list appears below:

- *Neil Bartlett* was elected to the National Academy of Sciences, as a Foreign Associate. He is one of three MMRD chemists elected to the Academy in 1979, which is probably a record for elections to a single institution. A total of only five chemists were elected nationally.
- *Leo Brewer* was elected to the Academy of Arts and Sciences.
- *Eugene Commins* received the 1979 Distinguished Teaching Award of the Academic Senate Committee on Teaching, sponsored by the California Alumni Associated.
- *Anthony G. Evans* won the first Richard M. Fulrath Award.
- *Charles B. Harris* was elected a Fellow of the American Physical Society.
- *Yuan T. Lee* was elected to the National Academy of Sciences, the second MMRD chemist on this list to be so honored.
- *C. B. Moore* presented the introductory lecture to the Faraday Discussion of the Chemical Society No. 67.
- *Sheree Hsiao Ru Chen* in Professor J. W. Morris's group has been announced as the 1980 winner of the Robert L. Hardy Gold Medal of the American Institute of Metallurgical and Mining Engineers given to "a young metallurgist of outstanding promise."
- *Donald Olander* was appointed Chairman of the Department of Nuclear Engineering.
- *Joseph Pask* was awarded the 1979 Gold Metal and Certificate of the Société d'Encouragement pour la Recherche et l'Invention of the French Academy of Sciences.
- *John Conway* was selected as the 1980 recipient of the William F. Meggers Award by the Optical Society of America.
- *Earl Muetterties* was awarded a Miller Research Professorship for the academic year 1980-81.
- *Glenn T. Seaborg*, who has already received a very wide range of awards, had two awards established in his name in 1979: one by the International Platform Association, entitled the Glenn T. Seaborg Award, and one by the Alpha Chi Sigma Chapter at UCLA, entitled the Glenn T. Seaborg Research Award.

- *David Shirley* was awarded a Miller Research Professorship for the academic year 1980-81.
- *Gabor Somorjai* was elected to the National Academy of Sciences, the third MMRD chemist on this list to be so honored.
- *Gareth Thomas* was elected a Fellow of The Metal Society, American Institute of Metallurgical and Mining Engineers. He also received a first prize in the 1979 American Society for Metals Metallographic Exhibit.

Once more many scientific achievements were reported by MMRD investigators in 1979. A somewhat eclectic list is given below, abstracted from among the many accomplishments that could equally well have been listed:

- *Neil Bartlett* and coworkers have synthesized conducting graphite salts intercalated with germanium fluoride. These salts have the formulae $C_{12}GeF_5$ and $C_{12}GeF_6$. They exist in equilibrium with gaseous fluorine, thereby providing the possibility of constructing an electrolytic cell with a potential of 5 volts when combined with an alkali metal half cell. These salts also provide a convenient means for storing gaseous fluorine.
- *John Clarke* and coworkers have conducted a magnetotelluric survey of a geothermal field at Cerro Prieto in Mexico. They found a high resistance region coinciding with a source of geothermal activity, bringing one step closer the possibility of prospecting with superconducting quantum interference devices.
- *Kenneth Raymond* and coworkers have synthesized sequestering agents for tetravalent actinide ions which show efficiencies in biological testing ten times as great as those of sequestering agents in present clinical use.
- *David Templeton* and coworkers have observed very large anomalous scattering effects which can be used for the study of complicated crystal structures, by studying crystals containing rare earth elements with synchrotron radiation.
- *Anthony Evans* has constructed a quantitative framework for predicting creep deformations and creep failure, using combined experimental and theoretical studies. This development should lead to the evolution of more failure-resistant ceramics.
- *Yuan Lee* has reported the first experimental observation of a quantum-mechanical dynamic resonance in an elementary chemical reaction. This effect, based on a Feshbach resonance, has been predicted theoretically but never before experimentally observed. Lee and coworkers observed the resonance in reactions of atomic fluorine with molecular hydrogen to form HF and atomic hydrogen.

This is the last Introduction that I shall write as Head of MMRD, a post which I have resigned effec-

tive June 30, 1980. It has been a pleasant duty (though at times a demanding one) to serve as Head of a Division possessing such an outstanding research staff, and to participate in a vicarious way in their scientific successes. It is a pleasure to acknowledge the assistance and support that I have received from all of my fellow investigators including Assistant Division Head Rolf Muller, Gabor Somorjai, Chairman of the Divisional Council which also served as the Divisional Staff Committee, all the members of this Council and the Chairman and members of the many other administrative committees in MMRD. I am particularly indebted to two individuals. Mr. Conway Peterson, Division Administrator, who with the help of his competent and diligent staff has effectively converted the position of Division Head from a potentially onerous and draining job to one in which the incumbent can not only have time to address the big issues facing a scientific division but can actually retain some personal scientific vitality. Dr. Andrew M. Sessler, Director of Lawrence Berkeley Laboratory, has been the ideal boss. He has been supportive in times of trouble and interactive and creative when opportunities

arose to build and strengthen MMRD. It has been a great pleasure to work with these two men and they are in no small measure responsible for the successes that have come to MMRD in the period 1975-1980.

Looking back, MMRD has evolved steadily, though not spectacularly, from a very strong base in IMRD and Nuclear Chemistry. Some fairly serious problems have been solved, staff has been strengthened, and several large interactive programs have been put into place. Looking forward, there are still some unsolved problems (though I hope no large ones), but they are certainly overshadowed by very strong staff and almost limitless opportunities. Having used my own creative energies to help develop MMRD over the last five years, I shall enjoy stepping aside and watching the new ideas and developments that will be brought in by the next Division Head. I have served with pleasure and I look forward to participating in the Division's future activities.

David A. Shirley
Division Head

I

Materials Sciences

A. Metallurgy and Ceramics

1. Structure of Materials

a. Microstructure, Properties and Alloy Design: Inorganic Materials*

Gareth Thomas, Investigator

Alloy Design: Medium Carbon Steels, "Qua-Tough Alloys"

Introduction. This continuing program on controlling combinations of high strength and good toughness has concentrated on optimizing the dislocated lath and stable interlath austenite duplex microstructures by controlling composition, heat treatment and melting practice. Because of considerable interest from the mining industries, the wear and corrosion aspects of these steels are now under investigation and the results are extremely promising, suggesting that stable retained austenite is also a significant factor in these properties. With the addition of a new analytical electron microscope, the problem of austenite stability can now be examined in more detail. Summaries of specific projects follow.

1. OPTIMIZATION OF Fe/Cr/C BASE STEELS FOR IMPROVED MECHANICAL PROPERTIES (FOR STRUCTURAL APPLICATIONS)[†]

M. Sarikaya, B. G. Steinberg, T. H. Rabe, and B. V. N. Rao[‡]

The effects of alloying and heat treatments on the microstructural changes and strength toughness properties were investigated in optimization of vacuum-melted Fe/Cr/C base steels. The structure of the steels in the as-quenched conditions consisted of the desired mixture of highly dislocated auto-tempered lath martensite (strong phase) and thin continuous films of retained austenite as has been shown previously. It is re-emphasized that the mechanical properties of the steels are sensitive to the amount distribution and stability of the retained austenite. To increase the stability of retained austenite in the as-quenched condition, 2 wt.% Mn or 2 wt.% Ni additions are made to the base steel, viz., Fe/3Cr/0.3C. Partial replacement of Cr by 0.5 wt.% Mo did not alter the beneficial microstructure, but these values of Mo addition had no influence on tempered martensite embrittlement (TME).¹

The steels were subjected to both conventional and non-conventional heat treatments (Fig. 1). With the latter, even in the as-quenched condition the steels had attractive mechanical properties (Fig. 2). Double heat treatments, designed for

* This work was supported by the Division of Materials Sciences, Office of Basic Energy Sciences, U. S. Department of Energy.

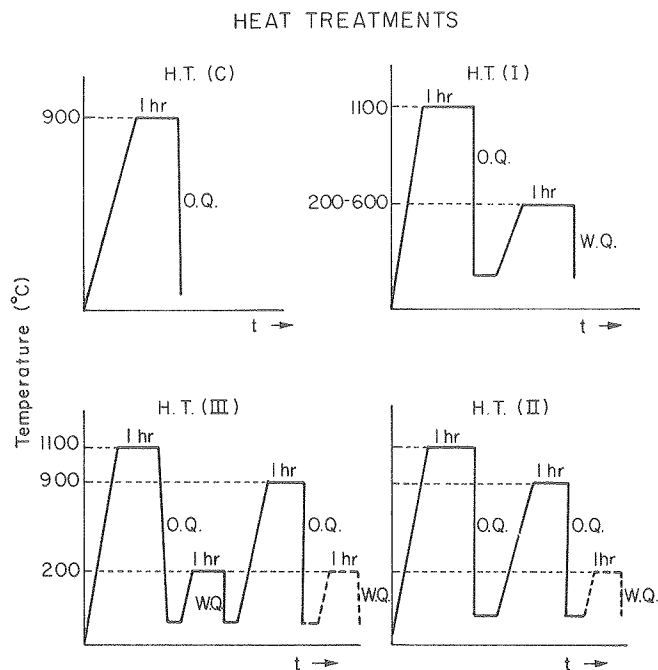


Fig. 1. Schematic illustration of the heat treatments employed. (XBL 7811-6085)

combining the benefits of high temperature austenitization with fine grain size, produced better properties. Heat treatment III, double heat treatment with intermediate tempering to obtain fine, uniform austenite grain sizes, yielded the best combination of strength and toughness (Fig. 2). Improvements in the toughness properties were attained without deteriorating the strength values by tempering at 200°C. Sudden decreases in the toughness values upon higher temperature tempering were attributed to temper martensite embrittlement (TME). The present alloys were found to have mechanical properties superior to many commercially available more complex structural steels.

Economical air-melting practice was applied to investigate the effects on structure and mechanical properties of these experimentally designed steels. Although tensile properties are not affected by the melting practice, air-melting lowers the toughness properties, especially in 2Ni containing alloys (see Fig. 3). These can be accounted for by a much higher volume fraction of second-phase inclusions (sulfides, oxides, nitrides, etc.) in the 2Ni alloy compared to the 2Mn alloy. In addition, as shown in the fractograph in Fig. 4, unique rib-like coalescence of voids is observed in the

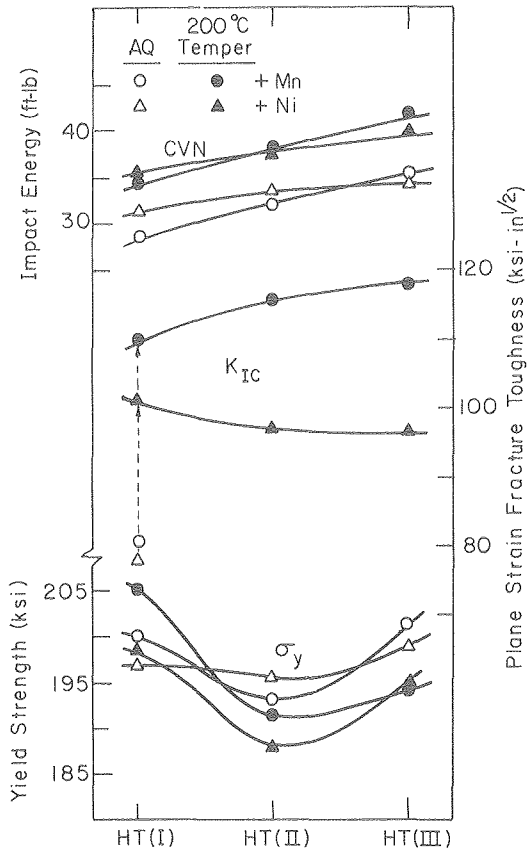


Fig. 2. Plot of strength, impact toughness, and fracture toughness variations with heat-treatment employed (refer to Fig. 1) in 2Mn and 2Ni quaternary alloys (refer to Fig. 3 for alloy compositions).
(XBL 794-6150)

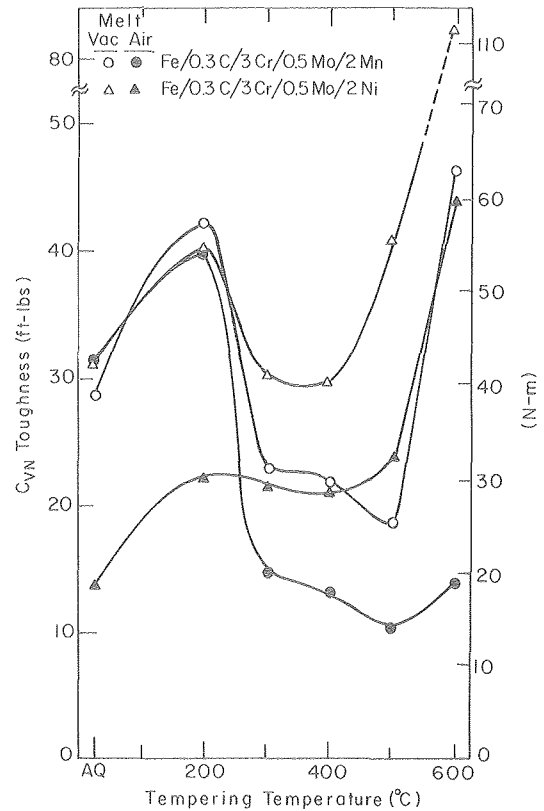


Fig. 3. Plot of impact toughness vs. tempering temperature after H.T. (I).
(XBL 793-5965)

2Ni alloy. The quaternary Fe/4Cr/2Mn/0.3 alloy has already been shown² to have excellent combinations of strength and toughness. It has also very high hardenability. Hence, another part of the objective of this investigation was to understand the behavior of this alloy upon different temperature austenitization and air-cooling (economical heat treatments). Low toughness properties resulted after slow cooling. The properties of conventionally heat-treated (900°C) specimens are somewhat better than the high temperature austenitized specimens. By high temperature austenitizing (1100°C), carbides and inclusions are taken into the solution. However, low temperature austenitization reduces the austenite grain size and modifies the segregation effect by tying up the segregating species in pre-existing inclusions. Therefore, an intermediate temperature (1050°C) can be chosen for austenitization. After slow cooling, various undesirable features appear in the microstructure: upper or lower bainite with large carbides, discontinuous retained austenite at the lath boundaries, microstructural twins, and inclusions, as well as auto-tempered martensite laths, (see Fig. 5).

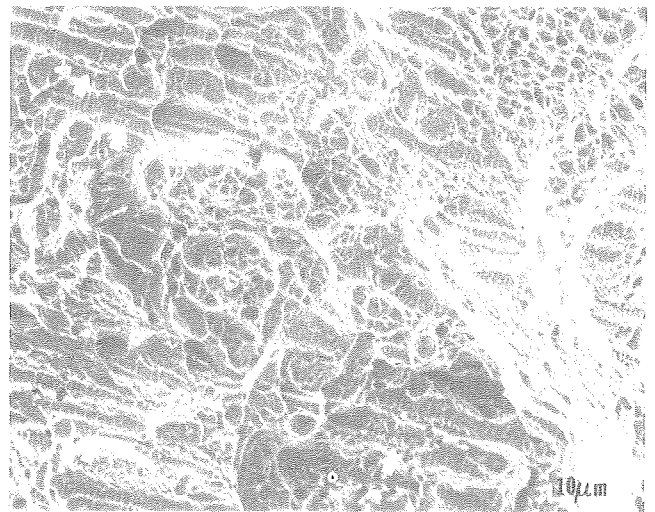


Fig. 4. Example of rib-like fracture (arrows) in 2Ni alloy as seen in a 300°C tempered CVN sample.
(XBB 793-3308)

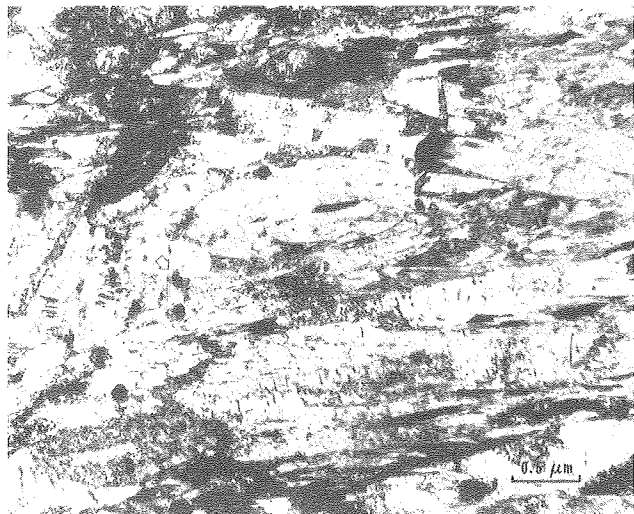


Fig. 5. BF micrograph showing dislocated auto-tempered martensite, upper and lower bainite with large spherical carbides in 1100°C heat-treated specimen. Also note microstructural twins (indicated by an arrow). (XBB 795-6578)

* * *

[†]Brief version of the following reports: LBL-9260, LBL-9103, and LBL-9262.

[‡]Permanent address: Analytical Chemistry Department, Research Laboratory, General Motors Technical Center, Warren, MI 48090.

1. G. Thomas, Met. Trans. 9A, 331 (1978).
2. B.V.N. Rao and G. Thomas, Met. Trans., in press, LBL-8064.

Low Carbon Dual Phase Steels

Introduction. This program is concerned with the effects of composition and heat treatment on the strength, fracture and corrosion resistance of simple low carbon steels. Although the initial motivation for this program came from the need to improve strong steels with high formability for automobile manufacture, to attain fuel savings (and which has been successful, e.g. the patented Fe/Si/C steels),¹ the potential for dual phase steels in structural applications is very broad indeed, e.g. a new joint program has been initiated with Sandia for geothermal applications.

The current program is concerned with the following effects on tensile and fracture properties:

1. Role of dual phase morphology and transformation path on microstructure-property relations.
2. Effect of cooling rates from the ($\alpha + \gamma$) phase field.
3. Effect of small amounts of alloying elements, e.g., boron on hardenability, and carbide formers, e.g. Mo, V on strength and ductility.
4. Grain size effects - especially to improve ductility at low temperatures.

5. Mechanistic understanding behind the empirical "law of mixtures" behavior.

6. New programs on wear and fatigue (corrosion properties already being obtained by cooperation with Battelle N.W. and Sandia). Summaries of current work follow.

* * *

1. J. Y. Koo and G. Thomas, Met. Trans. 8A, 525 (1977), US Patent #4,067,956.

1. METALLURGICAL FACTORS CONTROLLING IMPACT PROPERTIES OF DUAL-PHASE (DP) STEELS[†]

J. Y. Koo[‡] and G. Thomas

Impact properties have been investigated for the alloys in Table 1.

Table 1. Alloy compositions (wt.%)

| Alloy number | C | Cr | Si | Fe |
|--------------|------|-----|-----|------|
| 1 | 0.06 | 0.5 | - | Bal. |
| 2 | 0.07 | - | 0.5 | Bal. |
| 3 | 0.07 | - | 2.0 | Bal. |

Marked differences are developed in the morphology of the DP structures depending on the amount and type of alloying element X present in the Fe/X/0.1C ternary system. These are illustrated in the optical micrographs, Figs. 1 and 2. As can be seen in Fig. 1, martensite particles occur in a continuous network along the prior austenite grain boundaries with an acicular morphology in the interior of the prior austenite grains. In sharp contrast, a discontinuous, fibrous morphology was developed in the 2% Si-containing DP steel, Fig. 2.

The results of impact test data are plotted in Figs. 3 through 5. Figure 3 shows the impact energy curves of the 0.5Cr DP steels with two different volume fractions of martensite. The curve with 35% volume fraction of martensite does not exhibit a definite DBTT, while the one with 90% martensite volume fraction apparently does. The similar variations of DBTT with volume percent martensite in Si-containing DP steels are illustrated in Fig. 4. The apparent DBTT was lowered by increasing volume percent martensite from 30 to 60% in the case of the 0.5% Si DP alloy, whereas the 2% Si steel (alloy #3) showed no apparent DBTT and no significant difference in the impact energy as the volume percent martensite was varied.

Figure 5 compares the impact energy curves of the DP alloys 1 and 3, both having 35% martensite volume fraction.

The fracture surface of all the broken subsize CVN impact specimens, regardless of alloy composi-



Fig. 1. Optical micrograph of DP structure developed in alloy 1 (Fe/0.5Cr/0.06C). (XBB 778-7550)

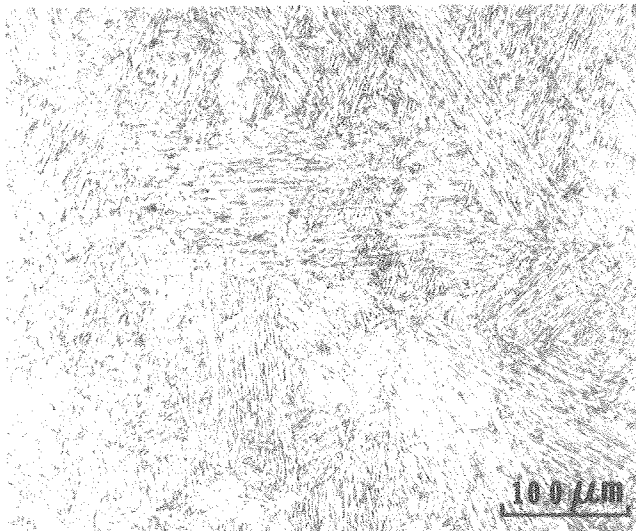


Fig. 2. Optical micrograph of DP structure developed in alloy 3 (Fe/2Si/0.07C). (XBB 798-10688)

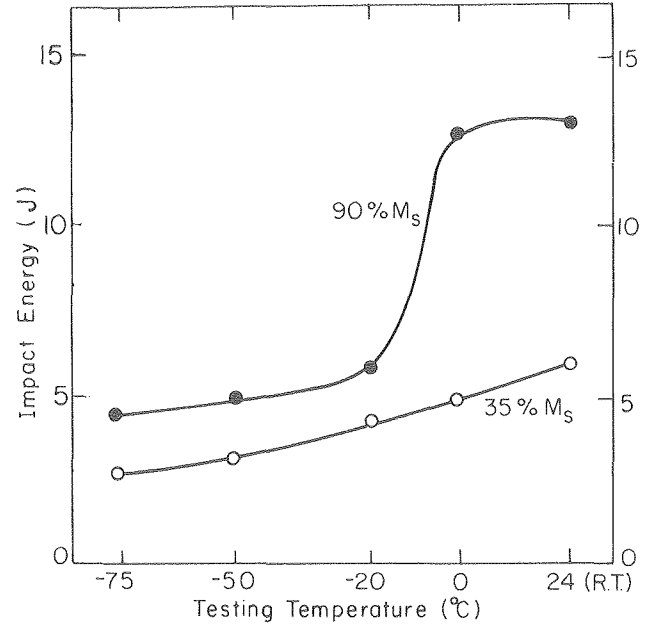


Fig. 3. Three-fourth subsize CVN impact energy as a function of testing temperature for DP alloy 1 containing 35% and 90% martensite volume fraction. (XBL 798-6737)

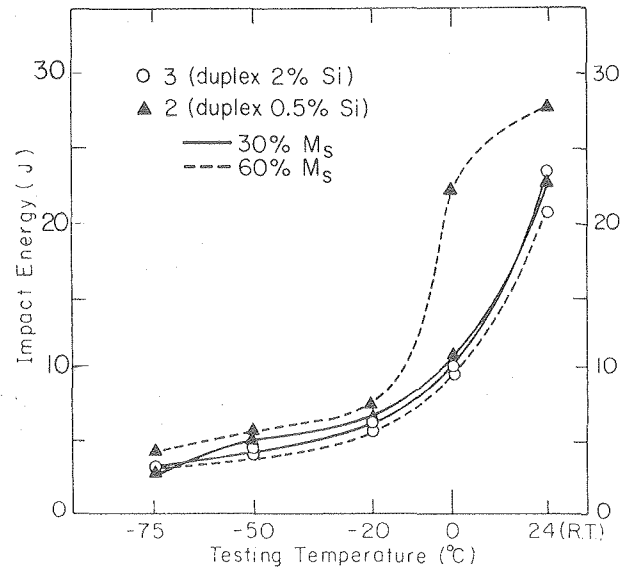


Fig. 4. Three-fourth subsize CVN impact energy vs. tempering temperature for the DP alloys 2 and 3 containing 30% and 60% martensite volume fraction. (XBL 798-6738)

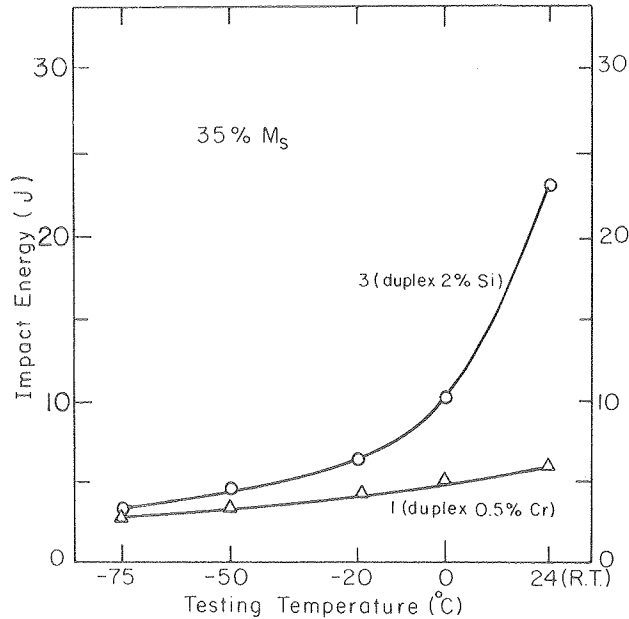


Fig. 5. Comparison of 3/4 subsize Charpy impact properties of the DP alloys 1 and 3, each having 35% martensite. (XBL 798-6739)

tion and martensite volume fractions, exhibited mainly quasi-cleavage-like morphology, Fig. 6, with a small quantity of ductile rupture the proportion of which depended on the testing temperature and the relative amount of each constituent phase in the DP steels. The mode of fracture changed significantly with the size of the impact specimen. Isolated experiments showed that when standard specimens were used, a large proportion of dimpled rupture features were associated with the fracture appearance.

From Figs. 1-5, one notes that the impact properties of the DP steels are strongly affected by the three major structural factors: morphology (shape, size and distribution) of DFM structure, volume fraction of martensite, and toughness (carbon content) of the martensite particles. The last two factors are correlated to each other since the carbon content is a linear function of the volume fraction of martensite.

As the volume fraction decreases, it is expected:

- (1) The connectivity of martensite will decrease, thus resulting in better impact properties.
- (2) Concurrently, toughness of the martensite will decrease due to increased carbon enrichment, thereby decreasing impact properties, since the carbon level has a drastic effect on reducing notched impact energy and DBTT.

Therefore, for a given morphology of DFM structures the observed effect of volume fraction on the impact properties will be determined by the balance between the two opposing factors.

For the 0.5Cr DP structure tested up to room temperature, the energy curve with higher volume

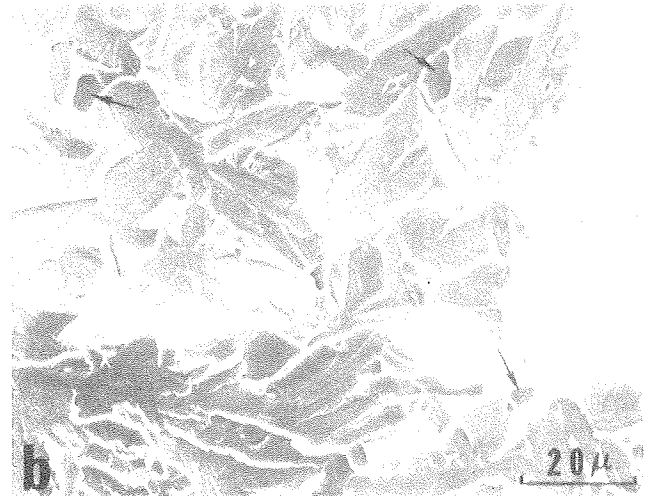


Fig. 6. Scanning electron fractographs of broken subsize CVN impact specimen of (a) DP alloy 1 having 90% martensite, and (b) DP alloy 3 having 30% martensite. Tested at 0°C. (XBB 788-7554A)

fraction (90% Ms, 0.07 wt.%C in the martensite) exhibited better impact energy, and showed an apparent DBTT, while no DBTT was present in the one with the lower volume fraction (35% Ms, 0.17 wt.%C in the martensite). This result may be due to the fact that the toughness factor has an overwhelming influence on the notched impact toughness compared to the connectivity factors, since in both cases the martensite phase was interconnected along the prior austenite grain boundaries (Fig. 1).

In contrast, the 2% Si DP structure yielded essentially identical energy curves for two different volume fractions of martensite, as is seen from Fig. 4. This indicates that toughness and connectivity factors counterbalanced each other to result in no variations in the curves. The

individual martensite particles are still separated and surrounded by the ferrite matrix at 60% martensite, maintaining the same fibrous morphology as that of 30% martensite, thereby resulting in identical energy curves for the two volume fractions. On the other hand, the martensite particles in the 0.5% Si DP steel revealed a high degree of connectivity at all volume fractions of martensite ($> 20\%$). The impact energy curves thus show similar behavior to those of 0.5% Cr DP steels, Fig. 4.

Silicon is known as a very detrimental alloying element in lowering impact toughness properties in carbon steels. Nevertheless, the impact properties of 2% Si DP steel are as good as those of 0.5% Si DP steel at 35% martensite volume fraction. This indicates that the connectivity of martensite constituents at a given volume fraction is an important factor in controlling impact properties, as can also be seen from Fig. 5. In general, it appears from the present study that the toughness or carbon content in the martensite is the single most important parameter in determining impact toughness, as has also been substantiated by Young.¹ It is therefore essential to limit the initial carbon content in the alloys to less than 0.1 wt.% for optimum impact toughness and tensile properties.² The influence of the prior austenite grain size and interparticle spacing on the impact properties of DP alloys is being investigated, and the results will be presented in a subsequent paper.

* * *

[†]Brief version of LBL-9535; to be published in Scripta Met.

[‡]Rutgers University, New Brunswick, N.J.

1. M. J. Young, M.S. thesis, LBL-6620.
2. J. Y. Koo and G. Thomas, "Formable HSLA and Dual-Phase Steels," A. T. Davenport, Ed., Proc. AIME, New York, N.Y., (1979) p. 42.
3. G. Thomas and J. Y. Koo, Proc. AIME Symposium on Formable Dual Phase Steels, New Orleans, 1979, in press; LBL-8650.

2. EFFECTS OF MORPHOLOGY ON THE MECHANICAL PROPERTIES OF DUAL PHASE Fe/Si/C STEELS[†]

N. J. Kim and G. Thomas

Although most of the alloy design principles for optimum combinations of tensile strength and elongation ductility have already been documented, there is a very important question which must be answered, viz., what is the effect of morphology on the mechanical properties of dual phase steels. Thus, the objective of this investigation is to clarify these points.

A coarse dual phase structure which was obtained by continuously annealing in the two phase range from the austenite range, resulted in very poor ductility (Fig. 1). In this case, a somewhat

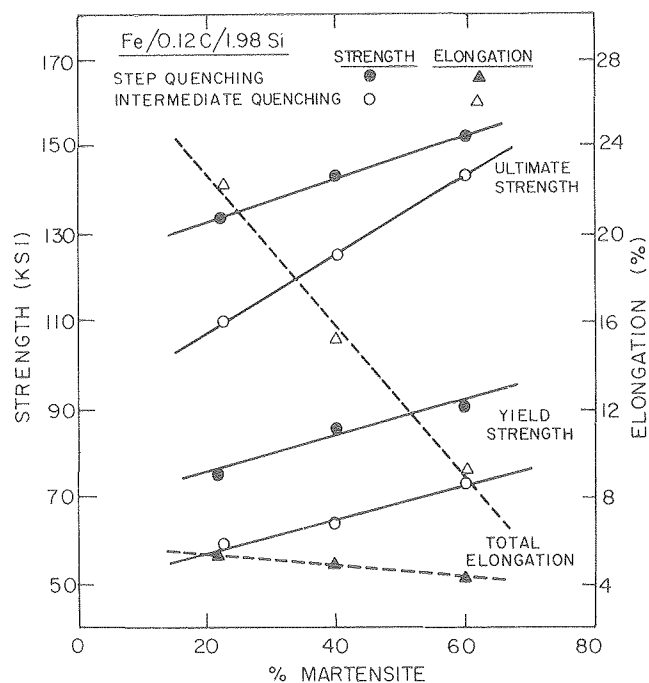


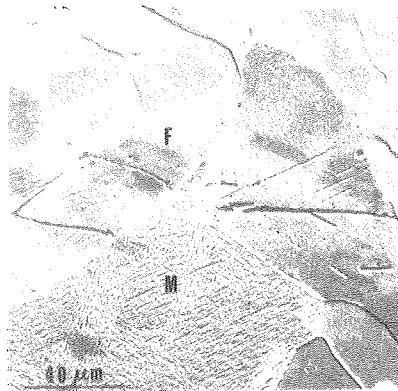
Fig. 1. Strength and elongation values vs. volume fraction of martensite in Fe/2Si/.1C steels.
(XBL 792-5702)

surprising observation was that premature failure occurs by the initiation of cracks in the ferrite (Fig. 2). However, upon obtaining fine, fibrous dual phase structures by annealing the martensitic structure in the two phase range, there was a significant improvement in ductility without much decrease in strength (Fig. 1) and no evidence of premature crack formation was found (Fig. 3). There are many factors which affect the mechanical behavior of dual phase steels: 1) morphology, 2) properties of ferrite and martensite; 3) volume fraction of martensite. By careful TEM and STEM-x-ray microanalysis studies it was found that there were no remarkable differences in the substructures and silicon distribution in both cases. So, differences in mechanical properties are mainly due to the different morphologies in both cases. From a continuum mechanics point of view, coarse microstructures cause more severe inhomogeneous strain distribution and restrict initial plastic flow to a smaller fraction of the total volume of ferrite matrix, which in turn causes premature crack formation in the ferrite matrix.

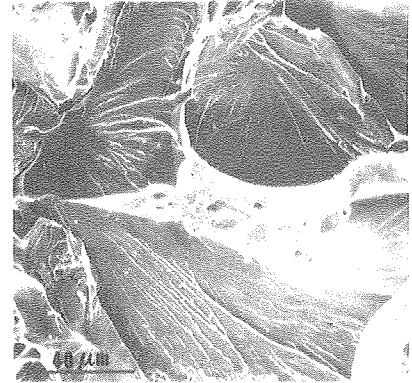
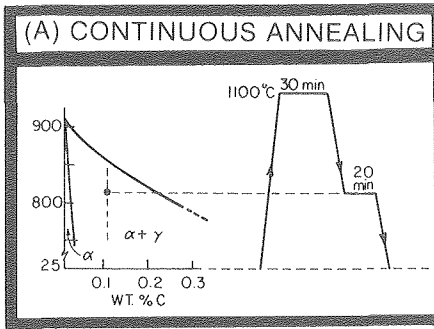
* * *

[†]Brief version of LBL-10457.

1. J. Y. Koo and G. Thomas, Proc. AIME Symposium, "Formable HSLA and Dual Phase Steels," A. T. Davenport, Ed., The Metall. Soc. AIME (1979) pp. 40-55; LBL-6995.

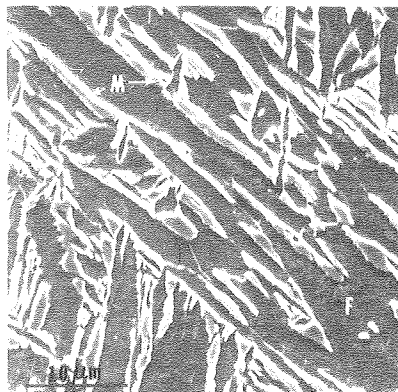


Scanning electron micrograph of the continuously annealed Fe-2Si-0.1C dual phase structure showing the morphology of ferrite and martensite and the cracks developed in the ferrite. 5% nital etch. M - martensite region, F - ferrite region.

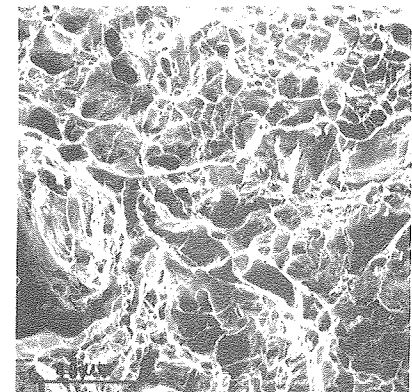
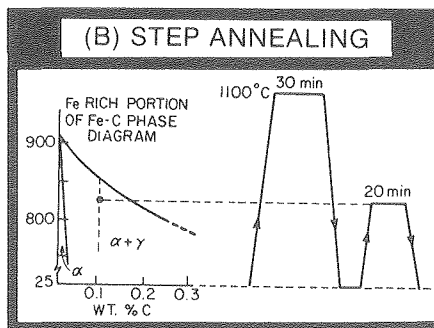


Cleavage fracture observed in the broken tensile specimen of the continuously annealed Fe-2Si-0.1C dual phase steels

Fig. 2. Scanning electron micrograph of step-quenched Fe/2Si/0.1C dual phase structure showing the morphology of ferrite and martensite and the cracks developed in the ferrite. 5% nital etch M - martensite region, F - ferrite region. (XBB 797-9313A)

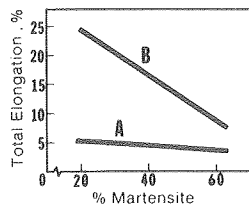


Scanning electron micrograph of the step annealed Fe-2Si-0.1C dual phase structure showing a fine dispersion of martensite in the ferrite. 5% nital etch.



Ductile fracture (dimpled rupture) observed in the broken tensile specimen of the step annealed Fe-2Si-0.1C dual phase steels

Dual phase ferrite-martensite steel is a "composite" which has emerged as a new generation of HSLA steels. The fracture characteristics of these dual phase steels are very sensitive to the transformation path by which the composite structure is obtained. A Fe/2% Si/0.1% C steel when subjected to the continuous annealing" treatment (Fig. A), which is a commercially attractive process, resulted in a very coarse dual phase structure as shown in Fig. 1. A careful scanning electron microscopy study indicated that in this case a premature failure occurs by the initiation of cracks in the ferrite region where maximum localized stress concentration takes place. This is illustrated in the scanning electron micrograph (Fig. 1) of the cross sectional surface of a tensile test specimen just before final fracture. The fracture surface of a broken tensile specimen revealed predominantly cleavage fracture (Fig. 2). As expected this dual phase structure resulted in very poor ductility (Fig. 5) which places a limiting factor on the potential structural applications.



Plot of elongation ductility vs. volume fraction of martensite for heat treatments A and B

A modified heat treatment, "step annealing", was designed to improve the ductility. Following the step annealing process (Fig B) a remarkable refinement in dual phase structure was obtained and no evidence of crack formation was found in the tensile specimen just prior to the final fracture. This is shown in Fig. 3. The fracture appearance of the broken tensile specimen exhibited a primarily dimpled rupture (Fig. 4). Thus the step annealing process allows a significant improvement in ductility with no sacrifice in strength, as illustrated in Fig. 5.

The drastic change in the fracture mode from brittle (heat treatment A) to ductile (heat treatment B) is attributed to the refinement of dual phase structure by the step annealing process which appears to be highly promising for the maximum utilization of the composite steels.

Fig. 3. Scanning electron micrograph of intermediate-quenched Fe/2Si/0.1C dual phase structure showing a fine dispersion of martensite in the ferrite. 5% nital etch. (XBB 797-9313B)

3. MECHANICAL PROPERTIES AND MICROSTRUCTURES OF DUAL PHASE STEELS CONTAINING SILICON, ALUMINUM, AND MOLYBDENUM[†]

T. O'Neil and G. Thomas

This investigation concerning the heat treatment of dual phase alloys containing silicon, aluminum, and molybdenum has been aimed at investigating the properties and microstructures of similar alloys, thus adding to the present understanding of dual phase steels. Aluminum, molybdenum and silicon all broaden the ($\alpha+\gamma$) field when added to the Fe-C system. This facilitates practical control of the volume fraction and composition of the martensite produced. The summary of the tensile data of these alloys which are intermediately quenched are shown in Fig. 1 with other alloys investigated so far. All these alloys show superior tensile properties to commercial HSLA steels.

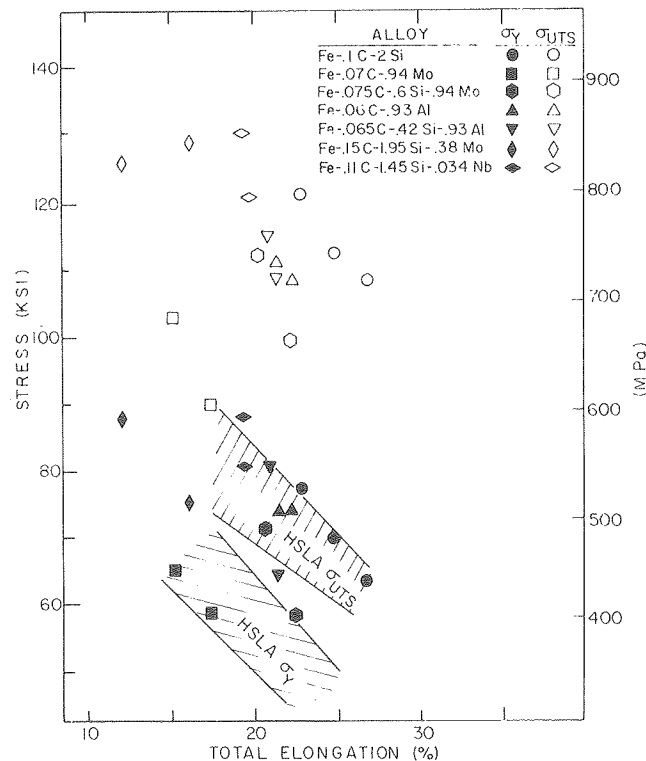


Fig. 1. Strength vs. total elongation for various alloys previously studied at the University of California, Berkeley. Each symbol of the same alloy reflects a different volume fraction of martensite. (XBL 7812-6281)

In the case of the Fe/Al/C alloy, a 20% increase in volume fraction of martensite from 20% to 40% has no substantial effect on either strength or ductility. Detailed examination by TEM and STEM has shown that this unusual behavior is due to a fine dispersion of precipitates (Fig. 2). The

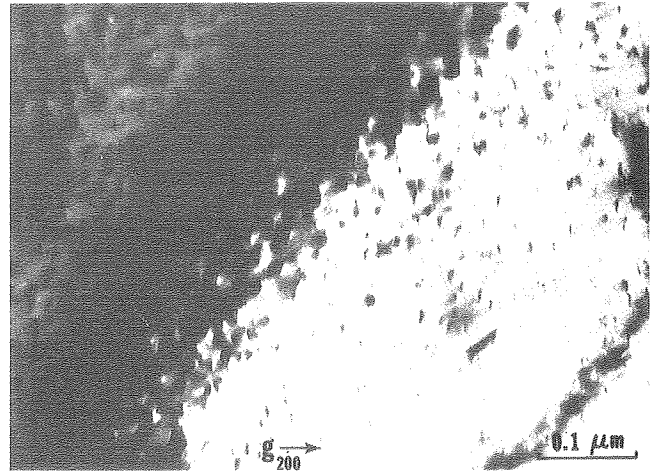


Fig. 2. High magnification micrograph of rods within the ferrite of the Fe/C/Al steels. These particles are thought to be AlN. (XBB 793-3352)

density of precipitates was greater in the ferrite than martensite presumably because ferrite has a high solubility for Al. This is confirmed by the x-ray microanalysis of Fig. 3. Furthermore, the precipitate density is expected to be higher in the ferrite with 20% martensite than that in the 40% martensite alloy since in the former case there is greater interstitial solubility. The presence of such precipitates in the ferrite will increase the strength of ferrite, and simultaneously lower ductility. Therefore, the strength increment expected through the increase in volume fraction of martensite by 20% will be balanced with a loss in strength of ferrite due to the reduced density of precipitates in alloy A containing 40% martensite. These findings are important in the practical sense that the reproducibility of such properties will be excellent with a wide flexibility of heat treatments available.

* * *

[†]Brief version of LBL-9047.

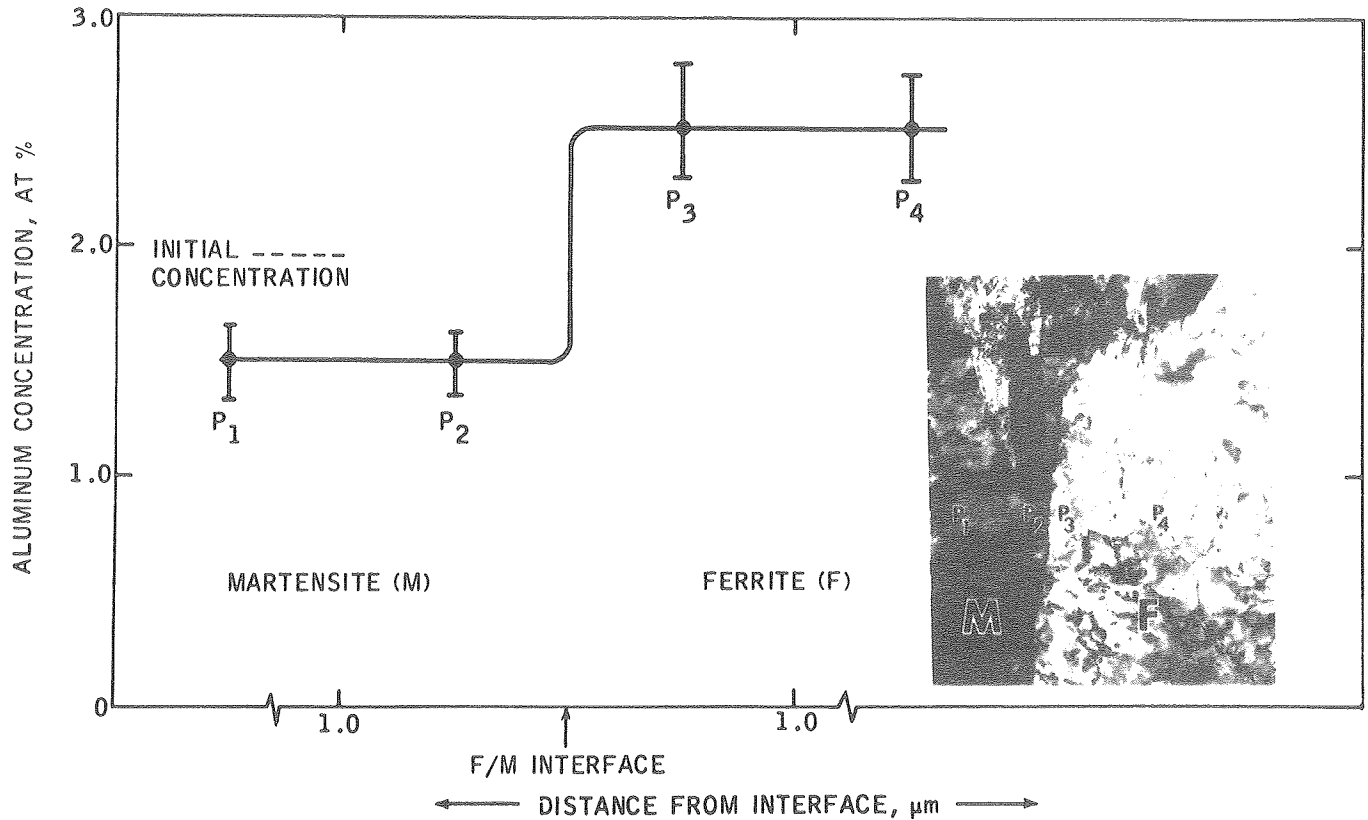


Fig. 3. Dual phase steel containing 1 wt.% aluminum; aluminum concentration profile in ferrite and martensite. The inset is a micrograph of an austenite/martensite interface. Points P₁ to P₄ are average concentrations of Al in ferrite and martensite, respectively. Points P₃ and P₄ were obtained using a 400 Å probe on either sides of the F/M interface. (XBB 795-7070)

4. DESIGN OF DUAL PHASE STEELS WITH CARBIDE FORMING ELEMENTS[†]

P. K. Costello and G. Thomas

As part of a continuing program aimed at understanding the microstructure-property relationships in dual phase steels, Fe/Si/C steels with carbide forming elements such as Mo, Nb have been investigated.

As shown in Table 1, the yield strength decreases with increasing volume fraction of martensite and this represents an anomaly in the usual "law of mixtures" behavior. Detailed analysis by TEM shows that this is due to precipitates in the ferrite. The precipitate in the system is a carbide, perhaps ϵ or M_3C . When the martensite volume fraction is increased by raising the holding temperature in the $(\alpha+\gamma)$ field, carbon content decreases. The higher yield strengths of these alloys with 20% martensite compared to those with

40% martensite is to be expected due to a greater density of carbide in the ferrite region in the former case. This is so because the yield strength of dual phase steels is primarily determined by the flow strength of ferrite. Thus, it should be emphasized that the properties of ferrite are as important an influence on the mechanical properties as are the strength and volume fraction of martensite. Also, alloys which are continuously air-cooled from austenite region exhibited superior e_T and e_n values. The e_T and e_n values ranged from 32-33% and 18-20%, respectively. The U.T.S. values extended from 84-91 ksi and the Y.S. values ranged from 55-69 ksi. These alloys contain pearlite and bainite as a second phase instead of martensite. This process appears to be an attractive one for potential technical applications.

* * *

[†]Brief version of LBL-8628.

Table 1. Tensile test summary.

| Specimen Designation | Heat Treatment | \bar{v}_m (%) | U.T.S. (ksi) | Y.S. (ksi) | e_T (%) | e_{11} (%) | R.A. (%) | U.T.S./Y.S. |
|---|---|-----------------|--------------|------------|-----------|--------------|----------|-------------|
| DUPLEX TREATMENTS: | | | | | | | | |
| A11 | Intermediate Quench | 40 | 129.1 | 76.6 | 16.3 | 12.2 | 23.7 | 1.7 |
| C11 | | 40 | 130.2 | 80.9 | 19.5 | 13.9 | 33.1 | 1.6 |
| A12 | | 20 | 126.2 | 87.8 | 12.3 | 10.0 | 21.2 | 1.4 |
| C12 | | 20 | 121.0 | 88.4 | 19.7 | 12.9 | 46.1 | 1.4 |
| A13 | Intermediate air cool | 40 | 137.9 | 89.8 | 7.5 | 7.0 | 11.4 | 1.5 |
| C13 | | 40 | 134.7 | 85.2 | 10.8 | 9.8 | 20.3 | 1.6 |
| A33 | | 20 | 111.3 | 81.5 | 7.7 | 7.3 | 8.0 | 1.4 |
| C33 | | 20 | 122.6 | 87.7 | 7.7 | 7.4 | 7.5 | 1.4 |
| NORMALIZING TREATMENT: | | | | | | | | |
| A31 | continuous air cooling from (γ) | | 90.8 | 68.6 | 33.4 | 19.5 | 63.5 | 1.3 |
| C31 | | | 84.8 | 55.1 | 33.0 | 18.0 | 56.7 | 1.5 |
| DIRECT ANNEALING TREATMENTS: | | | | | | | | |
| A32 | continuous air cooling from ($\alpha+\gamma$) | | 78.3 | 54.3 | 34.1 | 20.8 | 68.9 | 1.4 |
| C32 | | | | 76.6 | 53.0 | 46.10 | 22.3 | 65.8 |
| A42 | Quenching from ($\alpha+\gamma$) | 20 | 135.8 | 77.8 | 12.5 | 9.5 | 29.8 | 1.7 |
| C42 | | 20 | 133.7 | 79.1 | 16.9 | 13.4 | 40.9 | 1.7 |
| A = Fe/0.15 C/1.45 Si/0.38 Mo C = Fe/0.14 C/1.45 Si/0.034 Nb | | | | | | | | |

Phase Transitions

1. MORPHOLOGY AND CRYSTALLOGRAPHY OF LATH MARTENSITES^{††}

M. Sarikaya, B. V. N. Rao,[§] and G. Thomas

Martensites occurring in ferrous alloys have two types of morphology: twinned plate martensite and dislocated lath martensite. The former is usually associated with steels of C content greater than about 0.4 wt.%, while the latter is found in steels containing less than this amount of carbon with a total alloy content such that the bulk Ms temperature is not lower than 250°C. The morphology and crystallography of plate martensite occurring in steels of high alloy concentrations have been well studied and are now well understood.^{1,2} However, the same is not true for lath martensites occurring in technologically more important low alloy steels. As a result of the detection of retained austenite in these steels, it has been shown that direct crystallographic analysis on austenite serves to understand the lath martensite transformation more clearly.^{3,4} This project is mainly concerned with a detailed electron diffraction and microscopy examination of lath martensite in connection with retained austenite in medium and low C steels.

The strain created during the austenite to martensite transformation is two fold: (1) shape strain due to primary shear (homogeneous shear), and (2) dilatational strain primarily controlled by C in solution. The overall strain energy can be minimized by the cooperative nucleation of adjacent laths. Thus, orientations of adjacent laths change such that a 180° rotation is accomplished by a group of laths. Retained austenite is then trapped between these laths and it is highly deformed to accommodate part of the strain.

Analysis of the relative orientation of adjacent laths in packets was performed in low and medium C steels (Table 1). A sample set is given in Fig. 1.

Table 1. Analysis of alloys used.

| Alloy | Nominal Composition | Ms (°C) |
|-------|-----------------------|---------|
| 10 | Fe/2Si/0.1C | 450 |
| 20 | Fe/0.5Mn/0.2C/... | 400 |
| 5 | Fe/3Cr/0.5Mo/2Mn/0.3C | 320 |
| 6 | Fe/3Cr/0.5Mo/2Ni/0.3C | 340 |

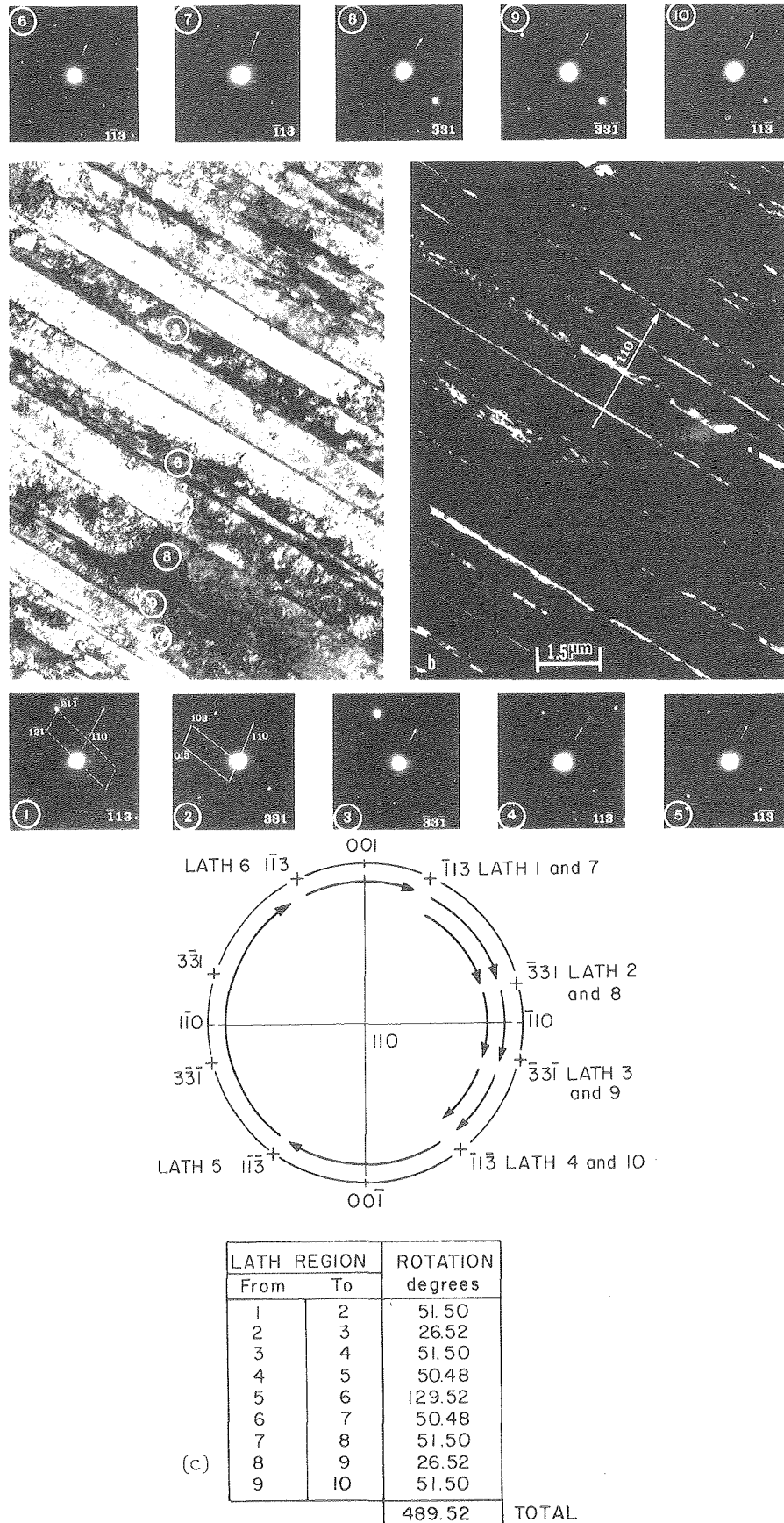


Fig. 1. Detailed analysis of orientation of adjacent 10 laths in 1040 steel (Alloy 10). (a) BF, (b) DF, from an austenite reflection, and (c) stereographic analysis showing rotation. Reference shear vector makes 2.7π rotation. [(a)&(b) XBB 799-11464; (c) XBL 799-7016]

In most cases $(110)_M$ remains parallel in a given packet. This indicates that the laths are separated by $(110)_M$ rotation boundaries [e.g., Fig. 1(a), (b)]. In few instances $(112)_M$ rotation axis have also been observed. It is assumed that the shear vector undergoes a systematic, but not random, rotation to minimize the shape deformation. Hence, stereographic analysis of the lath orientations can be made [e.g., Fig. 1c]. Martensite laths in a certain packet are not necessarily from a single variant of austenite; they may have different variants.

In the steels studied successive laths are separated in varying degrees. Lowering the C content decreases the dilational strain, and hence during transformation less accommodation of shape strain is necessary. Therefore, a higher number, n , of laths contribute to complete the π -rotation. The number " n " decreases as the C content increases, (Fig. 2a). The minimum value of " n " is equal to 2, when laths are twin-related (Fig. 3). Furthermore, at lower C contents, shear takes place over a broader thickness of the laths. Consequently, the lath width increases as C content decreases, (Fig. 2b).

Retained austenite in the form of thin films around the lath boundaries is always present, even in very low C steels (Figs. 1 and 3). This phase is absent at those lath boundaries where the adjacent lath orientation corresponds to a twin rela-

tion (Fig. 3). Both Kurdjumov-Sachs (K-S) and Nishiyama-Wasserman (N-W) orientation relationships were found to be obeyed in the same packet between retained austenite and adjacent laths, (Fig. 3). The relationships are: $(110)_M // (\bar{1}\bar{1}\bar{1})_A$ and $[001]_M // [110]_A$ for N-W and $(110)_M // (111)_A$ and $[\bar{1}\bar{1}\bar{1}]_M // [110]_A$ for K-S.

Current Work. The critical problem here is the question of lath orientation determination. Spot pattern analysis is not unique hence the model described above is still highly speculative.⁴ Current work utilizing microdiffraction and tilting experiments should help to sort out some of the ambiguities. Also TEM-STEM microanalysis is being performed to study such factors as chemical stabilization of austenite.

* * *

†Partially supported by NSF.

‡Brief version of LBL-9054.

§Permanent address: Analytical Chemistry Department, Research Laboratory, General Motors Technical Center, Warren, MI 48090.

1. C. M. Wayman, *Metallurgy* 8, 105 (1975).
2. G. Thomas, *Iron and Intl.* 46, 451 (1973).
3. B. V. N. Rao and G. Thomas, *Met. Trans. A*, to be published.
4. B. V. N. Rao and G. Thomas, *ICOMAT 5*, in press, LBL9058.

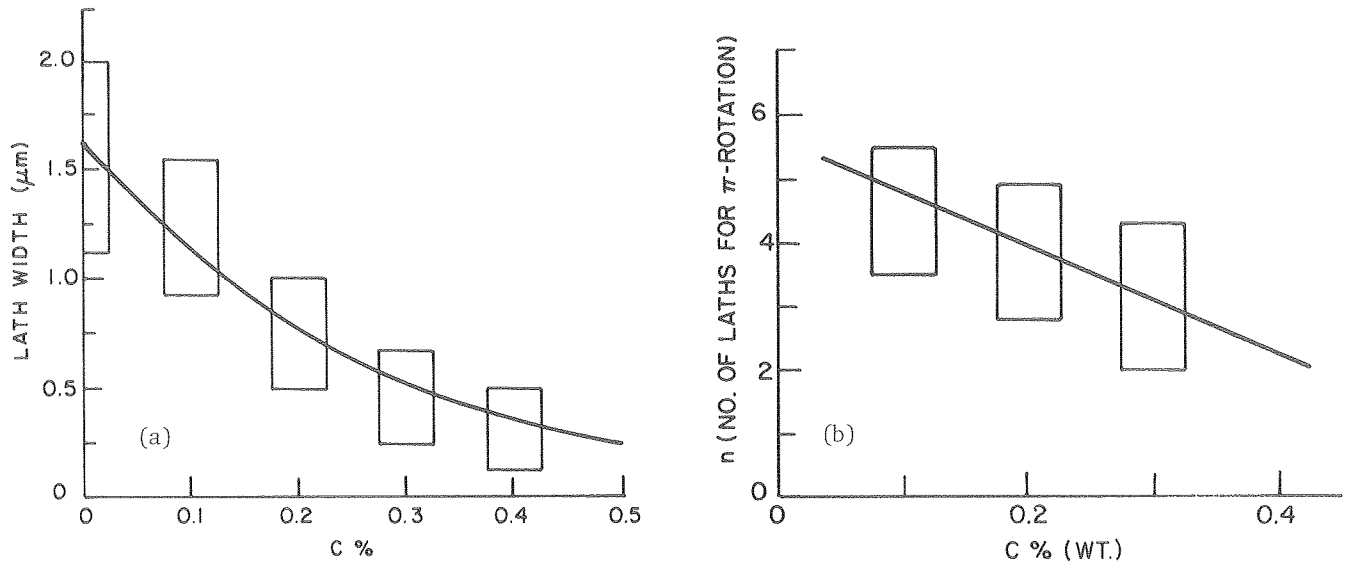


Fig. 2(a) Graph showing "lath width" vs. carbon content. (b) Graph showing " n ," the number of laths to complete π -rotation vs. C-content.

[(a) XBL 796-6418; (b) XBL 796-6417]

2. DETERMINATION OF LOCAL HYDROGEN CONCENTRATION USING COLD STAGE ELECTRON MICROSCOPY^{1,4†}

U. Dahmen

At room temperature, most transition metals have a high solubility for hydrogen. In tantalum for example up to 40 at wt.% hydrogen can be held in interstitial solution without any direct microstructural effects. However, as is well known, such hydrogen solute may cause severe embrittlement of the material due to solid solution hardening or stress-induced formation of hydrides at crack tips.

In a recent publication, it was determined that only minute amounts of hydrogen on the order of 10 parts per million are introduced into tantalum by chemical or electrochemical surface treatment.¹ Since it is likely that this hydrogen enrichment is concentrated near the surfaces, the effect was investigated in thin foils of tantalum prepared by chemical thinning in a mixture of HF and HNO₃.

Figure 1 shows the result of an in-situ cooling experiment on such a foil. The top row of diffraction patterns, taken at room temperature is typical for pure tantalum. This large angle tilt series shows that no hydrides were present. However, upon cooling the foil to liquid nitrogen temperature, extra spots appeared in the diffraction patterns (see arrows in central spot pattern). These extra spots originated from hydride precipitates such as the one shown in the two micrographs in the figures. Upon re-heating the precipitates dissolve at a temperature of -30°C, leaving an undistorted matrix diffraction pattern with no extra spots (bottom spot pattern). Using the well-established solubility data for hydrogen in tantalum,^{2,3} this solution temperature corresponds to a hydrogen concentration of ~8 at.%. Thus it has been shown that even though the overall concentration of hydrogen introduced by chemical surface treatment is low, a very high concentration can result near the surfaces, exceeding the average bulk concentration by more than three orders of magnitude.

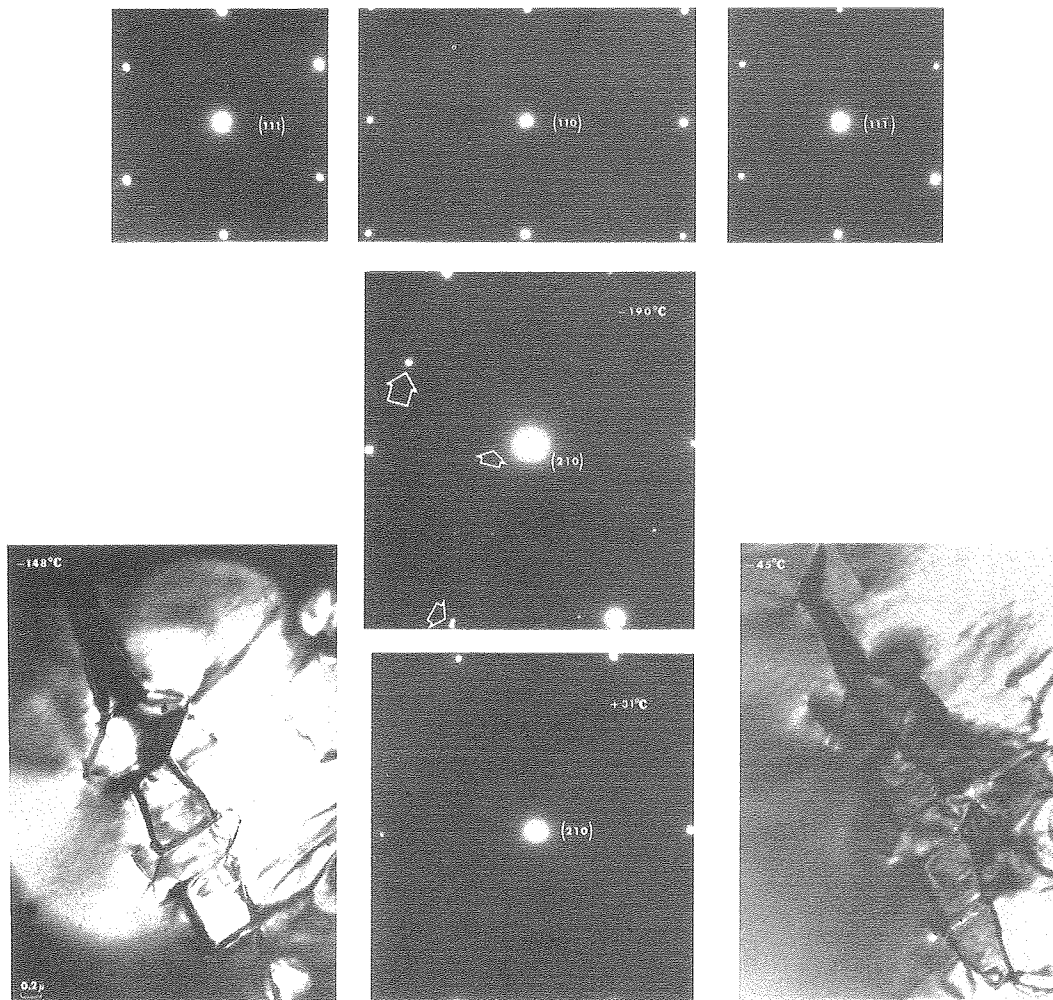


Fig. 1. In-situ cooling experiment on pure Ta-foil thinned chemically at 0°C. Top row of diffraction patterns: no hydride ordering is present at room temperature. Micrographs and center diffraction pattern: precipitation of hydride upon cooling to liquid nitrogen temperature. Bottom diffraction pattern: after dissolution of the hydride upon heating to room temperature. (XBB 782-1387)

* * *

⁺Partially supported by NSF.

[†]Brief version of LBL-8661.

1. K. Abe, H. Yoshinaga and S. Morozumi, *Trans. JIM* **17**, 551 (1976).
2. H. Asano, P. Yamada and M. Hirabayashi, *Trans. JIM* **18**, 155 (1977).
3. T. Schober and A. Carl, *Scr. Met.* **11**, 397 (1977).

Refractory Ceramics

Introduction. This effort has been divided fairly evenly between developing new state-of-the-art analytical instrumentation for ceramics research and applying the new techniques to significant ceramic problems, and research on the manufacture and properties of nitrogen ceramics and glasses.

1. THE CRYSTALLIZATION OF OXYNITRIDE GLASSES⁺

T. M. Shaw

The importance of residual glassy phases in Si_3N_4 -based ceramics has been extensively documented, but little is known about the intrinsic properties of the glass. Therefore the crystallization behavior of oxynitride glasses of compositions similar to that of the silicon nitride residual glassy phase has been characterized.

Glasses in the SiO_2 - Si_2N_2 - MgSiO_3 compatibility triangle with nitrogen contents of up to 5 at.% nitrogen were prepared in cooperation with Dr. R. Loehman of Stanford Research Institute. Good glass formation was found to be restricted to a narrow range of compositions near the SiO_2 - MgSiO_3 eutectic composition. Transmission electron microscopy showed that the milky appearance of the as-made glasses was caused by phase separation into Mg-rich and Si-rich glassy phases on cooling.

The crystallization behavior of a glass with a composition of 32 wt.% MgO , 59 wt.% SiO_2 , and 9 wt.% Si_3N_4 was investigated in detail using differential thermal analysis, x-ray diffraction and optical and electron microscopy. The glass was found to have a glass transition temperature of about 830°C. Isothermal heat treatment from 1000°C-1350°C of the glass crystallized the Mg-rich phase to enstatite after 2 hours. The Si-rich phase remained uncrystallized in the bulk of the sample after all heat treatments. Optical and electron microscopy showed that the Mg-rich phase crystallized by internal nucleation and growth of spherulites of about 50 μm diameter. The individual spherulites consisted of fan-like arrangements of plate-shaped clinoenstatite grains several microns long and ≈ 1000 Å thick, slightly misaligned with respect to each other. No nitrogen containing phases were detected by x-ray diffraction after crystallization heat treatments, however, TEM revealed a large number of very fine crystals at the grain boundaries between enstatite grains. These have been tentatively identified as $\text{Si}_2\text{N}_2\text{O}$.

Two-stage heat treatments were also tried and were found to produce a considerably finer ($\approx 3 \mu\text{m}$) spherulitic microstructure.

These results show that Mg-Si-O-N glasses can exhibit many features associated with glass ceramic formation, i.e., phase separation, internal crystallization, and response to two-stage heat-treatments for controlling the microstructure. The formation of grain boundaries containing $\text{Si}_2\text{N}_2\text{O}$ in this glass also suggests that refractory glass ceramics may be developed by crystallization of oxynitride glasses. Some of the initial applications of this system are described below.

* * *

⁺Partially supported by NSF.

2. C AND B IN SINTERED SiC ^{††}

M. F. Sung and O. L. Krivanek

The solid-state diffusion sintering of SiC and C and B additions is still not completely understood, partly because the role of the additives, and their distribution in the finished SiC and during sintering, is still not clear. SiC sintered with 1 wt.% B and 1 wt.% C has been studied by high-resolution scanning Auger microanalysis, and more recently by EELS. C is found at internal voids, which confirms its role as a surface-oxidant. B is mostly concentrated in boron carbide inclusions. EELS has detected a slight B enrichment of grain boundaries, but the amount ($\approx 2\%$) is very close to the present sensitivity limit of the technique (see E.1), and quantitative software is needed to confirm this result.

* * *

[†]Supported by NSF.

^{††}Brief version of LBL-9257.

Analytical Microscopy

1. DEVELOPMENT OF ENERGY LOSS SPECTROSCOPY[†]

O. L. Krivanek

Electron energy loss spectroscopy is a technique with promising applications in physics,¹ materials science,² biology,³ and other fields. Commercially built spectrometers are however still far from satisfactory. An energy loss spectrometer of the magnetic type,^{4,5} with a 10 cm bending radius and 90° degree deflection has therefore been designed and built at Berkeley.⁶ It combines several new design features, small physical size, good energy resolution, excellent flexibility of operation.

The spectrometer (Fig. 1) was designed for a Philips 400 electron microscope. The spectrometer magnet is asymmetric. The entrance focal plane is located 51 cm away from the magnet entrance plane, at the projector lens crossover where the

ELECTRON SPECTROMETER

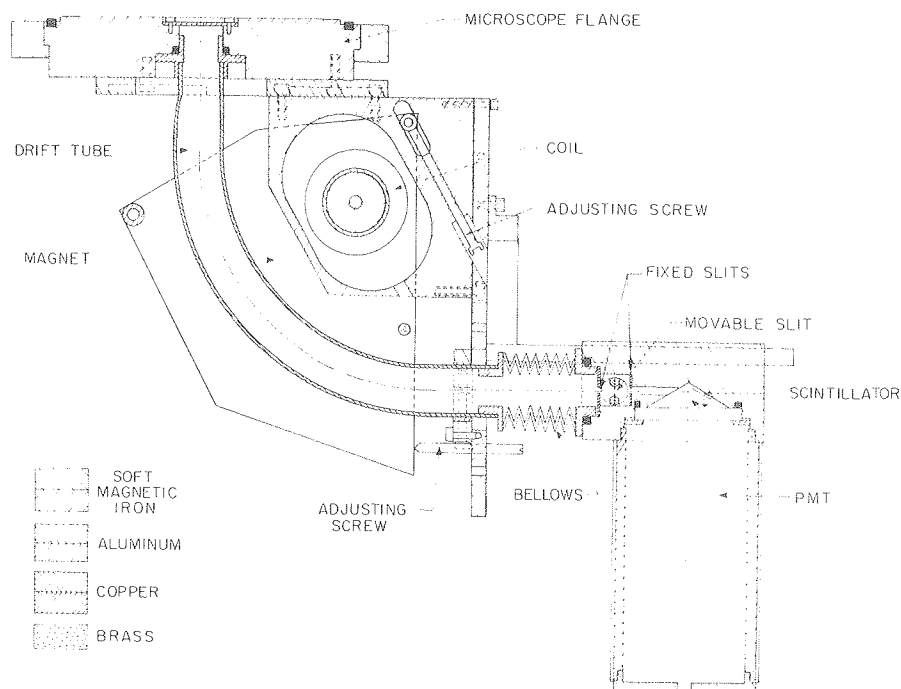


Fig. 1. Spectrometer cross section. (XBL 792-5747)

P400 has a 200 μm differential pumping aperture. The exit vertical and horizontal focussing planes are estimated to be 7.8 cm and 11.2 cm away from the exit plane of the magnet. The magnet pole-plates have three mechanical degrees of freedom for optimum adjustment, and $\epsilon_1 = 31^\circ$ and $\epsilon_0 = 0^\circ$. At present straight edged poleplates are used, but the design allows for an easy changeover of pole-plate geometry. The energy loss spectra dispersion is about 1 $\mu\text{m}/\text{eV}$ at 120 kV.

The detection chamber is attached to the electron drift tube via a welded bellows which allows ± 2.5 cm of travel for exact location of the focal plane. Because of the small dispersion of the magnet, the energy-selecting slit had to be made with better than 1 μm precision to allow 1 eV resolution. A special manufacturing procedure was therefore devised in which the slit is made from two polished blocks of Ge separated by a 50 μm thick sheet of glass. A slice is cut at 45° from this "sandwich," thinned to 40 μm , and polished to optical flatness on both sides. It is then glued over an aperture in a Mo support plate, and the glass is etched out in HF. The resultant 50 μm wide slit (Fig. 2), is mounted on a rotor, which allows the slit's projected width to be varied precisely and reproducibly. Fixed slits in front and behind the moveable slit eliminate electrons scattered from the electron drift tube and the moveable slit edges.

The electrons are detected by a plastic scintillator (NE 110). Approximately 100 photons are

produced per incident electron in a pulse 2 nsec wide. A large fraction of these photons enters a vertically mounted photomultiplier tube (RCA 8575). The resultant 4 nsec wide, roughly triangular pulses are processed at rates up to 100 MHz by a discriminator-amplifier (Canberra 1433) converted to Schottky TTL pulses (LeCroy 688 AL) and counted at up to 40 MHz (Kevex system 7000 front-ended with module 5180). The module 5180 also provides the magnet ramp which is fed to a separate winding of the main coil.

The whole spectrometer fits unobtrusively at the back of the available leg-space of the P400, and requires no alterations to the microscope. Magnetic shielding is provided by a μ -metal enclosure. Even so AC fields are expected to be the most serious resolution-limiting factor, and provisions are being made to compensate for the major AC components electronically. The magnet power supply (North Hills TC-602CR) is stable to 2 ppm.

Normal operation of the spectrometer makes use of the P400 scanning attachment to form a small probe on the specimen, and of the post-specimen lenses to give an image of the probe at the projector lens back-focal plane, and a stationary diffraction pattern at the level of the final viewing screen, where a 500 μm exchangeable aperture, which defines the entrance angle into the spectrometer, is located. This arrangement makes it possible to analyze electrons scattered by up to 100 mrad with little loss in energy resolution.

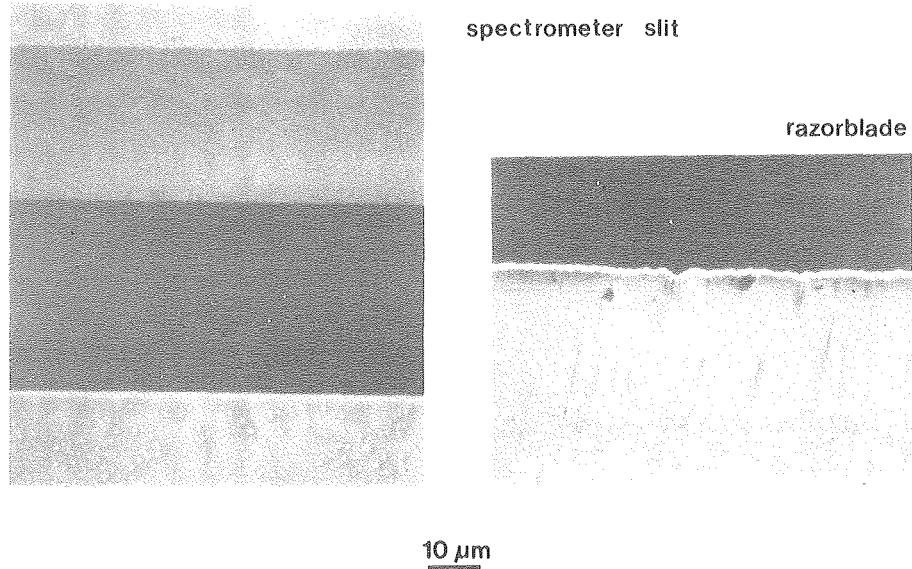


Fig. 2. Energy selecting slits, fully opened, compared to the edge of a new razor blade. (XBB 797-9145)

It is however also possible to operate the microscope without the scanning attachment, area selection being accomplished by the aperture in the viewing screen.

Initial tests show that stray magnetic fields limit the resolution of the spectrometer to 20-30 eV, but that simple dynamic compensation of 60 Hz AC fields can bring the resolution down to 4 eV, (Fig. 3), at which point the resolution limit comes mainly from 120 Hz AC. Improvements in the poor magnetic shielding of Philips 400 microscope, which are now being carried out, should bring the resolution down to the energy spread of the 120 kV electron beam (1 eV). Equally importantly, the electron counting system has proved itself capable of keeping the dark count below 100 counts/sec while detecting single electrons with close to 100% efficiency at rates up to 4×10^7 counts/sec.

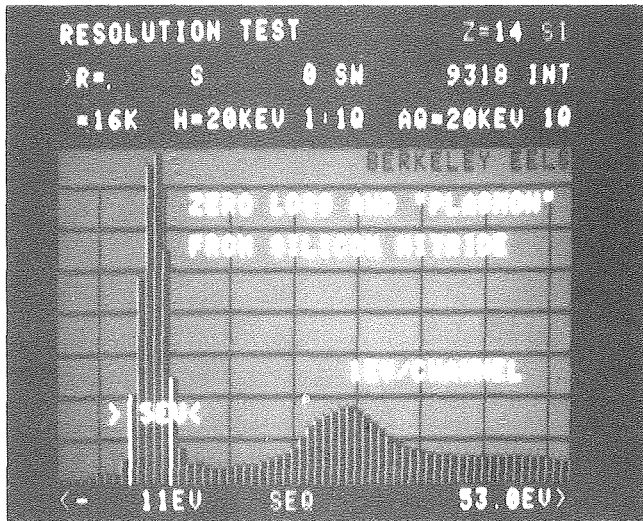


Fig. 3. Zero loss and first "plasmon" in silicon nitride. (CBB 7911-15001)

This kind of performance will be useful for studies of the fine structure of energy loss edges, where a good signal/noise ratio, and hence higher count rates, will be needed.

Initial applications of the spectrometer have been in the field of structural ceramics, where the ability to detect and map light elements presents the key to several long-standing problems. For instance, an energy-loss spectrum taken from a grain boundary in SiC sintered with small B and C additions shows a weak BK-edge (Fig. 4), thus indicating that B may be involved in increasing grain boundary diffusion during the sintering of this important ceramic.

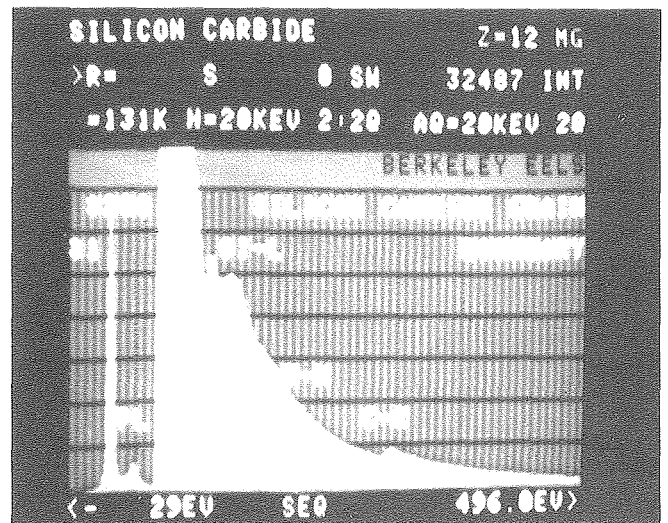


Fig. 4. Energy loss spectrum from a grain boundary region in SiC. Si L_{2,3} and L₁, and B-K and C-K edges can be seen. (CBB 7911-15003)

The spectrometer performance is now being further improved by adding electromagnetic alignment coils to replace the present mechanical alignments, magnetic sextupoles to correct second order aberrations, and an LSI-11-based minicomputer. In addition to quantifying the x-ray spectra that are also available on the Philips 400 microscope, the minicomputer will serve for the development (in collaboration with Dr. P. Rez of Kevex) of a comprehensive energy loss spectra quantification package. This will include the deconvolution of spectral features due to multiple scattering, automatic edge identification, calculation of compositions from the strength of the edges, and on-line EELFS analysis (extended energy loss fine structure, equivalent to EXAFS) to give radial distribution functions around each element in composite materials.

The possible applications of the fully developed system are too numerous to be described in detail. It will, however, be interesting to see how successful electron energy loss spectroscopy becomes in providing the types of information available until now only with synchrotron radiation, at a fraction of the cost.

* * *

⁺Partially supported by NSF; spectrometer built at LBL.

1. J. Silcox, Scanning Electron Microscopy 1, 393 (1977).
2. C. Colliex, V. E. Cosslett, R. D. Leapman and P. Trebia, Ultramicroscopy 1, 37 (1976).
3. J. L. Costa, D. C. Joy, D. M. Maher, K. L. Kirk and S. W. Huri, Proceedings 35th Annual EMSA Meeting (Boston), 238 (1977).
4. D. B. Whittrey, R. P. Ferrier and V. E. Cosslett, Brit. J. Appl. Phys. 2, 1967 (1969).
5. A. V. Crewe, M. Isaacson and D. Johnson, Rev. Sci. Instr. 42, 411 (1971).
6. O. L. Krivanek, Proceedings 37th EMSA Meeting (San Antonio), 530 (1979).

Physical Properties and Microstructures of Alloys and Ceramics

1. RARE EARTH-COBALT HARD MAGNETS^{††}

M. F. Sung and R. K. Mishra

Phase transformations in R-Co magnets are of primary importance, since nearly all the rare earth-cobalt magnets with good magnetic properties are multiphase alloys. However, identification of various phases that are present is generally not straight forward, particularly for the multi-component alloys that are being developed presently. Determination of the structure, chemical composition and magnetic domain behavior of the various phases in the material can be approached with electron microscopy techniques. Electron diffraction in conjunction with dark field techniques are essential for phase identification while Lorentz microscopy is very useful to study the magnetic domain patterns, and hence the mechanism of hardening.

The microstructure of sintered $(\text{Co,Cu,Fe,Zr})_{17}\text{Sm}_2$ alloy solution treated between 1100-1250°C and step tempered between 750°C to 400°C has been investigated. This alloy has been shown to have $(\text{BH})_{\text{max}}$ of ~ 30 MKGOe after step-aging up to 400°C.¹ The microstructure of the step aged alloy after aging at 400°C is shown in Figs. 1 (a) and (b). The microstructure in Fig. 1(a) taken from a section of the aged material containing the c-axis consists of a cellular microstructure with cell interiors having a 2:17 structure and cell boundaries a 1:5 structure. The cells are approximately 300 Å in size and the cell walls are ~ 40 Å in width, making it difficult to determine the chemical composition of these phases using the available STEM. Closely spaced stacking faults on the basal

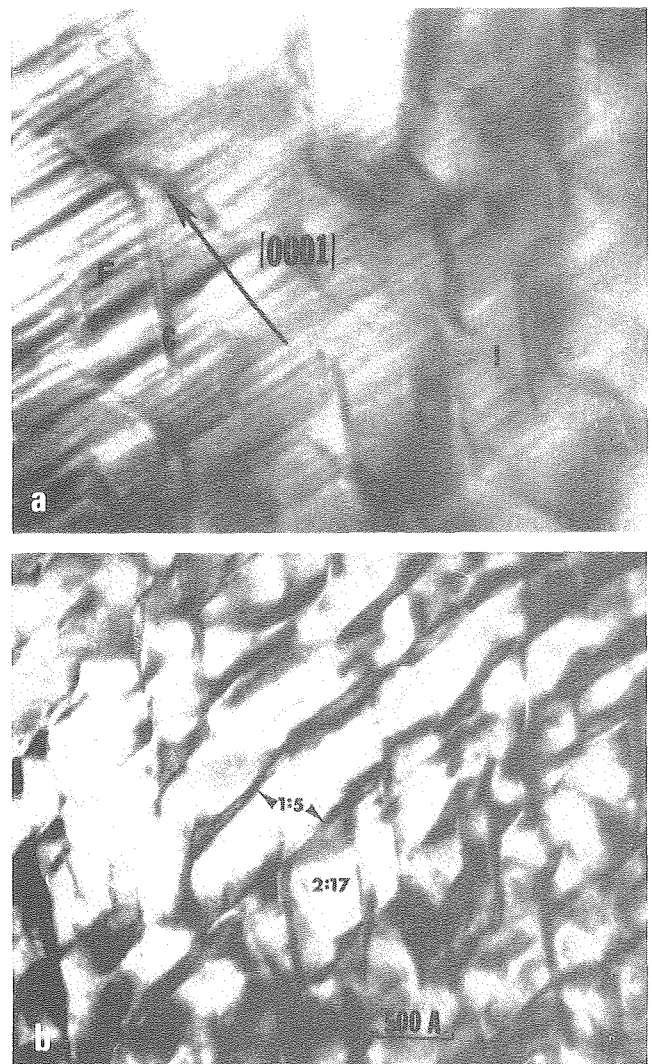


Fig. 1. (a) BF image of a step aged Sm_2 (Cu-Fe-Co-Zr)₁₇ alloy, sectioned parallel to the c-axis (easy axis) showing the cellular microstructure. The cell interior (I) has the 2:17 structure and the cell boundary C has the 1:5 structure. The cell interiors are heavily faulted (F) on (0001) planes. (b) Same as (a), from the alloy sectioned normal to the c-axis. The cell interiors are not faulted. The cell boundaries are aligned crystallographically. (XBB 795-6615)

planes are present in the cell interiors in Fig. 1(a) and these faults generally do not continue through the 1:5 phase at the boundary. In Fig. 1(b), taken from a section of the same magnet, normal to the c-axis, these faults are not seen. The cell morphology is not isotropic in this section, just as that in Fig. 1(a) where cell walls are parallel to crystallographic planes.

The microstructures from alloys step aged up to 600°C and 500°C are similar to those shown in Figs. 1(a) and (b).

The magnetic domain walls are imaged by Lorentz microscopy in Fig. 2 from a specimen of the aged alloy, sectioned parallel to the c-axis. The

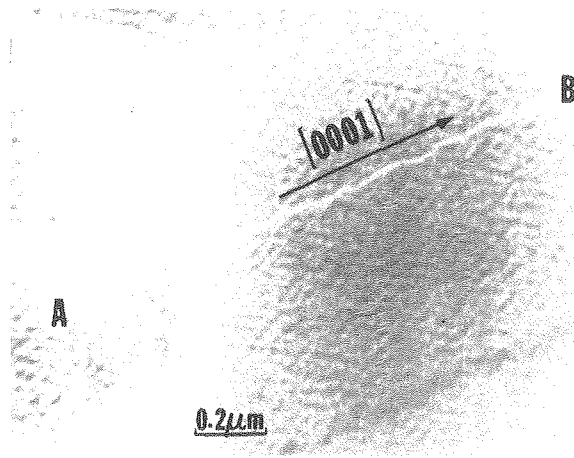


Fig. 2. Fresnel micrograph from a step aged $\text{Sm}_2(\text{Co-Cu-Fe-Zr})_{17}$ alloy showing the domain walls in an overfocussed condition. Note the wavy nature of the domain wall AB which tries to remain along the 1:5 phase preferentially. (XBB 795-6614)

domain wall is seen to be wavy in nature and lies parallel to the c-axis (easy axis). Careful comparison of these images with the focussed images shows that the wavy domain wall in Fig. 2 follows the cell boundaries. This is the case if the boundary phase is magnetically softer/harder than the cell interiors so that the domain walls are preferred energetically to lie in or near the 1:5 phase.

It can be concluded that the coercivity is controlled by domain wall motion and not by single domain particles in this magnet.² The high coercivity is a result of the changes in the chemical composition between the two phases during step tempering. It is suspected that the initial phase separation in this R-Co system proceeds via a mechanism where the two phases first separate out and any further step aging only enhances the composition differences. Further work in the characterization of the microstructure produced during aging of the R-Co alloys and the domain wall configurations in the partially aged alloys is necessary to discuss these points further, and is currently in progress.

- †Materials provided by TDK Electronics Co., Tokyo.
 ‡Brief version of LBL-9927.
 1. T. Ojima, S. Tomizawa, T. Yoneyama and T. Hori, IEEE Trans. MAG 13, 1317 (1977).
 2. R. K. Mishra and G. Thomas, Microstructural Characterization of Rare Earth-Cobalt Magnets, in Proc. IV International Workshop on Rare Earth-Co Permanent Magnets, May 22-24, 1979, Hakone, Japan, publ. by the Soc. of Non-Traditional Technology, p. 301.

2. HIGH PERMEABILITY Ni-Zn-Co FERRITES[†]

R. K. Mishra

Heat treatment of fabricated ferrites has been shown to affect the microstructures and properties, e.g. in LiFe_5O_8 , NiFe_2O_8 ,¹ $\text{NiZrCoFe}_2\text{O}_4$ ² etc. In the case of Fe-excess $\text{NiZrCoFe}_2\text{O}_4$ it has been established that when this material is annealed both above and below the Curie temperature ($\sim 470^\circ\text{C}$), the concentration of Fe^{+2} ion in the material is reduced. This in turn changes the permeability and the μQ factor. Formation of small precipitates and/or segregation of a grain boundary phase during the annealing has been suggested as factors affecting the changes in the permeability and μQ . The purpose of the present study is to examine the microstructure using TEM so as to determine the nature of the precipitates and the grain boundary segregates which may be affecting the high permeability properties.

Results show that, in specimens that are annealed at or above 425°C , the concentration of Fe^{+2} ions is significantly reduced and the d.c. resistivity increases. However, electron microscopy does not show any grain boundary phase in specimens annealed below 550°C . Also precipitates which might have formed during annealing are not present in samples aged below 550°C . In addition, when examined at 100 kV, samples annealed above 425°C exhibit a reduction reaction resulting in the precipitation of Ni on the free surfaces as shown in Fig. 1.

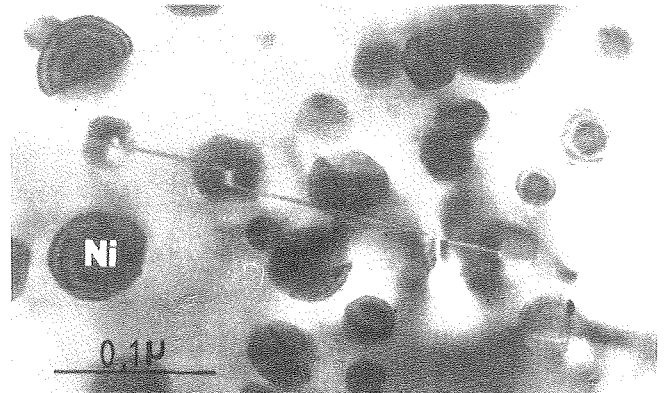


Fig. 1. Precipitates of Ni on the surfaces of (NiZnCo) ferrite, formed in the microscope due to beam heating. (XBB 794-5660)

The reduction reaction is similar to the one that occurs upon heating this material in a reducing atmosphere. It is seen that the ease of the reduction reaction depends on the amount of Fe^{+2} ions and the internal strain arising due to the oxidation of Fe_3O_4 to $\lambda\text{-Fe}_2\text{O}_3$ during annealing treatments. Thus the changes in μ and μ_0 are critically dependent on the internal stress and Fe^{+2} content rather than the presence of precipitates or grain boundary phases.

* * *

[†]Brief version of LBL-6675.

1. R. K. Mishra and G. Thomas, Proc. Magnetism Magnetic Materials 1976, Eds. J. Becker, G. Lander and F. Luborsky (1976) p. 66.
2. M. Dixon, T. S. Stakelon and R. C. Sundahl, IEEE Trans. Magnetics 13, 1351 (1977).

3. HIGHER PERMEABILITY (Mn,Zn) FERRITES[†]

R. K. Mishra and G. Thomas

The microstructures of six differently processed commercial grade MnZn soft ferrites have been studied using transmission electron microscopy and microanalysis, and the microstructural features correlated with the magnetic properties. Special emphasis has been placed on the grain boundaries. The permeabilities range from 1,200 to 18,000 and loss factors ($\tan\delta/\mu$) from 1.0×10^{-6} to 13.7×10^{-6} at 50 kHz. The pore distribution in these ferrites was quite diverse although the total porosities are nearly the same. In samples of low μ , fine precipitates of $\alpha\text{-Fe}_2\text{O}_3$ or MnO_2 (as detected by electron diffraction) were found associated with intergranular pores. In Sample 3 dark field and lattice imaging analyses near grain boundaries revealed the presence of a non-crystalline phase 30-50 Å wide and forming pockets at grain boundary junctions (Fig. 1). These were not detected in Sample 6.

X-ray microanalysis by STEM showed Ca and some Si segregation at the boundaries in Sample 3 [Fig. 2(a)], indicating that the glassy phase is probably a calcium silicate. This would be expected also from the chemical composition. Figure 2(b) shows little variation in Zn, Mn or Fe. In Sample 6 where no glassy phase could be seen, x-ray microanalysis (Fig. 3) failed to detect any Ca or Si.

Since no Ca is detected in Sample 6, either at the grain boundaries or in the grain interiors, one can conclude that Ca is distributed uniformly in the grains. In any case, the Ca concentration is below the detection limit of STEM.

Lattice imaging in conjunction with optical microdiffraction reveals that the lattice parameter is larger near the grain boundaries in the case of Sample 3 and not so in the case of Sample 6. An example of measurements for Sample 3 is shown



Fig. 1. Lattice image using 111 reflections simultaneously in two grains of Sample 3. The absence of fringe patterns at the edge-on grain boundary along A-A confirms the result of Fig. 3 that a non-crystalline phase exists at this boundary.

(XBB 795-7452)

in Fig. 4. The results indicate that the segregation of calcium is responsible for this effect. Such a change in lattice parameter introduces strain and hence stresses near the boundaries, which in turn affects magnetostriction and magneto-crystalline anisotropy and hence reduces μ . In the present case, lattice distortion due to Ca segregation and the presence of the glassy phase at the grain boundaries is thought to be responsible, in part, for the decreased value of μ in the case of Sample 3.¹ Thus, the large values of μ obtained in Sample 6 through processing control and use of higher purity powders can be attributed partly to the elimination of glassy phases and stress/strain gradients at grain boundaries.

We thank TDK Electronics, Co., Tokyo for providing samples and many helpful discussions.

* * *

[†]Brief version of LBL-9710.

1. G. Thomas, H. Tsunekawa, A. Nakata, T. Kamijo and K. Okutani, Microstructure and Properties of Commercial Grade Manganese Zinc Ferrites, IEEE Trans. Magnetics, 1980, in press, LBL-9710.

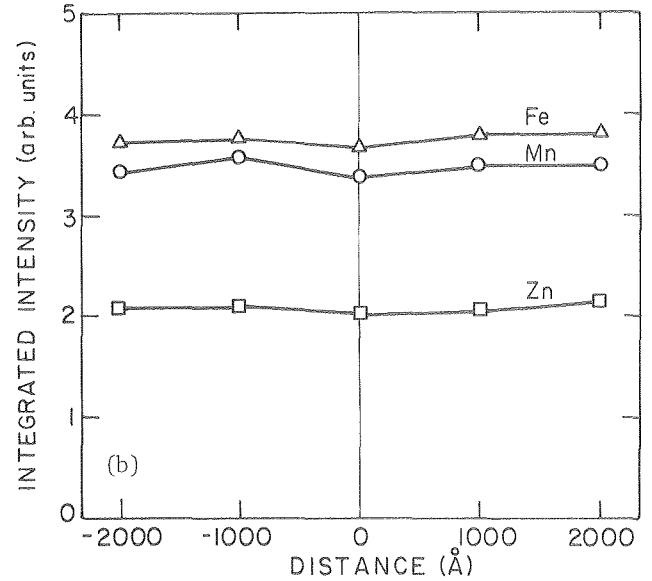
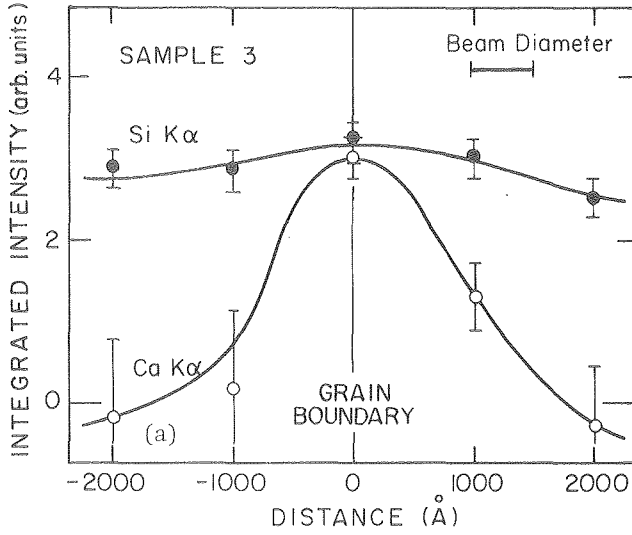


Fig. 2. (a) X-ray microanalysis using a STEM instrument across a grain boundary such as shown in Fig. 3 showing the presence and microsegregation of calcium and to some extent silicon; (b) As for Fig. 2(a) but for the elements Fe, Mn, Zn showing no detectable segregation.

[(a) XBL 795-6375; (b) XBL 794-6140]

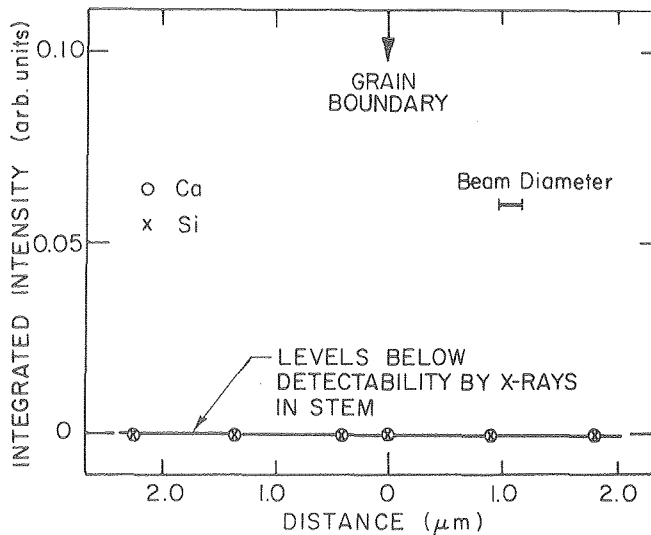
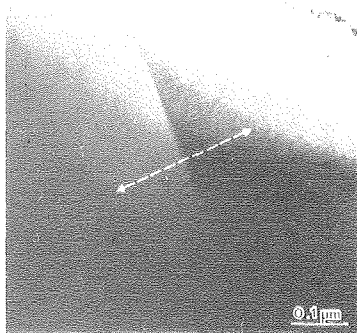


Fig. 3. X-ray STEM microanalysis across the grain boundary shown above for Sample 6. There is no glassy phase and no Ca nor Si could be detected. This is typical of Sample 6. (XBB 795-7386)

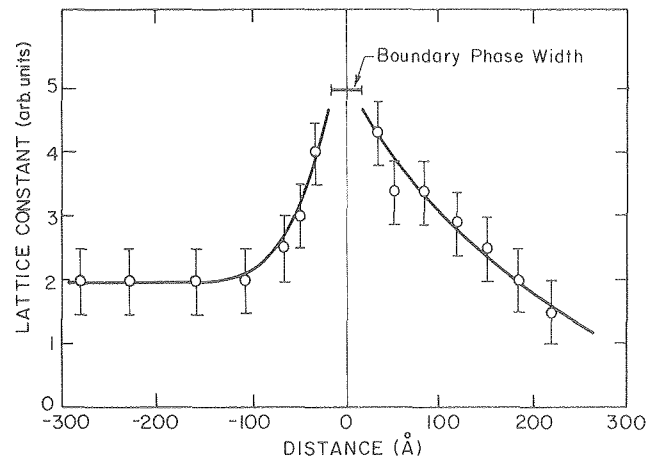


Fig. 4. Microdensitometer traces across the (111) lattice fringes. Notice the large increase in lattice parameter as the glassy phase is approached, indicating a concentration gradient and strain exists in these regions. Comparison to Fig. 2(a) indicated this effect is due to calcium segregation. (XBL 794-6141)

4. BUBBLE GARNET FILMS[†]

R. K. Mishra

Ferrimagnetic garnets are prime candidates for thin film bubble memory devices. For such applications, single crystal magnetic garnet films are epitaxially grown on nonmagnetic garnet substrates such as $\text{Cd}_3\text{Ca}_5\text{O}_{12}$ (GGG). Nonuniformity in the film composition with film thickness, segregation of certain alloying elements (added in order to tailor the magnetic properties and lattice parameters) in the film and related precipitation are some of the current practical problems. In addition, the nature of the epifilm-substrate interface region whose microstructure in an electron microscope scale (i.e. at a high enough resolution where structural defects and local compositional inhomogeneities can be identified) has not been characterized, is responsible for another kind of problem that affects static bubble properties as well as the bubble mobility.

LPE films grown on GGG substrate and with a nominal composition of $(\text{EuLu})_3\text{Fe}_5\text{O}_{12}$ containing Ca and Ge have been examined so far.

Chemical microanalysis in the STEM shows that the elemental composition profile across the boundary varies abruptly in some regions and smoothly in some other regions of the interface. TEM analysis shows the existence of interfacial dislocation network in some regions of the interface. Also evidence of how the matrix dislocations get replicated through the epifilm are seen. Work is in progress to completely characterize the interface structure and study the origin of growth induced anisotropy in the magnetic film.

* * *

[†]Brief version of LBL-8215.

5. MAGNETIC PROPERTIES OF PLASMA DEPOSITED IRON-IRON OXIDE THIN FILMS

R. K. Mishra and D. Hess

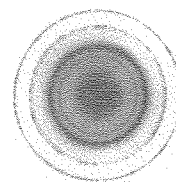
Magnetic thin films have been of great interest for many years. The large number of applications range from magnetic recording tapes to magnetic discs for bulk computer memories to magnetic recording heads, and finally to the more recent magnetic bubble devices. In the past, magnetic films have been deposited by techniques such as vacuum evaporation, electro-deposition, cathode sputtering etc. Plasma enhanced deposition (PED) has generated considerable recent interest. PED can be used to form compounds of various compositions at low temperatures in the plasma environment by controlling gas pressure, gas dynamics, substrate temperature, rf power, rf frequency, electrode spacings etc.

In the present work, thin films of iron and iron oxide are deposited by PED from an iron pentacarbonyl source in a glow discharge parallel plate reactor. Chemical analysis of the films show that the carbon and oxygen contents of the films increase with increasing rf power. Small crystallites

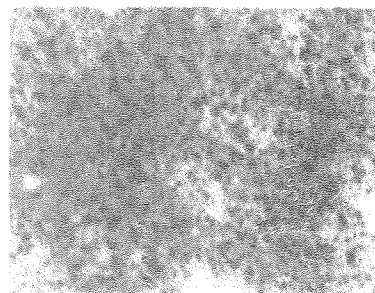
(30-300 Å) of α -Fe and iron oxide (Fe_3O_4 or γ - Fe_2O_3) are formed at substrate temperatures of 150°C or above (Fig. 1). The concentration of α -Fe crystallites increases with increasing substrate temperature (rf power).

Films deposited on substrates held at temperatures below 150°C, do not exhibit any hysteresis loop. Square hysteresis loops ($B_r/B_s \sim 1$) are observed for a substrate above 30 watts (Fig. 2). The magnetization, M , is found to lie in the film plane. The specific magnetization at saturation decreases from 2 to 0.4 weber-meter/kg by increasing the rf power from 10 to 100 watts. The coercive force ranges from 5 to 45 Oe, increasing with both increasing substrate temperature and increasing rf power (Fig. 3). Work is in progress to explain the changes in magnetic properties from chemical and morphological/microstructural considerations and establish these relationships.

(a)



(b)



(c)

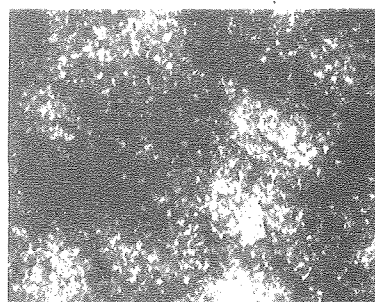


Fig. 1. Transmission electron micrographs for a film deposited onto NaCl at 300°C, 10 watts power. (a) SAD pattern showing the diffraction rings from α -Fe and spinel oxides (2 inner-most rings are from oxide only and the third ring is from α -Fe only). (b) BF image showing the particles of both α -Fe and iron oxide. (c) α -Fe dark field image showing the α -Fe crystallites. Magnification bar = 2000 Å.

(XBB 790-13250)

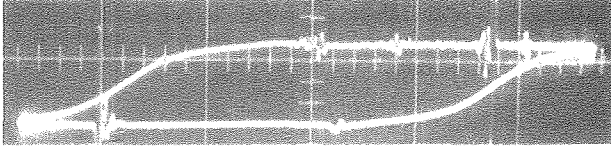


Fig. 2. The hysteresis loop resulting from a deposit run at 300°C and 100 watts power. ($H_c = 450e$, $Br/B_s = 1$, $\sigma_s = 0.7 \times 10^{-4}$ w-m/kg). (XBB 790-14173)

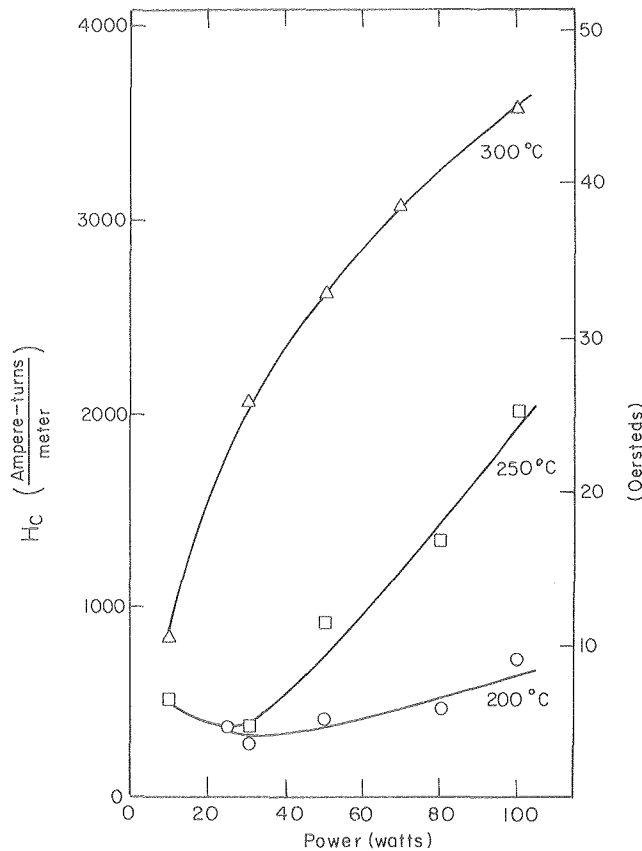


Fig. 3. The coercive force vs. substrate temperature and rf power level. (XBL 7910-7232)

RESEARCH PLANS FOR CALENDAR YEAR 1980

Alloy Design: Steels. Although it is clear that retained austenite is beneficial to strength and toughness, the detailed mechanism(s) for this are not yet established. The research work now being done will examine the question of austenite stability and crystallography of austenite decomposition with regard both to toughness and temper martensite embrittlement. For the latter work, modifications of the Fe/Cr/Mn/C "qua-tough" alloy with the carbide formers W and V will be studied.

The crystallography of the lath martensite in the whole range of steels being studied is under investigation with particular attention focused on orientation relationships and habit. Our model

for the transformation is quite speculative and requires detailed microelectron diffraction studies, e.g. by convergent beam methods now that we have a TEM-STEM microscope available.

A new program has started on fatigue and wear resistance of both the medium carbon (qua-tough) and low carbon (dual phase) classes of alloy developed in my group. The relationship between friction wear resistance and retained austenite will be established and the mechanisms of wear investigated. This aspect is of particular importance due to the great interest being expressed in the "qua-tough" steels by the mining industries. The fatigue program will concentrate particularly on mechanisms of crack propagation in our experimentally developed steels. In dual phase steels, current research is concerned with fracture behavior and improvement of low temperature toughness, e.g. by grain refinement. The role of carbide forming elements, especially vanadium, is being studied, in a collaborative effort with Sandia Laboratories, to obtain a better understanding of the potential of dual phase steels for geothermal applications (e.g. drill pipe casings). The corrosion properties will be studied at Sandia and the microstructure-ferrite-fracture research done here.

Another program in the dual phase alloy design project is concerned with increasing the hardenability of low carbon dual phase steels. In particular, alloying additions of boron, and cooling rate experiments from the ($\alpha+\gamma$) field are being studied. The latter is of interest for potential applications of dual phase steels for civil construction.

An analytical TEM/STEM facilities will be utilized for monitoring the solute and impurity distributions in all of the alloy design programs (NSF supported). Such information is essential for understanding such problems of austenite stability, relative properties of ferrite and martensite in dual phase steels. A critical, difficult problem being studied is a comparison of lattice imaging and microanalytical (spectroscopy) methods on the same alloys, e.g. the use of ELS for analysing light elements (C, N, B, etc.)

Magnetic Materials. The rare earth permanent magnet program involves a fundamental study of the phase transformations in Sm-Co-Cu-Fe-Zr alloys with particular emphasis on the initial phase separation and local chemical fluctuations during step aging. It is still not clear whether this decomposition is spinodal or not.

In amorphous alloys research started in 1979, studies of local magnetic fluctuations and chemical fluctuations are being carried out on Fe-Co-B-Si alloys annealed below the recrystallization temperature.

In ceramic magnets, boundary mobility is being investigated in Mn Zn ferrite containing CaO and SiO₂ as impurities. The permeability and other properties depend sensitively on localized segregation-strain effects. The emphasis is to manipulate the microstructure and remove unwanted segregation to optimize permeability.

In a collaborative program with Dr. D. Hess studies of the microstructures of plasma enhanced deposition (PED) films and the control of the magnetic properties H_c , B_s and $(BH)_{max}$ in PED films by alloying to change these microstructures are being carried out on iron.

The research on spinodal Fe/Cr/Co magnets has now been completed and no further work is currently planned for these alloys.

Ferroelectric Materials. Lead zirconate titanate (PZT) is a commercially important material for transducer applications. PZT can be sintered to a high density if 3 wt.% of excess PbO is added during sintering. The piezoelectric properties also improve upon adding small amounts of MnO₂. The role of these additives has not been conclusively established and a fundamental understanding of the densification and aging mechanisms in PZT is lacking. Thus, the current program involves detailed microstructure-property characterizations of this material.

Nitrogen Ceramics. In the nitrogen ceramics program sponsored by NSF, further characterization of commercial silicon nitrides obtained from Toshiba (Y₂O₃ treated) and Shinagawa (reaction sintered) is continuing to synthesize those intergranular phases which may be present. A new research program consisting of studies of the crystallization of nitrogen glasses has also been initiated. The research involves high resolution spatial and spectroscopic analyses of these ceramics using TEM/STEM techniques.

Varistors. The program on ZnO varistors has been completed and no further work is currently planned.

6. G. Thomas, R. Stevenson and D. J. Bailey, "High Strength Low Carbon Sheet Steel by Thermo-mechanical Treatment: 11, Microstructure," *Met. Trans. A* 10A, 57 (January 1979).

7. O. L. Krivanek, P. Williams, and Yi-Ching Lin, "Direct Observation of Voltage Barriers in Zinc Oxide Varistors," *Appl. Phys. Letts.* 34, (11), 1979 805 (1979).

Other Publications

1. J. Y. Koo, "High Resolution Electron Microscopy of γ' Precipitates," G. W. Bailey, Ed., 37th Annual Proc. Electron Microscopy Soc. Amer., San Antonio, Texas, August 13-17, 1979, p. 534 (1979).

2. O. L. Krivanek, G. Todd and M. F. Sing, "High Resolution Scanning Auger Microanalysis of High-Strength Silicon Carbides," G. W. Bailey, Ed., 37th. Annual Proc. Electron Microscopy Soc. Amer., San Antonio, Texas, August 13-17, 1979.

3. O. L. Krivanek, "Design of a Compact, Medium Resolution Electron Energy Loss Spectrometer, G. W. Bailey, Ed., 37th Annual Proc. Electron Microscopy Soc. Amer., San Antonio, Texas, August 13-17, 1979, p. 530 (1979).

4. M. F. Sung, "Microstructure-Mechanical Strength Relationship in Silicon Carbide," G. W. Bailey, Ed., 37th. Annual Proc. Electron Microscopy Soc. Amer., San Antonio, Texas, August 13-17, 1979, p. 630 (1979).

5. O. L. Krivanek, "Cross-Sectional Electron Microscopy of Electronic Interfaces," 37th. Annual Proc. Electron Microscopy Soc. Amer., San Antonio, Texas, August 13-17, 1979, p. 684 (1979).

6. G. Thomas and M. J. Goringe, Transmission Electron Microscopy, Wiley-Interscience (1979).

7. G. Thomas, B. V. N. Rao and M. Sarikaya, "High Resolution TEM Investigation of Austenite in 'lath': Martensite Steels," G. W. Bailey, Ed., 37th. Annual Proc. Electron Microscopy Soc. Amer., San Antonio, Texas, August 13-17, 1979, 538 (1979).

8. G. Thomas, J. Y. Koo, J. W. Morris, Jr., and K. M. Chang, "Coupled γ' and γ " Precipitation in Fe-Ni Base Austenites," G. W. Bailey, Ed., 37th. Annual Proc. Electron Microscopy Soc. Amer., San Antonio, Texas, August 13-17, 1979, p. 642 (1979).

9. G. Thomas and R. K. Mishra, "Microstructural Characterization of Rare Earth-Cobalt Magnets," 4th. International Workshop in Rare-Earth Cobalt Magnets, Hakone, Japan, May 1979, LBL-9927.

10. G. Thomas and J. Y. Koo, "Developments in Strong, Ductile Duplex Ferrite-Martensitic Steels," AIME Symposium, New Orleans, LA, February 18-22, 1979, LBL-8650.

11. T. M. Shaw and G. Thomas, "An Electron Microscopy Study of Crystallography and Phase Relationships in the Be₃N₂ - BeSiN₂ System," *Journal of Solid State Chemistry*, in press.

1979 PUBLICATIONS AND REPORTS

Refereed Journals

1. G. Thomas and R. K. Mishra, *Electron Microscopy of Ferrites*, *J. Am. Ceram. Society* 62, 1979, LBL-6675.

2. G. Thomas, M. Carlson and B. V. N. Rao, "The Effect of Austenitizing Temperature Upon the Microstructure and Mechanical Properties of Experimental Fe/Cr/C Steels," *Met. Trans. A* 10A, 1273, LBL-8462.

3. G. Thomas and U. Dahmen, "Significance of Oxygen on Interstitial Ordering in Tantalum (The Ta₆₄C Artifact)," *Scripta Met.* 13, 527 (1979), LBL-8544.

4. G. Thomas, J. Y. Koo and B. V. N. Rao, "Designing High Performance Steels with Dual Phase Structures," *Metal Progress* 116, 66 (1979), LBL-8922.

5. G. Thomas, S. Jin, J. W. Morris, Jr., Y. L. Chen and R. I. Jaffee, "An Investigation of Transformation Strengthening in Precipitation-Hardened Fe/Ni Austenite," *Met. Trans. A* 9A, 1625 (1978).

LBL Reports

1. U. Dahmen and G. Thomas, "A Study of Interstitial Ordering in Tantalum by Transmission Electron Microscopy," LBL-7640.
2. G. Thomas, "Duplex Steels," LBL-7675.
3. Y. Belli, K. Kubarych, M. Okada, R. Mishra and G. Thomas, "Influence of Microstructure on the Magnetic and Mechanical Properties of Fe-Cr-Co Hard Magnets," LBL-8384.
4. O. L. Krivanek, G. Todd and M. F. Sung, "High Resolution Scanning Auger Microanalysis of High-Strength Silicon Carbides," J. Amer. Ceramic Soc., in press, LBL-10045.
5. O. L. Krivanek and J. M. Mazur, "The Structure of Ultra-Thin Oxide on Silicon," Applied Phys. Letts, in press, LBL-10046.
6. G. Thomas and M. Raghavan, "Effect of Substructure on the Mechanical Properties of Fe/Ni/Co/C Alloys," Met. Trans., in press, LBL-8015.
7. G. Thomas and B. V. N. Rao, "Structure-Property Relations and the Design of Fe/4Cr/C Base Structural Steels for High Strength and Toughness," Met. Trans., in press, LBL-8064.
8. G. Thomas and Y. L. Cheng, "Structure and Mechanical Properties of Fe/Cr/Mo/C Alloys with and without Boron," Met. Trans., in press, LBL-8310.
9. G. Thomas and T. M. Shaw, "An Electron Microscopy Study of Crystallography and Phase Relationships in one Be_3N_2 - BeSiN_2 System," J. Solid State Chem., in press, LBL-8474.
10. G. Thomas and K. H. Westmacott, "The Role of Environmental Conditions on In-Situ Experiments in the High Voltage Electron Microscope," Proc. of the Halle Conference, Germany, April 1979, in press, LBL-8793.
11. G. Thomas, J. Y. Koo and M. Raghavan, "Compositional Analysis of Dual Phase Steels by Transmission Microscopy," Met. Trans., in press, LBL-9014.
12. G. Thomas and B. V. N. Rao, "Transmission Electron Microscopy Characterization of Dislocated "lath" Martensite," International Conference on Martensitic Transformation '79, Boston, MA, June 1979, LBL-9058.
13. G. Thomas and K. Westmacott, "The Role of Environmental Conditions in In-Situ Experiments in the High Voltage Electron Microscope," Crystal Research and Technology, in press, LBL-9144.
14. G. Thomas and B. V. N. Rao, "The "Lath" Martensite Transformation in Steels," Met. Trans., in press, LBL-9337.
15. G. Thomas, J. Y. Koo and M. J. Young, "On the Law of Mixtures in Dual-Phase Steels," Met. Trans., in press, LBL-9457.
16. G. Thomas, "Some Developments in Electron Microscopy Applications in Metals and Ceramics at U. C. Berkeley," 11th. USSR National Conference on Electron Microscopy, Tallinn, Estonia SSR, October 17-19, 1979, in press, LBL-9486.
17. G. Thomas, B. V. N. Rao and J. Y. Koo, "Mechanical Behavior of Dual Phase Steels with Strong Phase Martensite," U. S. Japan Conference Mechanical Properties of Martensite, June 15-17, LBL-9508.
18. G. Thomas and J. Y. Koo, "Metallurgical Factors Controlling Impact Properties of Two Phase Steels," Scripta Met., in press, LBL-9535.
19. G. Thomas, R. K. Mishra, H. Tsunekawa, A. Nakata, T. Kamiyo and K. Okutani, "Microstructure and Properties of Commercial Grade Manganese Zinc Ferrites," IEEE Trans. MAG 1980, in press, LBL-9710.
20. G. Thomas, P. Williams, O. L. Krivanek and M. Yodogaiva, "Microstructure-Property Relationships of Rare Earth-ZnO Varistors," submitted to J. Applied Physics, LBL-9805.
21. P. K. Costello, "Design of Duplex Low Carbon Steels with Carbide Forming Elements," M.S. Thesis, LBL-8628.
22. U. Dahmen, "Microstructures and Phase Transformations in Interstitial Alloys of Tantalum," Ph.D. Thesis, LBL-8661.
23. P. Williams, "Microstructure-Property Relationships of a Zinc Oxide Varistor Material," M.S. Thesis, LBL-8991.
24. T. J. O'Neill, Jr., "Mechanical Properties and Microstructure of Dual Phase Steels Containing Silicon, Aluminum and Molybdenum," M.S. Thesis, LBL-9047.
25. B. Steinberg, "The Effects of Air Melting on Fe/.3Cr/.5Mo/2Mn and Fe/.3C/.5Mo/2Ni Structural Alloy Steels," M.S. Thesis, LBL-9013.
26. M. F. Sung, "Microstructure, Sintering and Strength of Polycrystalline SiC," M.S. Thesis, LBL-9257.
27. M. Sarikay, "Alloying and Heat Treatment Optimization of Fe/Cr/C for Improved Mechanical Properties," M.S. Thesis, LBL-9620.
28. T. H. Rabe, "The Effect of Air-Cooling Heat Treatments on the Structure and Properties of Fe/4Cr/0.3C/2Mn Alloy," M.S. Thesis, LBL-9262.
29. K. Kubarych, "The Effects of Composition and Heat Treatments on the Strength and Ductility of Fe/Cr/C Alloys," Ph.D. Thesis, LBL-9941.

Invited Talks

1. G. Thomas, "A Study of Interstitial Ordering in Tantalum by Transmission Electron Microscopy," TMS-AIME Fall Meeting, St. Louis, MS, October 15-18, 1979.

2. G. Thomas, "On the Role of Electron Microscopy in Mineral Engineering Problems," Exxon Research and Engineering Company, Linden, New Jersey, January 4-5, 1979.
3. G. Thomas, "Principles and Applications of TEM in Materials Sciences," National Tsing Hua University, January 7-February 10, 1979.
4. G. Thomas, "Design of Structural Steels," National Tsing Hua University, January 7-February 10, 1979.
5. G. Thomas, "Current and Future Developments in TEM (High Resolution and High Voltages)," National Tsing Hua University, Taiwan, January 7-February 10, 1979.
6. G. Thomas, "Microstructure and Properties of Duplex Low Carbon Steels," AIME Annual Meeting, New Orleans, LO, February 18-22, 1979.
7. G. Thomas, "Morphology, Crystallography and Formation of Dislocated Lath Martensite "Lath: Martensite or Bainite?" 108th. AIME Annual Meeting, New Orleans, LO, February 18-22, 1979.
8. G. Thomas, "Application of Electron Microscopy in Materials Science," Stanford University, Stanford, CA, March 2, 1979 (special meeting to inaugurate the new TEM laboratory at Stanford University).
9. G. Thomas, "Developments in Characterizing Materials," ASM Seminar, Monterey, CA, April 28-29, 1979.
10. G. Thomas, "Application of High Resolution TEM in Materials Science," Ninth Western Regional Meeting of Electron Microscopists, Palm Springs, CA, April 30-May 3, 1979.
11. G. Thomas, "The Microstructure-Magnetic Properties Relationships in Magnetic Materials," Rare Earth-Cobalt Permanent Magnets Workshop, Hakone, Japan, May 21-29, 1979.
12. G. Thomas, "Crystallography, Morphology and Structure of Lath Martensites," International Conference on Martensitic Transformations (ICOMAT-79), Boston, MA, June 25-29, 1979.
13. G. Thomas, "Grain Boundaries in Ceramics," presented at the Gordon Conference, Wolfboro, NH, July 30-August 3, 1979.
14. G. Thomas, "Very High Resolution Studies of Alloys and Ceramics," Electron Microscopy Society of America and Microbeam Analysis Society Conference, San Antonio, TX, August 8-11, 1979.
15. G. Thomas, "The New World of Duplex Structural Steels," keynote address at South East Iron and Steel Institute, Kaohsiung, September 10, 1979.
16. G. Thomas, "Modern Electron Microscopy in Materials Science," keynote address of the 1st. National Electron Microscopy Conference, Taipei, Taiwan, September 3-19, 1979.
17. G. Thomas, "Materials Science" keynote lecture at the Electron Microscopy Conference in Tallinn, USSR Academy of Sciences, Moscow, Tallinn, October 12-20, 1979.

b. Atomic Resolution Microscopy*

R. Gronsky and G. Thomas, Investigators

Introduction. The objective of this program is the direct imaging of atoms in solids using simply-prepared thin specimens (allowing electron "transparency") and highly sophisticated electron optics. At the heart of the program is the Atomic Resolution Microscope (ARM), a unique instrument which is to be manufactured by one of the large commercial suppliers of transmission electron microscopes to specifications supplied by LBL. At this writing, the specifications are in the process of final revision and will be released by mid-December 1979.

In the interim before the arrival of the ARM, a number of research projects have been initiated which will derive maximum benefit from the application of atomic resolution imaging. These include the study of coherent transformations with emphasis on incipient interfacial structure, the relationship between grain boundary structure and properties in metallic, ceramic and semiconductor materials, and the theoretical analysis of the imaging capabilities of modern electron-optical systems.

The more advanced of these projects are summarized below.

1. ELECTRON MICROSCOPY OF SPINODAL STRUCTURES AT HIGH RESOLUTION†

R. Gronsky and G. Thomas

Even though theoretical descriptions of the spinodal reaction are highly developed,¹ there are deficiencies in the experimental characterization of spinodal structures which arise from their sampling of rather large specimen volumes. The present work describes a high resolution analytical method which is based upon direct imaging of the modulated lattice.

An alloy of Au-77at.%Ni was chosen for study due to its large difference in component lattice parameters. Specimens were viewed in a [100] zone axis orientation using a Siemens Elmiskop 102 equipped with double tilt-lift goniometer and pointed cathode. Images were formed by the two-beam tilted-illumination method² using the forward-scattered and 002 Bragg-scattered beams. The choice of "optimum" focus setting for imaging of the modulated lattice was reinforced by complementary optical diffractograms.³

A typical lattice image of the decomposed alloy is shown in Fig. 1, clearly revealing the 002 lattice planes at a modulation wavelength of 3 nm

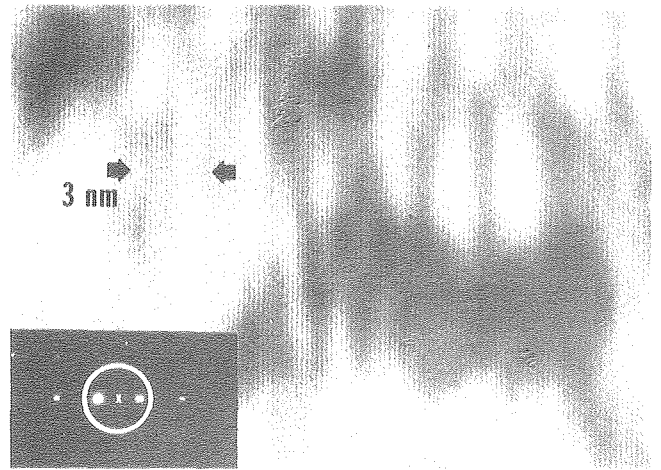


Fig. 1. Lattice image taken under two-beam conditions (shown in inset, x marks the optic axis) of a spinodally decomposed Au-Ni alloy. (XBB 790-14918)

(30 Å). The "amplitude" of the modulation corresponds to the extent of lattice strain reflected in the spacings of the fine fringes, as shown by the plot in Fig. 2. It is emphasized that this information depends critically upon the focus setting of the objective lens, and as Fig. 3 reveals, the structure can be completely misrepresented in an image taken at 240 Å underfocus.

These experimental results show that the range of harmonics present in a modulated microstructure are directly revealed by lattice imaging, but they can also be selectively filtered by the objective lens at controlled focus settings.

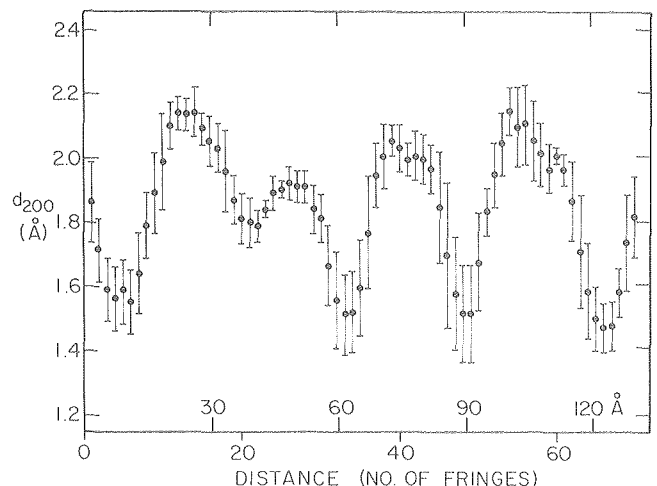


Fig. 2. Plot of d -spacing vs. distance obtained from microdensitometer scan of negative used in Fig. 1. Each point represents an average of 5 measurements with corresponding error indicated. (XBL 757-6648)

* This work was supported by the Division of Materials Sciences, Office of Basic Energy Sciences, U. S. Department of Energy.

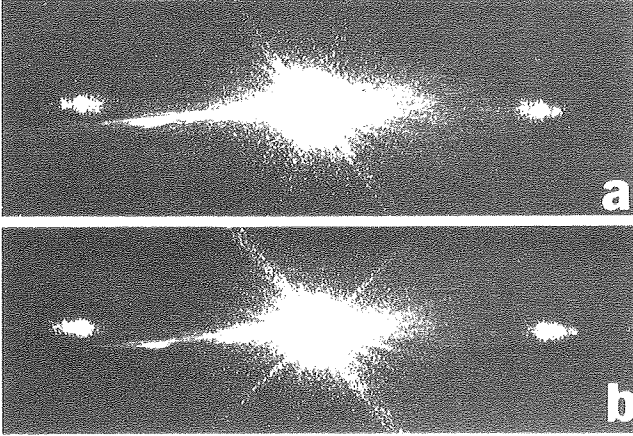


Fig. 3. Optical diffractograms from Au-Ni lattice images taken at (a) optimum focus Fig. 1; and (b) -240 angstroms under focus, which enhances the intensity of the high-angle satellite reflection. (XBB 793-4197)

* * *

[†]Brief version of LBL-8985; AIP Conference Proceedings on Modulated Structures, 1979.

1. J. W. Cahn, Trans. Met. Soc. AIME 242, 166 (1968).
2. W. C. T. Dowell, Optik 20, 535 (1963).
3. R. Gronsky, R. Sinclair and G. Thomas, 34th Ann. Proc. Elec. Mic. Soc. Am., G. W. Bailey, Ed. (Claitor's, New York, 1976) p. 494.

2. THE EFFECT OF LENS ABERRATIONS ON LATTICE IMAGES OF SPINODALLY DECOMPOSED ALLOYS

J. C. H. Spence,[†] J. M. Cowley,[†] and R. Gronsky

The purpose of this study is to propose a choice of objective lens focus setting Δf which allows reliable values of the spinodal amplitude to be estimated from lattice images (see preceding article). This choice is based upon a theoretical consideration of the contrast transfer function of the objective lens independent of any dynamical effects which may modify the relationship between local object and image periodicity.

We consider an idealized case of spinodal decomposition for a single atomic species in which the modulated crystal potential is proportional to:

$$f(x) = \cos(2\pi\mu_0 x + A \sin 2\pi\mu_L x), \quad (1)$$

where A is the amplitude of the modulation and $1/\mu_L$ is its wavelength. The average spacing of the lattice planes is $1/\mu_0$, but the local spacings is $1/\mu_x$ where:

$$\mu_x = \mu_0 + \mu_L A \cos(2\pi\mu_L x). \quad (2)$$

By comparison, the apparent local spacing in the image is $1/\mu'_x$ where:

$$\mu''_x = \mu'_x + \frac{1}{2\pi} \frac{d\chi(\mu_x)}{dx} \quad (3)$$

Here $\chi(\mu)$ is the phase distortion function taking account of lens aberrations, due to spherical aberration, C_S , and extent of defocus, Δf , i.e.,

$$\chi(\mu) = \frac{2\pi}{\lambda} \left(C_S \frac{\lambda^4 \mu^4}{4} + \Delta f \frac{\lambda^2 \mu^2}{2} \right), \quad (4)$$

and μ_x is given by

$$\mu_x = \mu_0/2 + \mu_L A \cos(2\pi\mu_L x). \quad (5)$$

The fractional change in image spatial frequency due to instrumental aberrations is thus

$$F(x) = \frac{1}{2\pi\mu'_x} \frac{d\chi(\mu_x)}{dx}, \quad (6)$$

which is plotted in Fig. 1 for a range of focus settings under typical experimental conditions ($C_S = 3 \text{ mm}$, $\lambda = 0.037 \text{ \AA}$, $\mu_0 = 1/1.8 \text{ \AA}^{-1}$, $\mu_L = 1/30 \text{ \AA}^{-1}$, $A = 1.66$).

It is observed from this result that the spinodal wavelength is correctly reproduced in a lattice image taken at any of the computed focal settings. However, even at the optimum focus setting, the spinodal amplitude is only 90% of the object period at that image point where the distortion is greatest. Hence, in any measurement of spinodal amplitude by this method, it is essential to use images recorded under known conditions of focus and spherical aberration coefficient.

* * *

[†]Department of Physics, Arizona State University, Tempe, Arizona 85281.

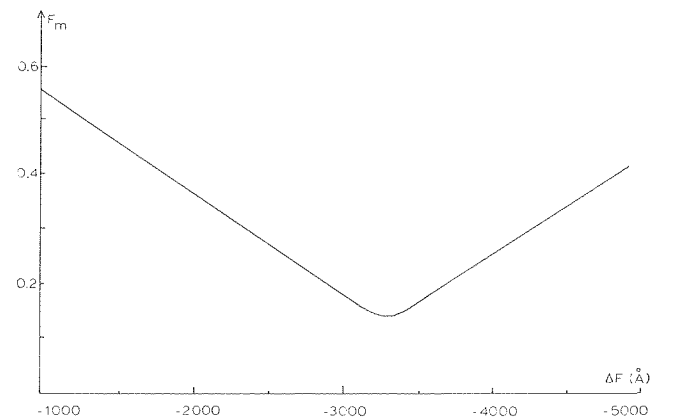


Fig. 1. The maximum value F_m of $F(x)$ given by Eq. (6) plotted as a function of defocus for a lens weakened from the Gaussian image. The minimum occurs at $\Delta f = C_S \lambda^2 (\mu_0/4)$. (XBL 7912-13631)

3. LATTICE IMAGING OF MODULATED STRUCTURES[†]

D. J. H. Cockayne[‡] and R. Gronsky

By including a full dynamical treatment¹ of the elastic diffuse scattering generated by a lattice with slowly varying changes in interplanar spacing and composition, a theoretical description of the appearance of lattice images in modulated structures has been completed. The method of periodic continuation² was used to calculate diffraction patterns and images for a spinodally decomposed Au-77at.%Ni alloy imaged at 100 kV under two-beam conditions.

Reference to Fig. 1(a) shows that the phase angle of the imaged 200 "beam" ($n=0$) including its satellites (at $n = \pm 1$) has a very strong dependence on foil thickness. This is also reflected in the diffracted amplitude Φ shown in Fig. 1(b). Note that the low-angle satellite reflection at $n = -1$, which corresponds to the large interplanar spacings where Au resides in the modulated lattice, increases more rapidly with thickness and has a shorter "extinction distance" than the $n = +1$ satellite reflection. Such a result is in accord with the larger scattering factor of Au compared with that of Ni. It is therefore not surprising that even for a "perfect" lens the image will show fringe spacings very different from the interplanar spacings of the object (Fig. 2). For example, in Fig. 2 although the actual object period consists of 18 fringes, the image shows 19 in one case and 22 in the other. This suggests that there may

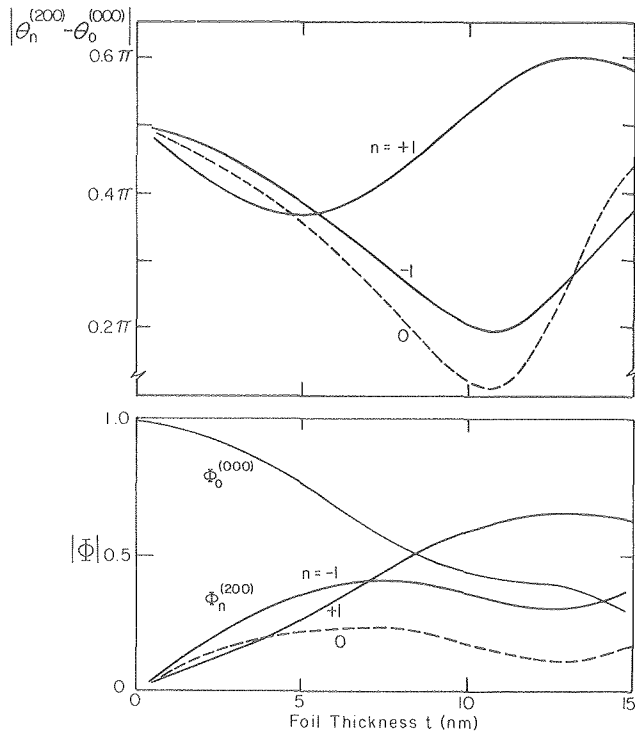


Fig. 1. The variation of phase angle $\theta_n^{(200)}$ and amplitude Φ_n as a function of foil thickness for the n^{th} satellite reflection of the spinodal Au-Ni alloy imaged in Fig. 3. (XBL 797-6612)

be fringe "terminations" present in a lattice image which do not correspond to dislocations, and experimental images (Fig. 3) in fact confirm this prediction.

It is concluded from this analysis that, for

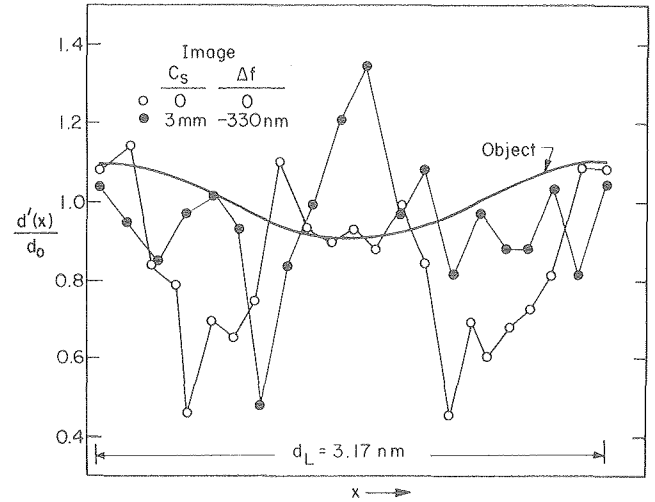


Fig. 2. Calculated fringe spacings $d'(x)$ across one period of a Au-Ni alloy, thickness 120 Å, at optimum defocus for a perfect lens ($C_s = 0$) and imperfect lens ($C_s = 3 \text{ mm}$). (XBL 797-6609)

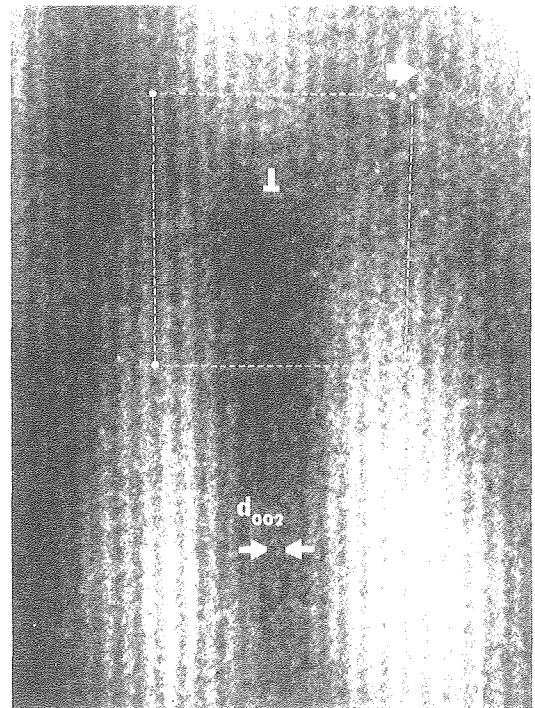


Fig. 3. High-magnification detail of a lattice image of spinodally decomposed Au-Ni showing a Burgers circuit around the 002 planes. An obvious closure failure is indicated and its source identified as the termination of one fringe. (XBB 798-10322)

slowly varying interplanar spacings, the variation of the contrast transfer function $\chi(\mu)$ across the distribution of elastic diffuse scattering must be considered when determining how closely interfringe (image) and interplanar (object) spacings match.

* * *

[†]Brief version of LBL-10158, submitted to Philosophical Magazine.

[‡]Permanent address: Electron Microscope Unit, University of Sydney, N.S.W. 2006 Australia.
1. G. R. Anstis and D. J. H. Cockayne, Acta Cryst. A35, 511 (1979).
2. G. R. Grinton and J. M. Cowley, Optik 34, 211 (1971).

4. GRAIN BOUNDARY PRECIPITATION IN ALUMINUM ALLOYS: EFFECT OF BOUNDARY STRUCTURE[†]

R. Gronsky and P. Furrer[‡]

This is the first of a series of studies on the topic of grain boundary precipitation with the objective of identifying active heterogeneous nucleation sites by their structural characteristics. Specimens of Al alloys were chosen for their commercial significance; and correlations were made between the structural defects, coincidence site lattice (CSL) models, and precipitate morphologies at the grain boundaries studied.

In highly ordered CSL boundaries, the occurrence of grain boundary precipitation was obviously reduced (see Fig. 1). In fact, any precipitates that were observed appeared to be associated with extrinsic grain boundary dislocations. At slight deviations from exact CSL orientations (e.g., Fig. 2), the density of grain boundary precipitates increased, but the tendency for particle alignment suggests an active intrinsic defect structure assisting in the nucleation event.

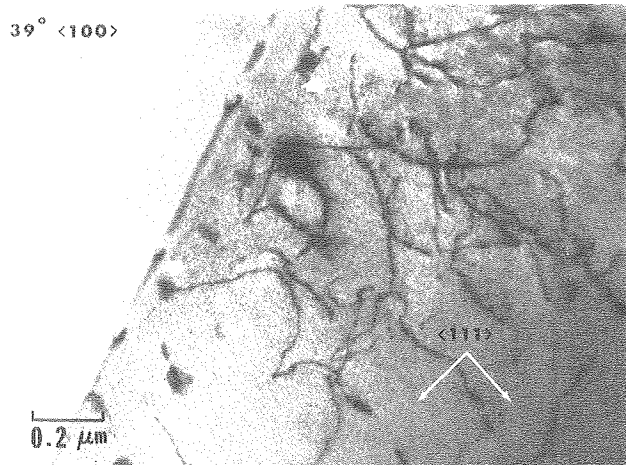


Fig. 1. Bright field TEM image of a $\Sigma = 5$ CSL boundary in an Al-Zn-Mg alloy showing coarse distribution of boundary precipitates connected to extrinsic defects. (XBB 792-2255)

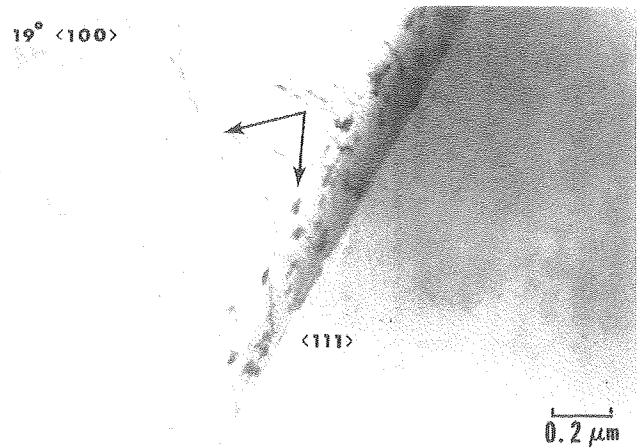


Fig. 2. Near-CSL boundary (3° from $\Sigma = 13$) in the Al-Zn-Mg alloy. The boundary plane is near $\{111\}$, and the particles have aligned themselves along the arrowed close-packed directions. (XBB 792-2251)

These intrinsic defects were found to be most significant when arranged as shown in Fig. 3. At this particular configuration, a segment of the grain boundary has been reoriented into a habit plane relationship with the emerging precipitate. This was found to be the most effective type of

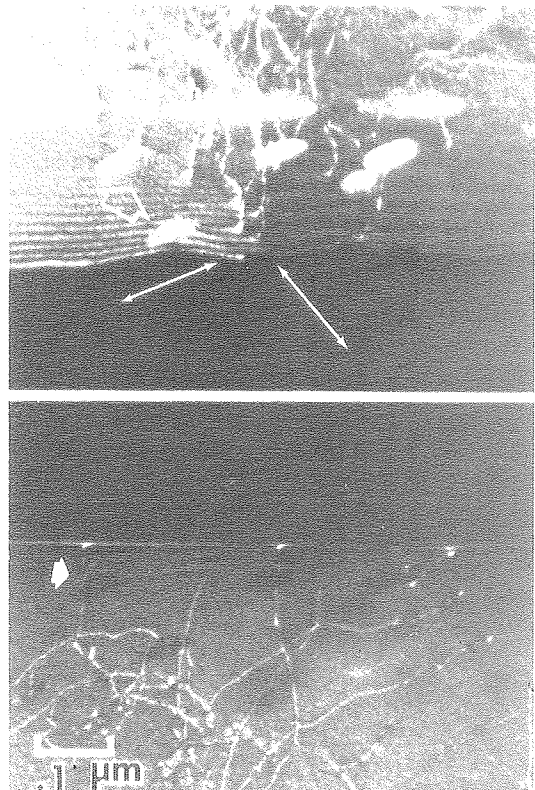


Fig. 3. Weak beam images of contiguous grains in the Al-Zn-Mg alloy. The large open arrow identifies an intrinsic defect array beneath the boundary precipitates which causes a local change in orientation of the boundary plane. (XBB 792-2259)

nucleation site for catalyzing second phase particles and completely dominated the decomposition reaction, even in the presence of a high density of extrinsic defects.

It is concluded that a transition lattice description of those grain boundaries which initiate precipitation reactions is much less useful than a complete characterization of the nonequilibrium defect structures present at such boundaries. Particularly with reference to the control of grain boundary phenomena in Al alloys, the nature and interactions of intrinsic defect arrays is of utmost importance.

* * *

[†]Brief version of LBL-9739, submitted to Metallurgical Transactions.

[‡]Permanent address: Swiss Aluminum Ltd. Research and Development, CH-8212, Neuhausen, Switzerland.

5. DIRECT IMAGING OF GRAIN BOUNDARIES[†]

R. Gronsky

The study of grain boundaries is best accomplished by experimental methods which provide a direct image of local atomic arrangements in the boundary vicinity. While some success has been obtained by indirect methods, i.e. diffraction,¹ there are still considerable problems in interpretation, particularly of the ambiguities present in diffuse scattering from nonperiodic defects. Diffuse scattering is also a major problem in imaging, but can be more readily interpreted with proper care.

The difficulties involved in imaging atomic positions at grain boundaries becomes obvious when it is realized that this requires sufficient breadth in the main contrast transfer interval to accommodate, not only the Bragg peaks from a single perfect crystal, but also the Bragg peaks from a second, misoriented, perfect crystal, and the diffuse scattering arising from the defect structure at the boundary as well. A typical experimental case might be as shown in Fig. 1.

An actual image of a grain boundary is shown in Fig. 2, where the problems outlined above (Fig. 1) are not as severe due to its small misorientation angle. The specimen is silicon and it has been imaged here in a $[110]$ zone such that all $\{111\}$ (and in some regions $\{002\}$ planes) are visible.

The interesting aspect of this image is the crystallography of the large-scale facets in the boundary plane, which follow the traces of all the low-index families. Detailed studies of atomic matching across the boundary show that the regions of greatest disturbance are at the intersections of these ledges and may represent extended core regions of the boundary dislocation net.

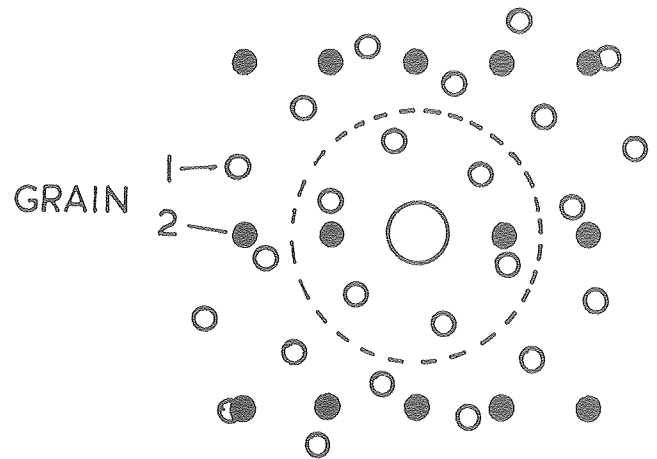


Fig. 1. Schematic electron diffraction pattern of a grain boundary. For the transfer limit shown by dashed lines, all the low index planes in grain 1 will be imaged, denoting atom positions by their intersection. However, only a single set of low index planes from grain 2 will appear and atomic level detail is therefore lost. (XBL 799-11682)

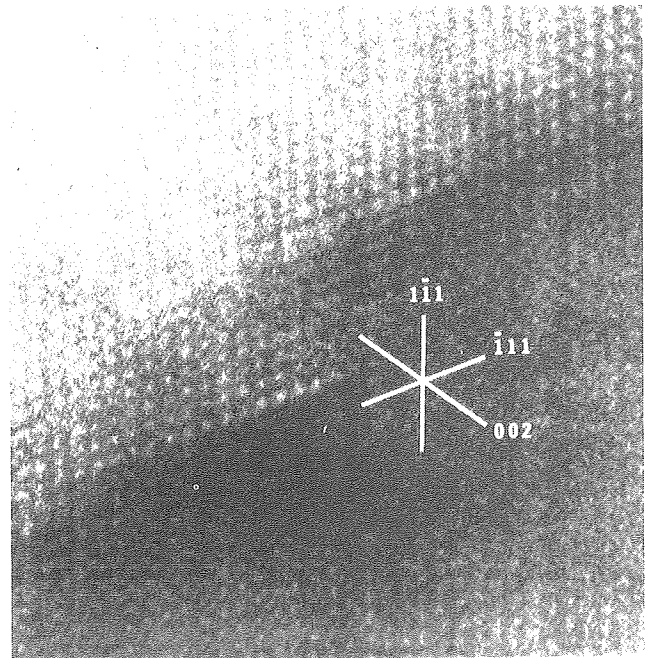


Fig. 2. Structural image of a small angle grain boundary in silicon formed by combining all of the first order reflections within a $[110]$ zone. (XBB 795-7087)

* * *

[†]Brief version of LBL-9779.

1. W. Gaudig and S. L. Sass, *Phil. Mag.* **39A**, 725 (1979).

6. THE STRUCTURE OF ULTRA-THIN OXIDE ON SILICON[†]O. L. Krivanek[‡] and J. H. Mazur[‡]

Ultra-thin oxide layers on silicon are of fundamental interest because they represent the initial stages of silicon oxidation and of practical importance because of their application in MIS solar cells.¹ This study seeks to determine the thickness, uniformity, and morphology of such oxides by high-resolution transmission electron microscopy.

Figure 1 shows an image of a 2300 Å long section of an ultra-thin oxide prepared by oxidation of a p-type 1 Ω - cm (100) Si wafer at 500°C. The specimen thickness in the direction normal to the image plane varies fairly linearly from ~100 Å at left to ~500 Å at right, as can be deduced from the thickness fringes within the crystalline silicon. The oxide thickness is fairly constant across the entire image. However there is evidence of a

periodic undulation with wavelength ~300 Å and amplitude ~3 Å over this surface, as seen more clearly in Fig. 2.

At higher magnification (Fig. 2), the thinnest sections of the oxide layer showed a number of crystalline protrusions where the largest (D) measures ~10 Å high by ~30 Å wide by 20-30 Å deep. The oxide-Al interface parallels the contour of the oxide-Si interface, suggesting that the roughness on the Si side may be due to the initial surface roughness of the silicon prior to its oxidation treatment.

* * *

[†]Brief version of LBL-10046.[‡]Supported by the National Science Foundation, Grant #DMR 77-24022.

1. R. G. Godfrey and M. A. Green, Appl. Phys. Lett. 34, 913 (1979).

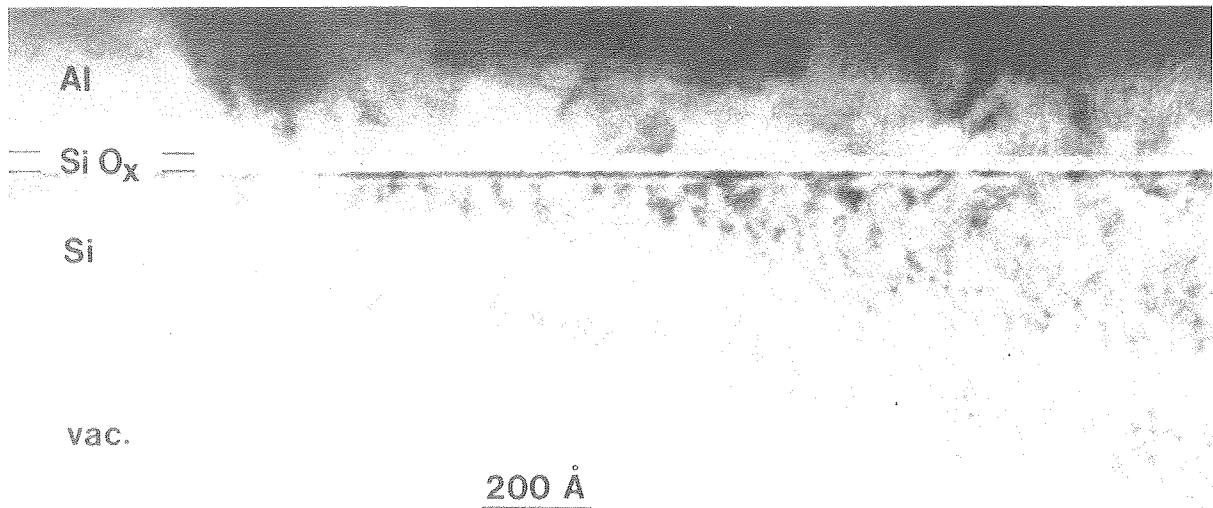


Fig. 1. TEM image of an ultra-thin oxide cross section. (XBB 799-12255)

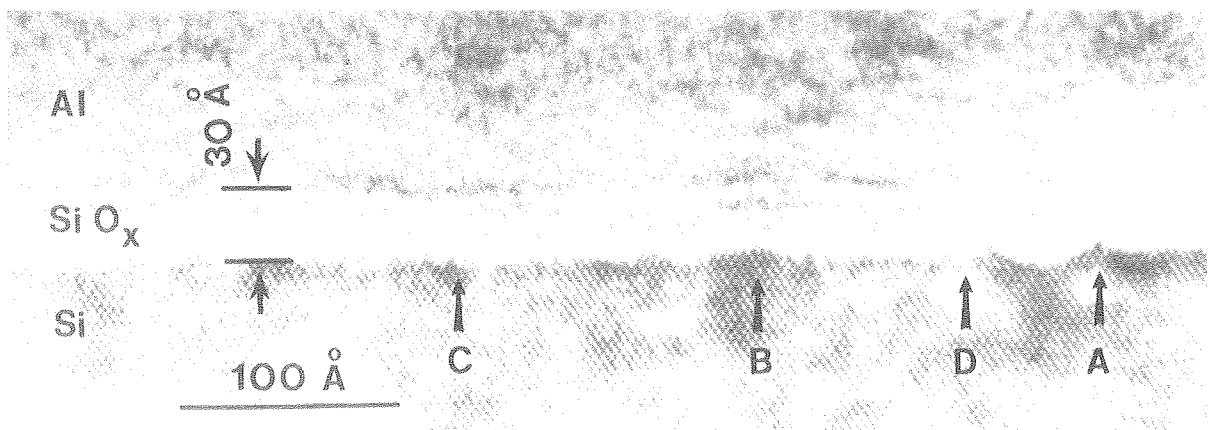


Fig. 2. High magnification image of the same oxide as Fig. 1. Arrows point to individual crystalline silicon protrusions (A,D) and to rough (C) and smoother (B) sections of the interface. (XBB 7910-14708)

7. HIGH-RESOLUTION STUDIES OF G.P. ZONE FORMATION IN Au-Ni ALLOYS[†]

C. K. Wu[‡] and G. Thomas

The Au-Ni alloy system is one of many binary systems in which the supersaturated solid solution may exhibit a multistage precipitation behavior during aging. Spinodal decomposition has been observed and characterized on a localized scale (see article 2), but other mechanisms may be induced by aging outside of the coherent spinodal. In this paper we report the formation of G. P. zones in a Au-15at.%Ni alloy after aging for 1 hour at 150°C.

The first evidence for such zones appears in the diffraction pattern as shown in Fig. 1, where reldods extend continuously along $\langle 100 \rangle$ directions.

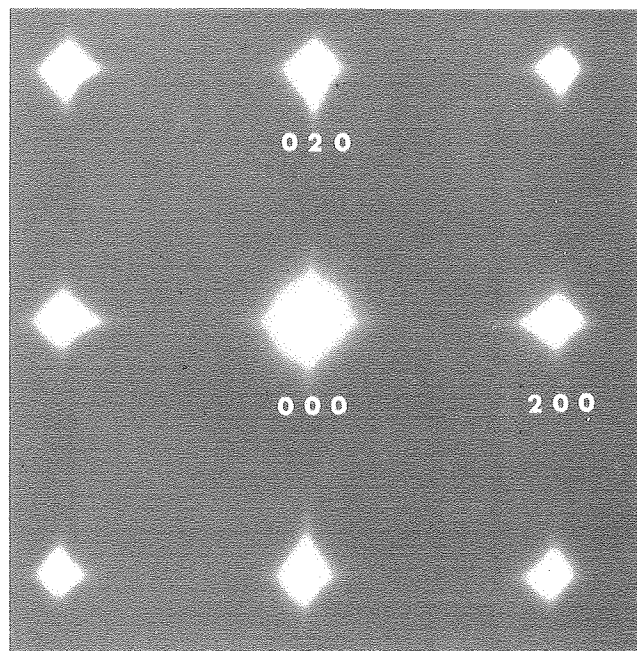


Fig. 1. Electron diffraction pattern, $[001]$ zone. (XBB 780-12895)

These streaks represent the shape transform of the solute atom clusters only 1-2 lattice planes thick along $\{100\}$ planes. These are observed directly in the corresponding lattice image (Fig. 2) taken under two-beam conditions. By direct measurement the zones are 2 to 4 Å thick and ~20 to 40 Å in diameter at this stage of development. They are completely coherent (no terminating fringes are observed) and the lattice shows obvious contraction in the Ni solute-rich cluster regions.

Financial support from NSF, Contract # DMR 78-03894 is gratefully acknowledged.

* * *

[†]Brief version of 37th Ann. Proc. Electron Microscopy Soc. Am., San Antonio, Texas, G. W. Bailey, Ed., (1979) p. 536.

[‡]Present address: Zilog Corporation, 10640 Bubb Road, Cupertino, California 95014.

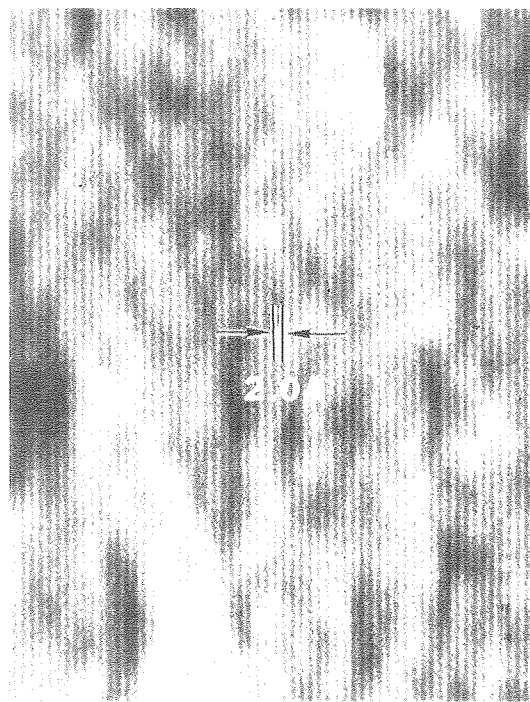


Fig. 2. Lattice image of (200) planes in Au-15at.% Ni alloy showing small zones. (XBB 7710-10851)

RESEARCH PLANS FOR CALENDAR YEAR 1980

Throughout the upcoming year, an expansion in effort is planned for studies of the relationship between grain boundary structure and properties. Results to date have indicated the optimum TEM methods for high resolution studies, and these will be applied in the following areas:

Grain boundary segregation. High resolution imaging, combined with compositional microanalysis in the STEM will be utilized in identifying the most likely boundary structures for segregation as well as the morphology and distribution of segregate species.

Grain boundary fracture. A detailed analysis of grain boundaries as dislocation sources has been initiated. The objective of this study is to also establish correlations with prior boundary structure, structural unit models and fracture behavior.

Grain boundary precipitation. Work will continue in this area with new emphasis placed on the morphological characterization of critical nuclei of the emerging phase.

Work will also continue on the theoretical analysis of atomic resolution microscopy, particularly the imaging of sharp structural discontinuities and non-periodic defect arrays. Simulations will incorporate the instrumental parameters characteristic of new-generation 200 kV microscopes.

1979 PUBLICATIONS AND REPORTS

Refereed Journals

1. R. Gronsky, O. L. Krivanek and G. Thomas, "Very High Resolution Studies of Alloys and Ceramics," 37th Annual Proc. Electron Microscopy Soc. Am., G. W. Bailey, Ed., San Antonio, Texas, 396 (1979).
2. J. C. H. Spence, J. M. Cowley and R. Gronsky, "The Effect of Lens Aberrations on Lattice Images of Spinodally Decomposed Alloys," Ultramicroscopy (in press).

Other Publications

1. R. Gronsky, D. R. Clarke and G. Thomas, "High Resolution Electron Imaging," Electron and Positron Spectroscopies in Materials Science and Engineering, O. Buck, J. K. Tien and H. L. Marcus, Eds., Academic Press (1979) p. 275.
2. R. Gronsky and G. Thomas, "Electron Microscopy of Spinodal Structures at High Resolution," Modulated Structures--1979, J. M. Cowley, J. B. Cohen, M. B. Salamon and B. J. Wuensch, Eds., American Institute of Physics (1979), p. 266.

LBL Reports

1. R. Gronsky and P. Furrer, "Grain Boundary Precipitation in Aluminum Alloys: Effect of Boundary Structure," Metallurgical Transactions (submitted), LBL-9739.
2. R. Gronsky, "Direct Imaging of Grain Boundaries," in Grain Boundary Structure and Kinetics, ASM Seminar Series, R. W. Balluffi, Ed., American Society for Metals (in press), LBL-9779.
3. D. J. H. Cockayne and R. Gronsky, "Lattice Imaging of Modulated Structures," submitted to Phil. Mag., LBL-10158.

Invited Talks

1. R. Gronsky, "Application of Advanced Techniques of Electron Microscopy in Materials Science," Department of Mechanical Engineering, U. C. Davis, January 1979.
2. R. Gronsky, "Grain Boundary Structure and Precipitation in Al-base Alloys," AIME Annual Meeting, New Orleans, February 1979.
3. C. K. Wu, R. Gronsky and G. Thomas, "On the Detection of Composition Variations by Optical Microdiffraction," AIME Annual Meeting, New Orleans, February 1979.
4. R. Gronsky, "Analysis of Interfacial Structure in Alloy Systems by High-Resolution Transmission Electron Microscopy," Northern California Society for Electron Microscopy, Pleasanton, California, May 1979.
5. R. Gronsky, "Direct Imaging of the Atomic Structure of Interfaces," Topical Meeting on Microchemical and Microstructural Analysis of Minority and Interface Phases, U. S. Department of Energy, Germantown, Maryland, May 30-31, 1979.
6. R. Gronsky, "Grain Boundaries, Intergranular Precipitation and Significance in Materials Properties," Department of Materials Science and Mineral Engineering Seminar, June 7, 1979.
7. R. Gronsky, "Direct Imaging of Grain Boundaries," Seminar on Grain Boundary Structure and Kinetics, American Society for Metals, Milwaukee, Wisconsin, September 15, 1979.
8. R. Gronsky and G. Thomas, "T.E.M. Characterization of Grain Boundaries," Symposium on Mechanisms of Intergranular Failure, Fall Meeting of TMS/AIME, Milwaukee, Wisconsin, September 17, 1979.
9. W. M. Kriven, R. Gronsky and J. A. Pask, "Dislocation and Low-Angle Grain Boundaries in Mullite," Fall Meeting, American Ceramics Society, New Orleans, October 1979.

c. 1.5 MeV Electron Microscope*

K. H. Westmacott, Investigator

Introduction. Activity during the year has been concentrated mainly in (1) developing the new 1.5 MeV High Voltage Microscope facility in Building 72, and upgrading the performance and utility of the old Hitachi 650 keV HVEM on Campus, (2) establishing base data from ex-situ experiments, principally on oxides and spinels, for subsequent comparison with controlled-environment in-situ studies, and (3) elucidating the nature of point-defect / solute-atom interactions and clarifying their role in phase transformations.

The in-situ techniques will be used in new direct studies of gas-solid reactions and phase transformations in important classes of both metallic and non-metallic materials, while the defect studies constitute part of a continuing attempt to understand the mechanisms of segregation and of second phase formation in a broad range of alloy systems. Close parallels have been observed between the early stages of graphite crystallite formation in supersaturated Pt-carbon alloys and carbide formation in Ta-C alloys, in both of which co-precipitation of vacancies and carbon atoms occurs. Present evidence suggests that this process is important in a variety of both FCC and BCC substitutional and interstitial alloys as a precursor to formation of the stable equilibrium phase. A detailed account of the precipitation sequence in the Ta-C system is given; further development will follow later.

1. PROGRESS REPORT OF FACILITY DEVELOPMENT

K. H. Westmacott

1.5 MeV HVEM Project. The final stages of the construction of the building to house the new instrument have been reached. The major construction phase is over, and all the essential items including isolation foundation, traveling crane, air-conditioning, and other utilities are installed. The building should be ready for acceptance before the end of the year. Delivery of the instrument has, however, fallen behind schedule by three months. The accelerator and generator are completed and in transit, but the column has suffered delays and is only now starting its final test phase. Acceptance tests at the factory are presently scheduled for late January 1980.

2. 650 keV HVEM Side Entry Conversion. Conversion of the Hitachi HU650 to side entry operation proved much more difficult than had been envisaged. The "Swann" system, while basically sound, must be custom-fitted since each of the Hitachi instruments is slightly different. These interfacing problems, which have serious repercussions for the rest of the system, have now been solved and the entire system,

including the environmental cell, is working in accordance with expectations. The first new results from direct in-situ studies of gas-solid interactions have recently been obtained.

2. PHASE TRANSFORMATION IN INTERSTITIAL ALLOYS[†]

U. Dahmen

It has recently become apparent that interstitial alloys bear more similarities to substitutional alloys than usually recognized. Among the most striking similarities are two features commonly attributed to the effect of vacancies in quench-aged substitutional alloys: the formation of homogeneously distributed coherent precipitates and the presence of precipitate-free zones (PFZ's) near vacancy sinks (e.g., grain boundaries, surfaces, etc.). Using quench-aging experiments in dilute alloys of (bcc) tantalum with carbon in interstitial solution, the precipitation sequence was followed by means of electron microscopy under special consideration of a possible vacancy effect due to carbon-vacancy binding.

When high-purity tantalum was alloyed with about 0.5 at.-% carbon and quenched rapidly in ultra-high vacuum, the carbon was held in supersaturated solution. Subsequent aging at $\sim 400^\circ\text{C}$ for 144 hr produced a high density of small coherent precipitates with image characteristics similar to dislocation loops, as shown in Fig. 1. A detailed trace analysis showed their habit planes to be the $\{310\}$ planes of the matrix. Due to the small volume fraction of precipitates no extra spots were observed in the diffraction patterns.

Since their visibility in electron micrographs results almost entirely from strain contrast, the precipitates could be analyzed as "dislocation loops." Three important pieces of information about the displacement vector \underline{R} of the precipitates could be obtained in this manner: the displacement vector is normal to the habit plane, i.e., the "loops" are pure edge, its magnitude is approximately $1/3 \langle 310 \rangle$ ($\sim 3\text{\AA}$), and its sign shows that the "loops" are slabs of increased volume. Such a contrast experiment is shown in Fig. 2 (for detailed analysis, see Ref. 1).

In contrast to carbon in platinum,² lattice vacancies are not necessary to explain the "loop" character at this stage of the precipitation process.

However, a number of features are difficult to explain without the involvement of vacancies. Vacancy sinks such as grain boundaries, dislocations, and interphase boundaries always exhibited precipitate-free zones (PFZ's). An example of the PFZ near a grain boundary is shown in Fig. 3, which demonstrates that no heterogeneous nucleation has occurred in the grain boundary. Since tantalum forms very stable carbides, it is highly unlikely that a film of

* This work was supported by the Division of Materials Sciences, Office of Basic Energy Sciences, U. S. Department of Energy.

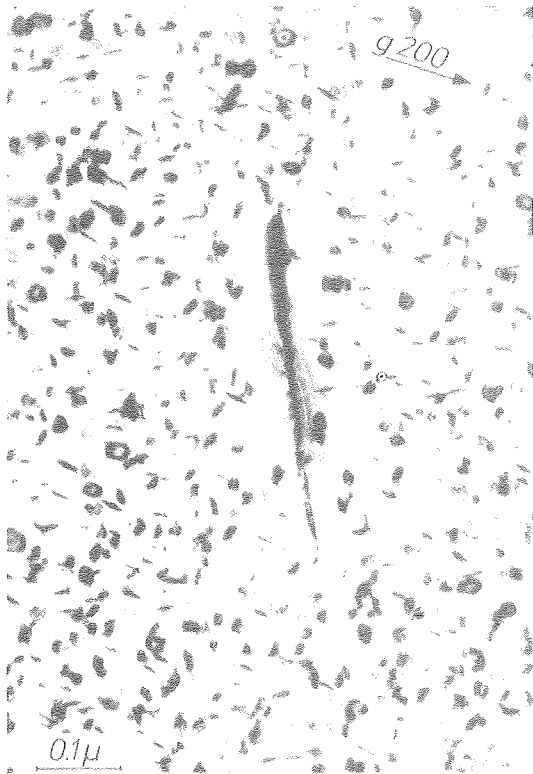


Fig. 1. TEM micrograph showing coherent precipitates in a quench-aged tantalum-carbon alloy.
(XBB 789-12291)

carbon has formed on the boundary. Hence a mechanism different from carbon depletion must be responsible for the PFZ. In aluminum alloys, the equivalent effect has been ascribed to a vacancy depletion³ and the same explanation seems reasonable in the present system.

Furthermore, on comparing the density of coherent precipitates in this system with reports in the literature on quench-aging of other bcc-metal/carbon alloys, it was found that there is remarkably little variation with carbon concentration. For example, a similar density of precipitates was found in the present alloy (Ta ~ 0.5 at.-%C) and a 10 times more dilute molybdenum-carbon alloy.⁴

In conjunction with the fact that these coherent precipitates are only found during low-temperature aging after a rapid quench, the evidence suggests that vacancies play an important part in this early stage of precipitation, analogous to their role in substitutional alloys.

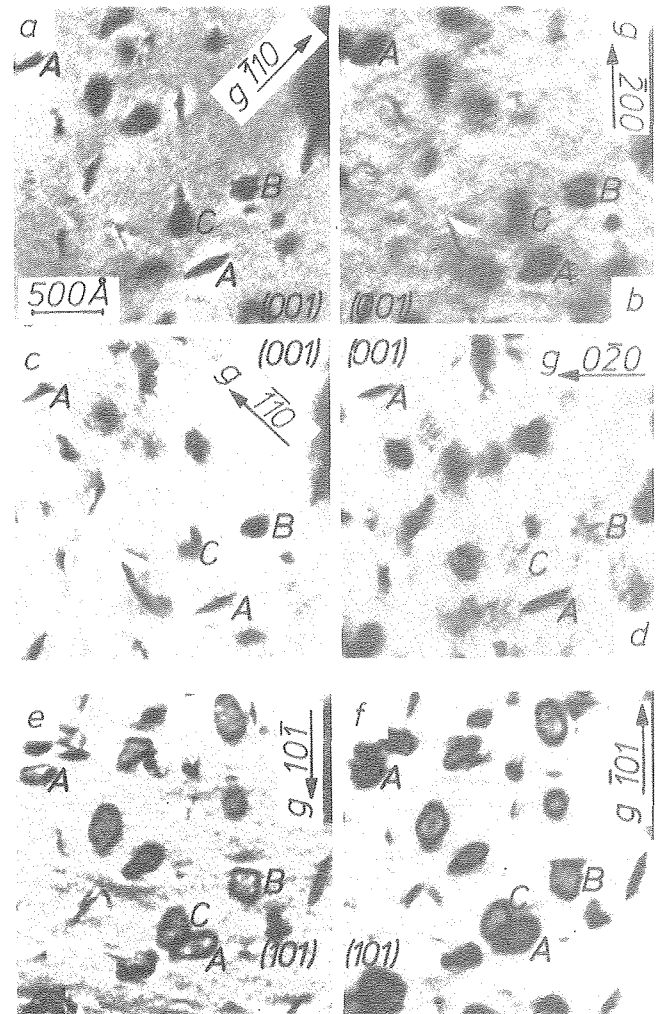


Fig. 2. Contrast analysis of coherent precipitates.
(XBB 789-12559)

* * *

† Brief version of LBL-8661.

1. U. Dahmen, Ph.D. Thesis, U. C. Berkeley, January 1979.
2. K. H. Westmacott and M. I. Perez, *J. Nucl. Mat.* **83**, 231 (1979).
3. P. N. T. Unwin, G. W. Lorimer and R. B. Nicholson, *Acta Met.* **17**, 1363 (1969).
4. K. Yoshioka and H. Kimura, *Scr. Met.* **9**, 361 (1975).

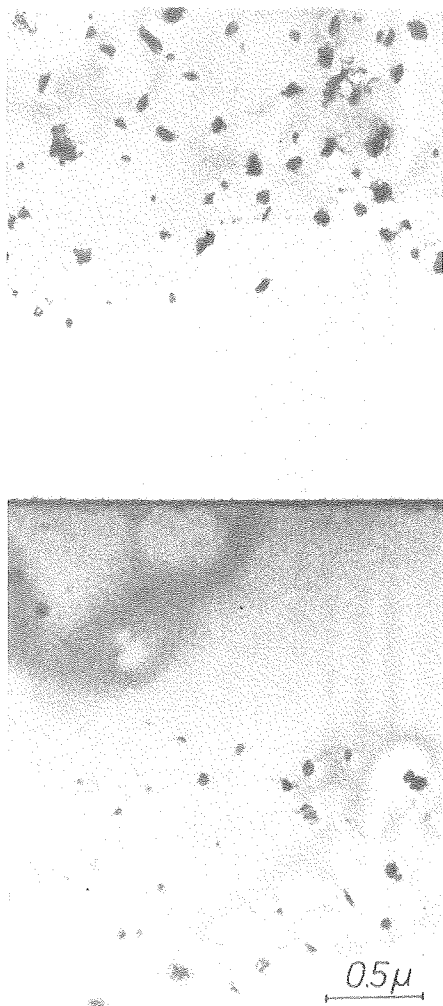


Fig. 3. Precipitate-free zone near a grain boundary. (XBB 789-12561)

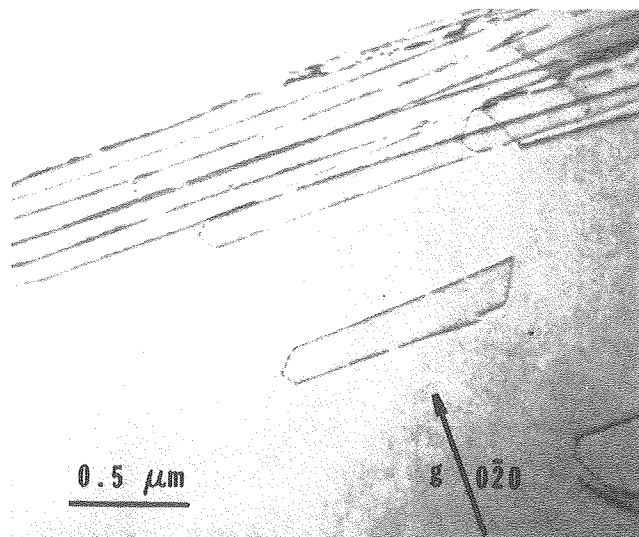


Fig. 1. Persistent slip traces in NiO single crystal running parallel to cleaved edge. The slip plane is $\{110\}$ and the dislocation Burgers vector $a/2\langle 110\rangle$. (XBB 801-1090)

Normally, when dislocations propagate in a foil during TEM observations, the surfaces do not impede their motion and only faint slip traces are observed marking their passage. In contrast to this, the strong persistent traces seen in Fig. 1 indicate that slip activity occurred before observation and the glide dislocations were retained near the foil surfaces. The anomalously strong diffraction contrast exhibited by the trailing dislocations is good evidence that they lie within about $1/10$ th of an extinction distance from the foil surface.² In all cases the dislocations lay in the usual $\{110\}$ slip plane and had $\frac{a}{2}\langle 110\rangle$ type Burgers vectors.

During prolonged observation in the microscope the near-surface dislocations were observed to slowly slip piecemeal out of the foil surface leaving discontinuous segments (Fig. 2).

These observations suggest that the surface layers of the ion-thinned NiO crystal have a structure of composition different from that of the bulk which impedes the motion of the gliding dislocations. This is analogous to the case in certain metals where surface oxide films are found to produce similar effects.² In the NiO the surface layers may be slightly reduced by the combined interaction with the ion beam and the relatively poor vacuum since many of the residual gas species in the atmosphere are hydrocarbon or other reducing agents. Such a process will be dependent on kinetic as well as thermodynamic factors, and beam heating of the specimen, which is known to occur, is probably a contributing factor. The disappearance of the dislocations during observation in the electron microscope is also explained in terms of the specimen environment. Under normal operating conditions, the ratio of hydrogen to water vapor in an electron microscope vacuum is about 1:20 and can be much higher when fresh photographic film is introduced into the system.³ Since the equilibrium H_2/H_2O ratio

3. THE ORIGIN OF UNUSUAL DISLOCATION STRUCTURES IN ION-THINNED NiO SINGLE CRYSTALS

J. A. Little and K. H. Westmacott

During the microstructural characterization of nickel oxide single crystals, some unusual dislocation configurations showing an anomalous contrast under certain diffracting conditions were observed that have not been previously reported. These observations were made in a study on the reduction of metallic oxides to metals in the gas-reaction cell of the Hitachi 650 keV HVEM.¹

The as-prepared ion-thinned specimens contained evidence that dislocation activity had occurred either during thinning or during subsequent specimen handling. Dislocation configurations consisting of a leading glissile segment threading the foil and a pair of trailing dislocations were observed (see Fig. 1) distributed non-uniformly throughout the foil.

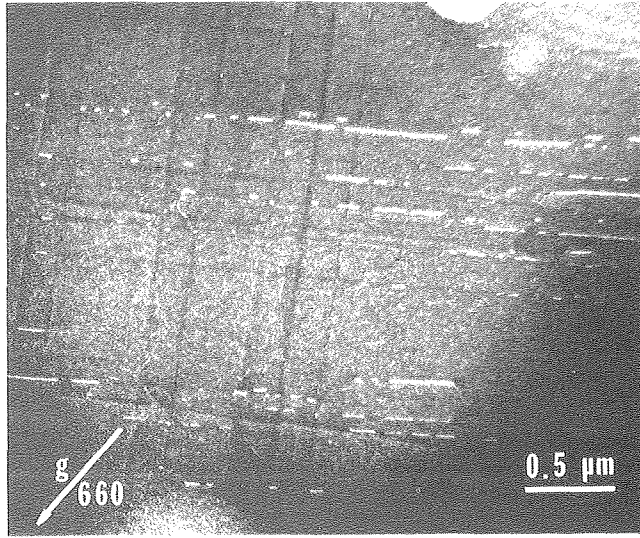


Fig. 2. Weak-beam dark-field micrograph showing anomalously strong contrast from near-surface dislocations and their progressive disappearance during reoxidation in the electron microscope. (XBB 801-1091)

for the Ni/NiO system is $\sim 1:30$ at room temperature, the microscope vacuum is probably an oxidizing environment, and heating of the specimen during examination will result in slow reoxidation of the reduced surface layers. This would account for the slow escape from the surface of the dislocations.

The second point of interest concerns the dislocations themselves. There is a nonrandom distribution of areas within foils where the dislocations are found to occur, and in every example studied these dislocations have been found to be adjacent to cleavage edges or cracks. It is thus probable that they arise from plastic deformation processes accompanying cleavage (i.e., slip of new, or pre-existing, dislocations), and further support for this was found when specimens which were ion-thinned and handled with extreme care contained neither cleavage edges nor persistent slip traces.

In conclusion, it should be emphasized that since ion thinning is a common, and increasingly used, technique the evidence that the surface layers of NiO, and perhaps ceramic materials, so prepared may have a structure different from the bulk should always be borne in mind.

* * *

1. J. A. Little, K.H. Westmacott and J. W. Evans, this annual report.

2. P. B. Hirsch, A. Howie, R. B. Nicholson, D. W. Pashley and M. J. Whelan, *Electron Microscopy of Thin Crystals*, Butterworth, London (1965), p. 271.

3. U. Dahmen, private communication.

4. PLASTIC DEFORMATION OF $\text{MgO}(\text{Al}_2\text{O}_3)_{1.1}$ SPINEL AT $0.28 T_M$

S. H. Kirby and P. Veyssi re

Plastic deformation has been observed in spinel single crystals deformed at temperatures below $0.5 T_M$ ($T_M \approx 2400\text{K}$)--where diffusion is not expected to play a role in the deformation mechanism--by the superposition of a uniaxial compressive and hydrostatic stress. Past attempts to deform crystals using compression only have been unsuccessful due to brittle failure at stresses too low to promote plastic yield.

The prism-shaped single crystals of $\text{MgO}(\text{Al}_2\text{O}_3)_\eta$ spinel ($\eta < 1.1$) were compressed to significant plastic strain at a temperature of 400°C ($\sim 0.28 T_M$) in controlled experiments under a superimposed hydrostatic stress of 1.4 GPa. Compression of crystals approximately parallel to $\langle 001 \rangle$, $\langle 111 \rangle$ and $\langle 011 \rangle$ resulted in simple yield behavior at axial stress differences of 1940, 3720 and 4300 MPa respectively (Fig. 1).

The tests were stopped at permanent strain of $\sim 1\%$ to permit metallographic examination of the specimen surfaces. Prominent glide lines were directly apparent on all the specimen faces (Fig. 2).

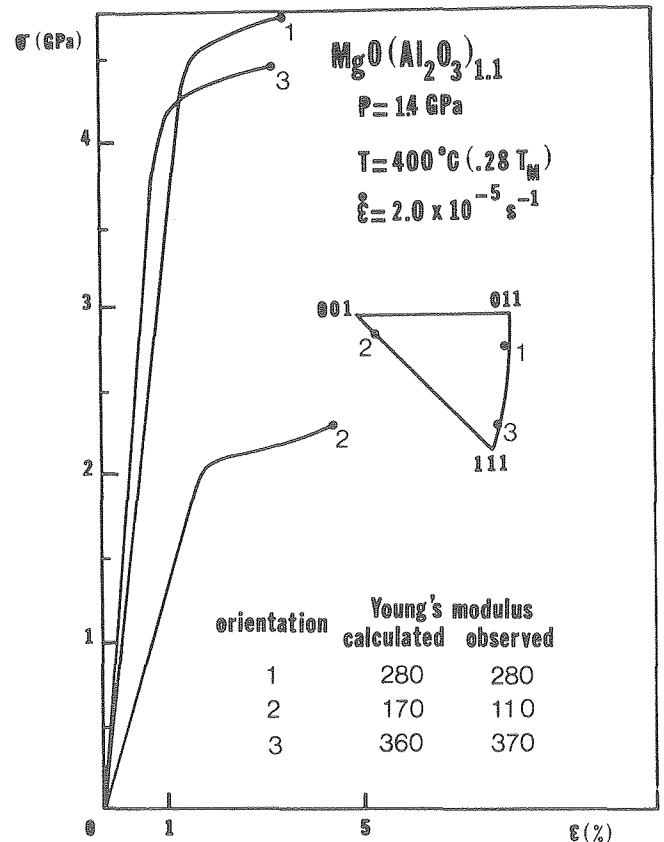


Fig. 1. Stress-strain curves for the constant strain rate tests on spinel single crystals, corrected for apparatus distortion. Conditions indicated on figure. Observed Young's modulus determined from the elastic slope and calculated modulus from the single crystal elastic constants.

(XBL 794-9444)

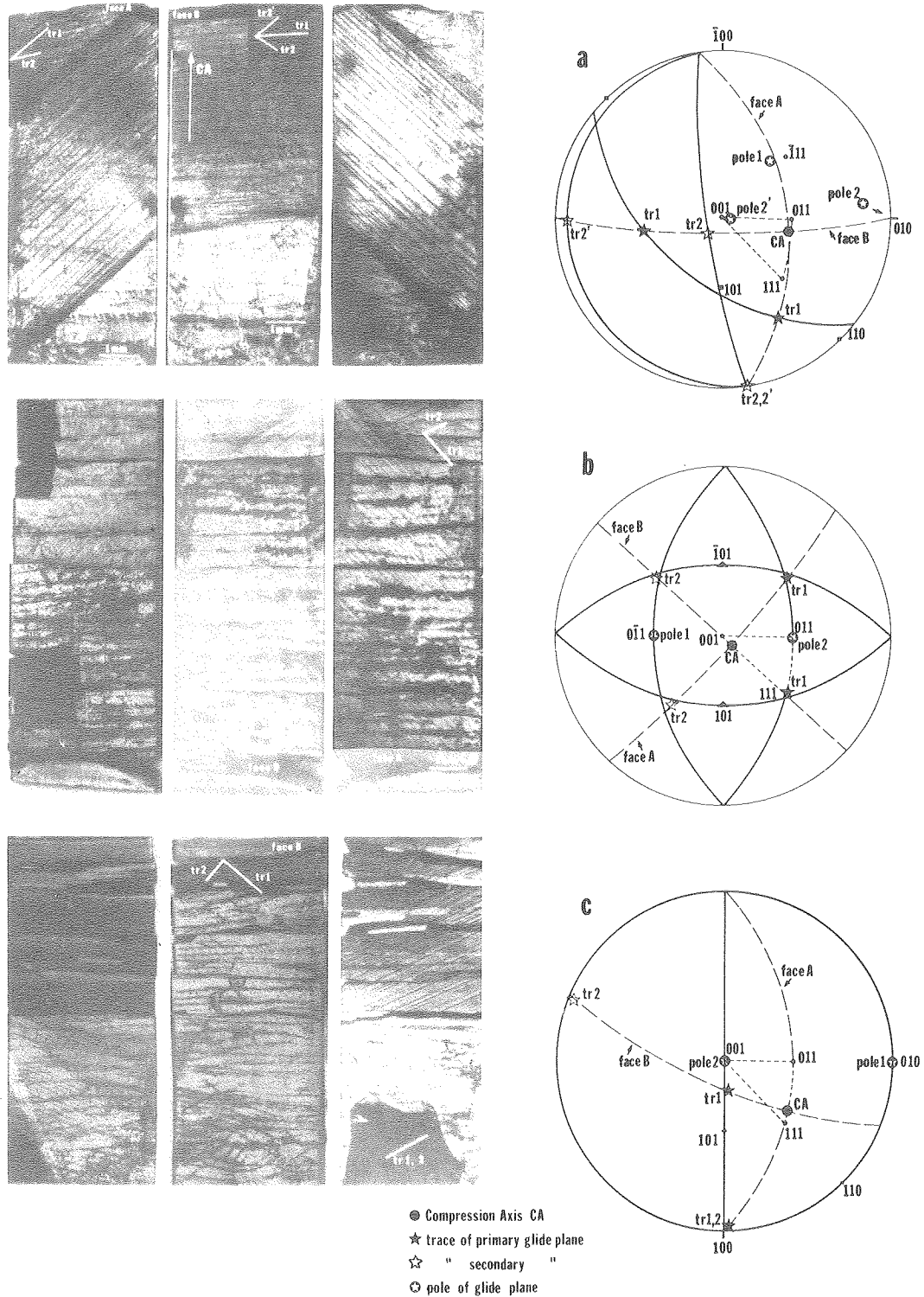


Fig. 2. Whole-specimen reflection micrographs of specimens compressed in the three principal orientations and supporting stereographic projections of slip line and specimen orientation data. One parallel polished pair of longitudinal surfaces was oriented approximately parallel to $\{110\}$ (face A) and flanked the one polished longitudinal surface (face B) which was orthogonal to face A. The dashed great circle lines are traces of the longitudinal prism surfaces and the heavy great circles are traces of the glide planes derived from slip line orientations. See legend for other symbols. (a) Orientation 1 (N-353) - Compression approximately parallel to $[011]$. (b) Orientation 2 (N-353) - Compression approximately parallel to $[001]$. (c) Orientation 3 (N-356) - Compression approximately parallel to $[111]$. (XBB 794-5806)

The well-defined and broadly-distributed lines and stress-optical effects of slip-bands permitted identification of the following operating slip families:

| Compression | Slip System | τ |
|---------------------------------|-----------------------------|--------------------|
| // \sim $\langle 001 \rangle$ | {110} $\langle 110 \rangle$ | 950 \pm 100 MPa |
| // \sim $\langle 111 \rangle$ | {100} $\langle 110 \rangle$ | 1810 \pm 100 MPa |
| // \sim $\langle 011 \rangle$ | {111} $\langle 110 \rangle$ | 1940 \pm 100 MPa |

where τ is critical resolved shear stress.

Typically, the members of the above slip families with the highest Schmid factors operated. Clear evidence for active cross-slip on the system {100} $\langle 110 \rangle$ was observed to nucleate from the {111} $\langle 110 \rangle$ slip bands in the \sim $\langle 001 \rangle$ specimen.

* * *

[†]Brief version of LBL-9129.

RESEARCH PLANS FOR CALENDAR YEAR 1980

The new 1.5 MeV High Voltage Electron Microscope will be installed in the Building 72 addition during 1980. When fully operational, the facility will be used by many different groups, both within and outside the U. C. community. The improved penetration at 1.5 MeV will permit more meaningful direct in-situ studies of gas-solid reactions in a variety of systems. In addition to the environmental cell reduction work described elsewhere in this report, studies of stress build-up during the initial stages of oxidation will be resumed. The effects of minor alloy additions on the mechanism of oxidation will be studied in collaboration with D. A. Whittle.

A continuation of the structural characterization of graphite intercalation compounds with N. Bartlett's group is also planned.

Studies on the role of lattice defects in the early stages of precipitation will be broadened, and it is expected that the concepts developed will be applicable to a wide variety of interstitial and substitutional alloys. Moreover, present indications are that the entire precipitation sequence is controlled in many systems by the initial precipitate geometry. These concepts are also being applied to

technologically important problems such as carbide precipitation in Fe-based alloys.

1979 PUBLICATIONS AND REPORTS

Refereed Journals

1. K. H. Westmacott and G. Thomas, "High Resolution and High Voltage Electron Microscopy at the University of California, Berkeley," Proc. Indian Academy of Sciences C2, 263 (1979).
2. K. H. Westmacott and M. I. Perez, "The Co-Precipitation of Vacancies and Carbon Atoms in Quenched Platinum," J. Nucl. Mat. 83, 231 (1979).
3. G. Thomas and K. H. Westmacott, "The Role of Environmental Conditions in In-Situ Experiments in the High Voltage Electron Microscope," Phys. Stat. Sol. (a) 55, 563 (1979).

Other Publications

1. J. Y. Laval and K. H. Westmacott, "Electron Beam Sensitivity and Structure of the Glassy Phase of Ceramics," Proc. EMAG 79, Paper 131, T. Mulvey, Ed. (1979).

LBL Reports

1. S. H. Kirby and P. Veysière, "Plastic Deformation of MgO (Al₂O₃)_{1.1} Spinel at 0.28 Tm: Preliminary Results" (Phil. Mag., in press), LBL-9129.
2. P. Veysière, "Study of the Precipitation in MgO 3.5 Al₂O₃ During Creep Experiments," J. de Phys. Lett. (in press), LBL-9044.
3. J. Y. Laval and K. H. Westmacott, "The Mechanism of Ionization Damage in Glassy Ceramics" (J. Am. Ceramic Soc., in press), LBL-9808.
4. M. I. Perez, "Secondary Defects in Quenched Platinum" (M.S. thesis), LBL-10178.

Invited Talks

1. K. H. Westmacott, "Vacancy-Interstitial Impurity Interactions in FCC Metals and A Mechanism for Solute Segregation," Max-Planck-Institut, Stuttgart, March 29, 1979.
2. K. H. Westmacott, "The Role of Environmental Conditions on In-Situ Experiments in the High Voltage Electron Microscope," Int. Symposium on HVEM, East Germany, April 3, 1979.

2. Mechanical Properties

a. Theoretical Problems in Alloy Design*

J. W. Morris, Jr., Investigator

Introduction. The research reported here is a multifaceted program of research in physical metallurgy which includes theoretical studies on phase transformation and mechanical properties; basic experimental studies in the influence of microstructure and microstructural transformation on physical and mechanical properties; and applied research in the development of new structural alloys, weld filler metals, and superconducting wires to meet advanced energy needs.

Theoretical Studies

1. PRECIPITATION AND COARSENING REACTIONS IN TWO-DIMENSIONAL ISING LATTICES[†]

E. S. Pundarika[‡] and J. W. Morris, Jr.

The dynamics of precipitation and coarsening reactions in a two-dimensional binary Ising lattice have been studied using computer simulation techniques. The studies are conducted by establishing an initially random distribution of A-type and B-type atoms over either a square or hexagonal lattice, a situation representative of equilibrium at very high temperature, and then permitting the system to evolve toward equilibrium at lower temperature through direct atom exchanges. These are governed by a Boltzmann probability which depends on the temperature and on the energetic consequence of the exchange. The atoms are assumed to interact pairwise with nearest neighbors, and the sign of the interaction is chosen such that the system naturally has a miscibility gap at low temperature. If the reaction temperature and composition is chosen such that the system lies within its miscibility gap, the evolution of the system will proceed through a decomposition into A-rich and B-rich regions. Through computer simulation this decomposition reaction can be followed, permitting a detailed study both of the kinetics and morphological aspects of the decomposition as a function of composition and temperature. The computer experiment amounts to a simulation of the precipitation and coarsening of precipitates rich in the minority species, B, in the matrix of the parent A.

Computer simulation studies have led to the division of the precipitation and coarsening reaction into four stages: a fast initial reac-

tion stage, a stage in which coarsening occurs through the direct coagulation of small mobile clusters of atoms, a transition stage, and a final stage of classic Lifshitz-Slosov coarsening through diffusion of individual atoms in the bulk. The appearance and characteristics of each of these phases are sensitive to the reaction temperature. During the past year it has also been demonstrated that each stage is characterized by particular morphological features of the coarsening particles, which are reflected in characteristic distributions of atom-bond types, and which vary in a systematic way with the reaction temperature. The evolution of the particle size distribution has also been studied in detail.

* * *

[†]Brief version of LBL-8456 and LBL-10005.

[‡]Present address: Department of Metallurgical Engineering, Cleveland State University.

2. THE ELASTIC ENERGY CONTRIBUTION TO SOLID STATE PHASE TRANSFORMATION[†]

Sheree Chen,[‡] A. G. Khachaturyan,[§] and J. W. Morris, Jr.

One of the most important influences on the nature of phase transformations in the solid state is the problem of elastic accommodation. The product phase will, in general, differ in size or crystal structure from the parent, and will therefore induce an elastic strain in the parent matrix, particularly if it forms initially as a coherent inclusion. One of the most important objectives of the theory of metallurgical phase transformations is to properly account for elastic effects.

Theoretical research on the elastic field of a misfitting inclusion within a solid phase and on its consequences for the thermodynamics, shape, and the habit of transformed inclusions has been underway for a great number of years. The greatest progress has been made in a model in which both the inclusion and matrix are assumed to be linear elastic, and the elastic constants of the composite system are assumed to be uniform. A variety of relevant problems has been solved in the context of this model, and give insight into such diverse reactions as ordering in solid solutions, the shape and habit of precipitate particles, and the characteristics of martensitic transformations. The wealth of research in the area has, however, led to a circumstance in which a variety of independent formulations exist which

* This work was supported by the Division of Materials Sciences, Office of Basic Energy Sciences, U.S. Department of Energy.

are not obviously consistent in either their starting premises or their most important results. As a consequence of the research reported here, a general formulation of the linear elastic theory of a solid containing substitutional defects was developed. The starting point for this treatment was microscopic, and it was shown to be consistent with the accepted "lattice statics" models of solid solution behavior. The model may then be taken to its macroscopic limit, and can then be shown to yield the continual elastic formulations of Khachaturyan and of Eshelby. The results provide a self-consistent formulation of the linear elastic theory of inclusions in solids, and, as a corollary, establish the consistency of a variety of earlier theoretical results obtained from independent starting points.

* * *

†Brief version of LBL-9264 and LBL-9800.

‡Present address: T. J. Watson Research Center, IBM, Yorktown, New York.

§Present address: Institute of Crystallography, Academy of Sciences of the U.S.S.R., Moscow, U.S.S.R.

3. THE THEORY OF MARTENSITIC TRANSFORMATIONS IN AN IDEALIZED ELASTIC SOLID[†]

Sheree Chen,[‡] A. G. Khachaturyan,[§] and J. W. Morris, Jr.

Despite the engineering importance of martensitic transformations in solids, particularly steel, there exists very little theoretical work on the development of the martensitic transformation and on the characteristics of the resulting microstructure. The work reported in this project was intended to advance the theory of the martensite transformation by constructing a computer model of a martensitic transformation in an idealized system. The model has its source in the general observation that the characteristics of martensitic transformations in solids are largely determined by the problem of accommodating the strain associated with the martensitic distortion of the crystal lattice. A review and adaption of prior theoretical work led to the development of a theory which allows a straightforward computation of the elastic energy associated with an arbitrary distribution of defects in an elastic anisotropic body under the assumptions that the body has uniform elastic constants and that anharmonic effects may be neglected. The relevant equations may be cast into a form in which the energy is the simple sum of binary interactions involving an elastic potential whose form can be readily calculated. With the use of this theory the martensitic transformation is modeled as a transformation which occurs through the sequential formation of individual martensitic elements, each of which carries the elementary transformation strain. Statistical equations have been developed which

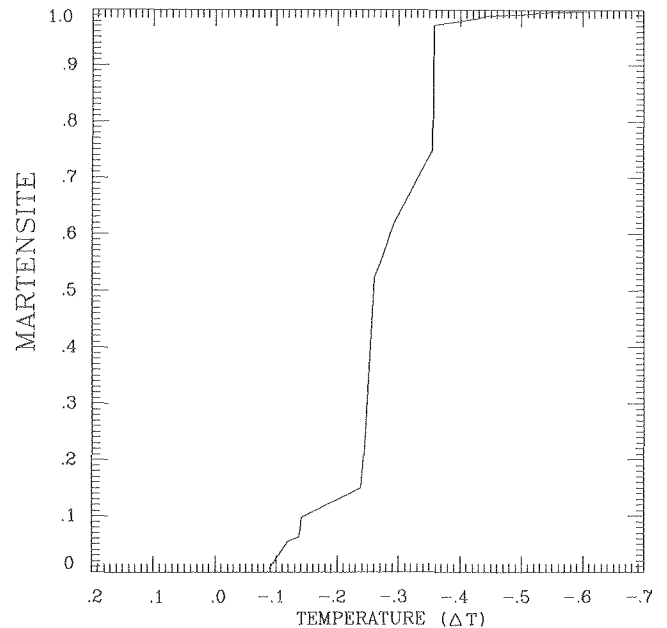


Fig. 1. The variation of martensite fraction with undercooling in a typical computer simulation experiment. (XBL 792-8196)

govern the selection of the transformation path or specific sequence in which elementary martensite particles appear in the model, and which specify the kinetics of transformations along any known path. The resulting model was then used for the detailed simulation of a martensitic transformation in a pseudo-two-dimensional system (see Figs. 1 and 2).

Despite the simplicity of the model, the features observed in the simulated transformations are encouragingly real. The initial martensite phase is heterogeneously nucleated and grows as a twinned plate along a definite habit plane. The overall transformation occurs through a series of bursts which are sequentially triggered as the temperature is lowered. These bursts involve the autocatalytic nucleation and growth of martensite plates which may parallel or branch with respect to the original plate. Bands of retained austenite are occasionally observed between parallel plates which are in an aggregate twin orientation to one another. Residual austenite is retained to a very late stage in the transformation (see Fig. 3), and is elastically stabilized to the extent that very large undercoolings are required to eliminate it.

* * *

†Brief version of LBL-9204 and LBL-9346.

‡Present address: T. J. Watson Research Center, IBM, Yorktown, New York.

§Present address: Institute of Crystallography, Academy of Sciences of the U.S.S.R., Moscow, U.S.S.R.

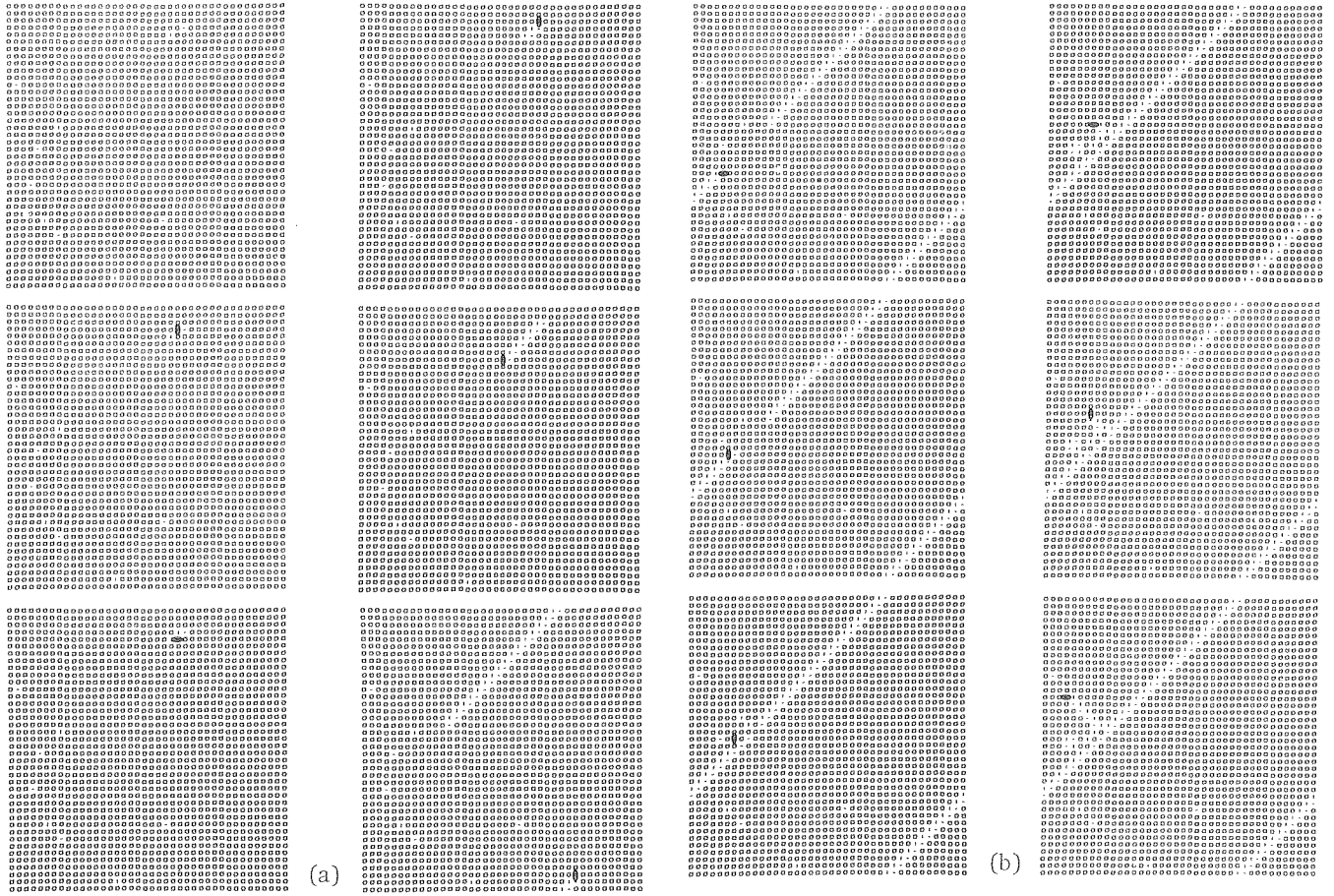


Fig. 2. Three snapshots of the martensite transformation in a two-dimensional system. (a) The nucleation of the transformation at an internal defect, (b) the growth of the initial martensite plate as a twinned plate along a definite habit, (c) a late stage in the transformation showing twinned plates and retained austenite, some of which appear as bands in the interstices between plates.

[(a) XBL 792-8415; (b) XBL 792-8420; (c) XBL 792-8417]

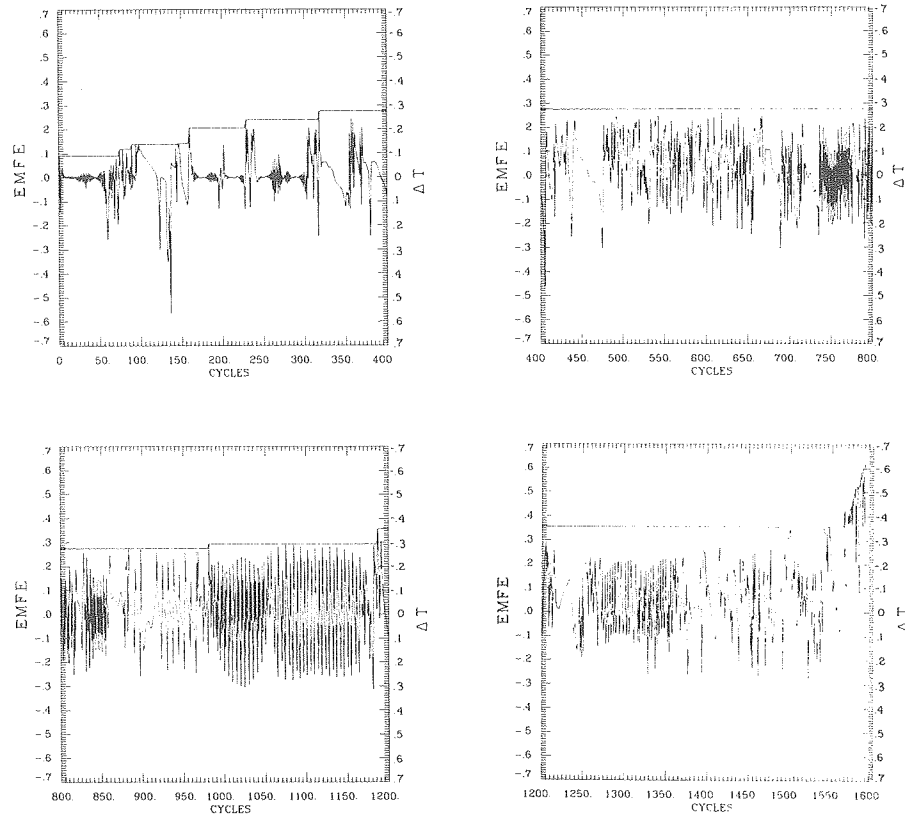


Fig. 3. The energetics of the transformation, showing the magnitude of the chemical driving force as a horizontal line, and the magnitude of the elastic energy change per transformation step as an oscillation function for the first 400 transformation steps. The steps in the chemical driving force correspond to increases in undercooling necessary to maintain the transformation. (XBL 792-8216)

4. TWEED AND COARSENING REACTIONS IN SIMPLE ELASTIC SOLIDS[†]

Sheree Chen,[‡] A. G. Khachaturyan,[§] and J. W. Morris, Jr.

Electron microscopic observations of the decomposition of alloys very often reveal regular substructures which arise during the aging process. These substructures are formed by new phase precipitates whose positions are correlated with one another. Regular structures have been observed in cubic alloys containing precipitates having either cubic or tetragonal structures. The morphology depends on the structure of the precipitate. When the precipitates are tetragonal the so-called "tweed" structure is formed which involves an alignment along $[110]$ directions of the cubic parent phase (see Fig. 1). When the precipitate is cubic the modulated structure displays an alignment along $[100]$ with a pseudo-periodical spatial distribution.

The formation process of the "tweed" or modulated structures was modeled through computer simulation of a hypothetical two-dimensional elastic solid containing a distribution of inclusions taken to be random (see Fig. 2). The inclusions are allowed to reconfigure through a stepwise diffusion process under the influence of

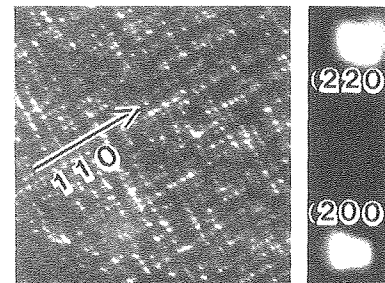


Fig. 1. The "tweed" structure in copper beryllium as observed by Rioja and Laughlin. (XBB 803-3100)

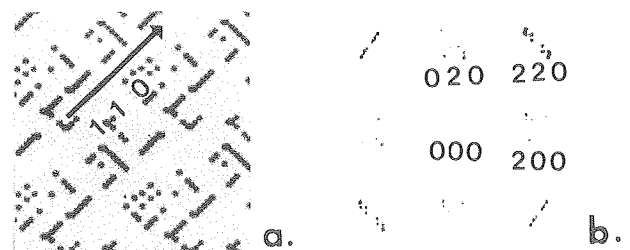


Fig. 2. Computer simulation of the "tweed" structure in an idealized two-dimensional solid. (a) Precipitate structure, (b) diffraction pattern. (XBB 803-3101)

their mutual elastic interaction energy. Utilizing the simulations, it was demonstrated that, in agreement with experimental observation, the inclusions take on an ordered preferential alignment whose nature depends upon the assumed symmetry of the inclusion particle. Inclusions of cubic symmetry align along the traces of [100] planes while inclusions of tetragonal symmetry align along traces of [110] planes. The diffraction patterns obtained from the computer-simulated patterns also bear a substantial resemblance to those observed experimentally.

* * *

†Brief version of LBL-9098.

‡Present address: T. J. Watson Research Center, IBM, Yorktown, New York.

§Present address: Institute of Crystallography, Academy of Sciences of the U.S.S.R., Moscow, U.S.S.R.

5. THE HABIT OF A TETRAGONAL PRECIPITATE IN A CUBIC MATRIX: ANALYTICAL RESULTS[†]

E. Kostlan, Sheree Chen,[‡] and J. W. Morris, Jr.

Analytical results obtained some years ago by Khachaturyan show that if a coherent inclusion of tetragonal symmetry is placed in a cubic matrix, and if the energetics of this inclusion are dominated by the elastic strain energy rather than by surface terms, then the inclusion will preferentially take on the form of a thin plate having a definite habit with respect to the parent matrix. Khachaturyan obtained a general relation giving the elastic energy of such an inclusion as a function of its habit orientation, and obtained the solution for this equation in special cases of high symmetry so as to predict precipitate habits. However, the Khachaturyan relation shows a rather complex dependence of the predicted habit plane on the elastic constants of the system and on the degree of tetragonality, and from the form of the relation there is no obvious reason to suspect that the preferred habit plane can be easily predicted.

In research done under this project it was shown that Khachaturyan equations can be cast in a simple analytic form which directly determines the habit plane which minimizes the elastic energy of a thin plate inclusion. Moreover, the habit plane is found to depend on the degree of tetragonality of the precipitate phase in a very simple way. The variation of habit plane with tetragonality follows one of two characteristic curves, depending on whether the anisotropy factor of the parent matrix is positive or negative. The two curves are shown in Fig. 1, and have been confirmed by direct computer solution of the Khachaturyan equation. These results constitute a complete solution to the problem of determining the preferred habit of a thin plate precipitate of tetragonal symmetry in an anisotropic cubic matrix, under the constraint that the elastic constants of the precipitate and the matrix are assumed the same.

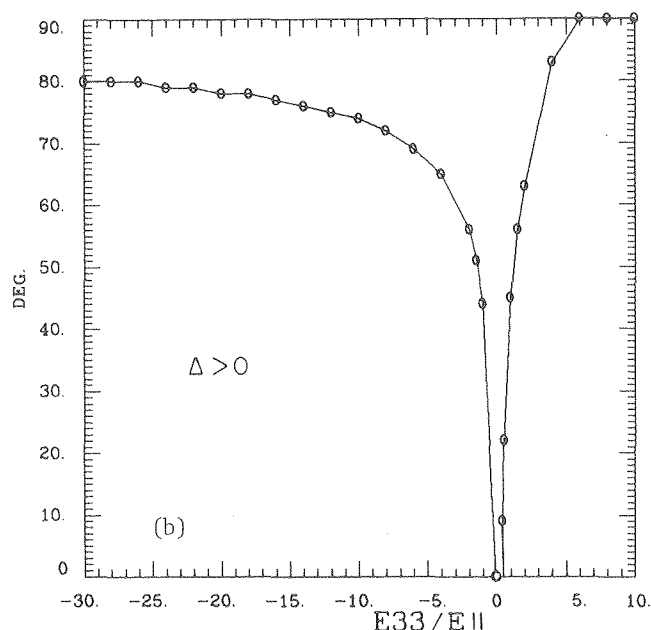
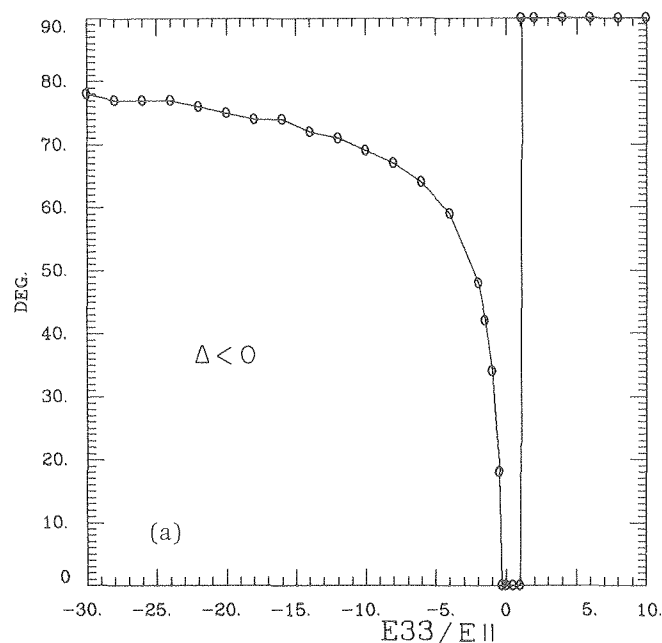


Fig. 1. The variation of the minimum energy habit of a thin-plate tetragonal precipitate in an anisotropic cubic matrix as a function of the degree of tetragonality. (a) Anisotropy factor $\Delta < 0$; (b) anisotropy factor $\Delta > 0$.

[(a) XBL 792-8203; (b) XBL 792-8204]

* * *

†Brief version of LBL-10262.

‡Present address: T. J. Watson Research Center, IBM, Yorktown, New York.

6. SHAPE AND HABIT OF TETRAGONAL PRECIPITATES IN ANISOTROPIC CUBIC MATRICES: PARTICLE SIZE AND SHAPE EFFECTS[†]

D. E. Wedge, M. Hong and J. W. Morris, Jr.

While linear elastic theory predicts that the preferred morphology of a coherent tetragonal inclusion in a cubic matrix will be that of an arbitrarily thin plane lying along a specific habit plane of the parent, such a morphology is not always obtainable in the early stages of precipitation reactions. Failure to achieve a thin-plate morphology is theoretically anticipated either if surface tension effects dominate the elastic energy, or if crystallographic constraints in precipitate nucleation have the kinetic consequence that a thin-plate morphology cannot be easily obtained. To gain theoretical insight into the energetics of these thick elastic inclusions, a general computer code has been written to compute the elastic energy of such an inclusion as a function of its size, shape, habit, and the elastic constants of the matrix, based on analytical results obtained by Khachaturyan. Questions of particular interest concern the preferred shape of the particle, the favored change in shape with increasing particle size during coarsening, and whether there is a predicted change in the habit of the particle as its thickness increases.

Computations have been carried out in detail for the specific case of early stage nitride precipitation in ferritic steels, since a significant body of experimental data exists for this case, and since the observed habit of the thick early stage precipitate differs from that predicted by linear elastic theory in the thin plate limit. The results of these calculations have been to show that there is a change in the most favored habit of the precipitate as it is made thicker, and that in the special case of nitride precipitates the predicted change is identical to that observed experimentally. The results also suggest that the aspect ratio of thick plate precipitates should vary in a systematic way with the precipitate size. This result can be phrased as a simple analytic relation which is shown to be in excellent agreement with the coarsening of nitride precipitates in ferritic steel, as shown in Fig. 1. Finally, studies of the variation of precipitate energy with particle shape have shown that, comparing plate-like morphologies with ellipsoidal morphologies to lens-like morphologies, there is an energetic preference for the lens figure, confirming the three-dimensional extrapolation of results obtained by Khachaturyan in the two-dimensional case.

* * *

[†]Brief version of LBL-10263.

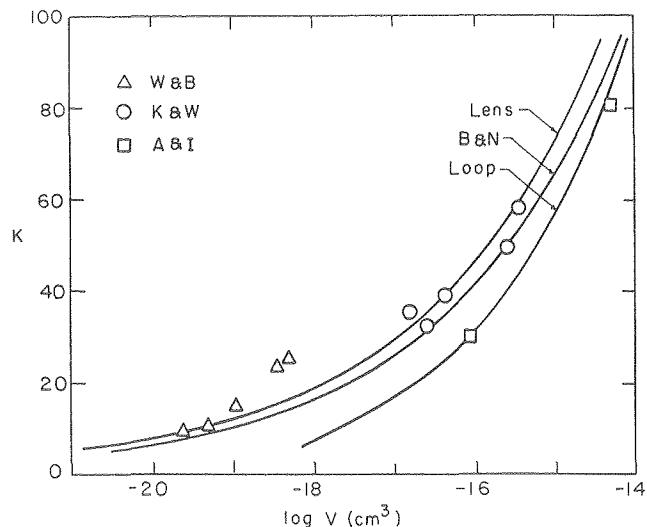


Fig. 1. The aspect ratio of plate-like nitride precipitates in ferritic steels as a function of particle radius compared with analytic predictions. (XBL 802-4727)

Fundamental Experimental Studies in Alloy Steels

1. RESEARCH ON THE COMPOSITION OF AUSTENITE PRECIPITATED DURING INTERCRITICAL TEMPERING IN Fe-Ni ALLOYS[†]

J. I. Kim

A variety of important engineering steels, for example, the common cryogenic steels and the so-called dual phase alloys of current interest for automotive applications, is given an intercritical treatment during their processing which has the consequence of introducing austenite phase into the parent martensite matrix. The stability of the precipitated austenite and its subsequent influence on the properties of the alloy is sensitive to its composition. It is hence essential to the metallurgical interpretation of intercritical treatments to identify the composition as the precipitation reaction proceeds. This sort of chemical characterization is, however, made extremely difficult by the small size of the austenite particles, which are in many cases $< 1 \mu\text{m}$ in effective diameter.

In this research project two techniques were used to estimate the composition of precipitated austenite in an Fe-5.5Ni cryogenic alloy. First, a chemical etchant was developed which preferentially etches the ferrite phase, leaving the austenite particles as a residue. This approach has the advantage of giving a mean composition of the austenite particles in a very straightforward way, but has the corresponding disadvantage that

it is not certain that all of the austenite particles have been captured, and it is possible that chemical contamination has occurred during the etching process. The second technique employed was scanning transmission electron microscopy. This high resolution technique permits the chemical analysis of individual austenite particles through energy dispersive x-ray analysis in thin foils. The technique has the advantage of exceptionally high resolution, but the disadvantage that the quantitative interpretation of the resulting spectrum is not yet fully established. Moreover, analysis by either technique is, in the form used here, confined to the heavier substitutional elements; important interstitial solutes such as carbon and nitrogen are not revealed.

The two methods for analyzing the composition of precipitation austenite give qualitative similar results. The results of STEM analysis are presented in Table 1. The results suggest three conclusions: First, chemical segregation during the initial precipitation of austenite is dominated by manganese and chromium, even though nickel is the predominate alloying species. Second, even when very long annealing times are allowed the nickel content in the precipitated austenite remains substantially below that predicted on the basis of the binary Fe-Ni phase diagram, presumably because of the influence of prior segregation in depressing nickel solubility. Third, very long annealing times, approximately 100 hours, are required to achieve maximum nickel contents in alloys intercritically tempered toward the lower end of the two phase region. Interestingly, as shown by the data in Table 1, a high nickel precipitated austenite can be obtained much more quickly through a two-step heat treatment in which the alloy is first treated at relatively high temperature to induce chemical segregation, and then treated at lower temperature to establish a high nickel content. This kinetic trick is believed to be important to the success of the so-called QLT treatment of low nickel cryogenic steels, as discussed further below.

* * *

†Brief version of LBL-9956.

2. THE SCAVENGING EFFECT OF RETAINED AUSTENITE IN LOW CARBON Fe-Ni ALLOY⁸

J. I. Kim and J. W. Morris, Jr.

The influence of intercritical tempering on the properties of cryogenic steels is very sensitive to the presence of interstitials of the parent matrix. In steels which are essentially carbon free or carbon gettered, an intercritical temper has the effect of lowering the ductile-brittle transition temperature, but does not have the significant effect on alloy toughness above the DBTT. In steels which contain a significant concentration of interstitials, on the other hand, the precipitation of austenite during an intercritical temper simultaneously lowers the DBTT and raises the shelf toughness of the alloy at higher temperatures. This effect is presumably associated with the role of precipitated austenite in gettering carbon or carbides from the parent matrix.

To investigate these phenomena the scavenging effect of retained austenite in a low carbon, commercial Fe-5.5Ni cryogenic alloy was investigated through the observation of dissolution of cementite precipitates during intercritical tempering and study of the associated change in Charpy impact toughness (see Figs. 1 and 2). Cementite precipitates initially located along prior austenite grain boundaries were gradually dissolved into reverted austenite as the intercritical tempering proceeded. The austenite tended to form at or around the carbide particles and may be catalyzed by their presence. The Charpy impact energy is changed through a decrease in the ductile-brittle transition temperature and an increase of the upper shelf energy. The latter

Table 1. Chemical composition of retained austenite and corresponding x-ray integrated intensity detected by EDAX in STEM as a function of thermal treatment.^{a,b}

| | | 600°C, 2 hr | 600°C, 100 hr | 670°C 1 hr | 670°C, 1 hr + 600°C, 1 hr |
|--|----|----------------|------------------|---------------|------------------------------|
| X-ray intensity count ^c | Fe | 19324 | 19838 | 20505 | 14575 |
| | Ni | 1613 | 1803 | 1710 | 1321 |
| | Mn | 496 | 910 | 902 | 779 |
| | Cr | 285 | 385 | 346 | 612 |
| | Si | 51 | 86 | 56 | 218 |
| Wt. % ^c | Fe | 90.4 | 85.5 | 86.8 | 84.7 |
| | Ni | 6.7 | 9.6 | 8.6 | 9.0 |
| | Mn | 2.1 | 3.5 | 3.3 | 3.9 |
| | Cr | 0.7 | 1.2 | 1.2 | 2.1 |
| | Si | 0.1 | 0.2 | 0.1 | 0.3 |

Note: (a) Total count: 50,000 counts.
 (b) All values are averaged from a minimum of 5 points.
 (c) Molybdenum is not analyzed.

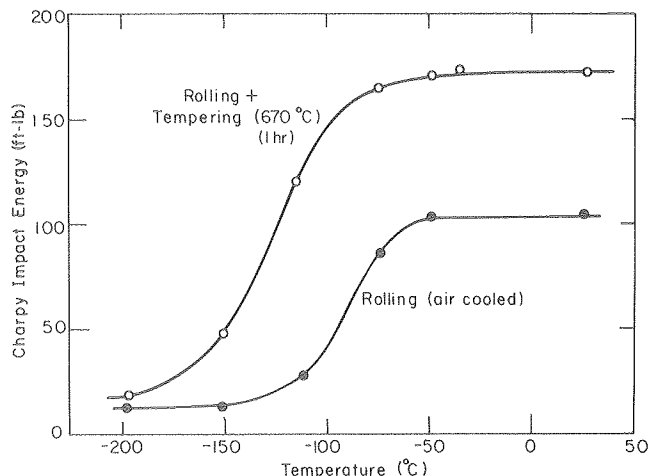
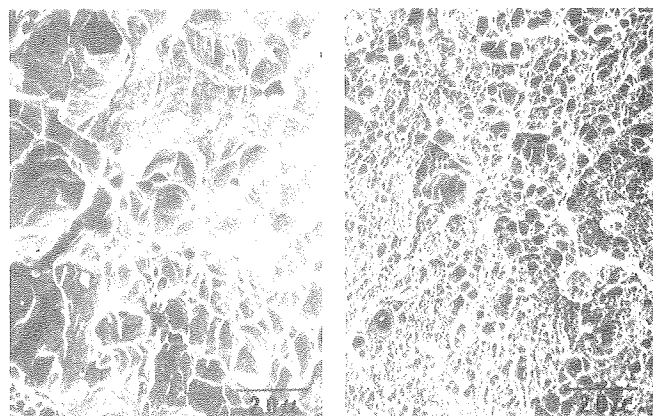


Fig. 1. Charpy impact energy as a function of temperature in Fe-5.5Ni before and after intercritical tempering treatment. (XBL 792-5739)



As - Cooled

670°C, 1hr/ WQ

Fig. 2. Comparative fractographs of Fe-5.5Ni broken at room temperature before and after intercritical tempering. The large ductile dimple size prior to tempering is due to the presence of precipitates which act as void nucleation sites. (XBB 792-2162)

effect is specifically associated with the dissolution of the carbides, which act as preferential void nucleation sites in the untempered alloy.

* * *

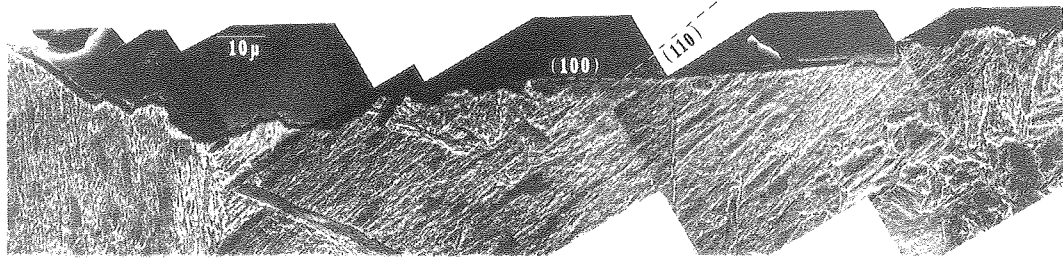
†Brief version of LBL-9835.

3. THE INFLUENCE OF RETAINED AUSTENITE ON THE TOUGHNESS OF FERRITIC CRYOGENIC STEELS.†‡

J. W. Morris, Jr., J. I. Kim, C. K. Syn and B. Fultz

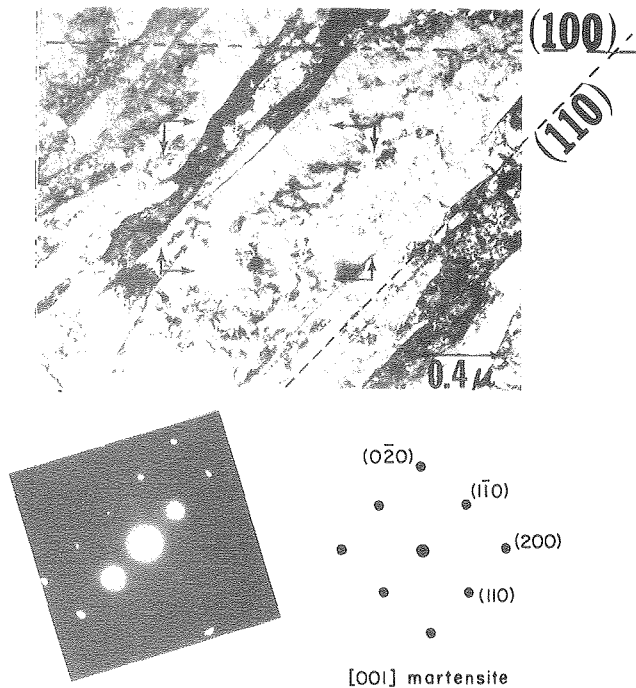
The central metallurgical question in the metallurgy of steels intended for low temperature use is the reason for the pronounced ductile-brittle transition behavior these steels often exhibit and the source of the suppression of the DBTT when the steels are intercritically tempered to introduce retained austenite. Until recently it was believed that the latter phenomenon had a fairly straightforward interpretation: The austenite, being a relatively soft structure, would act to block brittle fracture propagation through the ferritic or martensitic matrix. This interpretation was, however, called into serious question by Mössbauer spectroscopic studies at LBL and elsewhere which revealed that the retained austenite is not present during cryogenic fracture; it transforms mechanically at a rather early stage in mechanical deformation leading to fracture. These observations reopened the question of the influence of retained austenite on the ductile-brittle transition and led to series of microstructural studies under this project which have led to an alternate interpretation.

The ductile-brittle transition in ferritic cryogenic steels is associated with a shift in the fracture mode from ductile rupture to brittle quasi-cleavage. In the brittle mode the fracture surface shows large, flat cleavage facets which are large in dimension compared with the dimension of individual laths of dislocated martensite which make up the microstructure. Detailed analysis shows, however, that the martensite laths are organized into packets of many laths. The laths within a packet share a common crystallographic orientation, to the extent that they have an essentially common (100) cleavage plane. It is hence the packet size rather than the lath size which determines the effective grain size of the structure and hence the size of the observed cleavage facets. The introduction of austenite in bands along the lath boundaries appears to break up this packet alignment but, in fact, will not do so if the austenite is thermally unstable. The memory of the martensite transformation is such that retransformation of the austenite reestablishes the crystallographic orientation of the parent packet. If, however, the austenite is mechanically transformed during deformation, mechanical effects override the memory of the transformation and the austenite islands take on crystallographic orientations differing from those of the parent packet. The result is to break up the cleavage plane of the packet and hence to inhibit the cooperative cleavage of adjacent laths. This process, illustrated in the Figs. 1-3, suppresses the ductile-brittle transition temperature.



INTERCRITICALLY ANNEALED

Fig. 1. Scanning electron micrograph of the cross section of a brittle fracture surface in Fe-5.5Ni, illustrating the cooperative cleavage of lath martensite packets, presumably through cleavage along a shared (100) cleavage plane. (XBB 796-7888)



QUENCHED

Fig. 2. Transmission electron micrograph of a lath martensite packet in as quenched Fe-5.5Ni cryogenic steel, showing that the laths have essentially identical crystallographic orientation, and share (100) cleavage plane. (XBB 796-7884)

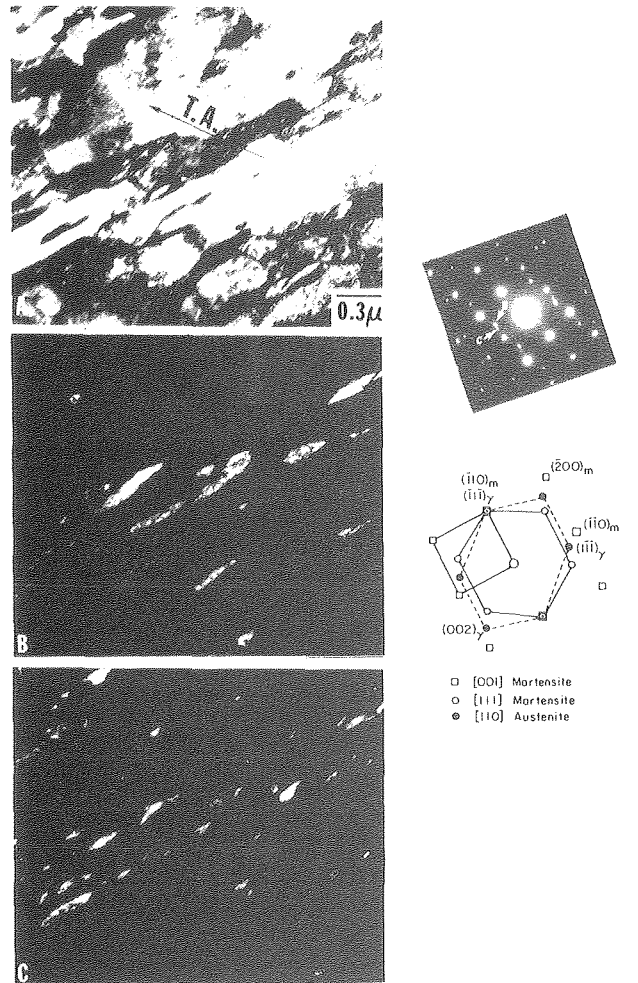


Fig. 3. Transmission electron micrograph of a packet of dislocated lath martensite into which thermally stable austenite has been introduced by intercritical tempering. The austenite was subsequently transformed by mechanical deformation. The fresh martensite caused by mechanical transformation of austenite has a crystallographic orientation different from that of the packet, causing the breakup of the (100) cleavage plane. (XBB 7910-13860)

* * *

†Brief version of LBL-9435 and LBL-10128.

‡This work was supported primarily by the Office of Naval Research under Contract No. N00014-75-6-0154.

Alloy Development Research in Ferritic Cryogenic Steels

1. THE ACHIEVEMENT OF CRYOGENIC TOUGHNESS IN LOW MANGANESE FERRITIC STEEL[†]

M. Niikura[‡] and J. W. Morris, Jr.

The steels commonly specified for structural applications at LNG and lower temperatures all have a relatively high nickel content. While the nickel addition contributes significantly to the good low temperature properties of these alloys, it also adds substantially to the cost. Consequently, there is an incentive to develop techniques for reducing or eliminating the nickel content of cryogenic steels while retaining good cryogenic properties. Because of the metallurgical similarity of manganese and nickel in ferritic steels, a program of research into the cryogenic potential of ferritic Fe-Mn steel was begun in this laboratory several years ago. This program took two rather different paths, which addressed the two distinct types of ferritic alloy which may be based on the Fe-Mn binary. For Mn contents for below about 10% Mn, the alloys develop a dislocated lath martensite substructure resembling that of Fe-Ni alloys of similar alloy content. For Mn contents in the range 10-14 wt.%, the alloys develop a blocky martensite structure with an admixture of hexagonal epsilon martensite. In previous research it was demonstrated that alloys having near 12 wt.% manganese could be toughened for cryogenic use by the addition of a small amount of boron. The information obtained in the alloy development effort which led to that success, however, coupled with our earlier research on the cryogenic behavior of Fe-Ni Alloys, suggested that it should be possible to obtain good cryogenic toughnesses at much lower manganese content.

During the past year it was demonstrated that a thermal treatment that combines grain refinement with an intercritical temper (the 2BT treatment originally developed for use with Fe-Ni cryogenic steels) may be used to achieve an excellent combination of strength and toughness in a nickel-free ferritic steel of nominal composition Fe-5Mn-0.2Mo-0.02C at temperatures as low as -196°C. The good properties achieved are attributed to a symbiotic interaction between the grain refinement treatment and the introduction of thermally-stable retained austenite during tempering, a conclusion supported by a comparison of the results to those obtained with simple heat treatments. The influence of carbon, manganese, and nickel additions to the base compositions was studied. Increasing carbon content above ~ 0.04 wt.% causes a deterioration in toughness, as does an increase in manganese to 8 wt.%. An addition of 1 to 3% nickel is beneficial, giving an increase in alloy strength at -196°C without loss of toughness.

The results of this research show that it is possible to treat low manganese, nickel-free ferritic steels so that they have cryogenic toughnesses approaching that of the commercial 9Ni grades. The comparison is documented in Fig. 1 and 2.

THERMAL CYCLING - T (2BT)

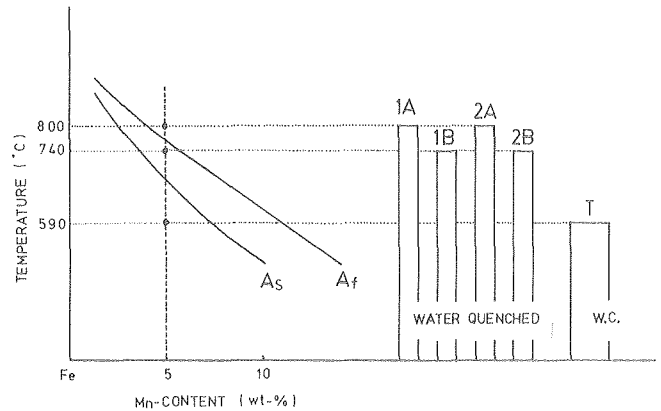


Fig. 1. Schematic of the 2BT treatment as used in the processing of the Fe-5Mn alloys.

(XBL 792-8393)

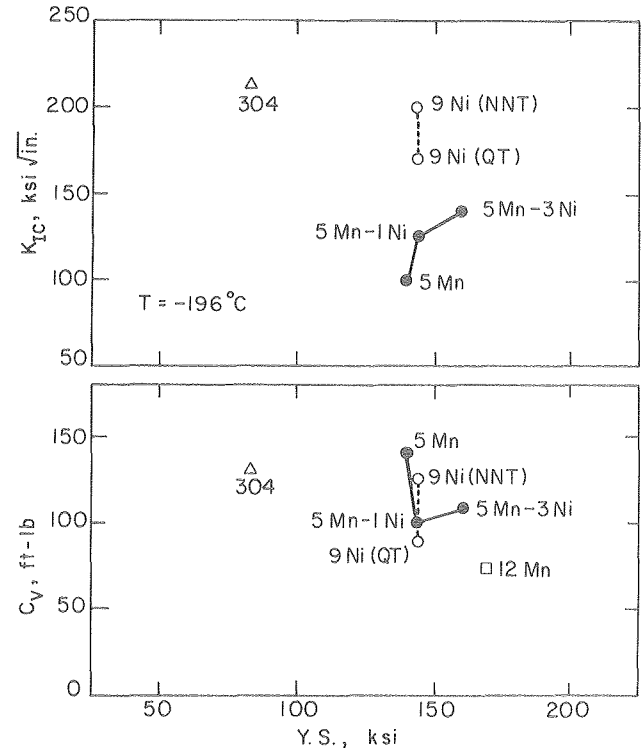


Fig. 2. Comparative plot of Charpy impact energy and estimated fracture toughness against yield strength for the Fe-5Mn and Fe-5Mn-XNi alloys at -196°C. These are compared with 9Ni steel in the QT and NNT conditions, 304 stainless steel, and the LBL-developed boron-modified Fe-12Mn alloy.

(XBL 798-6766)

* * *

†Brief version of LBL-9798.

‡Present address: Central Research Laboratories, Nippon Kokan K. K., Kawasaki, Japan.

2. METALLURGICAL INTERPRETATION OF THE QLT TREATMENT FOR LOW NICKEL CRYOGENIC STEELS†

J. I. Kim and J. W. Morris, Jr.

While steels with relatively high nickel content, e.g. 9Ni steel, have good properties at liquid nitrogen temperature in the quench and tempered condition, it has long been known that complex thermal treatments are required to establish outstanding low temperature properties in alloys which are leaner in nickel. The sophisticated heat treatment which has had the greatest commercial success in the processing of steels at liquified natural gas and liquid nitrogen temperature is the so-called QLT treatment developed by the Nippon Steel Company in Japan. In this treatment an alloy containing approximately 5.5Ni is austenitized, quenched, intercritically annealed at a temperature near the top of the two-phase $\alpha + \gamma$ region, quenched and then given a final intercritical temper toward the lower end of the two-phase range (see Fig. 1). There remains some mystery as to precisely what function the intermediate treatment served in imparting good cryogenic properties to the final alloy.

The benefit obtainable for the L treatment in the QLT sequence was investigated using a combination of transmission electron microscopy to monitor microstructural changes and scanning electron microscopy to monitor chemical redistribution during the treatment. These investigations lead

to what appears to be a self-consistent analysis of the benefit obtained from the intermediate L intercritical anneal in terms of its effect on the nature and distribution of thermally stable retained austenite in the final product. Specifically, if a low nickel alloy is intercritically tempered immediately after quenching, the low nickel content of the matrix has the consequence that very little austenite is introduced, and this austenite is relatively lean in nickel, unless very long tempering times are used. If exceptionally long tempering times are used, the austenite is rich in nickel and thermally stable, but appears in the form of relatively large, blocky austenite islands widely dispersed through the matrix. The intermediate L treatment, on the other hand, creates a segregated three-phase mixture of tempered martensite, fresh martensite, and retained austenite. The fresh martensite and the retained austenite are relatively high in nickel. When this structure is then intercritically tempered at a lower temperature, a dense distribution of thermally stable austenite is created within, and at the boundaries of the regions which already have a high nickel content. The consequence is that a dense distribution of fine, lath-like stable islands of austenite can be created through a short intercritical temper following the L treatment. The final microstructure strongly resembles that of intercritically tempered Fe-Ni alloys of much higher nickel content. In essence, the effect of the L treatment is apparently to deceive the alloy into behaving as if it had a much higher nickel content than it in fact does.

* * *

†Brief version of LBL-9956.

Welding Research

1. A REVIEW OF THE DEVELOPMENT OF FERRITIC CONSUMABLE FOR THE WELDING OF 9% NICKEL STEEL†

Kim W. Mahin, J. W. Morris, Jr. and I. Watanabe‡

Since its development in 1944 by the International Nickel Company, 9% nickel steel has been extensively used for the manufacture of liquified gas containment vessels. Its excellent toughness and strength make it suitable for use at temperatures as low as -196°C . However, the excellent properties of this material have not been used to their fullest due to the current necessity of joining 9% nickel steel plates with austenitic or modified austenitic weld consumables. The disadvantage in the use of these high alloy consumables are two-fold: their high cost destroys much of the economic incentive to utilize 9% nickel steel in preference to aluminum or stainless grades for cryogenic applications, and their relatively low strengths prevent the designer from taking full advantage of the high yield strength of 9% nickel steel in those cases where the relevant codes permit the use of yield strength as design criteria, as they almost inevitably do in Europe and in Japan. For these reasons the development of suitable ferritic consumables for the

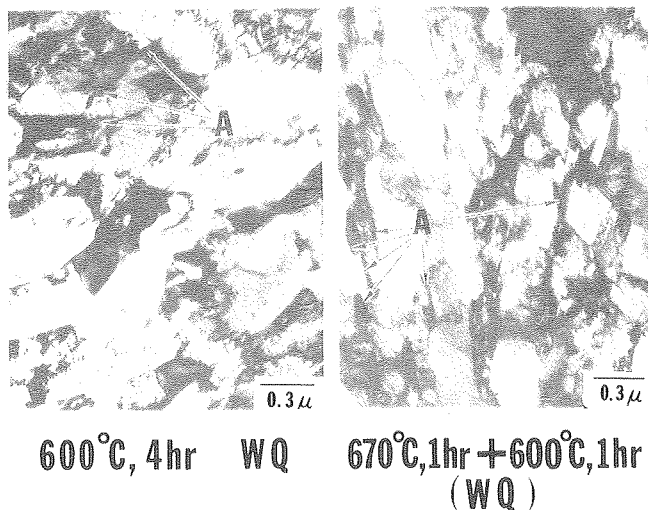


Fig. 1. Comparative transmission electron micrographs of Fe-5.5Ni (a) tempered at 600°C for 4 hours and (b) tempered at 670°C for 1 hour followed by tempering at 600°C for 1 hour showing the much denser and finer distribution of retained austenite in the latter case. (XBB 792-1343)

joining of 9% nickel steel is widely regarded as an important technological problem, and is the subject of active research in Japan, in the United States, and in the Soviet Union.

To help provide a base for increased collaboration in research on this problem, a review of prior research on the development of ferritic weld consumables in Japan and in the United States was prepared as a collaborative effort between MMRD personnel and personnel at Nippon Kokan KK, a Japanese steel company that has been very active in this research. This review was then collated with a similar study prepared by the personnel of the Paton Institute in the Soviet Union and made the basis for discussions at the most recent International Cryogenic Materials Conference. The purpose of the review and discussions was to identify the most promising avenues of future research. Two avenues were identified. The first, currently preferred in Japanese research, stresses the use of filler metals that closely match the base composition, in automated gas tungsten arc welding practice under carefully controlled conditions. The second, which is currently preferred in the United States and in the Soviet Union, in part because automated GTA welding practice is not so well developed in these countries, is the use of chemically modified ferritic consumables for gas metal arc welding practice. Promising results have been obtained with both approaches to the development of ferritic consumables, and continued research appears to offer a high probability of success.

* * *

†Brief version of LBL-10129.

†Present address: Nippon Kokan Kabushiki Kaisha, Kawasaki, Japan.

2. A STUDY OF FERRITIC WELD DEPOSITS IN Fe-9Ni STEEL†

Kim W. Mahin

LBL research toward the development of a ferritic weld consumable for Fe-9Ni steel has concentrated on consumables suitable for the gas metal arc process and has focused particularly on the microstructural analysis of factors influencing low temperature toughness levels in the weld deposit and heat affected zone. To date four ferritic wire compositions have been analyzed, which differ primarily in their contents of molybdenum, silicon, titanium, and aluminum. All are 11 to 12 wt.% nickel ferritic weld consumables.

Microstructural and Auger spectroscopic analysis of test weld consumables appears to show three major sources of brittleness in the weld deposit: weld defects, which are particularly severe when the weld consumable contains an inadequate concentration of deoxidizers, variation in the types of inclusions present and their morphology, and the large, columnar dendrite structures characteristic of weld deposits, which appear to offer relatively easy fracture paths along the boundaries of the columnar dendrites. The first two of these problems appear to have straightforward solutions, at least in the laboratory sense. The association between the preferred fracture path and the dendrite structure is, however, more subtle and requires further investigation. Auger spectroscopic analysis of weld fracture surfaces has verified that fracture occurs by cleavage through the dendrites, as shown in Fig. 1. Mössbauer analysis of weld surfaces reveals the absence of retained austenite, a puzzling feature since some austenite is present in materials given a weld-like thermal cycle in

AUGER SPECTRUM FOR CVN FRACTURE SURFACE

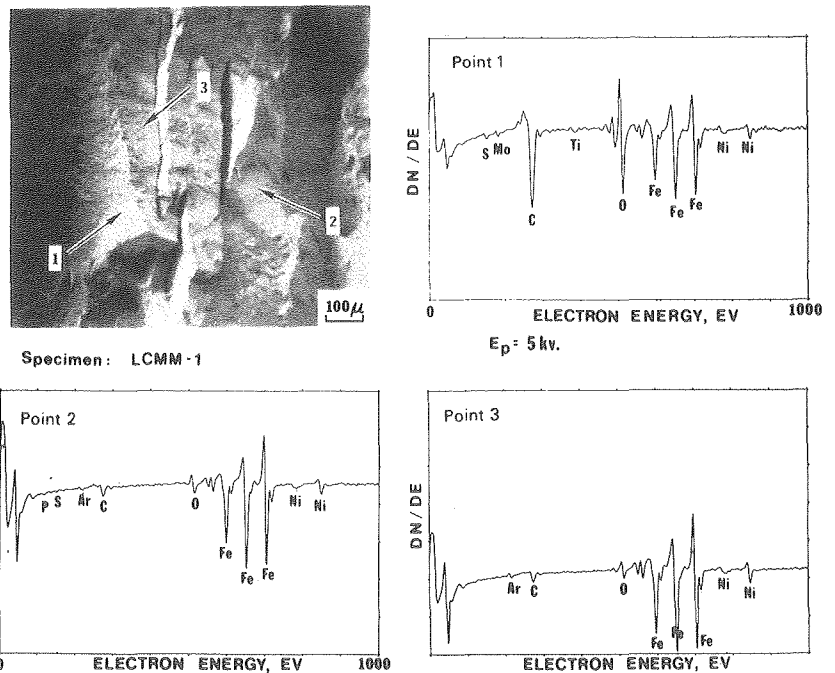


Fig. 1. Auger spectra of isolated points on brittle fracture surface in an 11-Ni ferritic weldment showing branches of the fracture through regions of different chemical composition. These regions correspond to differing locations within columnar dendrites. Points 1, 2, and 3 refer to various regions in the dendrite. Point 3 is taken from the dendrite core region, whereas points 1 and 2 are located nearer the inner dendrite region.
(XBB 798-10354)

the absence of constraint. The association between the preferred fracture path and chemical segregation in weld dendrites is under continued investigation, as are methods of accomplishing the refinement of the weld metal structure through sophisticated use of the welding process.

* * *

†Brief version of LBL-10130.

3. WELDABILITY STUDIES ON GRAIN-REFINED Fe-12Ni-0.25Ti FOR LIQUID HELIUM USE†

D. E. Williams

Research conducted at LBL some years ago established the possibility of thermally processing an Fe-12Ni-0.25Ti ferritic alloy to establish an extremely fine grain size with the consequence that the alloy remains tough at liquid helium temperature. Such an alloy may possibly find important applications in superconducting magnets and other devices intended for use in liquid helium, but, inasmuch as the most interesting of these applications require the alloy to be used in welded structures, procedures for welding this material without destroying its cryogenic properties must first be established. To initiate research along these lines an investigation was made of the possibility of welding the alloy with Inconel No. 92 filler metal. Inconel 92 is a very high alloy austenitic filler metal which was attractive for initial studies since it seemed safe to assume that this material would be tough at 4 K in the as-welded condition, with the consequence that plates welded with this alloy should remain tough unless their toughness is eliminated by embrittlement of the heat-affected zone.

Plates of Fe-12Ni-0.25Ti were grain refined by the conventional 2B grain refinement thermal treatment and welded with Inco 92 using the gas metal arc welding process with argon-15% helium gas shielding. For comparison purposes the alloy was also electron beam welded without filler metal addition, using both a single pass and a double-sided two pass welding process. The weldments were radiographed in sections and Charpy V notched specimens removed for testing at both liquid nitrogen and liquid helium temperatures. The results demonstrated very poor toughness in the electron beam weldment. However, the gas metal arc weldments exhibited toughness of 50 to 90 ft lbs. in both the weld metal and the heat affected zone in liquid helium, suggesting that reasonable cryogenic toughness could be established. Since there is considerable ambiguity in the proper conduct and interpretation of toughness tests involving the heat-affected zone in weldments, these results are not regarded as definitive, but do offer considerable encouragement that weld filler metals and weld procedures can be established to permit the use of ferritic cryogenic steels in welded structures at 4 K.

* * *

†Brief version of LBL-10259.

Superconductivity Research

1. MONOLITHIC PROCESSING OF V-Ga SUPERCONDUCTORS†

M. Hong and D. Dietderich

The A-15 superconducting phases have promising superconducting properties but are intrinsically brittle. Hence special processing techniques must be used to form them into wires or tapes. The metallurgically simplest method of wire manufacture involves casting an ingot of desired composition and extruding or drawing the case material into a wire. Virtually all conducting wires, including ductile Nb-Ti superconducting wires, are manufactured in this way. It is possible that variations on conventional wire-making practice may also be used for manufacture of A-15 superconducting wire or tapes.

A monolithic process has been successfully developed in this laboratory to produce superconducting wire from the V-Ga system by controlled precipitation of A-15 V₃Ga phase inside the bcc matrix of a V-rich solid solution. Ingots of V-17 to 19 at.% Ga were prepared by arc melting, homogenization, and quenching, were deformed at intermediate temperature into tape, and were then aged at temperatures in range 600 to 1000°C to precipitate the A-15 phase. Critical temperatures of approximately 14.8 K were found in materials aged for the appropriate time at temperatures of 750°C or below. This critical temperature compares favorably to the maximum previously obtained in the vanadium-gallium system. Research is currently in progress to increase the maximum amount of high quality superconducting phase obtainable in the cross section so as to produce a wire with promising current-carrying characteristics.

* * *

†Brief version of LBL-10007.

2. THE ATTAINMENT OF HIGH CRITICAL TEMPERATURES IN V-Ga MONOLITHIC WIRE THROUGH DIRECT PRECIPITATION†

M. Hong and D. Dietderich

Research on the monolithic processing of V-Ga superconducting wires has shown that it is possible to obtain very high critical temperatures (near 15 K) by direct precipitation in a wire or tape which has previously been severely worked. This result was initially surprising for two reasons: first, the equilibrium phase diagram of the vanadium-gallium system predicts that the A-15 phase precipitated from a vanadium-rich solid solution will deviate from V₃Ga stoichiometry to the vanadium-rich side, hence having a relatively low critical temperature. It is experimentally found, by contrast, that quite high critical temperatures may be obtained. Second, the equilibrium phase diagram further predicts that the deviation from stoichiometry will become more pronounced as the aging temperature is lowered. It is experimentally found, by contrast, that very

high critical temperatures are more easily obtained at lower aging temperatures, and that the optimum aging temperature lies in the range 600 to 750°C, a relatively low temperature in the vanadium-gallium system. More detailed investigations were undertaken to interpret this behavior.

Further research showed that the critical temperature of the directly precipitated A-15 vanadium-gallium phase depends upon the aging time as well as the aging temperature. Representative results are shown in Fig. 1. The data reveal that the critical temperature increases to a maximum and then decreases with longer aging time. Both the time and temperature dependence of the critical temperature bear an intriguing resemblance to curves of strength vs. aging time in precipitation hardening structural alloys. The interpretation of this phenomenon almost certainly lies in deviations from equilibrium behavior. A simple thermodynamic argument originally due to J. W. Gibbs seems to suffice. As illustrated in Fig. 2, the initial precipitates formed on precipitation from a supersaturated solid solution is thermodynamically anticipated to have a composition governed by the requirement of equal chemical potential, rather than the composition indicated by the equilibrium phase diagram. This has the consequence that the precipitate formed on initial precipitation from a highly supersaturated solution will tend to be relatively rich in solute, and in the case of V-Ga, is likely to be more stoichiometric than the equilibrium phase diagram would predict. As the precipitates are allowed to "overage" and approach equilibrium, their compositions will tend to take on that indicated by the equilibrium phase diagram. In the case of the V-Ga A-15 phase, where deviations from stoichiometry are associated with decreases in critical temperature, one would then expect that the critical temperature will decrease, as is experimentally observed. It is hoped that the phenomenon may be utilized to create superconducting wires of exceptional properties through direct precipitation processes.

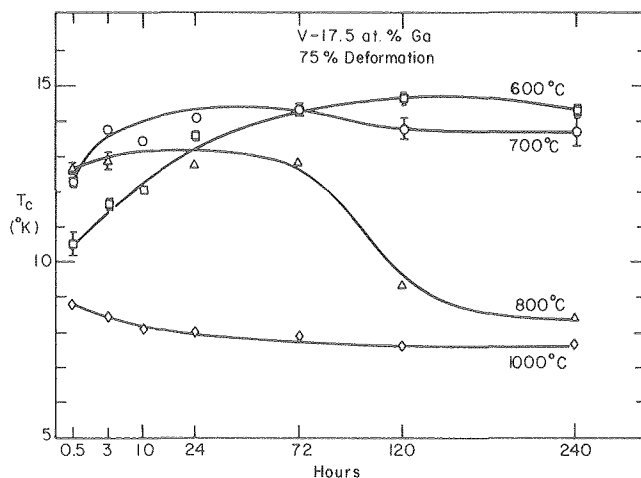


Fig. 1. The superconducting temperature of a V-17.5% Ga alloy deformed and then aged to precipitate the A-15 phase. (XBL 793-5871)

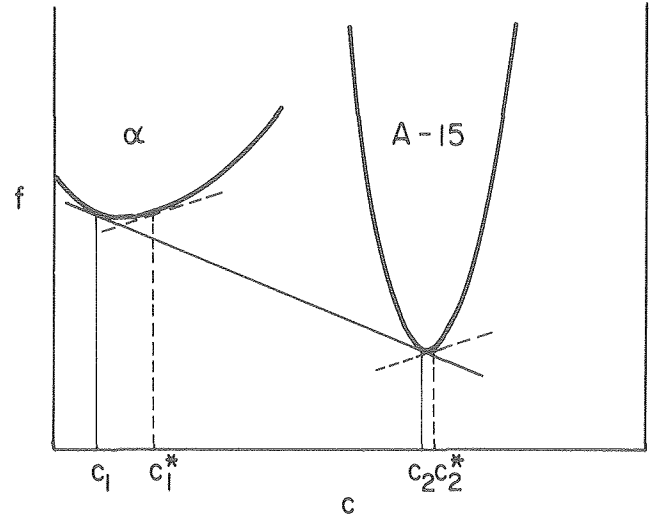


Fig. 2. Schematic illustration of Gibbs free energy vs. composition for a given aging temperature, showing the predicted solute enrichment in the precipitate phase when formed from a highly supersaturated solution. (XBL 793-5877)

* * *

†Brief version of LBL-9797.

RESEARCH PLANS FOR CALENDAR YEAR 1980

Theoretical studies. It is anticipated that the major thrust of our theoretical research under this program during calendar year 1980 will continue to focus on the influence of elastic energy in solid state phase transformations, including particularly martensitic transformations and solid state precipitation reactions. Outstanding problems under investigation include the simulation of martensitic transformations in more realistic two-dimensional cases and in three dimensions, the theoretical solution of predicted coherent precipitate habits in cases involving precipitate-matrix symmetry combinations other than tetragonal/cubic and the investigation of techniques for incorporating elastic modulus differences into the Khachaturyan theory of elastic interactions.

Fundamental experimental research in the metallurgy of alloy steels. It is anticipated that fundamental studies in steel metallurgy will expand considerably during calendar year 1980. Key problems identified for investigation include the role of chemical additives in modifying or destroying packet alignment in dislocated lath microstructures, a problem whose successful solution might create the possibility of developing outstanding structural alloys with very simple heat treatment; the grain boundary chemistry of chemically modified austenitic steels, a problem whose solution might help to overcome serious sensitization problems experienced with available austenitic alloys; and Mössbauer spectroscopic studies of magnetic transitions in austenitic steels at very low temperature, a problem whose

solution may resolve a set of curious anomalies in the mechanical behavior of austenitic cryogenic steels at temperatures near 4 K.

Alloy development research. It is anticipated that alloy development research during calendar year 1980 will concentrate on the exciting new class of low manganese ferritic cryogenic steels developed during the previous year's research and currently in the process of being patented. The research will concentrate on the microstructural properties of these steels and their response to chemical modification in the hope of identifying still simpler alloys for heat treatments.

Welding research. That portion of LBL welding research, which will be carried out under this project during calendar year 1980, will continue to emphasize the development of advanced welding techniques for ferritic structural alloys to be used at cryogenic temperatures. It is also anticipated, however, that this project will involve an increasing complement of fundamental metallurgical investigation into the detailed structure of weldments, the segregation of solute species within weldments, and the thermal histories experienced by the weldment and the base metal adjacent to the weld with the intent of devising techniques for using that thermal history to improve the properties of welded plates.

Superconductivity research. It is anticipated that superconductivity research during calendar year 1980 will continue to address the problem of manufacturing superconducting wires through monolithic processes which employ direct precipitation. A key problem is the development of wire drawing procedures for supersaturated solutions of A-15 forming elements so as to achieve exceptionally high dislocation densities, and create the possibility of depositing reasonable volume fractions of high quality superconducting phase. The research will also move away from V-Ga system to address the applicability of monolithic processing techniques to other A-15 forming compounds of particular promise which are incapable of manufacture by the currently popular "bronze" process.

1979 PUBLICATIONS AND REPORTS

Refereed Journals

1. L. J. Chen, "Mechanism of Austenite-Martensite Transformation and the Location of Carbon Atoms in Martensite Lattice," Chinese J. of Mat. Sci., 10, 3 (1978).
2. Kenton L. Hanson, "Determination of Grain Density in Space-Filling Geometries from Measurable Two-Dimensional Parameters," Acta Met. 27, 515 (1979).
3. S. K. Hwang and J. W. Morris, Jr., "The Improvement of Cryogenic Mechanical Properties of Fe-12Mn and Fe-8Mn Alloy Steels Through Thermal/Mechanical Treatments," Met. Trans. 10A (1979).

4. K. M. Chang and J. W. Morris, Jr., "Precipitation-Strengthened Austenitic Fe-Mn-Ti Alloys," Met. Trans. 10A (1979).

5. D. Grivas, K. L. Murty and J. W. Morris, Jr., "Deformation of Pb-Sn Eutectic Alloys at Relatively High Strain Rates," Acta Met. 27, 731 (1979).

Other Publications

1. K. M. Chang, J. Y. Koo, J. W. Morris, Jr. and G. Thomas, "Coupled γ' " Precipitation in Fe-Ni Base Alloys," in Proceedings of the Electron Microscopy Society of America, San Antonio, Texas, August 1979, G. W. Bailey, Ed.

2. S. K. Hwang and J. W. Morris, Jr. Patent #4,162,158, "Ferritic Fe-Mn Alloy for Cryogenic Application."

LBL Reports

1. K. W. Mahin, K. Hanson, and J. W. Morris, Jr., "Comparative Analysis of the Cellular & Johnson-Mehl Microstructures through Computer Simulation," LBL-8752.

2. D. Grivas, K. L. Murty, and J. W. Morris, Jr., "Deformation of Pb-Sn Eutectic Alloys at Relatively High Strain Rates," LBL-8790.

3. S. Chen, J. W. Morris, Jr. and A. G. Khachaturyan, "The Computer Simulation of the Formation of the 'Tweed' Structure & Modulated Structure in the Decomposition Reactions," LBL-9098.

4. Keh-Minn Chang, (Ph.D. thesis), "Precipitation Hardening in Fe-Ni Base Austenitic Alloys," LBL-9208.

5. Sheree Hsiao-Ru Chen, "The Computer Simulation of Martensitic Transformations in Idealized Systems," LBL-9264.

6. S. Chen and A. G. Khachaturyan, "Computer Simulation of the Martensite Transformation in a Model Two-Dimensional Body," LBL-9346.

7. J. W. Morris, Jr. and J. I. Kim, "Advances in the Heat Treatments of Steel," LBL-9435.

8. S. K. Hwang and J. W. Morris, Jr., "The Use of a Boron Addition to Prevent Intergranular Embrittlement in Fe-12Mn," LBL-9583.

9. M. Hong, O. Dietderich, and J. W. Morris, Jr., "Development of A-15 (V₃Ga) Superconducting Material through Controlled Precipitation," LBL-9797.

10. M. Niikura and J. W. Morris, Jr., "Thermal Processing of Ferritic-5Mn Steels for Toughness at Cryogenic Temperatures," LBL-9798.

11. J. W. Morris, Jr., K. M. Chang, D. H. Klahn, G. Thomas, and S. Jin, "Heat Treatment & Mechanical Properties of a Ta-Modified Fe-Base Superalloy," LBL-9799.

12. J. I. Kim and J. W. Morris, Jr., "On the Scavenging Effect of the Retained Austenite in a Low Carbon Fe-5.5 Ni Alloy," LBL-9835.

13. J. I. Kim and J. W. Morris, Jr., "The Mechanism of Microstructural Change & Its Consequences in a Low Carbon Fe-6Ni Alloy," LBL-9956.
14. E. S. Pundarika (Ph.D. thesis), "Kinetics of Clustering Reactions," LBL-10005.
15. M. Hong, D. Dietderich, and J. W. Morris, Jr., "Research on Monolithic Process of Making A-15 Superconducting Materials," LBL-10007.
16. S. K. Hwang and J. W. Morris, Jr., "The Improvement of Cryogenic Mechanical Properties of Fe-12Mn and Fe-8Mn Alloy Steels Through Thermal-Mechanical Treatments," LBL-10126.
17. K. M. Chang and J. Y. Koo, J. Morris, and G. Thomas, "Coupled γ' and γ'' Precipitation in Fe-Ni Base Austenites," LBL-10127.
18. J.W. Morris, Jr., C. Syn, J. I. Kin, and B. Fultz, "Consequences of the Re-Transformation of Precipitated Austenite in Ferritic Cryogenic Steels," LBL-10128.
19. K. W. Mahin, Y. Watanabe, and J. W. Morris, Jr., "A Review of the Development of Ferritic Consumables for the Welding of 9% Nickel Steel: Research in the U.S. and Japan," LBL-10129.
20. K. W. Mahin and J. W. Morris, Jr., "A Study of Ferritic Welded Deposits in Fe-9Ni Steel," LBL-10130.

Papers Presented

1. J. W. Morris, Jr., "Computer Simulation Studies of Dislocation Glide," ARPA Workshop on Constitutive Relations in High Temperature Cryogenics, La Jolla, July 1979.
2. K. W. Mahin, J. W. Morris, Jr., and I. Watanabe, "A Review of the Development of Ferritic Consumables for the Welding of 9% Nickel Steel: Research in the U.S. and Japan," International Cryogenic Materials Conference, Madison, Wisconsin, August 1979.
3. K. W. Mahin and J. W. Morris, Jr., "A Study of Ferritic Weld Deposits in Fe-9Ni Steel," International Cryogenic Materials Conference, Madison, Wisconsin, August 1979.
4. M. Hong, D. Dietderich, and J. W. Morris, Jr., "Development of A-15 Superconductors through Controlled Precipitation," International Cryogenic Materials Conference, Madison, Wisconsin, August 1979.
5. C. K. Syn, S. K. Hwang, and J. W. Morris, Jr., "Ferritic Fe-Mn Alloys for Cryogenic Use: I. Fe-12Mn," International Cryogenic Materials Conference, Madison, Wisconsin, August 1979.
6. M. Niikura and J. W. Morris, Jr., "Ferritic Fe-Mn Alloys for Cryogenic Use: II. Fe-5Mn," International Cryogenic Materials Conference, Madison, Wisconsin, August 1979.
7. M. Hong, D. E. Wedge, and J. W. Morris, Jr., "The Shape and Habit of Coherent Nitride Precipitates in Alpha Iron," TMS Fall Meeting, Milwaukee, Wisconsin, September 1979.
8. J. W. Morris, Jr., A. G. Khachaturyan and Sheree Chen, "The Free Energy of an Elastic Solid Containing an Arbitrary Distribution of Substitutional Defects," TMS Fall Meeting, Milwaukee, Wisconsin, September 1979.
9. Sheree Chen, A. G. Khachaturyan and J. W. Morris, Jr., "Low Temperature Clustering of Substitutional Defects in a Model Elastic Solid," TMS Fall Meeting, Milwaukee, Wisconsin, September 1979.
10. M. Hong, D. Dietderich, and J. W. Morris, Jr., "Superconducting Wire through Controlled Precipitation in V-Ga," TMS Fall Meeting, Milwaukee, Wisconsin, September 1979.
11. K. W. Mahin and J. W. Morris, Jr., "Developing Good Toughness Properties in Ferritic Weld Deposits at Cryogenic Temperature," TMS Fall Meeting, Milwaukee, Wisconsin, September 1979.
12. J. W. Morris, Jr. and K. W. Mahin, "Ferritic Alloys and Weldments for Cryogenic Use," Golden Gate Chapter, ASM, September 1979.
13. J. W. Morris, Jr., "Ferritic Cryogenic Steels for 4°K Use," NBS-DOE Workshop in Materials at Low Temperature, Vail, Colorado, October 1979.
14. J. W. Morris, Jr., "Advances in the Heat Treatment of Steel," Rutgers University, November 1979.

b. Structure-Property Relationships in Semiconductor Materials*

J. Washburn, Investigator

1. CROSS SECTION TRANSMISSION ELECTRON MICROSCOPY AS A POWERFUL NEW TECHNIQUE FOR THE STUDY OF DEFECTS IN THIN SURFACE LAYERS†

J. Washburn and D. K. Sadana

The secondary defect structures derived from the damage introduced by ion implantation and subsequent furnace, laser, or electron beam annealing has been studied by several workers using transmission electron microscopy (TEM). However, the TEM specimens have usually been prepared in the conventional manner (plane of the foil being parallel to the implanted surface). As a result, only damage distribution in "plan" view could be obtained. Although much useful information concerning defect structures has been obtained and characterization of many defects has been carried out, the depth distribution of the defects was difficult to ascertain even from stereo-microscopy. This is especially true for cases where either two discrete layers of defects separated by a defect-free region were present or where the defects of interest were buried under another dense band of damage.

The present work has been aimed at the development of a new specimen preparation technique permitting the damage distribution to be observed in 90° cross-sectional view. For this report, we have chosen three examples to demonstrate the power and usefulness of the technique developed. All the examples shown here are for P⁺ implanted (111) Si, implanted at 120 keV. The cross-sectional micrographs shown in Figs. 1-3 were taken using strong-beam bright-field contrast and all the plan-view micrographs were taken using weak-beam dark-field contrast methods. Figure 1(a) shows a cross-sectional micrograph for an implantation dose of $5 \times 10^{14}/\text{cm}^2$ implanted at RT and subsequently furnace annealed at 950°C for 20 minutes. The micrograph shows two discrete layers, A and B, each containing dislocation loops. Using the depth distribution information from the cross-sectional view, it was possible to prepare plan-view specimens corresponding to each damage layer. The TEM plan-view micrographs for each separate layer are shown in Figs. 1b and 1c. The detailed weak-beam, dark-field analysis of the defects from the plan-view specimens showed that layer A contained three sets of inclined $a/2\langle 117 \rangle$ type loops and only one set of $a/3\langle 111 \rangle$ type loops lying on the (111) plane parallel to the plane of the foil. The second layer, B, contained three sets of inclined $a/2\langle 110 \rangle$ type loops and all four sets of $a/3\langle 111 \rangle$ type loops. The loops in both layers were interstitial in nature. Such detailed information concerning the defects in each separate layer could not have been easily obtained without the cross-sectional micrographs.

Figure 2a shows a cross-sectional micrograph for a specimen implanted to a dose of $10^{15} \text{ P}^+/\text{cm}^2$ at 100°C and subsequently furnace-annealed at 850°C for 20 minutes. The micrograph shows a band of defects, C, and a discrete layer of dislocation loops, D. The bottom edge of band C and the top edge of layer D were separated by a damage-free region. Again, because the presence of layer C

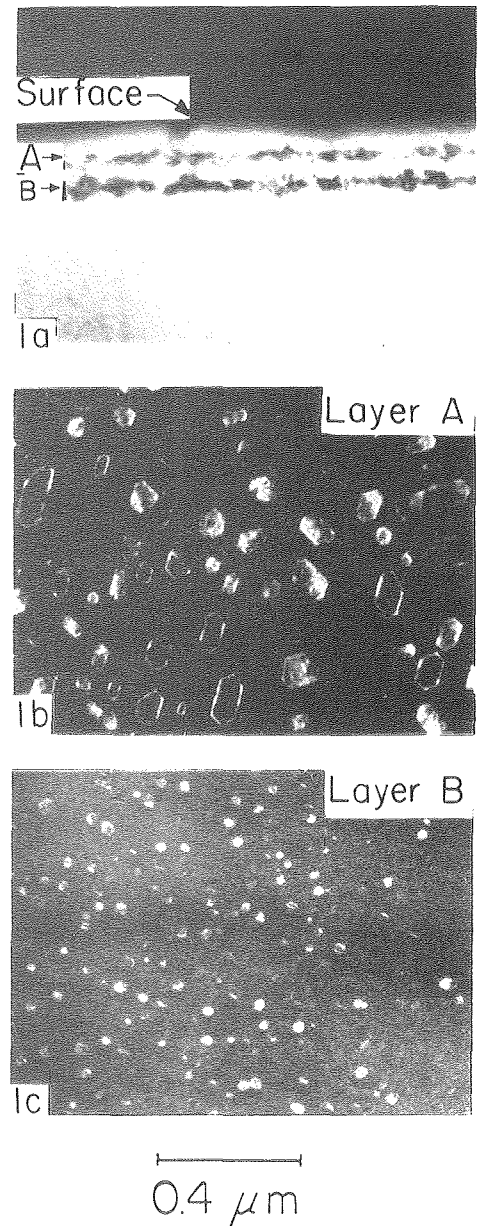
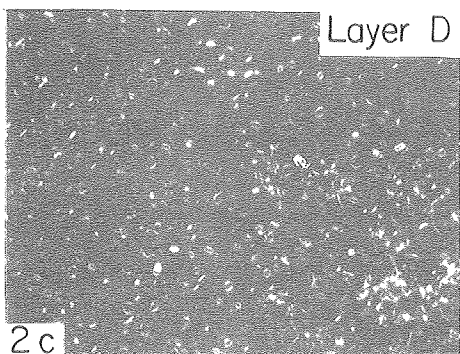
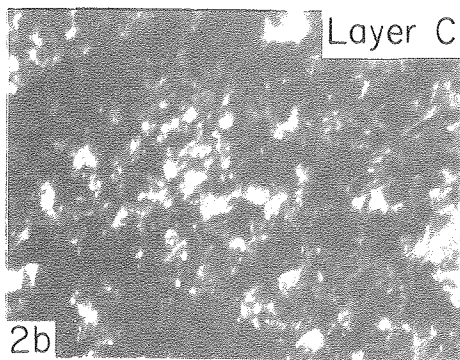
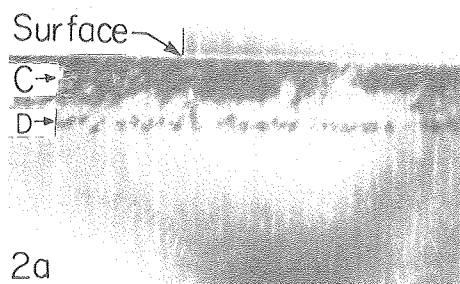


Fig. 1. P⁺-(111) Si, $5 \times 10^{14}/\text{cm}^2$, 120 keV, RT, Ta-950°C. (a) TEM 90° cross-sectional bright-field micrograph showing two discrete layers A and B containing dislocation loops. (b) TEM plan-view weak beam micrograph corresponding to layer A. (c) TEM plan-view weak-beam micrograph corresponding to layer B. (XBB 790-15810A)

*This work was supported by the Division of Materials Sciences, Office of Basic Energy Sciences, U.S. Department of Energy.

was known from Fig. 2a, layer D could be revealed in the plan-view micrograph by removal of layer C by ion-beam milling (Fig. 2c). Plan-view micrographs showed that layer C (Fig. 2b) contained twin lamellae, dislocation network, stacking faults, etc., and layer D contained three sets of inclined $a/2\langle 110 \rangle$ type loops and all four $a/3\langle 111 \rangle$ type loops. All the loops were interstitial in nature.

Figure 3a shows a TEM cross-sectional micrograph for the specimen implanted under similar conditions but subsequently laser-annealed at 0.7 J/cm^2 . The



0.4 μm

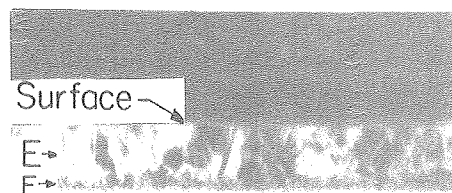
Fig. 2. $\text{P}^+\langle 111 \rangle \text{Si}$, $10^{15}/\text{cm}^2$, 120 keV, $T_i = 100^\circ\text{C}$, $T_a = 850^\circ\text{C}$. (a) TEM 90° cross-sectional bright-field micrograph showing a band of damages C and a discrete layer of loops D. (b) TEM plan-view weak-beam micrograph corresponding to layer C. (c) TEM plan-view weak-beam micrograph corresponding to layer D. (XBB 790-15810R)

micrograph shows a polycrystalline layer E continuous from the surface that is in direct contact with a heavily damaged layer F. The corresponding plan-view micrograph revealed only polycrystalline grains $\sim 1000 \text{ \AA}$ across (Fig. 3b). From the cross-sectional micrograph, the depth to which melting had occurred during laser annealing could be easily measured.

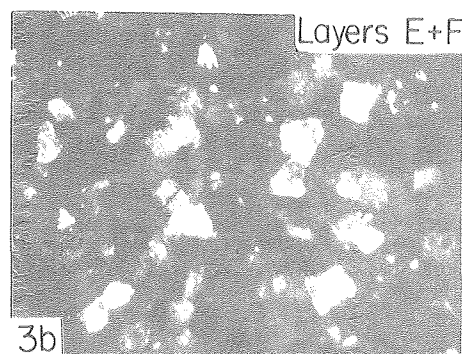
The technique for preparing cross-section TEM specimens of Si and GaAs and other semiconductor materials has been perfected to the point that even very thin surface layers of the order of 100 \AA thickness can be detected. The technique promises to be extremely important to the understanding of electrical property changes associated with laser and electron beam processing of thin surface layers.

* * *

[†]Brief version of LBL-i008, LBL-9209, and LBL-9793.



3a



3b

0.4 μm

Fig. 3. $\text{P}^+\langle 111 \rangle \text{Si}$, $10^{15}/\text{cm}^2$, 120 keV, $T_i = 100^\circ\text{C}$, L.A. = 0.7 J/cm^2 . (a) TEM 90° cross-sectional bright-field micrograph showing a polycrystalline layer E on a heavily damaged layer F. (b) TEM plan-view dark-field micrograph showing the polycrystal grains. (XBB 790-15810C)

2. ON THE INTERPRETATION OF CHanneLED RUTHERFORD BACKSCATTERING YIELDS FROM MULTILAYER SUBSURFACE DAMAGE[†]

J. Washburn and D. K. Sadana

Rutherford backscattering using a channeling orientation has been used extensively to detect lattice disorder and its depth distribution. However, this method alone is incapable of giving the detailed information concerning the nature of the disorder that can be obtained by transmission electron microscopy. Also, when more than one buried damage layer exists, quantitative interpretation becomes difficult. The present work was aimed at improving the interpretation of channeled RBS results when more than one damage layer is present. Cross-sectional TEM specimens were prepared from the same specimens used for channeled RBS observations. The specimens used were high dose rate P⁺ implanted Si wafer implanted to a dose of $7.5 \times 10^{15}/\text{cm}^2$. These implantation conditions provided several types of secondary damage structures in the same wafer due to non-uniform beam heating effects. Multicolored regions appeared at the surface due to optical interference effects at subsurface interfaces where changes in refractive index occurred. TEM 90° cross-sectional specimens were prepared to obtain damage-depth distribution for each region. The nature of the damage was further revealed by plan-view specimens. The damage distribution beneath each particular band was found to be entirely different from that present beneath the adjacent color band as can be seen in Figs. 1-4. Channeled RBS measurements were then also taken from each individual color band and the results were compared with the TEM results.

Figures 1-4 show that there was a good qualitative correlation between the results obtained by the two methods. The discrete damage layers as seen by TEM appear as discrete damage peaks in the channeled RBS spectra. The extent of disorder as revealed by the cross-section micrographs, also indicated by the diffraction patterns, correlated well with the scattering yield values obtained for the channeled spectra. For example, the first damage layer D₁ under the green band contained more disorder as compared to that in the first damage layer L₁ under the violet band and vice versa for the second damage layers. The scattering yield values in the channeled RBS spectra also followed precisely the same pattern. However, further comparison of the TEM and channeling data for the damage layers showed that, although the mean depth values for the damage layers obtained from the two methods were in close agreement, the widths of the damage layers calculated from the channeling data were consistently greater.

It was observed that dechanneling of the beam due to interaction with the disorder nearer the surface gave a background superimposed on the spectra due to the deeper damage at longer wavelengths. The dechanneling associated with the surface peak had a background on the lower energy side which was always approximately half the amplitude of the surface peak. Spectra containing single buried damage layers were also found to

have this background on the lower energy side of the peak, also half the magnitude of the peak height. Therefore, for calculations of the width of a second or third peak, the background level due to each scattering peak was assumed to be independent of that from the others and to have a magnitude of half the height of that peak at all lower energies. For peaks due to buried layers

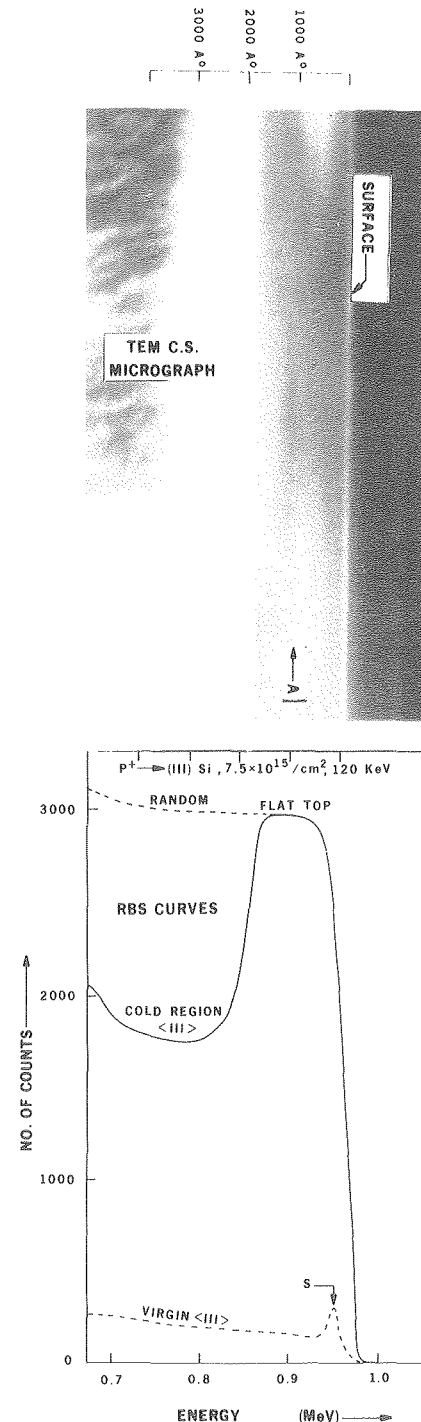


Fig. 1. Comparison of TEM cross-sectional micrograph with the channeled RBS spectrum from the "cold" region. (XBB 790-13568)

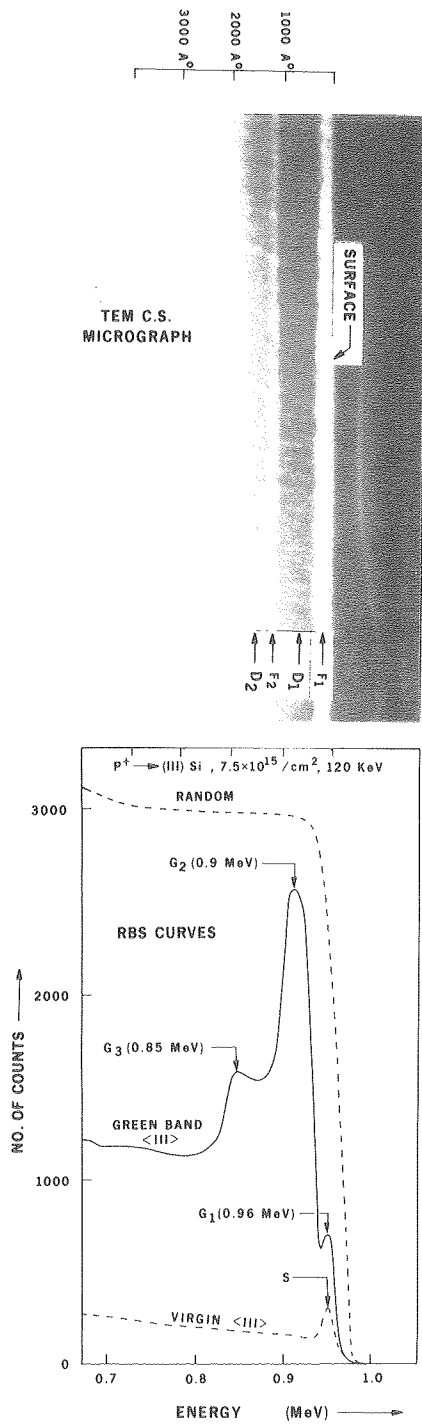


Fig. 2. Comparison of TEM cross-sectional micrograph with the channeled spectrum from the green region. (XBB 790-13567)

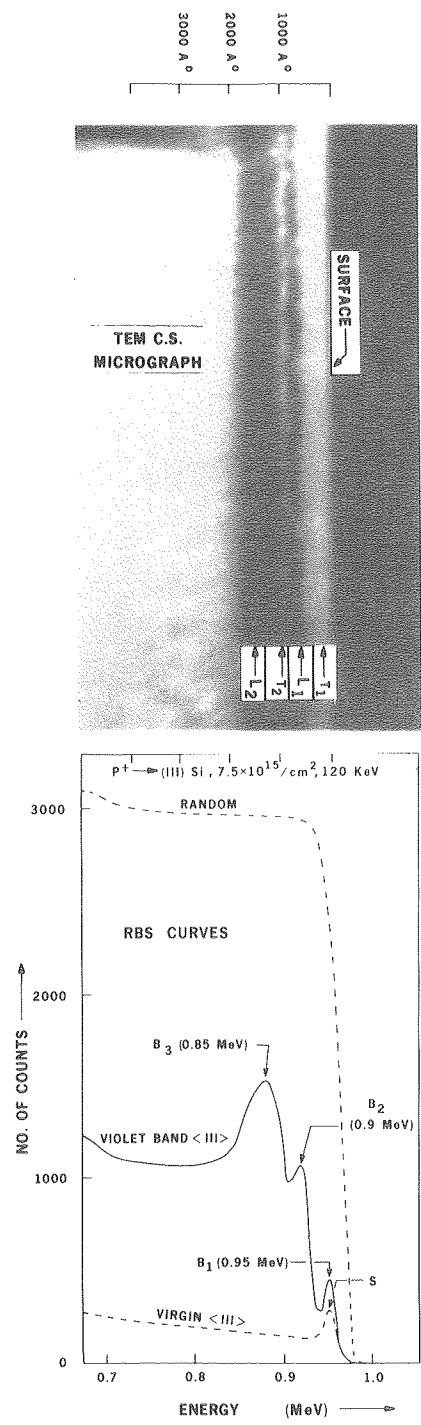


Fig. 3. Comparison of TEM cross-sectional micrograph with the channeled spectrum from the violet region. (XBB 790-13570)

of damage, the width of half-maximum was taken at a scattering yield half way between the background resulting from all the higher energy peaks and the top of the peak in question. The procedure is schematically shown in Fig. 5. The damage layer widths calculated after this background subtraction were then in close agreement with the TEM results.

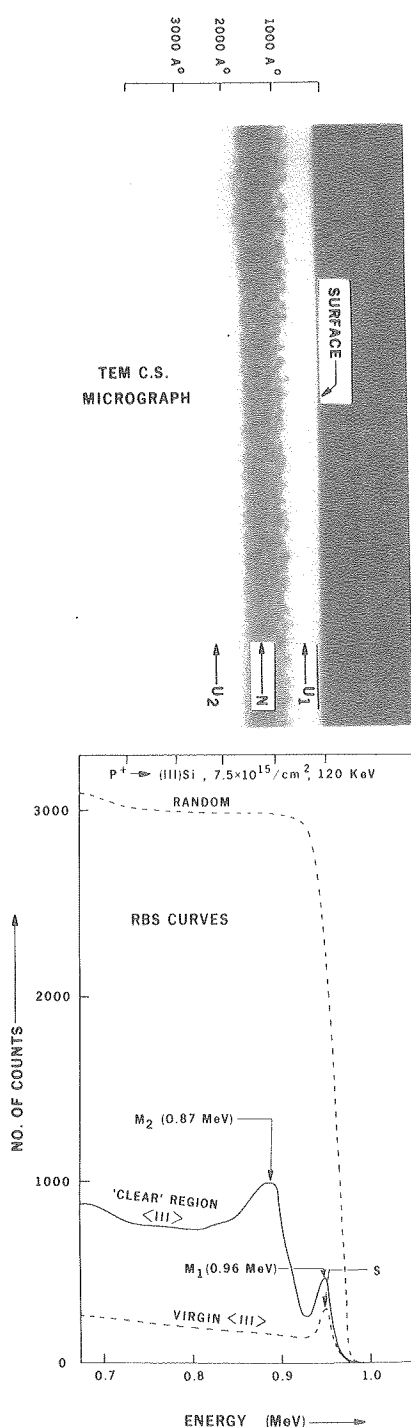


Fig. 4. Comparison of TEM cross-sectional micrograph with the channeled spectrum from the "hot" region. (XBB 790-13569)

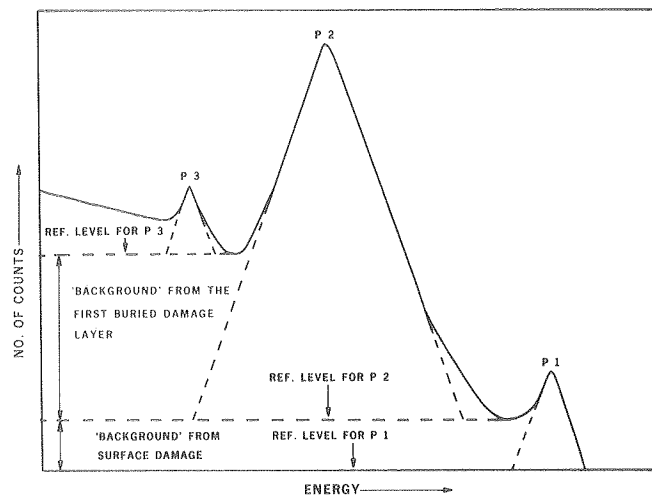


Fig. 5. Schematic diagram showing the background subtraction procedure. (XBL 7910-12209)

* * *

†Brief version of AIP Conference Proceedings on the Laser and Electron Beam Processing of Materials, November, 1979.

3. LASER AND ELECTRON-BEAM ANNEALING EFFECTS IN GALLIUM ARSENIDE †

J. Washburn and D. K. Sadana

High-energy, short pulse-length laser electron beams are being used with increasing success to recrystallize high-dose ion-implanted amorphous layers in Si and GaAs. This process is of particular interest for GaAs device fabrication where post-implantation annealing at temperatures above 800°C requires either an inert encapsulant, such as, Si_3N_4 or Si_2 or a suitable ambient pressure of As and Ga. By suitable choice of laser or electron beam parameters (such as the energy, the pulse length, etc.), epitaxial regrowth of the layers damaged by implantation can, in principle, be carried out either in the solid phase or by melting without requiring any protective layers. However, the mechanism of regrowth is not yet fully understood. This work was aimed at studying the regrowth behavior of different types of damage structures having different depth distributions in ion-implanted GaAs and Si on subsequent pulsed electron or laser beam annealing.

Gallium Arsenide

Semi-insulating Cr-doped (100) GaAs crystals were implanted with 300 keV Kr^+ ions in a non-channeling direction. This resulted in a continuous amorphous layer ~ 2100 Å thick extending from the surface (Fig. 1a). After a pulsed electron annealing at 0.4 J/cm^2 , a surface layer ~ 1350 Å thick converted into polycrystalline material

ELECTRON BEAM ANNEALING OF Kr^+ IMPLANTED GaAs
TEM 90° Cross-section Micrographs

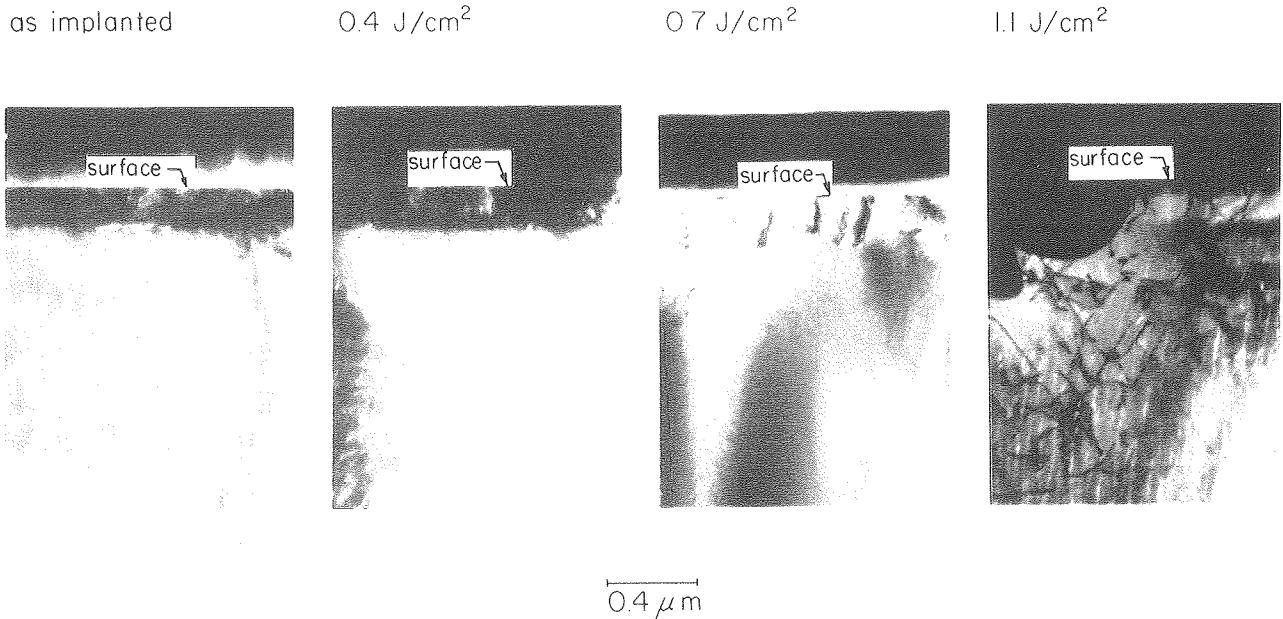


Fig. 1. TEM cross-sectional micrographs showing the electron beam annealing sequence for Kr^+ implanted GaAs [$\text{Kr}^+ \rightarrow (100)$ GaAs, $10^{15}/\text{cm}^2$, 300 keV, Ti = RT]; (a) as-implanted; (b) 0.4 J/cm^2 ; (c) 0.7 J/cm^2 ; (d) 1.1 J/cm^2 .

(XBB 799-12447)

which was in direct contact with a heavily damaged layer $\sim 800 \text{ \AA}$ wide immediately below it (Fig. 1b). This indicated that melting occurred during the annealing and that the melted region then regrew on top of a still heavily damaged deeper layer, resulting in the polycrystalline surface layer. At 0.7 J/cm^2 , dislocations looping down from the surface were seen to a depth of $\sim 2200 \text{ \AA}$ in single crystal material (Fig. 1c). This indicated that the melting this time went deeper than the depth of the as-implanted amorphous layer and that solidification resulted in epitaxial regrowth of single crystal material containing some dislocations. At 1.1 J/cm^2 microcracks at the surface were formed, and a dislocation network now extended to a depth of $\sim 1.5 \mu\text{m}$ into the material (Fig. 1d). The depth of the region with dislocations, in this case, is much deeper than the depth of the molten zone. This is evidence for high transient thermal stresses below the liquid/solid interface during the pulse.

Silicon

Amorphous layers in Si are also converted into polycrystalline material at a laser energy of 0.7 J/cm^2 (Fig. 3a in article 1).

In order to understand the effect of the crystallinity of the surface region on energy

absorption during pulsed annealing, specimens with a buried layer of damage clusters in the as-implanted condition were chosen (Fig. 2a). This kind of damage configuration was achieved by implanting P^+ into (111) Si in a nonchanneling direction at a dose rate of $\sim 0.8 \text{ mA/cm}^2/\text{sec}$ so that the temperature during implantation increased to $\sim 350^\circ\text{C}$. On subsequent laser annealing at 0.7 J/cm^2 , this layer remained practically unaffected (Fig. 2b). This is in contrast to the result for the amorphous layer where the surface layer converted into polycrystalline material (Fig. 3a in article 1). At 1.5 J/cm^2 , however, a high density of stacking faults and dislocations extended from the surface to a depth of $\sim 1800 \text{ \AA}$ and was in direct contact with a dense fine structure of defects $\sim 300 \text{ \AA}$ wide (Fig. 2c), indicating that melting occurred during the annealing but that the molten zone did not extend deeper than the tail of the as-implanted damage distribution.

The results described in this report are examples of the diverse secondary damage structures that can result for laser or electron beam annealing. A more complete understanding of the effects of numerous variables will require application of electrical measurements, TEM, and surface-layer analytical techniques to the same specimens.

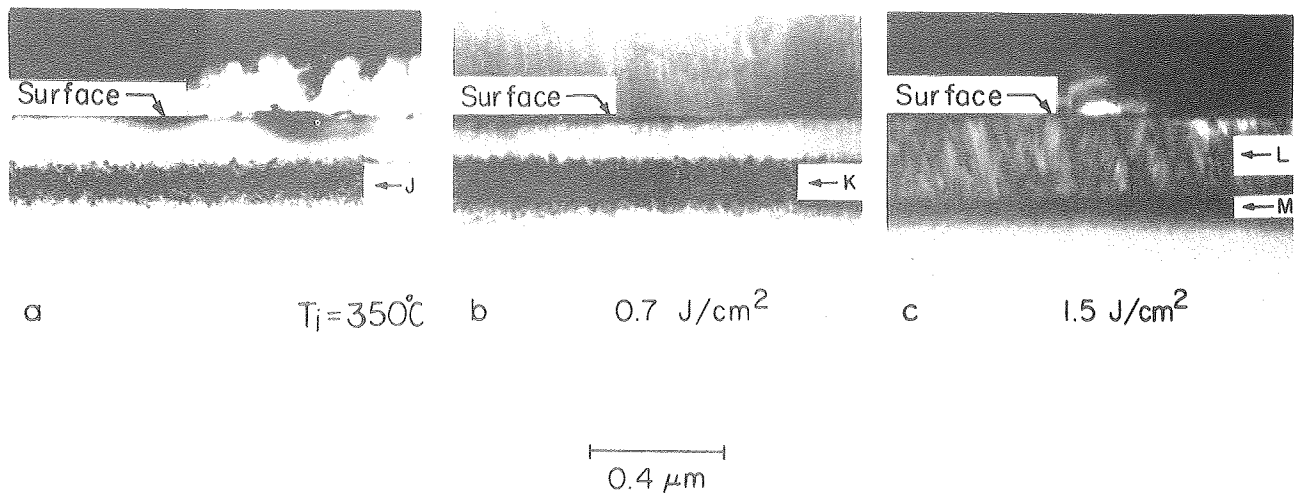


Fig. 2. TEM cross-sectional micrographs showing the laser annealing sequence for P^+ implanted Si [$P^+ \rightarrow (111)$ Si, $5 \times 10^{15}/\text{cm}^2$, 120 keV, $T_i = 350^\circ\text{C}$]; (a) as-implanted; (b) $0.7 \text{ J}/\text{cm}^2$; (c) $1.5 \text{ J}/\text{cm}^2$. (XBB 790-14331)

* * *

†Brief version of LBL-9793 and AIP Conference Proceedings on the Laser and Electron Beam Processing of Materials, November 1979, and Radiation Effects 42, 315 (1979).

4. EFFECT OF IMPLANTATION TEMPERATURE ON ION-IMPLANTATION DAMAGE IN SILICON†

R. Drosd and D. Sadana

The introduction of a high-energy ion into a crystalline substrate causes disorder along its trajectory in the crystal lattice. The extent of disorder and the length of the damage trajectory do not overlap; each damage track can be viewed as a small damage cluster by TEM. As the dose is increased, the individual damage tracks overlap to form amorphous regions. Since the distribution of the implanted ion and, hence, the damage has a Gaussian shape, the critical dose at which an amorphous region begins to form will occur just under the surface, forming a buried amorphous layer near the peak of the Gaussian distribution. Figure 1a shows a TEM 90° cross-sectional micrograph for a P^+ implanted (111) Si, implanted at 120 keV to a dose of $5 \times 10^{14}/\text{cm}^2$ at RT. The micrograph shows the presence of a buried amorphous layer. As the dose is increased to $10^{15}/\text{cm}^2$, the width of the amorphous layer increases and extends to the surface, forming a continuous amorphous layer. This is shown in Fig. 1b. Any further increase in the dose creates only minor changes in the damage structure or its distribution. However, if the temperature of implantation either is increased intentionally or increases due to ion beam heating during the implantation, the critical dose at which amorphous regions begin to form will increase because of partial annealing of the damage tracks during the implantation. An example of such behavior is shown in Fig. 1c where,

although the dose has been increased to $2.5 \times 10^{15}/\text{cm}^2$, due to beam heating, the as-implanted specimen does not show a continuous amorphous layer. Instead, a thin ($\sim 150 \text{ \AA}$) surface layer still remains crystalline. The temperature during the implantation was estimated to have increased to $\sim 200^\circ\text{C}$. Further increase in the implantation temperature to 400°C resulted in a buried layer of clusters (Fig. 1d) but no amorphous layer even though the dose was increased to $10^{16}/\text{cm}^2$.

Detailed investigations carried out using conventionally prepared plan-view specimens showed that the recrystallization of the continuous amorphous (α) layer type structures in low-temperature implanted (111) Si (Fig. 1b) causes the formation of microtwins on subsequent furnace annealing at 800°C for 1/2 hour (Fig. 2a). However, for (100) substrate orientation, only dislocation loops were present after an identical annealing treatment. Furthermore, if the implantation was carried out at temperatures $\geq 150^\circ\text{C}$, a dislocation network along with a few isolated dislocation loops was formed for both (111) and (100) substrate orientations.

It was observed that interface roughness increases with the temperature at which the implantation is carried out. Dark-field TEM micrographs of implanted but unannealed specimens exhibit bright "speckles" in the region of α/C interface but not in the α layer itself. These "speckles" reveal regions where crystalline silicon protrudes into the α layer and hence their size gives an indication of the scale of the interface roughness. The size of the bright spots and their contrast was found to increase for specimens implanted at elevated temperatures. The cross-sectional micrograph revealed the presence of a thin crystalline layer at the surface (Fig. 1c). Therefore, the effect of implantation temperature on regrowth behavior during subsequent furnace

annealing appears to be associated with the roughness of the as-implanted α/C interface, whether or not all crystallinity has been completely eliminated at the surface.

* * *

†Brief version of LBL-9990 and AIP Conference Proceedings on the Laser and Electron Beam Processing of Materials, November 1979.

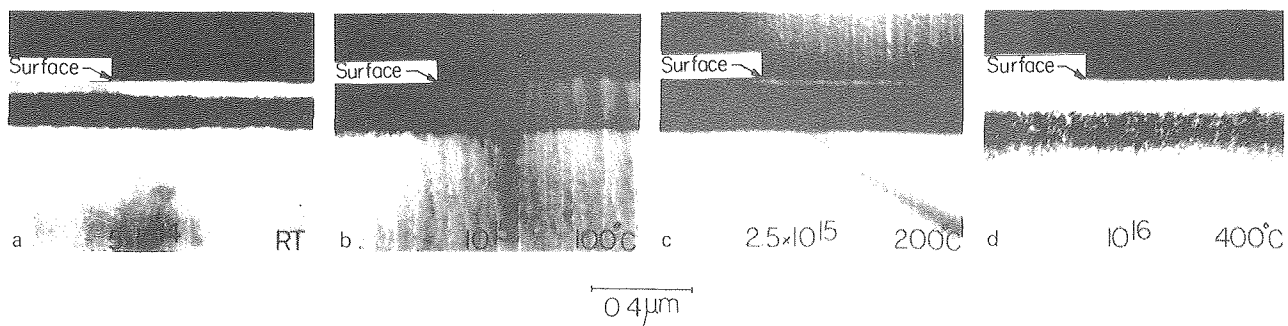


Fig. 1. TEM cross-sectional micrographs showing the damage-depth distributions for P^+ implanted into (111) Si under different implantation conditions.

(XBB 7911-15811)

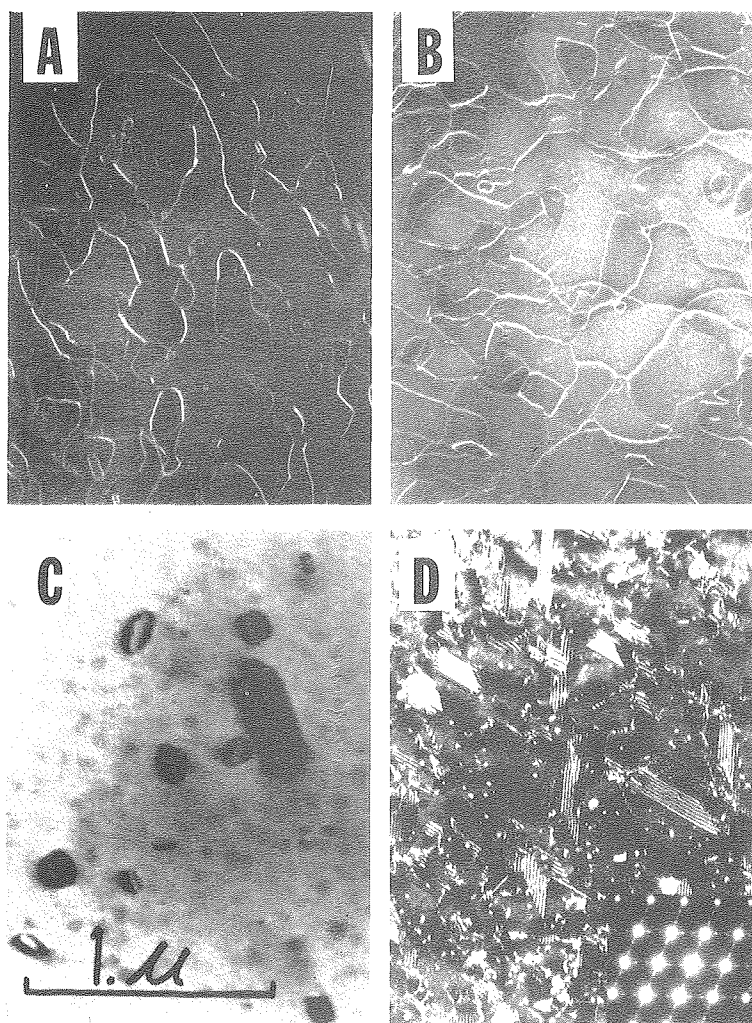


Fig. 2. TEM plan-view micrographs showing the effect of orientation and implantation temperature in P^+ implanted Si on subsequent furnace annealing at 800°C for 1/2 hour. (a) Substrate orientation \rightarrow (111), $T_i = 100^\circ\text{C}$; (b) Substrate orientation \rightarrow (100), $T_i = 100^\circ\text{C}$; (c) Substrate orientation \rightarrow (111), $T_i = 193^\circ\text{C}$; (d) Substrate orientation \rightarrow (100), $T_i = 193^\circ\text{C}$.

(XBB 802-1831)

5. A NEW EXPERIMENTAL TECHNIQUE FOR STUDYING THE REGROWTH OF AMORPHOUS LAYERS IN SEMICONDUCTORS[†]

J. Washburn and R. Drosd

A new experimental technique, using the transmission electron microscope (TEM), has been developed that makes possible the observation of the formation and growth of lattice defects during annealing of an amorphous (α) layer. In addition, measurements of recrystallization rate and its temperature dependence can be conveniently made. This is the first time that α layer recrystallization has been studied quantitatively in the TEM.

To perform this experiment a standard TEM specimen is made by chemical thinning from the unimplanted side of an unannealed wafer which contains an amorphous surface layer until a small hole is formed. This results in a portion of the amorphous (α) layer that is no longer in contact with the crystalline substrate, as shown in Fig. 1a. During annealing the α /crystalline inter-

face rotates away from the plane of the wafer and sweeps across the unsupported portion of the α layer as seen in Figs. 1b and 1c. Sequential micrographs of the same area may be taken to measure the $\alpha \rightarrow$ crystal transformation rate. Since different points along the interface are converging towards the center of the specimen all growth directions in the plane of the wafer may be observed. Figure 2 shows the [211] and [110] growth directions in $(\bar{1}11)$ specimen. The α layer was produced by 100 kV, $10^{16}/\text{cm}^2$ phosphorous ion implantation. Figure 3 displays the recrystallization rates for silicon, for the [100], [110], and [111] growth directions. The activation energy was 2.9 ± 0.1 eV for all growth directions. This experimental technique can be used for other semiconducting materials containing surface amorphous layers.

* * *

[†]Brief version of LBL-9990.

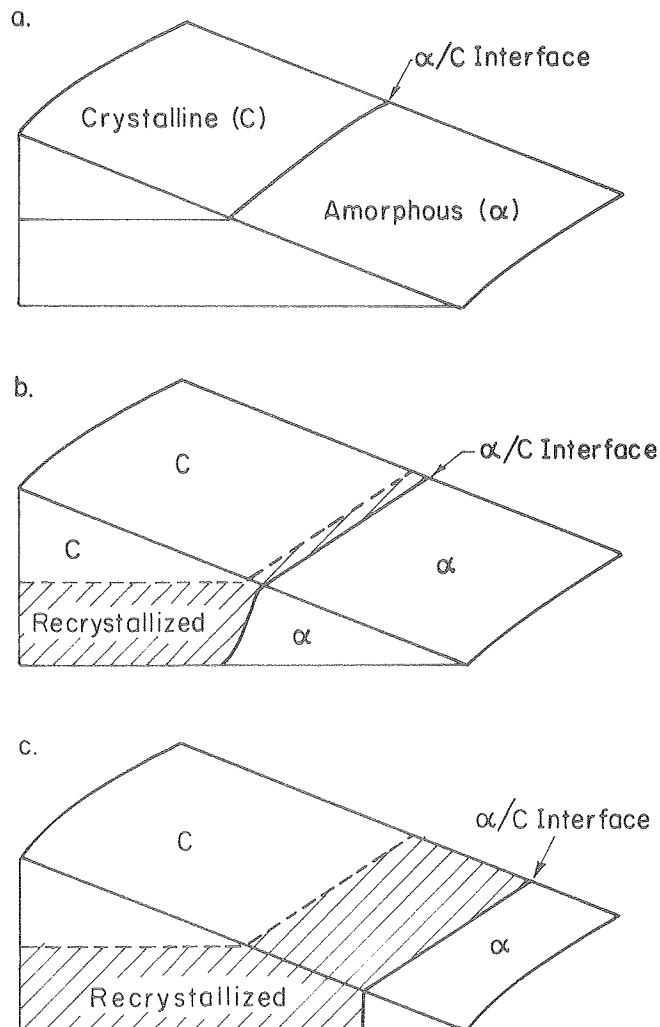


Fig. 1. A schematic annealing sequence of a thin foil specimen undergoing recrystallization.

(XBL 799-7152)



Fig. 2. Transmission electron micrographs of annealing sequences of amorphous silicon layers in the $\langle 112 \rangle$, (a), and $\langle 110 \rangle$, (b), directions. Micro-twins are found in both recrystallization directions.

(XBB 790-14131B)

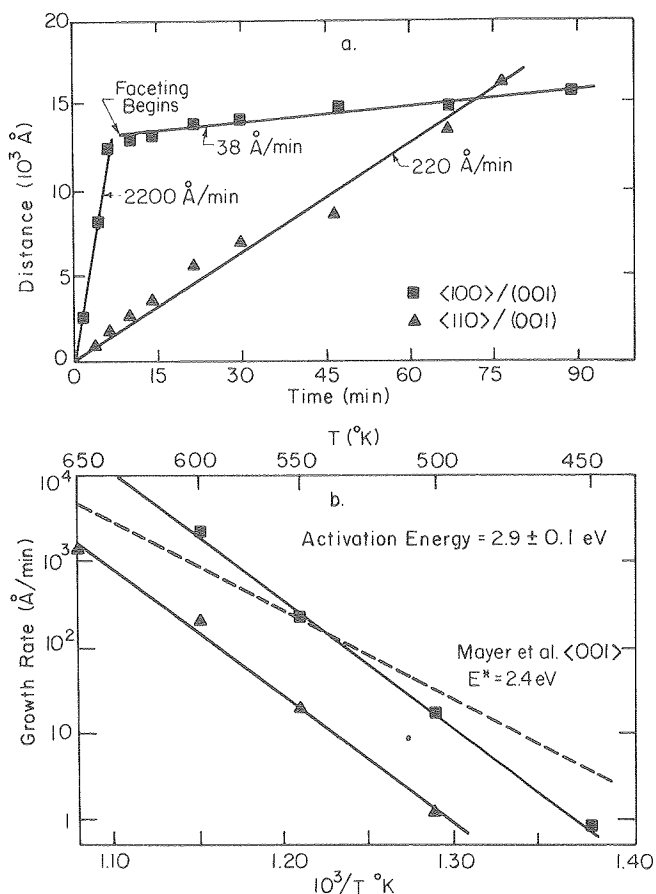


Fig. 3. A plot of recrystallization rate vs. temperature of amorphous silicon in the three major cubic directions. (XBL 799-7155)

6. A MODEL FOR REGROWTH OF AMORPHOUS SILICON WHICH EXPLAINS THE ORIENTATION DEPENDENCE OF REGROWTH RATE AND THE NATURE OF THE RESIDUAL DEFECT POPULATION[†]

J. Washburn and R. Drosd

A model has been developed for the recrystallization mechanism of an amorphous (α) silicon layer in contact with a crystalline substrate that successfully predicts the type of defects produced during annealing. In addition, the relative migration rates of the amorphous/crystalline (α/C) interface in the major crystallographic directions is now understood. During recrystallization of silicon wafers containing α layers (formed during low temperature implantation), it has been observed that twins are formed if the substrate orientation is (111) while only a low density of dislocation loops is found if a (100) wafer is used. In addition, the recrystallization rate is approximately 15 times slower for (111) substrates than for (100), with (110) being in between.

The new model is based on the ability of an atom leaving the α phase to find a stable bonding site at the crystal surface. To do this, the

incoming atom must complete two of its four possible bonds with the established crystal. On the (100) silicon surface a single atom may successfully attach itself to the crystal; but, on a (110) surface, a pair of atoms is required; and a cluster of three is needed on a (111) face. The schematic drawing in Fig. 1 is a [110] projection of a diamond cubic lattice where the critical size nucleus on each crystal face is shown. On the (111) face it is seen that there are two positions in which the group of three atoms can attach. In the one labeled "correct" the crystal has been continued, defect free. The nucleus labeled "incorrect" would start the growth of a twin. Since the atoms in the twin-oriented nucleus make only second nearest neighbor mistakes with atoms in the established crystal, twin mistakes are expected to occur frequently. Stacking mistakes on the (100) or (110) surface would involve first nearest neighbor mistakes and hence are unlikely to occur.

From consideration of the number of atoms required to form a stable surface nucleus at the α/C interface it would be expected that the [100] regrowth rate would be fastest, followed by [110] and then [111]. This is what is found experimentally. The experimental fact that twins and stacking faults are only found after recrystallization of an α layer on (111) substrates is also explained by the model.

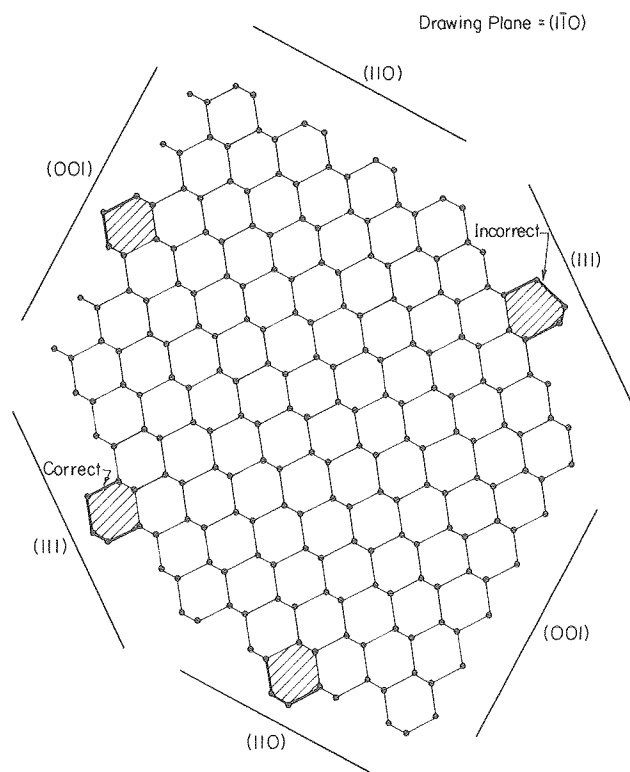


Fig. 1. A schematic $\langle 110 \rangle$ projection of the diamond cubic lattice showing the minimum size stable atomic clusters on the major crystal faces. (XBL 799-7157)

The model presented here explains the major features of α layer recrystallization. There are, however, other aspects that are not yet understood. It has been observed that the regrowth rate, and sometimes the activation energy, are sensitive to the type and dose of ion implanted. Some ions, such as phosphorous, boron, and arsenic accelerate the recrystallization rate as compared to pure silicon, while other ions, such as neon, argon oxygen, and nitrogen, slow it down. The present model will have to be refined before these chemical effects are understood.

* * *

[†]Brief version of LBL-9990.

7. ION THINNING AND ELECTRON BEAM DAMAGE IN CADMIUM SULFIDE DURING SPECIMEN PREPARATION AND TRANSMISSION ELECTRON MICROSCOPE OBSERVATION

J. Washburn and U. Dahmen

As possible low-cost photovoltaic cells, CdS, particularly in the form of vapor-deposited thin layers, has been studied extensively. However,

only very recently has an attempt been made to achieve a microstructural understanding by means of transmission electron microscopy. It was found that CdS is unusually sensitive to radiation damage and that great care must be taken to avoid the introduction of artifacts due to the techniques of preparation and observation.

Most nonconducting and semiconducting materials are thinned for electron microscopy by ion-beam milling. Figure 1 shows that this technique cannot be used for CdS because of extensive radiation damage caused by the incident Ar ions. An initially defect-free CdS film prepared by chemical thinning (Fig. 1a) became highly defected by ion milling at 5 kV (Fig. 1b). Reducing the ion-beam energy to 3 kV (Fig. 1c) and 1.1 kV (Fig. 1d) increased the thinning time to prohibitive length without completely eliminating the damage. Crystals were therefore prepared for electron microscopy by a special chemical-mechanical technique.

When this technique was employed to thin epitaxially grown CdS single crystals, the true grown-in dislocation structure was observed (Fig. 2). However, the material deteriorated rapidly under the 100 kV electron beam as shown in Fig. 2b, where a high density of dislocations

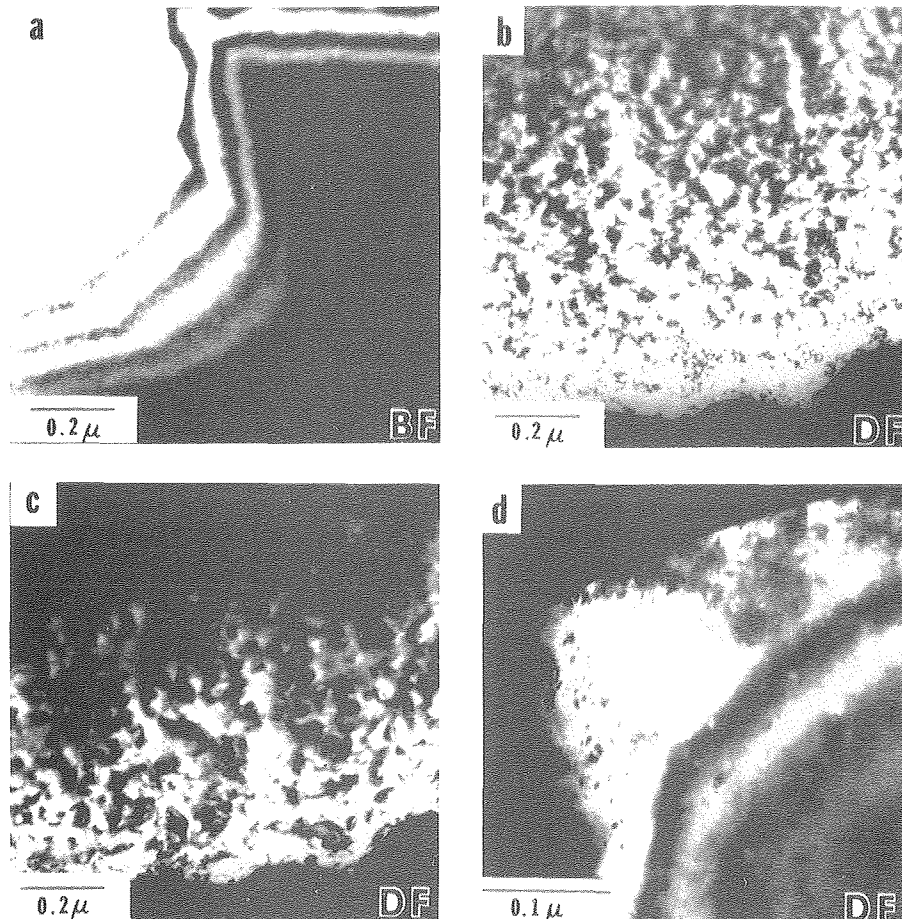


Fig. 1. Ion damage in bulk CdS: (a) before, (b) after exposure to 5 kV Ar-ion beam, (c) 3 kV, (d) 1.1 kV. (XBB 799-11723)

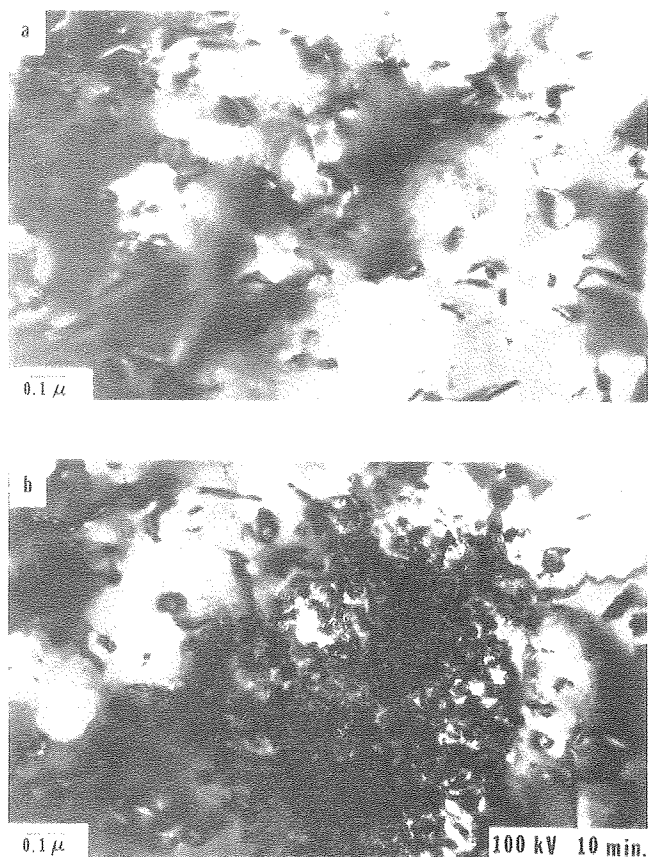


Fig. 2. Electron beam induced damage in epitaxially grown single crystal of CdS; (a) before, (b) after 10 min exposure to 100 kV electron beam. (XBB 791-14888)

and voids has formed in the area irradiated by the beam for 10 min. It was shown that these defects did not result from displacement of sulphur atoms by the high energy electrons because of the reduction of the electron energy to 40 keV. The same effect occurred although the reaction was somewhat slower. On the other hand, at 650 keV, no such damage was found even after long beam exposures, although this electron energy far exceeded that for the displacement of sulphur (115 keV) and Cd (320 keV).¹ A clue to a partial understanding of the processes involved was obtained from electron diffraction. Figure 3 shows selected area diffraction patterns from the center of the irradiated area (Fig. 3a) and the perimeter (Fig. 3b). The extra diffraction rings in Fig. 3b were identified as CdO rings, and dark-field imaging of these rings showed small CdO crystallites in a narrow band at the edge of the damage region. As evidenced by the widely spread intensity of the pure CdS pattern in Fig. 3a, the central region did not contain any foreign crystallites but was highly defected.²

These observations point to a mechanism involving a beam-induced chemical reaction with the residual gas in the microscope vacuum. An analysis of the microscope atmosphere showed the main contaminant to be water vapor with a total

vacuum of 3×10^{-5} Torr. Thus, a likely reaction would be the beam-induced dissociation of H_2O to produce adsorbed ions like OH^- or O^{--} . A reaction of these ions with CdS could then lead to the formation of the more stable oxide CdO. Whether this reaction occurs at the surface, in the bulk, or in the gas phase due to local evaporation by beam heating is uncertain. The formation of voids points to a bulk reaction involving the formation of gaseous reaction products like SO_2 , H_2S , and H_2 . The limitation of the CdO to the perimeter is likely to result from a thermal gradient causing surface diffusion or a vapor transport mechanism. It is felt that a similar mechanism is responsible for the damage structure observed in ion-milled samples. However, until a better understanding of these reactions is achieved, a damage-free characterization of CdS can be accomplished by high voltage electron microscopy of chemomechanically thinned samples.

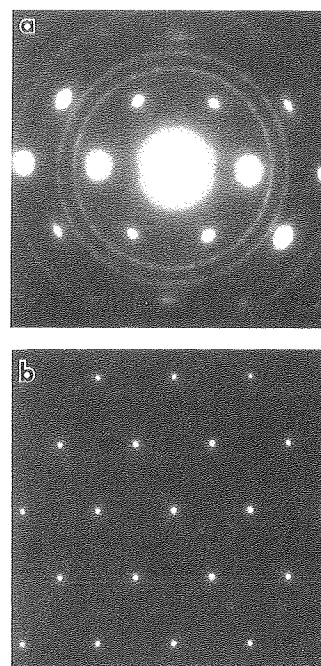


Fig. 3. Selected area diffraction patterns; (a) from central irradiated area, (b) from perimeter, showing CdO diffraction rings. (XBB 7911-15741)

* * *

1. G. D. Watkins, Inst. Phys. Conf. Ser. No. 31, 95 (1977).
2. M. Wilkens and P. Rapps, Phys. Stat. Sol. (a) 44, 173 (1977).

8. CHARACTERISTICS OF CdS-Cu_xS AND (Cd,Zn)S - Cu_xS HETEROJUNCTIONS

J. Washburn and B. Chin

Single-crystal CdS and (Cd,Zn)S thin films have been deposited on (111) Ge substrates for fabrication of test photovoltaic heterojunctions

with Cu_xS . Deposition conditions were determined for single-crystal growth using the hot-wall vacuum deposition technique. It was found that, for mixed crystal growth, an intermediate CdS layer between the Ge substrate and (Cd,Zn)S film was necessary to prevent attack of the substrate by Zn vapor. The grown films have been characterized using X-ray diffraction to determine composition and crystallinity, and SEM-EDAX to study surface morphology and perform compositional analysis.

It was found that the n-CdS/n-Ge heterojunction was ohmic and provided a good back contact for front-wall cells. The heterojunction with p- Cu_xS was formed by a solid-state ion exchange reaction in which CuCl is evaporated onto the single crystal film and then heat-treated to allow for the out-diffusion of the cations (Cd and Zn) and the in-diffusion of Cu. A modified heat treatment was developed to prevent cracking of the Cu_xS due to differences in lattice parameter and thermal expansion coefficients. Figure 1 is an SEM micrograph of a single crystal cell in which the surface

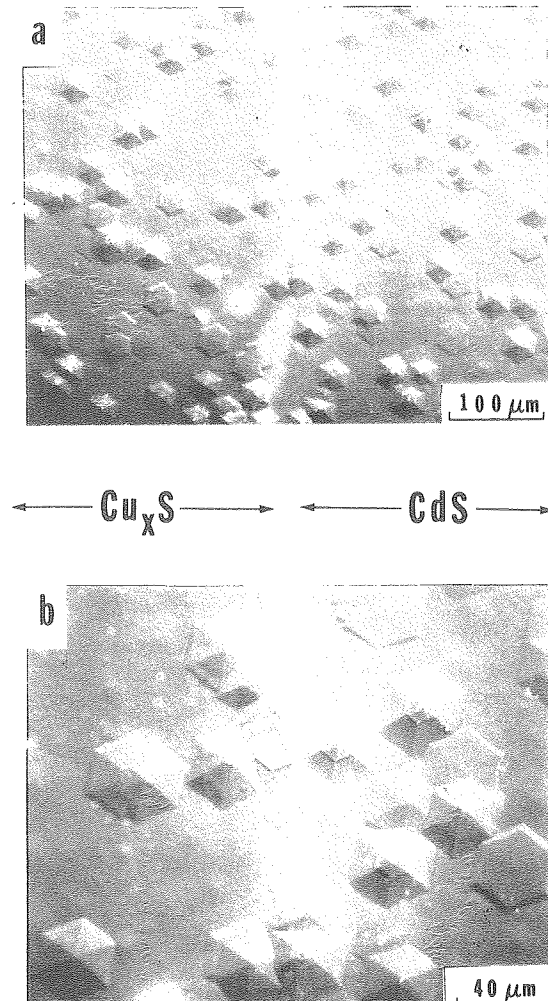


Fig. 1. SEM micrograph of CdS and region converted to Cu_xS . (XBB 7911-15812)

morphology of the converted region remains the same as the initial CdS area. EDAX analysis was used to locate the junction region as shown in Fig. 1 in which the detection of Cu (Fig. 2b) indicated the Cu_xS area.

Current-voltage characteristics of these cells were taken in the dark and under tungsten light illumination. The effect of conversion heat treatment is shown in Fig. 3a in which longer times resulted in a larger reverse saturation current and hence lower open-circuit voltage. Figure 3b shows improved current-voltage characteristics for a cell formed by a shorter heat treatment time. Steady-state spectral response equipment has been constructed to monitor the cell output under varying conditions of illumination, cell bias and temperature.

Transmission electron microscopy studies have been conducted to correlate the electro-optical properties of the grown films with structural perfection. Future plans are to study the Cu_xS and its formation and the heterojunction interface. Single crystal cells will be fabricated with (Cd,Zn)S of different compositions to determine those factors affecting cell performance.

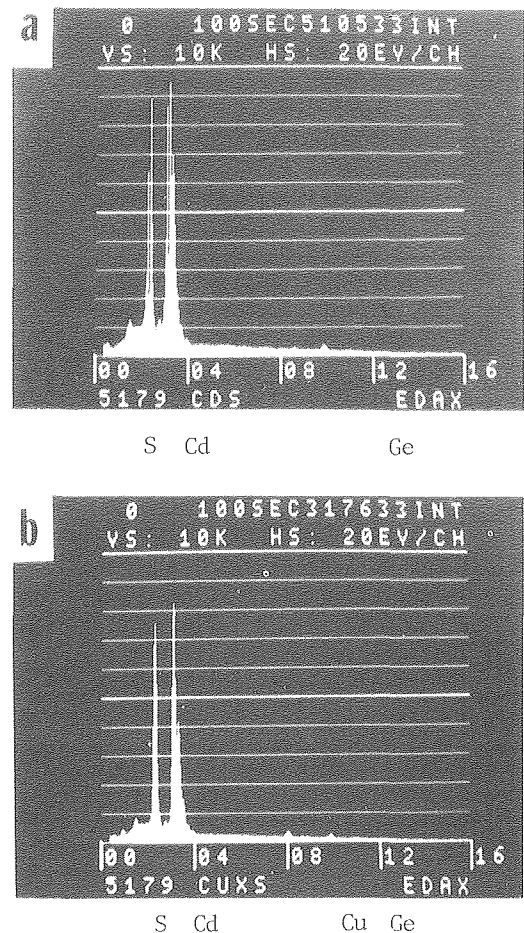


Fig. 2. EDAX analysis of (a) CdS area and (b) converted Cu_xS area. (XBB 7911-15814)

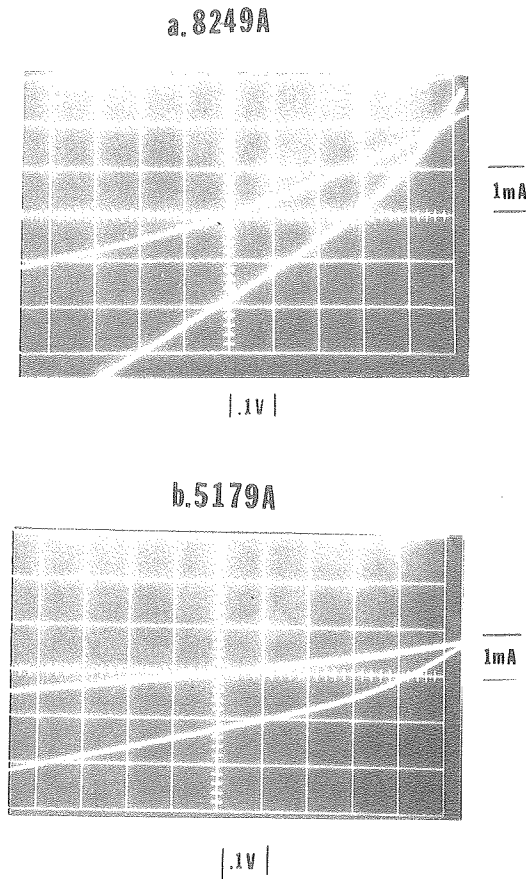


Fig. 3. Current-voltage characteristics of $\text{Cu}_x\text{S}/\text{CdS}$ cells showing effects of conversion heat treatment. (a) 2.5 hours at 60°C ; (b) 0.5 hours at 60°C . (XBB 790-15813)

9. ON THE DEGRADATION OF SPECTRAL SELECTIVITY OF BLACK CHROME SOLAR ABSORBER COATINGS DURING SHORT-TERM HIGH-TEMPERATURE EXPOSURES[†]

C. M. Lampert and J. Washburn

The very popular black chrome coating known as "Chromonyx"¹ was evaluated in terms of materials science to provide a correlation between its microstructure and observed optical properties. Furthermore, the effect of high temperatures upon the stability of this coating was investigated.

This study is important to users of the black chrome coating for solar collectors. Currently, it is the single most favored selective absorber because its wavelength-selective nature allows this coating to perform more efficiently than many other black coatings. Microstructural characterization is necessary to understand the high solar energy absorption property exhibited by this coating. Also, it is of paramount importance to be able to predict how this durable coating might fail when subjected to high temperatures, such as those experienced during stagnation.

Energy-dispersive analysis of X-rays (EDAX), as well as scanning and transmission electron microscopy, was employed for thin film analysis. A wide range of experiments has been reported previously,² which correlate both the as-electroplated and annealed microstructure to reflectance measurements. With supplemental information from Auger³ and x-ray photoelectron spectroscopy (XPS),⁴ it was possible to develop a physical metallurgical model for the wavelength-selective properties of black chrome. A schematic microstructure is shown in Fig. 1.

This model consists of agglomerated particles within the 0.05 - 0.3 micron size range. These particles exhibit a predominantly oxide surface. This oxide layer may behave as a transparent antireflective layer. Internally, these particles are composed of a distribution of fine metallic chromium grains (140 Å in diameter) suspended in amorphous or very fine crystalline Cr_2O_3 . Deeper into the coating, metallic chromium concentration increases. An intermediate Cr - Cr_2O_3 cermet region is responsible for the high solar absorptance. This property can be predicted from both the Maxwell-Garnett and Bruggeman effective medium theories. This essentially means that, in

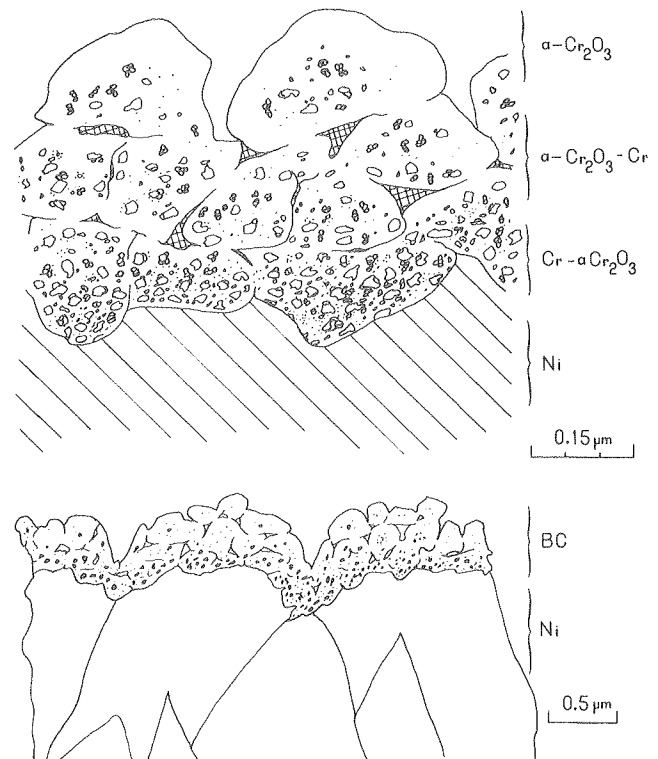


Fig. 1. Schematic cross-section for black chrome. Three distinct regions are shown in the as-prepared structures: a top layer consisting of Cr_2O_3 ; an intermediate area of metallic Cr in Cr_2O_3 ; and a bottom layer consisting principally of Cr and the nickel substrate. In all cases, Cr_2O_3 has an amorphous or very fine crystalline structure. Trapped water and the resulting hydride are also present but not shown.

(XBL 799-11767)

the high intensity solar region, the coating appears to be black and highly absorbing. Still deeper into the coating, close to the substrate, a high concentration of chromium is noted. This region accounts for the low infrared emittance. In other words, the upper layers are ineffective in the infrared and appear transparent, giving the coating a predominantly metallic character. The combined action of all layers results in a coating that is highly absorbing and allows very little loss by reradiation of energy, indicating high efficiency.

Microstructural analysis was performed on specimens annealed 1 to 100 hours over the 300 to 600°C temperature range.⁵ Below about 300°C this coating exhibits long-term stability. The effect of annealing in air was compared to that of medium vacuum (1.3×10^{-1} - 1.3×10^{-3} Pa). These conditions were chosen because they ideally simulate thermal effects this coating might experience during stagnation.

It was concluded that black chrome after 100-hour heat treatments shows minor instability below 300°C in air and 400°C in vacuum. Significant degradation appeared above 400°C in air and 500°C in medium vacuum. Within this region, crystalline Cr_2O_3 particles nucleate and grow; as they grow, metallic chromium is depleted. In Fig. 2 an electron micrograph reveals the growing Cr_2O_3 particles. Along with the occurrence of the predominant Cr_2O_3 phase, the grading of metallic chromium is reduced, thereby degrading the solar

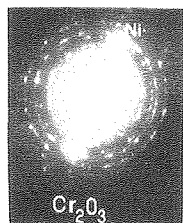
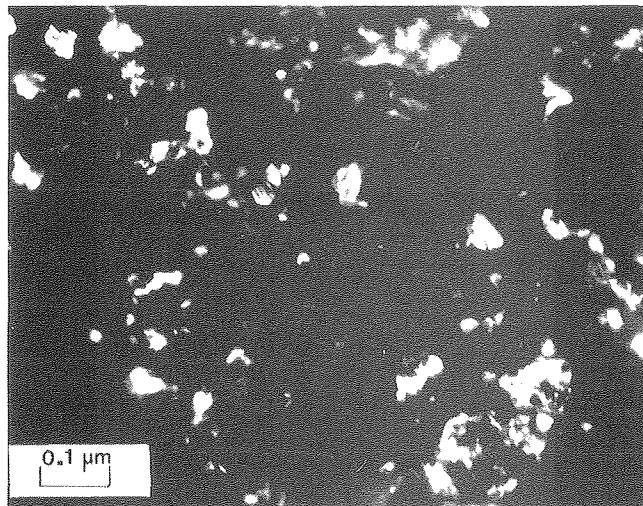


Fig. 2. Dark field transmission electron micrograph with corresponding diffraction pattern for 500°C 100-hour heat-treated black chrome in vacuum. (XBB 790-13605)

absorption properties. Crystallites of Cr_2O_3 have been observed growing on the black chrome surface at high temperatures. Also, the film densifies with outgassing of CO , CO_2 and water vapor.⁶ Presently, it is unknown if this absorber outgasses heavy species such as chromium hydrides or oxides. A schematic of degraded black chrome is depicted in Fig. 3.

The major mode of black chrome degradation appears to be diffusion-controlled oxidation in all cases, including medium vacuum. Diffusion of oxygen may be enhanced by the outgassing products. Their emanation may act to break up the coating, thereby providing paths for preferential diffusion.

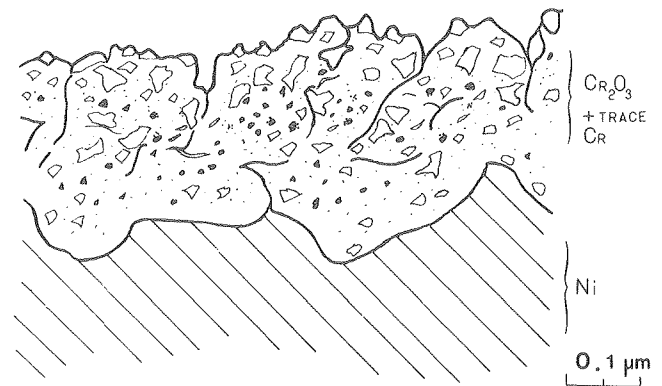


Fig. 3. Schematic of degraded black chrome at approximately 400°C in air or 500°C in vacuum for 100-hour heat treatment. (XBL 7910-12208)

* * *

†Brief version of LBL-8632, LBL-9123, and Proc. Int. Solar Energy Soc., May 1979.

1. Trade Name - Harshaw Chemical Company, Cleveland, Ohio.
2. MMRD Annual Report 1977, LBL-6016 and MMRD Annual Report 1978, LBL-8580.
3. R. B. Pettit and R. R. Sowell, Proceedings of SERI Second Annual Conference on Absorber Surfaces for Solar Receivers (1979), p. 33.
4. A. Ignatiev, P. O. Neill and G. Zajac, Solar Energy Materials **1**, 69 (1979).
5. C. M. Lampert, Ph.D. thesis, LBL-9123.
6. T. Beat, A Black Chrome Outgassing Study (LLL report to be published).

RESEARCH PLANS FOR CALENDAR YEAR 1980

The new technique for study of defect formation and crystal growth rates for the amorphous to crystalline transformation in silicon will be applied to study of the effect of phosphorous, boron, and arsenic concentrations on the perfection and growth rate of the crystalline phase. A modification of a model developed to explain the effect of crystallographic orientation of the growing face on crystallization rate may be able to explain impurity effects.

Research on the properties of polycrystalline silicon will focus attention on the effect of impurities or dopant atoms on the mobility of grain boundaries during grain growth and on the electrical properties of polycrystalline silicon produced by laser and electron beam pulse annealing of amorphous silicon. Microanalytical techniques utilizing the Philips 400 microscope operating in the STEM mode and microdiffraction information will be used to obtain information concerning segregation of impurities to grain boundaries.

The information on implantation-temperature effects and pulse-annealing parameters that has been obtained from the newly developed cross-section technique of transmission electron microscopy will be applied to P-N junction formation in silicon and gallium arsenide. Electrical properties of laser or electron beam melted surface layers will be correlated with their structural characterization.

The fundamental study of channeled Rutherford backscattering spectra from buried layers of different types, such as amorphous layers, small dislocation loops, and damage clusters produced by low dose implants, will be continued, using the cross-section transmission electron microscopy technique to independently monitor the depth of the scattering defects. This work should greatly improve understanding of RBS spectra from complex surface layers.

The techniques that have been developed for preparation of CdS foils and their observation in the transmission electron microscope without the introduction of artifacts will be used to study Cu₂S and interface between Cu₂S and CdS resulting from the replacement reaction between Cu and CdS. This research is of fundamental importance in understanding factors that limit efficiency and mechanisms of degradation of CdS - Cu₂S solar cells.

1979 PUBLICATIONS AND REPORTS

Refereed Journals

1. J. Washburn and K. Seshan, "Observations on the Development of Secondary Defects in Heavily Damaged Ion Implanted 110 and 111 Silicon," *Radiation Effects*, Vol. 40, 29 (1979).
2. C. Lampert, "Coatings for Enhanced Photothermal Energy Collection, I - Selective Absorbers," *Solar Energy Materials* 1, 319 (1979), LBL-8803.
3. C. Lampert, "Coatings for Enhanced Photothermal Energy Collection, II - Non-Selective and Energy Control Films," *Solar Energy Materials* 2 (1979) (in press), LBL-8803 Rev.
4. D. K. Sadana and G. R. Booker, "TEM Structural Studies on Se⁺ Implanted GaAs," *Rad. Eff.* 42, 35 (1979).
5. S. S. Kular, B. J. Sealy, M. H. Badawi, K. G. Stephens, D. K. Sadana and G. R. Booker,

"Laser Annealing of Capped and Uncapped GaAs," *Electronics Lett.* 15, 413 (1979).

Other Publications

1. C. Lampert, "Thermal Degradation of a Black Chrome Solar Absorber Short Term," Proceedings of International Solar Energy Soc., May 1979.
2. C. Lampert, "Metal Foils for Direct Application of Absorber Coatings on Solar Collectors," Proceedings of AES Second Symposium on Coatings for Solar Collectors, October 1979, LBL-9324.
3. J. Washburn and C. Lampert, "Microstructure and Optical Properties of Black Chrome Before and After Exposure to High Temperature," Proceedings of SERI/DOE Conference on Absorber Surfaces for Solar Receivers, January 1979, LBL-8632.
4. D. K. Sadana, M. C. Wilson, G. R. Booker, and J. Washburn, "Regrowth Behavior of Three Different Damage Structures in P⁺ Implanted and Subsequently Laser Annealed Si," AIP Conference Proceedings on the Laser and Electron Beam Processing of Materials, 156th Electrochemical Society Meeting, Los Angeles, October 1979, LBL-10008.
5. D. K. Sadana, M. C. Wilson, G. R. Booker and J. Washburn, "TEM Studies of P⁺ Implanted and Subsequently Laser Annealed Si," Extended Abstract 79 (2), 1293 (1979), Electrochemical Society Meeting, Los Angeles, LBL-9209.
6. I. Golecko, M. A. Nicolet, J. L. Tandon, P. M. Asbeck, D. K. Sadana and J. Washburn, "Transient Annealing of GaAs by Electron and Laser Beams," Extended Abstract 79 (2), 1279 (1979), Electrochemical Society Meeting, Los Angeles, LBL-9793.
7. D. K. Sadana, M. Strathman, J. Washburn and G. R. Booker, "TEM and RBS Studies of Single and Double Discrete Damage Layers in P⁺ Implanted Si on Subsequent Laser Annealing," AIP Conference Proceedings on the Laser and Electron Beam Processing of Materials, November 1979.
8. I. Golecki, M-A. Nicolet, M. Mäempä ä, J. L. Tandon, C. G. Kirkpatrick, D. K. Sadana and J. Washburn, "Transient Annealing of Ion Implanted GaAs," AIP Conference Proceedings on the Laser and Electron Beam Processing of Materials, November 1979.
9. M. Mäempä, M-A. Nicolet and D. K. Sadana, "Doping of Si by Pulsed Electron Beam Annealing of Deposited Sb Layers," AIP Conference Proceedings on the Laser and Electron Beam Processing of Materials, November 1979.

LBL Reports

1. J. Washburn and G. Hirsch, "High Resolution Biological Imaging Using Field Desorption Microscopy," LBL-8607.
2. C. M. Lampert, "Chemical, Structural and Optical Characterization of a Black Chrome Solar Selective Absorber" (Ph.D. thesis), LBL-9123.

3. R. Drosd, "A Model of the Recrystallization Mechanism of Amorphous Silicon Layers Created by Ion Implantation" (Ph.D. thesis), LBL-9990.

4. C. Lampert, "The Use of Coatings for Enhanced Solar Thermal Energy Collection," LBL-8072.

5. C. Lampert, "Black Absorber Coated Foils for Solar Collectors," LBL-10249.

Invited Talks

1. D. K. Sadana, "TEM Structural Studies of Ion Implanted Si and GaAs," California Institute of Technology, February 22, 1979.

2. D. K. Sadana, "Structural Studies of Furnace Annealed P⁺ Implanted Si and Se⁺ Implanted GaAs," Rockwell International Science Center, Thousand Oaks, Ca, March 26, 1979.

3. D. K. Sadana, "Comparison of Furnace Annealed and Laser Annealed Ion Implanted Si and GaAs," Oak Ridge National Laboratory, Tennessee, March 30, 1979.

4. D. K. Sadana, "TEM and STEM Studies of Laser Annealed Si and GaAs," Bell Telephone Laboratories, Murray Hill, N.J., April 16, 1979.

c. Mechanical Properties of Ceramics*

Anthony G. Evans, Investigator

Introduction. The research reported herein is an interdisciplinary study of the response of ceramics to stress. The generalized scope of the study is outlined in Fig. 1. The principal foci of the current research projects are problems that demand scientific attention by virtue of their considerable technological significance in the energy sphere. The research areas are: (1) high temperature deformation and failure and (2) microstructure and toughness relations.

The two research areas are new topics which are anticipated to continue for several years. The high temperature deformation and failure issue concerns the response of refractory materials to stress. A scientific basis for predicting high temperature failure and for relating the deformation and failure to microstructure does not pres-

ently exist. Research in this area is therefore devoted to the generation of a self-consistent scientific comprehension of the mechanisms of deformation and failure, leading eventually to a predictive capability. The enhancement of toughness in ceramics is pertinent primarily to the minimization of damage when a ceramic component is subject to impact, thermal shock, machining, etc. Toughness is thus a principal property involved in the structural integrity of ceramic components. Improved toughness can be induced by certain stress activated microstructural changes occurring in the vicinity of a crack tip, including martensitic transformations and microcracking. The study is devoted to a theoretical understanding of the microstructural conditions that afford optimum toughness, coupled with the experimental development of optimum microstructures.

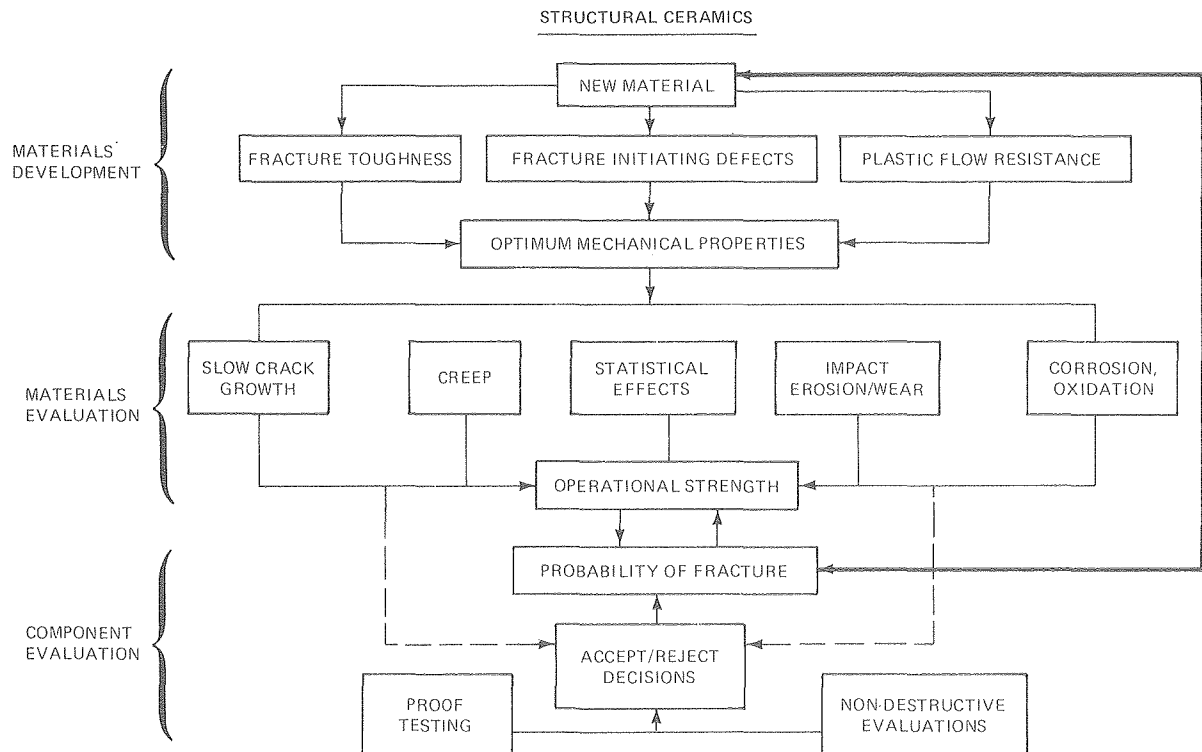


Fig. 1. A scheme for obtaining the information pertinent to structural design with brittle materials. (XBL 802-267)

* This work was supported by the Division of Materials Sciences, Office of Basic Energy Sciences, U. S. Department of Energy.

High Temperature Deformation and Failure

1. STATISTICAL MODELS OF FAILURE[†]

Anthony G. Evans and Amar Rana

High temperature failure in ceramics usually occurs by the formation and coalescence of grain facet sized cavities (Fig. 1). The fracture condition coincides with the formation of sufficient cavities on contiguous grain boundaries that the macrocrack propagation criterion is attained,

$$c \sim (K_C / \sigma^A)^2 \quad (1)$$

where c is the critical crack length, K_C is the fracture toughness and σ^A is the level of applied stress. The probability, P , of forming a crack of this size is related to the formation probability for individual facet-sized cavities, ϕ , by

$$P = \frac{A\phi^{1/2} \ell n \phi}{\ell^2 (\frac{1}{2} \ell n \phi - 1)} \exp[c/\ell] \ell n \phi \quad (2)$$

where ℓ is the grain facet length and A is the total area of grain boundary sampled. Hence, by recognizing the intrinsic variability of grain boundaries in ceramics, the probability of failure can be deduced. Assigning an extreme value probability for the boundaries most susceptible to cavitation, the median time to failure becomes:

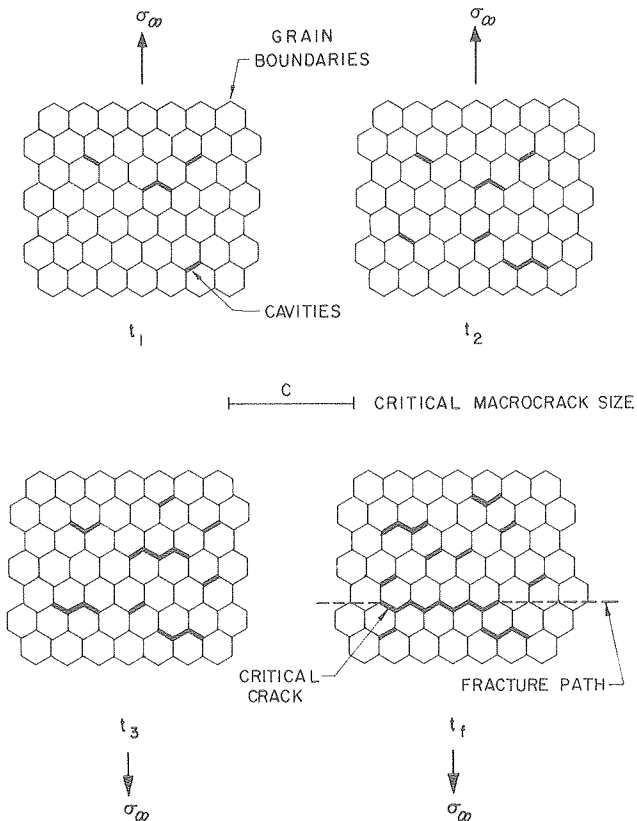


Fig. 1. A schematic of the sequence of events that lead to creep failure. (XBL 793-5995)

$$\ell n \theta_r = A - n \ell n \sigma^A - C \sigma^2 \quad (3)$$

where θ_r is the Orr-Sherby-Dorn parameter, n is the stress exponent of the intrinsic cavity formation mechanism, C is a parameter that depends on the fracture toughness of the material and the sample size, and A is a parameter that relates to the details of the cavity formation process. The utility of Eq. (3) as a description of failure in ceramics is exemplified by its correlation with extensive results for Al_2O_3 (Fig. 2) and SiC.

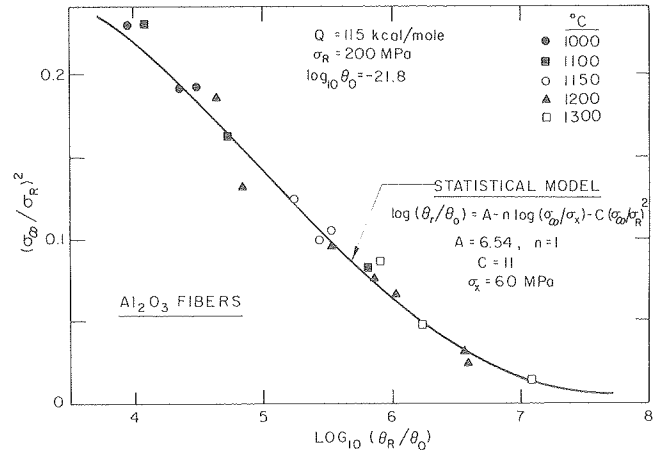


Fig. 2. A correlation of creep rupture data for Al_2O_3 with the predictions of the statistical model. (XBL 793-6002)

Further development of this approach for predicting failure requires the inclusion of specific cavitation processes. Three such processes have been examined; each is characterized by the requirement that the cavity opening be small compared with the grain diameter—a condition often encountered in ceramics. The three processes involve (1) cavitation of a contiguous second phase at grain boundaries, (2) crack-like diffusive growth along grain boundaries, (3) diffusive growth in the presence of an amorphous phase. These three processes yield different relations for the failure time. For example, the cavitation of a continuous second phase, typical perhaps of certain silicon nitrides, yields the relation:

$$\ell n \theta_r = \ell n [0.3 \eta (\ell / \delta_0)^2] - \ell n \sigma^A - (C^A / \sigma^A)^2 (4 \ell / \pi K_C^2) \ell n (4A / \ell^2) \quad (4)$$

where η and δ_0 are the viscosity and thickness of the second phase respectively. Application of this relation to the results for Al_2O_3 , (Fig. 2) yields a self-consistent description of the failure time through the microstructure dominated properties of the material, such as the fracture toughness, the grain size, the thickness and viscosity of the second phase.

The statistical approach has also been used to evaluate creep strains, based on solutions for the strain as a function of the (time dependent) crack

density. These yield non-linear relations for the creep strain even when the basic cavitation process is linear. The approach thus lends itself to the interpretation of the generally observed non-linear dependence of creep rates on the applied stress.

* * *

[†]Brief version of LBL-8692.

2. CREEP FRACTURE INDUCED BY GRAIN BOUNDARY SLIDING[†]

Anthony G. Evans

There are numerous suggestions in the literature that the deformation and failure of ceramics can occur through the formation of wedge cracks, induced by grain boundary sliding. However, the available analyses all make the invalid assumption that fully-brittle wedge cracks can propagate in the presence of significant diffusive mass transport. In fact, diffusion must modify the crack tip stress field and cause diffusive extension of the crack. Therefore, an analysis of sliding induced wedge cracking that excludes diffusion has been conducted in order to examine its significance as a deformation and failure mechanism.

The stress intensity factor for wedge cracks in the presence of grain boundary sliding have firstly been deduced from solutions for the kinked crack (Fig. 1). These solutions have then been used to determine the rate of growth of the wedge crack, as dictated by the rate of grain boundary sliding in its approach to elastic equilibrium. It is deduced that a critical wedge crack length a^* is reached, whereupon the crack extends unstably across the remainder of the grain facet (Fig. 2), length ℓ . The

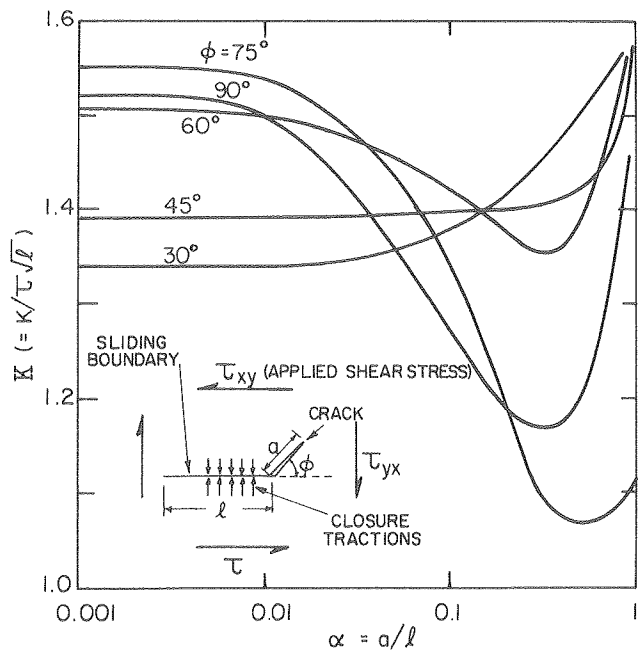


Fig. 1. Variation in stress intensity factor with wedge crack length. (XBL 798-6907)

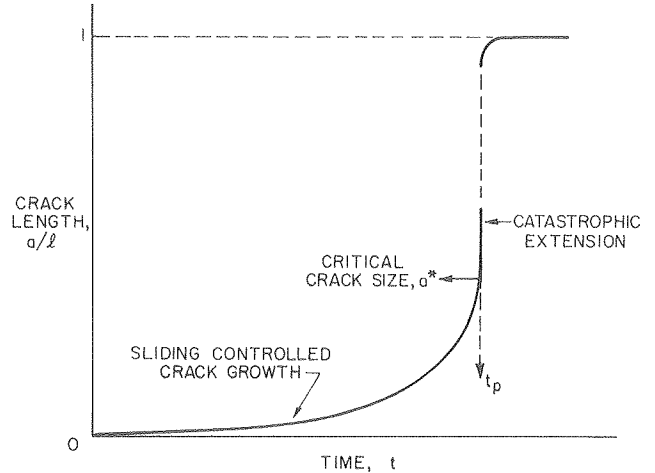


Fig. 2. The stable and unstable regions of crack extension across a grain facet. (XBL 798-6905)

time taken to attain this critical length is essentially the time t_p for formation of a grain facet sized cavity. A general relation for t_p derived from the analysis is,

$$t_p = \frac{\pi^2(1-\nu^2)}{4} \left(\frac{\eta}{E}\right) \left(\frac{\ell}{\delta_b}\right) \cos\phi A(\kappa, \phi, a^*) \quad (1)$$

where η is the grain boundary viscosity, δ_b is the boundary thickness, ϕ is the angle defined in Fig. 1, and A is a function of the applied stress, facet size, the critical crack length and the angle ϕ . Some typical results are plotted in Fig. 3. Several features of the results are of significance. First, the mechanism only pertains at relatively high stresses $\sigma^A > 2K_C^{\sigma, b}/\kappa\sqrt{\ell}$; it is thus most pertinent

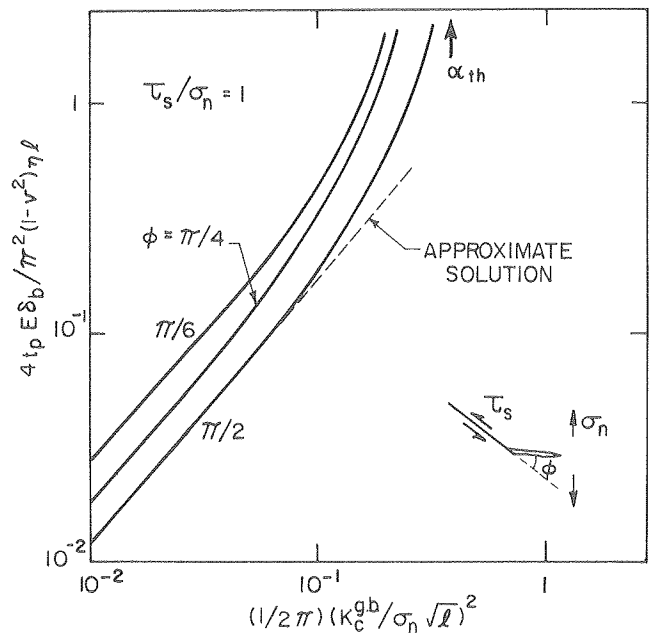


Fig. 3. Crack propagation times predicted by the analysis. (XBL 798-6909)

to creep at intermediate temperatures and/or to deformation in the vicinity of a crack tip (perhaps as a mode of slow crack growth). Second, since diffusion is prohibited, the mechanism can only proceed in materials with planar grain boundaries (a viable condition for ceramics formed by liquid phase sintering). Finally, it is noted that, for the most susceptible boundaries, Eq. (1) simplifies to

$$t_p \sim \left[\frac{K g \cdot b}{\frac{c}{\sigma \sqrt{\delta_b}}} \right]^2 \left(\frac{\eta}{E} \right) \quad (2)$$

The failure process is thus non-linear even at the basic cavity formation level. These non-linearities are augmented when this result is incorporated into the statistical relations for the failure time.

* * *

† Brief version of LBL-10342.

3. THE EFFECT OF CAVITATION ON THE TENSILE DEFORMATION BEHAVIOR OF ALUMINA

William Blumenthal and Anthony G. Evans

Cavities and microcracks have been observed in ceramics subjected to tensile stress at high temperatures. Recently, cavity propagation and growth have been proposed as a deformation and failure mechanism.

This study seeks to correlate the tensile deformation and failure behavior of high purity, hot-pressed alumina with the resulting microstructural effects produced by cavitation at various high temperatures.

Three-point bending is used to develop tensile stresses in a sample. The steady state applied load is measured as a function of time for an imposed constant displacement rate at a constant temperature. A series of scribes are placed at a constant interval along the side of selected samples in order to record the local strain produced over the sample cross section. The maximum local strain measured on a sample was found to be linearly related to the head displacement. The strain gradients also provide information concerning departures from linearity and incompatibilities of the tensile and compressive creep.

The stress distribution was deduced from the strain gradient and the strain-rate sensitivity of the steady state creep load. The steady state stress and strain rate were determined to be related in accord with the usual expression

$$\dot{\epsilon} \propto \sigma^n \quad (1)$$

where n (Fig. 1) is ~ 1.7 for the temperature and range of strain rates used in the present experiments. A deviation of the stress at the lowest strain rate from the extrapolated high stress behavior (Fig. 1) indicates an approach to a threshold

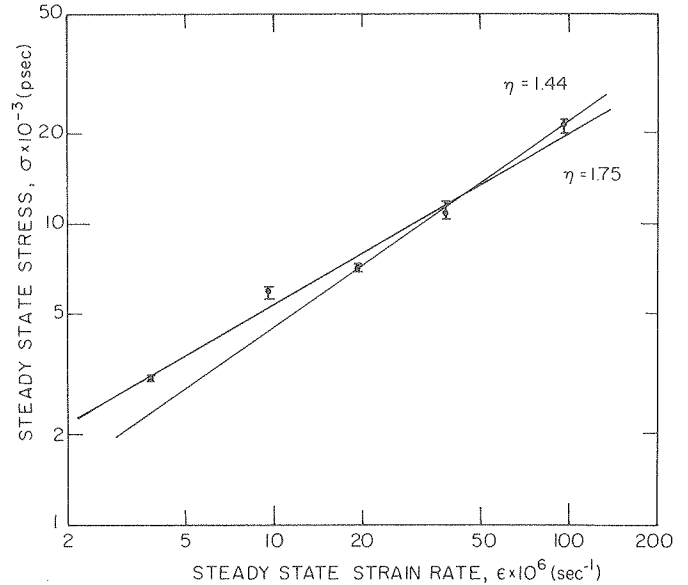


Fig. 1. The stress dependence of the strain rate for polycrystalline alumina. (XBL 7911-14544)

stress as a tentative interpretation of the nonlinear behavior. Alternatively, since the creep strain consists of components derived from diffusive creep and from cavity nucleation and growth, the non-linear creep may result from the nonlinearity of the cavitation component. These possibilities will be explored by estimating the cavitation component of the creep strain from both the cavity densities (and size distributions) and the location of the neutral axis. Also, threshold behavior will be examined by obtaining creep information at lower levels of applied stress. These results will be coordinated with transmission electron microscopic observations of cavity morphologies.

4. SOME EFFECTS OF CAVITIES ON CREEP IN CERAMICS[†]

John R. Porter and Anthony G. Evans

The failure of ceramics deforming under creep conditions occurs by the nucleation and growth of cavities at grain boundaries. For hot pressed alumina, the observed cavities often occupy whole grain boundary facets, unlike many metals which exhibit several small spherical cavities on each tensile grain boundary.

The mechanism for the nucleation and growth of facet-sized cavities in hot pressed alumina is being investigated by transmission electron microscopy of creep specimens deformed in a three-point bend mode at elevated temperatures. Electron transparent specimens have been prepared from regions in the three point bend specimens exhibiting the maximum tensile strain. Figure 1 shows such a region in a hot pressed alumina specimen deformed to a maximum tensile strain of 7% at 1340°C. The load time profile is shown in Fig. 2. During the initial period of deformation at low strain-rate, cavitation was not expected. The cavities would have been introduced

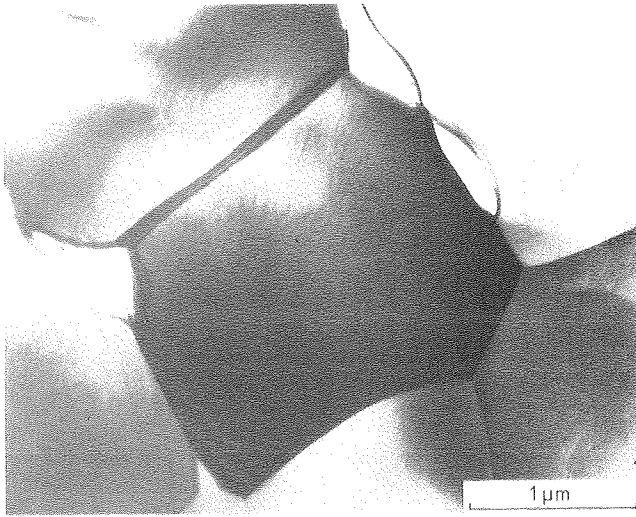


Fig. 1. Transmission electron micrograph of cavities formed at grain boundary during creep of alumina. (XBB 7911-15738)

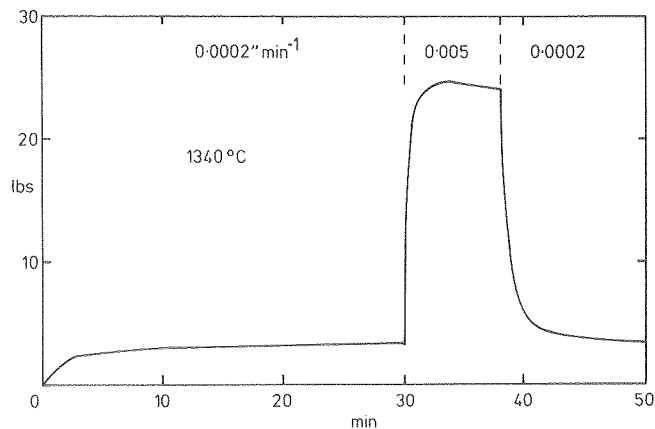


Fig. 2. Load-time profile of three point bend creep test. (XBL 7912-13527)

into the alumina during the short period of deformation at high strain-rate. The second period of deformation at high strain-rate established that the effect of the cavities on the resulting stress was negligible.

The reason for the undetectable effect of cavities on the creep stress at low strain-rates was established by developing a model for the contribution to the strain-rate as a result of the stress induced diffusive growth of grain facet sized cavities. The model system from which the stress strain-rate relationship was derived is shown in Fig. 3. Figure 3a shows two model cavities in a close packed array of hexagonal grains to which a stress is applied. The model calculates the strain-rate which would result from the growth of a cavity by the surface diffusion of material into the adjacent grain boundaries. From the symmetry of the model, only one quarter of a cavity needs to be considered and analyzed; the necessary fluxes are

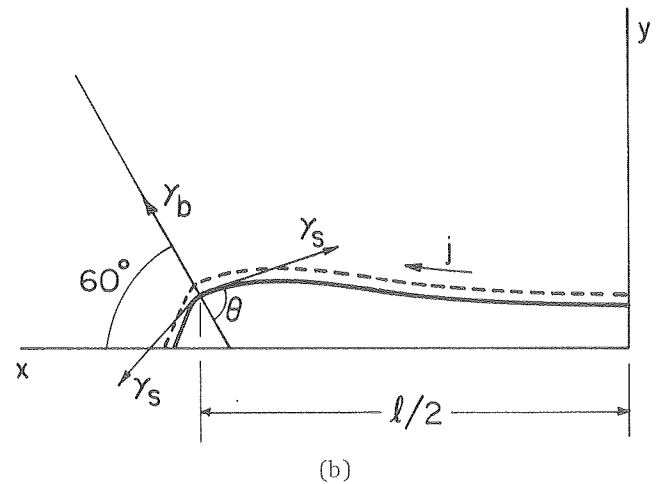
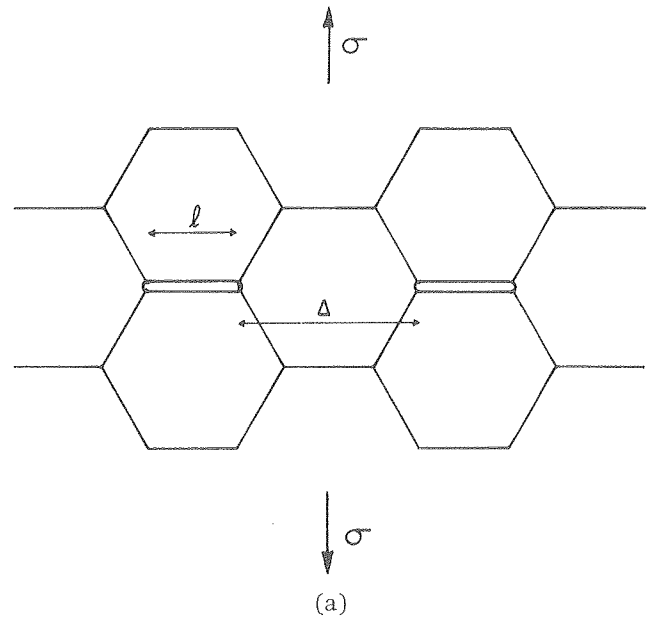


Fig. 3. (a) Schematic diagram of full facet grain boundary cavities in a hexagonal array of grains. (b) Flux diagram for the diffusive growth of a cavity. [(a) XBL 7910-7246; (b) XBL 7910-7248]

shown in Fig. 3b. For an equiaxed material exhibiting facets on alternate tensile grain boundaries, it has been demonstrated that the contribution to the strain-rate resulting from the growth of cavities will be:

$$\dot{\epsilon} = \frac{24\Omega_b \delta_b}{kTd^3 \left(1 + \frac{D_b \delta_b}{4D_s w}\right)} \sigma \quad (1)$$

where D_b and D_s are the grain boundary and surface diffusion coefficients respectively, δ_b and w are the thicknesses of the diffusing layer in the vicinity of the boundary and surface respectively and d is the grain size. Other symbols have their normal meaning.

When this equation is compared with the equation for Coble creep,

$$\frac{\dot{\epsilon}}{\sigma} = \frac{141\Omega D_b \delta_b}{kT d^3} \quad (2)$$

it becomes clear that the diffusive growth of cavities will normally provide a smaller contribution to the total strain-rate than Coble creep. The diffusive growth of cavities cannot therefore be used as a mechanism to explain either anomalously high observed creep-rates, or power law creep, unless all boundaries are cavitated and the deformation is dictated by the rate of extension of the cavities.

Further studies will involve correlations between creep strain, cavity morphologies and the deformations predicted from the permissible diffusive fluxes.

* * *

† Brief version of LBL-10601.

5. HIGH TEMPERATURE CREEP IN Al_2O_3 - SiO_2 CERAMICS[†]

Amar Rana and Anthony G. Evans

Creep strains result from time and temperature dependent processes when materials are subjected to stresses considerably less than the fracture stress. The resultant deformation strains are strongly dependent on microstructure. Most polycrystalline refractory materials are fabricated by sintering or hot-pressing at high temperatures; processes which usually yield microstructures containing residual voids, located on grain boundaries. The role of these pre-existing voids on creep have been examined for four types of microstructure. The concomitant modes of pore growth were distinguished.

The theoretical models involve the growth of pre-existing voids by mass transport (viscous flow or diffusion) with the material displaced from the voids being accommodated by small "thickening" [1] displacements and small cavity surface separations. The first, but least common, microstructure is an equiaxed grain structure with clean grain boundaries such as that present in mullite, 75 wt% Al_2O_3 . In this case

$$\dot{\epsilon}_\infty = \frac{9}{2d'} \left[\frac{\Omega D_b \delta_b}{kT} \frac{1}{b^3 (1-d)^2 2\xi} \right] a \cdot \sigma_\infty \quad (1)$$

where $\dot{\epsilon}_\infty$ is the creep strain rate, σ_∞ is the applied stress, $2a$ is the cavity size and $2b$ is the distance between their centers, $d = a/b$, Ω is the atomic volume, δ_b the grain boundary thickness, D_b the grain boundary diffusion coefficient, d' is the grain size, and

$$\xi = \frac{3d}{(1-d)^2} \left[\ln(1/d) - \frac{(3-d^2)(1-d^2)}{4} \right]$$

The second microstructure consists of grains completely encompassed by an amorphous second phase, typified by mullite, 71.8 wt% Al_2O_3 . In this case:

$$\dot{\epsilon}_\infty = \frac{3}{2d'} \frac{\delta_b^3}{b^2 \eta (1-d)^3} \quad (2)$$

where η is the intrinsic viscosity of the grain boundary.

The third microstructure has an amorphous phase confined to channels along three grain junctions or isolated at four grain junctions, as pertains for example in mullite, 73 wt% Al_2O_3 . In this case we replace $\delta_b D_b$ in Eq. (1) by $D_\ell C_\ell \xi'_\ell$ [2], where D_ℓ is the diffusivity of the solid in the liquid, C_ℓ is the concentration of solid in liquid and ξ'_ℓ is the average liquid film thickness on the cavity surface. Thus, we have

$$\dot{\epsilon}_\infty = \frac{a}{2d'} \left[\frac{\Omega (D_\ell C_\ell \xi'_\ell)}{kT} \frac{1}{b^3 (1-d)^2 2\xi} \right] a \cdot \sigma_\infty \quad (3)$$

It is to be noted that in Eqs. (1), (2) and (3), a , b , and hence d , are not time independent.

For the fourth microstructure, where particles (Al_2O_3 particles at mullite grain boundaries) control the grain boundary sliding rate,

$$\dot{\epsilon}_\infty = \frac{\pi^2}{2\alpha d'} \frac{\Omega}{kT} \frac{\lambda^2}{\delta_p^3} D_v^M \left[1 + \frac{D_v^A}{D_v^M} + \frac{5\delta_b}{\delta_p} \frac{D_b}{D_v^M} \right] \cdot \sigma_\infty \quad (4)$$

where λ is the interparticle spacing, δ_p the particle size, and D_v^A and D_v^M are the volume diffusion coefficients for Al_2O_3 and mullite respectively.

Creep tests have been initiated on the above Al_2O_3 , SiO_2 alloys to compare with the predictions of the creep models.

* * *

† Brief version of LBL-10602.

6. INTERNAL FRICTION IN Al_2O_3 , SiO_2 MATERIALS[†]

Amar P. Rana and Anthony G. Evans

Dynamic experiments as a function of temperature are an aid to understanding the nature of grain boundaries. The dynamic energy dissipated at grain boundaries is the product of shear stress and the shear displacement. At low temperatures, the shear displacement is small, while at high temperatures the boundaries become sufficiently mobile that the shear stress becomes essentially relaxed. Thus, at

low and at high temperatures the energy dissipated is small. Internal friction is the dissipation of energy when the stress and strain are not in phase. Thus at intermediate temperatures a peak in internal friction (Q^{-1}) obtains as a function of temperature.

In Figs. 1-3 the internal friction (Q^{-1}) vs. temperature is plotted for three different microstructures having (1) a continuous film of glassy phase (mullite with 71.8 wt% Al_2O_3), (2) isolated pockets of glassy phase (mullite with 73 wt% Al_2O_3) and (3) clean grain boundaries (mullite with 75 wt% Al_2O_3). All microstructures contain pores located at grain boundaries. We note that the internal friction peak temperatures vary appreciably, viz. 752°C, 762°C and 892°C respectively. A similar trend is apparent for the activation energies, viz. 95, 95 and 169 kcal/mol. The relaxation times for the three cases cited above are respectively:

$$\tau = \frac{\pi^2 d^2 b^2 \eta}{48 \delta^4 \beta} \quad (1)$$

$$\tau = \frac{\pi^2 d^2 k T b^3 (1-d^2)^2 \xi}{144 \delta \Omega \ell C_{\ell} \xi_{\ell} a \beta} \quad (2)$$

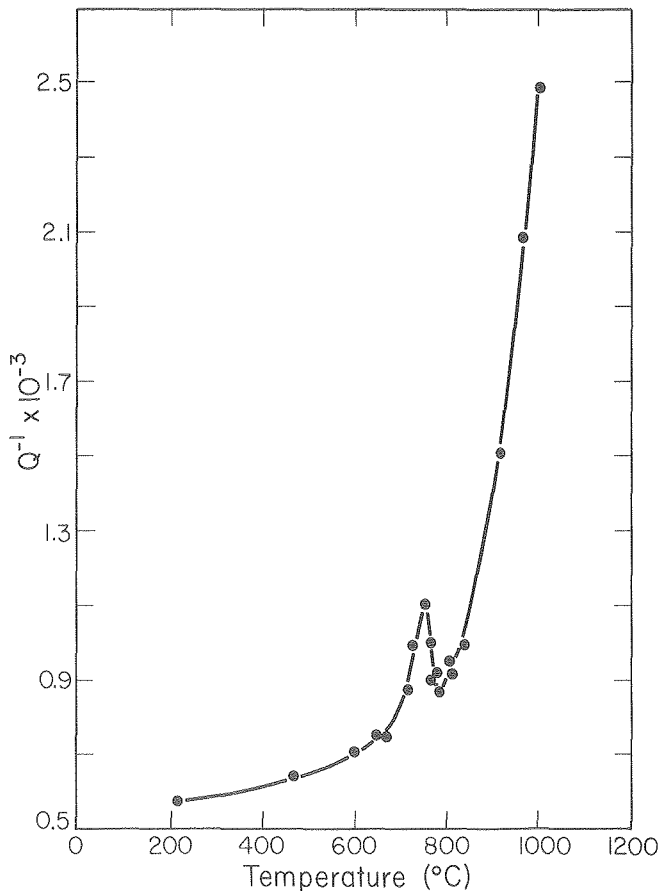


Fig. 1. Internal friction vs. temperature for mullite (71.8 wt.% Al_2O_3). (XBL 803-421)

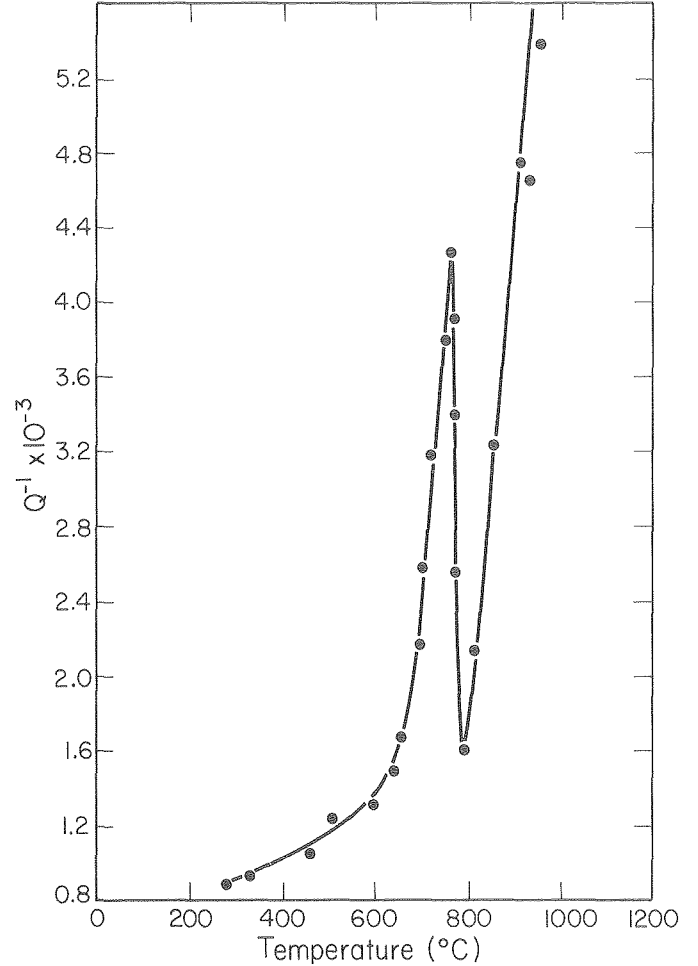


Fig. 2. Internal friction vs. temperature for mullite (73 wt.% Al_2O_3). (XBL 803-420)

and

$$\tau = \frac{\pi^2 d^2 k T b^3 (1-d^2)^2 \xi}{144 \delta \Omega \ell C_{\ell} \xi_{\ell} a \beta} \quad (3)$$

where

$$\beta = \frac{2E}{(1-\nu^2) \cos \phi (1+F \cdot \frac{\pi}{4 \ell} \cos \phi \sqrt{2 \pi a} (\kappa \sqrt{\ell} - \sin 2 \phi \sqrt{\pi (a/2)}))} \quad (4)$$

where τ is the relaxation time, 2ℓ in the grain facet length, ϕ is the extended angle between grain facets, κ is the normalized stress intensity factor [4], F is a factor depending on the number of triple points containing cavities and the rest of the terms have same meaning as in article (5).

These results are being compared with the models of grain boundary sliding for the three types of microstructure, models which invoke localized diffusive fluxes at grain boundary or the shear of a viscous phase.

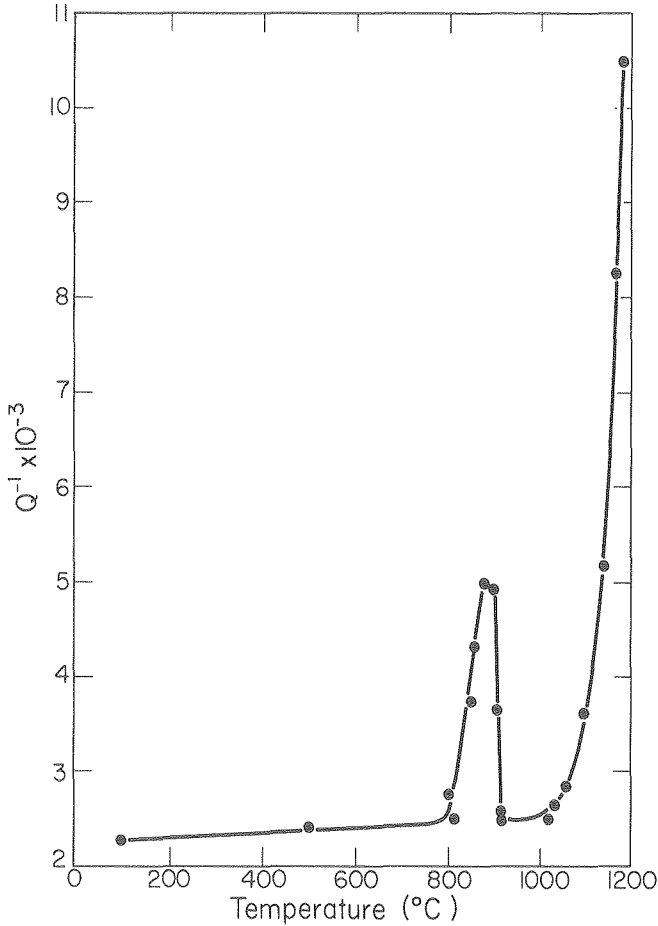


Fig. 3. Internal friction vs. temperature for mullite (75 wt.% Al₂O₃). (XBL 803-422)

* * *

† Brief version of LBL-10603.

1. A. G. Evans and A. Rana, High Temperature Failure Mechanisms in Ceramics, to be published in Acta Met., LBL-8962.
2. R. L. Stocker and M. F. Ashby, Reviews of Geophysics and Space Physics 11, 391 (1973).
3. A. S. Norwick and B. S. Berry, "Anelastic Relaxation in Crystalline Solids," Academic Press, p. 435 (1972).
4. S. N. Chatterjee, Int. J. Solids Structures 11, 521 (1975).

Toughening Mechanisms in Ceramics

1. MARTENSITIC TOUGHENING IN CERAMICS[†]

Anthony G. Evans and A. H. Heuer[‡]

It is now well established that appreciable toughening in ceramics can be achieved by inducing the martensitic transformation of a second phase particle in the vicinity of a crack tip. The most commonly used transformation is the tetragonal to monoclinic transformation in ZrO₂. The toughening

that can be achieved has therefore been analyzed, by examining the changes in strain energy and chemical free energy that accompany a martensitic transformation in the stress field around a crack tip.

The changes in strain energy ΔU have been ascertained using the basic relations developed by Eshelby

$$\Delta U = -V_p e_{ij}^T [p_{ij}^A + (1/2)p_{ij}^I] \quad (1)$$

where V_p is the particle volume, e_{ij}^T is the transformation strain, p_{ij}^A is the applied stress and p_{ij}^I is the transformation induced stress, e.g.,

$$p^I = \frac{e^T}{(1+\nu_m)/2E_m + (1-2\nu_p)/E_p} \quad (2)$$

where E is Young's modulus, ν is Poisson's ratio and the subscripts m and p refer to the matrix and particle respectively. Then, by presuming that the transformation will proceed when the thermodynamic requirements are satisfied (i.e., appropriate nuclei are always available), the critical applied stress p_c^A for transformation (for a dilational strain ΔV) becomes:

$$p_c^A \Delta V = -\Delta G_o + E_p \beta \left[\frac{(1/3)\Delta V^2}{(1+\nu_m) + 2\beta(1-2\nu_p)} \right] \quad (3)$$

where $\beta = E_m/E_p$. When the applied stresses are augmented in the vicinity of a crack tip, the field equations for a crack can be coupled with Eq. (3) to deduce the distance r from the crack tip at which particles will transform, as a function of the applied stress intensity factor K . The result is

$$r_c \left(\frac{\Delta V E_p}{K_I} \right)^2 = \frac{4.1}{\pi} \frac{[\cos(\theta/2)(1+\xi \sin\theta + 2\cos 3\theta/2)(1+\beta)]^2}{\beta(1+3\xi^2) - 3.6(1+\beta)\mathcal{F}} \quad (4)$$

where θ is the inclination with respect to the crack plane and $\mathcal{F} = \Delta G_o/E_p \Delta V^2$. Some typical transformation zones predicted by Eq. (4) are plotted in Fig. 1. The transformation zone size can now be used to predict the increment in toughness Γ_T imparted by the transformation, by requiring the crack to extend when the intrinsic crack extension resistance of the material Γ_o is exceeded. The resultant toughening is predicted to be

$$\frac{\Gamma_T}{\Gamma_o} = \frac{1+\phi}{1-\phi} \quad (5)$$

where

$$\phi = \frac{0.7V_f[\beta(1-\nu_f) + \nu_f][0.34\xi + 1]^2(1+\beta)}{\beta(1+3\xi^2) - 3.6(1+\beta)\mathcal{F}}$$

where V_f is the volume fraction of particles.

This prediction has several important implications for optimizing the toughening induced by a martensitic

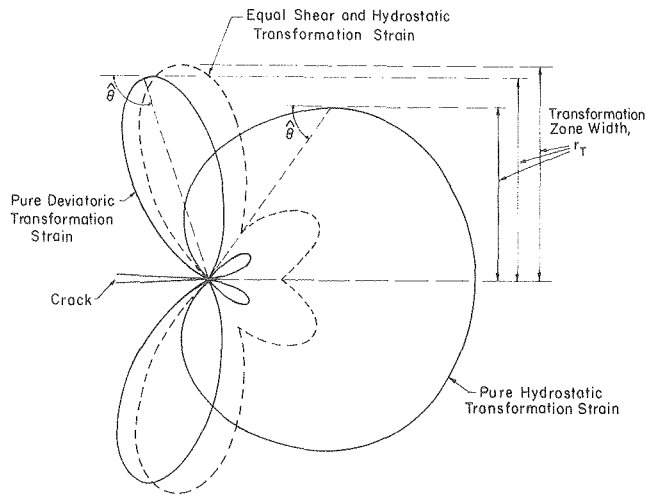


Fig. 1. Contours of crack tip martensitic transformations. (XBL 7812-6296)

transformation. There is an interdependence of toughness on the chemical composition of the martensite (which determines the chemical free energy), the elastic stiffness of the matrix and the twin/variant spacing within the transformed particles. The latter is rather poorly understood at this juncture and is the major impediment to quantitative predictions of toughening. However, the qualitative expectation that the maximum toughness should occur when the particles are close to spontaneous (stress free) transformation should generally pertain.

Finally, it is observed that the prediction of toughness, Eq. (5), provides an invaluable guidance for the design and interpretation of experiments. Specifically, effects of temperature and chemical composition are interpreted through their influence on ΔG_0 in the denominator of the toughening relation. The effects of the twinning and variant structure of the transformed particles and of the particle geometry appear through the strain energy terms; similarly the matrix elastic properties influence toughness by virtue of their effect on the strain energy change.

* * *

† Brief version of LBL-8442.

Permanent address: Division of Metallurgy & Material Science, Case Western Reserve University, Cleveland, Ohio 44106.

2. MARTENSITIC TRANSFORMATION IN ZIRCONIA

Waltraud M. Kriven and Anthony G. Evans

Martensitic transformations were first discovered in steels and contribute importantly to their strength. In the last decade, Garvie et al.¹ discovered that in partially stabilized zirconia (PSZ) fracture toughness and thermal shock resistance were considerably increased by the martensitic tetragonal to monoclinic transformation.

In the design of very tough ceramics, therefore, an understanding of the nature of martensitic transformations, coupled with the mechanism of crack arrest and optimum microstructure, is essential. The nature of martensitic transformations may be studied along the lines of their nucleation, thermodynamics and kinetics, and crystallography. Experimental elucidation of examples from both metal and non-metal systems may clarify these three aspects, which in turn may enable prediction and successful microstructural design.

To date, martensitic transformations have been found in the following, non-metallic substances:

| | |
|-----------------------------------|---|
| Ferro-electric perovskites: | BaTiO_3 , SrTiO_3 , $(\text{PbZrTi})\text{O}_3$ $\text{KTa}_{0.65}\text{Nb}_{0.35}$, KH_2PO_4 |
| Inorganic complexes: | RbNO_3 , TlNO_3 , KNO_3 , AgNO_3 Alkali halides, ammonium thiocyanate, MnS |
| Al ₁₅ superconductors: | V_3Si , NbSn , NbN - NbC |
| Organic compounds: | Polyethylene, solid monomers derived from anthracene |
| Rare earth oxides: | ZrO_2 , HfO_2 |

Recent work on PS zirconia has been directed to elucidate the crystallographic mechanism in ellipsoidal-shaped tetragonal particles which grow within the cubic matrix. Small particles of $\leq 0.2 \mu$ transform by numerous fine twins perpendicular to the long axis of the ellipsoid, while larger particles contain only a few wide variants whose lengths are parallel to the long axis of the ellipsoid. Previous TEM studies by Bailey² and Bansal and Heuer³ indicate twinning on $\{110\}_{\text{monoclinic}}$ and $(010)_m$ planes. Martensitic habit planes of the type $\{110\}_m$ form the long edge of lenticular plates containing no subtexture, while $(010)_m$ or $(100)_m$ form the midrib of twinned plates.⁴

Analysis of transformed product requires the differentiation between different twin types. Thus

- (1) fine twins provide the lattice invariant shear (LIS) for the martensite mechanism,
- (2) product variants may be twin related,
- (3) post-transformation deformational twins may accommodate misfit between nodules or packets of twin related variants.

Examples of each have been experimentally verified in steels and inorganic compounds.

The few, wide variants in the ellipsoidal particles of PSZ are similar in appearance to lath martensites in steels which are thought to occur by a slip mechanism.

Crystallographic martensite analyses were made by Bansal and Heuer³ and more extensively by Fraser, Kennedy and Kriven.⁴ The former analysis computes

solutions for slip LIS systems which only partially agree with experiments, while the latter use experimentally observed twin LIS systems as well. These predictions were applied to the ellipsoid particles in PSZ and found to agree with available experimental data.^{5,6} They are summarized in Table 1. Further detailed TEM analyses are underway to verify this agreement between experiment and predictions.

* * *

1. R. C. Garvey, R. H. Hannink, R. T. Pascoe, *Nature* 258, 703 (1975).
2. J. E. Bailey, *Proc. Roy. Soc.* 279, 395 (1964).
3. G. K. Bansal and A. H. Heuer, (I) *Acta Met.* 20, 1281 (1972); (II) *Acta Met.* 22, 409 (1974).
4. W. L. Fraser (and S. W. Kennedy), Ph.D. thesis, Adelaide (1974); W. M. Kriven (and S. W. Kennedy), Ph.D. thesis, Adelaide (1976).
5. L. H. Shoenlein and A. H. Heuer, Ph.D. thesis, Cleveland, (1979).
6. R. J. Hannink, *J. Mat. Sci.* 13, 2487 (1978).

Table 1. Martensite calculations.

| <u>Lattice</u> <u>Corre-</u> <u>spondence</u> | <u>Shear</u> <u>System</u> | <u>Habit</u> <u>Plane</u> | <u>Macroscopic</u> <u>Shape Strain</u> | <u>% Strain</u> <u>+ Habit</u> <u>Plane</u> | <u>% Strain</u> <u> Habit</u> <u>Plane</u> |
|---|-------------------------------|---|---|---|--|
| <u>Bansal and Heuer:</u> | | | | | |
| LC 2 | ($\bar{1}10$) [001] slip | (671) _m , (761) _m $\approx 7^\circ$ off (110) _m | .124 | 1.8 | 12.2 |
| LC 2 | ($1\bar{1}0$) [110] slip | (100) _m , (010) _m | .162 | 1.73 | 16.1 |
| <u>Fraser, Kennedy and Kriven⁴:</u> | | | | | |
| LC 3 | {110}<100> twin | {322} _m | .039 | 1.9 | 3.37 |
| LC 2 | ($1\bar{1}0$) [001] slip | (751) _m , $\sim 7^\circ$ off {110} | .110 | 1.9 | 10.5 |
| | | (105) _m | .110 | 3.01 | 10.5 |
| LC 2 | ($1\bar{1}0$) [110] | (010) _m | .153 | 1.9 | 14.8 |
| | | (019) _m | .153 | 1.87 | 15.1 |

3. TOUGHENING IN THE $\text{Al}_2\text{O}_3/\text{ZrO}_2$ SYSTEM[†]

Nick Burlingame and Anthony G. Evans

Fine dispersions of ZrO_2 particles can greatly increase the toughness of ceramic materials. This improvement can be related to the presence of tetragonal ZrO_2 particles, which, though stable when constrained by a matrix, transform to monoclinic when the constraint is relaxed in the stress field of a propagating crack. Upon transformation, there is a shape change and a size increase, effects creating compressive stresses at the crack tip, thereby increasing the energy required to further propagate the crack. Enhancement of toughness will depend on a combination of the matrix-dispersion, and the size, volume fraction, and chemical composition of the dispersed ZrO_2 .

Increasing the volume fraction V_f of ZrO_2 is expected to increase the toughness in proportion to V_f . However, this increase can be mitigated by the concomitant increase in particle size, because of the size dependence of spontaneous transformation, attributed to the relative influence of the twin boundary energy. These effects are demonstrated in Fig. 1, which plots the simultaneous variation in fracture toughness K_{IC} and the proportion of retained tetragonal phase as a function of the total volume fraction of ZrO_2 in an Al_2O_3 matrix. A peak toughness of $\sim 8 \text{MPa}\sqrt{\text{m}}$ is obtained for $\sim 15 \text{vol}\%$ ZrO_2 and a corresponding tetragonal phase content of $\sim 75\%$.

The effect of chemical composition has been examined for solid solutions created with the known stabilizing agents ($\text{CaO}, \text{MgO}, \text{Y}_2\text{O}_3$). These solutes decrease the chemical free energy and thereby allow an increased proportion of tetragonal phase to be retained. The influence of these solutes on both the toughness and proportion of tetragonal phase is indicated on Figs. 2-4. It is directly apparent that the maximum toughness occurs consistently when a significant proportion of the ZrO_2 is in its monoclinic option.

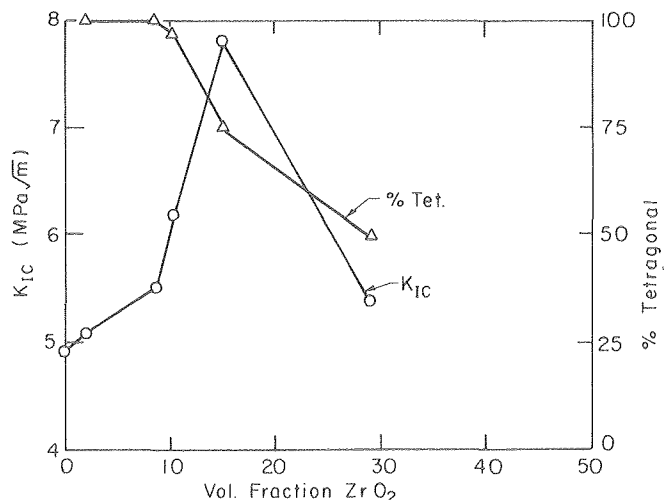


Fig. 1. Volume fraction ZrO_2 in Al_2O_3 matrix vs. K_{IC} and percent retained tetragonal.

(XBL 7911-14549)

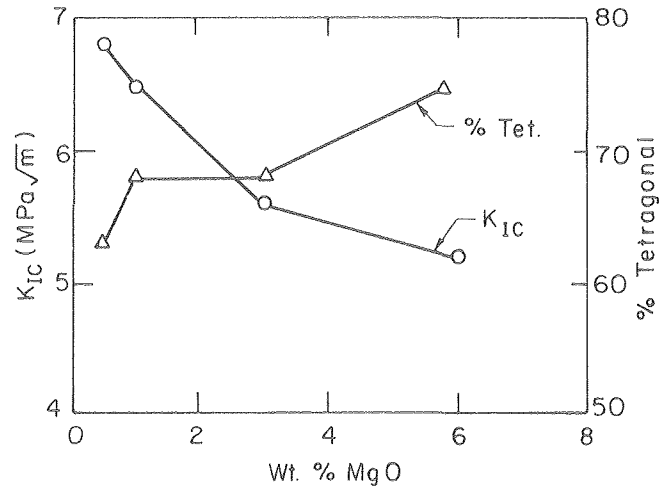


Fig. 2. Weight percentage MgO vs. K_{IC} and percent retained tetragonal (15 vol% ZrO_2).

(XBL 7911-14550)

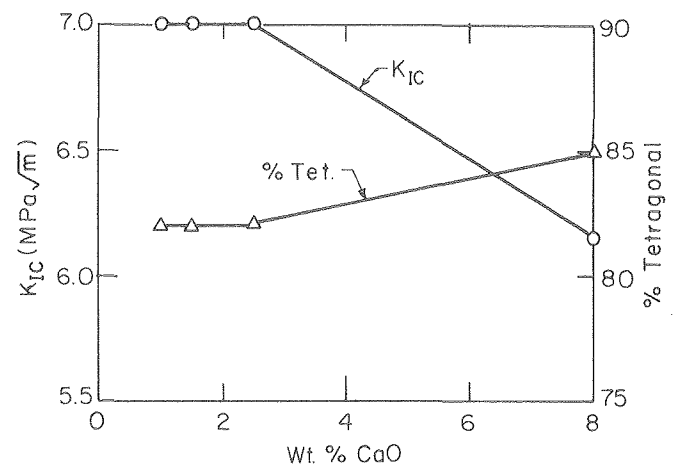


Fig. 3. Weight percentage CaO vs. K_{IC} and percent retained tetragonal (15 vol% ZrO_2).

(XBL 7911-14551)

The apparent prerequisite that a significant proportion of monoclinic ZrO_2 be present in order to attain maximum toughness is not consistent with the simple theory. This inconsistency has several possible interpretations, possibilities which might be distinguished by microscopy and further theoretical analyses. The deviations from the simple theory almost certainly reside in the following effects: (1) the statistical dispersion of ZrO_2 particle size, (2) the physical location of the ZrO_2 particles (within grains or at grain boundaries), (3) the thermal expansion mismatch between tetragonal ZrO_2 and Al_2O_3 , and (4) the incidence of crack tip microcracking following transformation, particularly of the thermally transformed particles. Subsequent microscopic studies will examine particle size distributions and the incidence of microcracking, as inputs to theoretical treatments of combined transformation, microcracking effects on toughness in the presence of a size distribution of particles.

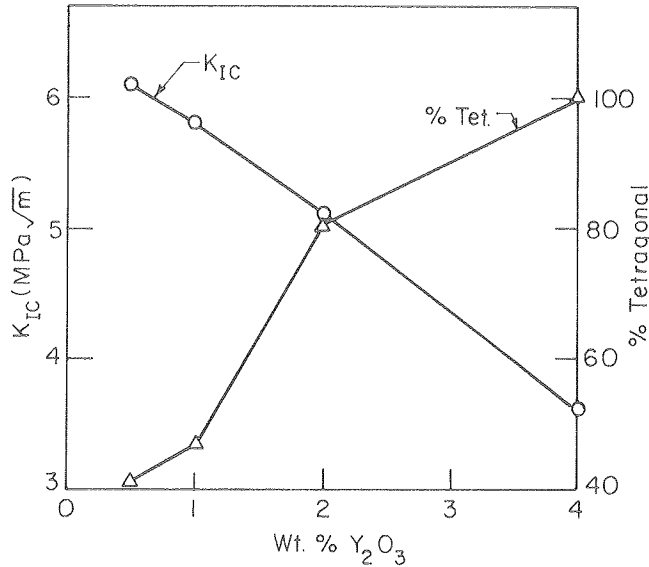


Fig. 4. Weight percent Y_2O_3 vs. K_{IC} and percent tetragonal (29 vol% ZrO_2). (XBL 7911-14552)

* * *

† Brief version of LBL-10604.

RESEARCH PLANS FOR CALENDAR YEAR 1980

1. High Temperature Deformation and Failure in Ceramics

Creep Strains. Recent experimental and theoretical results suggest that large creep strains in ceramic polycrystals cannot be induced by pre-formed cavities until large densities of cavities begin to form in the tertiary stage. This contrasts with the suggestions of prior investigators, based on qualitative arguments, that appreciable creep strains can result from cavitation. Creep strains determined exclusively by cavitation are small, a few times the elastic strain. These obtain at low temperatures and high stresses. Conversely, creep in porous ceramics can be appreciably affected by the pre-existent pores, a result explained by the location of the void space vis-a-vis the applied stress. These recent observations and the related theory will be amplified in the coming year and used to superimpose regimes of cavity and pore induced creep onto deformation mechanism maps. Specific implications with regard to the dominant diffusivities will also be deduced as a basis for correlation with final stage sintering results.

Failure Times. The failure times of ceramics subject to creep at elevated temperatures depend sensitively upon the mode of formation of grain boundary cavities and on the statistical dispersion of the cavities, as reflected by the variability of grain boundary properties. Experimental and theoretical studies conducted during the previous year have indicated various cavity growth mechanisms and have

derived statistical approaches for characterizing the evolution of failure by cavity formation and coalescence. In the coming year, detailed experimental results will be obtained on Al_2O_3 and the complementary theory will be developed. The experiments include determinations of cavity size distributions and morphologies as a function of stress, strain, and temperature obtained using SEM and TEM methods. Grain boundary chemistry will also be examined using STEM in order to ascertain possible correlations between grain boundary chemical composition and cavitation susceptibility. The theory will involve extensions of the Chuang-Rice model to include effects of voids terminating at grain triple points and of grain boundary sliding. Further developments of the statistical analysis of cavity coalescence will also be conducted, to include interaction effects between neighboring cavities.

2. Final Stage Sintering

A systematic study of final stage sintering will be conducted on Al_2O_3 . The study will entail the use of monodispersed powders, hot pressed to produce a characteristic final stage microstructure, i.e., isolated voids. The diminution of the voids and the onset of grain boundary migration will then be monitored during subsequent sintering. The results will be used to develop quantitative relations for void shrinkage and the onset of the breakway of pores from grain boundaries, the primary detriment to full densification.

3. Martensitic Toughening

The important interdependence of the matrix phase, and chemical composition of the martensite and twinning on the martensitic toughening have been established in the previous year. The major remaining uncertainties are connected with the characteristics of the twinning and with the nucleation condition (a simple thermodynamic energy balance has thus far been used to describe nucleation). These issues will be the focus of research in the forthcoming year. The twinning will be examined in the context of crystallographic martensite theory, coupled with the minimization of strain energy and twin boundary energy, using the generalized Eshelby approach. The role of nucleation on toughening will be examined using nucleation theories based on pre-existent shear inhomogeneities (e.g., defects located at interfaces) and the driving forces provided by the excess chemical free energy.

1979 PUBLICATIONS AND REPORTS

Refereed Journals

1. A. G. Evans, "Microfracture From Thermal Expansion Anisotropy, I. Single Phase Materials," *Acta Met.* 26, 1845 (1978).
2. D. L. Porter, A. G. Evans and A. H. Heuer, "Transformation Toughening in Partially Stabilized Zirconia," *Acta Met.* 27, 1649 (1979).

3. A. G. Evans, D. R. Biswas and R. M. Fulrath, "Some Effects of Cavities on the Fracture of Ceramics, I. Cylindrical Cavities," *J. Am. Ceram. Soc.* 62, 95 (1979).
4. A. G. Evans, D. R. Biswas and R. M. Fulrath, "Some Effects of Cavities on the Fracture of Ceramics, II. Spherical Voids," *J. Am. Ceram. Soc.* 62, 101 (1979).
5. F. F. Lange and A. G. Evans, "Erosive Damage Depth in Ceramics: A Study on Metastable Tetragonal Zirconia," *J. Am. Ceram. Soc.* 62, 62 (1979).
6. A. G. Evans, "Impact Damage Mechanics: Solid Projectiles," *Treatise on Materials Science and Technology*, 16, 1 (1979).
7. W. F. Adler and A. G. Evans, "Erosion Damage in Carbon-Carbon Composites at Hypersonic Impact Velocities," *ASTM STP* 664, 345 (1979).
8. A. G. Evans, "Fracture Toughness Determinations by Indentation," *ASTM STP* 678, 112 (1979).

Other Publications

1. A. G. Evans, "Abrasive Wear in Ceramics," in *Ceramic Machining*, R. W. Rice and B. J. Hockey, Eds., NBS Special Publication (Oct. 1979).
2. A. G. Evans, "Structural and Microstructural Design with Brittle Materials," in *ICM 3*, K. Miller, Ed., Vol. 3 (1979).
3. A. G. Evans, Y. M. Ito, and M. Rosenblatt, "Damage Thresholds for Brittle Materials Impacted by Water Drops," in *ELSI V*, J. E. Field, Ed., Cambridge (1979).

LBL Reports

1. A. G. Evans, "Abrasive Wear in Ceramics: An Assessment," LBL-8608 (January 1979).
2. A. G. Evans, "Acoustic Emission Sources in Brittle Solids," LBL-8335 (October 1978).
3. A. G. Evans and A. Rana, "High Temperature Failure Mechanisms in Ceramics," LBL-8692 (July 1979).

4. A. G. Evans and A. H. Heuer, "Transformation Toughening in Ceramics," LBL-8442 (July 1979).
5. A. G. Evans, "Fatigue in Ceramics," LBL-9529 (July 1979).

Invited Talks

1. A. G. Evans, "Structural and Microstructural Design with Brittle Materials," Third International Materials Conference, Cambridge, England (August 1979).
2. A. G. Evans, "Damage Thresholds in Brittle Materials Impacted by Water Drops," Fifth International Conference on Erosion, Cambridge, England (September 1978).
3. A. G. Evans, "Creep Fracture in Ceramics," Materials Research Council, La Jolla, California (July 1979).
4. A. G. Evans, "Erosion in Ceramics," DOE Workshop, Oak Ridge, Tennessee (June 1979).
5. A. G. Evans, "Non-Destructive Testing of Ceramics," American Ceramic Society Symposium, Cincinnati, Ohio (April 1979).
6. A. G. Evans, "Abrasive Wear in Ceramics," Ceramic Machining Conference, NBS Washington, D.C. (March 1978).
7. A. G. Evans, "Acoustic Emission in Brittle Solids," Joint American/Japanese Acoustic Society, Honolulu, Hawaii (October 1978).
8. A. G. Evans, "Erosion of Ceramics," ONR Workshop, NBS, Washington, D.C. (June 1979).
9. A. G. Evans, "Fracture of Ceramics," AIME Special Symposium, Milwaukee, Wisconsin (October 1979).
10. A. G. Evans, "Non-Destructive Testing of Ceramics," ARPA Review Meeting, La Jolla, California (July 1978).
11. A. G. Evans, "Creep of Ceramics," Stanford University, Palo Alto, California (May 1979).

3. Physical Properties

a. Superconductivity Effects—High Field Superconductivity*

J. W. Morris, Jr., and J. Wang, Investigators

Introduction. Application of multifilamentary superconductors to advanced energy research and technology, such as high energy particle accelerators and magnetic fusion energy systems is being seriously considered at the present time. A method has been developed for the fabrication of multifilamentary superconducting wires, employing a powder-metallurgy infiltration technique. The objectives of this program are to identify the process parameters, to study the chemistry of filamentary conductors and to measure the physical and mechanical properties of the superconducting wires.

1. AN INVESTIGATION OF THE EFFECTS OF PARTICLE SIZE ON THE MECHANICAL PROPERTIES OF POROUS AND TIN-INFILTRATED NIOBIUM RODS FABRICATED BY A THERMOPLASTIC-POWDER METALLURGY TECHNIQUE

Abid Noman, J. Ling-Fai Wang and Milton R. Pickus

A method has been developed for the fabrication of multifilamentary superconducting wires, employing a powder-metallurgy infiltration technique. This technique has been successfully extended to the Nb_3Sn , Nb_3Al , $Nb_3(Al,Ge)$ and $Nb_3(Al,Si)$ systems. For the fabrication of niobium rods, which are prepared from powder and are to be infiltrated at a later stage, two methods have been employed successfully. The first technique makes use of isostatic compaction and the second method employs as a binder a polymer, which is coated on the powder particles, thus imparting thermoplastic properties to the resulting powder. Taking advantage of the thermoplastic properties of the powder, the substance is extruded as a rod, after which the polymer is volatilized by means of a prescribed heating cycle. It remains to expose the niobium rod obtained after initial sintering to obtain strength and ductility and to facilitate the removal of oxide layer which hampers the infiltration of the rod. This investigation employs the thermoplastic-powder metallurgy technique and reports the effects on mechanical properties of three different particle size ranges and different sintering times at a given temperature.

The plot for residual porosity versus sintering time is shown in Fig. 1. This shows that larger

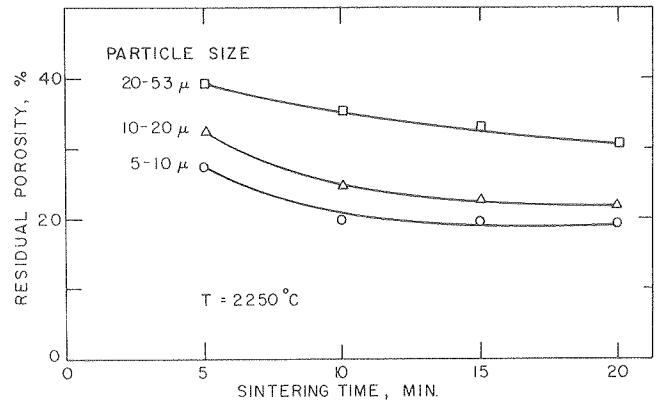


Fig. 1. Plot for residual porosity vs. sintering time. (XBL 7810-6011)

particles form a more porous body than particles of smaller size. The porosity decreases with sintering time as the bonding of particles causes the pores to shrink.

The tensile tests conducted show:

1. The relatively coarse particle rods sintered for the same length of time as finer particle rods, porous or infiltrated, were stronger (see Fig. 2).

2. Coarse particle rods were more ductile than the respective finer particle rods (see Fig. 3). This was presumably due to the lower surface to volume ratio of the coarser particles, which implied that less contaminants were present in the coarser particle rods.

* * *

†Brief version of LBL-8501.

* This work was supported by the Division of Materials Sciences, Office of Basic Energy Sciences, U.S. Department of Energy.

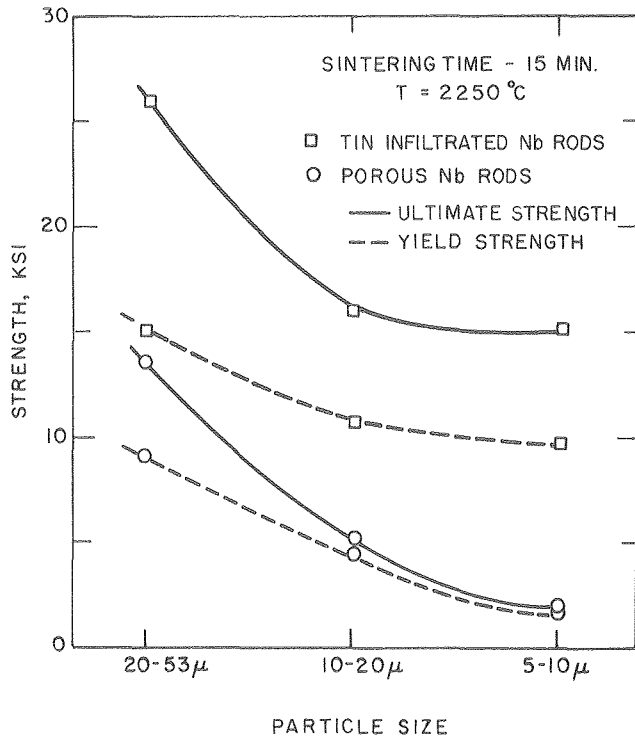


Fig. 2. Comparison of yield and ultimate strength of respective porous and as-infiltrated Nb rods.
(XBL 7810-6004)

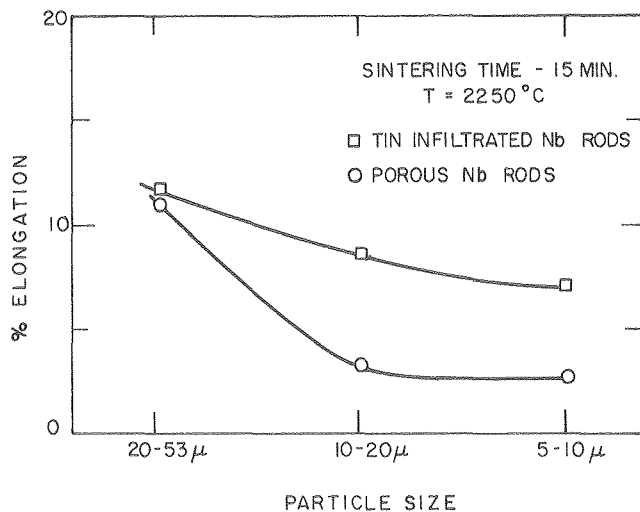


Fig. 3. Comparison of elongation of respective porous and as-infiltrated Nb rods.
(XBL 7810-6008)

2. HIGH FIELD CURRENT CARRYING CAPACITY OF NIOBIUM-TIN SUPERCONDUCTING WIRE PRODUCED BY THE INFILTRATION PROCESS[†]

J. Ling-Fai Wang, J. T. Holthuis and Milton R. Pickus

Application of superconducting materials to advanced energy research and technology, such as high energy particle accelerators and magnetic fusion is being seriously considered at the present time. The infiltration process developed has been applied to the niobium-tin system to produce multifilamentary tape and wire. High critical currents were previously reported by Hemachalam and Pickus for infiltrated samples tested in magnetic fields from 20 to 170 kG. The sample reacted at 950°C for 2 minutes exhibited a critical transition temperature, T_C , of 18 K. The objectives of the present investigation were to establish the reproducibility of the infiltrated wire, to extend the current carrying capacity measurements to a higher field region (~220 kG) and to study the effects of heat treatment on the critical current carrying capacity.

Most of the process parameters used were the same as previously reported except that the sintering time was increased from 15 to 30 minutes and the infiltration temperature was lowered from 675 to 575°C. These changes improved the formability of the composites and prevented premature breakage. The superconducting filaments of Nb₃Sn were formed by a heat treatment of wire specimens in an argon atmosphere. The reaction temperature ranged from 800 to 950°C while the duration varied from 30 to 2 minutes.

Superconducting critical current densities of Nb-Nb₃Sn cores were measured as a function of applied magnetic fields up to 190 kG for most cases and to 220 kG for a limited number of specimens. Critical current densities were determined by dividing critical currents by the cross sectional areas of the Nb-Nb₃Sn composite core for each wire. The variations in the critical current densities with applied magnetic fields are shown in Fig. 1. The present data for wire reacted at 950°C for 2 minutes matched very well with the data from Hemachalam and Pickus. This clearly shows the reproducibility of the infiltration process. The critical current density of 1×10^4 Amp/cm² at 200 kG shows that the infiltration process wires have a very high critical field without the need of third element additions.

* * *

[†]Part of this work was performed while the authors were guests at the Francis Bitter National Magnet Laboratory, which is supported at M.I.T. by the National Science Foundation.

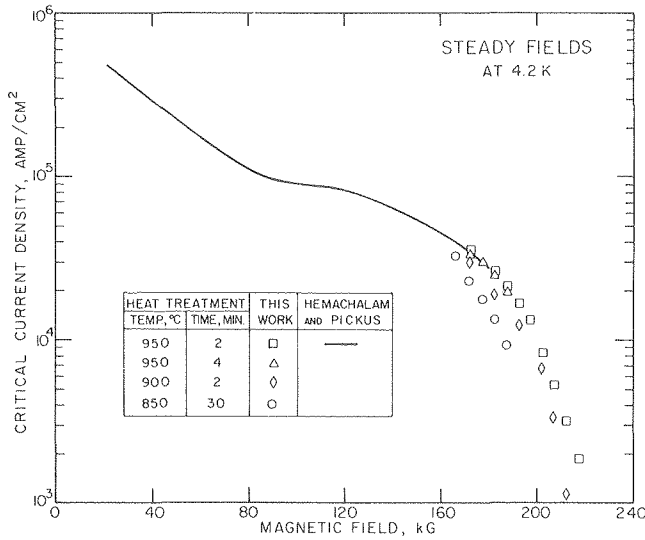


Fig. 1. Critical current density of the Nb-Nb₃Sn core as a function of magnetic field under steady field condition. (XBL 7911-14557)

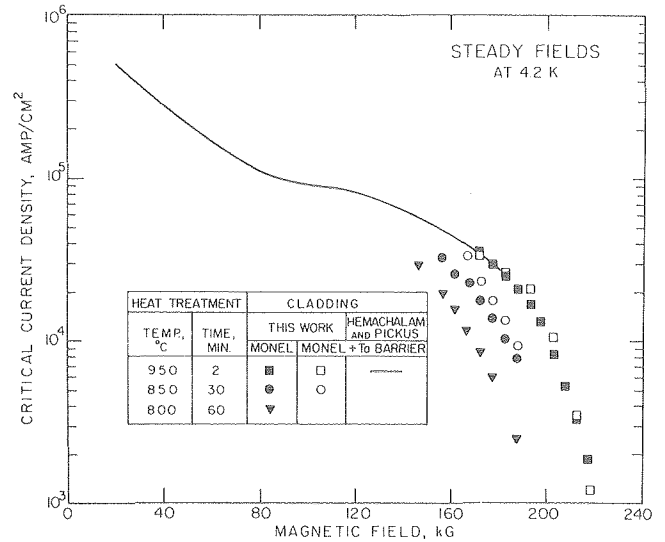


Fig. 1. Critical current density of the Nb-Nb₃Sn core as a function magnetic field under steady field condition. (XBL 7911-14558)

3. THE POSSIBILITY OF ELIMINATING THE TANTALUM DIFFUSION BARRIER IN NIOBIUM-TIN SUPERCONDUCTING WIRE FABRICATED BY THE INFILTRATION PROCESS[†]

J. Ling-Fai Wang, J. T. Holthuis and Milton R. Pickus

The "bronze" process for fabricating multifilamentary superconducting wire requires long heat treatment times. To provide adequate quench protection in large magnets, it was considered desirable to incorporate regions of high conductivity oxygen-free copper into magnet conductors. The copper is protected by an inert diffusion barrier to prevent poisoning during the processing and reaction stages. Tantalum metal tube is used for this purpose in most of the commercially available bronze process wires. The addition of the tantalum barrier has not only increased the cost of the superconducting wire but also increased the complexity of the manufacturing process.

A re-evaluation of the processing parameters suggested that tantalum diffusion barriers may be eliminated in infiltration-process wire since the infiltration-process wire depends on a liquid-solid interface reaction and requires much shorter reaction times.

In this study, tin infiltrated porous niobium was clad with monel tubing with and without a tantalum barrier and reduced down to wire as fine as 0.010" in diameter. Both types of wire were reacted at the same temperature and for the same duration. After reacting at 950°C for 2 minutes both types of wire have $T_C \sim 18$ K and approximately the same current carrying capacity (see Fig. 1). This seems to suggest that the tantalum barrier

can be eliminated from the infiltration process wire when the reaction time is short. At 850°C for 30 minutes the infiltrated wire without tantalum barrier definitely shows a deterioration of current-carrying capacity. This clearly shows that as reaction time increases the reaction between the infiltrated core and monel increases to such a degree that it affects the current-carrying capacity of the wire.

* * *

[†]Part of this work was performed while the authors were guests at the Francis Bitter National Magnet Laboratory, which is supported at M.I.T. by the National Science Foundation.

4. SCANNING AUGER MICROSCOPY STUDY OF THE ROLE OF OXYGEN ON THE FRACTURE OF TIN-INFILTRATED NIOBIUM ROD.[†]

J. Ling-Fai Wang and J. T. Holthuis

Niobium metal or alloys, like other group VB refractory metals are susceptible to embrittlement as a result of contamination from the interstitial elements (O, C, N and H). All niobium powder used for fabricating porous niobium rods for the infiltration process was produced by the hydride-crush-dehydride process. A typical chemical analysis of the niobium powder (-270 mesh) indicates that it has ~1700 ppm oxygen, <30 ppm carbon and <50 ppm nitrogen. For years this chemical specification was considered to be satisfactory and the effects of these interstitial elements on the formability were not considered. Premature breakages of samples during wire drawing were not considered to be a serious problem.

Recently there is a great interest to commercialize the infiltration process. This involves commencing with much larger diameters of as-infiltrated rods than were previously used. It was soon found that premature breakage during wire drawing was a serious problem.

Evidence was obtained on the basis of chemical analyses and hardness profiles that oxygen was a probable cause for the embrittlement. With special precaution to minimize oxygen content a substantial ductility was obtained.¹

During this fiscal year a scanning Auger microscope with an in-situ fracture mechanism was made available for metallurgical study. Tin infiltrated niobium rods were fractured in situ at room temperature and the elemental maps of the surfaces were obtained. Auger images for the elements oxygen, niobium and tin are given in Fig. 1. A SEM micrograph and x-ray maps for the elements niobium and tin are given in Fig. 2. These clearly show that oxygen atoms are not in tin but are homogeneously distributed in niobium and may be the cause of embrittlement.

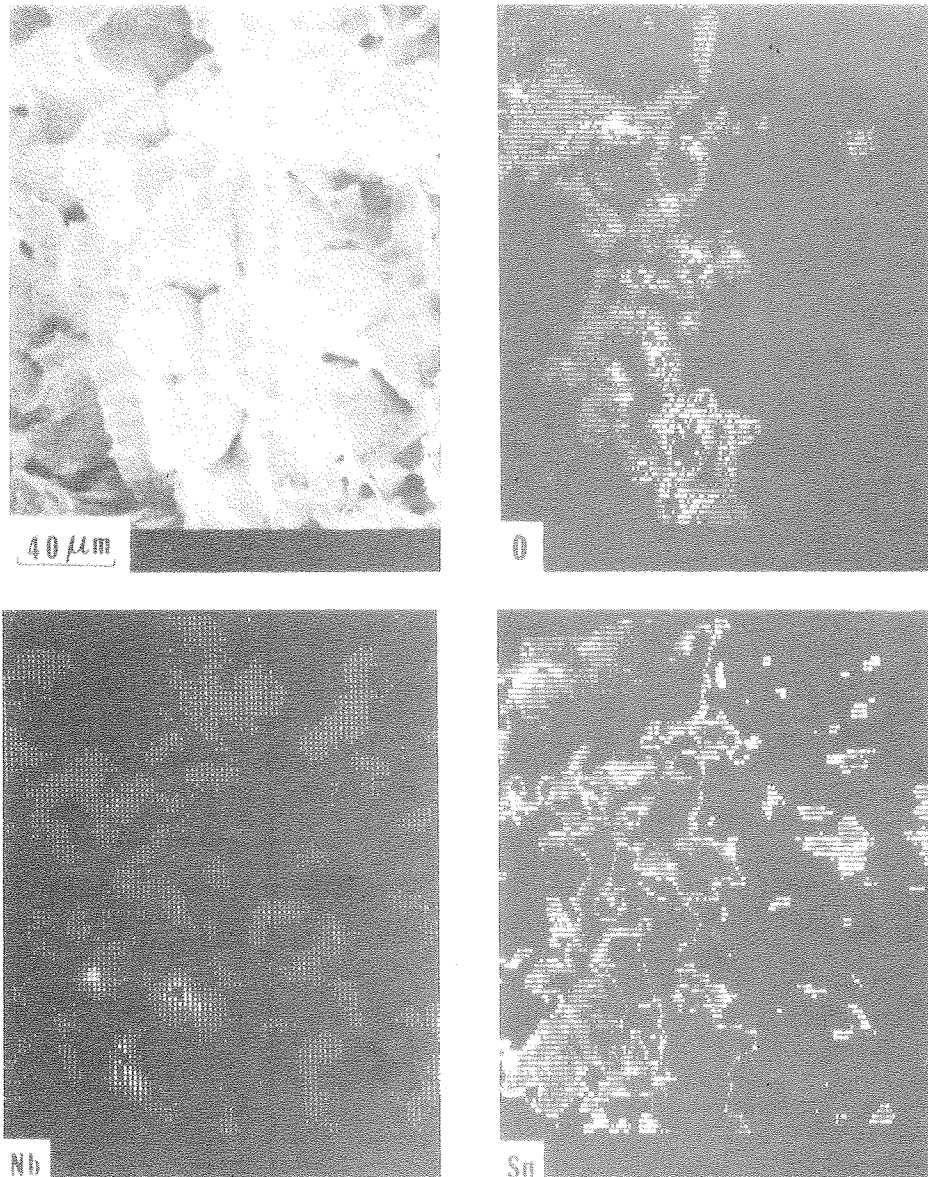


Fig. 1. SEM micrograph of the in-situ fractured tin-infiltrated niobium rod and Auger images for the elements oxygen, niobium and tin. (XBB 799-12565)

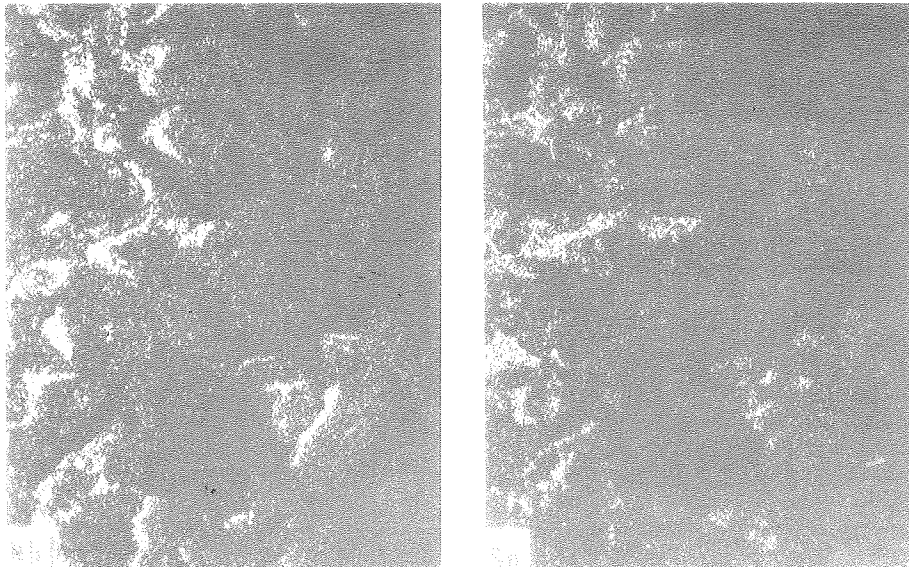
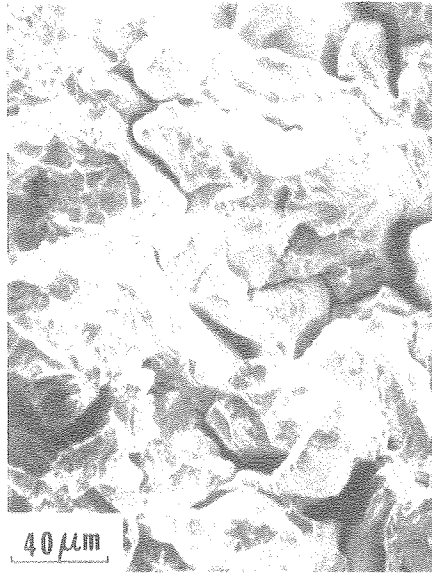


Fig. 2. SEM fractograph of the tin-infiltrated niobium rod and x-ray maps for the elements niobium and tin. (XBB 799-12566)

* * *

[†]Brief version of LBL-10584.

1. Craig Wojcik, Teledyne Wah Chang, Albany, Oregon, private communication.

1979 PUBLICATIONS AND REPORTS

Other Publications

1. J. Ling-Fai Wang, J. T. Holthuis, M. R. Pickus and R. W. Lindberg, "Direct Observation of the Growth of Voids in Multifilamentary Superconducting Materials via Hot Stage Scanning Electron

Microscopy," SEM/1979/I, SEM, Inc. AMF, O'Hare, IL, p. 399-403.

Papers Presented

1. J. Ling-Fai Wang, J. T. Holthuis, M. R. Pickus and R. W. Lindberg, "Direct Observation of the Growth of Voids in Multifilamentary Superconducting Materials via Hot Stage Scanning Electron Microscopy," Scanning Electron Microscopy Conference, Washington, D.C., April 1979.

2. J. Ling-Fai Wang, J. T. Holthuis and M. R. Pickus, "Infiltration Process--A Unique Way for Fabricating Multifilamentary Superconductor Based on the Aluminum-Containing A-15 Compounds," TMS-AIME Fall Meeting, Milwaukee, Wisconsin, September 1979.

b. Interfaces and Ceramics Microstructures*

J. A. Pask, Investigator

1. WETTING AND REACTIONS IN THE SODIUM SILICATE/IRON SYSTEM[†]

Antoni Tomsia and Joseph A. Pask

Interfacial reactions and wetting behavior of sodium disilicate (NS_2) glasses on substrates of high purity iron (Marz) and impure iron (Armco) were studied using the sessile drop technique combined with weight loss measurements. Two vacuum furnaces were used: one with a graphite core and heating element and an estimated P_{O_2} of $\sim 10^{-22}$ atm, and a second with an alumina core and an estimated P_{O_2} of 10^{-10} atm.

In similar studies^{1,2} pure NS_2 glass on Marz iron at 1000°C and $\sim 10^{-5}$ Torr vacuum for 2 hrs showed 55° contact angles in both of these furnaces and no reaction was observed. Also, no reaction was observed for glasses with FeO additions in the alumina furnace. In the graphite furnace, however, reactions were observed in configurations with glasses containing more than 9 wt.% of FeO . Preliminary kinetic experiments using the thermogravimetric technique in the graphite furnace indicated spreading of NS_2 glass with 95 wt.% loss of the total Na from the glass and in the alumina furnace, a contact angle of 10° with 55 wt.% loss of the Na both at 1000°C for 2 hrs at 2×10^{-6} Torr vacuum. In order to explain these differences a series of experiments were designed and performed with time, temperature and pressure as variables. Figure 1 shows the temperature dependence of the weight loss of Na and contact angle for the NS_2 - Marz iron system after 2 hrs, and Fig. 2 time dependence at 1000°C , both at a pressure of 2×10^{-6} Torr. After 2 hrs in a graphite furnace and 4 hrs in an alumina furnace at 1000°C the reaction was associated with the visible appearance of Na

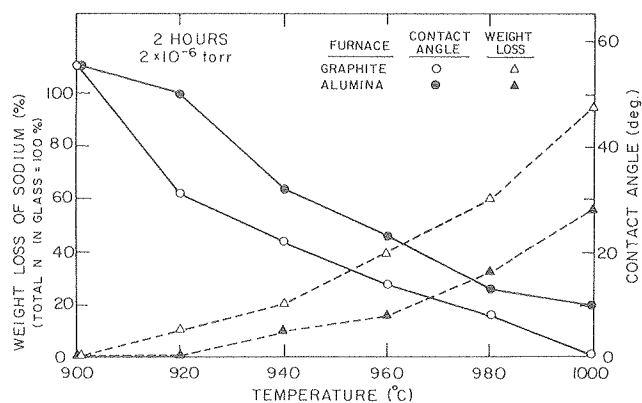


Fig. 1. Contact angles and weight loss of sodium from $\text{Na}_2\text{Si}_2\text{O}_5$ glass on Marz iron at 900 to 1000°C after 2 hrs at 2×10^{-6} Torr vacuum. (XBL 7910-7201)

*This work was supported by the Division of Materials Sciences, Office of Basic Energy Sciences, U. S. Department of Energy.

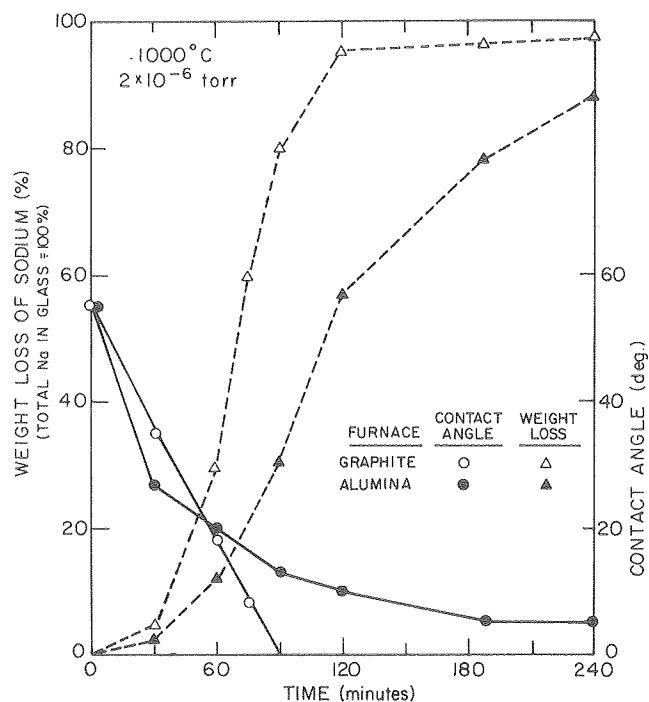


Fig. 2. Contact angles and weight loss of sodium from $\text{Na}_2\text{Si}_2\text{O}_5$ on Marz iron vs. time for 30 to 240 minutes at 1000°C and 2×10^{-6} Torr vacuum.

(XBL 7910-7200)

deposits in the cold parts of the furnaces and precipitation of cristobalite from the glass (Figs. 3a and 3b). It is thus evident that the extent of the reactions is dependent upon the experimental conditions (Table 1).

Another significant series of experiments indicated that for a given set of conditions the reactivities of as-received Marz iron, Marz iron aged for 8 months in a vacuum desiccator, and Armco iron were different. The results obtained with the aged Marz iron were similar to those reported in previous studies with Marz iron.

In the graphite furnace, the reaction presented by Eq. (1) has been identified. Because ΔG° for this reaction at 1000°C is positive, it will occur



only when the activity quotient will be sufficiently less than one which requires a low activity of FeO at the interface, a low P_{Na} , and a high activity of Na_2O in the glass. The FeO at the interface will readily diffuse into the glass and metal, but mostly glass because of the high solubility of FeO in the glass, since ΔG° for this process is negative. The critical factor in the graphite furnace is the P_{O_2} of 10^{-22} atm, which is less than the dissociation pressure for FeO (1.5×10^{-15} atm at 1000°C).

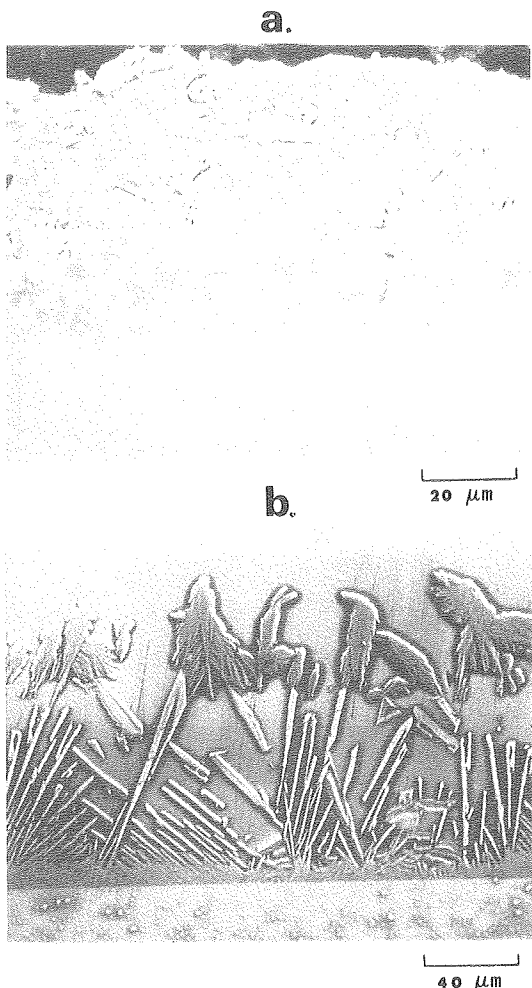


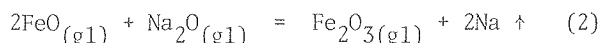
Fig. 3. (a) Cross section of $\text{Na}_2\text{Si}_2\text{O}_5$ glass sessile drop on Marz iron after 2 hrs at 1000°C with a total ambient pressure 2×10^{-6} Torr and P_{O_2} of $\sim 10^{-22}$ atm. Iron substrate at the bottom. Reaction resulted in precipitation of cristobalite, as observed after etching for 10 sec in 10% HF. (b) Same as (a) except that P_{O_2} was $\sim 10^{-10}$ atm, and time of experiment was 4 hrs. (XBB 802-2316)

Table 1. Contact angles and weight loss of sodium from $\text{Na}_2\text{Si}_2\text{O}_5$ glass on iron at 1000°C for 2 hrs and 2×10^{-6} Torr vacuum.

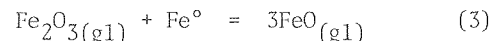
| Iron Grade | Graphite Furnace | | Alumina Furnace | |
|----------------------|------------------------|---------------|------------------------|---------------|
| | Na Weight loss percent | Contact angle | Na Weight loss percent | Contact angle |
| Marz Fe, as received | 95.37 | 0 | 57.35 | 10 |
| Armco Fe | 28.38 | 53 | 20.80 | 63 |
| Marz Fe, aged | 15.73 | 55 | 8.10 | 55 |

Under these conditions the $a(\text{FeO})$ in the iron and at the interface will approach zero. Another critical factor for the reaction to proceed is the pressure of Na gas formed at the interface, which must exceed the ambient pressure of sodium and the overall ambient pressure to proceed rapidly. This is possible only because the boiling point of liquid Na (880°C) is below the test temperature. In the alumina furnace with a P_{O_2} of $\sim 10^{-10}$ atm, the activity of FeO in the metal and at the interface will be at or approach unit value, which makes ΔG positive. Therefore, reaction (1) cannot account for the weight losses of Na observed in this furnace.

The current study has identified another reaction which can occur in both furnaces but is the one responsible for the observed large weight losses of Na in the alumina furnace. It is represented by Eq. (2).



The standard free energy for reaction (2) is also positive. Therefore, this reaction will only occur under conditions when the activity quotient is sufficiently smaller than one. It is thus favored when $a(\text{FeO}_{(\text{gl})})$ and $a(\text{Na}_2\text{O}_{(\text{gl})})$ in the glass are high, $a(\text{Fe}_2\text{O}_3_{(\text{gl})})$ approaches zero, and P_{Na} is low. Besides a low P_{Na} the most critical factor is a small $a(\text{Fe}_2\text{O}_3_{(\text{gl})})/a(\text{FeO}_{(\text{gl})})$ ratio. The Fe_2O_3 in the glass reacts readily with the substrate iron to form FeO at the interface [Eq. (3)] which diffuses into the glass because of ΔG° being negative.



Reaction (3) keeps the above activity ratio small permitting reaction (2) to continue.

Reaction (2) was verified with many wetting experiments of NS_2 glasses containing FeO, Fe_2O_3 or both on Au, Pt and fused silica. This reaction was also confirmed by color changes in both furnaces from blue to green, which indicates Fe^{3+} presence in the glass.

Before NS_2 can take part in a reaction represented by Eq. (2) in the alumina furnace, it must take into solution sufficient amount of FeO in order to raise $a(\text{FeO})$ in the glass. This can be realized by solution of a film of oxide on the surface of iron or an initial reaction of type (1). During wetting experiments with as-received Marz iron whose bulk $a(\text{FeO})$ is less than one, it is possible that some reaction of type (1) will occur before the iron becomes saturated with oxide and $a(\text{FeO})$ reaches one. The introduction of some FeO into the glass then would start the sequence of reactions (2) and (3).

The results show that the redox reactions are very sensitive to the degree of saturation of the iron with oxide. In a high vacuum and low P_{O_2} , pure iron loses any oxide film present on its surface. This occurrence increases the surface energy of iron and decreases the $a(\text{FeO})$ giving rise to favorable conditions for redox reactions which in turn will reduce the contact angles and

cause spreading if sufficiently severe. Oxygen present in the bulk of pure iron after aging and in Armco iron maintains a high $a(\text{FeO})$ at the interface for longer times. Although reactions proceed with all three types of iron, kinetics of reactions in the alumina furnace are much slower. It is interesting to note, however, that oxygen alone in aged high purity iron makes it less reactive than Armco iron with a larger total amount of impurities.

* * *

† Brief version of LBL-10443.

1. J. J. Brennan and J. A. Pask, J. Am. Ceram. Soc. 56(2), 58 (1973).

2. C. E. Hoge, J. J. Brennan and J. A. Pask, J. Am. Ceram. Soc. 56(2), 51 (1973).

2. WETTING AND ADHERENCE OF Na-BORATE GLASS ON GOLD †

Stephen T. Tso ‡ and Joseph A. Pask

The sessile drop technique was used to study the wetting behavior of sodium borate glass (nominally 94% B_2O_3 and 6% Na_2O) on gold. The contact angle 46° , and consequently the surface and interfacial energies, did not change in the vacuum range of 10^{-8} to 10^{-5} atm (<15 mHg) at 900°C . The interfacial energy values were $\gamma_{\text{SV}}-1370$, $\gamma_{\text{SL}}-1314$, and $\gamma_{\text{LV}}-80$ ergs/cm². The contact angle decreased sharply to 6° at ambient pressures greater than 10^{-5} atm or >15 mHg. Since oxygen chemisorbs on gold surfaces, γ_{SV} drops to 1209 ergs/cm². Surface energy of liquid glass is unaffected by oxygen pressure. γ_{SL} becomes 1130 ergs/cm². The decrease of γ_{SL} by 184 ergs/cm² on exposure to oxygen occurs with the development of chemical bonding. This deduction is consistent with the theory that adherence occurs when the glass and metal at the interface are saturated with substrate metal oxide.

It is of interest to note that, although both platinum and gold are noble metals, their behavior is different. The decrease in contact angle on platinum at about the same oxygen pressure occurred due to desorption of carbonaceous impurities when present and not to the appearance of an adsorbed oxide film and adherence. No evidence of carbonaceous contamination was observed on the gold surface. On exposure to water vapor absorption appeared to occur because of a resulting higher vaporization rate of the glass and the boiling that occurred at the glass/metal interface. Erratic contact angle measurements resulted. However, no reaction with gold or development of adherence occurred, which was not the case with platinum.¹

* * *

† Brief version of J. Am. Ceram. Soc. 62, 543 (1979).

‡ Permanent address: Texas Instruments, P.O. Box 225303, MS158, Dallas, TX 75265.

1. G. A. Holmquist and J. A. Pask, J. Am. Ceram. Soc. 59(9-10), 384 (1976).

3. MICROSTRUCTURE AND INTERFACE STUDIES IN THICK FILM CONDUCTOR SYSTEMS †

V. K. Nagesh ‡ and Joseph A. Pask

Thick Film Conductors. Studies have been conducted on acid-treated lead borosilicate (LBS) glass particle/silver thick film conductor systems. The effect of using different particle sizes on the sheet resistivity was determined (Fig. 1). Smaller particle sizes reduced the thickness of the silver film and hence increased the sheet resistivity (R_s) according to the relation

$$R_s = \frac{6\rho_{\text{Ag}} V_g}{K D_g V_m}$$

where R_s is in $\text{m}\Omega/\square$, ρ_{Ag} = bulk resistivity of silver, $K=0.1$ (a constant for the system), V_g, V_m = glass and metal volume content, and D_g = glass particle diameter. A good correlation between the theoretical and experimental results can be seen in Fig. 1.

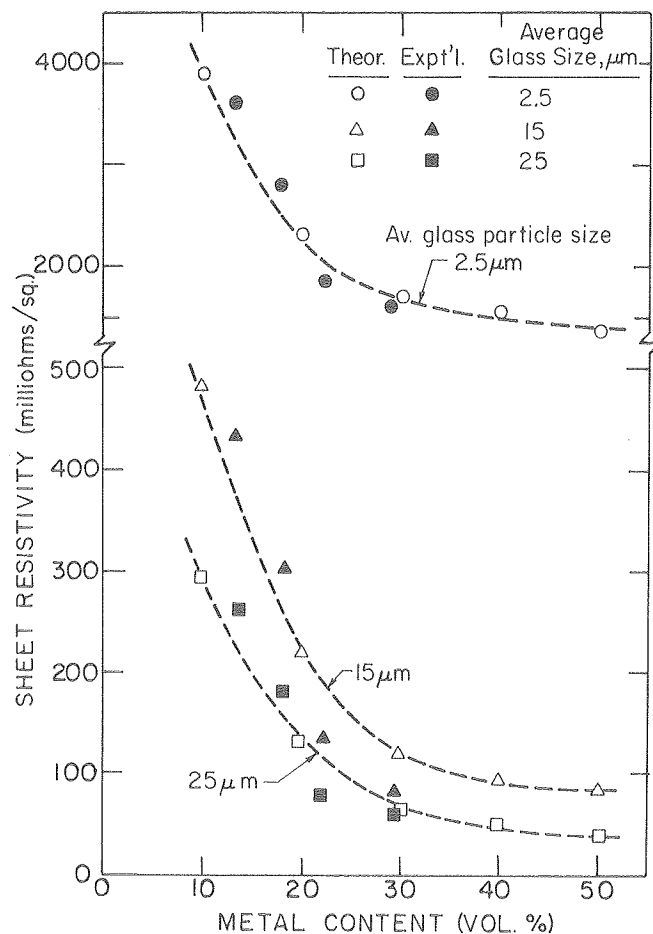


Fig. 1. Sheet resistivity vs. metal content in the thick film conductor for glass particles of different sizes. (XBL 7911-14532)

Effect on acid treatment on the composition of the surface of the glass was studied using the McPherson ESCA 36 electron spectrometer.¹ Finely powdered glass samples (etched in 0.01N HCl for 45 sec, and unetched) were used. Contaminant C_{1s} line (B.E. = 285 eV) was used as a reference. Due to etching, surface concentration of the component oxides changes. Pb/Si weight ratio decreased from 7 to 5.264 showing the leaching of lead during acid treatment. This result is in conformity with the model previously developed to explain the importance of acid treatment in interface bond development between glass and silver. The B/Si weight ratio decreased from 2 to 1.364 indicating that boron is leached out in addition to lead.

Studies were extended to nickel-silver thick film conductors fired in air. With silver contents as low as 25 wt.%, sheet resistivities as low as 15 m Ω /□ were obtained. Conventional thick film conductors using as much as 80-90 wt.% of precious metals give sheet resistivities in the order of 25-50 m Ω /□. Although base metal conductors are less expensive, they normally need to be fired in inert atmospheres. Thus, the new air-fired base metal-precious metal composite thick film conductor system is a significant advancement over the currently existing systems.

Wetting Studies. Most of the conventional thick film systems use lead borosilicate (LBS) as a binder between precious metals (Ag, Au, Pt) and the ceramic substrate (Al_2O_3). In order to understand the microstructure development in these systems appropriate glass/metal, metal/metal interface studies are important. Hence, sessile drop studies of LBS glass on Ag, Au, Pt and Ag on Ni were conducted (Table 1).

Table 1. Sessile drop measurements.

| System | Atmosphere | Temp. (°C) | Contact angle | Adherence (qualitative) |
|-----------------|-----------------|------------|---------------|-------------------------|
| LBS glass on Ag | Air | 600 | 0° | very strong |
| | Vacuum | 700 | 2° | good |
| | He | 700 | 48° | poor |
| LBS glass on Au | Air | 700 | 18° | strong |
| | Vacuum | 700 | 6.5° | poor |
| LBS glass on Pt | Air | 700 | 2-3° | strong |
| | Vacuum (no C) | 700 | 58° | poor |
| | Vacuum (with C) | 700 | 73° | poor |
| Ag on Ni | Air | 970 | 90° | strong |
| | He | 970 | 9.5° | very strong |

LBS: Lead borosilicate glass.
Vacuum: 3×10^{-6} Torr.

Firing LBS glass on silver in air caused extensive and rapid spreading of the glass and strong glass-metal bonding. This behavior occurs because of solution of silver oxide by the glass and corresponding saturation of the glass at the interface. In vacuum, adherence was stronger at the edges than in the center, color of the glass had slightly changed and there was a finite contact angle (2°). In the absence of adsorbed oxide on the metal, these factors indicate the possibility of a redox reaction between silver and lead oxide in the glass represented by the following overall reaction:



The free energy for this reaction ΔG is given by

$$\Delta G = \Delta G^\circ + RT \ln \frac{a(Ag_2O_{(glass)}) \cdot P_{Pb}}{a(PbO_{(glass)})}$$

ΔG° is positive. Therefore, the reaction proceeds if the equilibrium constant is sufficiently smaller than one to give a large enough negative second term to result in a negative ΔG . This could be realized easily at 700°C since Pb has a high vapor pressure and is removed from the site of the reaction. Stronger adherence at the edges is due to the easier escape of $Pb_{(g)}$ at the edges. In helium at atmospheric pressure this reaction does not take place since the Pb vaporization, and hence the reaction, are retarded at the interface. Consequently, the interface is not saturated with silver oxide and poor adherence results.

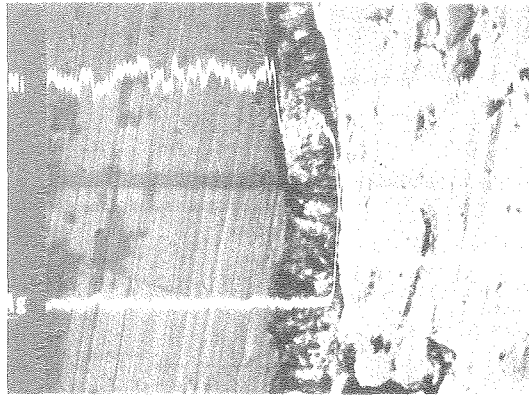
Strong adhesion of LBS glass to Au in the presence of oxygen is due to the dissolution of the surface oxide by the glass which leads to the formation of a chemical bond at the interface. Lower contact angle in vacuum (6.5°) compared to air atmosphere (18°) is explained by a higher driving force for wetting represented by $(\gamma_{sv} - \gamma_{sl})$. Even though γ_{sl} in air is lower than in vacuum, γ_{sv} in vacuum is sufficiently larger to give a larger overall value for $(\gamma_{sv} - \gamma_{sl})$. Weak adherence in vacuum is due to the lack of any reaction to form a chemical bond at the interface.

Strong adherence of LBS glass to Pt in air atmosphere (contact angle 2 to 3°) and poor adherence in vacuum (contact angle 58°) were observed. The analysis is similar to that for LBS glass on Au except that in this case the respective values for γ_{sv} and γ_{sl} were such as to result in a higher driving force for wetting $(\gamma_{sv} - \gamma_{sl})$ in air instead of vacuum. In the presence of carbon impurities (introduced by the graphite tube in the furnace) the adherence remained poor and the contact angle was increased to 73° due only to the reduction in the surface energy of Pt by carbon adsorption. This reduction was calculated to be ~ 43 ergs/cm².

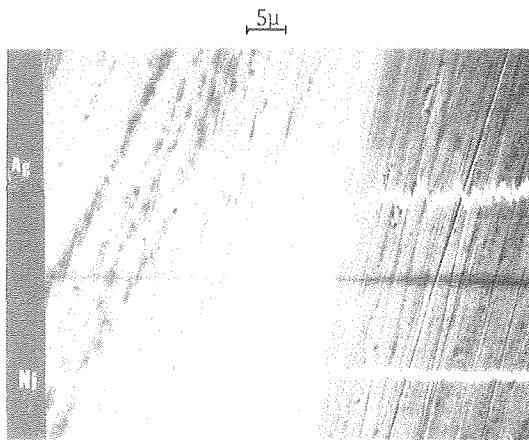
In helium atmosphere, the contact angle of silver on nickel was measured to be 9.5 at 970°C. In an air atmosphere it was 90°. Strong adherence was observed in both cases. Figure 2 shows the cross sections of the interfaces, as observed in SEM. In helium no layer is observed at the interface

and adherence is due to interdiffusion in the interfacial zone with $\gamma_{SV} > \gamma_{LV}$. There is a NiO layer (thickness $\sim 5 \mu\text{m}$) formed in the presence of oxygen. In this case, $\gamma_{LV} > \gamma_{\text{NiO}/\ell} > \gamma_{\text{NiO}}$. The interfacial energy between liquid silver and NiO is continuously reduced as the dissolution of NiO in silver goes on. When this interfacial energy reaches that of NiO which is not dissolving any Ag, a limiting contact angle of 90° is reached.² Chemical bonding is realized at this point because of chemical equilibrium at the interfaces.

SILVER - NICKEL INTERFACE



TEMPERATURE: 970°C ATMOSPHERE: AIR
CONTACT ANGLE (θ): 90°



TEMPERATURE 970°C ATMOSPHERE: He
CONTACT ANGLE (θ) $9^\circ 5'$

Fig. 2. Photomicrographs of cross sections of silver nickel interface on exposure to (top) air and (bottom) helium. (XBB 780-13348)

* * *

† Brief version of LBL-9274.

‡ Permanent address: Hewlett-Packard, 3500 Deer Creek Road, Palo Alto, CA 94304.

1. V. K. Nagesh, Ph.D. thesis, LBL-9274, December 1979.

2. I. A. Aksay, C. Hoge and J. A. Pask, LBL-1870, July 1973.

4. REACTION AND BONDING AT ZnO THIN FILM AND Si SUBSTRATE INTERFACES

Shu Sheng Chiang, Anthony G. Evans, and Joseph A. Pask

Adhesion has long been an elusive problem in the field of thin film technology. Consequently, reaction and bonding across the interface and their subsequent effect still remain poorly characterized. The first step toward solving these problems is to develop an effective and reproducible method for evaluating the bond strength across the interface. Then, the effect of different reactions and their influence on the bonding can be quantitatively evaluated.

In this study, a new adhesion test has been demonstrated using a microhardness indentation technique. The bond strength across the interface can be measured in terms of fracture toughness, which is a function of the load applied; the size of the lateral crack created along the interface; and the material parameters of Young's modulus and hardness.

Initial experiments have indicated that differences of bond strength across the interface for ZnO films annealed under different partial pressures of oxygen can be evaluated by comparing the size of lateral cracks. It was found that the film annealed at the lowest oxygen partial pressure exhibited the highest bonding strength as indicated by the smallest size of lateral cracks.

5. CORROSION OF SILICATE MATERIALS BY HYDROGEN GAS AND HF ACID SOLUTION^{†‡}

Stephen T. Tso[§] and Joseph A. Pask

The corrosion of silicate materials by hydrogen gas and HF acid solution was investigated by the gravimetric method. The reaction of silicate glasses with HF acid solution was found to be diffusion controlled as evidenced by the invariance of the reacted glass surface morphology, the monotonously increasing reaction rate with increased agitation of solution, and typical low activation energies ($< 10 \text{ kcal/mole}$). The corrosion resistance to the HF acid solution decreased with the addition of either alumina or lime to silica. This decrease in corrosion resistance was postulated to be due to the increased phase separation in the silicate glasses. The reaction was assumed to consist of two steps, hydration of silica glass surface followed by its reaction with HF.

The rate was kinetically controlled in the reaction with the hydrogen gas. The loss of pure silica glass in the hydrogen atmosphere in the temperature range of 1200°C to 1400°C was due to a reaction with hydrogen gas and not a decomposition as a result of the low partial pressure of oxygen. Surface devitrification of silica glass observed in hydrogen was attributed to a reaction with the

sodium vapor originating from the sodium oxide in the alumina tube and eliminated by heat treatment of the tube. A drilling phenomenon was observed on the reacted silica glass associated with redeposition of cristobalite on silica glass. Both phenomena were attributed to the temperature profile in the glass due to its transparency. The reaction mechanism of silica glass with hydrogen gas involved the formation of a reaction product whose desorption was deduced as probably the slowest step. The rate of weight loss at 1400°C was 10^{-2} gm/cm²/hr and ΔE was 82 ± 8 kcal/mole.

The addition of alumina and/or calcia to the silica glass decreased the reaction rate with the hydrogen gas as indicated for several glasses in the Arrhenius plot shown in Fig. 1. It also indicated that mullite ($3\text{Al}_2\text{O}_3 \cdot 2\text{SiO}_2$) has the lowest reaction rates. Since the silicate glasses were phase separated and not homogeneous and the reaction rates were different for the different phases, a transition layer was formed. This behavior is indicated in the concentration profile for a glass with 30 wt.% Al_2O_3 (Fig. 2). An alumina residue was left behind after reaction with hydrogen gas in all cases. The residue layers were porous and did not interfere with the reaction. The weight loss per unit area in the early stages of the reaction is linear with reaction time, indicating that the surface residue layer is not a barrier to the mass transport and that the reaction is kinetically controlled. The apparent activation energies for the aluminosilicate materials were ~ 90 kcal/mole. With further addition of 5 wt.% CaO , ΔE was ~ 68 kcal/mole. The reactions of the gases are complex due to the presence of intermediate layer and no correlation between the apparent activation energies is presently available. No empirical correlation was

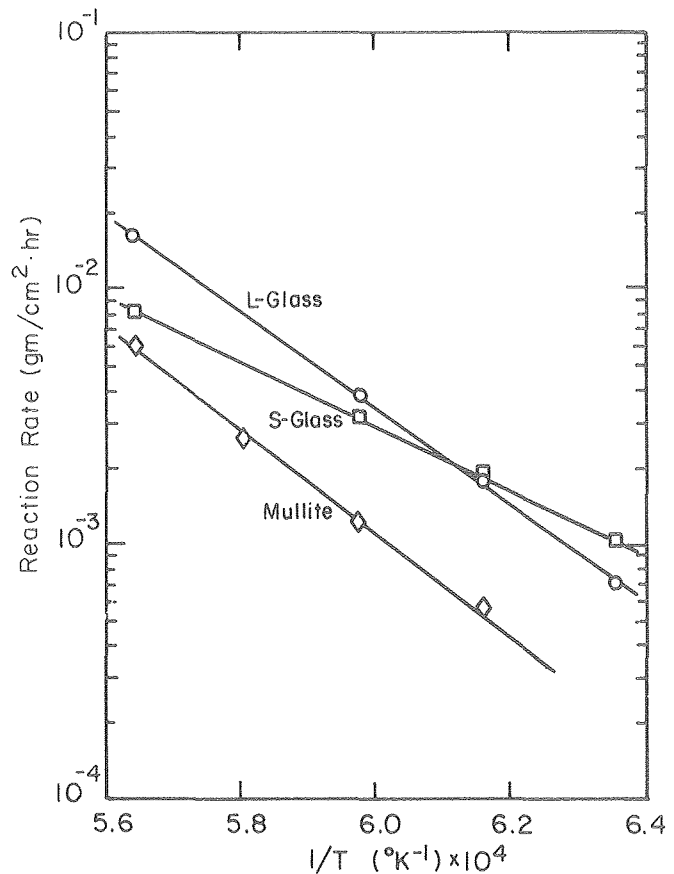


Fig. 1. Temperature dependence of total reaction rate of L glass (30 wt.% Al_2O_3 , 70 wt.% SiO_2), S glass (5 wt.% CaO , 38 wt.% Al_2O_3 , 57 wt.% SiO_2), and mullite (73 wt.% Al_2O_3 , 27 wt.% SiO_2).

(XBL 797-6547)

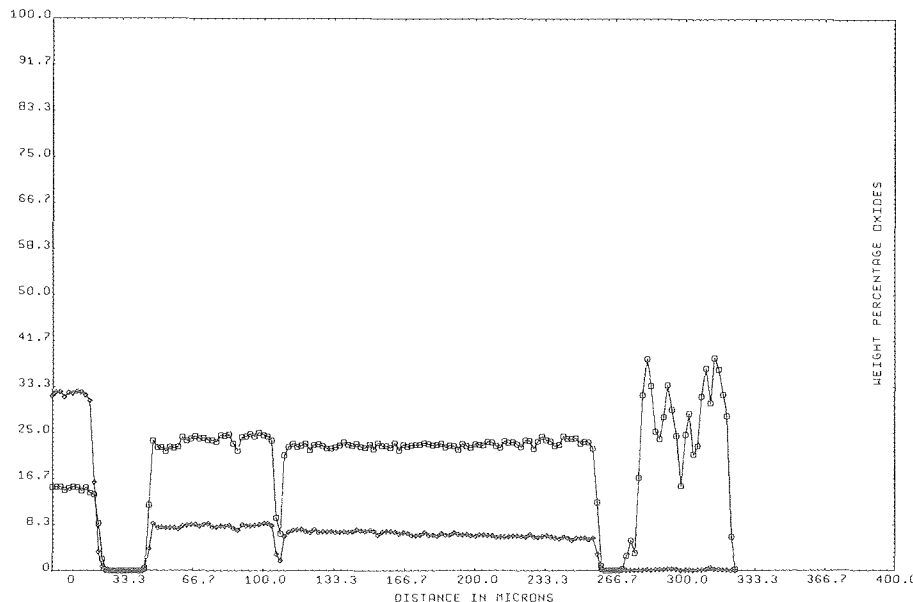


Fig. 2. Concentration profile of L glass without normalization obtained by electron microprobe. The low readings at about 110 m are the result of a pore in the specimen.

(XBL 799-11366)

found for the attack of the different gases by HF acid solution and hydrogen gas.

Efforts were made to sinter the porous alumina layer into a dense, protective layer. In the alumino silicate glasses, the sintered alumina layer cracked into pieces as a result of mismatch in the expansion coefficients. For the silicate glasses with lime, homogenization and mullitization occurred before alumina sintered. Mullite is the material with the most potential. It can withstand the temperature necessary for the sintering of the surface residue layer and good adherence exists between the unreacted mullite and the surface layer.

* * *

[†]This work was partially supported by the National Science Foundation.

[‡]Brief version of LBL-9887.

[§]Permanent address: Texas Instruments, P.O.Box 225303, MS158, Dallas, Texas 75265.

6. CORROSION AND MECHANICAL BEHAVIOR CORRELATIONS WITH COMPOSITION AND MICROSTRUCTURE OF ALUMINUM SILICATE REFRACTORIES ^{†‡}

Michael D. Sacks, Robert B. Langston, Stephen T. Tso,[§] and Joseph A. Pask

Seven commercial refractory specimens (SiO_2 content ranging from 11 to 51 wt.%), as-received and heat-treated at 1700°C , were exposed to corrosion by HF aqueous solutions of several strengths at room temperature, and by flowing H_2 at 1200°C .

The weight loss on exposure to an HF solution under constant conditions increases with the SiO_2 content of the specimens. A dense polycrystalline mullite specimen and $\alpha\text{-Al}_2\text{O}_3$ exposed to similar conditions showed no detectable loss of weight, indicating that an increase of SiO_2 of the refractory specimen means an increase of glass due either to an excess of SiO_2 beyond that needed to form mullite or to incomplete reaction to form mullite. Heat treatment of the refractories generally reduced the amount of weight loss, but the increasing trend with increase of SiO_2 was similar. This behavior can be attributed to an additional conversion of some of the amorphous phase to mullite by reaction. The weight loss data for heat-treated specimens after exposure to 15% HF solution for 24 hrs is shown in Fig. 1.

The weight loss on exposure to flowing H_2 at approximately atmospheric pressure at 1200°C for 24 hrs also increases with the SiO_2 content of the refractory specimens as seen in Fig. 1. Although the reactions with H_2 gas and with aqueous HF solutions are different in terms of mechanisms, corrosion in terms of weight loss occurs in both cases because of SiO_2 loss, primarily from the glassy or amorphous phases since crystalline mullite is the most resistant to corrosive attack. Detailed studies would also have to take into account microstructural features, such as pore volumes, sizes, and shapes.

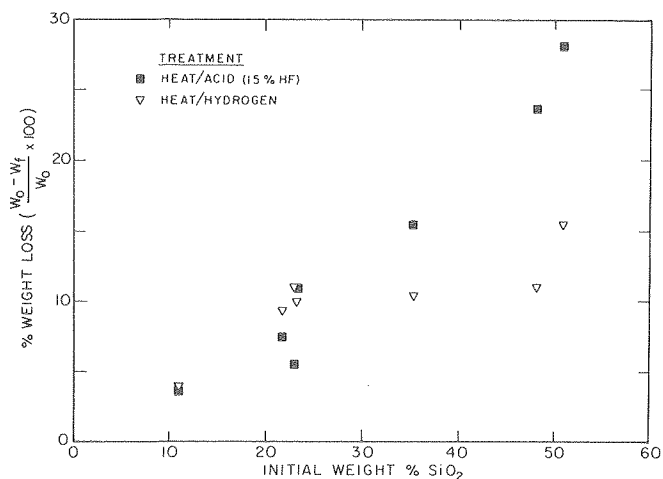


Fig. 1. Correlation of weight loss with initial SiO_2 content for heat-treated specimens after corrosion by 15% HF solution for 24 hrs at room temperature and H_2 for 24 hrs at 1200°C .
(XBL 777-5867)

High temperature erosion resistance to particulates is a complex behavioral characteristic that is dependent on a number of factors, one of them being strength at high temperatures. Stress-strain data were thus obtained in compression at 1200°C at a constant strain rate of $\sim 1.4 \times 10^{-5}$ /sec for the refractory specimens. Ultimate compressive stresses vs. initial SiO_2 content for as-received, as-received acid-treated, heat-treated, heat-treated acid-corroded, and heat-treated H_2 -corroded specimens are shown in Fig. 2. It is evident that in the case of mechanical behavior a correlation with SiO_2 content does not exist. The microstructure of the specimens controls their behavior.

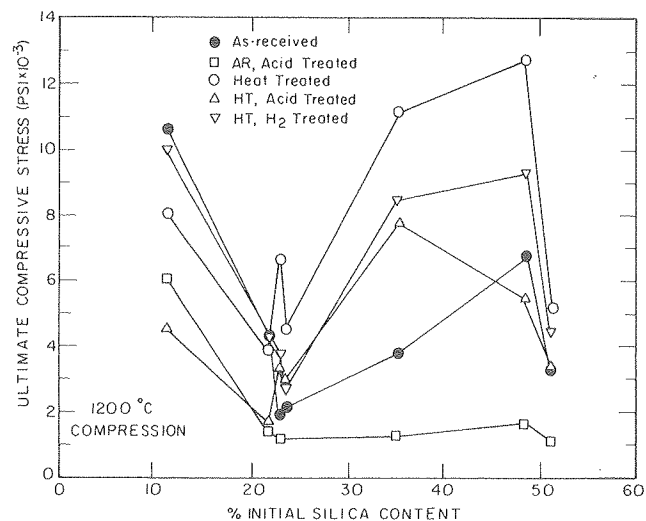


Fig. 2. Ultimate compressive stresses vs. initial SiO_2 content for as-received, as-received acid-treated, heat-treated, heat-treated acid-corroded, and heat-treated H_2 -corroded specimens tested in compression at 1200°C .
(XBL 782-4659)

Critical microstructure features are the nature of the grog particles relative to the matrix, the nature and amount of the matrix, and the nature of the porosity.

* * *

[†]This work was partially supported by the National Science Foundation.

[‡]Brief version of Bull. Am. Ceram. Soc. 58, 691 (1979).

[§]Permanent address: Texas Instruments, P.O. Box 225303, MS158, Dallas, Texas 75265.

7. SINTERING OF MULLITE-CONTAINING COMPOSITIONS ^{†‡}

Michael D. Sacks and Joseph A. Pask

The sintering behavior and microstructure development of mullite powder compacts are affected by many processing variables. Physical inhomogeneities in the green (pre-sintered) compact, due to variations in particle/pore size, shape, and packing characteristics, are important from technological and theoretical viewpoints. In respect to theory, most models of densification kinetics are based on the packing of particles in a geometrically regular fashion. In terms of practical considerations, the densification rate and the maximum density achieved during sintering are altered by inhomogeneities in the powder compact.

Figure 1 plots percent theoretical density (% ρ_{th}) vs. the logarithm of time ($\ln t$) for a mullite with an overall chemical composition of 73 wt.% Al_2O_3 /27 wt.% SiO_2 . The direct proportionality observed over a large range of densification (~60 - 75% ρ_{th}) is predicted by several models for intermediate stage sintering, i.e., the stage in which (1) the porosity evolves from continuous open channels along grain boundaries to discrete, isolated pores at grain corners, and (2) grain growth occurs.

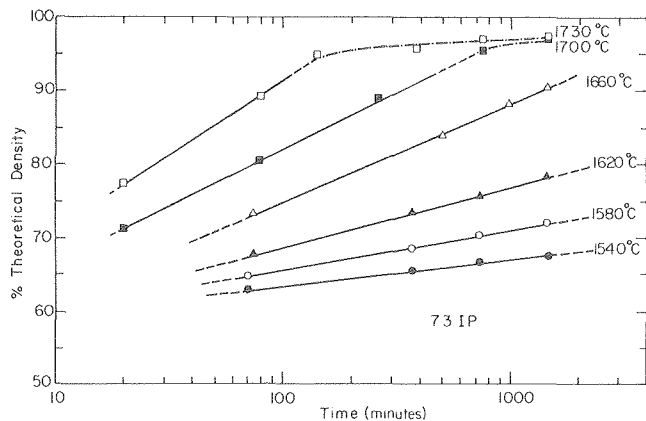


Fig. 1. Plots of % ρ_{th} vs. logarithm of time for samples sintered in the range 1540-1730°C. (XBL 7810-5889)

In a series of experiments with high surface area raw materials, aggregates/agglomerates were formed during processing. The effect on densification kinetics is shown in Fig. 2. The appearance of upward slope changes in the % ρ_{th} vs. \ln time plots at low temperatures indicates densification substages caused by packing irregularities. The sample in Fig. 3 is at a transition state in which (1) initially densely packed regions of the sample have sintered to theoretical density (complete elimination of pores), but (2) initially loosely packed regions of the sample are still in the initial stage of sintering in which only necks have formed between particles.

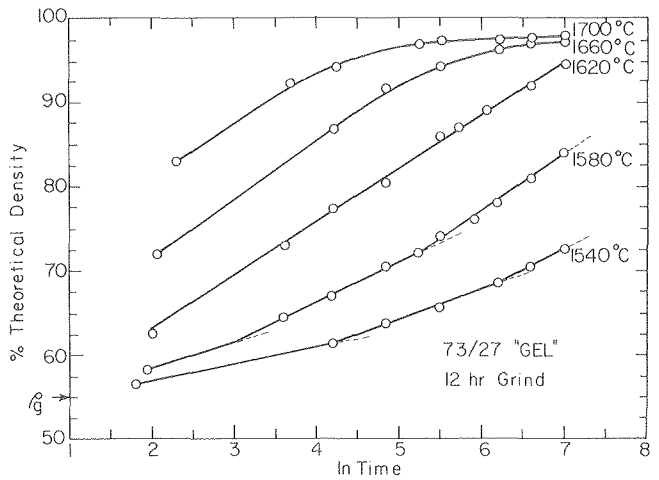


Fig. 2. Plots of % ρ_{th} vs. logarithm of time for samples sintered in the range 1540-1700°C. (XBL 7911-14500)

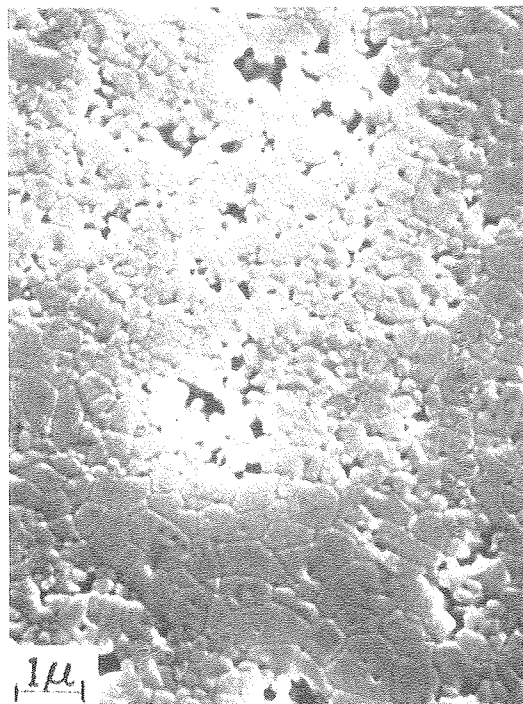


Fig. 3. SEM micrograph of sample sintered at 1580°C for 6 hrs. (XBB 785-5306)

73/27 "GEL": GREEN STATE

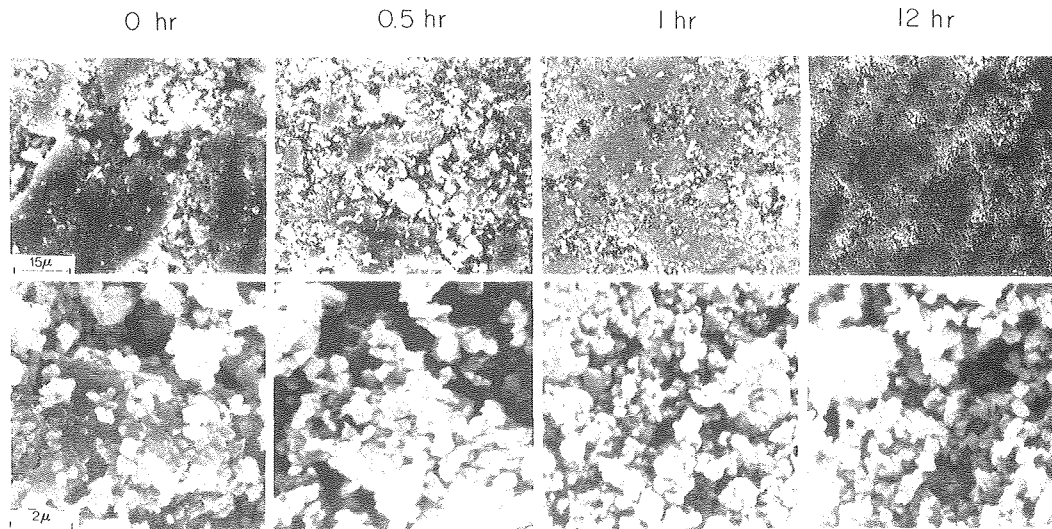


Fig. 4. Top: SEM micrographs of green compact surfaces of 73 wt.% Al_2O_3 mullites which illustrate the breakdown of large aggregates upon grinding (0-12 hrs). Bottom: Higher magnification micrographs which show individual crystallites. (XBB 780-14762)

The effect of packing inhomogeneity on maximum density achieved is shown by Figs. 4 and 5. Figure 4 contains the green compacts of 73 wt.% Al_2O_3 mullites which have been subjected to grinding from 0-12 hrs. As grinding time is increased, aggregates are broken down and packing becomes more regular. In Fig. 5, the maximum density achieved increases accordingly.

* * *

[†]This work was partially supported by the National Science Foundation.

[‡]Brief version of LBL-10372.

1. R. L. Coble, J. Appl. Phys. 32, 787 (1961).
2. Boon Wong, Ph.D. thesis, LBL-3957, June 1975.
3. J. H. Rosolowski and C. Greskovich, J. Am. Ceram. Soc. 58, 177 (1975).

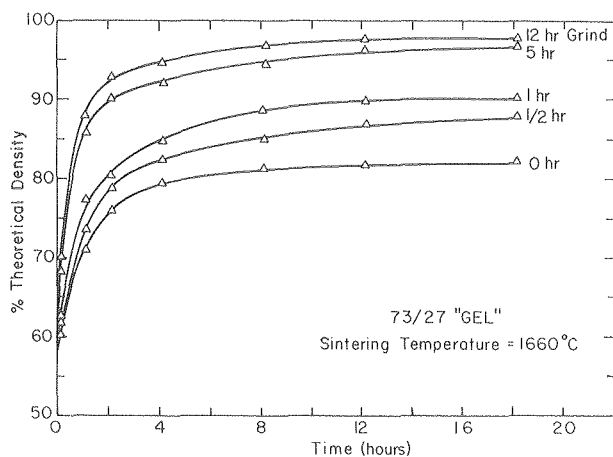


Fig. 5. Plot of % ρ_{th} vs. time after sintering at 1660°C for samples in Fig. 4. (XBL 7810-5883)

8. THERMODYNAMICS AND MECHANISMS OF SINTERING[†]

Joseph A. Pask

Sintering is a complex process which has been extensively studied but is still not completely understood. The objective of this ongoing study is to explore the thermodynamic and geometric factors that play a role in the process of densification of model compact systems consisting of crystalline spheres of uniform size in regular and irregular packing that form grain boundaries at every contact point. The thermodynamic driving force of negative free energy change exists in any system that is undergoing mass transport processes associated with densification. In sintering of crystalline single phase grains the driving force constitutes reduction of the overall interfacial free energy and can be expressed by

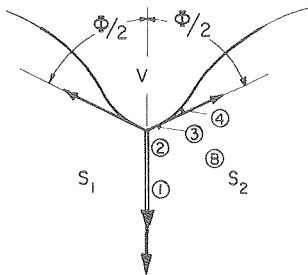
$$\delta(G_{\text{sys}}) = \delta \int \gamma_{\text{sv}} dA_{\text{sv}} + \delta \int \gamma_{\text{gb}} dA_{\text{gb}} \quad (1)$$

which says that the change in free energy of the system is equal to the change of the integrated surface free energy (negative) plus the change of the integrated grain boundary energy (positive). When the sum is negative the densification process proceeds.

Although there is no unique value of $\gamma_{\text{gb}}/\gamma_{\text{sv}}$ in a real system because of the anisotropy of interfacial energies, it does not exclude the requirement that the values for this ratio should be as small as possible. Theoretically, the smaller the percent theoretical density of the powder compacts, i.e. the more open the packing, the smaller the $\gamma_{\text{gb}}/\gamma_{\text{sv}}$ ratios should be to realize theoretical density in the sintered compacts. If the ratio is

too large, a thermodynamic end point density may be the result. Any additive that would reduce the γ_{gb}/γ_{sv} values is thus desirable.

In densifying systems, the mass transport must occur in two steps: movement from grain boundaries formed by contacts to the neck region, and movement from the neck region to the free surfaces. In most real systems a neck forms and the slow step in sintering is the movement of material from the neck region to the free surface regions due to a thermodynamic driving force of reverse curvature in the free surfaces (see Fig. 1). In special cases, a steady state neck does not form and the slow step is movement of material from the grain boundaries to the neck region due to a thermodynamic specific driving force of the presence of nonequilibrium dihedral angle formed at the contact grain boundary.



$$\begin{aligned} \gamma_{s_1 s_2} &< \gamma_{s_1 v} & \gamma_{s_2 s_1} &< \gamma_{s_2 v} \\ \gamma_{gb} &= \gamma_{s_1 s_2} + \gamma_{s_2 s_1} \\ \gamma_{gb} &< \gamma_{s_1 v} + \gamma_{s_2 v} \\ \gamma_{gb} &= \gamma_{s_1 v} \cos \phi/2 + \gamma_{s_2 v} \cos \phi/2 \\ \gamma_{gb} &= 2\gamma_{sv} \cos \phi/2 \\ \gamma_{gb}/\gamma_{sv} &= 2 \cos \phi/2 \\ \text{At nonequilibrium} \\ \mu_{(3)} &> \mu_{(2)} > \mu_{(1)} > \mu_{(4)} > \mu_{(0)} \end{aligned}$$

Fig. 1. Cross section through neck region in the early stages of sintering when reverse curvature exists. Relative magnitude of chemical potentials at several sites are indicated. Mass transport occurs continuously from 3 to 4, 2 to 3, and 1 to 2. Shrinkage or movement of centers towards each other then takes place. (XBL 789-5744)

The stages of sintering have been identified as follows. The PRELIMINARY STAGE includes any rearrangement of the grains or particles and formation of necks or a framework. The INITIAL STAGE corresponds to the period when shrinkage occurs with decreasing pore sizes but with no grain growth and no formation of closed pores. The INTERMEDIATE STAGE corresponds to the period when grain growth starts and closed pores are progressively formed in real systems, because of the presence of a range of particle sizes and shapes and anisotropy of interfacial energies. The FINAL STAGE of sintering corresponds to the period when no open pores are present; grain growth can occur and can also continue into an annealing period after the system has reached its maximum density, but not necessarily theoretical density. Inspection then indicates that the length of the intermediate stage is variable and is dependent on the character of the powder; for example, it is possible that in some systems with a broad particle size range the initial stage may be essentially nonexistent. Figure 2 shows the effect of sphere size on densification rates.

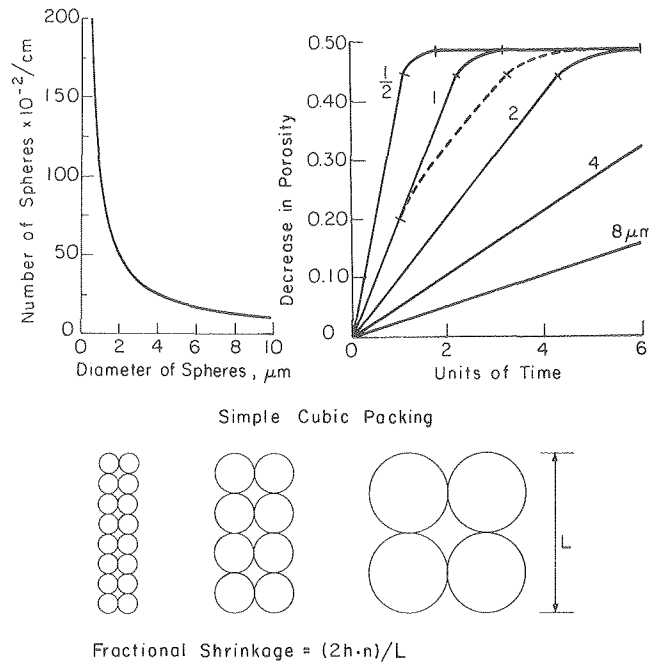


Fig. 2. Schematic showing the effect of sphere size in compacts with simple cubic packing on densification rates. (XBL 789-5748A)

It is thus evident that the nature of the mass transport or diffusion path is not the same for the identified three stages of sintering. It is then unrealistic to attempt to develop a single equation based on basic principles to cover the entire sintering process that would be applicable to all systems.

Analyses of model and real systems indicate that the most critical factors in realizing uniform microstructures are homogeneity and uniformity of packing in the powder compact. If agglomerates and aggregates are present, processing procedures should be devised that would prevent their formation or, if they form, break them down either in the powder processing or fabrication steps.

* * *

† Brief version of LBL-8419.

9. SINTERING OF MgO[†]

Boon Wong[‡] and Joseph A. Pask

Kinetic equations were formulated for the isothermal densification of a single-phase powder compact for the initial and intermediate stages of sintering. These stages are identified as continuous open-pore stages, with a decreasing number of voids and grains per unit volume accompanied by grain growth in the intermediate stage. The equations included one based on mass transport

along the forming grain boundary to the "neck" region as the rate-controlling step and one based on movement from the neck to the free surface regions as the rate-controlling step for each of these two stages.

Isothermal sintering studies were made on undoped and CaO-doped MgO powder compacts in static air and flowing water vapor atmospheres at 1230 to 1600°C. Analysis of microstructural changes and kinetic data supported the existence of distinct initial, intermediate, and final stages in the sintering of this powder in accordance with the theoretical analysis. The derived equations were applied to the initial and intermediate stages. In air, porosity was proportional to t in the initial stage and to $\ln t$ in the intermediate stage, both of which were based on the fact that the rate-controlling step is the transport of mass from the neck region to the adjoining free surface regions. In flowing water vapor, the porosity function of $\tanh^{-1}(-0.43P^{1/2} + 0.3)$ was proportional to t in the initial stage and to $t^{-1/3}$ in the intermediate stage, both of which were based on the fact that the rate-controlling step is the transport of mass from the grain-grain contact to the adjoining neck regions, during which the length of the diffusion path increased as densification progressed.

The apparent activation energies for the sintering of undoped MgO compacts in static air and flowing water vapor atmospheres in the initial stage were ~112 and 50 kcal/mole, respectively. The former corresponds to the value for bulk diffusion of oxygen whereas the latter corresponds to the value for grain-boundary diffusion, which is consistent with the suggested mechanisms. Not enough data were available to determine the apparent activation energies during the intermediate stage for undoped MgO and for both stages for CaO-doped MgO compacts.

* * *

† Brief version of J. Am. Ceram. Soc. 62, 138 (1979), and J. Am. Ceram. Soc. 62, 141 (1979).

‡ Permanent address: Spectrolab, 12500 Gladstone Avenue, Sylmar, California 91342.

10. ANALYSIS AND KINETICS OF SOLID STATE REACTIONS IN PbO-ZrO₂ SYSTEM†

Sudhir S. Chandratreya‡ and Joseph A. Pask

Existing models for solid state reaction kinetics have limitations because (a) they assume a geometry that can be realized only in gas-solid reactions which amounts to ignoring the pellet microstructure and does not account for the influence of prior processing steps, and (b) they cannot predict changes in rate limiting mechanism caused by localized microscopic volumetric changes accompanying the reaction. Theoretical equations were thus developed to estimate the external mass transport flux in terms of microstructural parameters of mixed powder solid-solid reactions. Using these equations, relative contributions of bulk, surface and vapor phase diffusion to the total external mass

transport can be evaluated. The "shrinking core"¹ and the "grain model"² equations were then modified whereby microstructural parameters explicitly appeared in the kinetic expressions.

A theory was developed which can predict abrupt changes in rate controlling mechanism in reactions accompanied by volumetric changes on a microscopic level. Accordingly, it becomes possible to predict the conditions under which contact between reactant particles can be maintained or broken from the radius ratio of reactant particles and densities of the products and reactants.

Experimental work was carried out on the solid state reaction between mixed powders of yellow lead monoxide and monoclinic zirconia to form lead zirconate. Reaction isotherms at temperatures between 710 to 810°C were determined for zirconia of two particle size ranges (Figs. 1 and 2). Dimensional changes accompanying the reaction were measured. Composition profiles in the cross-sections of partially reacted particles were obtained by electron beam microprobe analysis.

The reaction rate was strongly temperature dependent until approximately 85% of the reaction was completed. Apparent activation energy (Q_A), as determined from Arrhenius type of plots (Fig. 3),

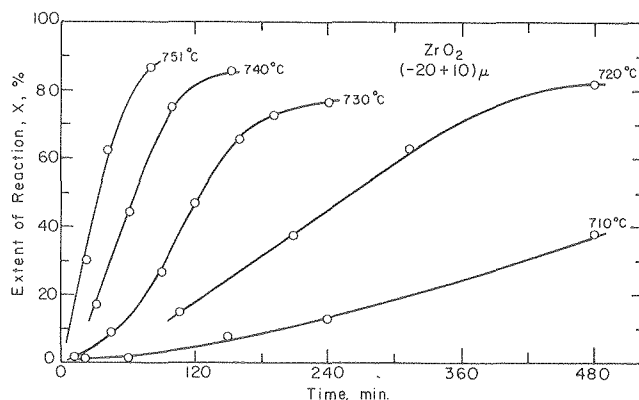


Fig. 1. Reaction isotherms for lead zirconate formation. (XBL 797-6633)

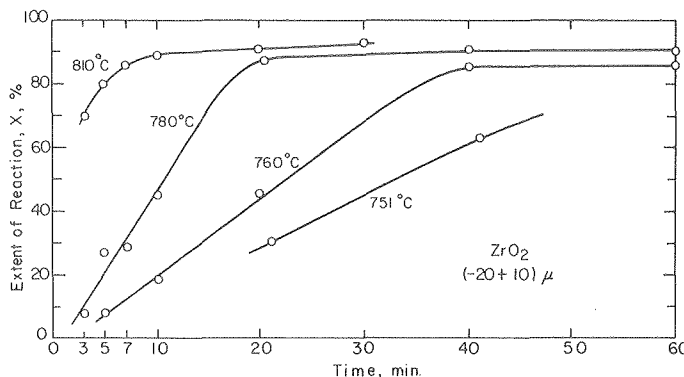


Fig. 2. Reaction isotherms for lead zirconate formation. (XBL 797-6634)

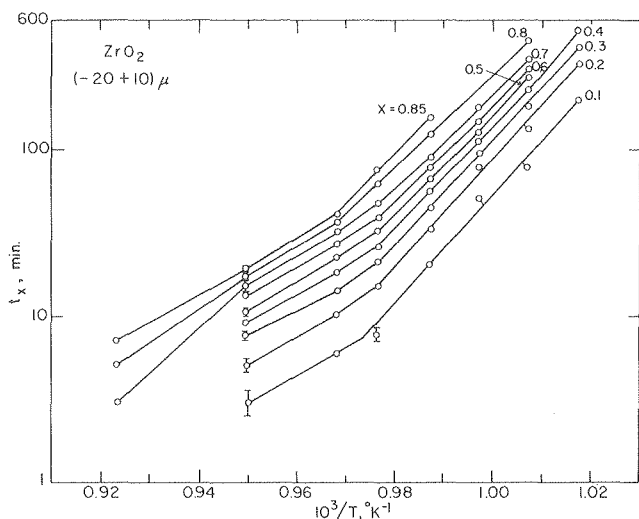


Fig. 3. Arrhenius plots for fixed amounts of reaction. (XBL 797-6638)

was dependent on the extent of reaction and decreased with increasing temperature indicating mixed rate control. Averaged over the temperature range but for a fixed extent of reaction (X), calculated values of Q_A ranged from 104 to 130 kcal/mole and the following relation was observed where $0 \leq X \leq 0.85$:

$$Q_A = 129.9 - 31.1 X .$$

The reaction rates suddenly decreased above 85% reaction and after a 15% linear expansion, and were relatively independent of the temperatures indicating a low activation energy. The low activation energy, which is typical of gaseous diffusion, suggests that external mass transport of PbO becomes the rate limiting factor above $X = 0.85$ which is predicted by the contact-maintenance theory after contact breakage. For an experimental value of $\Omega \approx 0.1$ and an assumed $Z \approx 2.0$, theoretically this breakage should occur at $X = 0.92$ with ~18% linear expansion if no shrinkage follows expansion.

Zirconia powder with larger particle size reacted faster than powder with smaller average particle size. The specific surface area measurement and pore structure analysis indicated that the coarser powder had higher specific surface area and higher proportion of finer pores. Therefore, the faster reaction rates observed in coarser zirconia can be attributed to reaction proceeding along the intraparticle pore surface in addition to the external surface of the particles. The "shrinking core" model frequently employed in solid-solid reaction studies would thus be inadequate in this case since it assumes nonporous particles and predicts faster reaction rates with decreasing particle size.

Microprobe profile analysis indicated a gradual composition change across the particle cross section. The absence of a sharp compositional change and uniform composition confirms mixed rate control by both diffusion and phase boundary reaction. Temperature dependence of Q_A can be attributed

to changes in relative importance of diffusion and interfacial reaction with changing temperature. Dependence of Q_A on the extent of reaction suggests that the pore structure changes during the reaction which affects the diffusive mass transport. If the pore structure changes are ignored, a modified "grain model" can be used to describe reactions with mixed control. However, for a meaningful analysis independently obtained data on various mass transport mechanisms would be required, which unfortunately are not available for the present case.

* * *

† Brief version of LBL-9839.

‡ Permanent address: Hewlett-Packard, Cupertino, California.

1. J. Szekely, J. W. Evans, and H. Y. Sohn, *Gas-Solid Reactions*, Chap. 3, p.65 (Academic Press, 1976).

2. *Ibid*, Chap. 4, p.108.

RESEARCH PLANS FOR CALENDAR YEAR 1980

Glass/metal interfaces. Studies are continuing on spreading, wetting, and reactions at interfaces at elevated temperatures between liquid glasses and metals. Factors being explored are the effect of impurities and adsorbed species. Extension of current concepts based on single element metals will be made to binary and ternary alloys. Elements of primary interest are iron, cobalt, nickel, and chromium. Of particular interest is the determination of the conditions under which adherence occurs in these complex systems.

ZnO/substrate interfaces. Conditions under which chemical bonding occurs at the interfaces between sputtered ZnO thin films and Si substrates are being evaluated. In addition correlations will be made between processing variables and microstructure of the ZnO thin film and interfacial zone; correlations will also be made between the microstructure and properties.

Hydrogen corrosion of Al silicate materials. NSF support for a project entitled "Structure, Strength and Corrosive Resistance of Aluminum Silicate Materials" will continue through the calendar year. The project objective is to determine the mullite-containing compositions and microstructures that have the best capability to resist corrosion by H_2 -containing atmospheres encountered in coal gasification processes. Kinetics and mechanisms of the corrosion processes, to which different phases in a normal microstructure are exposed, are being studied. A major effort is also being made to realize a theoretically dense polycrystalline mullite by pressureless sintering and to study the kinetics of sintering.

Liquid phase sintering. Studies are continuing on liquid phase sintering of alumina with anorthite (calcium aluminum silicate) liquids. The hot stage scanning electron microscope is a major tool. Correlations of the SEM, sessile drop and dihedral angle data will be made with the microstructure development and with liquid phase sintering theories.

1979 PUBLICATIONS AND REPORTS

Refereed Journals

1. Boon Wong and Joseph A. Pask, "Models for Kinetics of Solid State Sintering," J. Am. Ceram. Soc. 62, 138 (March-April 1979).
2. Boon Wong and Joseph A. Pask, "Experimental Analysis of Sintering MgO Compacts," J. Am. Ceram. Soc. 62, 141 (March-April 1979).
3. Subhash H. Risbud and Joseph A. Pask, "On the Location of Metastable Immiscibility in the System $\text{SiO}_2\text{-Al}_2\text{O}_3$," J. Am. Ceram. Soc. 62, 214 (March-April 1979).
4. Glenn A. Holmquist and Joseph A. Pask, "Reaction and Diffusion in Silver-Arsenic Chalcogenide Glass Systems," J. Am. Ceram. Soc. 62, 183 (March-April 1979).
5. V. K. Nagesh and Richard M. Fulrath, "Electrical Conduction in Glass-Metal Composite Materials," J. Am. Ceram. Soc. Bull. 58(4), 455 (April 1979).
6. Joseph A. Pask, Ilhan A. Aksay and Robert F. Davis, "Densities of $\text{SiO}_2\text{-Al}_2\text{O}_3$ Melts," J. Am. Ceram. Soc. 62, 332 (July-August 1979).
7. Michael D. Sacks, Robert B. Langston, Stephen T. Tso, and Joseph A. Pask, "Corrosion and Mechanical Behavior Correlations with Composition and Microstructure of Alumina Silicate Refractories," Bull. Am. Ceram. Soc. 58(7), 691 (July 1979).
8. D. R. Biswas, S. S. Chandratreya and Joseph A. Pask, "Thermal Expansion, Elasticity, and Internal Friction of Polycrystalline PZT Ceramic," Bull. Am. Ceram. Soc. 58(8), 792 (August 1979).
9. Philip C. Dokko and Joseph A. Pask, "High Temperature Stress-Strain Behavior of MgO in Com-

pression," J. Am. Ceram. Soc. 62, 433 (September-October 1979).

10. Stephen T. Tso and Joseph A. Pask, "Wetting and Adherence of Na-Borate Glass on Gold," J. Am. Ceram. Soc. 62, 543 (September-October 1979).

Other Publications

1. Joseph A. Pask, "Thermodynamics and Mechanisms of Sintering," in Factors in Densification and Sintering of Oxide and Non-oxide Ceramics, Proceedings of International Symposium held at Hakone, Japan, October 3-5, 1978, edited by Shigeyuki Somiya and Shinroku Saito (published by Gakujutsu Bunken Fukyu-kai, Tokyo Institute of Technology, Okayama, Meguro, Tokyo 152, Japan, 1979), pp.580-599.

LBL Reports

1. Paul R. Sharps, "Reactions and Spreading in the Cu-Ag System," M.S. thesis, January 1979, LBL-8600.
2. Sylvia M. Johnson, "Mullitization of Kaolinite and $\text{Al}_2\text{O}_3\text{-SiO}_2$ Mixtures," M.S. thesis, April 1979, LBL-9006.
3. Joseph A. Pask, "Ceramic Processing - A Ceramic Science," May 1979, LBL-9179.
4. Stephen T. Tso, "The Corrosion of Silicate Materials by Hydrogen Gas and Hydrofluoric Acid Solution," Ph.D. thesis, October 1979, LBL-9887.
5. V. K. Nagesh, "Microstructure Development and Conductivity in Thick Film Conductor Systems," Ph.D. thesis, December 1979, LBL-9274.
6. Sudhir S. Chandratreya, "Kinetics of Solid State Reaction in the PZT System," Ph.D. thesis, December 1979, LBL-9839.

c. High Temperature Reactions*

Alan W. Searcy, Investigator

1. PARTIAL MOLAL PROPERTIES OF CO₂ IN CaCO₃ AND THE SOLUBILITY OF CaO IN CaCO₃ AS A FUNCTION OF TEMPERATURE†

Rama K. Shukla, David J. Meschi, and Alan W. Searcy

The model developed by Searcy and Beruto for analyzing the kinetics of decomposition reactions emphasizes the importance of activity variations of the chemical components of the solid reactant, e.g., of CaO and CO₂ in CaCO₃.¹ As far as we know, little or no effort has previously been made to measure composition variations and the effect of this variation on partial molal properties in complex salts such as metal carbonates (as distinct from solids formed from pairs of complex salts such as the MgCO₃ - CaCO₃ phase, dolomite). The present study was directed toward measuring the partial molal thermodynamic properties for CO₂ in CaCO₃ as a function of its CaO to CO₂ composition ratio, and the solubility of CaO in the CaCO₃ phase at 770-1000 K.

The apparatus essentially consists of a manometer, gas burette, furnace with temperature control, mass spectrometer, and vacuum line assembly. Deviations from stoichiometry as small as $4 \times 10^{-3}\%$ were measured.

For calcite powder at low temperatures an irreversible conversion of about 1 monolayer of CO₃²⁻ to O²⁻ gave an initial composition change which was larger than the subsequent reversible composition changes that accompanied increases and decreases in CO₂ pressure in the system. Figure 1, in which points are numbered in the order in which data were taken, illustrates the irreversible and subsequent reversible changes. At higher temperatures with samples of lower surface area, the surface effect was not important (Fig. 2).

From the measurements the following values of partial molal quantities were calculated for the two components:

$$\Delta H^\circ_{\text{CaO}} = 35.6 \text{ K cal/mole}$$

$$\Delta H^\circ_{\text{CO}_2} = 76.47 \text{ K cal/mole}$$

$$\Delta S^\circ_{\text{CO}_2} = -56.8 \text{ eu/mole}$$

$$\Delta S^\circ_{\text{CaO}} = 21.8 \text{ eu/mole}$$

Using these values, values of the saturation concentration of CaO in the stoichiometric CaCO₃ phase were extrapolated to higher temperatures. This has led to a modified phase diagram for the CaO-CaCO₃ system (Fig. 3). Solution limits are shown as dashed lines because the data below the eutectic are calculated, not directly measured, and the data above the eutectic estimated.

* * *

† Brief version of LBL-9885.

1. D. Beruto and A. W. Searcy, *J. Phys. Chem.* **82**, 163 (1978).

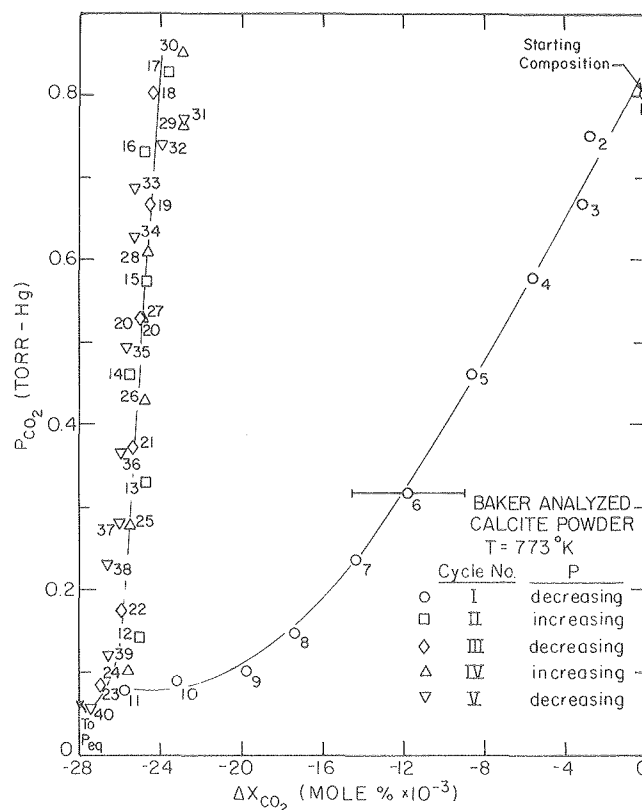


Fig. 1. P_{CO_2} vs. composition change, ΔX_{CO_2} for powder calcite (1-5 μm size) showing effect of irreversible CO₂ desorption. Points are numbered in order. (XBL 797-6517)

* This work was supported by the Division of Materials Sciences, Office of Basic Energy Sciences, U.S. Department of Energy.

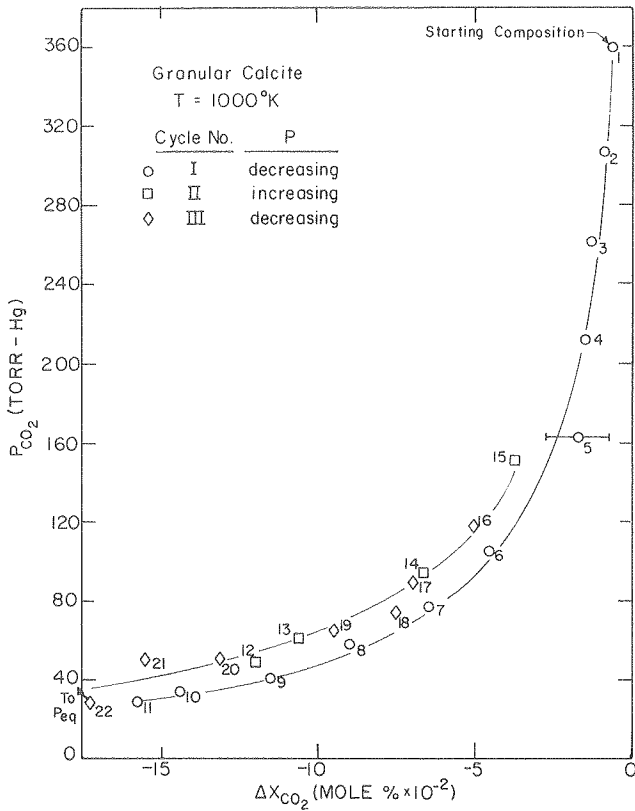


Fig. 2. P_{CO_2} vs. change in composition, ΔX_{CO_2} in the calcite phase at 1000 K for a granular calcite sample (5-10 mm particle size). Experimental points have been numbered to show the order in which they were generated. (XBL 797-6521)

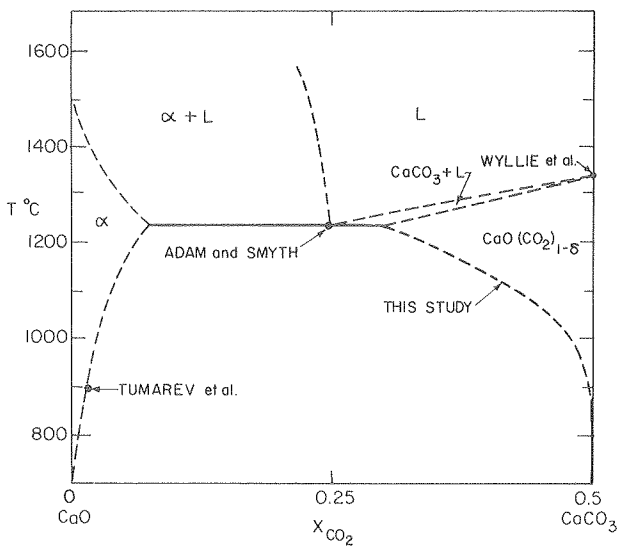


Fig. 3. Phase diagram for CaO-CaCO₃ as suggested by the current study. (XBL 797-6697).

2. THE KINETICS OF DECOMPOSITION OF CaCO₃ AT HIGH CO₂ PARTIAL PRESSURES†

Rama K. Shukla and Alan W. Searcy

Considerable controversy exists over the dependence of rate of decomposition of calcite at higher CO₂ pressure both in theoretical predictions and experimental measurements.¹⁻³ The apparatus which was developed for use in measuring the effect of CO₂ pressure on the composition of CaCO₃ (previous article) has been used to re-examine the effect of CO₂ pressure P on the rate of CaCO₃ decomposition in the range from $P/P_{eq} = 0.01$ to 0.8 in the temperature range of 500-700°C.

Decomposition cycles on a single crystal specimen were found to be extremely reproducible. Experiments with calcite powder showed that decomposition flux depended upon sample bed depth especially at low CO₂ pressures. The pressure dependence of the decomposition rate for single crystals was found not to follow either an equation of the form $j = k(1 - P/P_{eq})$ or $j = k(P_{eq}/P - 1)$, where j is the flux and k is a constant, as predicted by various theories,¹⁻⁴ and as seemingly confirmed by measurements over limited pressure ranges.¹⁻³

Figure 1 shows apparent linearity on a P_{eq}/P plot, but Fig. 2 shows curvature when P_{eq}/P approaches 1.

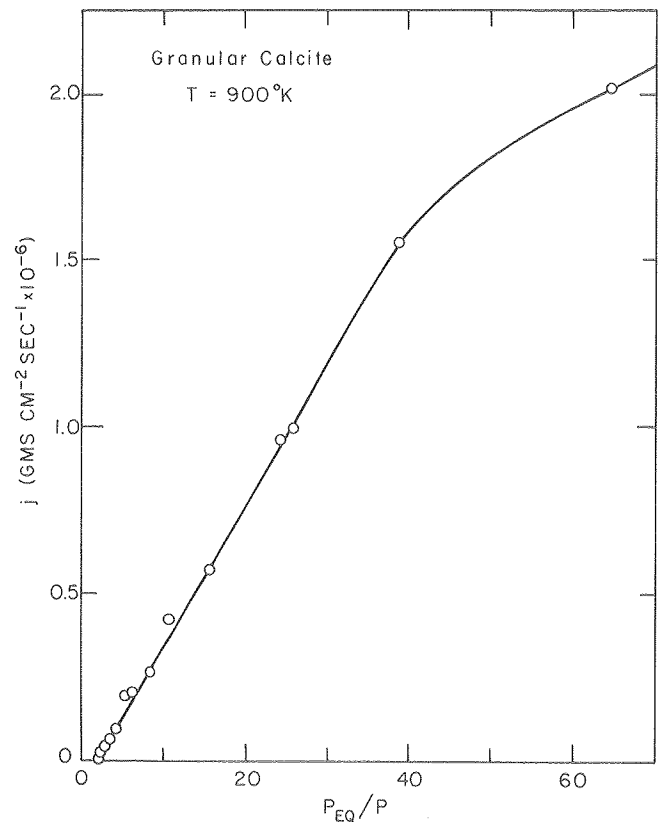


Fig. 1. Decomposition flux, j, vs P_{eq}/P_{CO_2} for granular calcite at 900 K, showing apparent linear relationship at pressures close to equilibrium. (XBL 797-6690)

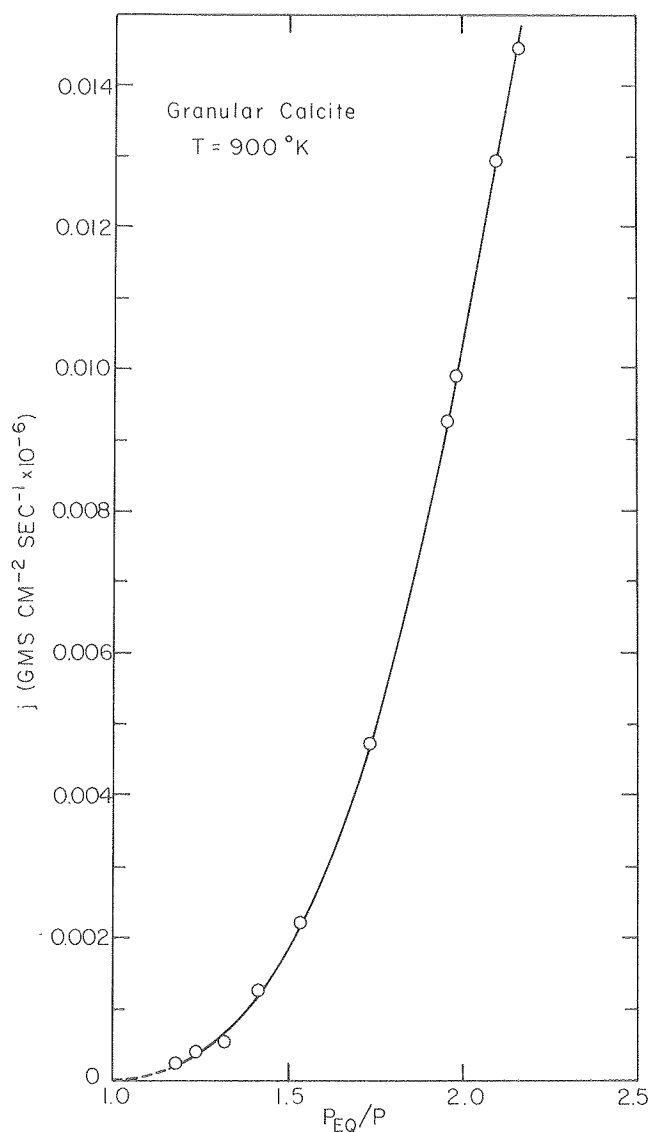


Fig. 2. Decomposition flux, j , vs P_{Eq}/P_{CO_2} at 900 K at pressures close to equilibrium showing non-linear behavior. (XBL 797-6689)

To determine the activation enthalpy of decomposition, Arrhenius plots were obtained for decomposition fluxes at different temperatures, but at constant value of departure from equilibrium, θ ($=P/P_{Eq}$). For single crystals, ΔH^* remains approximately constant at 49.2 ± 1.2 K cal/mole, for values of $\theta \leq 0.1$, which agrees very well with the activation enthalpy for single crystals decomposed in vacuum. For $\theta > 0.1$, ΔH^* rises to an average value of 61.8 ± 1.8 K cal/mole. It therefore follows that the decomposition of calcite has different rate limiting steps at low and relatively high CO_2 partial pressures.

* * *

† Brief version of LBL-9885.

1. E. P. Hyatt, et al., *J. Am. Ceram. Soc.* **41**, 70 (1958).

2. E. Cremer and W. Nitsch, *Z. Elektrochem. Ber. Bun Phys. Chem.*, **66**, 697 (1962).
3. J. Zawadzki et al., *Trans. Faraday Soc.* **34**, 951 (1938).
4. D. Beruto and A. W. Searcy, *J. Phys. Chem.* **82**, 163 (1978).

3. THE INFLUENCE OF SELF-COOLING ON THE APPARENT ACTIVATION ENTHALPY OF DECOMPOSITION OF $CaCO_3$ †

Elizabeth K. Powell and Alan W. Searcy

Recently investigators^{1,2} have argued that values reported for the activation enthalpy of decomposition of calcite are invalid because the reaction rates under the conditions of study were limited by thermal transport or gas phase diffusion. If such a conclusion were accepted for calcite decomposition, a similar conclusion would follow for essentially all endothermic decomposition reactions because the decomposition behavior of calcite is qualitatively similar to that of other solids. We have measured calcite decomposition fluxes in vacuum.³ Gas phase diffusion cannot limit such measurements. We summarize here the results of analyzing the thermal balance in that decomposition for which energy is supplied by radiation and removed by radiation and by the endothermic conversion of $CaCO_3$ to $CaO + CO_2$.

The straight line of Fig. 1 is a linear fit of the experimental data. The lowered curved line illustrates the kind of variation of flux J_{CO_2} with apparent sample temperature T_1 that would be observed if (a) the observed linear flux dependence correctly described a chemical rate dependence at low temperatures, but (b) self-cooling is sufficient to reduce the surface temperature at the midpoint of the experimental range to T_2 for which the flux is 75% of the flux at T_1 . The upper curved line illustrates the way that $\log J_{CO_2}$ must vary with $1/T_2$ if (a) the measured flux shows the experimentally recorded temperature dependence on $1/T_1$, but if (b) the flux measured when T_1 is 1000 K is only 75% of the true flux when T_2 is 1000 K.

Self-cooling should cause curvature qualitatively like that of the lower curve of Fig. 1, but no curvature is apparent in the plot of experimental data.³

The maximum extent of curvature from self-cooling that could be hidden by scatter in the apparently linear plot of experimental data would not introduce more than 1.5 kcal uncertainty into activation enthalpies calculated from the temperature dependence of the measured fluxes. The apparent enthalpy of activation for calcite decomposition in vacuum is^{3,4} 50 ± 3 kcal, compared to 40.5 kcal for the standard enthalpy of calcite decomposition at 1000 K.

* * *

† Brief version of LBL-9692.

1. P. K. Gallagher and D. W. Johnson, Jr., *Thermochemica Acta*, **6**, 67-83 (1973).

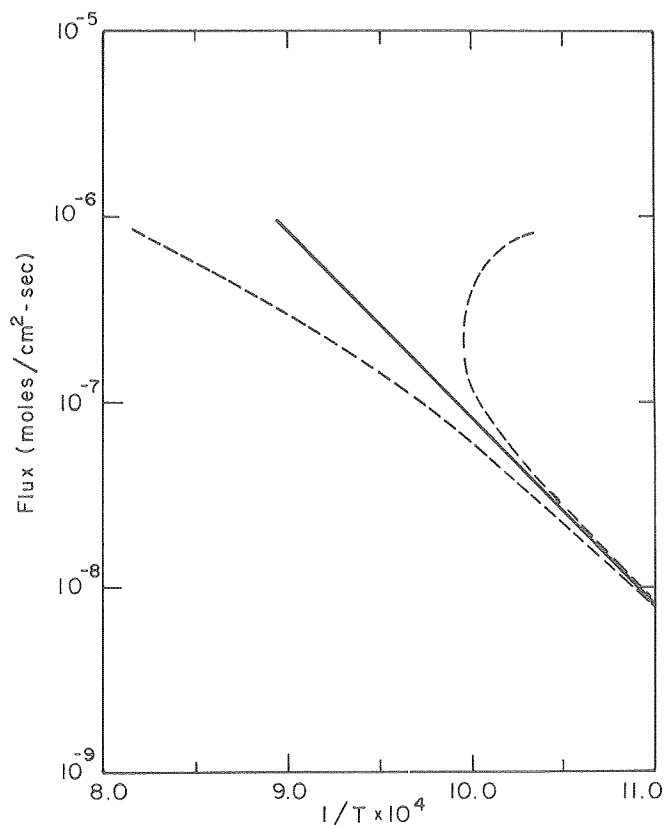


Fig. 1. The solid curve shows the measured flux densities of CO_2 as a function of temperature. The lower curve shows how self-cooling would change the apparent flux dependence and the upper curve shows the kind of (theoretically implausible) flux dependence that a self-cooling error could cause to yield a linear \ln flux vs. $1/T$ plot. (XBL 795-6368)

2. See K. M. Cladwell, P. K. Gallagher and D. W. Johnson, Jr, *Thermochimica Acta*, **18**, 15 (1977).
3. The experimental study was summarized in the 1978 Annual Report, LBL-8580.
4. D. Beruto and A. W. Searcy, *J. Chem. Soc., Far. Trans. I*, (1974).

4. CATALYSIS OF THE DECOMPOSITION OF CaCO_3 AND OF THE SINTERING OF CaO

Gary Knutsen and Alan W. Searcy

Recent studies in our laboratory have shown that CaCO_3 decomposition does not yield equilibrium CO_2 pressures from CaCO_3 in open crucibles or even in effusion cells with orifices as small as 0.23 mm diameter. Endothermic decomposition reactions, such as CaCO_3 decomposition, have commonly been called reversible, and the possibility that their rates can be increased by catalysts has previously received little or no attention. However, comparison of equilibrium pressures to pressures which correspond to fluxes generated from free surfaces of CaCO_3 crystals shows that the reaction rate could in principle be increased by a factor of 10^5 if a

suitable catalyst could be found. This article reports an effort to find a catalyst for CaCO_3 decomposition.

To simplify the experiments, a catalyst was sought that has a mass flux during vaporization which is at least an order of magnitude below that of the CO_2 from CaCO_3 but greater than the mass flux of Ca(g) and O_2 from CaO . Catalysts with this kind of vaporization behavior allow the CO_2 flux to be determined with little error from the sample weight loss. The catalyst can then be removed by vaporization to leave essentially pure CaO for x-ray diffraction and scanning electron microscopy studies. Promising possibilities turned out to be NaCl and LiCl . Of these, LiCl proved to be the better catalyst.

When 10 wt% of LiCl was added to CaCO_3 in an effusion cell with 0.23 mm orifice diameter, the CO_2 flux was increased by a factor of two over that from the uncatalyzed cell, and the equilibrium CO_2 pressure was attained. The rate of effusion of CO_2 was also constant until reaction was about 95% complete while the flux in the absence of a catalyst decreased by a factor of two from the time reaction began until reaction reached 85% of completion.

Cells were heated until the CaCO_3 was completely decomposed and the LiCl completely vaporized from the sample. The subsequent powder x-ray pattern showed highly crystalline CaO . The surface area of the CaO was $1 \text{ m}^2/\text{gm}$. In contrast, the product from the uncatalyzed reaction in a cell of 0.23 mm diameter orifice is poorly crystalline and has a surface area of $40 \text{ m}^2/\text{gm}$. The SEM micrographs in Figs. 1 and 2 show the difference between calcium oxide obtained from catalyzed CaCO_3 at 700 C.

It is evident that LiCl promotes extensive sintering of CaO at only 700 C. The sintered CaO particles must not adhere to CaCO_3 because an adherent CaO layer would reduce the rate of decomposition.

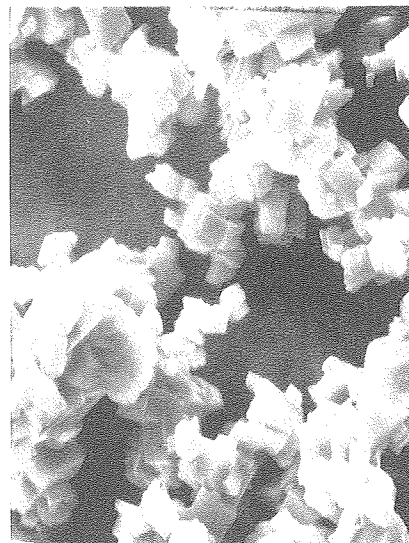


Fig. 1. SEM photograph of CaO prepared by decomposing CaCO_3 in an effusion cell without a catalyst. (XBB 784-4505)

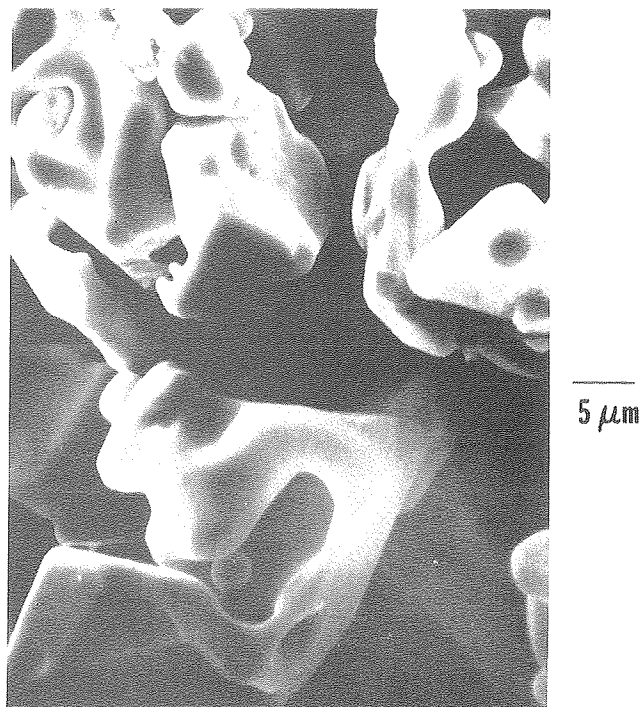


Fig. 2. SEM photograph of CaO prepared by decomposing CaCO_3 under the same conditions as used for the sample in Fig. 1 except for the presence of 10% LiCl which was removed by vaporization after decomposition was complete. (XBB 790-12874)

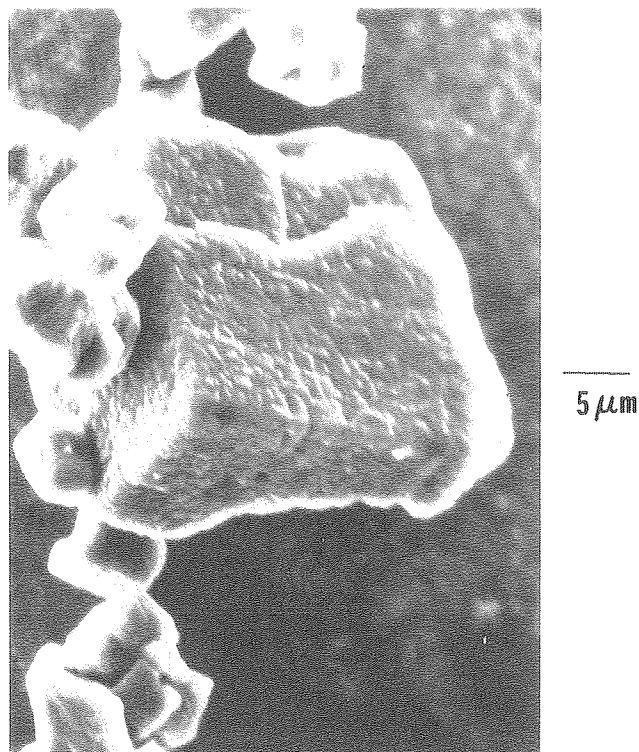


Fig. 1. SEM photograph of ~70% recarbonated particles of porous CaO powder. (XBB 790-15764)

5. THE KINETICS OF REACTION OF CO_2 WITH POROUS CaO POWDERS

Gary Knutsen and Alan W. Searcy

A new Cahn 1000 microbalance and an automated pressure controlling device have been incorporated in a system designed to study the reaction of CO_2 with porous CaO obtained from CaCO_3 decomposition in vacuum. After calibration of the system by measuring the vapor pressure of NaCl, ~0.7 grams of CaCO_3 was decomposed in vacuum at 600 C, the product porous CaO (~90 m^2/gm surface area) was then reacted with CO_2 gas.

The equilibrium CO_2 pressure was determined by finding the pressure that causes neither a weight gain or weight loss in the sample at 600, 650, 675 and 700°C. All values were about 40% below the reported CO_2 equilibrium values.¹ Samples of the porous CaO were reacted with CO_2 at 1.3 times the experimentally determined CO_2 equilibrium pressure at 600, 650, and 700 C. The rates of the back reaction of CO_2 with the porous carbonate are shown in Fig. 1 for 600, 650, and 700 C. The reaction rate was essentially linear until the sample reached 65 to 70% of theoretical recarbonation, regardless of the temperature of reaction. For the linear reaction, the activation enthalpy at constant CO_2 activity is calculated to be 13.6 kcal/mole.

The x-ray diffraction pattern showed the product to be crystalline CaCO_3 . The surface area was

<1 m^2/gm . An SEM micrograph (Fig. 1) shows the ruffled surface obtained from the 700 C sample. SEM photographs are similar for samples recarbonated at 600 and 650 C.

The initial linear reaction rate implies that the rate limiting process until the reaction is more than 50% complete is a surface step, rather than diffusion through the CaCO_3 product layer. The fact that the surface area measured for samples that were only ~70% reconverted to CaCO_3 is only ~1 m^2/g —about the area expected for nonporous powder particles—implies that the decrease in rate in the later phases of reaction is a consequence of blockage of pores well before the reaction is complete.

* * *

1. K. H. Stern and E. L. Weise, NBS Report NSRDS-NB530 (1969).

6. CHARACTERIZATION OF THE POROUS CaO PARTICLES FORMED BY DECOMPOSITION OF CaCO_3 AND $\text{Ca}(\text{OH})_2$ IN VACUUM†‡

Dario Beruto, Alan W. Searcy, Luigi Barco, and Giorgio Spinolo

Because of its high reactivity, further characterization of the properties of sr-CaO (the CaO

produced by decomposing CaCO_3 in vacuum) is of potential practical importance for removal of sulfur from steel, petroleum, and coal. The properties of CaO produced by decomposition of Ca(OH)_2 in vacuum are also of interest: first because this form of CaO (called h- CaO) has a higher surface area than does sr- CaO ; second because the layer structure of Ca(OH)_2 is likely to cause H_2O to escape by diffusion in two dimensions instead of three; and third because we disbelieved the report that the initial CaO formed from Ca(OH)_2 decomposition has a pseudo- Ca(OH)_2 structure.¹

Hot stage x-ray diffraction measurements showed that the normal crystallographic modification of CaO is produced from both CaCO_3 and Ca(OH)_2 from the time that decomposition commences. Earlier reports that pseudo-calcite and pseudo- Ca(OH)_2 forms of CaO are the initial product of decomposition are in error, probably because reaction of water vapor with h- CaO and sr- CaO occurs before CaO diffraction peaks can be detected.

Integrated breadths of the CaO XRD peaks were essentially constant through the course of either decomposition reaction. This result shows that the pressure of CO_2 or H_2O generated by the decompositions are too low to catalyze significant CaO crystal growth or annealing during the course of the reactions. Samples kept under vacuum at the temperature of decomposition for 15 hours after decomposition was complete also showed no XRD evidence of crystal growth. From the line broadening h- CaO and sr- CaO crystal dimensions are both calculated to be ~ 100 Å.

Surface areas were calculated from N_2 adsorption isotherms to be $79 \text{ m}^2/\text{g}$ for sr- CaO and $133 \text{ m}^2/\text{g}$ for h- CaO . Isotherms for h- CaO had forms consistent with the expected planar symmetry of pores, and isotherms of sr- CaO were consistent with De Boer's predictions for pores of cylindrical symmetry. Pore size distributions calculated for h- CaO and sr- CaO are shown in Fig. 1.

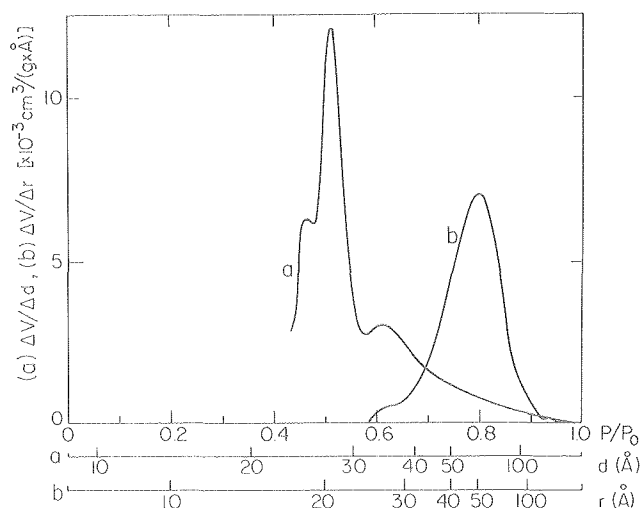


Fig. 1. Pore distributions as functions of the relative pressure of N_2 (P/P_0) and of pore slit width d for h- CaO (Curve a) and of pore radius r for sr- CaO (Curve b). (XBL 798-6894)

The porosity of particles of sr- CaO and of h- CaO are estimated to be $\sim 55\%$ and $\sim 50\%$ from the assumption that they have exactly the same exterior dimensions as the CaCO_3 or Ca(OH)_2 particles from which they were formed. The actual porosities of the two types of CaO particles were calculated from the volume of N_2 that they absorb when the N_2 pressure is infinitesimally below the equilibrium vapor pressure of N_2 at 78 K. By this means, the porosity of sr- CaO is found to be $41.5 \pm 5\%$, and that of h- CaO is $36 \pm 5\%$. These results indicate that although the porous particles of sr- CaO and h- CaO appear in SEM pictures to be unchanged in shapes and dimensions from the parent particles of CaCO_3 and Ca(OH)_2 , the decomposition reactions are accompanied by some particle shrinkage.

* * *

[†]This work was supported by the Division of Materials Sciences, Office of Basic Energy Sciences, U. S. Department of Energy and in part at Laboratorio de Chimica, Facolta di Ingegneria, University of Genova, Genova, Italy under partial sponsorship of the Centro Studi di Chimica e Chimica Fisica dei Materiali del CNR.

[‡]Brief version of LBL-9713.

1. D. R. Glasson, *J. Chem. Soc.*, 1506 (1956).

7. USE OF N_2 ADSORPTION ISOTHERMS TO DEDUCE REACTANT-PRODUCT ORIENTATION OF RELATIONSHIPS IN VAPOR PHASE HYDRATION OF SUB-MICRON PARTICLES OF $\text{CaO}^{\dagger\ddagger}$

Dario Beruto, Alan W. Searcy, Luigi Barco, and Gabriele Belleri

The porous CaO powders which are produced by decomposing nonporous CaCO_3 or Ca(OH)_2 powders in vacuum react very rapidly with water vapor at room temperature. As part of a study of the kinetics of that reaction, the authors have deduced the probable orientation of the product Ca(OH)_2 relative to the initial surfaces of the parent CaO crystallites from the pore size distribution before and after reaction. The orientation relationships would be difficult to obtain by diffraction techniques because the CaO crystallites that make up the porous particles have dimensions of the order of $0.01 \mu\text{m}$ (100 Å). The influence of pressure of water vapor on morphology, surface area, and pore size distribution, and the relative reactivity of Ca(OH)_2 powders of three different specific surface areas are reported.

The fact that rehydration occurs with only slight changes in particle shapes shows that reaction occurs primarily at internal pore surfaces. Pressures of water vapor are too low for capillary condensation. Reaction must proceed by solid state diffusion, presumably of water.

From the known crystal structures of CaO and Ca(OH)_2 it can be shown that the rehydration of porous CaO powders would be expected to cause highly anisotropic expansion of the solids in the plane of the pore surfaces. Pore size distribution data (illustrated by Fig. 1), however, indicate

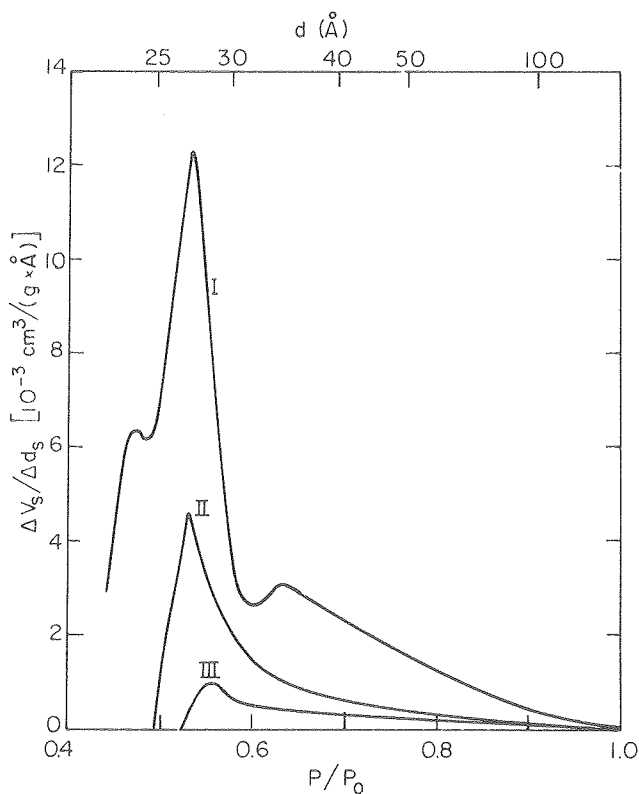


Fig. 1. Pore size distribution in CaO formed by $\text{Ca}(\text{OH})_2$ decomposition in vacuum (Curve 1), pore size distribution when that CaO is reacted with H_2O at 4 Torr pressure (Curve 2), and 15 Torr (Curve 3). (XBL 799-7108)

that the hydration reaction causes expansion principally normal to pore surfaces. It is suggested that shearing forces introduced by the expected anisotropic expansion causes extrusion into the pores of $\text{Ca}(\text{OH})_2$ crystallites formed at CaO particle surfaces.

The morphologies of $\text{Ca}(\text{OH})_2$ particles studied as a function of H_2O pressure show that water vapor catalyzes condensed phase movement of $\text{Ca}(\text{OH})_2$ at 25°C . The weight of $\text{Ca}(\text{OH})_2$ that reacts with CO_2 gas at 250°C is essentially a constant function of surface area.

* * *

†This work was supported by the Division of Materials Sciences, Office of Basic Energy Sciences, U. S. Department of Energy and in part at Laboratorio di Chimica, Facolta di Ingegneria, University di Genova, Genova, Italy under partial sponsorship of the Centro Studi di Chimica e Chimica Fisica dei Materiali del CNR.

‡Brief version of LBL-9943.

Measurements of the kinetics of decomposition of SrCO_3 single crystals in vacuum will be completed. No kinetic data have been available for this reaction. Its behavior is of particular interest because strontium belongs to the same chemical family as calcium and magnesium for which the carbonate decomposition behaviors differ significantly.

Preliminary observations of in-situ decomposition of CaCO_3 crystals in a scanning electron microscope reveal a process which appears to be a strain induced cooperative movement of porous CaO particles past each other. Further scanning observations are planned for CaCO_3 and for BaCO_3 . The BaO layer formed from BaCO_3 decomposition has a very different appearance from that of the CaO from CaCO_3 , which suggests that the BaO forms by a different mechanism.

Transmission electron microscope observations will be completed for in-situ decomposition of MgCO_3 and dolomite. These measurements are yielding the particle size and orientation relationships of the product porous oxides relative to the parent carbonate phases.

The use of a mass spectrometer to study the kinetics of decomposition of SO_3 gas to SO_2 gas plus O_2 gas in an experimental range intermediate between that commonly employed by chemical engineers and chemical physicists will be continued. The study is both a prototype test of a new approach to reaction kinetic studies and a source of new information about catalysis of an industrially critical reaction.

The influence of iron oxides and other catalysts on the rate of decomposition of SrSO_4 single crystals will be investigated in a mass spectrometer. The products of partial and completely decomposed crystals will be sectioned and submitted to microchemical analysis to ascertain whether or not the catalysts act by diffusion through the porous product layer to the advancing interface of the SrSO_4 .

A study of the thermodynamic stability of the MgO product of decomposing $\text{Mg}(\text{OH})_2$ in vacuum will be continued. Thermodynamic data derived from the apparent equilibrium pressure for the reaction $\text{Mg}(\text{OH})_2 \rightarrow \text{Mg}(s) + \text{H}_2\text{O}(g)$ in a Knudsen effusion cell are in disagreement with known data for the reaction from other sources. The calorimetric measurements will test whether or not the discrepancy is a consequence of very high metastability for the porous oxide formed by vacuum decomposition.

A collaborative study with Professor Dario Beruto's group at the University of Geneva on the kinetics of reaction of various porous forms of CaO with water vapor at room temperature will be

completed. The data so far obtained suggest that the reaction proceeds at a very high rate until access to the interior of the porous oxides is blocked by formation of the $\text{Ca}(\text{OH})_2$ reaction product. Experiments to test this interpretation are planned.

1979 PUBLICATIONS AND REPORTS

Refereed Journals

1. Alan W. Searcy, M. Huang, and D. Meschi, "Thermodynamic Properties of SeS gas," J. Electrochem. Soc. 126 (10), 1825 (October 1979).
2. Alan W. Searcy, J. Ewing, and D. Beruto, "The Nature of CaO Produced by Calcite Powder Decomposition in Vacuum and CO_2 ," J. Am. Ceram. Soc. 62, 580 (1979).

LBL Reports

1. Bob R. Powell, "Phase Equilibria in the $\text{PbO-Al}_2\text{O}_3$ System," Ph.D. thesis, September 1979, LBL-8219.

2. Rama Shukla, "Tensi-volumetric Studies of the $\text{CaCO}_3\text{-CaO-CO}_2$ System," Ph.D. thesis, December 1979, LBL-9885.

3. D. Beruto and A. W. Searcy, "The Kinetics of Reaction of Porous CaO Powders with Water Vapor," July 1979, LBL-9488.

4. E. Powell and A. W. Searcy, "The Rate and Activation Enthalpy of Decomposition of CaCO_3 ," August 1979, LBL-9692.

5. D. Beruto, A. W. Searcy, L. Barco, and G. Spinolo, "Characterization of the Porous Calcium Oxide Particles Formed by Decomposition of Calcium Carbonate and Calcium Hydroxide in Vacuum, August 1979, LBL-9713.

6. D. Beruto, A. W. Searcy, L. Barco, and G. Belleri, "Use of N_2 Adsorption Isotherms to Deduce Reactant-Product Orientation Relationships in Vapor Phase Hydration of Sub-Micron Particles of CaO," November 1979, LBL-9943.

Invited Talks

1. G. F. Knutsen and A. W. Searcy, "Metastable Equilibrium in Calcite Decomposition," Basic Science Division of the American Ceramic Society, New Orleans, LA, October 17, 1979.

d. Chemical Properties of Ceramic Alloys and Processing of Ceramic Materials*

L. C. De Jonghe, Investigator

1. GAS SOLID REACTION: REDUCTION OF OXIDES[†]

L. C. De Jonghe, J. Porter, and M. Chang

We have examined aspects of hydrogen reduction of cobalt ferrite in the temperature range between 500 and 800°C. We have used thermogravimetric analysis and electron microscopy to elucidate the nature of the various reaction steps in the reduction. It was found that in a temperature range between 500 and 650°C and under the reaction conditions used, the reduction reaction could be simply expressed as:

$$\dot{\xi} = \frac{p_{H_2}^b}{RTc_o} \left(\frac{1}{k_r} + \frac{\xi}{D_{eff}} \right)^{-1}, \quad (1)$$

where

- $\dot{\xi}$ = the rate of layer thickening,
- k_r = interface reaction rate coefficient,
- D_{eff} = the effective gaseous diffusion coefficient in the porous product scale, and
- $p_{H_2}^b$ = bulk pressure of hydrogen in the gas stream.

The mass transfer from the gas bulk to the sample appeared to be of negligible resistance. From Eq. (1), it can be seen that if the inverse rate is plotted vs. the layer thickness, a linear relationship should be obtained. Figure 1 shows how well the linear relationship is indeed obtained in the temperature range mentioned. However, it also shows serious deviations around 953 K. The strong deviation from the simple expression for the reduction rate (Eq. 1) is due to a reaction rate anomaly, as is evident from Fig. 2. Of special interest is the behavior at 973 K, where we observe an initially fast reaction rate that after some layer thickening changes to a slow reaction rate. Transmission electron microscopy has shown that the initial reaction is one where spinel is directly converted to metal. At longer times, a wüstite subscale appears which is associated with the slowdown of the reaction rate.

The reaction rate anomaly and the absence of wüstite in the early stage of the reaction are considered to be a kinetic effect. Indeed, the rate of growth of a small cobalt-wüstite precipitate at the metal/spinel interface, has to be compared to the rate of interface advance, $\dot{\xi}$ (Eq. 1). If the particle is consumed by the advancing interface more rapidly than it can grow, then a continuous wüstite layer cannot form. The growth rate of the wüstite precipitate, v_w , at the advancing

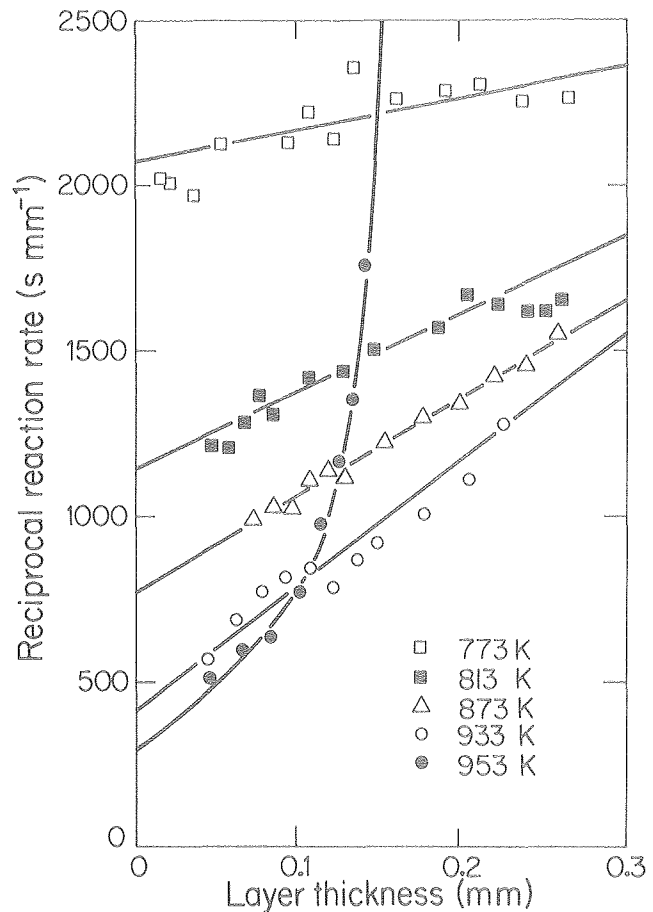


Fig. 1. Reduction kinetics at 100 Torr for specimens reduced between 773 and 953 K. The reciprocal interface advance rate is plotted against the layer thickness calculated from the weight loss data. Note that at 953 K the kinetics no longer follow the simple relationship expressed in Eq. (1).

(XBL 792-8370)

metal/spinel interface can be considered to a first approximation to be a constant for a constant temperature and pressure. From a comparison at $\dot{\xi}$ and v_w , a critical layer thickness, ξ_c , can be found at which wüstite can first appear. We find this critical layer thickness to be of the form:

$$\xi_c = \frac{D_{eff} p_{H_2}^b}{RT} \left[(C_o A^* \Delta\mu \exp(-Q_w/RT))^{-1} - RT/k_r p_{H_2}^b \right], \quad (2)$$

where

- C_o, A^* = constants,
- $\Delta\mu$ = chemical potential difference determining v_w ,
- Q_w = activation energy for v_w .

* This work was supported by the Division of Materials Sciences, Office of Basic Energy Sciences, U. S. Department of Energy.

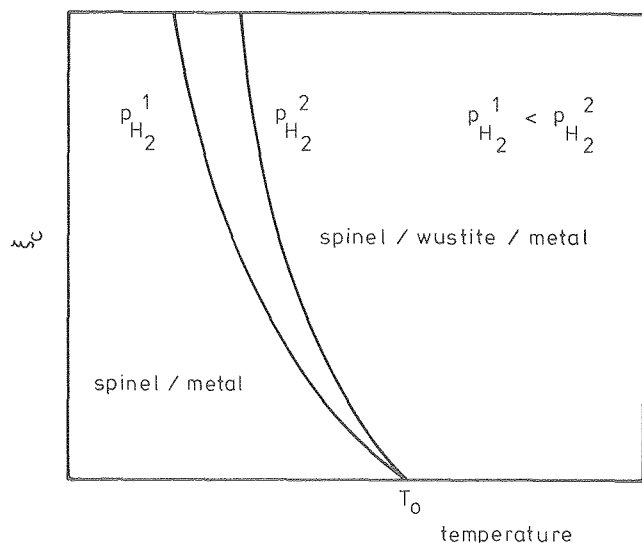


Fig. 2. Qualitative behavior of ξ_C as a function of temperature, according to Eq. (2).
(XBL 798-11035)

Also, there should be a temperature T_0 at which wüstite is initiated immediately at the beginning of the reaction. This temperature would be one where the rate of growth of the wüstite precipitate always exceeds the rate of spinel metal interface advance. T_0 is found to be of the form:

$$T_0 = - \frac{Q_w}{R \ln(k_3/C_0 \Delta \mu A^*)},$$

where k_3 = an interface transport coefficient.

Since all the kinetic parameters are not yet known, only the qualitative behavior of ξ_C can be considered (Fig. 2). It is apparent from this figure that the reduction rate will be characteristic of a direct spinel/metal reaction until $\xi = \xi_C$. At that point the reaction rate should become characteristic of the spinel/wüstite reaction. The pressure dependence of this critical thickness should be such that at a fixed temperature ξ_C would increase with increasing bulk hydrogen pressure, and at fixed pressure ξ_C would decrease with increasing temperature. This behavior has been confirmed experimentally.

A number of conclusions could be drawn from the present work.

1. Below 993 K, the reduction of cobalt ferrite by hydrogen at reduced pressures was shown to be under mixed control of the chemical reaction at the scale/cobalt ferrite interface and of the gaseous diffusion through the scale. The importance of the gaseous diffusion resistance through the scale increases with increasing temperature.

2. The effective diffusion coefficients of gas through the scales were determined to have both Knudsen and molecular components. The changes in

the diffusion coefficient as a function of the reducing conditions could be attributed to changes in the scale morphology.

3. The interface reaction was found to follow Langmuir-Hinshelwood kinetics.

4. The reaction rate minimum that was observed at 700°C was caused by the development of a continuous subscale of cobalt-wüstite. The incubation period for the development of the subscale could be attributed to the different velocities of the spinel/metal interface and of the wüstite/spinel interface. A critical layer thickness was defined as a thickness of the metal scale at the moment when the subscale became continuous. The temperature and pressure dependence of the critical layer thickness was found to be in agreement with the proposed model.

* * *

†Brief version of LBL-9801.

2. TRANSIENT LIQUID PHASE SINTERING OF CERAMICS

S. C. Hu and L. C. De Jonghe

Experiments have been performed to clarify the role of small amounts (up to 10 mole%) of transient, reactive liquid phases. In several ceramic systems, such transient liquid phases have been noted to increase significantly the rate of densification of the powder compacts. A number of binary systems where the second compound is the minority phase were examined. These included $\text{Al}_2\text{O}_3\text{-V}_2\text{O}_3$, NaCl-KCl , CaO-CoO , and $\text{CaF}_2\text{-MgF}_2$. The effects of the additive were noticeable only under the following conditions:

1. The matrix powder and the additive have a significant mutual solubility.

2. The densification rate of the pure powder should be low. This is the case, for example, when the presintered density is less than 55% of the theoretical one, and the average particle sizes are larger than 0.5 micrometers.

3. The heating rates have to be fast, i.e., more than 15°C per minute. Insignificant effects of minor amounts of additive were found for the $\text{Al}_2\text{O}_3\text{-V}_2\text{O}_3$ system and for the NaCl-KCl system because of low mutual solubility or because of high densification rates of the pure NaCl powder. Significant effects were observed in the CaO-CoO and in the $\text{CaF}_2\text{-MgF}_2$ systems at high heating rates. The CaO-CoO system proved to be unsuitable since water contamination of the CaO system cannot be completely eliminated, thereby complicating the effects of the additive. Our investigations have, therefore, centered on the calcium fluoride-magnesium fluoride system.

The results show that below 900°C, i.e., ~80°C below the eutectic temperature, the presence of magnesium fluoride decreases the rate of coarsening and grain growth of the ceramic powder compact.

From about 50° below the eutectic temperature and up, the presence of magnesium fluoride increases the densification rate although substantial grain growth does not yet occur. Above the eutectic temperature, magnesium fluoride containing calcium fluoride exhibits strongly enhanced grain growth and increased densification rates compared to the pure calcium fluoride. The microstructures of the magnesium fluoride and pure calcium fluoride are compared in Fig. 1.

The results also show that the difference in densification rates between eutectic additive and pure ceramic powders increases with increasing heating rates. The reason for this phenomenon, as well as the increased densification rates at sub-eutectic temperatures, is still unclear. It was also found that the ceramic systems were extremely deformable while the liquid phase was active. This should be of importance to ceramic technology concerned with forming by hot pressing: the high ductility permits high hot forming rates.

RESEARCH PLANS FOR CALENDAR YEAR 1980

Gas/Solid Reactions. In our previous study, it appeared that the gas/solid reaction at the interface between the porous metal product scale and the oxide contributed importantly to the control of the gaseous reduction process. This interface will be studied in more detail by the thermogravimetric measurements of reaction rates as a function of time, temperature, and pressure in

the temperature interval where the CoFe_2O_4 is following the kinetic expressions of Eq. (1) in article 1. Microstructural characterization with scanning electron microscopy and transmission electron microscopy will be carried out, and the microstructural observations will be related to the interface reaction model. Segregation of cobalt and iron to the reaction interface will be studied by STEM on quenched, partially reduced samples. This information should be helpful in clarifying the relation between the thermodynamics and the kinetics of the interface reaction. At temperatures below 500°C it was noted that strong preferential grain boundary reaction occurs. The nature of this preferential attack will be studied.

Transient Liquid Phase Sintering. Experiments will be conducted on transient liquid phase sintering in the $\text{CaF}_2\text{-MgF}_2$ system. In particular, efforts will be devoted to clarifying the nature of pre-eutectic densification phenomena, and to study the role of the transient liquid intergranular phases in densification and grain growth.

1979 PUBLICATIONS AND REPORTS

LBL Reports

1. M. C. Rey and L. C. De Jonghe, "Gas/Solid Reactions: Hydrogen Reduction of Cobalt Ferrites and Al^{3+} Containing Cobalt Ferrites," LBL-8684, January 1979.

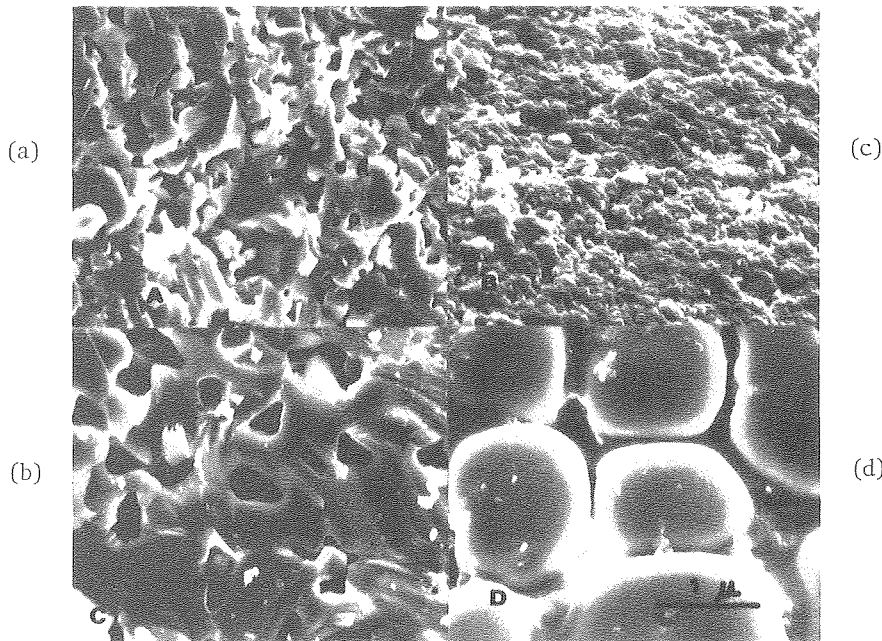


Fig. 1. Comparison of microstructures between pure CaF_2 and $\text{CaF}_2 + 10 \text{ wt.}\% \text{MgF}_2$. The eutectic temperature is 980°C. (A) Pure CaF_2 heated to 900°C at 15°C/min; (B) $\text{CaF}_2 + 10 \text{ wt.}\% \text{MgF}_2$, same conditions; (C) Pure CaF_2 heated to 1000°C at 15°C/min; (D) $\text{CaF}_2 + 10 \text{ wt.}\%$, same conditions.
(XBB 790-14711)

2. J. R. Porter and L. C. De Jonghe, "Hydrogen Reduction of Cobalt Ferrites," LBL-9801, June 1979.

Other Publications

1. J. R. Porter and L. C. De Jonghe, "Reduction Kinetics of Cobalt Ferrites," Abstract 140-B-79, Ceram. Bull. 58, 350 (1979).

2. M. C. Rey and L. C. De Jonghe, "Gas/Solid Reactions: Hydrogen Reduction of Cobalt Ferrites," Abstract 141-B-79, Ceram. Bull. 58, 350 (1979).

3. J. Allender and L. C. De Jonghe, "Gas/Solid Reactions: Hydrogen Reduction of Nickel Ferrites," Abstract 142-B-79, Ceram. Bull. 58, 350 (1979).

Invited Talks

1. L. C. De Jonghe, "Gas/Solid Reactions: Hydrogen Reduction of Mixed Oxides," Gordon Research Conference, Wolfeborough, N.H., August 1979.

2. L. C. De Jonghe, "Gaseous Reduction of Spinels," Cornell University, Ithaca, New York, August 1979.

e. Structure and Electrical Properties of Composite Materials*

Robert H. Bragg, Investigator

Introduction. The objective of our research on carbon materials is to delineate the relationship between the structure of hard carbon materials and their physical properties. These materials are said to be hard because they are difficult to graphitize, i.e., do not soften appreciably and remain unorderd or turbostratic even when heated to temperatures above 2000°C. Glassy carbon, GC, so-called because it is a black shiny material which fractures conchoidally, is used as the model material because it is obtainable in a chemically pure, monolithic form, and is thus convenient for a wide range of measurements of physical properties. X-ray diffraction and electron microscopy and diffraction studies have shown that GC consists of ribbons or laths of graphitic layers about 40 to 50 Å wide and 5 to 10 layers thick, intertwined somewhat like cooked macaroni or noodles so as to be impervious to gases, except He. Whereas the lath densities are those of turbostratic graphites, ca 2.26 g/cm³, the bulk densities of GC prepared at a 1000°C maximum process temperature is about 1.5 g/cm³. Glassy carbon thus has a pore volume approaching 40%, and our small angle x-ray scattering experiments show that the pores of GC have sharp edges, i.e., are slit shaped and have a specific surface area of the order of 500 - 1000 cm²/cm³. Glassy carbon is mechanically very hard with compressive strengths as high as 414 MPa (70,000 psi).

Our structural investigations have shown that GC is very similar to soft carbons in its response to heat treatments above 2200°C, and appears to graphitize with an activation energy of 225 ± 30 kcal/mole, close to the generally accepted 260 kcal/mole. However, our value was derived from kinetic studies of x-ray line broadening and it is not clear if the observed changes are due solely to crystallite growth, or possibly indicate a relief of local strain. Similarly our kinetic studies of internal specific surface area derived from small angle scattering measurements indicate that whereas the pore volume, or rather the density, is a nonkinetic function of HTT, the surface area decreases with an activation energy of 60 ± 10 kcal/mole close to the 70 kcal/mole accepted for a-direction vacancy migration in graphite. Both energies were derived from data for heat treatment temperatures, HTT, above 2200°C and are about 15% low, possibly because of poorly characterized heat treatment times, HTt. There seems to be a change in the mechanism at about 2200°C, and phase transformation is suspected.

Our data of electrical properties vs measurement temperature have heretofore been limited to 10 K. Following a disastrous fire which required rebuilding of many of our Dewar accessories, this in turn following extensive repairs of leaking joints with welds rather than solder, and repairs of our 5.0 tesla superconducting magnet, we have finally begun

to obtain electrical property data. In previous work we have shown that the magnetoresistance, $\Delta\rho/\rho$, can be expressed in terms of a single parameter, $H/T^{1/2}$, where H is the magnetic field strength, and T is temperature. Our main concern here is to see if $\Delta\rho/\rho$ saturates for sufficiently large $H/T^{1/2}$ and also to obtain accurate data of the Hall coefficient R_H vs HTT and T.

1. ELECTRICAL CONDUCTION AND HALL EFFECT IN GLASSY CARBON

Dennis F. Baker and Robert H. Bragg

Based on an extensive series of measurements Saxena¹ has shown that the electrical conductivity of GC can be expressed as

$$\sigma = \sigma_0 + [A \ln T / T_0] + B \exp(-CT^{-1/4}) \quad (1)$$

where T is temperature; σ_0 , A, and T_0 are functions of heat treatment temperature, HTT; and the term in brackets decreases with increasing HTT, becoming zero for $HTT > 2200^\circ\text{C}$. The term in $\exp(-CT^{-1/4})$ is unaffected by HTT up to 2750°C. While a σ versus $\exp(-CT^{-1/4})$ behavior has been reported by other workers,^{2,3} only in the present work have the first two terms been investigated. The term in $\ln T / T_0$ is associated with lattice defects, and σ_0 correlates with L_a , the mean lath width, and hence has been attributed to boundary scattering of charge carriers.

The magnetoresistance of our GC is negative for all HTT up to 2750°C, and for $HTT > 2200^\circ\text{C}$ can be expressed in terms of a single parameter, $H/T^{1/2}$, Fig. 1. It can be shown that negative magnetoresistance will occur when unpaired electron spins are present, and hence a correlation with paramagnetic susceptibility is implied. However, unpaired spins are also associated with lattice defects which should anneal when the material is heat treated, but instead the slope of $(\Delta\rho/\rho)^{1/2}$ versus $H/T^{1/2}$ increases as HTT increases. Furthermore $(\Delta\rho/\rho)$ does not appear to be time dependent, i.e., is a function only of HTT and not heat treatment time, HTt. Recently Bragg and Bose⁴ have found an explanation of this phenomenon in trying to rationalize the surprising decrease in density which occurs when GC is heated above its process temperature. As shown in article 2, the large anisotropy in thermal expansion coefficients leads to thermal stresses exceeding the fracture stress in GC, causing an irreversible volume increase. This local bond rupture increases the density of unpaired spins, and since the GC pores are not accessible to gases except He these unpaired spins remain unsaturated. Thus one expects the slope of $(\Delta\rho/\rho)^{1/2}$ vs $H/T^{1/2}$ to increase as HTT increases above the process temperature and this is shown in Fig. 2. However, while this correlation is consistent with the arguments just advanced what is needed is a direct demonstration that negative $\Delta\rho/\rho$ is associated with paramagnetism.

* This work was supported by the Division of Materials Sciences, Office of Basic Energy Sciences, U. S. Department of Energy.

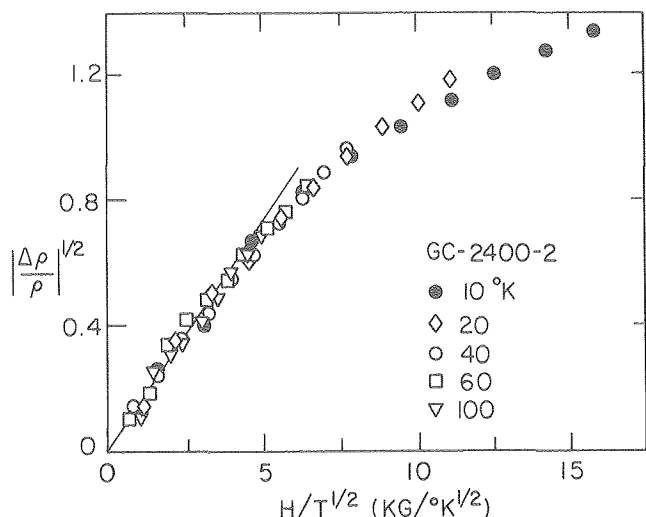


Fig. 1. Magnetoresistance in GC (taken from Ref. 1). H. has been held constant at 5.0 tesla (50 kG). (XBL 765-6927A)

and hence, by careful measurements of the temperature dependence of R_H and σ the temperature dependence of μ_H can be ascertained. However, it should be remembered that μ_H may not exhibit the same behavior as μ , the drift mobility. Only a few measurements of R_H in GC have been reported other than those of Saxena and Bragg.^{5,6} As shown in Fig. 3, the reported observations are in qualitative agreement in that R_H is not a strong function of T, is positive for $HTT < 1200^\circ C$, reaches a negative minimum for HTT around $1600^\circ C$, becomes positive as HTT increases. Also, all workers report that R_H is linear with H up to 2.2 Tesla, and in fact the linearity may extend to 15.0 Tesla.⁷ Unfortunately data have been obtained on only a few specimens, and typically measurements have usually been made at temperatures well above 4.2 K.

The $\exp(-CT^{-1/4})$ term in the expression for σ has been identified with hopping conduction between Anderson localized states, and Mott⁸ has classified GC as a Fermi glass. It has been shown that for hopping conduction the Hall mobility should be nearly independent of temperature,⁹ and the sign of R_H depends on the geometric arrangement of the microstructure. Also it changes sign depending

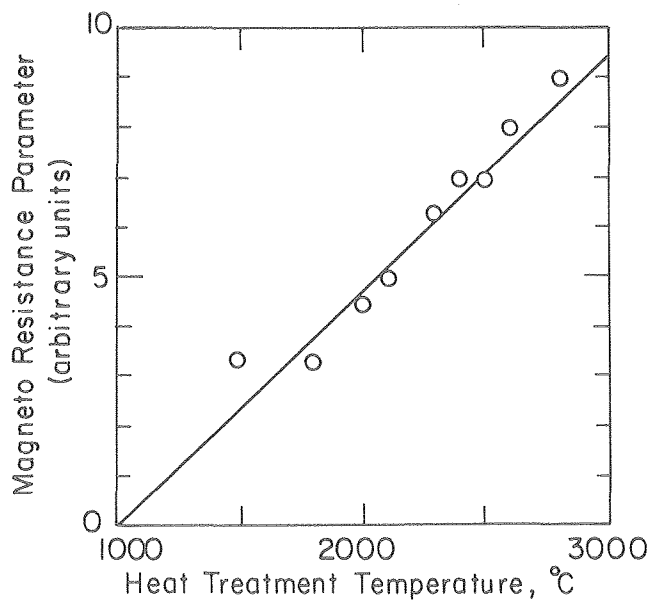


Fig. 2. Magnetoresistance parameter vs HTT. The ordinate is the initial slope of graphs in Fig. 1 for different HTT. (XBL 793-5991)

For conventional one or two band models of electrical conduction it is readily shown that

$$(\Delta\rho/\rho) = (\mu H)^2 \quad (2)$$

where μ is the mobility. If μ varies as $T^{-1/2}$ then apart from the negative sign $(\Delta\rho/\rho)^{1/2}$ will be proportional to $H/T^{1/2}$ at low fields, providing a natural explanation of the occurrence of $H/T^{1/2}$ as a single valued parameter. The Hall mobility μ_H can be obtained from

$$\mu_H = R_H \cdot \sigma \quad (3)$$

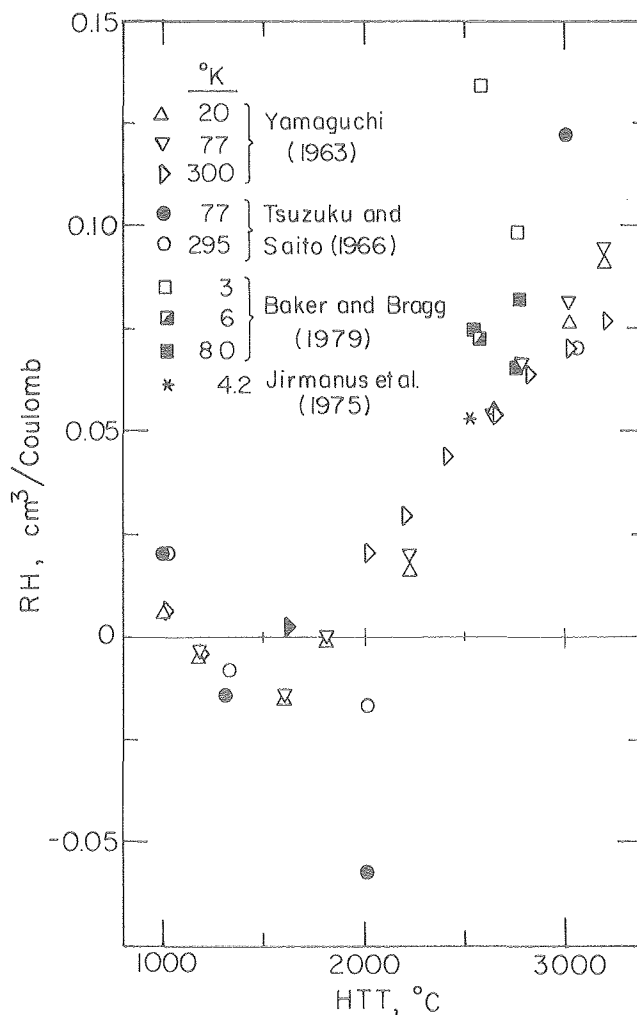


Fig. 3. Hall Coefficient of Glassy Carbon as a function of HTT. (XBL 7912-14579)

upon whether the local bonding is sp^2 or sp^3 , as well as whether the majority carriers are electrons or holes.¹⁰ One can thus anticipate that the observed sign reversals in R_H are most likely associated with changes in the density of states, since it has been shown that as HTT increases the bonding in GC (typically a mixture of sp^2 and sp^3) the proportion of sp^2 character increases.¹¹

A rapid change in the sign of R_H with HTT could give the temperature of a phase transformation, as has been discussed by Whittaker and Tooper.¹² The published data, plus our recent results, Fig. 3, show that near the sign reversal around 2000°C, the HTT at which the graphitization phase transformation is suspected, the changes in R_H are gradual. It happens that R_H in graphite is a strong function of temperature,¹³ increases with increase in grain size, decreases with increasing crystal perfection, and generally increases with increasing field especially at low temperatures.

Unfortunately there are few similarities between R_H in graphite and R_H in GC. What is needed is more data of R_H vs HTT and T. The present results indicate that R_H is not a strong function of T for T below 300 K, but can be measured with sufficient precision to examine the dependence on T and HTT.

* * *

1. R. Saxena, "The Structure and Electrical Properties of Glassy Carbon," Ph.D. thesis, LBL-5129, 1975.
2. W. Bucker, *J. Non-Cryst. Sol.* 12, 115 (1973).
3. T. Suzuki and K. Saito, *Jap. J. Appl. Phys.* 5, 738 (1966).
4. R. H. Bragg and S. Bose, Proceedings of the 14th Biennial Carbon Conference, University Park, Pennsylvania, June 1979, p. 189-190.
5. T. Yamaguchi, *Carbon* 1, 47 (1963).
6. M. Inagaki, Y. Komatsu, and J. Zanchetta, *Carbon* 7, 163 (1969).
7. M. Jirmanus, H. H. Sample, and L. Neuringer, *J. Low Temp. Phys.* 20, 229 (1975).
8. N. F. Mott and E. A. Davis, *Electronic Processes in Non-Crystalline Materials*, 2nd ed., Clarendon Press, Oxford (1979).
9. L. Friedman, *J. Non-Cryst. Sol.* 6, 329 (1971).
10. D. Emin, *Phil. Mag.* 35, 1189 (1977).
11. R. Saxena and R. H. Bragg, *Carbon* 12, 210 (1974).
12. A. Whittaker and B. Tooper, *J. Am. Ceram. Soc.* 57, 433 (1974).
13. I. L. Spain, "The Electronic Properties of Graphite," *Chemistry and Physics of Carbon*, P. L. Walker, Jr. and P. A. Thrower, eds., Marcel Dekker, Inc., New York, Vol. 8 (1973), p. 1-150.

2. EFFECT OF HYDROSTATIC PRESSURE AND GRINDING ON THE DENSITY AND PORE STRUCTURE OF GLASSY CARBON†

Dennis F. Baker, A. S. Rao, and Robert H. Bragg

It is well known that the density of GC decreases when the material is heated above its maximum process temperature, typically 1000°C. The density change is very large, going from about 1.5 g/cm³

for 1000°C HTT to about 1.3 g/cm³ for 2700°C HTT. Fischbach and Rorabaugh¹ studied the effects of heating and cooling rates on the density of GC. They concluded that about 10% of the density decrease could be attributed to a loss of weight; about 90% was said to result from volume expansion resulting from the internal pressure generated by the continued evolution of volatile pyrolysis products within the closed pores. Bose² has shown that once a maximum HTT is reached, prolonged isothermal heat treatment does not produce further density decreases and suggested that the density decrease is caused by an irreversible opening of cracks resulting from strains due to the mismatch of thermal expansion coefficients. Bragg³ analyzed the density vs HTT data and found that they imply a thermal expansion coefficient of $22.9 \times 10^{-6}/^\circ\text{C}$, close to the thermal expansion mismatch ($\alpha_c - \alpha_a$) of $25.0 \times 10^{-6}/^\circ\text{C}$ for graphite. Bragg and Bose⁴ subsequently refined the calculation of the implied strain as shown in Fig. 1, and showed that this would produce thermal stresses of the order of 53×10^4 MPa (7.69×10^6 psi) comparable to the failure stress of graphite in the presence of "Griffith flaws" of size ca. 1.0 nm. This implied flow size is consistent with the scale of the microstructure seen in lattice image photographs of GC.

In the experiments of Fischbach and Rorabaugh, densities were obtained from measurements of buoyancy. In the work reported here several experiments bearing on the density and pore structure of GC were performed. In one set both the weight and sample dimensions, nominally 6.0 gm and 5.0 cm x 2.5 cm x 0.32 cm, respectively, were measured to an accuracy of 0.0001 gm and 0.001 cm respectively before and

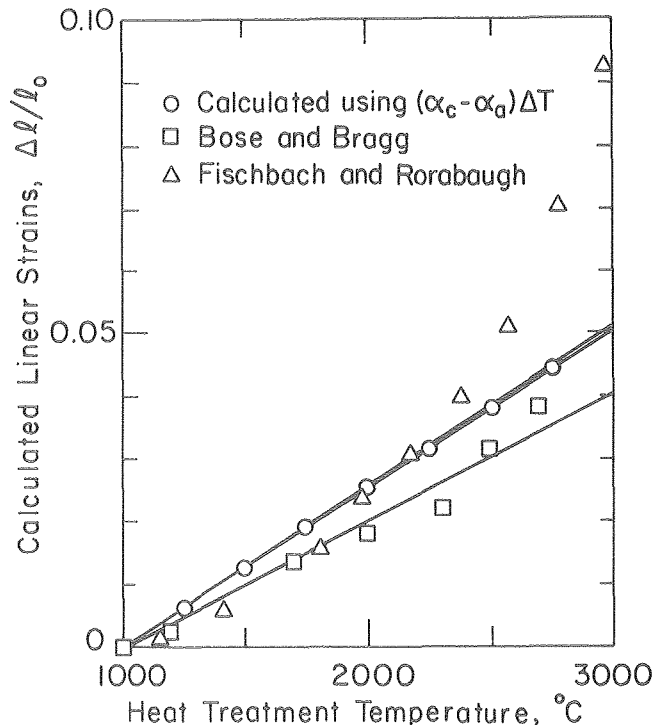


Fig. 1. Irreversible dilation caused by thermal expansion mismatch. Calculated from density vs HTT. (XBL 793-5989)

Table 1. Mass and volume changes in heat treated GC.

| Heat Treatment Temperature (°C) | Percentage Weight Loss | Percentage Increase in Dimensions | | |
|---------------------------------|------------------------|-----------------------------------|-------|-----------|
| | | Length | Width | Thickness |
| 1000 - 1 | 1.02 | 1.002 | 0.985 | 1.1 |
| 2700 - 1 | 1.29 | 4.275 | 3.26 | 3.92 |

after heat treatment. In Table 1 the directly measured mass and dimensional changes are shown. It can be seen that some mass loss occurs even when material previously heated at 1000°C is reheated at this temperature, and there is some volume expansion as well. However, the additional weight loss upon heating to 2700°C is negligible whereas the volume expansion is about 11%.

In another series of experiments done by Baker and Bragg⁵ samples of GC were compared before and after grinding in a vibrating ball mill. The initial objective was to determine if the intertwined "laths" in GC could be flattened. If this happens the wide range diffraction patterns will have narrower x-ray line profiles. The material chosen was GC given a 1000°C heat treatment and samples were ground dry or using 1,1,1-trichlorethane as a grinding aid. Careful measurements showed that grinding produced a slight sharpening of the line profiles. However, the most convincing evidence of structural change was obtained from small angle x-ray scattering measurements. As shown in Fig. 2 grinding caused an increase in the radius of gyration from about 8 to 8.5 Å. In Fig. 3 it can be seen that grinding wet or dry changes the pore structure as well as the specific surface area S/V. The samples were further analyzed for density, particle size using scanning electron microscopy, and specific surface area using both the BET single point method and calculations using the small angle x-ray scattering data. The results, Table 2, show that grinding closes off some surface while at the same time opening some pores to helium, but the internal surface area remains inaccessible to N₂ molecules.

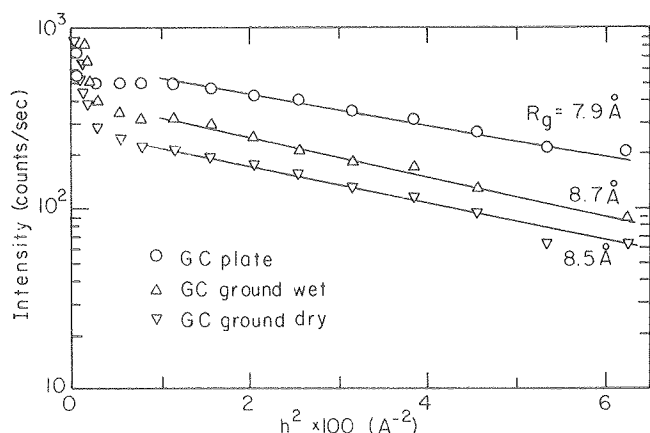


Fig. 2. Guinier plots of small angle scattering data. (XBL 793-5874)

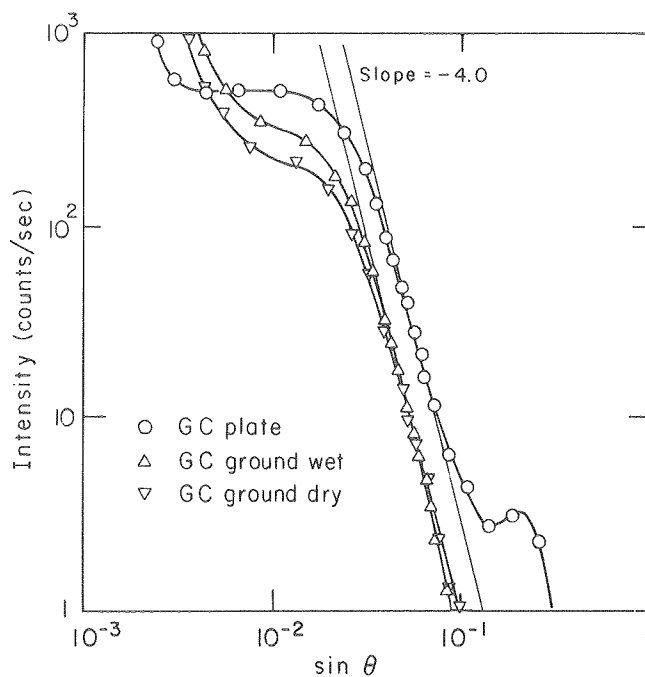


Fig. 3. Pored plots of small angle scattering data. (XBL 793-5875)

In a third series of experiments GC was subjected to an external hydrostatic compression instead of grinding. Samples heated in the range 1000 to 2700°C for one hour were placed in a pressure vessel using 20 wt% turbine oil as working fluid and pressurized up to 1331 MPa (225,000 psi) for periods of 5 minutes, after preliminary tests showed that the density was not altered by prolonged compression. The pre- and post-compression densities were measured in kerosene and water to an accuracy of ± 0.001 g/cm³. The results, shown in Figs. 4 and 5, indicate that very large mechanical stresses produce only small deformations in GC. Although one cannot extrapolate from these data to the properties of GC in tension, it seems unlikely that expansion of pyrolysis gases can be the cause of the observed density decreases. It seems most plausible that the density decreases are caused by the thermal stress mechanism.

* * *

† Brief version of LBL-10224.

1. D. B. Fischbaugh and M. E. Rorabaugh, 13th Biennial Carbon Conference, Irvine, July 1977 (Post Deadline Paper).

Table 2. Characterization of as received and ground GC.

| | As Received Plate | Ground Wet | Ground Dry |
|--|----------------------|---------------|---------------|
| S/V (m^2/cm^3) (calculated from SAXS) | 1325 | 954 | 1028 |
| S/V (m^2/cm^3) (using BET and N_2) | <10 | <10 | <10 |
| Rg (\AA) | 7.9 | 8.7 | 8.5 |
| Density (helium) | 1.50 | 1.98 | 1.94 |
| Density (water and kerosene) | 1.50 | 1.50 | 1.50 |
| Particle size (μm) | --- | 0.3 - 8.0 | 0.3 - 1.50 |
| Pore volume fraction | 0.321 | .735 | .754 |

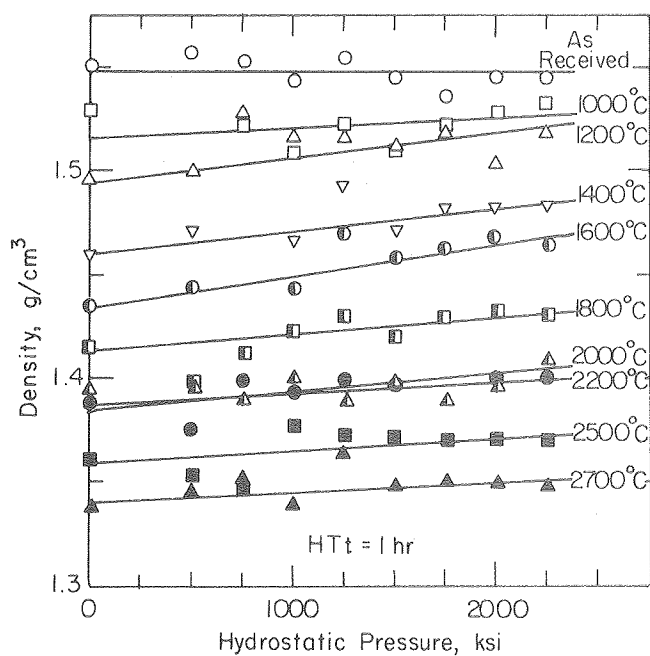


Fig. 4. Effect of hydrostatic pressure on the density of GC. (XBL 7912-14580)

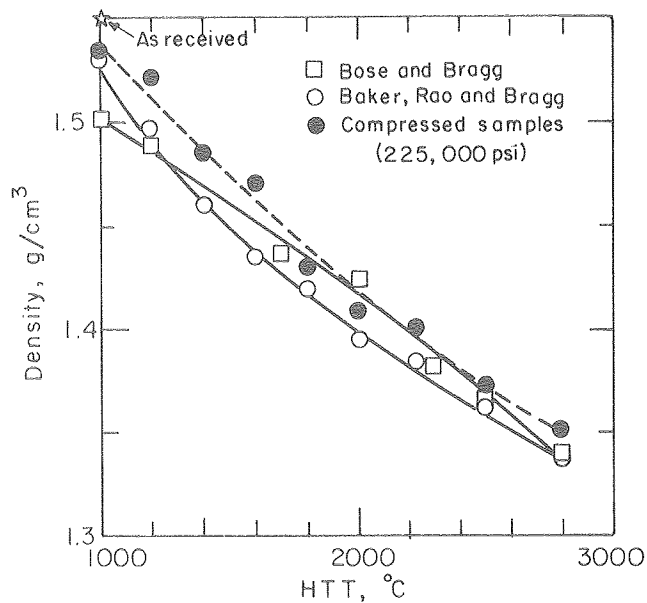


Fig. 5. Effect of 225,000 psi hydrostatic pressure on the density of GC. (XBL 7912-14581)

2. S. Bose, Pore Structure and Growth Kinetics in Carbon Materials, Ph.D. thesis, LBL-7638, (1978).

3. R. H. Bragg, "Density Decrease and Mrozowski Cracks in Glassy Carbon," MMRD Annual Report 1978, LBL-8580, pg. 121.

4. R. H. Bragg and S. Bose, Thermally Induced Density Changes in Glassy Carbon, 14th Biennial Carbon Conference, University Park, PA, June 1979, p. 189-190.

5. D. F. Baker and R. H. Bragg, Void Collapse in Glassy Carbon, 14th Biennial Carbon Conference, University Park, PA, June 1979.

3. CORRECTION FOR COMPTON SCATTERING IN GLASSY CARBON DIFFRACTION PATTERNS[†]

Leo G. Henry and Robert H. Bragg

In previous work we have used wide range x-ray diffraction or small angle x-ray scattering (SAXS) to characterize the structure of GC. In the latter, the SAXS was measured in transmission and used to calculate the specific surface area, S/V of samples. Since our measurements showed that at a given temperature the sample volume V is independent of time, the observed changes in S/V with HTT and HTt could be used to characterize surface area changes.¹ The relevant equation takes the form

$$S/V = 4c(1-c) \frac{\lim_{h \rightarrow \infty} [h^3 J(h)]}{\int_0^{\infty} hJ(h)dh}$$

or

$$S/V = \pi c(1-c) \frac{\lim_{h \rightarrow \infty} [h^4 I(h)]}{\int_0^{\infty} h^2 I(h)dh}$$

depending upon whether the experimental situation employs slit or point collimation. Here, c = fraction of sample occupied by matter, $h = 4\pi \sin\theta/\lambda$; J(h) = intensity for slit collimation; and I(h) = intensity for point collimation. There has been some uncertainty concerning which approximation is applicable to GC, because instances have been reported wherein the intensity was said to decrease as h^{-n} , where n might range from 2 to 3. Recent careful measurements have shown that these reports are in error. For the full range of heat treatment temperatures employed in this work, 1000 to 2800°C, the SAXS extends to such large values of h that our experimental situation always approximates point collimation, for which n = 4.

This result simplifies the correction of our wide range diffraction patterns for SAXS enormously. The corrections for Lorentz-Polarization, atomic scattering factor variations, and distortion due to low specimen² absorption are easily made. It appears that the procedures for correcting for Compton scattering that we have used heretofore are adequate for obtaining a fully corrected 002 line profile in GC as shown in Fig. 1. However, we need to determine if the observed narrowing of the widths of x-ray line profiles induced by heat treatment are due to "crystallite" growth or stress relief. To do this, it is necessary that at least two orders of 00l and hk0 reflections be measured in order to separate size and strain components. Since the GC reflections are weak and very diffuse, exact corrections for the large contribution of the Compton component to the total intensity in the regions where the (10) and (11) bands and the (004) reflections occur are mandatory.

In previous work we have assumed that in pyrolytic graphite, PG, the material is of high purity, and sufficiently close to a single crystal that far from a reciprocal lattice point the observed x-ray

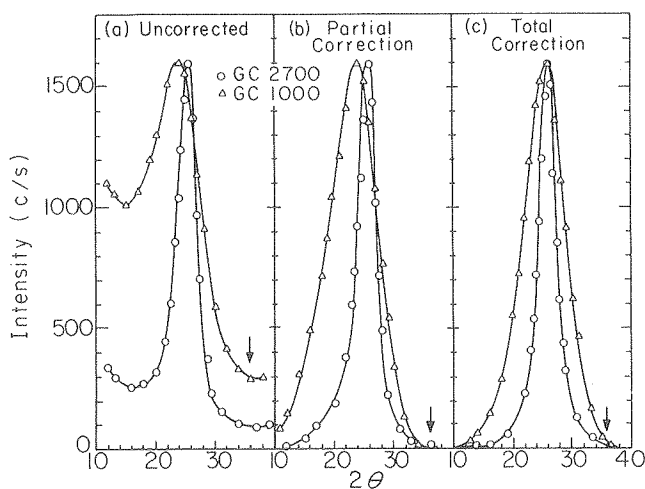


Fig. 1. Effect of corrections on the 002 line profile of glassy carbon. (XBL 793-5970)

intensity is due mainly to Compton scattering. Thus if the linear absorption coefficient is μ and the material is thick, the intensity will be totally caused by Compton radiation, and proportional to $1/\mu^2$. Thus a separate measurement of background intensity and μ on PG can be used to determine the background level, i.e., the contribution of Compton scattering to the total intensity for a GC sample having the same μ . A paper on this method submitted to Carbon has been returned with the (valid) criticism that this procedure of determining the Compton intensity level should be justified by comparison with an accepted method. We have decided to utilize a method which is based on the difference of the intensity of a diffracted beam when a filter is placed in the incident beam or in the diffracted beam. Our preliminary estimates of the Compton component obtained in this way differ from that obtained using PG by an order of magnitude. It is felt that the result obtained from PG is more nearly correct, and the low estimate obtained from the differences in absorption are caused by poor monochromatization. We have decided to use balanced filters to obtain better monochromatization and have just initiated this work.

* * *

[†]Brief version of LBL-10225.

1. S. Bose, Pore Structure and Growth Kinetics in Carbon Materials, Ph.D. thesis, April 1978, LBL-7638.
2. R. H. Bragg and C. M. Packer, Rev. Sci. Instrum. 34, 1202 (1963).

4. SHORT TERM HEAT TREATMENT OF GLASSY CARBON SAMPLES

B. N. Mehrotra and R. H. Bragg

As mentioned previously, it is felt that inaccurate specification of time at heat treatment temperature, HTt, is the major contributor to the slightly low activation energies obtained in our

studies of graphitization and S/V kinetics. Heretofore, in making a run samples were inserted in the furnace following which it was purged, back-filled with argon, and heated. In a typical run, several hours would elapse before the desired HTT was reached. After the desired HTT, the power was switched off, and the sample would be furnace-cooled until it could be removed from the furnace. It is obvious that, for time less than several hours, the effective HTT is difficult to specify but in general would be underestimated. As reported in the 1978 Annual Report it was decided to modify our ASTRO Furnace, Model 1000 - 2560 to permit a rapid insertion and rapid removal of samples from the hot zone. Because its design and operation are not standard in high-temperature heat treatment, it seems worthwhile to provide a few details here.

The furnace has the following features: (1) it can operate up to 3000°C in inert or reducing atmospheres (we use extra pure helium), (2) the heating and cooling is very fast, requiring less than one hour to and from room temperature to 3000°C, and (3) the power needed for the furnace is 20 kVA. The unique feature of the furnace is a graphite turnstile with radial slots to accommodate 10 samples of maximum size 2 in x 1 in x 0.1 in. This work charge is normally held outside the hot zone; and, when desired, quickly pushed into the hot zone. Thereafter any sample can be dropped individually out of the hot zone by rotating the turnstile to a slot over a bottom hearth assembly, falling into a lower chamber attached to the bottom of the furnace. Samples fall onto a graphite felt pad and if desired may be cooled very rapidly by admitting an inert gas. A removable cover is provided for taking out samples after the furnace is cooled. Furnace temperature is measured with a disappearing optical pyrometer calibrated for temperatures to 2800°C. A Rayotube pyrometer, which works on the blackening disk principle, is used to record temperature on an AZAR x-y recorder. The indicator pen works in conjunction with a set-point on the x-y recorder to control the power input to the furnace, so that temperatures are controlled to $\pm 20^\circ\text{C}$. The furnace has an interlock shut-off provision, in case of loss of cooling water.

Figure 1 shows operational characteristics for heat treatments at 1600°C. With the turnstile in the hot zone prior to power on curve (1) is obtained. With the turnstile initially outside the hot zone, curve (2) is obtained. Not surprisingly, the hot zone heats faster. The sharp dip in curve (2) is caused by the insertion of the turnstile into the hot zone. Figure 2 shows similar data for heat treatments at 2500°C. It can be seen that the time required to reach the desired HTT is about 7 minutes compared to nearly 2 hours in the normal mode.

It is felt that with the drop quench mechanism the uncertainties in our specification of HTT are minimized and far better kinetic data will be obtained than in our previous work.

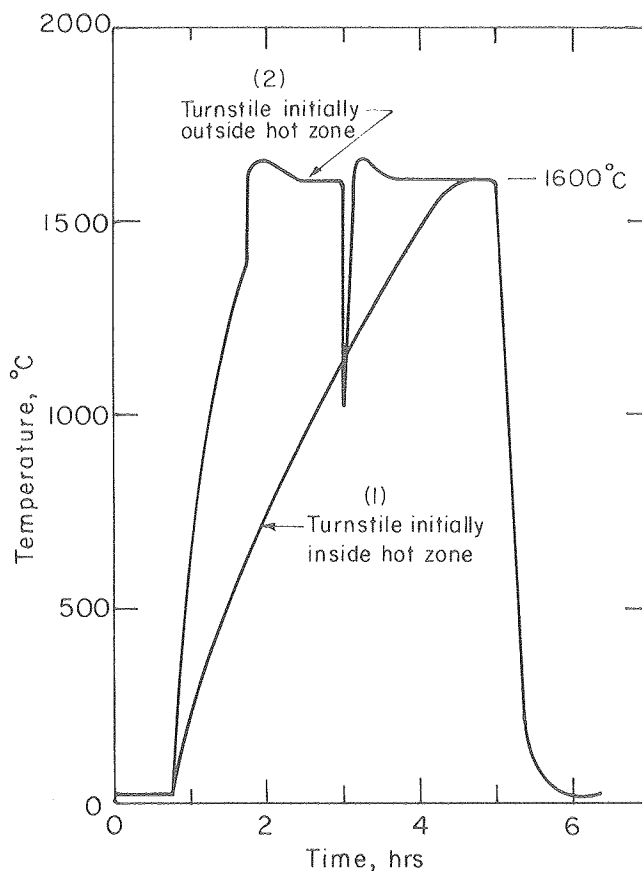


Fig. 1. Heat treatments of GC samples at 1600°C. The sharp dip in (2) indicates sample insertion. (XBL 7912-14582)

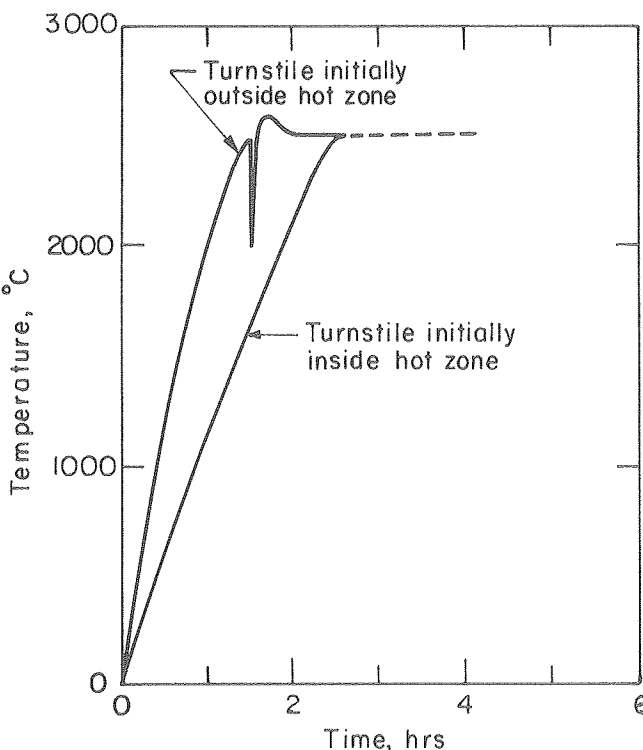


Fig. 2. Heat treatments of GC samples at 2500°C. The sharp dip in (2) indicates sample insertion. (XBL 7912-14583)

RESEARCH PLANS FOR CALENDAR YEAR 1980

Our research capability is far better at year end 1979 than a year ago. After many misfortunes, including a fire which damaged many of the accessories to our Dewar (which had already been out of operation several months due to a relocation in Bldg. 62), the low temperature electrical property facility is finally back in operation and electrical property data down to at least 3.0 K can be achieved. In addition, the drop quench mechanism for rapid insertion of samples in our ASTRO heat treatment furnace has been checked (see article 4), and it is now possible to do kinetic runs for which the uncertainties in HTt are reduced to a few minutes. The group was joined in January 1979 by Bhola Mehrotra, and shortly thereafter by Dr. A. S. Rao, a Postdoctoral Fellow. During the summer 1979, an intensive training session in x-ray diffraction and small angle x-ray scattering theory and practice was conducted. We plan to do the following in 1980:

Electrical Properties. Dennis Baker will concentrate on measurements of R_H and σ , with a few kinetic runs to verify our suspicion that $(\Delta\rho/\rho)$ is independent of HTt. The primary objective of the measurements of σ is to determine if B and C in Eq. (1) of article 1 are truly independent of HTt and HTt, what is their physical significance and what is the significance of the $\ln T/T_0$ term. With the new low temperature capability it should be possible to decide whether or not $\Delta\rho/\rho$ saturates. Still to be obtained is a direct correlation of $\Delta\rho/\rho$ with paramagnetic susceptibility, and Dr. A. S. Rao will investigate this problem. The measurement of R_H and σ will be combined to obtain μ_H and thus afford a test of the hypothesis that μ_H varies as $T^{-1/2}$.

Graphitization. Dr. A. S. Rao and B. Mehrotra will complete the series of heat treatments begun towards the end of summer 1979. It is intended that these samples be used in a re-determination of ΔH for graphitization (L. G. Henry), a re-determination of ΔH for point defect annealing (new student), as well as completing the measurements of electrical properties for the thesis of D. Baker. Following completion of the heat treatments, B. Mehrotra will begin to learn the techniques of measurements of electrical properties at cryogenic temperatures. Of primary importance will be the search for evidence of a phase transformation at about 2200°C, but techniques to measure electrical properties of intercalation compounds will be evaluated.

Point Defect Annealing. In addition to the GC samples, samples of pyrolytic graphite, PG, will be heat treated and kinetic studies of SAXS of these oriented materials will be made to verify that the activation energy obtained in the analysis of S/V in GC does in fact pertain to vacancy migration in the a-direction in graphitic layers. This work will probably be assigned to a new student, but may fall to L. G. Henry. Since the SAXS from PG is weak it will require use of the Oak Ridge National Laboratory, the national facility for small angle x-ray scattering. A Ferris wheel type holder for multiple specimen runs without breaking the system vacuum in the ORNL 10-meter facility has already

been built. Here our major problem is lack of well characterized specimens of PG.

Graphite Intercalation Compounds. Shortly after joining the group Dr. Rao was assigned to review the literature and recommend suitable binary, or more accurately pseudo-binary systems for study. The working hypothesis is that such systems can be regarded as two-dimensional binary solid solutions. Intercalation compounds containing $AlCl_3$ and $FeCl_3$ were selected as end members because, while difficult to prepare, they are said to be stable in room ambients. Our experience thus far has been that the preparation is difficult (sometimes explosive), owing perhaps to our use of commercial PG instead of the widely-used Union Carbide HOPG. Because of its scarcity we are attempting to replace HOPG with heat treated PG. Dr. Rao will accelerate this effort in preparation and continue his work to develop a magnetic susceptibility measurement capability.

Coal Characterization. The x-ray patterns of coals are strikingly similar to those of GC, with the addition of small amounts of a well-crystallized phase and a glass-like phase. Some SAXS is evident and the background obtained with $CuK\alpha$ radiation is high probably due to the presence of iron. As in GC, heat treatment induces some crystallinity. It seems highly relevant to ascertain if our x-ray techniques of characterizing GC are applicable to coals. Dr. O. O. Adewoye, Department of Physics, University of Ife, Nigeria, who spent several months in our x-ray laboratory during the summer, is expected to join us in the fall 1980 for a sabbatical year and will work on this problem.

1979 PUBLICATIONS AND LBL REPORTS

Other Publications

1. D. Baker and R. H. Bragg, "Void Collapse in Ground Glassy Carbon," in Proceedings of the 14th Biennial Carbon Conference, University Park, PA., June 1979, pp. 127-8.
2. L. G. Henry and R. H. Bragg, "Anomalous Large Layer Spacings in Glassy Carbon," in Proceedings of the 14th Biennial Carbon Conference, University Park, PA., June 1979, pp. 129-30.
3. R. H. Bragg and S. Bose, "Thermally Induced Density Changes in Glassy Carbon," in Proceedings of the 14th Biennial Carbon Conference, University Park, PA., June 1979, pp. 189-90.

LBL Reports

1. D. Baker, A. S. Rao, and R. H. Bragg, "Effect of Thermal and Mechanical Stress on the Density of Glassy Carbon," LBL-10224, December 1979.
2. S. Bose, L. G. Henry and R. H. Bragg, "Correction of Diffraction Patterns of Glassy Carbon," LBL-10225, December 1979.

Invited Talks

R. H. Bragg, "Carbon: An Old Dog Learning New Tricks," Percy Lavon Julian Memorial Lecture, 1978-79, Howard University Chapter, Sigma Xi, Washington, D.C.

f. High Temperature Oxidation and Corrosion of Materials*

David P. Whittle, Investigator

Introduction. The objective of this program is to gain an understanding of the corrosion chemistry and materials behavior in high temperature environments. Of particular interest are the mechanisms of attack in environments containing more than one reactive species, for example sulfur and oxygen. Sulfur is a critical impurity in almost all energy sources and leads to accelerated, and often unacceptable rates of metal degradation. In addition, the competitive formation of potentially more than one phase as a reaction product is an important fundamental problem, and can only be truly understood if the underlying thermodynamic and transport properties of the systems, and their interrelation, are identified. Sulfur can appear in a number of forms. In entirely gaseous environments it can appear as H_2S when the oxidizing potential of the atmosphere is low, such as might exist in energy conversion systems, or as SO_2/SO_3 at higher oxygen potentials, such as those produced by fuel combustion. It may also appear in sulfatic deposits, either as a solid, such as $CaSO_4$ in fluidized bed combustion systems, as inorganic and organic sulfur compounds in coal char, or as a liquid alkali-metal sulfate in coal-ash, or turbine-blade deposits. This last year has been spent primarily in establishing the typical behavioral patterns of common materials in these types of environments, and identifying the common mechanisms. In addition, development of definitive models of alloy reactions with single oxidants has continued. The individual projects are described below.

1. EQUILIBRIA IN GASEOUS SYSTEMS

D. P. Whittle, I. M. Allam, and H. Hindam

Correct interpretation of the behavior of metals and alloys in multicomponent gas mixtures at high temperature requires that the equilibrium conditions in the gas phase be known. In addition, it is also important to establish how the composition of the gas mixture, assuming it is at equilibrium, and in particular how the activities of the oxygen and sulfur reactants will change when one of the components is removed from the gas by reaction with the metal. This may not be critical in flowing, well-mixed systems, but where stagnant pockets of gas can exist, such as beneath inert deposits, in crevices, or within porous scales, it can have serious consequences.

In the S-O-H system, there are at least 14 possible gaseous species: H_2 , O_2 , S_2 , S_4 , S_8 , H_2O , SO_2 , SO_3 , SO , O , H , S , OH , etc. However, in the temperature, pressure and overall gas composition ranges of interest in the present context, sulfur species higher than the dimer, atomic oxygen, hydrogen and sulfur, and free radicals such as OH can be ne-

glected. The equilibrium composition of any gas mixture is calculated through the equilibrium constant approach. In essence two types of equations are involved: Mass balance equations which ensure that the total content of the three atomic species are conserved, and the intergaseous equilibria. A computer program has been written to solve the system of eight, nonlinear simultaneous equations for any given input composition. Solutions have been obtained at temperatures in the range 600-1200°C intervals, for a total system pressure of 1 atm. and for input compositions covering the whole range of oxygen and hydrogen contents and up to a sulfur level equivalent to 10% H_2S or SO_2 . Table 1 shows a sample output. Figure 1 shows the P_{S_2} in the equilibrated gas as a function of P_{O_2} at 1000°C for four different sulfur levels and a number of different oxygen levels.

As a whole, the S-O-H system can be divided into three sectors depending on the relative amounts of oxygen, sulfur and hydrogen in the gas mixture, best expressed as N_O , N_S and N_H where N_i is the fraction of total atoms of species i . At low oxygen contents, $N_S + N_O \leq 1/3$, H_2S - H_2O - H_2 are the major molecular species: the sulfur and oxygen potentials are relatively independent with the sulfur potential decreasing slightly with decreasing oxygen potential at a fixed sulfur content. At intermediate oxygen and sulfur contents, $N_S + N_O \geq 1/3$, $N_S \leq 1/3$ and $N_O - N_S \leq 1/3$, H_2O - H_2S - SO_2 are the major molecular species, and within this region sulfur and oxygen potentials are strongly interrelated, being inversely proportional to one another. In the third sector, $N_O - N_S \leq 1/3$, O_2 - SO_2 - H_2O are the major species; sulfur potentials are very low, and again are independent of oxygen potential.

These interdependencies between the sulfur and oxygen potentials have a considerable influence on likely corrosion behavior. The regime in which sulfur and oxygen potentials are strongly interdependent represents a very small change in overall composition, corresponding to almost exact, stoichiometric combustion of a fuel for example, and most practical combustion environments would be more oxygen-rich. It is nevertheless important since regions of stagnant gas within porous deposits or crevices, for example, could approach these conditions by reacting with oxygen to form oxides. In this context, the buffering capacity of the gas, or its ability to resist a change in sulfur potential caused by removal of oxygen in reaction is critical. These buffering capacities can be calculated from the equilibrated compositions computed above, and are equally important in determining corrosion behavior as the often quoted sulfur and oxygen potentials.

An additional feature evident from the calculations is the relative position of the maximum in sulfur potential as a function of oxygen potential with respect to the stabilities of the sulfides and oxides of the common alloying elements, Ni, Co, Cr, Fe, Al, etc. With the Ni-S-O system the maximum

* This work was supported by the Division of Materials Sciences, Office of Basic Energy Sciences, U. S. Department of Energy.

Table 1. Equilibrated compositions in the S-O-H system; input composition: $H_2S = 8.9\%$, $H_2O = 90.1\%$, $SO_2 = 1.0\%$, $N_S = 0.033$, $N_H = 0.66$, and $N_O = 0.307$.

| TEMP (C) | H ₂ S | H ₂ O | SO ₂ | H ₂ | SO ₃ | SO | O ₂ | S ₂ |
|----------|------------------|------------------|-----------------|----------------|-----------------|---------|----------------|----------------|
| 600. | -1.0737 | -.0442 | -2.0527 | -2.6350 | -10.4114 | -6.4515 | -18.6849 | -2.5416 |
| 650. | -1.0816 | -.0442 | -2.0492 | -2.3996 | -10.1494 | -6.0467 | -17.5553 | -2.4441 |
| 700. | -1.0917 | -.0445 | -2.0365 | -2.1916 | -9.9007 | -5.6783 | -16.5333 | -2.3544 |
| 750. | -1.1047 | -.0450 | -2.0135 | -2.0081 | -9.6597 | -5.3393 | -15.6010 | -2.2707 |
| 800. | -1.1210 | -.0457 | -1.9805 | -1.8465 | -9.4236 | -5.0252 | -14.7444 | -2.1924 |
| 850. | -1.1409 | -.0467 | -1.9387 | -1.7042 | -9.1914 | -4.7328 | -13.9529 | -2.1198 |
| 900. | -1.1648 | -.0481 | -1.8902 | -1.5788 | -8.9634 | -4.4602 | -13.2182 | -2.0537 |
| 950. | -1.1929 | -.0497 | -1.8369 | -1.4681 | -8.7407 | -4.2059 | -12.5339 | -1.9948 |
| 1000. | -1.2250 | -.0517 | -1.7809 | -1.3700 | -8.5243 | -3.9689 | -11.8947 | -1.9438 |
| 1050. | -1.2611 | -.0540 | -1.7239 | -1.2829 | -8.3153 | -3.7482 | -11.2962 | -1.9011 |
| 1100. | -1.3009 | -.0567 | -1.6670 | -1.2053 | -8.1143 | -3.5428 | -10.7345 | -1.8668 |
| 1150. | -1.3444 | -.0597 | -1.6115 | -1.1360 | -7.9220 | -3.3521 | -10.2065 | -1.8410 |
| 1200. | -1.3911 | -.0630 | -1.5580 | -1.0738 | -7.7385 | -3.1750 | -9.7093 | -1.8235 |
| 1250. | -1.4403 | -.0666 | -1.5072 | -1.0180 | -7.5641 | -3.0108 | -9.2403 | -1.8141 |

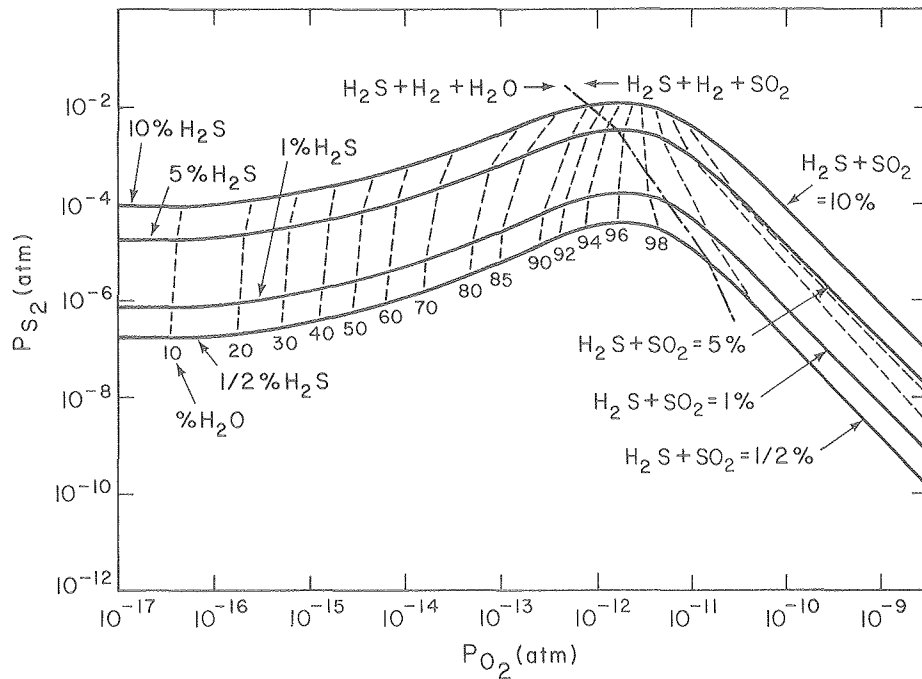


Fig. 1. Sulfur potential as a function of oxygen potential in equilibrated gas mixtures in the S-O-H system. (XBL 802-262)

lies close to the co-existence line for NiS and NiO, and as a consequence this interdependency between sulfur and oxygen potentials is much more critical for Ni-base materials. In other systems the maximum in the sulfur/oxygen potential curve lies to the right of the sulfide/oxide stability line and

it is unlikely that localized fluctuations in gas composition can ever shift the gas into a purely sulfide forming regime, although sulfides may form via other mechanisms.

* * *

2. CORROSION MECHANISMS IN COMPLEX ENVIRONMENTS OF LOW OXIDIZING POTENTIAL

I. M. Allam and D. P. Whittle

Pure Fe. Competitive formation of oxides and sulfides in environments that can sustain the formation of either or both phases has been studied in an attempt to establish the critical parameters which control the overall corrosion process. Pure iron samples were exposed to $H_2O-H_2-H_2S$ mixtures of various compositions introduced into the test rig through metered flows. A constant sulfur fugacity, 8.4×10^{-6} atm, was used for most of the experiments while the oxygen fugacity was varied over the range in which sulfide or oxide is the more stable phase.

Figure 1 shows a stability diagram for the Fe-S-O system with the gaseous environments included. At a $P_{O_2} = 3.2 \times 10^{-12}$ atm (point A), which is inside the Fe_3O_4 stability region, no sulfidation occurs and the growth rate of the FeO is independent of the presence of sulfur in the environment. The reaction path lies totally within the oxide region and this is related to the low solubility of sulfur in the Fe_3O_4 phase formed at the surface. When the P_{O_2} is reduced, 3.3×10^{-13} atm (point B), FeO is now in contact with the gas. It is possible that this phase has a higher solubility for sulfur than does magnetite and that sulfur can transport through the oxide giving rise to sulfide formation throughout the oxide layer and beneath it as shown in the scale cross-section in Fig. 2. However, a more consistent explanation relates to the location of the sulfide phase in the oxide scale: the sulfide is the lighter-colored phase appearing as globules with pores in the FeO and as continuous films, along the columnar grain boundaries of FeO. These boundaries, where they are in contact with the gas, represent deep cavities in which stagnant pockets of gas can collect. Further formation of oxide at these locations reduces the oxygen potential (or H_2O content) to the point where sulfide is the stable phase. Inclusion of the reactive gas in closing pores has the same effect. This continuous film of sulfide provides a path through which the sulfur is

transported down through the oxide scale. The sulfide is liquid at this temperature. Indeed, at the base of the oxide scale the FeS interacts with both oxide and metal, forming an even lower melting point ($925^\circ C$) liquid, which on post-exposure examination solidifies as a FeS-Fe-FeO eutectic: phase relationships in the Fe-O-S system are more complex than implied in Fig. 1 and need to be determined.

Changes in the oxide to sulfide ratio in the scale occur when the bulk H_2O content of the gas is lowered ($P_{O_2} = 1.0 \times 10^{-13}$ atm, point C, Fig. 1) and the gas mixture moves into a region where the sulfide should be stable in contact with the gas. Mixed sulfide and oxide protrusions grow outwards from the surface scale (Fig. 3) which is again consistent with a gaseous transport step being an important part of the overall growth process.

This is further substantiated by other observations. Variation in the volume flow rate of the reactive gas mixture produces two effects: (i) there is a marked change in the scale growth rate, and (ii) there is a change in the relative amounts

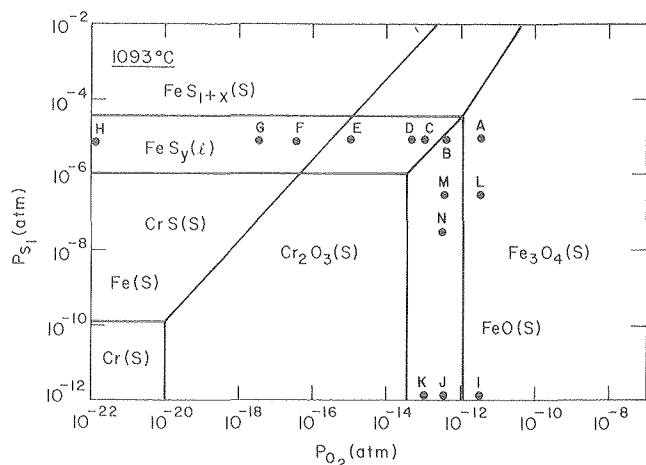


Fig. 1. Thermodynamic stability diagram of the Fe-S-O and Cr-S-O systems at $1093^\circ C$ showing gaseous compositions. (XBL 802-272)

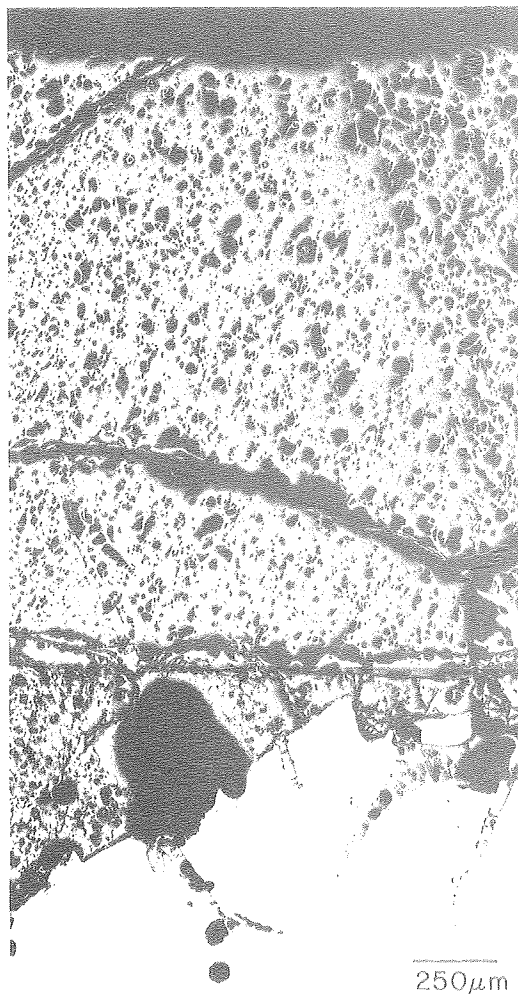


Fig. 2. Cross section of scale formed at gas composition B after 24 hr exposure. Note presence of globules of light-colored FeS phase associated with pores in oxide scale, and as continuous films at columnar grain boundaries. (XBB 802-2445)

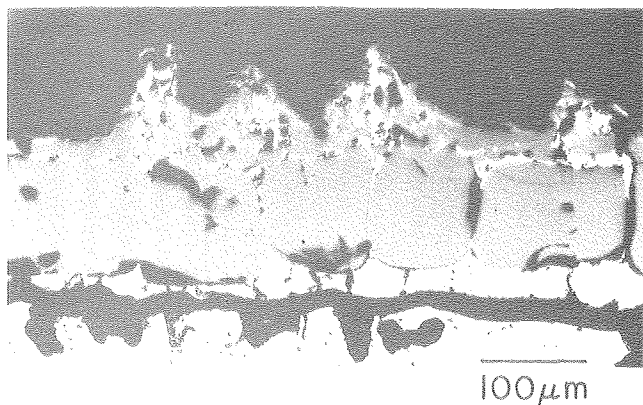


Fig. 3. Cross section of scale formed at gas composition C after 2 hr exposure. Note oxide/sulfide protrusions on outer surface of scale above columnar grain boundaries and layer of sulfide beneath oxide. (XBB 802-2443)

of sulfide and oxide formed. Increase in the flow rate from 200 cc/min, the condition producing the scale shown in Fig. 2, to 800 and 1200 cc/min produced scale thicknesses in 2h exposure of 350 and 810 μm respectively in comparison with 110 μm at the lower flow rate. The amount of sulfide formed decreased also, and was virtually nonexistent at the highest flow rate. In contrast, decrease of the flow rate to 50 cc/min produced a scale consisting essentially of only the liquid FeS-FeO phase, and virtually no FeO as a separate phase. This scale was only 10 μm after 2h, but this low figure may be somewhat misleading, since the liquid scale tends to run off the surface. With further decrease of the PO_2 (5.2×10^{-14} atm, point D), FeO disappears as a separate phase in the scale, and only the FeS-FeO liquid is formed. At still lower PO_2 (3.2×10^{-17} atm, point E), below the stability limit of FeO, the liquid scale is only FeS. The compositions of the liquid scales are not dependent on the gaseous flow rate: the liquid phase is not able to sustain crevices or pores at its growing surface.

Cr₂O₃ - Forming Alloys. Cr₂O₃ is considered to be among the best protective barriers for oxidation resistance. It is thermodynamically very stable (see Fig. 1), and grows slowly due to its low concentration of native defects. Whether it can remain as a protective barrier for Fe-base alloys in the presence of sulfur in the gas phase needs to be established, and has been investigated by exposing binary Fe-Cr alloys to H₂-H₂O-H₂S mixtures as outlined above. Generally, lower oxygen potentials were used, corresponding to conditions where Cr₂O₃ and FeS can be in equilibrium with the gas: these are marked in Fig. 1.

The thickness of the Cr₂O₃ grown at a $\text{PO}_2 = 1 \times 10^{-5}$ atm and $\text{PS}_2 = 8.4 \times 10^{-6}$ atm (point E) depends on the Cr content of the alloy, being 10, 20, 25, and 30 μm in 100h exposure on Fe-18, 25, 40% Cr and pure Cr respectively. In addition, on pure Cr, small, discrete particles of CrS form beneath the surface oxide, and to a lesser extent on Fe-40% Cr and pure Cr, but not with the more dilute alloys. Interestingly, the morphology of

the oxide changes from an apparently porous outer structure, to a very compact layer close to the metal interface. Calculations indicate that the diffusion rate of chromium in the alloy is sufficiently large that the flux of chromium out of the alloy is not a rate-limiting step, although a depletion of Cr does exist in the alloy behind the growing Cr₂O₃ scale. Instead, the oxygen potential gradient, and in turn the defect gradient, is influenced by the Cr concentration at the alloy surface, more so than when Cr₂O₃ grows in pure O₂ containing environments where the defect gradient is largely influenced by the conditions at the outer oxide/gas interface. The decrease in the defect gradient upon reducing the Cr content of the alloy, reduces the growth rate of the oxide, but more importantly reduces the inward diffusion of sulfur. The diffusion path cuts through the sulfide region for pure Cr and alloys rich in Cr, but remains in the oxide phase field. This cannot be shown on a two-dimensional stability diagram, such as Fig. 1, and diagrams with alloy composition as a third axis are required.

As the oxygen potential is reduced (point G in Fig. 1), the diffusion path cuts into the CrS region independently of the Cr content of the alloy, and CrS is formed as a separate phase beneath the Cr₂O₃ in all cases. Figure 4 shows a typical cross section. The overall consumption rate of Cr from the alloy is now somewhat higher and the Fe in the alloy cannot back diffuse into the alloy at a fast enough rate and is included into the growing scale as unoxidized metal, as indicated in the x-ray maps of Fig. 4. Note that the Fe forms neither a sulfide nor an oxide, and this is related quantitatively to the position of the diffusion path on the Fe-Cr-S-O stability diagram. Quantitative evaluation of the diffusion path is hindered by the lack of transport data in the Cr-rich sulfide and oxide phases.

Another feature of the behavior of these alloys relates to the formation of liquid iron-rich sulfides at some locations on the samples. These cannot have formed via a diffusional process and are related to a loss of adhesion of the Cr₂O₃, exposing the now Cr-denuded alloy to the sulfur-rich gas. As such, this breakdown is more prevalent near corners of the samples and the iron sulfide-rich liquid spreads out over the surface surrounding Cr₂O₃ scale seemingly without interacting further.

When the oxygen potential is reduced to 3.3×10^{-18} atm (point H), CrS becomes the stable phase in equilibrium with the gas, but the reaction path cuts into the Cr₂O₃ region. This reaction path is independent of the Cr content in the alloy. The scale thickness, however, increases from 250-300 μm for Fe-18Cr to 425-450 μm for Fe-40Cu and $\sim 850 \mu\text{m}$ for pure Cr. Except for the case of pure Cr, a CrS subscale forms within the alloy beneath the Cr₂O₃ that develops at the metal surface. The outer Cr scale contains substantial amounts of Fe, dissolved in solid solution.

Thus, the results show that two types of sulfur-induced degradation seem possible in these low oxygen potential atmospheres: the one is related to transport of sulfur through the Cr₂O₃ scale, and the other to a complete mechanical loss of the protective oxide.

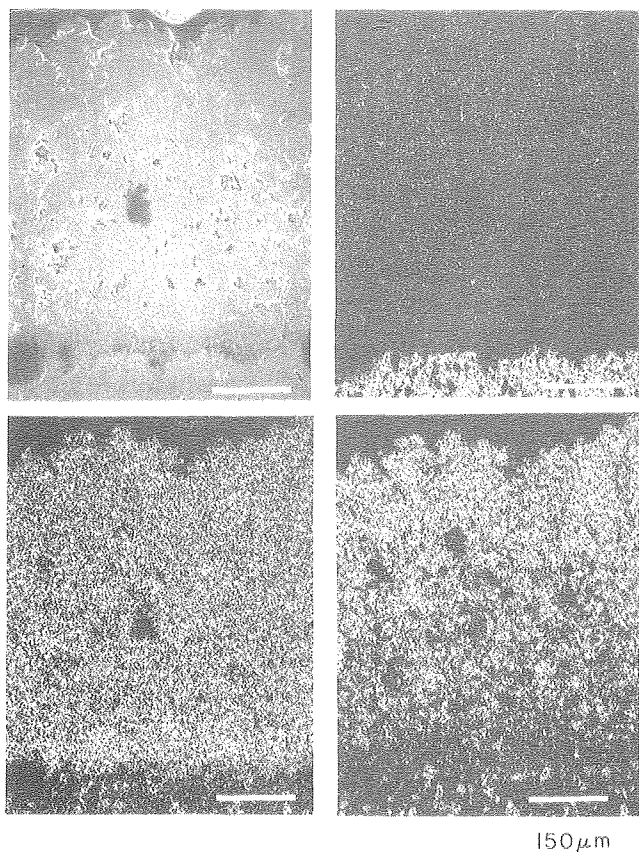


Fig. 4. Cross section of the scale formed at gas composition G after 190 hr exposure. Note Fe rich particle embedded in CrS protrusion below a Cr_2O_3 scale. (XBB 802-2446)

* * *

3. HOT CORROSION OF NICKEL-BASE ALLOYS AT INTERMEDIATE TEMPERATURES[†]

A. K. Misra and D. P. Whittle

It is now reasonably well established that there are two quite distinct types of hot corrosion involved in the degradation of turbine blading materials. Type I occurs at temperatures above 900°C and is caused by the deposition of molten Na_2SO_4 on the blades in air turbines. Type II occurs at somewhat lower temperatures, $700\text{--}850^\circ\text{C}$, and is more prevalent in marine and industrial turbines. Type II is also caused by sulfatic deposits. These are low melting point eutectics formed between the solid Na_2SO_4 deposit and NiSO_4 or CaSO_4 , formed by sulfation of NiO and CoO , the corrosion products of typical alloys. Propagation of type II corrosion, then, is dependent on a liquid sulfate being formed and the presence of significant, though small, concentrations of SO_3 in the gas phase. This project is aimed at identifying the factors controlling type II hot corrosion, and establishing mechanisms.

Ni-base Cr_2O_3 -forming alloys seem to be the most resistant to attack when coated with Na_2SO_4 in $\text{Na}_2\text{SO}_4\text{--NiSO}_4$ eutectic mixtures and exposed at

750°C to air containing $1.5 \times 10^{-3} \text{SO}_3$. Transport of the oxidant across the molten salt is a critical factor, and evidence points to oxygen diffusivities being very low; SO_3 may, however, transport as a pyrosulfate, $\text{S}_2\text{O}_7^{=}$ ion, and it has been shown that the continued propagation of the hot corrosion is via a sulfidation/oxidation mechanism. Dissolution or fluxing of Cr_2O_3 by the melt is not observed.

Al-containing alloys are very heavily corroded by the salt films, even Ni-25Cr-2.5Al which is still a Cr_2O_3 -forming alloy. Figure 1 shows a section through a sample coated with $2 \text{mg/cm}^2 \text{Na}_2\text{SO}_4$ and oxidized in air + $1.5 \times 10^{-3} \text{SO}_3$ for 15h at 750°C . The scale has a pronounced banded structure with alternate layers of Cr- and Ni-rich phases. This is typical of a fluxing type of process and it is clear that Al_2O_3 dissolves in the $\text{Na}_2\text{SO}_4\text{--NiSO}_4$ melt, probably as its sulfate. Thermodynamically, sulfation of Al_2O_3 would not be expected at the prevailing SO_3 partial pressure; however, the activity of $\text{Al}_2(\text{SO}_4)_3$ in the melt is probably quite low, promoting the reaction. The solution behavior of ternary sulfate melts of this type are not known.



Fig. 1. Cross section of Ni-25Cr-2.5Al coated with $2 \text{mg/cm}^2 \text{Na}_2\text{SO}_4$ and oxidized in air + $1.5 \times 10^{-3} \text{SO}_3$ for 15 hr at 750°C . (XBB 7910-13488A)

* * *

[†]Brief version of paper presented at Electrochem. Soc. Meeting, Los Angeles, California, October 1979.

4. CORROSION BY SOLID SULFATIC DEPOSITS[†]

H. C. Akuezie and D. P. Whittle

Fluidized bed combustion, although not a new concept, provides a novel process for burning a wide range of fuels efficiently at high combustion intensities, while keeping the emission of sulfur and nitrogen oxides well below any of the rigid standards currently being proposed or in force. Coal and suitably sized sorbent particles are introduced to the combustor where combustion of the coal occurs. The coal combusts at a relatively low temperature, in the range 750-950°C, which enables good sulfur retention by the sorbent in the bed; this temperature is also below the ash fusion point. Limestone or dolomite are the preferred sorbents: they react with the SO₂ released during combustion to form calcium or magnesium sulfates. Originally it was anticipated that fireside corrosion problems of in-bed steam-raising tubes by the ash/coal/calcium sulfate burden would be minimal; however, tests have shown that a severe sulfidation/oxidation type attack can occur even though most of the aggressive sulfur compounds that could have accounted for the sulfidation have reacted with the acceptor. The generation of sulfur activities sufficiently high to sulfidize the alloys implies that the oxygen potential of the system, at least locally, is relatively low, since the two potentials are related through the CaO/CaS/CaSO₄ equilibria. This study, then, examines the behavior of typical Cr₂O₃ - forming alloys in the presence of CaSO₄/CaO mixtures in atmospheres of controlled oxygen potential, in the range 10⁻¹⁹ - 1 atm, using CO/CO₂ mixtures.

The corrosion rate at a constant temperature, 850°C typical of operational temperatures, increased with increasing oxygen activity, and furthermore there was no sulfidation. This is contrary to the earlier expectation that the CaSO₄ - induced attack should depend only on the sulfur activity according to the Ca-O-S stability diagram. Interaction between the CaSO₄ and the oxides of iron which form on top of the protective Cr₂O₃ scale was responsible for the accelerated attack. CaFeO₂ was formed, which had a cubic structure with unit cell length of 4.726 Å and a composition of 72.6% CaO, 22.0% FeO and 4.9% Fe₂O₃. Direct observation of this interaction in the hot stage SEM indicated that the CaFeO₂ phase appeared to melt at around 927°C. Indeed, temperature was far more important than the oxygen potential in inducing sulfidation attack. Figure 1 shows a section through the scale formed on IN800 (Fe-32%Ni-20.5%Cr-0.35%Si-0.75%Mn-0.04%C-0.3%Cu) exposed to CaSO₄ containing C at 950°C in a static air environment. Heavy internal sulfidation occurs with the precipitation of Cr-rich sulfides within the alloy, primarily at grain boundaries. This concentrates the chromium in the grain boundaries and prevents the establishment of a continuous Cr₂O₃ protective layer. Once sulfides have been introduced into the alloy they continue to penetrate further by being oxidized at the alloy/state interface, with the released sulfur diffusing further into the alloy.

There appear to be two aspects of CaSO₄ - induced attack: (a) At low temperatures, below 950°C, a direct reaction between the oxide scales and CaSO₄ that does not involve sulfidation. In iron-base

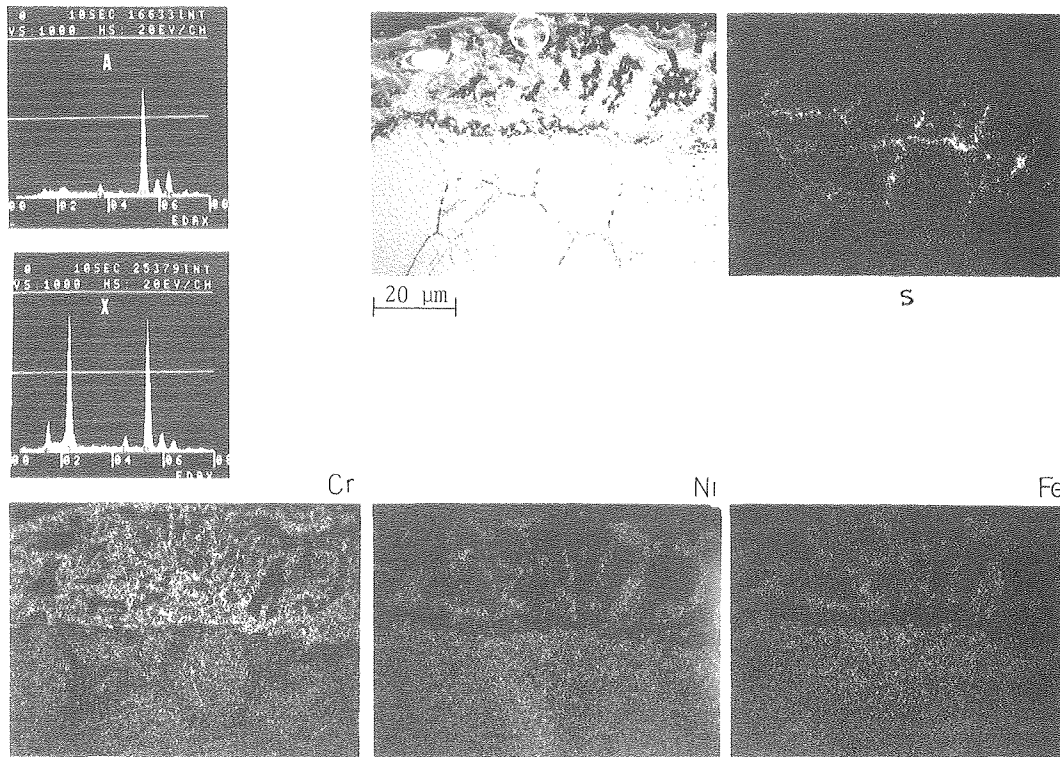


Fig. 1. Scanning electron image, x-ray maps and EDAX analyses of the cross section of the scale formed on alloy IN800 exposed to CaSO₄ + C deposit for 100 hr at 950°C in static air. (XBB 790-15069)

materials, the main scale contains nonprotective, porous CaFe_2O_4 spinel, and the outermost scale is a thin, sometimes loosely adhering complex calcium-iron sulfate. (b) A complex calcium-iron sulfate liquid phase attack that occurs at high temperature, above 950°C , and induces an oxidation/sulfidation attack that is catastrophic.

* * *

[†]Brief version of LBL-10286.

5. ADHERENCE OF Al_2O_3 OXIDE FILMS[†]

H. C. Akuezie, I. M. Allam, and D. P. Whittle

Adhesion between surface scale and alloy substrate is essential for good oxidation resistance. Poor adhesion can lead either to exfoliation of the oxide in response to thermal cycling, or to mechanically applied stresses, resulting in enhanced oxidation rates. Marked improvements in scale/substrate adhesion, however, can be achieved via the "rare-earth effect" whereby addition of a small amount of a rare-earth element or of a fine distribution of a stable oxide produces a significant increase in an alloy's resistance to cyclic oxidation. Recent work¹ has demonstrated that the major factor responsible for the improved scale adherence with Al_2O_3 -forming alloys is the formation of protrusions of oxide growing into the alloy. These act to key the protective scale to the surface and are more effective when a uniform distribution of small oxide pegs can be achieved at the alloy/scale interface. This is difficult to control with metallic additions since essentially the active element oxidizes internally during high temperature exposure, and these internally precipitated oxides form the nuclei around which the protective oxide forms the pegs. Clearly, the distribution of the internal oxides, and hence the subsequent pegs, depends on the exposure conditions and is thus not directly controllable.

Several reports have indicated that marked improvements in Al_2O_3 scale adherence are also achieved by the presence of Pt in the alloy, and it seemed possible that the formation of the intermetallic PtAl_3 might be involved, and that this might exist as a fine dispersion in the alloy which acted in the same way as an oxide dispersion. PtAl_3 is very stable, although its formation might reduce the effective Al content of the matrix. However, Pt and Hf additions could be made together, and the intermetallic HfPt_3 used as the dispersoid. This is even more stable, does not contain Al, and, if it did oxidize, would produce an HfO_2 -oxide dispersion anyway.

The principal alloy studied was Co-10Cr-11Al (wt.%), which forms an external scale of $\alpha\text{-Al}_2\text{O}_3$ over the temperature range studied. Additions of 1 Pt, 1 Hf-3Pt or 0.3Hf-0.9Pt (all wt.%) were made to this base alloy. Oxidation experiments were of two types: (a) isothermal exposure, and (b) repeated thermal cycles of 20hr duration each. The detailed morphology of the alloy/scale interface was studied by stripping the scale and examining its

underside and, when possible, the exposed surface of the alloy. Scales were stripped either mechanically by quenching in liquid nitrogen, or with particularly adherent scales, the substrate was dissolved away using a 10% bromine in methanol solution.

The alloy microstructures are very similar and consist principally of a dark, dendritic, $\beta\text{-CoAl}$ phase in a lighter, $\alpha\text{-Co}$ matrix. There is also a third, very dark precipitate phase identified by EPMA as the Hf-Pt-rich intermetallic which appears to be confined to the $\alpha\text{-Co}$ matrix.

Both Pt and Pt+Hf reduce the oxidation rate of the Co-10Cr-11Al alloy under isothermal conditions at 1100°C . Under cyclic oxidation conditions, Pt additions alone have little effect, but the 0.3Hf + 0.9Pt addition significantly improves the oxidation resistance. The alloy containing 1Hf + 3Pt shows a lower resistance. Weight gain/time curves are shown in Fig. 1.

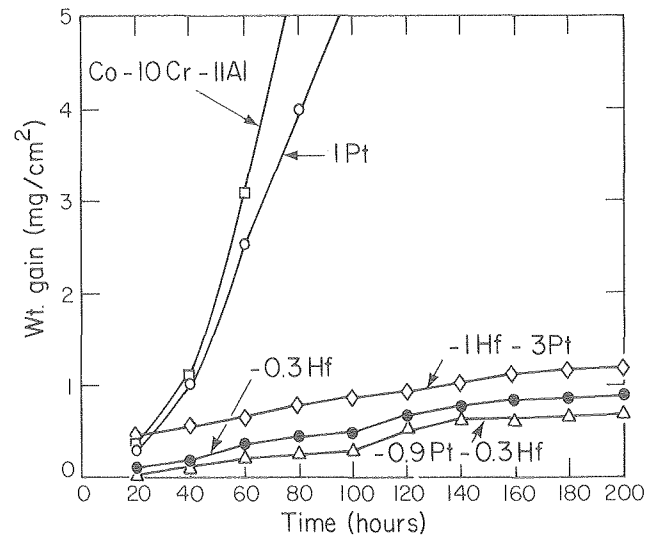


Fig. 1. Weight gain/time data for the cyclic oxidation of Co-10Cr-11Al alloys containing Pt and/or Hf at 1100°C . (XBL 798-2391)

The Al_2O_3 scale which formed on the alloy Co-10Cr-11Al-1Pt after 265 h oxidation at 1200°C was not adherent and spalled from the alloy on cooling. Similar features were observed with the ternary Co-Cr-Al alloy of the same composition oxidized under similar conditions.

Surface examination of the alloy Co-10Cr-11Al-0.3Hf-0.9Pt after oxidation at 1200°C indicated that the scale was tightly adherent to the substrate and spalled during cooling only from very small discrete areas. The major difference between this alloy and an alloy that was Pt-free but containing Hf¹ was that with the Pt-free alloy, the substrate surface appeared to be more heavily convoluted.

Figure 2 shows the underside of the Al_2O_3 scale after the alloy substrate has been dissolved away. This is the Co-10Cr-11Al-1Hf-3Pt alloy, oxidized isothermally for 200hr at 1100°C. This regular distribution of oxide protrusions compares well with those obtained in previous studies.¹ The protrusions do not penetrate so deeply and are not as tortuous in shape as those formed in the case of a Co-10Cr-11Al-0.3Hf alloy, but compare well with those formed when this latter alloy had been given a pre-internal oxidation treatment prior to exposure. This regular distribution of oxide protrusions is the most desirable in determining oxide/scale adherence. EPMA indicates that the pegs consist primarily of Al_2O_3 , encapsulating the dispersed phase. Presumably they grow by some form of short-circuit diffusion of oxygen along the incoherent interface between the matrix and the dispersed phase. As a consequence the composition of the dispersed phase is not critical.

The average spacings between the Al_2O_3 pegs and those of the dispersion phase in the alloy are quite similar for each alloy and typically are 3-4 μm along the interface. The length of the peg protruding into the alloy is also important. Typically these are in the range 5-10 μm with the alloy containing 1Hf-3Pt and slightly less than this for the 0.3Hf-0.9Pt alloy. Long protrusions tend to promote scale cracking above the pegs.

Thus, the intermetallic dispersions of Hf and Pt formed in Co-10Cr-11Al alloys are comparable in size and distribution to the HfO_2 dispersions produced by pre-internally oxidizing Co-10Cr-11Al-Hf alloys and seem to provide an alternative way of producing a dispersed phase in these alloys. This

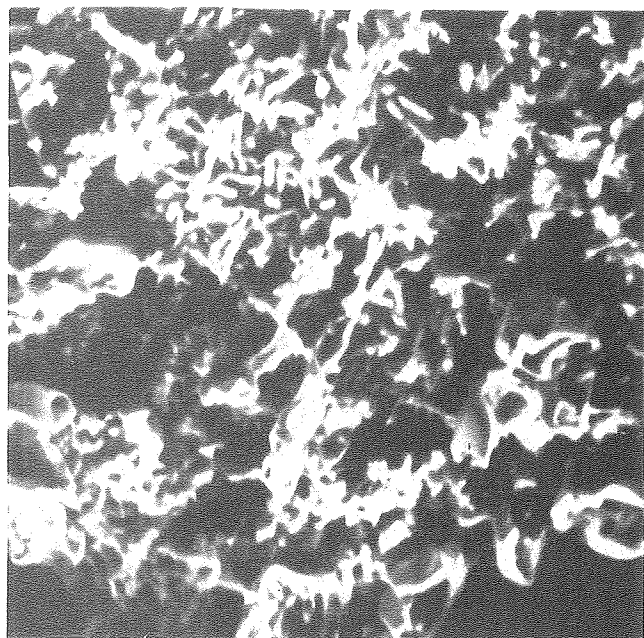


Fig. 2. Underside morphology of the Al_2O_3 formed on Co-10Cr-11Al-1Hf-3Pt after isothermal oxidation of 1100°C for 200 hr: alloy substrate has been dissolved away. (XBB 798-10392)

opens up the possibility of exploring other dispersion-containing metallic systems. The inwardly growing Al_2O_3 pegs which develop on subsequent exposure to oxidizing environments seem equally effective in keying the Al_2O_3 surface scale to the substrate and thereby improving the oxidation resistance of this type of alloy under both isothermal and particularly thermal cycling conditions.

* * *

† Brief version of LBL-9180; accepted for publication in *Oxid. Metals*.

1. I. M. Allam, D. P. Whittle and J. Stringer, *Oxid. Metals* 12, 35 (1978); 13, 381 (1979).

6. OXIDATION BEHAVIOR OF A TWO-PHASE ALLOY: Fe - 44%Cu†

F. Gesmundo,† P. Vianni,† and D. P. Whittle

During the high-temperature oxidation of alloys the scales that form often contain a number of different phases, each of which may contain more than one alloy component. Thus, the ratio of the metals in the scale is different from this ratio in the alloy because the various components have different affinities for oxygen, and the rate of transport in the scale is different for each cation and in each phase. The composition of the scale may also vary with position due to these differing diffusivities. Some success has been achieved in attempts to correlate the theories of alloy oxidation kinetics with diffusional, structural and compositional parameters of the metal oxides in systems in which a solid solution scale is formed. Here that theme is continued in attempting to analyze the behavior of systems in which the oxides of the constituent metals are virtually immiscible, and the overall oxidation rate depends heavily on the distribution of the various oxide phases in the scale. In addition, Fe and Cu are relatively immiscible in the metallic phase, and large compositional changes in the alloy due to preferential oxidation are therefore precluded even though there are considerable differences in stabilities between iron and copper oxides.

The microstructure of the alloy after annealing consists essentially of the as-cast, dendritic structure. The dendrites are the iron-rich phase which, according to the phase diagram, contains 5.81 wt% Cu; the copper-rich matrix contains 2.06 wt% Fe at 1000°C. The average size of the iron-rich phase particles is around 20-30 μm .

The isothermal oxidation rate follows, to a good approximation, a parabolic law, and the rate constants ($g^2 cm^{-4} s^{-1}$) as functions of temperature are reported in Table 1. Comparison of the alloy oxidation kinetic constants with those of the pure base metals shows an improved resistance of the alloy to oxidation; the alloy oxidizes marginally more slowly than pure copper, but substantially more slowly than iron. The ratio between alloy and pure copper parabolic rate constants remains almost constant up to 900°C and then decreases sharply, whereas for a similar ratio between alloy

Table 1. Comparison of parabolic rate constants for oxidation of Fe-44% Cu with pure Fe and pure Cu. [Data for Cu are from D. W. Bridges et al., J. Electrochem. Soc. 103, 475 (1956) and S. Mrowee and A. Stocklosa, Oxid. Met. 3, 291 (1971); those for Fe are from M. H. Davies et al., Trans. AIME 191, 889 (1951)].

| T (°C) | Parabolic rate constants (g ² cm ⁻⁴ s ⁻¹) | | | | |
|--------|--|-------------------------|---------------------------------|---|---|
| | Cu | Fe | Alloy | $\frac{k_{\text{Cu}}}{k_{\text{all.}}}$ | $\frac{k_{\text{Fe}}}{k_{\text{all.}}}$ |
| 700 | 1.72 x 10 ⁻⁹ | 6.0 x 10 ⁻⁹ | 2.61 ± 0.06 x 10 ⁻¹⁰ | 6.6 | 23 |
| 800 | 5.53 x 10 ⁻⁹ | 5.7 x 10 ⁻⁸ | 8.61 ± 0.85 x 10 ⁻¹⁰ | 6.4 | 66 |
| 900 | 2.80 x 10 ⁻⁸ | 2.5 x 10 ⁻⁷ | 4.73 ± 0.001 x 10 ⁻⁹ | 5.9 | 53 |
| 1000 | 8.1 x 10 ⁻⁸ | ~1.1 x 10 ⁻⁶ | 3.11 ± 0.03 x 10 ⁻⁸ | 2.6 | 35 |

and iron a maximum is observed at 800°C. There are four principal scale layers as shown in Fig. 1: an outer CuO, a layer of CuFeO₂ or magnetite layer, and an inner wüstite layer. In addition, there is a form of internal oxidation of the Fe-islands within the alloy. After longer oxidation times, the outer CuO layer develops considerable porosity, which tends to be elongated in the growth direction. The amount of Fe dissolved in this layer is about 7 wt% and the Cu concentration in the inner layers is 3.5 and 1.0 wt% in Fe₃O₄ respectively, at least for samples exposed at 900°C. Significantly less inter-solubility between the component oxides is observed at lower temperatures.

The main reason for the reduced oxidation rate of this alloy in comparison with pure Fe, is the reduced relative thickness of the inner FeO layer. Generally, on iron this phase constitutes about 95% of the total oxide scale formed in the temperature range 700-1200°C. In the case of the alloy, the oxygen activity at the alloy/scale interface is higher, since it can be noted that the iron-rich phase of the alloy is oxidized to FeO and the only remaining metal phase is the Cu-rich ε-phase. In the saturated ε-phase the Fe activity is as high as 0.9486 even though its atomic fraction is only 0.0234, so that the activity coefficient, γ° , assuming Henry's law, is 40.54. A lower limit for the Fe concentration in the ε-phase is equilibrium with FeO corresponding to an oxygen activity equal to that between FeO and Fe₃O₄. Using free energy data, this minimum Fe activity is 0.1284 with the corresponding atomic fraction of 0.0032. The growth rate for the direct formation of magnetite on an iron alloy having this metal activity then has been calculated from transport rates in Fe₃O₄, giving 3.5 x 10⁻¹⁰, 2.5 x 10⁻⁹, 1.3 x 10⁻⁸ and 5.1 x 10⁻⁸ g² cm⁻⁴s⁻¹ at 700, 800, 900 and 1000°C respectively. These are somewhat larger than the measured values, and the pressure of Cu₂O as an

outer layer may have reduced the oxygen activity at the outer interface of the magnetite layer, which would reduce the growth rate further. An additional contribution to the observed decrease in the scaling rate may also arise from the dissolution of Cu in the Fe oxides. In fact FeO, in spite of its large deviation from stoichiometry and the complex nature of its defects, is essentially a p-type semiconductor, so that the presence of copper--most probably in the form of Cu⁺ ions, owing to the low oxygen activity--should produce a decrease in the vacancy concentration and hence slow down the diffusion of iron. Actually, large additions would be thought necessary for this effect, due to the high concentration of native defects in FeO as compared to similar oxides like NiO or CoO.

Possible stress effects associated with the development of different oxides growing at different rates on the alloy seem to be absent from this system. In fact, the scale appears compact and of uniform thickness and shows no lateral variations in structure or composition, at least none which can be directly associated with the two-phase structure of the alloy only. The thickness of the wüstite layer sometimes shows large variations around the surface of the sample, where at some positions it is confined to the internal oxidation region, while in others it extends far into the scale. The relative uniformity of the scale structure is possibly related to the small grain size of the alloy, so that Cu-rich and Fe-rich regions in the alloy alternate frequently at the alloy/oxide interface and lateral diffusion is sufficiently rapid to even out these fluctuations: differences in the scale structure are in fact confined mainly in a direction perpendicular to the alloy surface rather than parallel to it.

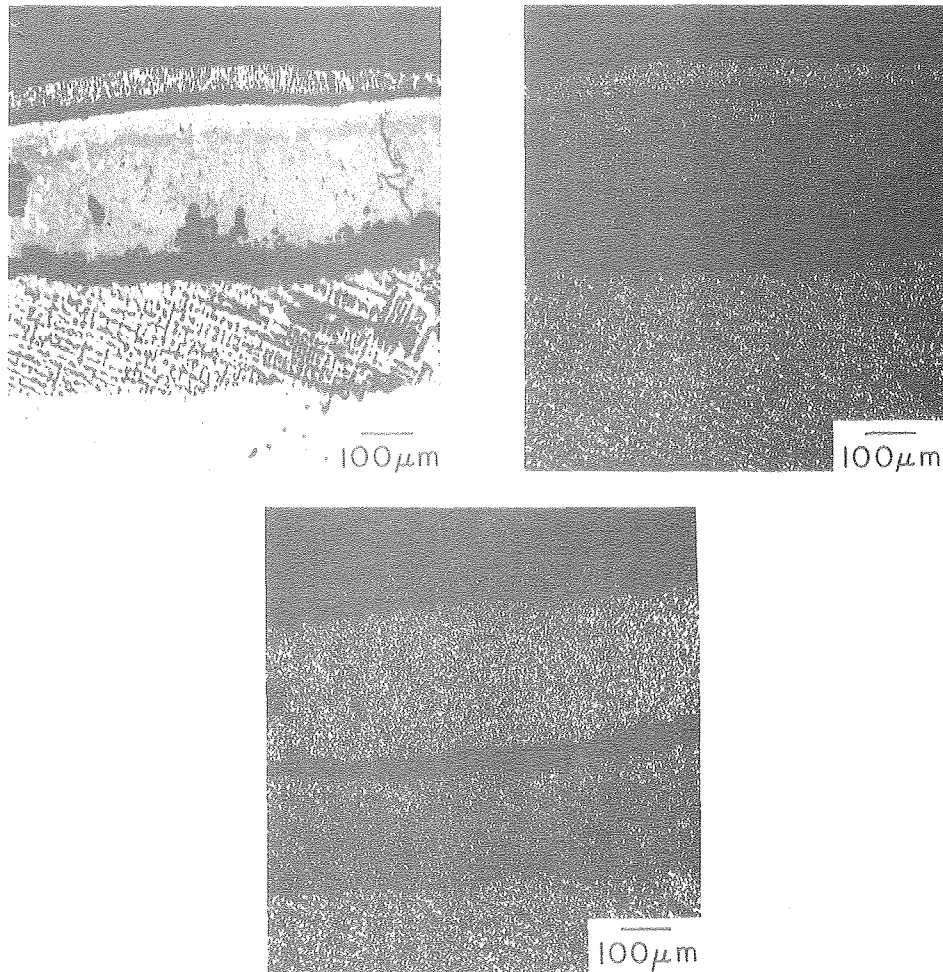


Fig. 1. Cross section of the oxide scale formed on Fe-44% Cu oxidized for 6 hr at 900°C in air. (XBB 802-2444)

* * *

[†]Brief version of LBL-10452; to be published in J. Electrochem. Soc.

*Centro Studi di Chimica e Chimica Fisica Applicata, Consiglio Nazionale delle Ricerche, Genoa, Italy.

7. FORMATION OF SUBSCALES OF VARYING COMPOSITION[†]

D. P. Whittle, F. Gesmundo,[‡] B. D. Bastow,[§] and G. C. Wood^{||}

Significant progress has been made recently¹ in the quantitative analysis of alloy oxidation phenomena, particularly in systems where a single phase scale, but containing both alloy components, is formed. This model, however, ignores the possibility of forming a subscale within the alloy beneath the surface scale and although this does not affect the validity of the original treatment in any way, a full description of the scaling

characteristics of this type of alloy requires analysis of the internal oxidation process also.

Internal oxidation in these systems, where both alloy components can and do enter the oxide phase forming an oxide solid solution, is somewhat different from that classically observed in other systems. The internally precipitated oxide is the same phase as the surface scale, and within the zone of internal oxidation, the fraction of internal oxide precipitated varies with position. Typical systems to which the analysis applies include binary alloys of Co, Fe, Mn and Ni with each other since the isotypic oxides CoO, FeO, MnO and NiO all have a simple cubic NaCl structure and form solid solutions over their entire composition ranges. Equally, the analysis is well suited to internal carbide precipitation when alloys are exposed to miscible. Degradation by internal carburization is rapidly increasing in significance in many studies relating to materials performance in coal conversion and petrochemical processing systems.

Figure 1 shows schematically a typical isothermal section of the alloy-oxygen phase diagram. The alloy and oxide systems referred to above approximate to thermodynamically ideal behavior, which simplifies the analysis, but does not limit its applicability. Included in Fig. 1 is the diffusion path which represents the locus of compositions through the alloy, subscale, and surface scale system. Portion ab represents the alloy behind the subscale zone, portions bc and de the compositions of alloy and oxide precipitates within the subscale region, with bd being the composite path in the subscale zone and indicating the relative fractions of the two phases, alloy and oxide. There is no overall change in composition in the subscale region, or in the alloy behind it, since the diffusivity of the interstitial oxygen within the alloy is far greater than that of the substitutional alloying elements. By the same token the average composition of metallic components in the oxide scale is identical to that in the alloy since the scale growth rate is orders of magnitude greater than interdiffusion in the alloy. There are concentration changes through the scale, ef, and these were calculated in the earlier paper.¹

By expressing the amount of precipitated oxide as a function of alloy composition, using the phase diagram, the transport equation for oxygen in the subscale zone is modified to allow for the consumption of oxygen by precipitation and a transcendental equation for the penetration of the subscale front into the alloy obtained. Fraction of subscale, composition of the alloy and the composition of the subscale throughout the internal oxide zone can also be calculated.

Figure 2 shows the variation of the subscale/surface scale thickness ratio, ξ , with alloy composition, N_B^0 , for different values of Ω and β which are the measures of the oxide stability: Ω is

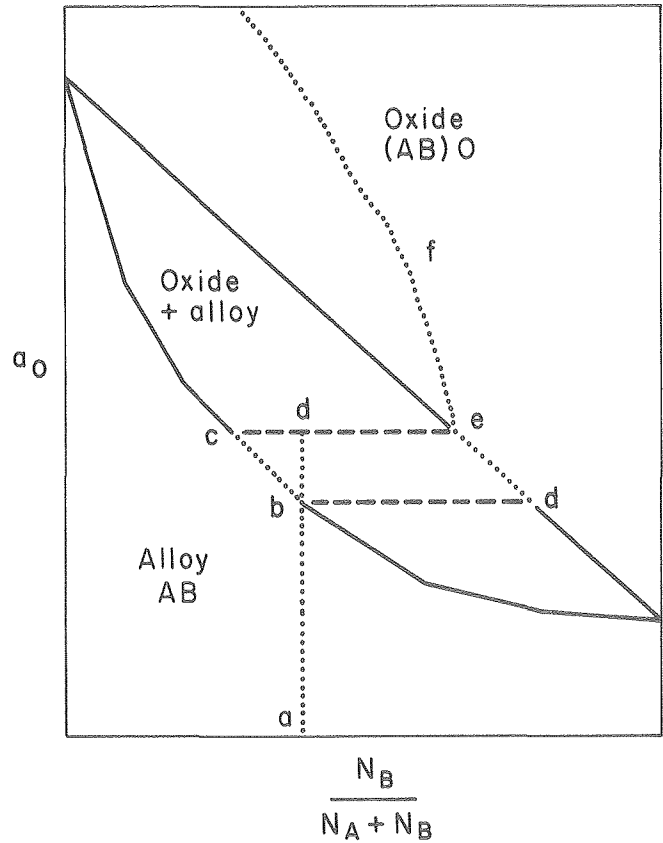


Fig. 1. Schematic phase diagram and diffusion path for the alloy-oxygen system. (XBL 802-317)

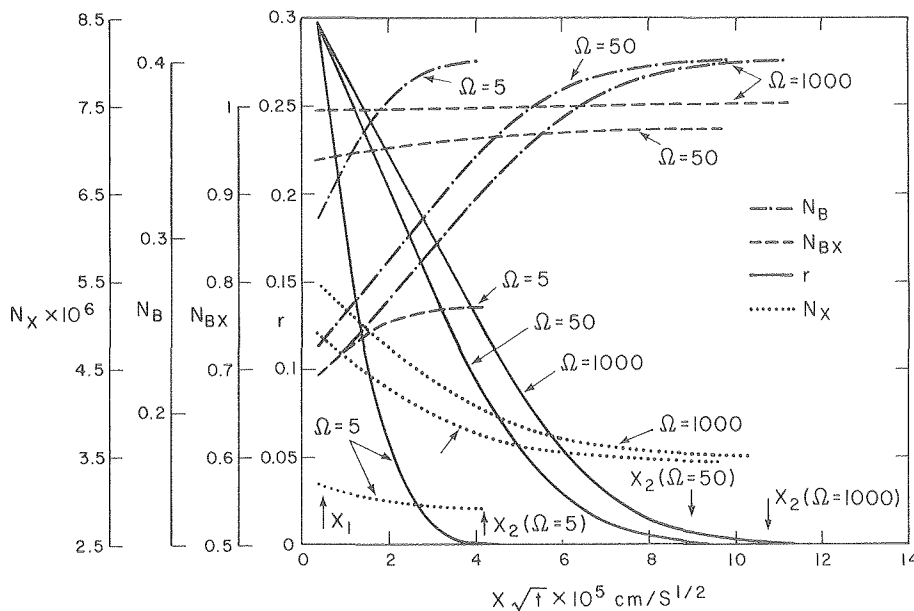


Fig. 2. Variation of internal oxide/surface oxide thickness as a function of alloy composition and the stability of the oxide components. (XBL 802-320)

essentially the difference in stabilities of the two scale components and determines the slope of the boundary between oxide and oxide + alloy fields on the phase diagram. Increase in Ω , which increases the slope and corresponds to a greater difference in stability between the scale components, has a strong influence on the depth of subscale penetration. Increase in Ω also causes the maximum value of subscale/surface scale thickness ratio to occur at smaller values of N_B^0 . β , which is a measure of the stability of the more stable scale component, has a lesser influence on the depth of subscale penetration. Its effect is opposite to that of Ω in that the larger the value of β , the smaller is the subscale penetration, and this is related to the lower overall solubility of the oxidant in the alloy. Other factors which affect the depth of subscale penetration include the diffusivity of oxygen in the alloy, and the rate of growth of the surface scale.

Swisher² measured the rate of internal oxidation of an Fe-1% Mn alloy exposed to a H_2O/H_2 mixture with $P_{H_2O}/P_{H_2} = 0.2$ at $1350^\circ C$ obtaining a rate constant of $7.4 \times 10^{-8} \text{ cm}^2/\text{s}$; the value calculated from our present analysis is $4.6 \times 10^{-7} \text{ cm}^2/\text{s}$. However, as shown in Fig. 3 which expresses the variation of the fraction of internal oxide, the composition of the oxide and that of the alloy as a function of position within the internal oxidation zone, the fraction of internal oxide is only 0.012 at the surface of the alloy, its maximum value, and falls off rather rapidly through the internal oxide zone, decreasing to about 0.004 half-way across it. This means that it would be very difficult to observe the precipitation front with an optical microscope, and the measured value of the rate constant almost certainly represents an underestimation. Indeed, a better indication of the depth of internal oxidation can be obtained from Swisher's measurement of the Mn concentration profile: this gives a rate constant of $1.1 \times 10^{-7} \text{ cm}^2/\text{s}$, somewhat closer to that given by the present analysis.

A better test of the analysis is to compare calculated and measured concentration profiles. The

fraction of internal oxide particles or their composition have not been measured, but Fig. 3 compares calculated and measured Mn profiles. The agreement in shape and in absolute value is considered an acceptable test of the current analysis. The concentration profile calculated according to Swisher's analysis is also included; due to the assumptions made this has a physically unlikely discontinuity at the alloy/internal oxide interface

* * *

†Brief version of LBL-10067.

‡Centro Studi di Chimica e Chimica Fisica Applicata, Genova, Italy.

§British Nuclear Fuels, Windscale, Cumbria, UK.

||Corrosion and Protection Center, U.M.I.S.T., Manchester, UK.

1. B. D. Bastow, D. P. Whittle and G. C. Wood, Proc. Roy. Soc. A356 177 (1977).

2. J. H. Swisher, TMS-AIME 242, 205 (1968).

RESEARCH PLANS FOR CALENDAR YEAR 1980

Studies of high temperature corrosion by gaseous environments containing sulfur and oxygen compounds will continue. Results to date have indicated that the buffering capacity of such gases, defined as the rate of change of sulfur potential with removal of oxygen, may be important, and this will be studied using gas mixtures in the S-O-H and C-O-S systems which have identical initial sulfur and oxygen potentials. Already it seems that the sulfur and oxygen potential of the gas are not necessarily the critical parameters in controlling behavior, and that the relative amounts of oxygen- and sulfur-containing species in the gas and the flow rate are involved. Studies will be extended to higher oxygen potentials where SO_2 is the major sulfidizing species. Transport through Cr_2O_3 has been shown to be critical and studies of the influence of dissolved sulfur on the defect chemistry and transport properties of Cr_2O_3 are planned using thermogravimetric measurements in controlled atmospheres. Sulfur solubility as a function of sulfur

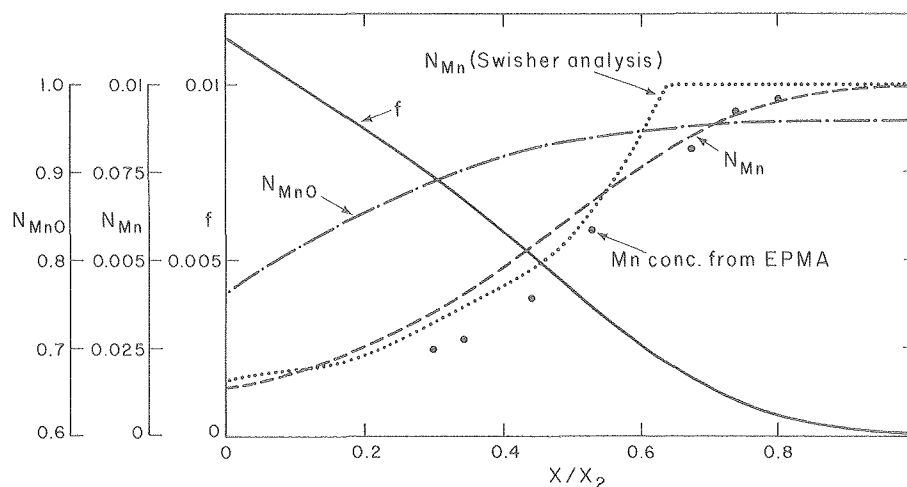


Fig. 3. Comparison of calculated and experimentally measured profiles for Fe-1% Mn oxidized in H_2O/H_2 (0.2) at $1350^\circ C$. (XBL 802-318)

and oxygen activity will also be determined. Attempts to construct meaningful alloy-O-S stability diagrams will be initiated, providing sufficient data exist.

Research into corrosion by liquid sulfate deposits has reached the stage at which the reactions of the sulfate melt should be studied in more detail. The formation of pertinent binary and ternary sulfates such as $\text{NaAl}(\text{SO}_4)_2$, $\text{Na}_3\text{Cr}(\text{SO}_4)_3$ and the CoSO_4 - NiSO_4 - Na_2SO_4 liquids as a function of SO_3 partial pressure will be studied. The mechanism of continued transport of SO_3 through the molten sulfate will be determined by SO_3 - solubility studies and Raman spectroscopy identification of the ionic state of sulfur compounds in the metal.

Oxide scale adhesion studies will be continued with attempts to develop a more quantitative description of the peg development at the alloy/scale interface. Low-angle erosion data will also be utilized as a potentially better method of quantifying scale adhesion. It is also planned to examine other parameters which can affect peg development: grain size, intermetallic and oxide dispersions, which can be varied more effectively by using actual PVD, sprayed and diffusion coatings. Microscopy studies of the early stages of oxide growth will also be initiated. A new program on the use of rare earth oxides added as surface deposited nitrates, to inhibit high temperature oxidation and scale spallation will be commenced.

Theoretical studies will concentrate on the growth of multiphase regions during diffusional-controlled reactions with particular reference to internal carburization as a degradation process. The ingress of interstitial elements such as oxygen and sulfur along alloy grain boundaries will be incorporated into the diffusion model.

1979 PUBLICATIONS AND REPORTS

Refereed Journals

1. D. P. Whittle and J. Stringer, "Improvements in High Temperature Oxidation Resistance by Additions of Reactive Elements or Oxide Dispersions," *Phil. Trans. Roy. Soc. A27* (56), 209 (1979).
2. I. M. Allam, D. P. Whittle and J. Stringer, "Improvements in Oxidation Resistance by Dispersed Oxide Addition: Al_2O_3 - Forming Alloys," *Oxidation of Metals* **13**, 381 (1979), LBL-9072.
3. O. T. Goncel, D. P. Whittle, and J. Stringer, "The Oxidation Behavior of Austenitic Fe-Cr-Ni Alloys Containing Dispersed Phases," *Corros. Sci.* **19**, 305 (1979).
4. G. W. Roper and D. P. Whittle, "Interdiffusion in Ternary Co-Cr-Al Alloys," *Metals Sci. J.* (1980); LBL-8791.
5. F. Gesmundo, P. Nami, and D. P. Whittle, "High Temperature Oxidation of Co-Mn Alloys," *Corros. Sci.* **19**, 675 (1979).

Other Publications

1. D. P. Whittle, "General Aspects of High Temperature Corrosive Attack: Influence of Gaseous Atmosphere," *High Temperature Corrosion*, Commission of European Communities, Brussels (1979),
2. D. P. Whittle, "Hot Corrosion," *High Temperature Corrosion*, Commission of European Communities, Brussels (1979),
3. D. P. Whittle, "Introduction to Session on Corrosion," *Proc. of Conf. on Corrosion/Erosion of Coal Conversion System Materials*, Berkeley (1979), NACE, pp. 218-222.
4. K. N. Strafford, D. P. Whittle, P. J. Hunt and A. K. Misra, "The Corrosion of M-Cr-Al-Y-Type Alloys: Evaluation Studies," *Proc. 4th Conf. on Gas Turbine Materials in the Marine Environment* (1979).

LBL Reports

1. I. M. Allam, H. C. Akuezue, and D. P. Whittle, "Influence of Small Pt Additions on Al_2O_3 Scale Adherence," LBL-9180.
2. I. M. Allam, D. P. Whittle and J. Stringer, "The Role of Active Elements and Oxide Dispersions in the Development of Oxidation-Resistant Alloys and Coatings," LBL-9516.
3. G. W. Roper and D. P. Whittle, "Multicomponent Diffusion," LBL-9758.
4. O. T. Goncel, D. P. Whittle, and J. Stringer, "The Oxidation Behavior of Fe-Cr Alloys Containing HfO_2 - Dispersed Phase," LBL-9709.
5. D. P. Whittle and A. V. Levy, "Oil Shale Retort Components," LBL-9792.
6. T. Hadishi, A. V. Levy, D. P. Whittle and E. Cuellar, "Determination of S_2 in Reactive Gas Mixtures by Tunable Atomic Line Molecular Spectroscopy," LBL-9678.
7. R. Stanley, D. P. Whittle, and A. V. Levy, "Characterization of the Degradation of Hydrodesulfurizing Catalysts," LBL-10026.
8. D. P. Whittle, F. Gesmundo, D. D. Bastow, and G. C. Wood, "Formation of Subscales of Varying Composition," LBL-10067.
9. H. C. Akuezue, "Calcium Sulfate-Induced Accelerated Corrosion," (M.S. thesis), LBL-10286.

Invited Talks

1. I. M. Allam, D. P. Whittle, and J. Stringer, "Improved Adhesion of Al_2O_3 Scales on CoCrAl Alloys," poster paper, Gordon Research Conf. on Corrosion, New London, New Hampshire, July 1979.
2. F. Gesmundo, F. Vianni, and D. P. Whittle, "High Temperature Oxidation of Two Phase Alloys," poster paper, Gordon Research Conf. on Corrosion, New London, New Hampshire, July 1979.

3. A. K. Misra and D. P. Whittle, "Hot Corrosion of Nickel-Base Alloys at Intermediate Temperatures," Electrochem. Soc. Meeting, Los Angeles, California, October 1979.
4. D. P. Whittle, "The Importance of the Metal/Scale Interface in High Temperature Oxidation," DOE Meeting on Microchemical and Microstructural Analysis of Minority and Interface Phases, Germantown, Maryland, May 1979.
5. K. N. Strafford, D. P. Whittle, P. J. Hunt, and A. K. Misra, "The Corrosion of M-Cr-Al-Y type Alloys: Evaluation Studies," 4th Conf. on Gas Turbine Materials in a Marine Environment, Annapolis, Maryland, June 1979.
6. T. Hadeishi, A. V. Levy, D. P. Whittle, and E. Cuellar; "Determination of S₂ in Reactive Gas Mixtures by Tunable Atomic Line Molecular Spectroscopy," 1979 Symposium on Instrumentation and Control for Fossil Energy Processes, Denver, Colorado, August 1979.

4. Engineering Materials

a. Erosion-Corrosion-wear Program*

Alan V. Levy, Investigator

Introduction. Erosion-corrosion studies have been conducted to gain a fundamental understanding of the mechanisms that are active when small particles entrained in gas or liquid carrier fluids impact the containment wall surfaces of coal conversion system components. Considerable advancements have been made in defining the mechanical and metallurgical interrelationship between an impacting particle and the surface which it impacts upon. A documented mechanism of material loss has been identified that markedly changes the basis for developing models for erosion loss in ductile materials. The forces transferred into a target material by a single impacting particle 600 μm in diameter have been measured.

The fluid mechanics of two-phase flow at low velocities has been defined in a manner that accounts for the aerodynamic contribution of the impacting particle's behavior to the erosion mechanism. By so doing it is now possible to account for experimentally determined velocity exponents in the erosion model up to values of 4, an impossibility heretofore. Also, the pattern of particle distribution in a three-dimensional curved pipe has been analytically established. A laser doppler velocimeter test apparatus is now in place to experimentally verify analytically determined two-phase flow behavior. The erosion behavior of thin scales formed on corrosion resistant stainless steels in elevated temperature oxidizing and sulfidizing gas systems has been determined to be morphology sensitive. An improved design for an elevated temperature, reactive gas erosion tester that can precisely control test conditions has been completed.

The effect of variations in brittle materials, both eroding particles and target surface material, has been investigated analytically and experimentally. The effect of brittle eroding particles of varying hardness and friability of six different minerals on the erosion of ductile aluminum and steel materials has been determined. The experimentally determined behavior patterns have been found to correlate well with the proposed basic mechanism of ductile metal erosion. The erosion of brittle materials as a function of stress and strain patterns in the region of particle impact has been analytically described.

The mechanism of corrosion of stainless steel

in contact with char particles has been determined for a number of environmental conditions of char composition variation and covering bulk gas composition and flow. It has been determined that the char can act as both a source for corroding species and a barrier against their reaching the metal surface from corrosive bulk gases. The behavior of the char as a barrier is more a function of its composition than its depth over the metal's surface.

The principals and diagnostic tools used to study elevated temperature oxidation-sulfidation behavior of metals in coal and oil shale conversion environments have been successfully used to observe surface and bulk characteristics of metal-alumina heterogeneous catalyst pellets and to potentially account for at least some of their change in activity as a function of their service in coal conversion system applications.

Erosion Behavior

1. EROSION MECHANISMS IN DUCTILE METALS[†]

R. Bellman, Jr.

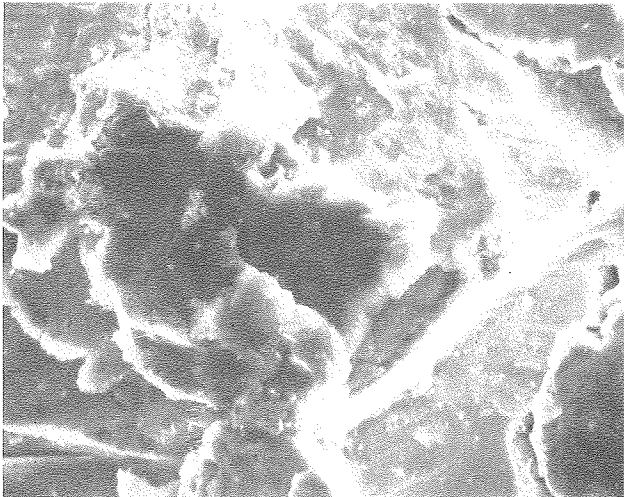
The mechanical mechanism of erosion of a ductile metal by impacting particles has been variously described as a micro machining action¹ or a ploughing behavior² or a brinnelling type of indentation deformation. These mechanisms have been used to establish analytical models, none of which completely defines the behavior. In order to establish a better foundation for modelling, an experimental technique has been developed that meticulously observes sequential deformation of metal surfaces, a particle impact at a time, using the SEM and considerable patience. By following the behavior of a specific area under the SEM from the beginning of erosion deformation of the surface to steady state erosion, a single, pervading mechanism has been documented that occurs at shallow and steep impingement angles alike. This mechanism is a smearing of surface material by a combined forging-extrusion of the surface that produces small platelets that are eventually knocked off the surface by succeeding particle impacts. No cutting action that would create fresh surface in the bottom of an impact formed crater was observed.

The platelet forming mechanism was observed at impingement angles of 30° and 90° on 1100-0 and 7075-T6 aluminum impacted by 600 μm SiC particles at 100 fps and on 1020 steel eroded at an angle of 30° by 250 μm SiC particles at 100 fps. SEM

* This work was supported by the Division of Materials Sciences, Office of Basic Energy Sciences, U. S. Department of Energy.

observations were made of single impacts on fresh and on steady state eroded surfaces and, sequentially, of surfaces impacted by 0.1, 0.2, 0.3, 0.4 and up to 2 gm of particles. Platelet formation is accompanied by localized adiabatic heating of the immediate area affected by the particle's impacting force to temperatures of the order of the annealing temperature in the case of the aluminum.³ The heating results in little difference in the appearance of the impacted area between soft, 1100-0 aluminum and the much harder 7075-T6 aluminum alloy. Cold working of the surface by the deformation from particle impacts does appear to occur below the surface smeared material, resulting in platelets being formed and broken off more readily as erosion continues, but no basic change in the smearing, platelet forming mechanism.

Figure 1 shows an area on the surface of a steady state eroded 7075-T6 aluminum specimen that was subsequently eroded with an additional 1 and 2 gm of particles. The deformed platelets on the surface can be seen in the upper photograph, which



20 μ m

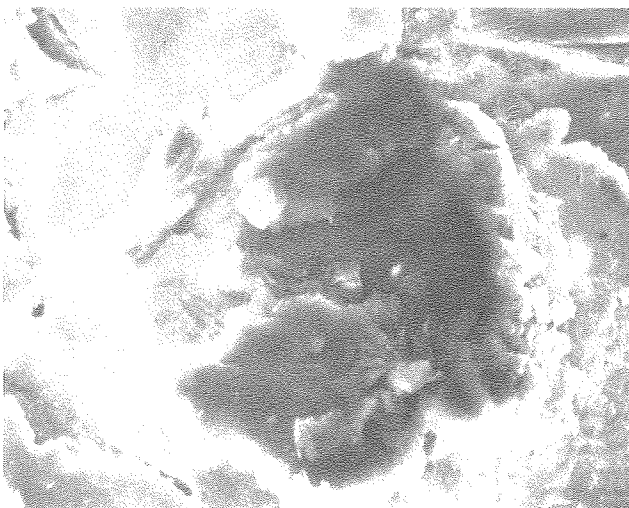
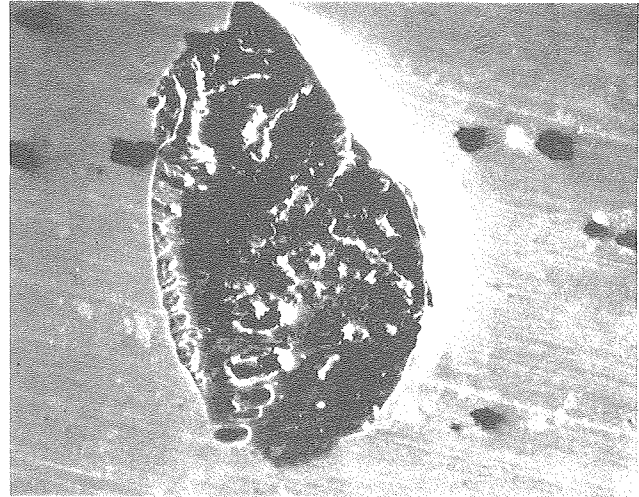


Fig. 1. Sequential removal and formation of platelets in 7075 Al by 600 μ m SiC particles at 100 fps.
(XBB 7910-13307)

is of a shallow crater. In the lower photo, after an additional gram of particles had been impacted upon the surface, some of the platelets are shown to have been removed and others formed. The nature of the platelet activity in the area shown is somewhat stylized and represents the mechanism in a simple form. Most material removal observed does not have as ideal a configuration of the platelets. However, essentially no cutting of chips has been observed.

Figure 2 shows a single particle impact crater on a 7075-T6 aluminum surface that was coated with gold before being impacted by a 600 μ m SiC particle at an angle of 30° and velocity of 150 fps. The particles in the unaffected areas of the surface and in the crater are the typical contaminant particles which occur in 7075 alloy. While the impact crater is relatively deep, some of these particles remain in its surface, indicating that the crater was formed by a smearing type rather than a cutting action. An x-ray map of gold was made of the crater area on the SEM and shows the



20 μ m

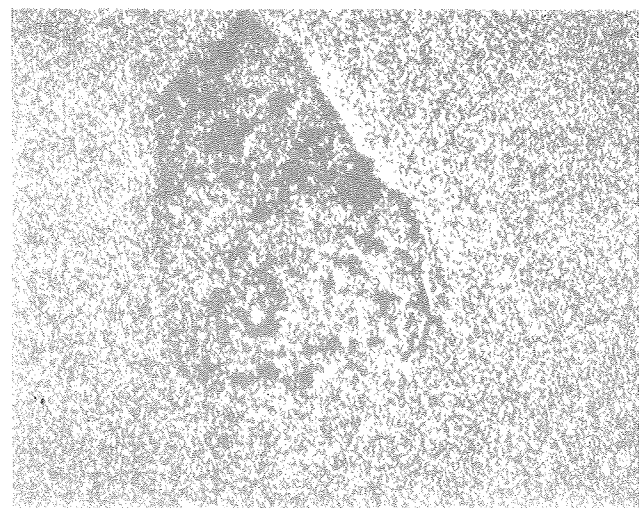


Fig. 2. Single impact crater in 7075 Al surface that was gold coated prior to particle impact.
(XBB 7910-13304)

presence of the gold deposited initially on the surface of the alloy across the entire crater surface, a further indication that cutting did not occur in the crater. The buildup of a lip of metal on the right side of the crater is the beginning of the formation of a platelet.

The metallographic observation of the sequential nature of erosion of ductile metals using eroding particle sizes that are representative of those in actual service will be continued to form the basis for an analytical model based upon forging-extrusion mechanisms.

* * *

[†]Brief version of LBL-10289.

1. I. Finnie, "Erosion of Surfaces by Solid Particles," *WEAR* 3, 87 (1960).
2. J. G. A. Bitter, "A Study of Erosion Phenomena Part I," *WEAR* 6, 5 (1963).
3. R. E. Winter and I. M. Hutchings, "The Role of Adiabatic Shear in Solid Particle Erosion," *WEAR* 34, 141 (1975).

2. EROSION OF THIN SCALES[†]

J. Maasberg

The surface degradation of stainless steels by the combined erosion-corrosion mechanism which occurs at elevated temperatures in coal gasification systems is a function of the formation rate of the protective scales on their surfaces and the removal of those scales by impacting solid particles. An investigation of the erosion behavior of the thin (1-5 μm) Cr_2O_3 barrier scales formed on 310SS in oxidizing and combined oxidizing-sulfidizing gases at 982°C has been carried out by eroding them at room temperature. The erosion behavior of Al_2O_3 barrier scales formed on an experimental Fe-18Cr-5Al-1Hf was also investigated.

Significant differences in the erosion behavior of the scales occurred as the result of variations in the oxygen content of the gas used to develop the scale, the presence of sulfur in the gas, the formation of SiO_2 at the scale-metal interface, and between Cr_2O_3 and Al_2O_3 protective scale compositions. Little difference in the erosion behavior occurred as the result of the surface condition of the alloy prior to scale formation, the temperature of scale formation, preoxidation, the activities of oxygen and sulfur in the gas at levels where sulfide formation did not occur, and the angle of impingement (30° and 90°) of the impacting 50 μm SiC particles at 100 fps velocity.

Figure 1 plots the erosion weight loss vs. amount of eroding particles for 310SS eroded in an air atmosphere ($P_{\text{O}_2} = 0.2$ atm) and in two low oxygen activity gases ($P_{\text{O}_2} = 10^{-15}$, 10^{-19} atm) and for a Fe-18Cr-5Al-1Hf alloy. The greater erosion loss for the air oxidized Cr_2O_3 barrier scale of the 310SS compared to the Cr_2O_3 formed in the low oxygen content gases was determined to be primarily due to the presence of internally

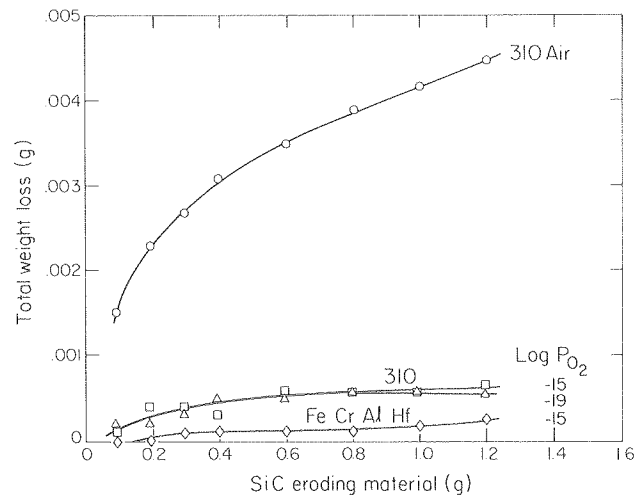


Fig. 1. Erosion of thin scales on 310SS and Fe-18Cr-5Al-1Hf formed at 982°C at different oxygen partial pressures. (XBL 793-803)

formed SiO_2 at the metal-scale interface. The more continuous SiO_2 layer in the air formed oxide scale and its orientation parallel to the scale-metal interface degraded the bond between the scale and the metal, enhancing its loss by erosion. Less SiO_2 formed in the low P_{O_2} exposures and no SiO_2 formed in the Al_2O_3 forming alloy, whose scale eroded the least. The presence of small amounts of Si in the 310SS was responsible for the formation of the SiO_2 .

Figure 2 compares 310 stainless steel with the Fe-18Cr-5Al-1Hf alloy. The Fe-Cr-Al-Hf alloy eroded less and this is attributed to the pinning seen in the scale-metal interface as well as the absence of SiO_2 near the scale-metal interface.

After comparing erosion rates with the morphologies of the scale-metal interfaces, it appears that there are three types of interfaces which can form, each corresponding to a different degree of susceptibility to erosion. Figure 3 shows the types of interfaces. The first type shows a pinning between the outer oxide scale and the metal due to the action of an internally formed oxide. This scale showed the least amount of erosion. The second type shows a smooth contact between the metal and the oxide, with the internally formed oxide having little influence over the erosion. This type of interface showed a moderate amount of erosion. The third type of interface shows an internal oxide running parallel under the surface scale. This type exhibited a high degree of erosion due to a lack of bonding between the metal and the scale.

* * *

[†]Brief version of "Erosion of Oxide Scales on Metal Substrates," Proceedings NACE Conference on Corrosion-Erosion of Coal Conversion System Materials, Berkeley, California, Jan. 24-27, 1979.

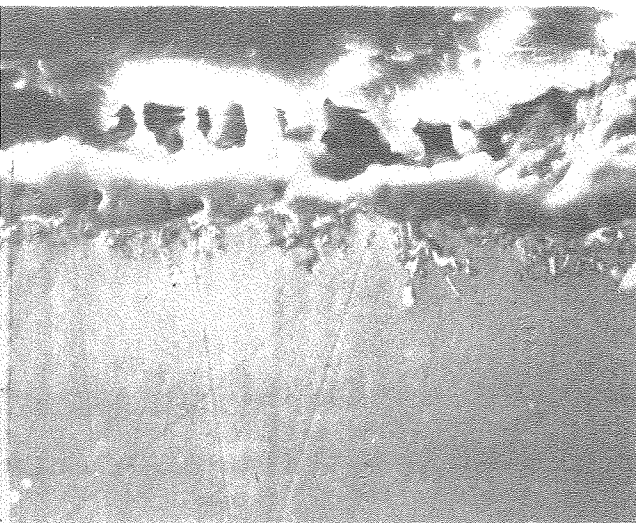
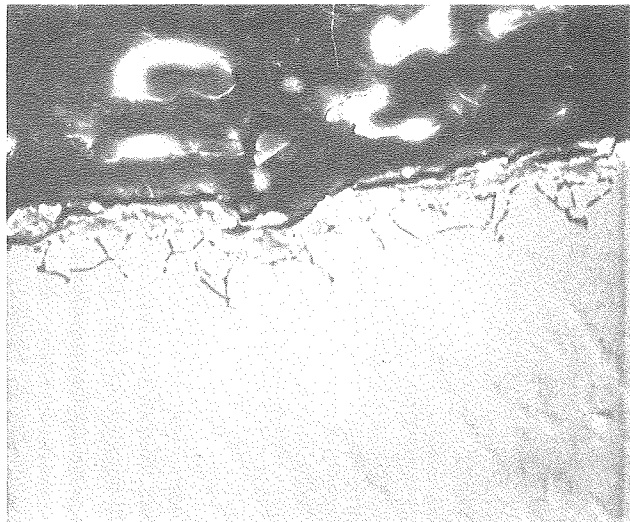
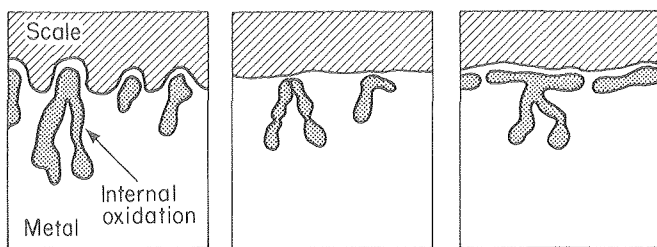


Fig. 2. Microstructure of 310SS and Fe-18Cr-5Al-1Hf formed at $PO_2 = 10^{-15}$ atmos at $900^\circ C$. (XBB 797-8943)



1. Pinning 2. Smooth contact 3. Parallel subscale
 — Increasing ease of erosion —>

Fig. 3. Sketches of morphologies of internally oxidized SiO_2 in 310SS. (XBL 7912-13356)

3. EROSION MECHANISMS IN BRITTLE SOLIDS

M. Khatibloo

An analytical model for erosion of brittle materials has been developed that agrees more closely with observed brittle material erosion cracking mechanisms than previous models in the literature.^{1,2} It relates the very complex stress and fracture distributions in the contact area of an eroding particle in terms of the target material's properties and the velocity, density and radius of the impacting particles. Because of the low velocity of erosive particle impacts in energy conversion system components, a quasistatic condition is assumed with negligible dynamic effects. Two types of particles were considered in the models, each of which results in a distinctive cone or radial crack formation when it impacts the target surface. The spherical particle induces an elastic response in the eroding material while the angular particle usually causes some plastic flow to occur.

The model considers the point of maximum stress intensity factor, K_I , as being the point where fracture as the result of particle impact will initiate. The stress intensities for positions along the surface of the target material out from the area of contact of the impacting particle were calculated for different crack lengths of small, pre-existing flaws in the brittle material's surface, designated C in Fig. 1. The calculations

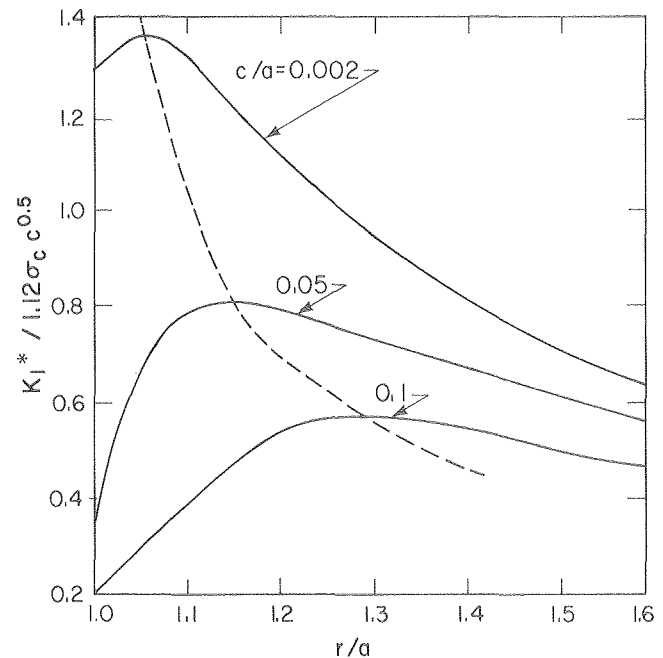
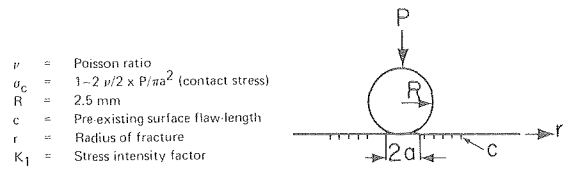


Fig. 1. Variations of the stress intensity factor, K_I^* , with the distance from the contact circle with different surface flaw sizes. (XBL 801-51)

were made for many points out from the particle's area of contact, designated 2a in Fig. 1, along the direction r and plotted, normalizing for the contact area of the particle. It can be seen that as the pre-existing flaw length increases, the normalized stress intensity K_{I}^* decreases and the position of its maximum out from the area of contact, r, increases (dotted line). Thus, the radius of fracture, r, of the eroding particle impact induced crack changes with the size of the pre-existing flaw. This is shown in Fig. 2. These predicted locations agree with data taken from several literature sources^{3,4} and constitute a major advancement in the development of erosion models for brittle materials.

* * *

1. F. C. Roesler, "Indentation Hardness of Glass as an Energy Scaling Law," Proc. Phys. Soc. B 69, 55 (1956).
2. F. C. Frank and B. R. Lawn, "On the Theory of Hertzian Fracture," Proc. Royal Soc. Series A 299, 291 (1967).
3. H. L. Oh and I. Finnie, "On the Location of Fracture in Brittle Solids," Int. J. of Frac. Mech. 6, 287 (1970).
4. A. S. Argon, Y. Hori, and E. Orowan, "Indentation Strength of Glass," J. Am. Ceram. Soc. 43, 86 (1960).

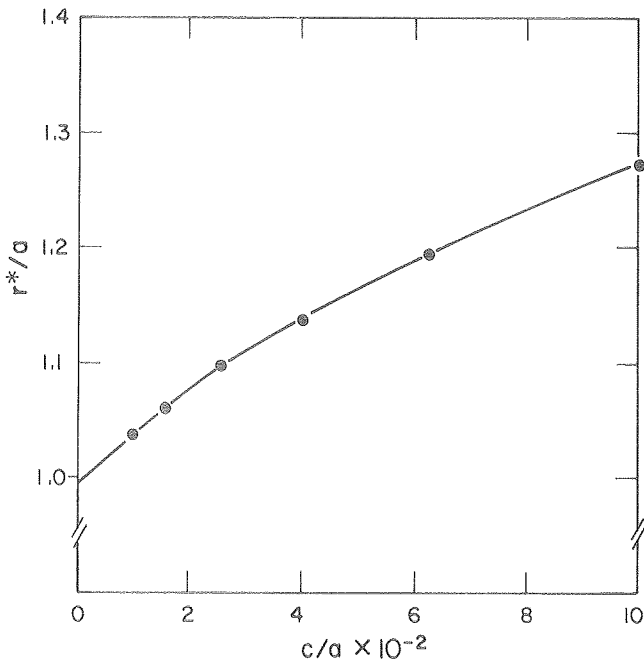
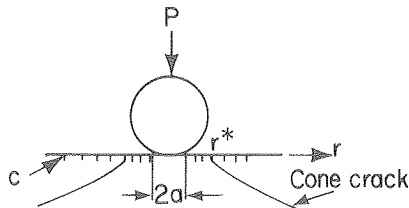


Fig. 2. Variation of the radius of fracture (r) with the surface having pre-existing flaw sizes of length C. (XBL 801-50)

4. EFFECT OF PARTICLE CHARACTERISTICS ON EROSION OF DUCTILE METALS[†]

J. Kim

The effect of the strength, hardness and friability of the impacting particles on the erosion of ductile metals at room temperature has been determined.¹ Most mechanical erosion tests are conducted with particles with Moh hardness greater than 7 and usually 9 or over.² Since char particles in coal gasifiers consist of materials with hardnesses considerably lower than 7, it is important to understand the erosive capabilities of softer particles. Table 1 lists the materials that were tested and the range of hardness they represent. All of the erosion tests were conducted with 50-70 mesh size particles at a velocity of 67 mps (220 fps) at impingement angles of 20° and 90°. The target materials were 1100-0 Al with a VHN = 37 kg/mm² and 1020 steel with a VHN = 194 kg/mm².

Table 1. Impacting particle materials.

| Abrasive Particle | MOHS Hardness | Vickers Hardness, VHN (kg/mm ²) |
|--|---------------|---|
| Calcite, CaCO ₃ | 3 | 115 |
| Fluorite, CaF ₂ | 4 | 180 |
| Apatite, Ca ₅ (PO ₄) ₃ (OH,F,Cl) | 5 | 300 |
| Sand, SiO ₂ | ~ 7 | 700 |
| Alumina, Al ₂ O ₃ | 9 | 1900 |
| Silicon Carbide, SiC | > 9 | 3000 |

It was determined that the nature of the abrasive particle has a significant effect on the erosion of the target materials, particularly in the lower hardness range of the particles. Figure 1 plots the erosion rate of the aluminum and steel as a function of eroding particle hardness. The soft particles are more friable than the hard particles and break up more easily upon impact, blunting the portion of them that transmits the eroding force to the target material and decreasing the effective size of the eroding particle mass. The higher hardness particles retain their size and shape better and this results in increased erosion. This increase is more due to the increasing integrity of the impacting particles than to their hardness.

Above a critical hardness, which was determined to be approximately VHN = 700 kg/mm, the mass and shape of the particles is adequate to have a maximum effect on the target material and further increases in particle hardness had little or no further effect on the erosion rate of the aluminum and steel. The peak in the erosion rate of the aluminum at a VHN = 400 kg/mm relates to the degree of secondary erosion from fragments of the initial particles and the degree of work hardening of the

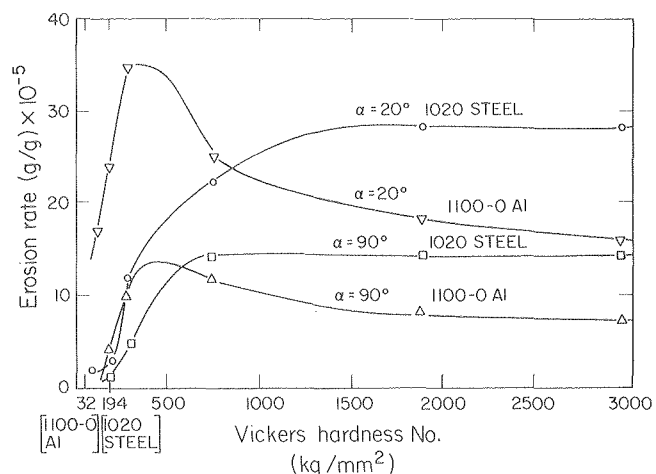


Fig. 1. Effect of impacting particle hardness on erosion behavior of 1100-OAl and 1020 carbon steel at impingement angles, α , of 20° and 90°.

(XBL 801-47)

subsurface area that is caused by the impacting particles and the resultant size of the eroding platelets that can be formed. The shape of the steel curve conforms to Tillys³ curve of particle size vs. erosion rate, further indicating that the size of the effective eroding particle is determining the erosion rate and not its hardness.

* * *

†Brief version of LBL-10268.

1. K. Nelliger and H. Uetz, *Wear* 1, 225 (1954).
2. Iain Finnie, *Wear* 19, 81 (1972).
3. J. Goodwin, W. Sage, and G. Tilly, "Study of Erosion by Solid Particles," *Proceedings of Institution of Mechanical Engineers (London)* vol. 184, 279 (1969).

5. THE HALO EFFECT IN JET IMPINGEMENT SOLID PARTICLE EROSION TESTING OF DUCTILE METALS†

L. Lapidés and A. Levy

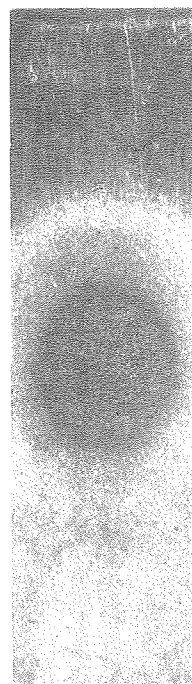
Two different areas of erosion occur on flat test specimens exposed to gas solid particle erosive streams where the stream diameter is smaller than the specimen surface dimensions. The inner area accounts for the majority of the weight loss (see Fig. 1). This area sees the set test conditions of velocity and impingement angle. Erosion also occurs outside this area in an area designated as the "halo area". The weight loss in this area depends on the impingement angle of the particles, and ranges from as high as 25% of the total weight loss at 15° to 3% of the total weight loss at 60°. Figure 2 shows the geometry of the impingement; Table 1 shows the values of the variables. A definite boundary was observed between the two areas. This halo erosion effect was found to be primarily due to the velocity distribution of the particles in a cone around the



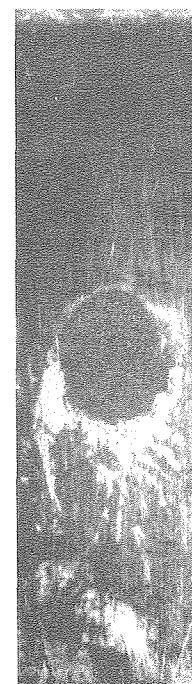
15° Unmasked



15° Masked



60° Unmasked



60° Masked

Fig. 1. Masked and unmasked specimen appearance after erosion at impingement angles of 15° and 60°. (XBB 7810-13575A)

principal column of particles striking the specimen. Table 1 shows that the velocities vary by a factor over 2 between the primary and halo areas. A

Corrosion Behavior

1. CORROSION OF METALS BY CHAR[†]

T. Foerster

The presence of char in coal gasification reactors provides a potential corrodent to metal surfaces that come in contact with it in a static or semi-static mode.^{1,2} A study has been completed to determine the mechanisms of the elevated temperature corrosion that occurs and the effects of variables such as the char composition, quantity of char and bulk gas composition over the char. The 304SS was exposed to the test chars at 982°C for times from 24 to 96 hours.

Figure 1 plots the weight gain of the 304SS for several gas conditions over the char for three different chars; FMC char from W. Kentucky coal, Husky char from North Dakota lignite and Synthane char from Illinois #6 coal. The FMC char was processed at a low temperature in the COED process and retained a significant amount of volatile sulfur while containing a relatively low amount of CaO in its low ash content. The Husky and Synthane chars were processed at higher temperatures which eliminate volatile sulfur from their chars and they contained high quantities of CaO in higher total ash contents compared to the FMC char. These factors explain the resulting weight gain differences.

In the closed exposure retort test with no circulating bulk gas over the char bed, the volatile sulfur in the FMC char was retained in the char, producing a high sulfur activity at the char-metal interface and a resultant greater degree of sulfidation and resultant weight gain. When the stopcock on the retort was opened, the volatile sulfur could escape from the FMC char and the weight gain was reduced. When a 1% H₂S bearing gas was flushed

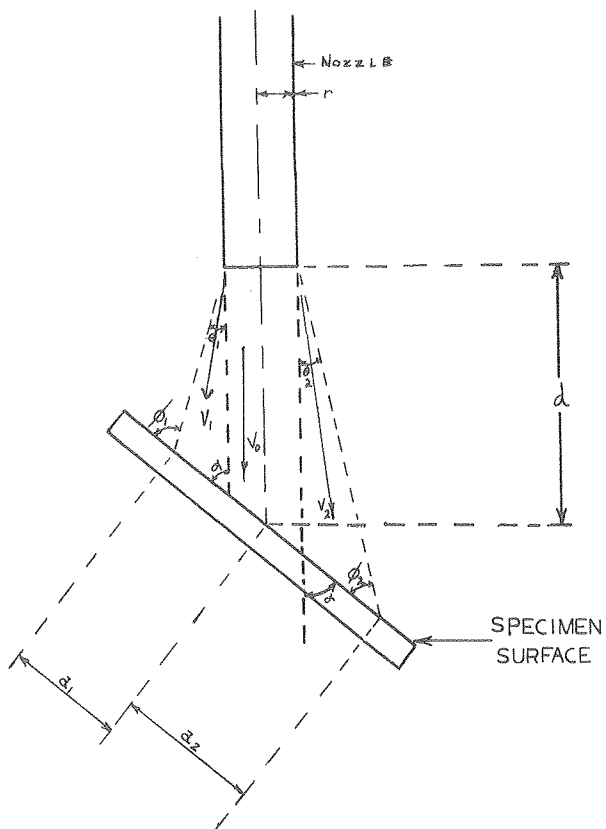


Fig. 2. Diagram of relationship between nozzle and specimen. (XBB 7811-12814A)

Table 1. Values of variables and erosive flow.^a

| Term | 15° | | | Angle 60° | | |
|------------|---------|----------|------|-----------|----------|------|
| | Primary | Boundary | Halo | Primary | Boundary | Halo |
| b_1 | 0.15 | 0.25 | 0.35 | 0.15 | 0.22 | 0.30 |
| b_2 | 0.75 | 0.94 | 1.25 | 0.17 | 0.26 | 0.40 |
| V_1 | 140 | 123 | 96 | 191 | 126 | 88 |
| V_2 | 151 | 134 | 116 | 172 | 117 | 81 |
| θ_1 | | 4.5° | | | 4.2° | |
| θ_2 | | 3.4° | | | 5.1° | |

^aSee Fig. 2.

^bThese are only relative velocities, not absolute velocities.

secondary effect is the change in the true angle of the particles striking the specimen from the set angle.

* * *

[†]Brief version of LBL-8525.

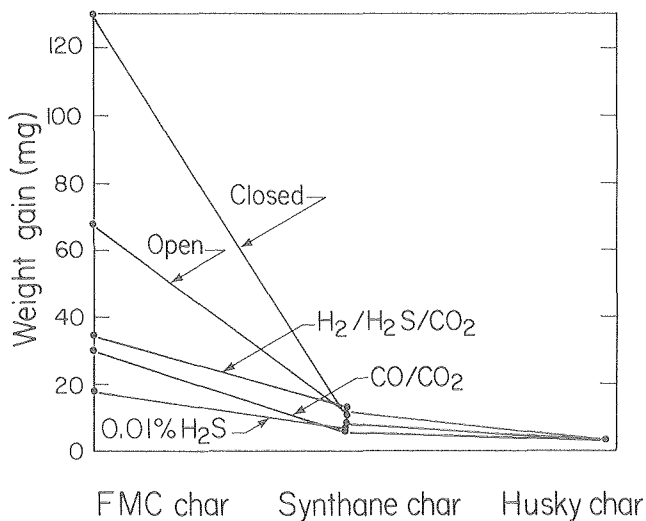


Fig. 1. Weight gain of 304SS exposed to three different chars at several gas conditions. (XBL 795-1670)

through the system, additional volatile sulfur was removed from the FMC char and the weight gain from sulfidation was further reduced, even though the bulk gas had its own sulfur content. When the sulfur activity of the bulk gas was reduced, the bottom two points for the FMC char on the weight gain plot resulted. The Synthane and Husky char specimens had lower weight gains than any of the FMC char specimens because the CaO in those chars acted as a getter for the sulfur that was present. The Husky char had the highest CaO content in its ash of the three chars tested, 13 wt.% composed to 6.5 wt.% for the Synthane char and 4% for the FMC char.

Figure 2 shows the external and internal sulfide scale formed on the 304SS when it was exposed to the FMC char in a closed test retort for 24 hours. Pieces of char were encapsulated in the scale that formed. Figure 3 shows the considerably reduced amount of scale that formed on the 304SS in the test where a 1% H₂S content, moving bulk gas was maintained over the FMC char bed in a 96 hour test.

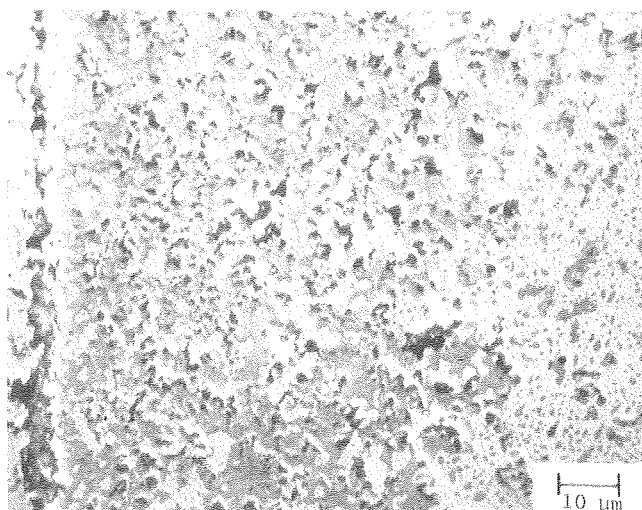
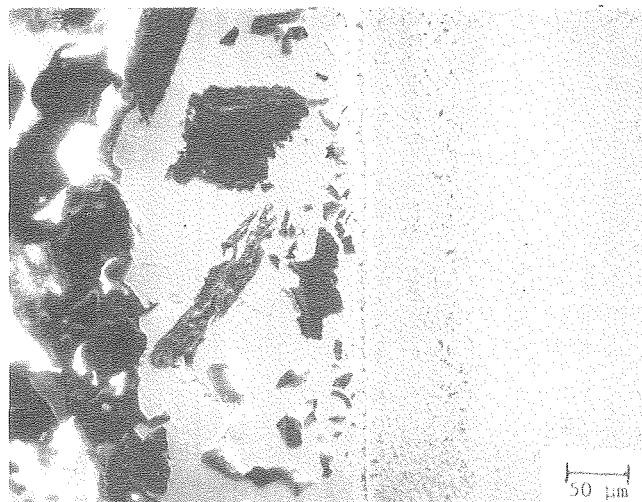


Fig. 2. External and internal sulfide scale formations on 304SS exposed to FMC char in a closed retort for 24 hrs. (XBB 795-6632)

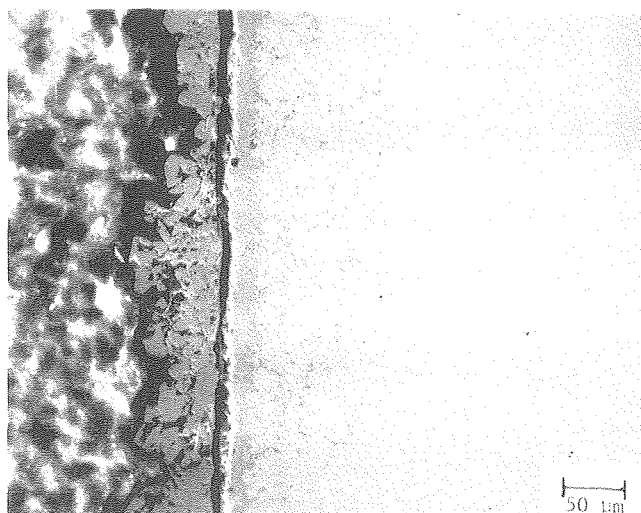


Fig. 3. External and internal sulfide scale formations on 304SS exposed to FMC char with 1% H₂S content flowing bulk gas. (XBB 795-7481)

The increased exposure time resulted in a decreased amount of sulfidation because of the removal of the volatile sulfur from the char by the moving bulk gas.

The Husky and Synthane chars acted as a barrier to the sulfur in the bulk gas, resulting in less sulfidation as the char thickness was increased over the specimens. However, the carbon in the char acted as a getter for the oxygen in the bulk gas and, as the char thickness over the 304SS was increased, the amount of Cr₂O₃ formation on the 304SS decreased.

This project demonstrated the sensitivity of stainless steels to corrosion in contact with chars of varying composition from different gasification processes and starting coals.

* * *

[†]Brief version of LBL-9308.

1. B. Gordon, "Corrosion of Iron Base Alloys by Coal Char at 871° and 982°C," M.S. thesis, LBL-7604, March 1978.
2. D. Douglass and V. Bhide, "Mechanism of Corrosion of Structural Materials in Coal Gasifier Atmospheres," UCLA, August 1978.

2. CATALYTIC DEACTIVATION[†]

R. Stanley, D. P. Whittle, A. Levy, and H. Heinemann

The use of heterogeneous desulfurization catalysts consisting of silica-alumina supports on which are deposited Ni-Mo, Co-Mo as oxides that could be susceptible to sulfidation in the operating environments of coal conversion systems were studied to determine the nature of the pellet surfaces after service and upon regeneration. Fresh, spent,

and spent and regenerated catalysts of two types were obtained from the Mobil Oil Corp. and metallurgically analyzed. It was determined that relatively thick scales up to 20 μm containing concentrations of sulfur and metallic elements from the environment and from the catalyst pellets formed on the pellet surfaces under some conditions. Surface areas and pore volumes were markedly reduced on those pellets where the scales formed.

Figure 1 shows two cross sections of a pellet of HDS-1441 catalyst that had been used to hydrodesulfurize crude oil. The fresh catalyst shows no scale while the spent and regenerated scale shows a heavy formation of scale. Figure 2 shows the scale highly magnified along with EDAX analyses of its composition at various points. It can be seen that the scale contains concentrations of

sulfur and vanadium, both of which decrease as the analysis moved toward the center of the pellet. The presence of peaks of S, V, Mo, Ti and Fe near the surface of various pellets studied indicates that the metallic constituents of the environment and the catalyst are reacting with sulfur and probably oxygen to form surface scales that can markedly reduce the activity of the catalysts. Concentrations of these elements were verified by electron probe micro analysis. Work is currently underway to use metallurgical techniques to further study surface behavior of desulfurization catalysts.

* * *

† Brief version of LBL-10026

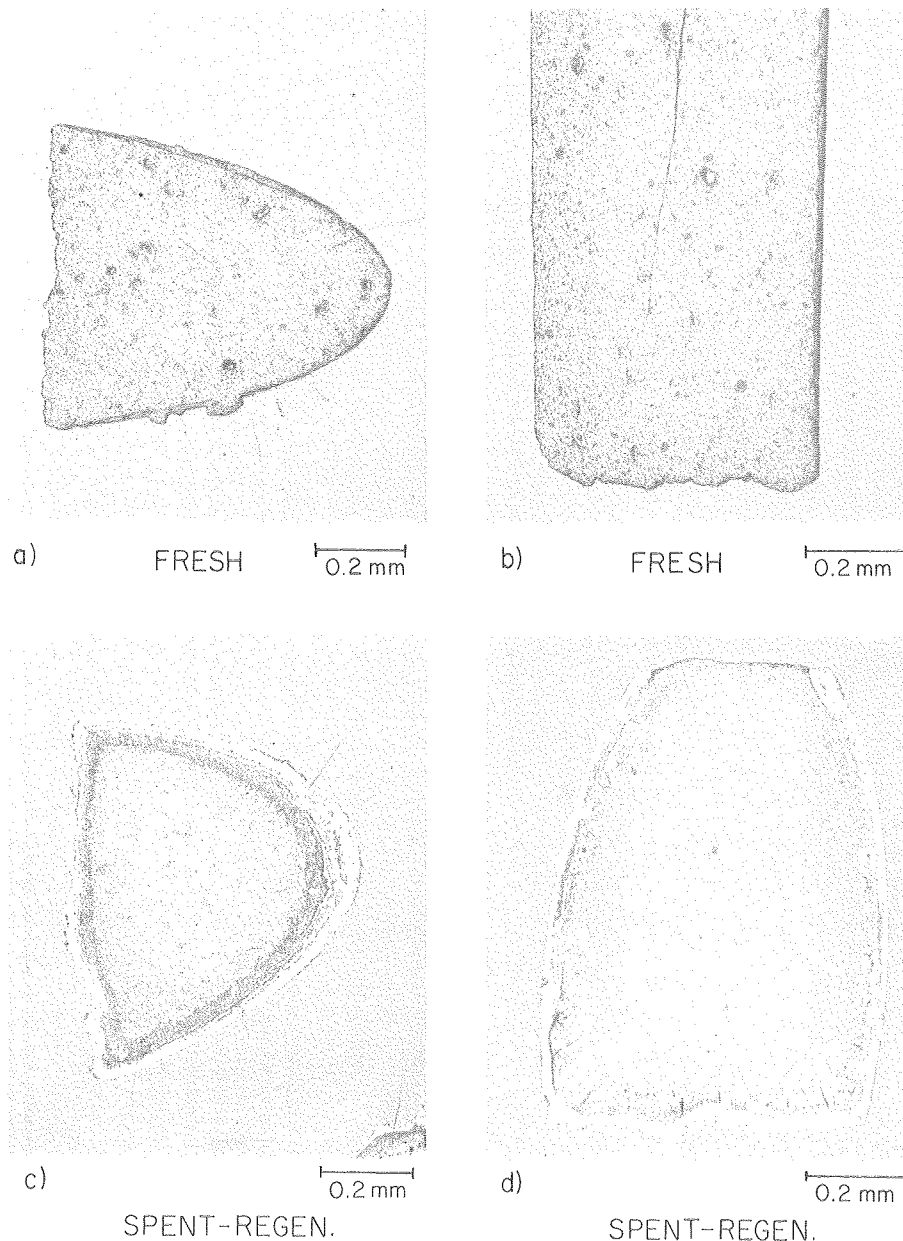


Fig. 1. Scale formation on spent and regenerated desulfurization catalyst pellet. (XBB 802-2169)

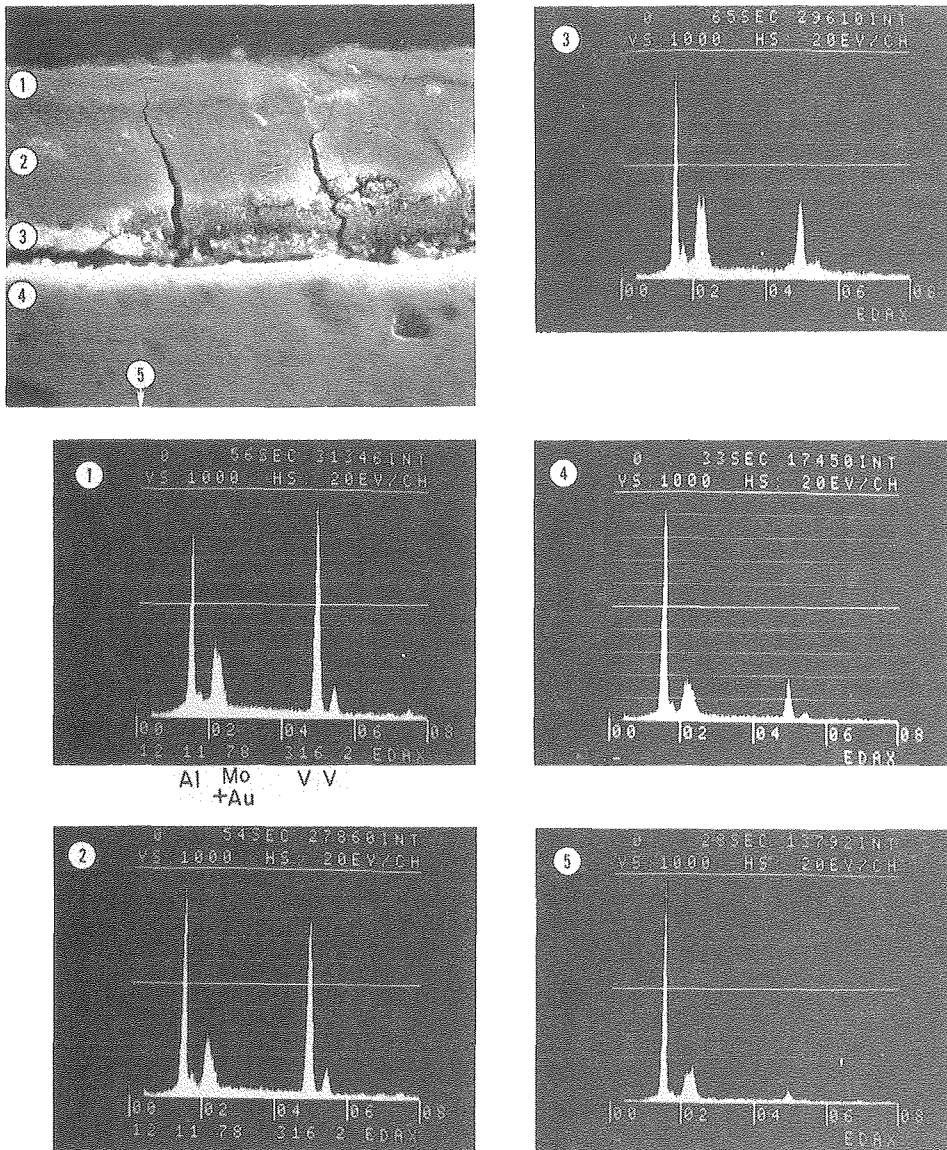


Fig. 2. SEM-EDAX analysis of composition variation of scale formed on desulfurization catalyst pellet. (XBB 802-2167)

Two Phase Flow Behavior

1. GAS-PARTICLE FLOW IN THE ENTRY REGION OF A CURVED PIPE[†]

Woon-Shing Yeung

The fluid dynamics of a dilute gas-particle mixture entering a circular curved pipe has been investigated. The fluid is assumed to be incompressible and the flow nonseparating and laminar. Individual numerical schemes have been devised to handle the two different regions of the fluid flow field, i.e., the irrotational core region and viscous boundary layer region. Thus, in the core region, the traditional Telenin's method is modified to obtain a numerical solution for the velocity potential function. For the viscous boundary

layer, the orthonormal version of the method of integral relations is applied together with a backward difference scheme for the cross derivative terms. Interaction between the two regions is also accounted for by means of a simple iteration scheme.

Since an irrotational core is assumed, the uniform entry profile changes to a two-dimensional potential vortex shortly downstream of the entry section. This is consistent with a recent experimental investigation on entry curved pipe flow by Agrawal, Talbot and Gong.¹ There is also a cross flow directed from the outer bend towards the inner bend in the immediate neighborhood of the entry section. Further downstream, the cross flow reverses its direction and moves from the inner bend towards the outer bend, as is generally

reported in all curved pipe investigations. The axial profile, however, does not change drastically from that of a uniform profile because of the weak interaction between the core and boundary layer region for the values of Reynolds number considered in this report ($Re\ 10^4 \sim 10^5$).

To assess the erosion of the pipe by the particles the dynamic equations of the particle phase are solved. Lagrangian equations of motion for the particle phase are used. Due to the complication of the momentum coupling between the two phases (i.e., the gas phase and the particle phase), only the first order solution for the particle phase has been obtained by neglecting its effect on the gas flow field. This has been proved adequate, for example, in the erosion calculation of a curved pipe carrying a gas-solid mixture. Figure 1 shows particle paths for flow in the

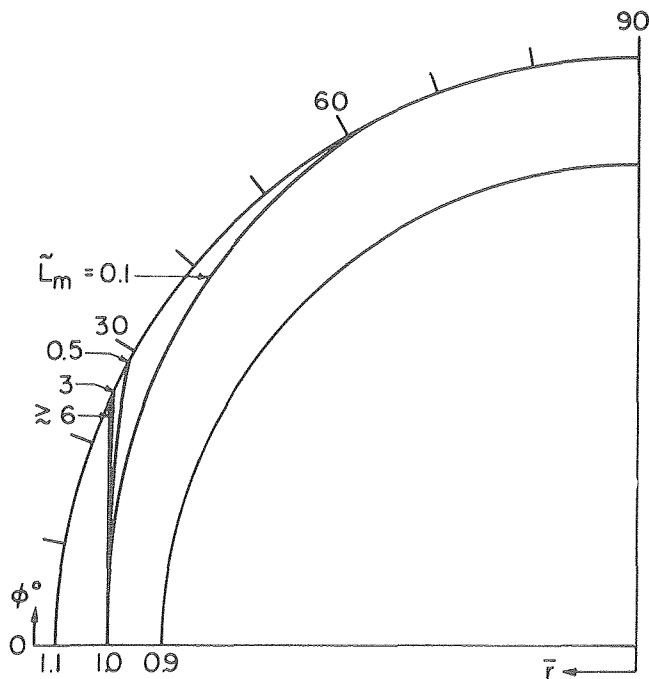


Fig. 1. Particle paths for values of $\tilde{\lambda}_m$, a measure of a particle's momentum. The gas flow is in the direct of ϕ° . \bar{r} is the nondimensional radius of curvature. (XBL 795-6224A)

curved pipe. The impact points indicate the position in the pipe where primary erosion occurs. Primary erosion points are the points at which the particles first strike the wall in the figure.

* * *

[†]Brief version of LBL-9905.
1. Y. Agrawal, L. Talbot, and K. Gong, J. Fluid Mech. 85, part 3 (1978).

2. SEPARATION EFFECTS IN GAS-PARTICLE FLOWS AT HIGH REYNOLDS NUMBERS[†]

Jonathan A. Laitone

Predicting the fluid mechanical characteristics such as particle trajectories and impact velocities of an eroding gas-solid two-phase flow in a containment vessel is crucial for the successful design and operation of coal gasification systems, coal fired turbines, and other energy conversion systems. The difficulties associated with the analysis of gas-particle flows have precluded general solutions, with most research being applied to simple geometries and often to flow conditions that are not particularly useful.

In the present work a general numerical solution is developed which extends a numerical scheme for gas flow developed by Chorin¹ to a solution suitable for dilute gas-solid particle flows over a much wider range of geometries than previously treated. The method is designed to solve the time dependent equations but may be used in the steady state case as well.

The numerical method is applied to the flow of gas and particles about a cylinder. Previously, gas-particle models have utilized a potential flow approximation for the gas motion. The present method predicts boundary layer growth and separation by introducing viscous effects in the gas flow. Figure 1 indicates the discrepancy between potential theory and the exact viscous case for Reynolds Number, $Re = 1000$. For values of λ (a measure of a particles' momentum) less than two, a cylinder placed in the flow is predicted by the viscous effects model to collect less particles than that predicted by potential theory. This is due to the effect of a viscous boundary layer which acts to deflect gas and particles away from the cylinder.

The method also predicts particle motion in the wake region. In Fig. 2 particles of different sizes are entrained in the Karman vortex street and ex-

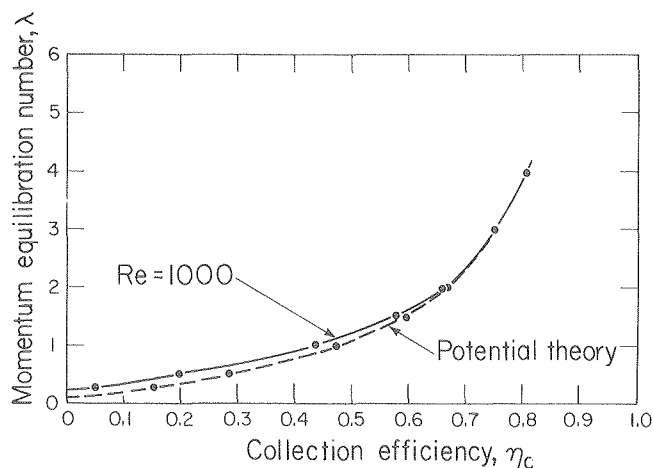


Fig. 1. Particle momentum equilibration number, λ , versus collection efficiency η_c for a cylinder placed in a two phase flow regime. (XBL 799-2769)

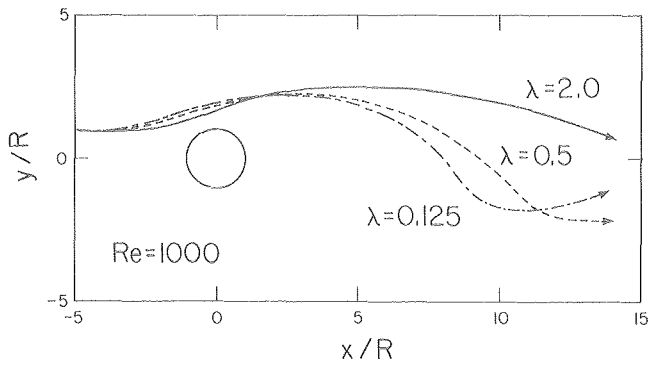


Fig. 2. Trajectories of particles of different particle momentum, λ , over a cylinder of radius R with spatial coordinates of x and y . (XBL 799-2775)

hibit sinusoidal trajectories. Good agreement is found between the numerical results² and experiment.³

* * *

†Brief version of LBL-9996.

1. A. J. Chorin, *J. Fluid Mech.* 57, 758 (1973).
2. J. A. Laitone, Separation Effects in Gas-Particle Flows at High Reynolds Numbers, LBL-9996 (1979).
3. G. Grant and W. Tabakoff, *J. of Aircraft* 12, (No. 5), 471 (1975).

3. AERODYNAMIC EFFECTS IN THE EROSION PROCESS[†]

J. A. Laitone

Experimental investigations of velocity effects on the erosion of a ductile material by aerodynamically entrained solid particles indicate erosion can vary with velocity raised to an exponent up to the order of four in normal or 90° impacts. For smaller angles of attack, the exponent is less than four but greater than two. Previous quantitative erosion models do not predict these high exponent values. In this study,¹ the two-phase fluid mechanical system is analyzed and an analytical expression is presented that predicts particle impact speeds varying with the fluid free stream speed squared in normal impacts (See Fig. 1).

The aerodynamic effects modify the particles impact kinetic energy by increasing the velocity dependence. Including the aerodynamic effect with an equation of motion type erosion model such as Finnie's² yields erosion rates varying with free stream velocity with exponents between 2 and 4; a result experimentally confirmed.³

This is a critical result for the study of erosion of materials. Researchers have attempted to explain why erosion varies with velocity exponents greater than two by considering only particle-surface interaction. Their results are valid only for particles that are not aerodynamically entrained. Experiments with single particles dropped on a surface are devoid of aerodynamic

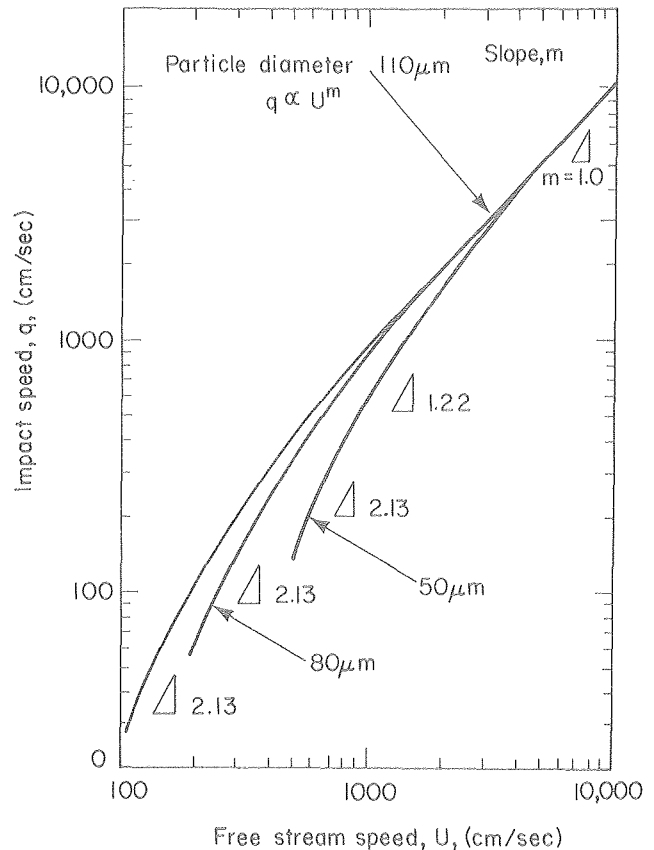


Fig. 1. Effect of free stream velocity on impact speed at the surface. The slope of the curve is given by m . The maximum value of m yields $q \propto U^{2.13}$. (XBL 794-1053)

effects and, thus, the impact speed, q , equals the free stream speed, U , far from the surface. This study indicates the role of aerodynamics in an erosion study. In order to utilize an erosion model in an aerodynamic system, the particle's impact speed which is different from its free stream speed must be used. The impact speed is determined from the free stream speed by solving the fluid mechanical system.

* * *

†Brief version of LBL-8962.

1. J. Laitone, Aerodynamic Effects in the Erosion Process, Proceedings of the 3rd International Tribology Conference, Paisley, Scotland, Sept. 10-13, 1979.
2. I. Finnie, *Wear* 19, 81 (1972).
3. G. Grant and W. Tabakoff, *J. Aircr.* 12 (No. 5) 471 (1975).

4. DEVELOPMENT OF A LASER TEST SYSTEM FOR TWO-PHASE FLOW STUDIES

A. Modavi

The major effort over the past three years to analytically describe particle trajectories and

velocities of eroding particles in two phase flows to determine precise particle impacting conditions on target surfaces has developed models for flow over various shaped surfaces. The nature of this flow was used to develop a refined experimental flow system that can test the predictions of the models. Verification of the models will considerably enhance the ability to predict erosion rates of surfaces of different geometries that are containing solid particle-fluid flow systems in coal conversion systems. The test system is particularly designed to be able to produce data that can be scaled to full size component flows. It is unique to the needs of the analytical models developed to describe flow in pipe bends and elbows, in sudden expansions and over sharp corners and about turbine blades, plates and cylinders.

Figure 1 shows the test system. The cold air flow system provides air velocities of 0 to 30 ft/sec up to 0.5 psia differential pressure in 2x2 inch curved rectangular ducting. The test section of the ducting is made of optically clear plastics which allow laser Doppler measurements to be carried out.¹ The Laser Doppler Velocimetry (LDV) is a nonintrusive velocity measurement technique which employs a laser light probe (the intersection of two beams of monochromatic light) to generate a modulated (Doppler shifted) light scattered off various particles' flow through the light probe.² This light scattering is detected by photomultiplier tubes, or other photo detectors, and processed electronically to translate such signals into velocity of the particles.

The diagram at the right side of the figure illustrates a simple LDV system, the actual LDV system employed is a more complex dual color back scattering LDV system. The dual color LDV provides simultaneous measurements of two components of velocity and employs the two primary frequencies of a 2 watt argon ion laser.

A minicomputer is used to provide the record keeping of the particle counts of up to 20 kHz from two Disa LDV processors. The minicomputer also provides the auto-positioning of the LDV optics by commanding a custom made SYZ motorized table to move in 1/1000 mm increments.

The data can be instantaneously processed and displayed/plotted on the computer terminals or can be stored on the magnetic discs for future processing. In addition to the LDV processors a real time signal digitizing capability is available.³

* * *

1. S. Mason and B. Smith, Erosion of Bends by Pneumatically Conveyed Suspensions of Abrasive Particles, Powder Technology, Netherlands, March 1972.
2. F. Durst, et al., Principles and Practice of Laser Doppler Anemometry, Academic Press, San Francisco, California (1976).
3. D. Holve and S. Self, An Optical Particle-Sizing Counter for In-situ Measurements, High Temperature Gas Dynamics Laboratory, Stanford Univ., Stanford, California (1978).

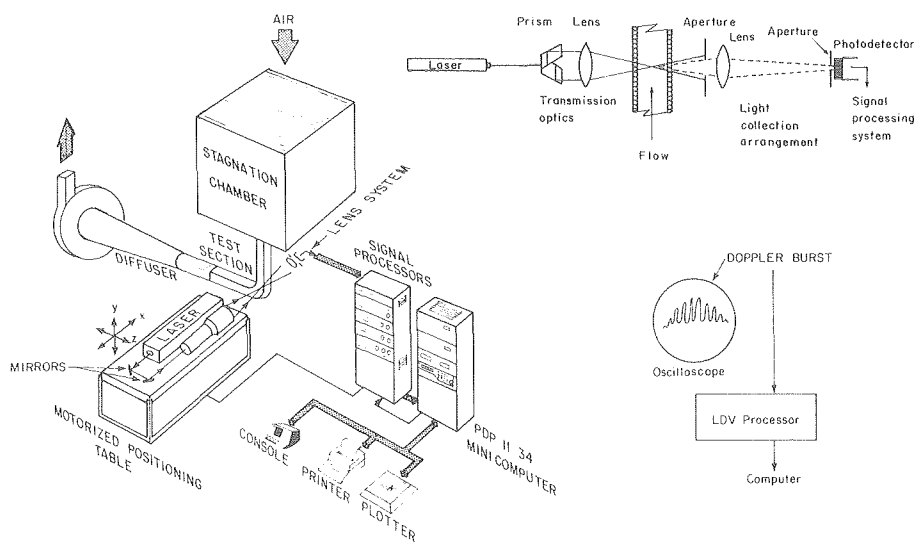


Fig. 1. Schematic of two-phase flow test system and laser Doppler velocimeter. (XBL 801-52)

RESEARCH PLANS FOR CALENDAR YEAR 1980

The mechanism of erosion by the formation of platelets on the surface of a ductile metal will be further experimentally documented and an analytical model will be developed based upon the forging-extrusion mechanism that forms the eroding platelets. Further efforts will be made to define the stresses and strains that occur upon impact of an erosive particle by experimental measurements using the techniques already developed and to utilize them in an analytical model and in defining what properties of a target material enhances erosion resistance. Elevated temperature erosion and combined erosion-corrosion will be studied further.

The effects of coatings of different types and compositions applied by several different mechanisms on the erosion and combined erosion-corrosion behavior of structural metals will be investigated. The combined erosion-corrosion behavior of thin scales on stainless steels will be studied to determine under what environmental conditions each of the mechanisms is governing and how synergistic the combined behavior is.

The fluid mechanics of two phase flow will be studied experimentally to verify model predictions using laser instrumentation. The analytical work will concentrate on adopting initial analytical models to fully turbulent flow conditions. The behavior of two phase flows where the carrier vehicle is a lubricating liquid such as an oil will be analytically described.

1979 PUBLICATIONS AND REPORTS

Refereed Journals

1. J. A. Laitone, "Aerodynamic Effects in the Erosion Process," *Wear* 56, 239-246 (1979), LBL-8962.
2. J. A. Laitone, "Erosion Prediction Near a Stagnation Point Resulting from Aerodynamically Entrained Solid Particles," *J. Aircraft*, AIAA, 16, No. 11 (1979), LBL-6990 Rev.
3. K. Chilquuri, G. Yee, and J. A. C. Humphrey, "Developing Laminar Flow and Heat Transfer in Strongly Curved Ducts of Rectangular Cross Section," *Journal of Heat Transfer* (in press).
4. L. Lapidés and A. Levy, "The Halo Effect in Jet Impingement Solid Particle Erosion Testing of Ductile Metals," *Wear* 58, (1979).
5. B. A. Gordon and V. Nagarajan, "Preliminary Observations of the Thermodynamic Predictions of Fe-Cr-Ni Alloys in Coal Gasifier Environments," *Oxidation of Metals* 13, (No. 2) 197 (April 1979).
6. K. T. Jacob, D. B. Rao, and H. G. Nelson, "Phase Relations in the Fe-Ni-Cr-S System and the Sulfidation of an Austenitic Stainless Steel," *Oxidation of Metals* 13 (No. 1) 25 (Feb. 1979).

Other Publications

1. A. V. Levy, "Corrosion-Erosion of Materials in Coal Liquefaction Environments," *Proceedings of NACE Conference on Corrosion-Erosion of Coal Conversion System Materials*; p. 174; Berkeley, Calif., Jan 24-26, 1979.
2. G. Zambelli and A. V. Levy, "Erosion of Scales on Metals," *Proceedings of NACE Conference on Corrosion-Erosion of Coal Conversion System Materials*; p. 480; Berkeley, Calif., Jan 24-26, 1979.
3. A. V. Levy and S. Jahannir, "The Role of Plasticity in the Erosion of Ductile Metals," *Proceedings of the 5th International Conference on Erosion by Liquid and Solid Impact*, p. 8-39; Cambridge Univ., England, Sept. 3-6, 1979.
4. G. Zambelli and I. Finnie, "Particulate Erosion of NiO Scales," p. 9-49; Cambridge Univ., England; Sept. 3-6, 1979.

LBL Reports

1. W.-S. Yeung (Ph.D. thesis), "Gas Particle Flow in the Entry Region of a Curved Pipe," LBL-9905.
2. G. Yee and J. A. C. Humphrey, "Developing Flow and Heat Transfer in Strongly Curved Ducts of Rectangular Cross-Section," LBL-9092.
3. J. A. C. Humphrey, J. H. Whitelaw, and G. Yee, "Turbulent Flow in a Square Duct with Strong Curvature," LBL-9650.
4. T. F. H. Foerster (M.S. thesis), "The Effect of Coal Char on the Corrosion of 304SS," LBL-9308.
5. J. A. C. Humphrey, "A Transition State Model for Predicting the Rate of Erosive Wear of Ductile Materials by Solid Particles," LBL-10011.
6. J. Kim (M.S. thesis), "Effect of Particle Characteristics on Erosion of Ductile Metals," LBL-10268.
7. R. Stanley, D. Whittle and A. Levy, "Characterization of the Degradation of Hydrodesulfurizing Catalysts," LBL-10026.
8. J. Laitone (Ph.D. thesis), "Separation Effects in Gas Particle Flows at High Reynolds Numbers," LBL-9996.

Presentations

1. A. V. Levy, "Role of Plasticity in Erosion," Naval Postgraduate School, February 1979.
2. A. V. Levy, "Erosion of Oxide-Sulfide Scales on Metals," Gordon Research Conference, New London, N.H., July 1979.
3. A. V. Levy, "Erosion Mechanisms in Metals," U. S. Army Research Office Conference; Sanibel Island, Fla., October 1979.

4. J. A. Laitone, "Erosion Prediction Near a Stagnation Point Resulting from Aerodynamically Entrained Solid Particles," Paper No. 79-0555, AIAA 15th Annual Meeting, Washington, D.C., February 1979.

5. J. A. Laitone, "Aerodynamic Effects in the Erosion Process," 4th International Tribology Conference, Paisley, Scotland, September 1979.

6. G. Yee and J. A. C. Humphrey, "Developing Laminar Flow and Heat Transfer in Strongly Curved Ducts of Rectangular Cross Section," Paper No. 79-WA/HT 15, ASME Winter Annual Meeting, Heat Transfer Div., New York, N.Y., December 1979.

b. In-Situ Investigations of Gas-Solid Reactions by Electron Microscopy*

J. W. Evans and K. H. Westmacott, Investigators

1. EARLY STAGES OF REDUCTION OF NICKEL OXIDE SINGLE CRYSTALS: AN INVESTIGATION BY TRANSMISSION ELECTRON MICROSCOPY

J. A. Little, J. W. Evans and K. H. Westmacott

Because of its practical importance, a great deal of work has been done on the reduction of metallic oxides to metals and in this investigation the reduction of nickel oxide to nickel is being studied at all stages of reduction using a transmission electron microscope. The main emphasis of the work is on examining the reaction in-situ in an environmental cell in the Hitachi 650 kV high voltage electron microscope. This environmental cell allows gases to be introduced into the vicinity of the specimen while isolating the same gases and the reaction products from the vacuum system of the microscope proper. This is achieved by a system of differential pumping within the cell and thus allows transmission of the electron beam through the system and direct observation of the reduction reaction as it occurs. However, such in-situ observations must be correlated with results gained by ex-situ reduction and in this report are presented the results of such ex-situ reductions of nickel oxide examined in a 100 kV microscope.

Small 3 mm discs of nickel oxide were prepared by conventional techniques and thinned until a hole appeared indicating thin areas suitable for microscopy. The reductions were then carried out by heating the specimens under helium to the required temperature, exchanging with hydrogen for the required time and then cooling under vacuum.

The reduction/time curves of this system show an appreciable period of time at low temperatures when nothing appears to happen as measured by conventional weight loss techniques and it was found that at 200°C this period, known as the induction period, was about 15 minutes in length and so reductions were carried out for 15, 20 and 25 minutes.

The specimen reduced for 15 minutes showed discrete nickel nuclei ranging in size from 100 to 2000 Å. Diffraction patterns from this area showed the nuclei to be epitaxial with the nickel oxide matrix with complete matching of the cube directions and planes in both structures. Figure 1 shows a bright field micrograph of a typical area and also a dark field micrograph taken with a (111) nickel reflection. Such imaging conditions show that most of the nickel nuclei are in the same orientation and stereo microscopy reveals them to be on the surface of the matrix. However, a small fraction of the nuclei do not appear to be in the same orientation and are thus non-epitaxial; the two

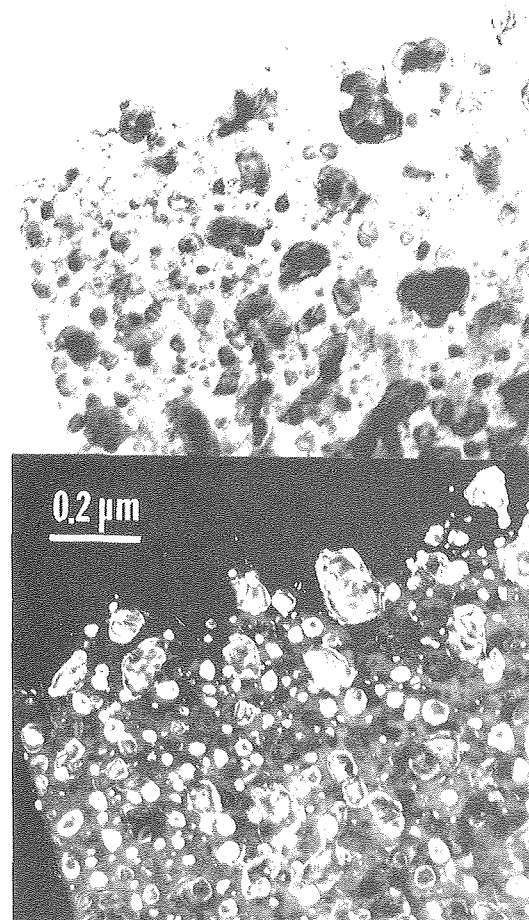


Fig. 1. Bright field and dark field micrographs of a typical area after 15 min. reduction.

(XBB 7911-15332)

types of nucleus are shown schematically in Fig. 2.

After 20 minutes at 200°C the majority of the nickel nuclei are not epitaxial with the oxide, as can be seen from the typical area plus associated diffraction pattern seen in Fig. 3. The diffraction pattern shows that the exact orientation relationship between the nuclei and matrix is slowly disappearing as the nickel reflections become powder rings, although the intensity of these rings is still higher at the original coincident nickel reflections. Also many of the nuclei are now associated with fissures, presumably arising from the strain mismatch between the matrix and the nickel which is of much smaller specific volume. These fissures may represent the first stage in the formation of the pores found on reducing many oxides.

After long exposure to the reducing environment, the nickel nuclei are found to have grown and

* This work was supported by the Division of Materials Sciences, Office of Basic Energy Sciences, U. S. Department of Energy.

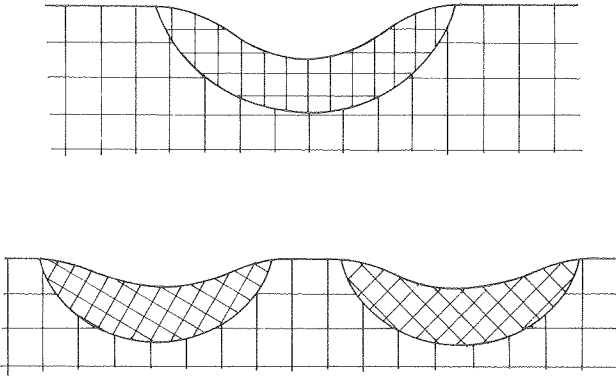


Fig. 2. Schematic figure of epitaxial and non-epitaxial nuclei. (XBL 799-7129)

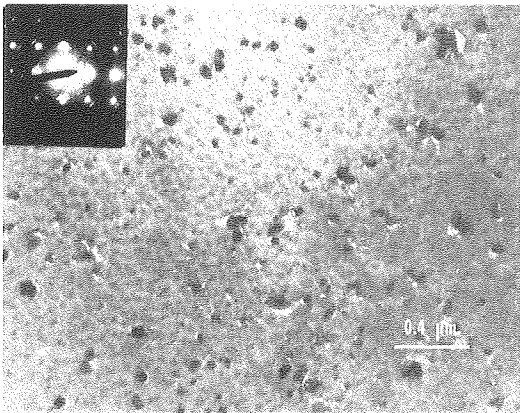


Fig. 3. Bright field micrograph plus diffraction pattern from typical area after 20 min. reduction. (XBB 7911-15337)

impinged upon other nuclei and formed large clusters of nickel metal. The associated diffraction patterns now show no evidence of epitaxy and the nickel is evident only as well-developed powder rings on the diffraction pattern.

Thus we have observed that during the early stages of nickel oxide reduction by hydrogen there exist both epitaxial and non-epitaxial nickel nuclei, the latter becoming predominant as time progresses. It is tempting to conclude, therefore, that a loss of epitaxy is a feature of the growth of the nuclei. However, such a loss would imply a rotation or similar movement of the nuclei, and it is difficult to see how this can take place for nuclei embedded in the host lattice. A more plausible explanation is that non-epitaxial nuclei are formed less rapidly in the initial stages but grow more rapidly once formed. Since nickel oxide is non-stoichiometric, the initial oxide (equilibrated in air) may be chemically quite different from that towards the end of the early reduction

period, where much oxygen has been removed from the surface. Figure 3 shows that the nuclei are frequently separated from the nickel oxide matrix by a fissure and it thus appears that the porosity which must form as nickel oxide reduced to nickel forms, not within the nickel but rather on parts of the nickel oxide/nickel interface. As the nuclei impinge and coalesce a large scale structure results with internal porosity observable by such techniques as optical microscopy.

RESEARCH PLANS FOR CALENDAR YEAR 1980

The current work has shown the relationships between the nickel oxide and nickel nuclei during the hydrogen reduction to change with time and to vary over the surface of the oxide. Thus further work will concentrate upon a detailed analysis of these factors by observing the reactions as they occur in the environmental cell in the transmission microscope. Both hydrogen and carbon monoxide/carbon dioxide mixtures will be used and the effects of varying both the partial pressures of reducing gases and the reduction temperatures will be investigated. The study will also be extended to cover both the ex-situ and in-situ reductions of polycrystalline nickel oxide and thus the effects of grain boundaries examined.

This work will also study the reduction of other metallic oxides, notably the iron oxides to iron, in a similar attempt to correlate the microstructure of the solids with the reactivity.

In all of the above work it is hoped to add a mass spectrometer system to the outlet side of the environmental cell to thus examine the kinetic data available during a reduction reaction and correlate this data with microstructural changes seen in the microscope.

1979 PUBLICATIONS AND REPORTS

Refereed Journals

- †1. J. W. Evans and B. J. Sabacky, "Electrodeposition of Metals in Fluidized Bed Electrodes; Part I, Mathematical Models," *J. of the Electrochemical Society*, 126, 1176-1180 (1979).
- †2. J. W. Evans and B. J. Sabacky, "Electrodeposition of Metals in Fluidized Bed Electrodes; Part II, An Experimental Study of Copper Electrodeposition at High Current Densities," *J. of the Electrochemistry Society*, 126, 1180-1187 (1979).
- †3. J. W. Evans and C-H. Koo, "Structural and Reduction Characteristics of Some Venezuelan Iron Ores," *Trans. Iron Steel Inst. Japan* 19, 95-101 (1979).
- §4. J. W. Evans and C. A. Natalie, "The Influence of Lime Properties on the Rate of Dissolution in CaO-FeO-SiO₂ Slags," *Ironmaking and Steelmaking*, 6, No. 5, 101-109 (1979).

[†]5. J. W. Evans and M. Ranade, "The Grain Model for Gas-Solid Reactions; a Refined Approximate Solution to the Equations," Chem. Eng. Sci., in press (1979).

[†]6. J. W. Evans and M. Ranade, "The Reaction Between a Gas and a Solid in a Non-isothermal Packed Bed: Simulation and Experiments, I. and E. C. Process Design and Development," in press (1979).

[†]7. J. W. Evans and A. Malazgirt, "Production of Aluminum and Aluminum Coatings by Thermal Decomposition of Aluminum Alkyls, Metallurgical Transactions," in press (1979).

^{||}8. J. W. Evans, A. Sarin and M. Abbasi, "A Monte Carlo Simulation of the Diffusion of Gases in Porous Solids," Journal of Chemical Physics, in press (1979).

Other Publications

[†]1. J. W. Evans and C-H. Koo, "The Reduction of Metal Oxides," in Rate Processes of Extractive Metallurgy, edited by Sohn and Wadsworth, Plenum, New York (1979).

LBL Reports

1. J. W. Evans, J. A. Little and K. H. Westmacott, "Early Stages of Reduction of Nickel and Oxide Single Crystals: An Investigation by Transmission Electron Microscope," LBL-10176.

Invited Talks

1. J. W. Evans, "Magnetic Fields, Current Densities, Melt Velocities and Current Efficiencies in Hall-Heroult Cells--Computations and Comparison with Measurements, Seminar on Heat and Mass Transfer in Metallurgical System," Dubrovnik, September 1979.

2. J. W. Evans, "Computation of Melt Velocities and Current Efficiency in Hall-Heroult Cells," The Electrochemistry Society Meeting, Boston, May 1979.

3. J. W. Evans, "Computation of Mass Transport and Current Efficiencies in Hall-Heroult Cells," International Society of Electrochemistry Meeting, Trondheim, August 1979.

4. J. A. Little, "The Physical and Chemical Properties of Copper β -alumina," The International Conference on Fast Ionic Conduction in Solid Electrolytes and Electrodes, Lake Geneva, Wisconsin, May 1979.

* * *

[†]This work was supported by the National Science Foundation.

[†]This work was supported by the U. S. Bureau of Mines.

[§]This work was supported by the American Iron and Steel Institute.

^{||}This work was unsupported.

B. SOLID STATE PHYSICS

1. Experimental Solid State Physics

a. Far Infrared Spectroscopy*

Paul L. Richards, Investigator

Introduction. The objective of our research is to use the infrared and near-millimeter wavelength range of the electromagnetic spectrum as a probe to do experiments which are selected for their technical novelty and their potential for revealing new physics. Our work includes development of new measurement techniques, such as new spectrometers, detectors, etc. In recent years considerable effort has been devoted to sensitive infrared detectors for use in experiments in which the background photon level is low. The Ge:Ga photoconductors, the uniaxially stressed Ge:Ga photoconductors, the composite bolometers, and the superconducting diode photon detectors developed in this project are now the most sensitive infrared and near-millimeter detectors ever produced over the wavelength range from 50 μm to 8 mm. The superconducting diode devices are also the most sensitive available heterodyne receivers at mm wavelengths.

Experimental projects not described in detail in this report include a recently completed balloon measurement of the spectrum of the cosmic (black body) background radiation which comprises 90% of the radiant energy in the universe. This experiment was the first to show that the spectrum of the microwave background falls at frequencies above the peak at 6 cm^{-1} . It also showed deviations from a black body spectrum at the confidence level of 5 standard deviations. A new experiment is being prepared to check these deviations. It will be different in most respects in order to reduce the possibility of common systematic errors. If the deviations are confirmed by new experiments, they will be a matter of highest importance for cosmology.

Other projects in progress, but not described in detail here, include a balloon experiment to survey the sky at far infrared wavelengths which had its first flight in the spring of 1979; a project to improve the performance of photoconductive infrared detectors and to test fundamental noise theory; a project to use adiabatic demagnetization to cool bolometric infrared detectors below 0.3 K; and a project to measure the thermal emission from molecules chemisorbed on metal surfaces. This work will be described in future annual reports as the projects are completed.

1. INFRARED SPECTRA OF CO CHEMISORBED ON Ni[†]

R. B. Bailey,[‡] T. Iri,[§] and P. L. Richards

We have developed a sensitive low-temperature thermal detection technique for measuring the infrared vibrational spectra of molecules chemisorbed on metals. We have used this technique to measure the detailed coverage dependence of the infrared spectrum of carbon monoxide molecules adsorbed on evaporated nickel films. The experimental apparatus we have developed detects the vibrational resonances of adsorbed molecules by attaching a germanium resistance thermometer to the sample, cooling the assembly to liquid helium temperatures, and measuring the temperature changes which occur when infrared radiation is absorbed. When combined with a rapid-scan Fourier transform infrared spectrometer, this technique produces vibrational spectra with high sensitivity and high resolution over a broad range of frequencies. These spectra can be used to identify molecules adsorbed on solid surfaces and to study the nature of their interactions with the surface and with other adsorbed molecules.

The sequence of spectra shown in Fig. 1 was produced by exposing an evaporated nickel film to CO gas at 77 K and then warming the sample during the brief intervals between low temperature spectral measurements to reduce the surface coverage. The appearance of distinct absorption lines indicates that CO molecules are bonded to different lattice sites on the nickel surface. Comparison of these spectra with published data for (100) and (111) nickel surfaces,^{1,2} suggests that the polycrystalline evaporated films consist mostly of (100) or other faces without the three-fold adsorption sites present on (111) surfaces. We associate the changes in the relative intensity of the two strong absorption lines with transitions between different ordered phases of the CO layer, each of which is stable over a limited range of surface coverage. The sum of the intensities of the two lines increases relatively smoothly with coverage. This interpretation is supported by the fact that the relative intensity changes do not occur when the measurement is repeated on a disordered ion-bombarded nickel film.

* * *

[†]Brief version of LBL-10159.

[‡]Present address: Electronics Research Center, Rockwell International, P.O. Box 4761, Anaheim, CA 92803.

[§]Permanent Address: Department of Materials Science, University of Electrocommunications, 1-5-1 Chofugaoka, Chofu-shi, Tokyo 182, Japan.

* This work was supported by the Division of Materials Sciences, Office of Basic Energy Sciences, U.S. Department of Energy.

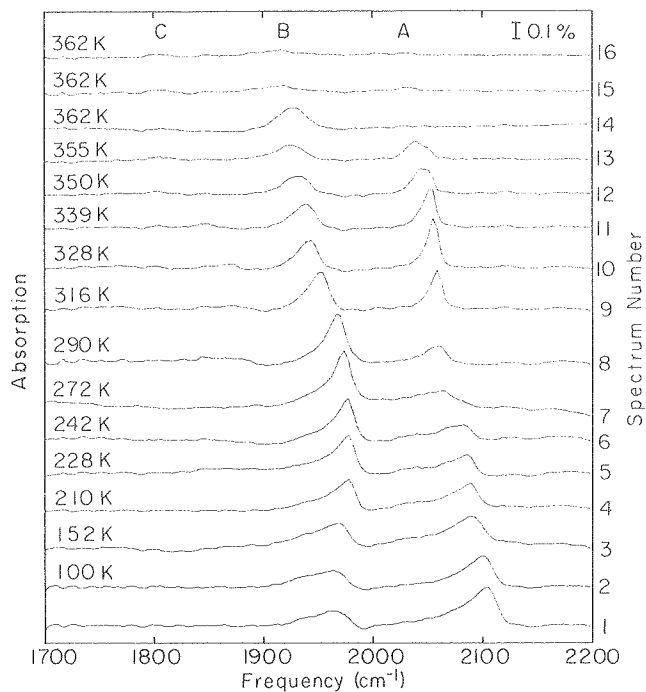


Fig. 1. Infrared spectra as a function of the surface coverage of CO molecules on an evaporated nickel film. The coverage increases monotonically from a value of approximately $\bar{\theta} = 0.05$ at the top to $\bar{\theta} = 0.85$ at the bottom of the figure.

(XBL 7912-5417)

1. S. Andersson, *Solid State Comm.* 21, 75 (1977).
2. W. Erley, H. Wagner, and H. Ibach, *Surface Sci.* 80, 612 (1979).

2. ELECTRONS ON THE SURFACE OF LIQUID HELIUM[†]

D. K. Lambert[‡] and P. L. Richards

Electrons pressed onto the surface of superfluid liquid helium from the gas by an external electric field can populate image-potential-induced surface states. Electrons in such states have large mobility along the surface and, to a good approximation, can be described as a two-dimensional electron gas. We have used a far infrared molecular laser to study transitions from the ground state to various excited states of this gas. The transition frequencies are a function of both the applied electric field and the surface charge density.

The measured values of the field at resonance for low surface charge densities shown in Fig. 1 are in excellent agreement with curves calculated from a one-dimensional Schrodinger equation. The Hamiltonian included an inverse-square-law image field, an infinite barrier at the helium surface, and the applied electric field.

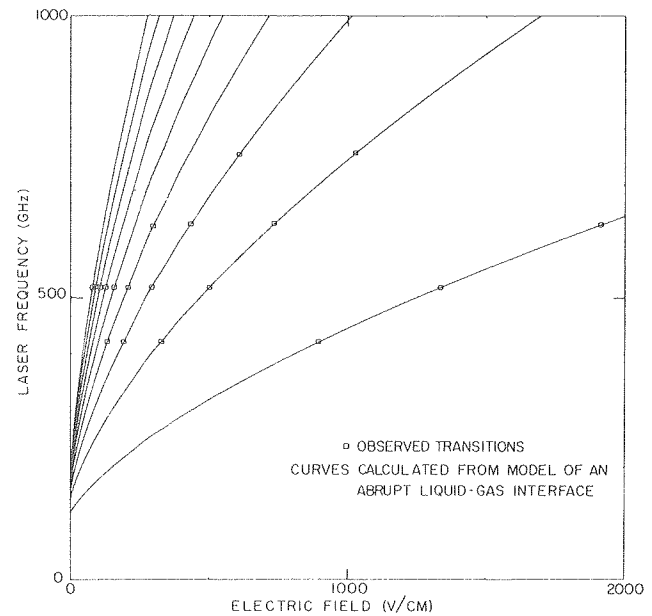


Fig. 1. Plot of the laser frequency versus the electric field at which transitions are observed. (XBL 798-6725)

The coverage of surface electrons was indirectly obtained by measuring the capacitance between electrodes placed above and below the surface of the helium. A self-consistent electrostatic shielding calculation was used to interpret these measurements and to obtain values for the surface charge density which were accurate to 1%. A dependence of the value of the applied field required for resonance on the surface charge density arises because of the electric dipole field from the surface electrons (and their image charges) surrounding the electron undergoing the transition. Although this surface charge density effect is small, it can be measured. It can also be calculated if a model for the radial distribution function of the surface electrons is available. In Fig. 2 we show that the measured field shift increases more rapidly with charge density than that calculated for a hexagonal lattice of the surface electrons. The slope of the line in Fig. 2 provides the first experimental measure of the disorder of the 2-dimensional electron gas. The measured value is about two standard deviations larger than theoretical predictions found in the literature.^{1,2}

* * *

[†]Brief version of LBL-9553 and LBL-10048.

[‡]Permanent address: Research Laboratories, General Motors Corporation, Warren, Michigan 48090.

1. H. Totsuji, *Phys. Rev. A* 17, 39 (1978).
2. R. C. Gann, S. Chakravartiz, and G. V. Chester, *Phys. Rev. B* 20, 326 (1979).

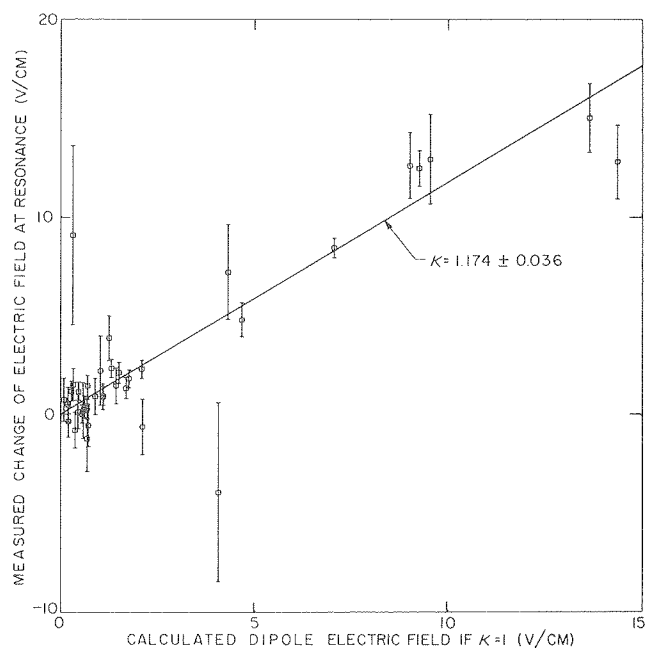


Fig. 2. Plot of the change of the electric field for resonance (as a function of surface charge density) versus the calculated contribution to the field for resonance from a hexagonal lattice of surface electrons with the same density.
(XBL 798-6724)

3. SUPERCONDUCTING RECEIVERS FOR MILLIMETER MICROWAVES[†]

T-M Shen, P. L. Richards, R. E. Harris,[‡] and F. L. Lloyd[‡]

The rapid onset of quasiparticle tunneling current at the full energy gap voltage in a superconductor-insulator-superconductor (SIS) tunnel junction is one of the strongest nonlinearities in any physical system. We are using this effect to make sensitive microwave detectors and mixers. Because of the interest in digital computers based on the Josephson effect, there has been extensive development of SIS tunnel junctions. Junctions made from Pb alloyed with small quantities of In and Au withstand many hundreds of cycles between helium temperature and room temperature. Structures with micron dimensions suitable for use at microwave frequencies can be produced by optical lithography. Junctions for our experiments have been produced at the National Bureau of Standards at Boulder using technology similar to that developed at IBM.

According to classical theory, the responsivity of a detector is proportional to the curvature of its I-V curve at the bias point. This quantity can become very large for an SIS quasiparticle detector biased at the full gap voltage. There is a quantum limit¹ of $R_i = e/h\nu$ to detector responsivity which corresponds to one tunneling quasiparticle for each incident microwave photon. Experimental results² at 36 GHz shown in Fig. 1 give a responsivity of more than half this quantum value and a shot-noise limited noise-

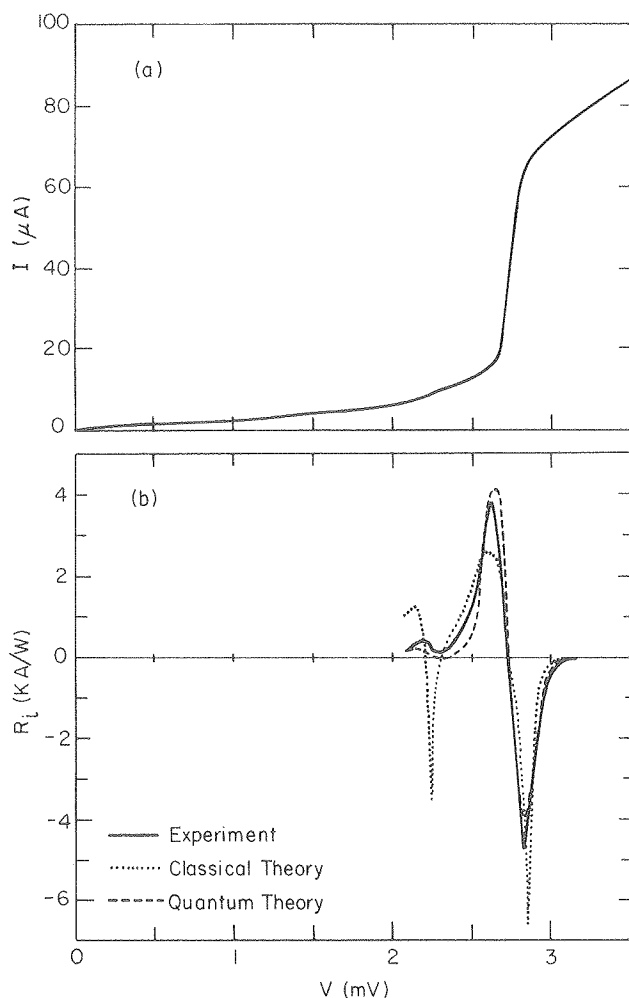


Fig. 1. (a) Measured I-V curve of Pb(In, Au) alloy SIS tunnel junction at 1.4 K. (b) Measured and calculated responsivities of the junction as a function of bias voltage. The experimental curve is measured with a constant rf source resistance which is close to optimum at the peak of the responsivity curve. The theoretical curves have been computed for a constant rf source resistance, chosen in each case to minimize the rms deviations between the theory and the experiment. Although the differences between classical and quantum predictions are not generally large for our experimental parameters, the latter theory does provide a significantly better overall fit. One important aspect of quantum theory is that it averages out the effects of features on the I-V curve which are narrow compared with $h\nu/e = 0.15$ mV. Classical theory predicts a sharp (negative) peak in responsivity at a bias of 2.25 mV which is not present in the quantum prediction and which is not observed. (XBL 798-6875)

equivalent power of 3×10^{-16} W/√Hz. This device is thus a microwave photodiode with unprecedented sensitivity.

When operated as a classical heterodyne mixer³ at 36 GHz as shown in Fig. 2, the SIS junction device gave a single-sideband mixer noise temperature of < 14 K and a conversion efficiency of 0.15

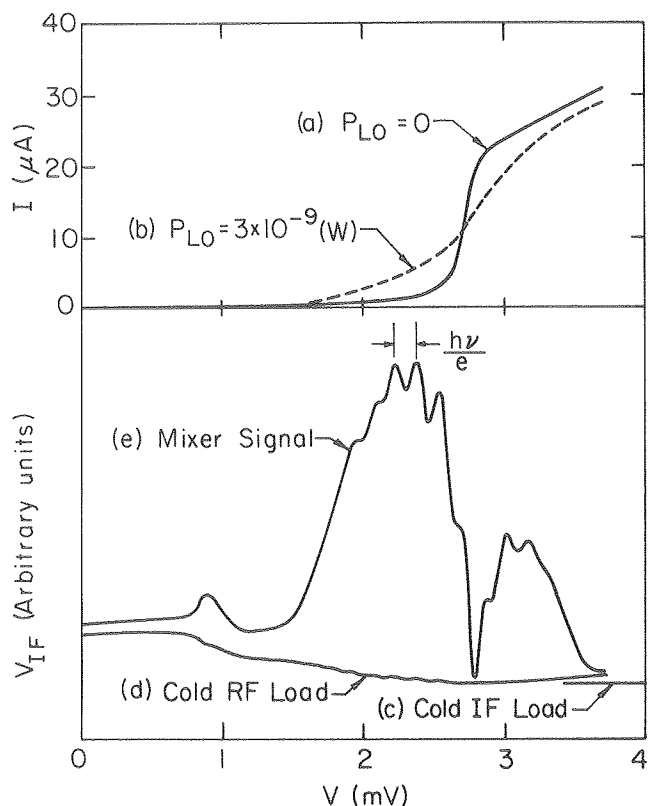


Fig. 2. Static I-V curves are shown above for a 1.5 K Pb(In, Au) alloy junction (a) without (b) with local oscillator power. Plots of IF amplifier output voltage in the frequency range from 30 to 80 MHz are shown as a function of junction bias voltage. Curve (c) was obtained with a 50Ω 1.5 K load in place of the mixer; curve (d) with a matched 1.5 K load in front of the mixer; curve (e) with a calibrated 36 GHz signal applied to the mixer from a Klystron oscillator. Values of mixer noise temperature were deduced from (c) and (d), and conversion efficiency from (e).

(XBL 789-5821)

for a local oscillator power of only 5×10^{-9} W. More recent results from junctions with a sharper corner on the static I-V curve require quantum photon assisted tunneling theory¹ for interpretation. This theory predicts conversion gain with very low noise temperatures.⁴ The best results thus far are a single sideband noise temperature of < 5 K and a conversion efficiency of 0.9.

The promise of the SIS heterodyne mixer is so great for radio astronomy that projects to exploit it have begun at eight institutions since our first results were announced.

* * *

†Work supported by the Office of Naval Research.

‡Present address: National Bureau of Standards, Boulder Colorado 80303.

1. J. R. Tucker and M. F. Millea, IEEE Trans. Magn. MAG-15, 288 (1979); J. R. Tucker, IEEE J. Quantum Electronics (invited paper IP#126, to be published).
2. P. L. Richards, T-M. Shen, R. E. Harris, and F. L. Lloyd, Appl. Phys. Lett. (to be published).

3. P. L. Richards, T-M. Shen, R. E. Harris, and F. L. Lloyd, Appl. Phys. Lett., 34, 345 (1979).
4. J. R. Tucker, Appl. Phys. Lett. (to be published).

4. GRID POLARIZERS FOR INFRARED FOURIER SPECTROMETERS^{†‡}

W. A. Challener, P. L. Richards, S. C. Zillio[§] and H. L. Garvin^{||}

Fourier transform infrared spectrometers have now become the conventional tool for laboratory infrared spectroscopy. Many changes of beam splitter are required to cover the far infrared frequency range from 5 to 500 cm^{-1} with the usual Michelson Fourier spectrometer. A design exists¹ for a Michelson polarizing interferometer which uses a wire grid polarizer for a beam splitter and thus will operate over the entire frequency range of the polarizer. This type of instrument has been used successfully over the range from 5 to 100 cm^{-1} with a free-standing wire grid beam splitter. The irregularities in wire separation, however, reduce its efficiency at higher frequencies.

We have prepared infrared grid polarizers consisting of copper lines with a $3.6 \mu\text{m}$ grid constant on a $4 \mu\text{m}$ thick Mylar polyester substrate by the techniques of photolithography and sputter-etching. Their polarization properties have been measured and found to be suitable for use at infrared frequencies below 700 cm^{-1} . These polarizers have been used for Fourier Transform spectroscopy. The efficiency of the interferometer has been measured over the frequency range from 50 to 700 cm^{-1} and compared to that of a conventional Michelson interferometer in Fig. 1.

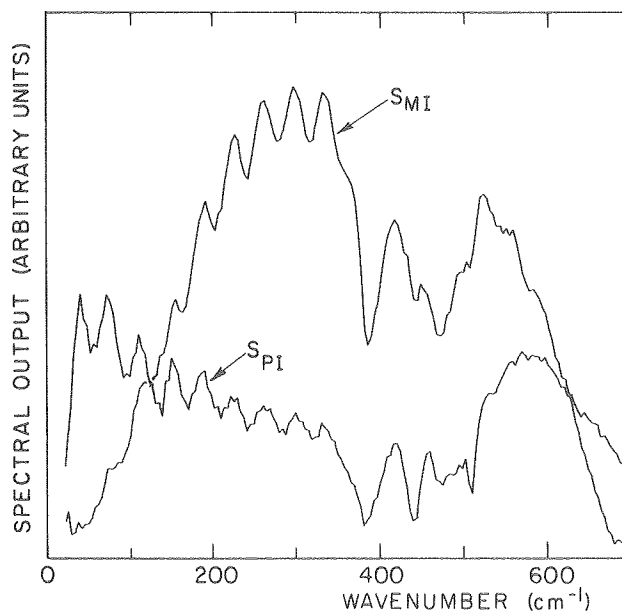


Fig. 1. Comparison of useful spectral range of polarizing interferometer with that of conventional Michelson interferometer with a $4 \mu\text{m}$ Mylar beam splitter.

(XBL 793-5853)

The results are shown to be in good agreement with the measured properties of the polarizers.

* * *

[†]A portion of this work was supported by NASA.

[‡]Brief version of LBL-8944.

[§]Present address: Departamento de Fisica e Ciencia dos Materials, Instituto de Fisica E Quimica de Sao Carlos, 13560 Sao Carlos, Sao Paulo Brazil.

^{||}Address: Hughes Research Laboratories, Malibu, CA 90265.

I. D. H. Martin and E. Puplett, *Infrared Phys.* **10**, 105 (1969).

RESEARCH PLANS FOR CALENDAR YEAR 1980

Surface Spectroscopy. The infrared thermal detection technique described above for measuring the vibrational spectra of molecules on metal surfaces will be extended to lower frequencies to observe the internal resonances of molecules larger than CO and to observe the molecule-metal vibrational modes. Improved techniques for measuring single crystal samples will be explored.

A second approach to this surface vibrational spectroscopy problem is to use a cooled spectrometer to measure the infrared emission from surfaces. Apparatus for this experiment is well advanced and development is being pursued vigorously. Emission experiments of the type contemplated have many of the advantages of the thermal detection scheme already in use, but are compatible with more conventional samples and with conventional surface characterization techniques such as LEED and Auger spectroscopy.

One-dimensional conductors. The one-dimensional conductor NbSe₃ shows evidence of pinned charge density waves which can be set into motion when sufficient current is passed through the material. Measurements of the temperature and magnetic field dependence of the resistance show evidence for electronic energy gaps whose behavior is not understood. Far infrared measurements are being made to search for independent evidence of the gaps.

Experimental cosmology. The conclusion from our previous measurement of the cosmic background radiation was that the spectrum is close to that of a black body, but with significant deviations. A new balloon experiment is being developed for flight in 1980 which will provide an independent test of these apparent deviations.

Our 1-meter aperture balloon telescope is being readied for a second flight. This experiment is designed to survey the northern sky in seven far infrared wavelength bands. The primary scientific goal is to measure the temperature, density and distribution of dust in our galaxy.

Instrument development. The demands of infrared surface spectroscopy have revealed some weaknesses in our spectroscopic capabilities. In

order to obtain optimal spectra in the 100-400 cm⁻¹ frequency range, a laser interferometer system is being installed in our mid-range Fourier transform spectrometer.

A simple portable adiabatic demagnetization system has been constructed and is undergoing tests. It will be used to test and operate a new generation of ultra-sensitive bolometric detectors for both surface spectroscopy and for cosmology.

Anomalous effects such as spontaneous spikes, saturation, and long time constants are being experimentally and theoretically investigated in Ge:Ga photoconductive infrared detectors. These effects now limit all ultra-sensitive applications of this class of detector, including our surface emission spectroscopy. When the detector performance is understood sufficiently it should be possible to test experimentally some aspects of the theory of photon noise from thermal sources which were originally proposed by Einstein, but not yet tested in detail.

1979 PUBLICATIONS AND REPORTS

Refereed Journals

1. E. Haller, M. Hueschen and P. L. Richards, "Ge:Ga Photoconductors in Low Infrared Backgrounds," *Appl. Phys. Lett.* **34**, 495 (1979).
2. D. P. Woody, N. S. Nishioka and P. L. Richards, "A New Measurement of the Cosmic Blackbody Radiation," *J. de Physique Colloq C6, Suppl. 8* **39** C-1629 (1978).
3. D. P. Woody and P. L. Richards, "Spectrum of the Cosmic Background Radiation," *Phys. Rev. Lett.* **42**, 925 (1979).
- [†]4. T. M. Shen, P. L. Richards and F. L. Lloyd, "Quasiparticle Heterodyne Mixing in SIS Tunnel Junctions," *Appl. Phys. Lett.*, **34**, 345 (1979).

Other Publications

1. D. K. Lambert and P. L. Richards, "Infrared Measurements of Surface Electrons on Liquid Helium," *Bull. Am. Phys. Soc. (Ser. II)* **24**, 473 (1979).
2. T-M. Shen, P. L. Richards, R. E. Harris, and F. L. Lloyd, "Quasiparticle Heterodyne Mixing in SIS Tunnel Junctions," *Bull. Am. Phys. Soc. (Ser. II)* **24**, 265 (1979).
3. R. B. Bailey and P. L. Richards, "Infrared Spectra of Molecules Adsorbed on Metal Surfaces," *Bull. Am. Phys. Soc. (Ser. II)* **24**, 405 (1979).
- [†]4. T-M. Shen, "Superconductor-Insulator-Superconductor Quasiparticle Tunnel Junctions as Microwave Receivers," Ph.D. Thesis, September 1979.
- [‡]5. E. F. Erickson, N. J. Evans II, R. F. Knacke, V. C. Kunde, H. P. Larson, J. C. Mather,

J. L. Pipher, P. L. Richards, S. T. Ridgeway, and R. I. Thompson, "The CFTS: a Composite Fourier Spectrometer for SIRTf," NASA Ames Research Center, August 15, 1978.

‡6. N. W. Bogges, L. T. Greenberg, M. G. Hauser, J. R. Houck, F. J. Low, C. R. McCreight, D. M. Rank, P. L. Richards and R. Weiss, "Infrared Receivers for Space Astronomy-Incoherent Detectors and Coherent Devices from One Millimeter to One Micron," NASA Ames Research Center, June 1979.

†7. P. L. Richards, T-M. Shen, R. E. Harris, and F. L. Lloyd, "SIS Quasiparticle Junctions as Microwave Photon Detectors," August 1979.

LBL Reports

1. P. L. Richards, "Direct Measurement of the Spectrum of the Near-Millimeter Cosmic Background," LBL-9374.

2. D. P. Woody and P. L. Richards, "The Spectrum of the Microwave Background," LBL-9843.

3. D. K. Lambert, "Electrons on the Surface of Liquid Helium," Ph.D. Thesis, LBL-9553.

4. D. K. Lambert and P. L. Richards, "Measurements of Local Disorder in a Two-Dimensional Electron Fluid," LBL-10048.

Invited Talks

†1. P. L. Richards, "New Techniques for the Measurement of Far Infrared Radiation-Photoconductors, Bolometers, and Super Heterodyne Mixers," Department of Physics, University of Minnesota, January 17, 1979.

2. P. L. Richards, "Spectrum of the Cosmic Background Radiation," Department of Physics, University of Minnesota, January 18, 1979.

3. P. L. Richards, "Spectrum of the Cosmic Background Radiation," Department of Physics, Simon Fraser University, Burnaby, British Columbia, January 31, 1979.

4. P. L. Richards, "Spectrum of the Cosmic Background Radiation," Department of Astronomy, Cornell University, February 6, 1979.

5. P. L. Richards, "Spectrum of the Cosmic Background Radiation," Department of Physics, University of Massachusetts, Amherst, February 7, 1979.

6. P. L. Richards, "Spectrum of the Cosmic Background Radiation," Department of Physics, Princeton University, February 8, 1979.

7. P. L. Richards, "Spectrum of the Cosmic Background Radiation," Department of Applied Physics, Yale University, February 9, 1979.

8. P. L. Richards, "Submillimeter Detectors," Rockwell International, Anaheim, California, February 14, 1979.

9. P. L. Richards, "Recent Measurements of the Spectrum of the Cosmic Background Radiation," Second West Coast Workshop on Cosmology, Stanford, May 5, 1979.

10. P. L. Richards, "Sensitive Infrared Spectroscopy: 1. Molecules on Surfaces, 2. The Early Universe," Physical Chemistry Colloquium, University of California, Berkeley, May 8, 1979.

11. P. L. Richards, "Spectrum of the Cosmic Background Radiation," Department of Physics, University of California, Santa Barbara, May 22, 1979.

12. P. L. Richards, "A New Measurement of the Spectrum of the Cosmic Background Radiation," Department of Physics, University of Utah, May 26, 1979.

13. P. L. Richards and D. P. Woody, "Direct Measurements of the Spectrum of the Near-Millimeter Cosmic Background," Conference on the Universe at Large Redshifts, Copenhagen, June 25, 1979.

14. P. L. Richards and D. P. Woody, "Spectrum of the Microwave Background, Conference on Objects at Large Redshifts," U.C.L.A., August 31, 1979.

†15. T-M. Shen and P. L. Richards, "SIS Tunnel Junctions as Low Noise Microwave Receivers," National Radio Science Meeting, Boulder, Colorado, November 5, 1979.

* * *

†Work supported by U.S. Office of Naval Research.

‡Partially supported by the National Aeronautics and Space Administration.

b. Experimental Solid State Physics and Quantum Electronics*

Y. Ron Shen, Investigator

1. SURFACE COHERENT ANTI-STOKES RAMAN SPECTROSCOPY[†]

Chenson K. Chen, A. R. B. de Castro, Y. Ron Shen, and Francesco DeMartini

The propagation of surface electromagnetic waves on solids and their applications have recently attracted considerable attention.¹ They have been used to study adsorbed molecules and overlayers on surfaces, and to probe phase transitions. In most cases, linear optics is employed in the excitation and detection of surface waves.

We have demonstrated that nonlinear mixing of four surface plasmons can be used to probe the Raman resonances of liquids.² The process we have been studying is surface coherent anti-Stokes Raman spectroscopy (CARS). Two surface plasmon waves at ω_1 and ω_2 propagate on the plane boundary between a metal and dielectric medium with wave vectors $(\vec{k}_1)_\parallel$ and $(\vec{k}_2)_\parallel$ respectively, parallel to the surface. These waves interact on the surface via the third-order nonlinearity of the medium to produce a third-order nonlinear polarization at $\omega_a = 2\omega_2$, which in turn generates a surface anti-Stokes plasmon wave at ω_a .

The theory of surface CARS is a straightforward extension of the theory of nonlinear generation and detection of surface polaritons.³ The theory predicts that the anti-Stokes output will be strongly enhanced if (1) the incoming waves \vec{E}_1 and \vec{E}_2 excite surface plasmons at ω_1 and ω_2 , (2) the surface anti-Stokes generation is phase-matched, i.e. $(\vec{k}_a)_\parallel = 2(\vec{k}_1)_\parallel - (\vec{k}_2)_\parallel$, and (3) $\omega_1 - \omega_2$ approaches the resonance excitation frequency of the dielectric medium so that $\chi^{(3)}$, the third-order nonlinear susceptibility, is enhanced.

Our experimental arrangement is shown in Fig. 1. The Kretschmann configuration was used to excite the surface plasmons.⁴ The electric fields \vec{E}_1 and \vec{E}_2 were provided by a Q-switched ruby laser, at 6943 \AA and a ruby pumped dye laser (NK 199 in acetone), tunable about 7456 \AA ; both lasers had line-widths $\leq 0.5 \text{ cm}^{-1}$ and pulsewidths $\approx 30 \text{ nsec}$. The two beams were then directed from the prism side onto the sample. The anti-Stokes surface wave was coupled out through the prism and was collected by the detection system consisting of an interference filter, monochromator, and photomultiplier. For the purpose of signal normalization and monitoring of the Raman resonance, a bulk CARS experiment on benzene was also set up in parallel.

Our experimental results on surface CARS are presented in Figs. 2-4 in comparison with the theoretical curves derived in Ref. 2. Figure 2 shows the variation of the anti-Stokes signal as ω_1 and ω_2 moves through the 992 cm^{-1} vibrational resonance in

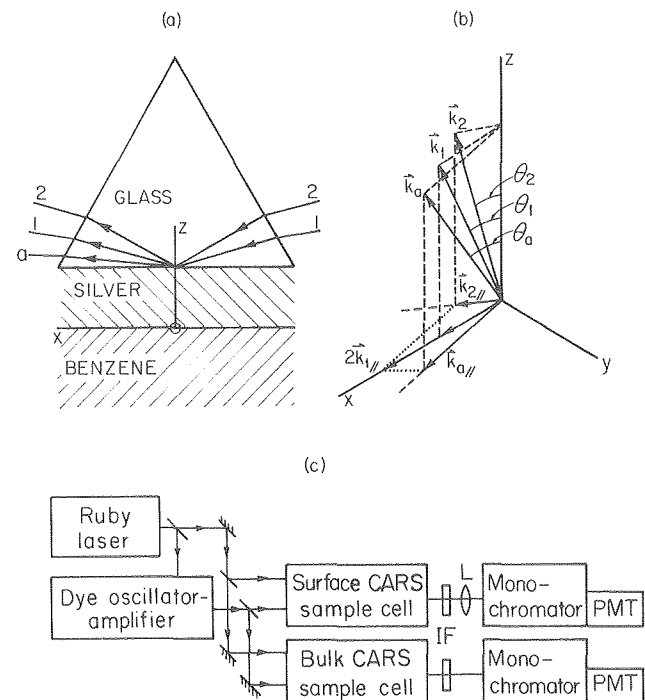


Fig. 1. (a) Prism-metal-liquid assembly. Beam 1 propagates in the x-z plane, beam 2 and the output do not. (b) Wavevectors in the glass prism; components in the x-y plane are phase matched. (c) Diagram of the apparatus. IF is an interference filter and L is a lens. (XBL 796-3540)

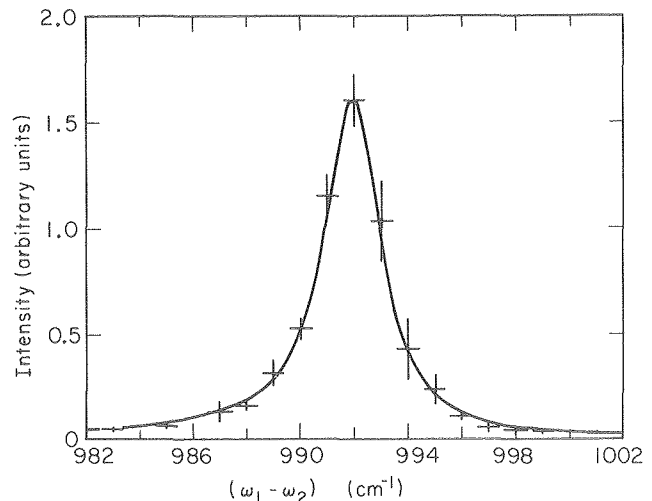


Fig. 2. Intensity of signal vs. $(\omega_1 - \omega_2)$ near resonance. (XBL 796-3537)

* This work was supported by the Division of Materials Sciences, Office of the Basic Energy Sciences, U. S. Department of Energy.

$\chi^{(3)}$ of benzene; in this case, the input beams were properly directed so that both ω_1 and ω_2 surface plasmons were optimally excited and the phase matching condition for surface CARS was satisfied. The theoretical curve describing this resonance peak was calculated by using a resonance linewidth determined from the parallel bulk CARS measurement. The nonresonant contribution to $\chi^{(3)}$ had to be included in the calculation to obtain a good fit to the experimental data in the wings. Aside from an amplitude normalization constant, no other adjustable parameters were used in the calculation of all the theoretical curves.

When both ω_1 and ω_2 beams were fixed in space and in frequency, but the prism-sample assembly was rotated about the \hat{y} axis, the surface CARS signal varied as a result of changing $(\vec{k}_1)_\parallel$ and $(\vec{k}_2)_\parallel$; first the resonance excitation conditions of the surface plasmons at ω_1 and ω_2 were changed, then the phase mismatch in the surface CARS was varied. The results are shown in Fig. 3. The peak is dominated by the effect due to resonance excitation of the surface plasmons at ω_1 and ω_2 . The effect of phase mismatch is of secondary importance in slightly reducing the width of the peak.

In Fig. 4, we show the results of the surface CARS signal versus the phase mismatch $\Delta k_\parallel = |2(\vec{k}_1)_\parallel - (\vec{k}_2)_\parallel - (\vec{k}_a)_\parallel|$, where $(\vec{k}_a)_\parallel$ is the wavevector for the surface plasmon at ω_a . In the experiment, Δk_\parallel was varied by changing the direction of $(\vec{k}_2)_\parallel$ through variation of k_2 , while keeping the surface plasmons at ω_1 and ω_2 still optimally excited. Here, the relatively large uncertainty in the experimental results came from the fact that for each change of Δk_\parallel , the beams had to be readjusted to optimize the beam overlap on the silver film.

The polarization of the anti-Stokes signal was found to be TM as expected and the signal disappeared when the ω_1 was made TE. With $\Delta k_\parallel = 0$ and both surface plasmons at ω_1 and ω_2 optimally excited, our theory predicted a maximum surface CARS output power $\mathcal{P}(\omega_a) = 1.1 \times 10^{-34} \mathcal{P}^2(\omega_1) \mathcal{P}(\omega_2) / W^4$ erg/sec at the resonance peak of $\chi^{(3)}$, where W is the incoming beam waist. With $\mathcal{P}(\omega_1) = 0.5$ mJ and $\mathcal{P}(\omega_2) = 5$ mJ in a 30 nsec pulse focused to 0.2 cm², we predicted an anti-Stokes output of 2.5×10^5 photons/pulse. From the actually observed signal from the photomultiplier, we estimated an output of $\sim 2 \times 10^5$ photons/pulse, in good agreement with the prediction. The power dependence of the anti-Stokes output on $\mathcal{P}(\omega_1)$ and $\mathcal{P}(\omega_2)$ was also experimentally verified over an order of magnitude in signal strength. When either the ω_1 and ω_2 beam was blocked, no signal at ω_a was detected after more than 10 shots, indicating that the signal-to-background ratio in our signal was greater than 10^5 . Furthermore, the anti-Stokes output was a coherent beam, as expected, with an experimental beam divergence of less than 2 mrad.

The sensitivity of the surface CARS technique with nanosecond pulses is limited by the maximum fluence incident on the film. However, because the signal is proportional to $\mathcal{P}^2(\omega_1) \mathcal{P}(\omega_2)$, the sensitivity can be greatly improved by use of picosecond pulses. Consider, for example, a 10-psec pulse with 10 μ J/pulse focused to a diameter of 400 μ m. Then, for the benzene-silver-glass system, we would expect to find an anti-Stokes signal of

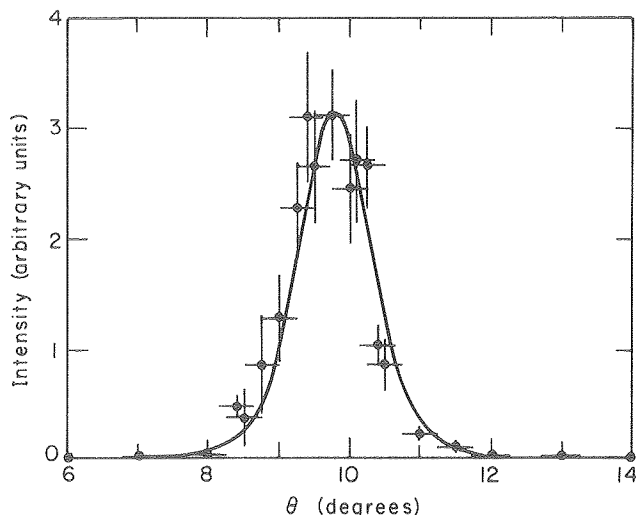


Fig. 3. Intensity of signal vs. angular position of prism assembly about the \hat{y} -axis. θ is the angle between the direction of beam 1 incident on the prism and to the prism normal. (XBL 796-3539)

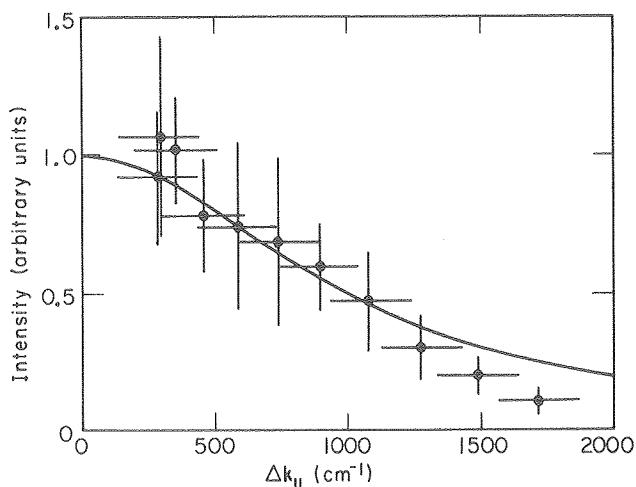


Fig. 4. Intensity of signal vs. phase mismatch Δk_\parallel . (XBL 796-3538)

1×10^{11} photons/pulse. This suggests that we should be able to detect a submonolayer of benzene molecules on silver.

In conclusion, we have reported the first results on a surface nonlinear four-wave mixing experiment, in which all input and output waves were surface plasmons. Our technique has a surface-specific nature and may find potential applications in surface science.

Acknowledgment. C. K. C. acknowledges partial support as an NSF Graduate Fellow from NSF grant No. SMI76-12375. A. R. B. C. acknowledges support from UNICAMP and CNPq, Brazil.

* * *

† Brief version of LBL-9341; Phys. Rev. Lett. 43, 946 (1979).

1. See, for example, the latest review article, G. Borstel and H. J. Falge, Appl. Phys. 16, 211 (1978) and references therein.
2. C. K. Chen, A. R. B. de Castro, Y. R. Shen, and F. DeMartini, Phys. Rev. Lett. 43, 946 (1979).
3. Detailed expressions for anti-Stokes power are given in Ref. 2.
4. E. Kretschmann, Zeit. Phys. 241, 313 (1971).

2. COHERENT SECOND HARMONIC GENERATION BY COUNTER-PROPAGATING SURFACE PLASMONS†

Chenson K. Chen, A. R. B. de Castro, and Y. Ron Shen

In a bulk nonlinear medium, counter-propagating electromagnetic waves will lead to second harmonic generation in all directions. On a surface, because of the required conservation of wavevector along the surface, counter-propagating surface electromagnetic waves generate second harmonic waves only in the direction perpendicular to the surface, an effect pointed out earlier.¹ Experimentally, on the other hand, second harmonic generation has been generated using counter-propagating evanescent² and guided³ waves, but not surface plasmons.

In our experiment, surface plasmons were excited along a quartz-silver interface in the Kretschmann geometry⁴ as shown in Fig. 1a. The second harmonic generation is due to the quartz nonlinearity. The solution of nonlinear Maxwell equations for this problem can be obtained fairly straightforwardly using appropriate boundary conditions.⁵

$$P(2\omega) = \frac{c\epsilon_q^{1/2}}{2\pi} A |F|^2 \left| \frac{4\pi(2\omega/c)^2 P_x^{(2)}}{4\beta^2 + (2\omega/c)^2 \epsilon_q} \right|^2 \quad (1)$$

$$\vec{P}^{(2)} = -\chi_{11}(E_x^2 + E_z^2)\hat{e}_x \quad (2)$$

where E_x, E_z are the field components of the surface plasmon at the silver-quartz interface, F is a Fresnel coefficient, ϵ_q is the dielectric constant of quartz, A is the beam overlap area, and χ_{11} is the nonlinear susceptibility of quartz.

The experimental arrangement is shown in Fig. 1b. A dye laser pumped by a Q-switched ruby laser produced 7 mJ, 20 nsec laser pulses at a rate of 10 pulses/min. The laser was tuned to 7456 Å with a linewidth less than 1 cm⁻¹ and was linearly polarized in the x - z plane. The silver film, 500 Å thick, was evaporated on the quartz crystal. A layer of α-bromonaphtalene provided optical contact between the Schott SF-10 equilateral prism and the silver film.

The experimental results are shown in Fig. 2 in comparison with theory. The observed maximum in the second harmonic signal occurs, as expected, at the

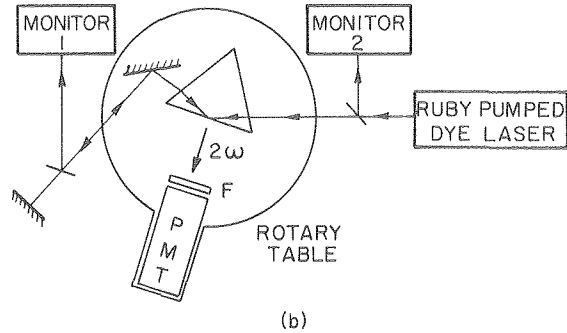
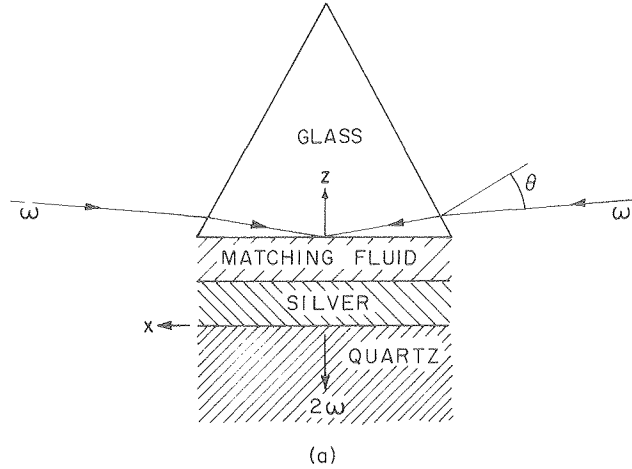


Fig. 1(a). The sample assembly. (b) Block diagram of the experimental set-up. F is a 10 cm long cell with saturated solution of CuSO₄ in water. (XBL 797-6702)

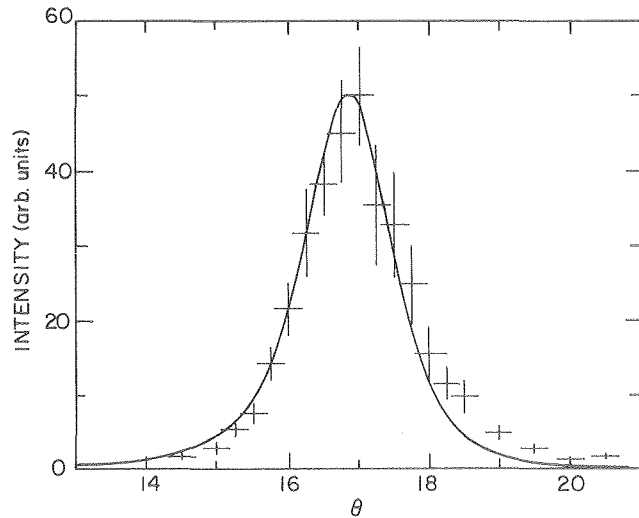


Fig. 2. Second harmonic intensity versus θ . θ is defined in Fig. 1(a). (XBL 797-6701)

angle where the counter-propagating surface plasmons were optimally excited and the width of the peak is approximately the width of the surface plasmon observed in attenuated total reflection (ATR) measurements. The theoretical curve was calculated from

Eq. 1 using Fresnel coefficients deduced from a fit to our ATR spectra. Apart from a normalization constant, it has no adjustable parameters. The agreement between experiment and theory is good.

We also verified that the second harmonic signal propagated as a highly directional beam with a divergence of ~ 1 mrad, and was linearly polarized along \hat{x} . It disappeared when either of the laser beams was blocked, or made transverse electric (so that surface plasmons were no longer excited), or when the quartz crystal was replaced by a glass substrate.

For the conditions of our experiment, Eq. 1 predicts an output of $\sim 2 \times 10^4$ photons/pulse, while we estimate the measured signal to correspond to $\sim 10^4$ photons/pulse.

The effect may be used to study second order nonlinear optical properties of thin crystalline films.

Acknowledgment. A. R. B. C. acknowledges support from UNICAMP and CNPq, Brazil. We also acknowledge partial support from NSF Grant INT76-05454 under the U. S.-Brazil Cooperative Science Program.

* * *

[†]Brief version of LBL-9542; to appear in Optics Letters.

1. M. Fukui, J. E. Sipe, V. C. Y. So, and G. I. Stegeman, *Solid State Commun.* **27**, 1265 (1978); R. Maddox and D. L. Mills, unpublished.
2. N. Bloembergen, H. J. Simon, and C. H. Lee, *Phys. Rev.* **181**, 1261 (1969).
3. R. Normandin and G. I. Stegeman, *Opt. Lett.* **4**, 58 (1979).
4. E. Kretschmann, *Z. Phys.* **241**, 313 (1971).
5. F. DeMartini and Y. R. Shen, *Phys. Rev. Lett.* **36**, 216 (1976); N. Bloembergen and P. S. Pershan, *Phys. Rev.* **128**, 606 (1962).

3. MEASUREMENT OF REFRACTIVE INDICES AND STUDY OF ISOTROPIC-NEMATIC PHASE TRANSITION BY THE SURFACE PLASMON TECHNIQUE[†]

Kung-Chao Chu, Chenson Chen, and Y. Ron Shen

We have used the surface plasmon technique to measure the refractive indices of liquid crystals with an accuracy better than 1×10^{-5} . We have measured the refractive indices of the liquid crystalline material 4-cyano-4'-pentylbiphenyl (PCB) as functions of temperature, particularly in the region near the isotropic-nematic phase transition. Because of the high sensitivity of the technique, we were able to probe the phase transition in great detail. We have found coexistence of the two phases, a hysteresis effect of the transition, and supercooling and superheating in a temperature range of 60 mK around the nominal transition temperature. That surface plasmons can be used to probe phase transition was proposed earlier by Agranovich.¹ Our experiment here is the first demonstration of his idea.

We excited the surface plasmons on a metal-dielectric interface by the Kretschmann⁴ method using a dielectric-metal film-prism configuration. The laser

beam with a TM-polarization is directed onto the metal-liquid crystal interface through the prism side, and the reflected beam is measured.

In our experiments, we used a cw Nd:YAG laser at $1.06 \mu\text{m}$. The sample assembly was composed of a prism with $n = 1.8117$, an evaporated film ($\sim 450 \text{ \AA}$) of gold, and a $\sim 100 \mu\text{m}$ layer of liquid crystal PCB sandwiched between the gold film and a glass plate. The sample assembly has a long-term temperature stability of better than 1 mK.

Typical reflectivity curves against the angle between the incident beam and the interface normal at $T < T_c$ and $T > T_c$ are shown in Figs. 1(a) and 1(c). The solid curves on the figures were theoretical curves by a nonlinear least-square fit program using the refractive index of the liquid crystal as a parameter to be deduced. The values of the optical constants and thickness of the gold film, required in the calculation, were on the other hand derived from a reflectivity curve in the isotropic

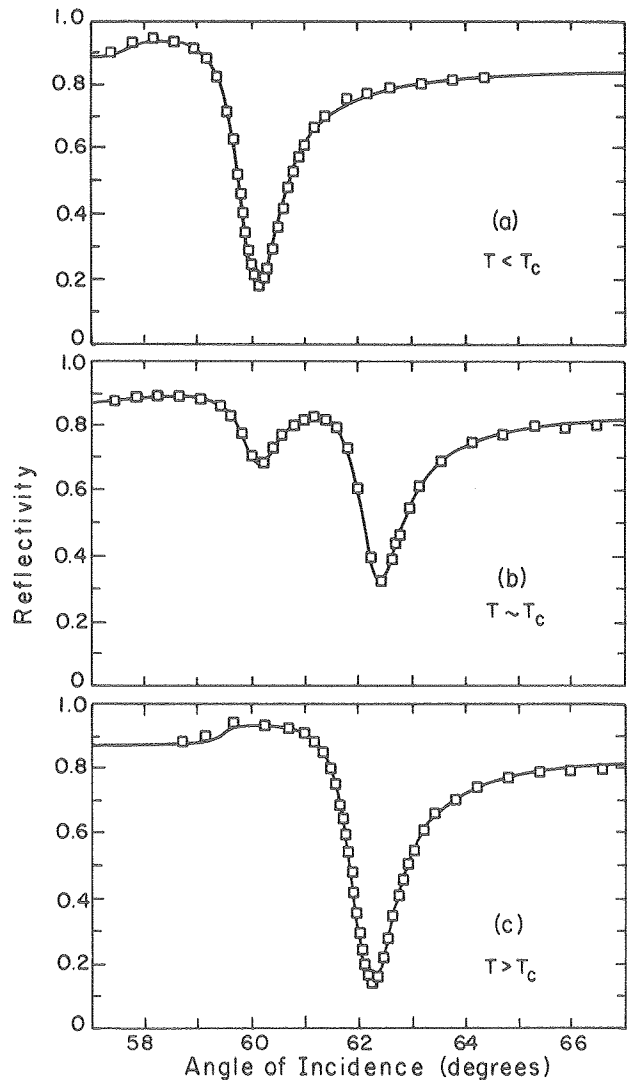


Fig. 1. Reflectivity vs. angle of incidence θ . The solid curves are theoretical curves obtained by nonlinear least-square fitting. (XBL 797-6535)

phase, the refractive index of the liquid crystal being known from a separate critical-angle measurement.

In the nematic phase, the liquid crystal has two refractive components: n_{\perp} and n_{\parallel} , perpendicular and parallel, respectively, to the direction of alignment \hat{n} . We deduced these components from measurements with different liquid-crystal alignments by the usual surfactant method.³ The accuracy of these n values is $\leq 1 \times 10^{-3}$ as checked by our separate measurements of n_{\perp} and n_{\parallel} with the critical-angle method.⁴

The most interesting aspect of the surface plasmon technique is its ability to probe the phase transition in detail. By raising or lowering the temperature of the sample in millidegree steps, we found that there was a ~ 60 mK transition region where the isotropic and nematic phases co-exist. Two reflectivity dips showed up in the region, as shown in Fig. 1(b); one corresponded to the nematic phase at $\sim T_C$ and the other to the isotropic phase at $\sim T_C$. Their positions remained unchanged as the temperature varied, but their relative magnitude did change. As seen in Fig. 1(b), the double-dip reflectivity curve can be fit very well by the theoretical expression $R = xR_{\text{isotropic}} + (1-x)R_{\text{nematic}}$, where x is the fraction of the medium in the isotropic phase, and $R_{\text{isotropic}}$ and R_{nematic} are evaluated at $\sim T_C$. With decreasing temperature, the nematic dip grew in strength while the isotropic dip gradually disappeared, and vice-versa for increasing temperature. In Fig. 2, the results of how x varies with temperature in the transition region are shown with the temperature change in one direction and then the other. There is a clear hysteresis effect, characteristic of the first-order transition. We can define the mid-point of the hysteresis loop as the transition temperature T_C , and the width of the hysteresis loop as the supercooling-superheating range. We believe this is the first time such a hysteresis loop for the nematic-isotropic transition has ever been measured. We also worked out a diffuse droplet model of nucleation to give a correct order-of-magnitude estimate on the supercooling and superheating range.

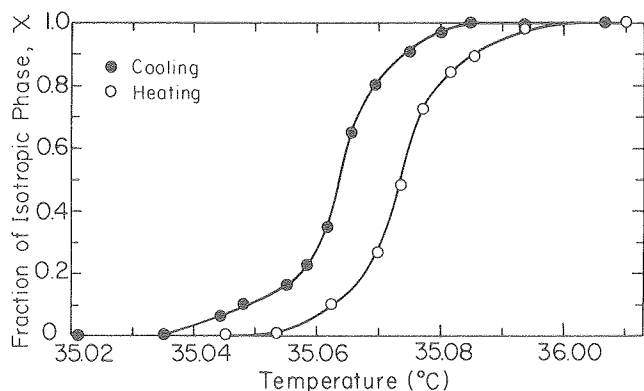


Fig. 2. Fraction of isotropic phase as a function of temperature in the transition region. Heating and cooling exhibit the hysteresis effect.

(XBL 797-6537)

Acknowledgment. K. C. C. and C. K. C. were supported by the Division of Materials Sciences, Office of Basic Energy Sciences, U. S. Department of Energy and Y. R. S. was supported by the NSF under Grant No. DMR78-18826. C. K. C. acknowledges partial support as an NSF Graduate Fellow from NSF Grant No. SMI76-12375.

* * *

† Brief version of LBL-9598; submitted to Mol. Cryst. Liq. Cryst.

1. V. M. Agranovich, JETP Lett. 24, 558 (1976).
2. E. Kretschmann, Zeit. Phys. 241, 313 (1971).
3. F. J. Kahn, Appl. Phys. Lett. 22, 386 (1973).
4. D. Riviere, Y. Levy, and C. Imbert, Opt. Comm. 25, 206 (1978).

4. POLARIZATION-SENSITIVE COHERENT ANTI-STOKES RAMAN SPECTROSCOPY†

Jean-Louis Oudar, Robert W. Smith, and Y. Ron Shen

In recent years, a number of coherent nonlinear optical spectroscopic techniques have been developed that have clear advantages over spontaneous scattering techniques when high resolution is required, and/or when fluorescence or thermal radiative emission is strong. Most notable of these nonlinear techniques is coherent anti-Stokes Raman spectroscopy (CARS) which is a widely accepted technique to study vibrational modes in both molecules and solids. However, CARS has a rather limited sensitivity in detecting weak resonances, due to the strong background from the nonresonant nonlinear contribution. The major source of noise comes from fluctuations in power or the mode structure of the input laser, thus masking small resonant signals. Variations of the basic CARS scheme have been proposed to suppress this background, but they make use of a third input beam so that three lasers are needed.^{1,2} We describe a simple polarization arrangement that allows continuous CARS spectra to be taken with only the usual two input lasers.

Recently, Akhmanov et al.³ have shown that ellipsometric measurements of the anti-Stokes beam in a CARS experiment can yield information on the dispersion of nonlinear susceptibility with high accuracy. However, it is a tedious procedure if the ellipsometry is to be performed over the entire spectrum, point by point.

In our arrangement CARS spectra are taken directly and continuously with the nonresonant background eliminated and considerable improvement in the detection of weak Raman resonances. In addition, by admixing the resonant contribution with a controlled (and properly phase-shifted) proportion on the nonresonant part, we can obtain spectra which are linear in either the real or the imaginary part of the resonant susceptibility.

Consider two input beams at frequencies ω_1 and ω_2 propagating in an isotropic medium along the \hat{z} axis. The ω_1 beam is polarized along \hat{x} and ω_2 beam along a direction at an angle ϕ with \hat{x} . The nonlinear

polarization, \vec{P} , at frequency $\omega_3 = 2\omega_1 - \omega_2$ will have components along \hat{x} and \hat{y} which are related to the input fields through the third order nonlinear susceptibility, χ_{ijkl} . In an isotropic medium P_x is determined by χ_{xxxx} , while P_y by χ_{xyyx} . We can describe the nonlinear susceptibility in terms of a resonant (dispersive) part and a nonresonant (non-dispersive background) part, which lead to distinct contributions to P . In our technique we exploit the fact that, in general $\chi_{xyyx}^{NR}/\chi_{xxxx}^{NR} \neq \chi_{xyyx}^R/\chi_{xxxx}^R$ (NR - nonresonant, R - resonant). The ratios are not equal because χ^{NR} derives its symmetry from the macroscopic medium, whereas χ^R has its symmetry determined by the Raman modes. We conclude that $P_y^{NR}/P_x^{NR} \neq P_y^R/P_x^R$, i.e. \vec{P}^{NR} and \vec{P}^R are not collinear. Having established that the two contributions to the nonlinear polarization have different directions, we can easily use polarization analysis to separate them.

The simplest way to take a polarization-sensitive-CARS (PS-CARS) spectrum is to null out \vec{P}^{NR} . As $\omega_1 - \omega_2$ is scanned across the Raman frequency, the signal will be proportional to only $|\chi^R|^2$ with the background suppressed. Usually it is necessary to introduce both a linear polarizer and a quarter-wave plate to achieve the best extinction of the background. Sensitivity now is limited only by the achievable extinction ratios.

If the polarizer is uncrossed by a small angle θ the signal will be proportional to $|\theta P^{NR} + P^R|^2 \approx |\theta P^{NR}|^2 + 2\text{Re}(\theta P^{NR} P^R)$, if $|\theta P^{NR}| \gg |P^R|$. By uncrossing the linear polarizer, the real part of P^R , is displayed, while uncrossing the quarter wave plate displays the imaginary part of P^R (effectively $\theta \rightarrow i\theta$). In all cases the part of the signal rejected by the analyzer is predominantly due to $|P^{NR}|^2$, which provides a convenient nondispersive reference signal for normalization.

To illustrate these possibilities, we have performed a CARS experiment with dilute mixtures of benzene in carbon tetrachloride. Two flashlamp-pumped dye lasers⁴ were used to provide the two tunable input beams of peak powers ~ 5 kW each. The polarization of the ω_2 beam could be rotated with respect to that of ω_1 by a half-wave Fresnel rhomb. Figure 1 shows spectra taken of the 992 cm^{-1} Raman modes of 0.1% benzene (by volume) in carbon tetrachloride. Figure 1(a) shows the background suppression spectrum and Figs. 1(b) and (c) show the imaginary and real parts of the resonance.

In conclusion, these spectra clearly demonstrate the sensitivity of PS-CARS for the detection of weak or dilute Raman modes. With our setup, the detection limit of benzene concentration in CCl_4 was 2×10^{-4} using the 992 cm^{-1} Raman mode, which is at least one order of magnitude improvement compared to other coherent Raman techniques.^{5,6} With the use of more powerful lasers, such as Nd:YAG pumped dye lasers in the 100 kW - 1 MW range, the detection limit should be less than 10^{-5} , that is 10 ppm for molecules with scattering cross-sections similar to that of benzene. This technique should also be very useful in the case of gaseous media where the nonresonant background nonlinearity also constitutes a major obstacle to the detection of small concentrations of a given species.⁷

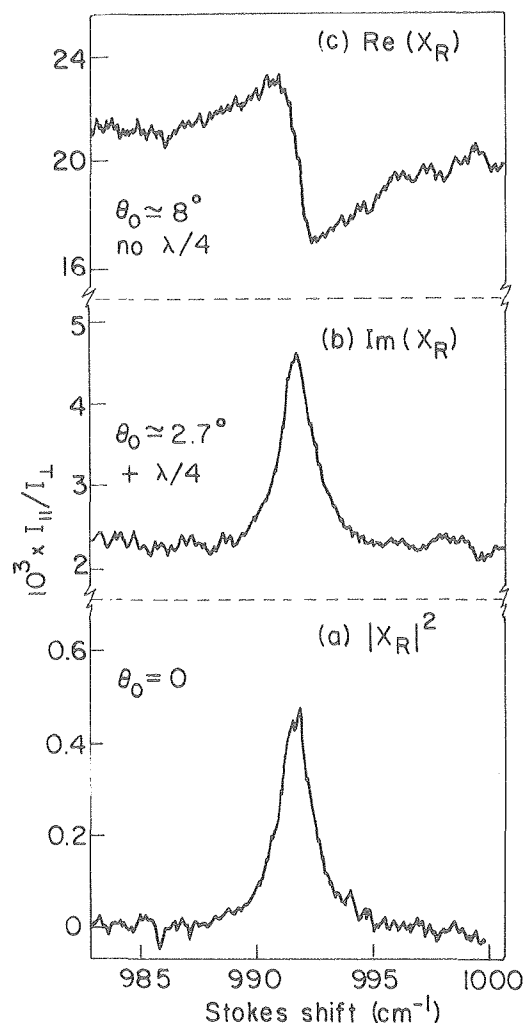


Fig. 1. PS-CARS spectra of 0.1% (by volume) benzene in carbon tetrachloride (a) background suppression, (b) and (c) interference between a small fraction of the coherent background and the imaginary part (b) or the real part (c) of the Raman contribution.

(XBL 791-5629).

Acknowledgment. This work was partially supported by a NATO fellowship (J.L.O.). One of us (J.L.O.) acknowledges a very fruitful discussion with N. I. Koroteev.

* * *

† Brief version of LBL-8749; Appl. Phys. Lett. 34, 758 (1979).

1. J. J. Song, G. L. Eesley, and M. D. Levenson, Appl. Phys. Lett. 29, 567 (1974).
2. H. Lotem, R. T. Lynch, Jr., and N. Bloembergen, Phys. Rev. A 14, 1748 (1976).
3. S. A. Akhmanov, A. F. Bunkin, S. G. Ivanov, and N. I. Koroteev, J. E. T. P. 74, 1272 (1978).
4. S. Chu and R. W. Smith, Optics Commun. 28, 221 (1979).
5. G. L. Eesley, M. D. Levenson, and W. M. Tolles, IEEE J. of Quant. Elect. QE-14, 45 (1978).
6. A. Owyong, IEEE J. of Quant. Elect. QE-14, 192 (1978).
7. J. P. Taran in Laser Spectroscopy III, p. 315, J. L. Hall and J. L. Carlsten, Eds. (Springer-Verlag, Berlin, New York, 1977).

5. DYNAMICS OF RESONANT STRONG INTERACTION OF LIGHT WITH ATOMS AND MOLECULES[†]

Aasmund Sudbø and Y. Ron Shen

We have developed a formalism for calculations of dynamics of resonant interaction of strong radiation with matter. The development is guided by the realization that such problems can be formulated as a set of eigenvalue equations, and can then be solved numerically with available computer software.

Briefly, the approach is as follows. We consider the problem of strong interaction of a monochromatic radiation with an N -level system. Using density matrix formalism, the dynamical response of the system can be described by a set of N^2 first-order differential equations, which form an eigenvalue problem of N^2 dimensions. In various physical situations, different approximations can be made to reduce the dimensionality. The eigenvalue problems can then be solved on a computer, and the time constants of the dynamic response can be deduced.

We have used the method to calculate the dynamics of optical pumping of the $S_{1/2} - P_{3/2}$ transition in an alkali atom. There are six states (neglecting hyperfine structure) involved in the optical pumping, giving rise to a 36-element density matrix. The solution should give the populations in the six states as a function of time. We deduce, for simplicity, only the smallest time constant for the dynamic response which basically tells us how rapidly the atoms can be oriented by the optical pumping. Figure 1 shows the steady state population in the $S_{1/2}$ ($m = 1/2$) state, after resonance pumping by a long laser pulse, as a function of the degree of circular polarization. In Fig. 2, the smallest time constant is plotted as a function of the laser field amplitude. It shows that the optical pumping speed increases rapidly with increase of laser intensity as expected, but it saturates at a certain value. Finally, in Fig. 3, the smallest time constant is shown as a function of detuning from resonance at several laser intensities. As expected, the optical pumping speed drops off quickly with increase of detuning, but the effect is less with higher laser intensities because of optical Stark broadening.

* * *

[†]Brief version of LBL-9796.

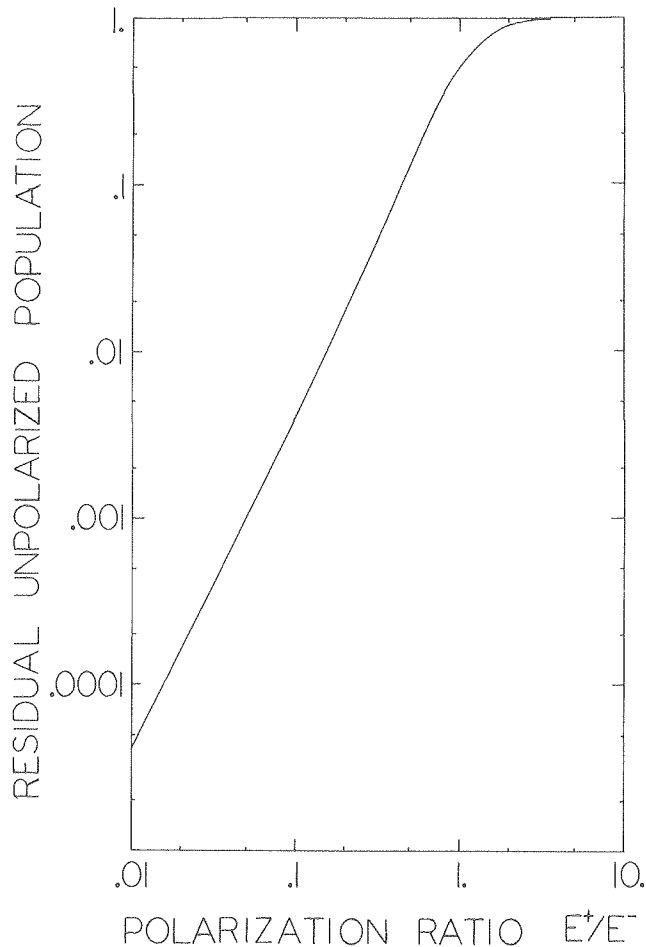


Fig. 1. Fraction of population in the $^2S_{1/2}$ ($m = 1/2$) state, after a long laser pulse excitation, tuned to resonance, as a function of the ratio of left circularly polarized amplitude to right circularly polarized amplitude, E^+/E^- . (XBL 799-11279)

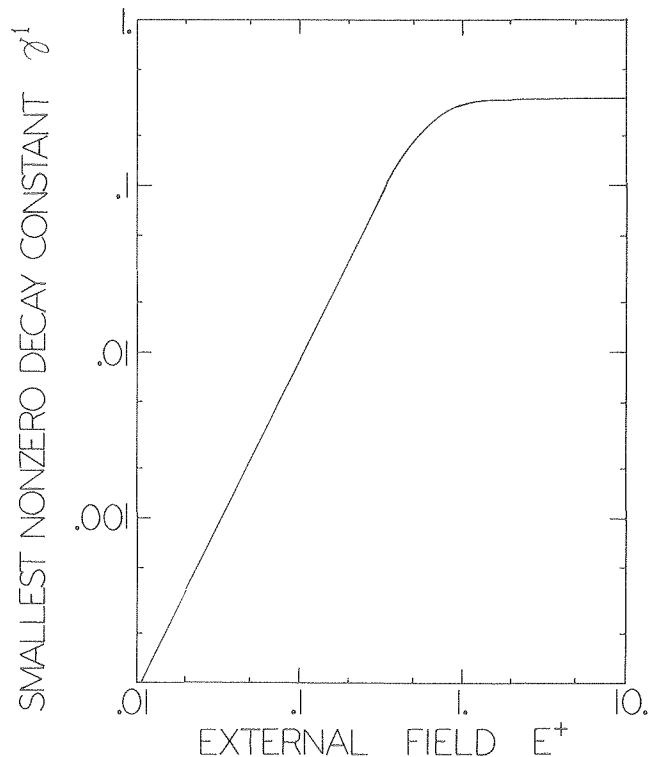


Fig. 2. Smallest nonzero response time constant for circularly polarized light on resonance as a function of laser field amplitude. (XBL 799-11277)

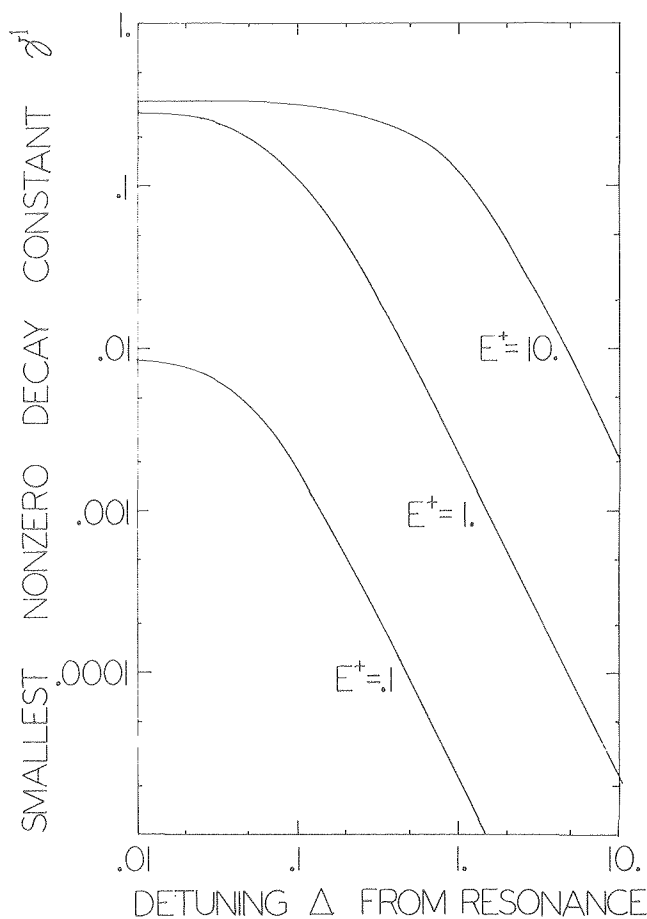


Fig. 3. Smallest nonzero response time for circularly polarized light, and for three different field amplitudes E^+ , as a function of detuning Δ from resonance. (XBL 799-11278)

6. MULTI-PHOTON DISSOCIATION OF MOLECULES

Aasmund Sudbø and Y. Ron Shen, in collaboration with Yuan T. Lee's group

See Section on Molecular Beam Laser Isotope Separation.

RESEARCH PLANS FOR CALENDAR YEAR 1980

The potential of surface CARS as a spectroscopic technique will be more carefully evaluated. First, the advantage of its application on absorbing and fluorescent materials will be tested. It is expected that both the Raman spectra and the two-photon absorption spectra of fluorescent dye molecules in solutions can be measured. Second, application of the technique to thin films will be tried. In particular, the possibility of detecting surface acoustic waves will be considered. Third, we will use picosecond mode-locked laser pulses, which should have the sensitivity of detecting monolayers of molecules on metal surfaces. Such sensitivity will be tested experimentally.

Resonant four-wave mixing as a new nonlinear spectroscopy technique will be studied theoretically and experimentally. Doubly and triply resonant cases are the main subject of investigation. The possibility of using the technique to reduce inhomogeneous broadening and to measure transitions between excited states, the transition matrix elements, and the relaxation lifetimes will be considered. Rare earth ions in solids will be the material systems to try out the spectroscopy technique.

Two-photon optical pumping in solids will be investigated experimentally. The results will be compared with those obtained from one-photon optical pumping. While the latter may suffer from the surface quenching effect, two-photon optical pumping is a pure bulk effect. Spin relaxations of electrons and excitons in the bulk can be deduced from our results.

A mode-locked laser system with picosecond pulse output tunable over a frequency range from $\sim 0.26 \mu$ to $\sim 4 \mu$ will be built. It will be used for studies of chemical dynamics, transient four-wave mixing, and dynamics of excitations in solids.

Collaboration with Prof. Y. T. Lee's group on laser-molecular beam interaction is being continued. Immediate problems to be investigated are the multi-channel, multiphoton dissociation of molecules, the resonant effect of one-photon predissociation of molecules, and the measurement of rotational energy distribution of laser-induced fluorescence.

Surface plasmons will be used to study optical properties of materials, in particular, the refractive indices and phase transitions in liquid crystals. The project is partially supported by the National Science Foundation. Thin films of materials can be studied by this technique because of its great sensitivity. Consequently, the problem of how the phase transition characteristics change from three-dimensional to two-dimensional as the film decreases can be thoroughly investigated.

1979 PUBLICATIONS AND REPORTS

Refereed Journals

1. C. K. Chen, A. R. B. de Castro, Y. R. Shen, and F. DeMartini, "Surface Coherent Anti-Stokes Raman Spectroscopy," *Phys. Lett.* **43**, 946 (1979), LBL-9341.
2. Aa. S. Sudbø, P. A. Schulz, D. J. Krajnovich, Y. T. Lee, and Y. R. Shen, "Photoionization Study of Multiphoton Excited SF_6 in a Molecular Beam," *Optics Lett.* **4**, 219 (1979), LBL-8765.
3. J. L. Oudar, R. W. Smith, and Y. R. Shen, "Polarization-Sensitive Coherent Anti-Stokes Raman Spectroscopy," *Appl. Phys. Lett.* **34**, 758 (1979), LBL-8749.
4. A. G. Jacobson and Y. R. Shen, "Coherent Brillouin Spectroscopy," *Appl. Phys. Lett.* **34**, 464 (1979), LBL-8448.
5. S. Chu and R. W. Smith, "A Reliable Thyatron-Switched Flashlamp-Pumped Dye Laser," *Opt. Commun.* **28**, 221 (1979).

†6. T. Bischofberger and Y. R. Shen, "A Nonlinear Fabry-Perot Filled with CS₂ and Nitrobenzene," *Opt. Lett.* 4, 40 (1979), LBL-8180.

†7. T. Bischofberger and Y. R. Shen, "Theoretical and Experimental Study of the Dynamic Behavior of a Nonlinear Fabry-Perot Interferometer," *Phys. Rev. A* 19, 1169 (1979), LBL-8179.

†8. K. Inoue and Y. R. Shen, "Study of Isotropic-Nematic Phase Transition by Optical-Field-Induced Molecular Alignment in Binary Mixtures," *Mol. Cryst. Liq. Cryst.* 51, 179 (1979).

9. Aa. S. Sudbø, P. A. Schulz, Y. R. Shen, and Y. T. Lee, "Three and Four Center Elimination of HCl in the Multiphoton Dissociation of Halogenated Hydrocarbons," *J. of Chem. Phys.* 69, 2312 (1978), LBL-6991.

10. Aa. S. Sudbø, P. A. Schulz, E. R. Grant, Y. T. Lee, and Y. R. Shen, "Simple Bond Rupture Reactions in Multiphoton Dissociation of Molecules," *J. of Chem. Phys.* 70, 912 (1979), LBL-7684.

Other Publications

1. Aa. S. Sudbø, P. Schulz, D. Krajnovich, Y. R. Shen, and Y. T. Lee, "Crossed Laser and Molecular Beams Studies of Multiphoton Dissociation," *Advances in Laser Chemistry*, A. H. Zewal, Ed., Springer Series in Chemical Physics (Springer-Verlag, Berlin, Heidelberg, New York, 1978), p. 308, LBL-7678.

2. P. A. Schulz, Aa. S. Sudbø, D. J. Krajnovich, H. S. Kwok, Y. R. Shen, and Y. T. Lee, "Multiphoton Dissociation of Polyatomic Molecules," *Ann. Rev. Phys. Chem.* 30, 379 (1979), LBL-8751.

3. Y. R. Shen, "Nonlinear Optical Effects," *Methods of Experim. Phys.* 15, 249 (1979), LBL-6091.

LBL Reports

1. Aa. S. Sudbø, D. J. Krajnovich, P. A. Schulz, Y. R. Shen, and Y. T. Lee, "Molecular Beam Studies of Laser Induced Multiphoton Dissociation," LBL-8993.

2. Aa. S. Sudbø, "Multiphoton Processes in Isolated Atoms and Molecules" (Ph.D. Thesis), LBL-9796.

3. P. A. Schulz, Aa. S. Sudbø, E. R. Grant, Y. R. Shen, and Y. T. Lee, "Multiphoton Dissociation of SF₆ by a Molecular Beam," LBL-9202.

4. C. K. Chen, A. R. B. de Castro, and Y. R. Shen, "Coherent Second Harmonic Generation by Counter-Propagating Surface Plasmons," LBL-9542.

†5. K. C. Chu, C. K. Chen, and Y. R. Shen, "Measurement of Refractive Indices and Study of Isotropic-Nematic Phase Transition by the Surface Plasmon Technique," LBL-9398.

Invited Talks

1. Y. R. Shen, "Coherent Light Scattering by Surface Polaritons," U. S.-Japan Seminar on Inelastic Light Scattering, Santa Monica, California, January 1979.

2. D. J. Krajnovich, A. Giardini-Guidoni, Aa. S. Sudbø, P. A. Schulz, Y. R. Shen, and Y. T. Lee, "Crossed Laser and Molecular Beam Study of Multiphoton Dissociation of C₂F₅Cl," European Physical Society Conference, Heriot-Watt University, Edinburgh, Scotland, September 20-22, 1978.

3. Y. R. Shen, "Surface Coherent Anti-Stokes Raman Spectroscopy," IBM, Yorktown Heights, New York, August 1979.

4. Y. R. Shen, "Lasers, Nonlinear Optics, Laser Spectroscopy, Laser Chemistry, and Other Laser Applications," a series of 11 lectures, Institute of Physics, Academia Sinica, Beijing, China, November 1978.

5. Y. R. Shen, "Nonlinear Optical Effects, Nonlinear Optical Spectroscopy, Multiphoton Dissociation of Molecules, Recent Advances in Quantum Electronics and Related Topics," lectures in various cities in China, November-December 1978.

† Partially supported by the National Science Foundation.

‡ Supported by the National Science Foundation.

c. Excited Quantum Fluids in Solids*

Carson D. Jeffries, Investigator

Introduction. When light strikes a cold semiconductor, for example Ge or Si, the excited electrons and holes quickly combine to form free mobile excitons (FE) and even multiexciton complexes; the free biexciton in Si, for instance, has been observed. These quasiparticles are bosons; a Bose condensation has been predicted by theory, but there is as yet no clear experimental evidence for this. Not predicted by theory was Pokrovskii's discovery that the exciton gas makes a first-order condensation into a Fermi liquid: electron-hole droplets (EHD) which are metallic and mobile. This transition has many of the classical aspects of the water vapor-fog droplet condensation. However, the medium of the EHD is a novel state of matter: in pure Ge it is a cold, dense, multicomponent, anisotropic, compensated plasma of constant density (2×10^{17} electrons and holes per cm^3). This liquid is a collective excited state of the crystal lattice with a lifetime of 10^{-4} sec and is the first example of a Fermi liquid in a periodic lattice. We have studied in detail many of its properties: the nucleation process; motion and diffusion of droplets; confinement of sizeable volumes of the liquid in potential wells of crystal strain; magneto-oscillatory phenomena; unusual magnetic properties: Alfvén wave dimensional resonances; lifetimes, decay mechanisms and phonon interactions in stressed and unstressed crystals; optical hysteresis and memory; droplet surface tension; compressibility of the liquid. These experiments are being extended, and we are also investigating the closely related Mott metal-insulator transition, as well as properties of the free excitons.

1. LIFETIME AND DIFFUSION OF FREE EXCITONS IN Ge^\dagger

James C. Culbertson, Robert M. Westervelt,[‡] and Carson D. Jeffries

Although the electron-hole liquid is more complex and varied, both in the phenomena observed and in the required theoretical treatment, the single free exciton (FE) in Ge has several properties not yet understood: The observed lifetimes (2 to 10 μsec) are 3 orders of magnitude shorter than the theoretical radiative decay lifetime, whereas the liquid lifetime is in reasonable agreement with theory. It is fairly clear that non-radiative decay modes involving, for example, dislocations, surfaces, and neutral impurities are important factors in FE decay, and it is our objective to measure and differentiate experimentally these various contributions to the FE decay and provide a quantitative explanation of the lifetimes. We are measuring the bulk FE lifetime τ_{ex} , the FE diffusion constant D , and the surface recombination velocity S using the experimental arrangement of Fig. 1.¹ A large

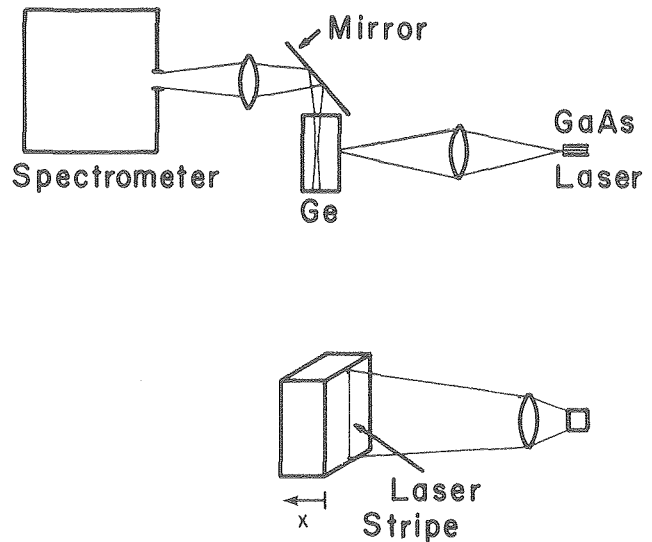


Fig. 1. Experimental geometry. A stripe of radiation from a GaAs laser diode is pulsed onto an ultrapure $8 \times 8 \times 4 \text{ mm}^3$ Ge crystal at $T = 4.2 \text{ K}$. The luminescence from the side of the crystal is then analysed by a spectrometer, using time resolution. (XBL 7912-13286)

ultrapure crystal of Ge $8 \times 8 \times 4 \text{ mm}^3$ is excited by a pulsed GaAs laser diode focused in a stripe. The FE luminescence from the side of the crystal is analysed by a spectrometer. Spatial profiles of FE luminescence intensity along the coordinate x are obtained by scanning the image past the spectrometer slit; time resolution is obtained by observing the luminescence of various time delays following excitation. The total luminescence from FE at 709 meV and EHD at 714 meV is recorded. Care is taken to select FE spatial profiles only after the EHD have evaporated. This avoids the complication of thermionic emission of FE from EHD. A temperature $T = 4.2 \text{ K}$ is used.

Luminescence intensity profiles at various times up until the first FE spatial profile taken are shown in Fig. 2 for a large dislocation-free crystal of Ge. The EHD are produced and remain near the front surface; they have essentially all decayed when the first FE scan is taken.

The total FE luminescence intensity for this unetched, dislocation-free crystal, Fig. 3(a), shows a lifetime $\sim 27 \mu\text{s}$. A smaller sample from the same crystal boule was measured earlier to have a $7 \mu\text{s}$ lifetime. This strongly suggests that surface recombination plays an important role in decay. Fig. 3(b) displays spatial profiles of FE luminescence intensity for the same sample. FE are seen to diffuse into the crystal from the excitation surface, indicated by the arrows on the right, to the interior of the crystal, the concentration being pulled down near the surface by

* This work was supported by the Division of Materials Sciences, Office of Basic Energy Sciences, U.S. Department of Energy.

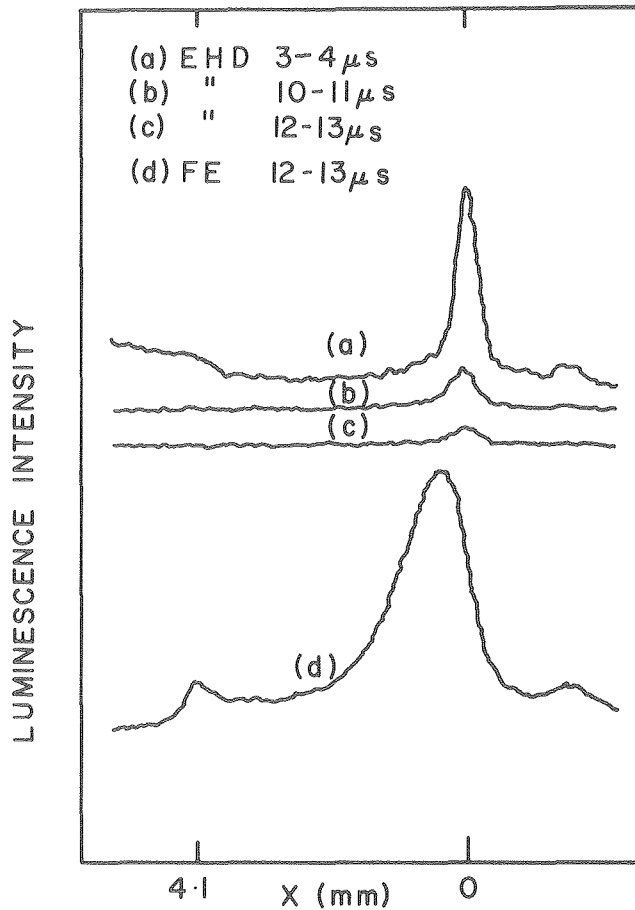


Fig. 2. Spatial scans of EHD (709 meV) luminescence intensity (a-c) at times up to 12 μ s, when the first FE profile is recorded. All profiles are to the same scale. (XBL 7912-13288)

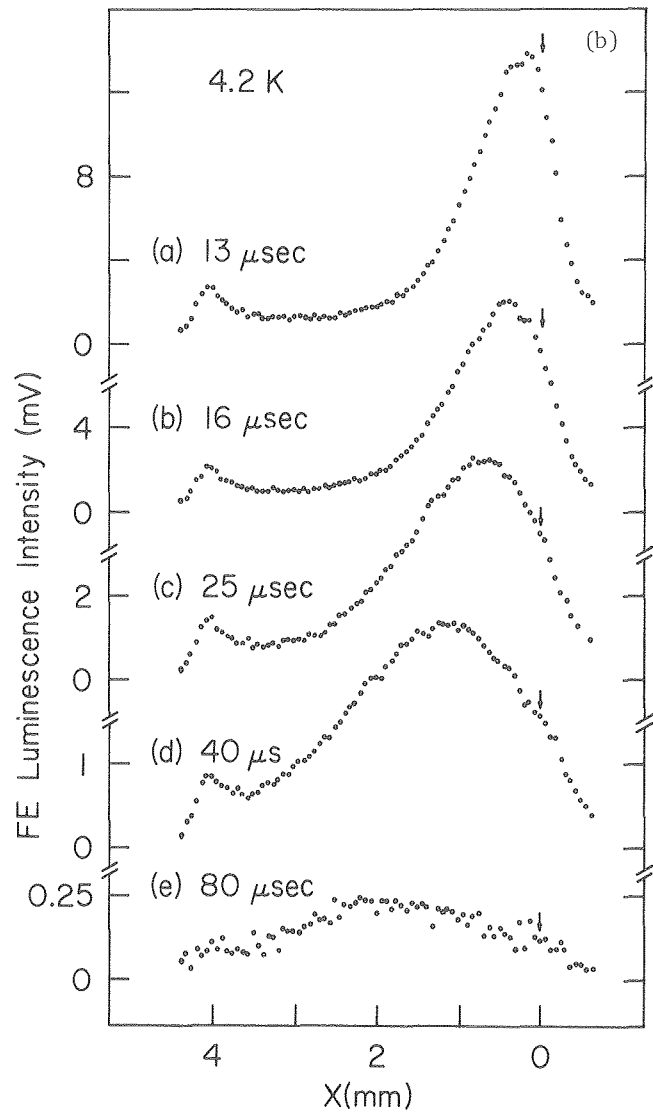
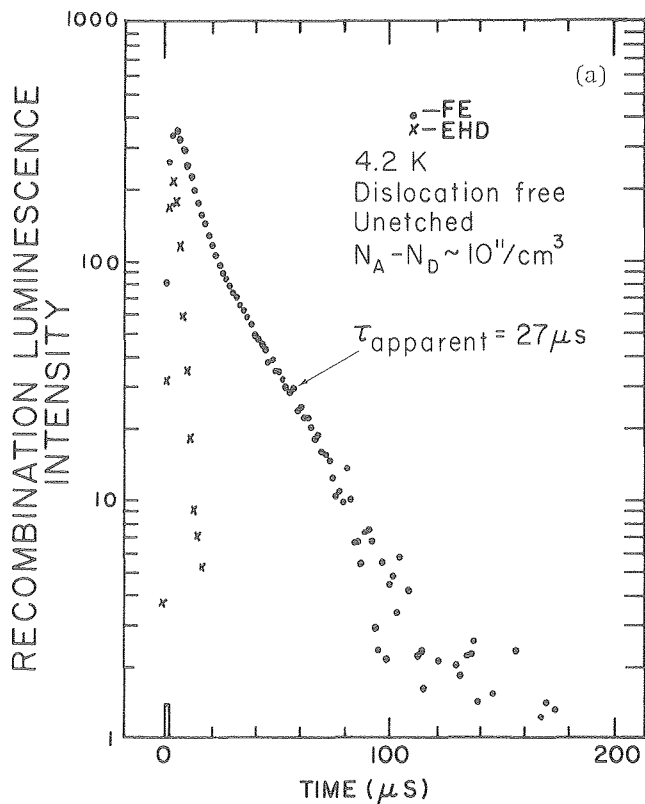


Fig. 3. (a) Decay of FE and EHD luminescence intensity for an $8 \times 8 \times 4 \text{ mm}^3$ unetched dislocation-free Ge crystal with impurity $N_A - N_D \sim 10^{11}/\text{cm}^3$. (b) FE luminescence intensity spatial profiles from 13 μ s to 80 μ s after laser excitation. The excitation surface is indicated by the arrows at the right. The FE are seen diffusing toward the back surface indicated by the peaks at $X = 4 \text{ mm}$, where internally reflected light is escaping through the corner of the crystal into the spectrometer.

[(a) XBL 7912-13289; (b) XBL 7912-13291]

surface recombination. The peaks at the left $x = 4$ mm occur at the back surface of the crystal where internally reflected FE luminescence escapes through the corner into the spectrometer. These are the first experiments to yield such long lifetimes for FE in Ge and, in addition, to show spatial resolution.

We use a model of FE diffusion, with acoustic phonon-FE scattering being the responsible mechanism, and a phenomenological boundary condition $J(\text{surface}) = S n(\text{surface})$ to account for surface recombination. This boundary condition states that the FE current, $J(\text{surface})$, into the surface is proportional to the FE density, $n(\text{surface})$, at the surface. S is called the recombination velocity.

Values of $D \sim 300 \text{ cm}^2/\text{sec}$, $S \sim 3 \times 10^3 \text{ cm/sec}$ and $\tau_{\text{ex}} \sim 30 \mu\text{s}$ appear to fit the data nicely. This value of D is about four times smaller than previous values.²

The results of the same experiment on an unetched Ge crystal $8 \times 8 \times 4 \text{ mm}^3$ with ~ 350 dislocations/cm² is shown in Fig. 4. A lifetime on the

order of $6 \mu\text{s}$ is observed, the shortness being attributed to FE recombination on dislocations. The other parameters appear to be about the same as in the dislocation-free sample.

With these data and results from further experiments, the actual dependence of the FE lifetime in bulk Ge on the features of the crystal can be determined. The ultimate goal of the project is the matching of experimentally determined FE lifetimes in Ge to theoretically calculated values.

Dr. Eugene Haller kindly provided the Ge crystals used.

* * *

†Brief version of LBL-8592.

‡Permanent address: Division of Applied Sciences, Harvard University, Cambridge, MA 02138.

1. J. C. Culbertson and R. M. Westervelt, Bull. Am. Phys. Soc. 24, 342 (1979), LBL-8592.

2. Ya. E. Pokrovskii and K. I. Svistunova, Fiz. Tverd. Tela. 13, 1485 (1971), [Sov. Phys.--Solid State 13, 1241 (1971)].

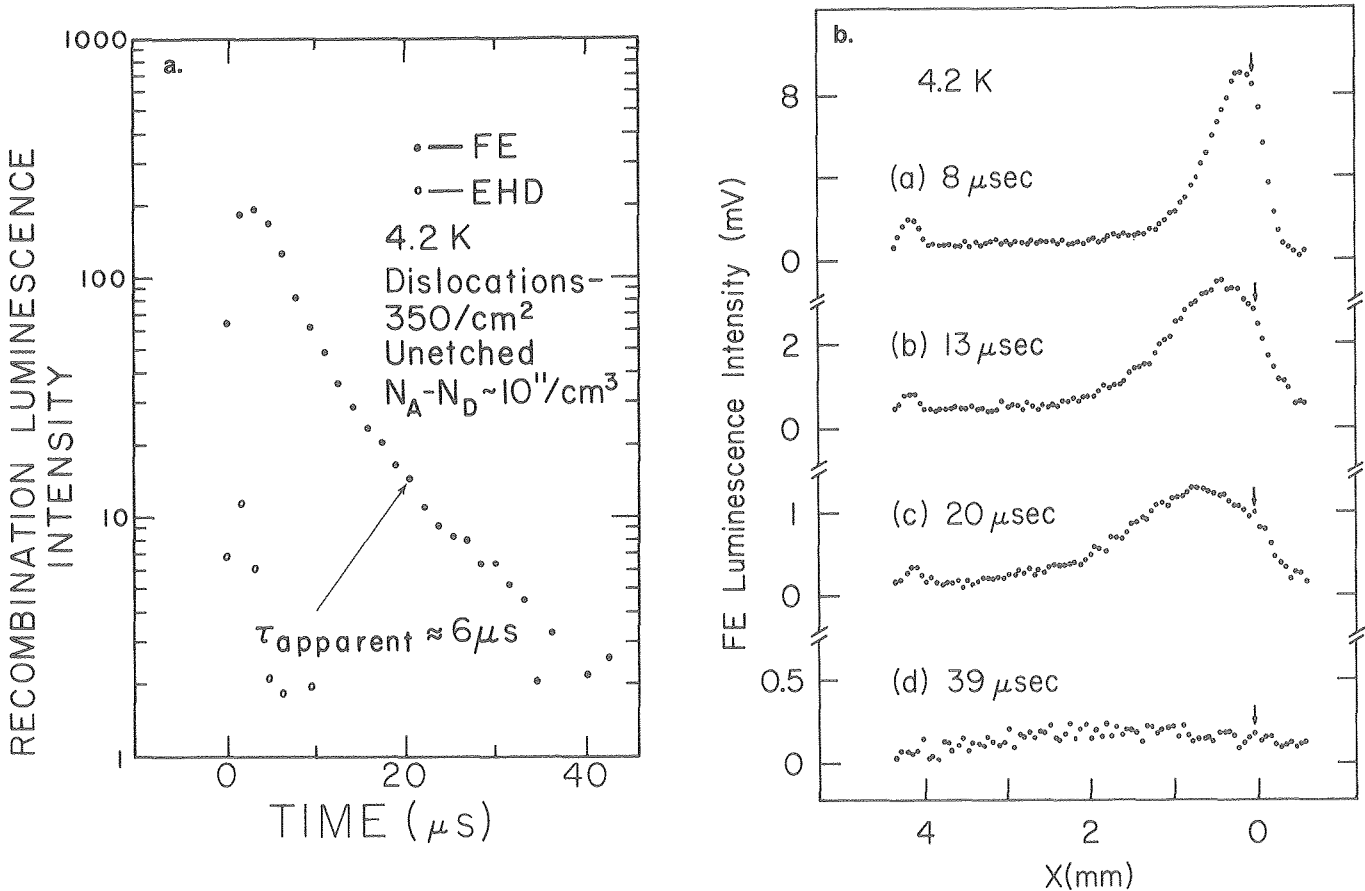


Fig. 4. (a) The decay of FE and EHD luminescence intensity for an $8 \times 8 \times 4 \text{ mm}^3$ unetched Ge crystal with ~ 350 dislocations/cm² and $N_A - N_D \sim 10^{11}/\text{cm}^3$. (b) FE luminescence intensity spatial profiles from $8 \mu\text{s}$ to $39 \mu\text{s}$ after laser excitation. The excitation surface is indicated by the arrows at the right. The FE are seen diffusing toward the back surface at $X = 4$ mm. The dislocations in this sample apparently account for the shortened life time relative to Fig. 3. [(a) XBL 7912-13287; (b) XBL 7912-13290]

2. EXPERIMENTAL LIMIT ON THE NET CHARGE OF ELECTRON-HOLE DROPS IN Ge

Robert M. Westervelt,[†] James C. Culbertson and Carson D. Jeffries

It has been predicted that EHD in Ge have a net electrical charge.¹ Experiments performed up to now² are in disagreement with each other as to the sign and magnitude of the charge. One experimental difficulty has been that the EHD must move distances $\sim 100 \mu\text{m}$ within $\sim 40 \mu\text{s}$ before the EHD decay in order for the motion and thus the charge of the EHD to be measured in an electric force field.

An experimental setup which bypasses this difficulty has been devised³ as shown in Figs. 1 and 2. In Fig. 2 a $1.52 \mu\text{m}$ wavelength source volume excites the free exciton (FE) gas. Due to a hysteresis in the formation of EHD, the intensity of this $1.52 \mu\text{m}$ light can be adjusted to be low enough to prevent EHD from being formed and at the same time high enough that any EHD already created will remain. With the $1.52 \mu\text{m}$ light source so adjusted a momentary stripe of Ar ion laser light on the crystal creates a stripe of EHD in the crystal. The strip of EHD remains and can be studied over periods of hours as opposed to $40 \mu\text{s}$.

To get the spatial profile of the EHD, the output lens is translated perpendicular to the spectrometer slit, thus translating the image of the EHD luminescence from the crystal across the slit.

To determine the net electrical charge or a limit of the net electrical charge on the EHD, we compare spatial profiles of EHD luminescence taken before and after a potential difference is applied across the ohmic contacts of boron implanted on the crystal. If the peak of the EHD luminescence is seen to translate, the net charge on the EHD can be determined. If the EHD are not seen to move, a limit on the net charge of the EHD may be obtained from the signal-to-noise ratio and the optical resolution.

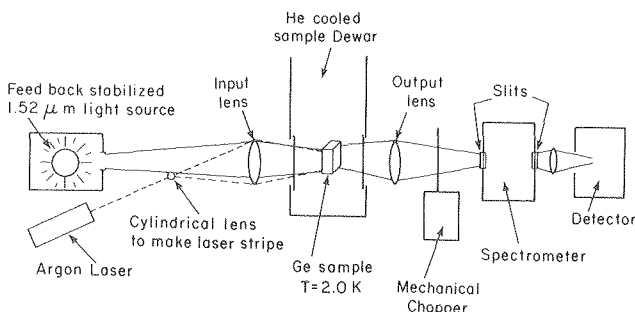


Fig. 1. Experimental apparatus. The output lens can be translated perpendicular to the paper and perpendicular to the spectrometer slit, generating spatial profiles of EHD luminescence.

(XBL 7912-13284)

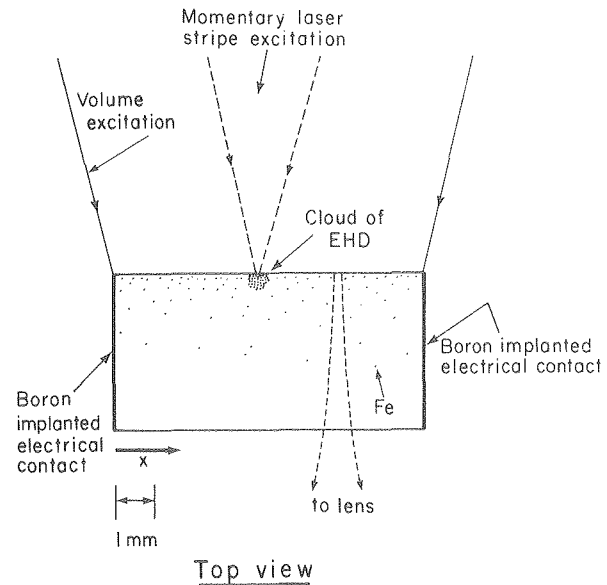


Fig. 2. Excitation and luminescence collection geometry to scale showing spatially-uniform gas of free excitons (FE) and localized packet of electron-hole drops (EHD) (XBL 7912-13285)

Figure 3 shows data taken in this manner. Each trace represents 16 minutes of accumulation in a multichannel analyzer. The top trace is the EHD luminescence profile before applying any fields. The bottom profile was taken while $10 \mu\text{s}$ pulses of 80 V were applied every millisecond between the boron contacts on the crystal. The crystal is an $8 \times 8 \times 4 \text{ mm}^3$ ultrapure Ge crystal with contacts 8 mm apart. The contacts were made by implanting boron into two opposite crystal faces, then annealing the crystal to repair crystal damage caused by the implant process. Finally, indium foil was attached to the implanted surfaces with a eutectic and wires attached to the indium. No motion is seen. This experiment thus sets a limit on the net charge on the EHD.

EHD are believed to be bound on impurities with a binding energy $BE \approx 7 \text{ meV}$. The binding energy is observed to be independent of drop size except for very small drops. This suggests the impurity can be anywhere within the EHD as long as it is further away from the surface than a surface thickness. The data in Fig. 3 indicate that for a force $F = |Z|eE = |Z|(1.6 \times 10^{-15} \text{ Nt})$ the EHD do not become dislodged, so $F = |Z|eE < BE/\Delta x$. This provides a limit on $|Z| < (BE)/eE\Delta x \approx 20$ electrons. We conclude that the charge on a drop is $Ze = (0 \pm 20)e$.

It is necessary to check that the $10 \mu\text{s}$, 80 V pulse is sufficient to move the EHD away from the vicinity of its binding site. The terminal drift velocity of the EHD is $V_d = F\tau_p/M$ where $\tau_p \approx 2 \times 10^{-9} \text{ sec}$ is the carrier-phonon scattering time, M is the inertial mass of the $0.2 \mu\text{m}$ radius drop and $F = ZeE$. Using $m_e = .58 m_0$, $m_h = .35 m_0$, we find $V_d \approx 5 \times 10^4 \text{ cm/sec}$ per net electron charge on the EHD. For a $10 \mu\text{s}$ pulse the EHD would move a distance $V_d(10 \mu\text{s}) = 5 \text{ mm}$ per net electron charge on the drop. Since the resolution of Fig. 3 is $\sim 50 \mu\text{m}$ we conclude that the observed limit on the

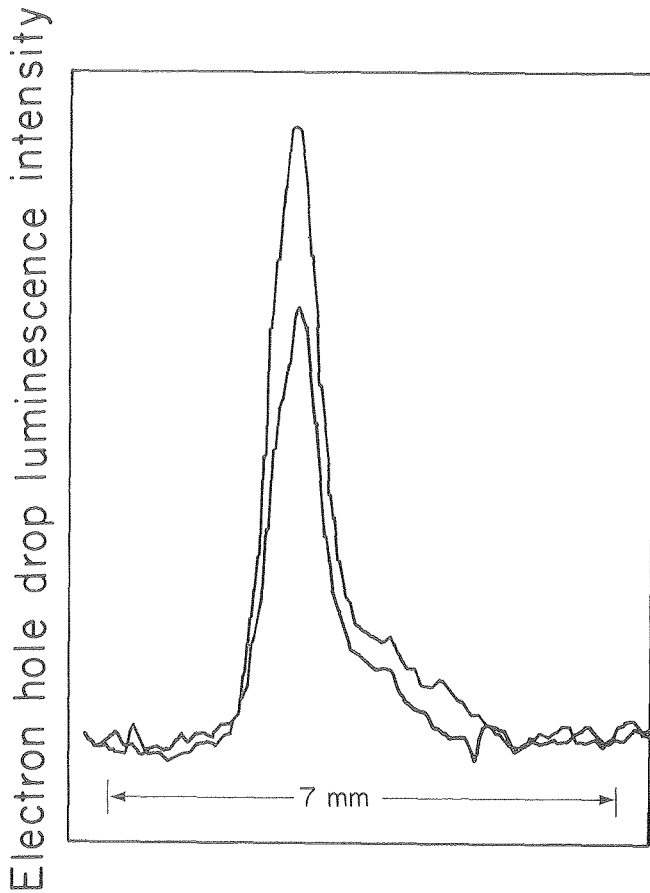


Fig. 3. Spatial scans of EHD luminescence intensity before (above) and after (below) applying 10 μ s pulses of 80 volts across the 8 mm wide crystal. The peak is not observed to move, indicating no net charge on the drops.

(XBL 7912-13283)

charge is accurate. It must be emphasized that this is the net charge on a drop and its surrounding free carriers. We expect that if the drop were charged it would attract a compensating charge cloud. This experiment will be improved and a lower limit set on the drop charge. Our conclusions are significantly different from those of other workers.

Dr. Eugene Haller kindly provided the Ge crystal with the ohmic contacts.

* * *

[†]Permanent address: Division of Applied Science, Harvard University, Cambridge, MA 02138.

1. T. M. Rice, Phys. Rev. B **9**, 1540 (1974); R. K. Kalia and P. Vashishta, Phys. Rev. **B17**, 2655 (1978).
2. Ya. E. Pokrovskii and K. I. Svistunova, JETP Lett. **19**, 56 (1974); T. Ugumori, K. Morigaki and C. Nagashina, J. Phys. Soc. of Japan **46**, 536 (1979).
3. R. W. Westervelt, J. C. Cubertson, and B. S. Black, Phys. Rev. Lett. **42**, 267 (1979).
4. P. Vashishta, R. K. Kalia and K. S. Singwi, Solid State Comm. **19**, 935 (1976).

3. THE METAL-INSULATOR TRANSITION IN UNIFORMLY STRAINED Ge[†]

Ivar Balslev,[†] John E. Furneaux and Carson D. Jeffries

Luminescence studies of the FE-EHL phase diagram in Ge are believed to show an additional structure displaying some aspects of a Mott type metal-insulator (M-I) transition.¹ However, pre-existing data have not been very convincing. The latest theoretical model for the system of excitons of density n_x and dissociated pairs of density n_f leads to an ionization catastrophe, typical of a M-I transition, as was first shown by Balslev.² This is illustrated in Fig. 1 where the ionization fraction $\eta = n_f/n_x$ is plotted vs. the total density of pairs $n_t = n_f + n_x$ for various temperatures. It can be seen that at low temperatures there is a bistability region where there are three solutions: two stable solutions and one unstable solution. At higher temperatures there is only one solution and the bistability region is gone. The absolute limits of this bistability region are defined by the singularities in dn/dn_t .³

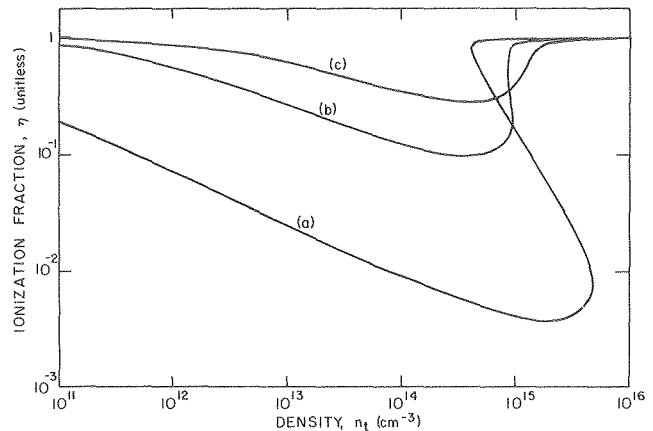


Fig. 1. Predicted ionization fraction η vs. total density n_t for Ge[1,1], curve: a) $T = 3$ K; b) $T = 5$ K; c) $T = 7$ K.

(XBL 796-6479)

In order to gain more information about this bistability region and M-I transitions in general we decided to study highly excited, uniformly stressed Ge. (This is explained more completely in the full version of this report.) By applying 16 kgf/mm² to our sample we were able to change the electronic configuration from Ge[4,2] to Ge[1,1], where the lower EHL critical temperature $T_c = 3.5$ K and critical density $n_c \approx 2 \times 10^{16}$ cm⁻³ allows easier experimental access to temperatures above the EHL critical point, where one can hope to observe only a M-I transition, since the EHL phase will not be coexistent.

Data obtained for 0.07 W of laser light absorbed in the sample are shown in Fig. 2. Dots correspond to data points, and the smooth curves are calculated free exciton luminescence lines, which approximately fit the data. At 0.07 W absorbed the fitted temperature of the FE gas was

found to be essentially the same as the He bath temperature. At 2.19 K the EHL line at 700 meV is also observed (Fig. 2a); however, at 3.15 K (Fig. 2b) this line is very weak, and at 4.2 K (Fig. 2c) is nonexistent. This is the expected behavior for the EHL phase with a critical temperature of 3.5 K. This figure shows that in stressed Ge[1,1] it is possible to pump the sample without producing the usual EHL. This situation thus allows for a search for the M-I transition.

This is done in Fig. 3 where data for higher absorbed power, 0.28 W, are shown with dots and smooth curves as for Fig. 2. At this absorbed power considerable heating, 2 to 3 K, is evident in the exciton gas. Further, a new broad line, which we interpret as being due to the high density phase of a M-I transition, is evident at 701 meV. This line shows very little temperature dependence.

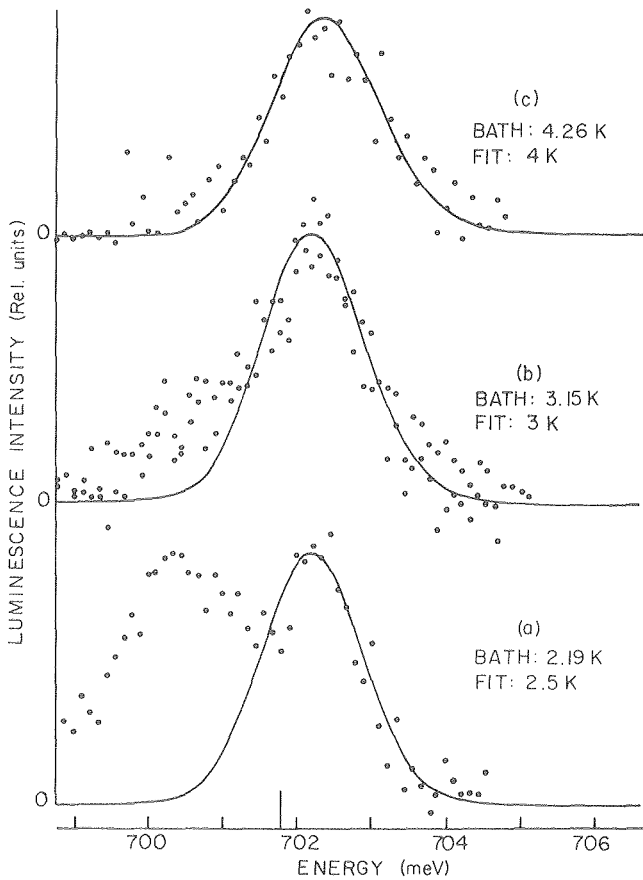


Fig. 2. Luminescence spectra with $P_a = 0.07$ W. The dots represent data points and the smooth curves are exciton lines which approximately fit the data with a slit width of 0.4 meV and 0.6 meV of Gaussian broadening. The large tick at 701.8 meV shows the low energy edge of all the exciton lines. a) He bath at 2.19 K; exciton lineshape at 2.5 K. Notice characteristic EHL luminescence at 700 meV. b) He bath at 3.15 K; exciton lineshape at 3 K. c) He bath at 4.25 K; exciton lineshape at 4 K. (XBL 796-6474)

We interpret the luminescence line at 701 meV shown in Fig. 3 as being due to free pairs by a process of elimination. The line cannot be due to EHL since it has the wrong temperature dependence and exists above the critical temperature for the EHL. It is very unlikely that the line is due to larger complexes such as biexcitons. Biexcitons have the largest binding energy of these complexes, but this energy is still approximately equal to the temperature, and they should therefore be completely disassociated.

Because the line at 701 meV is spectrally resolved and appears only at high pump powers, we interpret the line as due to the high density phase of a M-I transition. Since the strain is not homogeneous in this experiment it is not possible to fit this line. However, the shape does give good qualitative evidence that our interpretation is correct. The line is broad with a pronounced low energy tail. This shape can be understood qualitatively by assuming a nonuniform plasma: the emission from dense regions is broad and at low energies (large band renormalization),

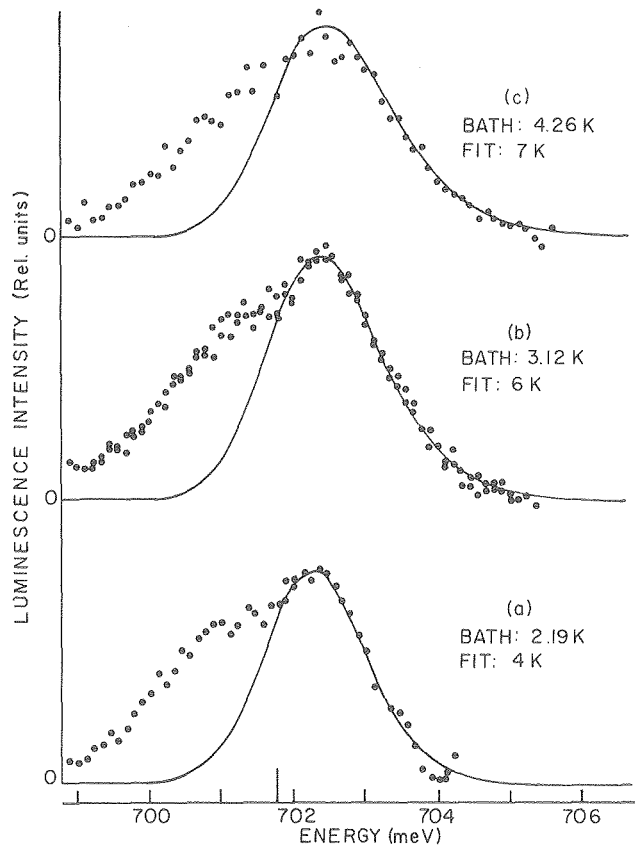


Fig. 3. Luminescence spectra with $P_a = 0.28$ W. All symbols and parameters as in Fig. 2 except temperature. a) He bath at 2.1 K; exciton lineshape at 4 K. b) He bath at 3.15 K; exciton lineshape at 6 K. c) He bath at 4.25 K; exciton lineshape at 7 K. Notice the temperature independent resolved peak at 701 meV which is interpreted as being due to the high-density metallic phase of a M-I transition. (XBL 796-6475)

while emission from less dense regions is narrower and at higher energies. To conclude, it is believed that these data present clear evidence for the M-I transition in Ge[1,1] for the first time.

* * *

†Brief version of LBL-8852.

‡Permanent address: Odense University, DK-5230 Odense M, Denmark.

1. H. Ehrenreich, F. Seitz and D. Turnbull, eds., *Solid State Physics*, Vol 32 (Academic press, New York, 1977).
2. I. Balslev, *Solid State Commun.* 27, 545 (1978).
3. J. E. Furneaux, *Experimental Studies of Excited Metallic Phases in Stressed Germanium* (Ph.D. thesis), September 1979 (LBL-9334).

4. BUILDUP OF THE STRAIN-CONFINED ELECTRON-HOLE LIQUID†

John E. Furneaux and Carson D. Jeffries

Once it has been established that the strain-confined electron-hole liquid (SCEHL) existed,¹ it was decided to investigate its formation process. The most appropriate experimental technique for initial investigations was Alfvén wave resonance studies. This technique can very effectively probe quite small volumes of SCEHL and has good time resolution ($\sim 0.1 \mu\text{s}$) due to the inherent speed of the microwave receiver. The experimental apparatus is pictured in Fig. 1. The laser was mounted on a precision x-y translation stage so the dependence of the buildup on laser pump position could be determined. A quartz lens was mounted on the tail of the Dewar, and the laser was positioned under the Dewar such that the $0.4 \text{ mm} \times 0.4 \text{ mm}$ laser surface was focused onto the germanium sample surface with a magnification of 1. This calibrated the movement of the laser with the x-y translator to correspond to the movement of the pumping spot on the sample.

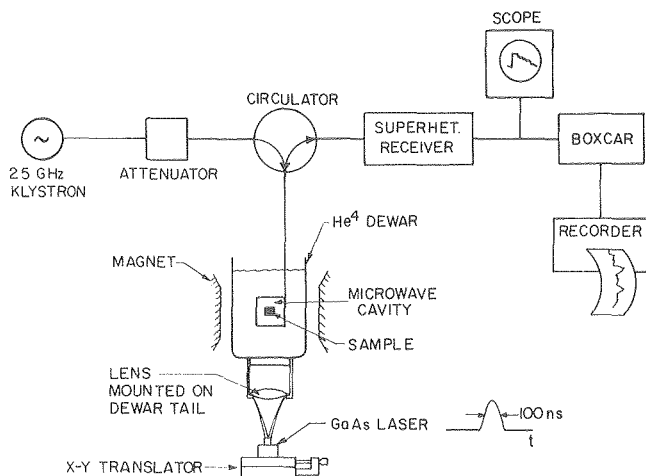


Fig. 1. Schematic of experimental apparatus used to measure buildup and decay of EHL with Alfvén wave absorption. (XBL 796-6454)

The drop buildup and decay are measured by monitoring the movement of the principal Alfvén resonance peak, H_C in magnetic field. We find that H_C increases rapidly (0.5 μsec) to a maximum field H_{max} , corresponding to a maximum drop size, and then decays exponentially with a characteristic 1400 μsec time constant. If we assign H_C as the lowest magnetic dipole mode of a sphere, the relation between radius and field is $R(\mu\text{m}) = 14[H_C(\text{kOe}) - 0.3]^2$ for a liquid density of $0.5 \times 10^{17} \text{ cm}^{-3}$. For this mode assignment the maximum resonant field of 13 kOe corresponds to a drop radius of 178 μm . This is approximately the same size obtained from assuming 100% pumping efficiency into the strain well. As would be expected for this mode assignment, $H_{\text{max}} \propto \epsilon_a^{1/3}$ where ϵ_a is the absorbed laser energy.

Figure 2 shows contours of constant pumping efficiency for two different laser powers. The t_d for buildup was then recorded at all possible positions. It can be seen that even for a constant final drop size and laser power, the buildup time is basically the time for carriers initially produced by the laser to move into the strain well, and not a time to cool down, which would be independent of position.

Some further information can be gained by studying contours. In this case the effect of the direction of the magnetic field, if any, on the buildup is found. This is illustrated in Fig. 3, where contours of constant buildup time to a given drop size with a constant energy are plotted for two field orientations, \vec{H} parallel to the stress and \vec{H} perpendicular to the stress. It can be seen that there are very small differences between the contours indicating that the field has very little if any effect on the buildup, even though the buildup time of 30 μs is quite long. This means that magnetohydrodynamic damping does not seem to be particularly important in this case.

The effect of carrier mass anisotropy on the motion of drops⁵ in the strain well is shown in Fig. 4 from Markiewicz. This shows how the equal energy contours of Fig. 4a are distorted. Carriers and small drops will flow perpendicular to the contours illustrated in Fig. 4b rather than perpendicular to the contours in Fig. 4a. This happens because although the force, \vec{F} , is perpendicular to the contours in Fig. 4b, the acceleration is $\vec{a} = \vec{m}^{-1} \cdot \vec{F}$ where $\vec{m} = m_e + m_{\parallel} \hat{I}$ and $m_{\parallel} \approx 0.3m_0$. The electron effective mass-tensor m_e , is quite anisotropic for stressed Ge; $m_{\parallel} = 1.58m_0$ (along the $\langle 111 \rangle$ axis), $m_{\perp} = 0.082m_0$. This leads to the distortions in the acceleration potential, E^* , pictured in Fig. 4b. E^* is defined so that $m_{\parallel} \vec{a} = -\nabla E^*$. There is a strong tendency for drops to pile up along the $\langle 111 \rangle$ axis and flow into the strain well predominantly along that axis because of the large longitudinal mass. This can be seen experimentally in Fig. 5. It is obvious especially from Figs. 5a and 5c that drops are channeled as expected from the contours in Fig. 4b.

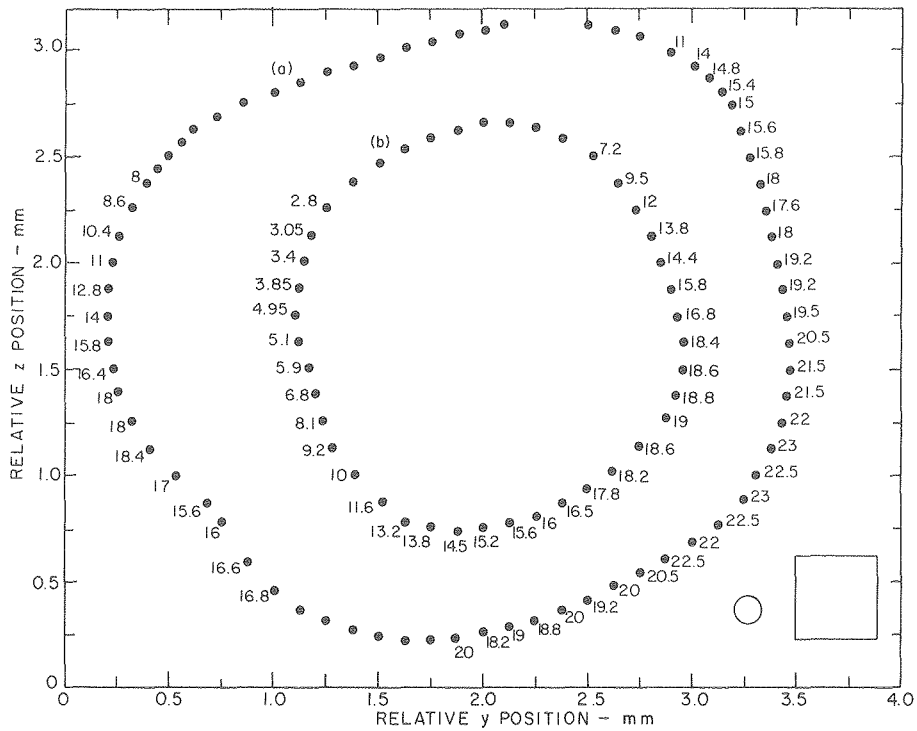


Fig. 2. Contours of constant pumping efficiency vs. position on the crystal. a) Absorbed energy is 7.2 ergs per pulse; b) absorbed energy is 1.6 ergs per pulse. Numbers next to the points indicate t_d in build-up. Circle and square indicate approximate drop size and laser spot size, respectively. (XBL 796-6465)

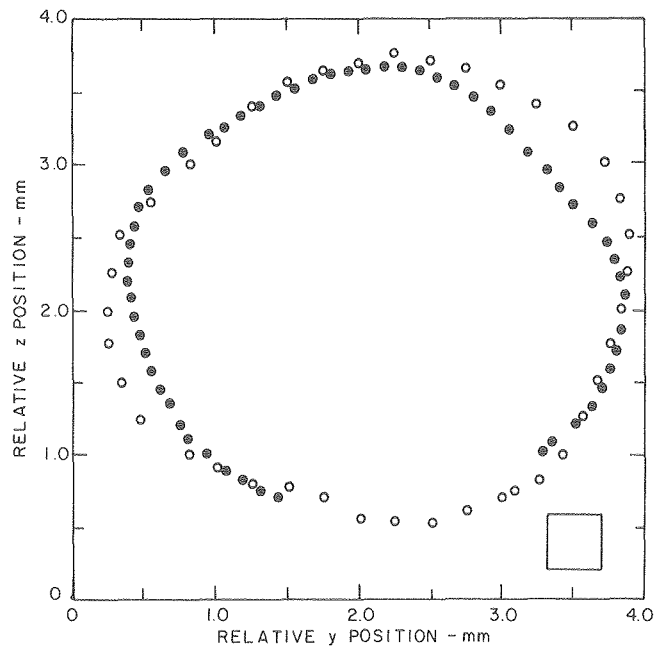


Fig. 3. Contours of constant buildup time as a function of magnetic field direction: Dots $H_{\parallel z}$, open circles $H_{\parallel y}$. Box in corner shows approximate laser spot size. $H_c = 6$ kOe; $t_d = 30$ μ s in build-up; absorbed energy is 7.2 ergs per pulse; $\eta = 24.3$ GHz; $T = 1.35$ K. Very little difference is seen for the different field orientations. (XBL 796-6464)

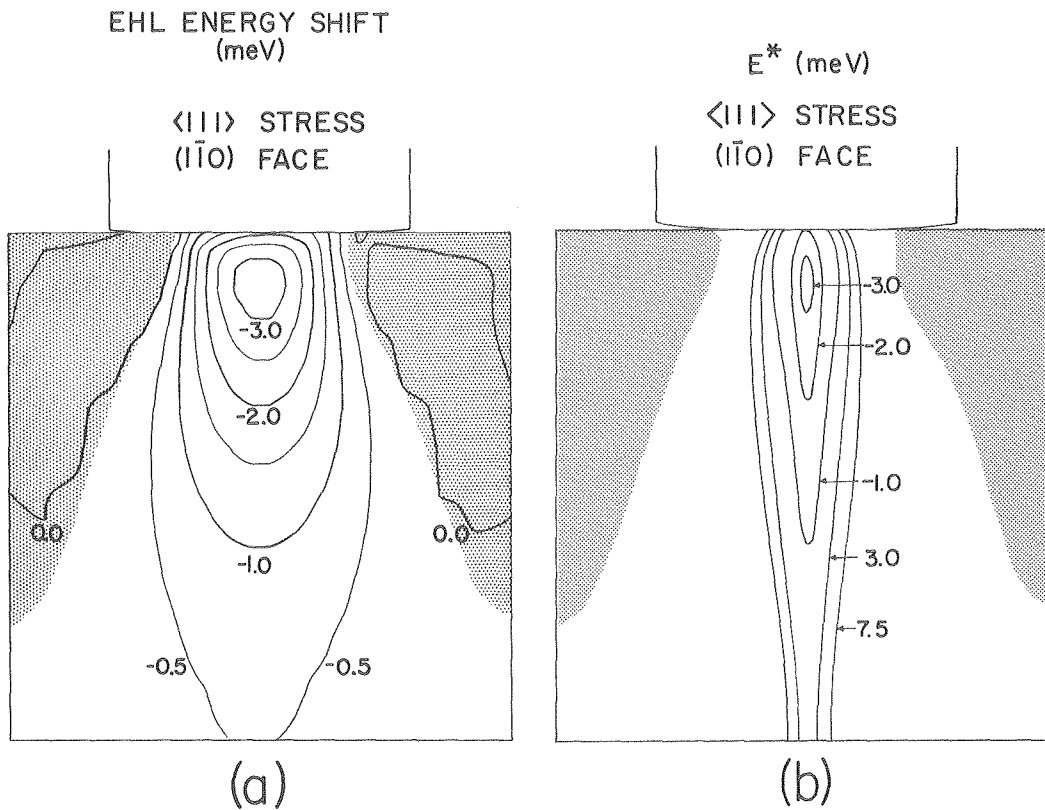


Fig. 4. (a) Calculated electron-hole liquid pair energy in nonuniformly strained Ge. Stress along $\langle 111 \rangle$ axis, viewed through $(1\bar{1}0)$ crystal face. In the unshaded region all electrons are in a single conduction band only. (b) Channeling of carrier flow. Due to effective mass anisotropy in the strain well of Fig. 5(a), the carriers and small drops would actually flow perpendicular to the contour lines drawn here. E^* is defined so that $m\hbar\vec{a} = -\nabla E$, where \vec{a} is the pair acceleration. (XBL 779-4830A)

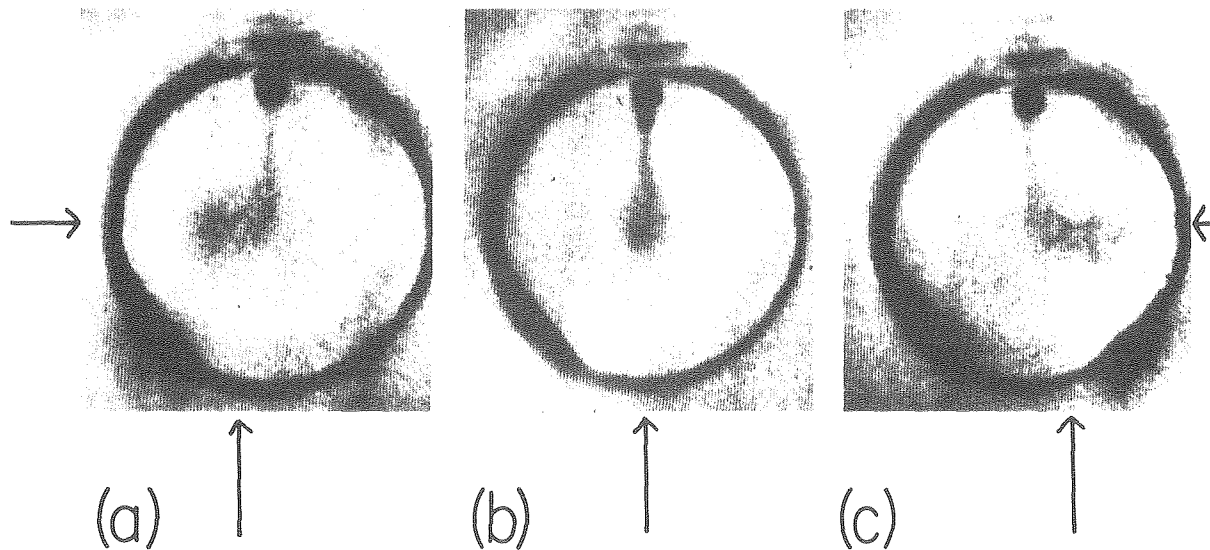


Fig. 5. Channeling of the carrier flow. The crystal is stressed along a $\langle 110 \rangle$ direction and viewed through a (001) face. For enhanced contrast, a negative photographic image is presented so that the glowing drop appears black. The three views correspond to three positions of the laser pumping spot on the sample surface. Arrows show the approximate position of the focused laser spot on the opposite face of the crystal. Carriers appear as a dark cloud of small drops formed about the laser spot. Leading away from the cloud is a narrow channel of drops flowing into the SCEHL near the top of the crystal. (XBB 770-9519)

Although quantitative information is very difficult to obtain about the buildup process, it is quite well understood qualitatively. Photons from the pumping light are absorbed within about a micron forming a dense fairly hot cloud of electrons and holes. This cools quite quickly ($\sim 10^{-9}$ sec) and forms small EHD. These EHD then move under the combined force of the strain gradient and phonon wind into the strain well at near the velocity of sound ($\sim 10^5$ cm/sec), and are strongly channeled into $\langle 111 \rangle$ directions due to the mass anisotropy. Finally, there seems to be very little effect of the magnetic field direction on the buildup as long as it is perpendicular to the direction of the incident light.

* * *

[†]Brief version of LBL-9334.

1. R. S. Markiewicz, J. P. Wolfe and C. D. Jeffries, Phys. Rev. B 15, 1988 (1977), (LBL-6225).
2. J. E. Furneaux, J. P. Wolfe and C. D. Jeffries, Solid State Commun. 20, 217 (1976); R. S. Markiewicz, Phys. Rev. B 18, 4260 (1978), (LBL-6942).
3. R. S. Markiewicz, Phys. Rev. B 17, 4788 (1978), (LBL-6694).

5. PROPERTIES OF THE ELECTRON-HOLE LIQUID IN Ge AND Si AS A FUNCTION OF DENSITY[†]

Susan M. Kelso[‡] and Carson D. Jeffries

A detailed study of the variation in electron-hole pair density in the electron-hole liquid (EHL) in stressed Ge and Si has been concluded. First, the variation of the density and other properties of the EHL was calculated theoretically as a function of uniaxial stress in both Ge and Si. Then the variation of the density with position was studied experimentally in the strain-confined electron-hole liquid (SCEHL) in Ge and compared with theory.

The calculation represents the first attempt to understand theoretically how EHL properties vary between their zero- and infinite-stress values, both at zero and at finite temperature, as continuous functions of stress, for $\langle 111 \rangle$ stress in Ge and $\langle 100 \rangle$ stress in Si. These properties include the ground state ($T=0$) equilibrium density, the ground state pair energy, the electron and hole Fermi energies, the luminescence linewidth, the electron-hole drop charge, and the liquid compressibility. The possibility of a phase transition would occur as the stress is varied, as the upper electron valleys become depopulated. The importance of including the nonparabolic valence band density of states in the fitting of the luminescence line-shape was found to be crucial. Theoretical results for the systematic low-temperature variation of the liquid density, Fermi energy, and chemical potential were calculated. The high-temperature properties were also calculated, including the critical temperature and density. These theoretical results were

found to be in reasonably good agreement with the available experimental data. The study of the EHL under uniform stress is a necessary prelude to the understanding of the EHL under nonuniform stress, i.e., confined in a strain well. All the properties of the EHL undergo a dramatic change as the liquid becomes confined in a strain well when the force reaches the critical force F_c at which the degeneracy of the 4 electrons is removed. Figure 1 is a representative display of the experimental results for a pure Ge crystal. At the critical force $F_c \approx 3$ kgf (corresponding to a stress ≈ 3 kgf/mm²) the small droplets coalesce into a sizably large pool of EHL with remarkably different properties.

The detailed properties of the strain-confined EHL are determined from further measurements of the recombination luminescence with spatial, time, and spectral resolution, as a function of excitation level, magnetic field, temperature, and stress. A single drop of EHL forms in the strain well, with radius as large as $R \approx 0.7$ mm and volume greater than 1 mm³. At high excitation levels the luminescence linewidth is found to increase and the recombination lifetime to decrease, indicating that the liquid becomes compressed. For smaller drop sizes ($R \leq 150$ μ m), however, the equilibrium properties of the liquid may be studied. From a fit of the luminescence lineshape the density is found to be $n_0 = 0.50 \pm 0.05 \times 10^{17}$ cm⁻³ for typical moderate stresses, and the lifetime is found from pulsed experiments to be $\tau \approx 500$ μ sec. The enhanced lifetime is understood qualitatively as a result of the reduced density (compared to the values for unstressed Ge), while the reduction in density is due to the stress. The size, shape, and kinetics of drops confined in strain wells are quite different from size, shape, and kinetics of clouds of small EHD in unstressed Ge. This is verified experimentally and theoretically.

The compression of the SCEHL at higher excitation levels was investigated in detail. It was shown theoretically that the density should vary with position, with the magnitude of the variation increasing with drop size. Experimentally, density profiles are measured using luminescence spatial profiles (box scans) and an Abel transform (see Fig. 2). The density is found to be largest at the center of the drop, decreasing at the drop surface, as predicted theoretically. The density at the center of the drop is found to increase with drop size from the equilibrium value by approximately a factor of three, in agreement with theory. The liquid chemical potential is measured as a function of density by varying the drop size, providing a very stringent test of the many-body theories used to describe the EHL. The compressibility of the SCEHL is measured to be $K_T = 0.058 \pm 0.024$ cm²/dyne. Finally, the liquid lifetime was studied as a function of density. The lifetime changes more slowly than the density, indicating that a density-independent decay mechanism is significant. In addition, the Auger recombination coefficient is significantly reduced from its value in unstressed Ge.

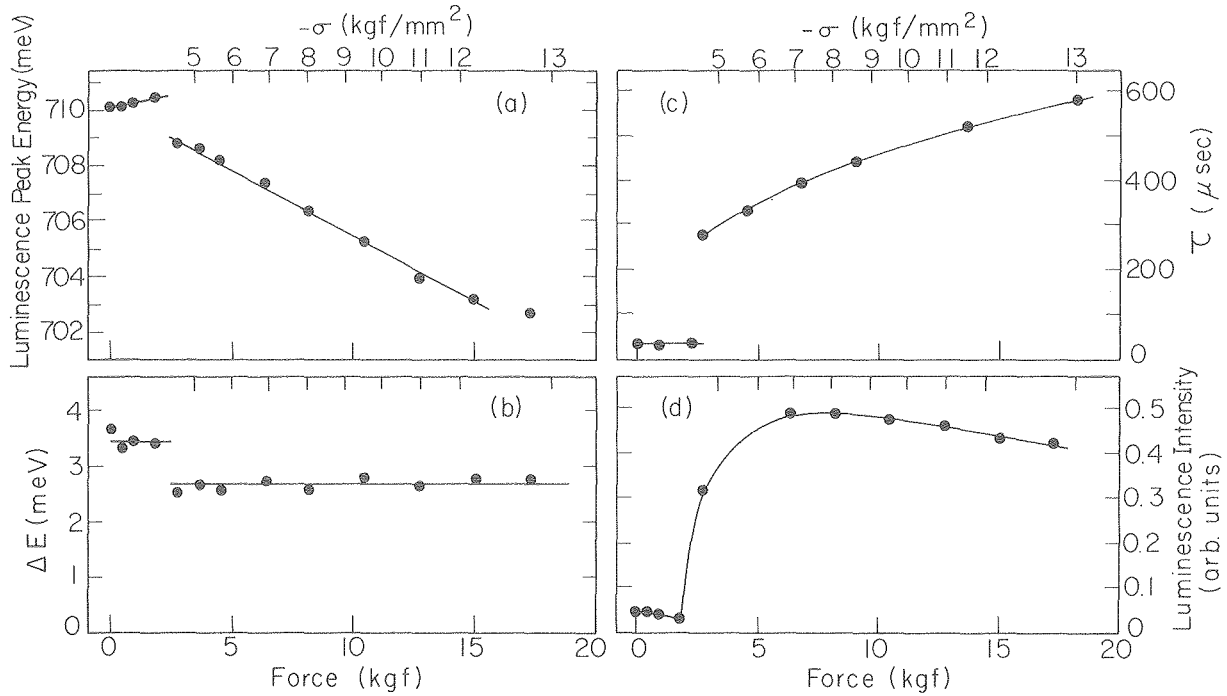


Fig. 1. (a) Luminescence peak energy of EHL vs. applied force F (kgf/mm²) for Ge sample stressed along $\langle 111 \rangle$ in a potential well. The liquid collects in the well above a threshold force F_C . (b) EHL linewidth ΔE vs. F ; since $\Delta E \propto E_{\text{Fermi}} \propto n^{2/3}$, this is a measure of the liquid density n and the change when the Ge configuration goes from Ge(4,2) to Ge(2,1). (c) EHL lifetime τ vs. F ; again, there is a sudden increase at F_C when the liquid become confined. (d) Total EHL luminescence intensity vs. F . Pump power $P_{\text{abs}} = 3.2$ mW, $T = 1.8$ K. (XBL 7711-6460)

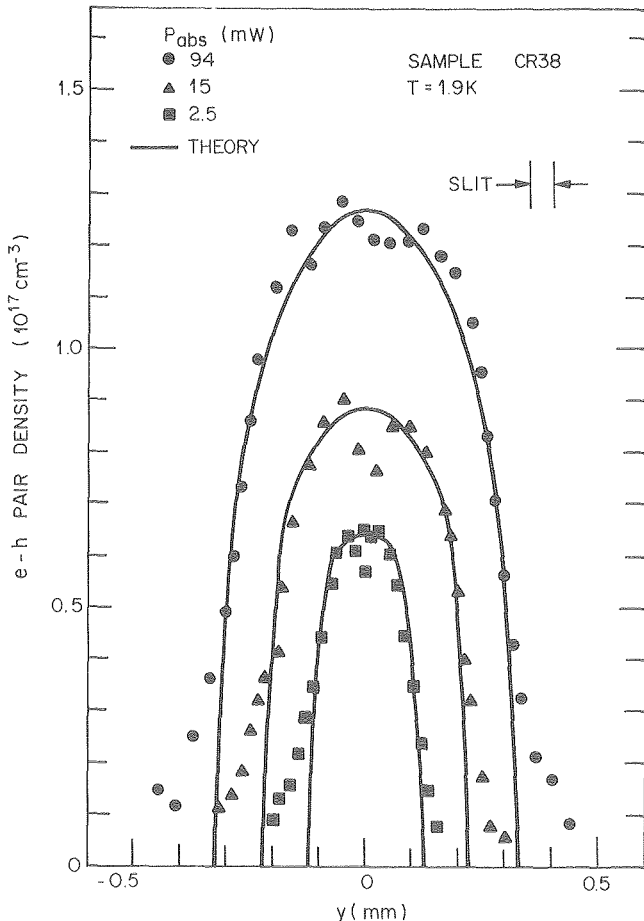


Fig. 2. Electron-hole pair density profiles of a strain-confined electron-hole drop for a series of excitation levels P_{abs} . The solid curves give the predicted profiles. (XBL 795-9618)

* * *

†Brief version of LBL-8786.

‡Permanent address: Bell Laboratories, Murry Hill, NJ 07974.

RESEARCH PLANS FOR CALENDAR YEAR 1980

Development of ultrasensitive IR detector. The proposed new spectrometer with an ultrasensitive detector ($\text{NEP} \approx 10^{-10} \text{ W/Hz}$) at 1.8 microns is nearing completion. This is 2 to 3 orders of magnitude more sensitive than any previous detector used in electron-hole drop research in Ge and will make possible a number of new experiments: direct search for the luminescence of biexcitons and multiexciton complexes in Ge; observation of the nucleation of individual small EHD in unstressed Ge and study of this by spatial imaging; study of the phase diagram near the critical temperature to see whether the droplets form a periodic array; using the new apparatus for general solid state spectroscopy in this range to see whether new excited states, complexes, condensations, and M-I transitions become observable.

Study of excitons and drops trapped on donors in Ge and Si by microwave paramagnetic resonances.

Experiments are underway using an ultrahigh-sensitivity microwave spectrometer in which the Ge crystal itself forms the cavity with a quality factor $Q \geq 10^5$. This is being used to observe the g-factor and hyperfine structure of shallow donors (As, P, Sb) in Ge and Si, as the crystal is pumped with light and excitons, drops, and other e-h species become trapped on the donor atoms. This is expected to produce an observable change in the wavefunction of the donor with consequent change in paramagnetic resonance structure. This is a direct and sensitive way to observe trapping and, via luminescence, to correlate it with the excited species. Preliminary results include new lines observed in the donor band in Ge ($g = 1.6$), very sensitive to light; and new lines observed at very low fields ($4\times$ lower than the light holes). They seem to be genuinely new phenomena--and will be resolved.

Study of long-lived free excitons in strain-confined EHL in Ge. We have discovered that the lifetime of FE can be as long as 300 to 400 μ sec in or around SCEHL. This interesting anomaly will be studied in detail using both spatial and temporal resolution. The whole problem of the exciton lifetime in Ge is very poorly understood as was discussed in article 1. This additional study will contribute to its understanding.

1979 PUBLICATIONS AND REPORTS

Refereed Journals

1. R. M. Westervelt, J. L. Staehli and E. E. Haller, "Nucleation Phenomena in Electron-Hole Drop Formation in Ge and Si. Part III: Experimental Results," Phys. Stat. Sol. (b) 90, 5571 (1979), LBL-7660.
2. R. M. Westervelt, J. C. Culbertson and B. S. Black, "Discovery of the Immobility of Electron-Hole Drops in Ge at Low Excitation," Phys. Rev. Lett. 42, 267 (1979), LBL-8049.
3. I. Balslev and J. E. Furneaux, "The Metal-Insulator Transition in Stressed Germanium," Solid State Commun. 32, 609 (1979), LBL-8852.

Other Publications

1. S. M. Kelso, "Properties of the Strain-Confined Electron-Hole Liquid in Ge as a Function of Density," Proceedings of XIV Int. Conf. Phys. Semiconductors, 1978, Inst. Phys. Conf. Ser. No. 43 (1979), ch. 11, pp. 363-366, LBL-7616.
2. R. M. Westervelt, J. C. Culbertson and B. S. Black, "Motion of Electron-Hole Drops in Ge," Proceedings of XIV Int. Conf. Physics of Semiconductors, 1978, Inst. Phys. Conf. Ser. No. 43 (1979), ch. 11, pp. 359-362, LBL-7617.
3. S. M. Kelso, "Calculation of Properties of the Electron-Hole Liquid in Uniaxially Stressed Ge and Si," Bull. Am. Phys. Soc. 24, 343 (1979), LBL-8590 Abstract.
4. S. M. Kelso and E. J. Pakulis, "Density Dependence of the Lifetime of the Strain-Confined Electron-Hole Liquid in Ge," Bull. Am. Phys. Soc. 24, 344 (1979), LBL-8591 Abstract.
5. J. C. Culbertson and R. M. Westervelt, "Free Exciton Lifetime and Diffusion in Ge," Bull. Am. Phys. Soc. 24, 342 (1979), LBL-8592 Abstract.
6. J. E. Furneaux and I. Balslev, "The Metal-Insulator Transition in Stressed Germanium," Bull. Am. Phys. Soc. 24, 280 (1979), LBL-8597 Abstract.

LBL Reports

1. Susan Mary Kelso, "Density Variation in the Electron-Hole Liquid in Stressed Germanium and Silicon" (Ph.D. thesis), LBL-8786, August 1979.
2. John Elson Furneaux, "Experimental Studies of Excited Metallic Phases in Stressed Germanium" (Ph.D. thesis), LBL-9334, September 1979.

Invited Talks

1. R. M. Westervelt, "Nucleation and Motion of Electron-Hole Drops in Germanium," Solid State Seminar, Bell Laboratories, Murry Hill, New Jersey, February 1979.

d. Superconductivity, Superconducting Devices, and 1/f Noise*

John Clarke, Investigator

1. MAGNETOTELLURICS AT A GEOTHERMAL SITE[†]

T. D. Gamble, W. M. Goubau, R. F. Miracky, and J. Clarke

The ultimate goal of magnetotellurics is to obtain an accurate picture of the electrical resistivity of the ground as a function of position. Such a representation may yield extremely valuable information about the location and magnitude of geothermal sources, oil deposits, and other anomalies. There are two distinct steps to this goal. In the first, one measures the horizontal components of the magnetic field fluctuations at the earth's surface, $\vec{H}(\omega)$, due to ionospheric disturbances, and, simultaneously, the horizontal components of the induced electric field, $\vec{E}(\omega)$. One can then estimate the impedance tensor $\underline{Z}(\omega)$, defined by the relation $\vec{E}(\omega) = \underline{Z}(\omega) \vec{H}(\omega)$. Our present techniques enable us to measure $\underline{Z}(\omega)$ to a typical accuracy of 1% or better. The second step in the procedure is to calculate the resistivity as a function of position from $\underline{Z}(\omega)$. In general, this is a formidable problem. However, where the ground is one-dimensional (layered) or two-dimensional (has a direction of translational invariance, known as the strike), considerable simplifications are possible, and one can often obtain quantitative results. In this article, we present results obtained at a geothermal site at Cerro Prieto, near Mexicali, Mexico, where a relatively simple modeling approach has produced rather intriguing results.

We have made two surveys in the vicinity of the site, one in 1978 and one in 1979. The magnetic field fluctuations were measured with a 3-axis SQUID magnetometer, and the two components of the electric field fluctuations by buried electrodes. A second (remote) 2-axis SQUID magnetometer was used as a reference to enable us to make accurate determinations of $\underline{Z}(\omega)$.¹ In 1978 the data were collected on tape. In 1979 the data were recorded on tape for frequencies <1 Hz, while for frequencies >1 Hz they were processed by our LSI-11-based in-field computer.² At the end of each data segment the seven channels were Fourier-transformed, the appropriate cross-power spectra were computed, and $\underline{Z}(\omega)$ was printed out.

The configuration of our 17 measurement sites is shown in Fig. 1. We shall confine ourselves to a discussion of the line FF', which is approximately the direction of a geological fault. First, we

calculate the best coordinate orientation by rotating the axes of the impedance tensor to maximize $|Z_{xy}|^2 + |Z_{yx}|^2$. We found that this procedure produced an approximate strike direction close to the direction of the geological fault. The apparent resistivity $\rho_{yx} = 0.2T |Z_{yx}|^2$ [ρ in Ω m, T in sec,

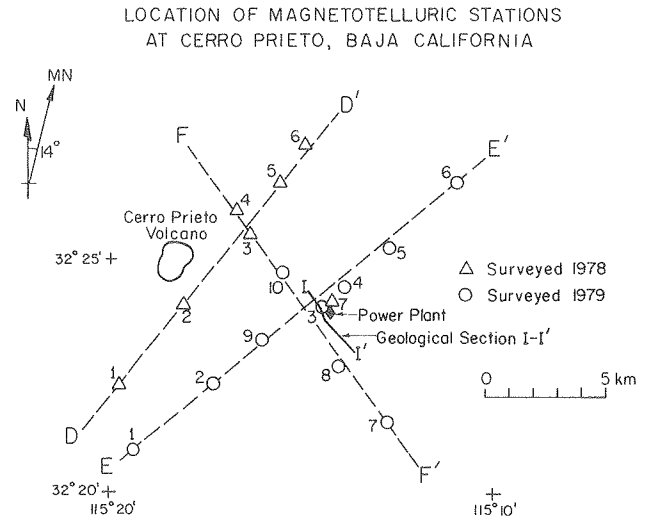


Fig. 1. Location of geothermal sites at Cerro Prieto, Mexico. (XBL 7911-12866)

Z in (mV/km)/ γ] for H along the strike (electric fields and currents perpendicular to strike) at 5 stations along FF' is shown in Fig. 2. Notice the region of relatively high resistivity at periods >2 sec found at the right-hand two stations. Figure 3 shows a rough model of the section FF' based on the data in Fig. 2. The important feature is the high resistivity (10 Ω m) region extending SE from the geothermal plant at a depth of 0.5 to 2 km. Finally, in Fig. 4, we show an expanded view of this high resistivity region together with a schematic of steam production zones for wells along this line, supplied by the Mexican Power Commission. The remarkable agreement between our model of a high resistivity region and the production zones of the wells is very gratifying.

* * *

[†]This work was supported in part by the Office of Geothermal Energy, U. S. Department of Energy.

1. MMRD Annual Report 1978, LBL-8580, pg. 165.
2. MMRD Annual Report 1978, LBL-8580, pg. 167.

* This work was supported by the Division of Materials Sciences, Office of Basic Energy Sciences, U. S. Department of Energy.

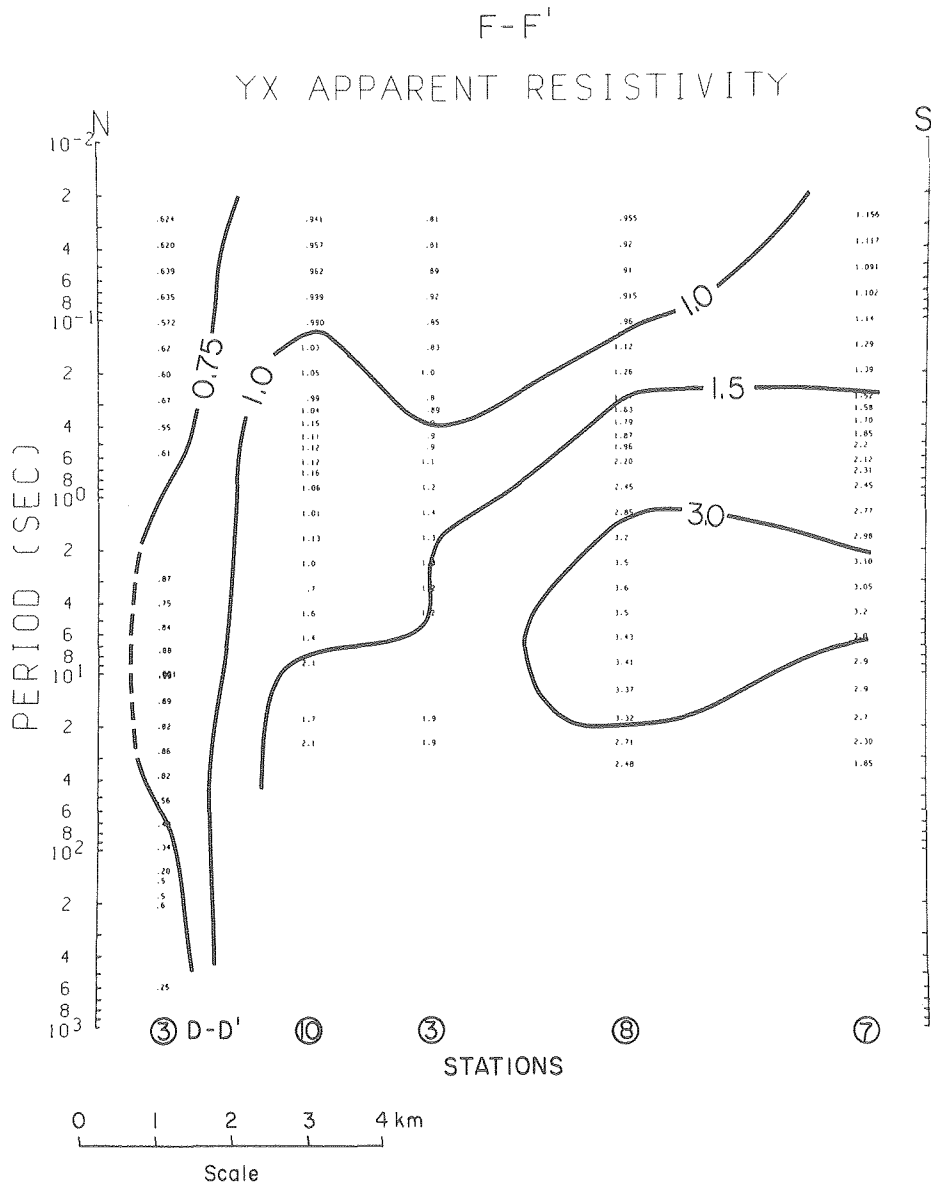


Fig. 2. Apparent resistivity ρ_{yx} along FF' for electric field perpendicular to strike. (XBL 799-11507)

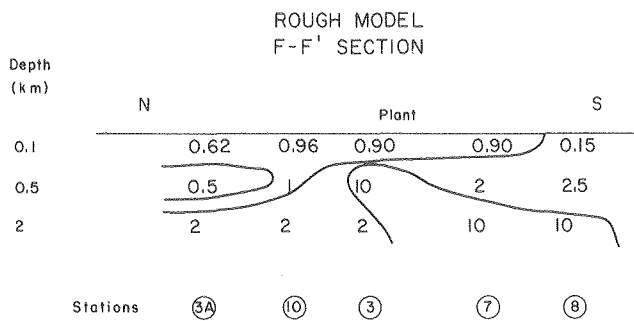


Fig. 3. Rough model of resistivity of ground along FF'. (XBL 799-11551)

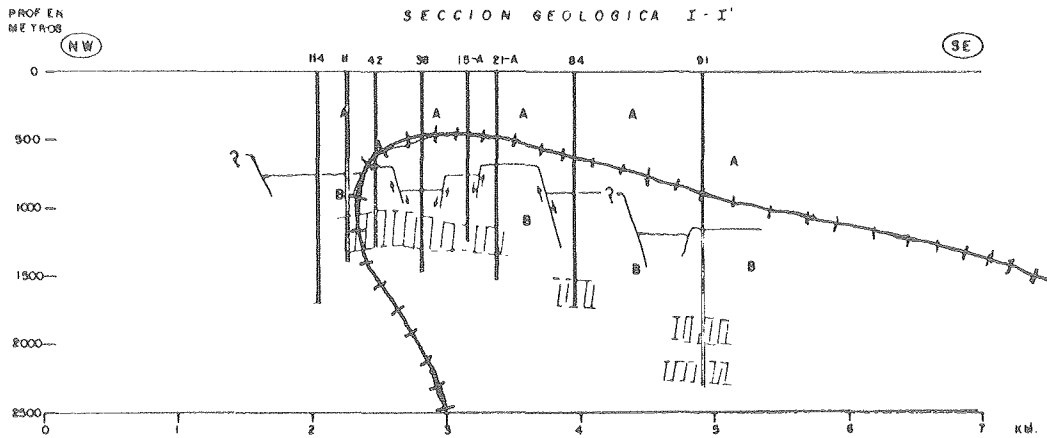


Fig. 4. 10 Ω m contour (hatched line) taken from Fig. 3 together with geothermal wells (vertical lines) and approximate positions of geothermal energy (rectangles). (XBL 7910-12260)

2. ALL Nb LOW NOISE DC SQUID WITH 1 μ m TUNNEL JUNCTIONS^{†‡}

J. Clarke, R. F. Voss,[§] R. B. Laibowitz,[§] and S. I. Raider[§]

Despite the great sensitivity of presently available dc SQUIDS, there are certain applications for which much greater sensitivity is necessary. Two examples are gradiometers, for example, for geophysical applications, and transducers for gravity wave detectors. The Tesche-Clarke model¹ of the dc SQUID with resistivity shunted tunnel junctions of negligible capacitance predicts that the optimum intrinsic energy sensitivity per Hz is given by

$$\epsilon = \frac{S_{\phi}}{2L} \approx 5\pi^{1/2} k_B T (LcA)^{1/2}. \quad (1)$$

Here, S_{ϕ} is the spectral density of the equivalent flux noise in the SQUID, L is the inductance, c is the capacitance per unit area of each junction of area A , and T is the ambient temperature of the SQUID. The model assumes that thermal noise in the resistive shunts is the only noise source, that $2LI_0 = \phi_0$, where I_0 is the critical current per junction and ϕ_0 is the flux quantum, and that $2\pi I_0 R^2 c A = \phi_0$, where R is the shunt resistance per junction. Equation (1) predicts that ϵ is proportional to $A^{1/2}$, a scaling that is in excellent agreement with results from our earlier $\ln H$ devices using $100 \times 100 \mu\text{m}$ and $10 \times 10 \mu\text{m}$ junctions. However, the absolute sensitivity predicted by Eq. (1) is roughly two times better than that achieved experimentally. In this article, we describe a $\ln H$ SQUID with $1 \mu\text{m}^2$ junctions: the sensitivity of this device shows the expected improvement.

The SQUIDS were fabricated on Si wafers using electron beam lithography to produce the masks for the metal films. A typical SQUID was about $300 \mu\text{m}$

square, and contained two $1 \times 1 \mu\text{m}$ Nb-NbOx-Nb tunnel junctions. The device was constructed entirely of Nb except for the resistive shunts, which were of Pd₂Si, formed by annealing a Pd film on the Si substrate. These devices appear to be virtually indestructible: they will resist severe abrasion and survive rapid thermal cycling with no detectable deterioration at all.

The SQUIDS were mounted in a Pb shield and immersed in liquid helium for testing. Figure 1 shows the current-voltage (I-V) characteristics of a typical device at 4.2 K and 1.5 K with an applied flux of $n\phi_0$ and $(n + \frac{1}{2})\phi_0$ in each case (n is an integer). The SQUID inductance was approximately $\ln H$, and the capacitance per junction was about 0.1 pF. Figures 2(a) and (b) and 3(a) and (b) show $V(\phi)$ and $|\partial V/\partial \phi|$ at 4.2 K and 1.5 K respectively, where ϕ is the applied flux. The smooth periodic behavior of $V(\phi)$ and the values of $|\partial V/\partial \phi|$ are in good agreement with theoretical predictions. We made noise measurements by coupling the SQUID to a low noise FET preamplifier via a cooled LC resonant circuit. Figures 2(c) and 3(c) show the measured voltage noise, V_n , at 40 kHz as a function of flux. We see that V_n is periodic in flux, with peaks corresponding to peaks in $|\partial V/\partial \phi|$. These peaks demonstrate the presence of circulating current noise in the SQUID, predicted by the model, that produces an additional voltage noise proportional to $|\partial V/\partial \phi|$. The equivalent flux noise, $\phi_n = V_n/|\partial V/\partial \phi|$, is shown in Figs. 2(d) and 3(d). The minimum values occur at the maxima of $|\partial V/\partial \phi|$, as expected, and are $3.4 \times 10^{-6} \phi_0 \text{ Hz}^{-1/2}$ and $2.3 \times 10^{-6} \phi_0 \text{ Hz}^{-1/2}$ at 4.2 and 1.5 K, respectively. Finally, Figs. 2(e) and 3(e) show $\epsilon = \phi_n^2/2L$ in units of Planck's constant h : the minimum values are 37h ($2.5 \times 10^{-32} \text{ J Hz}^{-1}$) and 17h ($1.1 \times 10^{-32} \text{ J Hz}^{-1}$) at the higher and lower temperatures, respectively. In both cases, the measured sensitivity is about $2\frac{1}{2}$ poorer than that predicted by Eq. (1). The increase in sensitivity with lowered temperature is close to the predicted value. As expected, the SQUIDS were relatively insensitive to changes in

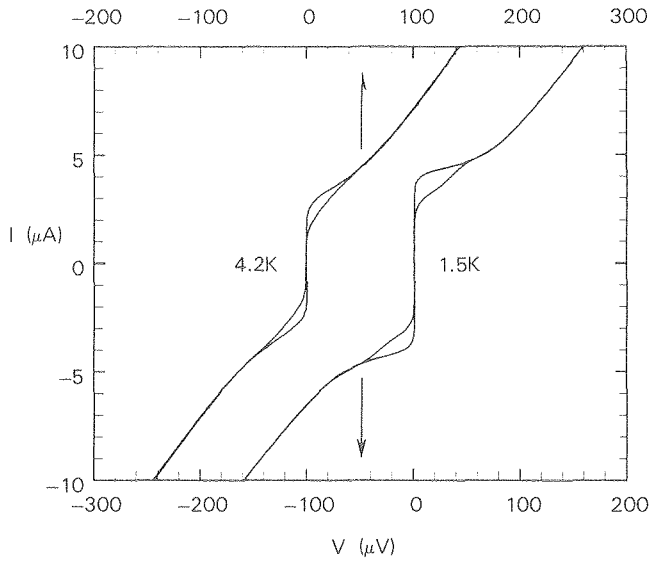


Fig. 1. Flux modulation of I-V characteristic for SQUID at 4.2 and 1.5 K. (XBL 7911-12873)

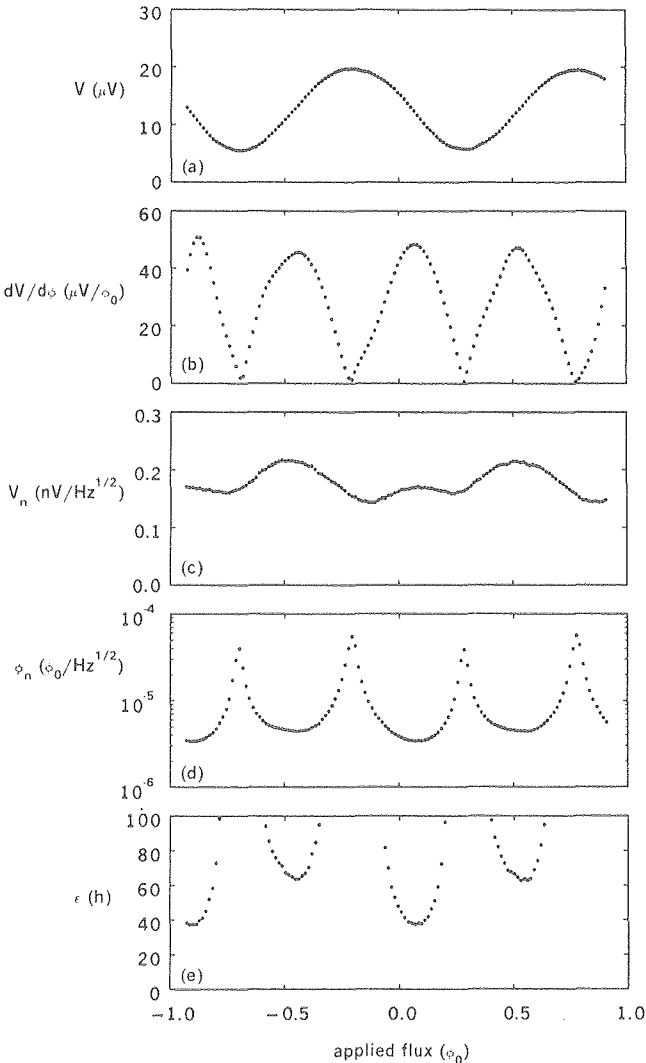


Fig. 2. Characteristics of SQUID shown in Fig. 1 with current bias of 2.8 μA at 4.2 K. (XBL 7911-12872)

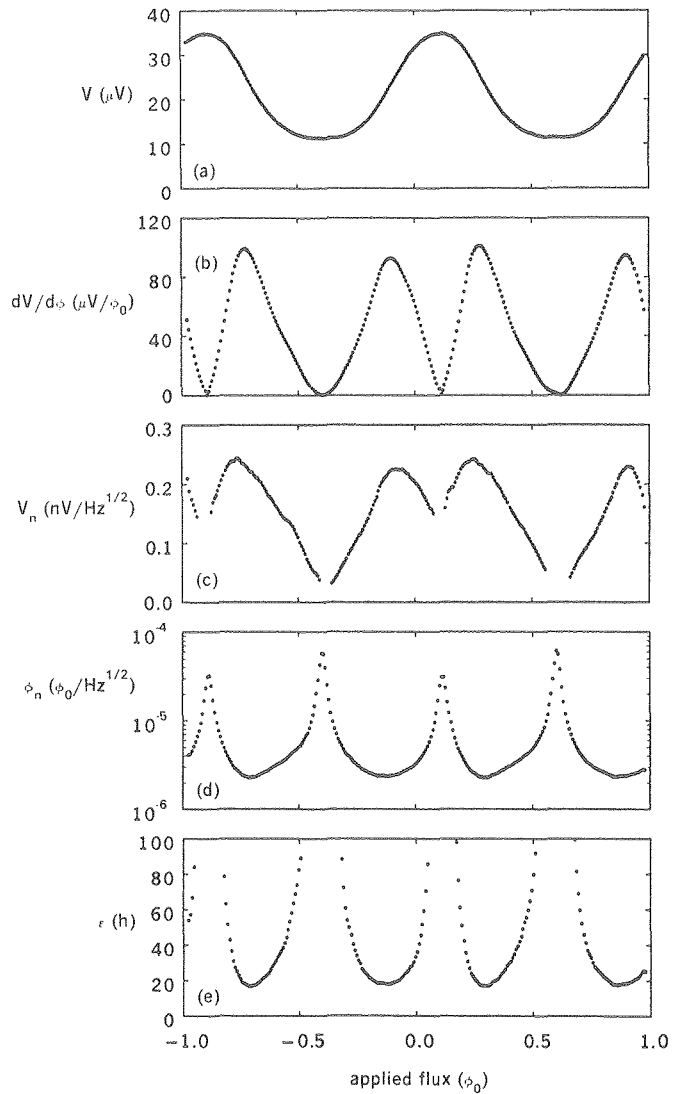


Fig. 3. Characteristics of SQUID shown in Fig. 1 with current bias of 3.7 μA at 1.6 K. (XBL 7911-12871)

current bias, and a change of $\pm 0.2 \mu\text{A}$ in bias current produced a change of less than 2% in the minimum value of ϵ .

We are very encouraged that our relatively simple model predicts the sensitivity of the dc SQUID so well over a wide range of parameters. It appears that Eq. (1) accurately predicts the scaling with junction area, but consistently overestimates the sensitivity by a factor of about 2. We believe that this discrepancy arises from the neglect of the capacitance in the noise computation; unfortunately, the inclusion of this effect is likely to be extremely costly in computer time. We also feel that there is every reason to believe that the ultimate energy sensitivity per Hz of h is achievable by appropriate scaling of the SQUID parameters. The present device is the most sensitive available that follows the general predictions of the theory, and that can be used in a feedback mode in a straightforward way. Its extreme ruggedness and very high sensitivity make it very attractive for both laboratory and field applications.

* * *

[†]This work was performed while J. Clarke was on leave at the IBM Research Center in New York.

[‡]Brief version of LBL-9893.

[§]IBM Thomas J. Watson Research Center, Yorktown Heights, N. Y. 10598.

1. MMRD Annual Report 1976, LBL-6016, pg. 146.

3. SUPERCURRENT-INDUCED CHARGE IMBALANCE IN THE PRESENCE OF A THERMAL GRADIENT[†]

J. Clarke, B. R. Fjordbøge,[‡] P. E. Lindelof,[‡] and M. Tinkham[§]

Pethick and Smith predicted that when a supercurrent I flows through a thermal gradient ∇T in a superconductor, a quasiparticle charge imbalance will be created that should be observable as a potential difference between the quasiparticle and the pair chemical potentials. Clarke, Fjordbøge, and Lindelof have observed this effect, but found its magnitude to be 2 to 3 orders of magnitude smaller than predicted. Clarke and Tinkham have subsequently developed a theory that is in good agreement with the magnitude and temperature dependence of the effect.

The sample configuration is shown in Fig. 1. A Sn film typically 300 nm thick and 0.1 mm wide was evaporated onto a 32x7x1 mm³ glass substrate and oxidized in air for 5-15 minutes. Three CuAl disks about 1 μ m thick were then deposited, followed by three Pb strips. In a given experiment, one of the three Sn-SnOx-Cu tunnel junctions was used to detect the quasiparticle potential in the Sn film relative to the pair potential. The sample was mounted in a vacuum can, with heaters and thermometers attached to enable us to establish and measure a temperature gradient. The voltage measurements were made with a SQUID in a feedback mode. The can was immersed in superfluid helium, and the cryostat was surrounded by a double mu-metal shield.

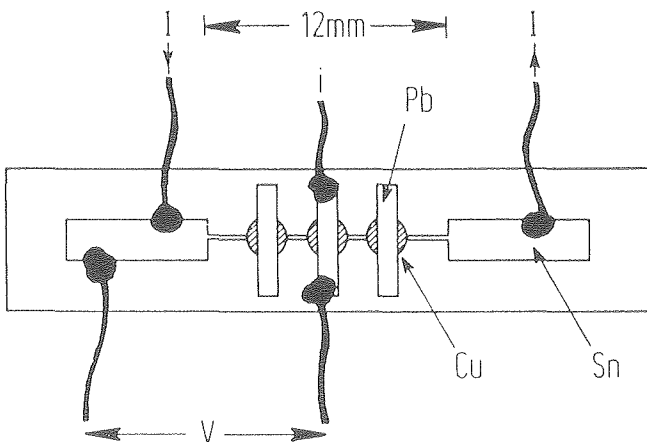


Fig. 1. Sample configuration. (XBL 7911-12877)

We made measurements by establishing a temperature gradient and then measuring the voltage generated when a given supercurrent was turned on.

In Figs. 2 and 3 for a typical sample we plot the voltage V vs. current for a given gradient and vs. gradient for a given current, respectively. It is immediately apparent that $V \propto I \nabla T$. To investigate the temperature dependence of the effect, in Fig. 4 we plot $V g_{NS} T / I \nabla T$ vs. $(1-t)$, where t is the reduced temperature, and g_{NS} is the measured normalized tunneling conductance of the Sn-SnOx-Cu tunnel junction. At reduced temperatures above about 0.8 the quantity $V g_{NS} T / I \nabla T$ diverges nearly as $(1-t)^{-1}$, while below about 0.8 it falls off more rapidly as the temperature is lowered. The dependence of V on $I \nabla T$ is as predicted by Pethick and Smith, but the magnitude of the effect is two to three orders of magnitude smaller than their prediction.

Clarke and Tinkham have developed a relatively simple theoretical model that is in good agreement with the observed effect. Consider first a superconductor with zero supercurrent but with $\nabla T \neq 0$. Quasiparticles moving into a given region from a colder region have an effective temperature $T - \delta T$, while those moving in the opposite direction from a hotter region have an effective temperature $T + \delta T$. Thus, there is an imbalance in the $k > k_F$ and $k < k_F$ populations on one side of the Fermi surface that is exactly canceled by an equal and opposite imbalance on the other side. As a result, the charge imbalance, Q^* , is zero. However, if we now apply a supercurrent and thus create a superfluid velocity \vec{v}_s , the excitation energy of a state with momentum \vec{p}_k is changed by $\vec{p}_k \cdot \vec{v}_s$, thereby introducing an asymmetry about the Fermi surface. As a result, in the presence of a thermal gradient the population imbalances on the two sides no longer exactly cancel, and a net Q^* results that in turn produces a

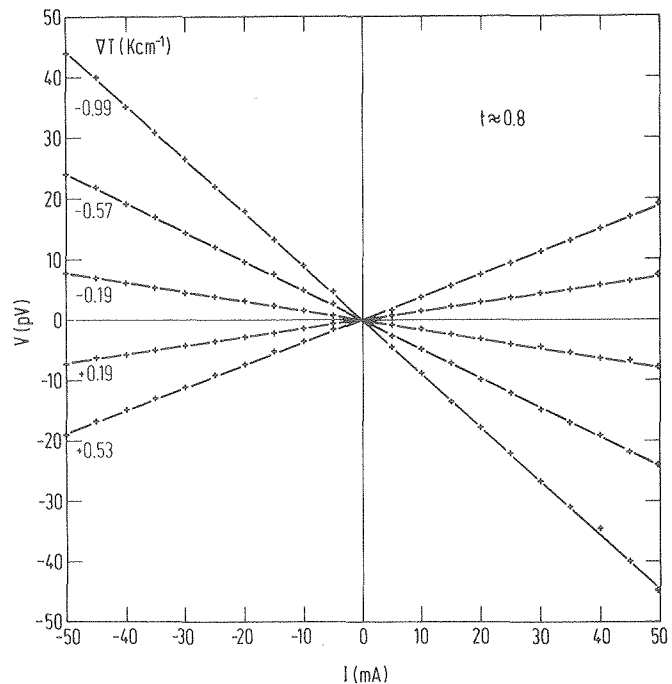


Fig. 2. V vs. I for 5 values of ∇T . (XBL 7911-12875)

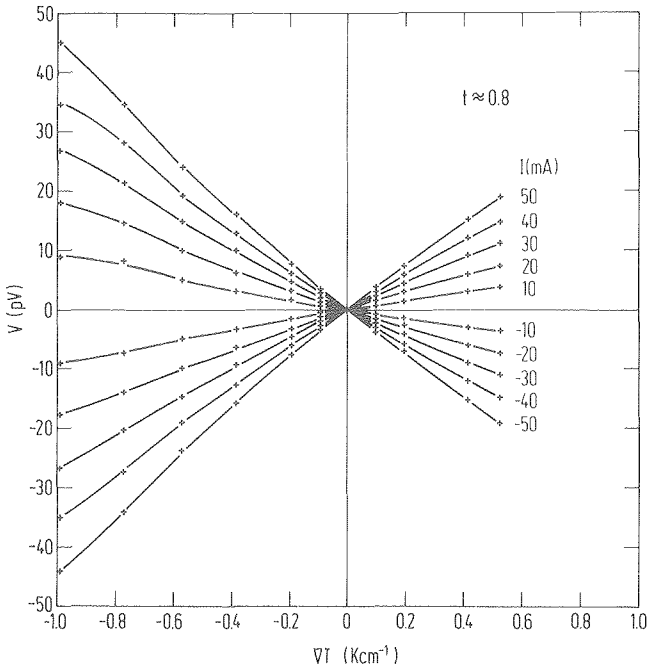


Fig. 3. V vs. \sqrt{T} for 10 values of I . (XBL 7911-12876)

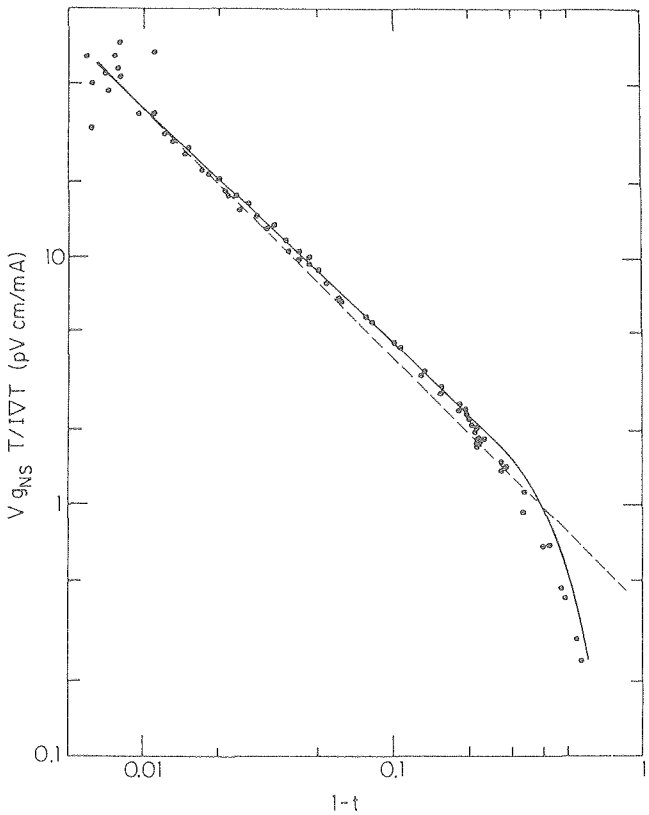


Fig. 4. $V g_{NS} T / I \sqrt{T}$ vs. $(1-t)$. Solid circles represent data, dashed line has slope -1, and solid line is Eq. (1). (XBL 7911-12874)

quasiparticle voltage. In the limit in which elastic scattering dominates, a detailed calculation yields

$$V = \frac{2\pi}{3} \frac{v_F}{c} \frac{\lambda^2(0)}{1-t^4} \tag{1}$$

$$\times \frac{\Delta(T)}{k_B T \cosh^2(\Delta/2k_B T) g_{NS} (1-Z)} \frac{\vec{J}_s \cdot \vec{\nabla} T}{c T},$$

where v_F is the Fermi velocity, ℓ is the electronic mean free path, $\lambda(0)$ is the zero temperature penetration depth, J_s is the supercurrent density, and $Z(T)$ is the function specified in article 5. Equation (1), fitted at a single point, is shown in Fig. 4. The fit to the data is remarkably good, and the absolute magnitude of the experimental results is within a factor of two of the theory. This excellent agreement strongly suggests that the simple theory contains the essential physics of the effect.

* * *

[†]Brief version of Phys. Rev. Lett. 43, 642 (1979).

[#]H. C. Ørsted Institute, Copenhagen, Denmark.

[§]Harvard University, Cambridge, MA 02138.

4. CALCULATIONS OF QUASIPARTICLE BRANCH RELAXATION RATES IN SUPERCONDUCTORS[†]

C. C. Chi and J. Clarke

There are many situations of physical interest in which a quasiparticle voltage may be induced in a superconductor by a charge imbalance

$$Q^* = 2N(0) \int_{\Delta}^{\infty} [\delta f_{>}(E) - \delta f_{<}(E)] dE \tag{1}$$

between the $k > k_f$ and $k < k_f$ quasiparticle branches. Here, $N(0)$ is the single spin density of states at the Fermi level, $\Delta(T)$ is the energy gap, $E^2 = \Delta^2 + \epsilon^2$ where ϵ is the one electron energy, and $\delta f_{>}(E)$ and $\delta f_{<}(E)$ are the deviations from the equilibrium distribution function. A charge imbalance may be created, for example, by tunnel injection into a superconductor (see article 6), by the passage of a current across a normal-superconducting interface (see article 5), by a phase slip center, or by the flow of a supercurrent in the presence of a temperature gradient (see article 3). Existing theories of the charge relaxation time, τ_{Q^*} , by Schmid and Schön, and Pethick and Smith are valid only in the limit $T \rightarrow T_c$, where they predict

$$\tau_{Q^*}^{-1} = (\pi \Delta(T) / 4k_B T) \tau_{E=0}^{-1}(T_c),$$

$\tau_{E=0}^{-1}(T_C)$ being the inelastic electron scattering rate at T_C for electrons at the Fermi energy. We have devised a computational scheme that enables us to calculate $\tau_{Q^*}^{-1}$ at any temperature, T , and as a function of injection voltage, V_{inj} .

The calculation was performed for the case of uniform injection of charge imbalance into a superconductor from a normal metal via a tunnel junction. One can readily compute the injection rate $Q_{inj}^*(T, V_{inj})$. The steady state value of Q^* is computed by first finding the deviation δf_ϵ from equilibrium as a function of $\epsilon = \pm(E^2 - \Delta^2)^{1/2}$ from the equation

$$d(\delta f_\epsilon)/dt = G_\epsilon - G_{in \epsilon} = 0. \quad (2)$$

In Eq. (2), G_ϵ is the injection rate at energy ϵ , and $G_{in \epsilon}$ is the inelastic collision integral. Integrating δf_ϵ enables us to find Q^* , and we finally obtain the relaxation rate from

$$\tau_{Q^*}^{-1} = \dot{Q}_{inj}^*/Q^*. \quad (3)$$

Figure 1 shows $\tau_{Q^*}^{-1} \tau_{E=0}^{-1}(T_C) \cdot 4k_B T / \pi \Delta(T)$ vs. $\Delta(T)/k_B T$ for $T \geq 0.9T_C$ and for three injection voltages: $eV_{inj} = 0.01\Delta(T)$, $10\Delta(T)$, $10k_B T_C$. Notice that as the injection voltage is raised, $\tau_{Q^*}^{-1}$ increases at all temperatures, reflecting the increase in the inelastic scattering rate with energy. In the low voltage limit and for $\Delta T/k_B T \leq 0.6$, we find that the computed curve is fitted to within 1% by the empirical formula.

$$\tau_{Q^*}^{-1} \tau_{E=0}^{-1}(T_C) \cdot 4k_B T / \pi \Delta(T) = 1 + \frac{1}{2} [\Delta(T)/k_B T] - \frac{3}{4} [\Delta(T)/k_B T]^2. \quad (4)$$

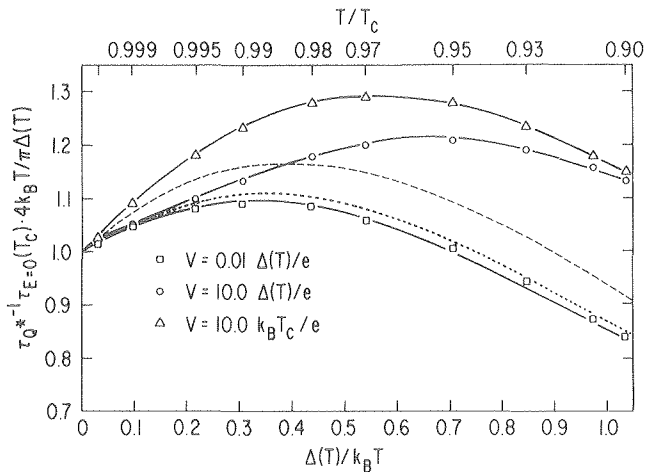


Fig. 1. $4\tau_{Q^*}^{-1} \tau_{E=0}^{-1}(T_C) k_B T / \pi \Delta(T)$ vs. $\Delta(T)/k_B T$ and T/T_C . Steady state calculation for $eV_{inj} = 0.01\Delta(T)$ (\square), $10\Delta(T)$ (\circ), and $10k_B T_C$ (\triangle); TC model (---), and PS model (—). (XBL 7911-12868)

Also shown in Fig. 1 are the relaxation rates computed from the Tinkham-Clarke (TC) and Pethick-Smith (PS) chemical potential models, in which the injected distribution is assumed to be represented by a Fermi function with a suitably shifted chemical potential. Interestingly, the calculated low voltage limit agrees more closely with the TC model, although the PS model is in fact more appropriate.

* * *

† Brief version of LBL-9695.

5. BOUNDARY RESISTANCE OF THE SUPERCONDUCTING-NORMAL INTERFACE[†]

T. Y. Hsiang and J. Clarke

Pippard, Shepherd, and Tindall were the first to show experimentally that the electrical boundary resistance of the superconducting-normal (SN) interface increased as the temperature was raised towards the transition temperature, T_C . They presented a theory for the increase that attributed the boundary resistance to the propagation of current-carrying quasiparticles into the superconductor. Subsequently, there was considerable theoretical interest in this subject. However, there has been no attempt to fit a theory quantitatively to experimental results, and to obtain values of the inelastic scattering time at the Fermi energy and at T_C , $\tau_{E=0}(T_C)$. We have developed a simple theory to account for the boundary resistance and applied it to our measurements on SNS samples to obtain values of $\tau_{E=0}(T_C)$ for four superconductors.

The theory is an extension of the tunnel injection theory for Q^* developed by Tinkham and Clarke. When a current I flows across an NS interface at a non-zero temperature, excitations with energies below the energy gap, Δ , are Andreev reflected, and their current is propagated into the superconductor as a supercurrent. Excitations with energies above Δ propagate into the superconductor generating a charge imbalance Q^* that decays from the interface as

$$Q^* = Q^*(0) \exp(-x/\lambda_{Q^*}), \quad (1)$$

where $\lambda_{Q^*} = (\ell v_F \tau_{Q^*}/3)^{1/2}$. Here, ℓ and v_F are the electronic mean free path and Fermi velocity of the superconductor, and $\tau_{Q^*} = 4k_B T \tau_{E=0}(T_C) / \pi \Delta(T)$ is the charge relaxation time. It is straightforward to show that

$$Q^*(0) = Z(T) I \tau_{Q^*} / e A \lambda_{Q^*}, \quad (2)$$

where A is the cross-section area of the sample, and

$$Z(T) = 2 \int_0^\infty N_S^{-1}(E) (-\partial f / \partial E) dE,$$

with $N_S(E) = [(1-\Delta^2/E^2)^{-1/2}]$, Δ the energy gap, and f the Fermi function.

The voltage generated by the charge imbalance is $Q^*(0)/2e N(0)$, where $N(0)$ is the single-spin density of states at the Fermi level. Combining this result with Eqs. (1) and (2) and using $\rho_S = 3/2e^2 N(0) \lambda_{Q^*} v_F$ for the normal state resistivity of the superconductor we find a boundary resistance

$$R_b = Z(T) \lambda_{Q^*} \rho_S / A. \quad (3)$$

This result has a simple interpretation. As $T \rightarrow T_C$, $Z(T) \rightarrow 1$, and the boundary resistance becomes the normal state resistance of a length λ_{Q^*} of the superconductor. As $T \rightarrow 0$, $Z(T) \rightarrow (k_B T / \Delta)^{1/2} \exp(-\Delta/k_B T)$, and R_b vanishes exponentially, as we would expect.

In our experiments, we made two different types of samples, one by successive evaporations of the appropriate materials, and the other by evaporating the superconducting material on to both sides of a foil cleaned by ion milling with argon. The samples, usually two or three at a time, were connected in series with a known resistor and the superconducting input coil of a dc SQUID with the usual feedback arrangement. The samples were mounted in a vacuum can surrounded by a superconducting shield and immersed in liquid helium. The resistance of each sample was measured as a function of current from about 1.2 K to T_C .

We found that the resistance was independent of current for densities up to $3 \times 10^6 \text{ Am}^{-2}$. The variation of resistance with temperature is shown in Fig. 1 for four samples. At low temperatures, the resistance was independent of temperature, and within the experimental error, equal to the value calculated from the dimensions and resistivity of the normal metal. This result indicates that boundary contamination is negligible. As the temperature was raised towards T_C , the resistance increased markedly. The curves in Fig. 1 show the excellent fit to the theory, using the values of $\tau_{E=0}(T_C)$ shown in Table 1. The measured times are generally in good agreement with those calculated by Kaplan et al.

* * *

† Brief version of LBL-9577.

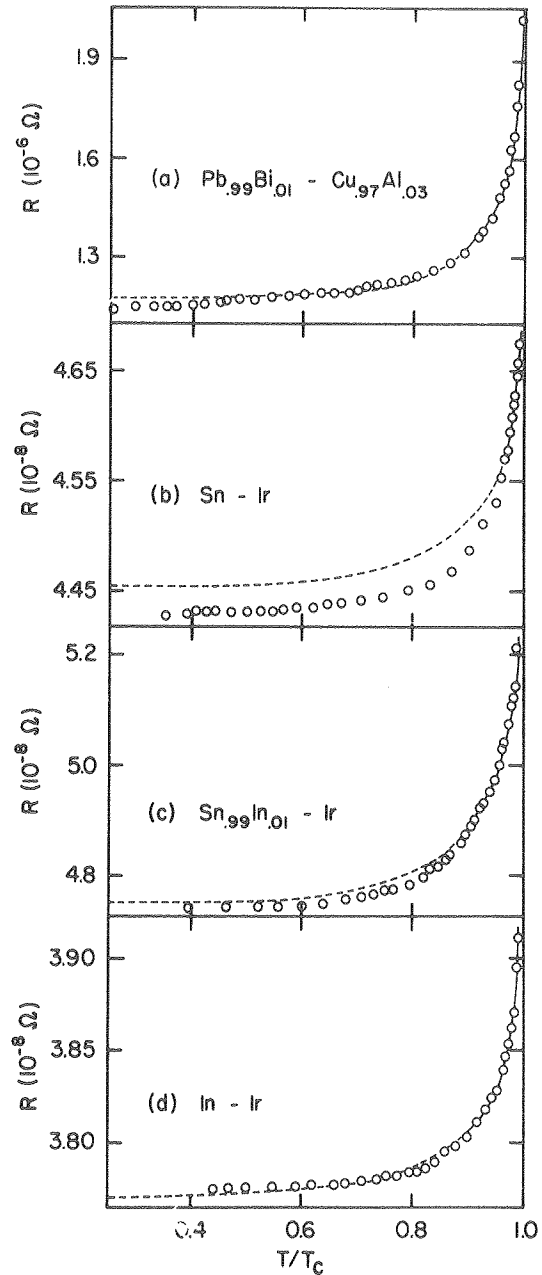


Fig. 1. Circles are measured dependence of the total resistance vs. reduced temperature of four SNS sandwiches. The solid lines above $0.9 T_C$ ($0.96 T_C$ for Sn) are the fit to Eq. (3) and the dashed lines shown the extrapolation of the theory to lower temperatures. (XBL 7911-12869)

Table 1. Experimental values of $\tau_{E=0}(T_C)$, together with computed values from Kaplan et al. In the case of alloy samples, the computed values for the pure materials are given in parentheses.

| Material | Pb _{0.99} Bi _{0.01} | Sn | Sn _{0.99} In _{0.01} | In | Pb |
|---|---------------------------------------|-----|---------------------------------------|-----|------|
| $\tau_{E=0}(T_C)(10^{-10}\text{s})$ (Experimental) | 0.25 | 2.6 | 1.1 | 1.1 | 0.20 |
| $\tau_{E=0}(T_C)(10^{-10}\text{s})$ (Kaplan et al) | (0.23) | 2.7 | (2.7) | 1.0 | 0.23 |

6. MEASUREMENT OF THE QUASIPARTICLE CHARGE RELAXATION RATE IN Al-Er ALLOYS

T. R. Lemberger and J. Clarke

In the 1978 MMRD annual report,¹ we reported measurements of the quasiparticle charge relaxation rate in superconducting aluminum-erbium alloy films, in which the Er is a magnetic impurity. Those measurements have been extended to lower reduced temperatures, and to cover two decades of Er concentration. In this article, these new results are presented, and compared to the analytic expression of Schmid and Schön, and to a computer calculation.

In this experiment a quasiparticle charge, Q^* , is created in an Al-Er film by tunnel injection at a rate $\dot{Q}_{inj} = F^* I_{inj} / e \Omega$, where I_{inj} is the injection current, Ω is the injected volume, and F^* is a calculable quantity which depends on temperature and injection voltage. For the measurements described here, $F^* = 0.95$. The induced charge $Q^* = \dot{Q}_{inj} \tau_{Q^*}$, where τ_{Q^*} is the charge relaxation time, gives rise to a quasiparticle potential $V = Q^* / 2N(0) e g_{NS}$ that is detected by means of a second tunnel junction; here, $N(0)$ is the single-spin density of states in the superconductor, and g_{NS} is the normalized tunneling conductance of the detector junction. The experimentally determined quantity is $I_{inj} / e \Omega Q^* = [F^* \tau_{Q^*}]^{-1}$.

The data, normalized so that the data from different samples overlap for $\Delta/k_B T_C \lesssim 0.5$, are shown in Fig. 1. We see that $[F^* \tau_{Q^*}]^{-1}$ is proportional to $\Delta/k_B T_C$ for $0.3 \lesssim \Delta/k_B T_C \lesssim 0.8$, while for $\Delta/k_B T_C \gtrsim 0.9$, it increases less rapidly with increasing $\Delta/k_B T_C$, possibly becoming constant at sufficiently low temperatures. The qualitative dependence on $\Delta/k_B T_C$ seems to be nearly independent of the Er concentration, which ranged from 21 ppm to 1660 ppm.

In the limit $\Delta/k_B T_C \lesssim 0.01$, Schmid and Schön (SS) obtained the analytic result

$$[F^* \tau_{Q^*}]^{-1} = \frac{3.2}{F^*} \frac{\Delta}{k_B T_C} \left[\frac{\Gamma}{\tau_0} \right]^{1/2}, \quad (1)$$

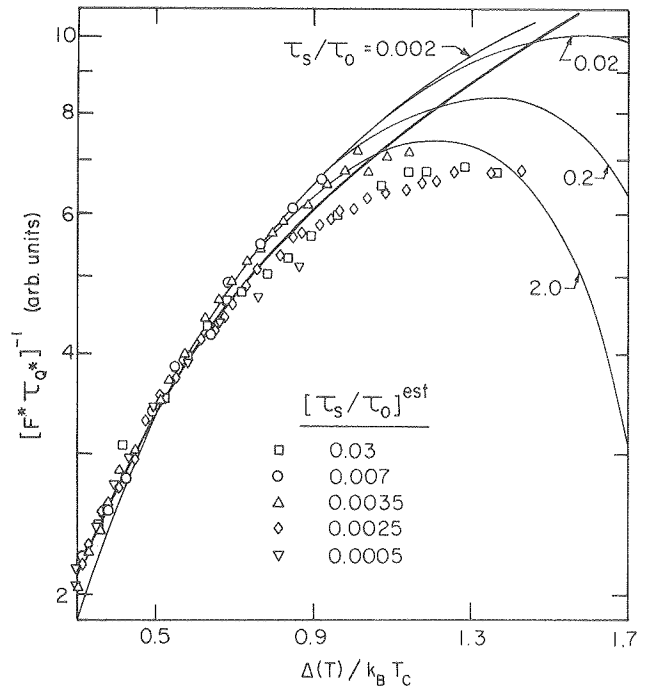


Fig. 1. $[F^* \tau_{Q^*}]^{-1}$ vs $\Delta/k_B T_C$. The discrete points are typical experimental data for one sample from each impurity concentration studied, normalized to agree for $\Delta/k_B T_C \lesssim 0.5$. The bold solid line represents a line proportional to $\Delta/k_B T_C$, while the other solid lines are calculated numerically.

(XBL 7911-7284)

where

$$\Gamma = \frac{4.2}{\tau_0} + \frac{1}{\tau_s} \quad (2)$$

Here, τ_0 is a characteristic electron-photon scattering time, and τ_s is the electron spin-flip scattering time. Although the data lie outside the

stated range of validity, it is instructive to compare them with the SS result. Equation (1) contains the observed linear dependence of $[F^* \tau_{Q^*}]^{-1}$ on $\Delta/k_B T_C$. In Fig. 2 we plot $d[F^* \tau_{Q^*}]^{-1}/d[\Delta/k_B T_C]$ vs. $3.4[\Gamma/\tau_0]^{1/2}$. The solid line through the data has a slope of unity, as predicted by Eq. (1). To plot these data, we assumed that $\tau_0 = 0.1 (1.2K/T_C)^{3\mu s}$, where T_C is the measured transition temperature, while we determined τ_S from the concentration of Er.

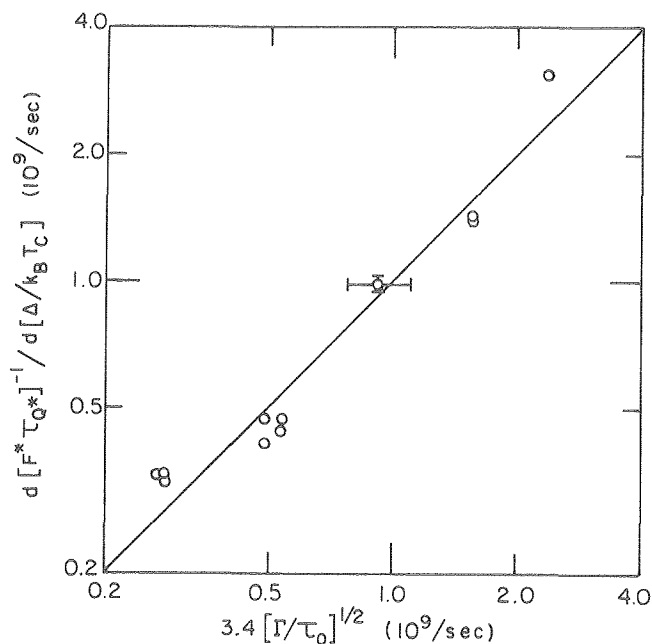


Fig. 2. The initial slope of the data, $d[F^* \tau_{Q^*}]^{-1}/d[\Delta/k_B T_C]$ vs. $3.4[\Gamma/\tau_0]^{1/2}$. The solid line has a slope of unity. (XBL 7911-7283)

To verify the validity of extrapolating the SS result to temperatures well below T_C , and to determine the low temperature dependence of $[F^* \tau_{Q^*}]^{-1}$ on $\Delta/k_B T_C$, we performed a computer calculation for $[F^* \tau_{Q^*}]^{-1}$. The Boltzmann equation is used to determine the occupation probabilities of quasiparticle states, given a steady-state injection of quasiparticles and quasiparticle scattering from phonons and magnetic impurities. The effect of the magnetic impurities on the order parameter and on the density of states is neglected, but this should be a valid approximation for the range of impurity concentrations and temperatures studied.

The numerical values of $[F^* \tau_{Q^*}]^{-1}$ vs. $\Delta/k_B T_C$ for different values of τ_S/τ_0 are shown in Fig. 1. The curves are normalized to have the same value at $\Delta/k_B T_C = 0.3$. The shapes of the curves depend on τ_S/τ_0 only through their ratio, τ_S/τ_0 . There are three important features: The magnitude of $[F^* \tau_{Q^*}]^{-1}$ at, say, $\Delta/k_B T_C = 0.5$ scales roughly with $[\Gamma/\tau_0]^{1/2}$; the curves are not proportional to $\Delta/k_B T_C$ for small values of $\Delta/k_B T_C$; and the shapes of the curves depend strongly on τ_S/τ_0 . Therefore, although the computer calculation gives approximately the observed dependence on τ_S , it does not

give the observed dependence on $\Delta/k_B T_C$ over any significant temperature range. Possible causes of the disagreement are under investigation.

* * *

1. MMRD Annual Report 1978, LBL-8580, pg. 171.

RESEARCH PLANS FOR CALENDAR YEAR 1980

Geophysics. We plan several new experiments to investigate fundamental aspects of magnetotellurics and to study the application of superconducting magnetometers to geophysical research. We hope to improve the sensitivity of our superconducting gradiometer further to 10^{-12} gauss $\text{cm}^{-1} \text{Hz}^{-1/2}$ or better and to use it to investigate fluctuations in the gradient of the earth's magnetic field. As a second method of studying gradient fluctuations, we propose to establish two 3-axis SQUID magnetometers at sites several kilometers apart, and to use a third remote magnetometer as a reference. This technique should enable us to make accurate estimates of the difference in field fluctuations at spatially separated sites. Another experiment is designed to investigate the source of magnetic noise in magnetotellurics. Keeping the magnetotelluric site fixed, we will vary the distance to the remote reference magnetometer from zero to perhaps 20 km. This will not only establish the minimum separation necessary for referenced magnetotellurics, but should enable us to estimate the coherence length of the noise. Finally, we hope to extend our modeling techniques to enable us to use the impedance tensor to calculate accurately the resistivity of the ground as a function of position.

Superconducting devices. We plan to measure the noise in a single Josephson junction in the quantum noise limit, and to use a simple model to compute the noise in a resistivity shunted junction. We hope to complete our program to investigate the noise limitations of SQUIDS with small area tunnel junctions and low inductances, and to be able to reach the quantum noise limit of these devices predicted from our measurements on single junctions. We propose to study various schemes to couple magnetic flux into SQUIDS in planar, cylindrical, or toroidal geometries in order to optimize the overall performance of systems such as gradiometers, voltmeters, and gravity wave detectors. The goal of this work is to investigate the ultimate limits of SQUID sensitivity, and to produce devices that are more sensitive, more reliable, and more straightforward to use than present devices.

Nonequilibrium superconductivity. This program is aimed at understanding fundamental nonequilibrium processes in superconductors; it is expected that this work will also lead to the understanding of noise in superconducting devices, thereby enabling us to improve their sensitivity. Three experiments are concerned with quasiparticle charge imbalance in superconductors: The relaxation of charge imbalance in the presence of a supercurrent, the generation of an imbalance by thermal gradients, and the relaxation of an imbalance under pulsed conditions are all to be investigated. The possibility

of gap enhancement and the establishment of a state with two energy gaps under phonon irradiation is to be studied.

1/f noise. It is hoped to initiate a new program to investigate the 1/f noise in extremely pure, strain-free single crystals. This study should yield information on whether or not the noise is generated by defects in the material.

1979 PUBLICATIONS AND REPORTS

Refereed Journals

[†]1. T. D. Gamble, W. M. Goubau, and J. Clarke, "Magnetotellurics with a Remote Magnetic Reference," *Geophys.* 44, 53 (1979).

[†]2. T. D. Gamble, W. M. Goubau, and J. Clarke, "Error Analysis for Remote Reference Magnetotellurics," *Geophys.* 44, 959 (1979).

3. C. C. Chi and J. Clarke, "Quasiparticle Branch Mixing Rates in Superconducting Aluminum," *Phys. Rev.* 19, 4495 (1979).

4. J. Clarke, B. Fjordbøge, and P. E. Lindelof, "Supercurrent-Induced Charge Imbalance Measured in a Superconductor in the Presence of a Thermal Gradient," *Phys. Rev. Lett.* 43, 642 (1979).

5. C. D. Tesche and J. Clarke, "DC SQUID: Current Noise," *J. Low Temp. Phys.* 37, 397 (1979).

6. J. Clarke, C. D. Tesche, and R. P. Giffard, "Optimization of DC SQUID Voltmeter and Magnetometer Circuits," *J. Low Temp. Phys.* 37, 405 (1979).

7. C. C. Chi and J. Clarke, "Enhancement of the Energy Gap in Superconducting Aluminum by Tunneling Extraction of Quasiparticles," *Phys. Rev.* B20, 4465 (1979).

8. J. Clarke, U. Eckern, A. Schmid, G. Schon, and M. Tinkham, "Branch Imbalance Relaxation Times," *Phys. Rev.* B20, 3933 (1979).

Other Publications

1. R. Koch and J. Clarke, "Small Area Tunnel Junction DC SQUID," *Bull. Am. Phys. Soc.* 24, 264 (1979).

2. R. F. Voss, R. B. Laibowitz, S. I. Raider, W. D. Grobman, and J. Clarke, "Niobium Thin Film DC SQUID with 1 μm Tunnel Junctions," *Bull. Am. Phys. Soc.* 24, 264 (1979).

3. T. R. Lemberger and J. Clarke, "Measurement of the Branch Imbalance in a Superconductor with Magnetic Impurities," *Bull. Am. Phys. Soc.* 24, 328 (1979).

4. T. Y. Hsiang and J. Clarke, "Temperature Dependent Resistance of Superconductor-Normal Metal Superconductor Sandwiches and Charge Relaxation Times of Superconductors," *Bull. Am. Phys. Soc.* 24, 328 (1979).

5. J. Clarke, "Josephson Effect Devices," Invited Article in *Physics Bulletin* 30, 206 (1979).

6. T. D. Gamble, W. M. Goubau, N. E. Goldstein, and J. Clarke, "Referenced Magnetotellurics at Cerro Prieto," Proceedings of the First Symposium on the Cerro Prieto Geothermal Field, Baja, California (1979).

LBL Reports

1. J. Clarke and M. Tinkham, "Theory of Charge Imbalance Induced in a Superconductor by a Super-current in the Presence of a Thermal Gradient," LBL-9559.

2. T. Y. Hsiang and J. Clarke, "Boundary Resistance of the Superconducting Normal Interface," LBL-9577.

3. C. C. Chi and J. Clarke, Addendum to "Quasiparticle Branch Mixing Rates in Superconducting Aluminum," LBL-9695.

4. R. F. Voss, R. B. Laibowitz, S. I. Raider, and J. Clarke, "All-Nb Low Noise DC SQUID with 1 μm Tunnel Junctions," LBL-9893.

Invited Talks

1. J. Clarke, "Gap Enhancement in Superconductors," invited talk at the Midwinter Solid State Research Conference, Laguna Beach, California, January 19, 1979.

2. J. Clarke, "Status of Stimulated Superconductivity," seminar at the H. C. Ørsted Institute, Copenhagen, February 15, 1979.

3. J. Clarke, "SQUIDS and Geophysics," seminar at Neils Bohr Institute, Copenhagen, March 14, 1979.

4. J. Clarke, "The SN Boundary Resistance," seminar at the H. C. Ørsted Institute, Copenhagen, March 29, 1979.

5. J. Clarke, "Nonequilibrium Superconductivity," seminar at the Physics Department, Oxford University, Oxford, U.K., June 15, 1979.

6. J. Clarke, "SQUIDS and Geophysics," Colloquium at the Physics Department Bristol University, Bristol, U. K., June 18, 1979.

7. T. D. Gamble, "Correlation Analysis of Simultaneous Electromagnetic Measurements," Ocean Floor Electromagnetics Workshop, Naval Postgraduate School, Monterey, August 20, 1979.

8. J. Clarke, "Supercurrent-Induced Charge Imbalance in Thin Films in the Presence of a Thermal Gradient," seminar at the National Bureau of Standards, Washington D. C., September 7, 1979.

9. T. D. Gamble, "Magnetotelluric Measurements at Cerro Prieto," Second Symposium on the Cerro Prieto Geothermal Field, Mexicali, Mexico, October 18, 1979.

10. J. Clarke, "SQUIDS and Geophysics," Colloquium at Sonoma State University, California, November 5, 1979.

11. J. Clarke, T. D. Gamble, W. M. Goubau, R. Koch, and R. F. Mirachy, Field Analysis of Magnetotelluric Data, 49th Annual Meeting, Society of Exploration Geophysicists, New Orleans, November 11, 1979.

12. J. Clarke, "SQUIDS and Geophysics," Colloquium at Stanford University, California, November 14, 1979.

13. J. Clarke, "SQUIDS and Geophysics," seminar at MacQuarie University, North Ryde, N.S.W., Australia, December 7, 1979.

14. J. Clarke, "Applications of SQUIDS to Audio Frequency Magnetotellurics, invited paper at the XVII General Assembly of the International Union of Geodesy and Geophysics, Canberra, Australia, December 11, 1979.

* * *

[†]Supported in part by the Division of Geothermal Energy, U. S. Department of Energy.

2. Theoretical Solid State Physics

a. Theoretical Solid State Physics*

Marvin L. Cohen, Investigator

1. PSEUDOPOTENTIAL TECHNIQUES AND ELECTRONIC PROPERTIES OF SOLIDS

Several important advances were made in pseudopotential theory and application (J12, R4)[†] which allowed more ambitious calculations of the electronic properties of solids. One aspect of these developments dealt with the form of the pseudopotential itself. A "first-principles" pseudopotential scheme (J2, R2) was developed in which the potentials were derived from atomic wavefunctions. This approach yields potentials which can be used for both atomic and solid electronic properties (J5). These potentials are relatively strong and a plane-wave basis set is often not sufficient. A mixed-basis set (J11) using plane waves and localized functions such as Gaussians can be used. This basis set was developed by our group to accommodate both localized states (e.g., d-orbitals) and itinerant states (e.g., s- and p-orbitals). This approach has been very successful in calculations of bulk and surface electronic properties of transition metals. Bulk electronic calculations using a mixed-basis set scheme include the high temperature Al5 superconductors (J9,10) like Nb₃Ge. Other d-band materials include Mo and W (J6,13). These calculations and other bulk electronic calculations (J16; R3,9,10) yield energy bands, density of states curves and charge densities. The theoretical results are compared with experiment where available.

Another new technique (R1) which has already had a significant impact on the applications of band theory is a total energy approach which can be applied using charge densities and potentials expressed in momentum space. This method allows the use of functions normally obtained in the process of doing a band structure calculation. The result is that a total energy calculation can be done without significant extra effort after a band structure calculation is done. The method was applied successfully to Si, Mo and W (J6,7; R13). The total energy expressions also allow a simplified approach for looking at specific contributions to the energy (R16).

* * *

[†]J and R refer to journal articles and reports under the section entitled "1979 Publications and Reports."

*This work was supported in part by the Division of Materials Sciences, Office of Basic Energy Sciences, U.S. Department of Energy and the National Science Foundation.

2. SOLID SURFACES AND INTERFACES

Research in this area concentrated on clean semiconductor surfaces (J4; R11,17), Schottky barriers (J1; R5,6), heterojunctions (J14; R12,18) and transition metal surfaces with and without H adsorbates (J3,8; R8,15). The GaAs (110) surface was studied in detail. This surface has been the subject of intense experimental and theoretical research during the past four or five years. The question whether intrinsic surface states exist in the semiconducting energy gap has been discussed actively in the literature and at conferences. Our recent self-consistent pseudopotential (SCP) results show that the ideal geometry yields states in the gap, but if a surface relaxation is imposed, the surface states move out of the gap. The relaxation model used was determined using LEED data. The calculated energy positions for the surface states are in good agreement with recent photoemission data.

The SCP approach was used to determine the electronic structure of a Ge (111)-metal interface (Schottky barrier). The results for the Schottky barrier height (0.55 eV) and the interface index ($S = 0.14$) are both consistent with measured values. The method was then applied to a diamond-metal interface. This interface is crucial to the theory of Schottky barriers because of diamond's large gap and zero ionicity. Predictions based on experimental extrapolations give $S = 0$ while our calculations give $S = 0.4$. The barrier height of 2.2 eV is in good agreement with experiment. The question of the S -value for diamond Schottky barriers will ultimately be settled by accurate experimental measurements. The results will determine the ionicity dependence of the interface index, S . The behavior of S is fundamental to Schottky barrier theory. An analysis based on our expressions for S shows that limits can be placed on S . We find that, for reasonable choices of the physical parameters, $0.03 \leq S \leq 1.5$. Although these results conflict with some other published theoretical estimates, they are consistent with all current measurements. They also indicate that measurements on high S materials are near or at the maximum value for S .

Two heterojunction (semiconductor-semiconductor) interfaces were studied using the SCP. The (110) GaAs-ZnSe interface was examined because this system has no lattice constant or symmetry change across the interface, but there is an ionicity change. No interface states are found in the fundamental gap, but interface states do split off from bulk states in other regions of the Brillouin zone. The calculation indicated the

role of ionicity in determining the properties of interface states. A second heterojunction, (001) InAs-GaSb, was analyzed. This heterojunction is of special interest because the electron affinity rule and some experimental measurements suggest that the bottom of the conduction band of InAs lies below the top of the valence band of GaSb. Although our SCP calculation was not sufficiently accurate to determine the band overlap, many features of this interface were exhibited.

Using the SCP in conjunction with the mixed-basis representation, the Mo (001) surface was examined. A complete analysis of the surface states was done by illustrating their distribution in the two-dimensional Brillouin zone, the charge-density distribution and the local density of states. The results are in good agreement with photoemission measurements. The calculation was extended to include a saturated monolayer of hydrogen on the ideal Mo (001) surface. This calculation was done for two values of the hydrogen-substrate interlayer distance, 0.75 Å and 0.0 Å. The former value gives a calculated work function in agreement with experiment while the latter is too small by 50%. Two adsorbate-induced bands are found to lie below the substrate bulk bands. Many of the intrinsic surface states found on the clean substrate continue to exist for the hydrogen-saturated surface but at slightly lower energies. Recent angular-resolved photoemission data give some support to these results.

3. SUPERCONDUCTIVITY

Research on superconductivity concentrated on nonphonon mechanisms (J15,16; R14). Using our calculation of the energy band structure of CuCl, we concluded that this system is a direct band gap material. This result is contrary to the proposal by Rusakov which suggested a small indirect gap model. This model was subsequently used by Abrikosov to explain anomalous diamagnetic properties of CuCl in terms of high-temperature superconductivity. Abrikosov's model was based on an electron-hole mechanism. Although our band structure model indicated that CuCl was not a good candidate for electron-hole superconductivity, the mechanism itself was of sufficient interest to warrant further exploration. Our detailed analysis showed that Abrikosov's estimate of transition temperatures above room temperature was an overestimate. Renormalization, stability requirements and Coulomb effects significantly reduce this estimate. We suggested that Umklapp and intervalley scattering might enhance the transition temperature. Another nonphonon mechanism of current interest is the s-d or "demon" model to produce Cooper pairs. This approach was used recently in an attempt to explain anomalous properties of d-band materials. Although our investigations did not bear on the above questions, preliminary results indicated that the s-d interaction can be promising. However, more detailed and careful analysis is necessary before any definite conclusions can be reached.

Projects planned for 1980 include more detailed calculations of the s-d mechanism for Cooper pairing. Surface and interface calculations include a SCP computation for the reconstructed Si (001) surface. Recent tight-binding calculations predict possible reconstructions, and these will be tested using the SCP method. The Si-Pd interface will be examined, and the characteristics of the interface states of this Schottky barrier system will be determined. A cubic-hexagonal ZnS interface (heterojunction) is being examined to determine whether a symmetry change across an interface will bind interface states. An analysis of the GaAs-AlAs mixed compound is in progress to determine the charge density and electric field gradients for mixed-bond configurations. A frozen phonon calculation for Si will be attempted at the x-point of the Brillouin zone using the SCP method. First-principles pseudopotentials are now tabulated numerically; analytic forms will be tested for convenience in using these potentials.

1979 PUBLICATIONS AND REPORTS

Journals

1. J. Ihm, S. G. Louie and M. L. Cohen, "Electronic Structure of Ge and Diamond Schottky Barriers," *Phys. Rev. B* 18, 4172 (1978).
2. A. Zunger and M. L. Cohen, "A First-Principles Non-Local Pseudopotential Approach in the Density Functional Formalism, I: Development and Application to Atoms," *Phys. Rev. B* 18, 5449 (1978).
3. G. P. Kerker, K. M. Ho and M. L. Cohen, "Self-Consistent Electronic Structure of Transition Metal Surfaces: The Mo (001) Surface," *Phys. Rev. B* 18, 5473 (1978).
4. J. R. Chelikowsky and M. L. Cohen, "Electronic States on the Relaxed (110) Surface of GaAs," *Solid State Comm.* 29, 267 (1979); "Erratum," *Solid State Comm.* 30, 819 (1979).
5. M. Schlüter, A. Zunger, G. P. Kerker, K. M. Ho and M. L. Cohen, "Reliability of Pseudopotential Charge Densities," *Phys. Rev. Lett.* 42, 540 (1979).
6. A. Zunger and M. L. Cohen, "Self-Consistent Pseudopotential Calculation of the Bulk Properties of Mo and W.," *Phys. Rev. B* 19, 568 (1979).
7. J. Ihm and M. L. Cohen, "Self-Consistent Pseudopotential Calculation of the Equilibrium Properties of Bulk and Surface Si," *Solid State Comm.* 29, 711 (1979).
8. M. L. Cohen, "Adsorbates on Transition Metals," *Nature* 278, 688 (1979).
9. W. E. Pickett, K. M. Ho and M. L. Cohen, "Electronic Properties of Nb₂Ge and Nb₂Al from Self-Consistent Pseudopotentials. I. Band Structure and Density of States," *Phys. Rev. B* 19, 1734 (1979).

10. K. M. Ho, W. E. Pickett and M. L. Cohen, "Electronic Properties of Nb_3Ge and Nb_3Al from Self-Consistent Pseudopotentials. II. Bonding, Electronic Charge Distribution, and Structural Transformation," *Phys. Rev. B* 19, 1751 (1979).
11. S. G. Louie, K. M. Ho and M. L. Cohen, "Self-Consistent Mixed-Basis Approach to the Electronic Structure of Solids," *Phys. Rev. B* 19, 1774 (1979).
12. M. L. Cohen, "The Pseudopotential Panacea," *Physics Today* 32, 40 (1979).
13. A. Zunger, G. P. Kerker and M. L. Cohen, "Calculation of the Electronic Properties of Mo in a First-Principles Nonlocal-Pseudopotential Approach," *Phys. Rev. B* 20, 581 (1979).
14. J. Ihm and M. L. Cohen, "Self-Consistent Calculation of the Electronic Structure of the (110) GaAs-ZnSe Interface," *Phys. Rev. B* 20, 729 (1979).
15. M. L. Cohen, "High-Temperature Electron-Hole Superconductivity," *Phys. Rev. B* 20, 1022 (1979).
16. A. Zunger and M. L. Cohen, "Electronic Structure of CuCl," *Phys. Rev. B* 20, 1189 (1979).
6. M. L. Cohen, "Electrons at Interfaces."
7. M. L. Cohen, "Science Citation Classic: M. L. Cohen and T. K. Bergstresser," *Physical Review* 141, 789 (1966).
8. G. P. Kerker, M. T. Yin and M. L. Cohen, "Self-Consistent Electronic Structure for a Mo (001) Surface with Saturated H Adsorption."
9. G. P. Kerker, A. Zunger, M. L. Cohen and M. Schlüter, "A Solid-State Approach to the Electronic Structure of Molecules: Self-Consistent First-Principles. Pseudopotential Calculations for O_2 ."
10. W. E. Pickett, M. L. Cohen and C. Kittel, "Theory of the Hydrogen Interstitial Impurity in Germanium."
11. J. R. Chelikowsky and M. L. Cohen, "A Self-Consistent Pseudopotential Calculation for the Relaxed (110) Surface of GaAs."
12. J. Ihm, Pui K. Lam and M. L. Cohen, "Electronic Structure of the (001) InAs-GaSb Superlattice."

13. J. Ihm and M. L. Cohen, "Calculation of Structurally Related Properties of Bulk and Surface Si."

14. M. L. Cohen, "Theoretical Overview--Emphasis on New Mechanisms."

15. G. P. Kerker, M. T. Yin and M. L. Cohen, "Self-Consistent Electronic Structure of a Transition Metal Surface with an Adsorbate: H on Mo (001)."

16. J. Ihm and M. L. Cohen, "Comment on 'Correction to Fuch's Calculation of the Electrostatic Energy of a Wigner Solid.'"

17. J. R. Chelikowsky and M. L. Cohen, "The (110) Surface of GaAs."

18. J. Ihm and M. L. Cohen, "Electronic Structure of the (100) InAs-GaSb Superlattice."

Reports

1. J. Ihm, A. Zunger and M. L. Cohen, "Momentum-Space Formalism for the Total Energy of Solids Using Pseudopotentials."
2. A. Zunger and M. L. Cohen, "A First-Principles Nonlocal Pseudopotential Approach in the Density Functional Formalism II: Application to Electronic and Structural Properties of Solids."
3. M. L. Cohen and D. J. Chadi, "Temperature Dependence of Semiconductor Band States."
4. M. L. Cohen and J. R. Chelikowsky, "Pseudopotentials for Semiconductors."
5. M. L. Cohen, "The Schottky and Bardeen Limits for Schottky Barriers."

C. MATERIALS CHEMISTRY

1. Chemical Structure

a. Low Temperature Properties of Materials*

Norman E. Phillips, Investigator

1. USE OF A MICROCOMPUTER FOR ON LINE CALCULATIONS OF LOW TEMPERATURE HEAT CAPACITY DATA

J. D. Boyer

Although automated calorimeters with on-line data reduction capability have been developed for use at temperatures above 4 K, full automation at lower temperatures has not been realized. In fact, automation is not as practical or useful at lower temperatures because the important sources of heat leaks are different and long internal equilibrium times are more likely to be encountered. On-line data reduction, which is a natural feature of automated operation, is, however, quite practical and offers several advantages over hand calculations done only after the data have been collected. In addition to the inherent time and labor savings, on-line processing allows an opportunity for tailoring the details of the experimental procedures to the specific experiment. Since the long time lag between data collection and review of the resultant heat capacities is eliminated, the judgment as to when adequate data are available is more certain.

The development of the microprocessor and supporting integrated circuitry and their evolution into small but powerful and inexpensive computers makes implementation of a dedicated on-line computing system much more practical. Not only is the cost an order of magnitude less than that of their predecessor, the mini-computers, but the simpler timing and bus control logic ease the task of interfacing to a diverse array of instruments. A microprocessor-based on-line data reduction system has been developed in this laboratory over the last several years. It has been in operation for the past year, and while further refinements will be made in the future, it has already proven to be a great advance in taking low-temperature heat capacity data.

The traditional heat pulse technique of measuring heat capacities is used with this system at present as it is the most general and reliable. The basis of this approach is to measure the change in temperature produced in a system by the introduction of a known quantity of energy. The quantities which must be determined are thus an initial and final temperature and the net energy input. The system description logically separates into three well-defined but tightly linked subsystems. These

are the thermometry system, the energy control and measurement system, and the computer and its operating system which links the operator and the other two segments. The structure and operation of each of these subsystems and their interaction with each other are described prior to evaluation of overall system performance.

Figure 1 is a block diagram of the thermometry subsystem. A four lead germanium resistor is used as a temperature sensor for its ability to retain calibration through many thermal cyclings and over long time periods. However, to span a wide temperature range and achieve low power dissipation in the sensor it is necessary to work with signal levels of a few hundreds of microvolts. The change in signal for a temperature change of 10% ranges from 20 to 80 microvolts. Therefore, achieving better than .1% precision in heat capacity measurement requires resolution of this signal to a few hundredths of a microvolt. Current is supplied to the sensor from a battery power supply and passes through one of several precision standard resistors. The potentials across the standard resistor and the sensor are brought into a six decade potentiometer with a resolution of ten nanovolts. The potentiometer has an internal switch matrix giving a read-out of the dial positions which are encoded by simple TTL circuitry and read by the computer as necessary. The galvanometer output from the potentiometer is amplified by a Keithly model 147 nanovolt null-detector and displayed on a strip recorder for visual monitoring of temperature drifts. The amplified signal is also filtered and digitized by a 3 1/2 digit D.V.M. for input to the computer. A real time clock, which is a string of cascaded TTL counters driven by a 1 MHz crystal oscillator, is read along with the potentiometer signal. Collected pairs of voltage, V, and time, t, are used to derive a best fit equation for V(t).

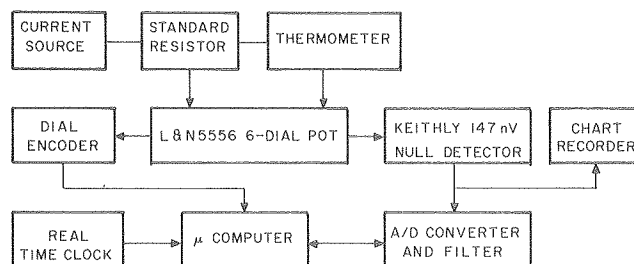


Fig. 1. Block diagram of temperature measurement subsystem. (XBL 7912-13694)

* This work was supported by the Division of Materials Sciences, Office of Basic Energy Sciences, U. S. Department of Energy.

The low signal levels mandate the careful handling of spurious effects such as thermal emf's and zero offsets generated in the circuit and accurate measurement of the signal gain. The measurements of these quantities are made by sending commands to the computer from a typewriter style keyboard which cause the computer to execute a sequence of steps which determine the desired quantity. For example, the operator enters a command consisting of the letter T followed by the return key. This informs the computer that it is to measure the thermal emf across the thermometer. The computer will then collect V and t measurements while deriving an equation $V_n(t)$ until the operator decides that enough data have been accumulated and presses the space key, telling the computer to enter a pause state. The operator then reverses the direction of the thermometer current and the thermometer potential leads. When the signal has settled, the operator presses the return key, signaling the computer to begin deriving $V_T(t)$. When the operator again decides enough data have been taken, the space key is again pressed at which point the computer calculates, displays and stores a thermal emf correction which is used to correct all measured thermometer voltages until the procedure is executed again. Zero offsets, gain and thermometer currents are handled in a similar fashion.

The energy control and measurement system is diagrammed in Fig. 2. Energy measurement is much simpler as the measured potentials are two to three orders of magnitude larger than those encountered during temperature measurement. Current is provided by a dc voltage standard and passes through a standard resistor and a resistance wire heater attached to the sample. The heater is switched on and off by a guarded low thermal relay under computer control. A separate 1 MHz driven counter is used to measure the heat pulse width. The computer reads the heater current and potential for each heat capacity point by multiplexing the potentials across the standard resistor and the heater through a H.P. 3455 D.V.M. operating in the high resolution mode. The measurement is enhanced by averaging multiple measurements of heater voltage and current. Introduction of energy, like other operations, is initiated and terminated by operator command through the keyboard. Measurement of the energy is, however, completely automatic.

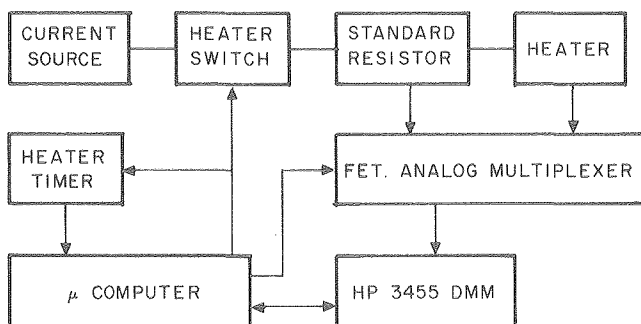


Fig. 2. Block diagram of energy control and measurement subsystem. (XBL 7912-13696)

The final section illustrated in Fig. 3 is the operator control system. The operator enters commands and data into the computer through a typewriter style keyboard. The computer displays output on a sixteen line by sixty-four character alphanumeric CRT. The display consists of updated values of important parameters as well as prompting signals denoting the status of operations in progress. A teletype printer provides printed listings of selected raw data as well as listings of processed results. An audio frequency based cassette tape provides program storage and also allows storage of raw data for reanalysis if desired.

The computer is based upon a computer hobbyist system called the S-100 buss. The memory consists of forty kilobytes of read-write memory and eight kilobytes of erasable read only memory. The read only memory contains an assembly language based operating system as well as the routines for extended precision arithmetic, number conversion, input-output routines, and an assortment of routines for linking the instrument interfaces to the computer. The read-write memory is used for both program and data storage. At present all programming is done in assembly language which, while somewhat inconvenient, offers maximum speed and flexibility.

The actual program used in taking heat capacities appears to the user as a command oriented language. The operator types a one- or two-character symbolic command followed by one or more arguments. In most cases, if a needed value of an argument is not given the last assigned value is used. The computer acts on these commands and prompts the operator where an outside action, such as changing the position of a switch, is required. An updated display of experimental parameters is maintained on the CRT. These parameters include initial and final as well as current values for thermometer current, potentiometer setting, temperature, value of the offnull signal, thermal emf, zero offset and sensitivity. Also displayed are the last value for heater current, potential, resistance, and pulse width. Available on command are values for many quantities such as total heat capacity, addenda heat capacity, their difference, fractional temperature change and a large number of other quantities.

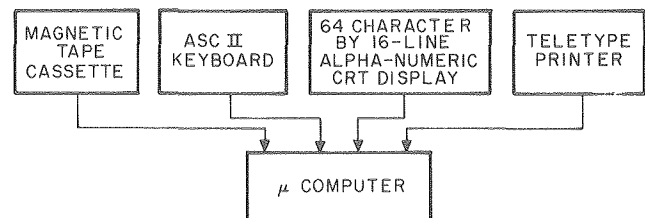


Fig. 3. Block diagram of operator control subsystem. (XBL 7912-13695)

Flexibility requires a large and versatile assortment of commands. Except for a few miscellaneous exceptions, commands fall into four major categories: data entry, control, computation, and output. In addition to the general purpose enter command, which assigns a specified value to any one of the named variables, there are commands which accept lists of values from the keyboard in specific formats for simpler operation. For example, one command accepts sequentially the coefficient of a polynomial to be subtracted from each heat capacity point. Another data entry command allows entry of alphanumeric data defining titles for listings and data files. The control group consists of the commands which initiate sequences of operations to measure quantities such as sensitivity, thermals, temperature drifts, and etc. This group also includes commands to control the heater circuitry. The computational group controls functions such as calculation of heat capacities, evaluation of polynomials, corrections for curvature, and etc. Output commands cause the computer to print lists of raw data, heat capacities, and quantities such as $(C-C_{addenda})/T$ and T^2 for plotting. A few miscellaneous commands control sampling rate, digital filtering, and dumping or retrieving data from cassette tape.

A description of the procedure followed in taking a single heat capacity point demonstrates the use of the system. Prior to a heat capacity point, parameters such as sensitivity, zero offset, and thermal emf's must be measured or defined. While sensitivity is very stable and varies little even from run to run, both zero offset and thermal emf's depend upon the experimental environment and change from point to point. In practice, the variation is slow enough so that measurement at every other point is usually sufficient. The thermometer current supply is not a true constant current source, therefore it is necessary to measure initial and final values for the thermometer current which varies with the resistance of the thermometer. The sequence of operations is then to measure the thermometer current, take an initial temperature drift, apply energy, take a final temperature drift after the system has settled into a steady state, and read the final thermometer current. A single command then initiates calculation of the heat capacity, stores the raw data and computed results in the appropriate file, and dumps selected raw data to the teletype.

The calculation of a heat capacity point involves computation of the thermometer resistance as a function of time from the potentiometer setting, $V(t)$, zero offset and thermal emf corrections, amplifier sensitivity, and thermometer current. Both the initial and final resistance as a function of time are linearly extrapolated into the center of the energy input period to derive an initial and final resistance. The initial and final resistances are converted to temperatures by third order Lagrangian interpolation of a dense table of temperatures derived from smoothing a set of calibration. The energy, computed as the product of the heater voltage, current, and pulse width divided by the temperature difference yields the uncorrected heat capacity. Corrections include subtraction of an addenda heat capacity, calculated by interpolation of another table, possibly subtraction of a poly-

nomial of up to twelve terms, and correction for curvature based on a Taylor series expansion of an assumed power law temperature dependence of the heat capacity. After collection of a set of heat capacity data, listings can be printed on the teletype for review.

The system has been in use for about one year and has met or exceeded all expectations. In addition to eliminating the long time lag between data collection and review of the results, the inevitable human errors in manual workup have been greatly reduced. Furthermore, the signal averaging inherent in digital sampling and curve fitting enhance the signal-to-noise ratio and results in a noticeable improvement in precision. Current work on the system is in refinement of the command structure and improvement in sampling techniques.

2. LOW-TEMPERATURE HEAT CAPACITY OF AuGd , A WEAKLY INTERACTING SPIN GLASS

W. E. Fogle and N. E. Phillips

Some time ago the effect of low concentrations of Gd in Au on the Kapitza resistance to ^3He was studied.¹ It was hoped that the indirect exchange interactions between the Gd ions via the RKKY mechanism would be weak enough so that the Gd ions would behave approximately as free spins and provide a mechanism for heat transfer by magnetic-dipole coupling to the ^3He nuclei as was believed to happen at the cerium magnesium nitrate - ^3He interface. Although there were no independent experimental data from which the Gd-Gd exchange interaction could be estimated the $\text{Au Gd} - ^3\text{He}$ Kapitza resistance did turn out to be anomalously low. Shortly thereafter heat capacity measurements were undertaken on AuGd to obtain an estimate of the strength of the Gd-Gd interaction. It was also expected that the results would be of interest in connection with general theories of the properties of spin glasses. The relatively well defined localized moments expected for 4f ions should be easier to treat theoretically than the virtual bound states that occur in the theory of solutions of 3d ions in noble metal hosts, the type of spin glass on which most measurements have been made to date. The measurements were made using germanium thermometers that had been calibrated only approximately below 0.3 K. A detailed analysis of the results was postponed until the results of the more accurate thermometer calibration that was recently completed were available. At this time the main features of the results can be given a qualitative interpretation but, as will be brought out in the following, there are significant crystal-field splittings that make a quantitative comparison with existing theories of spin glasses inappropriate.

Heat capacity measurements were made on "pure" Au and Au-Gd alloys with nominal Gd concentrations of 0.01, 0.05, and 0.2 at %, and from 0.07 K to

above 20 K. Heat capacity measurements on Cu on the same temperature scale show the expected $\gamma T + AT^3$ temperature dependence to the lowest temperatures, confirming the accuracy of the scale. The gold data show a 3% upturn at the lowest temperature which is therefore presumed to arise from magnetic impurities. In calculating the excess heat capacity associated with the Gd in the Au-Gd alloys the actual measured heat capacity of the Au, including that of the magnetic impurities, was subtracted. This is of course not really justified but the magnitude of associated errors is small.

The results are shown in Fig. 1 as the excess heat capacity (over that of pure Au), C , divided by the concentration of Gd in at %, c , vs $\log T/c$. The expected maximum in C is observed only for the most concentrated alloy, and at approximately 0.18 K. This characteristic "ordering temperature" is smaller than that of CuMn alloys by a factor of 25. From this result and from the magnitude of C one can obtain rough estimates of the strength of the local moment-conduction electron exchange interaction. It is, for example, a factor of 5 to 8 smaller than in CuMn. For the 0.01 and 0.05 at % samples the maximum occurs below the lowest temperature of the measurements.

When one attempts a more detailed comparison of the heat capacity with existing spin-glass theories substantial discrepancies become apparent. First, for sufficiently low concentrations the strength of the interaction varies as r_{ij}^{-3} where r_{ij} is the distance between two Gd ions. This leads to a "law of corresponding states" such that C/c should be a uni-

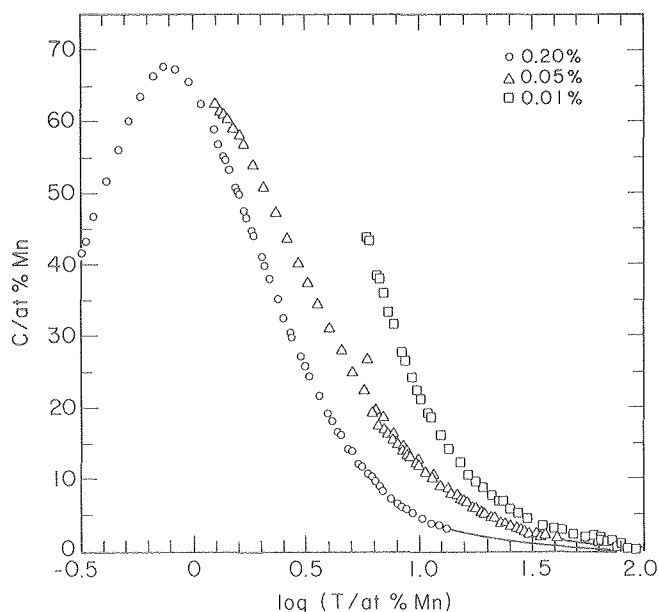


Fig. 1. The heat capacity of Au-Gd alloys in excess of that of pure Au, divided by the concentration, c , and plotted as a function of T divided by c . Units are mJ/mole of alloy - K for C , at % for c , and K for T .
(XBL 7912-13697)

versal function of T/c . Although exact agreement with this result has never been observed, the deviations shown in Fig. 1 are substantially greater than those found in other systems at comparable concentrations. Second, it also follows from the form of the RKKY interaction that in the high-temperature limit $C \propto T^{-1}$. In the high-temperature limit, the heat capacity of AuGd cannot be fitted by this temperature dependence, although it is observed in other systems for which the necessary data are available including, for example, CuMn. The quantitative discrepancies with spin glass theory are probably associated with crystal field effects. Although one expects a 8S state for the Gd^{+3} ion crystal field splittings can occur as a result of mixing with higher multiplets by the spin-spin interaction. Paramagnetic resonance data² on AuGd can be interpreted in terms of a zero-field splitting of the 8S state into a two-fold degenerate ground level with four-fold and two-fold degenerate excited levels at 0.033 and 0.088 K, respectively. The overall splitting is too small to cause a large error in the estimate of the strength of the exchange interaction mentioned above, but it seems very probable that it can account for the quantitative discrepancies with spin glass theory.

* * *

1. O. Avenal, M. P. Berglund, T. G. Gylling, N. E. Phillips, A. Vetleseter, and M. Vuorio, Phys. Rev. Lett. **31**, 76 (1973).
2. E. P. Chock, R. Chui, D. Davidov, R. Orbach, D. Shaltiel, and L. J. Tao, Phys. Rev. Lett. **27**, 582 (1971).

RESEARCH PLANS FOR CALENDAR YEAR 1980

Norman E. Phillips

We will continue to apply a major part of our effort to problems in very-low-temperature thermometry related to heat capacity measurements on ^3He . The new dilution refrigerator has been installed in a cryostat and has been used several times but so far it has not gone below 10 mK except in the "one-shot" mode. (The failure to meet specifications may be associated with limitations on the pumping speed that is available.) At this point we are developing apparatus of three kinds for attachment to the refrigerator: (1) for thermometer intercomparison, in particular to calibrate diluted CMN thermometers against nuclear orientation and nuclear susceptibility thermometers; (2) for heat capacity measurements on ^3He using a diluted CMN working thermometer; (3) for extending the temperature range of these measurements to below that of dilution refrigerator by adding a nuclear cooling stage.

Measurements of heat capacities under pressure had been discontinued while the on-line data reduction system described in article 1 above was being developed. Since these measurements depend on taking large numbers of data points with high precision and for a series of pressures they can now be made much more conveniently. Work on the pressure

dependence of the heat capacity of metallic Ce has been resumed.

The collaboration with Neil Bartlett's group on the heat capacities of intercalated graphites was

set back by the discovery of run-to-run irreproducibility in the measurements on a single sample. This has recently been shown to be associated with absorption of N_2 , and work on new samples will be continued.

b. Electrochemical Processes*

C. W. Tobias, Investigator

Introduction. The purpose of this program is to advance scientific methods for the analysis of scale-dependent cell processes and to provide means by which the design and operation of such processes may be optimized with respect to energy efficiency and capital cost. Physical description and quantitative characterization of transport of charged and uncharged specie to and from electrode surfaces by convective diffusion represent a core interest in this program. The analysis of high rate processes, such as electromachining and electroforming, is undertaken to point the way to new applications in electrometallurgy. A smaller part of this program is devoted to the exploration of electrochemical synthesis processes. Emphasis is placed on investigations in aprotic solvent systems which may be of potential use in galvanic cells, or in electrowinning or refining of reactive metals.

1. GAS-ELECTROLYTE-ELECTRODE INTERFACES--PRIMARY POTENTIAL AND CURRENT DISTRIBUTION AROUND A BUBBLE ON AN ELECTRODE†

Paul J. Sides and Charles W. Tobias

The effect of gas dispersed in an electrolyte on the effective conductivity can be predicted with satisfactory accuracy.¹ However, bubbles still attached to the electrode surface may cause a significant ohmic loss, especially in electrolysis at high current densities. As a first step toward developing a quantitative method for predicting this effect, we have solved the Laplace equation for a single dielectric sphere touching an equipotential plane when the field is linear at large distances from the plane. Tangent sphere coordinates were used, as described by Moon and Spencer² and an analytical solution was obtained following a development similar to that of Witze et al.³

The field around the bubble and the dimensionless current distribution on the plane electrode are shown in Figs. 1 and 2, respectively. Zero at the contact point, the current density reaches only 1% of its undisturbed value at 30% of the radius. A current density maximum exists somewhat beyond the area shadowed by the sphere, exceeding that at large distances. Since the current flowing to an area of $0.09 r^2$ is negligibly small, we can insulate this area with a surface coinciding with a surface of flow, and calculate the contact angle with which a nearly spherical bubble having this base area would meet the planar electrode. This angle is 17.5° . We conclude that at least for a primary distribution the effect of a tangent in-

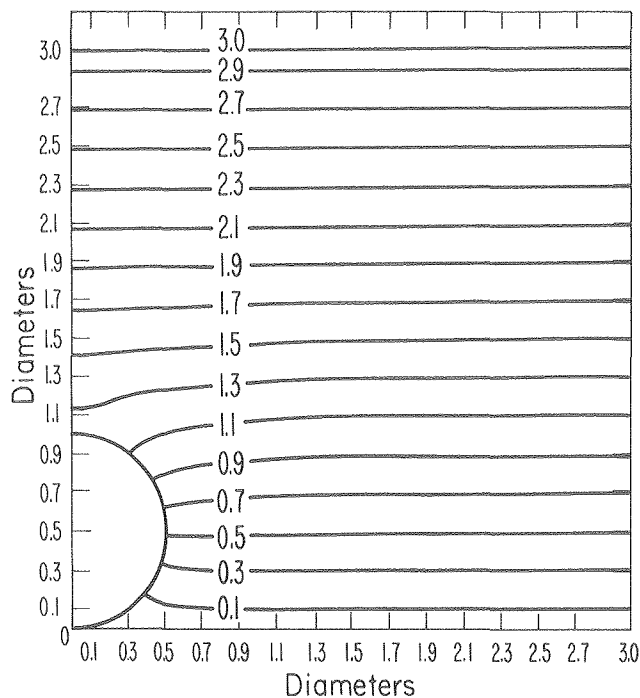


Fig. 1. Potential field around an insulating sphere tangent to an electrode. (XBL 793-997)

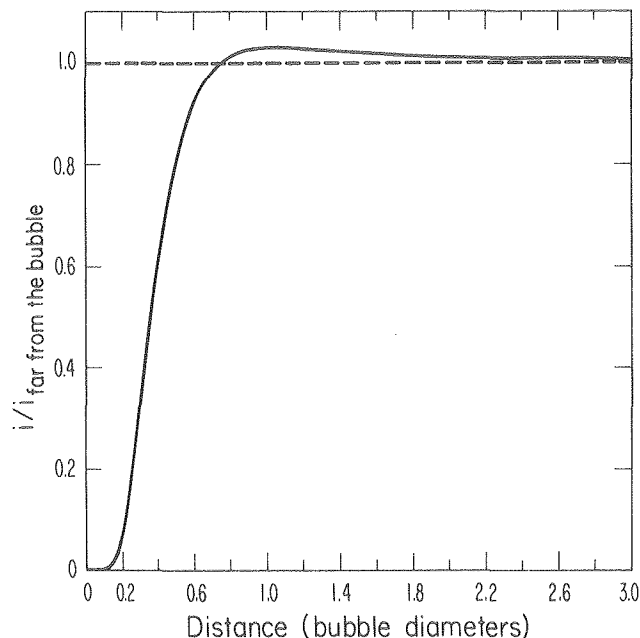


Fig. 2. Current distribution on an electrode around an insulating sphere. (XBL 793-998)

* This work was supported by the Division of Materials Sciences, Office of Basic Energy Sciences, U. S. Department of Energy.

ulating sphere well approximates that of a nearly spherical bubble having a base area less than $0.1 r^2$, and a contact angle less than 17.5° .

The effect of a single bubble on the ohmic drop to the electrode can now be evaluated. Dilute arrays of bubbles have negligible effect on the effective resistance between electrodes, but at high current densities ($> 0.5 \text{ amp/cm}^2$) bubbles are close to each other, and may form close-packed arrays on the surface. For the evaluation of the effective resistance of concentrated bubble arrays, there is no suitable analytical technique available. For this reason we are measuring the resistance of precise scaled-up geometric models that simulate a hexagonal planar array of spherical bubbles attached to an electrode surface. Results so far demonstrate that at low surface occupancy the well-known Maxwell relation may be used to predict effective resistance with reasonable accuracy, while at high surface coverage the resistivities somewhat exceed those predicted by the relation derived by Meredith and Tobias for three-dimensional quadratic arrays of dielectric spheres suspended in a conductor.¹

* * *

[†]Brief version of LBL-8745.

1. R. E. Meredith and C. W. Tobias, Advances in Electrochemistry and Electrochemical Engineering (Wiley, Interscience, New York, 1962), vol. 2, pp. 15-48.

2. P. Moon and D. E. Spencer, Field Theory Handbook (Springer-Verlag, Berlin, 1961), p. 104.

3. C. P. Witze, V. E. Schrock, and P. L. Chambre, Int. J. Heat Mass Transfer, **11**, 1637 (1968).

2. HIGH RATE ELECTROLYSIS PROCESSES--THE EFFECT OF SUSPENDED INERT PARTICLES ON LIMITING CURRENTS TO A ROTATING DISK

David Roha, Rolf H. Muller, and Charles W. Tobias

Ionic mass transport represents a serious limitation to achieving higher specific rates in electrolysis and galvanic cell processes. The presence of moderately large volume fractions of small, inert particles in the electrolyte has long been recognized as intensifying mass transport in forced flow.^{1,2} For a quantitative approach to evaluating the effect of the presence of suspended inerts, we employed a rotating disk electrode, which has very well understood hydrodynamic and mass transfer characteristics. Particle diameters investigated ranged from 0.2 - 250 micrometers. Limiting currents were measured for the reduction of ferric (0.04 M) to ferrous (0.2 M) cyanide in the presence of large excesses of NaOH (2 M). Volume fraction of inerts ranged from zero to 40%. Rotational speeds of up to 2870 rpm were employed, corresponding to velocity gradients of up to $52,000 \text{ sec}^{-1}$.

The increase of limiting current with rotational speed, and its dependence on volume fraction of inert particles in the 1 - 5 μm diameter range, is shown in Fig. 1. The enhancement of limiting

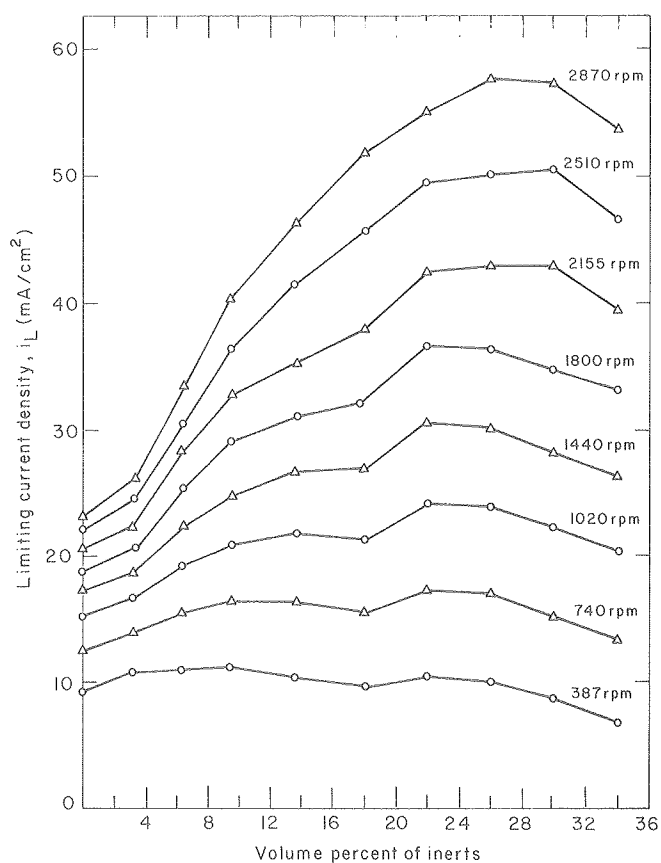


Fig. 1. Dependence of enhancement of mass transfer to a rotating disk electrode on the volume fraction of suspended inert particles. Size range of suspended glass spheres: 1-5 μm . Electrode reaction: reduction of ferric to ferrous cyanide in the presence of large excess of NaOH. Disk diameter: 2.82 cm.

(XBL 802-319)

currents relative to the clear solution depends not only on particle volume fraction, but also on rotational speed. Further, for each rpm, the enhancement factor reaches a maximum beyond which it declines with increasing volume fraction of inerts. This maximum is the more pronounced the higher the rpm and the larger the diameter of the disk. The dependence of limiting current on ω , the angular velocity, follows the general form:

$$i_L = A \cdot \omega^n$$

where A is a constant, and the exponent, $n = 0.5$ for clear solutions. As the particle concentration is increased, n approaches unity and the value of A, which depends on viscosity, decreases. We have found that the highest enhancement factor is obtained when the particle diameter is roughly the same as the thickness of the mass transfer boundary layer. Maximum enhancement factor, 3.6, was observed at 2870 rpm, using an average particle diameter of 8 microns.

* * *

1. D. C. Carbin and D. R. Gabe, *J. Appl. Electrochem.* **5**, 129 (1975).
 2. G. Kroysa, P. Piontek, and E. Heitz, *J. Appl. Electrochem.* **5**, 305 (1975).

3. RESEARCH LEADING TO NEW ELECTROCHEMICAL PROCESSES—ANODIC PROCESSES IN PROPYLENE CARBONATE[†]

Suen-Man G. Yu, Philip N. Ross, and Charles W. Tobias

Propylene carbonate, a solvent which demonstrates satisfactory stability in respect to strong reducing agents,¹ could serve as a medium for electrowinning of reactive metals from their simple salts, provided a suitable anodic reaction, e.g., liberation of a halogen, is possible without significant attack of the solvent. The possibility of direct decomposition of KCl to the metal and chlorine gas was chosen for investigation. The solvent from Jefferson Chemical Co. contains significant levels of various impurities, of which water, propylene oxide, and propylene glycols predominate. Following treatment with a 50-50 mixture of Linde type 13X and vacuum dried alumina, helium was bubbled through the solvent overnight. The solvent

was then distilled at 5 mm Hg pressure, and a head temperature below 65°C. The first 10 volume % and the last 30% were discarded. The middle fraction contained less than 2 ppm water, and less than 5 ppm propylene oxide; the other impurities were below the detection limit in the gas chromatograph. Contaminants in the solvent before and after purification are shown in Table 1.

The effect of contact with chlorine gas was evaluated both with simply bubbling the gas through the solvent, and also by anodically generating chlorine, in two different electrolysis cells. In cell no. 1, the anode and cathode compartments were not separated. In cell no. 2, a Nafion #425 membrane separated the two compartments, each containing 15 cc electrolyte. Aliquot samples (2 μliters each) were taken through an airtight rubber septum by means of a syringe. Sample analytical results are shown in Table 1.

It is noteworthy that the attack on the solvent slows down considerably after the initial period of rapid attack. Additions of up to 10 ppm water initially to the solvent resulted in increased rate of attack, but virtually the same decomposition contents after 2 - 10 hours, as was observed without water addition. It is likely that 2 - 3 ppm water present in the purified solvent has a major role in the decomposition mechanism, as a source of protons upon reaction with chlorine.

Table 1. Contaminants in propylene carbonate before and after purification treatment.

| Impurity/decomposition product (concentrations in ppm) | Before After purification | Following electrolytic generation of Cl ₂ ^a | | |
|---|--|--|-------------------|-------------------|
| | | 1 min | 2 hrs | > 12 hrs |
| Water H ₂ O | 10 ³ -10 ⁴ < 3 | < 3 | < 3 | < 3 |
| 1,2 and 1,3 Propylene (1,2) glycol CH ₃ -CH(OH)-CH ₂ (OH) | ~2×10 ⁴ < 1 | 150 | 2×10 ⁴ | 5×10 ⁴ |
| (1,3) CH ₂ (OH)-CH ₂ -CH ₂ (OH) | | | | |
| Propylene oxide CH ₃ -CH(O)-CH ₂ | 500 < 5 | 25 | 2×10 ⁴ | 5×10 ⁴ |
| Allyl alcohol H ₂ C=CH-CH ₂ -OH | 200 < 1 | < 10 | 500 | 1000 |
| Propionaldehyde CH ₃ -CH ₂ -C(=O)H | 200 < 1 | 30 | 1000 | 1000 |
| Acetone CH ₃ -C(=O)-CH ₃ | < 100 < 1 | | | |
| Formaldehyde HCHO | < 1000 < 1 | | | not measured |
| CO ₂ CO ₂ | negligible | | | not measured |

^aResults presented here were obtained in an H-type cell; anolyte and catholyte were separated by a Nafion # 425 membrane. 0.5 M KAlCl₄ electrolyte. Figures refer to changes in composition in the anode compartment. The composition in the cathode compartment, where potassium was deposited, remained unchanged, corresponding to the "purified" solvent.

A likely mechanism that could lead to the appearance of the degradation products is illustrated in Fig. 1. Water has an autocatalytic role in

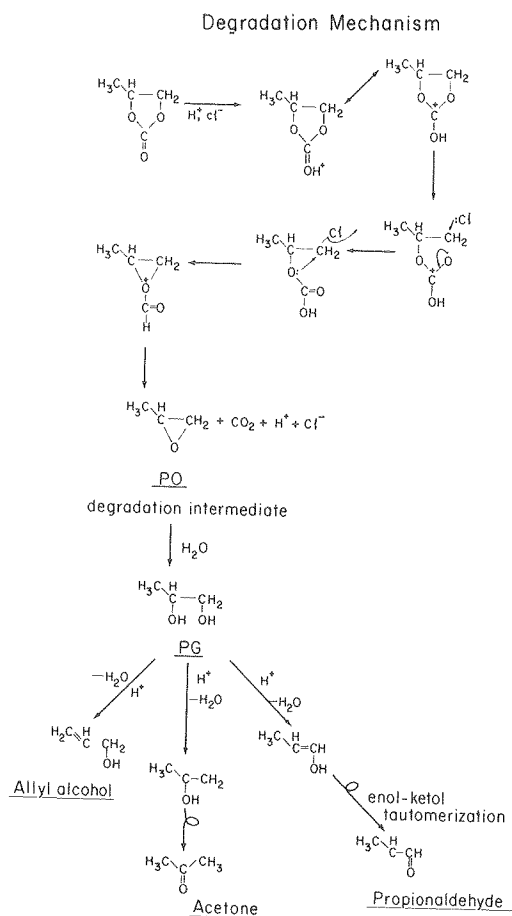


Fig. 1. Proposed mechanism for the degradation of propylene carbonate contaminated with water, upon saturating it with chlorine gas. (XBL 799-4255)

this decomposition process, and it remains to be established whether reduction of water content by a factor of 10 - 100 could stabilize the solvent in the presence of elemental chlorine. As confirmed by gas chromatographic analysis of the catholyte, and by the undisturbed progress of the potassium deposition process, Nafion membranes effectively confine the dissolved chlorine, as well as the degradation products, to the anode chamber.

* * *

†Brief version of LBL-10069.

1. Henry H. Law, "Studies on the Electrochemical Behavior of Potassium in Propylene Carbonate," Ph.D. thesis, LBL-1111, May 1979.

1. Fundamental Studies of Mass Transport Phenomena in Electrochemical Cells

Studies of Events Occurring at Gas-Evolving Electrodes. Measurements of incremental resistances offered by single- and multilayered dielectric spheres on electrode surfaces will be completed, and the effective resistance will be correlated as a function of volume fraction and of void structure. A cell for measurement of resistance of actual gas bubble layers, already constructed, will be employed to measure differential resistance by the interruptor technique. Work is continuing on the high speed cinematographic study of gas evolution on transparent and metal electrodes.

High Rate Electrolysis Processes. After completing measurements of the effect of suspended particles on the thinning of mass transfer boundary layers at rotating disk electrodes, results will be correlated, taking into consideration the basic mechanism by which suspended particles interact with the boundary layer. Studies on high-rate anodic dissolution of refractory compounds will include those of tungsten. The nature of the anion used, and the type of binder present in the work piece, as they affect dissolution stoichiometry and surface roughness, will receive special emphasis.

2. Anodic Processes in Propylene Carbonate

For the electrolytic decomposition of alkali halides in propylene carbonate, the major stumbling block is the anodic reaction, because chlorine and bromine attack the solvent. A double membrane scheme will be evaluated, in which the anodic process will occur in aqueous solution, while the cathodic process--the deposition of alkali metal--will proceed in propylene carbonate. A central compartment containing propylene carbonate will be separated from the anode and cathode chambers by an anion and a cation exchange membrane, respectively. In addition, the electrolyte in the central compartment will be continuously dehydrated through an external reprocessing loop. This scheme, if it proves feasible, could have applications in electroorganic synthesis processes as well.

1979 PUBLICATIONS AND REPORTS

Refereed Journals

1. Frank R. McLarnon, Rolf H. Muller, and Charles W. Tobias, "Interferometric Study of Forced Convection Mass Transfer Boundary Layers in Laminar Channel Flow," *I&EC Fundamentals* **18**, 97-108 (1979).

Other Publications

†1. Milan Jaksic and Charles W. Tobias, "Hydrodynamics Flow Visualization by the Electrochemical Method," Extended Abstracts, 6th Yugoslav Symposium on Electrochemistry, Dubrovnik, June 1979.

2. Paul J. Sides and Charles W. Tobias, "Primary Current and Potential Distribution Around a Bubble on an Electrode," Extended Abstracts, vol. 79-2, Electrochemical Society, October 1979.

[†]3. Geoffrey A. Prentice and Charles W. Tobias, "Simulation of Electrode Profiles Undergoing Deposition or Dissolution," Extended Abstracts, vol. 79-2, Electrochemical Society, October 1979.

[‡]4. Peter C. Foller, "The Kinetics and Mechanism of the Evolution of Ozone by the Anodic Oxidation of Water," Ph.D. thesis (with C. W. Tobias), University of California, Berkeley, November 1979.

LBL Reports

1. J. B. Riggs, R. H. Muller, and C. W. Tobias, "A Model for Prediction of Work Piece Geometry for Electrochemical Hole Sinking," submitted to Electrochim. Acta, LBL-6282 Preprint, Rev., December 1979.

2. Paul J. Sides and Charles W. Tobias, "Primary Potential and Current Distribution Around a Bubble on an Electrode," accepted for publication in the Journal of the Electrochemical Society, LBL-8745 Preprint, March 1979.

3. Karrie Jo Hanson, "Interferometric Study of Mass Transfer Enhancement by Turbulence Promoters," M. S. thesis (co-directed with R. H. Muller), LBL-9038, April 1979.

[†]4. Henry H. Law, "Studies on the Electrochemical Behavior of Potassium in Propylene Carbonate" (Ph.D. dissertation) LBL-9207, May 1979.

5. John F. Cooper, Rolf H. Muller, and Charles W. Tobias, "Periodic Phenomena During Anodic Dissolution of Copper at High Current Densities," submitted to J. Electrochem. Soc., LBL-9404 Preprint, Rev., December 1979.

6. Suen-Man G. Yu, Philip N. Ross, and Charles W. Tobias, "An Investigation of the Degradation of Propylene Carbonate by Chlorine," LBL-10069, November 1979.

Invited Lectures

1. Charles W. Tobias, "A Close Look at Electrolytic Gas Evolution," Symposium on Electrochemical Reaction Engineering, sponsored by the Society of Chemical the Industry and the Institution of Chemical Engineers, University of Southampton, England, April 18-20, 1979.

2. Charles W. Tobias, "Gas Evolution at Electrodes," Bell Laboratories, Murray Hill, New Jersey, May 4, 1979.

[†]3. Milan Jaksic and Charles W. Tobias, "Hydrodynamic Flow Visualization by the Electrochemical Method," 6th Yugoslav Symposium on Electrochemistry, Dubrovnik, June 1979.

4. Paul J. Sides and Charles W. Tobias, "Primary Potential and Current Distribution Around a Bubble on an Electrode," paper presented at 156th Meeting of the Electrochemical Society, Los Angeles, October 14-19, 1979.

[†]5. Geoffrey A. Prentice and Charles W. Tobias, "Simulation of Electrode Profiles Undergoing Deposition or Dissolution," paper presented at 156th Meeting of the Electrochemical Society, Los Angeles, October 14-19, 1979.

* * *

[†]Supported by the Division of Solar, Geothermal, Electric and Storage Systems, Office of Energy Technology, U. S. Department of Energy.

[‡]Supported entirely from University funds.

2. High-Temperature and Surface Chemistry

a. High-Temperature Thermodynamics*

Leo Brewer, Investigator

1. HIGH-TEMPERATURE SOLID-ELECTROLYTE ELECTRO-MOTIVE CELL MEASUREMENTS OF GENERALIZED-LEWIS-ACID-BASE INTERACTIONS IN BINARY TRANSITION METAL ALLOYS[†]

D. Goodman and D. Davis

Work was carried out this past year on electro-motive cells using a variety of electrolytes made from ZrO_2 , HfO_2 , and ThO_2 using CaO and Y_2O_3 doping to increase oxygen anion conductivity. The electrodes are made of mixtures of Ta_2O_5 with tantalum-iridium alloys and mixtures of Nb_2O_5 and niobium-palladium alloys combined with various standard electrodes. As the phase diagrams of some of these systems are incompletely known, the phase relations of these systems and a number of related systems are being investigated in a gradient furnace. Such a furnace, which is designed to obtain a steep temperature gradient along the length of the furnace, is being used to fix the temperature range of stability for a number of the high-temperature phases of transition metal systems.

* * *

[†]Brief version of LBL-7691.

2. HIGH-TEMPERATURE GASEOUS EQUILIBRIA MEASUREMENTS OF GENERALIZED-LEWIS-ACID-BASE INTERACTIONS IN BINARY TRANSITION METAL ALLOYS

B.-J. Lin, D. Davis, J. Gibson and K. Miller

Equilibration of water-hydrogen mixtures with the electrode materials is a useful method of obtaining thermodynamic data for some of the systems that are being studied using Solid-Electrolyte Electrochemical Cells. This work has been carried out using a thermal balance provided by Professor J. W. Evans. As a given gaseous mixture of water and hydrogen is passed over a mixture of Nb_2O_5 and a niobium-palladium alloy, variation of temperature causes a change from weight loss to weight gain. This procedure brackets the equilibrium constant for the formation of the alloy by reduction of the oxide by hydrogen. As the thermodynamic data are known for water and for the oxide, the thermodynamic data for the alloy can be fixed.

Additional values are being obtained by equilibrating mixtures of oxides such as Nb_2O_5 and NbO_2 with an alloy of niobium and palladium. Diffusion couples also provide equilibrium phase boundaries that provide additional thermodynamic data.

3. CRITICAL EVALUATION AND COMPILATION OF HIGH-TEMPERATURE THERMODYNAMIC DATA[†]

L. Brewer and R. Lamoreaux

After an effort covering many years, a major milestone has been the completion of a tabulation of the thermodynamic data, diffusion constants, and phase diagrams for 100 binary systems of molybdenum. Our contributions will constitute three chapters of Special Issue No. 7: Molybdenum (Atomic Energy Review Special Issue on Molybdenum, Physicochemical Properties of its Alloys and Compounds: Vienna) which is currently scheduled to be published in December 1979. This achievement is noteworthy not only because of its value to scientists and engineers who will need the properties of molybdenum and its compounds for the design of high-temperature systems, but because it also constitutes an important theoretical advance in that it has been demonstrated that bonding models are now available which can predict practical thermodynamic values for metallic systems. These values can then be used to calculate phase diagram boundaries within practical accuracy ranges.

* * *

[†]Brief version of "Principles of Critical Evaluation and Compilation of Phase Diagrams and Thermodynamic Data," in Proceedings of the TMS-AIME Symposium on Calculation of Phase Diagrams and Thermochemistry of Alloy Phases, Milwaukee, Wisconsin, September 17-18, 1979.

4. STABILITIES OF HOMONUCLEAR DIATOMIC MOLECULES[†]

L. Brewer and J. Winn

The bonding models that have proved to be so useful in predicting the thermodynamic properties of condensed metallic systems have also been found to be capable of predicting thermodynamic data for gaseous molecules. This is of particular importance for the understanding of chemical behavior of materials ranging from gaseous atoms and diatomic molecules through metallic clusters to the bulk metals. In contrast to the solid phases for which elements such as Mg, Al, and Si

* This work was supported by the Division of Materials Sciences, Office of Basic Energy Sciences, U. S. Department of Energy.

promote from s^2p^{n-2} ground atomic states to sp^{n-1} valence states, thus increasing the number of electrons used in bonding, the calculations indicate that the bonding in diatomic non-transition gaseous molecules is not sufficient to offset the promotion energies, and thus that not all of the valence electrons are available for bonding.

The alkaline earths provide a particularly dramatic contrast in that the diatomic molecules are weakly bound with bonding energies comparable to those of the diatomic noble gases. In fact, it has been demonstrated that magnesium vapor will behave as a permanent noble gas at room temperature in a container coated with hydrocarbons to prevent nucleation of metallic crystals.¹ John Winn will discuss the alkaline earth dimers in more detail in his section.

The transition metals are found to be intermediate in behavior with some promoting to the same valence states as in the solid metal while others, particularly to the right of the transition series, promote to a smaller extent than in the solid metal. Values of the dissociation energies have been calculated for all diatomic molecules for which no data were available. A complete set of values for all elements from hydrogen to lawrencium will be published in December 1979 as a preprint for the Faraday Society Discussion to be held in England in January 1980.

* * *

[†]Brief version of LBL-9690.

1. L. B. Knight, Jr., R. D. Brittain, M. Duncan and C. H. Joyner, "Unusual Behavior of Vaporized Magnesium under Low Pressure Conditions," *J. Phys. Chem.* 79 (12), 1183 (1975).

5. TERNARY PHASE EQUILIBRIA OF A-B-X SYSTEMS WITH X+B, C, N, AND O.

D. Goodman, D. Davis, J. Gibson, and K. Miller

Previous studies of ternary diagrams of this type by our group have demonstrated that valuable thermodynamic data can be obtained that are difficult to obtain by other techniques.¹ In previous work A was zirconium and B was one of the elements in the series ruthenium to silver or rhenium to gold. This work is now being extended to titanium, niobium, and tantalum for the A elements with the same group of B elements. This work is being carried out in the graphite tube furnace that we have been using in previous studies up to 3200K. The principal aim of this work is to characterize strong Generalized-Lewis-Acid-Base interactions between transition metals with unused orbitals and the platinum group metals.

* * *

1. P. R. Wengert and L. Brewer, "Transition Metal Alloys of Extraordinary Stability: An Example of Generalized-Lewis-Acid-Base Interactions in Metallic Systems," *Met. Trans.* 4, 83 (1973).

RESEARCH PLANS FOR CALENDAR YEAR 1980

The very strong interactions of transition metals of the left-hand side of the Periodic Table, which have unused d orbitals, with platinum group metals, which have non-bonding pairs of electrons, constitute a challenge to bonding models to provide a quantitative prediction of the extraordinary stability of the resulting intermetallic compounds. These Generalized-Lewis-Acid-Base interactions bring about many surprising and unexpected chemical reactions.

A three-fold attack on this problem will be continued to provide a check on the reliability of the various methods. High-temperature solid-electrolyte electromotive cell measurements on the tantalum-iridium and niobium-palladium systems will be checked by thermal balance determinations of water-hydrogen equilibrium and by ternary phase equilibrium involving interstitial elements such as boron, carbon, nitrogen, and oxygen.

Additional checks on the bonding models will be made using thermal gradient furnaces and diffusion couples to fix the temperature ranges of stability of phases undergoing peritectic reactions. A new project will be initiated to obtain experimental tests of the predictions of bonding models on the solute stabilization of the bcc and hcp phases of Ti, Zr, and Hf. The initial studies will involve the transition metals from the fifth group of the Periodic Table through Cu, Ag, and Au. All of these metals, which have bcc, hcp and fcc structures, are predicted by the Engel model to stabilize the bcc structures of Ti, Zr, and Hf because of their d electron bonding. The available data show no contradictions to the predictions of the model. All missing experimental results will be obtained to determine if the predictions of the model will continue to be 100% reliable. These studies will mainly cover the range of temperatures of 700 to 2000°C although some measurements may be extended to higher temperatures.

With the completion of the molybdenum monograph, compilation efforts will be reduced to a small fraction of our effort. However, some collaboration will continue with the JANAF Tables and a joint project with Stanford Research Institute dealing with thermodynamic properties of vaporizing oxide systems at high temperatures is under consideration.

1979 PUBLICATIONS AND REPORTS

Refereed Journals

1. K. Pitzer and L. Brewer, "Simplification of Thermodynamic Calculations Through Dimensionless Entropies," *High Temp. Sci.* 11(1), 49 (1979).

2. K. Pitzer and L. Brewer, "Simplification of Thermodynamic Calculations Through Dimensionless Entropies," *J. Phys.-Chem. Ref. Data* 8(3), 917 (1979).

3. L. Brewer and L. Hagan, "The Oscillator Strength of the C₂ Swan Bands," *High Temp. Sci.* 11, 233 (1979).

4. G. Rosenblatt, "Estimation of Activity Coefficients in Concentrated Sulfite-Sulfate Solutions," LBL-9671, submitted to *AIChE*.

5. B. Meyer, M. Ospina, and L. Peter, "Raman Spectrometric Determination of Oxysulfur Anions in Aqueous Systems," LBL-9974, submitted to *Anal. Chem. Acta*.

Other Publications

1. Leo Brewer, "Bibliography on the High-Temperature Chemistry and Physics of Materials, Vol. 22, Part 2, Gases: (A) Spectroscopy of Interest to High-Temperature Chemistry, and (B) Reactions Between Gases and Condensed Phases," published by IUPAC Commission on High Temperatures and Refractory Materials, edited by M. G. Hocking and V. Vasantasree, London, 1979.

2. Leo Brewer, "Development of a Critical Data Base," High-Energy Workshop, Reston, Virginia, March 16-21, 1979, contributed to book Report on High-Temperature Science, Chapter 8.

3. L. Brewer, "Principles of Critical Evaluation and Compilation of Phase Diagrams and Thermodynamic Data," in Proceedings of the TMS-AIME Symposium on Calculation of Phase Diagrams and Thermochemistry of Alloy Phases, edited by Y. A. Chang and J. F. Smith, Milwaukee, Wisconsin, September 17-18, 1979.

Papers Presented

1. J. Winn and L. Brewer, "Models for Calculation of Dissociation Energies of Homonuclear Diatomic Models," Faraday Society Meeting, England, January 1980, LBL-9690.

2. Leo Brewer, Seminar entitled "Prediction of Structure and Thermodynamic Properties of Metals," Stanford University, January 26, 1979.

3. Leo Brewer, "High Temperature Science and Technology," Bay Area High-Temperature Conference, Ames Research Center, Moffett Field, California, March 8, 1979.

4. Leo Brewer, "CaO/SO₂/H₂ System," Flue Gas Desulfurization Meeting, Morgantown, Virginia, June 7-8, 1979.

5. Leo Brewer, Symposium on "Present and Future Energy Demands on Thermodynamics," Richland, Washington, June 13-15, 1979.

6. Leo Brewer, Basic Energy Sciences (BES) Committee, Ames, Iowa, June 20-22, 1979.

7. Leo Brewer, High-Temperature Materials for Energy Production Meeting, Toronto, Canada, July 16-19, 1979.

8. Leo Brewer, Special Lecture Series: Oak Ridge, Tennessee, September 10-14, 1979:

- (a) "Electrons, the Universal Glue"
- (b) "Thermodynamics of Redwood Trees and Metals"
- (c) "Metals as Acids and Bases"
- (d) "Calculation of Binary Phase Diagrams from Thermodynamic Data and Vice-Versa"
- (e) "Prediction of High-Temperature Multi-component Phase Diagrams"
- (f) "What are the Odds That We Can Resolve the Energy Crisis?"

9. Leo Brewer, (presented by R. Lamoreaux), "Evaluation and Prediction of Binary Phase Diagrams of Molybdenum with the Other Elements," Lawrence Livermore Laboratory, Livermore, California, October 11, 1979.

10. Leo Brewer, Basic Energy Sciences (BES) Committee, Livermore, California, December 3-4, 1979.

b. Chemistry and Materials Problems in Energy Production Technologies*

D. R. Olander, Investigator

1. BUBBLE MIGRATION IN STRESS GRADIENTS[†]

D. R. Olander

During irradiation in a nuclear reactor, the gaseous fission products xenon and krypton precipitate as tiny bubbles in the oxide fuel. The presence of these bubbles causes the fuel to expand against the cladding, which can thereby fail by creep-rupture. Alternatively, if the fission gas bubbles are released from the fuel, the liberated gas internally pressurizes the fuel rod and constitutes a source of highly mobile radioactivity in the event of an accident which breaches the cladding. Prediction of gas release rates, which requires knowledge of the mechanisms of bubble mobility, is therefore of direct practical significance. The release mechanism based upon bubble migration in the temperature gradient in the fuel is well established, but the possibility of bubble migration in a stress gradient (which also exists in the fuel rod) has not been satisfactorily resolved theoretically.

The velocity of biased migration of bubbles due to temperature and stress gradients in the host solid can be computed by "global" or "local" methods. The former technique determines the change in system free energy as the bubble is displaced in the direction of the potential gradient, which is equivalent to calculation of the force on the bubble. Application of the Nernst-Einstein equation then yields the velocity. In the local method of analysis, the distribution of the temperature or stress on the bubble surface is calculated from the equations of heat conduction and elasticity theory for a specified distribution of these potentials far from the bubble. The surface atom flows are then determined from the flux equation which consists of a term containing the gradient of the chemical potential of atoms on the surface and one involving the surface Soret effect arising from the local temperature gradient. Stress gradients induce surface atom flows via the former term, and a connection between stress and chemical potential of a solid surface has to be established. Most analyses requiring such a relationship have incorrectly replaced the pV term of fluid thermodynamics with σV , where σ is a single measure of the stress (e.g., mean normal stress or uniaxial stress). However, Gibbs' original investigation of this subject showed that the stress effect is contained in second order terms such as the strain energy, which is $\sim \sigma^2 V/E$, and hence is only $\sigma/E \approx 10^{-3}$ of σV (E is Young's modulus). The chemical potential of atoms in a solid surface includes a surface energy component, which Gibbs also treated. Stress variations on the surface of a bubble cause corresponding chemical potential

variations via the stress dependence of the solid atomic volume and elastic energy and by deviations from spherical shape, which activates the surface tension component of the chemical potential. The surface flows are converted to a surface normal velocity which, when expanded in spherical harmonics, contains terms identified with volume change, translation, and distortion.

Application of the analysis to a spherical bubble in vacancy equilibrium with the uniform hydrostatic stress component in the solid shows that a stress gradient cannot cause bubble motion. If the bubble can exchange vacancies with the host solid, additional contributions to the bubble migration velocity appear. The nonuniform temperature or stress distributions far from the bubble set up nonuniform vacancy concentration distributions in the solid around the bubble. The vacancy flows to the bubble in such a field are nonuniform as well, and hence lead to bubble translation and distortion in addition to growth. The nonuniform bulk vacancy concentration also causes motion of the entire body containing the bubble, and careful attention must be paid to the proper frame of reference in determining bubble velocities when lattice vacancies are mobile.

In addition, the local method of analysis can be applied to calculate the distortion of a bubble in a deviatoric stress state. This calculation is based on the requirement of uniform chemical potential of the solid atoms everywhere on the bubble surface. In the case of a bubble in a solid subjected to uniform uniaxial stress, the distortion is found to be small.

The final application of the local analysis method is to a faceted bubble. Motion of such a cavity is controlled by the rate of nucleation of atomic ledges on the facets. A potential gradient affects motion by altering the nucleation free energy barrier on the facets at opposite ends of the bubble along the direction of the potential gradient. However, a faceted bubble is not driven by a stress gradient if the bubble is in vacancy equilibrium with the spatially uniform hydrostatic portion of the external stress field. The magnitude of the velocity of a non-equilibrium faceted bubble in a stress gradient is very much smaller than that achievable by a practical temperature gradient in a ceramic such as UO_2 .

* * *

[†]Brief version of LBL-9739.

2. SOLUBILITY AND DIFFUSION OF RUTHENIUM IN UO_2

Rosa Yang and D. R. Olander

Ruthenium is one of several noble metals which have significant fission yields in nuclear reactor

* This work was supported by the Division of Materials Sciences, Office of Basic Energy Sciences, U.S. Department of Energy.

fuels. The chemical and physical behavior of this group of fission products has a strong influence on the performance of the fuel during irradiation. Although ruthenium is a noble metal, the great stability of the Brewer-type intermetallic compound URu_3 can render ruthenium reactive towards UO_2 . This chemical reactivity, which is accompanied by significant mobility, was demonstrated by the following experiments.

A thin layer of powdered ruthenium metal was placed between two UO_2 wafers, the assembly encapsulated in a refractory metal crucible, and annealed at $\sim 2000^\circ\text{C}$ in a hydrogen-containing gaseous atmosphere. After annealing for about 20 hours, the sample was cut in a direction perpendicular to the plane of the ruthenium powders. Figure 1 shows a photomicrograph of a section of the UO_2 cut surface about $300\ \mu\text{m}$ away from the interface. The grain boundaries are seen to be decorated with a metallic phase (white) which electron microprobe analysis showed to contain only uranium and ruthenium. No ruthenium was detected within the UO_2 grains. An additional experiment was conducted to determine whether the ruthenium particles migrated as entities or whether the mechanism was one of solution of ruthenium in the UO_2 followed by diffusion in atomic form, and precipitation as URu_3 particles upon cooldown. To clarify this point, the ruthenium powder was replaced by a massive ruthenium disk. After a high temperature anneal, essentially the same type of ruthenium migration as shown in Fig. 1 was observed. Since the ruthenium disk could not break up into small particles, we concluded that ruthenium dissolves in UO_2 and migrates as atoms.

The next question to be answered was whether the diffusion process occurred via the grain boundaries or the UO_2 crystal lattice. For this test, ruthenium powder was placed between two UO_2 single crystal wafers and the assembly was annealed.

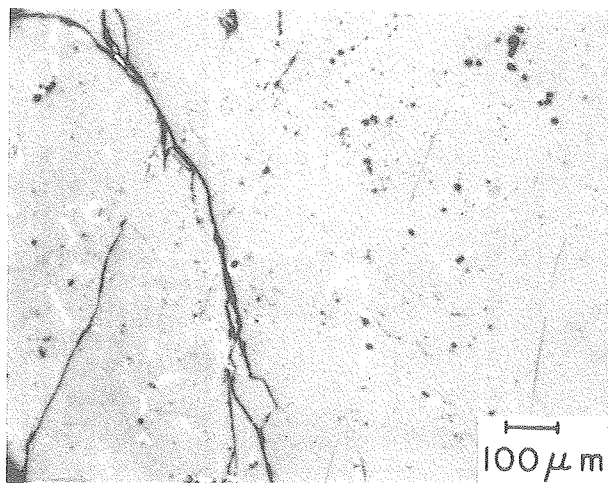


Fig. 1. Ruthenium precipitates outlining UO_2 grain boundaries after isothermal annealing at 2250°C for 31 hr; tungsten capsule, $\text{H}_2(4\%)\text{-Ar}(96\%)$ atmosphere; interface of powdered Ru metal located $200\ \mu\text{m}$ to the left of the photomicrograph.

(XBB 802-2016)

Post-anneal microscopy revealed that essentially no ruthenium had penetrated the UO_2 single crystals, which demonstrates that the dissolution and diffusion process occurs through the grain boundaries of the UO_2 .

In order to obtain quantitative information on the solubility and diffusion coefficient of ruthenium in the grain boundaries of UO_2 , an annealed specimen was polished parallel to the interface. Approximately $100\ \mu\text{m}$ thick layers were ground off at a time and the ruthenium-to-uranium ratio of the exposed surface was determined after each polishing step by x-ray fluorescence. The resulting data, illustrated in Fig. 2, was fitted to the solution of Fick's second law appropriate to the geometry of the experiment. The curve drawn through the data points in Fig. 2 shows the best fit, which simultaneously produces values of the solubility (the maximum of the curve times a calibration factor) and the diffusion coefficient. The excellent fit of a diffusion model to the data further substantiates the assumption of a diffusion-controlled migration process.

The solubilities and diffusivities of ruthenium in UO_2 determined as described above were found to be strongly dependent upon the crucible used to contain the specimen during the anneal; both the solubility and the diffusion coefficient were much larger when the crucible was molybdenum than when tungsten was used. The most reasonable

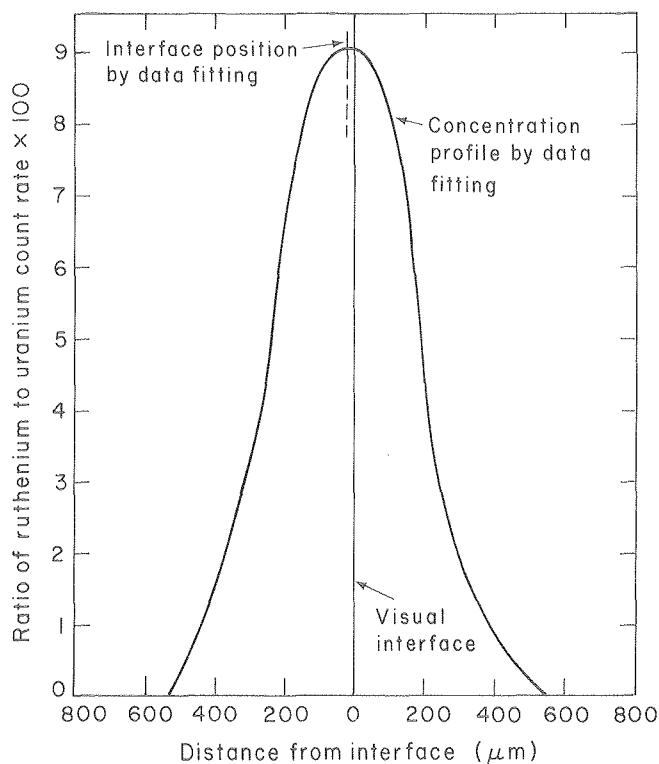
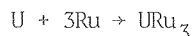


Fig. 2. Ruthenium concentration profile for the conditions of Fig. 1. Data fitted to diffusion using MINUIT with three adjustable parameters; diffusion coefficient, Ru solubility in UO_2 (i.e., the maximum of the profile times calibration factor) and the interface location. (XBL 802-268)

explanation of this behavior is that these properties of the Ru/UO₂ interaction are strongly dependent on the stoichiometry of the urania. At high temperatures, molybdenum is more permeable to oxygen than is tungsten, and in the former crucible, the urania is more easily reduced by the hydrogen-containing gas in which the anneal is conducted. Since the activity of uranium is higher in hypostoichiometric urania (UO_{2-x}) than in stoichiometric or hyperstoichiometric material, the reaction:



is enhanced in reduced urania and greater ruthenium solubilities should be observed.

3. THERMAL GRADIENT BRINE INCLUSION MIGRATION IN SALT^{††}

D. R. Olander, M. Balooch, A. J. Machiels and S. K. Yagnik

Natural salt deposits contain small cubical inclusions of brine distributed through the salt. Temperature gradients, resulting from storing heat-generating nuclear wastes in the salt, can cause the inclusions to move through the salt. Prediction of the rate and amount of brine-inclusion migration is necessary for the evaluation of bedded or domed salts as possible media for nuclear waste repositories.

An experimental investigation of the migration velocity of all-liquid brine inclusions in single crystal NaCl has been conducted. The inclusion velocity was measured as a function of inclusion size, temperature and applied temperature gradient. The mechanism involves the solution at hot face, diffusion across the liquid, and deposition on the cold face.

All liquid inclusions were produced by drilling a 0.3 mm diameter by 3 mm deep hole in an end (100) face of a 15 × 5 × 5 mm NaCl or KCl crystal. The hole was filled with deionized water and the crystal was sandwiched between two copper blocks (which also served to generate the temperature gradient field). By applying a temperature gradient of about 30°C/cm for two to five days, all liquid inclusions with a size distribution ranging from 7 to 150 μm could be produced. It has been suggested that migration velocities (and the pinning of small inclusions) can be the result of dislocation interaction with the inclusion. Therefore, one would suspect that drilling a hole directly into the crystal would increase the dislocation density with respect to as-fabricated crystal. To avoid this problem, a sample was cleaved. One cleaved face was drilled and filled with liquid and then sandwiched with the other half prior to applying the temperature gradient. In this way the inclusions were formed in the drilled half and, by the temperature gradient, moved to the fresh half. The results showed no observable change in the migration rate of these inclusions with respect to earlier results.

By applying temperature gradients in the [100]

direction, the larger inclusions flattened in a plane perpendicular to the thermal gradient and assumed the form of thin square platelets (See Fig. 1). Figure 2 shows the migration velocities of these inclusions measured in the two types of alkali halide single crystals. Inclusions move about an order of magnitude faster in KCl than in NaCl. This difference is due in part to the larger temperature coefficient of salt solubility in KCl compared to NaCl, and to a larger interfacial resistance to dissolution and/or crystallization in the latter solid. Other data demonstrates a critical size-temperature gradient relationship which has important consequences in modeling the performance of inclusions in nuclear waste repositories. For a given size of inclusion, there is a minimum temperature gradient below which it will not migrate at all, or conversely, at a fixed temperature gradient, only inclusions larger than a particular size can be induced to move. This aspect of the phenomenon is due to the existence of a nonzero supersaturation required for salt crystallization from solution or to a nonzero subsaturation needed for dissolution.

The data in Fig. 2 exhibit a degree of scatter which is far greater than the precision with which the velocities of a single inclusion can be measured. Such a phenomenon suggests the presence of a physical feature of the process which is not accounted for in the current theory: two possibilities come to mind. First, the kinetic resistances to dissolution or to crystallization and the departures from equilibrium required to induce these processes may depend upon the number of screw dislocations which intersect the faces of the inclusion, and thereby influence the migration velocity. Such a condition is stochastic in nature, and would lead to intrinsically large variations in the velocities of inclusions with the same macroscopic parameters (e.g., size, temperature and temperature gradient).

Second, the inclusions are mounted on the hot stage of the microscope by mechanically clamping between copper heating blocks. This procedure produces a state of stress in the specimen which may affect the migration velocity. The solubility of the salt is a function of the state of stress

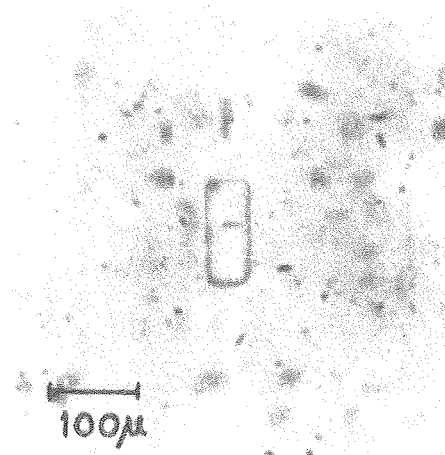


Fig. 1. Brine inclusion in single crystal NaCl. (XBB 802-2017)

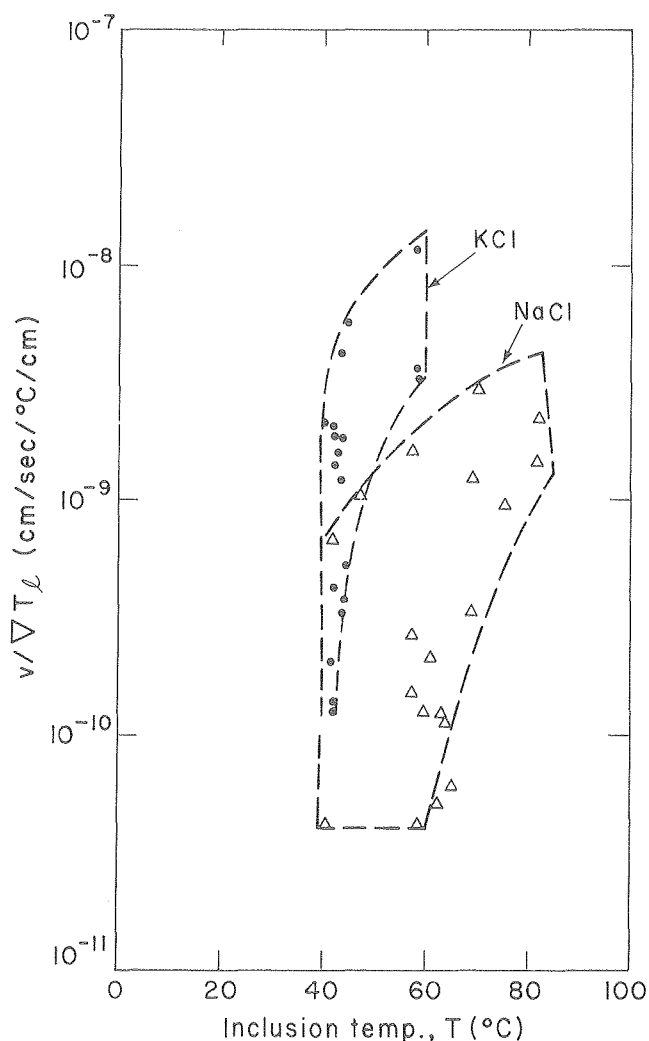
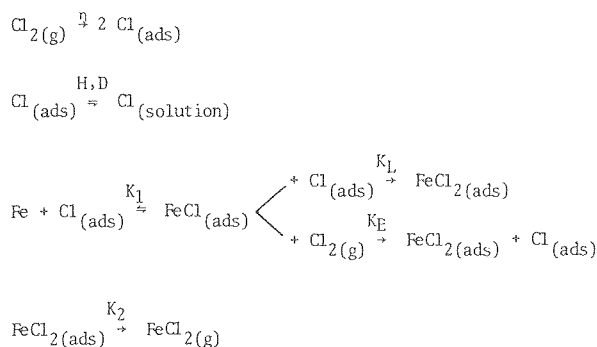


Fig. 2. Migration velocities of brine inclusions in NaCl and KCl. (XBL 802-261)

During the reaction taking place at low pressure, a reaction product is present at the surface, growing in a thin continuous layer out of which islands protrude. ESCA studies, performed at 400°C and $\text{PCl}_2 \sim 10^{-7}$ Torr, show that more than one species is present. A laser-stimulated desorption experiment during which an iron target heated to 625°C in an environment of 10^{-7} Torr in Cl_2 is rapidly heated to a high temperature by a laser pulse of 16.5 Joule energy shows that both FeCl and FeCl_2 desorb.

Molecular beam data support the existence of a diffusion and two parallel reaction mechanisms. The diffusion could correspond to either chlorine diffusing into iron or iron diffusing into FeCl_2 . The two parallel reaction mechanisms are probably a combination of Ely-Rideal and Langmuir-Hinshelwood processes.

A good fit to the data has been obtained with the following mechanism:



* * *

† Brief version of UCRL-82524.

5. OXYGEN SELF-DIFFUSION IN HYPOSTOICHIOMETRIC URANIA

Kee Kim and D. R. Olander

Oxygen self-diffusion in hypostoichiometric uranium oxides is of importance in predicting the rate of oxygen redistribution and other physico-chemical processes occurring in an irradiated fuel pin. Although there have been many measurements of oxygen diffusion in ordinary oxides and in hyperstoichiometric urania, similar measurements in hypostoichiometric urania have been proven very difficult mainly because it is a defect structure stable only at high temperature, and its oxygen diffusivity is likely to be large enough to render conventional methods unworkable (i.e., gas phase mass transfer of isotopic exchange are rate-limiting). The method utilized here involves a diffusion couple consisting of $\text{U}^{18}\text{O}_{2-x}$ wafer sandwiched to a $\text{U}^{16}\text{O}_{2-x}$ wafer by a bond of liquid uranium. When heated, the ^{18}O and ^{16}O interdiffuse. The liquid uranium at the interface is intended to eliminate a gap resistance to oxygen transfer.

at the dissolving and crystallizing surfaces; thus, any stress gradient introduced by the specimen mounting process can influence the migration velocity.

* * *

† Brief version of LBL-10252.

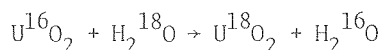
‡ Work partially supported by the Office of Nuclear Waste Isolation, U. S. Department of Energy.

4. INVESTIGATION OF THE IRON-CHLORINE REACTION BY MODULATED MOLECULAR BEAM MASS SPECTROMETRY†

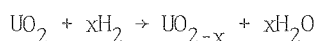
W. Siekhaus, M. Balooch and D. R. Olander

The reaction mechanisms which are involved when gaseous chlorine reacts with a solid iron surface maintained at high temperature have been studied by modulated molecular beam spectrometry, ESCA and laser-stimulated desorption.

Two identical UO_2 wafers, each 1.3 cm in diameter and 0.93 mm thick, were prepared. They were polished by diamond abrasive to promote a good contact. The ^{16}O in one of the wafers was exchanged by ^{18}O using an H_2^{18}O - H_2 mixture at 1500°C :



The ratio $\text{H}_2^{18}\text{O}/\text{H}_2$ was approximately 10^{-2} , which yielded the oxygen potential for $\text{UO}_{2.00}$ at the temperature. The desired $\text{H}_2^{18}\text{O}/\text{H}_2$ ratio was obtained by flowing hydrogen through H_2^{18}O the temperature of which was controlled. By measuring the weight of the wafer before and after a 43-hour treatment, it was determined that approximately 70% of the ^{16}O was replaced by ^{18}O . The same procedure was exactly applied to the other UO_2 wafer (using normal H_2^{16}O) in order to have the same history. Then the samples were reduced at the same time by hydrogen at 1950°C :



The stoichiometry of the reduced samples was determined by thermogravimetric method to be 1.96. Thus, the diffusion couple consists of two nearly identical wafers of UO_{2-x} , the only difference being the oxygen isotope content. When annealed in the diffusion experiment at a temperature well below the reduction temperature, liquid uranium metal is present in the specimens and the oxygen-to-metal ratio of the oxide phase is buffered at the value corresponding to that of the lower phase boundary at the diffusion temperature. This procedure was necessary in order to maintain a known oxide stoichiometry during the diffusion anneal. Single phase substoichiometric uranium would risk composition changes during the experiment by oxygen exchange with the furnace atmosphere. Figure 1 shows the set-up of the diffusion experiment. The diffusion couple was enclosed by molybdenum plugs. Rhenium foils were used in

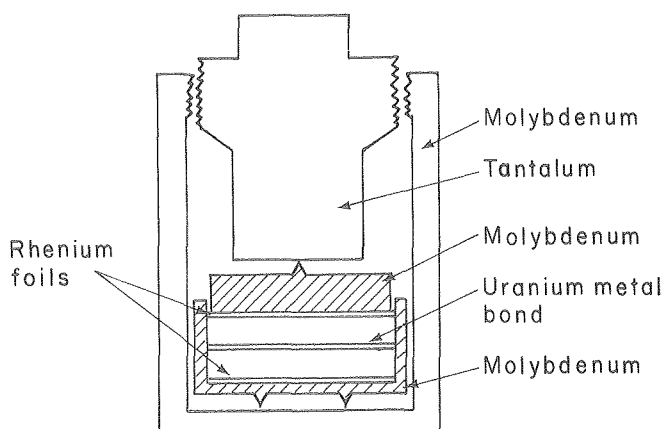


Fig. 1. Apparatus for mounting a diffusion couple to measure oxygen self-diffusion in UO_{2-x} . (XBL 802-260)

order to prevent any possible reaction between molybdenum and urania. The two wafers were pressed by a tantalum rod in order to promote a better contact. After the experiment, the diffusion couple was cut in half perpendicular to the interface and the profile of ^{18}O concentration was obtained by using an ion microprobe.

Shown in Fig. 2 is the normalized profile of ^{18}O concentration after a 20-minute anneal at 1330°C .

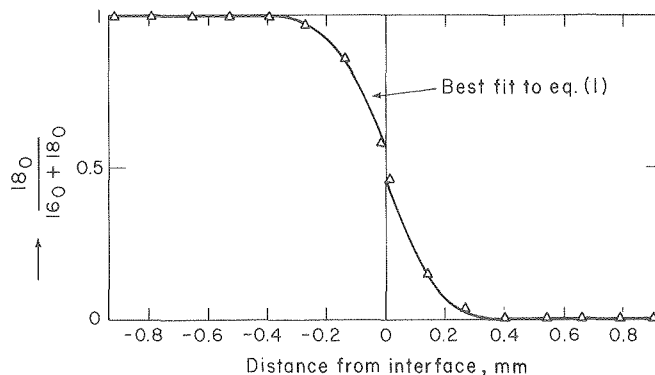


Fig. 2. Distribution of oxygen-18 in the diffusion couple after annealing for 20 min at 1330°C . (XBL 802-259)

The lower phase boundary at this temperature corresponds to $\text{UO}_{1.985}$. Data were fitted to the analytic solution:

$$\frac{^{18}\text{O}}{^{18}\text{O} + ^{16}\text{O}} = \sum_{n=0}^{\infty} e^{-D\alpha_n^2 t} \quad (1)$$

$$\times \frac{\left\{ \left(\frac{B}{\ell} \right)^2 + \alpha_n^2 \right\} \cos \alpha_n z}{\left\{ \left(\frac{B}{\ell} \right)^2 + \alpha_n^2 \right\} \ell + \left(\frac{B}{\ell} \right)} \cdot \frac{\sin \alpha_n \ell}{\alpha_n}$$

D = oxygen self-diffusion coefficient
 α_n = constants
 t = time
 z = distance from the interface
 ℓ = thickness of the wafer
 B = Unknown dimensionless parameter which characterizes liquid uranium resistance to oxygen transport (If there were no resistance, $B = \infty$).

Fitting the data to Eq. (1) using the least square program MINUIT gave $D = 0.89 \times 10^{-7} \text{ cm}^2/\text{sec}$ and $B = 71$. In the absence of the uranium bond between the two wafers, the interface resistance would have been so large that gap transport rather than solid state diffusion would have controlled the kinetics of the exchange. Thus, the method appears to be suitable for measuring the diffusivity of the very mobile anion in UO_{2-x} .

6. THE THEORY OF URANIUM ENRICHMENT BY THE GAS CENTRIFUGE[†]

D. R. Olander

The next series of uranium enrichment plants to be constructed in the United States for producing fuel for light water reactors will utilize gas centrifuges. Theoretical understanding of the hydrodynamics and separative capabilities of the centrifuge is needed to predict performance of the device. The gas centrifuge shown in Fig. 1 consists of a rotor containing uranium hexafluoride gas and spinning at high speed. The primary separation effect is the depletion of the gas at the periphery in $^{235}\text{UF}_6$, due to the centrifugal force, leaving the center enriched in this species. This effect alone, however, is not sufficient to make a practical isotope separation device. In addition, a weak countercurrent gas circulation shown by the arrows in Fig. 1 is induced by applying a temperature gradient along the length of the rotor wall. The resulting internal circulation has the effect of changing the direction of isotope separation from radial to axial, thereby permitting extraction of enriched product from the top and depleted waste from the bottom, which renders the machine practical for large-scale uranium enrichment.

In order to predict the extent of isotope separation due to the combined effects of the radial centrifugal field and the axial gas circulation, it is necessary to solve the equations of motion for the gas in the rotor. Onsager¹ first demonstrated that this set of conservation equations could be reduced to a single sixth order partial differential equation which can be solved by the eigenfunction expansion method.

Once the velocity profiles in the rotor have been determined, the diffusion-convection equation must be solved to determine the degree of isotope separation in the device. This solution is effected by adapting Onsager's method originally devised for analysis of the thermal diffusion column.

The theoretical analysis thus produces a prediction of the separative power of the centrifuge as a function of the throughput (feed rate) and cut (ratio of product and feed rates) at which the machine operates. This function is called the performance function of the centrifuge and is the basic information needed to design an ideal cascade composed of a large number of centrifuges, which constitutes an isotope separation plant. Operation of centrifuges in an ideal (i.e., no-isotope mixing) cascade effectively fixes the cut at which the centrifuges must operate. The classical ideal cascade is symmetric in the sense that the waste from a stage is sent to the stage immediately below for further stripping and the product is delivered to the next stage up for additional enrichment. The cut which this sort of cascade requires of its constituent centrifuges is well below the maximum separative power of the latter. However, it is possible to invent other cascades, which are still ideal or no-mixing, which better exploit the separative properties of the individual centrifuges. The computed

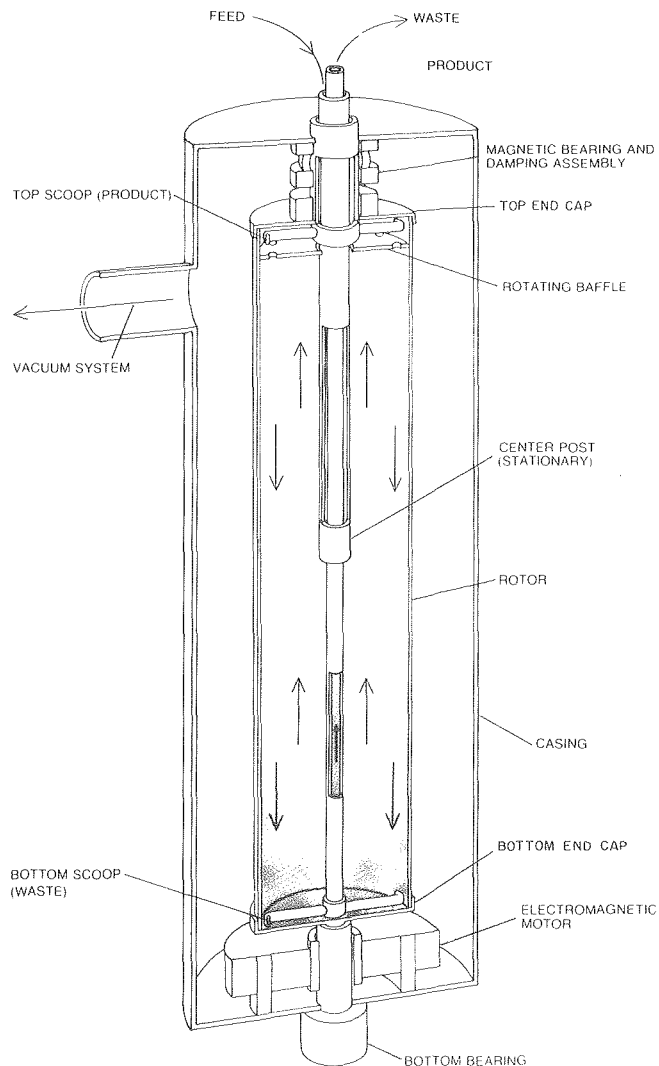


Fig. 1. A gas centrifuge for uranium enrichment.
(XBB 793-3060-A)

performance functions for the centrifuges studied show that the separative power increases as the cut decreases. In order to utilize this feature of the physics of the machines, they must be operated at as low a cut as possible, which can be accomplished in an asymmetric ideal cascade. In this type of cascade, the product from a stage is delivered two stages forward instead of just one. It is shown that by use of this type of cascade, more separative work can be extracted from a gas centrifuge, and therefore the cost of producing enriched uranium by this method is correspondingly reduced.

[†]Brief version of LBL-10253.

1. Lars Onsager, "Approximate Solutions of the Linearized Flow Equations," SWLO-001 (1965).

RESEARCH PLANS FOR CALENDAR YEAR 1980

The projects will continue to investigate the high temperature chemical and physical behavior (with emphasis on kinetics) of reactions pertinent to nuclear reactor fuels and other energy production technologies. The rapid vacuum vaporization of UO_2 project will seek to determine the high temperature evaporation kinetics of UO_2 by laser pulsing of solid specimens coupled with fast pyrometer temperature measurement and *in situ* mass spectrometric detection of the vaporization pulse. The electron-bombardment-heated temperature gradient furnace will be used to complete the investigation of ruthenium mobility in UO_2 by providing a variable temperature environment which permits the activation energy for diffusion to be determined in a single experiment. The study of oxygen self-diffusion in hypostoichiometric urania will provide data on this transport property at a series of temperatures along the lower phase boundary $U(x)/UO_{2-x}$. The zircaloy stress corrosion cracking experiment will be directed towards determination of the efficacy of cesium iodide as a stress corrosion cracking agent. Analysis of the desorption kinetics of water from UO_2 will be completed and a model for this process developed. The project of thermal gradient migration of liquid brine inclusions in NaCl (partially supported by ONWI) will examine the effect of dislocations in the solid and applied stress gradients on the migration process. The silane cracking experiment using modulated molecular beam methods will use isotope exchange techniques to elucidate the mechanism of the surface reaction.

1979 PUBLICATIONS AND REPORTS

Refereed Journals

1. D. R. Olander and S. Shamm, "Iodine Stress Corrosion Cracking of Zircaloy," *Trans. Am. Nucl. Soc.* 32, 268 (1979).
2. D. R. Olander, "Separative Performance Transients in a Gas Centrifuge," *Nucl. Technol.* 44, 307 (1979).

3. D. R. Olander, "Separation of Flowing Gas Mixtures by Thermal Diffusion," *High Temp. Sci.* 10, 223 (1979).

4. D. R. Olander and M. Balooch, "Platinum-Catalyzed Gasification of Graphite by Hydrogen," *J. Catalysis* 60, 41 (1979).

Other Publications

1. D. R. Olander, "Overview of Fuel Element Design," *Mechanical Engineering*, p. 30, April (1979).

LBL Reports

1. M. Balooch and D. R. Olander, "Migration of Brine Inclusions in Single-Crystal NaCl," LBL-10252.
2. D. R. Olander, "Bubble Migration in Stress Gradients," LBL-9739.
3. D. R. Olander, "The Theory of Uranium Enrichment by the Gas Centrifuge," LBL-10253.
4. W. Siekhaus, M. Balooch and D. R. Olander, "A Molecular Beam Study of the Iron-Chlorine Reaction," UCRL-82524.
5. D. R. Olander and A. J. Machiels, "Thermal Gradient Brine Inclusion Migration in Salt Study: Gas-Liquid Inclusions--Preliminary Model," LBL-10275.

Invited Talks

1. D. R. Olander, "Uranium Enrichment by the Gas Centrifuge Method," Massachusetts Institute of Technology, Department of Nuclear Engineering, March 19, 1979.
2. D. R. Olander, "Thermodynamic Treatment of Bubble Migration in Potential Gradients," Symposium on Rare Gases in Metals and Ionic Solids, Harwell, U.K., Sept. 13, 1979.

c. Plasma Enhanced Deposition of Thin Films*

D. W. Hess, Investigator

1. PLASMA-ENHANCED DEPOSITION OF IRON/IRON OXIDE FILMS

D. M. Wroge and D. W. Hess

Magnetic thin films have been of great interest for many years, owing to their wide applicability. For instance, current applications range from magnetic recording tape to magnetic disks for bulk computer memories, to magnetic recording heads, and finally to the recent magnetic bubble memory

devices. A specific application depends strongly upon the magnetic properties of the film, which in turn are determined by the structure and chemical properties of the film.

Thin films (1-2 μm) of iron/iron oxide were deposited by striking an rf glow discharge in iron pentacarbonyl vapor at ~ 0.2 Torr pressure. Unlike the powdery deposits obtained from thermal decomposition of iron pentacarbonyl, plasma-enhanced deposition (PED) results in reflective, adherent, and uniform films. The crystallinity of the PED films, as measured by x-ray diffraction and by transmission electron microscopy, increases with increasing substrate temperature. Further, the diffraction intensity of the α -iron peak decreases with increasing rf power level, as shown in Fig. 1. These results indicate that the relative amount of amorphous iron (or iron as Fe_3O_4 or $\gamma\text{-Fe}_2\text{O}_3$) in the film increases with power, and this trend is probably a result of an increase in electron and/or ion bombardment as well as enhanced incorporation of carbon and oxygen from decomposition of CO molecules at the higher power levels. Chemical analyses substantiate this latter conclusion, since the film stoichiometry varies from $\text{FeO}_{0.9}\text{C}_{0.18}$ at 10W, to $\text{FeO}_{0.52}\text{C}_{0.23}$ at 100 W, when the substrate temperature is 300°C .

Magnetic properties of the iron/iron oxide films are determined by measuring the inductance (B) of

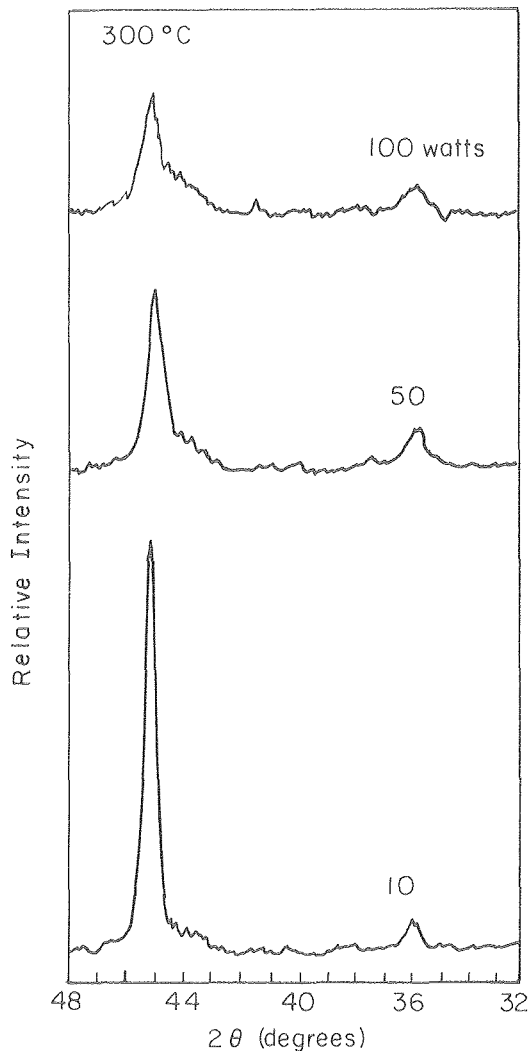


Fig. 1. X-ray diffraction patterns observed for iron/iron oxide films deposited at 300°C as a function of rf power. The peak at 45° is due to $\alpha\text{-Fe}$, and the peak at 36° is due to Fe_3O_4 and $\gamma\text{-Fe}_2\text{O}_3$. (XBL 7910-7227)

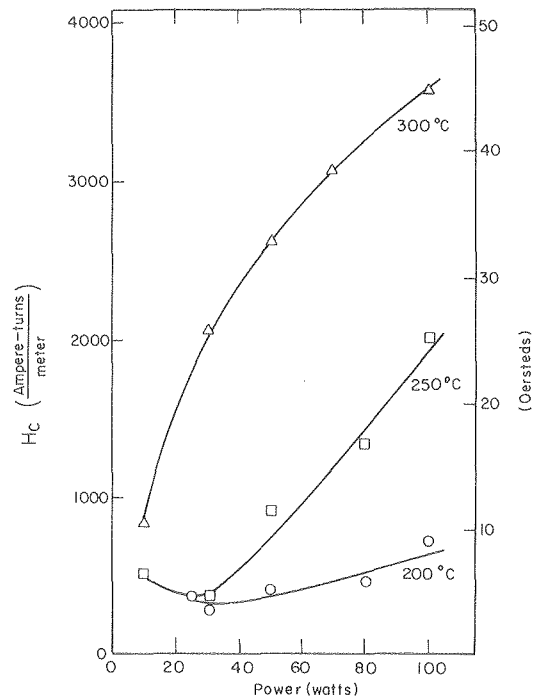


Fig. 2. Coercive force (H_c) of the iron/iron oxide films as a function of substrate temperature and rf power. (XBL 7910-7232)

*This work was supported by the Division of Materials Sciences, Office of Basic Energy Sciences, U. S. Department of Energy.

the films as a function of applied magnetic field (H). For our system sensitivity, no magnetization curves (B vs. H) are obtained for substrate deposition temperatures below 150°C. Above 150°C, the shape of the magnetization curve is a strong function of the rf power and substrate temperature. The coercive force (H_C) increases with increasing substrate temperature and rf power level as shown in Fig. 2. Since an increase in H_C is generally due to structural imperfections and inhomogeneities, it appears that an increase in power increases the number of structural defects in iron films, as discussed previously. Similarly, the ratio of the remanent induction (B_r) to the saturation induction (B_s) increases with increasing substrate temperature and power. Therefore, PED allows the magnetic properties of iron/iron oxide films to be varied during deposition.

RESEARCH PLANS FOR CALENDAR YEAR 1980

Extensive kinetic data will be taken so that the deposition rate of iron/iron oxide films can be expressed as functions of various plasma parameters such as gas pressure and rf power. These studies will generate insight into the relationship between

plasma variables, plasma chemistry, and the resulting film properties.

In order to utilize magnetic films in solid state devices, it is necessary to pattern these films. Thus, acid baths such as HCl will be studied in order to determine the appropriate bath conditions (temperature, pH, etc.) for controllable pattern definition. Scanning electron micrographs of pattern cross sections will be taken so that the exact pattern geometries resulting from various etching procedures can be investigated.

1979 PUBLICATIONS AND REPORTS

Other Publications

1. D. W. Hess, "Process Technology of Silicon Integrated Circuits," in Chemical Technology 9, 432 (1979).

LBL Report

1. D. M. Wroge (M. S. thesis), with D. W. Hess, "The Plasma Enhanced Deposition of Iron and Iron Oxide Thin Films," LBL-9879.

d. Electrochemical Phase Boundaries

Rolf H. Muller, Investigator

Introduction. The purpose of this work is to advance the understanding of boundary layers and thin films at electrochemical interfaces. Chemical and physical processes at electrochemical phase boundaries are investigated, primarily by experimental means, to determine mechanisms of transport and film formation, to find new means to accelerate electrochemical mass-transport and to define the effect of surface layers on electrochemical processes.

The formation of solid surface layers on metals is investigated because such layers determine the chemical properties of most metals in liquid or gaseous environments. These layers are therefore important in electro-deposition and -dissolution, in the functioning of most batteries and in corrosion processes. Boundary layers at electrodes are investigated because they control the chemical environment in which electrode processes take place and because they limit the specific rate, material-and energy efficiency of high-rate electrochemical processes.

New experimental equipment and techniques are developed and used for the characterization of electrochemical phase boundaries. These include a unique self-compensating ellipsometer that can be combined with ultra-high vacuum techniques and used with new interpretation procedures for the measurements, and a laser interferometer of special design with new optical data analysis, optical thin-film interference, and laser Doppler velocimetry.

Work on high-rate electro-deposition and -dissolution, conducted jointly with C. W. Tobias, is described in the section, "Electrochemical Processes," C. W. Tobias, Investigator. Applied research, "Anodic Surface Layers on Battery Materials," supported by the Division of Energy Storage Systems, Office of Conservation and Solar Energy, DOE, is described under "Electrochemical Synthesis and Energy Storage."

1. USE OF FILM-FORMATION MODELS FOR THE INTERPRETATION OF ELLIPSOMETER MEASUREMENTS[†]

Rolf H. Muller and Craig G. Smith[‡]

Multiple-film models of electrochemical surface layers have been successfully used to interpret ellipsometer measurements of anodic film formation. The models consider the simultaneous or sequential formation of up to six layers with time-varying properties. Controlled mass-transport conditions are maintained and mass-transport between layers is allowed to occur by diffusion, migration and convection. Continuous mass and charge balances are applied to the mathematical model. The simultaneous measurement of current and potential provides additional input on the rates of surface reactions and the nature of products formed (Figs. 1 and 2).

The two measured parameters of an isolated ellipsometer measurement, normally permits multiple interpretations. The time-dependence of transient measurements, which can now be obtained with automatic instruments, however, permits a fuller use of the experimental data. Thus, up to seven of the 28 parameters required to describe the model, have been considered unknown and have been determined by fitting the ellipsometer measurements in multidimensional space.

Limits of uncertainty for the parameters thus derived have been determined by fitting a parabola through the partial derivative of each parameter near the best fit. A linear regression analysis was also performed to identify independent variables. A Monte Carlo routine was used to search the multidimensional space for multiple roots.

* * *

[†]Brief version of LBL-9428, submitted to Surface Sci.

[‡]Present address: Bell Laboratories, Murray Hill, N.J. 07974

* This work was supported by the Division of Materials Sciences, Office of Basic Energy Sciences, U. S. Department of Energy.

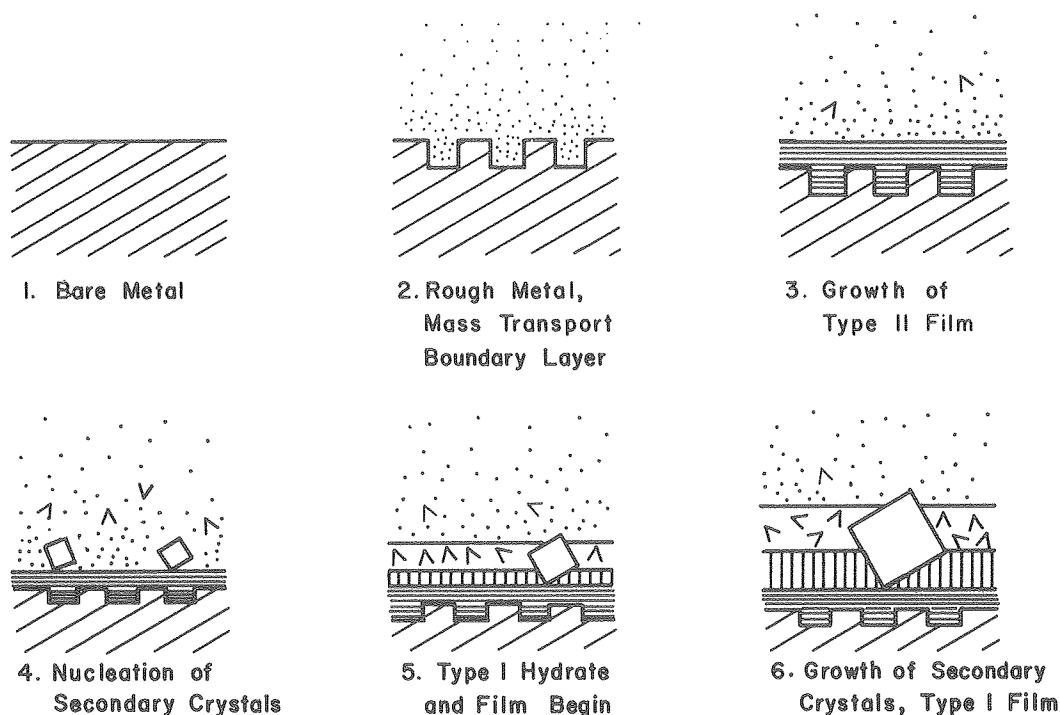


Fig. 1. Time sequence of events used in the modeling of anodic film formation for the interpretation of in situ ellipsometer measurements. (XBL 787-9519)

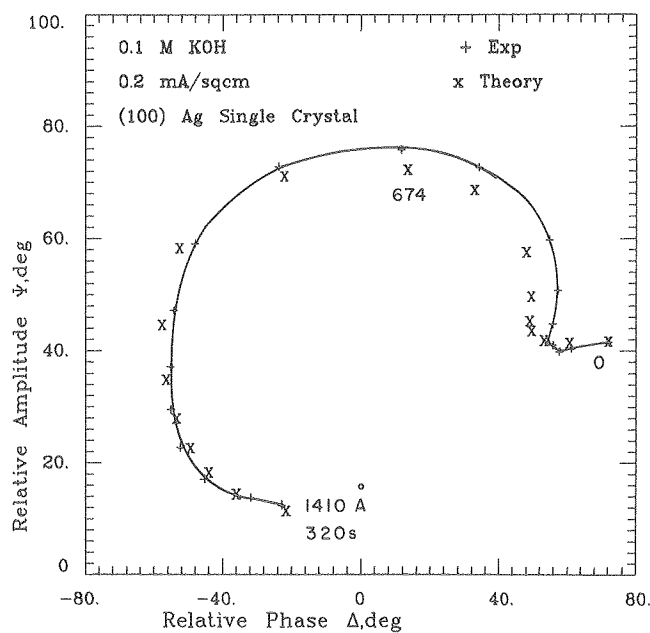


Fig. 2. Interpretation of the ellipsometer measurement of anodic oxide formation. Comparison of experiment (+) and model prediction (x). Anodic formation of Ag_2O on Ag (100) in stagnant 0.1 M KOH at 0.2 mA/cm². Thickness of primary layer indicated along the curve. (XBL 786-9084)

2. CONVENTIONS AND FORMULAS FOR USING THE MUELLER-STOKES CALCULUS IN ELLIPSOMETRY[†]

P. S. Hauge,[‡] R. H. Muller, and C. G. Smith[§]

The effect of conventions and definitions on the presentation of ellipsometer measurements had been analyzed earlier¹ and the preferred conventions proposed then have been widely accepted since.² While only the state of polarization, described by two parameters (usually relative phase and relative amplitude) is considered in classical ellipsometry, present developments, in addition, are concerned with reflectance and partial polarization. A complete description of polarized light is then necessary for which the Stokes Parameters provide a convenient means. A number of arbitrary choices, particularly the sign of the fourth Stokes Parameter, however are again available. The effect of these choices on the Mueller-Stokes calculus has been investigated. Conventions are proposed and the formulation for converting the Jones matrix into the transformation matrix for the coherency vector or the Stokes vector are described. In order to maintain the previously determined principal conventions of ellipsometry and the established Mueller-Stokes matrix calculus, it has been found necessary to invert the coordinates on the Poincaré Sphere.

* * *

[†]Brief version of LBL-10172, submitted to Surface Sci.

[‡]IBM Thomas J. Watson Research Center, Yorktown Heights, N.Y. 10598

[§]Bell Laboratories, Murray Hill, N.J. 07974

1. Rolf H. Muller, Surface Sci. 16, 14 (1969).

2. Proceedings 3rd International Conference on Ellipsometry, Surface Sci. 56 (1976).

3. FOURTH INTERNATIONAL CONFERENCE ON ELLIPSOMETRY

Rolf H. Muller

The Fourth International Conference on Ellipsometry was held at LBL August 20-22, 1979. Five invited speakers opened sessions devoted to the different conference topics which were optical theory, instrumentation and technique, and applications. The invited review papers were followed by 38 contributed papers. Several important developments were brought into focus at the conference. Among them are the continuing development of the optical theory for reflection from rough and inhomogeneous surfaces, the use of spectroscopic ellipsometry for the identification of surface states and adsorbates and new developments in corrosion and biomedical research. The conference was attended by 103 participants from 15 countries. The proceedings of the conference, consisting of the full papers and a record of the discussions, will be published as a special volume of Surface Science, approximately August 1980.

4. INTERFEROMETRY OF MASS-TRANSFER BOUNDARY LAYERS[†]

Karrie J. Hanson, Rolf H. Muller, and Charles W. Tobias

The use of flow obstacles or turbulence promoters to enhance the rate of electrochemical mass-transfer in flow channels, with a minimal increase in pressure drop, has been investigated by observing mass-transfer boundary layers with a traveling dual-beam laser interferometer.

Figure 1 illustrates the effect of three flow obstacles of different cross-section, attached to the electrode surface, on the boundary layer thickness: after a precipitous reduction at the location of the obstacle, indicated by the arrow, the boundary layer gradually increases in the downstream direction to approach the thickness in the absence of the obstacle (marked "calculated"). Of the three shapes studied, the triangular obstacle was most effective in reducing downstream boundary layer thickness (curve C). Similar experiments with varying obstacle location from the surface showed the optimal position to be approximately one obstacle height away from the surface. The effectiveness of obstacles increased with increasing Reynolds Number over the range investigated (395 to 1903).

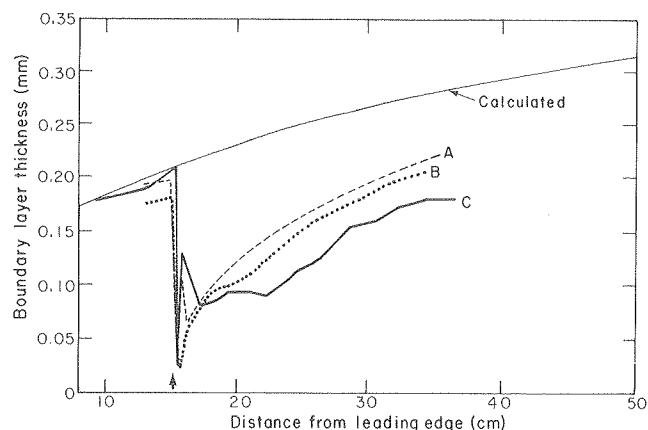


Fig. 1. Comparison of the effect of obstacle shape on the downstream mass-transfer boundary layer. (A) Attached round, (B) Attached square, and (C) Attached triangle. $Re = 756$, $i = 3 \text{ mA/cm}^2$. Obstacle height, 0.762 mm. (XBL 793-933)

To describe the performance of flow obstacles, three parameters were introduced. These are the average reduction β in boundary layer thickness, expressed as the relative difference between the integrated unobstructed boundary layer thickness and the reduced thickness in the wake of the obstacle,

$$\beta = \frac{\delta_{\text{unobstructed}} - \delta_{\text{with obstacle}}}{\delta_{\text{unobstructed}}}$$

the minimum boundary layer thickness in the wake of the obstacles, δ_{min} , and the distance over which the obstacle has an effect, the recovery distance

ℓ_R , which is the distance in the downstream direction, expressed in obstacle heights, at which the boundary layer immediately upstream from the obstacle is re-established. A summary of results in terms of these three parameters is shown in Tables 1 and 2. The detached obstacle of triangular cross-section is seen to be most effective in Table 1, while Table 2 illustrates the beneficial effect of increased Reynolds Numbers.

In addition to increasing the local current density, the obstacles had a pronounced effect on the morphology of the metal deposit which showed streaks and ridges, indicative of the flow pattern, that subside as laminar flow is re-established and provide another measure for the length of the recovery distance.

The results of this study can be used to design a turbulence promoter system to maintain a predetermined average boundary layer thickness in an electrochemical flow cell. Figure 2 illustrates

Table 1. Effectiveness of flow obstacles, comparison of obstacle shape and position at $Re = 756$. D_1 - Detached 0.762 mm, D_2 - Detached 1.524 mm, D_3 - Detached 2.286 mm, A - Attached.

| Type of Obstacle | δ_{min} mm | β % | ℓ R |
|------------------|----------------------|--------------|-------------|
| Round - A | .033 | 37 | 201 |
| Square - A | .033 | 44 | 216 |
| Triangle - A | .033 | 50 | 275 |
| Square - D1 | .033 | 67 | 249 |
| Square - D2 | .177 | 45 | 209 |
| Square - D3 | .171 | 37 | 190 |

Table 2. Effectiveness of flow obstacles, comparison of Reynolds Numbers.

| Type of Obstacle | Re | δ_{min} mm | β % | ℓ R |
|------------------|------|----------------------|--------------|-------------|
| Square - A | 395 | .131 | 32 | 209 |
| | 756 | .033 | 44 | 216 |
| | 1328 | .033 | 48 | 393 |
| | 1903 | .033 | 50 | 380 |
| Round - D1 | 395 | .190 | 45 | 157 |
| | 1328 | .092 | 59 | 183 |
| | 1903 | .052 | 66 | 350 |

how a boundary layer thickness of 0.075 mm was maintained at $Re = 750$ by use of four attached square obstacles 5 cm apart. In an unobstructed cell, under the same conditions, the average boundary layer thickness would be 0.25 mm.

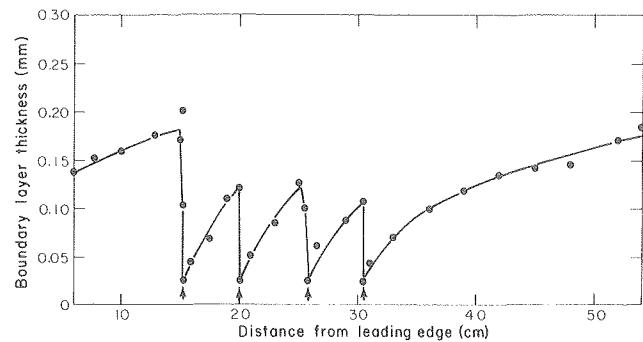


Fig. 2. Reduction of average boundary layer thickness by the use of multiple obstacles in series. Four attached square obstacles located at 15, 20, 25, and 30 cm from leading edge. $Re = 756$, $i = 3 \text{ mA/cm}^2$. Obstacle height, 0.762 mm. (XBL 793-885)

* * *

† Brief version of LBL-9038.

RESEARCH PLANS FOR CALENDAR YEAR 1980

Critical assumptions in film-formation models for the interpretation of ellipsometer measurements will be tested experimentally. Among them are variations in composition and porosity in multi-layer structures, the role of adsorbed reaction intermediates and the optical effect of growing particulate aggregates. Auger spectroscopy and ion etching will be used for this purpose. The installation of an Argon ion laser as a light source will make it possible to examine specimens of smaller surface area (approximately 3 mm^2 vs 30 mm^2) and greater roughness than could be investigated so far. Fast spectral scanning capabilities will be constructed for the spectroscopic characterization of surface layer materials.

Investigation of new means to accelerate electrochemical mass-transport by use of current pulses and vibrating electrodes is planned. Transient local mass-transport boundary layers will be observed by interferometry to established details of the processes needed to define the effectiveness of these approaches (with C. W. Tobias).

Studies on the use of suspended particulates in the high-rate electrodeposition of metals will be completed. Optimum size and concentration of solids will be established for transport to a rotating disk (with C. W. Tobias).

Limiting factors in the electrochemical machining of cemented transition metal borides and carbides will be determined. Means to predict the behavior of the materials on the basis of the properties of the pure components will be sought (with C. W. Tobias).

Local electrolyte velocity in boundary layers along electrodes will be determined by laser velocimetry to identify hydrodynamic causes of non-uniform current distribution on extended electrodes. Based on a survey and test of commercial equipment, the optical components of a double-beam system have been designed and built. These components are expected to provide spatial resolution not otherwise attainable. A reference-beam module of similar capabilities will be developed, and combined with commercial frequency counters for spectrum analysis.

1979 PUBLICATIONS AND REPORTS

Refereed Journals

1. F. R. McLarnon, R. H. Muller and C. W. Tobias, "Interferometric Study of Forced Convection Mass-Transfer Boundary Layers in Laminar Channel Flow," *Industrial and Engineering Chemistry Fundamentals* **18**, 97 (1979).

LBL Reports

1. Karrie J. Hanson, "Interferometric Study of Mass-Transfer Enhancement by Turbulence Promoters," M.S. Thesis, Department of Chemical Engineering, University of California, Berkeley, LBL-9038, April 1979.

2. John F. Cooper, Rolf H. Muller and Charles N. Tobias, "Periodic Phenomena During Anodic Dissolution of Copper at High Current Densities," LBL-9404, July 1979, submitted to *J. Electrochem. Soc.*

3. J. B. Riggs, R. H. Muller and C. W. Tobias, "Prediction of Geometry in Electrochemical Machining," LBL-6282 Rev., Dec. 1979, submitted to *Electrochim. Acta*.

4. Rolf H. Muller and Michael L. Sand, "Optimum Angle of Incidence for Monochromatic Interference in Transparent Films on Absorbing Substrates," LBL-7662 Rev., June 1979, accepted for publication by *J. Opt. Soc. Am.*

5. R. H. Muller and C. G. Smith, "Use of Film-Formation Models for the Interpretation of Ellipsometer Measurements," LBL-9428, Oct. 1979, submitted to *Surface Sci.*

6. P. S. Hauge, R. H. Muller and C. G. Smith, "Conventions and Formulas for Using the Mueller-Stokes Calculus in Ellipsometry," LBL-10172, December 1979, submitted to *Surface Sci.*

Invited Talks

1. Rolf H. Muller, "Anodic Film Formation Phenomena," Gordon Research Conference for Electrochemistry, Santa Barbara, California, January 7-12, 1979.

e. Solid State and Surface Reactions*

Gabor A. Somorjai, Investigator

Surface Structure and Chemisorption By Low Energy Electron Diffraction

1. SURFACE STRUCTURE ANALYSIS OF THE RECONSTRUCTED (100) CRYSTAL FACES OF IRIDIUM, PLATINUM AND GOLD†

M. A. Van Hove and G. A. Somorjai

Low energy electron diffraction (LEED) intensities have been measured for the Ir and Pt(100) reconstructed surfaces. These have been analyzed with multiple-scattering calculations to determine the location of the surface atoms. The most likely structure consists of a hexagonal close-packed top monolayer resting on the underlying square substrate lattice. The hexagonal layer is not flat but buckled with atoms positioned up to ± 0.2 Å out of plane. For Ir(100) the structure has the relatively small unit cell (1×5), whereas Pt(100) and Au(100) have the larger unit cells $\begin{pmatrix} 14 & 1 \\ -1 & 5 \end{pmatrix}$ and $c(26 \times 68)$, respectively, due to contractions within the hexagonal layer and, in the case of Pt, an additional small rotation of this layer.

* * *

†Brief version of LBL-10340.

2. MEASUREMENT OF THE LEED DIFFRACTION BEAM INTENSITIES FROM CHEMISORBED CO ON THE Rh(111) CRYSTAL FACE

R. J. Koestner and G. A. Somorjai

A structural determination via a LEED dynamical analysis of CO, CO₂ bonding to the Rh(111) surface with each adsorbate forming a ($\sqrt{3}c \times \sqrt{3}$ R30°) or, at higher coverage, a (2×2) LEED pattern is underway. At present, intensity electron voltage curves for the clean Rh(111) at $\theta=0$ as well as Rh(111)-($\sqrt{3} \times \sqrt{3}$ R30°)-CO at $\theta=0^\circ, 10^\circ, 20^\circ, \phi=0$ have been produced. Intensity electron voltage curves for Rh(111)-($\sqrt{3} \times \sqrt{3}$ R30°)-CO₂ at $\theta=0^\circ, 10^\circ, 20^\circ, \phi=0$, Rh(111)-(2×2)-CO at $\theta=0^\circ, 10^\circ, 20^\circ, \phi=0$ and Rh(111)-(2×2)-CO₂ at $\theta=0^\circ, 10^\circ, 20^\circ$, will be completed within the next few months. We expect a full LEED dynamical analysis of the above I-V profiles to confirm HREELS studies¹ which suggest CO₂ dissociates into CO (adsorbed) + O (the fate of this O is not well understood), the ($\sqrt{3} \times \sqrt{3}$ R30°)-CO unit cell has one CO molecule bonded to the surface at an atop site, and the (2×2)-CO unit cell consists of one bridge-bonded and two atop site CO molecules.

* * *

†Brief version of LBL-10581.

* This work was supported by the Division of Materials Sciences, Office of Basic Energy Sciences, U. S. Department of Energy.

1. L. H. Dubois and G. A. Somorjai, Surface Sci. 91, 000 (1980).

3. LOW ENERGY ELECTRON DIFFRACTION STUDIES OF THE SURFACES OF MOLECULAR CRYSTALS (ICE, AMMONIA, NAPHTHALENE, BENZENE)†

L. E. Firment and G. A. Somorjai

Low energy electron diffraction (LEED) has been used to study the surface structures of thin films of molecular crystals. The samples were grown epitaxially on metal single crystal substrates at low temperatures. Both Pt(111) and Ag(111) surfaces were used as substrates in order to identify the influence of the substrate on molecular film structure. Previous observations of ice (0001) and naphthalene (001) surfaces on films grown on Pt(111) substrates¹ were confirmed using the Ag(111) substrate. The NH₃(111) and benzene (111) surfaces were also studied on films grown on either substrate. All observed molecular crystal surfaces showed no evidence of surface reconstruction. To minimize sample charging and electron beam induced damage, LEED experiments were performed on samples of thickness less than 10-10² nm, with low energy electron exposures less than 1 C cm⁻². The maximum thickness and exposure values were characteristic of the particular molecular crystal. The relationship between the structure of the initial adsorbed monolayer and the molecular crystal orientation is discussed.

* * *

†Brief version of Surface Sci. 84, 275 (1979).

1. L. E. Firment and G. A. Somorjai, Surface Sci. 55, 413 (1976).

4. LEED STUDY OF THE ADSORPTION OF ACETIC ACID AND PROPANOIC ACID ON Ag(111)†

L. E. Firment and G. A. Somorjai

The adsorption of acetic acid and of propanoic acid on Ag(111) and Pt(111) single crystal surfaces have been studied with LEED. Both acetic acid and propanoic acid formed 2-dimensional structures in two different types of orientation on Ag(111) and propanoic acid apparently formed the same structure on graphite covered Pt(111). Neither acid formed ordered monolayers when adsorbed on clean Pt(111). The similar LEED data and physical properties of the acid molecules suggested similar structures for both acids consisting of closely packed arrays of hydrogen bonded dimers.

* * *

†Brief version of J. Vacuum Technology, in press.

5. A LEED-AES STUDY OF THE RECONSTRUCTED Pt(110) SURFACE AND THE EFFECTS OF OXYGEN TREATMENT[†]

M. Salmerón and G. A. Somorjai

The Pt(110) crystal face has been studied by low energy electron diffraction (LEED) and Auger electron spectroscopy (AES). The stable reconstructed (2×1) surface structure transforms, reversibly, to the (1×1) structure upon heating in vacuum to 830±30°C. Ion bombardment at 25°C also stabilizes the metastable (1×1) surface structure which converts, irreversibly, to the stable (2×1) structure upon heating in vacuum at ≤500°C. The diffraction beam intensity vs. electron energy curves (I(hk) vs. eV) exhibit complex behavior when monitored as a function of temperature. Heat treatments in oxygen at high crystal temperatures (>800°C) result in the appearance of new (3×1), (5×1) and ("7×1") surface structures while oxygen remains undetectable by AES. Adsorbed CO causes the (2×1)→(1×1) transformation while it does not effect the (3×1) surface structure.

* * *

[†]Brief version of LBL-8464.

6. LEED, AES AND THERMAL DESORPTION STUDIES OF THE OXIDATION OF THE Rh(111) Surface[†]

D. G. Castner and G. A. Somorjai

The oxidation of the Rh(111) surface was studied by low energy electron diffraction (LEED), Auger electron spectroscopy (AES), and thermal desorption mass spectroscopy (TDS). Four different oxygen species were detected during the oxidation. Initially chemisorbed oxygen atoms are produced from the low temperature dissociative adsorption of oxygen and undergo an activated ordering process to form three domains of a (2×1) structure. The chemisorbed oxygen was readily removed by exposure to hydrogen above 350 K. Heating the Rh(111) crystal in the presence of oxygen resulted in oxygen diffusing into the near surface region. Prolonged high temperature annealing produced an unreactive surface oxide. The epitaxial growth of Rh₂O₃(0001) on Rh(111) occurred during high temperature annealing in 1 Torr of O₂. This epitaxial oxide did not adsorb detectable amounts of either hydrogen or CO at 300 K and could be decomposed by heating the crystal to 800 K in vacuum.

* * *

[†]Brief version of LBL-9288.

7. ADSORBED MONOLAYERS ON SOLID SURFACES

G. A. Somorjai and M. A. Van Hove

In this review, we cover the various experimental parameters that can be used to characterize the adsorbate layer in the submonolayer to few-

monolayers range. We discuss the principles of ordering of the adsorbate layer since one of the most exciting observations of low energy electron diffraction studies is the predominance of ordering within these layers. We list the ordered adsorbate layer structures and summarize what can be learned about the nature of their bonding from the available structural data. This is done separately for the many surfaces whose two-dimensional unit cells are known in terms of shape, size and orientation, and for the fewer surfaces for which additionally the contents of the unit cell are known (adsorption site, bond lengths). Many types of adsorption are covered including atomic and molecular adsorption, co-adsorption, metallic adsorbates, non-metallic adsorbates, and organic adsorbates.

* * *

[†]Brief version of LBL-8566.

8. A NEW MICROFACET NOTATION FOR HIGH MILLER INDEX SURFACES OF CUBIC MATERIALS WITH TERRACE, STEP AND KINK STRUCTURES[†]

M. A. Van Hove and G. A. Somorjai

The ideal, i.e. unreconstructed and unrelaxed, structure of arbitrary high Miller index surfaces of cubic crystals is analyzed in terms of terraces, steps and kinks, and a new, simple, useful microfacet notation is proposed. The cubic crystals include the simple cubic, face-centered cubic, body-centered cubic, diamond, zinblende, NaCl and CsCl crystals.

* * *

[†]Brief version of LBL-9363.

9. SURFACE STRUCTURES OF METALLIC MONOLAYERS ON METAL CRYSTAL SURFACES[†]

J. P. Biberian and G. A. Somorjai

The structures of adsorbed metals on single crystal surfaces of other metals have been reviewed and tabulated. Most of the adsorbates of over 100 systems studied form ordered surface structures that may undergo changes as the coverage in the monolayer is increased. At low coverages, the adsorbate and substrate surface structures are closely related indicating the predominance of the adsorbate-substrate interaction in determining ordering. At higher coverages, there are more complex ordering characteristics. Although the relative atom sizes and magnitudes of adsorbate-substrate and substrate-substrate interactions influence the ordering in the monolayer general, conclusions that have predictive value must await the availability of more experimental results on more metal adsorbate-substrate systems.

* * *

[†]Brief version of LBL-8996.

10. THE STRUCTURE AND COMPOSITION OF POTASSIUM LAYERS DEPOSITED ON Ni(111) CRYSTAL SURFACES

H. Nozoye and G. A. Somorjai

Potassium is well known as a promotor of catalysts, but its role is not yet known. Potassium was adsorbed on nickel(111) surface which was used as a methanation catalyst by a potassium ion gun. The coverage of potassium was determined by means of Auger intensity versus evaporation time method and its structure was monitored by LEED. Potassium is adsorbed on the substrate as a neutral species until one monolayer completion, and this neutral species is easily oxidized by the ambient gas and by further evaporation of potassium which forms one monolayer of potassium oxide. By the strict analysis of LEED and Auger, we can determine the composition and structure of potassium oxide. Potassium oxide forms a layer compound on Ni(111) and the topmost layer is potassium. An oxygen layer sits between potassium Ni substrate. We intend to investigate the potassium effect on the catalytic reaction by this well defined potassium-covered single crystal.

Electron Spectroscopy Studies of Solid Surfaces and Adsorbates

1. THE CHEMISORPTION OF ACETYLENE AND ETHYLENE ON Rh(111): A HIGH RESOLUTION ELECTRON ENERGY LOSS AND LEED STUDY[†]

L. H. Dubois, D. G. Castner and G. A. Somorjai

We reported the results of a detailed investigation of the chemisorption and reactivity of C₂H₂ and C₂H₄ on the Rh(111) single crystal surface. Below 270 K ELS measurements indicated that acetylene chemisorbs on Rh(111) with its C-C bond oriented parallel to the surface forming an approximately sp² hybridized species. LEED investigations show that both C₂H₂ and C₂H₄ formed metastable (2×2) surface structures on Rh(111) below 270 K. An irreversible order-order transformation occurred between 270 and 300 K to a stable c(4×2) hydrocarbon overlayer. The stable species formed from both molecules were identical. Hydrogen addition to chemisorbed acetylene was necessary to complete this conversion. The geometry of the adsorbed ethylene species did not change during this transformation, although the overlayer structure did. This stable hydrocarbon fragment is identical to the hydrocarbon species formed from the chemisorption of either C₂H₂ or C₂H₄ and hydrogen on the Pt(111) single crystal surface at 300 K. The addition of H₂ to chemisorbed C₂D₂ or C₂D₄ resulted in H-D exchange, but no change in the adsorbate geometry was detected by ELS.

* * *

[†]Brief version of LBL-9946.

2. EVIDENCE OF THE WEAKENING OF THE CO BOND UPON COADSORPTION WITH HYDROCARBONS[†]

H. Ibach and G. A. Somorjai

The chemical bond of CO to transition metal surfaces becomes stronger in the presence of chemisorbed hydrocarbons of different types. High resolution electron energy loss spectroscopy studies of the vibrational frequencies of adsorbed CO on the Ni(111) and Pt(111) crystal faces reveal a large red shift in the presence of coadsorbed hydrocarbons which indicates the weakening of the C=O bonds. This, in turn, implies the formation of stronger metal-CO bonds. Furthermore, thermal desorption studies of chemisorbed CO from clean and carbon-covered rhodium surfaces show the presence of dissociated CO on the carbon contaminated surfaces, while only molecular CO is present on the clean metal surface.

* * *

[†]Brief version of Appl. Surface Sci. 3, 293 (1979).

3. THE CHEMISORPTION OF CO AND CO₂ ON Rh(111) STUDIED BY HIGH RESOLUTION ELECTRON ENERGY LOSS SPECTROSCOPY[†]

L. H. Dubois and G. A. Somorjai

The techniques of high resolution ELS, TDS and LEED were applied to a study of CO and CO₂ chemisorption on the Rh(111) single crystal surface at 300 K. The vibrational spectra of carbon monoxide indicated two distinct binding sites (atop and bridged) whose relative populations and vibrational frequencies were determined by both the substrate temperature and the background pressure. TDS measurements showed the bridge bonded CO to have an approximately 4 kcal/mole lower binding energy to the surface than the species located in the atop site. Surface pretreatment also had a marked effect on CO adsorption; carbon and oxygen both inhibited carbon monoxide chemisorption and weakened the metal-adsorbate bond strength. Hydrogen had no observable effect. The adsorption of carbon dioxide yielded identical spectra to those of chemisorbed CO, indicating dissociative adsorption. By combining our data with earlier infrared and inelastic electron tunneling spectroscopic studies, we calculated a consistent set of force constants for the two types of chemisorbed carbon monoxide.

* * *

[†]Brief version of LBL-9280.

Molecular Beam-Surface Interactions

1. THE KINETICS OF AMMONIA DECOMPOSITION ON THE (111) AND STEPPED CRYSTAL FACES OF PLATINUM[†]

W. Guthrie, J. Sokol and G. A. Somorjai

Ammonia adsorbs associatively on the Pt(111) and Pt(557) surfaces. The sticking coefficients are high ($s_{111}=0.74$, $s_{557}=0.49$). The probability of adsorption on the stepped surface is 66% smaller than on the flat surface. In spite of this, approximately 15 times more adsorbed ammonia decomposes to produce N_2 and H_2 on the stepped surface. On the stepped surface at peak temperatures (725 K), 10% of the adsorbed ammonia decomposes. Hence the steps enhance decomposition while diminishing the probability of reactant adsorption.

There is essentially no reactant angle of incidence dependence to adsorption on either crystal, nor to decomposition on the (557) surface. The sticking coefficient on the (111) surface was shown to have a weak coverage dependence. The production of hydrogen on the stepped surface was first order in ammonia pressure.

Hydrogenic atom exchange between NH_3 and D_2 takes place on the (557) surface at temperatures where there is little or no decomposition ($T \leq 700$ K). Approximately 10% of adsorbed ammonia undergoes exchange. This presumably occurs through a short-lived NH_3D intermediate.

The interaction of NH_3 with Pt(111) can be described by a simple adsorption and desorption model. The best fit parameters for this model are $s=0.74$, $K=2.65 \times 10^{10} d^{-15,500/RT}$. Decomposition is not a significant pathway on the (111) surface and can be assumed to take place only at defect sites on the surface.

* * *

[†]Brief version of LBL-9712.

2. THE VELOCITY AND ANGULAR DISTRIBUTIONS OF PRODUCTS FROM THE PLATINUM SURFACE CATALYZED REACTIONS OF H , H_2 AND O_2 [†]

S. Ceyer, J. Lin, W. Guthrie and G. A. Somorjai

The dynamics of the oxidation of deuterium on platinum has been studied in a molecular beam surface scattering experiment. A D_2 and an O_2 beam are aimed at a single crystal Pt(111) surface and the angular and velocity distribution of the reaction product, D_2O , is measured. By comparison of these results with the results obtained when the starting products are D and O_2 , the most probable mechanism involves a reaction between a D atom and an adsorbed OD radical in the last step of the reaction. Since the angular distribution is broad, there is no preferred orientation for the exiting D_2O molecule. The velocity distribution shows that very little of the exothermicity is liberated into the translational motion of the molecule away from the surface. In fact, the

exiting D_2O molecule has less translational energy than the energy of the surface. This indicates the reaction is occurring when the Pt-OD bond is at the classical turning point.

* * *

[†]Brief version of LBL-9838.

Studies of Catalyzed Surface Reactions

1. CORRELATIONS OF CYCLOHEXENE REACTIONS ON PLATINUM CRYSTAL SURFACES OVER TEN ORDERS OF MAGNITUDE PRESSURE RANGE: VARIATIONS OF STRUCTURE SENSITIVITY, RATES AND REACTION PROBABILITIES[†]

S. M. Davis and G. A. Somorjai

The hydrogenation and dehydrogenation of cyclohexene have been studied in the 10^{-7} to 10^2 Torr pressure range. The reaction of cyclohexene in excess hydrogen over the Pt(223) stepped platinum crystal surface at 25-150°C predominantly produces benzene at low pressures ($\sim 10^{-7}$ Torr) and cyclohexane at high pressures ($\sim 10^2$ Torr). While the low pressure reactions are structure sensitive and proceed on the clean metal surface, the high pressure reaction is apparently structure insensitive due to the continuous presence of a near monolayer of carbonaceous species. Widely differing coverages of reactive, weakly adsorbed hydrogen influence the reversal in selectivity between high and low pressures. The catalytic efficiency (reaction probability) decreases markedly with increasing pressure.

* * *

[†]Brief version of LBL-9869.

2. HIGH PRESSURE STUDIES OF CYCLOHEXANE DEHYDROGENATION AND HYDROGENOLYSIS OVER PLATINUM CRYSTAL SURFACES.[†]

W. Gillespie, R. Herz and G. A. Somorjai

Single crystal platinum surfaces are being used to study the fundamental principles which govern hydrocarbon reactions over heterogeneous catalysts. These single crystal surfaces serve as model reforming catalysts and are readily amenable to surface structure determination by low energy electron diffraction (LEED) and compositional analysis by Auger electron spectroscopy (AES). The relationship between catalyst structure and composition on an atomic scale and the resultant activity, selectivity and stability of the catalyst can thus be explored. The reactions we are studying are the dehydrogenation and hydrogenolysis of cyclohexane and the dehydrocyclization and hydrogenolysis of n-heptane in the pressure range of 100-500 Torr and temperature range of 200-300°C. The apparatus used to study these reactions consists of an ultrahigh vacuum system within which is mounted a movable reaction cell capable of isolating the catalyst from the main vacuum chamber. This arrangement allows high pressure reaction

studies to be performed on surfaces which have been characterized by LEED and AES under ultrahigh vacuum conditions.

For the reaction of cyclohexane we find that the activity and selectivity of the catalysts are sensitive to surface structure, but rather insensitive to the presence of surface oxide. The most densely packed surface, the (111), exhibits the highest hydrogenolysis rates and the lowest benzene formation rates. Highly stepped or kinked surfaces have benzene formation ratio about a factor of 3 lower than the (111) surface. Thus the selectivity of dehydrogenation to benzene versus hydrogenolysis varies by at least a factor of 10, depending on surface structure. These high pressure reaction studies exhibit quite different characteristics than similar studies on platinum single crystals at pressures of less than 10^{-5} Torr. The apparent activation energy, the structure sensitivity and the reaction probability are all substantially different between the two pressure extremes. These differences are the result of fundamental differences in the nature of the active surface in the two cases. At less than 10^7 Torr the inherent activity of "clean" platinum is being measured. At high pressure the surface is covered with a layer consisting of adsorbed products, reactants, reaction intermediates and deactivating residues, thus making the surface much more complex than in the low pressure case. It is apparent from these studies that the nature of the active surface must be considered as dependent on reaction conditions.

In addition to being sensitive to surface structure, the reaction of n-heptane, unlike cyclohexane, depends also on the presence of surface oxide. On clean surfaces the rate of hydrogenolysis varies by a factor of 3 as the surface structure is changed. The rate is lowest on the (111) surface and highest on the highly kinked surfaces. The dehydrocyclization of n-heptane to toluene varies by about a factor of 4 as a result of changes in surface structure and is highest on surfaces with intermediate step density. This results in changes of selectivity of about a factor of 7. Preoxidation of all surfaces studied produced large changes in the selectivity of hydrogenolysis versus dehydrocyclization. This preoxidation caused enhancement of hydrogenolysis and a decrease of toluene production resulting in selectivity changes as large as a factor of 50.

* * *

[†]Brief version of LBL-10576.

3. THE STRUCTURE AND REACTIVITY OF ORDERED PLATINUM STRUCTURE AND MONOLAYERS EPITAXIALLY DEPOSITED ON THE Au(100) CRYSTAL FACE

A. Sachtler and G. A. Somorjai

The dehydrogenation of cyclohexene has been studied on monolayers of platinum which were deposited on gold single crystal surfaces of (100) orientation. Two monolayers of ordered platinum

were necessary to obtain optimum reaction rates. The rate of reaction on the evaporated layer was seven times greater than that on a Pt(100) crystal face. The effects of other substrates, such as copper and tungsten, and the effect of gold deposited on platinum crystal surfaces, are being explored.

RESEARCH PLANS FOR CALENDAR YEAR 1980

Surface structure analysis of small molecules, CO, CO₂, C₂H₂ and C₂H₄ on the rhodium and platinum crystal surfaces will be carried out using LEED and ELS.

A high pressure cell will be built to combine catalytic and ELS studies.

The velocity distribution of molecules after surface reactions will be measured to determine the nature of surface-gas energy transfer and reaction dynamics.

Epitaxial deposition of metals on other metal crystal surfaces will be studied (Au on Rh, Cu on Pt, Na on Ni) and the reactivities of the metal monolayers will be investigated.

Carbon-14 dating will be employed to characterize the exchange ratios of hydrocarbon fragments deposited on platinum surfaces during hydrocarbon reactions.

The effect of chlorine additive on the reactivity of platinum will be studied.

1979 PUBLICATIONS AND REPORTS

Refereed Journals

1. L. E. Firment and G. A. Somorjai, "LEED Study of the Surface of Thin Crystals and Monolayers of Normal Paraffins and Cyclohexane on the Ag(111) Crystal Surface," *J. Chem. Phys.* **69**, 3940 (1978).
2. I. Toyoshima and G. A. Somorjai, "Heats of Chemisorption of O₂, H₂, CO, CO₂, and N₂ on Polycrystalline and Single Crystal Transition Metal Surfaces," *Catal. Rev. Sci. Eng.* **19**, 150-159 (1979).
3. G. A. Somorjai, "Active Sites for Hydrocarbon Catalysis on Metal Surfaces," IUPAC Meeting Proc. Tokyo Sept. 1-11, 1977, *Pure and Appl. Chem.* **50**, 963 (1978).
4. J. T. Yates Jr., W. Clinton and G. A. Somorjai, "Report of the Surface Science Workshop," ERDA Report (1977) *Matl. Sci. and Eng.* **35**, 15 (1978).
5. D. J. Dwyer, K. Yoshida, and G. A. Somorjai, "Hydrogen of CO and CO₂ on Clean Rhodium and Iron Foils. Correlations of Reactivities and Surface Composition," *Proc. of the Petro. Div. of the ACS* (1978), *Energy Res. Abstr.* **3**, No. 30498; *Adv. in Chemistry No. 178*, Eds. Kugler and Steffgen Chapt. 7 (1979).

6. "Catalysis on the Atomic Scale," 1977 Emmett Lecture, *Catal. Rev.* 18, 173 (1978).
7. J.-P. Biberian and G. A. Somorjai, "On the Calibration of Monolayer Coverage by Auger Electron Spectroscopy. Application to Carbon on Platinum," *Appls. of Surface Sci.* 2, 352 (1979).
8. D. Dwyer and G. A. Somorjai, "The Role of Readorption in Determining the Product Distribution During CO Hydrogenation over Fe Single Crystals," *J. Catal.* 56, 249 (1979).
9. J. C. Hemminger, E. L. Muetterties and G. A. Somorjai, "A Coordination Chemistry Study of a Nickel Surface. The Chemistry of Ni(111) with Triply Bonded Molecules," *J. Amer. Chem. Soc.* 101, 62 (1979).
10. M. Salmerón, R. J. Gale and G. A. Somorjai, "A Modulated Molecular Beam Study of the Mechanism of the H₂-D₂ Exchange Reaction on Pt(111) and Pt(332) Crystal Surfaces," *J. Chem. Phys.* 70, 2180 (1979).
11. L. L. Kesmodel, L. H. Dubois and G. A. Somorjai, "LEED and ELS Analysis of Ethylene Chemisorption on the Pt(111) Surface, Evidence for Ethylidyne Formation," *J. Chem. Phys.* 70, 2180 (1979).
12. D. G. Castner and G. A. Somorjai, "LEED and Thermal Desorption Studies of Small Molecules (H₂, O₂, CO, CO₂, NO, C₂H₄, C₂H₂ and C) Chemisorbed on the Stepped Rh(755) and (331) Surfaces," *Surface Sci.* 83, 60 (1979).
14. G. A. Somorjai, "Studi LEED delle Reazioni Catalitiche," *Enciclopedia della Scienza e della Tecnica Mondadori*, pp. 130-36 (1978).
15. D. G. Castner and G. A. Somorjai, "Surface Structures of Adsorbed Gases on Solid Surfaces, A Tabulation of Data Reported by LEED Studies," *Chem. Rev.* 79, 233 (1979).
16. L. E. Firment and G. A. Somorjai, "LEED Studies of the Surfaces of Molecular Crystals (Ice, Ammonia, Naphthalene, Benzene)," *Surface Sci.* 84, 275 (1979).
5. L. H. Dubois and G. A. Somorjai, "The Chemisorption of CO and CO₂ on Rh(111) Studied by High Resolution Electron Energy Loss Spectroscopy," LBL-9280.
6. D. G. Castner and G. A. Somorjai, "LEED, AES and Thermal Desorption Studies of the Oxidation of the Rh(111) Surface," LBL-9288.
7. G. A. Somorjai, "Catalysis and Surface Science," 2nd European Conf. on Surface Sci., Plenary Lecture, Cambridge, England, March 19-23, 1979, LBL-9043.
8. M. A. Van Hove, and G. A. Somorjai, "Adsorbed Monolayers on Solid Surfaces," LBL-8566.
9. J.-P. Biberian and G. A. Somorjai, "Surface Structures of Metallic Monolayers on Metal Crystal Surfaces," LBL-8996.
10. M. A. Van Hove and G. A. Somorjai, "A New Microfacet Notation for High Miller Index Surfaces of Cubic Materials with Terrace, Step and Kink Structures," LBL-9363.
11. S. M. Davis and G. A. Somorjai, "Correlation of Cyclohexene Reactions on Platinum Crystal Surfaces over Ten Orders of Magnitude Pressure Range: Variations of Structure Sensitivity Rates and Reaction Probabilities," LBL-9869.
12. F. T. Wagner, S. Ferrer and G. A. Somorjai, "Photocatalytic Hydrogen Production from Water over SrTiO₃ Crystal Surfaces, Electron Spectroscopy Studies of Adsorbed H₂, O₂, H₂O," LBL-9942.
13. L. H. Dubois, D. G. Castner and G. A. Somorjai, "The Chemisorption of Acetylene and Ethylene on Rh(111): A Low Energy Electron Diffraction (LEED), High Resolution Electron Energy Loss (ELS) and Thermal Desorption Mass Spectrometry (TDS) Study," LBL-9946.
14. D. G. Castner, R. L. Blackadar and G. A. Somorjai, "CO Hydrogenation over Clean and Oxidized Rhodium Foil and Single Crystal Catalysts. Correlations of Catalyst Activity, Selectivity and Surface Composition," LBL-10018.
15. F. T. Wagner and G. A. Somorjai, "Photocatalytic and Photoelectrochemical Hydrogen Production on Strontium Titanate Single Crystals," LBL-10020.
16. S. Ferrer and G. A. Somorjai, "UPS and UXP Studies of the Chemisorption of O₂, H₂ and H₂O on Reduced and Stoichiometric SrTiO₃(111) Surfaces," LBL-10037.

LBL Reports

1. J. C. Hemminger, R. Carr, W.-J. Lo and G. A. Somorjai, "Photochemical Processes at the Solid-Gas Interface: The Adsorption and Reactions of Gaseous CO₂ and H₂O on Pt-SrTiO₃ Single Crystal Sandwiches," LBL-8441.
2. L. H. Dubois, and G. A. Somorjai, "The Dissociative Chemisorption of CO₂ on Rhodium Surfaces," LBL-8976.
3. M. Salmerón and G. A. Somorjai, "A LEED-AES Study of the Reconstructed Pt(110) Surface and the Effect of Oxygen Treatment," LBL-8464.
4. S. M. Davis and G. A. Somorjai, "The Effect of Surface Oxygen on Hydrocarbon Reactions Catalyzed by Platinum Crystal Surfaces with Variable Kink Concentrations," LBL-8992.

Invited Talks

1. G. A. Somorjai, "Low Energy Electron Diffraction Studies of the Surfaces of Simple Molecular Crystals," Vacuum Society Meeting, San Francisco, Dec. 2, 1978.
2. G. A. Somorjai, "The Organic Surface Chemistry of Platinum. An Atomic Scale View of Bonding and of the Ingredients for Catalytic Selectivity," Linden Research Department Colloquium, Linden, N.J. Dec. 13, 1978.

3. G. A. Somorjai, "Active Sites for Hydrocarbon Catalysis on Metal Surfaces," Union Carbide, Tarrytown, New York, Dec. 13, 1978.
4. G. A. Somorjai, "Heterogeneous Catalysis," DOE Research Meeting, Gaithersburg, Maryland, Dec. 14-15, 1978.
5. G. A. Somorjai, "Reactivity of Hydrocarbon over Metal Surfaces," UCLA Physical Chemistry Seminar, January 9, 1979.
6. G. A. Somorjai, "The Structure and Catalytic Activity of Hydrocarbons on Metal Surfaces," University of Colorado, Boulder CO, Feb 20, 1979.
7. G. A. Somorjai, "The Surface Chemical Bond," Colorado State University, Ft. Collins, CO, Feb. 21, 1979.
8. G. A. Somorjai, "Photochemical Reactions of H₂O and CO₂ on Solid Surfaces," UC Berkeley, Dept. of Physics, Feb. 28, 1979.
9. G. A. Somorjai, "Organic Surface Character of Platinum: Investigation on the Atomic Scale," California Institute of Technology, Pasadena, CA, March 7, 1979.
10. G. A. Somorjai, "The Effect of Surface Oxygen on Hydrocarbon Catalysis by Platinum Crystal Surfaces with Variable Kink Concentration," (presented by L. H. Dubois) California Catalysis Society Meeting, Stanford University, March 16-17, 1979.
11. G. A. Somorjai, "The Structure of Ir(100)(5×1) Analyzed by Dynamical LEED" (presented by M. A. Van Hove) American Physical Society Meeting, Chicago, March 19-23, 1979.
12. G. A. Somorjai, "Structure of Adsorbed Gases on Solid Surfaces," University of Madrid, Madrid, Spain, March 20, 1979.
13. G. A. Somorjai, "Catalysis of Hydrocarbon over Metal Surfaces," Surface Science Consejo, Madrid, Spain, March 21, 1979.
14. G. A. Somorjai, "The Structure and Activity of Organic Molecules on Platinum Surfaces," University of Milani, Milan, Italy, March 25, 1979.
15. G. A. Somorjai, "Catalysis and Surface Science," European Conference on Surface Science(2), Plenary Speaker, Cambridge, England, March 28, 1979.
16. G. A. Somorjai, "The Organic Surface Chemistry of Pt. An Atomic Scale View of Catalytic Activity for Hydrocarbon Reactions," University of Minnesota, Physical Chemistry Seminar, April 16, 1979.
17. G. A. Somorjai, "The Effect of Chemisorbed Oxygen on the Hydrogenation and Dehydrogenation of Platinum Catalysts," 11th Central Regional Meeting of ACS, Columbus, Ohio, May 7, 1979.
18. G. A. Somorjai, "Molecular Beam Studies of Chemisorption and Catalysis on Metal Surfaces," University of British Columbia, Vancouver, BC June 5, 1979.
19. G. A. Somorjai, "High and Low Pressure Studies of the Dynamics of Surface Catalyzed Reactions on Single Crystals," Gordon Conference, Plymouth State College, NH, Aug. 16, 1979.
20. G. A. Somorjai, "Heterogeneous Catalysis on the Atomic Scale," 6th Canadian Symposium on Catalysis, Ottawa, Canada, Aug. 20, 1979.

f. Nuclear Magnetic Resonance*

Alexander Pines, Investigator

1. SELECTIVE EXCITATION OF n-QUANTUM TRANSITIONS[†]

W. S. Warren, S. Sinton, D. P. Weitekamp, and A. Pines

Previous work in our group has demonstrated the excitation of all symmetry allowed transitions in systems of coupled nuclear spins, in contrast to the usual single quantum ($\Delta m=1$) selection rule common to magnetic resonance and other branches of spectroscopy.¹ The sequences of wideband irradiation used were either nonselective or, at best, selectively excited either the even or odd quantum transitions.² This year for the first time wideband excitation sequences were demonstrated which are n-quantum selective.³ These produce coherent superpositions of those states connected by absorption of kn quanta from the radiation field ($k=0, 1, 2, \dots$) and require no detailed prior knowledge of the energy levels.

The spectra of Fig. 1 illustrate the selective excitation of the zero and four quantum transitions in oriented benzene as detected by multiple quantum Fourier transform NMR. The essential feature of the

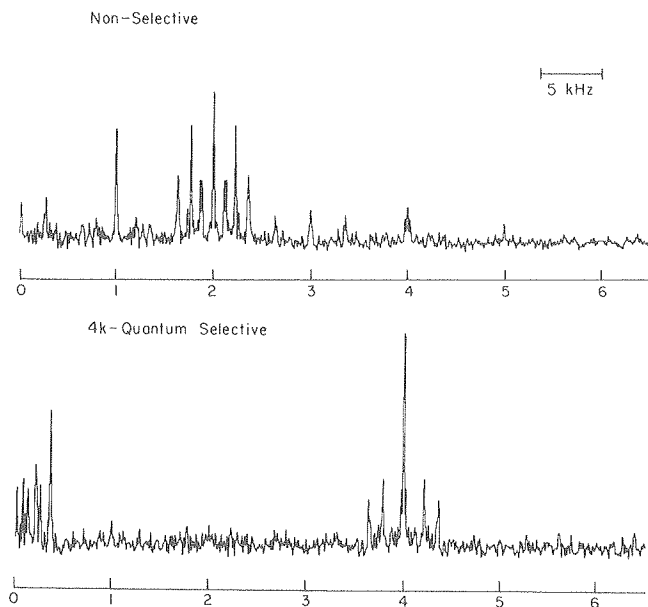


Fig. 1. Selective excitation of zero and four quantum transitions in benzene oriented in a liquid crystal. The selective spectrum and the nonselective control were obtained under identical conditions except for the omission of phase shifts in the control. (XBL 7912-5200)

excitation sequences is systematic permutation of the phase of the coherent radiation. Analysis of the general class of such sequences by the methods of average Hamiltonian theory has demonstrated the possibility of constructing sequences selective to arbitrary accuracy, limited only by relaxation processes.⁴ This approach promises to be generally applicable to selective excitation of coherence and selective population inversion in multilevel systems. Ongoing experimental work is aimed at improving the signal-to-noise ratio in multiple quantum Fourier transform NMR by use of highly selective and efficient excitation and detection sequences.

* * *

[†]Brief version of LBL-9820.

1. G. Drobny, A. Pines, S. Sinton, D. P. Weitekamp, and D. Wemmer, "Fourier Transform Multiple Quantum NMR," Faraday Symposium of Chemical Society, No. 13, 1979, LBL-8565 and references therein.
2. D. Wemmer, Ph.D. thesis, 1979, LBL-8042.
3. W. S. Warren, S. Sinton, D. P. Weitekamp, and A. Pines, "Selective Excitation of Multiple Quantum Coherence in Nuclear Magnetic Resonance," Phys. Rev. Lett. 43 1791 (1979).
4. W. S. Warren, D. P. Weitekamp, and A. Pines, "Theory of n-Quantum Selectivity in Multiple Quantum Spectroscopy," 1979, LBL-10161.

2. INFORMATION THEORY TREATMENT OF MULTIPLE-QUANTUM COHERENCE

R. D. Levine, S. Mukamel, W. Warren, and A. Pines

Multiple-quantum spectra tend to have fewer lines than their single-quantum counterparts, but this enhanced simplicity has to be balanced against a reduced overall intensity. An average of many multiple-quantum experiments reveals a decrease in overall intensity as a function of number of quanta that is roughly Gaussian. A somewhat more sophisticated model can be formulated by specifying the strength of single-quantum coherences and finding the density matrix which maximizes the information entropy subject to this constraint. The resultant intensity pattern confirms the validity of a "dynamic random-phase approximation," which assumes that transitions between adjacent manifolds of total z-component of spin angular momentum add incoherently. This information theory treatment also permits qualitative calculation of the effects of temperature on multiple-quantum coherences.

An example of the predicted n-quantum intensities from information theory as a function of pumping strength is shown in Fig. 1.

* This work was supported by the Division of Materials Sciences, Office of Basic Energy Sciences, U. S. Department of Energy.

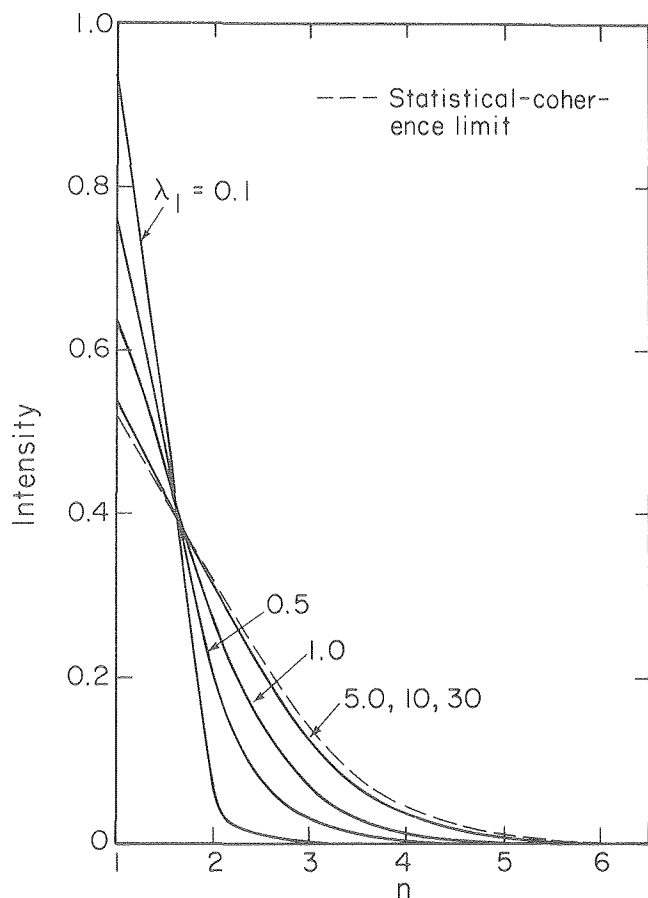


Fig. 1. Comparison of experimental n -quantum intensity with those from a dynamic random phase theory. (XBL 796-10080)

3. RELAXATION OF MULTIPLE QUANTUM TRANSITIONS[†]

J. Tang and A. Pines

A particularly interesting feature of multiple quantum NMR is the information available from the n -quantum relaxation. Stoll et al. have shown that relaxation of the forbidden double quantum transition in two spin AX spin systems contains information on the correlated fluctuations at the A and X sites. In a thorough discussion, Wokaun and Ernst also presented the theory for n -quantum relaxation and showed experimental results on a two-spin system in an isotropic field. Further, Poupko et al. and Bodenhausen et al. have demonstrated the applicability of multiple quantum NMR to the study of relaxation and motion in coupled systems of deuterium nuclear spins.

We have been interested in the multiple quantum NMR of strongly dipolar coupled spin-1/2 nuclei in oriented systems (solids, liquid crystals). These illustrate the behavior of systems with high symmetry, for example a CH_3 group or benzene. Normally, radiofrequency irradiation can induce only transitions between eigenstates belonging to the same irreducible representations of the spin Hamiltonian.

However, relaxation by fluctuating random fields may induce symmetry-breaking transitions and the study of n -quantum spectra and their relaxation should allow a complete determination of the fluctuations, correlations and symmetry-breaking pathways. We have performed a first study of the relaxation of dipolar coupled 3-proton system (CH_3 group) by paramagnetic impurities in a liquid crystal solvent. The 1-, 2-, and 3-quantum linewidths were studied over a wide concentration range and the accurate linewidth ratios allowed a determination of the fact that fluctuations are correlated and a measurement of the correlation times. Figure 1 shows the relaxation broadening of the 1, 2, and 3 quantum transitions in agreement with the solid lines based on a model of completely correlated fluctuation. This approach is being used to study correlations of sequential motion in ordered molecular chains.

* * *

[†]Brief version of LBL-9853.

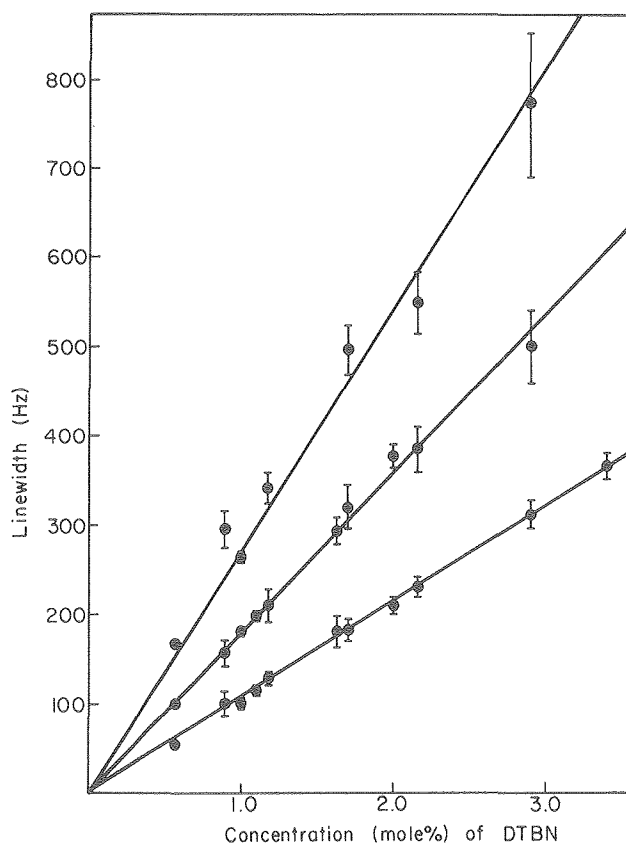


Fig. 1. The linewidths of multiple quantum transitions is linearly proportional to the concentration of DTBN. The ratios of the relaxation rates can be determined accurately by measuring the ratios of the slope. The solid lines indicate the behavior expected for completely correlated fluctuations at the 3 proton sites. (XBL 796-10118)

4. ANALOGY OF MULTIPLE-QUANTUM NMR TO ISOTOPIC LABELING[†]

W. S. Warren and A. Pines

The number of allowed transitions in the NMR spectra of oriented molecules increases dramatically as the number of spins increases. For this reason, large molecules often require selective isotopic substitution to give resolvable spectra. However, the synthesis of selectively substituted molecules can be difficult, and in some cases the substitutions change molecular geometries or reaction rates.

Multiple-quantum NMR provides an alternative means of simplifying spectra which does not require any chemical alterations, see Fig. 1. Group theoretical arguments indicate that the M-quantum transitions of an N spin system inherently label M of the spins, and that the number of allowed transitions can be counted by considering only molecules that have M isotopic substitutions. We have derived simple counting schemes for the number of lines in

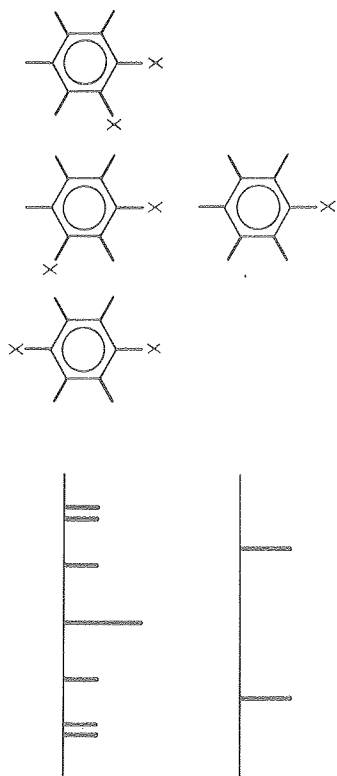


Fig. 1. The isotopic labeling analogy with multiple-quantum NMR. If five protons of benzene are each replaced by a single different nucleus, only one species results. The remaining proton can be up or down, giving one pair of lines in the five-quantum spectrum. Four substitutions leave three possibly different species, each configuration (ortho, meta, or para) gives a triplet, so the four-quantum spectrum has three pairs of lines plus a highly degenerate central peak.

(CBB 794-4431)

N-quantum, (n-1)-quantum, and (N-2)-quantum spectra, and verified our predictions experimentally on oriented benzene and other molecules.

* * *

[†]Brief version of NMR article in 4th European Experimental NMR Conference, Grenoble/Austans, June 26-29, 1979.

5. STATISTICAL CONFIGURATIONS OF ALIPHATIC CHAINS[†]

D. P. Weitekamp, G. Drobny, and A. Pines

A full understanding of the liquid crystal state of matter requires a characterization of both the external and internal configurations of the constituent molecules. The microscopic quantities are not only of descriptive interest, but constitute a large set of experimental data which, in conjunction with thermodynamic quantities, can be used to develop and discriminate among statistical mechanical models of these phases. Figure 1 illustrates the possible single bond conformations, the probabilities of which are among the unknowns of interest.

Magnetic resonance studies of the anisotropic terms of the nuclear spin Hamiltonian constitute an unparalleled set of techniques for measurement of the microscopic degrees of order in partially fluid systems. Previous work in our group has focused on measurement of the motionally averaged nuclear quadrupole interactions and resolved direct dipolar interactions in specifically deuterated liquid crystals.¹ Current work is on the use of proton multiple quantum Fourier Transform spectroscopy to obtain resolved spectra from species with unresolved single quantum spectra. The advantages of this approach over deuterium studies include: higher accuracy due to the longer relaxation times of the protonated species; the ability to measure internuclear geometry over greater distances due to the larger gyromagnetic ratio of the proton; and the vastly simpler chemical synthesis required. Preliminary spectra indicate that attainable resolution in measurement of dipolar couplings is about one part per thousand for butyl bromide (nine spin system) dissolved in a nematic liquid crystal. Future work aims toward analysis of the multiple quantum spectrum of the same proton spin system incorporated into an otherwise deuterated nematogen.

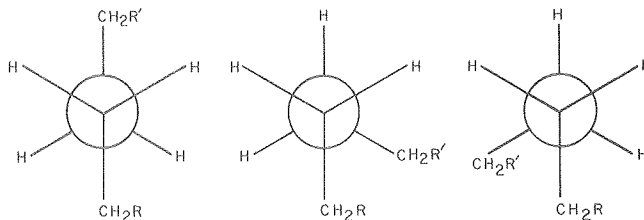


Fig. 1. Projection diagram of possible rotamers at a carbon-carbon single bond in a chain.

(XBL 771-7397)

* * *

†Brief version of LBL-6976.

1. S. Hsi, H. Zimmerman, and Z. Luz, "Deuterium Magnetic Resonance of Some Polymorphic Liquid Crystals: The Conformation of the Aliphatic End Chains," *J. Chem. Phys.* **69**, 4126 (1978).

6. CORRELATION IN THE MOTION OF COUPLED METHYL GROUPS†

J. Tang, Y. S. Yen, and A. Pines

An interesting question to chemists, and one that has been consistently difficult to approach, is the characterization of conformation and correlated motion of molecular groups which are "sterically hindered." An example is two methyl groups in proximity on the same molecular framework. In the limit of vanishing coupling between the groups we expect no correlation in the motion of the two methyl groups, and they should reorient independently. This is indicated schematically in Fig. 1(a). In the opposite limit of strong coupling, we expect completely correlated motion as indicated in Fig. 1(b). Since there are six protons in this problem, 4-quantum NMR spectra should be sensitive to two body correlations and should allow a distinction between the two cases. In fact, experiments in liquid crystals have demonstrated this to be true. Experiments are continuing on a variety of single crystals at low temperatures to see the effects of tunneling and correlation when phonon interruption of the phases is diminished.

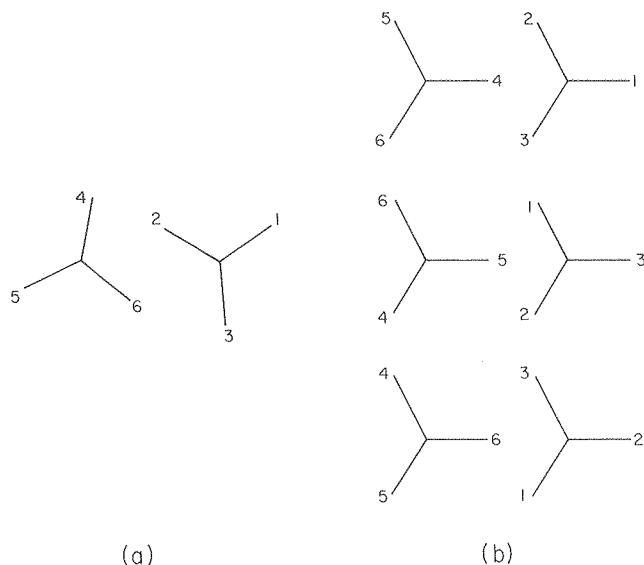


Fig. 1. (a) Two methyl groups with uncorrelated motions, random positions of all 6 protons. (b) correlated motions of methyl groups. Only 3 different configurations are allowed.

(XBL 7912-5207)

* * *

†Brief version of LBL-10162.

7. BIPHENYL CONFORMATION IN A LIQUID CRYSTAL MOLECULE†

S. Sinton, D. P. Weitekamp, and A. Pines

A study of biphenyl structure is important to an understanding of the physics and chemistry of liquid crystal molecules containing this subunit. Of particular interest are the ring deformations and the dihedral angle which is related to the potential for the partially hindered rotation about the carbon-carbon ring bridge. The NMR of molecules forming or dissolved in a liquid crystalline matrix has proved to be an invaluable tool to the investigation of molecular structure and potentials. The NMR spectra contain information on the structure sensitive intramolecular dipolar couplings among the nuclei. Fourier Transform Multiple Quantum NMR (FTMQNMR) can be used to yield simplified higher quantum spectra ($\Delta M > 1$) when the one quantum spectrum ($\Delta M = 1$) is too complex and unresolved to analyze. Group theoretical considerations for a symmetrically para substituted biphenyl indicate that, whereas there are hundreds of one quantum transitions possible, the number of unique 5, 6, 7, and 8 quantum transitions are 46, 11, 2 and 1 respectively. Together, these may be used for an analysis of molecular structure.

Shown in Fig. 1 is the multiple quantum spectrum of the biphenyl protons in d_{11} -pentylcyanobiphenyl which is in the nematic phase. The lower order ($\Delta M = 1, 2, 3, \dots$) transitions overlap to give unresolved subspectra. The higher order ($\Delta M = 5, 6, 7, 8$) transitions result in a set of resolved lines which can be fit with theory to yield the desired molecular parameters. Further applications of FTMQNMR to this and other substituted biphenyls and the development of computer simulations of model structures are underway.

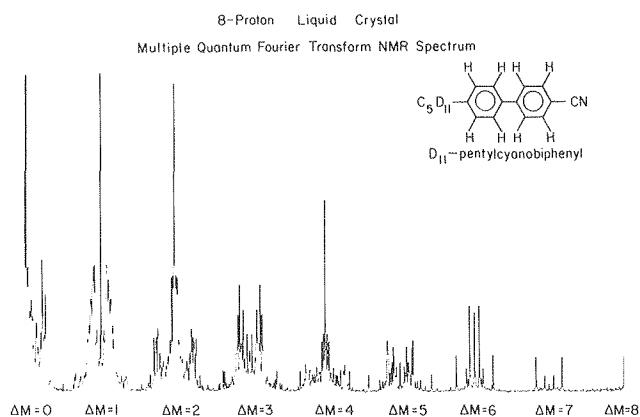


Fig. 1. Multiple-quantum NMR spectra of 8-proton system from biphenyl part of molecule. From the $n = 5, 6, \text{ and } 7$ region the conformation and dynamics are studied.

(XBL 7912-5203)

* * *

†Brief version of LBL-8565.

8. SYNTHESIS OF LIQUID AND SOLID CRYSTALS

S. Wolfe and A. Pines

In many anisotropic systems, it has been necessary to align the molecules of the sample so that they share some common mode of orientation in the magnetic field. This can be accomplished by 1) growing the molecules into a single crystal, 2) dissolving the compound in a liquid crystal, or 3) by synthesizing a liquid crystal which contains an isotopically labeled moiety of interest.

Solid single crystals of about 5-20 mm in length are grown from either synthesized or commercially available material. The material is first zone refined to provide a very pure material. The crystals are then grown by the classical technique of slowly evaporating a saturated solution of the compound in a suitable solvent or for some compounds the crystals are grown by lowering a melt of the compound through a heat gradient in a Bridgeman apparatus. Both materials for single crystals and liquid crystals have been synthesized with deuterium and carbon-13 labeling. Labeled material has been used to grow single crystals of perdeuterated material doped with 5% protonated material to provide a means for observing protons in single crystals without intermolecular couplings. Liquid crystals such as, 4-n-alkyl-4'-cyanobiphenyls, for example, as shown in Fig. 1, have been synthesized with various labelings in order to study the conformations of aliphatic chains and biphenyl rings. Liquid crystals have been synthesized in a perdeuterated manner for use as a solvent for future applications in multiple quantum NMR studies.

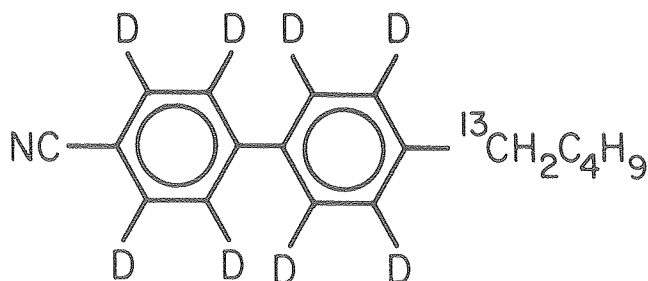


Fig. 1. Isotopically labeled cyanobiphenyl liquid crystal molecule. (XBL 7912-5204)

9. ANISOTROPIC RELAXATION OF DEUTERATED HEXAMETHYLBENZENE

J. Tang, L. Sterna, and A. Pines

Molecules in solids may exhibit various kinds of symmetric motion. Hexamethylbenzene (NMB) is a good example. The methyl groups (CD_3) of the molecule reorient about their C_3 -symmetry axes rapidly. In addition, the whole molecule may reorient about its C_6 -axis at a slower rate. The spin-lattice relaxation at room temperature of deuterated hexa-

methylbenzene- d_{18} is caused mainly by the fluctuation of nuclear quadrupole coupling by molecular motion about the C_6 -axis. The contribution of fluctuating dipole-dipole interactions is rather small and can be neglected.

We have observed the anisotropic relaxation of HMB- d_{18} . The anisotropy changes as the temperature changes from 70°C to -36°C as predicted by our model (see Fig. 1). The measurements of the temperature dependence of the spin-lattice relaxation also confirm our model. Further investigations on lineshape changes and other HMB compounds with different degrees of deuteration are in progress. These techniques are essential for an understanding of molecular dynamics in solids.

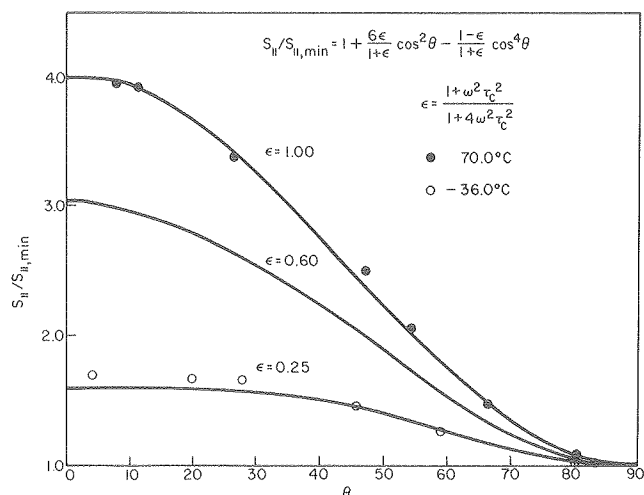


Fig. 1. Orientation dependence of the spin-lattice relaxation rate S_{11} of deuterium in HMB- d_{18} for two temperatures. The anisotropy changes as temperature changes from 70°C ($\omega^2\tau_c^2 \ll 1$) to -36°C . (XBL 7912-5202)

* * *

† Brief version of LBL-8042.

10. SPIN-LATTICE RELAXATION OF REORIENTING OR TUNNELING DEUTERATED METHYL GROUPS

J. Tang, S. Emid, and A. Pines

Unlike methyl groups (CH_3), the deuterated methyl group (CD_3) has different features in spin-lattice relaxation. The fluctuation of quadrupole coupling of the deuterons by random reorientation or tunneling about their C_3 symmetry axis is the dominant relaxation mechanism. For random reorientation at high temperature (≥ 77 K) Zeeman, quadrupole, tunneling and the rotation polarization systems are predicted to be uncoupled, in contrast to the CH_3 case in which Zeeman and rotational polarization systems are coupled, respectively. For tunneling CD_3 groups at low temperature ($\ll 77$ K) the Zeeman and tunneling systems are coupled and, consequently, the Zeeman spin-lattice relaxation is predicted to become non-exponential, see Fig. 1a, b.

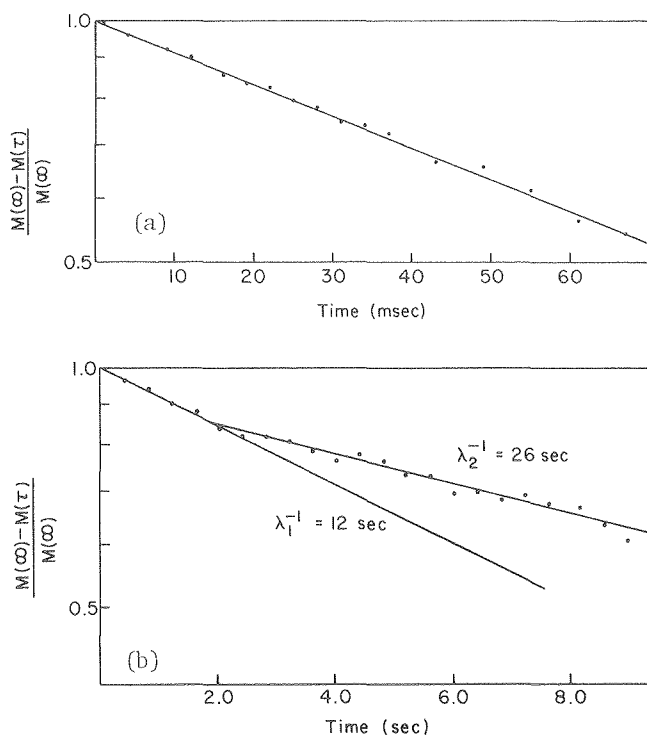


Fig. 1. The recovery of the intensity of the spectrum is plotted on the semi-logarithmic scale; (a) shows the spin-lattice relaxation at liquid nitrogen temperature and is exponential with $T_1 = 1.1 \pm 0.1$ sec; (b) shows the spin-lattice relaxation at liquid helium temperature and is the sum of two exponentials.

[(a) XBL 7912-13586;
(b) XBL 7912-13585]

The experimental results show that the relaxation is exponential at liquid nitrogen temperature and becomes non-exponential at liquid helium temperature, thus verifying the unique expectations for CD_3 relaxation. These effects arise from statistical interference of the boson wavefunctions at low temperatures.

* * *

† Brief version of LBL-10162.

11. ROTATIONAL POLARIZATION OF SOLID METHYL IODIDE[†]

S. Emid, L. Sterna, and A. Pines

In the gas phase the rapidly rotating ($\approx 10^{13}$ Hz) methyl group of the methyl iodide molecule CH_3I generates a magnetic moment which can be detected through shifts in the rotational spectrum of CH_3I in a magnetic field. The question arises as to whether this magnetic moment can be detected in the solid state. In the solid where the rotation is strongly hindered by the nearest neighbor molecules, the methyl group is most accurately described as a torsional oscillator. The torsional energy levels are subdivided into three distinct symmetries A, E_1 and E_2 corresponding to the three irreducible

representations of a C_3 -rotor. The A-states do not rotate and may be viewed as pure torsional oscillations. The E -states do rotate, and within a given torsional level E_1 and E_2 rotate in opposite directions (see Fig. 1). The population difference E_1 - E_2 is termed "Rotational Polarization." The nuclear spins on the methyl group are coupled to the torsional sublevels by symmetry. As such, the spin states and rotor states constitute two thermodynamic systems in contact with one another. By altering the populations in one system (i.e. changing the temperature), the populations in the other system will be altered through the contact.

We have been able to induce preferential population of the E_1 -states over the E_2 -states (i.e. Rotational Polarization) in solid CH_3I by using rf pulses to pump the nuclear spin states and then allowing them to relax. Since the orientation of the methyl groups is fixed in the solid, the rotational polarization can be inverted by a 180° -flip of the sample (Note: although rotational relaxation is very fast, relaxation of rotational polarization can be very slow ~ 1 -100 sec). By performing sample flipping experiments and measuring subsequent changes in the nuclear spin state populations, we are measuring the methyl group magnetic moment. Future work will be facilitated by the use of a new sample flipping probe allowing 180° -sample flips in 0.1 sec with 1° accuracy.

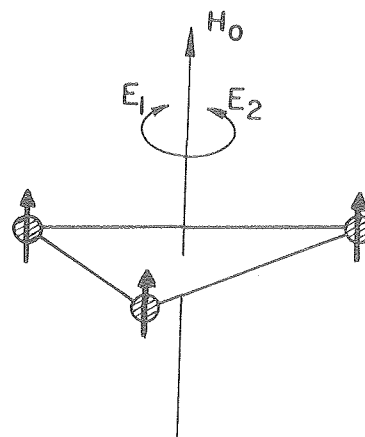


Fig. 1. Relation of E -states to methyl group rotation. The pulsed NMR induces a preferential population of E_1 . (XBL 783-4788)

* * *

† Brief version of LBL-9997.

12. EXCHANGE OF ROTATIONAL POLARIZATION IN METHYL GROUPS

S. Emid, L. Sterna, Y. S. Yen, and A. Pines

As a consequence of the Pauli Exclusion Principle, the magnetization of the protons on a methyl group is coupled to the rotational polarization, where rotational polarization is a quantity asso-

ciated with a preferential rotation of the methyl group in one sense. From the coupling to the rotational polarization, the spin-lattice relaxation of the magnetization is non-exponential. This coupling can be used to probe the rotational dynamics and relaxation of methyl groups.

In particular, rotational polarization can be used to measure the degree of steric hindrance between methyl groups. If two adjacent methyl groups are so sterically hindered that they rotate in a gear-like manner, the rotational polarization of the two methyl groups tend to cancel. (In fact, it is identically zero when the two methyl groups have their C_3 axes at the same polar angle with respect to the external magnetic field.) To demonstrate this, we have measured the relaxation curve of the proton magnetization of 1, 4, 5, 8 tetramethylnaphthalene (molecule a) and of 1, 4, 5, 8 tetramethylantracene (molecule b) in powdered form (Fig. 1a,b). The relaxation of molecule a was found to be exponential and of molecule b to be non-exponential. This is consistent with our expectations using the concept of rotational polarization. Molecule a has methyl groups that are more sterically hindered than b and hence would have a small net rotational polarization. Its relaxation curve should appear exponential. The methyl groups of molecule b are further separated and thus much less sterically hindered. Its rotational polarization should be larger and is in fact measurable, leading to a non-exponential relaxation. The above argument considered only intramolecular interferences. Certainly the intermolecular interference should be taken into account. We are using rotational polarization to study the transfer of rotational polarization in molecules with various separations of the methyl groups.

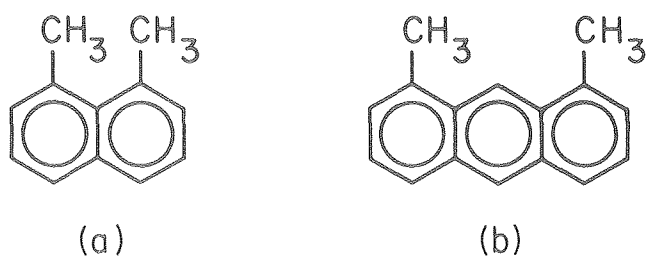


Fig. 1. (a) Molecule a - 1, 4, 5, 8 Tetramethylnaphthalene. No rotational polarization (spatial polarization of the methyl rotor) can be formed due to strong coupling of the methyl groups. (b) Molecule b - 1, 4, 5, 8 Tetramethylantracene. Rotational polarization is formed easily since the methyl groups are essentially uncoupled. In the intermediate case the transfer of rotational polarization from one methyl group to another will be measured. (XBL 7912-5201)

13. VISCOSITY DEPENDENCE OF THE MAGNETIC ISOTOPE EFFECT[†]

L. Sterna, P. Mayeda, S. Wolfe, and A. Pines

In a free radical chemical reaction two radicals, each of electron spin = 1/2, diffusively encounter and form a radical pair in either a singlet (spin =

0) or triplet (spin = 1) electronic state. Typically, only those radical pairs in the singlet state can combine to form product molecules while those in the triplet state undergo only unreactive collisions. The hyperfine coupling between the unpaired electrons and the nuclei present in the radicals can serve as an efficient means for inducing intersystem crossing of the radical pair from the triplet to the singlet state. By preparing the radical pairs preferentially in a triplet state, those radical pairs containing nuclei of large hyperfine coupling strength have a much greater probability of forming product than those without large hyperfines. In the presence of other chemical processes competing for the consumption of the radicals, it is possible to chemically separate isotopes of different spin (i.e. different hyperfine coupling). The Russian group of Buchachenko, et al. first reported using such a technique for enriching dibenzyl ketone in ¹³C, and we subsequently enhanced the effect by several means. Our calculations predict a strong viscosity dependence for this enrichment process. The enrichment is expected to exhibit a maximum in the viscosity dependence and then fall away to zero at either extreme away from the maximum. Experiments have been performed using dibenzyl ketone in which the viscosity has been varied over four orders of magnitude. The experimental data in Figs. 1 and 2 show the expected features in the viscosity dependence. Work is being done to determine the position of the enrichment maximum and to further elucidate the behavior at high viscosity. In addition we are developing model calculations in order to use these data to gain a better understanding of the microscopic diffusion of radicals in liquids and glasses.

* * *

[†]Brief version of LBL-10594.

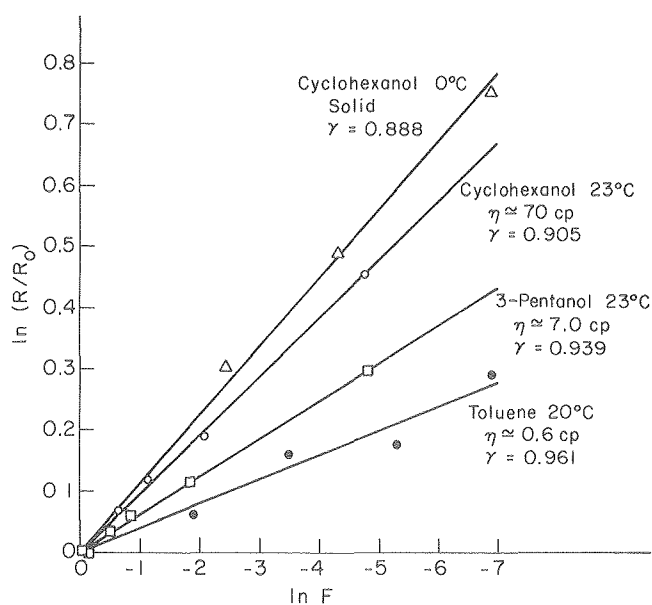


Fig. 1. Dependence of ¹³C enrichment in dibenzyl ketone on conversion for several viscosities. (XBL 785-8675)

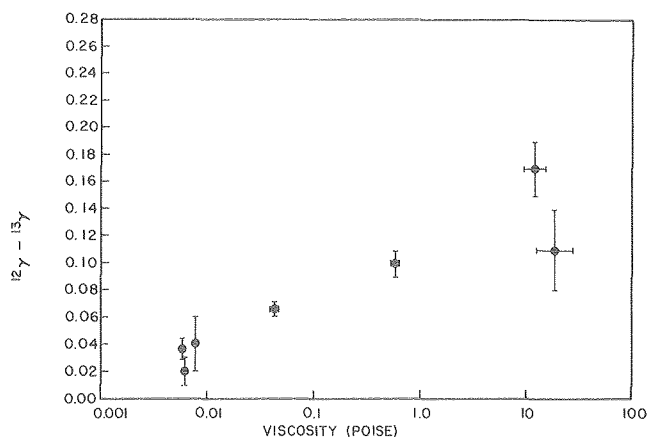


Fig. 2. Enrichment of dibenzyl ketone in ^{13}C as a function of solvent viscosity. The radical pairs are produced in a triplet state through photolysis of dibenzyl ketone and must undergo intersystem crossing to reform the ketone. $^{12}\gamma$ and $^{13}\gamma$ are the quantum yields for loss of ^{12}C and ^{13}C containing molecules, respectively. (XBL 802-8214)

14. COMPUTER PROGRAMS FOR NMR AND CONFORMATIONAL ANALYSIS[†]

J. Murdoch, S. Sinton, H. Weeks, and A. Pines

The need for computer analysis is an important part of all areas of spectroscopy and of NMR in particular. Computer programs and computational efforts in our group extend over a variety of topics but center around three in particular. These involve the simulation of spin dynamics, theoretical spectral fitting routines and the statistical analysis of carbon chain conformations. Currently, we are using both on- and off-site computer facilities in these applications.

Computer simulated spin dynamics involves the use of the computer to simulate an "experiment" in which a pulse sequence is applied to a system of coupled spins. The time evolution of the spin density matrix is followed during the pulse sequence and requires matrix multiplications of the sort:

$$\rho(t+t_1) = e^{-iHt} \rho(t_1) e^{iHt}$$

for each time ordered portion of the pulse sequence. Crucial in this application is the availability of large amounts of computer memory storage and CPU time. For N spin-1/2 nuclei each of the above

arrays requires $\binom{N}{(N/2)-M} \times \binom{N}{(N/2)-M}$ elements of storage where M is the Zeeman quantum number. This approach is applied to pulse sequences (such as selective excitation in MQNMR) on a large number of spins to see the effect of phase cycling on the n -quantum selectivity.

Another area of computer applications currently being developed is that of theoretical simulation of single and multiple-quantum NMR spectra for various types of molecular dynamics. Such theoretical spectra are produced from a calculation of molecular parameters based on a model of geometry and dynamics. An optimized fit of the theory to an experimental spectrum yields refined parameters which can be used to describe molecular structure, motionally averaged couplings and molecular potentials. Computer requirements are similar to those in the case of spin dynamics. Currently, a program using standard least squares analysis and capable of simulating the n -quantum spectra for up to ten spin - 1/2 nuclei has been written. Figure 1 shows a block diagram of the program flow involved in such a calculation.

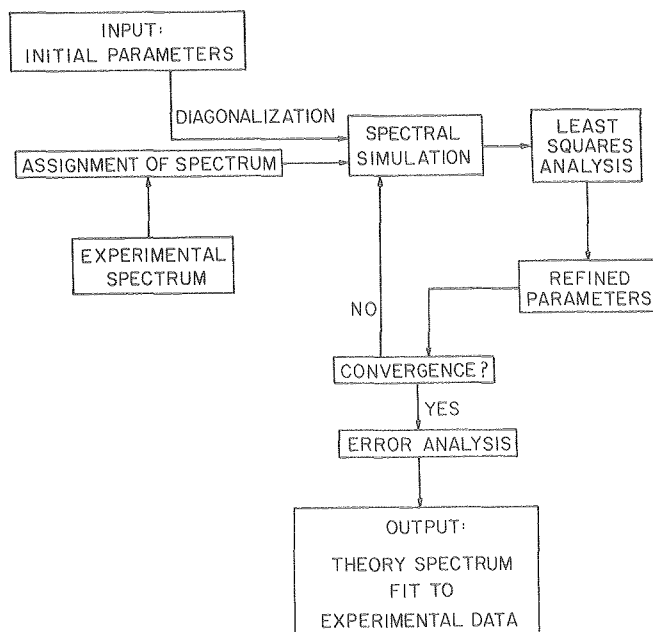


Fig. 1. Flow diagram for a least-squares iterative computer program used in Multiple Quantum NMR spectral simulation. (XBL 7912-5205)

* * *

[†]Brief version of LBL-10593.

RESEARCH PLANS FOR CALENDAR YEAR 1980

Research will continue in the following areas:

Selective excitation and detection of n -quantum transitions. After developing further the phase cycling technique, an effort will be made to produce high n -quantum excitation (e.g. $n=12$) with good sensitivity.

Correlated motions studied by multiple-quantum relaxation. Applications will include coupled molecular groups and sequential motion in liquid crystal chains. Extension to tunneling motions at low temperatures will begin.

Rotational polarization will be produced by Zeeman saturation and by optical pumping. The relaxation to phonons and the migration of the rotational polarization will be studied.

Molecular orientation at liquid interfaces will be studied. This will include hydrocarbon chain ordering in ternary mixtures. The relationship to liquid phases will be investigated. Statistical mechanics of oriented chains will be studied.

1979 PUBLICATIONS AND REPORTS

Refereed Journals

1. D. Suwelack, M. Mehring, and A. Pines, "Quantitative Aspects of Deuteron (Spin 1) Spin-Decoupling in Solids," *Phys. Rev. B* **19**, 238 (1979).
2. S. Emid, A. Bax, J. Konijnendijk, J. Smidt, and A. Pines, "Multiple Quantum Coherence in Dipolar Relaxation Measurements," *Physica* **96B**, 333 (1979).
3. W. Warren, D. P. Weitekamp, S. Sinton, and A. Pines, "Selective Excitation of Multiple Quantum Coherence in Nuclear Magnetic Resonance," *Phys. Rev. Lett.* **43**, 1791 (1979).
4. J. L. Ackerman, R. Eckman, and A. Pines, "Experimental Results on Deuterium NMR in the Solid State by Magic Angle Sample Spinning," *Chem. Phys.* **42**, 423 (1979).
5. J. Tang, A. Pines, and S. Emid, "Spin-Lattice Relaxation of Reorienting or Tunneling Deuterated Methyl Groups," to be published in *J. of Chem. Phys.*
6. J. Tang and A. Pines, "Multiple-Quantum NMR and Relaxation of an Oriented CH₃ Group," *J. Chem. Phys.*, March 1 issue (1980).

LBL Reports

1. G. Drobny, A. Pines, S. Sinton, D. Weitekamp, and D. Wenner, "Fourier Transform Multiple Quantum NMR," Symposium 13 of the Faraday Society, University of London, 1979, LBL-8565.
2. M. Alla, R. Eckman, and A. Pines, "Enhanced Resolution in Deuterium Chemical Shift Spectra of Powders," LBL-9537.
3. S. Emid, S. Konijnendijk, J. Smidt, and A. Pines, "On the Short Time Behavior of Dipolar Relaxation," LBL-9261.
4. M. Alla, R. Eckman, and A. Pines, "Dipolar Spin Diffusion and Spin-Lattice Relaxation of Deuterium in Rotating Powders," LBL-9852.
5. J. Tang and A. Pines, "Multiple-Quantum NMR and Relaxation of an Oriented CH₃ Group," LBL-9853.
6. L. Müller, R. Eckman, and A. Pines, "Proton-Deuterium Cross Polarization in Magic Angle Spinning Solids," LBL-10245.

7. L. Müller, R. Eckman, and A. Pines, "High Resolution Deuterium NMR in Polycrystalline Solids," LBL-10281.

8. S. Vega, T. W. Shattuck, and A. Pines, "Double Quantum Cross Polarization NMR in Solids," LBL-10338.

Other Presentations and Lectures

1. G. Drobny, A. Pines, S. Sinton, D. Weitekamp, J. Tang, and W. Warren, "Multiple Quantum Fourier Transform NMR in Liquid Crystals," 20th Experimental NMR Conference, Asilomar, California, February 1979, Invited Talk.
2. A. Pines, Chemistry Department, University of California, Irvine, California, February 1979, Seminar.
3. J. Ackerman, M. Alla, R. Eckman, and A. Pines, "High Resolution Deuterium NMR in Solids," 20th Experimental NMR Conference, Asilomar, California, February 1979.
4. A. Pines, "New Developments in Solid State NMR," Pittsburgh Conference on Chemistry and Spectroscopy, Symposium on New Techniques, Cleveland, Ohio, March 1979, Invited Talk.
5. A. Pines, Chemistry Department, Colorado State University, Fort Collins, Colorado, April 1979, Seminar.
6. A. Pines, Chemistry Department, University of Colorado, Boulder, Colorado, April 1979, Seminar.
7. A. Pines, Harvard-M.I.T. Seminar, Harvard University, Cambridge, Massachusetts, April 1979, Seminar.
8. A. Pines, Chemistry Department, University of California, Los Angeles, California, May 1979, Seminar.
9. A. Pines, "Nuclear Magnetic Resonance with Lots of Photons," IBM, San Jose, California, May 1979, Invited Lecture.
10. A. Pines, Chemistry Department, University of Texas, Austin, Texas, May 1979, 5 Invited Lectures in Distinguished Visiting Lectures Series.
11. A. Pines, International Symposium on Magnetic Resonance in Chemistry, Biology and Physics, Argonne National Laboratory, June 1979, Invited Talk.
12. A. Pines, "The Analogy of Multiple Quantum Spectroscopy to Isotopic Labeling and Supersonic Beams," Fourth European Experimental Nuclear Magnetic Resonance Conference, Grenoble, France, June 1979, Invited Talk.
13. A. Pines, "Development in Multiple Quantum NMR," Gordon Research Conferences, Wolfeboro, New Hampshire, June 1979, Invited Talk.
14. A. Pines, University of Witwatersrand, Johannesburg, South Africa, Presented 10 Invited Lectures, August 1979.

15. A. Pines, "Multiple Quantum Spectroscopy," Bat-Sheva Workshop on Magnetic Resonance, Israel, Presented 6 Invited Lectures, September 1979.
16. A. Pines, "Nuclear Magnetic Resonance With Lots of Photons," University of California, Berkeley, California, September 1979, Seminar.
17. A. Pines, "Magnetic Resonance With Lots of Photons," Chemistry Department, Purdue University, West Lafayette, Indiana, November 1979, Seminar.
18. A. Pines, "Magnetic Resonance With Lots of Photons," Chemistry Department, University of Pennsylvania, Philadelphia, Pennsylvania, November 1979, Seminar.
19. A. Pines, "Nuclear Magnetic Resonance with Lots of Photons," Symposium on Magnetic Resonance in Biology, Stanford University, November 1979, Invited Talk.
20. A. Pines, "Recent Developments in High Resolution Deuterium NMR in Solids by Magic Angle Spinning," 21st Annual Mountain Conference, Denver, Colorado, August 1979, Invited Lecture.

II

Chemical Sciences

A. FUNDAMENTAL INTERACTIONS

1. Photochemical and Radiation Sciences

a. Photon-Assisted Surface Reactions, Materials and Mechanisms*

Gabor A. Somorjai, Investigator

1. PHOTOCATALYTIC HYDROGEN PRODUCTION FROM WATER OVER SrTiO₃ CRYSTAL SURFACES[†]

F. T. Wagner and G. A. Somorjai

Sustained photogeneration of hydrogen was observed on metal-free as well as platinized SrTiO₃ single crystals illuminated in aqueous alkaline electrolytes or in the presence of electrolyte films. Hydrogen evolution rates increased with electrolyte hydroxide concentration most strongly at hydroxide concentration above 5 N. Both stoichiometric and prerduced metal-free crystals were active for hydrogen photoproduction. No activity was observed from crystals in neutral or acidic solutions or in water vapor in the absence of a crust of basic deliquescent compound. Metal-free crystals appear to evolve hydrogen via a photocatalytic mechanism in which all chemistry occurs at the illuminated surface. The results allow direct comparison of photocatalytic and photoelectrochemical processes and have implications for the development of heterogeneous photocatalysis at the gas-solid interface.

* * *

[†]Brief version of LBL-9942 and LBL 10020.

2. ELECTRON SPECTROSCOPY (XPS AND UPS) STUDIES OF THE ADSORPTION OF H₂, O₂, AND H₂O ON REDUCED AND STOICHIOMETRIC SrTiO₃[†]

S. Ferrer and G. A. Somorjai

About one monolayer of Ti³⁺ species is detectable at the surface of reduced SrTiO₃(111) single crystals by XPS and UPS. O₂, H₂, and H₂O have been adsorbed in the dark and the decrease on the concentration of Ti³⁺ species has been monitored as a function of the gas exposures. Subsequent band gap illumination partially restores the Ti³⁺ initial concentration in the cases of O₂ and H₂ exposures but not in the case of H₂O. The Ti³⁺ photogeneration on the oxygen covered surface is associated with oxygen photodesorption as indicated by XPS and UPS. UPS measurements give evidence for surface hydroxylation resulting from water and hydrogen adsorption.

The activity of the stoichiometric SrTiO₃(111) crystal face for O₂ and H₂ adsorption is very low when compared with the reduced SrTiO₃ samples.

* * *

[†]Brief version of LBL-10037.

3. HIGH TEMPERATURE PHOTOCATALYTIC DISSOCIATION OF H₂O ON SrTiO₃ AND TiO₂

R. Carr and G. A. Somorjai

Dissociation of H₂O on SrTiO₃ appears to involve a catalytic surface reaction in which hydroxylation of the surface is necessary. In order to investigate this idea it was proposed to hydroxylate the surface with steam and not an electrolyte solution as is conventionally done. A steam atmosphere cell was constructed and connected to a gas chromatograph for analysis of reaction products.

It was found that TiO₂ and SrTiO₃ both yielded H₂ from dissociation of H₂O upon exposure to band-gap light in the presence of 1-3 atm of steam at 120°C. Some metal, usually Pt or Rh deposited on the surface by evaporation, was found to be necessary, probably for H₂ recombination. There are temperature effects which might not show up in electrochemical cells at room temperature; but these results, at pH 7 and with no external bias on the TiO₂, as is necessary in the electrochemical cell, indicate a reaction mechanism different from conventional electrochemistry. This will be explored further.

RESEARCH PLANS FOR CALENDAR YEAR 1980

The photodissociation of water on other oxides (Fe₃O₄, TiO₂) will be explored. The high temperature reactivity of SrTiO₃ for photodissociation will be explored using steam. The photodissociation of H₂O will be combined with other catalytic reactions involving CO₂, CO and N₂.

1979 PUBLICATIONS AND REPORTS

LBL Reports

1. F. T. Wagner, S. Ferrer and G. A. Somorjai, "Photocatalytic Hydrogen Production from Water

* This work was supported by the Division of Chemical Sciences, Office of Basic Energy Sciences, U. S. Department of Energy.

over SrTiO₃ Crystal Surfaces, Electron Spectroscopy Studies of Adsorbed H₂, O₂ and H₂O," LBL-9942.

2. S. Ferrer and G. A. Somorjai, "UPS and XPS Studies of the Chemisorption of O₂, H₂ and H₂O on Reduced and Stoichiometric SrTiO₃(111) Surfaces. The Effects of Illumination," LBL-10037.

3. F. T. Wagner and G. A. Somorjai, "Photocatalytic and Photoelectrochemical Hydrogen Production on Strontium Titanate Single Crystals," LBL-10020.

4. J. C. Hemminger, R. Carr, W. J. Lo and G. A. Somorjai, "Photochemical Processes at the Solid-Gas Interface: The Adsorption and Reactions of Gaseous CO₂ and H₂O on Pt-SrTiO₃ Single Crystal Sandwiches," LBL-8841.

Invited Talks

1. G. A. Somorjai, "Photochemical Reactions of H₂O and CO₂ on Solid Surfaces," UC Berkeley, Department of Physics, Feb. 2, 1979.

2. G. A. Somorjai, "Photochemical Dissociation of Water over SrTiO₃ Crystal Surfaces," 3rd Solar Photochemistry Research Conference, Asilomar, CA, June 19, 1979.

3. G. A. Somorjai, "Surface Structure and Water Adsorption," International Conference on Non-Traditional Approaches to the Study of the Solid-Electrolyte Interface, Snowmass, Colorado, Sept. 24-25, 1979.

b. Photochemistry of Materials in the Stratosphere*

H. S. Johnston, Investigator

1. ABSOLUTE QUANTUM YIELDS FOR TWO CHANNELS OF PHOTOLYSIS OF NO₃ FREE RADICAL[†]

F. Magnotta[†] and H. S. Johnston

The absolute photodissociation quantum yields for NO₃ along two channels, (1) NO₃ + hv → NO + O₂ and (2) NO₃ + hv → NO₂ + O, were obtained by tunable laser flash photolysis and resonance-fluorescence detection of the products O and NO. The maximum quantum yield for channel 1 was 0.32 and was observed at 592 nm; the maximum quantum yield for channel 2 was 1.00 and was observed at 585 nm. The calculated first-order rate coefficients for photolysis at the surface of the earth by the overhead sun was: j₁ = 0.022 ± 0.002 s⁻¹ and j₂ = 0.18 ± 0.018 s⁻¹.

The photochemistry of the nitrate free radical, NO₃, is of possible importance in the tropospheric and stratospheric ozone balance. Nitrogen dioxide and ground-state atomic oxygen, O(³P), are energetically possible for light of wavelengths less than 580 nm, and NO and O₂ could be produced at any wavelengths below 8 μm. Using red, yellow, green, and blue fluorescent lamps, Graham and Johnston¹ demonstrated that both channels of reaction occur, but they could not get the wavelength-dependence nor sharp values for the quantum yields.

A complete description of the apparatus and procedure is given elsewhere,² but the salient features are described here. The photolytic source is a pulsed, PHASE-R dye laser with 400 ns pulse widths, capable of producing 1 to 2 Joules of visible radiation per pulse and between 6 and 10 millijoules of ultraviolet radiation upon doubling. Wavelength measurements were made with a one-meter grating monochromator and Princeton Applied Research optical multichannel analyzer with a resolution of 0.04 nm. The laser beam passed through a photolysis cell of 10 cm length; at right angles passed the beam of radiation which excited the resonance line of either O(³P) or NO; and along the third perpendicular axis the resonance fluorescence was detected by photon counting. The fluorescent signal was processed by a thousand channel analyzer, and multiple laser flashes (2⁹ to 2¹⁰) were averaged to generate a decay curve. Baseline subtraction and data analysis were carried out with one-line minicomputers. The linear regime for NO and for O analysis was established, and calibration curves were constructed.

A flowing stream of carrier gas, usually N₂, picked up a small concentration of N₂O₅ vapor from a temperature-controlled saturator; the concentration of N₂O₅ and HNO₃ in the stream was measured by infrared absorption; and just before entering the photolysis cell the concentration of nitrogen

dioxide in the stream (formed by the slow irreversible decomposition of N₂O₅) was measured by laser-excited NO₂ fluorescence. From the measured values of N₂O₅ and NO₂, the concentration of NO₃ could be calculated from the equilibrium constant.



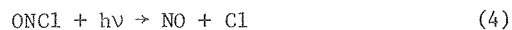
$$K = [\text{NO}_2][\text{NO}_3]/[\text{N}_2\text{O}_5] \quad (2)$$

since N₂O₅ is in rapid, reversible equilibrium with respect to NO₂ and NO₃.

The absolute calibration of the resonance fluorescence measurements of atomic oxygen and of nitric oxide was carried out by photolysis of NO₂ in the near ultraviolet spectral region



and also the calibration was carried out for nitric oxide in the visible region of the spectrum by photolysis of nitrosyl chloride



The quantum yields were already known both for NO₂ photolysis and for ONCl photolysis.

The laser "fluence," E, is defined as the total number of photons per unit area in the pulse. The fraction of molecules that absorb radiation in one pulse is (1 - e^{-Eσ}) where σ is the cross section. There are two relatively simple regions: for low intensities 1 - e^{-Eσ} is equal to Eσ, and at high intensities 1 - e^{-Eσ} approaches one. An example of the time decay of the atomic-oxygen resonance-fluorescence signal at high fluence is given by Fig. 1. The decay of the signal was caused by flow and by diffusion of atomic oxygen out of the region of observations. An example of the NO fluorescence signal is given by Fig. 2. In this case, there is an initial value for NO and then an increase followed later by a decay. The increase of NO over the first few milliseconds is caused by the reaction



and the decrease in signal is the result of gas flow and diffusion. By extrapolation to zero time, the amount of NO produced by the photolysis of NO₃ was obtained and by evaluation of the initial slope on Fig. 2 the amount of O produced by photolysis of NO₃ could be determined also.

Quantum yields for O and for NO were obtained both for high fluence and for low fluence in order to check on possible two-photon photolysis. All studies were made at 296 K and 10 Torr total pressure. The quantum yields for NO production are given as a function of wavelength at high and low Eσ in Fig. 3. The quantum yield for NO falls to zero at short wavelengths where the second channel

* This work was supported by the Division of Chemical Sciences, Office of Basic Energy Sciences, U. S. Department of Energy.

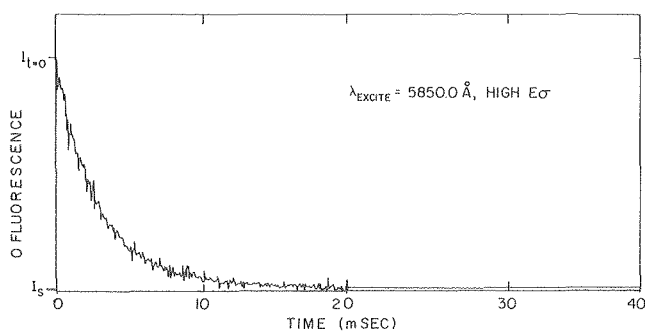


Fig. 1. Resonance fluorescence of atomic oxygen as a function of time after flash photolysis of NO_3 at 585.0 nm with high value of $E\sigma$. (XBL 799-7105)

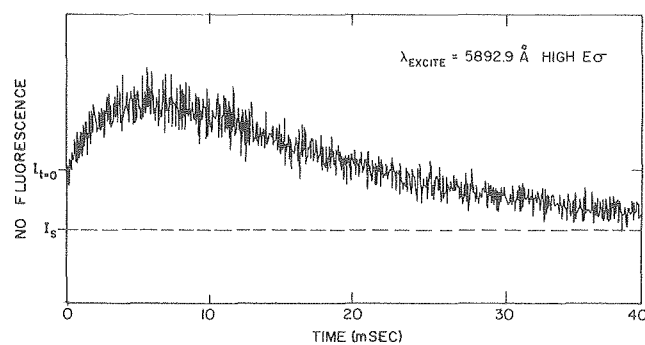


Fig. 2. Resonance fluorescence of nitric oxide as a function of time after flash photolysis of NO_3 at 589.3 nm with high value of $E\sigma$. (XBL 799-7107)

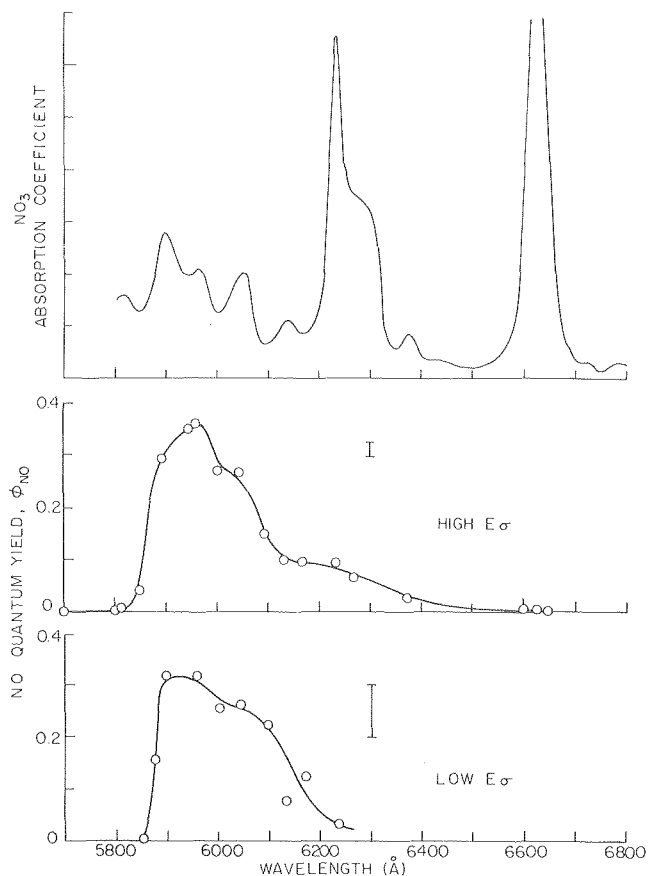


Fig. 3. The relative absorption cross section of NO_3 above 580 nm (top panel); the absolute quantum yield of nitric oxide with high $E\sigma$ (middle panel); and the quantum yield of NO with low $E\sigma$. (XBL 799-7078)

($\text{NO}_2 + \text{O}$) becomes energetically allowed; but, curiously, the NO quantum yield also falls to zero at long wavelengths, even though NO_3 has very intense absorption bands in this region (the top panel of Fig. 3). Under these intense absorption bands, some two-photon production of atomic oxygen was found. After excluding such two-photon processes, the absolute quantum yields for atomic oxygen are given by Fig. 4, which also includes the quantum yields for NO production. For atomic oxygen production the quantum yield is 1.0 at the threshold, falls rapidly to zero at energies below the threshold (the finite values presumably arising from "hot bands" in NO_3), and it falls to a plateau with value 0.8 below 540 nm.

The quantum yield functions $\phi(\lambda)$ of Fig. 4 were combined with the cross section functions $\sigma(\lambda)$ and with the distribution of solar radiation³ at the earth's surface with an overhead sun $I(\lambda)$ to calculate the NO_3 photolysis coefficient

$$j = \sum_{\lambda} I(\lambda)\sigma(\lambda)\phi(\lambda) \quad (6)$$

The values are

$$j(\text{O} + \text{NO}_2) = 0.18 \pm 0.018 \text{ s}^{-1} \quad (7)$$

$$j(\text{NO} + \text{O}_2) = 0.022 \pm 0.002 \text{ s}^{-1} \quad (8)$$

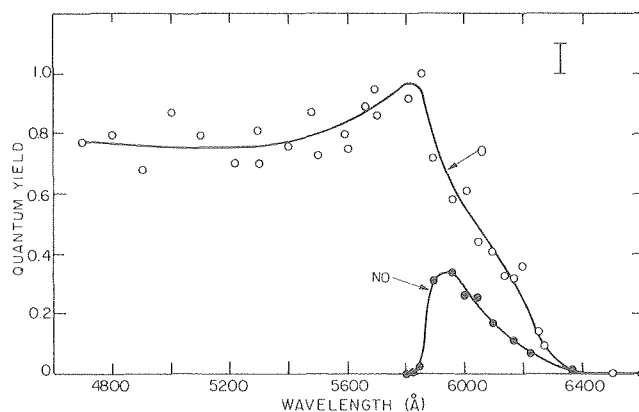


Fig. 4. Comparison of absolute quantum yields of $\text{O} + \text{NO}_2$ and of $\text{NO} + \text{O}_2$ in the one-photon photolysis of the NO_3 free radical. (XBL 799-7077)

At long wavelengths and under the intense absorption peaks at 623 and 660 nm, the total quantum yield, $\phi_1 + \phi_2$, is very nearly zero. An effort was made to observe resonance fluorescence or fluorescence shifted to longer wavelengths, but no fluorescence could be seen under conditions where the signal-to-noise ratio should have exceeded 100 if the fluorescence quantum yield was unity. This study leaves unanswered the question as to what happens to the energy absorbed at long wavelengths, especially so for the peaks at 623 and 660 nm.

* * *

† Brief version of LBL-9981.

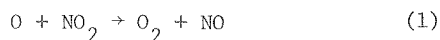
‡ Permanent address: Joint Institute for Laboratory Astrophysics, University of Colorado, Boulder, Colorado 80309.

1. R. A. Graham and H. S. Johnston, *J. Phys. Chem.* **82**, 254 (1978). LBL-4147
2. F. Magnotta, Ph.D. Dissertation, University of California, 1979. LBL 9981
3. R. J. Gelinis, R. P. Dickinson, and K. E. Grant, "Solar Flux and Photodissociation Calculations for LLL Physics Program," Lawrence Livermore Laboratory (1973).

2. RATE CONSTANT FOR THE REACTION OF O(³P) WITH NITROGEN DIOXIDE †

F. Magnotta and H. S. Johnston

During the course of a separate study to determine the absolute oxygen atom quantum yields from photolysis of NO₃ and N₂O₅, a substantial amount of data was accumulated, measuring the reaction rate of atomic oxygen with nitrogen dioxide.



This reaction has been studied by several investigators in the past,¹⁻³ but the rate constant is still judged⁴ to be uncertain to 10 percent

$$k(298 \text{ K}) = 9.3 \pm 0.93 \times 10^{-12} \text{ cm}^3 \text{ molecule}^{-1} \text{ s}^{-1} \quad (2)$$

In this study atomic oxygen was produced by the flash laser photolysis of NO₂, NO₃, and N₂O₅, and the consumption of the atomic oxygen was followed by its resonance fluorescence.

The apparatus is the same as that used to measure the quantum yields for NO₃ photolysis. The concentrations of nitrogen dioxide in the reaction cell was determined by fluorescence as excited by a helium-cadmium laser. Careful consideration of this measurement was made, because of its criticality in determining an accurate rate constant. The apparatus was calibrated with eight separate preparations of variously purified NO₂. A tank mixture with 115 parts per million of NO₂ in nitrogen was used for regular recalibration of the system, and the concentration of the tank mixture was

analyzed before and after the series of runs by optical absorption using a Cary 118C in a three meter absorption cell at 400 nm. A slow flow was maintained to prevent NO₂ loss to the walls, and the total pressure was measured with an MKS capacitance manometer.

Photolyses were carried out during fourteen series of experiments, and rate constants were obtained for 144 individual runs. Data were obtained by photolysis of NO₃ with visible light, by photolysis of NO₂ at 351.8 nm with and without the presence of N₂O₅, by photolysis of N₂O₅ at 290 to 300 nm, and by two-photon photolysis of NO₂ between 470 and 585 nm. All runs were made at 296 K and with 10 Torr of N₂ as buffer gas. Atomic oxygen was observed by its resonance fluorescence, and it underwent a first-order decay, which included both the reaction of interest and diffusion of the beam of atoms. In some cases a small correction was made for the rate of the reaction of atomic oxygen with the nitrate free radical, NO₃ + O → NO₂ + O₂. By extrapolating the empirical first-order rate constant, 1/τ for atomic oxygen, to the initial time, the effect of diffusion was evaluated and eliminated. The first-order rate constant (corrected for diffusion and for reaction with NO₃) divided by the concentration of NO₂ gives the second-order rate constant for the reaction of interest (Eq. 1)

The corrected first-order rate constants were averaged into fourteen sets, and these averaged rate constants are plotted against the average concentration of NO₂ in each set, Fig. 1. The slope

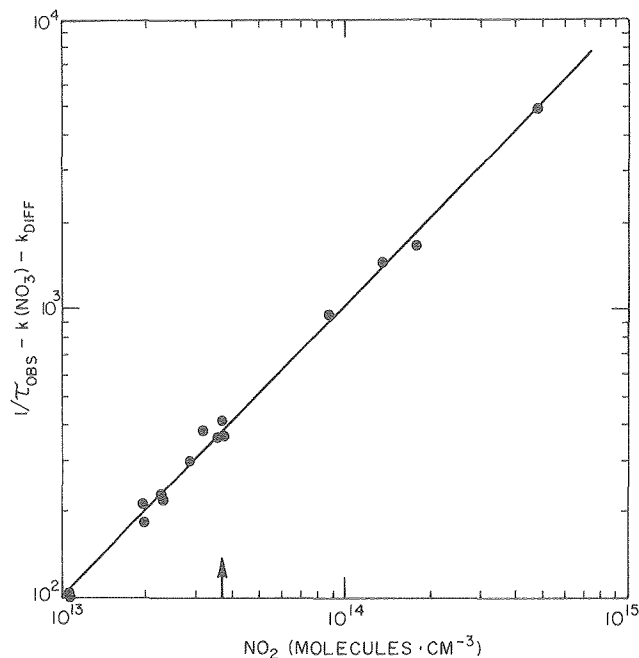


Fig. 1. A plot of the empirical first order rate constant corrected for reaction of O(³P) with NO₃ and corrected for diffusion against the concentration of nitrogen dioxide in the cell. The slope is the second order rate constant. (XBL 799-7099)

of the line is the second order rate constant, k_i . Giving equal weight to each of the 144 runs represented by the data in Fig. 1, a linear least-squares analysis gave the rate constant

$$k_1 = (1.033 \pm .008) \times 10^{-11} \text{ cm}^3 \text{ molecule}^{-1} \text{ s}^{-1} \quad (3)$$

and the first-order diffusion constant was found to be

$$k(\text{diffusion}) = 102.7 \pm 8.4 \text{ s}^{-1} \quad (4)$$

where the error range is the standard error based on the precision of these data.

This rate constant is about 10 percent higher than the currently recommended value.⁴ Because of this discrepancy, this experimental method was scrutinized for possible systematic errors. All aspects of the absolute calibration for NO_2 were closely checked. No systematic errors could be found.

Since this method differs from the previous results and since no systematic errors could be found, one can ask if this method has any possible advantages over the previous methods. This study used slow continuous flow of NO_2 , which equilibrated NO_2 in the gas phase with that absorbed on the walls. Several previous studies were static and absorption of NO_2 by the walls was an unknown factor. This method carried out in-situ monitoring of NO_2 concentration, which was not usually done by previous investigators.

It may be that there is an unrecognized systematic error in this study, or it may be that previous investigators had unrecognized systematic errors. The precision of the present study is 0.8 percent.

* * *

[†]Brief version of LBL-9981.

1. D. D. Davis, J. T. Herron, and R. E. Huie, *J. Chem. Phys.* **58**, 530 (1973).
2. P. P. Bemand, M. A. A. Clyne, and R. T. Watson, *J. Chem. Soc., Faraday Trans. II* **70**, 564 (1973).
3. T. G. Slanger, B. J. Wood, and G. Black, *Int. J. Chem. Kin.* **5**, 615 (1973).
4. "Chemical Kinetic and Photochemical Data for Use in Stratospheric Modeling, Evaluation #2," NASA, Jet Propulsion Laboratory, Pasadena, California, April 15, 1979.

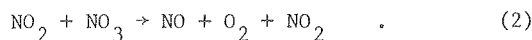
3. ABSOLUTE QUANTUM YIELDS FOR PHOTOLYSIS OF DI-NITROGEN PENTOXIDE[†]

P. Connell,[†] F. Magnotta, and H. S. Johnston

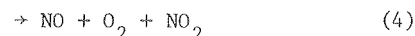
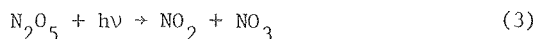
Di-nitrogen pentoxide reversibly dissociates to nitrogen dioxide and the NO_3 free radical



The rate-determining step in the irreversible decomposition of N_2O_5 is the reaction of nitrogen dioxide and NO_3 to produce nitric oxide.



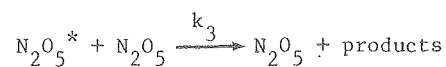
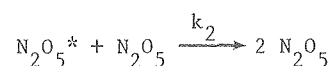
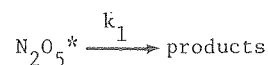
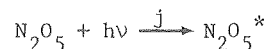
Upon photolysis, both NO_2 and NO_3 give primarily atomic oxygen as product. On such considerations as these, it has been considered possible that photolysis of N_2O_5 could be by way of any of the three channels



The method of laser flash photolysis of N_2O_5 and resonance-fluorescence detection of O and of NO, as described in the section above, was used to measure the absolute quantum yield for reactions (4) and (5),¹ at 10 Torr pressure and 296 K. By studying the photolysis of N_2O_5 in a static cell, a flowing cell, and in a flowing cell with modulated photolysis lamps, information was obtained about reaction (3), as well as about the other two channels over a wide range of temperature and total pressure.²

The concentrations of N_2O_5 , HNO_3 , and NO_2 were measured by infrared absorption in a silica reaction cell 28 cm in diameters and 100 cm long, which was contained in a large thermostated box. The cell was irradiated by four low pressure mercury arcs contained inside one-meter long silica dewar flasks containing chlorine gas as a filter. These lamps were modulated to give square-wave photolysis pulses, and the modulation amplitude and phase shift of reactants and products were measured. The general method has been described in detail by Graham.³ The experiments were supported by extensive model calculations for various assumed chemical mechanisms.

Previous investigators^{4,5} have found the quantum yield of N_2O_5 photolysis to be about 0.6, which was interpreted to mean that the primary products were $\text{NO}_2 + \text{NO}_3$ and the low observed quantum yield was caused by recombination of NO_2 and NO_3 to reform N_2O_5 . At constant initial concentrations of N_2O_5 and with widely varied concentration of inert gas, N_2 and O_2 , these old findings were confirmed. However, a wide variation of initial N_2O_5 concentrations gave a different result. At low concentrations of N_2O_5 the quantum yield approaches unity and at high concentrations of N_2O_5 at room temperature it approaches a finite value.¹ These findings suggest the mechanism



With this mechanism the steady-state quantum yield is

$$\phi = \frac{k_1 + k_3[N_2O_5]}{k_1 + (k_2 + k_3)[N_2O_5]}$$

At high concentration of N_2O_5 the quantum yield approaches one, and at low concentrations of N_2O_5 the quantum yield approaches $k_3/(k_2 + k_3)$, which agrees with observations if the primary products are not NO_2 and NO_3 .

To obtain the absolute and relative quantum yields for the other channels of photolysis, $2 NO_2 + O$ and $NO + O_2 + NO_2$, N_2O_5 was photolyzed between 250 and 300 nm at 10 Torr total pressure, at 298 K, and with N_2O_5 concentrations between 7 and 18×10^{14} molecules cm^{-3} . The quantum yield for production of atomic oxygen is shown in Fig. 1; the dashed line is based on the quantum yield for N_2O_5 destruction with a steady-state photolysis. The quantum yield for forming atomic oxygen appears to be about 10 percent below the curve for N_2O_5 destruction as found by the other method; however the results agree within the range of their mutual experimental errors.

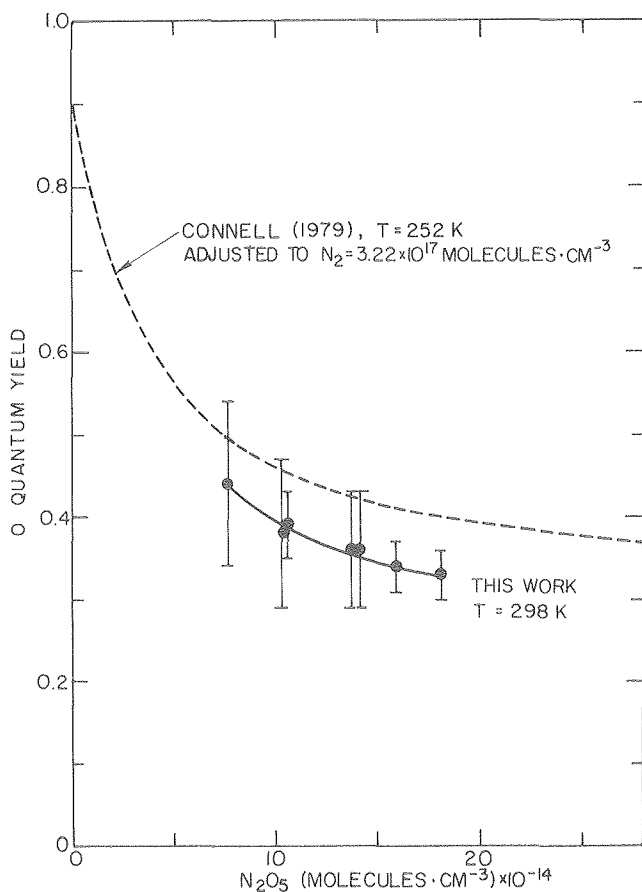


Fig. 1. Data points and estimated error bars for quantum yield for production of atomic oxygen from the photolysis of N_2O_5 at 250 nm, 298 K. The dashed line is derived from observed quantum yield for N_2O_5 destruction by steady-state method. (XBL 799-7094)

Experiments were performed to detect nitric oxide as a product from N_2O_5 photolysis at 295 nm. After sufficient laser pulses easily to detect 2×10^{10} molecules cm^{-3} of NO , no primary production of nitric oxide could be detected. From the conditions of the experiment, an upper limit can be placed on nitric oxide quantum yield, $\phi_{NO} \leq 0.1$.

The primary products in the photolysis of N_2O_5 between 250 and 300 nm are $2 NO_2 + O(^3P)$, and the primary quantum yield is one. The other possible channels of photolysis, $NO_2 + NO_3$ and $NO + O_2 + NO_2$ occur with a quantum yield of less than 0.1.

* * *

† Brief version of LBL-9034 and LBL-9981.

‡ Permanent address: U. S. Department of Commerce, National Oceanic and Atmospheric Administration, Environmental Research Laboratories, Boulder, Colorado 80303.

1. F. Magnotta, Ph.D. Dissertation, University of California, Berkeley, California, December 1979. LBL-9981.

2. P. S. Connell, Ph.D. Dissertation, University of California, Berkeley, California, June 1979. LBL-9034.

3. R. A. Graham, Ph.D. Dissertation, University of California, Berkeley, California, December 1975. LBL-4147.

4. H. H. Holmes and F. Daniels, J. Am. Chem. Soc. 56, 630 (1934).

5. R. Murphy, Ph.D. Dissertation, University of California at Los Angeles, University Microfilms, Ann Arbor, Michigan, 1969.

4. ISOTOPE EFFECT ON THE ULTRAVIOLET ABSORPTION SPECTRUM OF NITROUS OXIDE†

G. Selwyn and H. S. Johnston

The absorption spectrum of nitrous oxide in the 170 to 200 nm wavelength range is forbidden, but allowed by bending.¹⁻⁴ This feature leads to a strong increase in the absorption intensity as the temperature is raised. The molecule is thought to be bent in the excited electronic state,^{2,5,6} and it is linear in the ground electronic state. To obtain information about the excited electronic state, a study was made here with four isotopic species: NNO , ^{15}NNO , $N^{15}NO$, and $^{15}N^{15}NO$, where unlabeled N refers to ^{14}N . The absorption spectrum of each species was measured between 173 and 197 nm wavelength and at six temperatures between 150 and 490 K. The spectral resolution was 0.05 nm, and 1250 data points were collected for each spectrum. An example of the experimental data is given by Fig. 1, showing the strong effect of temperature on the spectra of $^{15}N^{15}NO$.

There is a weak continuous spectrum arising from the ground (000) vibrational state and a relatively strong banded spectrum arising from the (010) vibrational state. By calculating the thermally excited population of the (010) state for each of the various temperatures, one can separate the (000) and (010) spectra. An example of the separated NNO

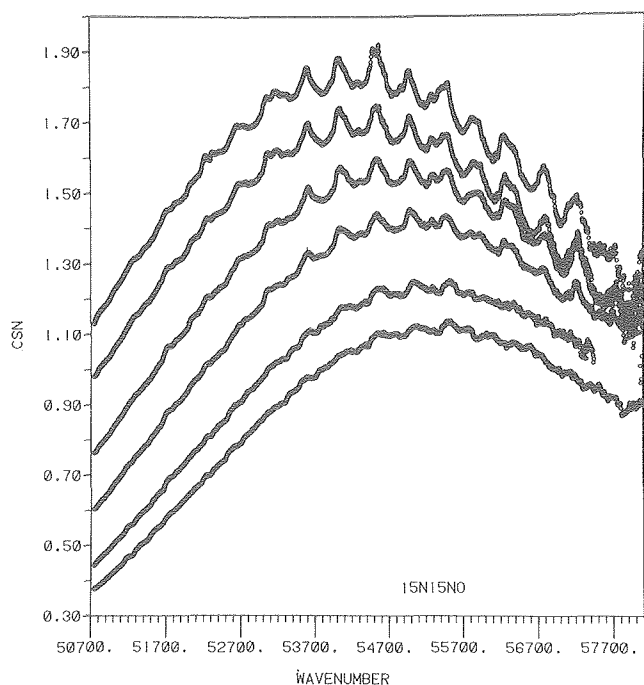


Fig. 1. Optical absorption cross-section (CSN) in multiples of 10^{-19} cm^2 as a function of wave number for six temperatures between 150 and 490 K for $^{15}\text{N}^{15}\text{NO}$. The intensity of absorption increases with increasing temperature. (XBL 792-8588)

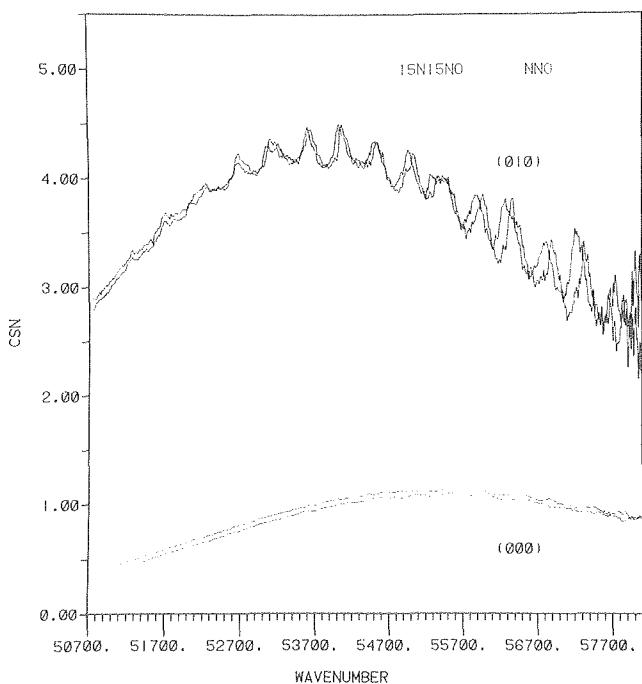


Fig. 2. Temperature-resolved spectra for ground vibrational state (000) and first excited bending vibrational state (010) for two isotopic species of nitrous oxide, $^{14}\text{N}^{14}\text{NO}$ and $^{15}\text{N}^{15}\text{NO}$. (XBL 792-8605)

spectra and $^{15}\text{N}^{15}\text{NO}$ spectra is given by Fig. 2, and a good separation of the two spectra can be seen. At low energies the peaks are not well defined and an isotopic shift could not be evaluated. The highest energy band is noisy because the wavelength limit of the instrument (Cary 118C) is being approached. For 10 bands, isotope shifts could be evaluated, and these are labeled $K = 0$ to 9, where the relation of K to the origin of the vibrational progression is unknown, on the basis of the spectrum itself.

The origin of these spectra is the (010) vibrational state of the ground electronic state. The fundamental frequencies of this state are defined as ν_1'' for NNO and as ν_2'' for $^{15}\text{N}^{15}\text{NO}$, where energies and frequencies are expressed in units of cm^{-1} . The energies of these states then are

$$E_1'' = (3/2)\nu_1''$$

$$E_2'' = (3/2)\nu_2''$$

The observed infrared spectra⁷ give the frequencies ν_1'' and ν_2'' . The energies of the vibrational bands in the excited electronic states are

$$E_1' = T_e + (n' + 1/2)\nu_1' + Q_1'$$

$$E_2' = T_e + (n' + 1/2)\nu_2' + Q_2'$$

where T_e is the difference in energy between the bottom of the potential wells in upper and lower electronic states and the Q 's represent anharmonic and other higher order terms. The observed spectral transitions for each isotopic species correspond to the energy changes

$$\Delta E_1 = T_e + (n' + 1/2)\nu_1' - 3/2 \nu_1'' + Q_1'$$

$$\Delta E_2 = T_e + (n' + 1/2)\nu_2' - 3/2 \nu_2'' + Q_2'$$

The isotope effect on the spectra is the double difference between initial and final state for one isotopic species and the other. Since the energies ν_1'' and ν_2'' are known from infrared spectra, an observable double difference is defined as

$$\Delta\Delta E = (\Delta E_1 + 3/2 \nu_1'') - (\Delta E_2 + 3/2 \nu_2'')$$

In terms of theory this observable quantity is interpreted as

$$\Delta\Delta E = (n' + 1/2)\nu_1' - (n' + 1/2)\nu_2' + (Q_1' - Q_2')$$

where $n' = 0, 1, 2 \dots$ but its origin is unknown. By dividing through by $n' + 1/2$, one obtains

$$\frac{\Delta\Delta E}{(n' + 1/2)} = \nu_1' - \nu_2' + \frac{Q_1' - Q_2'}{(n' + 1/2)}$$

The difference in anharmonicity terms, $Q_1' - Q_2'$ is expected to be small compared to $\nu_1' - \nu_2'$ and to increase no faster than $n' + 1/2$, and this term is dropped to give

$$\frac{(\Delta\Delta E)_{\text{OBS}}}{N + K + 1/2} = \nu_1' - \nu_2'$$

where $n' = N + K$, K numbers the sequence of observed vibrational bands, and N is the unknown vibrational quantum number of the first evaluated band ($K = 0$). Numbers between 0 and 14 were tentatively assigned to N , and $\Delta\Delta E/(N + K + 1/2)$ was plotted against K for each of 10 observed bands; examples for $N = 2, 5, 8$, and 14 are plotted in Fig. 3. For the proper value of N , each term should be the same and equal to $\nu_1' - \nu_2'$. If N is too large, the terms increase with increasing K ; and if N is too small, the terms decrease with increasing K . From Fig. 3, it can be seen that the function $\Delta\Delta E/(N + K + 1/2)$ decreases

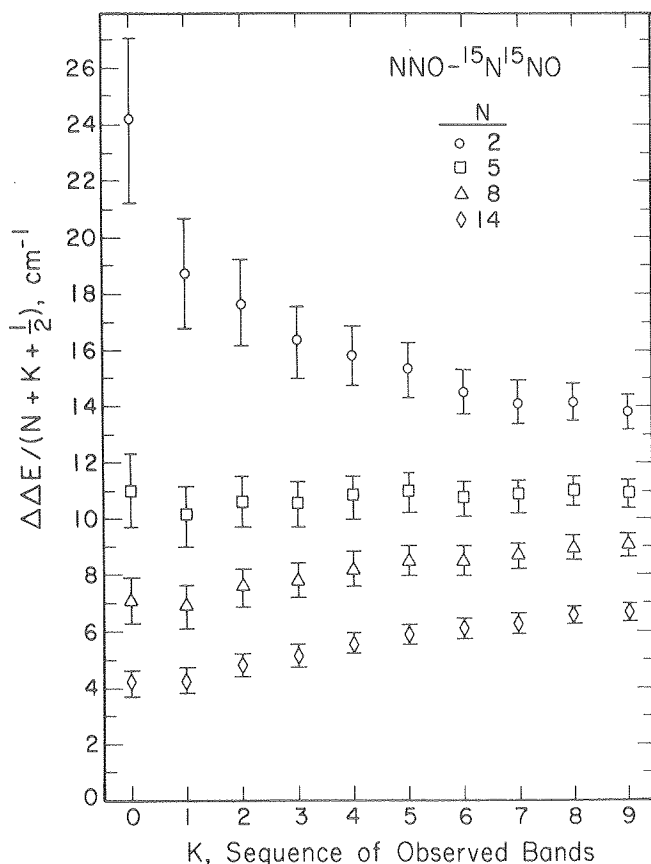


Fig. 3. Plot to determine origin of bending-vibration progression in upper electronic state of nitrous oxide. The sequence of observed spectroscopic isotope shift is plotted for various assumed origins of the progression. The correct origin should give a horizontal line and the value of the isotope effect. (XBL 801-7808)

Table 1. The isotope shift for the (010) vibrational band of the upper electronic state of nitrous oxide.

| Isotopic species | $\Delta\nu'$, cm^{-1} |
|-----------------------|---------------------------------|
| NNO - $N^{15}NO$ | 4.9 ± 1.5 |
| NNO - ^{15}NNO | 8.0 ± 1 |
| NNO - $^{15}N^{15}NO$ | 10.8 ± 1 |

for $N = 2$, is very nearly constant for $N = 5$, and increases for $N = 8$. Plots for $N = 3, 4, 5, 6, 7$ show that this test is uncertain to plus or minus one quantum number; but for all pair-wise comparisons of the isotope effect the best value of N is 5 ± 1 . These results are summarized in Table 1. This assignment identifies the origin of energy of the upper electronic state: $T_W = 51210 \pm 480 \text{ cm}^{-1}$ or 6.35 eV.

* * *

† Brief version of LBL-8739.

- Rabelais, J. W., J. M. McDonald, V. Scherr, and S. P. McGlynn, Chem. Rev. **71**, 73 (1971).
- Fortune, P. J., D. G. Hörner, B. J. Rosenberg, W. B. England, G. Das, A. C. Wahl, and T. O. Tierman, ARL-TR-75-0202, Vol. III, Air Force Systems Command, June 1975.
- Krauss, M., D. G. Hopper, P. J. Fortune, A. C. Wahl, and T. O. Tierman, ARL-TR-75-0202, Vol. I, Air Force Systems Command, June 1975.
- Chutjian, A., and G. A. Siegal, J. Chem. Phys. **57**, 3069 (1972).
- Herzberg, G., Electronic Spectra and Electronic Structure of Polyatomic Molecules, Vol. III, Van Nostrand Reinhold Co., 1966.
- Herzberg, G. and H. C. Longuet-Higgins, Disc. Faraday Soc. **35**, 77 (1963).
- Pliva, J., J. Mol. Spect. **12**, 360 (1961).

5. INSTANTANEOUS GLOBAL OZONE BALANCE INCLUDING OBSERVED NITROGEN DIOXIDE†

S. Solomon,[†] H. S. Johnston, M. Kowalczyk, and I. Wilson[§]

The importance of the oxides of nitrogen in affecting the stratospheric ozone balance has been a subject of interest in atmospheric chemistry for several years.¹ Recent measurements of stratospheric nitrogen dioxide from ground-based stations as well as aircraft and balloons have provided a first approximation to a global distribution of NO_2 vertical columns. Noxon and co-workers have presented measurements of the stratospheric column of nitrogen dioxide, NO_2 , at numerous latitudes and seasons.^{2,3} There are now several NO_2 profiles up to the middle stratosphere observed from balloons.⁴⁻⁷

Dütsch has reviewed all of the available data on the vertical ozone distribution measured with chemical sondes and one year of ozone data obtained by back-scattered ultraviolet radiation from the Nimbus 4 satellite.⁸

These recent measurements of temperature, ozone, and nitrogen dioxide have been taken, and by use of a photochemical model the observed NO₂ columns (Fig. 1) have been translated into time-dependent vertical profiles, which were then extended to

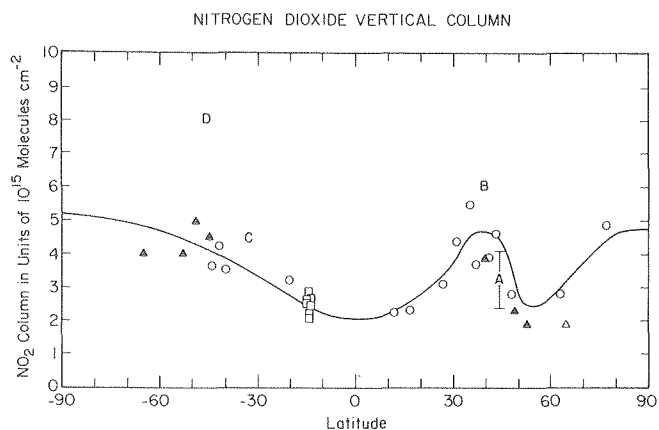
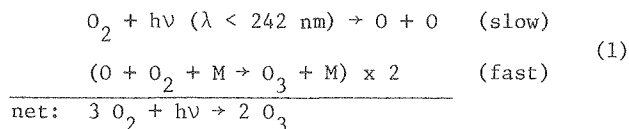


Fig. 1. Observed PM vertical columns of stratospheric nitrogen dioxide, fall-spring: \odot Noxon,^{2,3} Fig. 1; \square Noxon, Fig. 2; Δ Noxon, Fig. 3; D, Harries et al.;⁵ C, Murcray et al.;⁶ B, Ogawa;⁷ A, Ackerman et al.⁴ The line is that used as the primary case for this study. (XBL 801-7809)

global stratospheric distributions (Fig. 2). The global distribution of the rate of NO_x catalyzed destruction of ozone was evaluated by the method of instantaneous rates.

The method of instantaneous rates has been described previously.^{9,10} Briefly the observed distribution of temperature, oxygen, ozone, and incoming solar radiation outside the atmosphere are used to calculate photolysis rates on a grid containing 1 km vertical intervals, 10° latitude intervals, and 15° longitude intervals. Rayleigh scattering and albedo effects are treated by the method of Isaksen et al.¹¹ The concentration of O(³P) is calculated at each grid point using the steady-state approximation. At each grid point three independent components of the global ozone balance were evaluated:¹⁰ (a) The rate of ozone production from the photolysis of oxygen, P(O₃), which is 2 j[O₂],



(b) The rate of ozone destruction by the pure oxygen family of reactions, L(O_x), which is 2 k[O][O₃],

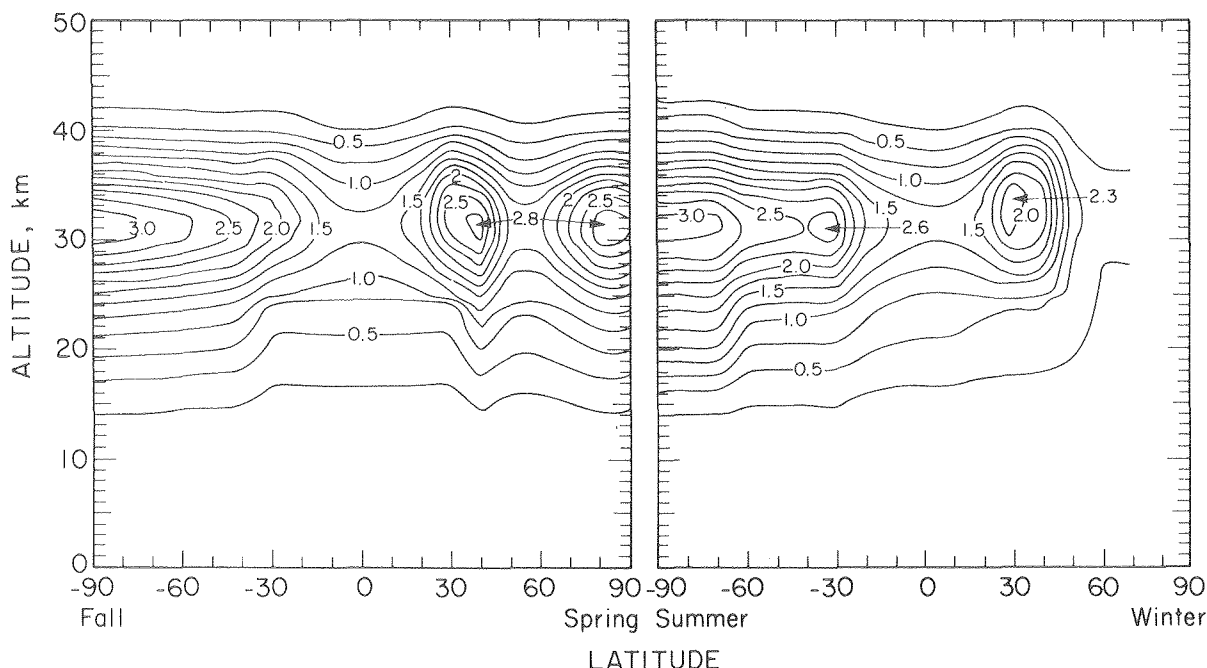
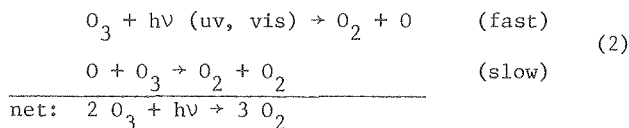
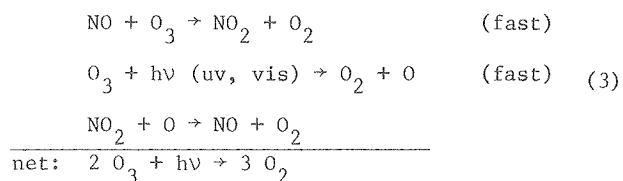


Fig. 2. Daytime average nitrogen dioxide concentrations in units of 10⁹ molecules cm⁻³. (XBL 801-7807)

(c) The rate of ozone destruction by the oxides of nitrogen, $L(\text{NO}_x)$, which is $2 k' [\text{O}][\text{NO}_2]$,



In each of the above cases the loss or production of ozone resulting from the catalytic cycle is given by the rate determining step in each cycle.

The relative role of the pure oxygen species and the oxides of nitrogen in the global ozone balance is examined in Tables 1 and 2. The 24 hour average column rates between 15 and 45 km for ozone photochemical production $P(\text{O}_3)$ for ozone destruction by O_x reactions $L(\text{O}_x)$, and for ozone destruction by NO_x

are listed for each latitude between 80°S and 80°N in Table 1. For fall-spring conditions, the rate of ozone production at 80°N or 80°S is very slow (about 10 percent of that at the equator), and the destruction rates, $L(\text{O}_x) + L(\text{NO}_x)$, are about twice as fast as the photochemical production. At mid-latitudes ($30^\circ - 60^\circ$) the 15 to 45 km column rate of ozone destruction by O_x is about 14 percent and that by NO_x reactions is about 55 percent of the rate of ozone production. In tropical regions the percentages are 14 for $L(\text{O}_x)$ and 35 for $L(\text{NO}_x)$.

The global sums of $P(\text{O}_3)$, $L(\text{O}_x)$, and $L(\text{NO}_x)$ over various altitude bands of 5 km width are given in Table 2. Between 45 and 50 km the role of NO_x is quite small, $L(\text{NO}_x)$ being only seven percent of $P(\text{O}_3)$; over this range $L(\text{O}_x)$ is 23 percent of $P(\text{O}_3)$. Between 40 and 45 km, the O_x and NO_x reactions are about equally important in balancing ozone, and each destroys ozone about 25 percent as fast as it is produced. Between 30 and 40 km, the O_x reactions destroy ozone about 10 percent as fast as it is pro-

Table 1. Twenty-four hour average column rates (15 to 45 km) in units of 10^{11} molecules $\text{cm}^{-2} \text{ s}^{-1}$. Spring NH, fall SH (south pole is -90°).

| Lat. | Prod. O_3 $2 j [\text{O}_2]$ | Loss of O_3 | | Ratio L/P | | |
|------|---|--|---|--------------|---------------|------|
| | | O_x $2 k [\text{O}][\text{O}_3]$ | NO_x $2 k' [\text{O}][\text{NO}_2]$ | O_x | NO_x | Both |
| -80 | 14 | 2 | 28 | 0.13 | 1.95 | 2.08 |
| -70 | 33 | 3 | 20 | 0.09 | 0.61 | 0.70 |
| -60 | 51 | 5 | 21 | 0.11 | 0.40 | 0.51 |
| -50 | 67 | 9 | 26 | 0.14 | 0.39 | 0.53 |
| -40 | 81 | 13 | 49 | 0.16 | 0.60 | 0.76 |
| -30 | 94 | 14 | 64 | 0.15 | 0.68 | 0.83 |
| -20 | 106 | 16 | 47 | 0.15 | 0.44 | 0.59 |
| -10 | 112 | 17 | 36 | 0.15 | 0.32 | 0.47 |
| 0 | 119 | 16 | 35 | 0.13 | 0.29 | 0.42 |
| 10 | 117 | 16 | 37 | 0.13 | 0.31 | 0.44 |
| 20 | 110 | 14 | 45 | 0.13 | 0.41 | 0.54 |
| 30 | 100 | 13 | 53 | 0.13 | 0.53 | 0.66 |
| 40 | 83 | 12 | 44 | 0.15 | 0.53 | 0.68 |
| 50 | 67 | 9 | 39 | 0.13 | 0.58 | 0.71 |
| 60 | 48 | 5 | 32 | 0.11 | 0.66 | 0.77 |
| 70 | 28 | 3 | 26 | 0.11 | 0.93 | 1.04 |
| 80 | 9 | 2 | 20 | 0.19 | 2.18 | 2.37 |

Table 2. Global-sum column rates over various altitude bands, in units of 10^{29} molecules s^{-1} . Spring NH, fall SH.

| Alt. Band km | Prod. O_3 $2 j[O_2]$ | Loss of O_3 | | Ratio L/P | | |
|--------------|---------------------------|---------------|--------|-----------|--------|------|
| | | O_x | NO_x | O_x | NO_x | Both |
| 45-50 | 140.2 | 32.4 | 9.2 | 0.23 | 0.07 | 0.30 |
| 40-45 | 171.2 | 42.4 | 45.2 | 0.25 | 0.26 | 0.51 |
| 35-40 | 155.4 | 19.0 | 89.2 | 0.12 | 0.57 | 0.69 |
| 30-35 | 104.0 | 7.2 | 57.4 | 0.07 | 0.55 | 0.62 |
| 25-30 | 43.4 | 2.6 | 15.4 | 0.06 | 0.35 | 0.41 |
| 20-25 | 8.8 | 0.52 | 1.8 | 0.06 | 0.30 | 0.36 |
| 15-20 | 0.9 | 0.04 | 0.12 | 0.04 | 0.13 | 0.17 |
| 15-45 | 484 | 72 | 209 | 0.15 | 0.43 | 0.58 |

duced, and NO_x destroys about 57 percent. Between 25 and 30 km, $L(O_x)$ is six percent of $P(O_3)$, and $L(NO_x)$, is 35 percent. Below 25 km both the rate of photochemical production of ozone and its destruction by O_x and NO_x become slow. Over the range 15 to 45 km on the global scale the O_x reactions destroy 15 percent of the photochemically produced ozone and NO_x reactions destroy 43 percent for the fall-spring season. This total percentage of 58 leaves ample room for major effects by HO_x and Cl_x reactions.

The global role of NO_x in destroying ozone between 15 and 45 km is explored as a function of season in Table 3. Ozone destruction by NO_x is 43 percent of $P(O_3)$ in spring, 50 percent in summer, 39

percent in fall, and 43 percent in winter of the northern hemisphere. The average of these four seasons is 44 percent. The inventory of NO_2 in the sunlit half of the globe is about 1.3×10^{34} molecules, with some apparent seasonal changes.

This single number for the effect of nitrogen oxides on stratospheric ozone should be used with great caution. Emphatically, it is not an index for the sensitivity of stratospheric ozone to a perturbation by added NO_x . At present model calculations predict that an increase of stratospheric NO_x would decrease ozone in the upper stratosphere, would increase ozone in the lower stratosphere, and would have only a small effect of uncertain sign on the total ozone column.¹²

Table 3. Comparison of four seasons in terms of global instantaneous rates between 15 and 45 km. The total daytime NO_2 is summed over the sunlit hemisphere

| Season NH | $P(O_3) s^{-1}$ (10^{29}) | Total Daytime NO_2 (10^{32}) | $L(NO_x)$ (10^{29}) | $\frac{L}{P}$ |
|-----------|----------------------------------|---------------------------------------|----------------------------|---------------|
| SP | 484 | 146 | 209 | 0.43 |
| SU | 449 | 119 | 222 | 0.50 |
| F | 480 | 135 | 187 | 0.39 |
| W | 527 | 134 | 228 | 0.43 |

* * *

[†]Brief version of LBL-9607.

[‡]Permanent address: NCAR-ASP, P. O. Box 3000, Boulder, Colorado 80307.

[§]Permanent address: Department of Chemistry, Monash University, Wellington Road, Clayton, Victoria, Australia 3168.

1. Crutzen, P. J., *Quart. J. Roy. METEOROL. Soc.* **96**, 320 (1970).

2. Noxon, J. F., E. C. Whipple, Jr., and R. S. Hyde, *J. Geophys. Res.*, in press (1979).

3. Noxon, J. F., *J. Geophys. Res.*, in press (1979).

4. Ackerman, M., J. C. Fontanella, D. Frimout, A. Girard, N. Louisnard, and C. Muller, *Planet. Space Sci.* **23**, 651 (1975).

5. Harries, J. E., D. G. Moss, N. R. W. Swann, G. F. Neill, and P. Gildwang, *Nature* **259**, 300 (1976).

6. Murcray, D. G., A. Goldman, W. J. Williams, F. H. Murcray, J. N. Brooks, J. Van Allen, R. N. Stocken, J. J. Kusters, D. B. Barker, and D. E. Snider, *Proceedings of the Third Conference on CIAP*, U. S. Department of Transportation, DOT-TSC-OST-74-15, 1974, pp. 184-192.

7. Ogawa, T., private communication, 1979.

8. Dütsch, H. U., *Pure Applied Geophys.* **116**, 511 (1978).

9. Johnston, H. S., and G. Whitten, *Int. J. Chem. Kinet.*, Symposium No. 1, 1-26 (1975).

10. Johnston, H. S., *Rev. Geophys. Space Phys.* **13**, 637 (1975).

11. Isaksen, I. S. A., K. Midtbø, J. Dundee, and P. J. Cruzen, *Institute for Geophysics, University of Oslo, Oslo, Norway, Report 20*, 1976, pp. 1-21.

12. Rundel, R. D., D. M. Butler, and R. S. Stolarski, *J. Geophys. Res.* **83**, 3063 (1978).

6. THUNDERSTORMS AS POSSIBLE MICROMETEOROLOGICAL SINK FOR STRATOSPHERIC WATER

H. S. Johnston and S. Solomon

The stratosphere has been observed to have a low mixing ratio of water.^{1,2} In his classic paper, Brewer³ explained this phenomenon by a "dynamic process ... of a circulation in which air enters the stratosphere at the equator, where it is dried by condensation, travels in the stratosphere to temperate and polar regions, and sinks into the troposphere." The dryness of the stratosphere was interpreted in terms of what has come to be called a "cold trap" mechanism. The rising branch of the Hadley cell model of the general circulation supplied stratospheric water vapor, and the descending branches provided the sink.

Ellsaesser⁴ reviewed the literature on the net mass flux of air from troposphere to stratosphere in the tropical Hadley cell and on the mean tropical tropopause temperatures. He stated that there appeared to be a discrepancy in the water budget with respect to the global circulation model and asked, "How does the stratosphere maintain a mean mixing ratio of around 2.5 ppmv when all air entering the stratosphere passes through a cold trap whose characteristic mixing ratio is not less than

3.4 ppmv [saturation at mean tropical tropopause temperature] and when there is presumptive evidence for direct stratospheric injections of additional H₂O via CH₄ oxidation, the subtropical tropopause gaps, and cumulonimbus penetration of the tropopause?"

We believe that the discrepancy that Ellsaesser perceived in the general circulation model proposed by Brewer may be removed if one examines the physical processes occurring in the upward branch of the Hadley cell. There is a standard, meteorological, idealized theory that gives a first-order approximation to the physical processes that occur during cumulonimbus activity.⁵ Although many of the assumptions of the theory are not realized under actual conditions, classical parcel theory provides simple limiting predictions against which real phenomena can be compared and classified. Briefly, a diagram such as the inset in Fig. 1 is constructed. The observed environmental temperature profile⁶ is indicated by the line ABCD. In our example the temperature profile is that for Panama, 9° north, February 21, 1963.

The calculated parcel temperature profile is AECF in Fig. 1. The parcel cools less rapidly than the environment along AEC, is warmer than the surrounding air, and being buoyant, rises upward. At the neutral point C, the parcel has the same temperature and pressure as the surrounding air; but it has upwardly directed kinetic energy, equal to the area I. The idealized parcel overshoots the neutral point C and rises to a maximum height F, where area II equals area I. After it comes to rest at F, the parcel spontaneously descends. For this example the numbers on the expanded diagram in Fig. 1 repre-

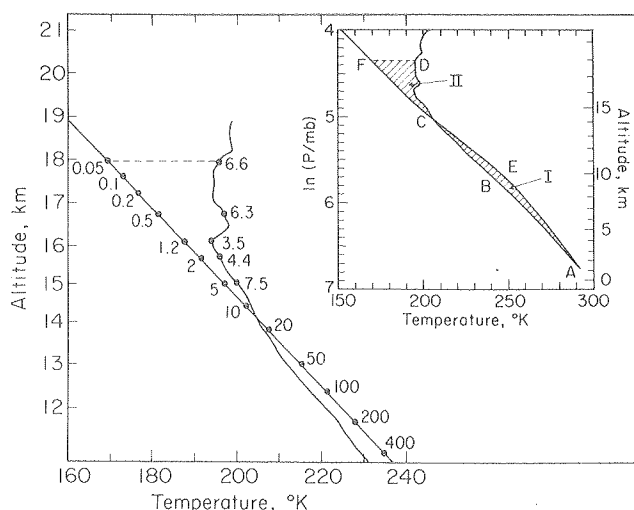


Fig. 1. (Inset) Pseudo-adiabatic lapse rate and an environmental profile for Panama, 9°N, February 21, 1963.⁶ Surface temperature assumed to rise to 304 K. Absolute temperature T and natural logarithm of pressure in millibars. (Expanded scale) Portion of curve above plotted as absolute temperature and altitude in kilometers. Numbers indicate saturation water vapor mixing ratios with respect to ice on the environmental and calculated "parcel theory" profiles (parts per million by mass). (XBL 801-7810)

sent the saturation mixing ratios of water vapor (parts per million by mass) with respect to ice on both the environmental and the parcel profiles. At the tropopause the saturation mixing ratio of water vapor is 1.2 ppm in the parcel but 3.5 ppm in the environment. At its maximum altitude the parcel has a temperature of 170 K and a saturation mixing ratio of water vapor over ice of 0.95 ppm. However, for actual storms the process of entrainment (mixing of environmental air with the parcel) acts to prevent the parcel from reaching the heights predicted by the theory, and a line intermediate between CF and CS is more nearly to be expected.

Intense thunderstorms that penetrate the stratosphere are exceedingly more complicated than the representation in Fig. 1, but the regions in Fig. 1 still supply useful nomenclature. The temporary existence of large parcels of air above and colder than the tropopause suggests mechanisms whereby the overshooting cumulonimbus clouds could provide a cold trap effectively colder than the mean tropopause.

* * *

† Brief version of *J. Geophys. Res.* **84**, 3155 (1979).

‡ This research was supported in part by the National Science Foundation.

1. Mastenbrook, H. J., *J. Atmos. Sci.* **28**, 1495 (1971).
2. Harries, J. E., *Rev. Geophys. Space Phys.* **14**, 565 (1976).
3. Brewer, A. W., *Quart. J. Roy. Meteorol. Soc.* **75**, 351 (1949).
4. Ellsaesser, H. W., *Proceedings of the Third Conference of the Climatic Impact Assessment Program*, pp. 273-283, Department of Transportation, Washington, D. C., 1974.
5. Rogers, R. R., *A Short Course in Cloud Physics*, Pergamon, New York, 1976.
6. Hering, W. S., Report AFCRL-64-30, U. S. Department of Commerce, Office of Technical Services, Washington, D. C., 1964.

7. DEVELOPMENT OF STABLE ELECTRICAL WAVEFORM SOURCES FOR A MOLECULAR MODULATION†

J. Podolske

In the course of developing a molecular modulation spectrometer for studying a number of gas phase reactions of the HO₂ radical, the need arose for two unusual signal sources. The first was a sine wave generator capable of operating a very low frequency, with stable amplitude and well known frequency. The second was a closed loop device which transforms a roughly sinusoidal waveform of varying amplitude, derived from the pickup coil of a tuning form chopper, into a constant amplitude sinusoidal waveform, with the same frequency and phase as the pickup signal, to drive the chopper.

Stable, Low-Frequency Sine Wave Generator. A circuit was developed for the generation of low-frequency (0.002 Hz to 63 kHz) sine waves possessing stable amplitude and frequency characteristics using

digital techniques.¹ The circuit produces a 32 step approximation to a sine wave at a frequency 1/32nd of the digital time base frequency by nonrecursive filtering of binary wave forms produced by a twisted ring counter. The crystal controlled time base has a switch selectable frequency range of 2.048×10^7 times the base frequency, with half octave resolution. A switch programmable active filter is included for removing the high order harmonics produced by the generator.

Stable Sinusoidal Tuning Fork Driver. An electronic circuit was developed which can drive tuning fork choppers, such as the Bulova L40 and L2 series units.² The advantages of this circuit over the factory supplied 5A-type driver are better drive amplitude stability, freedom from drift due to line voltage variations, and a cleaner, transient free sinusoidal reference signal. Test results indicate an improvement in long-term stability by as much as a factor of four.

* * *

† Brief version of LBL-8610 and 8611.

1. Podolske, J., *Rev. Sci. Instrum.* **50**, 1010 (1979), LBL-8610.

2. Podolske, J., *Rev. Sci. Instrum.* **50**, 1025 (1979), LBL-8611.

RESEARCH PLANS FOR CALENDAR YEAR 1980

We are developing new methods, based on lasers, for measuring free-radical intermediates in photochemical reactions. By use of a diode laser, we plan to measure simultaneously the hydroxyl HO and perhydroxyl HOO radicals in a molecular modulation system. Trace amounts of ozone or hydrogen peroxide or both will be sinusoidally photolyzed as they are carried by a stream of nitrogen through a long-path cell. The amplitude and phase shift of the monitoring beam of near infrared radiation should give spectroscopic and kinetic information about HO and HOO in this system. Using a tunable dye laser driven by a continuous wave argon-ion laser, we plan to study the molecular modulation of the NH₂ free radical. We are developing the use of an external cavity, such as that used for lasers, as a compact, small-volume, long-path absorption cell. Our pulsed high-intensity dye laser will be used to photolyze molecules containing chlorine atoms, which will be detected by resonance fluorescence.

Presumably all elementary reactions that occur in the carbon-monoxide-smog process are identified and have known rate constants. We have underway a combined experimental and theoretical study of this relatively simple smog reaction. The object of this experiment is to verify the completeness, or establish the incompleteness, of theoretical models for these processes under controlled laboratory conditions.

Modeling studies of photochemistry in the global stratosphere will continue. These studies are different from the conventional stratospheric models, which are now in operation in at least ten labora-

tories; our studies take observations of trace species in the atmosphere and interpret them; the conventional approach sets up a model of chemical reactions radiation, and atmospheric motions and predicts the concentrations of trace species. These two approaches are complementary, not competitive.

1979 PUBLICATIONS AND REPORTS

Refereed Journals

1. P. Connell and H. S. Johnston, "The Thermal Dissociation of N_2O_5 in N_2 ," *Geophys. Res. Lett.* 6, 553 (1979). LBL-8943.
2. H. S. Johnston and S. Solomon, "Thunderstorms as Possible Micrometeorological Sink for Stratospheric Water," *J. Geophys. Res.* 84, 3155 (1979). LBL-8633.
3. J. Podolske, Stable, Inexpensive, "Low-Frequency Sine Wave Generator Using Digital Techniques," *Rev. Sci. Instrum.* 50, 1010 (1979). LBL-8610.
4. J. Podolske, "Stable Sinusoidal Driver Circuit for Tuning Fork Choppers," *Rev. Sci. Instrum.* 50, 1025 (1979). LBL-8611.
5. H. S. Johnston, O. Serang, and J. Podolske, "Instantaneous Global Nitrous Oxide Photochemical Rates," *J. Geophys. Res.* 84, 5077 (1979). LBL-8055.

LBL Reports

1. G. S. Selwyn, "The Ultraviolet Spectroscopy of Nitrous Oxide (N_2O): A Temperature-Resolved Study," Ph.D. Thesis, University of California, Berkeley, March 1979, LBL-8739.
2. P. S. Connell, "The Photochemistry of Dinitrogen Pentoxide," Ph.D. Thesis, University of California, Berkeley, May 1979, LBL-9034.
3. F. Magnotta, "Absolute Photodissociation Quantum Yields of NO_3 and N_2O_5 by Tunable Laser Flash-Photolysis Resonance-Fluorescence," Ph.D. Thesis, University of California, Berkeley, December 1979, LBL-9981.
4. P. S. Connell and S. Solomon, "Temporal Behavior of NO_3 and N_2O_5 in the Stratosphere, June 1979, LBL-9862.
5. S. Solomon, H. S. Johnston, M. Kowalczyk, and I. Wilson, "Instantaneous Global Ozone Balance Including Observed Nitrogen Dioxide, June 1979, LBL-9607.

2. Chemical Physics

a. Energy Transfer and Structural Studies of Molecules on Surfaces*

C. B. Harris, Investigator

Introduction. As in the past, our laboratory has been engaged in developing new methods for investigating energy transfer processes in condensed phase on metal surfaces and studying a variety of questions associated with the electronic and molecular structure of molecules on single crystal metal surfaces. Progress in this field has been contingent on the development of new instrumentation. In 1979, we completed construction of a surface chamber designed to probe surface-adsorbate interactions using some new laser techniques. In addition, modification of the existing instrumentation used in the optical spectroscopy studies has been completed. This has resulted in a tenfold increase in the signal-to-noise ratio of the data. As a result of these two technical developments, normal unenhanced Raman scattering of molecules on metal surfaces and the optical spectroscopy of chemisorbed species on metal surfaces are reported for the first time. We have also been developing picosecond nonlinear optical laser techniques for studying energy transfer and relaxation in condensed phase and on metal surfaces. Our first definitive experiments related to the question of the structure of liquids on the picosecond time scale have been completed and are presented.

1. OPTICAL SPECTROSCOPY OF CHEMISORBED MOLECULES ON Ni(111).†

C. B. Harris, A. R. Gallo, H. J. Robota, and P. M. Whitmore

We have obtained the optical electronic spectrum of chemisorbed species on Ni(111) using a refined and optimized scanning ellipsometer.

As an example, the spectrum of chemisorbed pyrazine is shown in Fig. 1 with the previously obtained¹ spectrum of physisorbed and condensed pyrazine shown in Fig. 2 for comparison. The chemisorbed pyrazine spectrum is characterized by a strong absorption near 2600 Å and a less intense, broad feature near 3100 Å. Nonquantitative preliminary thermal desorption spectra indicate molecular pyrazine as the adsorbed species. This agrees with similar behavior for benzene on Ni(111).² Finally, the relationships between gas phase, physisorbed, and chemisorbed spectra lead us to identify the adsorbed species as an

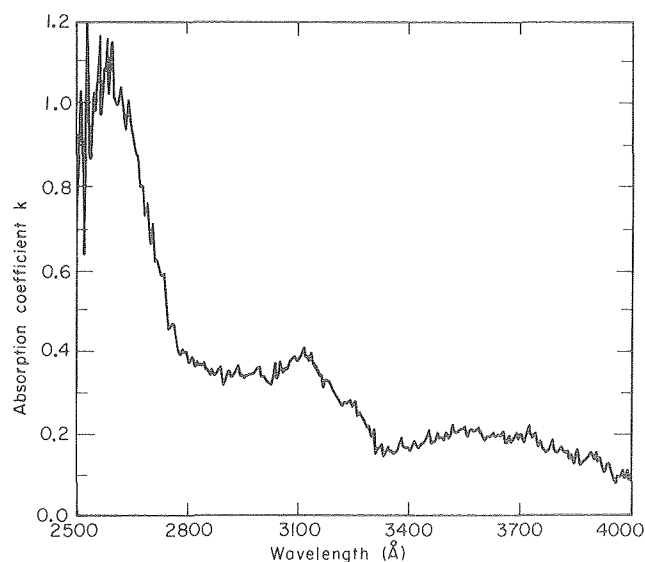


Fig. 1. The analyzed 30 K spectrum of chemisorbed pyrazine on Ni(111) deposited at room temperature, obtained by rotating analyzer ellipsometry.
(XBL 7911-3896)

undissociated molecular pyrazine entity. We assign the 2600 Å absorption as a $1\pi\pi^*$ type and the 3100 Å absorption as a $1n\pi^*$ type transition.

This spectral assignment leads immediately to two further implications regarding the nature of the pyrazine-Ni(111) bond. From a comparison of the transition energies in the gas phase, the interaction with the surface apparently produces a uniform shift in adsorbate state energies. This allows the molecule to remain intact and behave as a separate species at the surface. Also, the blue shift of the $1n\pi^*$ transition and the lack of vibronic structure suggests the bonding of the pyrazine through the nitrogen lone pair electrons. The possibility of further bonding through the aromatic π ring electrons, as in benzene at higher temperatures, remains an open one.

In summary, the utilization of optical techniques for studying chemisorbed molecules has been demonstrated in which the spectra obtained reveal features of the chemisorption bond not easily obtained with other techniques. The techniques should be generally applicable to a variety of problems in many systems.

*This work was supported by the Division of Chemical Sciences, Office of Basic Energy Sciences, U. S. Department of Energy.

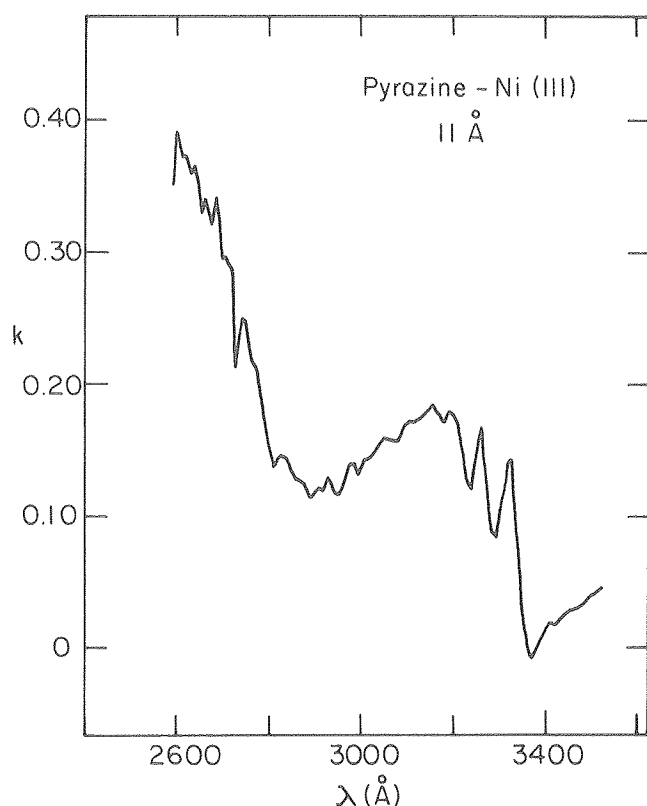


Fig. 2. The spectrum of condensed, annealed pyrazine on Ni(111) at 10 K revealing vibronic structure in the 1_{nm}^* transition. (XBL 786-5178)

* * *

[†]Brief version of LBL-8546; *Surface Sci.* **85**, 1, L205 (1979).

1. C. B. Harris, D. A. Zwemer, A. R. Gallo, and H. J. Robota, *Surface Science*, **85**, L205 (1979).
2. S. Lehwald, H. Ibach, and J. E. Demuth, *Surface Sci.* **78**, 577 (1978).

2. RAMAN SPECTROSCOPY OF MOLECULES ADSORBED ON Ni(111) AND Ag(111).

C. B. Harris and A. Campion

Two approaches have been designed to increase the sensitivity of Raman spectroscopy to the point where it may be used to obtain vibrational spectra of adsorbed species at submonolayer coverage. The first program is directed towards the elucidation of the mechanism of the surface-enhanced Raman effect,¹ which has been reported for electrode surfaces, primarily silver. We find, for a number of molecules physisorbed on Ag(111) and Ag(110) surfaces, no appreciable enhancement of the scattering cross section. Our findings bear directly upon the validity of various theories² which have been advanced to explain the effect and indicate that the

nature of the plasmon wavevector in the Ag surface are important for enhanced scattering.

The second approach uses an optical multichannel analyzer to improve efficiency. The parallel nature of this detector results in an efficiency improvement of up to 10^3 , over conventional photon counting, making it possible to obtain spectra even in the absence of enhancement.

Figure 1 shows the Raman spectrum of nitrobenzene physisorbed on Ni(111). All bands in the lower spectrum correspond closely to literature values for the pure liquid, with some deviations in intensity ratios that may be ascribed to new selection rules imposed by the boundary conditions on the electromagnetic fields at the surface. All features of the lower spectrum are preserved in the upper spectrum of a much thinner layer, one that is only a few monolayers thick. By improving the optical configuration used in these experiments, and using a second generation optical multichannel analyzer, detectivities into the submonolayer regime should be possible.

* * *

1. R. P. Van Duyne in *Chemical and Biochemical Applications of Lasers*, Academic Press, New York, p. 101 (1979).
2. F. W. King, R. P. Van Duyne, and G. C. Schatz, *J. Chem. Phys.* **69**, 4472 (1979).
3. S. Efrima and H. Metiu, *J. Chem. Phys.* **70**, 1602 (1979).

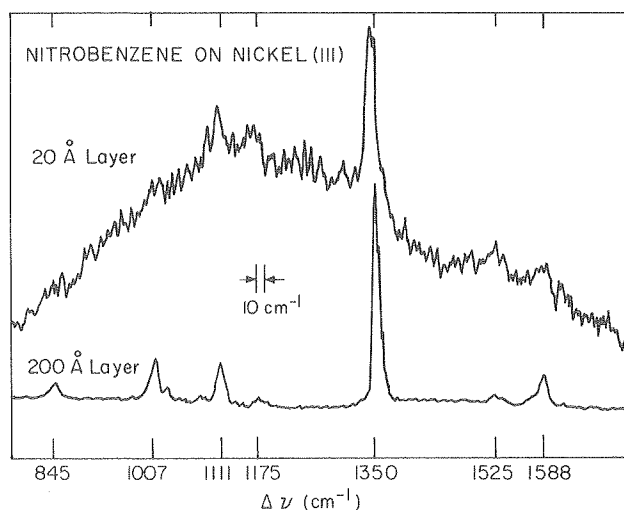


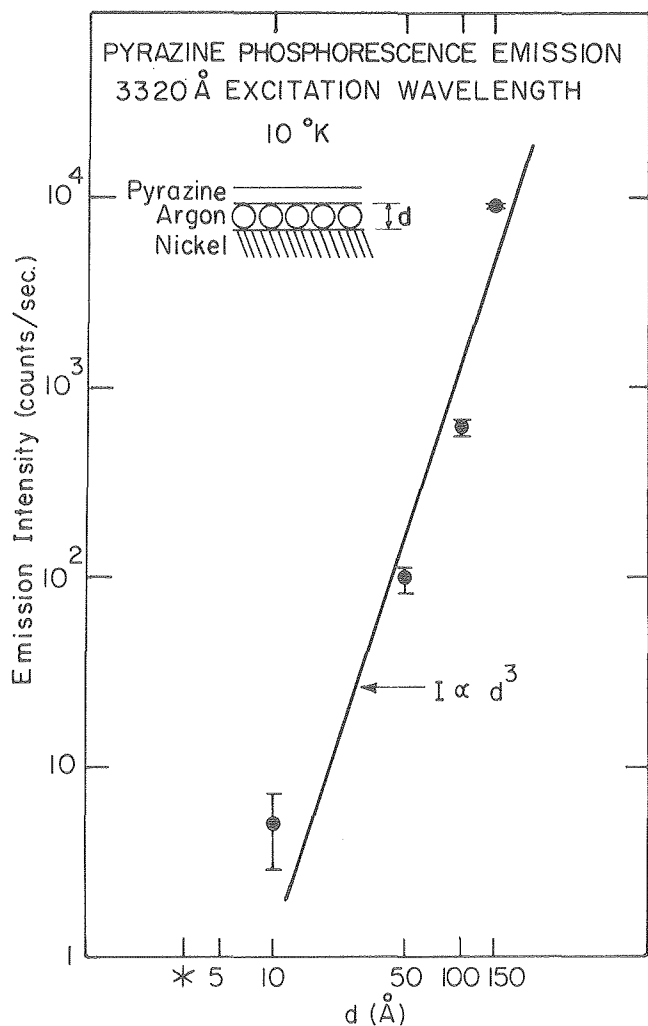
Fig. 1. Raman spectra of nitrobenzene physisorbed on Ni(111). Lower spectrum is for a layer estimated to be ~ 200 Å thick. Spectral resolution is ~ 10 cm^{-1} . Upper spectrum is for a 20 Å layer (estimated from an Auger electron spectrum). The high background intensity arises from the detector. (XBL 7910-7273)

3. THE DYNAMICS OF ENERGY TRANSFER FROM PHOTO-EXCITED MOLECULES TO METAL SURFACES[†]

C. B. Harris, A. Campion, and A. R. Gallo

A new technique has been developed for investigating the mechanism of nonradiative electronic energy transfer from excited molecules to metal surfaces at very short ($< 50 \text{ \AA}$) distances. A monolayer of luminescent molecules is deposited on top of a thin layer of argon which has been condensed onto a metal surface at 10K, under ultrahigh vacuum. The thickness of each layer is controlled during deposition by monitoring the film growth with an ellipsometer. The distance dependence of the energy transfer rate is then obtained by measuring the luminescence intensity, or lifetime as a function of the thickness of the argon spacer layer. This short distance regime has been inaccessible until now. Previous studies have employed the Langmuir-Blodgett method, in which monomolecular layers of a fatty acid are used to separate the dye molecule from the surface.¹ The shortest separation achieved by this method was approximately 50 \AA .

Figure 1 shows the distance dependence of the relative phosphorescence quantum yield for the system pyrazine-argon-nickel. Classical image dipole theory¹ predicts an inverse cubic dependence of the energy transfer rate upon distance to the surface.



This same distance dependence is also obtained by invoking a Förster dipole-dipole mechanism. The data obtained in this experiment are relatively consistent with the cubic dependence shown although some deviation is to be noted.

This method should be generally applicable to the study of energy transfer processes occurring near surfaces and allow one to investigate the multipolar nature of the electronic coupling, which may be obtained by more careful measurements of the distance dependence. In addition, this method can be used to elucidate the role of the surface plasmons,² which act as energy acceptors, by obtaining the frequency dependence of the transfer rate.

* * *

[†]Brief version of LBL-10134; submitted to Phys. Rev. Lett.

1. R. R. Chance, A. Prock, and R. Silbey, Adv. Chem. Phys. XXVII, (1978).
2. R. R. Chance, A. Prock, and R. Silbey, J. Chem. Phys. 62, 2245 (1975).

4. LOW LEVEL LIGHT SIGNAL AVERAGING USING AN OPTICAL MULTICHANNEL ANALYZER (OMA)[†]

C. B. Harris and J. L. Chao

The use of an optical multichannel analyzer (OMA) operating system for the data collection and signal processing of extremely low level light signals has been developed. A programmable optical multichannel analyzer has been employed to signal average high resolution ($0.05 \text{ cm}^{-1}/\text{channel}$) emission spectra from sources having as few as 1.2 photon/sec./channel. By developing extended delay target integration capabilities, we have been able to achieve photoelectron statistics comparable to single channel photon counting schemes.¹

The SIT (silicon intensified target) detector consists of a 500×500 array of silicon diodes. Photoelectrons are formed and allowed to integrate on the target in order to improve the counting statistics in each discrete channel. Furthermore, cooling of a detector to -50°C by using a liquid cooler refrigeration unit greatly reduces the dark current associated with the thermal population around the Si band gap. It was found that signal-to-noise can be improved by more than 10:1 by proper detector cooling.

Figure 1 shows a spectrum collected using extended delay techniques with target integration of six minutes. The first plot shows the signal collected with the concomitant dark current while the second shows the spectrum after background subtraction.² One should note in this particular spectrum that the dark current/background level is approximately four

Fig. 1. Pyrazine phosphorescence intensity as a function of distance to the (111) surface of a nickel single crystal. The theoretical d^{-3} dependence is shown for comparison. (XBL 7910-7272)

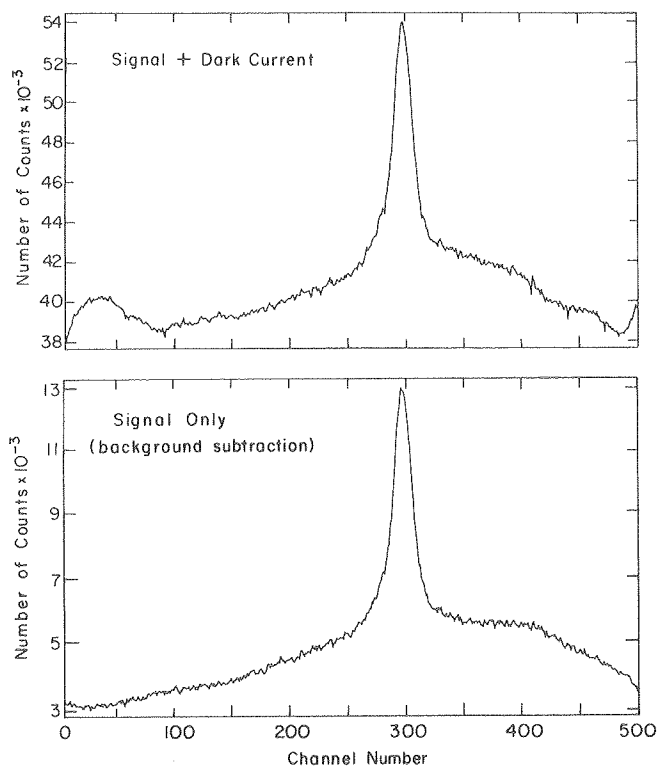


Fig. 1. Spectrum collected using extended delay target integration techniques. The first plot shows the emission before background subtraction and the second plot shows the signal only after digital background subtraction. (XBL 7911-14523)

times that of the signal peak. Furthermore, the detected photoelectron flux is 43 counts/sec-channel! We have been able to integrate light on the silicon target for periods as high as three hours where the flux was below 0.3 counts/sec and still achieve S/N ratios greater than 10:1.

The use of an optical multichannel analyzer for low level light imaging can often mean the difference between success and failure in many signal-limited applications. The development of the programmable detector optimization techniques will be useful for a number of UV/Vis experiments. In particular, we have observed Raman scattering from organic molecules physi- and chemisorbed to metal surfaces using the instrumentation. Raman spectroscopy using an optical multichannel analyzer should allow one to study interactions in such systems at sub-monolayer coverages when integration techniques are developed.

* * *

[†]Brief version of LBL-10135; submitted to Rev. Sci. Instrum.

1. J. L. Weber and P. W. Roehrenbeck, Optical Spectroscopy, March 1979.

2. Background subtraction is performed by first scanning the detector with no light signal and storing it in computer memory. Light is then allowed to collect on the target and the spectrum is then extracted by digitally subtraction out the

background counts. This serves to eliminate any DC offset associated with A/D conversion as well as to subtract out any other sources of non-photon generated counts such as the dark current.

5. INVESTIGATIONS OF LIQUID STRUCTURE BY PICOSECOND LASER SPECTROSCOPY^{††}

C. B. Harris, H. Auweter, and S. M. George

Using picosecond probe techniques,^{1,2} we have determined the dephasing times of the symmetric CH₃ stretching vibration in various liquids. Because the homogeneous linewidth is proportional to the inverse of the dephasing time, we have been able to determine the amount of inhomogeneous broadening in liquid linewidths by comparing isotropic spontaneous Raman linewidths to our experimentally determined linewidths. We have found that almost all symmetric CH₃ stretching vibrations linewidths are inhomogeneously broadened and have been able to correlate the amount of inhomogeneous broadening with specific characteristics of the liquids.

The results of our study are compiled in Table 1. The dephasing times are remarkably similar, with the exception of dimethylsulfoxide and acetonitrile. Dimethylsulfoxide has the shortest dephasing time and the largest viscosity, which suggests that the collision frequency may be playing a role in dephasing since the collision frequency is proportional to the viscosity.³

When the inhomogeneous broadening magnitude is compared to various liquid physical characteristics, such as the dielectric, thermodynamic, and ultrasonic parameters, very little correlation is apparent. An interesting connection, shown in Fig. 1, is observed between the amount of inhomogeneous broadening and the excess volume fraction in the liquid. This suggests that inhomogeneous broadening arises not just because of structural associativity, but by distributions of free space in liquids which tend to maximize the number of interactions of molecules with other molecules and/or free space.

Since our results show that almost all symmetric CH₃ stretching vibrational linewidths are inhomogeneously broadened, our results seriously jeopardize spontaneous Raman linewidth investigations which assume that vibrational linewidths are homogeneous. Recent pressure, temperature and dilution studies on symmetric CH₃ stretching vibrational linewidths in liquids may just be monitoring the inhomogeneous rather than the homogeneous linewidth's functional dependence of pressure, temperature and dilution.⁴⁻⁶ Our results illustrate the picosecond time domain techniques' importance in studying homogeneous liquid vibrational linewidths.

We have begun to understand how liquid structure affects inhomogeneous broadening. We have preliminary evidence that suggests how liquid dynamics affect homogeneous broadening. By studying more molecules and specific molecules under varying conditions, one can elucidate how liquid dynamics and liquid structure act to determine homogeneous and inhomogeneous broadening in liquid vibrational linewidths.

Table 1. Comparison of experimental data with liquid parameters.

| Molecule | $w(\text{cm}^{-1})$ | Spontaneous $\Delta w(\text{cm}^{-1})$ | T_2 (psec) | Homogeneous $\Delta w(\text{cm}^{-1})$ | Normalized Broadening (cm^{-1}) | $\alpha(\text{\AA}^3)$ | $\frac{\Delta H^V}{T}$ ($\frac{\text{cal}}{\text{deg mol}}$) | $\frac{\text{BP}}{\text{MW}}$ | $\frac{\alpha_{\text{exp}}}{\alpha_{\text{class}}}$ | Excess Volume (%) Fraction |
|---------------------------|---------------------|---|--------------|---|--|------------------------|---|-------------------------------|---|----------------------------------|
| Methanol | 2836 | 18.75 | 2.4 | 4.4 | 3.26 | 3.28 | 24.97 | 1.96 | 2.29 | 18.2 |
| Ethanol | 2929 | 18.0 | 2.5 | 4.6 | 2.91 | 5.12 | 26.36 | 1.70 | 2.09 | 12.4 |
| Acetone | 2925 | 16.5 | 3.0 | 3.4 | 3.85 | 6.41 | 21.11 | 0.97 | 4.10 | 16.2 |
| CH_3CCl_3 | 2941 | 4.5 | 2.6 | 4.2 | 0.07 | 10.35 | 22.17 | 0.50 | 28.53 | 5.7 |
| DMSO | 2915 | 11.8 | 1.5 | 7.6 | 0.55 | 7.97 | 22.32 | 2.41 | 2.60 | 0.6 |
| CH_3CN | 2945 | 6.6 | 5.4 | 2.0 | 2.30 | 4.39 | 20.16 | 1.99 | 12.49 | 8.7 |
| Pentane | 2885 | ≈ 20 | 2.7 | 3.9 | 4.10 | 10.02 | 19.93 | 0.50 | 7.14 | 18.5 |

α = polarizability.

$\Delta H^V/T$ = Trouton's ratio.

BP/MW = boiling point divided by molecular weight.

$\alpha_{\text{exp}}/\alpha_{\text{class}}$ = an ultrasonic ratio used to classify liquids.

Excess volume = $V_{\text{liquid}} - V_{\text{solid}}/V_{\text{liquid}} \times 100$, where V is molar volume.

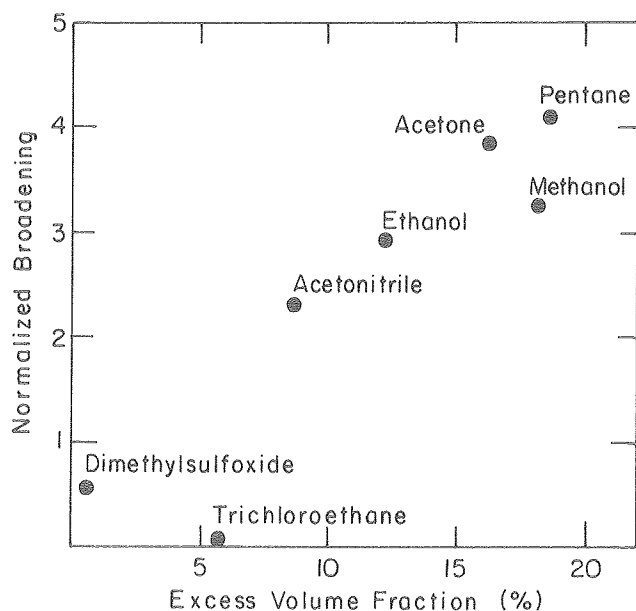


Fig. 1. Plot of inhomogeneous broadening (normalized by dividing by the homogeneous linewidth) versus the excess volume fraction in the liquid.

(XBL 7911-14545)

* * *

[†]Brief version of LBL-10141.

[‡]Partially supported by National Science Foundation.

1. A. Laubereau and W. Kaiser, *Rev. Mod. Phys.* **50**, 607 (1978).

2. A. Laubereau, G. Wochner, and W. Kaiser, *Chem. Phys.* **28**, 363 (1978).

3. K. F. Herzfeld and T. A. Litovitz, *Absorption and Dispersion of Ultrasonic Waves*, Academic Press, New York City, p. 376 (1959).

4. K. Tanabe and J. Jonas, *Chem. Phys.* **38**, 131 (1979).

5. J. Shroeder, V. H. Schieman, P. T. Sharko, and J. Jonas, *J. Chem. Phys.* **66**, 3215 (1977).

6. J. Yarwood, R. Arndt, and G. Döge, *Chem. Phys.* **25**, 387 (1977).

6. A CRITICAL TEST OF VIBRATIONAL DEPHASING THEORIES IN LIQUIDS USING SELECTIVE COHERENT PICOSECOND STOKES SCATTERING^{†‡}

C. B. Harris, H. Auweter, and S. M. George

The highly selective collinear stokes probing technique[†] has been used to detect the homogeneous contribution to inhomogeneously broadened vibrational transitions in liquids. Our investigations have been focused on the dephasing of the symmetric CH_3 -stretching mode of a series of simple organic solvents. The isotope effect on the vibrational dephasing time in methanol and acetone has been studied extensively. Figure 1 shows typical time-resolved dephasing curves on a picosecond time scale for acetone and deuterated acetone. The ratio of the measured dephasing times, T_2^d/T_2^h , is given by approximately 1, which implies that there is no change in the vibrational dephasing time upon isotopic substitution.

Numerous theoretical models on the problem of pure vibrational dephasing in liquids and solids have recently been proposed. The major approaches,² yielding quantitative expressions for the vibrational dephasing time, are based on energy exchange mechanisms,³ hydrodynamic theories,⁴ binary collision theories,⁵ and molecular dynamics simulations.⁶ The study of the isotope effect on the vibrational dephasing time presents a critical test on the frequency and effective mass dependence of theoretically

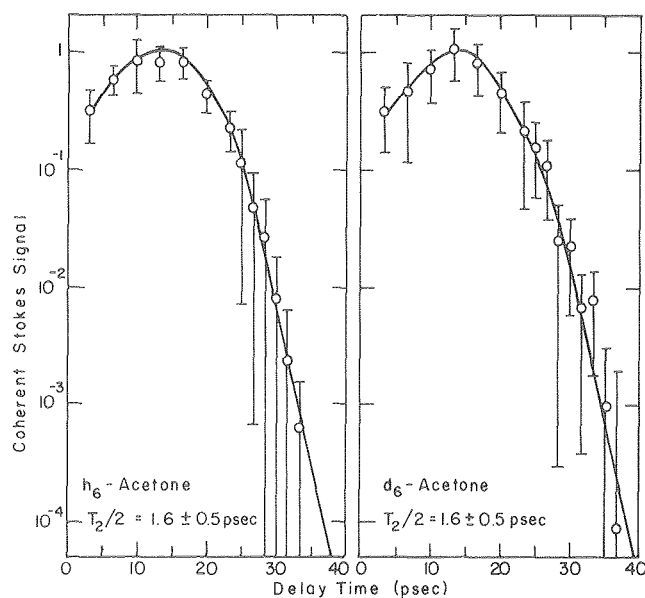


Fig. 1. Coherent Stokes signal as a function of delay time t_D for protonated acetone (h_6 -acetone) and deuterated acetone (d_6 -acetone). (XBL 7911-14546)

predicted dephasing times. Table 1 gives the experimental results together with the results from the binary collision theory. We come to the conclusion that neither the binary collision model nor the hydrodynamic theory correctly account for the isotope effect on the vibrational dephasing of the CH-stretch in methanol and acetone.

We note that, in general, vibrational transitions in liquids are inhomogeneously broadened, therefore, highly selective time-resolved probing experiments on either isotopically substituted molecules or experiments as a function of hydrodynamic parameters provide the only means to elucidate the origin of vibrational dephasing in liquids and the relation to molecular structure and dynamics.

[†]Brief version of LBL-10142; submitted to Phys. Rev. Lett.

[‡]Partially supported by National Science Foundation.

1. A. Laubereau and W. Kaiser, Rev. Mod. Phys. 50, 607 (1978).

2. D. W. Oxtoby, to be published.

3. C. B. Harris, R. M. Shelby, and P. A. Cornelius, Phys. Rev. Lett. 38, 1415 (1977).

4. D. W. Oxtoby, J. Chem. Phys. 70, 2605 (1979).

5. S. F. Fischer and A. Laubereau, Chem. Phys. Lett. 35, 6 (1975).

6. D. W. Oxtoby, D. Levesque, and F. F. Weis, J. Chem. Phys. 68, 5528 (1978).

7. A CRITICAL TEST OF VIBRATIONAL DEPHASING THEORIES IN SOLIDS USING SPONTANEOUS RAMAN SCATTERING IN AN ISOTOPIC MIXED CRYSTAL^{†‡}

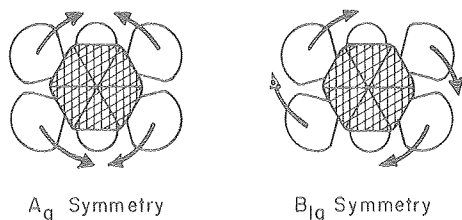
C. B. Harris, P. A. Cornelius, and S. Marks

By means of temperature dependent spontaneous Raman scattering and a theory based on intermolecular energy exchange,¹ we have analyzed the C-D stretches in d_{14} -durene in various stages of isotopic dilution. Results of an exchange analysis yield parameters such as what low frequency mode is coupled to a particular stretch, that low mode's resident lifetime, τ , and the anharmonic coupling between the low and high modes. In addition, the Fourier transform infrared spectroscopy has confirmed the presence of combination bands in accordance with the prediction of exchange theory.

The effect of energy exchange on the Raman spectrum in pure systems is shown in Fig. 1. In both isotopes of durene, various stretches are coupled to the methyl rocking modes--a motion which is expected to be anharmonically coupled to stretches by steric considerations. The fact that there appears to be two different methyl motions for a given molecule is borne out by the low-temperature ($\sim 12K$)

Table 1. Experimental and theoretical results of the isotope effect on the vibrational dephasing of the symmetric CH_3 -stretching mode in methanol and acetone: vibrational frequency $\tilde{\nu}$, experimental dephasing time T_2 , inhomogeneous linewidth $\Delta\tilde{\nu}_{inhom}$, homogeneous linewidth $\Delta\tilde{\nu}_{hom}$ [$\Delta\tilde{\nu}_{hom} = (\pi CT_2)^{-1}$], hydrodynamic collision time τ_c , and theoretical dephasing time, $iBC-T_2$, as predicted by the isolated binary collision theory.

| | $\tilde{\nu} [cm^{-1}]$ | Exptl. T_2 [ps] | $\Delta\tilde{\nu}_{inhom} [cm^{-1}]$ | $\Delta\tilde{\nu}_{hom} [cm^{-1}]$ | $\tau_c [10^{-13}s]$ | $iBC-T_2$ [ps] |
|-----------------|-------------------------|-------------------|---------------------------------------|-------------------------------------|----------------------|----------------|
| Methanol | 2836 | 3.2 | 18.8 | 3.3 | 0.37 | 0.55 |
| d_4 -Methanol | 2074 | 3.0 | | 3.5 | 0.41 | 1.39 |
| Acetone | 2925 | 3.0 | 16.5 | 3.5 | 0.99 | 2.31 |
| d_6 -Acetone | 2108 | 3.3 | | 3.2 | 1.09 | 5.62 |

RAMAN ACTIVE IN-PLANE METHYL ROCKING MODES
IN DURENE

Methyl Rock as Observed Dephasing Channel

| | PEAK (cm^{-1}) | E_i (cm^{-1}) | τ (psec) | Symmetry of Methyl Rock |
|-----------------------|------------------------------|-------------------------------|------------------|----------------------------|
| Pure h_{14} -durene | 2970.3 | 265 ± 6 | 0.19 | A_g |
| | 3027.5 | 263 ± 19 | 0.36 | B_{1g} |
| Pure d_{14} -durene | 2035.4 | 252 ± 10 | 0.66 | B_{1g} |
| | 2191.1 | 240 ± 20 | 0.30 | A_g |
| | 2225.9 | 240 ± 15 | 0.36 | A_g |

Fig. 1. The methyl rocking motion in both forms of durene is the most common mode observed coupling to a C-H or C-D stretch. Note that there appear to be two different modes with two different lifetimes—a result substantiated by the low frequency spectrum. (XBL 794-6105)

Raman spectrum in which a second peak (B_{1g} mode) is seen. The behavior of the linewidths and position for these low frequency modes as a function of temperature and concentration as well as the concentration dependent resident lifetime, τ , led to the conclusion that the A_g low frequency vibrational mode has significant excitonic properties while B_{1g} is localized.

Figure 2 illustrates the effect of isotopic dilution on the energy relaxation time, τ , for the low frequency mode (B_{1g} methyl rock) coupled to the 2035 cm^{-1} stretch. Based on the finite slope and the intercept we conclude that the mode degrades into the lattice in 1.42 psec and the resonant energy transfer time is 1.18 psec/mole fraction. This is dynamical information about vibrational energy relaxation that is difficult to obtain by any other means.

The applicability of intermolecular energy exchange has proved very valuable as a probe of vibrations in solids. Information on properties such as coherence in certain low energy vibrations as well as resonant energy transfer times and degradation into lattice modes has been obtained. This approach can be extended to the liquid phase where the results can be used to differentiate between various theories for liquid structure.

* * *

† Brief version of LBL-10181; submitted to J. Chem. Phys.

‡ Partially supported by National Science Foundation.

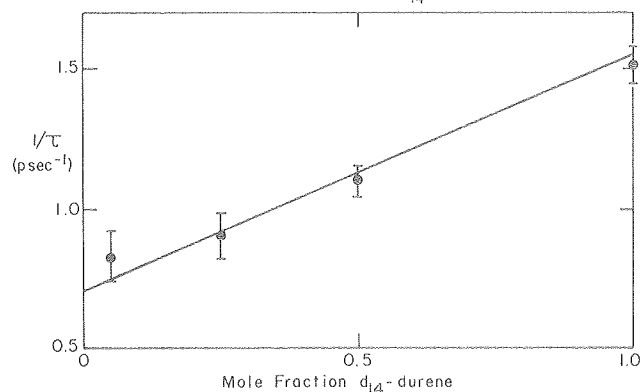
DEPENDENCE OF INVERSE EXCHANGE TIME ON CONCENTRATION
(2035 cm^{-1} C-D STRETCH d_{14} -DURENE)

Fig. 2. This shows the dependence of the resident lifetime for the 2035 cm^{-1} C-D stretch in d_{14} -durene upon dilution with h_{14} -durene. The zero concentration intercept yields the rate of transfer at that mode into the lattice (or other modes); the slope yields the resonant energy transfer rate.

(XBL 794-6106)

- C. B. Harris, R. M. Shelby, and P. A. Cornelius, Phys. Rev. Lett. **38**, 1977; C. B. Harris, R. M. Shelby and P. A. Cornelius, Chem. Phys. Lett. **57**, 8 1978.

8. FREQUENCY MIXING THROUGH SELF-PHASE MODULATION
IN PICOSECOND PULSES^{†‡}

C. B. Harris and P. A. Cornelius

The theory of self-phase modulation¹ has been used to calculate the spectrum of a pulse traversing a nonlinear medium which has gain at two or more well-separated frequencies. The theory which is based on transient stimulated Raman scattering² predicts the appearance of new components in the spectrum of the phase-modulated pulse, spaced by the frequency between a pair of components of the input pulse (see Fig. 1a). In the simplest case, in which the input pulse contains two components at ω_1 and ω_2 ($\omega_2 > \omega_1$) the output pulse contains additional frequencies at $\omega_2 + (\omega_2 - \omega_1)$, $\omega_2 + 2(\omega_2 - \omega_1)$, $\omega_1 - (\omega_2 - \omega_1)$, $\omega_1 - 2(\omega_2 - \omega_1)$, etc. The number and intensity of these satellite peaks vary with input pulse shape and intensity.

The predicted effect was subsequently observed in the transient stimulated Raman spectrum of methanol, which is known to exhibit two peaks corresponding to the symmetric and asymmetric C-H stretching modes. At low pump pulse intensity, only these two peaks were observed. By changing the pulse energy and focus, satellite peaks could be made to appear, as predicted by the theory (see Fig. 1). Some spectra were also obtained which showed the semi-periodic frequency spacing characteristic of phase modulation of the pulse envelope, which is also explained by the calculations (see Fig. 2).

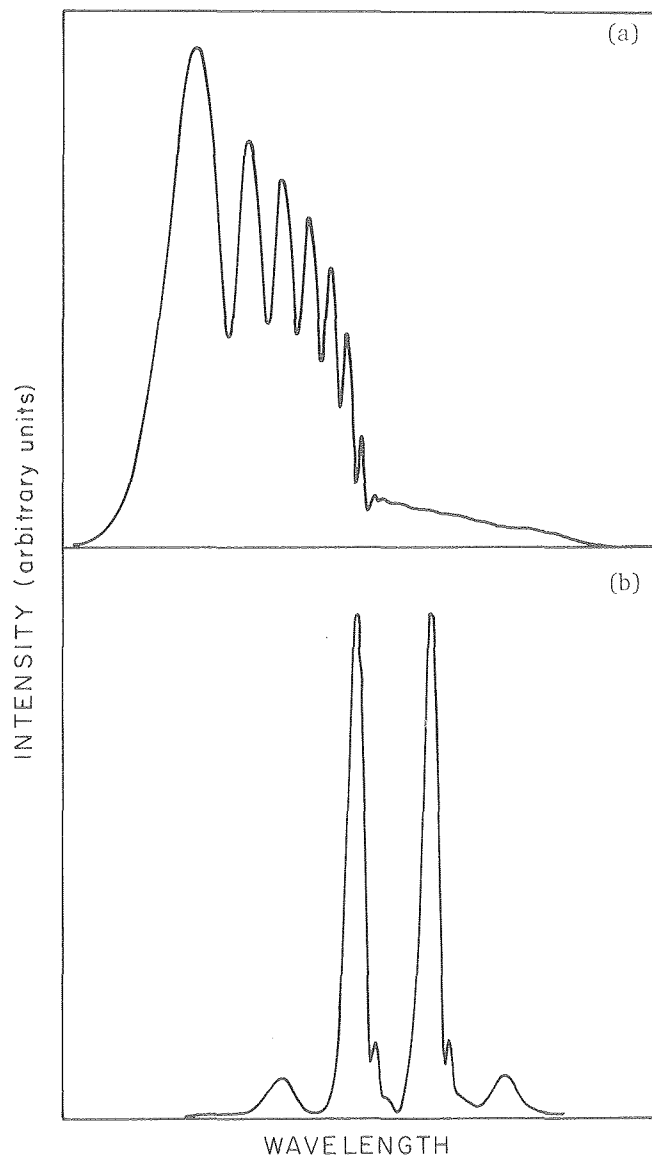


Fig. 1. Examples of calculated self-phase modulated spectra. The smaller peaks in (a) result from frequency factors appearing in the nonlinear refractive index. Spectrum (b), at higher intensity, shows the effect of envelope modulation. (XBL 7911-14548)

The calculations have shown that the production of satellite peaks as in Fig. 1 occurs at lower light intensities than the envelope modulation as in Fig. 2. For this reason, self-phase modulation becomes an important factor in understanding stimulated Raman spectra of molecules in which more than one mode has transient gain. In addition, the phase-modulated spectra in such systems may yield insight into those dynamical processes known to be related to time-dependent nonlinear optical constants.³

* * *

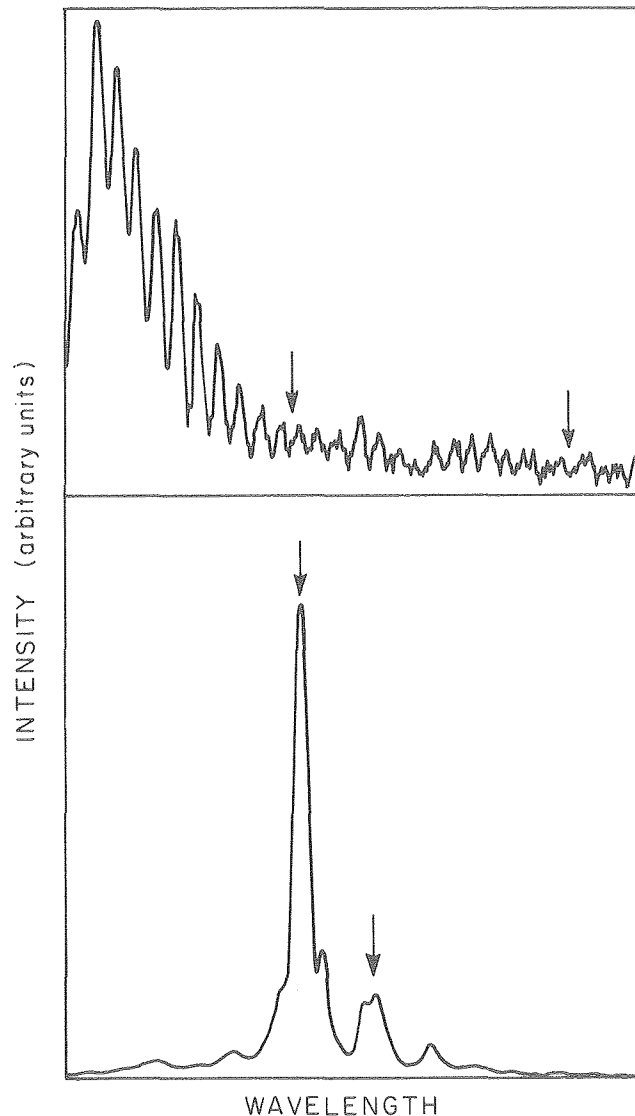


Fig. 2. Observed spectra in methanol. The arrows indicate the unmodulated peak position in each case. These can be compared to calculated spectra in Fig. 1. (XBL 7911-14547)

[†]Brief version of LBL-10143, submitted to Optics Comm.

[‡]Partially supported by National Science Foundation.

1. W. Zinth, A. Laubereau, and W. Kaiser, *Opt. Comm.* **22**, 161 (1977); R. R. Alfano, L. L. Hope and S. L. Shapiro, *Phys. Rev. A* **6**, 433 (1972); T. K. Gustafson, J. P. Taran, H. A. Haus, J. R. Lifshitz, and P. L. Kelley, *Phys. Rev.* **177**, 306 (1969).
2. R. L. Carman, M. E. Mack, F. Shimizu, and N. Bloembergen, *Phys. Rev. Lett.* **23**, 327 (1969).
3. R. Polloni, C. A. Sacchi, and O. Svelto, *Phys. Rev. Lett.* **23**, 690 (1969); V. S. Starunov, *Opt. i. Spektroskopiya* **18**, 300 (1965).

RESEARCH PLANS FOR CALENDAR YEAR 1980

Since many of the preliminary experiments designed to test the feasibility of several new spectroscopic methods for studying surfaces have been completed and have been shown to be successful, the nature of our research has changed in the past year. Given the fundamental nature of the problems, the following plans should be read with long range views in mind.

Since we have demonstrated that the spectra of both physi- and chemisorbed molecules can be obtained routinely on metal surfaces, a major effort will now be mounted to understand the nature of the chemisorbed state and its relationship to optical spectra from a fundamental point of view. The study of series of molecules on simple single crystal surfaces, step surfaces and alloy surfaces will be begun to ascertain the nature of the chemisorbed state as determined from the optical transitions, the adsorbate-adsorbate transition and/or the adsorbate-metal charge transfer spectra. In addition, given the results reported this year on laser Raman scattering, a systematic study will now be begun to investigate Raman scattering on single crystal metal surfaces. The study of the enhanced Raman scattering effect will be continued on single crystal (111) and (110) silver surfaces in order to determine the importance surface plasma states, plasma localization and surface dielectric properties have in the mechanism for enhancement. Finally, a new series of experiments will be designed to study the nature of energy transfer processes from adsorbed molecules to metal surfaces at the one monolayer level. These will be designed to ascertain whether or not photocatalysis can compete with energy relaxation processes and metal surfaces.

1979 PUBLICATIONS AND REPORTS

Refereed Journals

- *1. R. M. Shelby, C. B. Harris, and P. A. Cornelius, "The Origin of Vibrational Dephasing of Polyatomic Molecules in Condensed Phases," *J. Chem. Phys.*, 70[1], 34 (1979), LBL-7309.
2. M. E. Tarrasch and C. B. Harris, "Coherent Averaging of Electron Spins by Rotary Echoes in Excited Triplet States," *Chem. Phys.* 37[2], 293 (1979), LBL-7307.
3. C. B. Harris, D. A. Zwemer, A. R. Gallo, and H. J. Robota, "Optical Spectroscopy of Aromatic Hydrocarbons on Ni(111) Surface," *Surface Sci.* 85, 1 (1979), LBL-8546.
4. D. A. Zwemer and C. B. Harris, "Energy Transfer in One-Dimensional Substitutionally Disordered Systems. II. Experimental Results for 1,2,4,5-tetrachlorobenzene," *Chem. Phys.* 38, 139 (1979), LBL-8249.
5. J. C. Brock and C. B. Harris, "Use of an 'ordered' Electron Spin State in Molecular Spectroscopy: Theoretical and Experimental Considerations

of Spin-Ordering in Excited States," *Chem. Phys.* 43, 55 (1979).

6. C. B. Harris, "The Use of Electron Spin Coherence Techniques to Study Properties of Excited Triplet States," Abstract to the Conference on Dynamical Processes in the Excited State of Ions and Molecules in Solids, Madison, Wisconsin, June 1979.

7. A. R. Burns and C. B. Harris, "Heat Pulses in Molecular Solids: Phonon Induced Delocalization of Trapped Excited Triplet States," *Molecular Crystal and Liquid Crystal*, special issue, in press (1979), LBL-9127.

8. J. Chao and C. B. Harris "Low Level Light Signal Averaging Using an Optical Multichannel Analyzer (OMA)," submitted to *Rev. Sci. Instrum.* (1979), LBL-10135.

*9. C. B. Harris, H. Auweter, and S. M. George, "Investigations of Liquid Structure by Picosecond Laser Spectroscopy," submitted to *Phys. Rev. Lett.*, LBL-10141.

*10. C. B. Harris, H. Auweter, and S. M. George, "A Critical Test of Vibrational Dephasing Theories in Liquids Using Selective Coherent Picosecond Stokes Scattering," submitted to *Phys. Rev. Lett.*, LBL-10142.

*11. S. Marks, P. A. Cornelius, and C. B. Harris, "A Critical Test of Vibrational Dephasing Theories in Solids Using Spontaneous Raman Scattering in Isotopic Mixed Crystal," submitted to *J. of Chem. Phys.*, LBL-10181.

*12. P. A. Cornelius and C. B. Harris, "Frequency Mixing Through Self-phase Modulation in Picosecond Pulses," submitted to *Optics Comm.*, LBL-10143.

LBL Reports

1. Antonio R. Gallo (Ph.D. thesis), "Optical Spectroscopy of Molecules Adsorbed on the Nickel (111) Surface," August 1979, LBL-9278.
2. C. B. Harris and A. Champion, "Raman Spectroscopy of Molecules Adsorbed on Ni(111) and Ag(111)," LBL-10133.
3. C. B. Harris, A. Champion, and A. R. Gallo, "The Dynamics of Energy Transfer from Photoexcited Molecules to Metal Surface," LBL-10134.

Invited Talks

1. A. Champion, "Electron-Phonon Interactions in Amorphous Solids," presented at the University of Texas, Austin, Texas, February 1979.
2. A. Champion, "Electron-Phonon Interactions in Amorphous Solids," presented at the Indiana University, Bloomington, Indiana, February 1979.
3. A. Champion, "Electron-Phonon Interactions in Amorphous Solids," presented at the University of Wisconsin, Madison, Wisconsin, February 1979.

4. C. B. Harris, Introductory remarks, "Coherent Processes in Molecular Systems," American Physical Society, Chicago, March 1979.

5. A. Campion, "Electron-Phonon Interactions in Amorphous Solids," presented at the University of Illinois, Urbana, Illinois, April 1979.

6. C. B. Harris, "The Use of Electron Spin Coherence Techniques to Study Properties of Excited Triplet States," Dynamical Processes Conference, Madison, Wisconsin, June 1979.

7. C. B. Harris, "Intermolecular Energy Exchange as the Origin of Vibrational Dephasing in Liquids and Its Effects on Spontaneous and Stimulated Raman Scattering," at the Gordon Conference on Chemistry and Physics of Liquids, Plymouth, New Hampshire, August 1979.

* * *

* Partially supported by National Science Foundation.

b. Molecular Beam Spectroscopy*

John S. Winn, Investigator

1. ANALYTICAL POTENTIAL FUNCTIONS FOR WEAKLY-BOUND MOLECULES†

J. H. Goble and J. S. Winn

Our program on the inversion of spectroscopic data to accurate analytical potential functions for weakly-bound diatomic molecules¹⁻³ has progressed to the point where we can now compare classes of weakly-bound molecules and make quantitative statements about the differences in the detailed shape of the potential function and the origins of the binding forces operative in these molecules. The general potential function we employ is that suggested by Thakkar:

$$V(R) = e_0 \lambda^2 \left[1 + \sum_{n=1} e_n \lambda^n \right]$$

where $\lambda = 1 - (R_e/R)^p$. This function contains a distance parameter, R_e , an energy scaled parameter, e_0 , correction terms, e_n , and an expansion exponent, p . The parameter p may be chosen however one wishes, but the choice

$$p = \alpha_e \omega_e / 6B_e^2$$

has the effect of making $e_1=0$ and relating equilibrium spectroscopic constants to all parameters of the potential function in an unambiguous way.

We have applied this function to a number of weakly-bound diatomics in both their ground and certain excited states, and have found it capable of exceptionally good accuracy in terms of giving correctly spaced vibrational levels and accurate dissociation energies. In the case of NaAr, this inversion method was used to confirm an uncertain spectroscopic assignment. This assignment would not have been possible without the ability to predict dissociation energies accurately.

This potential function is not only capable of representing the bound states of the molecule, but also the unbound differential scattering cross-section. For Ar₂, we have found a potential function based on spectroscopic constants of the bound levels which reproduces the differential cross-section with essentially the same accuracy as the more awkward piecewise analytic functions of Lee and co-workers. The function also gives quite accurate second virial coefficients for Ar gas.

Perhaps the greatest advantage of this functional form is the opportunity it offers to correlate and compare the interatomic potentials of many weakly-bound molecules in a uniform way. Of particular interest in this regard is the observation that the

function, through the parameter p , can give a direct measure of the importance of long range (electrostatic, induction, and dispersion) forces at the equilibrium internuclear separation. Another telling measure of differences among weakly-bound molecules is the reduced force constant (the reduced curvature) of the weak bond. This quantity, denoted κ , is defined by

$$\kappa = \frac{R_e^2 V''(R_e)}{D_e}$$

and is unusually large for weakly-bound molecules. For ordinary chemically-bound diatomics, κ lies in the range 4-24, while weakly-bound molecules exhibit κ values significantly greater than 20.

Table 1 summarizes certain of these correlations. Note how weakly-bound molecules fall into periodic families, with only a few notable exceptions. The small p values for Mg₂ and Ca₂ indicate the importance of excited state mixing in otherwise weakly-bound ground states. The anomalous shape of the XeF potential well is evident from the high curvature of this potential when compared to other rare gas halides.

Table 1. Thakkar p values and reduced curvatures for several diatomics (ground states).

| | p | κ |
|-------------------|------|----------|
| Ar ₂ | 5.73 | 81 |
| Kr ₂ | -- | 82 |
| Xe ₂ | -- | 78 |
| Mg ₂ | 3.58 | 35.2 |
| Ca ₂ | 3.54 | 37 |
| ArF | -- | 37 |
| KrF | -- | 37 |
| XeF | 6.51 | 112 |
| BeAr ⁺ | 3.16 | 27.5 |
| BeKr ⁺ | -- | 29.1 |
| NaAr | 4.31 | 51.4 |

* This work was supported by the Division of Chemical Sciences, Office of Basic Energy Sciences, U. S. Department of Energy.

* * *

[†]Supported in part by NSF and NRCC.

1. J. H. Goble, D. C. Hartman, and J. S. Winn, *J. Chem. Phys.* **67**, 4206 (1977).
2. J. H. Goble and J. S. Winn, *J. Chem. Phys.* **70**, 2051 (1979).
3. J. H. Goble and J. S. Winn, *J. Chem. Phys.* **70**, 2058 (1979).

2. EMPIRICAL METHODS OF ESTIMATING DIATOMIC BINDING ENERGIES[†]

L. Brewer and J. S. Winn

The dissociation energy of a diatomic molecule is at once among the most important constants to know and among the most difficult to measure. Two approaches toward the estimation of dissociation energies have been devised which may be of value not only in providing the energies, but also in understanding the origins of the binding.

Spectroscopic data can, in principle, give an exact measure of the dissociation energy. But limited spectroscopic data (which is the usual case) cannot be treated without further assumptions about the potential energy function.^{1,2} If one assumes a Morse function, then the usual expression for the dissociation energy is in terms of the harmonic force constant and the anharmonic correction:

$$D_e = \omega_e^2 / 4\omega_e x_e. \quad (1)$$

This is not the only expression for the Morse dissociation energy which one can write. We have found a previously unknown expression which uses the vibrational-rotation constant α_e , instead of the anharmonicity constant. This new expression is

$$D_e = 9\omega_e^2 B_e^3 / (\alpha_e \omega_e + 6B_e^2)^2. \quad (2)$$

These expressions are most readily applied to strongly bound diatomics, but they are not very accurate, nor do they necessarily give the same values, as is demonstrated in Table 1.

For weakly-bound molecules, we found the expression

$$D_e = \frac{9B_e^2}{\alpha_e^2} \left(\frac{n^2}{(n+1)^2} \right)$$

where n is the integral power of R^{-1} which leads an expansion of the long-range portion of the potential. This expression is based on a simple Lennard-Jones $(2n,n)$ potential function, for which the dissociation energy is simply given by $9B_e^3/\alpha_e^2$. The factor $n^2/(n+1)^2$ is a semi-empirical correction factor.

When spectroscopic data are lacking, one can turn to empirical correlations based on the idea

Table 1. Dissociation energies predicted by Morse potential relationships and compared to experimental values. The energies are in eV units.

| Molecule | Eq. (1) | Eq. (2) | Experiment |
|------------------------------|-----------------------|-----------------------|-----------------------|
| CO | 10.982 | 10.387 | 11.226 |
| N ₂ | 12.037 | 11.793 | 9.905 |
| NO | 7.969 | 7.754 | 6.614 |
| O ₂ | 6.460 | 5.874 | 5.213 |
| HF | 5.906 | 4.988 | 6.123 |
| HCl | 5.249 | 4.681 | 4.618 |
| HBr | 4.810 | 4.324 | 3.921 |
| HI | 4.168 | 3.884 | 3.196 |
| OH | 5.101 | 4.477 | 4.621 |
| CH | 4.020 | 3.563 | 3.640 |
| F ₂ | 2.317 | 2.172 | 1.658 |
| Cl ₂ | 3.630 | 3.578 | 2.514 |
| Br ₂ | 3.044 | 3.146 | 1.991 |
| I ₂ | 2.322 | 2.518 | 1.555 |
| H ₂ | 4.948 | 3.822 | 4.747 |
| Na ₂ | 1.081 | 1.309 | 0.730 |
| He ₂ ⁺ | 2.533 | 2.517 | 2.469 |
| NaAr | 4.82x10 ⁻³ | 4.86x10 ⁻³ | 5.14x10 ⁻³ |

that binding energies are the result of offsetting electron promotion energies and valence binding from excited states. In this way, we have estimated the dissociation energies of all the homonuclear diatomics in the periodic table.³

* * *

[†]Brief version of LBL-9690.

1. J. H. Goble and J. S. Winn, *J. Chem. Phys.* **70**, 2058 (1979).
2. J. S. Winn, LBL-10171, submitted to *J. Chem. Ed.*
3. L. Brewer and J. S. Winn, LBL-9690, accepted by *Trans. Faraday Symposia*, 1980.

3. DYNAMICS OF CHEMILUMINESCENT CHEMI-IONIZATION[†]

D. C. Hartman[†] and J. S. Winn

Chemi-ionization, whereby two neutral species react to produce either an ion pair or a positive ion-electron pair, is a well known process in discharge and combustion phenomena. The dynamics of elementary Penning and associative ionization phenomena have been studied by molecular beams methods. Both the angular distributions of ionic products and the Penning electron energy spectrum have been measured. In these experiments,^{1,2} chemiluminescence detection has been applied to the Ar* + Ca chemi-ionization reactions to study for the first time the branching of chemi-ionization processes among several states as well as the internal energy content of a nascent associative ionization product.

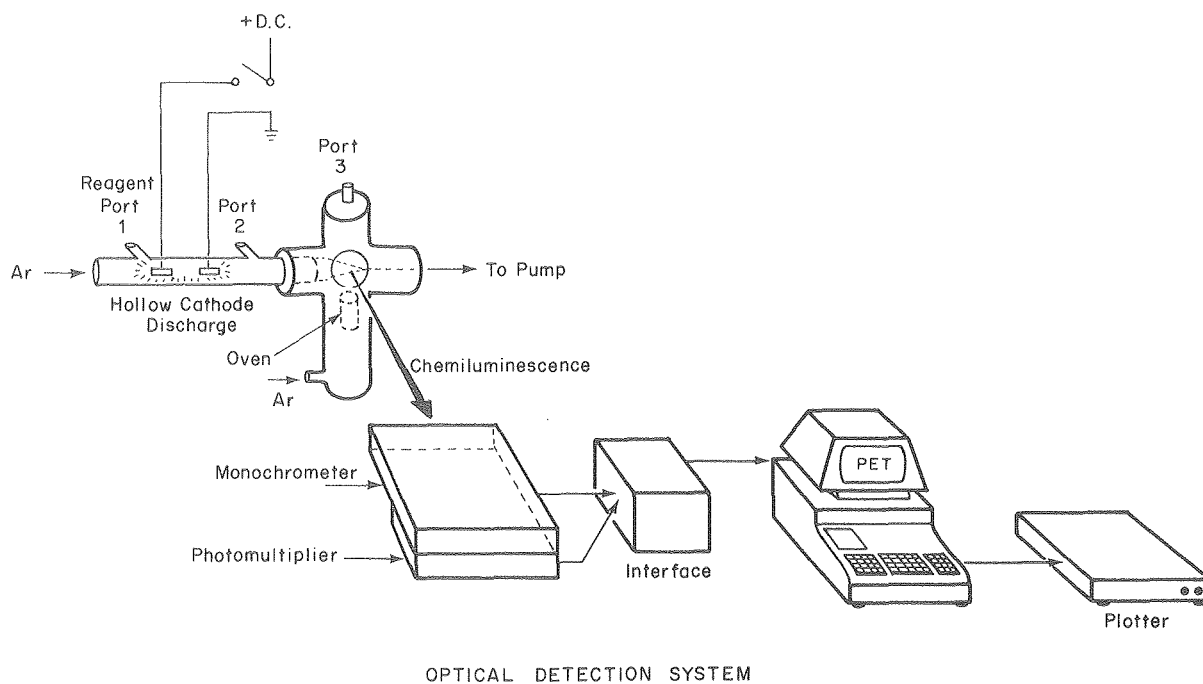


Fig. 1. Chemiluminescence flowing afterglow apparatus. (XBL 792-8369)

The flowing afterglow chemiluminescence reactor used in these experiments is shown in Fig. 1. Metastable Ar is produced by a D.C. hollow cathode discharge in a 1 Torr flow of purified Ar. Ca metal is vaporized in the oven, entrained in a second Ar flow, and reacted with Ar*. The resultant flame is analyzed by a high resolution 1.5 m monochromator equipped with a photomultiplier detector. Photon signals are counted and averaged by a micro-computer interface, which also controls the monochromator scan.

Metastable Ar* ($^3P_{0,2}$) has sufficient energy to ionize Ca to the ion states 2S , $^2D_{3/2}$, $^2D_{5/2}$, $^2P_{1/2}$, and $^2P_{3/2}$. In addition to atomic Penning ionization to these excited states, one may also observe associative ionization, forming CaAr* in a variety of excited states. In the spectral region to the red of the 2P - 2S resonance doublets, we observed the band system shown in Fig. 2. This band system extends to the red beyond the region shown in Fig. 2, but only as an unstructured, oscillatory continuum. We attribute this spectrum to the CaAr* $A^2\Pi \rightarrow X^2\Sigma^+$ molecular transition.

Our kinetic analysis of the atomic Penning ionization rate constants for production of the $^2P_{1/2,3/2}$ fine structure states showed that production of the 3/2 component was favored by a factor of five. This is in excess of the statistical amount, and our analysis of the spectrum in Fig. 2 was based on an assumption that only the $A^2\Pi_{3/2}$ state contributed significantly to the molecular emission.

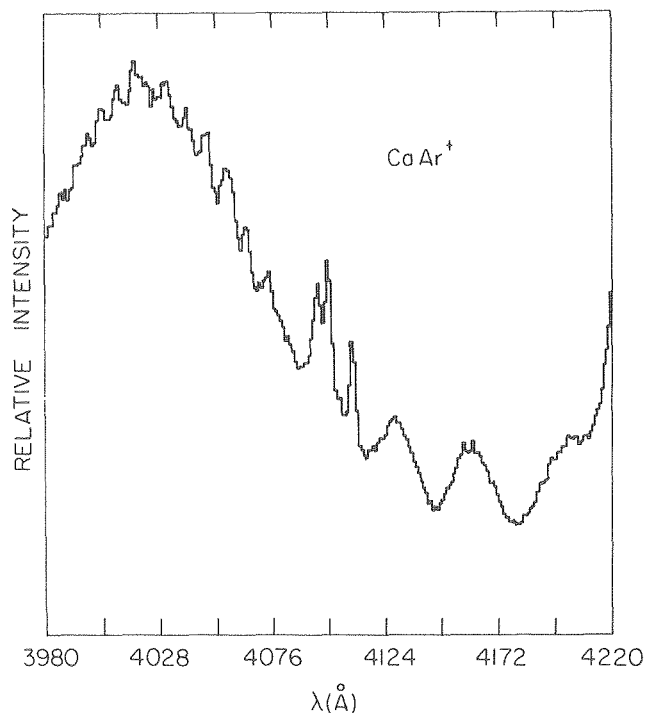


Fig. 2. CaAr⁺ emission spectrum produced by excitive associative ionization. (XBL 7910-12400)

These spectra were inverted using the (Exp-Z4) model potential

$$V(R) = A \exp(-BR) - Z^2 e^2 \alpha / 2R^4$$

which we had found³ to give an excellent representation of the analogous molecular states of BeAr⁺. The inversion method used potentials of this form for both the A and X states, setting Z = 1 in the X state and Z = 2 in the A state, and varying the remaining parameters until a synthetic spectrum could be generated which gave good agreement with the observed spectrum. It was also necessary, of course, to assume the initial vibrational level distribution in the A²Π state and to vary this distribution to achieve agreement.

Table 1. Spectroscopic constants for CaAr⁺.

| | Z | R _{oe} (Å) | ω _e (cm ⁻¹) | D _e (cm ⁻¹) |
|-------------------------------|---|------------------------|---------------------------------------|---------------------------------------|
| X ² Σ ⁺ | 1 | 2.8 | 87 | 970 |
| A ² Π | 2 | 2.6 | 200 | 4940 |

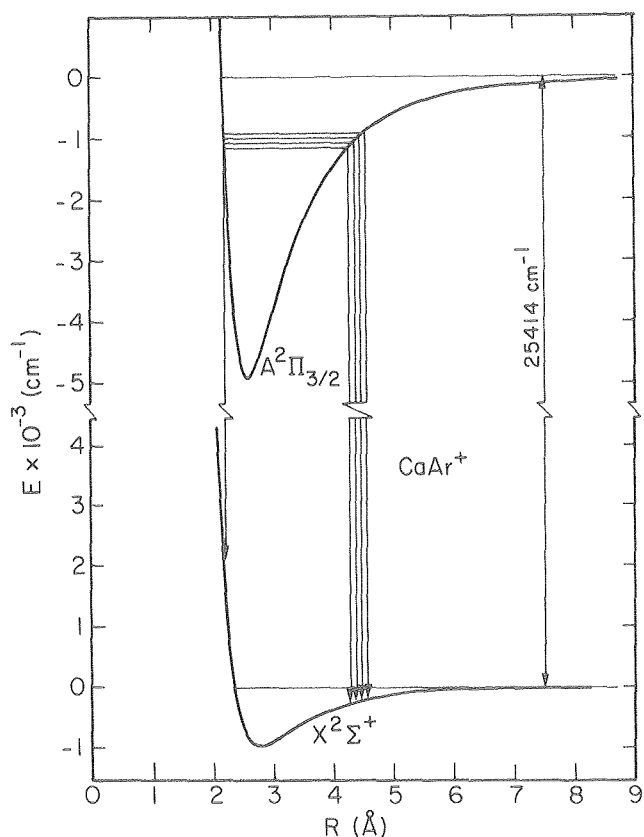


Fig. 3. Potential energy curves for CaAr⁺. The arrows indicate the origins of the bound-bound and bound-free emissions. (XBL 7910-12397)

The results of this inversion are given as spectral constants for the A and X potentials in Table 1 and as a diagrammatic graph of the potentials in Fig. 3. Note in Fig. 3 that the A state is produced with considerable vibrational excitation localized around only a few (three or so) vibrational levels. In many respects, the dynamical processes leading to these molecular excitations are very similar to those in excimer systems such as the rare gas-halide lasers.

* * *

† Brief version of LBL-9819 and LBL-10168.

‡ Current address: Central Research Laboratories, Texas Instruments, Inc., Dallas, TX 75265

1. D. C. Hartman (Ph.D. thesis) LBL-9819.
2. D. C. Hartman and J. S. Winn, LBL-10168 (submitted to J. Chem. Phys.).
3. J. H. Goble, D. C. Hartman, and J. S. Winn, J. Chem. Phys. 67, 4206 (1977).

4. MECHANISM OF METAL CARBONYL DISSOCIATION BY METASTABLE RARE GASES[†]

D. C. Hartman,[‡] W. E. Hollingsworth, and J. S. Winn

The bimolecular electronic energy transfer reaction between a rare gas metastable and a monometal carbonyl leads to complete metal-ligand dissociation and electronic excitation of the metal atom. The discovery¹⁻⁵ of this unusual mode of a metastable atom quenching pathway has been investigated in detail, and the several unique features it involves have been explained by a restricted statistical model, to be described below.

Chemiluminescence spectra of flowing afterglow flames of He*, Ne* and Ar* with Fe(CO)₅ and Ni(CO)₅ were recorded with our flowing afterglow optical spectrometer. Over the 2000-4000 Å region, only Fe or Ni atomic emission was observed in each case. The observed emission rates were converted to rates of formation of each excited state using the relationships

Rate of formation

$$= \text{rate of depletion} \propto I(\sum_j A_{uj} / A_{ul})$$

where I is the observed intensity (counts per second) and A is the Einstein coefficient for spontaneous emission. The effects of collisional relaxation were assumed to be negligible in comparison to radiative relaxation. Subsequent analysis showed collisional intramultiplet relaxation in the long-lived Fe and Ni states of highest spin to be observable at the ca. 1 Torr pressure of these experiments.

A statistical model was used to predict these relative rates of formation. The model has the following conceptual steps:

- (1) a certain (known) amount of energy is used to break all metal-ligand bonds,

- (2) a second amount of energy is used to provide electronic excitation of the metal atom, and
- (3) the remainder of the energy is statistically partitioned among selected degrees of freedom of the exciting ligands.

The rate of formation of each excited metal state is then taken to be proportional to the density of states of products computed from semiclassical partition functions according to the assumptions in step (3) above.

In Fig. 1, the data and the theoretical results for two different assumptions in step (3) are shown. These data are for the $\text{Ar}^* + \text{Ni}(\text{CO})_4$ reaction. The solid circles are the long-lived quintet states, identified by the J quantum number of the term symbol for each state. The effect of intramultiplet collisional relaxation is evident in several of these states. The dashed line is the prediction of a full statistical model in which the CO products are allowed to vibrate and to rotate and translate

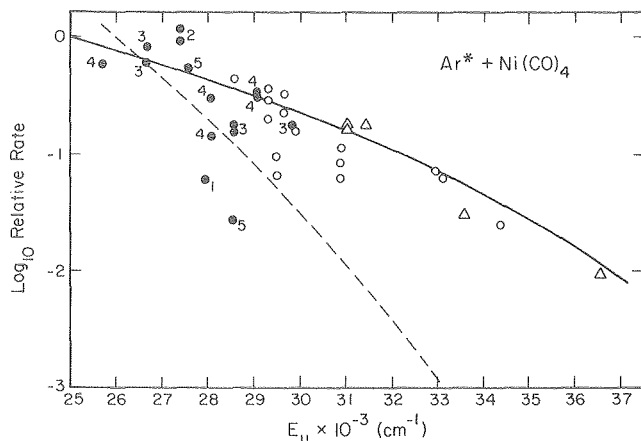


Fig. 1. Relative rates of production of various states of Ni in the $\text{Ar}^* + \text{Ni}(\text{CO})_4$ flame. The solid and dashed lines are theoretical predictions described in the text. (XBL 7910-12394)

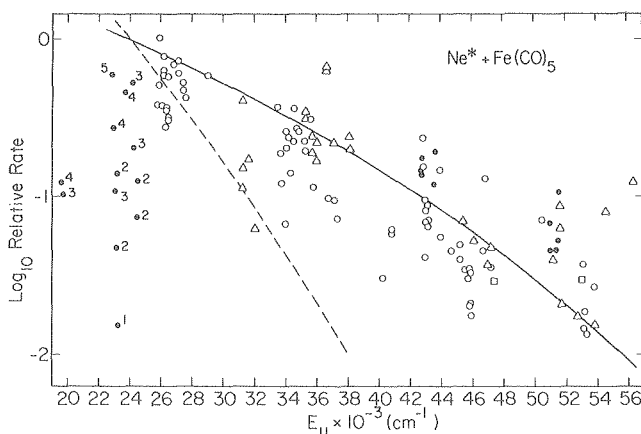
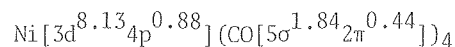


Fig. 2. As Fig. 1, but for the $\text{Ne}^* + \text{Fe}(\text{CO})_5$ flame. (XBL 7910-12385)

in three dimensions. The solid line is the prediction of a restricted model in which the CO products are allowed to vibrate, but to translate in only one dimension (the radial reaction coordinate) and not to rotate. Clearly, the restricted picture is more realistic. Figure 2 shows the same analysis of the $\text{Ne}^* + \text{Fe}(\text{CO})_5$ reaction, with the same conclusion.

In terms of electronic excitations, it is clear that the metal is undergoing an excitation to a state which is highly metal-ligand repulsive. Starting from the carbonyl ground electronic configuration, which population analysis has shown to be (for the case of $\text{Ni}(\text{CO})_4$)



electron exchange with the metastable will remove a bonding $9t_2$ electron (of 3d or 2π parentage) and produce an electron (from the metastable) in the 4s or 3d metal vacancies. The resultant Ni^* will be in states derived from $3d^94p$ or $3d^84s4p$ configurations, as we observed in the flame spectra. Similar arguments explain the $\text{Fe}(\text{CO})_5$ spectra.

* * *

† Brief version of LBL-10169.

‡ Present address: Central Research Laboratories, Texas Instruments, Inc., Dallas, TX 75265.

1. D. C. Hartman, (Ph.D. thesis), LBL-9819.
2. D. C. Hartman and J. S. Winn, *J. Chem. Phys.* **68**, 2990 (1978).
3. D. C. Hartman, W. E. Hollingsworth, and J. S. Winn, *J. Chem. Phys.* **72**, 0000 (1980), LBL-10169.

5. PRODUCTION AND CHEMISTRY OF METAL ATOMS AND METAL CLUSTERS BY MOLECULAR BEAMS METHODS†

B. C. Hale, H. S. Luftman, and J. S. Winn

The chemistry of transition metal atoms and atomic clusters is traditionally in the domain of high temperature chemists. To study this chemistry under less severe conditions yet still in the gas phase has long been a challenge.¹ We have approached this problem by exploiting the volatility of metal carbonyls and their thermal dissociation at moderate temperatures. In this way, we can use molecular beam techniques to monitor the dissociation process itself, subsequent recombination events during a supersonic beam expansion, and reaction or rearrangement chemistry of the complex when co-expanded with various other gases. The conditions (temperature, pressure, and composition) under which we perform these experiments allow us to simulate many of the conditions of real thermally initiated processes catalyzed by metal centers.

The supersonic molecular beam expansion is a well-known method for the production of molecular and atomic clusters.² We have used such an expansion to explore cluster formation with $\text{Fe}(\text{CO})_5$ as the metal carrier. The technique involves monitoring the beam composition with a mass spectro-

meter universal beam detector as a function of the expansion gas composition and source temperature. With neat $\text{Fe}(\text{CO})_5$ vapor, thermal degradation starts at ca. 80°C , and a beam of atomic Fe can be easily produced. Co-expansion with Ar at a pressure of 1 atm or higher produces a variety of clusters containing one or more Fe atoms and varying amounts of ligands, depending on the expansion temperature.

When $\text{Fe}(\text{CO})_5$ is expanded with H_2 gas (at a total pressure again near 1 atm and with a $\text{Fe}(\text{CO})_5$ mole fraction of about 5%), the mass spectrum shows new features appearing as the temperature is raised through the thermal dissociation region of $\text{Fe}(\text{CO})_5$. Experiments with both H_2 and D_2 indicate the production of CO_2 and ketene, CH_2CO . The reaction of H_2 with CO to yield CO_2 and CH_2CO is exothermic by 30 kcal/mol, and apparently a hydride intermediate is formed between H_2 and some $\text{Fe}(\text{CO})_5$ fragment which rearranges to the observed products. The role of Fe in facilitating the H_2 bond rupture has been inferred from many surface and solution studies, and we expect to be able to monitor this effect as a function of mean Fe cluster size in future experiments.

* * *

[†]Brief version of LBL-10170.

1. J. S. Winn, LBL-10170 (accepted by Trans. Faraday Symposia).
2. B. L. Blaney and G. E. Ewing, *Ann. Rev. Chem.* **27**, 553 (1976).

6. MOLECULAR BEAM ELECTRIC RESONANCE SPECTROSCOPY[†]

H. S. Luftman, S. A. Sherrow, and J. S. Winn

Our research on weakly-bound molecular structures using molecular beam electric resonance spectroscopy has centered around rare gas-hydrogen halide dimers,¹ rare gas-halogen dimers, and halogen-halogen dimers.² These species form a class of weakly-bound donor-acceptor complexes for which a large body of structural data has been measured, especially in regards to rare gas-hydrogen halide dimers.

The structure of XeHCl was completed in collaboration with the Harvard MBER group, and data are now available on HCl complexes with all rare gases

except He, which is assumed to behave like Ne. The NeHCl molecule does not exhibit a permanent dipole moment, indicating essentially free rotation of the HCl molecule in the field of the Ne atom. In other words, the anisotropy of the potential is very weak. Table 1 summarizes the structural data on the rare gas-HCl complexes. Particularly striking is the similarity of these data for the heavier rare gases. The bond angles are zero-point average deviations from a collinear equilibrium geometry, while R is the rare gas-Cl distance. The general trend in these data are consistent with the increase in polarizabilities of the rare gases, but the data cannot be explained by simple induction forces alone.

We have also begun work on the HeClF molecule. This species is the most probable He-containing complex to be amenable to study by MBER methods. ClF is a strong Lewis acid, and the structure of this molecule will determine the importance of p versus s electron donation in the anisotropy of the intermolecular potential between an atom and a Lewis acid diatomic. The high source pressures available in our MBER spectrometer beam source make this experiment uniquely suited to our apparatus. The only other He complex for which structural data are available is the He I_2 molecule, which appears from optical spectra to be T-shaped, rather than linear as is the case for ArClF and KrClF .

* * *

[†]Supported in part by NSF.

1. K. V. Chance, K. H. Bowen, J. S. Winn, and W. Klemperer, *J. Chem. Phys.* **70**, 5157 (1979).
2. K. V. Chance, K. H. Bowen, J. S. Winn, and W. Klemperer, *J. Chem. Phys.* **71**, 0000 (1979).

RESEARCH PLANS FOR CALENDAR YEAR 1980

The role of coordinately unsaturated metal carbonyls in various chemical processes will continue to be explored using both afterglow-discharge methods and molecular beam methods. We will use electric and magnetic deflection to analyze product distributions. The electric deflection analysis of, for instance, *cis* to *trans* 2-butane isomerization by Fe or Ni is among the type of experiments we will undertake.

Table 1. Structural data on rare gas-HCl dimers.

| | R ○ (Å) | θ (deg) | B (MHz) | μ_a (D) |
|-------|---------------|-----------------------------|------------|----------------|
| NeHCl | -- | $80^\circ\text{--}90^\circ$ | --- | --- |
| ArHCl | 4.006 | 41.5° | 1678.511 | 0.81144 |
| KrHCl | 4.078 | 39.8° | 1205 | --- |
| XeHCl | 4.258 | 34.77° | 989.262 | 1.0901 |

We also plan to analyze the magnetic properties of Fe and Ni clusters via magnetic deflection. There is evidence from matrix isolation spectra that as few as five Fe atoms form an ordered magnetic system. We hope to probe this phenomenon as a function of cluster size.

The electric resonance spectra of selected rare gas-halogen complexes will be sought. Particular emphasis will be given to HeClF and XeF radical. Our MBER apparatus will be used in these experiments, and a high temperature F atom source will be developed for the XeF experiments.

The program on analytic potential functions for weakly-bound molecules will be continued, with particular emphasis being placed on differential scattering inversions in the rare gas-halide systems and on the spectroscopic inversion of alkaline earth diatomics.

1979 PUBLICATIONS AND REPORTS

Refereed Journals

- ^{††}1. J. H. Goble and J. S. Winn, "Analytic Potential Functions for Weakly Bound Molecules: The X and A States of NaAr and the A State of NaNe," *J. Chem. Phys.* 70, 2051 (1979).
- ^{††}2. J. H. Goble and J. S. Winn, "Estimation of the Dissociation Energy of Weakly Bound Molecules from Spectroscopic Data," *J. Chem. Phys.* 70, 2058 (1979).
- [†]3. K. V. Chance, K. H. Bowen, J. S. Winn, and W. Klemperer, "Microwave and Radio Frequency Spectrum of XeHCl," *J. Chem. Phys.* 70, 5157 (1979).
- [†]4. K. V. Chance, K. H. Bowen, J. S. Winn, and W. Klemperer, "Electric Deflection Studies of Halogen and Interhalogen Polymers," *J. Chem. Phys.* 71, 0000 (1979).
5. D. C. Hartman, W. E. Hollingsworth, and J. S. Winn, "Dissociation of Metal Carbonyls by Metastable Rare Gases: Fe and Ni Emission Analysis," *J. Chem. Phys.* 72, 0000 (1979); LBL-10169.

LBL Reports

1. D. C. Hartman, "Quenching of Metastable Rare Gases by Calcium Atoms and Metal Carbonyls," (Ph.D. thesis), LBL-9819.
2. L. Brewer and J. S. Winn, "Models for Calculation of Dissociation Energies of Homonuclear Di-

atomic Molecules," LBL-9690 (to appear in Faraday Symposium Proceedings, 1980).

3. J. S. Winn, "Gas Phase Production and Chemistry of Transition Metal Atoms and Clusters from Polynuclear Metal Carbonyls," LBL-10170 (to appear in Faraday Symposium Proceedings, 1980).

4. D. C. Hartman and J. S. Winn, "Chemiluminescent Chemi-ionization: Ar* + Ca and the CaAr⁺ Emission Spectrum," LBL-10168 (submitted to *J. Chem. Phys.*).

^{††}5. J. S. Winn, "Analytical Potential Functions for Diatomic Molecules: Some Limitations," LBL-10171 (submitted to *J. Chem. Ed.*).

Invited Talks

1. J. S. Winn, "Weakly bound diatomic molecules--How are they different?," Chemistry Colloquium, U.C. Irvine, Feb. 15, 1979.
2. J. S. Winn, "Weakly bound diatomic molecules--How are they different?," Physical Chemistry Seminar, Cal Tech, Feb. 16, 1979.
3. J. S. Winn, "Production and chemistry of long-lived excited states of Fe and Ni," ACS National Meeting, Honolulu, Hawaii, April 4, 1979.
4. J. S. Winn, "Weakly bound ions: BeAr⁺ and CaAr⁺," Symposium on van der Waals Molecules, Quebec, Canada, Aug. 2, 1979.
5. J. S. Winn, "Weakly bound diatomic molecules--How are they different?," Physical Chemistry Seminar, Harvard University, Nov. 16, 1979.
6. J. S. Winn, "Gas phase transition metal chemistry--the metal carbonyl way," Physical Chemistry Seminar, MIT, Nov. 20, 1979.
7. J. S. Winn, "Novel chemiluminescent reactions of metastable rare gases," Physical Chemistry Seminar, Rutgers University, Dec. 10, 1979.
8. J. S. Winn, "Novel chemiluminescent reactions of metastable rare gases," Research Seminar, Exxon Corporate Research Laboratories, Dec. 11, 1979.
9. J. S. Winn, "Qualitative differences among weak bonds," Chemistry Seminar, IBM T. J. Watson Laboratory, Dec. 14, 1979.

* * *

[†]Supported in part by NSF.
^{††}Supported in part by NRCC.

c. Selective Photochemistry*

C. Bradley Moore, Investigator

Introduction. Emphasis of this program has been on the study of high vibrational overtone excitations to understand coupling among vibrational modes at high internal energies and to explore the possibility of photochemistry following excitation. The techniques of optoacoustic spectroscopy and intra-cavity dye laser spectroscopy are used for these studies. Results are described in the following sections. Dye laser absorption spectroscopy is also being developed for studying the dynamics and chemistry of HCO. HCO reaction rate measurements will commence shortly. Other work in progress includes vibrational relaxation and chemistry in matrix isolated systems, spectroscopy in the condensed phase and photopredissociation of formaldehyde.

1. PRESSURE BROADENING OF SINGLE VIBRATIONAL-ROTATIONAL TRANSITIONS OF ACETYLENE AT $\nu = 5^+$

James S. Wong

Properties of high vibrational overtones of polyatomic molecules are a subject of intense study following the suggestion of possible mode-selective chemistry after single photon excitation of these overtones.¹⁻³ Due to the extremely weak absorption strength of the high overtones, the technique of optoacoustic spectroscopy is the most suitable detection scheme. The high overtone spectra of molecules provide valuable pieces of information. For small molecules, linewidth measurements of discrete single vibration-rotation transitions may reveal the onset of intramolecular energy transfer. Pressure broadening measurements allow one to study collisions between the excited molecules and the vibrationless ground state molecules. For large molecules the large ($>100 \text{ cm}^{-1}$) but Lorentzian lineshapes allow one to extract intramolecular energy transfer and dephasing rates which are essential for the understanding of mode-coupling at high vibrational levels.

For a first study, we have obtained the spectra of acetylene excited with five vibrational quanta in the C-H stretching motions. The apparatus is shown in Fig. 1. A single frequency mode tunable dye laser, continuously scannable over 10 GHz with 30 MHz resolution, is used to excite 20 to 200 Torr of acetylene. The laser beam is chopped at 40 Hz to allow for the generation of an optoacoustic signal following absorption by acetylene. The 5" long gas cell is equipped with a Knowles BT 1759 miniature electret microphone. This microphone detects the optoacoustic signal which is directly proportional to the absorption cross section. Phase-sensitive detection is used to improve the sensitivity.

A low resolution (1 cm^{-1}) spectrum is shown in Fig. 2. Acetylene at $\nu = 5$ exhibits a well-defined rotational structure with distinct P and R branches.

*This work was supported by the Division of Chemical Sciences, Office of Basic Energy Sciences, Sciences, U. S. Department of Energy.

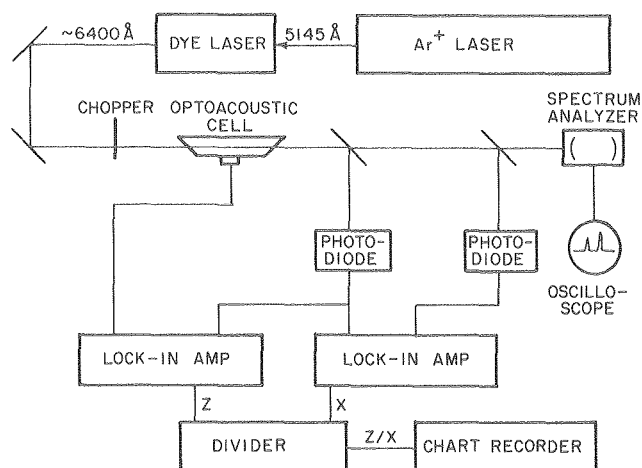


Fig. 1. Schematic diagram of the experimental apparatus. (XBL 802-8027)

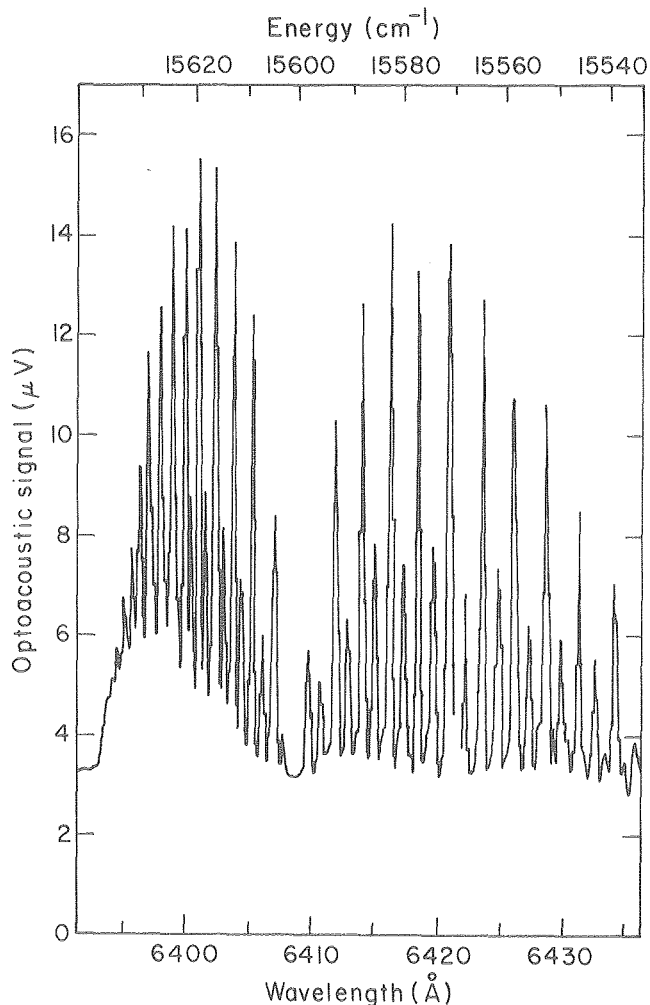


Fig. 2. Spectrum of acetylene at 6400 Å at 1 cm^{-1} resolution. (XBL 791-174)

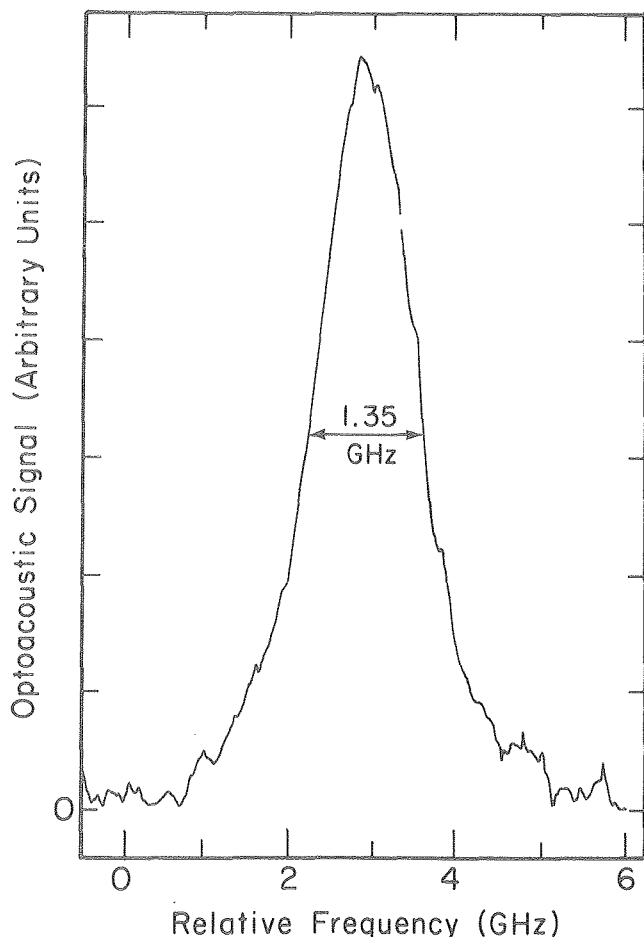


Fig. 3. High resolution spectrum of the R(9) rotational line of 49 Torr of acetylene. (XBL 802-8026)

The alternating intensity with odd and even rotational quantum number is characteristic of the C_2H_2 molecule. The discrete structure even at $16,000\text{ cm}^{-1}$ of internal energy is a result of the low density of states.

High resolution spectra were taken as a function of acetylene pressure from 20 to 200 Torr for the R(3), R(9), and R(15) lines at $v=5$. A typical spectrum of the R(9) line at 49 Torr is shown in Fig. 3. The room-temperature, self-broadened full-widths at half-maximum of the absorption profile are shown in Fig. 4 as a function of pressure for the R(3) and R(9) lines. The slope of the points gives the self-broadening coefficients of each individual line. The measured self-broadening coefficients for the R(3), R(9), and R(15) lines are $8.59 \pm 0.25\text{ MHz/Torr}$, $7.29 \pm 0.32\text{ MHz/Torr}$, and $6.10 \pm 0.23\text{ MHz/Torr}$, respectively. The decrease in pressure broadening as the rotational quantum number increases is consistent with previous measurements of the $\nu_1 + \nu_3$ band at about 6500 cm^{-1} (Ref. 4) and is believed to be due to the larger amount of energy that must be exchanged in rotationally inelastic collisions. The observed

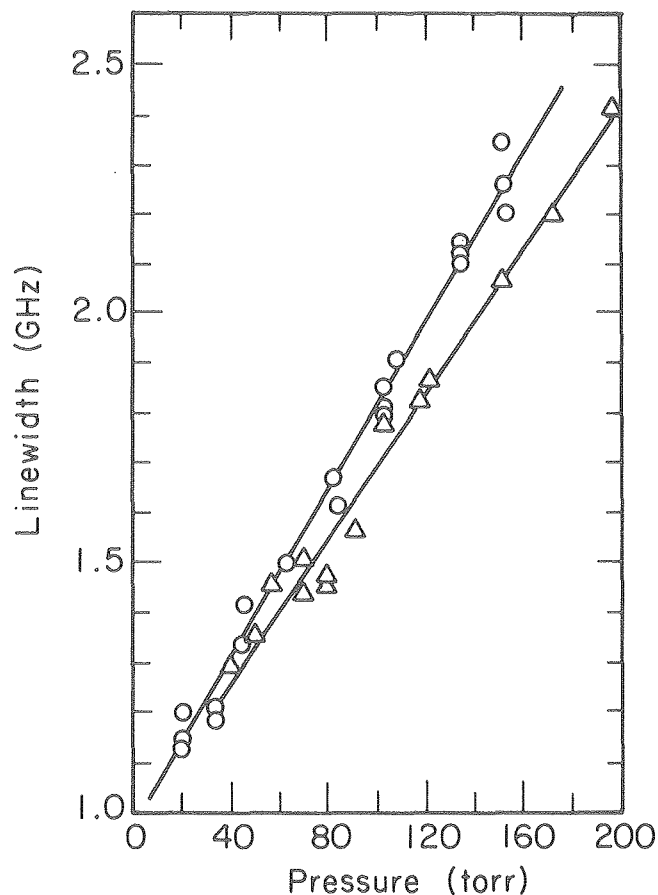


Fig. 4. A plot of the full width at half maximum height vs. pressure for the R(3) (o) and R(9) (Δ) rotational lines for the $\Delta v = 5$ transition. The solid lines represent least squares fits to the data. (XBL 802-8025)

pressure broadening coefficients for the R(9) and R(15) levels were 10.2 MHz/Torr and 9.8 MHz/Torr , respectively, at 295 K. There has been little theoretical treatment of the change in pressure broadening as a function of vibrational excitation and work in the literature is limited to diatomic molecules.⁵ It is hoped this work will generate new interest in extending the theoretical understanding to polyatomic molecules.

* * *

[†]Brief version of LBL-10251.

1. K. V. Reddy and M. J. Berry, *Chem. Phys. Lett.* 52, 111 (1977).
2. M. J. Berry, *Bull. Am. Phys. Soc.* 23, 78 (1978).
3. C. B. Moore and Ian W. M. Smith, "Vibrational-Rotational Excitation--Chemical Reactions of Vibrationally Excited Molecules," Proceedings of the Faraday Discussion No. 67, Birmingham, England, April 9-11, 1979.
4. P. Varanasi and B. R. P. Bangaru, *J. Quant. Spectrosc. Radiat. Transfer* 15, 267 (1975).
5. M. Giraud, D. Robert and L. Galatry, *J. Chem. Phys.* 59, 2204 (1973).

2. ANALYSIS OF THE FIFTH OVERTONE SPECTRUM OF PROPANE

James S. Wong

The high overtone one photon spectra of organic molecules with visible light are dominated by "local mode" transitions in which only one C-H oscillator is excited.¹ Since this optically prepared local mode state is not a true eigenstate of the system, collisionless intramolecular energy transfer and dephasing will occur spreading the vibrational energy throughout the molecule.² From the linewidths of the observed spectra, one can obtain the energy transfer rate of the lifetime broadened state.

Since the absorption oscillator strength is derived from a single C-H oscillator, one might expect to resolve splittings in the spectra due to inequivalent C-H stretches. Other workers^{3,4} have resolved two peaks in the liquid phase spectra of alkanes: one from the methylene (CH₂) groups and one from the methyl (CH₃) groups at higher energy. Unfortunately, the intermolecular interactions in the liquid phase obscure the free molecule homogeneous linewidth and no intramolecular lifetime information could be extracted. From the gas phase spectrum taken in this work, one can obtain information on the intramolecular energy transfer rate under essentially collisionless (on the picosecond timescale) conditions.

Optoacoustic spectra were obtained with the apparatus shown schematically in Fig. 1 of the preceding article. The optoacoustic cell is now placed within the cavity of the cw dye laser to take advantage of the higher intracavity circulating power. Wavelength scanning is performed at 1 cm⁻¹ resolution by the birefringent filter and the optoacoustic signal is normalized to the intracavity power by monitoring the small amount of light scattered off the Brewster angle window of the OA cell.

The spectrum of propane at $\Delta v = 6$ is shown in Fig. 1. The raw spectrum from the strip chart recorder was digitized and resolved into a sum of three Lorentzians by the program, GAMET, which was originally written for resolving photoelectron

spectra. The results of the deconvolution with the full width at half maximum height (FWHM) for the two higher energy peaks constrained to be equal are given in Table 1. The methylene peak again lies at lower energy at 15559 cm⁻¹ but the methyl group is split into two peaks. Since the methyl groups can undergo a hindered internal rotation with a barrier height of approximately 3.3 kcal/mole,⁵ the symmetry point group of propane is C_{2v} with one of the hydrogens on each methyl group lying in the plane of the molecule and the other two lying out of the molecular plane. The difference in the steric environment shifts the in-plane C-H stretch to higher energy at 15846 cm⁻¹. The observed relative areas of 1:1.5:1 qualitatively support the assignment, but the cross sections for each local mode C-H transition are expected to depend on many factors, such as anharmonicity, which vary from oscillator to oscillator. Experiments in progress indicate that a splitting of the methyl C-H stretches of alkanes may be a general phenomenon. A point of interest is that the

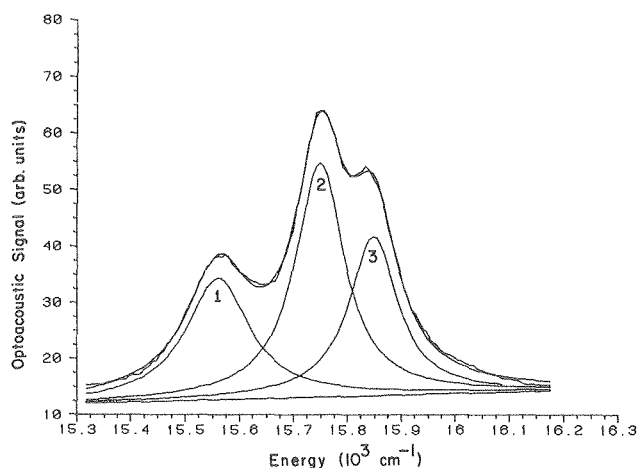


Fig. 1. Experimental and deconvoluted spectrum of propane at $\Delta v = 6$. The three Lorentzians from the computer calculation are labeled 1, 2 and 3. Peak #1 corresponds to the C-H's of the methylene (CH₂) group and peaks 2 and 3 correspond to the two inequivalent C-H's of the methyl groups.

(XBL 802-8024)

Table 1. Results of computer deconvolution.

| Peak | Location (cm ⁻¹) | FWHM (cm ⁻¹) | Relative area |
|------|------------------------------|--------------------------|---------------|
| 1 | 15559 ± 3 | 141 ± 13 | 1.0 ± .1 |
| 2 | 15747 ± 1 | 109 ± 4 | 1.49 ± .06 |
| 3 | 15846 ± 2 | 109 ^a | 1.01 ± .04 |

^aConstrained to be equal to the FWHM of peak 2.

methylene peak is considerably broader than the methyl peaks (141 vs. 109 cm^{-1}), indicating that the dephasing and energy transfer rates are faster for the methylene C-H modes. Studies under way on the local mode spectra of cycloalkanes and cycloalkenes show even larger differences in linewidths and a more general treatment of theory of intramolecular energy transfer is being developed. Since splittings in the local mode spectra of chemically equivalent C-H bonds are observable, the chances of achieving mode-selective vibrational photochemistry following one photon excitation of a single C-H local mode appear excellent. The reaction system currently under investigation is HCl elimination from 1,2-dichloropropane which has four different photolysis products and at least three different groups of C-H bonds.

* * *

1. See, for example, B. R. Henry, *Acc. Chem. Res.* **10**, 207 (1977).
2. D. F. Heller and S. Mukamel, *J. Chem. Phys.* **70**, 463 (1979).
3. W. R. A. Greenlay and B. R. Henry, *J. Chem. Phys.* **69**, 82 (1979).
4. M. S. Burberry, J. A. Morrell, A. C. Albrecht and R. L. Swofford, *J. Chem. Phys.* **70**, 5522 (1979).
5. S. Weiss and G. E. Leroi, *Spectrochim. Acta.* **A25**, 1759 (1969).

3. VIBRATION-VIBRATION ENERGY TRANSFER IN METHANE[†]

P. Hess[‡] and A. H. Kung

Methane is a relatively simple polyatomic molecule whose structure and spectroscopy are well studied.¹ The presence of four fundamental vibrations makes the energy level diagram, Fig. 1, sufficiently complex that methane should be a useful prototype for understanding energy transfer processes in larger molecules. In many molecules CH stretching vibrations are clustered near 3000 cm^{-1} and bending vibrations in the 1200 - 1500 cm^{-1} range.² The proximity of bending overtones and stretches provides a relaxation path which is

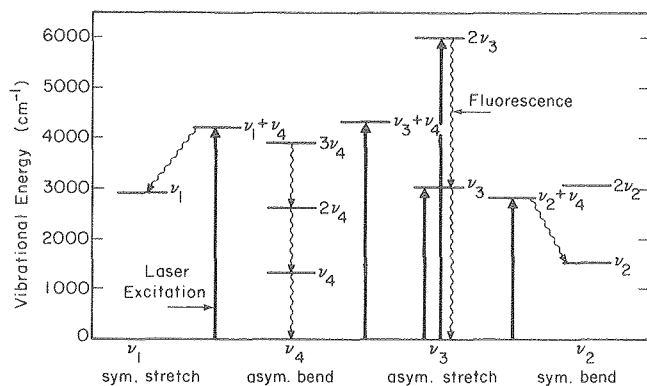


Fig. 1. Energy levels of CH_4 with laser excitation (—→) and some fluorescence (~~~~→) transitions indicated. (XBL 787-9565)

undoubtedly important in most hydrocarbons. Laser excited vibrational fluorescence experiments have given rates for V-V transfer between stretching and bending vibrations in methane.²⁻⁴ V → T,R relaxation rates have also been measured by many methods. The results have helped to establish a good quantitative understanding of the role of rotation in vibrational relaxation.

In this article a powerful new tunable ir laser source is used to excite a variety of combination and overtone levels as well as the ν_3 mode in the 2800 - 6000 cm^{-1} range. There are too many levels even in methane for a complete determination of rate constants coupling each possible initial and final vibrational level. However, rates are determined for the various types of V-V transfer processes and overall relaxation pathways are mapped in a general way. The method of laser-induced fluorescence is used. Emission is monitored from both infrared active modes. A summary of the measurements was presented in a previous report.⁵ The result of the analysis is described here.

Table 1 gives approximate rates for the various types of V → V energy transfer processes which occur in pure CH_4 . All of the rates fall in the range of roughly 0.1 to 1 $\mu\text{sec}^{-1} \text{Torr}^{-1}$, or $(0.3 \text{ to } 3) \times 10^{-11} \text{cm}^3 \text{molecule}^{-1} \text{sec}^{-1}$, corresponding to probabilities per gas kinetic collision between 10^{-2} and 10^{-1} . The scaling factor appropriate for first order perturbations of harmonic oscillators is listed for each measured rate or type of rate. If these V → V transfer rates scale in this way, then the rates for the process involving transitions between levels $v=0$ and $v=1$ may be found by dividing the reported rate by the factor n . The fastest rate is for transfer of energy within a single molecule between the symmetric and asymmetric stretching modes. The analogous process for bending vibrations, intramolecular conversion between ν_2 and ν_4 excitation, is also fast. The stretch-to-bend transfers are dominated by intramolecular conversion of ν_3 primarily to $2\nu_4$ and $\nu_2 + \nu_4$. In any case $\nu_2 + \nu_4$ and $2\nu_4$ are rapidly equilibrated. Presumably $2\nu_2$ also equilibrates rapidly with these levels by this rapid intramolecular interconversion of ν_2 and ν_4 quanta. For the stretch-to-bend relaxation of ν_3 it has been observed previously⁴ that rare gases are comparably effective to methane itself as energy transfer collision partners. This should be true for all of the intramolecular transfer processes. The intermolecular V → V transfers are slower than the intramolecular ones even though they involve smaller changes in total vibrational energy. The rates for transfer of a bending or a stretching quantum from one molecule to another are listed at the bottom of Table 1.

In conclusion, approximate values are found for the different types of V → V energy transfer processes which relax the higher vibrational levels of methane. In systems which are only partially relaxed the relative speed of intramolecular processes vs. intermolecular ones will tend to keep the excitation energy concentrated in the molecule that is excited. Thus in experiments on gas-surface interactions the populations of $\text{CH}_4(2\nu_4)$ will be more important than the production of $2\text{CH}_4(\nu_4)$ following ν_3 excitation. To the extent

Table 1. Rates of collisional V → V energy transfer in CH₄ at 294 K.

| | n ^a | (pτ) ⁻¹ (μsec ⁻¹ Torr ⁻¹) | k x 10 ¹¹ (cm ³ molec ⁻¹ sec ⁻¹) | p ^b |
|--|----------------|--|---|----------------|
| <u>Processes predominantly intramolecular</u> | | | | |
| v ₃ ↔ v ₁ | 1 | k ₁ = 1.2 ± 0.3 | 3.6 | 0.09 |
| v ₂ + v ₄ ↔ 2v ₄ | 2 | k ₁₇ = 1 ± 0.5 | 3 | 0.08 |
| v ₃ → 2v _b | 1 | k ₉ ' = 0.28 ± 0.06 | 0.8 | 0.022 |
| 2v ₃ → v ₃ + 2v _b | 2 | k ₁₂ ' + k ₁₃ ' = 0.6 ± 0.2 | 1.8 | 0.05 |
| v ₃ + v ₄ → 3v _b | 1-2 | k ₈ ' = 0.7 ± 0.2 | 2.1 | 0.05 |
| <u>Intermolecular single quantum transfer</u> | | | | |
| v ₄ | 2 | k ₂₀ = 0.6 ± 0.2 | 1.8 | 0.05 |
| stretch | 2 | k ₁₁ ' + 2k ₁₄ ' = 0.25 ± 0.15 | 0.8 | 0.02 |
| bend and stretch | 1 | k ₂ ' = 0.2 ± 0.1 | 0.6 | 0.02 |

a. Normalization factor for first order perturbation of harmonic oscillators

b. Probability per gas kinetic collision, (pτZ)⁻¹.

that intramolecular transfers are faster than intermolecular ones, laser-induced chemical reactions of small molecules may be favored by keeping the total energy of a molecule above threshold while energy is transferred to the most effective modes for reactions.

* * *

† Brief version of LBL-10060.

‡ Permanent address: Physikalisches-Chemisches Institut der Universität Heidelberg, Neuenheimer Feld 1, 69 Heidelberg, West Germany.

1. K. Fox, "Analysis of Vibration-Rotation Spectra of Methane," U. S. National Technical Information Service, AD Rep. 1974, No. 776061/4GA.

2. G. Herzberg, "Molecular Spectra and Molecular Structure. II. Infrared and Raman Spectra of Polyatomic Molecules," (Van Nostrand, Princeton, 1945).

3. J. T. Yardley and C. B. Moore, J. Chem. Phys. 49, 1111 (1968).

4. P. Hess and C. B. Moore, J. Chem. Phys. 65, 2339 (1976).

5. P. Hess and A. H. Kung, MMRD Annual Report for 1978, p.270.

RESEARCH PLANS FOR CALENDAR YEAR 1980

The primary emphasis of research plans for 1980 is to understand the possibilities for and limitations on selective photochemical processes. Part of the efforts are devoted to the study of relaxation of selectively excited states to thermally heated states, part to chemical dynamics of the unrelaxed states and part to the chemistry of the comparable thermal systems.

Research will include:

Spectroscopy and Kinetics of High Vibrational States. High overtone spectra of the C-H stretching motions of methane, acetylene and halogenated acetylenes in the visible region will continue to be studied. These spectra reveal the nature of coupling among vibrational modes and of collisionless intramolecular energy transfer for high vibrational states. The chemistry of these highly excited molecules will be observed. Bond selective vibrational photochemistry will be attempted following single photon absorption into specific quantum states of these and more complex molecules such as 1,2-dichloropropane.

Energy Transfer of Molecules on Surfaces.

Studies of vibrational energy transfer in condensed phase at low temperature are beginning to yield interesting results. Diatomic molecules isolated in inert gas matrices show that the rate of vibrational relaxation is slow. We propose to extend this study to investigate the vibrational relaxation of molecules adsorbed on a surface. Knowledge of relaxation rates is an important first step to understanding the kinetics of surface chemistry and to successful selective photochemistry involving surface molecules. Carbon monoxide adsorbed on amorphous silica is a convenient system to begin this study. The technique of laser-induced, time-resolved infrared fluorescence will be used. Energy relaxation will be monitored by time-resolved emission from the adsorbed CO. Energy transfer rates will be measured as a function of temperature, surface coverage and surface preparation.

Photochemistry of Matrix-Isolated Metal Carbonyls. Mode-selective vibrational photochemistry can best be demonstrated in an isolated molecule since collisions are known to disrupt selective excitation. The system of cobalt carbonyls in inert gas matrices at 10 K is most suitable for this purpose. The interconversion of bridging and terminal carbonyls has a low activation energy and the isomerization can easily be observed by monitoring the position of ^{13}CO in partially labeled $\text{Co}_4(\text{CO})_{12}$ using infrared absorption spectroscopy. The dynamics of CO ligand exchanges are important for understanding the catalytic behavior of this type of molecule.

Radical-radical Reactions and Combustion Chemistry. Accurate values of the rate constants for radical-radical reactions are essential for the modeling of combustion processes. The use of laser flash kinetic spectroscopy for quantitative measurements of these reaction rates has recently been demonstrated in this laboratory. Accurate absolute radical concentration measurements are made simply

by measurement of the laser power absorbed when radicals are produced by laser photodissociation. Approximate rate constants for $\text{H} + \text{HCO}$ and $\text{HCO} + \text{HCO}$ have been determined by monitoring HCO absorption following formaldehyde photolysis. The measured rates are one order of magnitude larger than those previously predicted and used for combustion modeling. It is proposed to refine the experimental system to produce rate constants as a function of temperature with better than 20% accuracy. The potential surface for the $\text{H} + \text{HCO}$ reaction is being investigated by H. F. Schaefer's group. The combined results should produce an excellent model for this unusually fast reaction and the ability to estimate accurate rate constants for experimentally inaccessible conditions.

Many radicals may be produced in high concentration by photolysis with uv excimer laser lines. It is also possible to study reactions between two molecular excited species. New types of reactions may be expected in just the way that correlation arguments show that photochemically accessed reaction paths lead to different products than do thermal reaction paths.

1979 PUBLICATIONS AND REPORTS

Refereed Journals

- [†]1. J. M. Wiesenfeld and C. B. Moore, "Vibrational relaxation of Matrix-Isolated HCl and DCl," *J. Chem. Phys.* 70, 930 (1979), LBL-8052.
- [‡]2. F. E. Hovis and C. B. Moore, "Temperature Dependence of Vibrational Energy Transfer in NH_3 and H_2^{18}O ," *J. Chem. Phys.* (in press).

LBL Reports

1. D. M. Goodall, M. Whittle, and C. B. Moore, "Single Photon Vibrational Photochemistry of Protic Liquids," Proceedings of the Chemical Society Conference on Mechanisms of Reactions in Solution, Canterbury, England, July 1979, LBL-9780.
- [§]2. C. B. Moore and Ian W. M. Smith, "Vibrational-Rotational Excitation--Chemical Reactions of Vibrationally Excited Molecules," Proceedings of the Faraday Discussion No. 67, Birmingham, England, April 9-11, 1979, LBL-9781.
- ^{||}3. P. Hess, A. H. Kung and C. B. Moore, "Vibration \rightarrow Vibration Energy Transfer in Methane," submitted to *J. Chem. Phys.*, LBL-10060.
- ^{||}4. Floyd E. Hovis, Jr., "Vibrational Energy Transfer in Gas Phase Water and Ammonia," LBL-9955.

Invited Lectures

1. C. Bradley Moore, "Laser-Induced Chemistry," General Motors Research Laboratory, Warren, MI.
2. C. Bradley Moore, Series of 8 lectures and 3 discussions on laser spectroscopy, energy transfer, and photochemistry at the Fudan University, Dept. of Physics II, Shanghai, China.
3. C. Bradley Moore, "Laser-Induced Chemistry," She Bay University, Sian, China.
4. C. Bradley Moore, "Selective Photochemistry with Lasers," Institute of Chemistry, Academia Sinica, Peking, China.

5. C. Bradley Moore, "Laser-Induced Chemistry," Tsing-hua University, Peking, China.
6. C. Bradley Moore, "Laser Photochemistry Research at Berkeley" and "Laser-Induced Chemical Reactions," Institute for Molecular Science, Okazaki, Japan.
7. C. Bradley Moore, "Laser-Induced Chemistry," Chemical Society of Japan, Tokyo, Japan.
8. C. Bradley Moore, "Laser Photochemistry and Energy Transfer Research at Berkeley," University of Tokyo, Komaba Campus, Komaba, Japan.
9. C. Bradley Moore, "Vibrational Photochemistry," University of Tokyo, Hongo Campus, Tokyo, Japan.
10. C. Bradley Moore, "Laser-Induced Chemistry," Nagoya University, Nagoya, Japan.
11. C. Bradley Moore, "Laser-Induced Chemistry," Chemical Society of Japan, Osaka Branch, Osaka, Japan.
12. C. Bradley Moore, "Vibrational Photochemistry," Kyoto University, Kyoto, Japan.
13. C. Bradley Moore, "Laser-Induced Chemistry," Kyushu University, Fukuoka, Japan.
14. C. Bradley Moore, "Vibrational Photochemistry," Göttingen University, Göttingen, West Germany.
15. C. Bradley Moore, "Vibrational Photochemistry," Université de Paris-Sud, Orsay, France.
16. C. Bradley Moore (with I. W. M. Smith), "Vibrational Photochemistry," Faraday Discussions of the Chemical Society.

* * *

[†]Partially sponsored by the U. S. Army Research Office, Triangle Park, NC, and the National Science Foundation.

[‡]Partially sponsored by the U. S. Air Force Office of Scientific Research and the U. S. Army Research Office, Triangle Park, NC.

[§]Partially sponsored by the National Science Foundation.

^{||}Partially sponsored by the U. S. Air Force Office of Scientific Research.

d. Physical Chemistry with Emphasis on Thermodynamic Properties*

Kenneth S. Pitzer, Investigator

1. IMPROVED AB INITIO EFFECTIVE CORE POTENTIALS FOR MOLECULAR CALCULATIONS†

Phillip A. Christiansen, Yoon S. Lee and Kenneth S. Pitzer

During the last ten years, effective potentials (EP) based directly or indirectly on the pseudo-potential theory of Phillips and Kleinman¹ (PK) have become popular for the study of molecular systems containing atoms with large numbers of electrons. However, because of the approximations involved and because of the erratic results sometimes obtained, electronic structure theorists have remained skeptical of the usefulness of these procedures for obtaining quantitative chemical information. Some of the more widely employed EPs yield disastrously poor results for molecular dissociation curves. This was particularly well documented in the F₂ and Cl₂ studies of Hay, Wadt and Kahn.² Using the PK type EPs generated by Kahn et al,³ they observed unreasonable shortening of bond lengths, increases in dissociation energies, and lowering of inner repulsive walls of the dissociation curves relative to all-electron calculations or experimental results. Although they were able to reduce greatly the errors by ad hoc modifications of the Kahn EPs, substantial errors in bond lengths and inner repulsive walls still remained. Furthermore some of their modifications lead to inconsistencies in the EP formalism.

We have recently investigated this problem in terms of the EP formalism and have concluded that these problems are not the result of the frozen core and local potential approximation as is often suggested, but rather they are due, at least in large measure, to incorrect partitioning of core and valence electron space as implied by the Phillips-Kleinman pseudoorbital. The PK pseudo-orbital has the general form

$$\chi_V^{PK} = C_V \phi_V + \sum_C C_C \phi_C,$$

where the ϕ_V and ϕ_C are the valence and core atomic Hartree-Fock orbitals. Since χ_V^{PK} and all ϕ 's are normalized, C_V is always less than unity and electron density is transferred from the valence region into the core. As a result in molecular calculations the χ_V^{PK} cannot accurately describe either the electronic structure in the bonding region or the valence-core potential terms.

To correct for this defect we have abandoned the PK definition for χ_V and replace it with

$$\chi_V = \phi_V + f_V$$

where the function f_V is zero outside the core region and is otherwise chosen to cancel the oscillations of ϕ_V within the core region so that χ_V will be smooth and have no radial nodes. In practice, χ_V is defined in two regions. For values of r greater than some r_{match} we set χ_V equal to ϕ_V . In the region between $r = 0$ and $r = r_{\text{match}}$, χ_V is defined as a five term polynomial in r with the coefficients chosen so as to match the amplitude and first three derivatives of ϕ_V at r_{match} and to ensure normalization of χ_V . The value of r_{match} is chosen to be the innermost point for which χ_V is smooth in the core region with at most two inflexions in its entire range. Plots of χ_V and χ_V^{PK} (from Ref. 3) can be seen in Fig. 1.

From the above definition of χ_V we have generated pseudoorbitals and EPs for chlorine and fluorine. We have used these potentials, expanded in terms of Gaussian functions, to compute dissociation curves for the ground states of F₂ and Cl₂. For these calculations we used two-configuration MC-SCF wavefunctions, identical in form, to those used in the studies by Kahn et al and by Hay et al. In Table 1 we list the resulting equilibrium bond lengths and dissociation energies. For comparison we have included the all-electron results from Hay et al., as well as their results generated from the PK type EPs of Kahn et al. and from their modification of the Kahn EP.

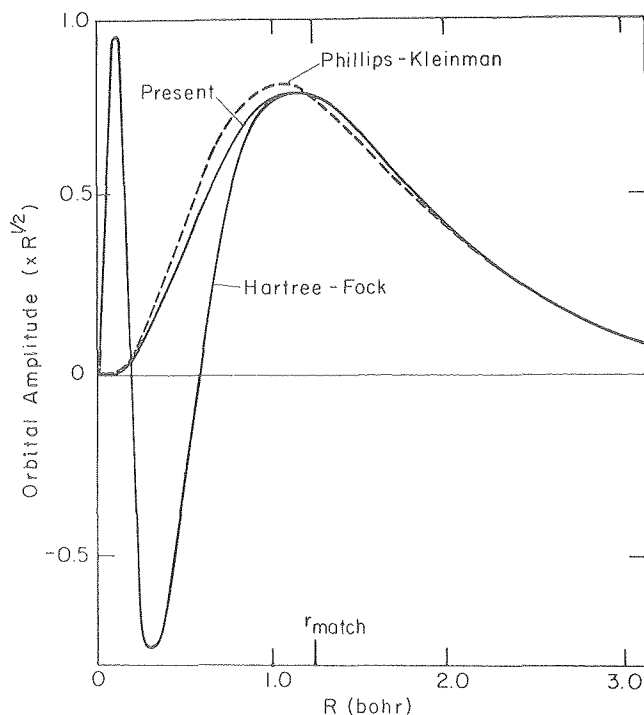


Fig. 1. A comparison of our chlorine 3s pseudo-orbital with the Phillips-Kleinman type pseudo-orbital of Refs. 2 and 3, and the HF orbital.

(XBL 802-8356)

* This work was supported by the Division of Chemical Sciences, Office of Basic Energy Sciences, U.S. Department of Energy.

Table 1. Bond length (Bohr) and dissociation energies (kcal/mole) for the ground states of F_2 and Cl_2 from 2-configuration MCSCF wavefunctions.

| Potential | F_2 | | Cl_2 | |
|---------------------------|-------|-------|--------|-------|
| | R_e | D_e | R_e | D_e |
| All Electron ² | 2.84 | 14.8 | 4.04 | 27.0 |
| Hay EP ² | 2.82 | 16.1 | 3.94 | 24.6 |
| Kahn EP ^a | 2.70 | 21.2 | 3.76 | 45.7 |
| Present | 2.86 | 14.6 | 4.04 | 25.7 |

^aValues were computed by Hay et al.,² using potentials from Kahn et al.⁵

For both F_2 and Cl_2 the agreement between our EP results and the all-electron results is excellent. Our results are even better than those which Hay et al. obtained with their modified PK type EP (for Cl_2 the difference is substantial). These improvements are apparent in Figs. 2 and 3 where we have plotted the corresponding potential curves for F_2 and Cl_2 for the regions near the equilibrium geometries.

The differences between the present and previous EP calculations become very apparent at short internuclear separations. For the shortest bond distances studied; 2.2 Bohr for F_2 and 3.0 Bohr for Cl_2 , the curves generated from the PK type EPs of Kahn et al. were far too low (insufficiently repulsive). Even the modified EPs of Hay et al. yielded potential curves which were too low by about 0.007 and 0.03 a.u., respectively. This is contrary to what one would expect from the frozen core approximation since core polarization, if treated rigorously, will undoubtedly lower the molecular energy. In contrast, using the present procedure the potential curves for both molecules were too repulsive by about 0.002 a.u. for the same geometries. This is a relatively small error and in the proper direction.

In summary we have shown that effective potential calculations of molecular properties can reliably yield results in close agreement with all-electron calculations if the atomic pseudoorbitals retain the correct radial distribution of charge in the valence region as given by all-electron atomic calculations. The problems with previous EP calculations stem from the improper partitioning of core and valence electron space in the Phillips-Kleinman formalism.

* * *

[†]Brief version of LBL-9351; J. Chem. Phys. 71, 4445 (1979).

1. J. C. Phillips and L. Kleinman, Phys. Rev. 116, 287 (1959).
2. P. J. Hay, W. R. Wadt, and L. R. Kahn, J. Chem. Phys. 68, 3059 (1978).
3. L. R. Kahn, P. Baybutt and D. G. Truhlar, J. Chem. Phys. 65, 3826 (1976).

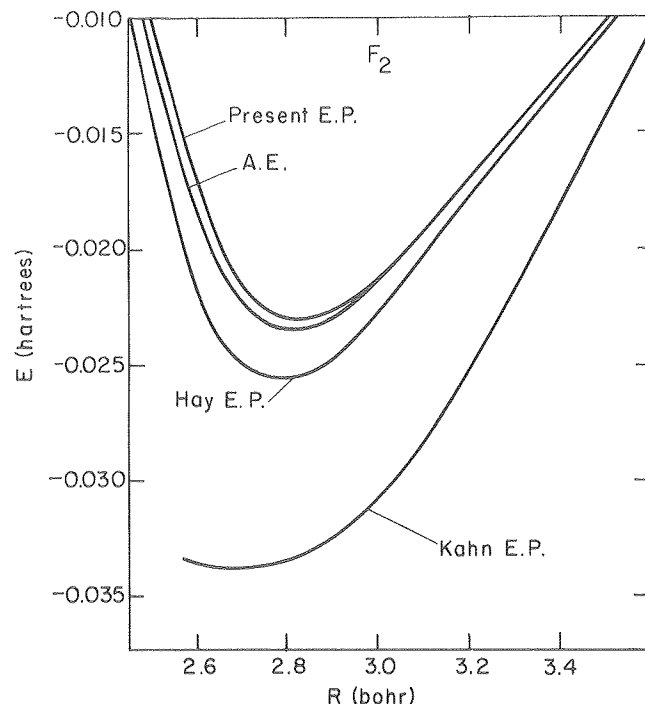


Fig. 2. Potential energy curves for the ground state of F_2 from all-electron (AE) and effective potential (EP) calculations using 2-configuration MCSCF wavefunctions. (XBL 794-6126)

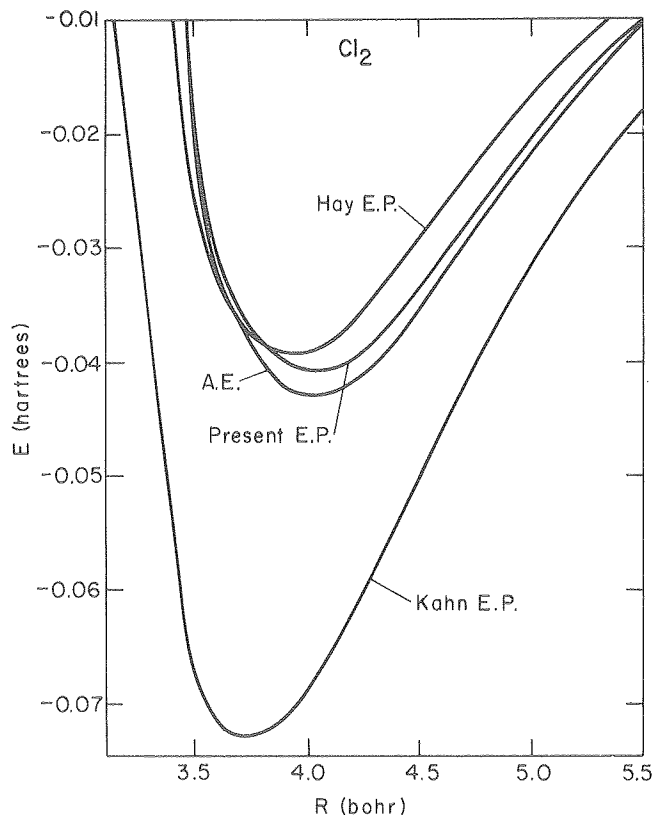


Fig. 3. Potential energy curves for the ground state of Cl_2 from all-electron (AE) and effective potential (EP) calculations using 2-configuration MCSCF wavefunctions. (XBL 794-6127)

2. RELATIVISTIC EFFECTS ON MOLECULAR PROPERTIES:
Au₂, TlH, PbS, and PbSe.[†]

Yoon S. Lee, Walter C. Ermler, and Kenneth S. Pitzer

Previously we have developed and reported a method of generating relativistic effective core potentials (REP)¹ from atomic Dirac-Hartree-Fock (DHF) calculations and applications to the diatomic molecules Xe₂ (Ref. 2) and Au₂.^{3,4} In these applications, we averaged the p_{1/2} and p_{3/2} potentials (also d_{3/2} and d_{5/2}, etc.) with the proper weights so that the spin-orbit splittings were removed from the potentials and the usual programs based on LS coupling can be used for the molecular calculations. Other workers have also used averaged relativistic effective core potentials (AREP) in molecular calculations.

Since the spin-orbit splitting is comparable in order of magnitude with other relativistic effects, it is theoretically more consistent to avoid this averaging and to carry out molecular calculations in ω - ω coupling. In this article we describe a method for self-consistent-field (SCF) molecular calculation using the non-averaged REP from our earlier treatment of atoms and thus retaining the spin-orbit effect in a direct manner. The application of our REP in molecular calculations requires a SCF formalism that is based upon two-component molecular spinors. A brief discussion of the method has been reported in an earlier paper³ for diatomic molecules with closed-shell configurations. We have extended the theory to treat molecules with no more than one open shell of a given symmetry. Electronic structure calculations for Au₂⁺, TlH, PbS and PbSe are reported as examples of this procedure. In linear molecules, the angular symmetry of a state is defined by the total electronic angular momentum Ω as in the Hund

case c and that of ith molecular orbital by $m_i = \pm\omega_i$. The two orbitals with $m_i = +\omega_i$ and $m_i = -\omega_i$ are degenerate and constitute a shell. With spin incorporated in the orbital, each molecular orbital can accommodate only one electron. With these characteristics, one can derive the SCF theory of the two-component molecular spinors (TCMS) for diatomic molecules by applying the approximations that have been developed for the conventional non-relativistic molecular calculations. The rather extensive mathematics of these procedures is given in LBL-10101.

Some of the results are given in Tables 1-4. For Au₂⁺ columns three and four of Table 1 compare the vertical ionization energy from the difference of total energies of Au₂ and Au₂⁺ with that from Koopman's theorem. The agreement is good and indicates that our open-shell calculations are adequate for Au₂⁺ and that Koopman's theorem is a good approximation. As would be expected, the (1/2)_g state of Au₂⁺ has a slightly larger equilibrium bond length (5.18 a.u.) and a smaller vibrational frequency (94 cm⁻¹) compared with the 0_g⁺ state of Au₂ according to our calculations. The dissociation energy is expected to be smaller for Au₂⁺ than for Au₂ although the exact estimate of D_e is not available in the SCF approximation. We are not aware of experimental values for Au₂⁺ for comparison.

The ground state of TlH has been calculated with 3 and 13 electron valence shells and with REP, AREP and NREP for the Tl atom. The spectroscopic constants are summarized in Table 2, from which it is apparent that relativity reduces the interatomic distance significantly; this may be ascribed to the relativistic contraction of the 6s orbital on Tl and to a smaller contraction of the 6p_{1/2} orbital. Also the bond is weakened, although consideration

Table 1. Total valence energies of Au₂⁺, vertical ionization energies of Au₂ (calculated from the total valence energies of Au₂ and Au₂⁺) and the orbital energies of the least-bound (1/2)_g electron of Au₂ at various interatomic distances. (all in a.u. and based on 11-electron REP's for Au)

| R | E(Au ₂ ⁺) - E(Au ₂) | -E[(1/2) _g] of Au ₂ |
|------|--|--|
| 4.5 | 70.5181 | .260 |
| 4.75 | 70.5266 | .254 |
| 5.0 | 70.5300 | .249 |
| 5.5 | 70.5292 | .238 |
| 8.0 | 70.5022 | .202 |

of the spin-orbit splitting of the atomic states of Tl complicates the argument.

The difference in R_e between the 3 and 13 electron bases for Tl is surprisingly large. Presumably the outer radius of the 5d orbitals is important in determining R_e and this should be more reliably established when these 5d electrons are included explicitly in the calculation.

The population analysis for TlH was considered but the interpretation is rather complex. The most striking results are: (1) the large ionic character Tl⁺H⁻ with about 0.35e charge, and (2) the small ratio of the ($p_{3/2}/p_{1/2}$) populations for the relativistic calculations compared to the non-relativistic value of 2.0.

Our interest in PbS and PbSe was stimulated by the simultaneous measurements of Professor Shirley and associates of the photoelectron spectra.⁶ The results for PbS are shown in Table 3; the results for PbSe are similar in all respects. For both molecules the lower frequency photoelectron peak is broad and presumably includes both the lowest $\Omega = 1/2$ state and the $\Omega = 3/2$ state for the positive ion. The agreement of our calculated energies with experiment is as good as could be expected. Also our results show a rapid variation of ϵ with interatomic distance for the 4-1/2 orbital and hence predict a broad band which would overlap the 1-3/2 band. For the second transition removing an electron from the 3-1/2 orbital, the agreement between calculation and experiment is perfect--doubtless in some degree by accident.

Also shown in Table 3 are results of the X α calculations of Yang and Rabii⁷ which yield the correct order of orbital energies but the quantitative values do not agree. More recent and improved X α calculations⁸ yield better agreement.

In Table 4 are shown our calculated values of R_e , ω_e , and D_e together with experimental data.⁹ The agreement with the experimental values of R_e is quite satisfactory. Since electron correlation is not included in our calculation, it is expected that our calculated D_e will be too small, and this effect will also influence the ω_e values in the same direction.

* * *

[†]Brief version of LBL-10101.

1. Y. S. Lee, W. C. Ermler and K. S. Pitzer, *J. Chem. Phys.* **67**, 5861 (1977).
2. W. C. Ermler, Y. S. Lee, K. S. Pitzer and N. W. Winter, *J. Chem. Phys.* **69**, 976 (1978).
3. Y. S. Lee, W. C. Ermler, K. S. Pitzer and A. D. McLean, *J. Chem. Phys.* **70**, 288 (1979).
4. W. C. Ermler, Y. S. Lee and K. S. Pitzer, *J. Chem. Phys.* **70**, 293 (1979).
5. P. Pyykkö, and J. P. Desclaux, *Chem. Phys. Lett.* **42**, 545 (1976).
6. D. A. Shirley, M. G. White, and associates, private communication.
7. C. Y. Yang and S. Rabii, *J. Chem. Phys.* **69**, 2497 (1978).
8. M. G. White and C. Yang, private communication.
9. K. P. Huber and G. Herzberg, *Molecular Spectra and Molecular Structure. IV. Constants of Diatomic Molecules*, Van Nostrand Reinhold Co., New York (1979).

Table 2. Spectroscopic constants obtained from the SCF calculation of TlH with various EP's and from the one-center calculations of Pyykkö and Desclaux.⁵

| | Effective Core Potentials | | | | | One-center | | Exp ^b |
|------------------------------------|---------------------------|-------------------|-------------------|-------------------|-------------------|------------|-------|------------------|
| | REP13 | REP3 | AREP3 | NREP13 | NREP3 | R | NR | |
| R_e (a.u.) | 3.47 | 3.39 | 3.39 | 3.67 | 3.55 | 3.529 | 3.795 | 3.53 |
| D_e (a.u.) | .057 ^a | .050 ^a | .065 ^b | .062 ^b | .064 ^b | | | 0.072 |
| ω_e (cm ⁻¹) | 1450 | 1380 | 1380 | 1380 | 1410 | 1500 | 1390 | 1391 |
| ($p_{3/2}/p_{1/2}$) ^c | .37 | .50 | 2.0 | 2.0 | 2.0 | .65 | 2.0 | - |
| I.P. (a.u.) ^d | .298 | .290 | .286 | .266 | .267 | | | |

^a $E(\text{Tl } 2p_{1/2}) + E(\text{H}) - E(\text{TlH at } R_e)$.

^b $E(\text{Tl } 2p) + E(\text{H}) - E(\text{TlH at } R_e)$.

^c From the atomic population analysis.

^d Ionization potential from Koopman's theorem and orbital energies at near-equilibrium distance.

Table 3. Orbital energies and ionization energies for PbS (in a.u. at $R = 4.25$).

| Orbital | REP | $X\alpha$ | | Exp ⁷ |
|---------|------|-----------|-------|--------------------------|
| | | Ref 8 | Ref 9 | |
| 4 - 1/2 | .326 | .227 | .334 | .33 ₈ (broad) |
| 1 - 3/2 | .344 | .243 | .345 | |
| 3 - 1/2 | .359 | .260 | .353 | .36 ₀ |
| 2 - 1/2 | .591 | .510 | .566 | |
| 1 - 1/2 | .884 | .632 | - | |

Table 4. Calculated and experimental quantities for PbS and PbSe.

| | | PbS | PbSe |
|--------------------------------|-----|-------|-------|
| R_e (a.u.) | REP | 4.28 | 4.55 |
| | Exp | 4.321 | 4.539 |
| ω_e (cm ⁻¹) | REP | 351. | 210. |
| | Exp | 429.4 | 277.6 |
| D_e (a.u.) | REP | 0.043 | 0.033 |
| | Exp | 0.128 | 0.113 |

3. THERMODYNAMIC PROPERTIES OF ELECTROLYTES: FROM DILUTE SOLUTIONS TO FUSED SALTS⁷

Kenneth S. Pitzer

Electrolyte systems extending in the liquid phase from a dilute solution in a polar molecular solvent (such as water) to a pure fused salt constitute an interesting but infrequently studied type. They are of interest as extremely concentrated brines. Kraus¹ summarized the information available in 1954 concerning such systems. In the following 25 years, the vapor pressure and thereby the activity of water has been measured for the systems (Li,K)NO₃-H₂O (Refs. 2 and 3) and (Ag,Tl)NO₃-H₂O (Ref. 4) over the entire range from pure water to fused salt. In each case there is a fixed, nearly equal ion fraction of cations so that either can be regarded as a two component MNO₃-H₂O system. The mixing of the salts reduces the melting point and allows the experiments to be carried out at low pressure near 100°C. With the availability of these thermodynamic data it seemed worthwhile to examine again the nature of these novel systems.

Figure 1 presents a survey of data for the activity of water in very concentrated solutions. The composition variable is the mole fraction on an ionized basis, i.e., $x_1 = n_1/(n_1 + \nu n_2)$ where n_1 and n_2 are moles of water and salt, respectively, and ν is the number of ions in the salt. On this basis Raoult's law applies in the very dilute range, with the Debye-Hückel correction applicable as the concentration increases. The similarity of the curves on Fig. 1 to those for nonelectrolyte solutions is striking. The dashed line representing $a_1 = x_1$ can be called "ideal-solution behavior" for these systems, as it is for nonelectrolytes; but it is realized that a statistical

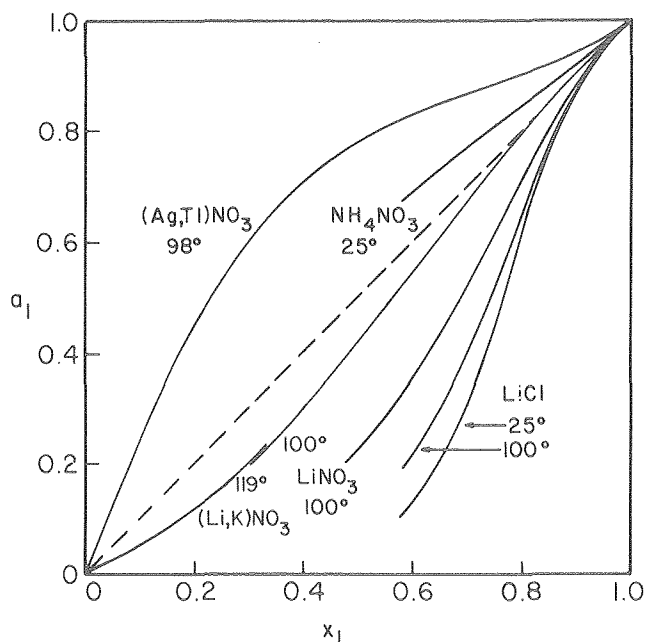


Fig. 1. The activity of water for water-salt solutions over the full range of composition. (XBL 802-8357)

model yielding that result would be more complex for the ionic case. Also the Debye-Hückel effect is a departure from this ideal behavior. Nevertheless it seems worthwhile to explore the use for these systems of the simple equations for nonelectrolytes. One of the simplest and most successful had its origin in the work of van Laar⁵ and has been widely used since. For the activity of either component, referenced to the pure liquid, one has

$$\begin{aligned} \ln a_1 &= \ln x_1 + w_1 z_1^2 \\ \ln a_2 &= \ln x_2 + w_2 z_2^2 \\ z_1 &= n_1 / [n_1 + \nu n_2 (b_2/b_1)] \\ z_2 &= \nu n_2 / [n_1 (b_1/b_2) + \nu n_2] = 1 - z_1 \\ w_2 &= (b_2/b_1) w_1 \end{aligned} \quad (1)$$

The non-ideality parameter w (sometimes written w/RT) arises from the difference between the intermolecular attraction of unlike species as compared to the mean of the intermolecular attraction for pairs of like species. The second parameter (b_1/b_2) is sometimes ascribed to the ratio of the volumes of the molecules or to the ratio of molal volumes in the liquid. For fused salt-water mixtures it seems best to regard (b_1/b_2) as a freely adjustable parameter and subsequently to compare the values with ratios of molal volumes.

Equation (1) was fitted to the two systems remaining liquid over the full range of composition with the results $w_1 = 1.02$, (b_1/b_2) = 0.50 for (Ag,Tl)NO₃-H₂O and $w_1 = -0.89$, (b_1/b_2) = 1.2 for (Li,K)NO₃-H₂O. Water is component 1 and the salt component 2. The calculated curves based on equation (1) are compared with the experimental data in Fig. 2 where it is apparent that the agreement is excellent.

The molal volume ratio for (Ag, Tl) NO₃-H₂O is 0.82 compared to (b_1/b_2) = 0.50 while for (Li,K) NO₃-H₂O the volume ratio is 0.87 compared to 1.2. Thus (b_1/b_2) does not follow the volume ratio very closely.

This treatment of very concentrated electrolytes in a manner analogous to that of nonelectrolytes seems to me to be the simplest and most useful initial approach, but it has not been used to the writer's knowledge. A favorite method has been the use of the Brunauer-Emmett-Teller adsorption isotherm as proposed by Stokes and Robinson.⁶ Equation (1) fits the data better, especially at $x_1 > 0.6$.

Although Eq. (1) gives a remarkably accurate representation over most of the composition range of the activity of water in a water-fused salt system, it becomes somewhat inaccurate for dilute solutions in water and it does not include the Debye-Hückel limiting law. Clearly electrostatic forces cause a departure from a random distribution of ions which may be nearly constant over most of the composition range except in the limit of infinite dilution. However, the shift to a random

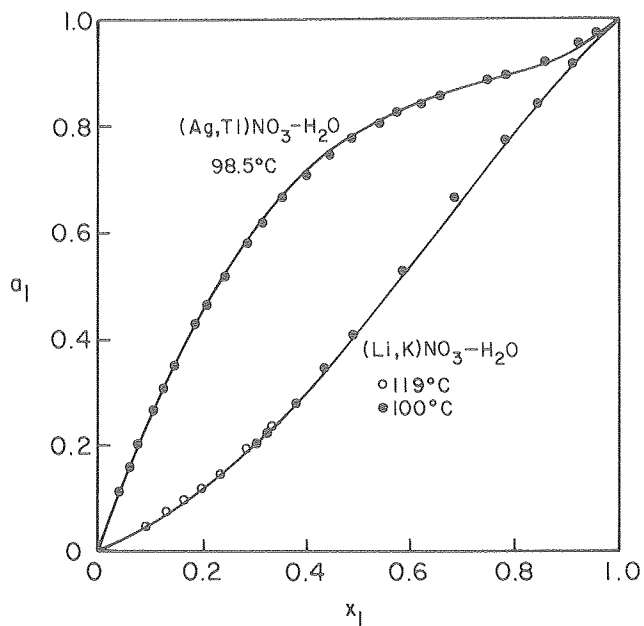


Fig. 2. Comparison of the experimental activity of water with that calculated from Eq. (1). (XBL 802-8358)

distribution in the limit of zero solute concentration can be included by adding a Debye-Hückel term to Eq. (1).

New definitions are required for the use of mole fractions in electrolyte thermodynamics and Debye-Hückel equations. Thereafter, equations are obtained combining Debye-Hückel terms with Eq. (1). The resulting fits to experimental data are shown on Figs. 3 and 4 which also include the electrical (D-H) contributions to the activity coefficients and the total activity coefficients of each component. Details and numerical parameters are given in the full report (LBL-9708).

Most apparent on Figs. 3 and 4 is the large electrostatic effect for γ_{\pm} as compared to the small effect for γ_1 in the region of dilute aqueous solution. Thus, without the guidance from Debye-Hückel theory, one would not obtain even approximately correct curves for the activity of the salt on the infinitely dilute standard state. However, on the fused salt standard state, where $\gamma_{\pm} = 1$ at $x_2 = 1$, the major portion of the curve for γ_{\pm} is reasonably well defined by the experiments on water activity with the simple equations of the non-electrolyte type. The postulate mentioned above, that the departure from random distribution of ions is roughly constant from concentrated solutions through to the pure fused salt, is supported by the relative constancy of γ_{\pm}^{el} over that range of composition.

* * *

[†] Brief version of LBL-9708.

1. C. A. Kraus, J. Am. Chem. Soc. 58, 673 (1954).
2. T. B. Tripp and J. Braunstein, J. Am. Chem. Soc. 73, 1984 (1954).
3. H. Braunstein and J. Braunstein, J. Chem. Thermodynamics 3, 419 (1971).

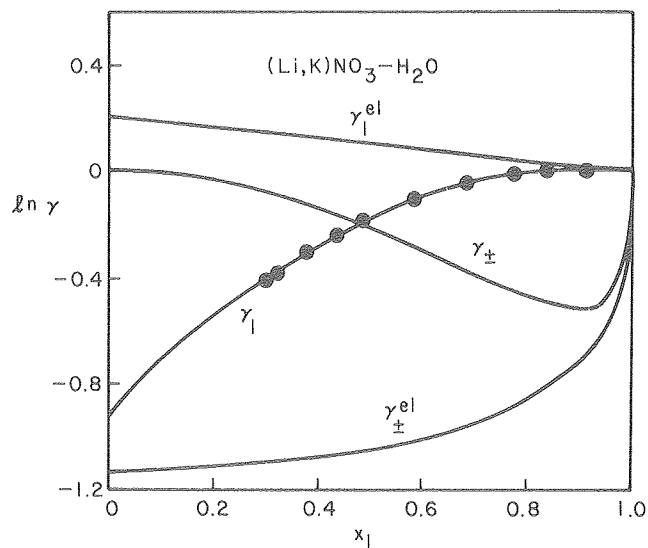


Fig. 3. Activity coefficients for both water and salt for the system $(\text{Li,K})\text{NO}_3\text{-H}_2\text{O}$ at 100°C . It is a numerical accident that the curves for γ_{\pm} based on the pure liquid or the infinitely dilute standard states are indistinguishable on the scale of the graph. (XBL 802-8359)

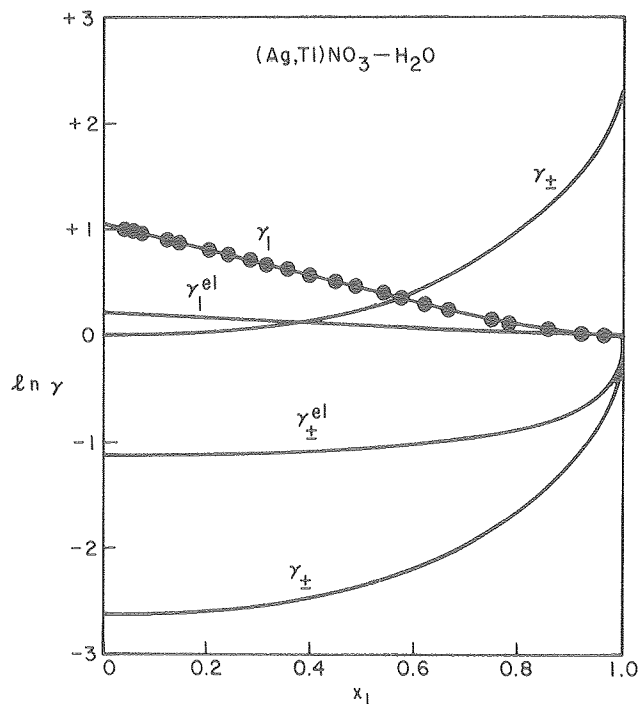


Fig. 4. Activity coefficients for both water and salt for the system $(\text{Ag,Tl})\text{NO}_3\text{-H}_2\text{O}$ at 98°C . Separate curves give γ_{\pm} on the pure liquid standard state (above) and the infinitely dilute standard state (below). (XBL 802-8360)

4. M-C Trudelle, M. Abraham, and J. Sangster, *Can. J. Chem.* **55**, 1713 (1977).
5. J. J. van Laar, *Sechs vortrage uber das thermodynamische potential*. Vieweg-Verlag (1906). See also *Z. physik. Chem.* **72**, 723 (1910).
6. R. H. Stokes and K. A. Robinson, *J. Am. Chem. Soc.* **70**, 1870 (1948).

RESEARCH PLANS FOR CALENDAR YEAR 1980

The improved effective-potential method described above will be incorporated into our relativistic program for the quantum chemistry of molecules containing heavy atoms. Also we expect to extend this program to allow multi-configuration calculations; this is needed for the satisfactory calculation of dissociation energies in most cases. Collaboration with the IBM Laboratories (San Jose) in all-electron relativistic calculations will continue. With these improved methods, meaningful calculations can be made for a number of additional molecules. One example is Tl_2 whose properties are experimentally essentially unknown (there is only an upper limit for the dissociation energy). Tl_2 is of particular interest, theoretically, in connection with spectroscopic experiments examining parity non-conservation for the Tl atom. The molecules Tl_2 , Pb_2 , and Bi_2 are all of interest with regard to trends in chemical bonding as relativistic effects become substantial.

An experimental program will be initiated to measure the thermodynamic properties of extremely concentrated aqueous electrolytes including systems continuously miscible from the fused salt to the dilute solution. We plan to measure the vapor pressure of water above such solutions in the temperature range 100-175°C. Salt activity can then be calculated from the Gibbs-Duhem relationship. Simultaneously, the theoretical treatment initiated in 1979 will be extended to a more fundamental level if possible. These extremely concentrated systems have received very little attention, hence their exploration is of particular scientific interest. Also they are surely relevant to the behavior of concentrated brines of geological or industrial significance. Related aqueous electrolyte research for systems of more moderate concentration will continue with support from the Geoscience program at LBL.

1979 PUBLICATIONS AND REPORTS

Refereed Journals

1. Yoon S. Lee, Walter C. Ermler, Kenneth S. Pitzer, and A. D. McLean, "Ab Initio Effective Core Potentials Including Relativistic Effects. III. Ground State Au_2 Calculations," *J. Chem. Phys.* **70**, 288 (1979), LBL-8056.

2. Walter C. Ermler, Yoon S. Lee and Kenneth S. Pitzer, "Ab Initio Effective Core Potentials Including Relativistic Effects. IV. Potential Energy Curves for the Ground and Several Excited States of Au_2 ," *J. Chem. Phys.* **70**, 293 (1979), LBL-8057.

3. Kenneth S. Pitzer, "Statistical Thermodynamics of Dissociating Gases and Plasmas," *J. Chem. Phys.* **70**, 393 (1979), LBL-8231.

4. Kenneth S. Pitzer, "Relativistic Effects on Chemical Properties," *Acc. Chem. Res.* **12**, 271 (1979), LBL-8395.

5. Daniel J. Bradley and Kenneth S. Pitzer, "Thermodynamics of Electrolytes. 12. Dielectric Properties of Water and Debye-Hückel Parameters to 350° and 1 kbar," *J. Phys. Chem.* **83**, 1599 (1979), LBL-8549.

6. Kenneth S. Pitzer and Leo Brewer, "Simplification of Thermodynamic Calculations Through Dimensionless Entropies," *J. Physical and Chemical Reference Data* **8**, 917 (1979) and also *High Temperature Science* **11**, 49 (1979), LBL-8077.

7. P. A. Christiansen, Yoon S. Lee, and Kenneth S. Pitzer, "Improved Ab Initio Effective Core Potentials for Molecular Calculations," *J. Chem. Phys.* **71**, 4445 (1979), LBL-9351.

LBL Reports

1. Kenneth S. Pitzer, "Electrolytes: From Dilute Solutions to Fused Salts," LBL-9708, submitted to *J. Am. Chem. Soc.*

2. Yoon S. Lee, Walter C. Ermler, and Kenneth S. Pitzer, "Ab Initio Effective Core Potentials Including Relativistic Effects. V.S.C.F. Calculations with ω - ω Coupling Including Results for Au_2^+ , TlH , Tl_2H , PbS , and $PbSe$," LBL-10101 submitted to *J. Chem. Phys.*

Invited Talks

1. Kenneth S. Pitzer, D. J. Bradley, P. S. Z. Rogers, and J. Christopher Peiper, "Thermodynamics of High-Temperature Brines," *The Am. Chem. Soc. -ASTM Joint Symposium, Hawaii, April 1979*, LBL-8973.

2. K. S. Pitzer, "Characteristics of Very Concentrated Aqueous Solutions," *Nobel Symposium on Chemistry and Geochemistry of Solutions at High Temperature and Pressure*, Royal Swedish Academy of Sciences, September 1979, LBL-9660.

3. K. S. Pitzer, "Thermodynamics of Aqueous Electrolytes at Various Temperatures, Pressures, and Compositions," *Conference on Thermodynamics of Aqueous Systems with Industrial Applications (NSF-NBS-AICHE)*, October 1979, LBL-9788.

e. Chemical Dynamics Studies*

Bruce H. Mahan, Investigator

1. LASER INDUCED FLUORESCENCE STUDIES OF MOLECULAR IONS[†]

F. Grieman,[‡] B. H. Mahan, and A. O'Keefe

We have completed spectroscopic studies on several gas phase molecular ions using a recently developed technique which allows us to mass selectively store ions under collision free conditions for periods of milliseconds. We have completed the analysis of selected electronic transitions in both the 1,3,5-trifluorobenzene cation and the BrCN cation.¹

Ions are formed within a three dimensional RF quadrupole trap by electron impact ionization of parent neutral molecules maintained at a pressure of $\sim 5 \times 10^{-5}$ Torr. The trap may be tuned to confine ions of a given charge to mass ratio for periods of several milliseconds. The ions are then studied using laser induced fluorescence. Resulting spectra are stored in a PDP-8 computer interfaced to the detection electronics.

a. The $\tilde{B} A_2'' - \tilde{X} E'$ Band System of 1,3,5-Trifluorobenzene Cation.

In an attempt to resolve the controversy concerning the number of bands in the photoelectron spectrum of benzene and the ordering of its molecular orbitals, the PE spectra of many fluoro-substituted benzenes have been obtained by several groups. The $\tilde{B}-\tilde{X}$ transition in several fluoro-benzene cations, which appears in the visible wavelength region, has been obtained in emission studies by Maier and co-workers² but complete analysis was not possible due to the complexity of the spectra. This prompted our study of the 1,3,5-trifluorobenzene cation using laser induced fluorescence (LIF). The two most significant advantages to be found in this approach are the high resolution associated with optical spectroscopy and the likelihood of an easily analyzed spectrum, consisting of only a few vibrational progressions.

The LIF studies were carried out over a wavelength region spanning 1000 Å, from 4000 Å - 5000 Å. The spectrum we observed for this transition is reproduced in Fig. 1. We find a series of bands on top of a pseudocontinuum. The assignment of the 0_0^0 (vibrationless) peak is made by comparison with existing PE spectra and is determined to be $21830 \text{ cm}^{-1} \pm 10 \text{ cm}^{-1}$. The uncertainty in the peak positions is due primarily to the extensive overlap of the bands. All other observed peak positions are given in Table 1 relative to the 0_0^0 position. Irregularity in the progressions is believed to be caused by strong Jahn-Teller interaction. The assignments given are in good agreement with recently published flow tube studies by Bondybey, et al.³

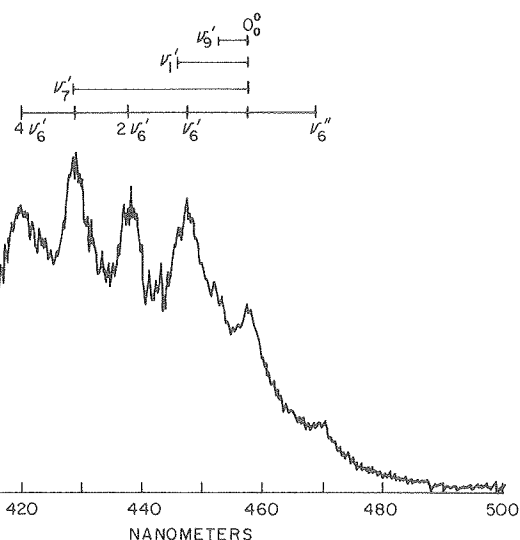


Fig. 1. Fluorescence excitation spectrum of the $\tilde{B} 2A'' - \tilde{X} 2E'$ Band System of the 1,3,5-Trifluorobenzene cation. (XBL 799-7115)

Table 1. 1,3,5-Trifluorobenzene cation vibrational assignments.

| $\Delta\nu(\text{cm}^{-1})$ | Assignment | Symmetry Class |
|-----------------------------|----------------------------|-------------------------|
| - 535 | ν_6'' (hot band) | E' |
| 0 | 0_0^0 | A_1' |
| 245 | ν_9' | E' |
| 484 | ν_6' | E' |
| 579 | ν_1' | A_1' |
| 769 | $\nu_9' + \nu_6' (?)$ | $A_1' \& E'$ |
| 988 | $2\nu_6'$ (ν_{12}') | $A_1' \& E'$ (A_1') |
| 1496 | ν_7' ($\nu_8' ?$) | E' (E') |
| 2008 | $2\nu_{12}'$ ($4\nu_6'$) | A_1' ($A_1' + E'$) |

*This work was supported by the Division of Chemical Sciences, Office of Basic Energy Sciences, U. S. Department of Energy.

b. The $\tilde{B} \ ^2\Pi - \tilde{X} \ ^2\Pi$ Band System of BrCN Cation

From the band separation in the photoelectron spectrum of BrCN obtained in 1970,⁴ the $\tilde{B}-\tilde{X}$ electronic transition in the molecular ion BrCN⁺ was found to lie in the visible wavelength range. Emission studies⁵ were unsuccessful in providing an assignment of vibrational progressions or of determining the spin orbit splitting in the \tilde{B} state. A study of this system using our LIF system⁶ has resulted in the vibrational assignment (although strong Fermi interaction is apparent) and determination of the spin orbit splitting. The resulting spectrum is shown in Fig. 2. The \tilde{X} and \tilde{B} states are found to belong to Hund's case (a), and so the transition consists of $^2\Pi_{3/2} - ^2\Pi_{3/2}$ and $^2\Pi_{1/2} - ^2\Pi_{1/2}$ components. Examination of the spectrum reveals a splitting of each band into two subbands. This behavior, along with the irregular progression and spin orbit splitting, has been observed in other linear triatomics and has been attributed to a Fermi resonance. In the

present case we believe this to be due to interaction between the vibrational levels (v_1, v_2, v_3) and (v_1, v_2+2, v_3-1) which are of the same symmetry.

Assignments of the bands are made in Table 2. These assignments are based upon the O_0^0 band seen in the PE spectra as this band was not observed in the present work. Values given are band center frequencies.

From these values a mean frequency of 441 ± 18 cm^{-1} is obtained for V^* ($= V_3' + 1/2 V_2'$). Because no bands unaffected by Fermi resonance were observed, no estimate of the magnitude of this effect can be made. In Fig. 2 the two different components involved in the most intense V^* band are connected by lines labeled α and β . The frequency difference between the subbands of a spin orbit doublet pair is an approximation to the difference in spin-orbit coupling constants ΔA . The average of our most accurate ΔA values gives ΔA of -280 cm^{-1} .

Table 2. $\tilde{B} \ ^2\Pi - \tilde{X} \ ^2\Pi$ subband heads for BrCN⁺. All transitions are from the (0,0,0) level of the \tilde{X} state. $v^* = (v_3' + 1/2 v_2')$. The different Fermi resonance components are represented by α and β .

| v^* | $^2\Pi_{1/2} - ^2\Pi_{1/2}$ | | $^2\Pi_{3/2} - ^2\Pi_{3/2}$ | | Δv^* |
|-------|-----------------------------|--------------------|-----------------------------|-----------------------------|--------------|
| | α | β | α | β | |
| 4 | 20205 (426) | 20275 (449) | 20482 (455) | 20537 (463) | Δv^* |
| 5 | 20631 | 20724 (450) | 20937 (450) | 21000 (466) | Δv^* |
| 6 | --- | 21174 (466) | 21387 (421) | 21466 (402) | Δv^* |
| 7 | 21592 [†] (449) | 21640 (481) | 21808 (442) | 21868 (454) | Δv^* |
| 8 | 22041 [†] (443) | 22121 (447) | 22250 (433) | 22322 [†] (431) | Δv^* |
| 9 | 22484 (438) | 22568 (447) | 22683 (424) | 22753 (434) | Δv^* |
| 10 | 22922 [†] (441) | 23015 [†] | 23107 (441) | 23187 | Δv^* |
| 11 | 23363 [†] (407) | --- | 23548 [†] (416) | --- | Δv^* |
| 12 | 23770 [†] (432) | --- | 23964 (443) | --- | Δv^* |
| 13 | 24202 | --- | 24407 | --- | |

[†]The uncertainty in these frequencies is ± 20 cm^{-1} . All of the others are $\leq \pm 10$ cm^{-1} . Note that these frequencies have not been corrected to vacuum.

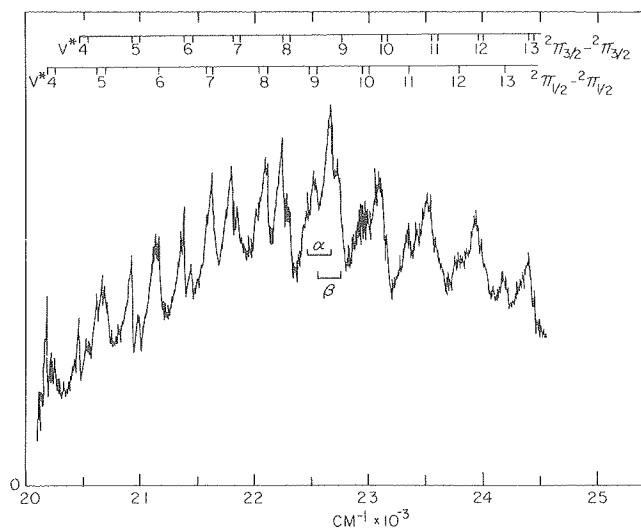


Fig. 2. Fluorescence excitation spectrum of BrCN^+ : $\tilde{\text{B}}^2\Pi - \tilde{\text{X}}^2\Pi$ band system. (XBL 799-7116)

* * *

[†]Brief version of LBL-10021.

[‡]Current address: Department of Physics, University of Oregon, Eugene, OR 97403.

1. F. J. Grieman, Ph.D. thesis, LBL-10021.
2. M. Allan and J. P. Maier, Chem. Phys. Lett. 34, 442 (1975).
3. V. E. Bondybey and T. A. Miller, J. Chem. Phys. 70(1), 138 (1979).
4. R. F. Lake and Sir H. Thompson, Proc. Roy. Soc. Lond. A. 317, 187 (1970).
5. M. Allan and J. P. Maier, Chem. Phys. Lett. 41, 231 (1976).
6. F. J. Grieman, B. H. Mahan, and A. O'Keefe, to appear in J. Chem. Phys.

2. DYNAMICS OF $\text{CO}_2^+ - \text{D}_2$ COLLISIONS[†]

S. G. Hansen and B. H. Mahan

Work has been completed on the reactions $\text{CO}_2^+(\text{D}_2, \text{D}) \text{DCO}_2^+$ and $\text{CO}_2^+(\text{H}_2, \text{OH}) \text{HCO}^+$. Previous work in our group¹ showed that the reaction $\text{CO}_2^+(\text{D}_2, \text{D}) \text{DCO}_2^+$ proceeds by a direct mechanism at relative collision energies above 2.0 eV. Using our low energy crossed ion-molecular beam apparatus, we now have established² that this reaction remains direct down to 0.27 eV. This is somewhat surprising as the intermediate D_2CO_2^+ lies 1.7 eV below the products, and our previous work¹ demonstrated the importance of a long-lived collision complex in the reaction $\text{CO}_2^+(\text{D}_2, \text{OD}) \text{DCO}^+$. Figure 1 shows a typical final velocity vector distribution for DCO_2^+ formed by $\text{CO}_2^+ - \text{D}_2$ collisions. The forward peaking indicates the predominance of a direct reaction channel; however, the lower intensity contours are more symmetric about the $\pm 90^\circ$ line. The decay of a long-lived complex would yield symmetric contours, and hence the distribution in Fig. 1 can be explained in terms of a dominant direct reaction channel and weaker long-lived complex channel.

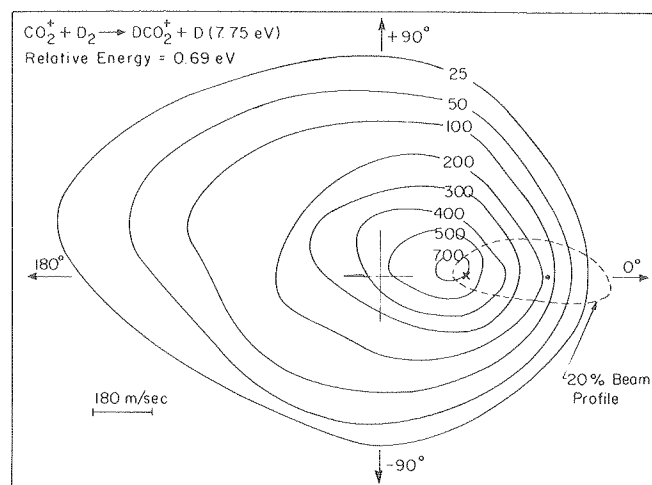


Fig. 1. A contour map of the specific intensity of DCO_2^+ from $\text{CO}_2^+ - \text{D}_2$ collisions at an initial relative energy of 0.69 eV. The intensity maximum occurs near the spectator stripping velocity which is marked by a small cross. (XBL 799-7021)

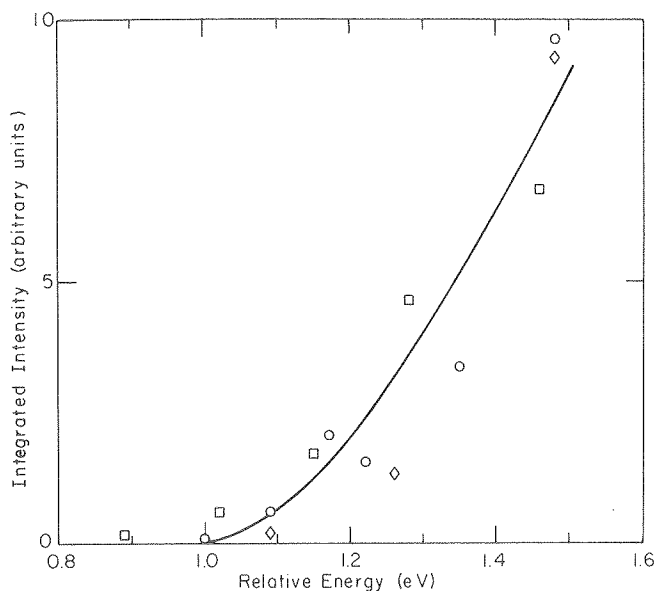


Fig. 2. Plot of the integrated intensity of HCO^+ as a function of initial relative energy for the reaction $\text{CO}_2^+(\text{H}_2, \text{OH}) \text{HCO}^+$. Different symbols denote data taken on different runs. A smooth line is drawn through the data points. (XBL 799-7020)

Our interest in the reaction $\text{CO}_2^+(\text{H}_2, \text{OH}) \text{HCO}^+$ has been to measure its kinetic energy threshold. Because this reaction is exothermic, the existence of a barrier is surprising, as such barriers are rare in ion-molecule reactions. Data were obtained by directing CO_2^+ beams of various energies through a scattering cell containing H_2 and measuring HCO^+ velocity spectra in the direction of the ion beam. From the velocity spectra, contour maps were synthesized and integrated. Figure 2 shows a plot of HCO^+ integrated intensity vs. relative collision energy and yields a threshold

of about 1.0 eV. Using D_2 , and measuring DCO^+ intensity, a similar value is obtained. In spite of this agreement, a note of caution is appropriate. The apparatus used was designed to measure differential, not total cross sections. Also, variations in detector transmission efficiency can lead to systematic errors. We therefore report the threshold to be 1.0 ± 0.3 eV.

* * *

† Brief version of LBL-9806.

1. B. H. Mahan, P. J. Schubart, *J. Chem. Phys.* **66**, 3155 (1977).
2. S. G. Hansen and B. H. Mahan, (Accepted by *J. Chem. Phys.*), LBL Report #9806.

3. DYNAMICS OF N^+ - H_2 COLLISIONS

S. G. Hansen and B. H. Mahan

Previous work^{1,2} in our laboratory on the reaction $N^+(H_2, H)NH^+$ in the low energy (0.5-2.0 eV) range has shown several interesting points. Although there exists a well of ~ 6 eV depth associated with the NH_2^+ intermediate, the reaction takes place via a direct interaction mechanism at energies above ~ 1.5 eV. Below this energy the reactants sample the deep well, and products are seen to result from the decay of a long-lived complex. We have also detected the reaction of a metastable state (presumably 1D). This reaction remains direct down to a few tenths of an eV relative collision energy. Recent work³ has concentrated on studying the non-reactive scattering of N^+ from H_2 . Figure 1 shows a final velocity vector distribution for N^+ scattered non-reactively from H_2 at an initial relative energy of 1.42 eV. The scattering pattern is similar to that of other systems we have studied, with the exception of the prominent back-scattered peak. This feature cannot be explained by impulsive scattering. Therefore it results from the decay of a long-lived NH_2^+ complex. A forward peak would also be expected, so that there would be symmetry about the $\pm 90^\circ$ line; however, it is obscured by the main beam. Since the reaction $N^+(H_2, H)NH^+$ is nearly thermo-neutral, the non-reactive channel can effectively compete with the reactive channel in the breakup of the complex. There is a large difference in the dynamics though, because in the non-reactive case the initial relative translational energy remains as translation whereas in the reactive case it is converted to internal energy of NH^+ .¹ In principle, non-reactive scattering may be a more sensitive means to detect a long-lived complex than reactive scattering. When direct reaction channels open up, they tend to shift the scattering pattern, making long-lived complex evaluation difficult. Such complications do not exist in the interpretation of these non-reactive maps. Thus, the complete absence of a back-scattered peak in Fig. 2 indicates that at 2.5 eV long-lived complex formation is negligible in this system.

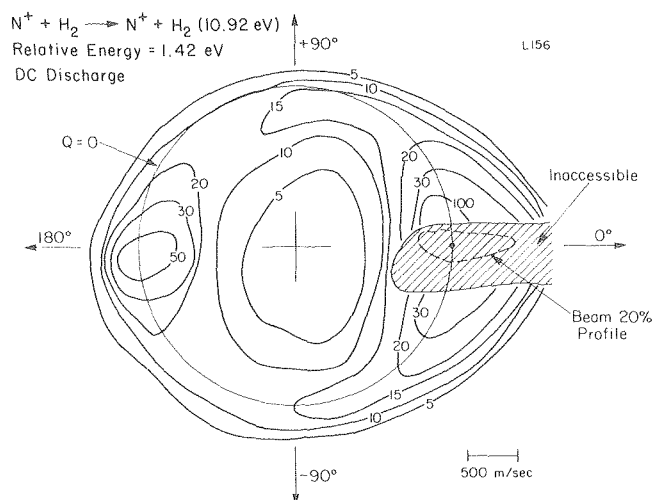


Fig. 1. A contour map of the specific intensity of N^+ scattered non-reactively from H_2 at an initial relative energy of 1.42 eV. The $Q=0$ circle is the theoretical locus of all elastic scattering events. (XBL 801-7821)

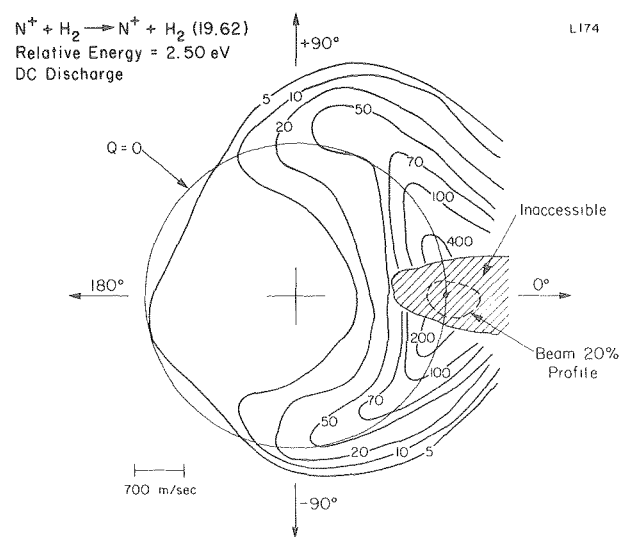


Fig. 2. A contour map of the specific intensity of N^+ scattered non-reactively from H_2 at an initial relative energy of 2.50 eV. (XBL 801-7820)

* * *

1. J. A. Fair and B. H. Mahan, *J. Chem. Phys.* **62**, 515 (1975).
2. J. M. Farrar, S. G. Hansen, and B. H. Mahan, *J. Chem. Phys.* **65**, 2908 (1976).
3. S. G. Hansen and B. H. Mahan (to appear in *J. Chem. Phys.*).

RESEARCH PLANS FOR CALENDAR YEAR 1980

We plan to continue work on the S^+ -D₂ collision system and initiate work on the CF^+ -D₂ system. Further experiments will involve studies of the electronic state distributions of F^+ and S^+ from various ion sources and implementation of a Wien filter to reduce the energy spread of the primary ion beam.

We have begun studies on CH^+ using our laser induced fluorescence technique. We plan to measure the radiative lifetimes for several vibronic transitions of the ion. Attempts will be made to measure the rotational and vibrational state distributions of CH^+ formed in the reaction $C^+ + H_2 \rightarrow CH^+ + H$ and the analogous D₂ reaction. In addition we plan to continue spectroscopic studies on other small ions such as NH_2^+ and CH_2^+ which are of importance in astrophysical and combustion processes.

1979 PUBLICATIONS AND REPORTS

Refereed Journals

1. S. T. Ceyer, P. W. Tiedemann, B. H. Mahan, and Y. T. Lee, "Energetics of Gas Phase Proton

Solvation by NH_3 ," J. Chem. Phys. 70, 14 (1979), LBL-7695.

2. S. T. Ceyer, P. W. Tiedemann, C. Y. Ng, B. H. Mahan, and Y. T. Lee, "Photoionization of Ethylene Clusters," J. Chem. Phys. 70, 2138 (1979), LBL-7694.

3. P. W. Tiedemann, S. L. Anderson, S. T. Ceyer, T. Hirooka, C. Y. Ng, B. H. Mahan, and Y. T. Lee, "Proton Affinities of Hydrogen Halides Determined by the Molecular Beam-Photoionization Method," J. Chem. Phys. 71, 605 (1979), LBL-8858.

LBL Reports

1. T. Hirooka, S. L. Anderson, P. W. Tiedemann, B. H. Mahan, and Y. T. Lee, "Vibrational Pre-dissociation of Vibronically Excited Hydrogen Molecule Dimers," submitted to J. Chem. Phys., LBL-8934.

2. S. G. Hansen and B. H. Mahan, "Dynamics of CO_2^+ -D₂ Collisions, II," submitted to J. Chem. Phys., LBL-9806.

3. Frederick J. Grieman, Ph.D. thesis, "Laser Induced Fluorescence of Trapped Molecular Ions," LBL-10021.

f. Theory of Low Energy Atomic and Molecular Collision Processes*

William H. Miller, Investigator

1. CLASSICAL MODEL FOR THE ELECTRONIC DEGREES OF FREEDOM IN NON-ADIABATIC COLLISION PROCESSES^{†‡}H. D. Meyer[§] and W. H. Miller

We have shown in several recent papers^{1,2} how the electron states participating in an electronically non-adiabatic collision process can be replaced by a classical degree of freedom. This is important when treating molecular collision systems (as opposed to the collision of two atoms) since it means that the electronic degrees of freedom can be treated on a footing dynamically equivalent to the rotational and vibrational (and translational) degrees of freedom. It has been noted³ that models which do not treat electronic and heavy particle degrees of freedom on a dynamically equivalent footing will fail to describe certain features of the process correctly.

For the simplest case of two electronic states, for what the quantum mechanical matrix representation of the Hamiltonian is

$$\begin{pmatrix} H_{00} & H_{01} \\ H_{10} & H_{11} \end{pmatrix}, \quad (1)$$

the classical Hamiltonian which our theory determines is^{1,2}

$$H_{CL}(n,q) = (1-n)H_{00} + nH_{11} + 2\sqrt{n(1-n)} H_{01} \cos q, \quad (2)$$

where (n,q) are the classical action-angle variables for the (collective) electronic degrees of freedom. To test how accurately this classical Hamiltonian models the two-state dynamics, we have considered the case of a general time-dependent two-state system, i.e., the matrix elements of Eq. (1) become functions of time, $H_{n,n'}(t)$, $n,n' = 0,1$. The $0 \rightarrow 1$ transition probability is then calculated classically, using the classical Hamiltonian of Eq. (2), and compared to the correct quantum mechanical transition probability (obtained by solving the time-dependent Schrödinger equation with the Hamiltonian of Eq. (1)).

Figure 1 shows the results obtained at various levels of approximation. (These comparisons are universal, i.e., they pertain to any, and all, two

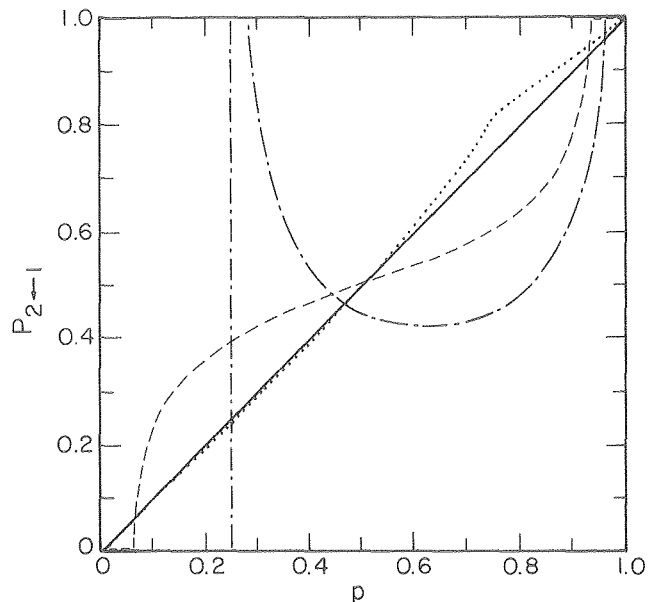
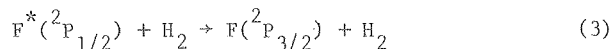


Fig. 1. Electronic transition probability for the two-state model, as a function of the parameter p . The correct quantum mechanical transition probability is the solid line (—) $P_{2 \rightarrow 1} = p$, and the results of the primitive classical (— · — ·), quasiclassical (---), and uniform semiclassical (····) models are shown. (XBL 7811-13175)

state systems!) The solid curve is the correct quantum mechanical transition probability, and one sees that even the relatively primitive "quasiclassical" model gives reasonably good results, never being in error more than ~10-20% over the whole range of transition probabilities; this would be quite adequate for classical Monte Carlo simulations of the collision process. The "semiclassical" results are seen to be in essentially quantitative agreement (a few percent error) with the quantum mechanical results.

A more interesting application, and the one that originally motivated this line of research, is the quenching of the excited fine structure state of fluorine atoms, $F(^2P_{1/2})$, by collision within H_2 :



The question of whether or not this reaction has a significant cross section has been of considerable interest in relation to the chemical reaction $F + H_2 \rightarrow HF + H$, which pumps the HF chemical laser.

Early theoretical treatments suggested that the cross section for reaction (3) is small, $< 1 \text{ \AA}^2$, and F^* thus essentially non-reactive, but a more recent tour de force quantum mechanical coupled channel

* This work was supported by the Division of Chemical Sciences, Office of Basic Energy Sciences, U.S. Department of Energy.

calculation⁴ obtained a large value, $>10 \text{ \AA}^2$. These latter calculations showed that the quenching cross section is large because H_2 undergoes a simultaneous $0 \rightarrow 2$ rotational excitation. The earlier theoretical models were unable to describe this resonance effect and thus failed to obtain a large quenching cross section.

The $\text{F} + \text{H}_2$ system involves three electronic states, for which the quantum mechanical electronic Hamiltonian matrix is⁴

$$H_{el} = \begin{pmatrix} H_{xx} & 0 & 0 \\ 0 & H_{yy} & H_{yz} \\ 0 & H_{zy} & H_{zz} \end{pmatrix}, \quad (4)$$

and the classical electronic Hamiltonian corresponding to this is

$$\begin{aligned} H_{CL}(m,q) &= (1-m^2)H_{zz} + m^2 \frac{1}{2} (H_{xx} + H_{yy}) \\ &\quad - 2m\sqrt{1-m^2} H_{yz} \sin q \\ &\quad - (1-m^2) \frac{1}{2} (H_{zz} - H_{yy}) \cos^2 q. \end{aligned} \quad (5)$$

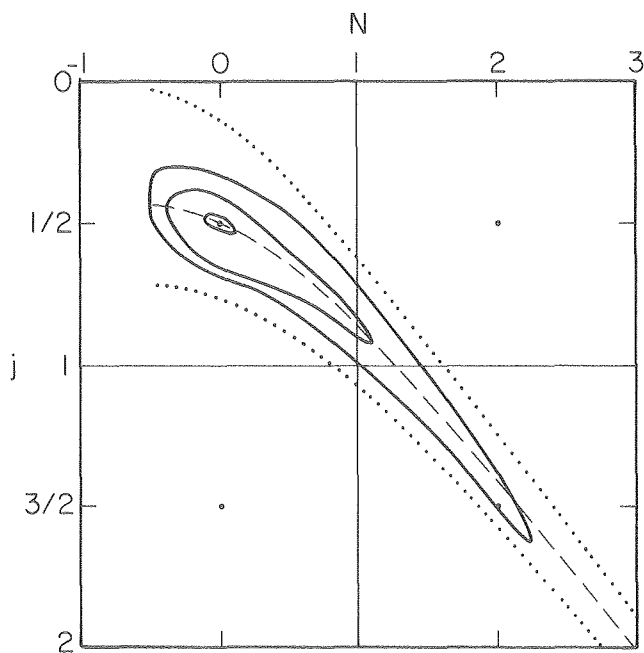


Fig. 2. Contour plot of the distinction of final (j,N) -values resulting from the classical trajectory calculation with $(j_1, N_1) = (1/2, 0)$ and energy $E = 10 \text{ meV}$. The dashed line is the "resonance line" $\epsilon_F(j) + \epsilon_{\text{H}_2}(N) = 0$, and the dotted lines correspond to 10 meV increments off resonance. The points are the locations of the discrete quantum values of j and N . No classical trajectories give (j,N) -values outside the largest contour (solid line). (XBL 795-9569)

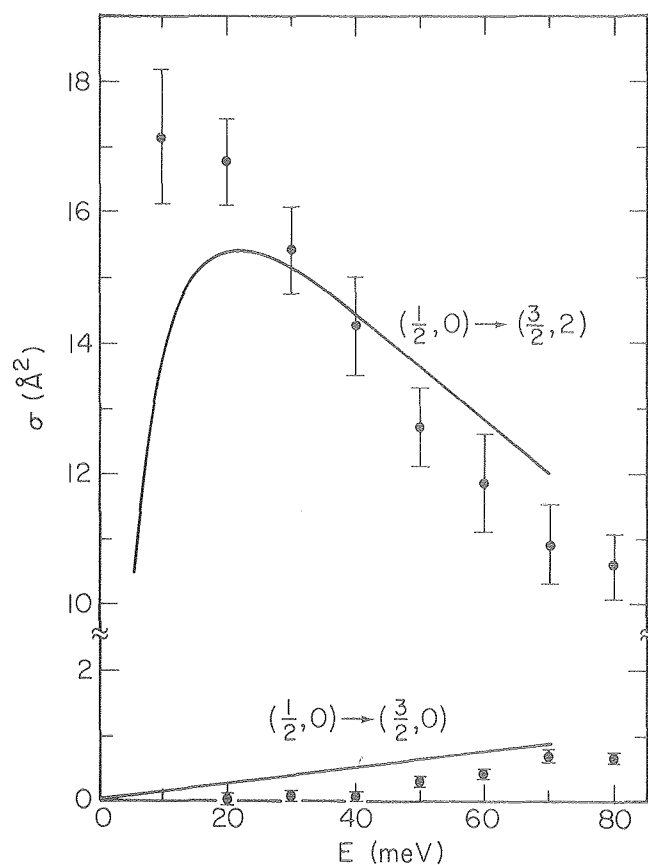


Fig. 3. Cross sections for quenching of $\text{F}^*(2\text{P}_{1/2})$ by non-rotating (i.e., $N_1 = 0$) H_2 , as a function of initial translational energy E . The solid curves are the quantum mechanical results of Ref. 4, and the points are the results of the quasi-classical trajectory calculation (with Monte Carlo error estimates indicated). Note the break in the scale. (XBL 795-9567)

For the initial rotational quantum number of H_2 $N=0$ and $\text{F}(2\text{P}_j)$ initially in the excited state $j = 1/2$, Fig. 2 shows the distribution of final values of N and j resulting from a Monte Carlo classical trajectory calculation using the above classical electronic Hamiltonian. The dashed line is the curve of exact resonance, i.e., zero translation energy transfer, and one sees that the contours of the distribution obtained from the trajectory calculation peak along this resonance curve. It is clear that the nearly resonant transition, final $(N,j) = (2, 3/2)$, will have a large cross section, while the non-resonant quenching of F^* , final $(N,j) = (0, 3/2)$, will have a smaller cross section. Figure 3 shows these cross sections as a function of translational energy, which indeed corroborate these ideas.

* * *

[†]Brief version from J. Chem. Phys. 70, 3214 (1979) and 71, 2156 (1979).

[‡]All calculations were carried out on a Harris Slash Four minicomputer funded by a National Science Foundation Grant CHE-7622621.

⁵Postdoctoral fellow supported by the Deutsche Forschungsgemeinschaft. Present address: Abteilung Molekulare Wechselwirkung, MPI-für Strömungsforschung, Böttingerstrasse 6-8, 3400 Göttingen, West Germany.

1. W. H. Miller and C. W. McCurdy, *J. Chem. Phys.* **60**, 5163 (1978).
2. C. W. McCurdy, H. D. Meyer and W. H. Miller, *J. Chem. Phys.* **70**, 3177 (1979).
3. W. H. Miller, *J. Chem. Phys.* **68**, 4431 (1978).
4. F. Reberstrost and W. A. Lester, Jr., *J. Chem. Phys.* **67**, 3367 (1977).

2. EFFECT OF TUNNELING ON UNIMOLECULAR RATE CONSTANTS, WITH APPLICATION TO FORMALDEHYDE^{††}

W. H. Miller

The effect of tunneling on thermally averaged bimolecular rate constants of chemical reactions has received considerable attention,¹ primarily within the framework of transition state theory, but there has been little discussion of such effects in unimolecular reactions. One reason for this is that unimolecular reactions have traditionally been studied under less well-defined conditions than bimolecular reactions, and corrections due to tunneling are thus obscured. Modern experimental techniques involving laser excitation and/or molecular beam methods, however, are making it possible to monitor the unimolecular dynamics under collisionless conditions, and it is thus interesting to consider the effects of tunneling on the rates of such processes. Furthermore, it turns out that tunneling has a qualitatively more significant effect on the unimolecular rate constant of isolated molecules than on thermally averaged bimolecular rate constants. This is particularly evident with regard to experiments by C. B. Moore and co-workers² on the photodissociation of formaldehyde, an example discussed below.

Within the framework of transition state theory, the microcanonical (i.e., fixed energy) rate constant for unimolecular reaction of an isolated molecule is given by the standard RRKM expression,¹

$$k(E) = \frac{N(E)}{2\pi\hbar \rho(E)} \quad (1)$$

where $N(E)$ is the integral density of states of the activated complex,

$$N(E) = \sum_{\tilde{n}} h(E - \epsilon_{\tilde{n}}^{\ddagger}) \quad (2)$$

and $\rho(E)$ is the density of states of the stable molecule,

$$\rho(E) = \sum_{\tilde{n}} \delta(E - \epsilon_{\tilde{n}}) \quad (3)$$

$\delta(E - \epsilon_{\tilde{n}})$ is the usual delta function, $h(E - \epsilon_{\tilde{n}}^{\ddagger})$ the step function,

$$h(x) = \begin{cases} 1, & x > 0 \\ 0, & x < 0 \end{cases} \quad (4)$$

and $\epsilon_{\tilde{n}}^{\ddagger}$ and $\epsilon_{\tilde{n}}$ are the energy levels of the activated complex and the stable molecule, respectively. Within the approximation that the reaction coordinate is separable from the other degrees of freedom, tunneling modifies Eq. (1) by³ replacing the step function h of Eq. (2) by the tunneling probability P ,

$$h(E - \epsilon_{\tilde{n}}^{\ddagger}) \rightarrow P(E - \epsilon_{\tilde{n}}^{\ddagger}) \quad (5)$$

$P(E_1)$ is the one-dimensional tunneling probability for motion along the reaction coordinate, as a function of the energy E_1 in that degree of freedom.

For zero total angular momentum the energy levels $\epsilon_{\tilde{n}}^{\ddagger}$ are usually approximated by a harmonic oscillator expression,

$$\epsilon_{\tilde{n}}^{\ddagger} = V_0 + \sum_{i=1}^{s-1} \hbar\omega_i^{\ddagger} \left(n_i + \frac{1}{2}\right) \quad (6)$$

where V_0 is the barrier height, $\{\omega_i^{\ddagger}\}$ the vibrational frequencies of the activated complex, and $s = 3N - 6$ (N = number of atoms in the molecule). Neglecting tunneling, the rate $k(E)$ is zero for energies E less than \tilde{V}_0 , the "zero-point energy adjusted" barrier height \tilde{V}_0 ,

$$\tilde{V}_0 = V_0 + \sum_{i=1}^{s-1} \frac{1}{2} \hbar\omega_i^{\ddagger} \quad (7)$$

whereas inclusion of tunneling allows a non-zero rate for $E < \tilde{V}_0$.

H. F. Schaefer and co-workers⁴ have carried out extensive quantum mechanical calculations for the ground electronic state of formaldehyde, determining all the parameters necessary for calculating the rate of decomposition of formaldehyde to molecular species,



It was Moore's observations² that reaction (8) appeared to take place at energies significantly below \tilde{V}_0 with rates $k \sim 10^6 \text{ sec}^{-1}$ which initially suggested that tunneling might be involved in this reaction.

Figure 1 shows the schematic potential energy surface for reaction (8) with the energetics as determined by Schaefer et al.,⁴ and the rate constant as a function of energy E , as calculated from the above expressions, is shown in Fig. 2. The dashed curve is the classical result without tunneling, and this rate constant goes to zero at $E = \tilde{V}_0$. The solid curve is the result which includes tunneling. The energy corresponding to the Moore et al.'s experiments is $\sim 96 \text{ kcal/mole}$, and Fig. 2 indicates that tunneling can indeed produce

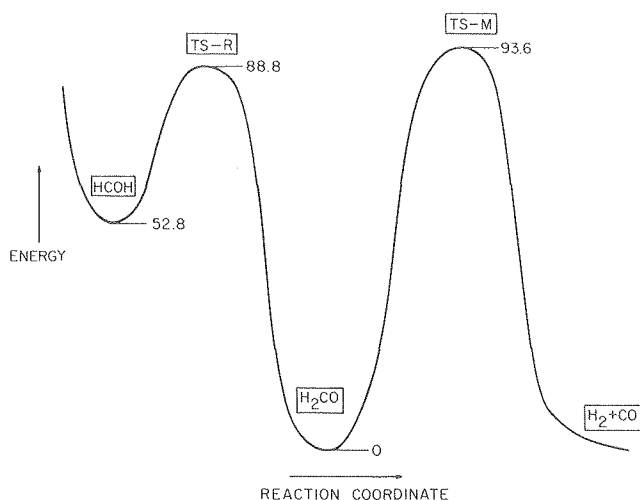


Fig. 1. Schematic of the potential energy surface for the ground electronic state (S_0) of formaldehyde. Units of energy are kcal/mole, and the values shown are from the work in reference 4. (XBL 791-8083)

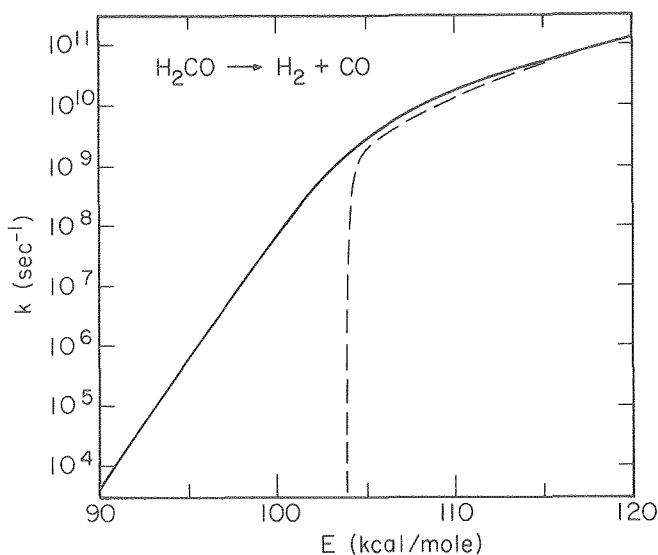


Fig. 2. Unimolecular rate constant for the reaction indicated, as a function of total energy, for total angular momentum $J = 0$. The broken curve is the classical rate, computed from Eqs. (1)-(4), and the solid curve is the result of including tunneling via the modification indicated by Eq. (5). (XBL 794-9378)

rates of $\sim 10^6 \text{ sec}^{-1}$ even for energies 5-10 kcal/mole below V_0 .

Although the simple theoretical model used above can be in considerable error in the "deep tunneling" region, the qualitative conclusion should still be

valid, namely that tunneling is a significant feature in the collisionless photochemistry of formaldehyde.

* * *

† Brief version of LBL-8649; J. Am. Chem. Soc. 101, 6810 (1979).

‡ All calculations were carried out on a Harris Slash Four minicomputer funded by a National Science Foundation Grant CHE-7622621.

1. See, for example, H. S. Johnston, Gas Phase Reaction Rate Theory, Ronald Press, New York, 1966. pp. 37-47.

2. See (a) E. S. Yeung and C. B. Moore, J. Chem. Phys. 58, 3988 (1973); (b) P. L. Houston and C. B. Moore, J. Chem. Phys. 65, 757 (1976); and other references cited therein.

3. See, for example, W. H. Miller, Accts. Chem. Res. 9, 306 (1976); R. A. Marcus, J. Chem. Phys. 45, 2138 (1966).

4. J. D. Goddard and H. F. Schaefer, J. Chem. Phys. 70, 5117 (1979).

3. REACTION PATH HAMILTONIAN FOR POLYATOMIC MOLECULES†

W. H. Miller, N. C. Handy‡ and J. E. Adams

A rigorous treatment of the reaction dynamics of polyatomic systems is severely complicated by the number of degrees of freedom which are involved in the description. Since the potential energy surface for a N -atom system depends on $3N-6$ coordinates, the complete determination of the potential surface, for example, would require that it be calculated at $\sim 10^{3N-6}$ points. For $N > 3$ one immediately sees that it is out of the question to imagine that one will normally have available this amount of information.

It is possible, however, for quantum chemists to carry out usefully accurate calculations for polyatomic ($N > 3$) systems, simply not the enormous number of such calculations necessary to map out the complete potential surface in the $(3N-6)$ -dimensional configuration space. A technique which has recently proved useful involves calculations of the potential at a sequence of points along the reaction path, the curve of steepest descent (if mass-weighted cartesian coordinates are used) from a saddle point on the potential surface to various local minima. We have shown that it is possible to define a set of $(3N-7)$ normal coordinates $\{Q_k\}$, $k=1, \dots, 3N-7$, which describe vibrations orthogonal to the reaction path. In terms of the $3N-6$ internal coordinates $(s, \{Q_k\}, k=1, \dots, 3N-7)$ -- where s is the arc length along the reaction path -- the potential energy is approximated by

$$V(s, Q_1, Q_2, \dots, Q_{3N-7}) \approx V_0(s) +$$

$$+ \sum_{k=1}^{3N-7} \frac{1}{2} \omega_k(s)^2 Q_k^2, \quad (1)$$

where $V_0(s)$ is the potential on the reaction path and $\{\omega_k(s)\}$ are the normal frequencies for vibration in the hyper-plane orthogonal to the reaction path. The potential is thus approximated as a "harmonic valley" about the reaction path.

The more difficult task is to express the kinetic energy in terms of the coordinates $(s, \{Q_k\})$ and their conjugate momenta $(p_s, \{P_k\})$, $k = 1, \dots, 3N-7$. We have done this, however, and the complete classical Hamiltonian for the case of zero total angular momentum is given by

$$\begin{aligned}
 H(p_s, s, \{P_k, Q_k\}) &= \sum_{k=1}^{3N-7} \left(\frac{1}{2} P_k^2 + \frac{1}{2} \omega_k(s)^2 Q_k^2 \right) + V_0(s) \\
 &+ \frac{\frac{1}{2} [p_s - \sum_{k, k'=1}^{3N-7} Q_k P_{k'} B_{k, k'}(s)]^2}{[1 + \sum_{k=1}^{3N-7} Q_k B_{k, 3N-6}(s)]^2} \quad (2)
 \end{aligned}$$

where the coupling elements $\{B_{k, k'}(s)\}$ are defined explicitly in terms of properties of the reaction path. The coupling elements in the numerator of the last term in Eq. (2) are Coriolis couplings between different vibrational modes k and k' which are induced because the vibrational modes change with s ; i.e., the vibrational modes can wind about the reaction path. The couplings in the denominator are the direct coupling between the vibrational mode k and the reaction coordinate ("mode" 3N-6) which are due to the curvature of the reaction path.

The important point is that all of the quantities necessary to determine the Hamiltonian in Eq. (2) -- $V_0(s)$, $\{\omega_k(s)\}$, and $\{B_{k, k'}(s)\}$ -- are generated by a relatively modest number ($\sim 10^2$) of calculations of the potential surface. With this Hamiltonian one can then begin to describe the dynamics of the reacting system. One may wish to compute the full classical trajectories of the system from this Hamiltonian, or simpler dynamical models may be investigated. For example, since some vibrational modes will be only weakly coupled to the reaction coordinate, one expects that the oscillator part of the Hamiltonian can be partitioned into "active" and "passive" modes, and the passive modes effectively eliminated from the problem.

Some applications of this reaction path Hamiltonian to tunneling effects through the saddle point region of the potential surface have already been made, with encouraging results, and this and other applications are being pursued.

* * *

[†]Brief version of J. Chem. Phys. 72, 99 (1980).

[‡]Sabbatical visitor. Present address: Department of Physical Chemistry, University Chemical Laboratories, Cambridge, England.

4. UNIFIED MODEL FOR DIFFRACTIVE AND INELASTIC SCATTERING OF A LIGHT ATOM FROM A SOLID SURFACE[†]

J. E. Adams and W. H. Miller

Scattering of gas atoms from solid surfaces is usually described as either (1) scattering from a rigid periodic surface, whereby diffraction is the process of interest, or (2) scattering from a flat but moveable surface, whereby energy transfer between the gas atom and the surface is of interest. Our motivation in this work is to construct a theoretical model capable of describing both diffraction and energy transfer in a single unified framework but one also simple enough to allow an essentially analytic solution.

The theoretical model which accomplishes this is the sudden approximation. The quantity of interest is the intensity $I(\Delta E, \vec{k}_f \leftarrow \vec{k}_i)$ for the gas atom being scattered from the initial wavevector (or momentum) \vec{k}_i to final wavevector \vec{k}_f , with a change of energy $\Delta E \equiv \hbar^2 k_f^2 / 2m - \hbar^2 k_i^2 / 2m$. The formally exact expression for I is

$$\begin{aligned}
 I(\Delta E, \vec{k}_f \leftarrow \vec{k}_i) &= \sum_{\vec{n}_2, \vec{n}_1} \frac{e^{-\beta \epsilon_{\vec{n}_1}}}{Q} \\
 &+ \delta(\Delta E + \epsilon_{\vec{n}_2} - \epsilon_{\vec{n}_1}) |S_{\vec{k}_f \vec{n}_2, \vec{k}_i \vec{n}_1}^{\vec{n}_2 \vec{n}_1}|^2 \quad (1)
 \end{aligned}$$

where \vec{n} refers to all the phonon quantum numbers of the surface atoms and S is the S-matrix for the scattering process. Within the sudden approximation, and also assuming a one-dimensional surface for notational simplicity, S is given by

$$\begin{aligned}
 S_{\vec{k}_f \vec{n}_2 \leftarrow \vec{k}_i \vec{n}_1}^{\vec{n}_2 \vec{n}_1} &= \int_{-\infty}^{\infty} dx \int dq \phi_{\vec{n}_2}(q)^* \phi_{\vec{n}_1}(q) \\
 &+ \frac{-i\Delta k_x}{e} \frac{-i\Delta k_z}{e} Z(x; q) \quad (2)
 \end{aligned}$$

where $\phi_{\vec{n}}$ are the oscillator wavefunctions of the phonons and $Z(x; q)$ is the surface contour (which depends not only on x , the distance along the surface, but also on the configuration of the surface atoms). $Z(x; q)$ is in general energy dependent since it is the root of the equation

$$V(x, z, q) = E \quad (3)$$

where V is the interaction potential between the surface and gas atoms.

If the surface contour $Z(x; q)$ is linearized in the phonon coordinates q , then after considerable manipulations the scattering intensity can be expressed as

$$\begin{aligned}
I(\Delta E, \vec{k}_f \leftarrow \vec{k}_i) &= (2\pi\hbar)^{-1} \int_{-\infty}^{\infty} dt e^{-i\Delta E t/\hbar} \int dx \int dx' \\
&+ e^{-i\Delta k_x(x-x')} \\
&\times e^{-i\Delta k_z[Z(x)-Z(x')]} C(x, x'; t), \quad (4)
\end{aligned}$$

where $Z(x) \equiv Z(x;0)$ is the undistorted surface contour, and the coordinate-dependent correlation function C is given by

$$C(x, x'; t) = \exp[-W(x) - W(x') + \Delta W(x, x'; t)] \quad , \quad (5)$$

where $W(x)$ is a coordinate-dependent Debye-Waller factor,

$$W(x) = \frac{1}{2} \Delta k_z^2 \sum_j \langle q_j^2 \rangle \zeta_j(x)^2 \quad (6)$$

$$\zeta_j(x) = \left. \frac{\partial Z(x; q)}{\partial q_j} \right|_{q=0} \quad , \quad (7)$$

and ΔW the non-separable term

$$\begin{aligned}
\Delta W(x, x'; t) &= \Delta k_z^2 \sum_j \langle q_j^2 \rangle \zeta_j(x) \zeta_j(x') \\
&+ [\cos(\omega_j t) - i \tanh\left(\frac{\hbar\omega_j\beta}{2}\right) \sin(\omega_j t)] \quad . \quad (8)
\end{aligned}$$

It is the time-dependence of ΔW that gives rise to inelastic processes. This is easy to see by expanding the exponential factor in Eq. (5) which involves ΔW :

$$e^{\Delta W} \approx 1 + \Delta W + \frac{1}{2} \Delta W^2 + \dots \quad . \quad (9)$$

The intensity is then a sum of terms related to the power of ΔW in the expansion:

$$I(\Delta E, \vec{k}_f \leftarrow \vec{k}_i) = I_0 + I_1 + I_2 + \dots \quad . \quad (10)$$

I_0 is elastic scattering, and one can show that it becomes

$$I_0 = Na^2 \delta(\Delta E) \sum_{\ell} \delta\left(\ell - \frac{\Delta k_x a}{2\pi}\right) P_{\ell} \quad , \quad (11)$$

where N is the number of surface atoms, and P_{ℓ} is the probability of diffraction of order ℓ , including the Debye-Waller factor:

$$P_{\ell} = \left| \frac{1}{a} \int_0^a dx e^{-W(x)} e^{-i\Delta k_x x} e^{-i\Delta k_z Z(x)} \right|^2 \quad . \quad (12)$$

I_1 is the contribution from 1-phonon processes, I_2 that from 2-phonon processes, etc.

By assuming the particular potential model,

$$V(x, z, \underline{q}) = V_0 \sum_j e^{-\alpha(x-x_j)^2} e^{-\gamma(z-z_j)} \quad , \quad (13)$$

where $(x_j, z_j) \equiv q_j$ are the instantaneous positions of the surface atoms, we are able to obtain simple explicit expressions for the elastic (diffractive) and inelastic scattering. The elastic scattering is given by Eq. (11) with

$$P_{\ell} = e^{-2\bar{W}} J_{\ell}(\lambda)^2 \quad , \quad (14)$$

where J_{ℓ} is the usual Bessel function, and

$$\bar{W} = \frac{a\sqrt{\alpha}}{4\pi} \Delta k_z^2 \langle q_z^2 \rangle \quad (15)$$

$$\lambda = \frac{2\Delta k_z}{\gamma} e^{-\pi^2/\alpha a^2} \quad , \quad (16)$$

and the 1-phonon contribution to the inelastic scattering is

$$\begin{aligned}
I_1 &= Na^2 \left\{ \delta(\Delta E - \hbar\omega_z) \left[1 - \tanh\left(\frac{\hbar\omega_z\beta}{2}\right) \right] \right. \\
&\quad \left. + \delta(\Delta E + \hbar\omega_z) \left[1 + \tanh\left(\frac{\hbar\omega_z\beta}{2}\right) \right] \right\} \\
&\times \frac{1}{2} \Delta k_z^2 \langle q_z^2 \rangle \sum_{\ell} P_{\ell} e^{-\frac{2\pi^2}{\alpha a} \left(\ell - \frac{\Delta k_x a}{2\pi} \right)^2} \quad . \quad (17)
\end{aligned}$$

The basic result, therefore, is elastic diffraction, which produces delta-function peaks whenever Δk_x is equal to a reciprocal lattice vector, although the intensities of these peaks are attenuated by Debye-Waller factors. This structure is augmented by inelastic lobes on either side of a diffraction peak, the "line shape" of these lobes being gaussian about the values of Δk_x determined by the diffraction condition. Note that the relative

magnitude of I_1 to I_0 , $1/2 \Delta k_z^2 \langle q_z^2 \rangle$, and the width parameter of the gaussian line shape of I_1 , $2\pi^2/\alpha a^2$, can be combined to extract the Debye-Waller factor of Eq. (15).

* * *

†Brief version of Surface Sci. 85, 77 (1979).

5. ON THE QUANTUM MECHANICAL IMPLICATIONS OF CLASSICAL ERGODICITY†

R. M. Stratt, N. C. Handy and W. H. Miller

For some time it has been recognized that classical mechanics permits what is essentially ergodic-like behavior in systems with just a few degrees of freedom. Thus it is possible to understand, classically at least, how purely deterministic dynamics can lead to statistical behavior. It has not been clear, however, how this classical behavior will manifest it quantum mechanically. This paper has considered several ways of characterizing quantum systems with regard to their regular (i.e., separable-like) or ergodic behavior.

One of the most revealing of these methods of characterization is the nodal structure of the wavefunction. The model Hamiltonian considered is that of two coupled anharmonic oscillators, the Casati-Ford Hamiltonian,

$$H(p_x, p_y, x, y) = \frac{p_x^2}{2m_x} + \frac{p_y^2}{2m_y} + e^{-x} + e^y + e^{x-y}, \quad (1)$$

which for small x and y is harmonic about $x = y = 0$. For $m_x = m_y$ the system is rigorously separable and thus has regular, intersecting nodal lines. For

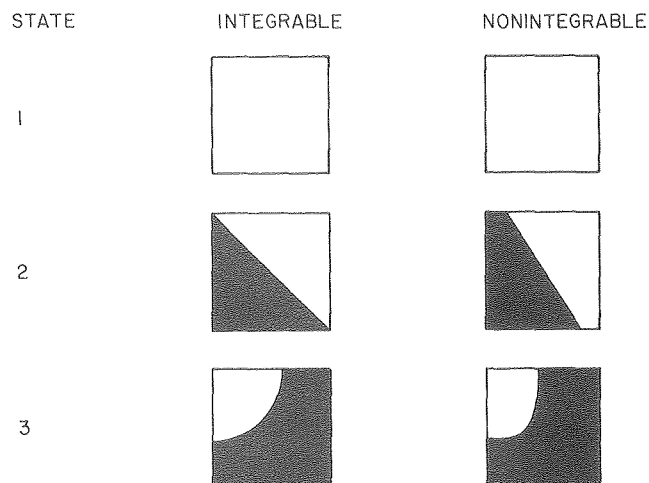


Fig. 1. Nodal plots of eigenstates 1, 2, and 3 of the Casati-Ford Hamiltonian with equal masses (classically integrable) and with unequal masses (nonintegrable). The square boundary is arbitrary. (XBL 795-9725)

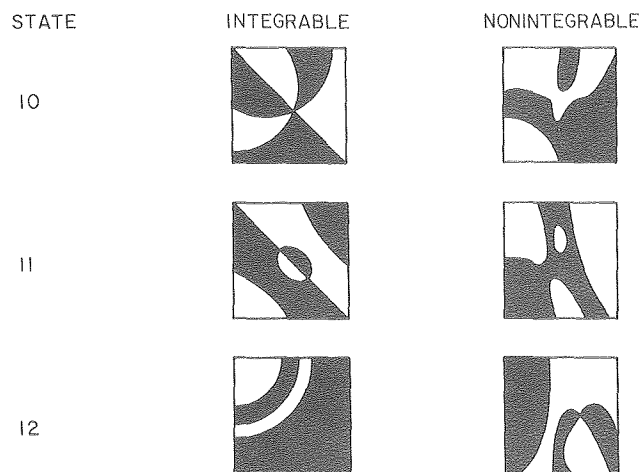


Fig. 2. Nodal plots of Casati-Ford eigenstates 10, 11, and 12. (XBL 795-9728)

$m_x \neq m_y$, however, the system is non-separable and the nodal structure need not remain intact. Nevertheless, for some states the nodal structure does remain intact, with only distortions, even for the non-separable case $m_x \neq m_y$. Figure 1 shows some examples of these. States with higher energy, however, do show the expected break-up of nodal structures for the case $m_x \neq m_y$, cf. Fig. 2. Furthermore, the energy at which the nodal structure appears to change most significantly is roughly the same as the energy at which the classical mechanics changes from regular to ergodic.

Characterization of states by their nodal structure thus gives a picture that is qualitatively consistent with the character of the classical mechanics of the system. Other methods of characterization which were explored were a natural orbital analysis of the wavefunctions and calculation of the power spectrum (the Fourier transformation of the dipole correlation function), and these lead to similar correspondences between the classical and quantum character. It appears, therefore, that the quantum mechanics of systems of coupled oscillators does parrot the classical mechanics with regard to regular or ergodic character.

* * *

†Brief version of J. Chem. Phys. 71, 3311 (1979).

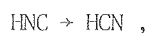
RESEARCH PLANS FOR CALENDAR YEAR 1980

Tunneling Corrections to Microcanonical Rate Constants. The discussion in article 2 above suggests that tunneling may be a significant feature in the unimolecular decomposition of formaldehyde under collisionless conditions. The theoretical model used for these calculations, however, is rather primitive; to draw more quantitatively reliable conclusions one needs to treat the tunneling dynamics more accurately.

The reaction path Hamiltonian model described in article 3 above provides a way to do this. It has

already been possible to construct a more rigorous (and accurate) vibrationally adiabatic approximation using this approach, and even more dynamically accurate models are possible.

Plans are first to test the new theoretical models on the simpler reaction



for which Professor H. F. Schaefer and associates are carrying out the quantum chemistry calculations to provide the quantities necessary for constructing the reaction path Hamiltonian. Because the reaction primarily involves motion of a hydrogen atom, tunneling corrections should be significant.

Studies of Mode-Specificity in Reaction Dynamics. There is much interest nowadays in the question of whether mode-specific laser excitation of molecules will cause mode-specific chemical reactions. For example, to what extent does the rate of a unimolecular reaction depend on the specific mode of the molecule that is excited. With regard to the reaction $\text{HNC} \rightarrow \text{HCN}$ mentioned above, the question would be how the rate of isomerization depends on the mode of HNC that is initially excited.

It is also possible to approach this question using the reaction path Hamiltonian discussed in article 3. Most rigorously, one can compute (numerically) classical trajectories with this Hamiltonian, but it is also possible to construct simpler dynamical models based on this form of Hamiltonian.

Using the reaction path Hamiltonian, therefore, it is possible to address many aspects of the dynamics of polyatomic systems.

Classical Models of Electronic Degrees of Freedom. There are still some interesting theoretical questions to be explored regarding the classical models for electronic degrees of freedom discussed in article 1. Already, though, this approach is a powerful one that can be usefully applied to a variety of nonadiabatic collision processes. Work in both directions is planned.

1979 PUBLICATIONS AND REPORTS

Refereed Journals

- [†]1. A. D. Isaacson and W. H. Miller, "Calculation of Siegert Eigenvalues for Molecular Systems: Results for $\text{He}(2^1, 3\text{S}) + \text{H}_2$," *Chem. Phys. Lett.* 62, 374 (1979), LBL-8067.
- [†]2. A. E. Orel and W. H. Miller, "Infrared Laser Enhancement of Chemical Reactions via Collision Induced Absorption," *J. Chem. Phys.* 70, 4393 (1979), LBL-8575.
- [†]3. J. E. Adams and W. H. Miller, "On Expansion of Exchange Kernels for Reactive Scattering," *J. Phys. Chem.* 83, 1505 (1979), LBL-8086.

- [†]4. C. W. McCurdy, H. D. Meyer, and W. H. Miller, "Classical Model for Electronic Degrees of Freedom in Non-Adiabatic Collision Processes: Pseudo-Potential Analysis and Calculations for $\text{F}(2\text{P}_{1/2}) + \text{H}^+$, $\text{Xe} \rightarrow \text{F}(2\text{P}_{3/2}) + \text{H}^+$, Xe ," *J. Chem. Phys.* 70, 3177 (1979), LBL-8425.

- [†]5. H. D. Meyer and W. H. Miller, "A Classical Analog for Electronic Degrees of Freedom in Non-Adiabatic Collision Processes," *J. Chem. Phys.* 70, 3214 (1979), LBL-8282.

- [†]6. A. D. Brandrauk and W. H. Miller, "Analysis of the Generalized Stueckelberg Method of Non-Adiabatic Transitions," *Mol. Phys.* 38, 1893 (1979).

7. W. H. Miller, "On the Periodic Orbit Description of Tunneling in Symmetric and Asymmetric Double-Well Potential," *J. Phys. Chem.* 83, 960 (1979), LBL-8255

8. J. E. Adams and W. H. Miller, "A Unified Model for Diffractive and Inelastic Scattering of a Light Atom from a Solid Surface," *Surface Sci.* 85, 77 (1979), LBL-8691.

- [†]9. W. H. Miller, "Tunneling Corrections to Unimolecular Rate Constants, with Application to Formaldehyde," *J. Chem. Soc.* 101, 6810 (1979), LBL-8649.

- [†]10. H. D. Meyer and W. H. Miller, "Classical Models for Electronic Degrees of Freedom: Derivation via Spin Analogy and Application to $\text{F}^* + \text{H}_2 \rightarrow \text{F} + \text{H}_2$," *J. Chem. Phys.* 71, 2156 (1979), LBL-9087.

- [†]11. R. M. Stratt, N. C. Handy, and W. H. Miller, "On the Quantum Mechanical Implications of Classical Ergodicity," *J. Chem. Phys.* 71, 3311 (1979), LBL-9197.

- [†]12. R. M. Stratt, "Semiclassical Statistical Mechanics of Hard Wall Potentials via the Transformed Potential Approach," *J. Chem. Phys.* 70, 187 (1979); LBL-8084.

- [†]13. R. M. Stratt, "Semiclassical Statistical Mechanics of Fluids: Non-Perturbative Incorporation of Quantum Effects in Classical Many Body Models," *J. Chem. Phys.* 70, 3630 (1979); LBL-8478.

Other Publications

- [†]1. A. E. Orel and W. H. Miller, "Infrared Laser Induced Chemical Reactions; Calculations for $\text{X} + \text{H}_2 \rightarrow \text{HX} + \text{H}$," in Rarefied Gas Dynamics, ed. R. Campargue. Commissariat a L'Energie Atomique, Paris, 1979, p. 1061, LBL-8256.

LBL Reports

- [†]1. R. M. Stratt, "Semiclassical Statistical Mechanics," (Ph.D. thesis), LBL-9095.
2. J. E. Adams, "Topics in Bound-State and Dynamical Processes: Semiclassical Eigenvalues, Reactive Scattering Kernels and Gas-Surface Scattering Models," (Ph.D. thesis), LBL-9196.

Invited Talks

1. William H. Miller, "Recent Advances in the Semiclassical Theory of Electronically Non-Adiabatic Processes," ACS National Meeting, Honolulu, April 1-6, 1979.
2. William H. Miller, "Recent Progress in the Semiclassical Theory of Adiabatic Non-Adiabatic Collision Processes," International Symposium on Reaction Dynamics and Energy Transfer in Systems with Many Accessible States, Munich, March 26-30, 1979.
3. William H. Miller, "Classical Models for Electronically Non-Adiabatic Collision Processes," Sherwin-Williams Lecture, University of Illinois, Urbana, May 8, 1979.
4. William H. Miller, "Semiclassical Scattering Theory," Invited Lecture Series, Department of Theoretical Chemistry, University of Sydney, Australia, July 1979.
5. William H. Miller, "Semiclassical Theory of Molecular Collision Processes," Invited Lecture Series (five lectures), Institute of Chemical Physics, Chinese Academy of Sciences, Dalian, China, August 6-10, 1979.
6. William H. Miller, "Laser Enhancement of Chemical Reactions," Symposium on Atomic and Molecular Science, Taipei, Taiwan, August 23-25, 1979.

* * *

[†]All calculations were carried out on a Harris Slash Four minicomputer funded by a National Science Foundation Grant CHE-7622621.

g. Photoelectron Spectroscopy*

David A. Shirley, Investigator

Introduction. The main research theme in this program is electron spectroscopy, with emphasis on spectroscopic studies based on synchrotron radiation research in the 6-4000 eV range, supported by research with laboratory sources. Emphasis is given to new types of experiments, based on new effects. The projects completed in 1979 are naturally divided into two groups: (a) solid-state and surface research, and (b) gas-phase research. These are discussed separately below.

Solid-State and Surface Research

Overview. All of the projects reported below are based on angle-resolved photoemission. Three angular distribution effects are involved. In article 1, condensed-phase photoelectron asymmetry is described for the first time. Photoelectron diffraction, reported in 1978, is extended to molecules (article 2) and to new atomic systems (article 3). The remaining articles (5 through 8) deal with dispersion relations in solids and surfaces, including the first determination of a "complete" valence-band structure of metallic silver (article 6).

1. CONDENSED PHASE PHOTOELECTRON ASYMMETRY: A NEW EFFECT†

R. F. Davis, S. D. Kevan, B.-C. Lu,‡ J. G. Tobin, and D. A. Shirley

Large directional asymmetries were observed in photoelectron distributions from core and valence levels in metals and adsorbate atoms, with incident photon energies in the range $40 \text{ eV} \leq h\nu \leq 252 \text{ eV}$. Intensities varied by factors up to 25 as the angle (α) between \vec{A} (vector potential of the photon field) and \vec{p} (photoelectron momentum) was varied. The energy dependence of asymmetry showed atomic behavior similar to that calculated for free atoms by Manson and coworkers,^{1,2} modified by a tendency for photoemission to occur parallel to \vec{A} .

According to Yang's theorem,³ the general form of the photoelectron angular distribution from a randomly oriented system excited by \vec{A} via a dipole process is

$$\frac{d\sigma(\epsilon)}{d\Omega} = \left(\frac{\sigma(\epsilon)}{4\pi}\right) [1 + \beta(\epsilon)P_2(\cos \alpha)] , \quad (1)$$

where σ is the angle-averaged photoionization cross-section, ϵ is the photoelectron kinetic energy, and $\beta(\epsilon)$ is termed the asymmetry parameter. Equation (1) has been shown to hold for free atoms; extensive calculations of $\beta(\epsilon)$ for free atoms are now available, and a number of measurements have been made with rare-gas samples.¹ The extent to which Eq. (1) may be explicitly applicable to condensed phases is a question that has received little attention, and we have undertaken a comprehensive study to elucidate this important question.

The angular dependence of $d\sigma/d\Omega$ for each system was found to support the $P_2(\cos \alpha)$ form of Eq. (1), but we chose to emphasize the energy dependence of $\beta(\epsilon)$. Figure 1 shows $\sigma(\epsilon)$ and $\beta(\epsilon)$ for the 4s and valence-band (4d) shells of Ag, compared with theoretical values of these parameters for Xe calculated by Kennedy and Manson.² The agreement is remarkable (experimental σ values are on a relative scale). The 4s peak shows near maximum asymmetry--i.e., $\beta = 2$ --as expected from atomic theory on rather general grounds,¹ while the 4d peak shows the distinctive atomic character expected for shells with Cooper minima^{1,4} in their photoionization cross-sections. These measurements, as well as results for Se(3d), Pt(4f), and Ag(4p)

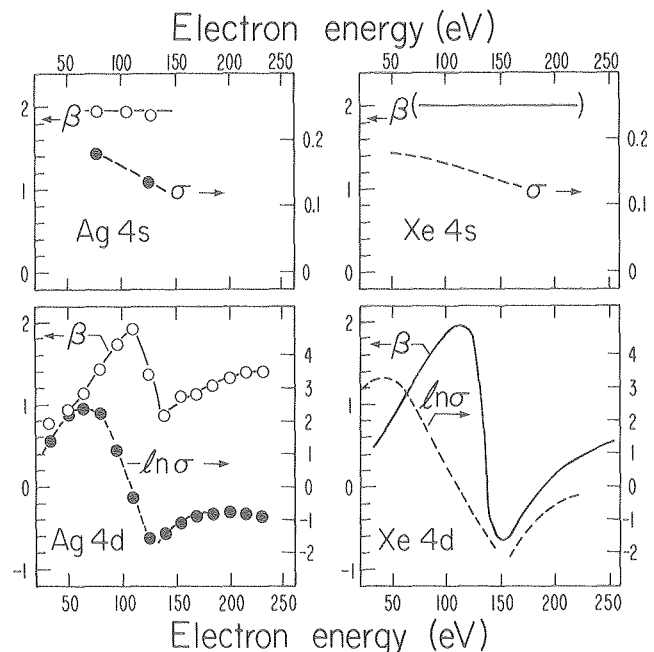


Fig. 1. Cross-section $\sigma(\epsilon)$ and asymmetry parameters $\beta(\epsilon)$ for Ag 4s and 4d peaks (left) compared to theoretical values calculated for Xe by Kennedy and Manson (right). (XBL 797-2104)

*This work was supported by the Division of Chemical Sciences, Office of Basic Energy Sciences, U. S. Department of Energy. All projects except articles 4 and 8 under Solid State and Surface Research, and article 4 under Gas Phase Research were performed at the Stanford Synchrotron Radiation Laboratory, which is supported by the NSF Grant No. DMR 77-27489, in cooperation with the Stanford Linear Accelerator Center.

support our main conclusion that intermediate-energy photoemission in solids shows $\beta(\epsilon)$ behavior with atomic character, modified by a tendency toward higher asymmetry. The latter result is consistent with larger plane-wavelike character in the conduction-band final state.

Aside from its intrinsic interest, this phenomenon has considerable implications for angle-resolved photoemission experiments that make quantitative comparisons of peak intensities, and it should be useful in characterizing orbital symmetries and identifying the origins of photoemission lines.

* * *

[†]Brief version of LBL-9384; submitted for publication in *Chemical Physics Letters*.

[‡]Permanent address: INTEL Corporation, 3065 Bowers Avenue, Santa Clara, CA 95051.

1. Steven T. Manson, *Advances in Electronics and Electron Physics* **41**, 73 (1976); **44**, 1 (1977).

2. D. J. Kennedy and S. T. Manson, *Phys. Rev. A*, **5**, 227 (1972).

3. C. N. Yang, *Phys. Rev.* **74**, 764 (1948).

4. J. W. Cooper, *Phys. Rev. Lett.* **13**, 762 (1964).

2. PHOTOELECTRON DIFFRACTION STUDIES OF CARBON MONOXIDE OVERLAYERS[†]

S. D. Kevan, R. F. Davis, D. H. Rosenblatt, B.-C. Lu,[‡] C. C. Parks, and D. A. Shirley

The application of angle-resolved photoemission to surface structure determination has been the subject of several investigations in the past. Here, we report two new effects that are potentially useful in such studies. Both involve measurements of adsorbate core level differential photoemission cross-sections in the systems CO/Ni(001) and CO/Ni(111).

The first effect is photoelectron diffraction, in which the photoelectron intensity of the carbon or oxygen 1s level is measured normal to the surface as a function of kinetic energy in the range $30 \text{ eV} \leq E_K \leq 200 \text{ eV}$. This range, attainable only with synchrotron radiation, is the LEED range, and diffraction effects due to scattering of the final-state electron off the surface layer are expected. Such effects are easily measurable and have been shown to be interpretable in terms of a particular adsorbate registry with the surface.^{1,2} The advantage of using photoelectron diffraction in molecular systems is first its nondamaging nature and second that the intensity of a particular atom's core level is measured so that a structure determination of that species may be accomplished independently.

Data on the carbon (1s) level in the CO/Ni(001) system are shown in Fig. 1. Also shown are calculations by Tong with the CO positioned in the atop site and d_{CNi}^{\perp} , the interplanar spacing between the outermost nickel and the carbon layers, equal to 1.8 Å. While the agreement in intensities is

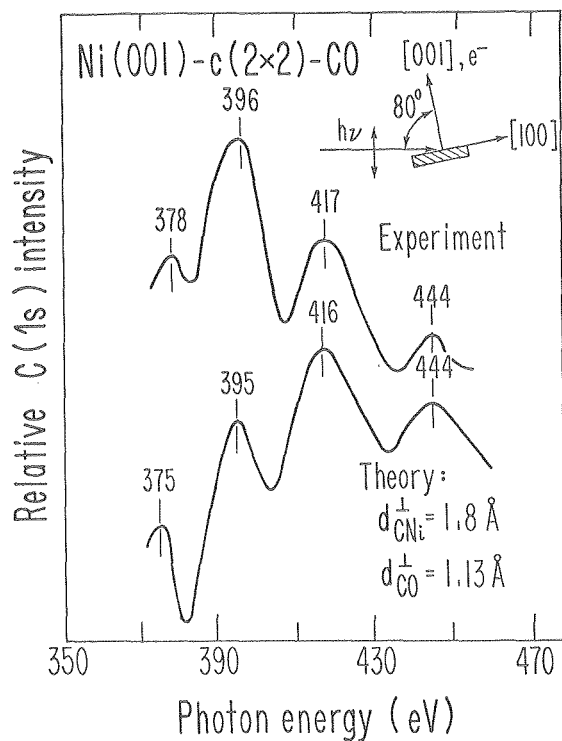


Fig. 1. Cross-section of the C(1s) level in the CO/Ni(001) system. Top: experimental. Bottom: theoretical curve calculated for the d-spacings shown. (XBL 7911-13243A)

fair at best, excellent correspondence of peak energies is observed. Previous results on model systems have shown that such agreement is typical, and that agreement in peak energy positions is sufficient for an accurate structure determination.^{1,2} We conclude, in agreement with previous LEED and ELS studies for similar coverages, that the atop site is populated.

A complete structure determination must await similar data on the O(1s) level. We have accumulated data on both the C(1s) and O(1s) levels in the (2×2)CO/Ni(111) system. These data are shown in Fig. 2. Structure determination is awaiting theoretical treatment.

The second effect that may prove useful in surface structure determination is seen in Fig. 2 as a near-threshold resonance in the C(1s) cross-section. The resonance is clearly not atomic-like, and shows several characteristics very similar to those predicted for a shape resonance for gas phase CO.³ In particular, the variation of the resonance intensity with electron emission and photon polarization angles is significant: the intensity is maximized when the molecular axis, the photon polarization vector, and the outgoing electron momentum are aligned. This is exactly as predicted for the fixed molecule gas-phase differential photoemission cross-section. On the other hand, the resonance energy is higher by ~5 eV than predicted, and in addition a similar

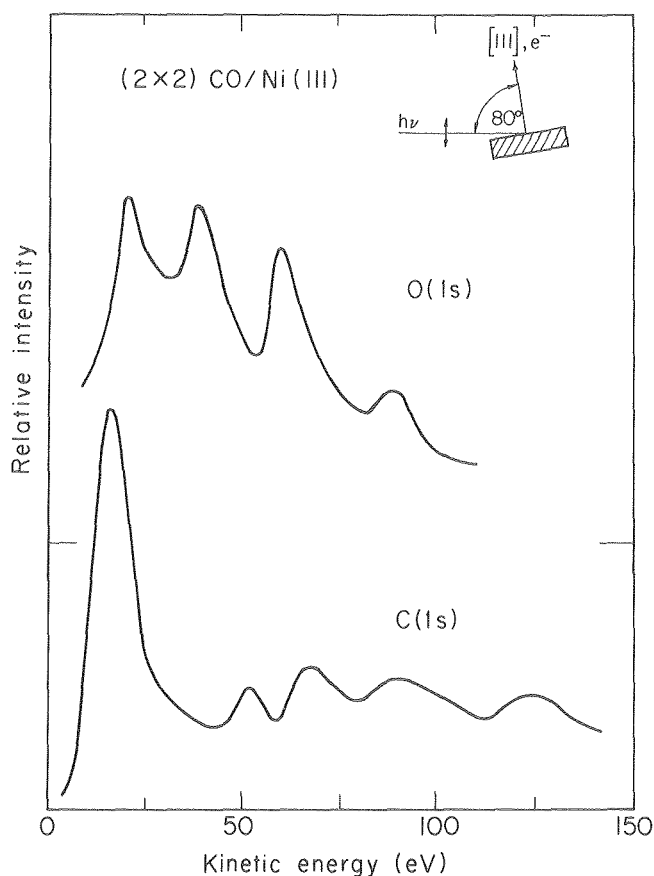


Fig. 2. Cross-section of the C(1s) and O(1s) levels in the CO/Ni(111) system. (XBL 7912-3933)

resonance predicted to exist in the O(1s) cross-section is not observed. We conclude, therefore, that the resonance is closely related to the gas-phase shape resonance, but the presence of the surface does introduce some perturbation. In any case, the sharp angular features should allow interesting experiments to be performed concerning molecular bond axis orientation.

* * *

[†]Brief version of LBL-10024; to be submitted to Physical Review Letters.

[‡]Permanent address: INTEL Corporation, 3065 Bowers Avenue, Santa Clara, CA 95051.

1. S. D. Kevan, D. H. Rosenblatt, D. Denley, B.-C. Lu, and D. A. Shirley, Phys. Rev. Lett. **41**, 1565 (1978).

2. S. D. Kevan, D. H. Rosenblatt, D. Denley, B.-C. Lu, and D. A. Shirley, Phys. Rev. **B20**, 4133 (1979).

3. J. L. Dehmer and Dan Dill, Phys. Rev. Lett. **35**, 213 (1975).

3. PHOTOELECTRON DIFFRACTION MEASUREMENTS OF SULFUR AND SELENIUM ADSORBED ON Ni(001)[†]

S. D. Kevan, D. H. Rosenblatt, D. R. Denley, B.-C. Lu,[‡] and D. A. Shirley

The technique of photoelectron diffraction, which we have recently shown to be capable of determining the structure of adsorbates on metal surfaces,¹ has been utilized to study sulfur and selenium overlayers on Ni(001).² Normal photoelectron diffraction (NPD) is sensitive to adsorbate registry through d_{\perp} , the spacing between the overlayer plane of atoms and the top substrate layer. The mechanism is a two-step process--there is first an atomic-like excitation followed by scattering in the final state that introduces oscillations in the photoelectron intensity as a function of energy. These oscillations are very large and can easily be distinguished from an atomic-like cross-section.

These experiments were done on the 4° branch of Beam Line I at the Stanford Synchrotron Radiation Laboratory. The photoemission intensities of the Se(3d), Ni(3p), and Ni valence band for the p(2x2)Se overlayer on Ni(001) were measured as functions of electron kinetic energy over the range $90 \text{ eV} \leq h\nu \leq 250 \text{ eV}$. The results are shown in Fig. 1. Note that diffraction maxima occur at different energies on each curve. Both adsorbate and substrate levels show large NPD oscillations, including multiple scattering peaks. In addition, the peak positions and intensities of these curves do not seem to depend sensitively on the azimuthal or polar orientation of the photon polarization vector in the photon energy range we have studied.

We have used the NPD curve for the Se(3d) core level to show that the selenium atoms of a p(2x2)Se overlayer lie in the fourfold hollow site on Ni(001) with a d_{\perp} of 1.55 Å. This result was determined from the excellent agreement between the experimental NPD curve and the curve calculated by Li and Tong³ for $d_{\perp} = 1.55 \text{ Å}$, as shown in Fig. 2. Note the similarity of the peak positions of the NPD curves and the LEED (00) I-V curve, although the intensities are quite different. The system c(2x2)S-Ni(001) was also studied, and the sulfur atoms were found to lie in the fourfold hollow site, with a d_{\perp} of 1.3 Å, the same value reported from LEED and other photoemission analyses. As was the case for the Se(3d) level, the S(2p) intensity-kinetic energy curve behaves like an atomic cross-section, modulated by photoelectron diffraction peaks.

NPD can also be used to study disordered adsorbate systems. Disordered, low coverages of selenium on Ni(001) were found to give almost identical NPD curves as the c(2x2) overlayer, as shown in Fig. 3. This result shows that the dominant scattering mechanism in NPD is off the substrate and not the

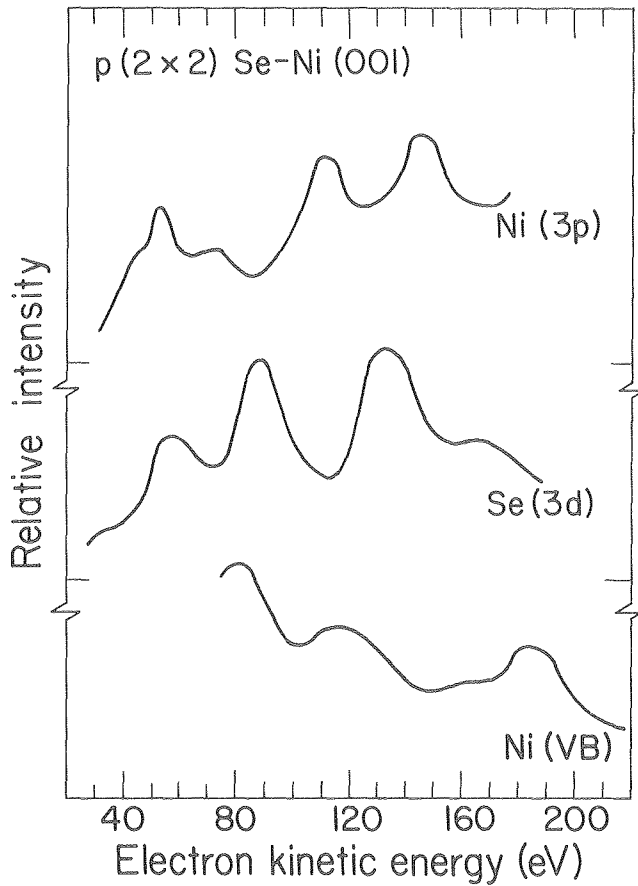


Fig. 1. Normal photoemission intensity versus kinetic energy curves for (a) Ni(3p), (b) Se(3d), (c) Ni valence band (VB) electrons from p(2x2)Se-Ni(001). (XBL 794-1374)

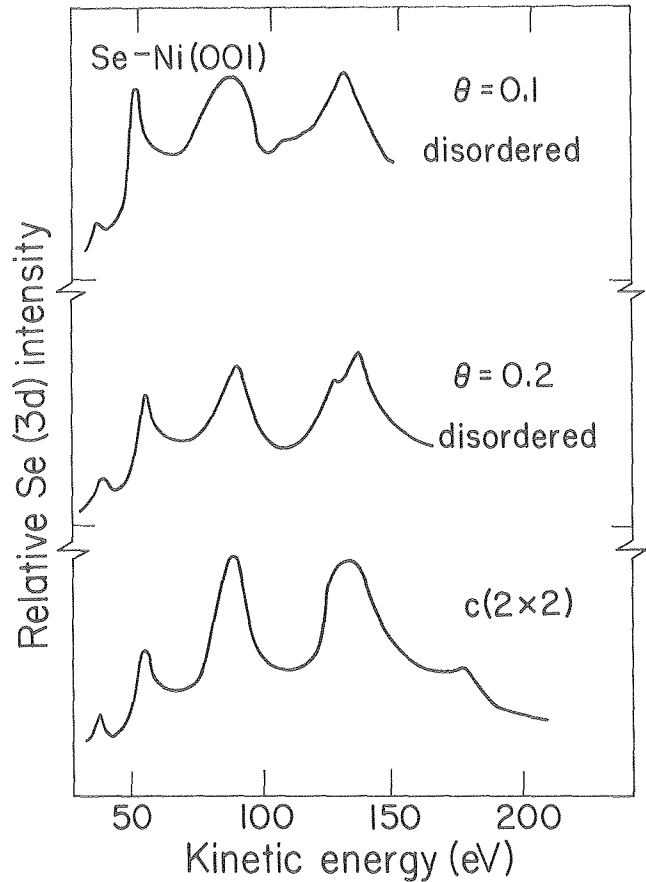
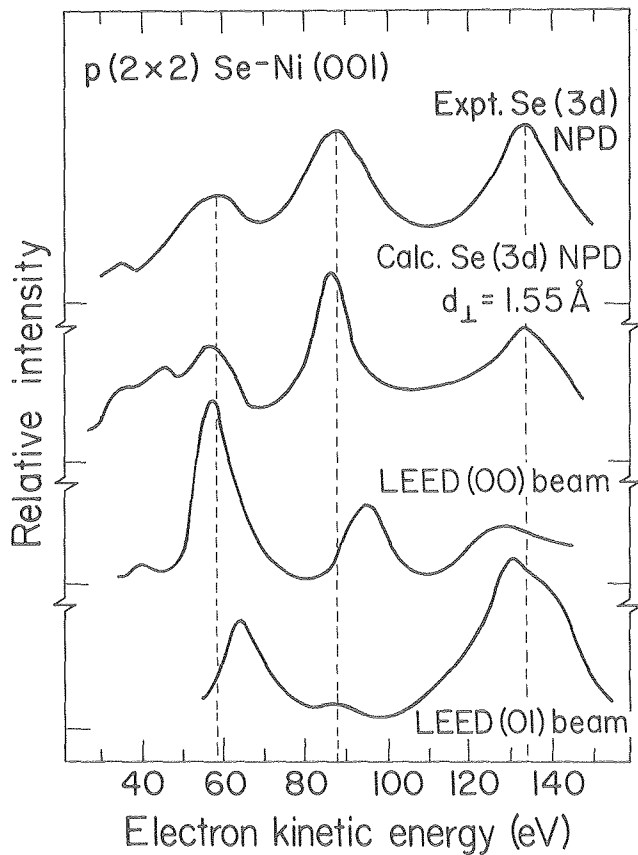


Fig. 3. Comparison of NPD curves for Se(3d) in disordered Se on Ni(001) at 0.1 monolayer, and 0.2 monolayer, with the c(2x2) pattern. (XBL 794-1376)



overlayer itself; otherwise, the effect in the disordered overlayer would not be so large. Off-normal emission studies on ordered overlayers were also carried out. The resulting curves are rich in structure, but the intensity modulations are not nearly as pronounced off-normal as they are at normal emission. Careful theoretical analysis will be required to determine the extent to which these curves can provide structural information.

Fig. 2. NPD curve for Se(3d) electrons from p(2x2)Se-Ni(001), compared with theoretical curve by Li and Tong, and LEED-beam curves by Demuth and Rhodin (Ref. 4). (XBL 794-1373)

† Brief version of LBL-9024; published in Phys. Rev. B 20, 4133 (1979).

‡ Permanent address: INTEL Corporation, 3065 Bowers Avenue, Santa Clara, CA 95051.

1. S. D. Kevan, D. H. Rosenblatt, D. R. Denley, B.-C. Lu, and D. A. Shirley, Phys. Rev. Lett. 41, 1565 (1978).

2. S. D. Kevan, D. H. Rosenblatt, D. R. Denley, B.-C. Lu, and D. A. Shirley, Phys. Rev. B20, 4133 (1979).

3. C. H. Li and S. Y. Tong, Phys. Rev. Lett. 42, 901 (1979).

4. J. E. Demuth and T. N. Rhodin, Surf. Sci. 45, 249 (1974).

4. HIGH-RESOLUTION PHOTOEMISSION STUDY OF THE COPPER (100) SURFACE STATE†

S. D. Kevan and D. A. Shirley

Angle-resolved photoemission (ARP) is the technique of choice for studying the surface electronic structure of materials. Of particular interest in the last few years has been the investigation of occupied states localized at clean metal and semiconductor surfaces. Such a state has been observed on Cu(001) near the \bar{M} point of the two-dimensional Brillouin zone at an energy slightly above the d-bands.¹ We have undertaken high angular and energy resolution studies of this state with the intent of producing a more complete characterization than has been done previously.

The fact that the state lies above the d-bands means that the final-state hole lifetime will be quite long, since there are few occupied electron states with energies greater than the surface state. This in turn means that the peak width is quite small by photoemission standards (≤ 60 meV) and accurate studies relevant to both surface-state character and the photoemission process in general are possible.

An important aspect of any electron state is its symmetry, since a knowledge of that parameter yields information concerning orbital character. Using polarized HeI radiation, we have shown that the surface state has odd symmetry with respect to the (100) mirror plane.² This is consistent with a d_{xy} atomic orbital character as hypothesized in the earlier study.

A surface state will in general possess two-dimensional dispersion relations. By changing k_{\parallel} , the component of the outgoing electrons's momentum parallel to the surface, we can determine these $E(k_{\parallel})$ dispersion relations. We have done so for this state along part of the $\bar{\Gamma} \rightarrow \bar{M} \rightarrow \bar{\Gamma}$ line, and the result is shown in Fig. 1. A roughly parabolic curve is seen, symmetric about $k_{\parallel} = 1.74 \text{ \AA}^{-1}$, which is the \bar{M} point. Figure 2 shows the experimental peak width $\Gamma(k_{\parallel})$, which is inversely proportional to photoelectron and hole lifetimes. A model based on several simple assumptions yields the relation

$$\Gamma(k_{\parallel}) \propto \beta(E_0 - E) + \gamma,$$

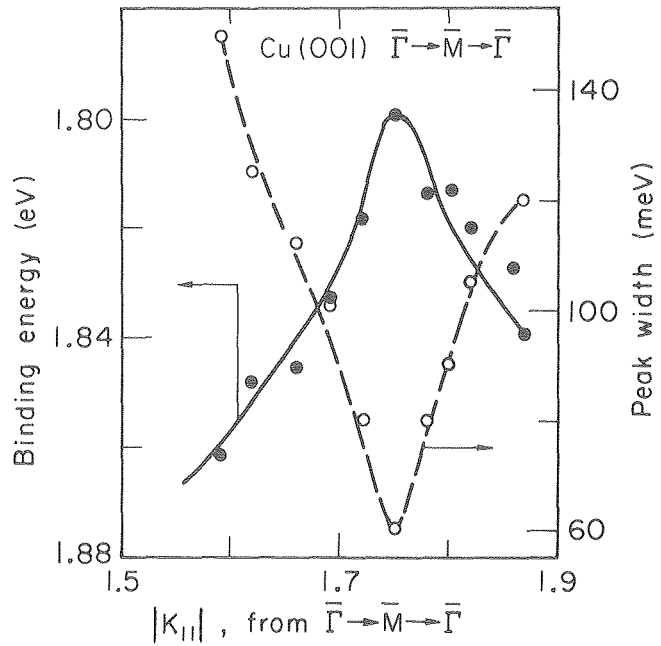


Fig. 1. Experimental dispersion relations and peak widths for the surface state near the \bar{M} point. $(k_{\parallel}) = 1.74 \text{ \AA}^{-1}$ for initial states at the \bar{M} point. (XBL 7912-3929)

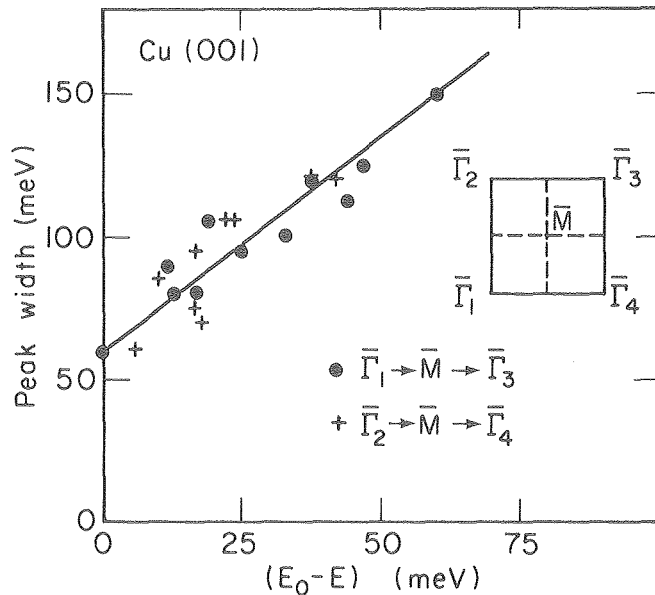


Fig. 2. Variation of the surface-state peak width with initial energy. (XBL 7912-3928)

where β and γ are constants and E_0 is the energy of the surface state at \bar{M} .² A plot of $\Gamma(k_{\parallel})$ against $(E_0 - E)$, shown in Fig. 2, is seen to be roughly linear.

The final result of interest is the temperature dependence of the surface-state intensity. In Fig. 3 we show photoemission spectra taken with

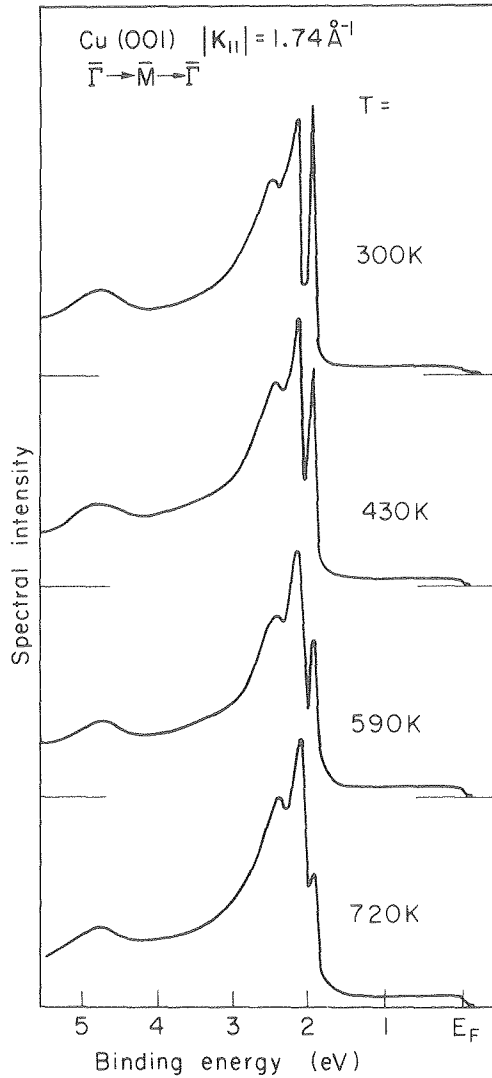


Fig. 3. High resolution AREDCs of Cu(001) for initial states at the \bar{M} point at various temperatures. Note dramatic decrease in surface-state intensity at high temperatures. (XBL 7912-3934)

$\bar{k}_{||}$ at the \bar{M} point for various temperatures. The surface state is unusually sensitive to temperature. The effect is much larger than a Debye-Waller or lattice expansion effect and also of the wrong functional form. We hypothesize that the higher energy surface phonon modes produce enough disruption of the local order to destroy the surface state itself.

* * *

[†]Brief version of LBL-10025; to be submitted to Physical Review B.

1. P. Heimann, J. Hermanson, H. Miosga, and H. Neddermeyer, Phys. Rev. Letters **42**, 1782 (1979).
2. S. D. Kevan and D. A. Shirley, submitted for publication in Physical Review B.

5. ANGLE-RESOLVED PHOTOEMISSION DETERMINATION OF A-LINE VALENCE BANDS IN Pt AND Au USING SYNCHROTRON RADIATION[†]

K. A. Mills,[‡] R. F. Davis, S. D. Kevan, G. Thornton,[§] and D. A. Shirley

For the 3d and 4d transition metals, variable photon energy angle-resolved photoemission (ARP) studies have shown that accurate and detailed information about valence bands may be obtained within the framework of the direct-transition model (DTM).¹ The extension of such investigations to the 5d metals is therefore of great importance.

We have studied Pt(111) and Au(111) faces in the photon energy range $6 \text{ eV} \leq h\nu \leq 34 \text{ eV}$. Clean crystal surfaces were prepared in situ by standard ion-sputtering and annealing techniques; impurity levels were monitored by Auger spectroscopy and were negligible throughout the experiments. The Pt photoemission spectra were recorded using a hemispherical analyzer,² and a cylindrical mirror analyzer was used for the Au spectra.³

Selected spectra for Au(111) are shown in Fig. 1. Most of the features could be assigned to direct

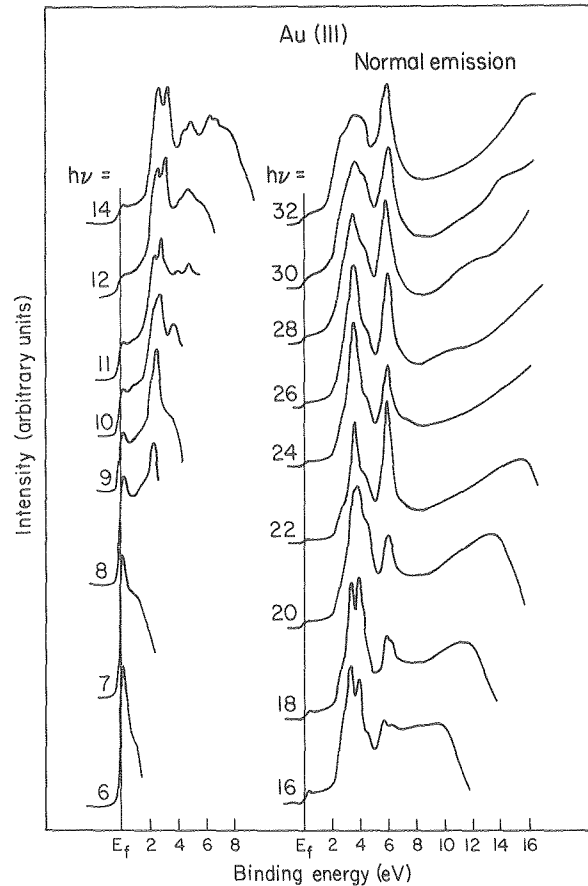


Fig. 1. Selected spectra for normal emission from Au(111) in the photon energy range $6 \text{ eV} \leq h\nu \leq 33 \text{ eV}$. (XBL 797-2111)

transitions for both Pt and Au. Using a quasi-free-electron fit to the Au (RAPW) theoretical conduction levels⁴ as the final states, we were able to determine empirical dispersion relations along Λ for both metals, as summarized in Figs. 2 and 3. Unlike the case of the 3d and 4d metals, substantial disagreement is observed between the theoretical and experimental valence bands, indicating that further theoretical work is needed for these more complicated elements.

Several other features were observed and assigned. The Pt(111) peak intensities were strongly (light) polarization dependent, and when combined with group theoretical selection rules⁵ these results indicated that the band symmetries are: Λ_6 for bands 3, 5, and 7, and Λ_{4+5} for bands 2, 4, and 6. From the experimental band splitting at Γ , ligand field parameters were derived: $\xi(5d) = 0.71 \pm 0.05$ eV (Au), 0.66 ± 0.05 eV (Pt); $10Dq = 1.22 \pm 0.05$ eV (Au), 1.78 ± 0.05 eV (Pt). We investigated the effect of cooling Au to 150 K, and found a significant enhancement of the spectral features over background. This is interpreted as arising from an attenuation of both thermal-diffuse and phonon-assisted scattering processes. In addition, peak-intensity resonances were observed in both materials; they may be explained as being caused by the mixing of f-wave character into the final states near the center of the Brillouin zone. From the energy maxima of these resonances, we determined the position of band 7 near Γ : $E_7(\Gamma) = 16.6$ eV (Pt), 16.4 eV (Au).

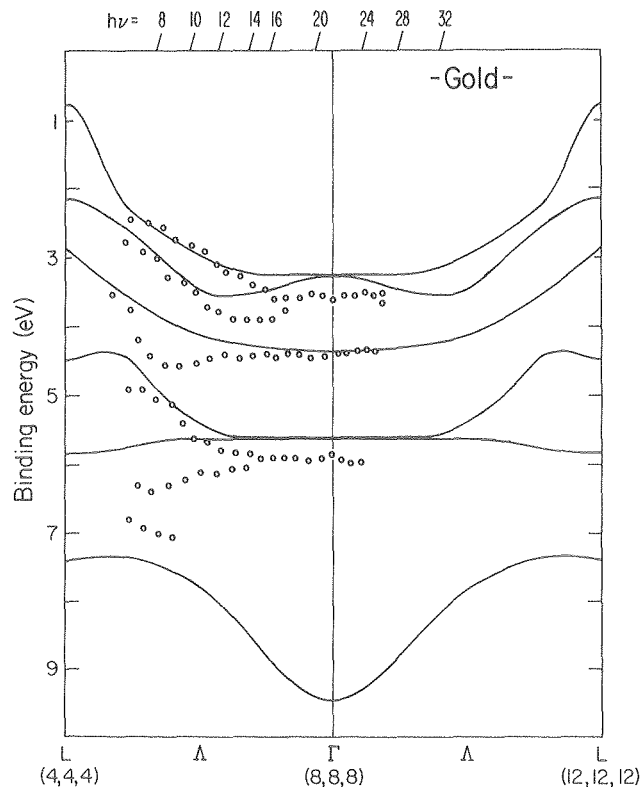


Fig. 2. Empirical (circles) and theoretical (lines, Ref. 4) valence bands for Au along Λ . (XBL 797-2117)

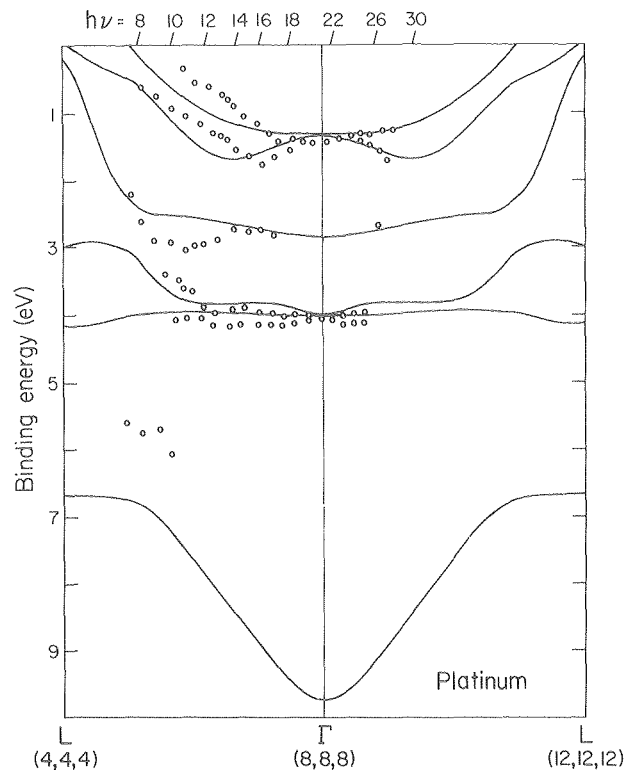


Fig. 3. Empirical (circles) and theoretical (lines, Ref. 6) valence bands for Pt along Λ . (XBL 797-2109)

These studies show that the direct-transition model may be extended to the 5d metals over a wide range of photon energies. They also demonstrate that the use of quasi-free-electron final states to determine the empirical dispersion relations from ARP data is justified, and that the experimentally derived valence bands are sufficiently precise to enable the critical evaluation of theoretical band calculations.

* * *

[†]Brief version of LBL-9430; submitted for publication in Physical Review B.

[‡]Permanent address: Hewlett-Packard Company, Palo Alto, CA 94304.

[§]Permanent address: Department of Chemistry, University of Manchester, Manchester M13-9PL, England.

1. J. Stöhr, P. S. Wehner, R. S. Williams, G. Apai, and D. A. Shirley, Phys. Rev. **B17**, 587 (1978); and P. S. Wehner, R. S. Williams, S. D. Kevan, D. Denley, and D. A. Shirley, Phys. Rev. **B19**, 6164 (1979).

2. This apparatus is described in LBL-10025, by S. D. Kevan and D. A. Shirley.

3. P. S. Wehner, Ph.D. thesis, University of California, Berkeley, LBL-7622, 1978; the angular acceptance of the analyzer was reduced to $\pm 2.5^\circ$.

4. N. E. Christensen and B. O. Seraphim, Phys. Rev. **B4**, 3321 (1971).

5. G. Dresselhaus, Phys. Rev. **100**, 580 (1955).

6. O. K. Anderson, Phys. Rev. **B2**, 883 (1970).

6. INVESTIGATION OF THE VALENCE-BAND STRUCTURE ALONG Δ , Σ , AND Σ' IN Ag USING ANGLE-RESOLVED PHOTOEMISSION[†]

K. A. Mills,[‡] R. F. Davis, G. Thornton,[§] R. Watson,^{||} and D. A. Shirley

Recently, we studied the valence bands of silver along Λ using angle-resolved photoemission (ARP) and synchrotron radiation.¹ Employing the direct-transition model in the data analysis, excellent agreement was found between the experimentally derived and theoretical dispersion relations. The extension of these studies to the other high-symmetry directions in Ag is thus both timely and important.

We investigated Ag(100) and Ag(110) faces in the photon energy ranges $11 \text{ eV} \leq h\nu \leq 34 \text{ eV}$ and $6 \text{ eV} \leq h\nu \leq 34 \text{ eV}$, respectively, using an apparatus described previously.² Selected spectra are shown for Ag(110) in Fig. 1. For both faces, most of the peaks are associated with primary-cone direct transitions. For Ag(110), a surface state is observed with low ($h\nu \leq 10 \text{ eV}$) photon energies; in addition, there is considerable structure near the Fermi level (E_F) for $h\nu \geq 30 \text{ eV}$ which cannot be assigned at this time, but may include peaks due to direct transitions from band 6.

To determine experimental valence band dispersion relations along Σ , Σ' , and Δ using these data, we used the direct-transition model in conjunction with a quasi-free-electron final-state dispersion relation. The agreement of the experimental curves with the theoretical RAPW valence bands calculated by Christensen³ is extremely good. In conjunction with our previous Λ direction data, these new results allow us to present the entire high-symmetry empirical band structure for silver in Fig. 2.

Two additional aspects of this work are particularly noteworthy. First, it clearly shows that experimental band dispersion occurs for photon energies corresponding to excitation into bulk-conduction band-gap states ($E_k = 6\text{-}11 \text{ eV}$ for Ag(110), $E_k = 16\text{-}21 \text{ eV}$ for Ag(100), where E_k is the photoelectron kinetic energy), in contradiction to the work of Dietz and Himpel based on a study of Cu(110).⁴ Second, peak intensity resonances associated with the bulk conduction-band structure are observed, analogous to results with Ag(111),¹ Pt(111) and Au(111),⁵ and Pt(100).⁶

These results further demonstrate the viability of using angle-resolved photoemission in conjunction with synchrotron radiation to determine all major portions of bulk valence-band structures in transition metals. To our knowledge, this silver work and our previous lower-resolution studies of copper,⁷ represent the first such complete band structure determinations in these metals.

* * *

[†]Brief version of LBL-9552; submitted for publication in Physical Review B.

[‡]Permanent address: Hewlett-Packard Company, Palo Alto, CA 94304.

[§]Permanent address: Department of Chemistry,

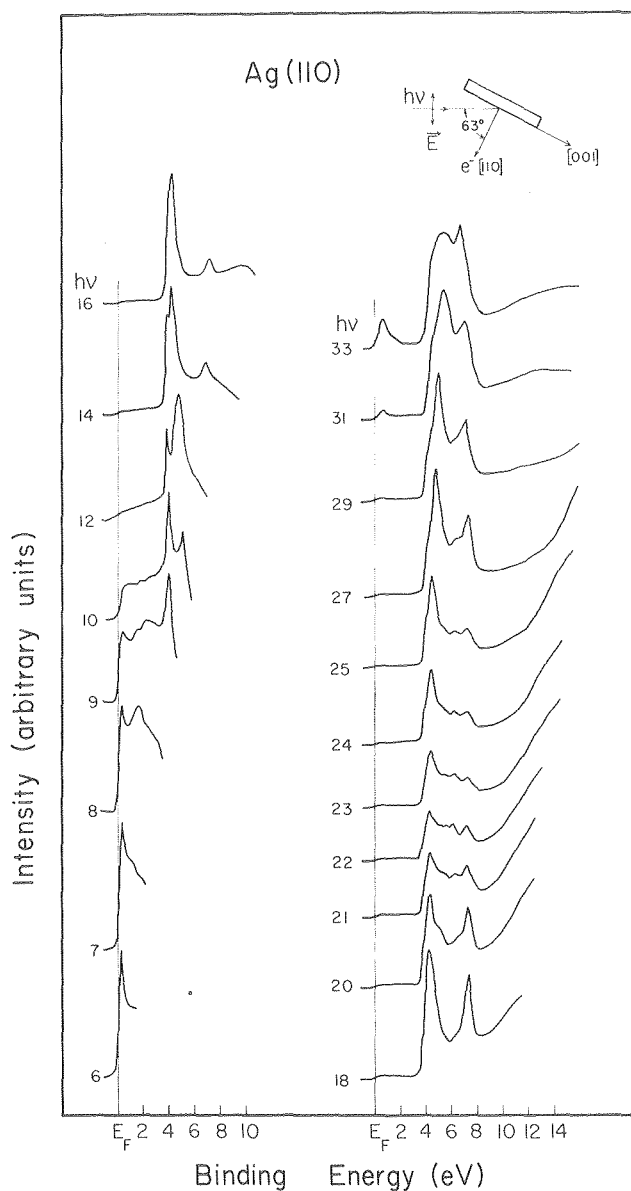


Fig. 1. Selected normal photoemission spectra for Ag(110); the inset gives the experimental geometry. (XBL 797-10717)

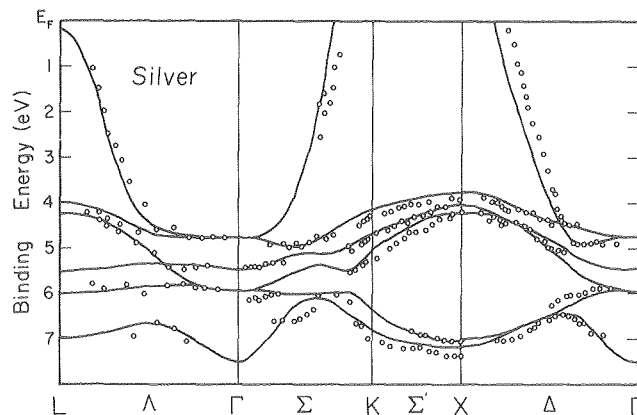


Fig. 2. Empirical valence-band structure (circles) of silver, compared to Christensen's RAPW calculation (lines). The experimental data along Λ are from Ref. 1. (XBL 797-10723)

- University of Manchester, Manchester M13-9PL, England.
- Permanent address: The Cyclotron Institute, Texas A&M University, College Station, Texas 77843.
1. P. S. Wehner, R. S. Williams, S. D. Kevan, D. Denley, and D. A. Shirley, *Phys. Rev.* **B19**, 6164 (1979).
 2. J. Stöhr, P. S. Wehner, R. S. Williams, G. Apai, and D. A. Shirley, *Phys. Rev.* **B17**, 587 (1978); and P. S. Wehner, Ph.D. thesis, University of California, Berkeley, LBL-7622 (1978); the only change was a decrease in the angular resolution of the CMA to $\pm 2.5^\circ$.
 3. N. E. Christensen, *Phys. Stat. Solidi* **B54**, 551 (1972).
 4. E. Dietz and F. Himpsel, *Solid State Commun.* **30**, 235 (1979).
 5. K. A. Mills, R. F. Davis, S. D. Kevan, G. Thornton, and D. A. Shirley, LBL-9430, submitted for publication in *Phys. Rev. B*.
 6. G. Thornton, R. F. Davis, K. A. Mills, and D. A. Shirley, LBL-9790, submitted for publication in *Solid State Commun.*
 7. D. A. Shirley, J. Stöhr, P. S. Wehner, R. S. Williams, and G. Apai, *Physica Scripta* **16**, 398 (1977).

7. AN ANGLE-RESOLVED PHOTOEMISSION DETERMINATION OF THE VALENCE-BAND STRUCTURE OF Pt BETWEEN Γ AND X^\dagger

G. Thornton,[†] R. F. Davis, K. A. Mills,[§] and D. A. Shirley

We have recently established the viability of using angle-resolved normal photoemission (ARNP), in conjunction with synchrotron radiation, to obtain experimental valence-band dispersion relations, $E_n(\vec{k})$, for the high-symmetry (k -space) directions of transition metals.¹ Recent ARNP studies of low-index faces of Ag,² Au,³ and Pt³ suggest that the direct-transition model (DTM), along with a quasi-free-electron parabolic final-state dispersion relation, can be used to determine $E_n(\vec{k})$ even when the photoelectron energy and momentum correspond to a bulk conduction-band gap. This choice is related to the surface sensitivity of photoemission. The present work extends these studies, because it represents an attempt to investigate $E_n(\vec{k})$ for the Δ line of a 5d metal for which no bulk conduction bands have been calculated. It also addresses the relative contributions of direct transitions and density-of-states (DOS) features in ARNP spectra.

The ARNP spectra of Pt(100) were taken in the range $6 \text{ eV} \leq h\nu \leq 32 \text{ eV}$ using an apparatus described elsewhere.⁴ Representative spectra are shown in Fig. 1. Also shown is the experimental geometry used. In order to determine an empirical $E_n(\vec{k})$ relation from the direct-transition features in these spectra, it is first necessary to construct suitable final states. As in our studies of Ag and Au, we require the final-state dispersion relation to be of the form $(\hbar^2/2m^*)|\vec{k}+\vec{G}|^2 + V_0$ (where $\vec{G} = (\vec{1}\vec{6},0,0)\pi/4a$), fitting this relation to the appropriate calculated bulk conduction band

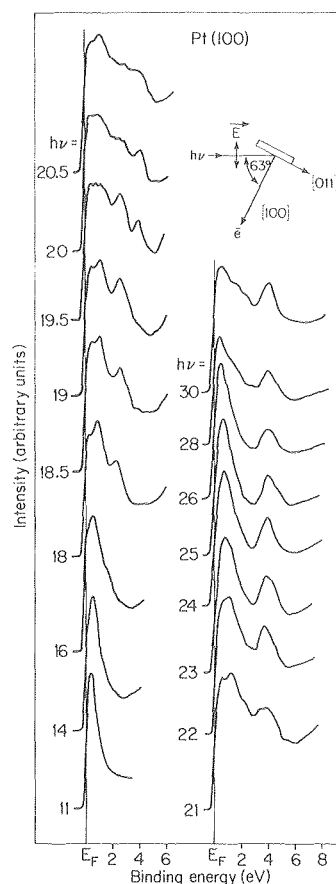


Fig. 1. Selected normal emission spectra of Pt(100) in the photon energy range $11 \leq h\nu \leq 30 \text{ eV}$. The inset gives the experimental geometry. (XBL 798-2700)

(band 7) near the center of the line under investigation. Because Anderson's RAPW band structure calculation⁵ did not include the high energy bands, we followed the procedure used for Pt(111),⁵ where the effective mass m^* was taken to be the value found for the analogous band in Au ($m^* = 1.4 m_e$, where m_e is the free-electron mass). The band minimum was adjusted to $V_0 = 3.3 \text{ eV}$, which gave the best overall agreement between the experimentally derived $E_n(\vec{k})$ and Andersen's RAPW calculation.⁵ A comparison between the empirical and theoretical valence bands along Δ in Pt is shown in Fig. 2. The agreement is generally very good, although some discrepancies are observed. Band 5 is seen to lie higher than calculated, although it should be noted that for $h\nu \geq 20 \text{ eV}$ the positions of peaks associated with this band were difficult to determine. Apart from band 2, which was also found to be higher than calculated, the remaining discrepancy is in band 3 between $(4,0,0)$ and $(6,0,0)$ where there is a deviation in the curvature. Band 1 was not observed in our spectra, presumably because of a low cross-section due to its s-p character.

In addition to the direct-transition peaks in the spectra, there are features arising from the density-of-states (DOS). The most intense DOS peak occurs in the spectra for $19 \text{ eV} \leq h\nu \leq 32 \text{ eV}$,

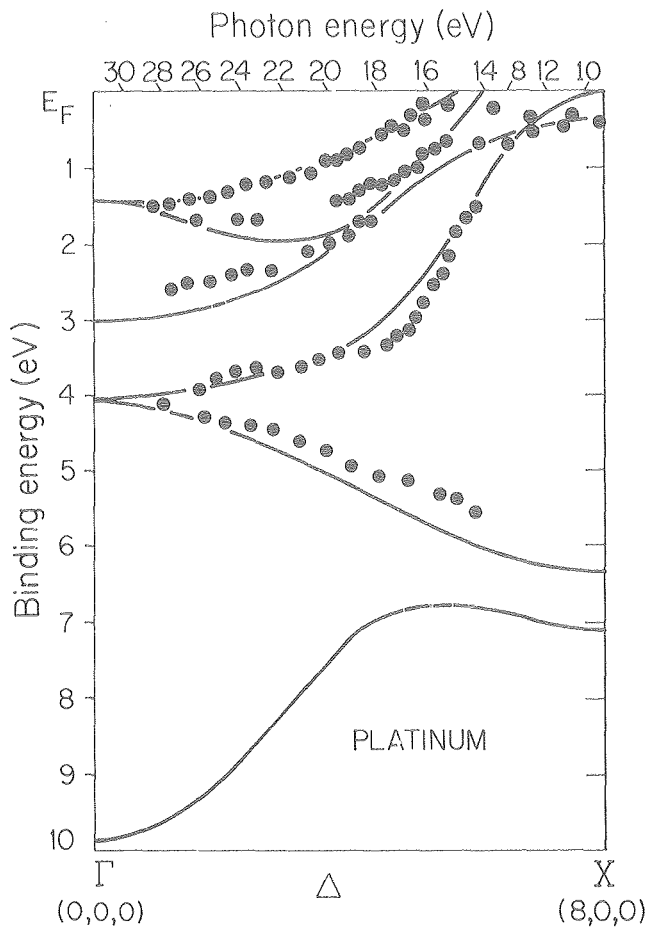


Fig. 2. Empirical dispersion relations (circles) and theoretical bands (lines) along Δ for platinum. The scale at the top gives the final state shifted down by the indicated photon energy. The final state crosses from the first to the second Brillouin zone at ca. $h\nu = 11$ eV. (XBL 798-2699)

with a binding energy of 0.5 eV. The relative intensity increase of this peak with photon energy is interpreted as arising from a decrease in the electron mean free path, reducing the extent of \vec{k}_{\parallel} conservation and leading to an enhancement of DOS features.⁶

As in our earlier studies, direct transitions into the derived final-state band could be assigned even when a gap was present in the bulk conduction-band structure. This study therefore adds further credence to the idea of a surface-modified final state in the analysis of ARNP data.

* * *

[†]Brief version of LBL-9790; Solid State Commun., to be published.

[‡]Permanent address: Department of Chemistry, University of Manchester, Manchester M13-9PL, England.

[§]Permanent address: Hewlett-Packard Company, Palo Alto, CA 94304.

1. D. A. Shirley, J. Stöhr, P. S. Wehner, R. S. Williams, and G. Apai, *Physica Scripta* **16**, 398 (1977).

2. K. A. Mills, R. F. Davis, G. Thornton, R. Watson, and D. A. Shirley, LBL-9552, submitted for publication in *Phys. Rev. B*.

3. K. A. Mills, R. F. Davis, S. D. Kevan, G. Thornton, and D. A. Shirley, LBL-9430, submitted for publication in *Phys. Rev. B*.

4. J. Stöhr, P. S. Wehner, R. S. Williams, G. Apai, and D. A. Shirley, *Phys. Rev. B* **17**, 587 (1978); and P. S. Wehner, Ph.D. thesis, University of California, Berkeley, LBL-7622 (1978); the only change was a decrease in the angular acceptance of the CMA to $\pm 2.5^\circ$.

5. O. K. Andersen, *Phys. Rev. B* **2**, 883 (1970).

6. See, for example, L. F. Ley, *J. Electron Spectroscopy* **15**, 329 (1979).

8. ELECTRONIC STRUCTURE IN GaAs/Ge FROM ANGLE-RESOLVED PHOTOEMISSION[†]

D. R. Denley,[‡] K. A. Mills,[§] P. Perfetti,^{||} and D. A. Shirley

The nature of the electronic structure of metal-semiconductor and semiconductor-semiconductor interfaces, and the process by which very thin films evolve toward the limit of two bulk materials joined at an interface, are of considerable scientific and technological interest. Until now, however, most studies of these interfaces have been concerned primarily with the elucidation of general interface electronic properties such as band discontinuities.¹ We present here the preliminary results of experiments which show that angle-resolved photoemission (ARP) may be used to more fully elucidate the detailed evolution of electronic structure in the initial stages of interface formation. In particular, we have found a number of features, some of which correspond to recent calculations of interface states.² These features follow regular trends as successively greater amounts of Ge are deposited on GaAs.

The ARP spectra were taken at 21.2 eV (He I) photon energy for an n-type GaAs(110) single crystal cleaved in situ, using a cylindrical mirror analyzer (CMA) with an energy resolution of 0.07 eV. The sample orientation was fixed, following cleavage along the $\bar{\Gamma}\bar{X}'$ direction, by laser autocollimation. Successive layers of Ge were produced by evaporative deposition with the substrate held at the epitaxial growth temperature³ of 350°C. Coverage was determined by calibrating the oven with a piezoelectric thickness monitor. Spectra were taken as a function of θ , the polar angle from the surface normal, for azimuths corresponding to electron wavevectors along $\bar{\Gamma}\bar{X}$ ($\phi = 0^\circ$) and $\bar{\Gamma}\bar{X}'$ ($\phi = 90^\circ$) in the surface Brillouin Zone (SBZ); the geometry is summarized in Fig. 1.

The spectral changes that were observed were rather subtle, and to better analyze them we have calculated difference spectra for the various evaporations relative to the clean substrate. Several rather sharp features appear; their energies are summarized in Fig. 2. The features are found to fit one of two cases for the location of at least some of their associated (E_B , k_{\parallel}) paired values: (1) in a region that is calculated

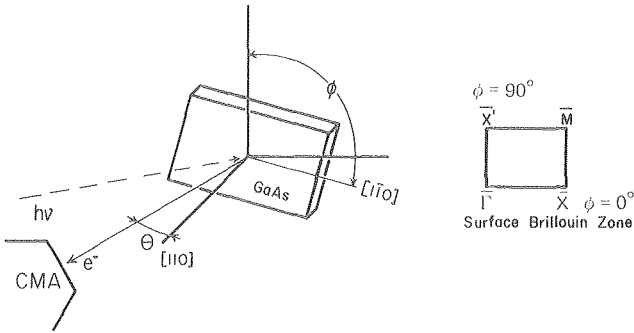


Fig. 1. Experimental geometry and surface Brillouin Zone for GaAs. (XBL 792-8386)

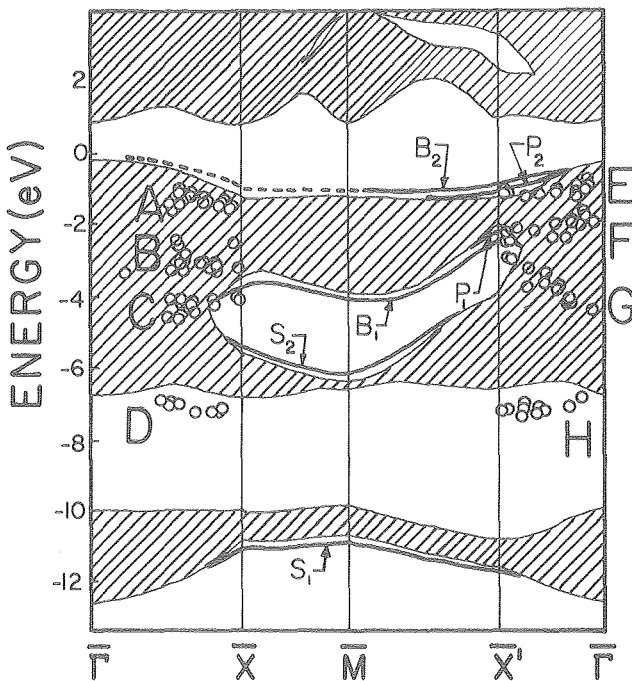


Fig. 2. Observed ARP features and projected surface band structure for GaAs/Ge (after Ref. 2). Cross-hatched areas are GaAs bulk-forbidden regions. Interface states are labeled with the notation of Pickett et al. Peaks are plotted from data for all evaporations, but not all data are shown. (XBL 792-8387)

to be forbidden to itinerant (bulk-like) states, or (2) within or at the edge of a region in which itinerant states are allowed. The first case is necessary for the formation of a truly localized state, while the second is typical for the occurrence of resonances.⁴ In the present experiment, all features falling below -7 eV are found to persist in the region of itinerant states, regardless of whether or not they can be found in gaps. For case (1), this is shown by features C for the $\bar{\Gamma}\bar{X}$ azimuth and E, F, and G, for the $\bar{\Gamma}\bar{X}'$ azimuth, all of which penetrate from a gap into the bulk-forbidden region. The features D and H are noteworthy in that they fall in the ionic gap of GaAs.

The effect on the surface of the Ge deposition, in the limit of a thick overlayer, will be to partially close the gap at \bar{X}' , and completely close it at \bar{X} . This will prevent the formation of localized states, and it is therefore consistent that D (and to a degree H) is strongly damped for greater depositions; in fact, feature D has disappeared by an early evaporation, whereas all other features are persistent. Features corresponding to the second case are peaks A and B for the $\bar{\Gamma}\bar{X}$ azimuth.

We have further found correspondence with the main features of available calculations.² It is clearly important to extend these results to higher coverages to study any further evolution that is observable in the spectra, with the hope of following the observed features until a heterojunction has been effectively formed.

* * *

[†]Brief version of LBL-8718; published in *J. Vac. Sci. Technol.* **16**, 1501 (1979).

[‡]Permanent address: Shell Development Company, Houston, TX 77001.

[§]Permanent address: Hewlett-Packard Company, Palo Alto, CA 94304.

^{||}Permanent address: Laboratori Nazionale di Frascati, Rome, Italy.

1. See, for example, P. E. Gregory and W. E. Spicer, *Phys. Rev.* **B12**, 2370 (1975); and G. Margaritondo, J. E. Rowe, and S. B. Christman, *Phys. Rev.* **B14**, 5396 (1976).

2. W. E. Pickett, S. G. Louie, and M. L. Cohen, *Phys. Rev.* **B17**, 815 (1978).

3. R. S. Bauer and J. C. McMenamin, *J. Vac. Sci. Technol.* **15**, 1444 (1978).

4. B. Feuerbacher and R. F. Willis, *J. Phys.* **C9**, 169 (1976).

Gas-Phase Research

Overview. The time-of-flight photoelectron analyzer, in conjunction with the time-structured SSRL beam, has been exploited to study two "classic" systems in atomic photoelectron spectroscopy (articles 1 and 2), and to measure asymmetries in the halogen acids (article 6). Fluorescence studies at SSRL include the observation (with R. N. Zare's group) of polarized fluorescence from reaction products, which yields information about mechanisms of photolysis reactions.

1. ANGULAR DISTRIBUTION OF Xe5s \rightarrow ϵ p PHOTOELECTRONS NEAR THE COOPER MINIMUM[†]

M. G. White,[†] S. H. Southworth, P. Kobrin, E. D. Poliakov,[§] R. A. Rosenberg,^{||} and D. A. Shirley

We use the time structure (0.3 nsec pulse width, 780 nsec repetition period) of the synchrotron radiation at the Stanford Synchrotron Radiation Laboratory (SSRL) to obtain photoelectron spectra of gases by time-of-flight (TOF) kinetic energy analysis of the ejected electrons. Recently, two

TOF analyzers have been positioned at angles of 0° and 54.7° (magic angle) with respect to the polarization axis of the radiation. The analyzers are operated simultaneously, and a comparison of the photoelectron intensities observed at the two angles yields the "asymmetry parameter" β , which completely describes the photoelectron angular distribution. The β value is determined by the relative transition strengths to the final continuum channels and by their interference. The transition amplitudes, and hence β , are sensitive to relativistic and many-electron interactions.

VUV radiation from the 8° branch line at SSRL was used to measure β for photoionization of the 5s-subshell of xenon at three energies near the Cooper minimum. Our results are plotted in Fig. 1 along with theoretical predictions¹⁻⁵ and the data point of Dehmer and Dill.⁶ All of the calculations treat the spin-orbit interaction, but only the many-body RPA calculations which include all of the 5s, 5p, and 4d interchannel interactions are in good agreement with the experimental data.

* * *

[†]Brief version of LBL-9740; Phys. Rev. Lett. 43, 1661 (1979).

[‡]Permanent address: Department of Chemistry, University of British Columbia, Vancouver V6T 1W5, Canada.

[§]Permanent address: Argonne National Laboratory, Argonne IL 60439.

^{||}Permanent address: Physics Division, Naval Weapons Center, Michaelson Laboratory, China Lake, CA 93555.

1. Dirac-Fock (DF): W. Ong and S. T. Manson, J. Phys. B11, L65 (1978).

2. Dirac-Slater (DS): T. E. H. Walker and J. T. Waber, J. Phys. B7, 674 (1974).

3. Random-Phase Approximation with Exchange (RPAE): N. A. Cherepkov, Phys. Lett. A66, 204 (1978).

4. Relativistic Random-Phase Approximation (RRPA): W. R. Johnson and K. T. Cheng, Phys. Rev. Lett. 40, 1167 (1978); Phys. Rev. A20, 978 (1979).

5. K-matrix: K. N. Huang and A. F. Starace, Bull. Am. Phys. Soc. 22, 1325 (1977).

6. J. L. Dehmer and D. Dill, Phys. Rev. Lett. 37, 1049 (1973).

2. RESONANCE PHOTOELECTRON SPECTROSCOPY: A NEW METHOD--THE PHOTOELECTRON SPECTRA OF ATOMIC Ba AT SELECTED AUTOIONIZING RESONANCES[†]

R. A. Rosenberg,[‡] M. G. White,[§] G. Thornton,^{||} and D. A. Shirley

Using the VUV continuum radiation available from the 8 degree beam line at the Stanford Synchrotron Radiation Laboratory (SSRL) and a recently developed time-of-flight electron energy analyzer,¹ we have recorded the photoelectron spectra of atomic Ba at several autoionizing resonances. Autoionization occurs via resonant excitation of an intermediate highly excited state of Ba I which decays to many Ba II continuum states. Strongly enhanced populations of electron correlation satellite states were observed previously upon excitation by He I (21.22 eV) resonance radiation,^{2,3} a result of the fortuitous overlap of the He I line with an autoionizing level of Ba I. Use of the tunable continuum source at SSRL allowed photoelectron spectra to be recorded at selected autoionizing resonances in the present work. We shall call this new method resonance photoelectron spectroscopy.

A total electron-yield spectrum of Ba, taken between 700 Å and 490 Å, is shown in Fig. 1. All the major features of the absorption spectrum of Connerade et al.⁴ are reproduced. Photoelectron

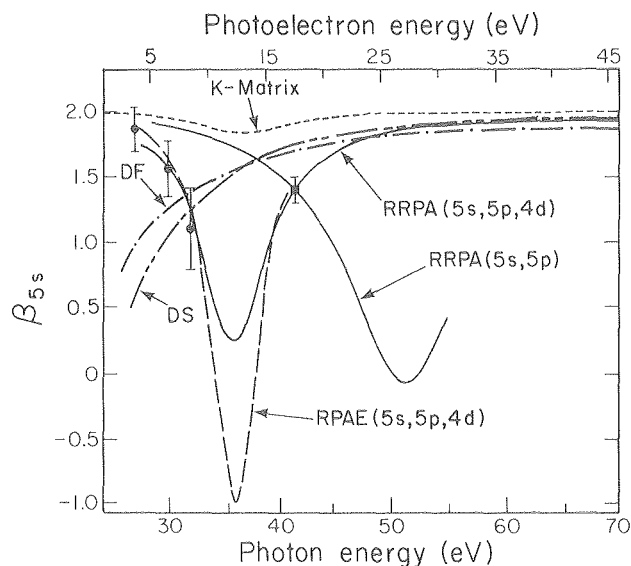


Fig. 1. Theoretical and experimental asymmetry parameters for Xe5s \rightarrow 5p photoionization versus energy. (XBL 799-2500A)

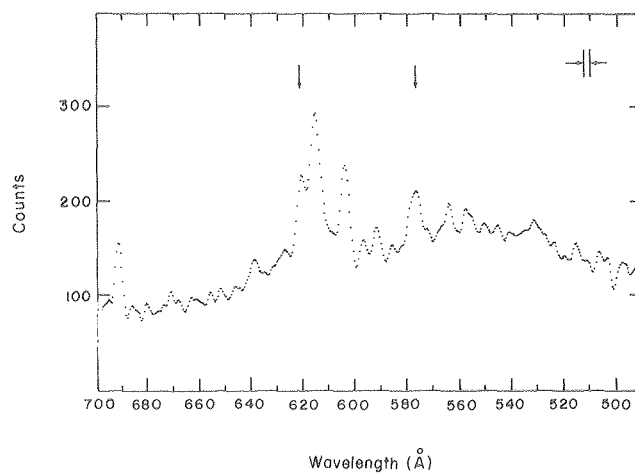
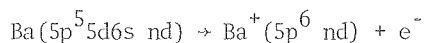


Fig. 1. Total electron yield spectrum of Ba. Photoelectron spectra (Fig. 2) were taken at the two wavelengths indicated by the arrows. The bandpass of the excitation monochromator (2.5 Å) is indicated in the upper right-hand corner. (XBL 793-8812)

spectra taken at the two resonances indicated by arrows in Fig. 1 are shown in Fig. 2. Based on the work of Connerade et al.,⁴ the two autoionizing levels involved are assigned to the same Rydberg series in which an electron is excited to an nd orbital. The corresponding photoelectron spectrum shows extensive population of the nd satellite line, implying that Auger-type decay, e.g.,



is a dominant decay channel of the autoionizing level.

The electronic structures of the resonant states are characterized by the peak intensities recorded in the photoelectron spectra, with strong variations in peak intensities observed among resonances. Thus, resonance photoelectron spectroscopy should have general applicability in elucidating the electronic structure of many-electron systems.

* * *

[†]Brief version of LBL-9170; published in Phys. Rev. Lett. 43, 1384 (1979).

[‡]Permanent address: Physics Division, Naval Weapons Center, Michaelson Laboratory, China Lake, CA 93555.

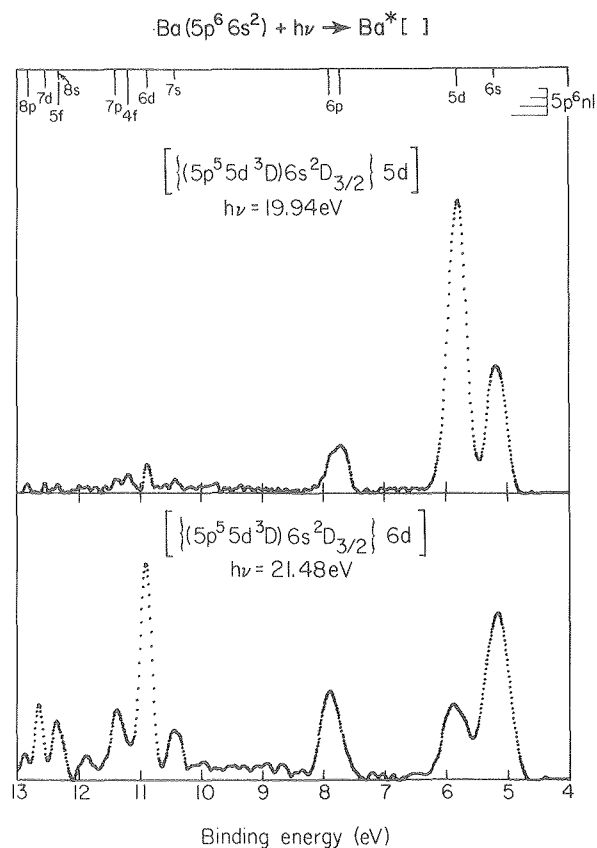


Fig. 2. Photoelectron spectra of Ba taken at two autoionizing resonances. The assignments are based on the work of Connerade et al.⁴ (XBL 792-610A)

[§]Permanent address: Department of Chemistry, University of British Columbia, Vancouver V6T 1W5, Canada.

^{||}Permanent address: Department of Chemistry, University of Manchester, Manchester M13 9PL, England.

1. M. G. White, R. A. Rosenberg, G. Gabor, G. Thornton, E. D. Poliakoff, S. H. Southworth, and D. A. Shirley, Rev. Sci. Instrum. **50**, 1268 (1979).

2. S.-T. Lee, S. Süzer, E. Matthias, R. A. Rosenberg, and D. A. Shirley, J. Chem. Phys. **66**, 2496 (1977).

3. H. Hotop and D. Mahr, J. Phys. B8, L301 (1975).

4. J. P. Connerade, M. W. D. Mansfield, G. H. Newsom, D. H. Tracy, M. A. Baig, and K. Thimm, Phil. Trans. R. Soc. Lond. **A290**, 327 (1979).

3. POLARIZED FLUORESCENCE FROM PHOTODISSOCIATION FRAGMENTS: A STUDY OF ICN PHOTOLYSIS USING SYNCHROTRON RADIATION[†]

E. D. Poliakoff,[‡] S. H. Southworth, D. A. Shirley, K. Jackson,[§] and R. N. Zare^{||}

Polarized fluorescence has been observed in the CN(B → X) transition following VUV photolysis of cyanogen iodide (ICN). Highly polarized radiation ($P_{\text{ex}} > 95\%$) from the Stanford Synchrotron Radiation Laboratory (SSRL) was used as an excitation source, and the fluorescence polarization, P_{fl} , was determined by measuring the fluorescence intensities I_{\parallel} and I_{\perp} with a polarization analyzer oriented parallel and perpendicular, respectively, to the polarization axis of the excitation radiation.

$$P_{\text{fl}} = \frac{I_{\parallel} - I_{\perp}}{I_{\parallel} + I_{\perp}} \quad (1)$$

The radiation at SSRL is pulsed with a 0.3 nsec (FWHM) pulse width and 780 nsec repetition period. Because of these excellent timing parameters, polarized fluorescence was measured as a function of time following the pulse, i.e., decay curves were generated¹ for both the parallel and perpendicular fluorescence components. Thus, collisional and time-dependent depolarization could be investigated. Figure 1 shows a pair of polarized fluorescence decay curves with the intensity of the parallel component clearly stronger than the perpendicular component. Data were collected at ICN pressures from 10 to 100 mTorr, however the data analysis revealed no effects of pressure on the polarization. In addition, no time-dependence was observed for the degree of fluorescence polarization, suggesting that collisional depolarization (alignment destruction) by ICN does not compete with collisional quenching.

Figure 2 shows CN(B → X) fluorescence intensity versus excitation wavelength along with values of P_{fl} (see Eq. 1) measured at the indicated wavelengths. We note some interesting trends. Population of the first three members of the lowest-lying Rydberg series ($\lambda_{\text{ex}} = 1698 \text{ \AA}$, 1331 \AA , 1247 \AA) all led to vanishing values for P_{fl} . There is

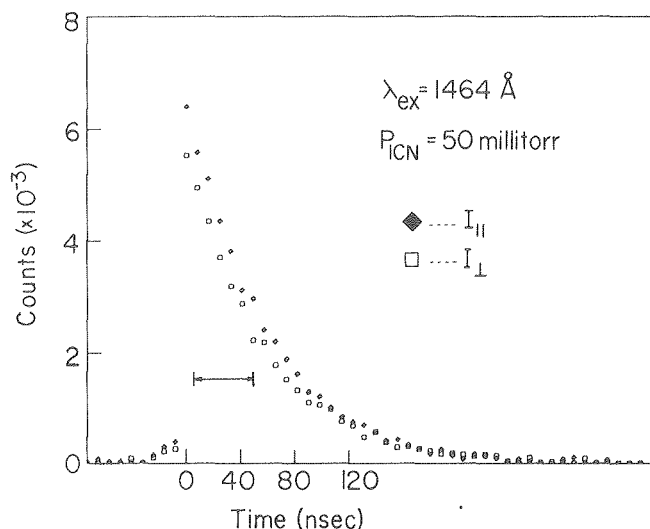


Fig. 1. Fluorescence decay curves of the polarized emission (background subtracted). The horizontal bar indicates the time period over which the fluorescence polarization was analyzed. (XBL 794-9374)

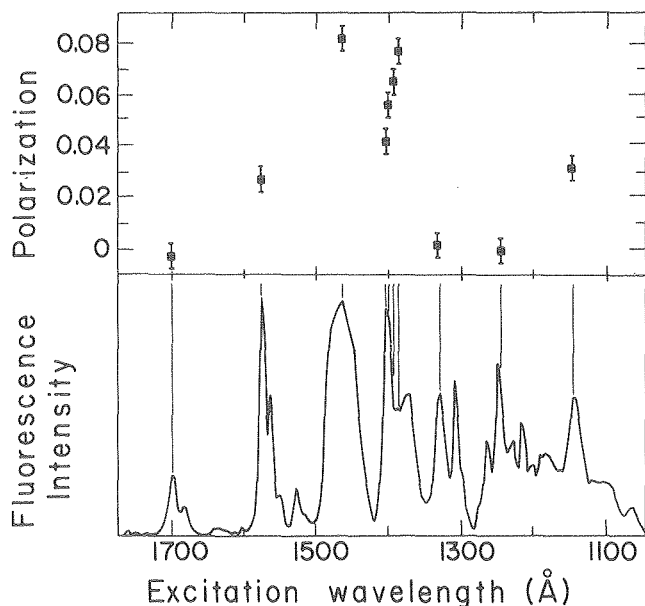


Fig. 2. Degree of polarization and fluorescence intensity of the CN fragment as a function of excitation wavelength. (XBL 794-1347)

a strong variation in P_{fl} near 1400 Å as the excitation wavelength is scanned over a peak. All the observed polarizations are positive, indicating² that the transition dipole moment lies in the triatomic plane or along the triatomic axis if the equilibrium geometry of the ICN dissociative state is bent or linear, respectively.

* * *

[†]Brief version of LBL-9081; published in Chem. Phys. Letters 65, 407 (1979).

[‡]Permanent address: Argonne National Laboratory, Argonne IL 60439.

[§]Permanent address: Department of Chemistry, Stanford University, Stanford CA 94305.

^{||}Permanent address: Department of Chemistry, Stanford University, Stanford CA 94305.

1. E. Matthias, R. A. Rosenberg, E. D. Poliakoff, M. G. White, S.-T. Lee, and D. A. Shirley, Chem. Phys. Lett. 52, 239 (1977).

2. G. A. Chamberlain and J. P. Simons, J. Chem. Soc. Far. Trans. II 71, 2043 (1975); M. T. Macpherson, J. P. Simons, and R. N. Zare, Mol. Phys., submitted for publication.

4. THE EJECTED ELECTRON SPECTRA OF ATOMIC Yb AND Ba[†]

R. A. Rosenberg,[‡] S.-T. Lee,[§] and D. A. Shirley

By utilizing the glow discharge lamp on a Perkin-Elmer PS-18 photoelectron spectrometer as a source for low-energy electrons,¹ we have recorded the ejected electron spectra of atomic Yb ($5p^6 4f^{14} 6s^2$) and Ba ($5p^6 6s^2$). The electrons observed in this work are due to either decay of autoionizing levels in the neutral or Auger decay of the singly ionized atom. Autoionization occurs by excitation of a 5p electron and the Auger process results from ionization of a 5p electron. In general, the Auger electrons will have lower kinetic energies than those stemming from autoionization.

The ejected electron spectra of atomic Yb is shown in Fig. 1. Using the absorption data of Tracy,² the group of peaks between 17 eV and 23 eV is assigned to decay of two autoionizing levels to both the ground and excited states of Yb II. Peak 13 is a result of Auger decay of the Yb II ($5p^5 4f^{14} 6s^2 \ 2p_{3/2}$) state to the ground state of Yb III ($5p^6 4f^{14}$). Many of the additional lower-energy peaks may be assigned to Auger decay to excited states of Yb III ($5p^6 4f^{13} n\ell$).

Figure 2 shows the ejected electron spectra of atomic Ba. Due to the complexities exhibited

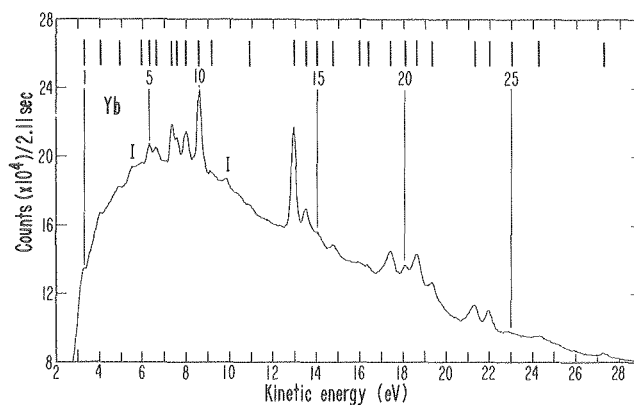


Fig. 1. Ejected electron spectrum following excitation or ionization of a 5p electron in Yb. (XBL 763-2573)

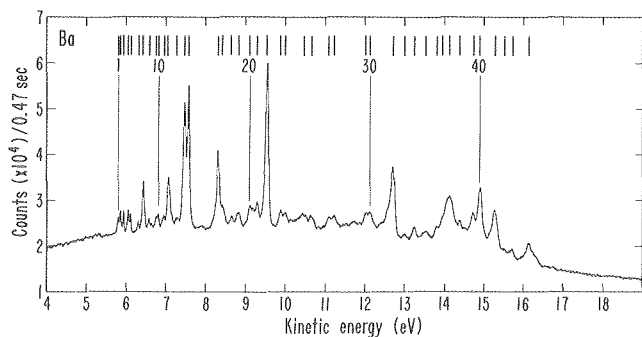


Fig. 2. Ejected electron spectrum following excitation or ionization of a 5p electron in Ba. (XBL 763-2476)

in the absorption spectra of Ba I³ and Ba II⁴ analysis of this spectrum is very difficult. However, by utilizing this absorption data most of the lines may be classified. In addition, a series of lines due to decay of a single auto-ionizing level to excited states of Ba II is indicated.

* * *

[†]Brief version of LBL-9120; submitted for publication in Phys. Rev. A.

[‡]Permanent address: Physics Division, Naval Weapons Center, Michaelson Laboratory, China Lake CA 93555

[§]Permanent address: Eastman Kodak Research Labs., 1999 Lake Avenue, Rochester NY 14615

1. S.-T. Lee, R. A. Rosenberg, E. Matthias, and D. A. Shirley, J. Elec. Spec. and Rel. Phen. 10, 203 (1977).

2. D. H. Tracy, Proc. R. Soc. Lond. A357, 485 (1977).

3. J. P. Connerade, M. W. D. Mansfield, G. H. Newsom, D. H. Tracy, M. A. Baig, and K. Thimm, Phil. Trans. R. Soc. Lond. A290, 327 (1979).

4. R. A. Roig, J. Opt. Soc. Am. 66, 1400 (1976).

5. DECAY DYNAMICS OF XeF* (B²Σ⁺ AND C²Π_{3/2}) STATES[†]

E. D. Poliakoff,[‡] G. Thornton,[§] S. H. Southworth, M. G. White,^{||} R. A. Rosenberg,[¶] and D. A. Shirley

The electronic structure of XeF has been a topic of current interest due to its relatively deep ground-state potential well.^{1,2} The radiative lifetimes of excited states of XeF serve as stringent tests of theoretical wavefunctions used to compute the electronic structure of this radical.

The XeF₂ sample was photodissociated using 1690 Å radiation. Decay curves were generated using the timing apparatus described in Ref. 3.

The XeF₂ sample was ≥99.9% pure for the volatile components. Our measurements used XeF₂ pressures between 1.75 × 10⁻² and 1.21 Torr. The fluorescence detection photomultiplier tube (RCA C31000 M) was placed perpendicular to both the

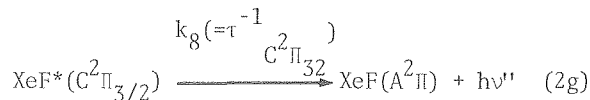
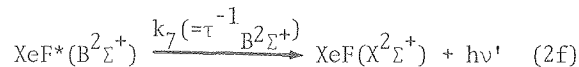
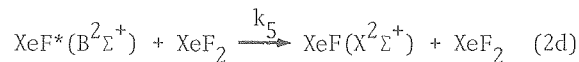
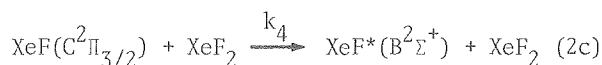
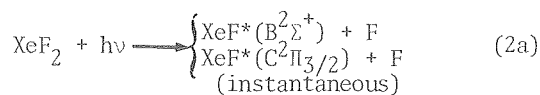
propagation vector and the ε vector of the exciting radiation.

The XeF* decay curves were fitted to an equation of the form

$$I(t) = C_0 + C_1 \exp(-t/\tau_1) + C_2 \exp(-t/\tau_2) \quad (1)$$

A typical decay curve with its least-squares fit is shown in Fig. 1. Plots of both τ_1^{-1} and τ_2^{-1} vs. pressure yielded straight lines (see Fig. 2). Each set of data was fitted with linear least-squares and the results are $\tau_1 = 14.2 \pm 0.2$ nsec and $\tau_2 = 98 \pm 10$ nsec.

Decay of the XeF*(B²Σ⁺ and C²Π_{3/2}) can be modeled simply using the following scheme:



The light intensity I(t), predicted by Eqs. (2a)-(2g) is

$$I(t) \approx k_1 \exp\{-[k_8 + (k_4 + k_6)C_{\text{XeF}_2}]t\} + k_2 \exp\{-[k_7 + (k_3 + k_5)C_{\text{XeF}_2}]t\} \quad (3)$$

provided the transfer rates are much smaller than the difference of the exponential arguments, which is the case.⁴ Thus, we conclude that τ_1 and τ_2 are equated with $[k_7 + (k_3 + k_5)C_{\text{XeF}_2}]$ and $[k_8 + (k_4 + k_6)C_{\text{XeF}_2}]$, respectively. Therefore

$$\tau_{\text{B}^2\Sigma^+} = 14.2(2) \text{ nsec} \quad \text{and} \quad \tau_{\text{C}^2\Pi_{3/2}} = 98(10) \text{ nsec.}$$

* * *

[†]Brief version of LBL-9491; submitted for publication in J. Chem. Phys.

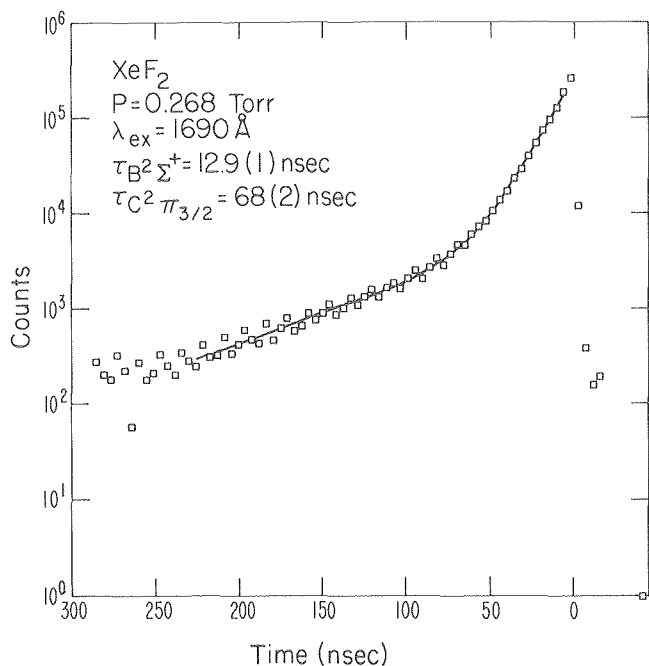
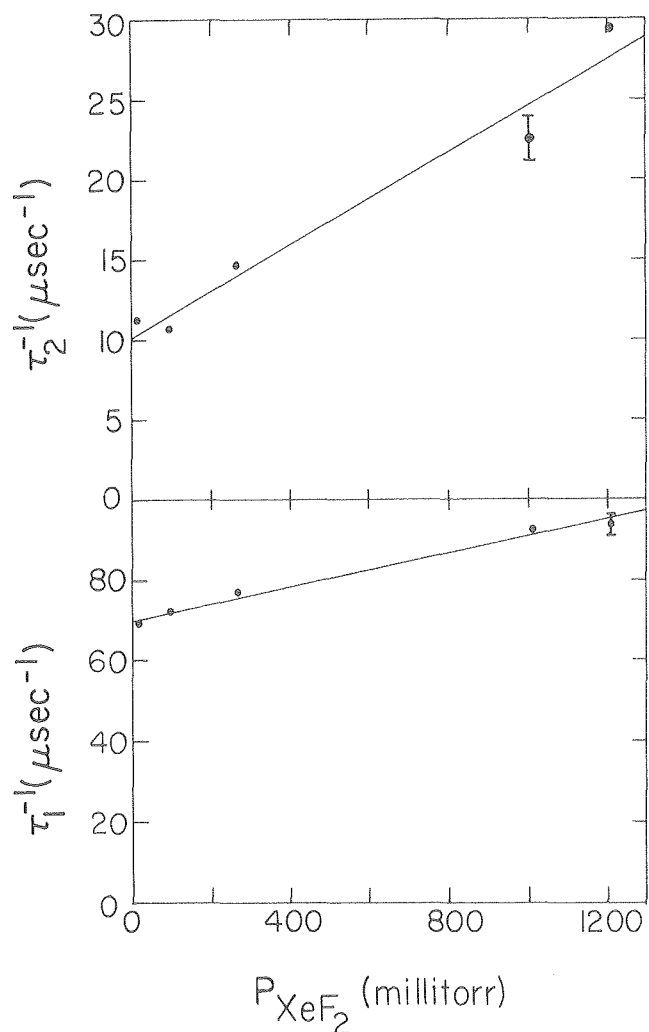


Fig. 1. XeF* decay curve. (XBL 797-2096)



[‡]Permanent address: Argonne National Laboratory, Argonne IL 60439.

[§]Permanent address: Department of Chemistry, University of Manchester, Manchester M13-9PL, England.

^{||}Permanent address: Department of Chemistry, University of British Columbia, Vancouver V6T 1W5, Canada.

[¶]Permanent address: Physics Division, Naval Weapons Center, Michaelson Laboratory, China Lake CA 93555.

1. T. H. Dunning and P. J. Hay, *J. Chem. Phys.* **69**, 134 (1978).

2. C. H. Becker, P. Casavecchia, and Y. T. Lee, *J. Chem. Phys.* **69**, 2377 (1978).

3. E. Matthias, R. A. Rosenberg, E. D. Poliakoff, M. G. White, S.-T. Lee, and D. A. Shirley, *Chem. Phys. Lett.* **52**, 239 (1977).

4. H. C. Brashears, Jr. and D. W. Setser, *Appl. Phys. Lett.* **33**, 821 (1978).

6. THE PHOTOELECTRON ANGULAR DISTRIBUTIONS OF HBr AND HI AT $h\nu = 21.2$ eV[†]

M. G. White,[‡] S. H. Southworth, P. Kobrin, and D. A. Shirley

The photoelectron angular distributions for the $2\pi_{3/2,1/2}(p\pi)^{-1}$ and $2\Sigma_{1/2}^+(p\sigma)^{-1}$ ionic states of HBr and HI have been measured at a photon energy of 21.2 eV. Highly plane-polarized (>97%), pulsed synchrotron radiation at the Stanford Synchrotron Radiation Laboratory was used to obtain time-of-flight (TOF) photoelectron spectra.¹ The asymmetry parameter β , which completely characterizes the photoelectron angular distribution, was determined by operating two TOF detectors simultaneously at angles of 0 degrees and 54.7 degrees with respect to the polarization direction of the radiation. The HI sample contained sufficient HBr impurity that TOF spectra of both gases were obtained at the same time, as shown in Fig. 1.

The measured β -values are listed in Table 1. along with those for HCl measured with the 21.22 eV HeI line.²

Table 1. Experimental asymmetry parameters for photoionization ($h\nu = 21.2$ eV) from the $p\pi_{3/2}$, $p\pi_{1/2}$, and $p\sigma_{1/2}$ orbitals of the HX (X = Cl, Br, I) molecules.

| X | $p\pi_{3/2}$ | $p\pi_{1/2}$ | $p\sigma_{1/2}$ |
|-----------------|--------------|--------------|-----------------|
| Cl ^a | 1.40(5) | 1.40(5) | .75(10) |
| Br ^b | 1.2 (2) | 1.1 (2) | .9 (1) |
| I ^b | 1.47(9) | 1.47(9) | .89(8) |

^aFrom Ref. 2.

^bThis work.

Fig. 2. XeF* Stern-Volmar fits. (XBL 797-10657)

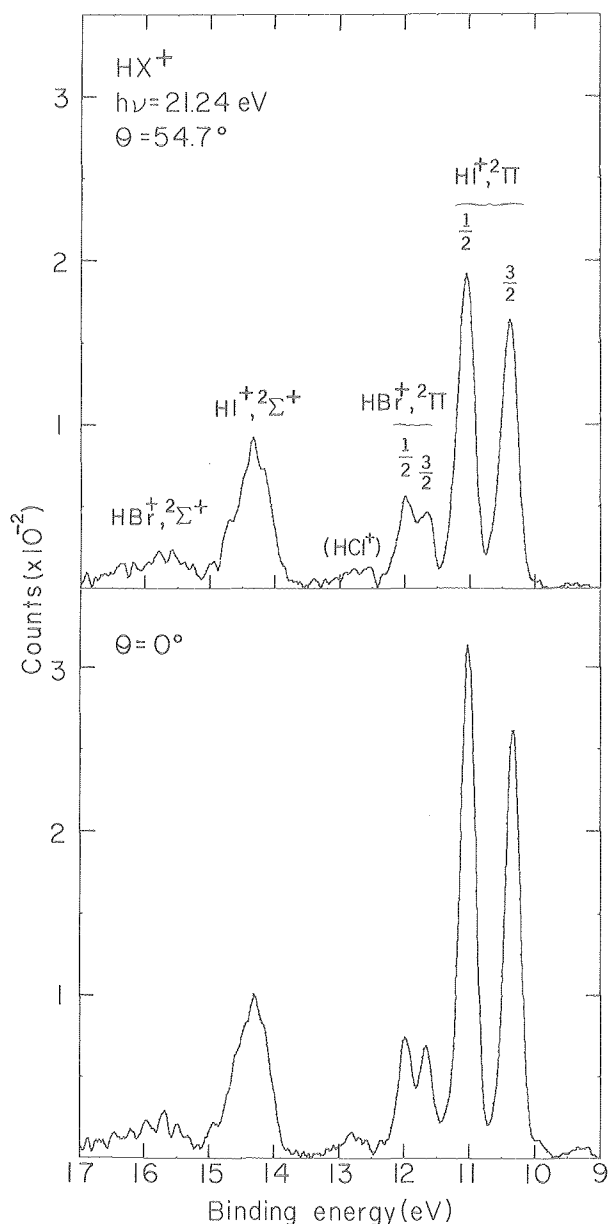


Fig. 1. The 0° and 54.7° TOF spectra of HBr^+ and HI^+ taken at $h\nu = 21.24$ eV. (XBL 798-11138)

[†]Brief version of LBL-9807; submitted for publication in *J. Elect. Spectros.*

[‡]Permanent address: Department of Chemistry, University of British Columbia, Vancouver V6T 1W5, Canada.

1. M. G. White, R. A. Rosenberg, G. Gabor, G. Thornton, E. D. Poliakoff, S. H. Southworth, and D. A. Shirley, *MMRD 1978 Annual Report*, p. 309; *Rev. Sci. Instrum.* **50**, 1268 (1979).

2. T. A. Carlson, G. E. McGuire, A. E. Jonas, K. L. Cheng, C. P. Anderson, C. C. Lu, and B. P. Pullen, in *Electron Spectroscopy*, edited by D. A. Shirley (North-Holland, Amsterdam, 1972), p. 207.

3. E. S. Cheng, *J. Phys.* **B11**, L293 (1978).

4. J. L. Dehmer, W. A. Chupka, J. Berkowitz, and W. T. Jivery, *Phys. Rev.* **A12**, 1966 (1975).

RESEARCH PLANS FOR CALENDAR YEAR 1980

With the advent of 50% dedication of the SPEAR storage ring to synchrotron radiation research (which started in October 1979), our group is looking forward to higher photon flux in the 6-4000 eV vacuum ultraviolet-soft x-ray range. Two branches of Beam Line III will be commissioned in 1980 at SSRL. Beam Line III-1 will enhance the SSRL capability in the 32-100 eV range, while Beam Line III-3 will provide an entrée into the new range 1000-4000 eV. Our own group will help to develop a new "windowless" branch line, for gas-phase studies in the 5-160 eV range, to be completed in 1981. These new lines will greatly facilitate the spectroscopic exploitation of a heretofore relatively inaccessible range of the electromagnetic spectrum.

A strong laboratory program in electron spectroscopy in LBL will also be maintained. A high-resolution electron energy loss spectrometer for surface studies will be completed, and a high-resolution energy analyzer for gas-phase photoemission from molecular beams will be put into operation. Initial construction on the Chemical and Materials Science Laboratory (CMSL) addition to Building 62 will be started, and our group will ultimately move into this new building, where we will participate in the development and use of some of the special equipment that will be associated with CMSL.

David Shirley will also be a Miller Research Professor during the 1980-81 academic year, and will concentrate on this research program.

Specific topics to be studied in the surface and solids area include photoelectron diffraction, studies of adsorbates by surface EXAFS in the soft x-ray regions, photoelectron asymmetry, and characterization of surface states. Gas-phase studies will include photoelectron asymmetries and photoelectron spectroscopy with molecular beams, as well as fluorescence angular distributions.

The asymmetry parameters for the spin-orbit split $2\Pi_{3/2}$ and $2\Pi_{1/2}$ states are in each case larger than for the $2\Sigma_{1/2}^+$ state, in disagreement with the qualitative predictions of Cheng,³ in which β -values for $\Sigma^\pm \rightarrow \Sigma^\pm$ ionization transitions should be greater than those for $\Sigma^\pm \rightarrow \Pi$ transitions. The deviation from the Cheng result is most likely a result of the fact that the $p\pi$ orbitals are essentially atomic, closely resembling the corresponding united atom (rare gas) np orbitals, which have large β -values.⁴ The asymmetry parameters for the $2\Sigma^+(p\sigma)^{-1}$ states of HX^+ are more like those obtained for ionization of strongly bonding σ orbitals of other molecules, with $\beta(\sigma) \approx 1.2$

1979 PUBLICATIONS AND REPORTS

Refereed Journals

1. S. D. Kevan, P. S. Wehner, and D. A. Shirley, "Evidence for the Itinerant Electron Model of Ferromagnetism and for Surface Photoemission from Angle-Resolved Photoemission Studies of Iron," *Solid State Commun.* 28, 517 (1978).
2. P. M. A. Sherwood, F. R. McFeely, S. P. Kowalczyk, and D. A. Shirley, "d-Orbital Directed Photoemission from Manganese Fluoride Single Crystals Using AlK α Radiation," *J. Chem. Soc., Faraday Trans. II* 75, 201 (1979).
3. D. Denley, R. S. Williams, P. Perfetti, D. A. Shirley, and J. Stöhr, "X-ray Absorption Fine Structure above the Ti L Edge," *Phys. Rev. B* 19, 1762 (1979).
4. D. Denley, K. A. Mills, P. Perfetti, and D. A. Shirley, "Electronic Structure in GaAs/Ge Through Angle-Resolved Photoemission," *J. Vac. Sci. Technol.* 16, 1501 (1979).
5. E. D. Poliakoff, S. H. Southworth, D. A. Shirley, K. H. Jackson, and R. N. Zare, "Polarized Fluorescence from Photodissociation Fragments: A Study of ICN Photolysis Using Synchrotron Radiation," *Chem. Phys. Lett.* 65, 407 (1979).
6. K. A. Mills, D. Denley, P. Perfetti, and D. A. Shirley, "Mapping of Conduction Bands in GaAs by Angle-Resolved Photoemission," *Solid State Commun.* 30, 743 (1979).
7. P. S. Wehner, R. S. Williams, S. D. Kevan, D. Denley, and D. A. Shirley, "Valence-Band Structure of Silver along Λ from Angle-Resolved Photoemission," *Phys. Rev. B* 19, 6164 (1979).
8. G. Thornton, E. D. Poliakoff, E. Matthias, S. H. Southworth, R. A. Rosenberg, M. G. White, and D. A. Shirley, "Fluorescence Decay of the O_u and I_u States of Xe $_2$," *J. Chem. Phys.* 71, 133 (1979).
9. M. G. White, R. A. Rosenberg, G. Gabor, E. D. Poliakoff, G. Thornton, S. H. Southworth, and D. A. Shirley, "Time-of-Flight Photoelectron Spectroscopy of Gases Using Synchrotron Radiation," *Rev. Sci. Instrum.* 50, 1268 (1979).
10. M. G. White, R. A. Rosenberg, S.-T. Lee, and D. A. Shirley, "The He(I) Photoelectron Spectroscopy of Heavy Group IV-VI Diatomics," *J. Elect. Spectros. and Rel. Phen.* 17, 323 (1979).
11. R. A. Rosenberg, M. G. White, G. Thornton, and D. A. Shirley, "Selective Resonant Enhancement of Electron-Correlation Satellites in Atomic Barium," *Phys. Rev. Lett.* 43, 1384 (1979).
12. M. G. White, S. H. Southworth, P. Kobrin, E. D. Poliakoff, R. A. Rosenberg, and D. A. Shirley, "Angular Distribution of Xe5s \rightarrow ϵp Photoelectrons Near the Cooper Minimum," *Phys. Rev. Lett.* 43, 1661 (1979).

LBL Reports

1. R. S. Williams, D. Denley, D. A. Shirley, and J. Stöhr, "Soft X-Ray Absorption Spectroscopy: Electronic and Morphological Structure of Polyvinylidene Fluoride," LBL-8681, submitted to *J. Amer. Chem. Soc.*
2. S. D. Kevan, D. H. Rosenblatt, D. R. Denley, B.-C. Lu, and D. A. Shirley, "Photoelectron Diffraction Measurements of Sulfur and Selenium Adsorbed on Ni(001)," LBL-9024, accepted for publication, *Phys. Rev. B*.
3. R. A. Rosenberg, S.-T. Lee, and D. A. Shirley, "Observation of a Collective Excitation in the Ejected Electron Spectra of Yb and Ba," LBL-9120, submitted to *Phys. Rev. A*.
4. D. A. Shirley, R. S. Williams, P. S. Wehner, R. F. Davis, and S. D. Kevan, "Angle-Resolved Normal Photoemission from Cu(111) for 7 eV $\leq h\nu \leq$ 200 eV," LBL-9344.
5. R. F. Davis, S. D. Kevan, B.-C. Lu, J. G. Tobin, and D. A. Shirley, "Condensed Phase Photoelectron Asymmetry," LBL-9384, submitted to *Chem. Phys. Lett.*
6. K. A. Mills, R. F. Davis, S. D. Kevan, G. Thornton, and D. A. Shirley, "Angle-Resolved Photoemission Determination of Λ -Line Valence Bands in Pt and Au Using Synchrotron Radiation," LBL-9430, submitted to *Phys. Rev. B*.
7. D. Denley, P. Perfetti, R. S. Williams, D. A. Shirley, and J. Stöhr, "Carbon K-Edge Fine Structure in Graphite Foils and in Thin Film Contaminants on Metal Surfaces," LBL-9431, accepted for publication, *Phys. Rev. B*.
8. E. D. Poliakoff, S. H. Southworth, M. G. White, G. Thornton, R. A. Rosenberg, and D. A. Shirley, "Decay Dynamics of the CN*(B $^2\Sigma^+$) and XeF*(B $^2\Sigma^+$ and C $^2\Pi_{3/2}$ States," LBL-9491, submitted to *J. Chem. Phys.*
9. K. A. Mills, R. F. Davis, G. Thornton, R. Watson, and D. A. Shirley, "Investigation of the Valence-Band Structure along Δ , Σ , and Σ' in Silver Using Angle-Resolved Photoemission," LBL-9552.
10. D. A. Shirley, "Surface and Adsorbate Structural Studies by Photoemission in the $h\nu = 50$ -500 eV Range," LBL-9596, to be published in ISISS book.
11. G. Thornton, R. F. Davis, K. A. Mills, and D. A. Shirley, "An Angle-Resolved Photoemission Determination of the Band-Structure of Platinum Between Γ and X, LBL-9790," accepted for publication, *Solid State Commun.*
12. M. G. White, S. H. Southworth, P. Kobrin, and D. A. Shirley, "The Photoelectron Angular Distributions of HBr and HI at $h\nu = 21.2$ eV," LBL-9807, submitted to *J. Elect. Spectros.*
13. S. D. Kevan, R. F. Davis, D. H. Rosenblatt, B.-C. Lu, C. C. Parks, and D. A. Shirley, "Photoelectron Diffraction Studies of Carbon Monoxide Overlayers," LBL-10024, to be submitted to *Phys. Rev. B*.

14. S. D. Kevan and D. A. Shirley, "High Resolution Angle-Resolved Photoemission Studies of the M-Point Surface State on Cu(001)," LBL-10025, submitted to Phys. Rev. B.
15. Richard Allen Rosenberg, "Studies of Electron Correlation in the Photoionization Process" (Ph.D. thesis), LBL-8948.
16. Kenneth Alan Mill, "The Determination of Electronic States in Crystalline Semiconductors and Metals by Angle-Resolved Photoemission" (Ph.D. thesis), LBL-9429.
17. Erwin David Poliakoff, "Time-Resolved Spectroscopy Using Synchrotron Radiation" (Ph.D. thesis), LBL-9475.
18. David R. Denley, "Determination of Morphology and Electronic Structure in Solids with 20-1000 eV Radiation" (Ph.D. thesis), LBL-9482.
19. Michael George White, "Photoelectron Spectroscopy of Heavy Atoms and Molecules" (Ph.D. thesis), LBL-9527.
5. D. A. Shirley, "Physical Chemistry with Low-Energy Synchrotron Radiation: Status and Prospects," Sam Houston State University, Huntsville, Texas, March 6, 1979.
6. D. A. Shirley, "Physical Chemistry with Low-Energy Synchrotron Radiation: Status and Prospects," North Texas State University, Denton, Texas, March 7, 1979.
7. D. A. Shirley, "Normal Photoelectron Diffraction," American Physical Society Meeting, Chicago, Illinois, March 23, 1979.
8. D. A. Shirley, "Surface and Adsorbate Structures from Synchrotron Radiation: Results and Possibilities," American Chemical Society Meeting, Honolulu, Hawaii, April 2, 1979.
9. D. A. Shirley, "Surface and Adsorbate Structural Studies by Photoemission in the $h\nu = 50-500$ eV Range," Fourth International Summer Institute in Surface Science (ISISS) 1979, Milwaukee, Wisconsin, August 13-17, 1979.

Invited Talks

1. D. A. Shirley, "Surface Structural Studies from Angle-Resolved Photoemission," Surface Science and Catalysis Seminar, Materials and Molecular Research Division, Lawrence Berkeley Laboratory, January 31, 1979.
2. D. A. Shirley, "Efficiency and Information in Photoelectron Spectroscopy," Chemical Sciences Review, Department of Energy, Materials and Molecular Research Division, Lawrence Berkeley Laboratory, February 7, 1979.
3. D. A. Shirley, "Adsorbate Geometries from Photoelectron Diffraction," Department of Physics, Montana State University, February 23, 1979.
4. D. A. Shirley, "Physical Chemistry with Synchrotron Radiation: Status and Prospects," Department of Chemistry, Texas A&M University, College Station, Texas, March 5, 1979.
10. D. A. Shirley, "New Angular Distribution Effects in Photoemission from Solids," Physics Departmental Colloquium, University of California, Santa Barbara, October 16, 1979.
11. D. A. Shirley, "Photoelectron Diffraction," SSRL Users Meeting, October 26, 1979.
12. D. A. Shirley, "Photoelectron Angular Distribution from Solids: Three New Effects," Physical Chemistry Seminar, University of California, Berkeley, October 30, 1979.
13. S. D. Kevan, "Normal Photoelectron Diffraction Studies of Adsorbed Atoms and Molecules," 1979 Gordon Conference on Synchrotron Radiation, Plymouth, New Hampshire, July 9-13, 1979.
14. S. D. Kevan, "Photoelectron Diffraction Studies at the Stanford Synchrotron Radiation Laboratory (SSRL)," 12th Annual Synchrotron Radiation Users Group Meeting, Madison, Wisconsin, October 22-23, 1979.

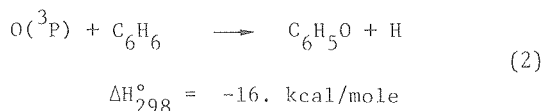
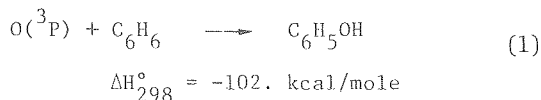
h. Crossed Molecular Beams*

Y. T. Lee, Investigator

1. COMPETITIVE DECAY OF THE COMPLEX FORMED IN THE REACTION $O(^3P) + C_6H_6$ AND $C_6D_6^{\dagger}$ R. J. Buss, P. Casavecchia, T. Hirooka,
S. J. Sibener and Y. T. Lee

The reactions of oxygen atoms with hydrocarbons are of great interest because they are important in combustion processes, atmospheric chemistry and photochemical air pollution. Although the reaction of $O(^3P)$ with benzene has been studied by a variety of techniques, uncertainty remains concerning the products of the primary reactive event. We have now completed a crossed molecular beam study of this reaction which eliminates the previous difficulties of secondary reactions and has enabled us to identify the primary products unambiguously.

The crossed beam apparatus and supersonic oxygen atom beam have been previously described.¹ About 90 Torr of the pure vapor of C_6H_6 or C_6D_6 was expanded from a 0.1 mm nozzle orifice heated to 326 K to prevent condensation. The reactions were studied at two mean collision energies, 2.5 and 6.5 kcal/mole by seeding the oxygen beam in argon and helium respectively. Two reaction channels were observed in this study:



The most intense product signal occurred at masses 65 and 66 which are daughter ions produced by ionizer fragmentation of the parent C_6H_5O and C_6H_5OH molecules. The laboratory angular distributions of product are shown for the higher collision energy in Fig. 1. The narrow distribution of mass 66 is found to coincide with the calculated distribution proving that it is indeed the result of oxygen attachment, Eq. (1). The mass 66 cannot be the result of CO elimination from the complex because momentum conservation would greatly broaden the mass 66 distribution. The angular distribution of mass 65 is wider than the centroid distribution as a consequence of the elimination of a hydrogen atom from the complex. The angular distribution of product from the low energy reaction is shown in Fig. 2 with a calculated centroid distribution (dashed line) and a best fit calculation (solid curve), assuming an isotropic angular distribution and the translational energy distribution shown in Fig. 3.

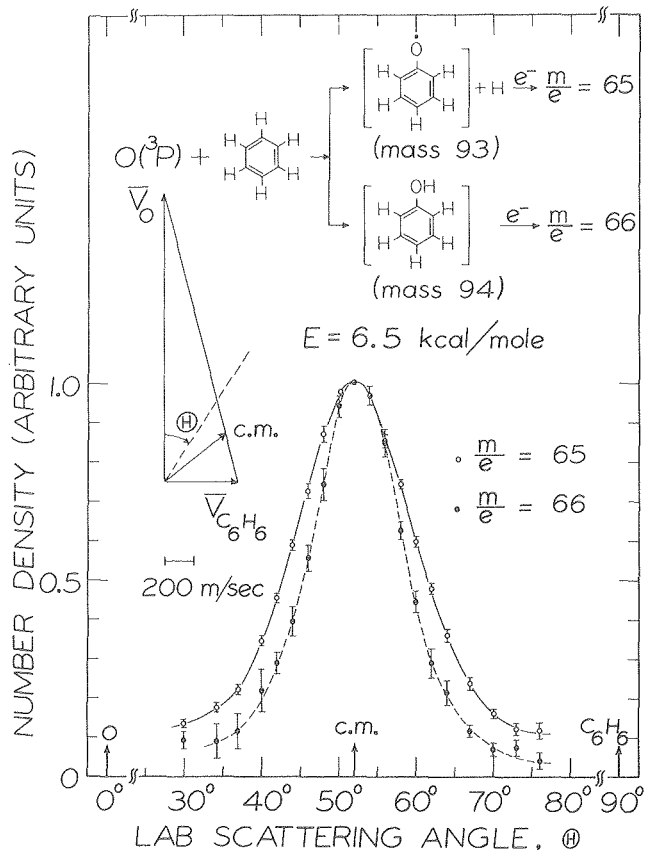


Fig. 1. Angular distributions from the reaction $O(^3P) + C_6H_6$, mean collision energy $E = 6.5$ kcal/mole. The primary reaction products formed were C_6H_5O and C_6H_5OH , which subsequently fragmented during electron bombardment ionization. The solid and dashed lines are drawn through the data for clarity. (XBL 794-9157A)

The results of the C_6D_6 reaction are qualitatively the same but the effect of deuteration is to alter the branching ratio of the two channels. The relative intensities of the detected masses are shown in Table 1. Because of the uncertainties in the fragmentation patterns of the parent species, these intensities do not give actual branching ratios but show only the trends. At both collision energies, deuteration has the effect of increasing the 66/65 and 72/70 ratios, indicating that the formation of phenol is favored by deuteration. Also evident is a strong enhancement of phenol production at the higher collision energy. The reaction of $O(^3P)$ with benzene apparently proceeds through formation of a triplet biradical intermediate. This can decay by one of two routes, non-radiative transition to the S_0 manifold of phenol or decomposition by hydrogen atom loss. We have determined that the complex does not dissociate by elimination of CO as was previously thought.² While this scheme is the simplest interpretation

*This work was supported by the Division of Chemical Sciences, Office of Basic Energy Sciences, U. S. Department of Energy.

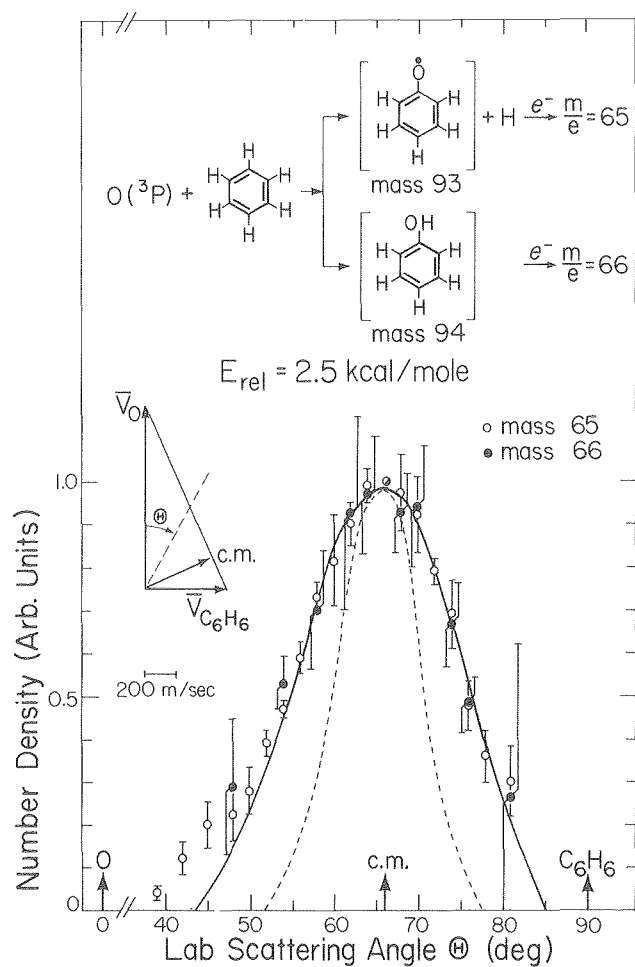


Fig. 2. Angular distributions from the reaction $O(^3P) + C_6H_6$, relative collision energy $E_{rel} = 2.5$ kcal/mole. The dashed line is a calculation of the centroid distribution. The solid line is the calculated distribution described in the text. (XBL 798-2454)

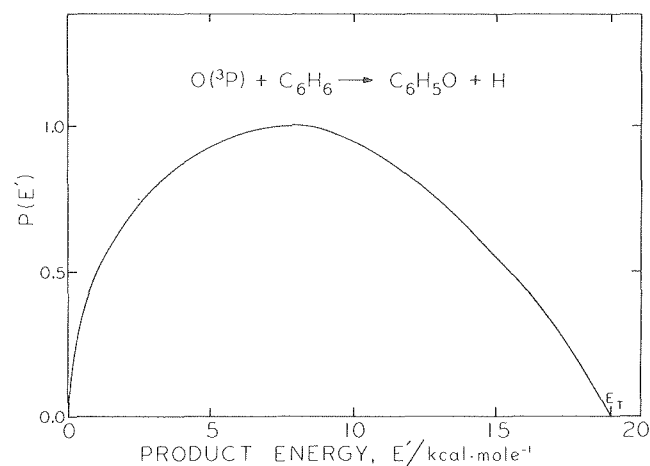


Fig. 3. Translational energy distribution of the C_6H_5O product from the reaction $O(^3P) + C_6H_6$, $E_{rel} = 2.5$ kcal/mole. (XBL 7910-12122)

of our results, further experiments will be necessary to determine whether the 94 product is actually formed by a radiative process, by a ring opening, or if, indeed, it is ground state phenol formed by a nonradiative curve crossing.

* * *

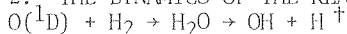
† Brief version of LBL-9975, submitted to J. Chem. Phys.

1. Y. T. Lee, J. D. McDonald, P. R. LeBreton and D. R. Herschbach, Rev. Sci. Instrum. 40, 1402 (1969); S. J. Sibener, R. J. Buss, C.-Y. Ng and Y. T. Lee, Rev. Sci. Instrum., in press.
2. T. M. Sloane, J. Chem. Phys. 67(5) 2267 (1977).

Table 1. Relative intensities of the detected ion masses.

| | Mass | Species | Collision Energy | |
|--------------|------|------------|------------------|---------------|
| | | | 6.5 kcal/mole | 2.5 kcal/mole |
| $O + C_6H_6$ | 94 | C_6H_5OH | 0.01 | < 0.005 |
| | 93 | C_6H_5O | 0.08 | 0.01 |
| | 66 | C_5H_6 | 0.21 | 0.08 |
| | 65 | C_5H_5 | 1.00 | 1.00 |
| $O + C_6D_6$ | 100 | C_6D_5OD | 0.04 | < 0.005 |
| | 98 | C_6D_5O | 0.04 | < 0.005 |
| | 72 | C_5D_6 | 1.05 | 0.18 |
| | 70 | C_5D_5 | 1.00 | 1.00 |

2. THE DYNAMICS OF THE REACTION



R. J. Buss, P. Casavecchia, T. Hirooka,
S. J. Sibener and Y. T. Lee

The reaction of $\text{O}(^1\text{D})$ with H_2 is of particular interest to theoreticians because while it is a sufficiently small system as to be manageable, the theory must accurately account for the participation of a manifold of low lying electronic states. The experimental determination of product state distributions in crossed molecular beams can provide a sensitive test of the dynamical theories. We have used our $\text{O}(^1\text{D}_2)$ beam source to obtain angular and velocity distributions of OH and OD product from the reaction of $\text{O}(^1\text{D})$ with H_2 and D_2 .

We have found that the radio frequency discharge supersonic oxygen atom source¹ can produce a high flux of $\text{O}(^1\text{D})$ when helium is used as the seeding gas because helium is ineffective at quenching the excited state oxygen. The hydrogen or deuterium was expanded at a stagnation pressure of 17 atm through a room temperature 30-micron-diameter nozzle orifice. The mean collision energy was 2.7 kcal/mole. The cross correlation time of flight method was used to obtain velocity distributions at 17 angles. The angular distribution of OH product is shown in Fig. 1 with a calculated curve, obtained by optimizing the product translational energy $P(E')$ and the center of mass angular distribution $T(\theta)$ to obtain a best fit to the data. The optimum $P(E')$ and $T(\theta)$ (which was found to be symmetric) are shown in Fig. 2. The results for the deuterium reaction, while not yet fully analyzed, appear to be qualitatively similar.

The reaction of $\text{O}(^1\text{D})$ with H_2 might proceed by insertion of the oxygen into the H_2 bond to form a

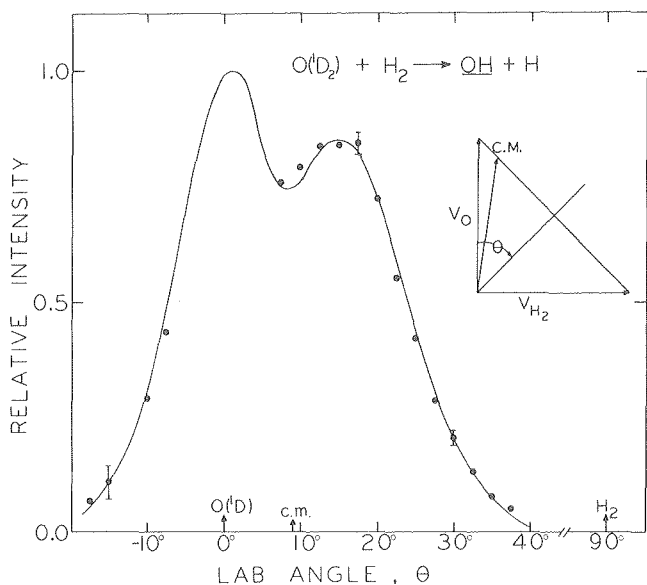


Fig. 1. Laboratory angular distribution of OH product from the reaction of $\text{O}(^1\text{D}) + \text{H}_2$. The line is a calculated curve using a decoupled angular and energy distribution. (XBL 7911-12907)

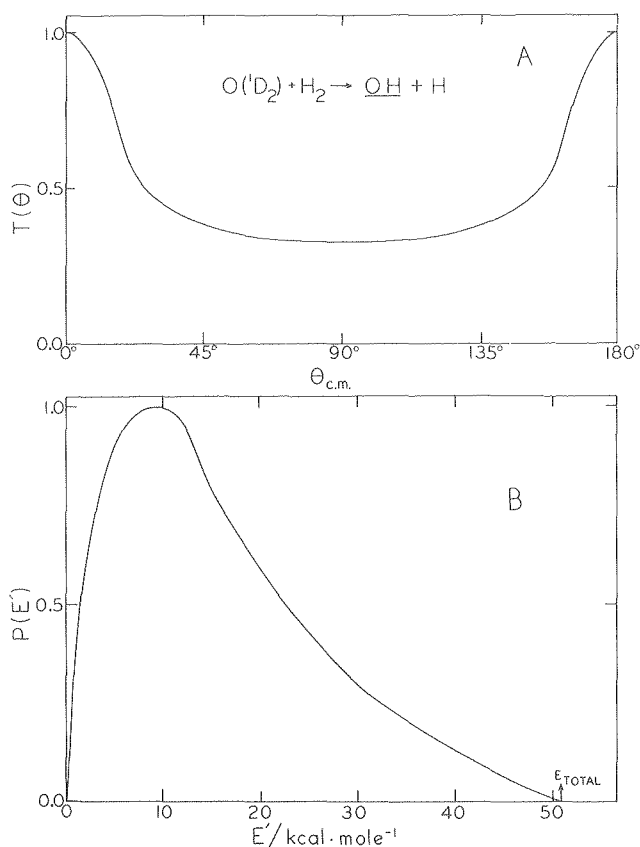


Fig. 2. (A) Center of mass angular distribution of product OH flux. (B) Product translational energy distribution obtained for the $\text{O}(^1\text{D}) + \text{H}_2$ reaction. (XBL 7912-13560)

vibrationally hot water molecule which subsequently dissociates. Alternatively the oxygen might attack collinearly, abstracting an H atom and rebounding. Our product angular distribution is found to be forward-backward symmetric, consistent with the insertion mechanism in which the direction along which the products depart is uncorrelated with the incident direction except for angular momentum constraints. The ab initio potential energy surface (PES) of Howard, McLean and Lester² has no barrier to insertion with a perpendicular approach of the oxygen but indicates a small barrier 1-3 kcal/mole to collinear approach, and thus gives qualitative agreement with our results. Whitlock, Muckermann and Fisher³ have performed classical trajectory studies on a PES they have obtained using a valence bond method. They have found considerable asymmetry in the product angular distributions, even when only the trajectories which involve insertion of the oxygen are chosen.⁴ However, the product translational energy distribution obtained by them is in quite good agreement with the results of our experiment.

Future studies with improved resolution may help us to derive differential cross sections of the individual product vibrational states for this reaction. Additionally we will extend these studies to include the reaction with HD in which we will look at the competition for formation of OH and OD. These studies provide the theoretician with a

sensitive standard with which to compare the accuracy of the PES as well as of the dynamical theories.

* * *

† Brief version of LBL-10565.

1. S. J. Sibener, R. J. Buss and Y. T. Lee, *Rev. Sci. Instrum.*, in press.
2. R. E. Howard, A. D. McLean and W. A. Lester, Jr., *J. Chem. Phys.* **71**(6), 2412 (1979).
3. P. A. Whitlock, J. T. Muckermann and E. R. Fisher, "Theoretical Investigations of the Energetics and Dynamics of the Reactions $O(^3P, ^1D) + H_2$ and $C(^1D) + H_2$," (Research Institute for Engineering Sciences, Wayne State University, Detroit, 1976).
4. J. T. Muckermann, private communication.

3. PRIMARY PRODUCT IDENTIFICATION IN THE REACTION OF OXYGEN ATOMS WITH TOLUENE

R. J. Baseman,[†] R. J. Buss, P. Casavecchia[‡] and Y. T. Lee

We have investigated the reaction of ground state oxygen atoms with toluene under single collision conditions. Previous studies of the rate of this reaction have been reasonably consistent, but there has been uncertainty in the identity of primary products formed.¹⁻⁹ Products reported from bulk phase studies include o-, m-, p-cresol, anisole, benzaldehyde, phenol, methane, ethane, carbon monoxide, benzyl alcohol, and a red-yellow tar. We have observed at least two primary reaction products, C_7H_7O and C_6H_5O , (corresponding to loss of H and loss of CH_3 from an O-toluene adduct) and have failed to observe some previously reported products (i.e., benzaldehyde, cresol, anisole, and benzyl alcohol).

Supersonic beams of $O(^3P)$ atoms produced in a radiofrequency discharge¹⁰ and toluene molecules from a supersonic expansion of the vapor in equilibrium with liquid toluene at ca. 400 K were crossed at 90° in our crossed beams spectrometer equipped with a rotatable electron bombardment ionizer-electric quadrupole mass spectrometer detector assembly.¹¹ Angular and time of flight (TOF) distributions were measured by monitoring parent and daughter ion intensities. Product was detected as masses 78, 79, 106, 107 and 108.

All angular distributions of these masses were found to be superimposable, and all are wider than the distribution of centroids (Fig. 1). The intensity of mass 108 product is approximately one-tenth that of mass 107, about equal to that expected from ^{13}C isotopic impurity.¹² This data then is consistent with mass 107, C_7H_7O being a primary product with masses 78, 79 and 106 being fragments formed in the ionizer. The mass 106 cannot be a primary product of H_2 elimination because this would have resulted in broadening of its angular distribution.

Evidence for C_6H_5O product (CH_3 elimination from C_7H_8O) was found in the mass 65 (C_6H_5O losing CO in the ionizer) spectrum. Angular scans proved fruitless as fragmentation of elastically scattered

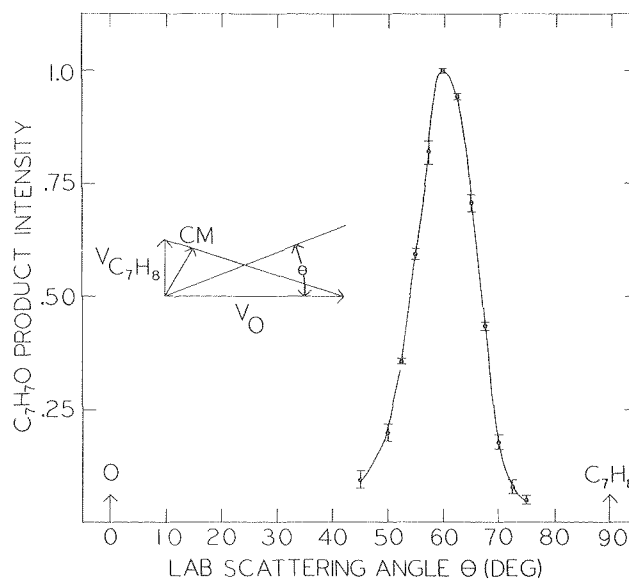


Fig. 1. Angular distribution of mass 107 (C_7H_7O) product formed in the reaction of $O(^3P) +$ toluene. (XBL 7912-13563)

toluene obscures any reaction features in the mass 65 spectrum. TOF spectra measured with daughter ions of elastically scattered toluene (e.g., mass 91) show two maxima, one due to the elastically scattered secondary beam, the other to main chamber background gas. The mass 65 spectrum shows the same two lines, however with added intensity between the peaks. We believe that this is due to a third line in the mass 65 TOF spectrum, from a mass 65 (C_5H_5) daughter ion of a C_6H_5O reaction product. This line obtained as the difference between normalized (corrected) mass 91 and 65 TOF spectra, is shown in Fig. 2 with the corresponding line from C_7H_7O product. The increased breadth and displacement of the C_6H_5O product associated line relative to that from C_7H_7O product confirms a difference in molecular origin for the two lines.

We have observed H and CH_3 elimination in the reaction of oxygen atoms (3P) and toluene. We have seen no evidence for H_2 elimination. Future considerations of this reaction will allow us to describe the reactive dynamics and product structures more fully.

* * *

† Fannie and John Hertz Foundation Fellow.

‡ Permanent address: Dipartimento di Chimica dell'Università, 06100, Perugia, Italy.

1. G. R. H. Jones and R. J. Cvetanovic, *Can. J. Chem.* **39**, 2444 (1964).
2. R. Atkinson and J. N. Pitts, Jr., *J. Phys. Chem.* **78**, 1780 (1974).
3. R. Atkinson and J. N. Pitts, Jr., *J. Phys. Chem.* **79**, 295 (1975).
4. S. Furuyama and N. Ebara, *Int. J. Chem. Kin.* **7**, 689 (1975).
5. A. J. Colussi, D. L. Singleton, R. S. Irwin, and R. J. Cvetanovic, *J. Phys. Chem.* **79**, 1900 (1975).
6. J. S. Gaffney, R. Atkinson, and J. N. Pitts, Jr., *J. Am. Chem. Soc.* **98**, 1828 (1976).

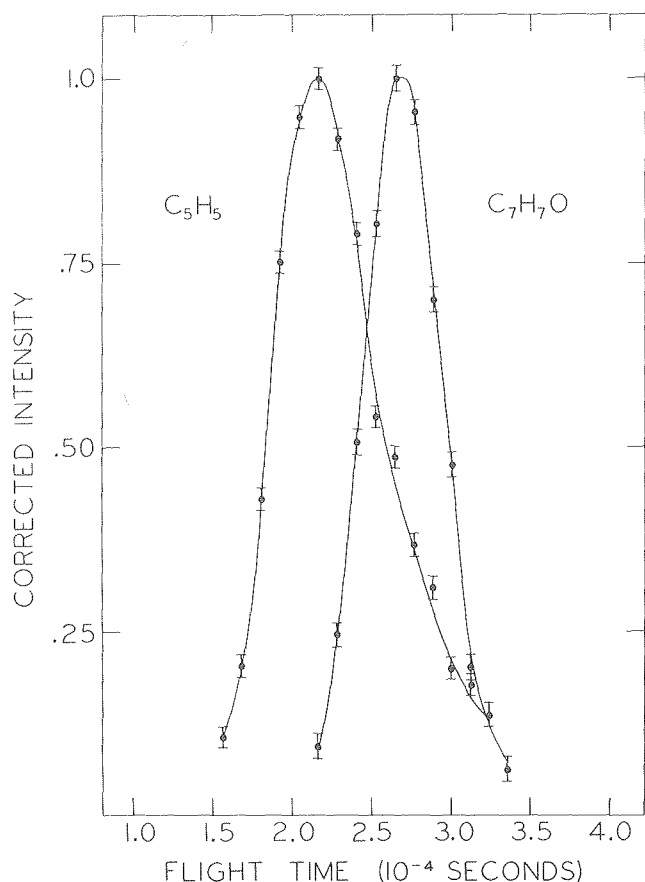


Fig. 2. Time of flight spectra of C_7H_7O and C_6H_5O products formed in the reaction of $O(^3P) + \text{toluene}$ (C_6H_5O product intensity represented by the C_5H_5 daughter ion). (XBL 7910-13564)

7. T. M. Sloane, *J. Chem. Phys.* **67**, 2267 (1977).
8. H. Akimoto, M. Hoshino, G. Inoue, M. Okuda, and N. Washida, *Bull. Chem. Soc. Japan* **51**, 2496 (1978).
9. R. Atkinson and J. N. Pitts, Jr., *Chem. Phys. Lett.* **63**, 485 (1979).
10. S. J. Sibener, R. J. Buss, C. Y. Ng, and Y. T. Lee, *Rev. Sci. Instrum.*, in press.
11. Y. T. Lee, J. D. McDonald, P. R. LeBreton, and D. R. Herschbach, *Rev. Sci. Instrum.* **40**, 1402 (1969).
12. E. Stenhagen, S. Abrahamsson, and F. W. McLafferty, eds., "Atlas of Mass Spectra Data" (Wiley, New York, 1969).

4. OBSERVATION OF CH_3O PRODUCT IN THE CROSSED BEAM STUDY OF THE $O(^1D_2) + CH_4$ REACTION[†]

P. Casavecchia, R. J. Buss, S. J. Sibener and Y. T. Lee

The reaction of $O(^1D_2)$ with methane has been a matter of considerable interest in the past, primarily for its role in stratospheric chemistry.¹ UV photolysis of N_2O-CH_4 or O_3-CH_4 mixtures has been used to study this reaction in gas phase²⁻⁶ and also in a liquid argon medium.⁷ At the present time the reaction is understood⁶ to proceed along two distinct pathways: a) by insertion of $O(^1D_2)$

into the C-H bond to form "hot" methanol, which fragments in the absence of stabilizing collisions; b) by abstraction of H atoms to form OH and CH_3 radicals. H_2 elimination from "hot" methanol resulting in the formation of formaldehyde has also been observed in liquid Ar and inferred in gas phase as a minor channel. Uncertainty remains whether other precursor radicals, such as CH_3O or CH_2OH , are formed at all. Dimethyl ether has been observed in a low pressure study,³ but there is no direct experimental evidence on the identity of the precursor radicals.

In order to understand the reaction mechanism and to elucidate the dynamics and energetics of the $O(^1D_2) + CH_4$ reaction, we have performed a crossed molecular beam investigation of this reaction using a novel supersonic $O(^1D_2)$ beam source developed recently in our laboratory. The seeded $O(^1D_2)$ atomic beam is produced from a high pressure, radio frequency discharge nozzle beam source which has been previously described in detail.⁸ Although the beam also contains $O(^3P)$, undissociated O_2 molecules as well as the He carrier gas, only $O(^1D_2)$ reacts with CH_4 appreciably at low collision energies.⁴ The $O(^1D_2)$ beam was crossed at 90° with a room temperature supersonic beam of pure CH_4 in a collision chamber maintained at $\sim 1 \times 10^{-7}$ Torr. Reaction product angular distributions are measured as a function of in-plane scattering angle by a triply differentially pumped rotatable electron bombardment quadrupole mass spectrometer, kept at $\sim 10^{-11}$ Torr in the ionization region.⁹ Product velocity distributions at selected angles are determined by a cross correlation time-of-flight (TOF) technique.¹⁰ Although $C^{13}H_4$ impurity prevents our studying the hydrogen abstraction channel, we observed scattered signal at $m/e = 30$, 31 and 32. Possible origins of $m/e = 32$ are either CH_3OH^+ or O_2 , but since the lifetime of CH_3OH^+ is expected to be too short ($\lesssim 10^{-12}$ sec)⁶ for it to reach the detector, the $m/e = 32$ signal is believed to be entirely due to elastic scattering of O_2 from CH_4 , as demonstrated by TOF analysis. $m/e = 31$ product cannot be identified directly from a mass spectrometric detection, since it can be either formaldehyde (H_2CO) or a fragment of $m/e = 31$ product. But in a crossed molecular beam experiment it is possible to positively identify the origin of $m/e = 30$ from precise measurement of angular and velocity distributions because of the dynamical and energetic constraints imposed on the reaction system. The $m/e = 30$ angular distribution is rather narrow and is peaked at the center of mass and is shown to come from the fragmentation of mass 31 product (CH_3O or CH_2OH) in the ionizer. Since the $m/e = 31$ signal is strongly contaminated, especially at small angles, by the low mass tail of the intense $m/e = 32$ elastic signal, a reliable angular distribution of $m/e = 31$ is difficult to obtain. However, in the TOF data the reactive $m/e = 31$ signal is separated from that due to elastic contamination. Figure 1 shows the TOF spectra of $m/e = 30$, 31 and 32 at the center-of-mass angle. The $m/e = 30$ and 31 spectra appear similar and peak at the same velocity with the strong elastic contribution of $m/e = 32$ appearing as a shoulder on the high velocity side of $m/e = 31$ spectrum. By subtracting the $m/e = 32$ contribution from the $m/e = 31$ distribution we obtain a spectrum (solid line in Fig. 1b) which is identical to the $m/e = 30$ spectrum (Fig. 1a). This strongly

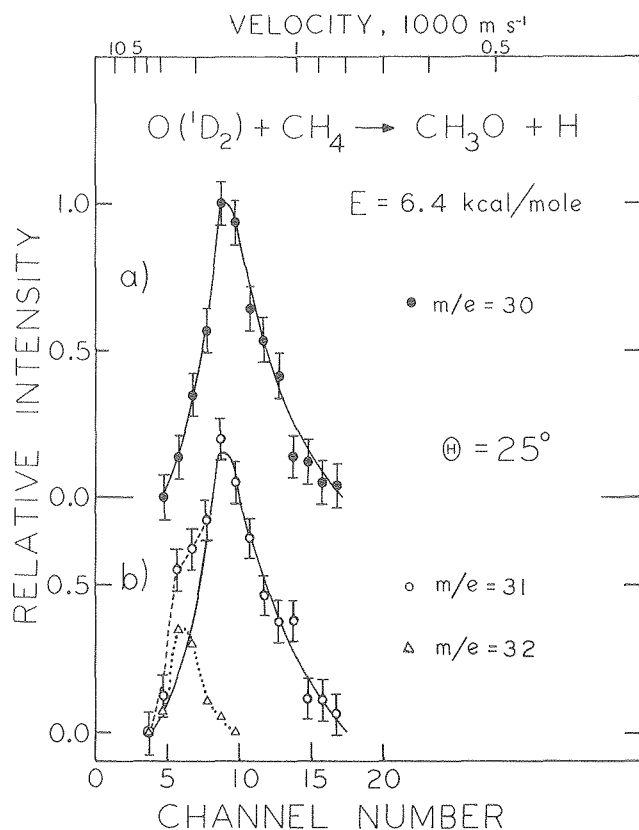


Fig. 1. a) Experimental TOF distribution of m/e 30 product in time space. The dark line is drawn through the data for clarity. b) Experimental TOF distributions of m/e 31 (\circ) and m/e (Δ) in time space. The dark line represents m/e 31 TOF distribution corrected for m/e 32 contribution (see text). Other dotted or dashed lines are drawn through the data for clarity. Error bars ($\pm 2\sigma$) are of the size of the data points for m/e 32 TOF distribution. (XBL 798-11136)

suggests that m/e 31 and m/e 30 have the same origin. Moreover, the intensity ratio of the m/e 30 and 31 TOF spectra is constant at different angles, giving further support that m/e 30 detected is a fragment of CH_3O (or CH_2OH), the primary reaction product, in the ionizer of the mass spectrometer. The narrow angular distribution of m/e 30 product also supports our contention that the primary reaction is not the highly exoergic ($\Delta H = -113$ kcal/mole)¹¹ $\text{H}_2\text{CO} + \text{H}_2$ reaction. The H elimination channel can be accompanied by either CH_3O or CH_2OH radical formation, having slightly different exoergicities¹² (33 and 43 kcal/mole, respectively), but the two pathways cannot be distinguished in our experiment. The fact that we do not observe formaldehyde as a product suggests that the H_2 elimination channel from $\text{CH}_3\text{OH}^\ddagger$ plays a very minor role. The identification of the CH_3O (or CH_2OH) radical as one of the primary reaction products from the single bimolecular reactive collision of $\text{O}(^1\text{D}_2)$ with CH_4 is unambiguous in our experiment. This certainty is not possible using mass spectrometric identification alone.

[†]Brief version of LBL-9762, submitted to J. Chem. Phys.

1. M. Nicolet, *Ann. Geophys.* **26**, 531 (1970); R. P. Lowe and D. McKinnon, *Can. J. Phys.* **50**, 668 (1972).
2. N. Basco and R. G. W. Norrish, *Can. J. Chem.* **38**, 1769 (1960).
3. J. N. Bradley, A. D. Edwards and J. R. Gilbert, *J. Chem. Soc. A* **326** (1971).
4. R. I. Greenberg and J. Heicklen, *Int. J. Chem. Kinet.* **4**, 417 (1972).
5. F. I. Vilesov and A. M. Privilov, *High Energy Chem.* **4**, 475 (1970).
6. C. L. Lin and W. B. DeMore, *J. Phys. Chem.* **77**, 863 (1973).
7. W. B. DeMore and O. F. Raper, *J. Chem. Phys.* **46**, 2500 (1967); W. B. DeMore, *J. Phys. Chem.* **73**, 391 (1969).
8. S. J. Sibener, R. J. Buss, C. Y. Ng, and Y. T. Lee, *Rev. Sci. Instrum.*, in press.
9. Y. T. Lee, J. C. McDonald, P. R. LeBreton, and D. R. Herschbach, *Rev. Sci. Instr.* **40**, 1402 (1969).
10. K. Sköld, *Nucl. Instrum. Meth.* **63**, 114 (1968).
11. S. W. Benson, "Thermochemical Kinetics," (John Wiley & Sons, Inc., New York, 1968). The heats of formation of CH_3O and CH_2OH radicals are taken from J. A. Kerr, *Chem. Rev.* **66**, 465 (1966).

5. VIBRATIONAL PREDISSOCIATION SPECTRA OF WEAKLY BOUND VAN DER WAALS COMPLEXES[†]

H. S. Kwok, M. F. Vernon, D. J. Krajnovich, Y. R. Shen and Y. T. Lee

In the past year, we have developed a high power tunable infrared laser source using the process of optical parametric oscillation (OPO) in a LiNbO_3 crystal and used this to study the infrared absorption spectra and the dynamics of van der Waals complex dissociation. The pumping source was the unstable resonator Nd:Yag laser at 1.064μ . The output from the OPO consisted of two frequencies, with the signal frequency tunable from 1.4 to 2.1μ and the idler frequency tunable from 2.1 to 4.2μ . At the present stage, a total output energy of 15 mJ was routinely available, with a frequency bandwidth of 3.5 cm^{-1} .

We employed these IR pulses to investigate the vibrational predissociation of weakly bound van der Waals complexes in a crossed laser-molecular beam experiment. The experimental arrangement is depicted in Fig. 1. The Nd:Yag laser was allowed to travel >10 m to convert to its far field spatial profile to achieve optimum pumping of the OPO. The van der Waals complexes were obtained by the supersonic expansion of a mixture of argon gas and the benzene or cyclohexane vapor through a 7 mil diameter quartz nozzle. The stagnation pressure of the gas mixture was controlled by adjusting the Ar pressure and the partial pressure of the molecule of interest was varied by changing the temperature of the corresponding liquid bath.

When the van der Waals complex absorbs an infrared photon, it will predissociate according to the equation

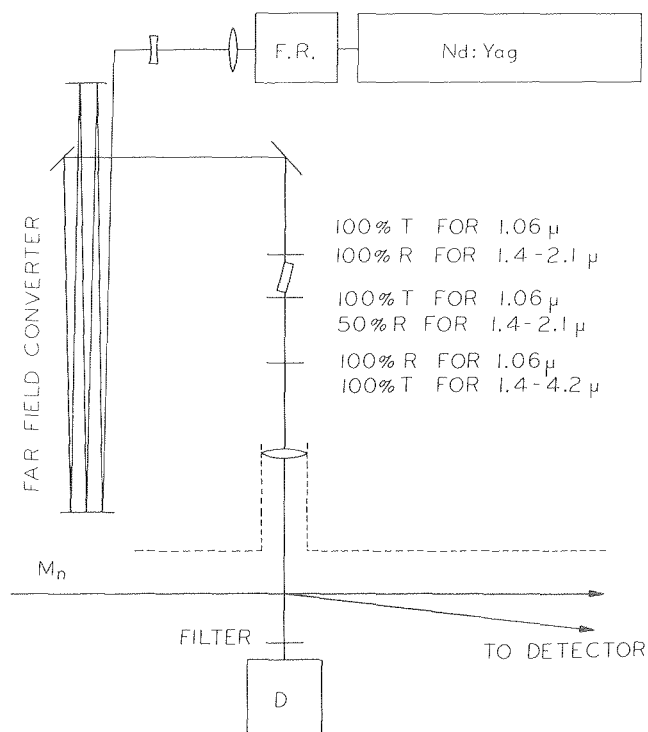
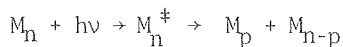


Fig. 1. Experimental setup to obtain the vibrational predissociation spectra of polymeric complexes using a crossed laser-beam configuration. (XBL 7911-12653)



($n = 2, 3$ or 4). Product was detected at 5° from the molecular beam with the mass spectrometer tuned to the product ion M_{n-1} . In order not to have higher polymers contaminating the dissociation signal, we operated at a beam condition by adjusting the stagnation pressure such that there was negligible higher polymer signal.

Figure 2 shows the $C_6H_6^+$ signal from such a measurement. Since the binding energy of the van der Waals complex is much less than a photon energy,

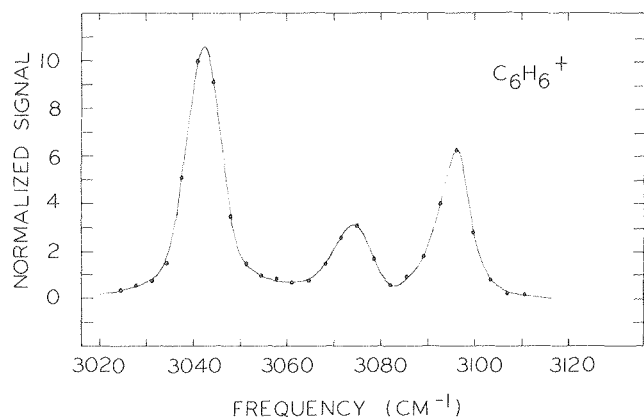


Fig. 2. Vibrational dissociation spectra of benzene polymers. (XBL 7911-12651)

we expect the dissociation spectrum to be the same as the absorption spectrum of the complex itself, in this case the benzene dimer $(C_6H_6)_2$. We observed that the spectrum in Fig. 2 is quite sharp, depicting the three dominant peaks identical to those in the benzene liquid and solid spectrum.¹ The same spectrum was obtained by monitoring $(C_6H_6)_2^+$ at a different molecular beam condition. The only change is that the hexamer spectrum appears red-shifted by $\sim 1.5 \text{ cm}^{-1}$ from the dimer spectrum.

The broadening of the absorption lines, FWHM about 10^{-1} cm^{-1} , should contain contribution from lifetime and rotational broadening. The rotational constant, β , can be estimated by assuming a geometry for the benzene dimer. With an internuclear spacing of 5 \AA , β is calculated to be 0.15 cm^{-1} and, at 100 K the corresponding rotational broadening² is $\sim 7 \text{ cm}^{-1}$. The rotational broadening is expected to decrease as the cluster size increases, but the linewidth of the hexamer was observed to be the same as that of the dimer, suggesting that its rotational temperature might be much colder than 100 K and/or the dominant broadening effects come not from rotation but from lifetime broadening. The 10 cm^{-1} linewidth would correspond to a lifetime of 1 psec which then constitutes a lower bound on the predissociation time.

Figure 3 shows a similar study with cyclohexane. Again, we observe that the peaks are quite narrow ($\sim 10 \text{ cm}^{-1}$) and the absorption spectrum of the dimer is almost identical to the cyclohexane liquid spectrum with a constant red-shift of $\sim 8 \text{ cm}^{-1}$.

In conclusion, the absorption spectrum of van der Waals polymers are found to be very similar to the liquid state spectra. This is consistent with the notion that in a weakly coupled system the energy of the individual components is only slightly perturbed.

For the coming year we plan to incorporate line narrowing elements into the OPO to obtain a linewidth of $\sim 0.5 \text{ cm}^{-1}$ at 3000 cm^{-1} . We shall also interface the OPO with a minicomputer to automate the frequency scanning.

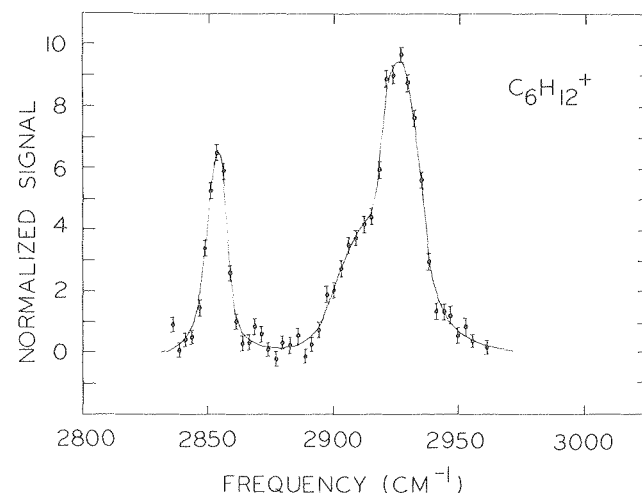


Fig. 3. Vibrational dissociation spectra of cyclohexane polymers. (XBL 7911-12652)

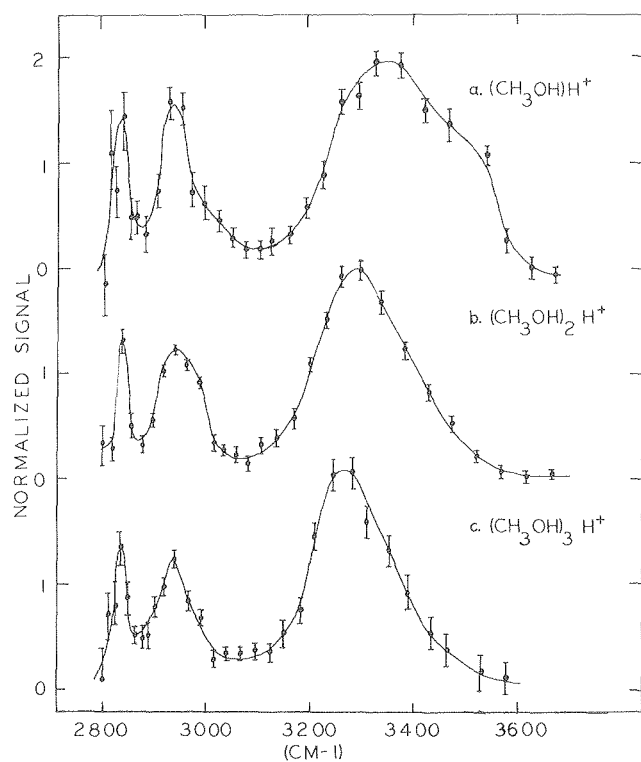


Fig. 2. Photodissociation spectra of $(\text{CH}_3\text{OH})_n^+$.
(XBL 799-11720)

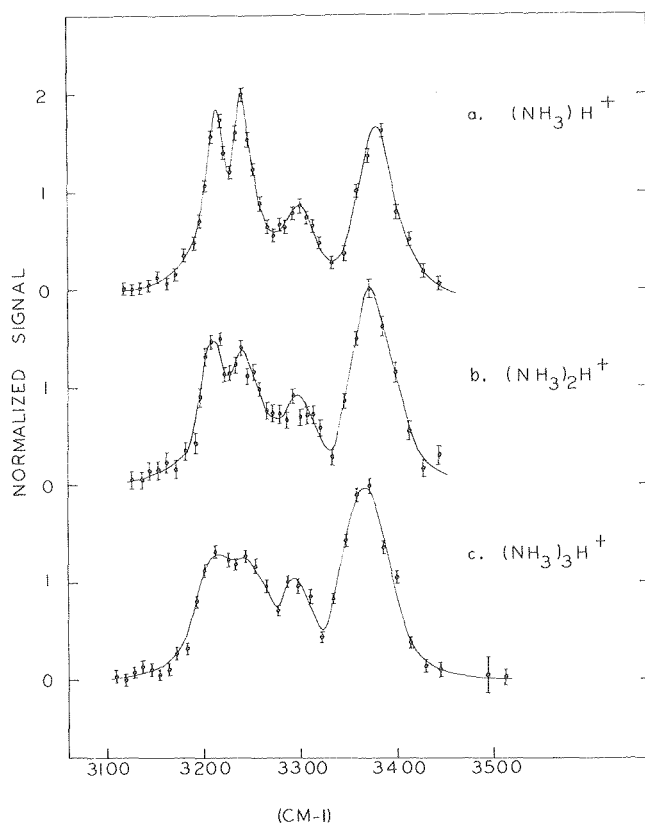


Fig. 3. Photodissociation spectra of $(\text{NH}_3)_n^+$.
(XBL 799-11718)

to be tetrahedral, with one water molecule donating both of its protons to form hydrogen bonds. The feature of 3550 cm^{-1} which dominates the higher polymer spectra could be assigned to the latter type of protons, with the postulate that the majority of the additional water molecules are of this doubly hydrogen bonded type. Further calculations on the high frequency spectrum of water polymers will indicate whether the remaining peaks are characteristic of certain proton types, or the coincidental grouping of slightly disparate frequencies.

* * *

†Brief version of LBL-10288.

1. H. R. Carlson, ARCSL-TR-78914 (1977), and K. R. Wilson in Abstracts of the ACS Meeting, Washington, D.C. (1979).

2. M. Van Thiel, E. D. Becker and G. C. Pimentel, *J. Chem. Phys.* **27**, 95 (1957).

3. J. C. Owicki, L. L. Shipman and H. A. Scheraga, *J. Phys. Chem.* **79**, 1794 (1975).

7. STATE SELECTED ION-MOLECULE REACTIONS: $\text{H}_2^+ + \text{He}$ AND $\text{H}_2^+ + \text{D}_2$

S. L. Anderson, D. Gerlich, F. A. Houle and Y. T. Lee

One of the most serious problems in the interpretation of ion-molecule reaction data, is that in many cases, the ionic reagent is formed in a distribution of excited states. Often this distribution is poorly characterized. A case in point is the simplest molecular ion, H_2^+ . H_2^+ formed by electron bombardment is highly vibrationally excited, with typical estimates of the average internal energy of 0.5 (Ref. 2) to 0.9 (Ref. 1) eV. This uncertainty in the vibrational state distribution makes analysis of low energy reaction data difficult, sometimes obscures the reaction dynamics² and makes comparison with the extensive theoretical³ literature almost impossible.

The use of photoionization allows preparation of ions with well characterized vibrational state distributions. Experiments of Chupka and coworkers⁴⁻⁵ and more recently by Tanaka,⁶ have demonstrated that the reactivity of H_2^+ changes dramatically with the vibrational state. However, these experiments have rather limited energy range and resolution and have been carried out for very few systems. There is a need to extend and redefine our knowledge of internal energy effects on reaction dynamics of ionic systems.

We have recently completed construction and testing of a novel experiment for measuring integral cross sections of an ion molecule reaction. By using a combination of photoionization and the guided beam technique of Telow and Gerlich,⁷ we are able to produce a state selected ion beam with very narrow kinetic energy spread ($<25\text{ meV}$). The ions are reacted with the neutral species either by passing them through a scattering cell (low resolution), or by crossing them with a molecular beam

(high resolution). All primary and product ions are collected by the ion guide and subsequently mass analyzed and counted by a Daly detector. We have near unit collection and detection efficiency independent of mass and thus directly measure integral cross sections. More experimental detail will be given in a subsequent paper. Here we present preliminary data obtained using this instrument.

$\text{H}_2^+ + \text{D}_2 \rightarrow \text{D}_2\text{H}^+ + \text{H}$. This is an isotopic variant of one of the simplest exothermic reactions. There is some controversy, however, about the mechanism of the reaction at low energies.² Experiments to date have not resolved this because of the difficulties outlined above. The $\text{H}_2^+ + \text{H}_2$ reaction has considerable significance theoretically since it is relatively easy to study, and there is a great deal of experimental data.^{1,2} We have studied the reaction channel for collision energies from 0 to 6.3 eV for the first five vibrational states. Figure 1 shows an example of the raw data. The primary beam transmission function and the cross section for $\text{H}_2^+ (v=0) + \text{D}_2 \rightarrow \text{D}_2\text{H}^+ + \text{H}$ are shown. The slow rise of the transmission function is not indicative of the energy spread of the H_2^+ beam, but rather of a discrimination against slow ion transmission at junction of the segments of the ion guide. This skews the energy scale at energies below 0.5 eV. A computational technique for correcting the skewing is under development. The shape of the cross section for $v=0$ is typical of that for the other vibrational states. However, close comparison of the cross sections reveals some important differences. Figure 2 shows the cross sections for $v=0$ through 4 for a number of energies. These were obtained by fixing the collision energy and scanning the ionization wavelength and thus the vibrational state of the H_2^+ . Cross sections here have been corrected for the actual vibrational

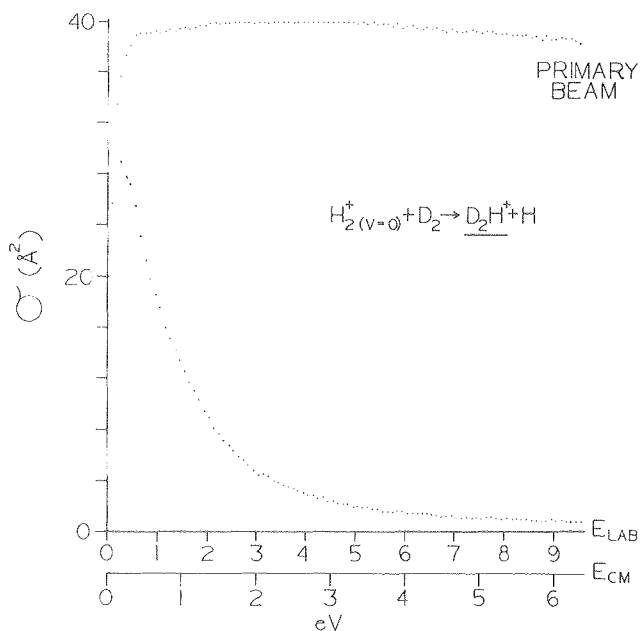


Fig. 1. Primary beam transmission function and cross section for $v=0$ state. (XBL 7911-12752)

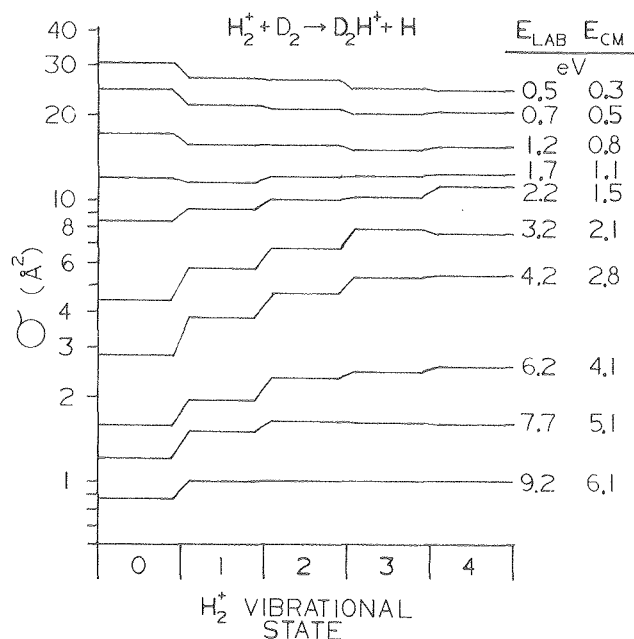


Fig. 2. Comparison of reactivity of different vibrational states of H_2^+ at different energies. (XBL 7911-12754)

populations, but not for averaging due to D_2 target motion. Several trends are clear. At low energies the cross section decreases as v increases. As the collision energy increases this effect rapidly dies out and is replaced by a strong positive effect at ~ 3 eV cm. This effect has been observed qualitatively previously,^{4,6} and interpreted as a change from a complex mechanism at low E to a direct reaction at higher energies. This seems unreasonable in light of the lack of a deep well in the H_4^+ potential surface, and the low reduced mass of the system. We are presently measuring the cross sections for the dissociative and charge exchange channels and the vibrational dependence of the branching ratio between proton transfer and H atom transfer in the reactive channel. Hopefully a more coherent picture of the H_4^+ system will emerge when the interplay between the different channels is known.

$\text{H}_2^+ + \text{He}$. The $\text{H}_2^+ + \text{He}$ system has been the subject of many experimental and theoretical investigations. Chupka and coworkers⁵ have measured cross sections for HeH^+ and H^+ formation over the range 0 to 10 volts (lab). Figure 3 shows our data for the dissociative channel as a function of collision energy and vibrational state. Agreement with Chupka's data is excellent.

Calculations on the $\text{H}_2^+ + \text{He} \rightarrow \text{HeH}^+ + \text{H}$ reaction have predicted the existence of resonances in the total cross section as a function of energy.⁸ In our crossed beam mode of operation we have sufficient resolution to observe features separated by only ~ 20 meV. We are planning to study this reaction at high resolution in the energy range around 1 eV and look for fine structure.

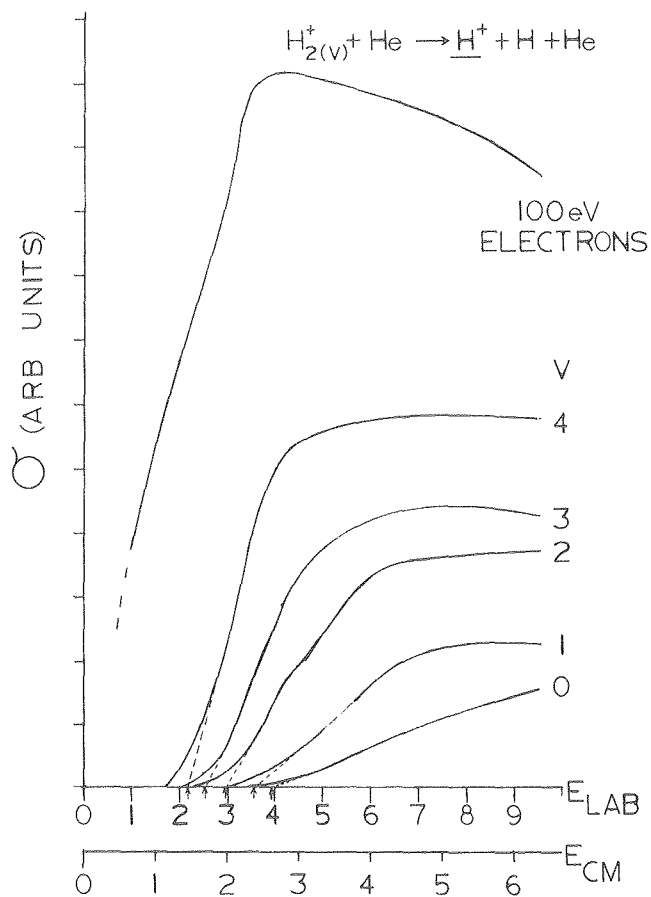


Fig. 3. Relative cross sections for H_2^+ for various vibrational states and for H_2^+ formed by 100 eV electrons. (XBL 7911-12753)

* * *

1. C. H. Douglass, D. J. McClure, and W. R. Gentry, *J. Chem. Phys.* **67**, 4931 (1977).
2. J. R. Krenos, K. K. Lehmann, J. C. Tully, P. M. Hierl, and G. P. Smith, *Chem. Phys.* **16**, 109 (1976).
3. F. Schneider, U. Havemann, L. Zulicke, and Z. Herman, *Chem. Phys. Lett.* **48**, 439 (1977); P. J. Kuntz and W. N. Whitton, *Chem. Phys. Lett.* **34**, 340 (1975); R. D. Poshusta and D. F. Zetik, *J. Chem. Phys.* **58**, 118 (1973).
4. W. A. Chupka in "Ion Molecular Reactions," edited by J. L. Franklin, (Plenum, New York, 1972), Chapter 3.
5. W. A. Chupka and W. E. Russell, *J. Chem. Phys.* **49**, 5426 (1968).
6. I. Koyano and K. Tanaka, "Atomic Collision Research in Japan," Progress Report #5 (1979).
7. D. Gerlich (1971) Diplomarbeit, University Freiburg/Br, W. Germany; E. Telov and D. Gerlich, *Chem. Phys.* **4**, 417 (1974).
8. D. J. Kouri and M. Baer, *Chem. Phys. Lett.* **24**, 37 (1974); J. T. Adams, *Chem. Phys. Lett.* **33**, 275 (1975).

8. MOLECULAR BEAM STUDIES OF THE REACTION DYNAMICS OF F + H₂, D₂[†]

C. C. Hayden, R. K. Sparks, D. M. Neumark, K. Shobatake and Y. T. Lee

The reaction of fluorine atoms with hydrogen molecules has attracted extensive experimental and theoretical attention in the past and undoubtedly will be very important to the detailed understanding of reaction dynamics in the future. The calculation of a limited ab initio potential energy surface for this reaction has been carried out.¹ The basic features of this surface were adopted in the determination of more complete semiempirical potential energy surfaces which have been used in classical trajectory studies,^{2,3} exact one-dimensional scattering calculations,^{4,5} and very recent three-dimensional quantum calculations.⁶ In the one-dimensional quantum mechanical calculations a sharp resonance in the production of HF (v=2) was predicted at a collision energy of ~1 kcal/mole. This sharp enhancement of the production of HF (v=2) at a specific collision energy was not observed in the three-dimensional calculations, although a similar resonance phenomenon is evident as the collision energy is varied at a fixed reactant orbital angular momentum. The experimental observation of these resonance phenomena via their effect on the state and angular distribution of the products could provide a very stringent test of the accuracy of the theoretical calculations.

We have recently measured laboratory velocity and angular distributions for the F + H₂ and F + D₂ reactions at several collision energies. The experiments were performed by crossing supersonic beams of H₂ or D₂ with a high temperature (~700 C) beam of fluorine seeded in nitrogen, and detecting the HF or DF product as a function of angle around the collision center. The collision energy was varied by adjusting the H₂ or D₂ nozzle temperature. Velocity distributions of the products were determined from time-of-flight measurements. The information was then used to construct contour maps of the center-of-mass product distributions. This was done with a forward convolution procedure where trial center-of-mass energy and angular distributions were used to calculate laboratory angular and time-of-flight distributions for comparison with experimental data. The trial functions were then adjusted until a satisfactory fit was obtained.

The center-of-mass angular distribution for HF product from the F + H₂ → HF + H reaction at collision energy of 2.0 kcal/mole is shown in Fig. 1. The distributions clearly peak along the relative velocity vector for products formed in each vibrational state, and the peak direction corresponds to backward scattering of product with respect to the direction of the incident fluorine atom. Very similar results were obtained for the F + D₂ → DF + D reaction at nearly the same collision energy. The center-of-mass distribution for HF product at a collision energy of 3.17 kcal/mole is shown in Fig. 2. The distributions for products in individual vibrational levels at this energy seem to be

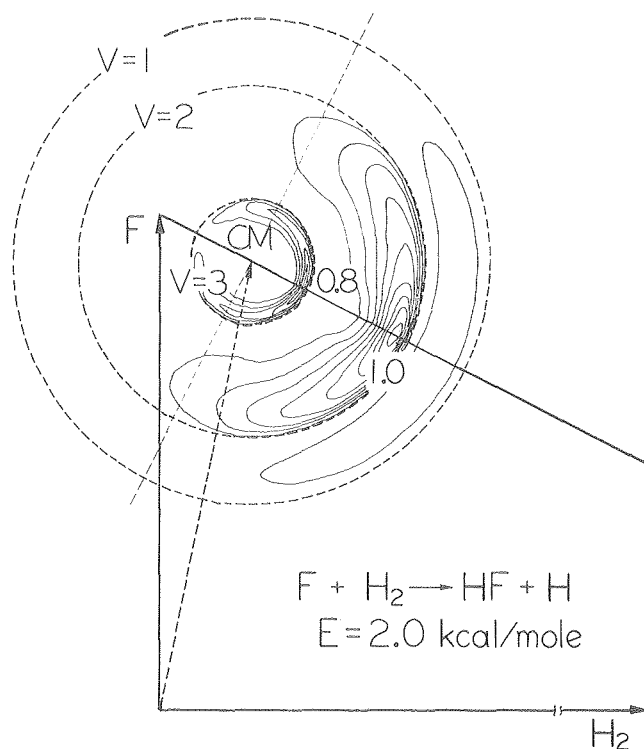


Fig. 1. Center-of-mass velocity-space contour plot of HF product distribution from $F + H_2$ reaction at 2.00 kcal/mole. (XBL 7910-12374)

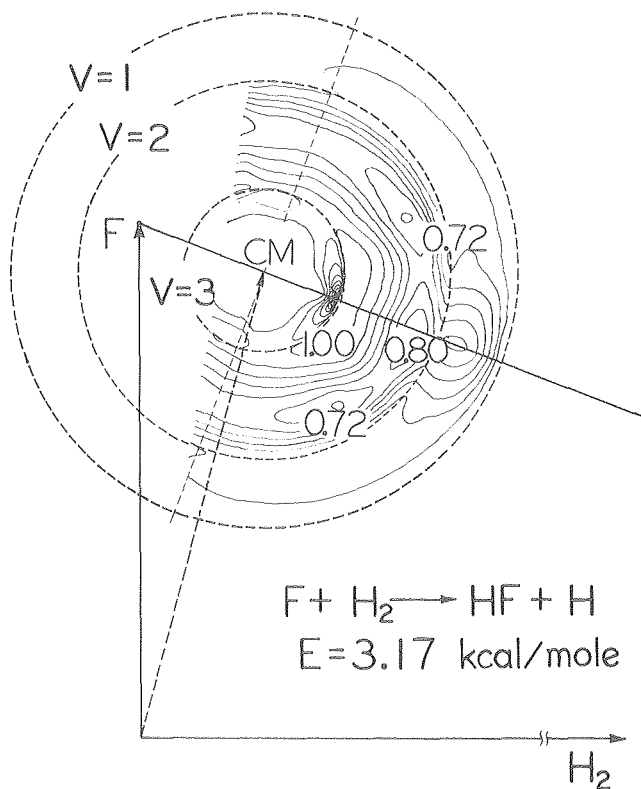


Fig. 2. Center-of-mass velocity space contour plot of HF product distribution from $F + H_2$ reaction at 3.17 kcal/mole. (XBL 7910-12376)

completely decoupled. The products in $v=1$ and $v=3$ peak in the backward direction, but for product $v=2$ the intensity remains high as the center-of-mass angle decreases, and even shows a sideways peaked relative maximum. The dramatic change in the center-of-mass angular distribution for product formed in $v=2$ at 3.17 kcal/mole compared to that at 2.0 kcal/mole is consistent with the reactive resonance phenomenon predicted by the three-dimensional calculations of Redmon and Wyatt.⁶ In that study it was shown that the effect of the resonance is to change the dependence of the reaction probability on reactant orbital angular momentum, and hence the collision impact parameter. While at low collision energies (~ 2 kcal/mole) the reaction probability for $v=2$ product is predicted to peak at zero orbital angular momentum, for collision energies around 3 kcal/mole the probability is calculated to peak at non-zero orbital angular momentum. This is what we observed experimentally, at the higher collision energy more $v=2$ product scatters at smaller center-of-mass angles, indicating that it resulted from collisions with non-zero impact parameter. Thus our results qualitatively agree with the calculation of Redmon and Wyatt.⁶

Several further experiments are planned on these reactive systems. Figure 3 shows data on the $F + D_2$ reaction at 4.51 kcal/mole collision energy. This data has not been fully analyzed, but a surprising feature is immediately apparent. The sharp peak at small lab angles probably indicates a large degree of correlation between reactant and product orbital angular momentum. This feature of the reaction will be very interesting to study in more detail. In addition, we intend to extend the range of collision energies studied for both the $F + H_2$ and $F + D_2$ reactions, as well as improve the resolution of the experiment, by reducing the collision energy

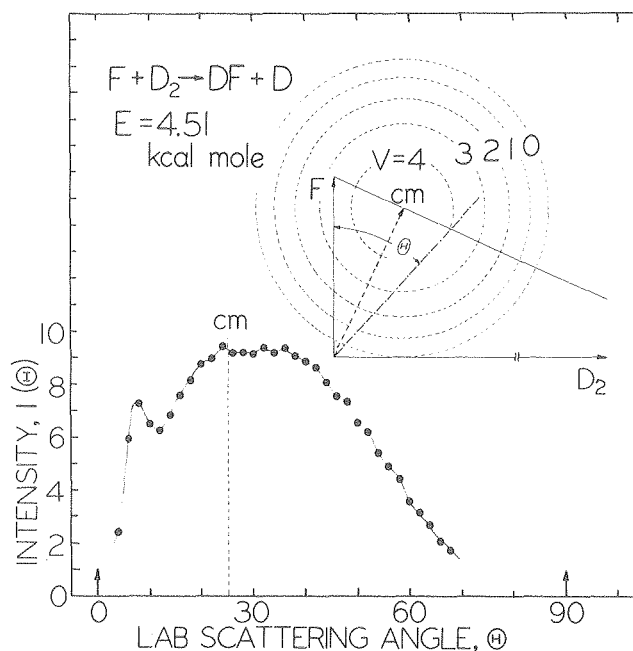


Fig. 3. Experimental LAB angular distribution of the DF product from the $F + D_2$ reaction at 4.51 kcal/mole. (XBL 7910-12373)

spread. We are also in the process of synthesizing HD, in order to study resonance features in the F+HD reaction.

* * *

† Brief version of LBL-9688.

1. C. F. Bender, P. K. Pearson, S. V. O'Neil, and H. F. Schaefer III, *J. Chem. Phys.* **56**, 4626 (1972).
2. J. T. Muckermann, *J. Chem. Phys.* **54**, 1155 (1971).
3. R. L. Wilkins, *J. Chem. Phys.* **58**, 3038 (1973).
4. G. C. Schatz, J. M. Bowman, and A. Kupperman, *J. Chem. Phys.* **58**, 4023 (1973).
5. S. L. Latham, J. F. McNutt, R. E. Wyatt, and M. J. Redmon, *J. Chem. Phys.* **69**, 3746 (1978).
6. M. J. Redmon and R. E. Wyatt, *Chem. Phys. Lett.* **63**, 209 (1979).

9. DYNAMICS OF THE REACTION $\text{Li} + \text{HF} \rightarrow \text{LiF} + \text{H}$ †

P. Casavecchia, C. H. Becker, P. W. Tiedemann, J. J. Valentini and Y. T. Lee

A crossed molecular beam study of reactive and nonreactive scattering of $\text{Li}(^2\text{S}) + \text{HF}(^1\Sigma^+, v=0)$ has been carried out at collision energies ranging from approximately 2 to 9 kcal/mole under single collision conditions. A far reaching motivation has been to provide experimental results for a future test of ab initio and semiempirical potential energy surfaces (PES) and reactive scattering computational methods. $\text{Li} + \text{HF}$ is a good prototype system because of the simplifications of dealing with only light atoms, only one reactive product channel, $\text{LiF} + \text{H}$, and only one PES at collision energies up to ~ 0.5 eV. A partial ab initio and semiempirical PES have been reported for LiFH .^{1,2} Another more complete ab initio PES has recently been carried out.³ These studies show the existence of an exit potential energy barrier relative to the HF zero point vibrational energy for breaking H atoms from LiF. At a bent configuration the height of the barrier of LiFH is smallest and is calculated to be 6.35 kcal/mole.³

The crossed molecular beam apparatus employed in this study has been described in detail previously.⁴ Supersonic beams of Li atoms and HF molecules are crossed at 90° in a liquid N_2 -cooled collision chamber maintained at $\sim 1.5 \times 10^{-7}$ Torr. The supersonic Li atom beam is produced by seeding in a rare gas carrier. The Li source consists of a tantalum reservoir with a gas inlet tube and a tantalum nozzle tube. The reservoir and the nozzle are radiatively heated to a temperature of 960 C and 1150 C, respectively. The second beam is pure HF at room temperature. The HF nozzle is a resistively heated nickel tube, maintained at 380 C to prevent HF dimer formation.

Angular distributions of reactively scattered LiF and nonreactively scattered Li are measured in the plane defined by the two beams as a function of LAB scattering angle θ , measured from the Li beam by a triply differentially pumped rotatable electron bombardment quadrupole mass spectrometer, kept at $\sim 10^{-10}$ Torr. Product velocity distributions at

selected angles are determined by a cross correlation time-of-flight technique.^{5,6}

The angular distributions recorded at m/e 7 show a "hump" in the data at large angles due to fragmentation of reactively scattered LiF in the ionizer. The other dominating feature is the nonreactive scattering of Li at small angles. Rainbow structure is observed at the two lowest collision energies, E_c . From the analysis of these nonreactive distributions a best fit spherically symmetric $v_O(R)$ potential is derived ($\epsilon = 0.46$ kcal/mole; $R_m = 4.34 \text{ \AA}$). The laboratory angular distributions $I(\theta)$ of LiF are shown in Fig. 1 for the four E_c investigated. $I(\theta)$ at the lower E_c are obtained

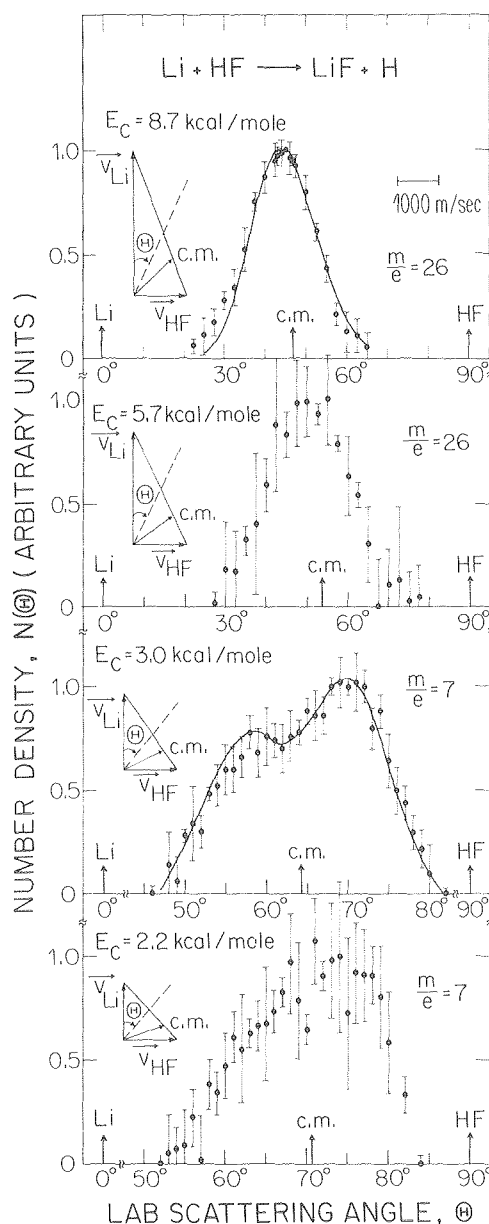


Fig. 1. Laboratory angular distributions of LiF at four E_c . The solid lines are calculated curves. (XBL 7910-4572)

from the reactive "hump" in the m/e 7 measurements, because the LiF signal was very low as a result of the high fragmentation in the ionizer. The low E_c data show a bimodal structure indicating formation of a complex living comparable or longer than a rotational period. This disappears at higher E_c where the distribution shows a weighting toward forward direction. Data have been analyzed to obtain the center-of-mass (c.m.) product distribution. A forward convolution trial and error fitting technique⁶ is used, in which the c.m. angular and energy distribution is input as a trial function. The corresponding laboratory angular and velocity distributions are then calculated from it and compared to the experimental data. The initial trial function is adjusted and the process repeated until a satisfactory fit is obtained simultaneously to both the TOF spectra and the angular distribution. The final result of the analysis is a c.m. product flux contour map. The results are shown in Figs. 2 and 3 for two E_c . The forward-backward symmetry at $E_c = 3.0$ kcal/mole indicates that this reaction is proceeding through a long-lived complex at low collision energy, while at higher E_c the reaction shifts toward a more forward scattering. An estimate of the integral reactive cross section σ_R has been carried out by using the small angle elastic scattering data to calibrate the apparatus. The values obtained at $E_c = 3.0$ and 8.7 kcal/mole are $\sigma_R = 0.80 \text{ \AA}^2$ and $\sigma_R = 0.94 \text{ \AA}^2$, respectively. The small size of σ_R speaks strongly in favor of the existence of a barrier for this slightly exoergic ($\Delta H = -1.1$ kcal/mole) reaction. However, the fact that LiF formation has been observed in this work for a collision energy of ~ 2 kcal/mole

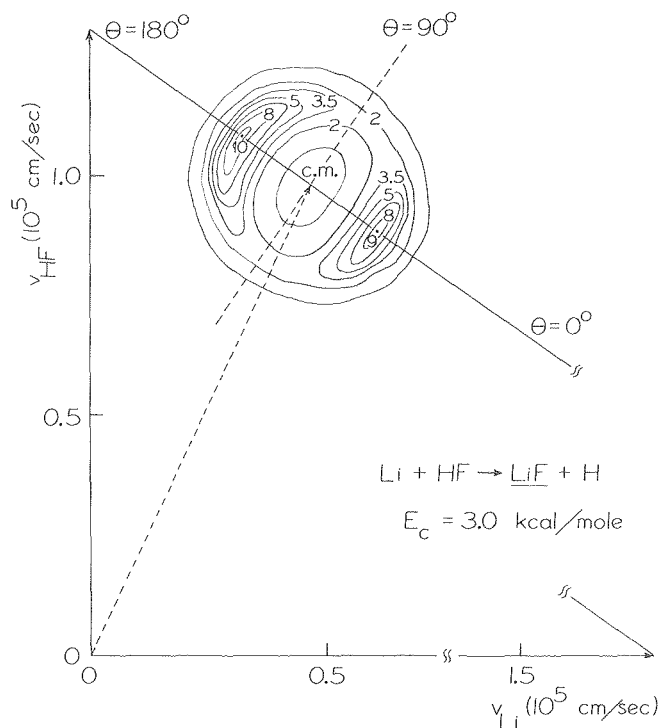


Fig. 2. Contour map of LiF flux in the center-of-mass system produced in the reaction $\text{Li} + \text{HF}$ at a collision energy E_c of 3.0 kcal/mole.

(XBL 7911-12646)

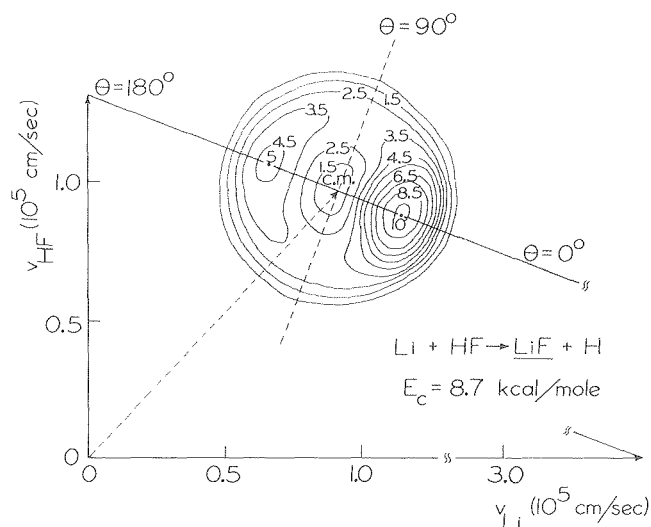


Fig. 3. Contour map of LiF flux in the center-of-mass system produced in the reaction $\text{Li} + \text{HF}$ at a collision energy E_c of 8.7 kcal/mole.

(XBL 7911-12647)

raises the questions of both the accuracy of the computed barrier and the importance of hydrogen tunneling.

* * *

[†]Brief version of LBL-10564.

1. W. A. Lester, Jr. and M. Krauss, *J. Chem. Phys.* **52**, 4775 (1970).
2. G. G. Balin-Kurti and R. M. Yardley, *Faraday Disc. Chem. Soc.* **62**, 77 (1977); M. Shapiro and Y. Zeiri, *J. Chem. Phys.* **70**, 5264 (1979).
3. M. M. L. Chen and H. F. Schaefer III, submitted to *J. Chem. Phys.*
4. Y. T. Lee, J. C. McDonald, P. R. LeBreton, and D. R. Herschbach, *Rev. Sci. Instrum.* **40**, 1402 (1969).
5. K. Sköld, *Nucl. Instrum. Meth.* **63**, 114 (1968).
6. J. M. Farrar, Ph.D. dissertation, University of Chicago, 1974.

10. CHEMILUMINESCENCE MEASUREMENTS FOR THE REACTIONS OF FLUORINE ATOMS WITH I_2 , ICl AND Br_2 [†]

C. C. Kahler and Y. T. Lee

Orbital symmetry arguments have been used for many years to explain the lack of reactivity in systems that are energetically allowed. For the reaction of $\text{I}_2 + \text{F}_2 \rightarrow \text{IF}^* + \text{IF}$, the results of Birks, Gabelnick and Johnston¹ indicated that the mechanism may involve a four-center reaction in violation of symmetry rules. The chemiluminescence was found to increase linearly with both I_2 and F_2 pressure and transitions from both $\text{IF}(B^3\Pi_0^+)$ and $\text{IF}(A^3\Pi_1)$ were observed. Johnston, et al., suggested that either an atom recombination mechanism or a four center reaction mechanism was responsible for the observations. Coggiola, Valentini and Lee² studied $\text{I}_2 + \text{F}_2$ (as well as $\text{F}_2 + \text{ICl}$ and HI) in a crossed molecular beam machine. Their results indicated that the four center reaction is not the major reaction channel. Most of the reaction

proceeds through a trihalogen intermediate. They detected I_2F , $ClIF$ and HIF with reaction thresholds of 4, 6 and 11 kcal/mole, respectively, and for I_2 and ICl , they found the production of IF at higher collision energies, 7 and 21 kcal/mole, respectively, when the product channel such as $I + IF + F$ opens up. The product distributions were not forward-backward symmetric as would be expected of a four-center reaction. The experiments we have just completed on $I_2 + F_2$ combine the molecular beam approach with photon detection to provide a bridge between the two experiments discussed above.

Using the chemiluminescence molecular beam machine previously described,³ light from the reactions of I_2 , ICl and Br_2 with F_2 was measured as a function of collision energy, I_2 pressure and F_2 pressure. The supersonic beam of F_2 was seeded in He, Ar or a mixture of He and Ar and could be heated to 700 K to produce collision energies of 2-20 kcal/mole. A chopper on the F_2 source was used with a gating circuit and dual channel scalar to extract signal from background light. The quasi-effusive source for I_2 , ICl and Br_2 was also heated to prevent condensation of the gases in the nozzle. The data near the threshold for the reactions of $I_2 + F_2$ and $ICl + F_2$ are shown in Figs. 1 and 2. The collision energy scale represents a cross

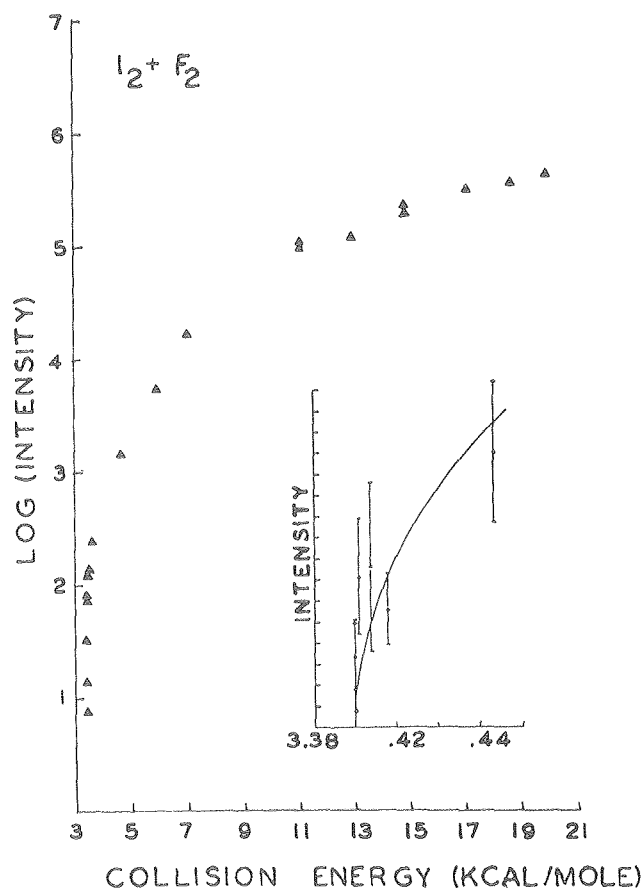


Fig. 1. Energy dependence of the total signal for $I_2 + F_2$. Inset is an enlargement of the threshold region. (XBL 7912-13566A)

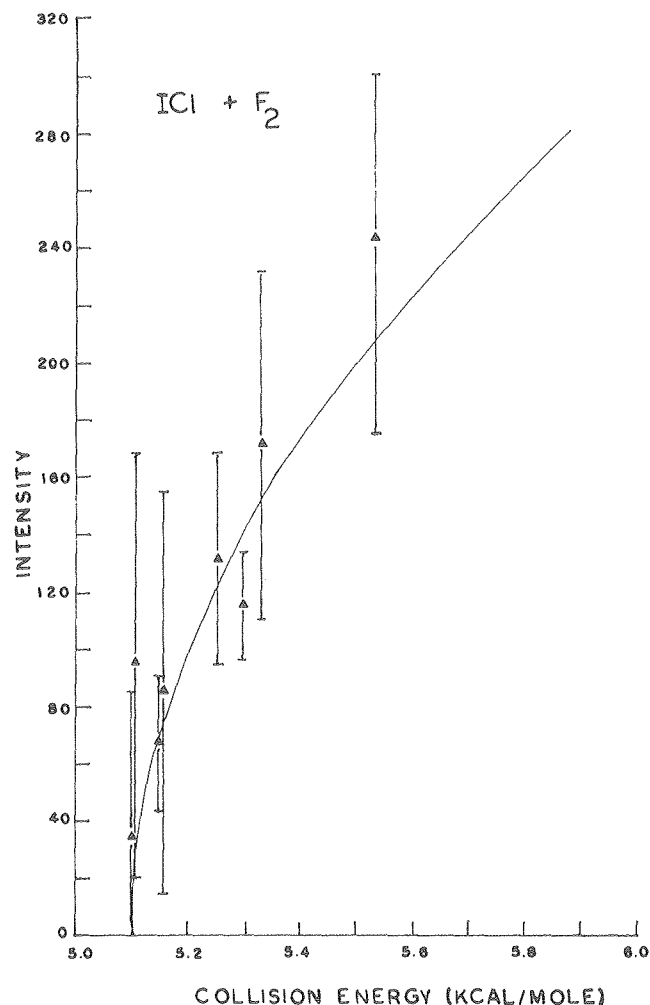


Fig. 2. Energy dependence of the total signal for $ICl + F_2$ near reaction threshold. (XBL 7912-13569)

section weighted mean of the collision energy spread in the beams. The curve going through the points represents a fit of the data to the following equation for the reaction cross section,

$$\sigma \propto (1 - E/E_t)^{0.5} \text{ (Ref. 4),}$$

where E is the collision energy and E_t is the threshold energy. $E_t = 3.4$ kcal/mole for $I_2 + F_2$ and 5.1 kcal/mole for $ICl + F_2$. If we include contributions of internal energy (with the assumption of relaxation of the translational and rotational degrees of freedom and no vibrational relaxation in the beam expansion) we obtain thresholds of 4.6 and 6.1 kcal/mole, in good agreement with Valentini et al.'s thresholds for production of I_2F and $ClIF$.

Figure 3 shows the relative energies of the molecules involved, using Valentini et al.'s values for I_2F and $ClIF$. No level for Br_2F is indicated because it has not been previously observed. We expect to obtain an estimate of its energy relative to $Br_2 + F_2$ when an analysis of the data is complete.

The agreement of our threshold values with those of Valentini et al., implies that the light-emitting

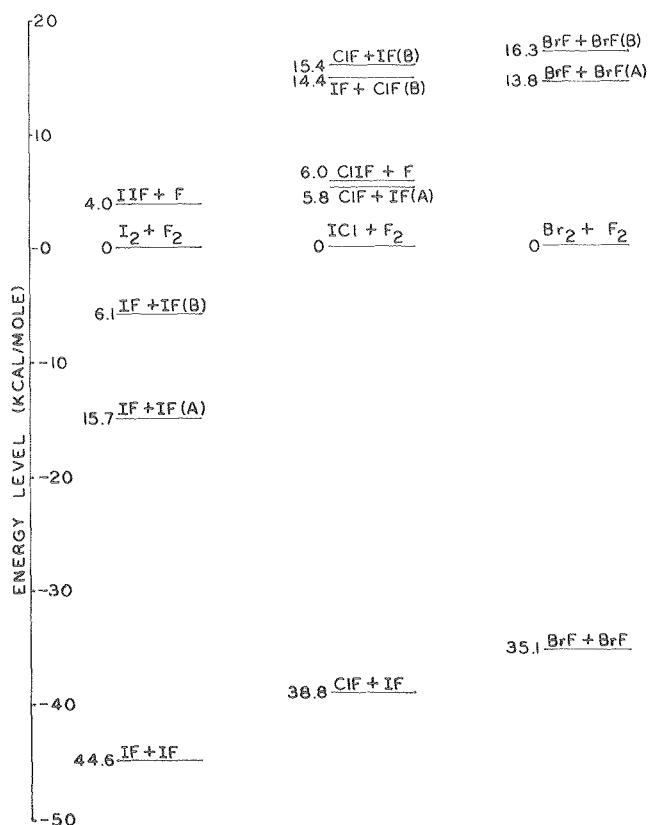


Fig. 3. Energy diagram indicating relative stabilities for species in the reaction $F_2 + X$, $X=I_2, ICl, Br_2$. All energies are in kcal/mole. The values for trihalogen stabilities are from Ref. 2. (XBL 7912-13570)

products are related to the production of I_2F and $ClIF$. In the case of $F_2 + ICl$, our threshold value also matches the endoergicity of $ICl + F_2 \rightarrow ClF + IF(A)$, so the agreement with the $ClIF$ threshold could be fortuitous. We also observe the same leveling off of the signal at high collision energies that Valentini, et al., observed for I_2F . The signal was found to be linear with respect to both I_2 and F_2 pressure which rules out six center reactions (as observed by Herschbach⁵) or reaction of I_2F produced by the beam collision reacting subsequently with background F atoms. $I_2F + F_2 \rightarrow IF^* + IF + F$ is energetically inaccessible. We propose that, although the formation of $I_2F + F$ is the major reaction channel, the light is produced by a reaction of I_2F (or $ClIF$) with the newly released, but still loosely associated F atom in a secondary encounter. This allows excitation of either $IF(A)$ or $IF(B)$ for $I_2 + F_2$, as observed by Johnston,¹ but only $IF(A)$ or $ClF(A)$ (which has not been previously observed) near the threshold of $ICl + F_2$. Unfortunately, our signal was too low to allow the chemiluminescence to be dispersed and the species identified. The fact that Valentini et al., did not see IF at low collision energies is not surprising since this light-producing reaction with a cross section of 0.05 \AA^2 is a minor branch compared to I_2F production.

[†]Brief version of LBL-10545.

1. J. W. Birks, S. D. Gabelnick and H. S. Johnston, *J. Molec. Spec.* **57**, 23 (1975).
2. J. J. Valentini, M. J. Coggiola and Y. T. Lee, *Disc. Faraday Soc.* **62** (1977).
3. MMRD Annual Report (1976), p.369.
4. C. B. Eu and W. S. Liu, *J. Chem. Phys.* **63**, 592 (1975).
5. D. L. King, D. A. Dixon, D. R. Herschbach, *J. Am. Chem. Soc.* **96**, 3328 (1974).

11. ELASTIC SCATTERING OF HF WITH Xe^{\dagger}

C. H. Becker, P. W. Tiedemann, J. J. Valentini, R. B. Walker,[†] and Y. T. Lee

The rare gas-hydrogen halide (RG-HX) interactions have been studied extensively as a simple prototype anisotropic interaction (see, e.g., citations in Ref. 1). Earlier work has been done on $Xe-HF$ by infrared spectroscopy of HF trapped in a Xe matrix near 4 K, (Ref. 2), and measurements of gas phase infrared linewidths and shifts.³ An estimate of the well depth⁴ of the $Xe-HF$ potential of $\sim 0.037 \text{ eV}$ and of the $Xe-HF$ separation⁴ of 3.5 \AA (where $V=0$) are given. However, further investigation of $Xe-HF$ is warranted because the interpretation of the matrix vibrational band displacements are model dependent, infrared linewidths and shifts are not quantitatively reproduced, and because $Xe-HF$ is an extreme of the RG-HX class which has received intense study.

We have measured¹ total angular distributions $I(\theta)$ (including both elastic and inelastic contributions) of $HF(^1\Sigma^+)$ scattered off $Xe(^1S_0)$ by the crossed molecular beam method at collision energies of 0.044 and 0.153 eV in an attempt to further the understanding of this interaction. The apparatus and technique used has been described in detail elsewhere.⁵ The $I(\theta)$ show rainbow and supernumerary rainbow structure, with diffractive oscillations being just resolved in the low energy data. They are reported in Fig. 1. A spherically symmetric potential $V_0(R)$ is fit to the data with well depth and minimum position 0.016 eV and 3.77 \AA . Using this $V_0(R)$, four model potential surfaces $V(R,\gamma)$ are constructed and scattering calculations are performed¹ employing the centrifugal sudden approximation.⁶ The calculation treats HF as a rigid rotor and uses a collision energy of 0.044 eV. The calculations emphasize the role of the initial rotational state as well as the effect of the type and degree of anisotropy of $V(R,\gamma)$ upon the total and state-to-state center-of-mass differential cross sections. In particular, it is found that when $V(R,\gamma)$ is strongly attractive for one limited range of atom-diatom orientations, the elastically scattered rainbow is shifted to larger angles compared to the rainbow from $V_0(R)$ scattering — if the initial rotational state $j_{in}=0$. For $j_{in}=1$ and 2 the $V(R,\gamma)$ scattering tends to resemble that for $V_0(R)$. Results which show this effect (Fig. 2) also indicate that the rotational state of a molecule can have a profound influence on the $d\sigma/d\omega$,

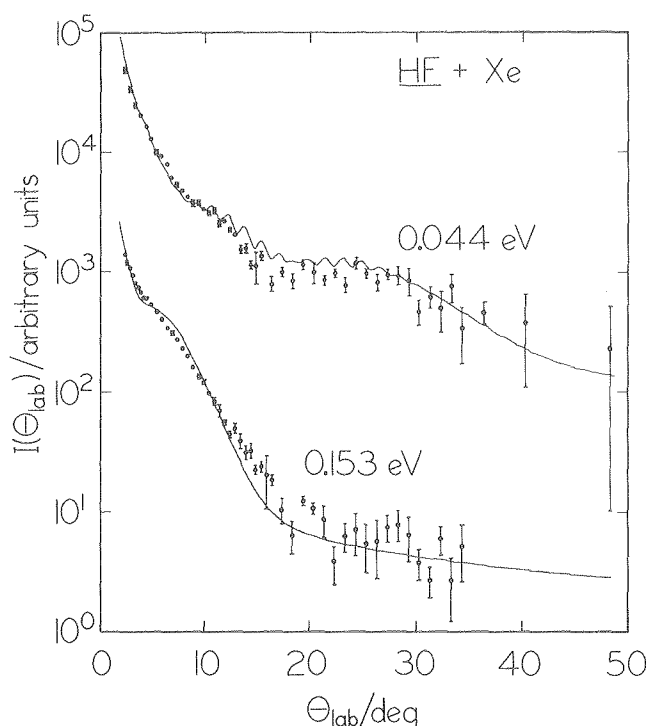


Fig. 1. Experimental angular distributions $I(\theta)$ (solid circles) of HF scattered off Xe at the nominal collision energies shown. The solid line is calculated from the best fit spherically symmetric potential (parameters given in Table I of Ref. 1). (XBL 7812-14109)

and that as the molecule rotates considerably during the collision time the spherically symmetric description of the interaction becomes more useful – which is physically intuitive.

Because the j_{in} distribution in the HF beam is not well characterized, and because it is shown that very similar total differential cross sections at one energy can be generated from qualitatively different $V(R, \theta)$ with similar $V_0(R)$, even for the same j_{in} , conclusions about the HF-XE anisotropy of $V(R, \gamma)$ from $I(\theta)$ are precluded. However, the extracted $V_0(R)$ is thought to be realistic based on the consistency of fits to the two $I(\theta)$ at significantly different collision energies (see Fig. 1) and the likelihood of a relatively high rotational temperature of the HF beam due to heating of the nozzle source.

* * *

† Brief version of LBL-8637.

‡ Associated with Los Alamos Scientific Laboratory.

1. C. H. Becker, P. W. Tiedemann, J. J. Valentini, Y. T. Lee and R. B. Walker, *J. Chem. Phys.* **71**, 481 (1979).
2. M. G. Mason, W. G. Von Holle and D. W. Robinson, *J. Chem. Phys.* **54**, 3491 (1971).
3. J. Jarecki and R. M. Herman, *J. Quant. Radiat. Transfer* **15**, 707 (1975); J. Jarecki, *J. Chem. Phys.* **65**, 5318 (1976).
4. H. Friedman and S. Kimel, *J. Chem. Phys.* **43**, 3925 (1965).

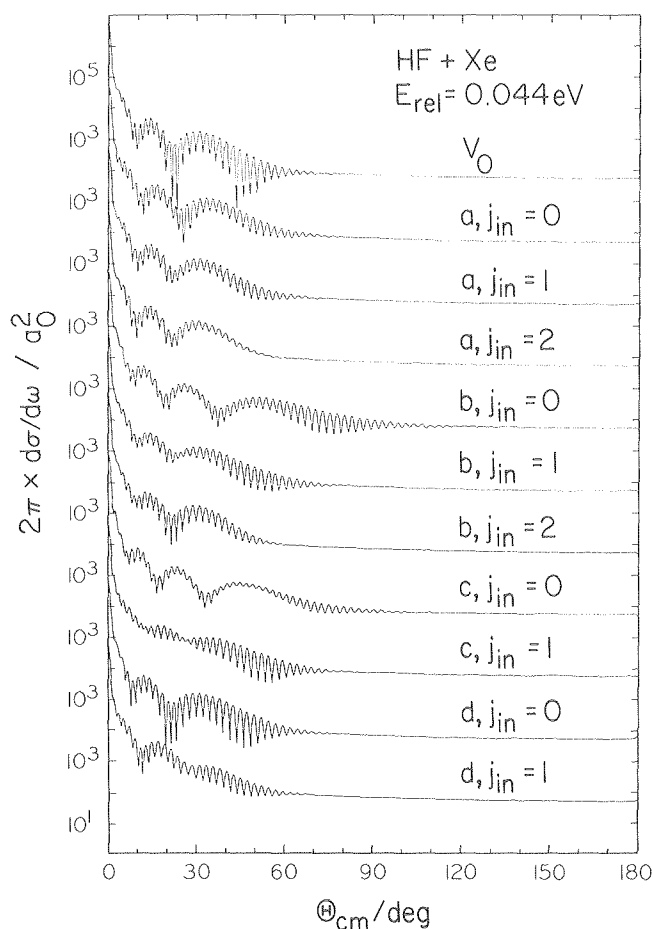


Fig. 2. Total $d\sigma/d\omega$ for the four model surfaces a, b, c and d described in Ref. 1 at $E_{rel} = 0.044$ eV for given initial rotational states.

(XBL 7812-14112)

5. Y. T. Lee, J. D. McDonald, P. R. LeBreton and D. R. Herschbach, *Rev. Sci. Instrum.* **40**, 1402 (1969). See Ref. 1 for experimental details.
6. G. A. Parker and R. T. Pack, *J. Chem. Phys.* **68**, 1585 (1978); R. T. Pack, *J. Chem. Phys.* **60**, 633 (1974); R. B. Walker and J. C. Light, *Chem. Phys.* **7**, 84 (1975). See also citations in Ref. 1.

12. CLOSE-COUPPLING STUDY OF HALOGEN (2P) + RARE GAS (1S) SCATTERING†

C. H. Becker, P. Casavecchia, R. E. Olson,‡
W. A. Lester, Jr.‡ and Y. T. Lee

There is considerable need for ground state interaction potentials for rare gas-halides (RG-X) because of the development of RG-X ultraviolet lasers and for the theory of termolecular recombination of these systems (see, e.g., citations in Ref. 1). Although these states are not easily accessible to standard optical spectroscopy, it is possible from crossed atomic beam scattering experiments to measure total differential cross section $I(\theta)$ and, where the data are adequate, to extract the potentials from this data. $I(\theta)$ have been measured

for $F(^2P)$ scattered off Ne, Ar, Kr (Ref. 1) and Xe (Ref. 2) and for $Cl(^2P)$ scattered off Xe (Ref. 3) at several collision energies in a universal crossed beam apparatus.⁴ An elastic approximation¹⁻³ appropriate to Hund's coupling case (c) has been employed to derive the potential $X\ 1/2$, $I\ 3/2$ and $II\ 1/2$ arising from the $X(^2P) + RG(^1S)$ interaction.

In order to test this elastic approximation and obtain information on intra and intermultiplet transitions among $RG-X$, quantum mechanical coupled-channel (CC) computations have been carried out⁵ for the $F + Ar$, Xe and $Cl + Xe$ systems employing the potentials previously derived¹⁻³ from the measured $I(\theta)$. The multichannel Schrödinger equations, derived in a space fixed frame, are solved numerically by the log-derivative integration technique⁶ to obtain the scattering matrices S^J . Differential cross sections for $j \rightarrow j'$ transitions are conveniently constructed from the S in the helicity representation.⁷ Integral inter- and intramultiplet changing cross section are expressed conveniently in terms of Grawert's $B(j, j'; g)$ coefficient.⁸ Information on the collision dynamics is extracted by following the partial wave dependence of selected $B(j, j'; g)$. Classical turning point analysis, based on the values of the large l -waves for which these partial wave contributions $B_1(j, j'; g)$ begin to rise above zero, leads to the conclusion that both intermultiplet and first order forbidden intramultiplet transitions are caused by a single localized nonadiabatic coupling region at the position of complex crossing of the $\Omega = 1/2$ adiabatic potentials. Small amplitude oscillations or perturbation in the CC calculated differential cross sections $d\sigma/d\omega$ and in the experimental $I(\theta)$ are thought to be examples of Stükelberg oscillations, though quantitative agreement between these quantities is not obtained. Comparison of the $d\sigma/d\omega$ derived by the CC and elastic methods were carried out at energies chosen to coincide with nominal laboratory collision energies E_{rel} . The calculated $d\sigma/d\omega$ were converted to the lab frame and the results are shown in Figs. 1 and 2 for the $F + Xe$ system for two different E_{rel} . Agreement between the CC and elastic $I(\theta)$ for both these collision energies is extremely good. Good agreement is obtained also for $F + Ar$ and $Cl + Xe$. This close agreement between the $I(\theta)$ computed by the CC and elastic methods shows that the simple single channel approach to these $RG-X$ three channel scattering problems is useful for extracting realistic $V(R)$ from experimental $I(\theta)$. Use of realistic $V(R)$ then makes the coupled channels calculation meaningful for comparison or prediction of experimental quantities. The validity of the elastic approximation is supported also by its ability to corroborate accurate spectroscopically determined $V_X\ 1/2$ for $F-Xe$ (Ref. 2) and $Cl-Xe$ (Ref. 3). This approximation is expected to allow a valid $I(\theta)$ analysis also for the $Br-$ and $I-RG$ systems, presently under investigation in our laboratory.

* * *

† Brief version of LBL-8533.

‡ Stanford Research Institute International, Menlo Park, California.

§ NRCC, Lawrence Berkeley Laboratory.

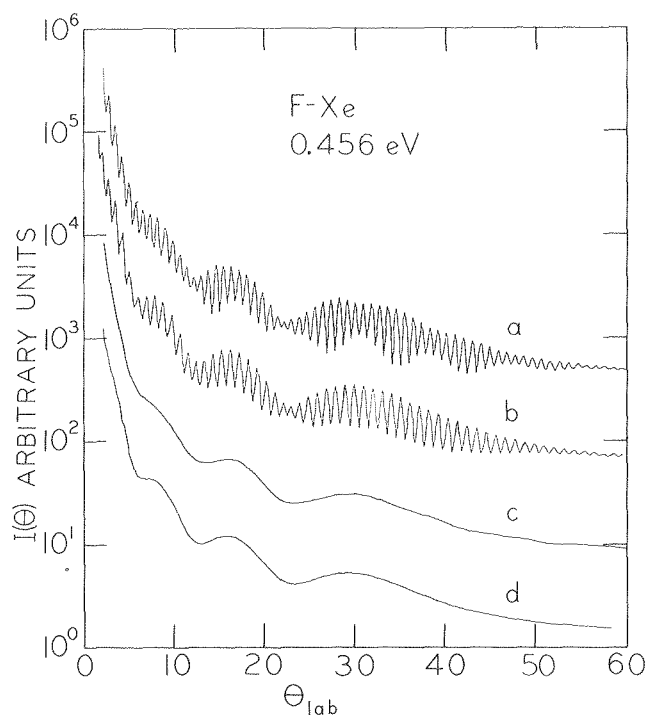


Fig. 1. Comparison of $F-Xe\ I(\theta)$ derived by CC and elastic methods for $E_{rel} = 0.456\ eV$. Arbitrary scaling is employed. (a) CC result with no angular averaging. (b) Elastic result with no angular averaging. (c) Angular average of curve (a). (d) Angular average of curve (b). (XBL 7811-12996)

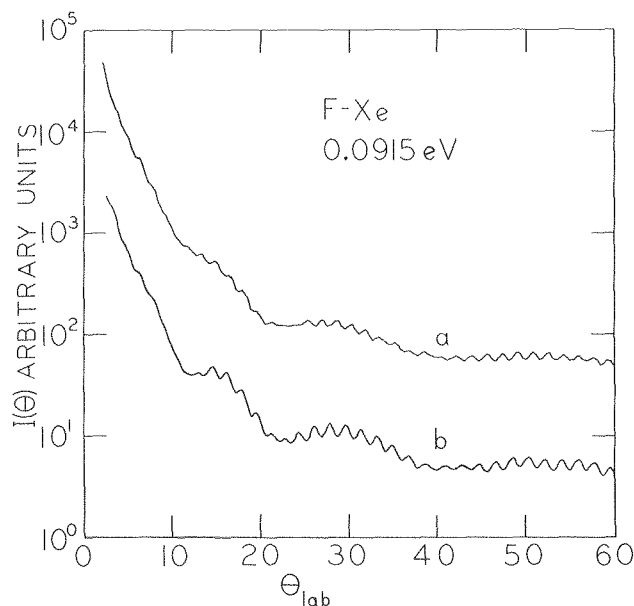


Fig. 2. Comparison of $F-Xe\ I(\theta)$ derived by CC (curve a) and elastic methods (curve b) for $E_{rel} = 0.0915\ eV$. (XBL 7811-12995)

1. C. H. Becker, P. Casavecchia and Y. T. Lee, *J. Chem. Phys.* **70**, 2986 (1979).
2. C. H. Becker, P. Casavecchia and Y. T. Lee, *J. Chem. Phys.* **69**, 2377 (1978).
3. C. H. Becker, J. J. Valentini, P. Casavecchia, S. J. Sibener and Y. T. Lee, *Chem. Phys. Lett.* **61**, 1 (1979).
4. Y. T. Lee, J. D. McDonald, P. R. LeBreton and D. R. Herschbach, *Rev. Sci. Instrum.* **40**, 1402 (1969).
5. C. H. Becker, P. Casavecchia, Y. T. Lee, R. E. Olson and W. A. Lester, Jr., *J. Chem. Phys.* **70**, 5477 (1979).
6. B. R. Johnson, *J. Comput. Phys.* **13**, 445 (1973).
7. W. H. Miller, *J. Chem. Phys.* **50**, 407 (1969); see also J. Schaefer and W. A. Lester, Jr., *J. Chem. Phys.* **62**, 1913 (1975).
8. F. H. Mies, *Phys. Rev. A* **7**, 942, 957 (1973); R. H. G. Reid, *J. Phys.* **B6**, 2018 (1973); G. Grawert, *Z. Phys.* **225**, 283 (1969).

RESEARCH PLANS FOR CALENDAR YEAR 1980

Crossed molecular beam studies of the reaction of oxygen atoms with unsaturated hydrocarbons will move from aromatic to aliphatic hydrocarbons as well as alkyl radicals in the coming year. Investigations of the initiation processes of combustion, especially the formation of HO₂ by high energy O₂ collisions with hydrocarbons and the reaction of alkyl radicals with O₂ will also be carried out.

The exciting dynamic resonance phenomena in reactive scattering will be further pursued by obtaining the translational energy dependence of total reactive cross sections of state-selected H₂⁺ + He and by measuring the energy-dependent branching ratio of the state-resolved F + HD reaction. These resonance phenomena will provide the most stringent test of the accuracy of potential energy surfaces and scattering calculations which will become available in the near future.

With a new single frequency ring laser, reactions of electronically excited molecules will be carried out under single collision conditions. The effect of vibrational rotational excitation in these molecule-molecule reactions will be of particular interest.

A new apparatus will be constructed for the investigation of the infrared absorption spectroscopy and for measurement of the heat of formation of radical molecules. Infrared absorption spectra of radicals will be obtained with the molecular beam method using photoionization detection of IR laser excited radicals. The heat of formation will be derived from the threshold energy of vibrational energy controlled unimolecular decomposition of complex ions which produce radicals and protonated molecules as products. Proton affinities determined in previous experiments will be the key with which to obtain the heat of formation of radicals.

Interaction potentials of bromine atoms with Kr and Xe will be studied from the measurements of elastic differential cross sections. These open shell systems will be compared with corresponding closed shell Kr + Kr and Kr + Xe systems in order

to understand the subtle differences between van der Waals forces and weak chemical forces.

1979 PUBLICATIONS AND REPORTS

Refereed Journals

1. Richard J. Buss and Yuan T. Lee, "Crossed Beam Studies Related to Gas Kinetics," *J. Phys. Chem.* **83**, 34 (1979), LBL-7625.
2. S. T. Ceyer, P. W. Tiedemann, B. H. Mahan and Y. T. Lee, "Energetics of Gas Phase Proton Solvation by NH₃," *J. Chem. Phys.* **70**, 14 (1979), LBL-7695.
3. S. T. Ceyer, P. W. Tiedemann, C. Y. Ng, B. H. Mahan and Y. T. Lee, "Photoionization of Ethylene Clusters," *J. Chem. Phys.* **70**, 2138 (1979), LBL-7694.
4. C. H. Becker, P. Casavecchia and Y. T. Lee, "Crossed Molecular Beam Studies on the Interaction Potentials for F(²P) + Ne, Ar, Kr(¹S)," *J. Chem. Phys.* **70**, 2986 (1979), LBL-8406.
5. C. H. Becker, J. J. Valentini, P. Casavecchia, S. J. Sibener and Y. T. Lee, "Crossed Molecular Beam Studies on the Interaction Potentials for Cl(²P) + Xe(¹S)," *Chem. Phys. Lett.* **61**, 1 (1979), LBL-8574.
6. C. H. Becker, P. Casavecchia, Y. T. Lee, R. E. Olson and W. A. Lester, Jr., "Coupled-Channel Study of Halogen (²P) + Rare Gas (¹S) Scattering," *J. Chem. Phys.* **70**, 5477 (1979), LBL-8533.
7. C. H. Becker, P. W. Tiedemann, J. J. Valentini, Y. T. Lee and R. B. Walker, "Experimental and Computational Study of HF + Xe Scattering," *J. Chem. Phys.* **71**, 481 (1979), LBL-8637.
8. P. W. Tiedemann, S. L. Anderson, S. T. Ceyer, T. Hirooka, C. Y. Ng, B. H. Mahan and Y. T. Lee, "Proton Affinities of Hydrogen Halides Determined by the Molecular Beam - Photoionization Method," *J. Chem. Phys.* **71**, 605 (1979), LBL-8858.

LBL Reports

1. Richard J. Buss and Yuan T. Lee, "Molecular Beam Studies Unimolecular Reactions, Cl, F + C₂H₃Br," Faraday General Discussion No. 67, Univ. of Birmingham, England, April 9-11, 1979, LBL-7686.
2. Christopher H. Becker, "Collisions of Halogen (²P) and Rare Gas (¹S) Atoms," (Ph.D. Thesis), LBL-8589.
3. T. Hirooka, S. L. Anderson, P. W. Tiedemann, B. H. Mahan and Y. T. Lee, "Vibrational Predissociation of Vibronically Excited Hydrogen Molecule Dimers," submitted to *J. Chem. Phys.*, March 1979, LBL-8934.
4. H. Haberland, Y. T. Lee and P. E. Siska, "Scattering of Noble Gas Metastable Atoms in Molecular Beams," submitted for a chapter in "The Excited State in Chemical Physics, Part 2," edited by J. Wm. McGowan, March 1979, LBL-8959.

5. Richard J. Buss, "Crossed Molecular Beam Studies of Unimolecular Reaction Dynamics," (Ph.D. Thesis), LBL-9057.
 6. Lee R. Carlson, "Photodissociation Processes in Molecular Beams," (Ph.D. Thesis), LBL-9219.
 7. R. K. Sparks, L. R. Carlson, K. Shobatake, M. L. Kowalczyk, and Y. T. Lee, "Ozone Photolysis: A Determination of the Electronic and Vibrational State Distributions of Primary Products," submitted to *J. Chem. Phys.*, July 1979, LBL-9555.
 8. Steven J. Sibener, Richard J. Buss, Cheuk Yiu Ng and Yuan T. Lee, "Development of a Supersonic $O(^3P_j)$, $O(^1D_2)$ Atomic Oxygen Nozzle Beam Source," submitted to *Rev. Sci. Instrum.*, September 1979, LBL-9722.
 9. P. Casavecchia, R. J. Buss, S. J. Sibener and Y. T. Lee, "Observation of CH_3O Product in the Crossed Beam Study of the $O(^1D_2) + CH_4$ Reaction," submitted to *J. Chem. Phys.*, September 1979, LBL-9762.
 10. Steven J. Sibener, "Crossed Beam Reactive Scattering of Oxygen Atoms and Surface Scattering Studies of Gaseous Condensation," (Ph.D. Thesis), LBL-9811.
 11. Syliva T. Ceyer, "Molecular Beam Photoionization and Gas-Surface Scattering," (Ph.D. Thesis), LBL-9838.
 12. D. Gerlich, S. W. Bustamente, H. S. Kwok, L. R. Carlson, and Y. T. Lee, "Measurement of the Decay Lifetime of the Metastable $O_2(a^4\pi_u)$ State," submitted to *Chem. Phys. Lett.*, October 1979, LBL-9972.
 13. Steven J. Sibener, Richard J. Buss, Piergiorgio Casavecchia, Tomohiko Hirooka, and Yuan T. Lee, "A Crossed Molecular Beams Investigation of the Reactions $O(^3P) + C_6H_6$, C_6D_6 ," submitted to *J. Chem. Phys.*, October 1979, LBL-9975.
 14. Randal K. Sparks, "Crossed Beam Studies of Full and Half Collisions," (Ph.D. Thesis), LBL-10138.
- Invited Talks
1. Y. T. Lee, "Energetics and Dynamics of Molecule Ions by Molecular Beam Photoionization of van der Waals Molecules," Pauling Award Symposium on van der Waals Molecules, Seattle, Washington, January 20, 1979.
 2. Y. T. Lee, "Dynamics of Infrared Multiphoton Dissociation of Polyatomic Molecules," Department of Chemistry, Rice University, Houston, Texas, March 7, 1979.
 3. Y. T. Lee, "Investigation of Reaction Intermediates and Transient Species by the Molecular Beam Method," Department of Chemistry, Arizona State University, Tempe, Arizona, March 9, 1979.
 4. Y. T. Lee, "Dynamics of Multiphoton Dissociation in Molecular Beams," ACS/CSJ Chemical Congress: 1979, Laser Chemistry Symposium, Honolulu, Hawaii, April 2-6, 1979.
 5. R. J. Buss, "Molecular Beam Studies of Unimolecular Reactions, $Cl, F + C_2H_3Br$," Faraday General Discussion No. 67, "Kinetics of State-Selected Species," University of Birmingham, England, April 9-11, 1979.
 6. Y. T. Lee, "Molecular Beam Studies of Infrared Multiphoton Dissociation of Polyatomic Molecules," Department of Chemistry, University of California Los Angeles, California, April 24, 1979.
 7. Y. T. Lee, "Energetics and Dynamics of Radical Molecules," Department of Chemistry, University of California, Berkeley, May 1, 1979.
 8. Y. T. Lee, "Intramolecular Energy Transfer of Vibrationally Excited Molecules," Naval Weapons Laboratory, Washington, D.C., May 23, 1979.
 9. Y. T. Lee, "State to State Reactive Scattering," VI International Molecular Beam Symposium, Riva Del Garda, Italy, May 26-30, 1979.
 10. S. Ceyer, "Energetics and Dynamics of Molecule-Ions by Photoionization of van der Waals Molecules," Symposium on "Fundamental Aspects of Processes Relevant to Formation and Reaction of Ions," 27th Annual Meeting on Mass Spectrometry and Allied Topics, Seattle, Washington, June 4-8, 1979.
 11. Y. T. Lee, "Infrared Multiphoton Dissociation of Polyatomic Molecules," CNEN, Centro di Frascati (Roma), June 7, 1979.
 12. Y. T. Lee, "Infrared Multiphoton Excitation and Dissociation of Molecules," Europhysics Study Conference on Multiphoton Processes, Benodet, France, June 18-22, 1979.
 13. Y. T. Lee, "Dynamics of IR Multiphoton Processes," Summer School on Chemical Photophysics, Les Houches, France, June 26, 1979.
 14. Y. T. Lee, "Molecular Beam Studies of Elementary Chemical Reactions," Summer School on Chemical Photophysics, Les Houches, France, June 27, 1979.
 15. Y. T. Lee, "Photoionization of Molecular Clusters," Summer School on Chemical Photophysics, Les Houches, France, June 28, 1979.
 16. Y. T. Lee, "Photoionization and Vibrational Predissociation of van der Waals Molecules," Herzberg International Conference on van der Waals Molecules, Quebec, Canada, August 1-3, 1979.
 17. Y. T. Lee, "Dynamics of Multiphoton Excitation Processes," Symposium on Atomic and Molecular Science, Taipei, China, August 23-25, 1979.
 18. R. J. Buss, "Molecular Beam Studies of Substitution Reactions," American Chemical Society Meeting, Washington, D.C., September 9-14, 1979.
 19. R. J. Buss, "The Crossed Beam Studies on Reactions of $O(^3P)$ and $O(^1D)$," Combustion Symposium,

Brookhaven National Laboratory, Upton, New York, October 9-11, 1979.

20. Y. T. Lee, "Reaction Dynamics of F + H₂, D₂," Third International Congress of Quantum Chemistry, Kyoto, Japan, October 29-November 3, 1979.

Presentations

1. L. R. Carlson, "Dynamics of Photodissociation of Ozone," ACS/CSJ Chemical Congress: 1979, Laser Chemistry Symposium, Honolulu, Hawaii, April 2-6, 1979.

2. R. K. Sparks, "Dynamics of Photodissociation of O₃," VI International Molecular Beam Symposium, Riva Del Garda, Italy, May 26-30, 1979.

3. Tomohiko Hirooka, "A Crossed Molecular Beam Study of the Reactions of O(³P) + C₆H₆, C₆D₆," XI International Conference on the Physics of Electronic and Atomic Collisions, Kyoto, Japan, August 29-September 4, 1979.

4. K. Shobatake, "Energy Disposal in the Photodissociation of CH₃I at 266 nm," XI International Conference on the Physics of Electronic and Atomic Collisions, Kyoto, Japan, August 29-September 4, 1979.

i. Potential Energy Surfaces for Chemical Reactions*

Henry F. Schaefer III, Investigator

1. CONFORMATIONAL PREFERENCES AND ELECTRONIC STRUCTURES OF $\text{Ni}(\text{C}_2\text{H}_4)_2$ AND $\text{Ni}(\text{C}_2\text{H}_4)_3^+$

Russel M. Pitzer[†] and Henry F. Schaefer III

One of the most remarkable organometallic species synthesized in recent years is the tris(η^2 -ethene) nickel(0) molecule. This was the first transition metal complex prepared in solution with ethylenes alone as its ligands. In 1973 Fischer, Jonas, and Wilke prepared $\text{Ni}(\text{C}_2\text{H}_4)_3$ in a diethylether solution, which was found to be pale yellow in color. Upon crystallization from solution at 195 K they obtained colorless, needle-shaped crystals. Fischer, Jonas and Wilke assumed the molecule to have the "planar" D_{3h} structure seen in Fig. 1 and reported nuclear magnetic resonance and infrared spectroscopic data consistent with this assumption. More recently the analogous $\text{Pt}(\text{C}_2\text{H}_4)_3$ molecule has been synthesized by Green, Howard, Spencer, and Stone.

Two other experimental reports of tris(η^2 -ethene) nickel(0) have appeared since the pioneering synthesis of Fischer, Jonas and Wilke. In the first, Atkins, McKenzie, Timms and Turney made $\text{Ni}(\text{C}_2\text{H}_4)_3$ in an ethylene matrix in the course of preparing a number of palladium complexes. Even more recently, Huber, Ozin, and Power made $\text{Ni}(\text{C}_2\text{H}_4)_3$ at 15 K in C_2H_4 and $\text{C}_2\text{H}_4/\text{Ar}$ matrices. Ozin and co-workers also prepared the simpler members $\text{Ni}(\text{C}_2\text{H}_4)$ and $\text{Ni}(\text{C}_2\text{H}_4)_2$ of the series and obtained infrared and visible ultraviolet spectra for all three molecules. Primarily on the basis of Rösch and Hoffman's theoretical work, Ozin assigned as $\text{Ni}(d) \rightarrow \text{C}_2\text{H}_4(\pi^*)$ the electronic transition at 280 nm (mono), 250 nm (bis), and 236 nm (tris complex). In addition, these workers demonstrated the weakly bound nature of $\text{Ni}(\text{C}_2\text{H}_4)_3$ by observing that the fragmentation reaction



occurs at about 273 K.

Over the past five years, *ab initio* studies of transition metal complexes have in several cases nicely complemented experimental findings. However, it cannot be realistically stated that work to date compares with the spectacular successes achieved for molecules composed entirely of atoms smaller than neon. This gap between reliability of theoretical predictions for hydrocarbons (for example) and those for organometallic systems is due to a very practical problem--the basis set problem. For first-row molecular systems it is usually possible to approach rather closely the Hartree-Fock limit by adopting successively larger basis sets. In this way, all errors remaining at the self-consistent-field (SCF) level of theory may accurately be ascribed to the effects of electron correlation. Once chemically significant correla-

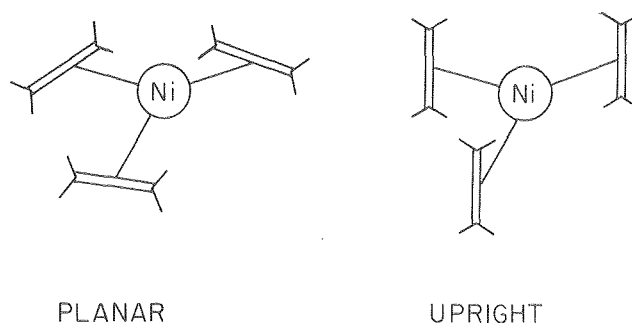


Fig. 1. Geometries of the "planar" (left) and upright (right) geometries of tris(η^2 -ethene) nickel(0). (XBL 793-8747)

tion effects are identified, these may be systematically treated through successively more elaborate configuration interaction (CI) procedures.

For no real (i.e., experimentally characterized) organotransition metal complex has the Hartree-Fock limit been reasonably approached to date. Probably the closest approach to date has been that of Bagus for the ferrocene molecule $\text{Fe}(\text{C}_5\text{H}_5)_2$. The only significant deficiency of their ferrocene basis set was a third set of d functions, needed to allow the expansion of the 3d orbital relative to the isolated transition metal atom. Here we report *ab initio* SCF studies of the conformers of $\text{Ni}(\text{C}_2\text{H}_4)_2$ and $\text{Ni}(\text{C}_2\text{H}_4)_3$ using relatively large and flexibly contracted basis sets. We should concede at the outset that there are still notable absolute differences between the present SCF energies and the (unknown) exact Hartree-Fock energies. However, major differences between the present relative energies (conformation differences, electronic excitation energies, ionization potentials) and experiment should be primarily due to correlation effects.

Three types of contracted gaussian basis sets were used in conjunction with restricted self-consistent-field theory. The middle basis set may be labeled $\text{Ni}(14s\ 9p\ 6d/10s\ 6p\ 3d)$, $\text{C}(10s\ 6p/6s\ 3p)$, $\text{H}(5s/3s)$ and is perhaps the most complete basis set used to date for an experimentally known organotransition metal complex such as $\text{Ni}(\text{C}_2\text{H}_4)_3$. The chosen basis comes very close to reproducing the exact Hartree-Fock term splittings for the nickel atom. For $\text{Ni}(\text{C}_2\text{H}_4)_2$ the twisted (D_{2d}) and "planar" (D_{2h}) conformations are predicted to lie energetically within 0.1 kcal of each other. For the $\text{Ni}(\text{C}_2\text{H}_4)_3$ complex, however, the planar conformation lies ~24 kcal lower than the upright form. Surprisingly, for the positive ion $\text{Ni}(\text{C}_2\text{H}_4)_3^+$, the energetic ordering of conformers is reversed, with the upright form lying 2.4 kcal lower. However, this result was readily explained in

*This work was supported by the Division of Chemical Sciences, Office of Basic Energy Sciences, U.S. Dept. of Energy.

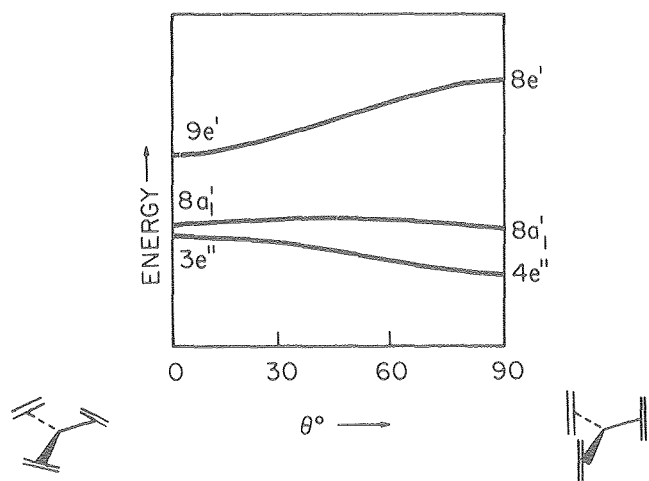


Fig. 2. One-electron energies for the three highest occupied molecular orbitals of $\text{Ni}(\text{C}_2\text{H}_4)_3$ as a function of rotation between the planar and upright conformers. (XBL 797-10484)

terms of the Walsh-like diagram, Fig. 2. The lowest D_{2h} triplet state of $\text{Ni}(\text{C}_2\text{H}_4)_2$ is of ${}^3B_{3u}$ symmetry, and a number of other electronic states were also investigated. The ionization potentials of both molecules were predicted and large deviations from Koopman's Theorem were found. Mulliken population analyses are also reported (see, for example, Table 1) and used to qualitatively discuss the electronic structures.

* * *

† Brief version of LBL-8956.

‡ Permanent address: Department of Chemistry, Ohio State University, Columbus, Ohio.

Table 1. Mulliken populations for the planar and upright (see Fig. 1) geometries of $\text{Ni}(\text{C}_2\text{H}_4)_3$. These results were obtained with the standard large basis set.

| | Nickel | | | Carbon | | Hydrogen |
|-----------------------------|--------|--------|-------|--------|-------|----------|
| | s | p | d | s | p | s |
| Planar | 6.265 | 12.024 | 9.371 | 3.261 | 3.095 | 0.850 |
| Upright | 6.239 | 12.014 | 9.490 | 3.253 | 3.090 | 0.850 |
| Free C_2H_4 | -- | -- | -- | 3.221 | 3.075 | 0.852 |

| Mulliken Charges | Ni | C | H |
|-----------------------------|--------|--------|--------|
| Planar | +0.340 | -0.356 | +0.150 |
| Upright | +0.258 | -0.344 | +0.150 |
| Free C_2H_4 | -- | -0.296 | +0.148 |

| d orbital populations | $d_{3z^2-r^2}$ | $d_{x^2-y^2}$ | d_{xy} | d_{xz} | d_{yz} |
|-----------------------|----------------|---------------|----------|----------|----------|
| Planar | 1.930 | 1.705 | 1.705 | 2.016 | 2.016 |
| Upright | 1.985 | 1.977 | 1.977 | 1.775 | 1.775 |

2. 1,1-DILITHIOETHYLENE: A GROUND STATE TRIPLET OLEFIN WITH NEARLY FREE ROTATION ABOUT THE DOUBLE BOND†

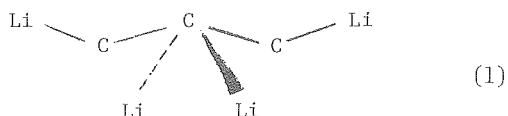
William D. Laidig and Henry F. Schaefer III

In recent years Schleyer, Pople and their colleagues have made some remarkable predictions concerning the equilibrium geometrical structures of lithiated hydrocarbons. For example, the planar form of dilithiomethane CH_2Li_2 was predicted to lie only a few kcal/mole above the conventional "tetrahedral" isomer. More complete theoretical studies of CH_2Li_2 here at MMRD have resoundingly confirmed this qualitative prediction and suggested the following order for dilithiomethane electronic states:

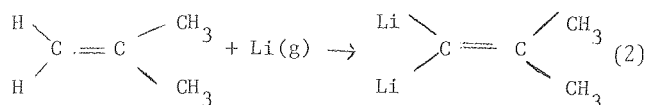
| | |
|---------------------|----------|
| planar triplet | 5.9 kcal |
| tetrahedral triplet | 4.7 kcal |
| planar singlet | 4.2 kcal |
| tetrahedral singlet | 0.0 kcal |

Although the above predictions are probably still only reliable to ± 3 kcal, it is clear that there is a near degeneracy of isomers and electronic states. Further, the barrier separating the planar and tetrahedral singlet states is small, of the order of 1 kcal (from the planar side).

In a second key paper Apeloig, Schleyer, Binkley and Pople (ASBP) have predicted equally unexpected properties for the olefin 1,1-dilithioethylene. These results are, if anything, more important since related molecules have already been prepared in the laboratory. For example, the reaction of lithium atoms with CCl_4 at 800°C yields the product tetralithioethylene C_2Li_4 to the extent of $\sim 60\%$. However, considering the remarkable structure predicted by Jemmis, Poppinger, Schleyer and Pople for C_2Li_4 ,



it is not clear that C_2Li_4 contains a "normal" $\text{C}=\text{C}$ double bond. A more conventional 1,1-dilithioolefin is probably provided by the reaction of 2-methylpropene with *n*-butyllithium and potassium *t*-amyloxyde. But the clearest experimental evidence for such a lithiated olefin comes from the research of Morrison, Chung and Lagow. They found the reaction of isobutene with gaseous lithium atoms to give a $\sim 20\%$ yield of the 1,1-dilithio compound



In their paper ASBP note that not only is the rotational barrier about the $\text{C}=\text{C}$ double bond low, but the triplet or perpendicular form may even be the true equilibrium geometry. Although ASBP note that the theoretical methods chosen artificially favor triplet states relative to singlets, the predicted triplet-singlet energy separations were thought to be so large as to suggest a triplet ground state for CH_2CLi_2 . This is also experimentally significant since it would allow identification of CH_2CLi_2 by matrix isolation electron spin resonance techniques.

We consider the ASBP predictions for 1,1-dilithioethylene to be sufficiently unorthodox and the possibility of laboratory preparation of this species sufficiently high to mandate further theoretical studies of this intriguing molecule. In the present work the theory has been pushed to essentially state-of-the-art levels of reliability through (a) extension of the basis set, and (b) an explicit description of the effects of electron correlation. In addition some qualitative aspects of the electronic structure of $\text{CH}_2=\text{CLi}_2$ are discussed in terms of dipole moments, Mulliken populations, and orbital energies.

Geometry optimizations were carried out at the self-consistent field (SCF) level of theory using a basis set of better than double zeta quality: $\text{C}(9s\ 5p\ 1d/4s\ 2p\ 1d)$, $\text{Li}(9s\ 4p/4s\ 2p)$, $\text{H}(4s/2s)$. The predicted $\text{C}=\text{C}$ bond distances are 1.356 Å (planar singlet), 1.334 Å (twisted singlet), 1.322 Å (planar triplet), and 1.323 Å (twisted triplet), (see Figs. 1 and 2). The analogous $\text{Li}-\text{C}-\text{Li}$ bond angles are 133.6° , 104.1° , 73.9° , and 75.5° , while the corresponding $\text{C}-\text{Li}$ bond distances are 2.000 Å, 1.866 Å, 2.106 Å, and 2.064 Å. SCF theory predicts the twisted triplet to be the ground state, followed energetically by the planar triplet (1.2 kcal), twisted singlet (28.4 kcal), and planar singlet (29.3 kcal). The effects of electron correlation were investigated by configuration interaction (CI) including single and double excitations. The ordering of states is unchanged, with the relative energies being 0.0, 1.4, 14.0, and 15.5 kcal. After Davidson's correction for the effects of unlinked clusters, the same relative energies become 0.0, 1.4, 10.5, and 12.5 kcal.

* * *

† Brief version of LBL-9070.

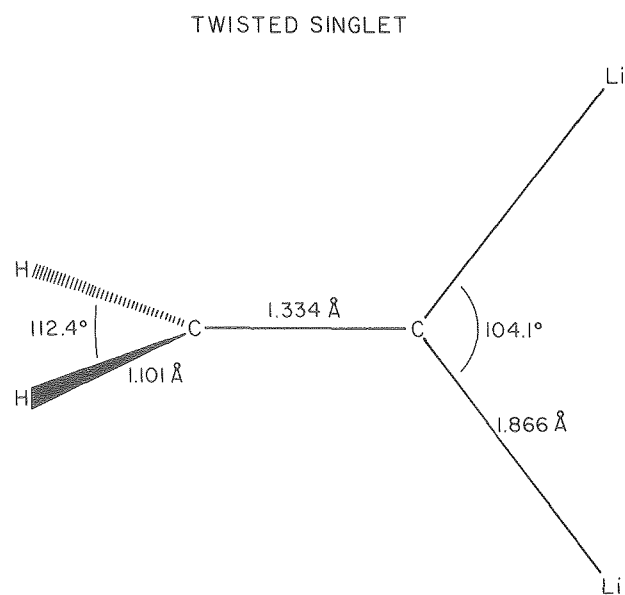
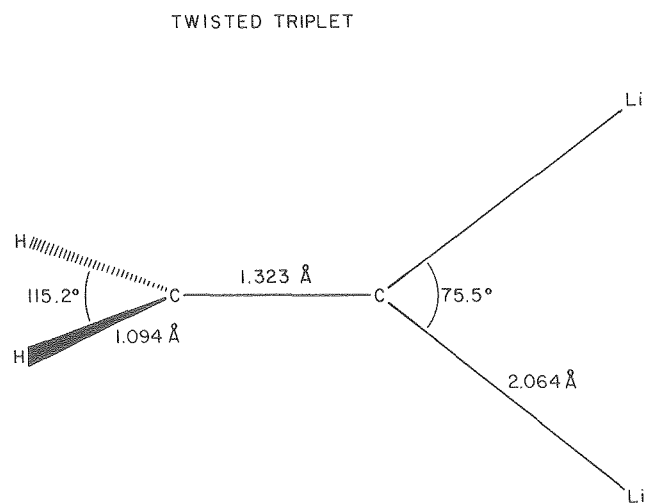
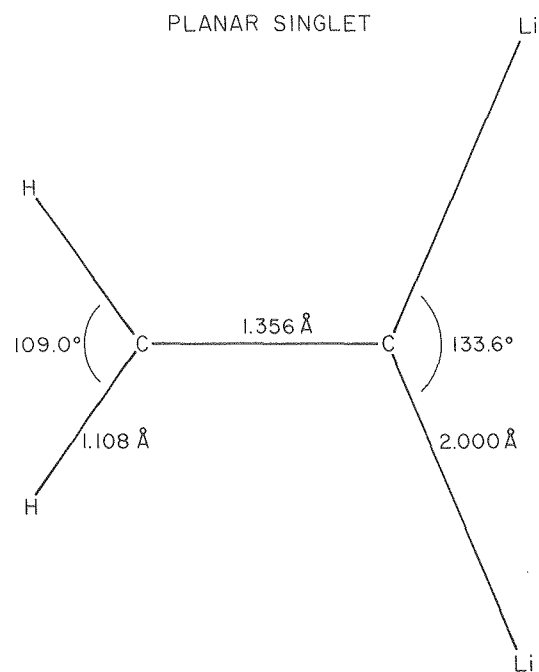
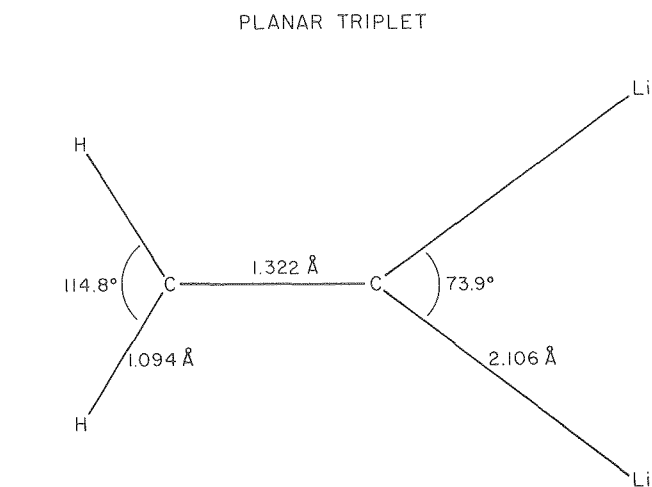


Fig. 1. Predicted planar and twisted geometries for triplet 1,1-dilithioethylene. Bond distances are in angstroms. (XBL 7812-14022)

Fig. 2. Theoretical structures for the lowest singlet electronic state of CLi_2CH_2 . Bond distances are in Å. (XBL 7812-14023)

3. THE GAS PHASE STRUCTURES OF TRANSITION METAL DIHYDRIDES[†]Jean Demuynck[‡] and Henry F. Schaefer III

The electronic and molecular structures of the transition metal hydrides is an established area of research where an increasing amount of experimental data has revealed some interesting variations, thus stimulating theoretical studies on several of these molecules. Considerably less is known about the transition metal hydrides and most experimental studies have been restricted to the monohydrides MH. However the electronic structures and potential energy curves of these hydrides are of interest due to the insight they may give into chemisorption, surface chemistry and catalysis, and several quantum mechanical studies have been reported for such systems (mainly for diatomic hydrides).

The MH_n investigations show that for the transition metal hydrides there is often a tendency to maintain as high a multiplicity as possible, with the $3d^n$ configuration of the metal surviving essentially unchanged during the formation of the molecule. In other words, the interaction between the metal 3d orbitals and the hydrogen 1s orbitals is found to be very weak, probably because the partially occupied d orbitals are localized within the transition metal atom and are to a significant degree screened by the 4s orbital.

The main question we address in the present work is the prediction of the molecular structure of the dihydrides. If the $3d_M-1s_H$ interaction is weak for all the elements of the first transition metal series (Sc-Cu) then a linear geometry is expected for every MH₂ molecule. This is based on a bonding scheme involving the interaction of the 1s orbitals of the hydrogen atoms with the two 4s-4p hybrid orbitals available from the transition metal (see Fig. 1). That is, in fact, what was found for NiH₂ by Guse, Blint and Kunz. They state that the ground state of NiH₂ is derived from the $3d^8 4s^2$ configuration on nickel and not from the $3d^9 4s^1$ configuration, because the $3d_{Ni}-1s_H$ interaction is too weak. Further, they reported a relatively high resistance of this molecule to C_{2v} bending.

Recent cryospectroscopic experiments have suggested that the previously unknown molecules MnH₂ and CrH₂ trapped in argon at 4 K are bent, with bond angles of ~120° proposed for both of them. Although it is well known that the geometries of matrix isolated molecules may differ from their gas phase structures, a bent structure for the lightest elements of transition metal series could also be rationalized on the basis of a stronger $3d_M-1s_H$ interaction. For example, there seems to be a consensus developing that TiF₂ is bent.

Here we present the most sophisticated and complete theoretical work to date on an MH₂ species. However, rather than carrying out self-consistent-field calculations on each of the transition metal dihydrides, a more qualitative approach was adopted. We decided to choose the molecule MnH₂ and construct an ab initio Walsh diagram from which it might be possible to predict the geometries of the entire

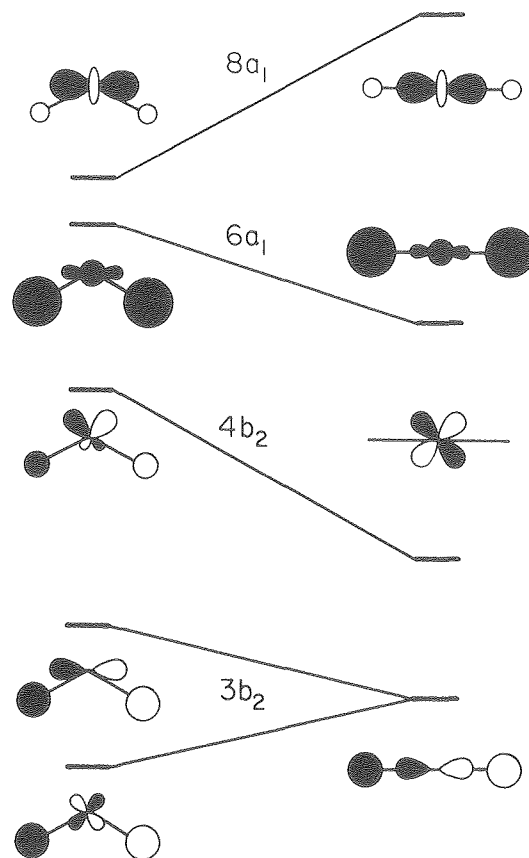


Fig. 1. Bond angle sensitive molecular orbitals for MH₂. (XBL 801-7825)

series of transition metal dihydrides. MnH₂ is a good choice for the present study since it was the subject of a Weltner's recent spectroscopic study, lies halfway through the series, and is the first molecule for which each of the five transition-metal d-like orbitals becomes occupied. We later checked the validity of such a diagram by an explicit examination of TiH₂, the MH₂ molecule most likely to be bent.

A large contracted gaussian basis set [Mn(14s 11p 6d/9s 8p 3d), H(5s 1p/3s 1p)] was used in conjunction with self-consistent-field and configuration interaction methods. These suggest that the 6A_1 ground state of MnH₂ is linear. Further studies of the 5A_1 state (one of several low-lying states) of TiH₂ also favor linearity, although this potential energy surface is extremely flat with respect to bending. Thus it appears probable that most MH₂ molecules, like the related MX₂ family, are linear. These results are summarized in Fig. 2.

[†]Brief version of LBL-9509.

[‡]Permanent address: Equipe de Recherche N° 139 du CNRS, Université Louis Pasteur, 67008 Strasbourg, France.

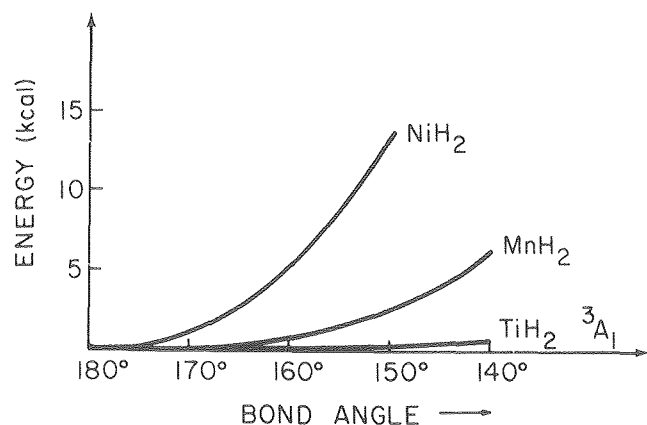


Fig. 2. Potential energy curves for the bending of HMH molecules. (XBL 801-7822)

4. SULFUR OXIDE: LOW-LYING BOUND MOLECULAR ELECTRONIC STATES OF SO †

William C. Swope, ‡ Yuan-Pern Lee, and Henry F. Schaefer III

Sulfur oxide, SO, was first identified from $B^3\Sigma^- \rightarrow X^3\Sigma^-$ emission by Martin in 1932 and later in a number of systems by various techniques. This radical is believed to play an important role in the oxidation of sulfur and sulfur compounds. However, it is still a molecule about which much is yet to be learned and for which quality ab initio calculations might contribute to an understanding of low-lying excited electronic states.

It is well known that molecules with isoelectronic structure do not necessarily have similar potential surfaces for all electronic states. For instance, the three lowest states of O_2 , $X^3\Sigma_g^-$, $a^1\Delta_g$, and $b^1\Sigma_g^+$, dissociate into two ground state atoms, $O(^3P) + O(^3P)$. Quite differently, the ground state $X^3\Sigma^-$ of the isoelectronic molecule NF dissociates into ground state atoms $N(^4S) + F(^2P)$ while the $a^1\Delta$ and $b^1\Sigma^+$ states must dissociate into $N(^2D) + F(^2P)$ according to the Wigner-Witmer rules. This results in a slightly higher vibrational frequency ($\omega_e = 1197 \text{ cm}^{-1}$) for the b state than the ground state (1141 cm^{-1}) of NF. Such behavior would not be expected for diatomic molecules in which both constituting atoms have the same valence structure if the states considered correlate with both ground state atoms. For example, each of the X, a, and b states of O_2 , S_2 , and SO are spectroscopically similar and they all dissociate into two 3P atoms. However, this similarity may not hold for molecular states which correlate with excited atoms. Furthermore, the loss of g/u symmetry in the case of heteronuclear diatomic molecules may result in a great extent of mixing between certain electronic states. Hence, the potential surfaces of the higher excited states of SO might be quite different from those of its close homonuclear companions, S_2 and O_2 . SO serves as the best candidate for the study of these effects since S_2 , O_2 , and SO are relatively well studied experimentally and accurate ab initio studies of O_2 and S_2 are available.

Six excited valence states of SO have been observed. The relative energies of these low-lying states of SO as well as those for O_2 and S_2 are listed in Table 1. Among the six, only three states, $B^3\Sigma^-$, $A^3\Pi$, and $b^1\Sigma^+$ have been well-characterized by accurate molecular constants.

Table 1. Comparison of experimentally determined excitation energies (T_0 , in cm^{-1}) of O_2 , S_2 , and SO for the electronic states studied in this work.

| | O_2 | | SO | | S_2 | | | |
|---|----------------|-------|-----|--------------|---------|----|----------------|---------|
| B | $^3\Sigma_u^-$ | 49358 | B | $^3\Sigma^-$ | 41629 | B | $^3\Sigma_u^-$ | 31689 |
| A | $^3\Sigma_u^+$ | 35007 | A'' | $^3\Sigma^+$ | -- | A | $^3\Sigma_u^+$ | 21971 |
| C | $^3\Delta_u$ | 34319 | A' | $^3\Delta$ | ~ 28400 | A' | $^3\Delta_u$ | 20974 |
| c | $^1\Sigma_u^-$ | 32664 | c | $^1\Sigma^-$ | ~ 27700 | c | $^1\Sigma_u^-$ | ~ 20250 |
| b | $^1\Sigma_g^+$ | 13121 | b | $^1\Sigma^+$ | 10510 | b | $^1\Sigma_g^+$ | ~ 8500 |
| a | $^1\Delta_g$ | 7882 | a | $^1\Delta$ | 6150 | a | $^1\Delta_g$ | ~ 4700 |
| X | $^3\Sigma_g^-$ | 0 | X | $^3\Sigma^-$ | 0 | X | $^3\Sigma_g^-$ | 0 |

Although the a $^1\Delta$ state was observed by an electron spin resonance (ESR) technique in 1966, it was not until recently that accurate vibrational constants and the equilibrium bond distance were determined. The energy of this state relative to the ground state is still not accurately known.

Lee and Pimentel recently observed chemiluminescence, from the reaction of sulfur and oxygen atoms in cryogenic matrices, which they assigned to the c $^1\Sigma^- \rightarrow$ a $^1\Delta$ transition of SO with $\nu_{00} = 21,363 \text{ cm}^{-1}$. Tevault and Smardzewski also observed the same emission as well as a relatively weak progression which was assigned to the A' $^3\Delta \rightarrow$ X $^3\Sigma^-$ of SO. However, they obtained a ν_{00} value of $22,543 \text{ cm}^{-1}$ for the c \rightarrow a transition (due to differences in vibrational number assignments) and a ν_{00} value of $28,400 \pm 1,150 \text{ cm}^{-1}$ for the A' \rightarrow X transition. The uncertainty of this latter value is quite large because of uncertainties in vibrational number assignments. All the assignments concerning these two transitions were made on the basis of estimated T_0 values for the c $^1\Sigma^-$, A' $^3\Delta$, and A'' $^3\Sigma^+$ states of SO obtained by simple (perhaps naive) scaling of corresponding T_0 values of O₂ and S₂.

By rationalizing the differences between experimental values and ab initio studies of some well-characterized states of O₂, SO, and S₂, we have obtained good estimates of the molecular constants for other low-lying electronic states based on our

ab initio studies. With these estimates we hope that the assignments for the cryogenic matrix chemiluminescence can be verified, and furthermore, the correct molecular constants of these states can be determined.

Self-consistent-field (SCF) and configuration interaction (CI) theoretical studies of seven low-lying electronic states of sulfur oxide have been completed. The basis set was of double zeta quality augmented with polarization functions. The CI space for each electronic state consisted of all configurations constructed from single and double substitutions of electrons from the valence orbitals of the Hartree-Fock reference occupation. Spectroscopic constants as well as dipole moments for each electronic state were predicted both at the SCF and CI levels of theory. Of particular significance is the prediction of excitation energies and properties for three low-lying states for which experimental information is either unavailable or only very recently available. These states are the c $^1\Sigma^-$ state ($T_e = 28100 \pm 300 \text{ cm}^{-1}$), the A' $^3\Delta$ state ($29200 \pm 300 \text{ cm}^{-1}$) and the A'' $^3\Delta^+$ state ($30200 \pm 300 \text{ cm}^{-1}$). These and other results are summarized in Table 2.

* * *

[†]Brief version of LBL-9142.

[‡]Present address: Department of Chemistry, Stanford University, Stanford, California.

Table 2. Comparison of theoretical and experimental results for SO.

| State | Method | Number of C _{ov} Configurations | T _e , cm ⁻¹ ^b | r _e , Å | ω _e , cm ⁻¹ | B _e , cm ⁻¹ | μ, Debye |
|------------------|----------------|---|--|--------------------|-----------------------------------|-----------------------------------|----------|
| B $^3\Sigma^-$ | CI, 2[ref.+NO] | 3098 | 48200 | 1.868 | 460 | 0.453 | 3.48 |
| | CI, 2[ref.] | 3098 | 49500 | 1.818 | 570 | 0.478 | 3.18 |
| | SCF | | 17300 | 1.730 | 820 | 0.528 | 1.31 |
| | Expt. | | 41888 | 1.775 | 630.4 | 0.502 | --- |
| A'' $^3\Sigma^+$ | CI | 2349 | 26200 | 1.797 | 680 | 0.489 | 1.25 |
| | SCF | | 18200 | 1.735 | 810 | 0.525 | 1.32 |
| | Expt. | | --- | --- | --- | --- | --- |
| A' $^3\Delta$ | CI | 2615 | 25400 | 1.789 | 700 | 0.494 | 1.25 |
| | SCF | | 17500 | 1.729 | 820 | 0.529 | 1.27 |
| | Expt. | | ~ 28600 ± 1150 | --- | --- | --- | --- |
| c $^1\Sigma^-$ | CI | 2041 | 24400 | 1.788 | 680 | 0.494 | 1.24 |
| | SCF | | 16700 | 1.723 | 820 | 0.532 | 1.26 |
| | Expt. | | ~ 27900 | --- | --- | --- | --- |
| b $^1\Sigma^+$ | CI | 898 | 12400 | 1.518 | 1160 | 0.686 | 1.76 |
| | SCF | | 16400 | 1.464 | 1350 | 0.738 | 2.10 |
| | Green | | 17159 | --- | --- | --- | 1.83 |
| | Expt. | | 10550 | 1.5004 | 1067.7 | 0.7026 | --- |

(Table cont'd.)

Table 2. Comparison of theoretical and experimental results for SO (cont'd).

| State | Method | Number of $C_{\infty v}$ Configurations | T_e, cm^{-1} ^b | $r_e, \text{\AA}$ | ω_e, cm^{-1} | B_e, cm^{-1} | μ, Debye |
|---------------|--------------|--|------------------------------------|-------------------|----------------------------|-----------------------|---------------------|
| $a^1\Delta$ | CI | 959 | 7140 | 1.506 | 1200 | 0.697 | 1.82 |
| | SCF | | 8300 | 1.460 | 1260 | 0.742 | 2.23 |
| | Green | | 8848 | --- | --- | --- | 1.997 |
| | Expt. | | ~ 6150 | 1.4889 | 1115.3 | 0.709 | 1.31 |
| $X^3\Sigma^-$ | [CI, 2 ref.] | 3098 | 0 | 1.506 | 1150 | 0.696 | 1.99 |
| | CI | 1046 | 0 | 1.499 | 1200 | 0.703 | 1.95 |
| | SCF | | 0 | 1.457 | 1350 | 0.745 | 2.42 |
| | Expt. | | 0 | 1.4810 | 1148.19 | 0.7208 | 1.55 |
| | | | | | | | |

5. POTENTIAL ENERGY HYPERSURFACE FOR THE PROTOTYPE M + HF REACTION: $\text{Li} + \text{HF} \rightarrow \text{LiF} + \text{H}^\dagger$

Maynard M. L. Chen and Henry F. Schaefer III

The first chemical reaction to be studied using crossed molecular beams was the $\text{K} + \text{HBr}$ system, investigated in 1955 by Taylor and Datz. In the intervening 25 years this and many other examples of alkali atom plus hydrogen halide reactions have been the subject of related experimental studies. Considering the central role of $\text{M} + \text{HX}$ reactions in the development of chemical dynamics, it is surprising that no definitive quantum mechanical study of such a potential energy surface has appeared. This is all the more perplexing in light of Herschbach's identification, no less than nine years ago, of the $\text{Li} + \text{HF}$ system as a critical prototype. In the Proceedings of the Conference on Potential Energy Surfaces in Chemistry, Herschbach stated that "An *ab initio* calculation of $(\text{H}, \text{Li}, \text{F})$ would be of interest both to study a new species of 'hydrogen bond' and to elucidate the problem of connecting the $\text{H} + \text{K}^+\text{Br}^-$ portion of the surface to the regions involved in the 'electron jump' process."

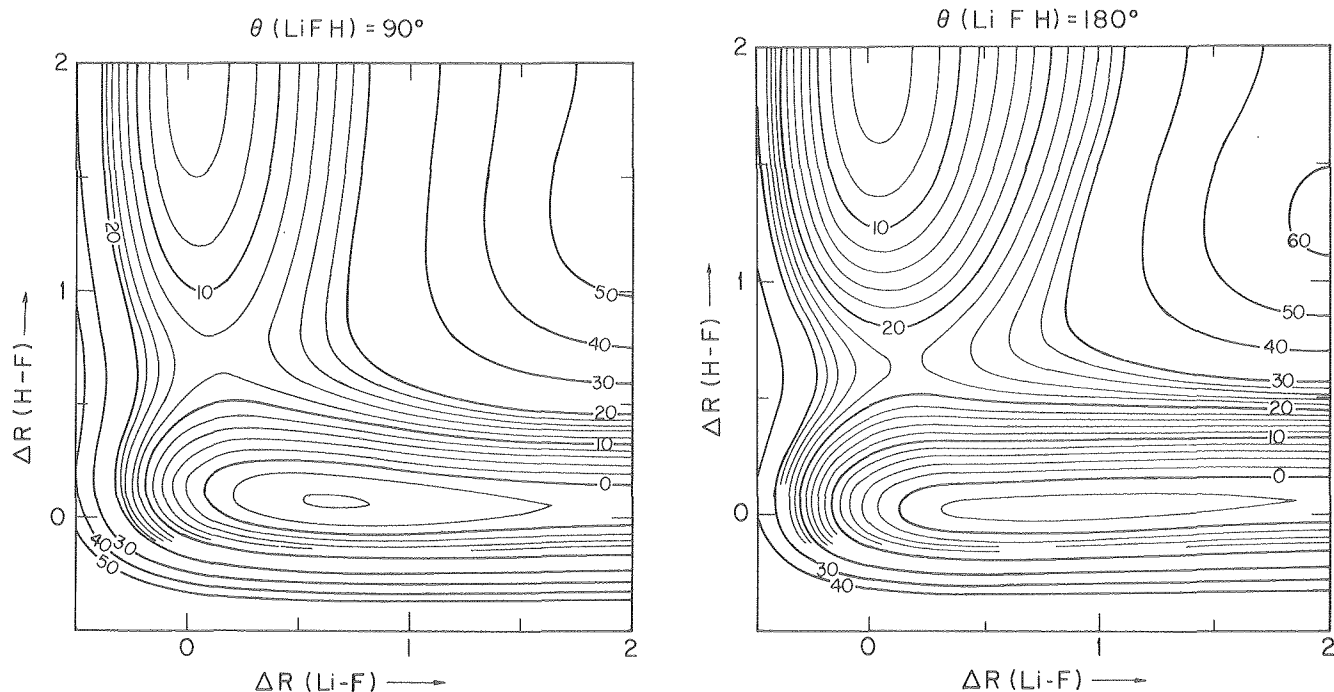
A second goal of the present research was to evaluate the reliability of three proposed-semi-empirical potential energy surfaces for $\text{Li} + \text{HF} \rightarrow \text{LiF} + \text{H}$. In particular, if the Zeiri-Shapiro surface were to be found accurate, this would allow a fair amount of confidence in their analogous energy surfaces for the other $\text{M} + \text{HX}$ reactions ($\text{M} = \text{Li}, \text{Na}, \text{K}, \text{Rb}$; $\text{X} = \text{F}, \text{Cl}, \text{Br}, \text{I}$). Since the alkaline earth plus hydrogen halide reactions have often been compared with the alkali atom reactions, it will also be of interest to compare the present $\text{Li} + \text{HF}$ results with those of Schor, Chapman, Green and Zare for collinear $\text{Be} + \text{FH}$. However, the real driving force for our investigation was the series of elegant molecular beam experiments now being carried out at MMRD LBL by Lee and coworkers. These experiments promise a very complete description of the $\text{Li} + \text{HF}$ reaction,

and with the theoretical results presented herein and dynamical studies which hopefully will follow, should ultimately allow a comprehensive comparison between theory and experiment.

Here the three-dimensional potential energy hypersurface for $\text{Li} + \text{HF} \rightarrow \text{LiF} + \text{H}$ has been studied at the self-consistent-field (SCF) and configuration interaction (CI) levels of electronic structure theory with a medium-sized basis set that included polarization functions. The "corner" of the reaction channel was first mapped (see Figs. 1 and 2) by calculation of a lattice of points; then further calculations were carried out to characterize selected points along the minimum energy pathway more precisely. The classical reaction endothermicity was 2.9 kcal/mole, but with zero-point corrections, the reaction was found to be exothermic by 1 kcal/mole. As the Li atom approaches the diatomic, it first forms a bent complex with 4.5 kcal/mole of stabilization energy before reaching the transition state. The latter, also bent with an angle of 74° was located in the exit channel and is predicted to be 10 kcal/mole above the reactants. These stationary points and relative energies are sketched in Figs. 3 and 4. Force constants, vibrational frequencies and zero-point energies of the complex and transition state were calculated. After applying zero-point corrections to the transition state, the threshold energy for reaction was reduced to 6.4 kcal/mole, which will probably be further reduced to ~ 4 kcal by higher order correlation effects. Our results were compared with previous theoretical efforts and with qualitative theories concerned with the transition state angle and its exit bias. A qualitative discussion of the dynamics over the surface emphasizing interrelationships between the translational energy, vibrational energy and the LiFH angle θ is also presented.

* * *

[†]Brief version of LBL-10111.



Figs. 1 and 2. Contour maps of the CI potential energy as a function of Δr_{LiF} and Δr_{HF} with LiFH angle θ fixed at 90° and 180° , respectively. The distances are expressed in terms of their differences in a.u. from the calculated diatomic equilibrium values. Thin contours are at 2 kcal/mole intervals, thick ones are at 10 kcal/mole and zero corresponds to the energy of the reactants Li+HF at infinite separation. [(XBL 798-3671) and (XBL 798-3669)]

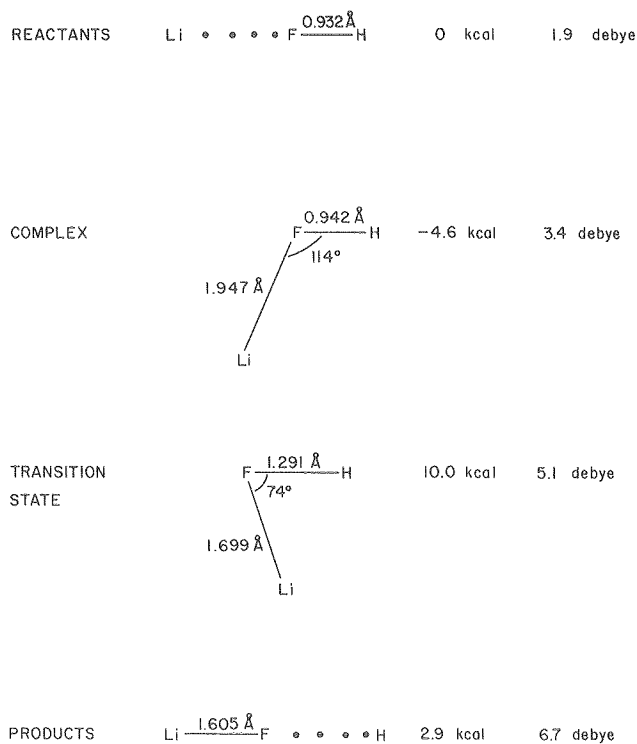


Fig. 3. The geometry, energy and dipole moment of LiFH at stationary points along the minimum energy pathway from reactants to products. (XBL 801-7824)

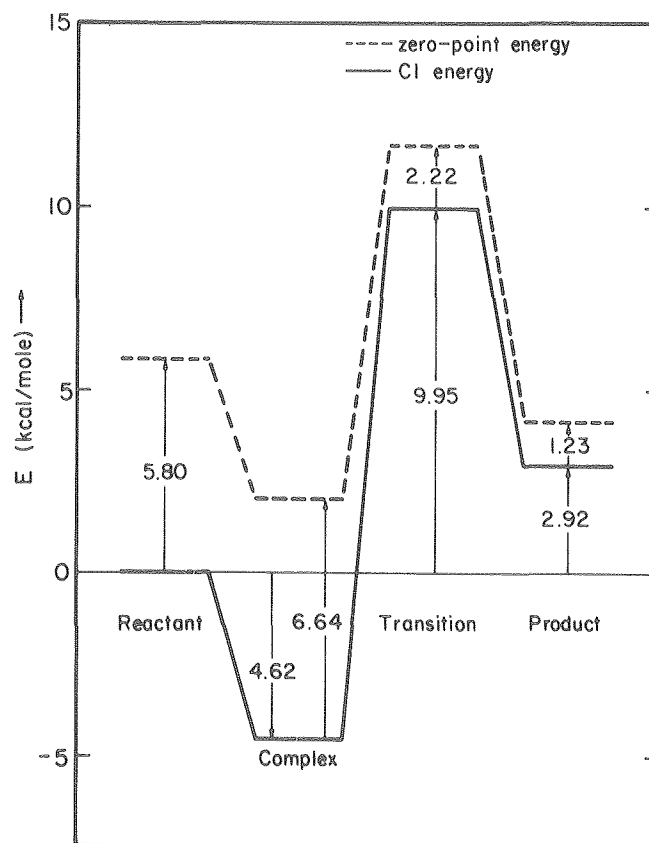
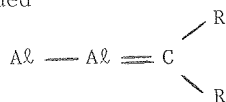


Fig. 4. A schematic diagram showing the CI energies and the estimated zero-point energies of the reactants, complex, transition state and products. (XBL 801-7823)

RESEARCH PLANS FOR CALENDAR YEAR 1980

The critical role of organotransition metal carbenes as catalysts for the olefin metathesis reaction has become firmly established during the past three years. We expect to complete in 1980 the first reliable theoretical study of a realistic metal carbene complex, $(\text{CO})_3\text{Ni}=\text{CH}_2$. Detailed comparisons with the stable $\text{Ni}(\text{CO})_4$ reference compound as well as the "naked" carbene $\text{Ni}=\text{CH}_2$ should be extremely helpful in establishing the role of electronic factors in homogeneous catalysis. In a related vein, J. L. Beauchamp (Cal Tech) has recently made the remarkable discovery that the naked ion MnCH_2^+ is able to readily exchange its methylene group with one in ethylene. Thus there is now an established experimental example of gas phase olefin metathesis, and we plan to determine the detailed molecular mechanism by which this process occurs. The stability of silicon-carbon multiple bonds is of simultaneous interest to surface chemists and physicists and to organometallic chemists. It now appears that the evanescent silaethylene molecule is nearly degenerate with its previously unrecognized isomer, methylsilylene. During the 1980 calendar year, the precise energetic relationship (± 2 kcal) between the two will be established and the potential energy surface connecting $\text{H}_2\text{Si}=\text{CH}_2$ and $\text{CH}_3-\ddot{\text{S}}\text{iH}$ will be explored in detail. An area in which a major effort is planned is the interaction between small aluminum clusters (Al , Al_2 , Al_3 , Al_4) and organic fragments (C , CH , CH_2 , CH_3 , etc.). Although aluminum makes up 8% of the earth's crust and is of great technological importance, relatively little is known about its elemental chemistry. Among the many questions of immediate interest, we plan to compare the terminal bonded



and bridging



isomers of aluminum carbenes. Finally, continued collaboration with the MMRD experimental groups of C. B. Moore (on the electronic spectrum of HCOH) and Y. T. Lee (reactions of atomic oxygen with hydrocarbons) is planned.

1979 PUBLICATIONS AND REPORTS

Refereed Journals

1. M. P. Conrad and H. F. Schaefer, "Absence of an Energetically Viable Pathway for Triplet 1,2-Hydrogen Shifts. A Theoretical Study of the Vinylidene-Acetylene Isomerization," *J. Am. Chem. Soc.* 100, 7820 (1978).
2. B. R. Brooks and H. F. Schaefer, "The BERKELEY System. III. General Configuration Interaction Methods for Open-Shell Molecular Electronic States," *Int. J. Quantum Chem.* 14, 603 (1978).

3. B. R. Brooks and H. F. Schaefer, "Sudden Polarization: The Pyramidalization of Twisted Ethylene," *J. Amer. Chem. Soc.* 101, 307 (1979).
4. D. M. Hood, H. F. Schaefer and R. M. Pitzer, "Planar $^3A_2'$ - Orthogonal 1B_1 Energy Separation for Trimethylenemethane," *J. Amer. Chem. Soc.* 100, 8009 (1978).
5. W. C. Swope, Y. T. Lee and H. F. Schaefer, "Diatomic Sulfur: Low Lying Bound Molecular Electronic States of S_2 ," *J. Chem. Phys.* 70, 947 (1979), LBL-8073.
6. M. E. Zandler, J. D. Goddard and H. F. Schaefer, "Effects of Electron Correlation on the Geometrical Structure of HCCN ," *J. Amer. Chem. Soc.* 101, 1072 (1979).
7. M. Trenary, M. E. Casida, B. R. Brooks, and H. F. Schaefer, "Three Isomers of the $\text{Al}-\text{C}_2\text{H}_2$ System," *J. Amer. Chem. Soc.* 101, 1638 (1979), LBL-8097.
8. B. R. Brooks and H. F. Schaefer, "The Graphical Unitary Group Approach to the Electron Correlation Problem. Methods and Preliminary Applications," *J. Chem. Phys.* 70, 5092 (1979).
9. M. P. Conrad, R. M. Pitzer and H. F. Schaefer, "Geometrical Structure and Energetics of Gloss's Diradical: 1,3-Cyclopentadiyl," *J. Amer. Chem. Soc.* 101, 2245 (1979).
10. J. D. Goddard and H. F. Schaefer, "The Photodissociation of Formaldehyde: Potential Energy Surface Features," *J. Chem. Phys.* 70, 5117 (1979), LBL-8545.
11. D. M. Hood, R. M. Pitzer and H. F. Schaefer, "Electronic Structure of Homoleptic Transition Metal Hydrides: TiH_4 , VH_4 , CrH_4 , MnH_4 , FeH_4 , CoH_4 , NiH_4 ," *J. Chem. Phys.* 71, 105 (1979), LBL-8235.
12. N. C. Handy, J. D. Goddard and H. F. Schaefer, "Generalization of the Direct Configuration Interaction Method to Hartree-Fock Interacting Space for Doublets, Quartets, and Open-Shell Singlets. Applications to NO_2 and NO_2^- ," *J. Chem. Phys.* 71, 426 (1979).
13. C. F. Bender, T. N. Rescigno, H. F. Schaefer and A. E. Oreil, "Potential Energy Curves for Diatomic Zinc and Cadmium," *J. Chem. Phys.* 71, 1122 (1979), LBL-8753.
14. J. D. Goddard, N. C. Handy, and H. F. Schaefer, "Gradient Techniques for Open-Shell Restricted Hartree-Fock and Multiconfiguration Self-Consistent Field Methods," *J. Chem. Phys.* 71, 1525 (1979).
15. H. F. Schaefer, "The 1,2-Hydrogen Shift: A Common Vehicle for the Disappearance of Evanescent Molecular Species," *Accounts Chem. Res.* 12, 288 (1979).
16. S. Bell, "Ab Initio Study of the \tilde{X}^1A_1 , \tilde{a}^3A_1 and \tilde{A}^1A_1 States of Formaldehyde," *Molec. Phys.* 37, 255 (1979).

17. C. E. Dykstra and W. C. Swope, "The H_3^{\ddagger} Potential Surface," *J. Chem. Phys.* **70**, 1 (1979).

18. W. C. Swope and R. A. Harris, "A Harmonic Oscillator Model for the Magnetic Properties of a Closed Shell System. II: The Magnetic Shielding," *Mol. Phys.* **38**, 287 (1979).

Other Publications

1. H. F. Schaefer, "Atom-Molecule Potentials," Chapter 2(a) of *Atom-Molecule Collision Theory: A Guide for the Experimentalist*, R. B. Bernstein, ed., (Plenum, New York, 1979), pp.45-77.

LBL Reports

1. R. M. Pitzer and H. F. Schaefer, "Conformational Preferences and Electronic Structures of $Ni(C_2H_4)_2$ and $Ni(C_2H_4)_3$," *J. Amer. Chem. Soc.*, LBL-8956.

2. W. D. Laidig and H. F. Schaefer, "1,1-Dilithioethylene: A Ground State Triplet Olefin with Nearly Free Rotation About the Double Bond," *J. Amer. Chem. Soc.*, LBL-9070.

3. W. C. Swope, "Selected Topics on the Electronic Structure of Small Molecules," (Ph.D. Thesis), LBL-9094.

4. W. C. Swope, Y. T. Lee and H. F. Schaefer, "Sulfur Oxide: Low-Lying Bound Molecular Electronic States of SO ," *J. Chem. Phys.*, LBL-9042.

5. J. Demuyck and H. F. Schaefer, "The Gas Phase Structure of Transition Metal Dihydrides," *J. Chem. Phys.*, LBL-9509.

6. W. C. Swope, H. F. Schaefer and D. R. Yarkony, "A Geneological Electronic Coupling Procedure Incorporating the Hartree-Fock Interacting Space and Suitable for Degenerate Point Groups. Application to Excited States of BH_3 ," LBL-9580.

7. B. R. Brooks, "The Loop-Driven Graphical Unitary Group Approach to the Electron Correlation Problem, Including Configuration Interaction Energy Gradients," (Ph.D. Thesis), LBL-9998.

8. M. M. L. Chen and H. F. Schaefer, "Potential Energy Surface for the $Li + Hf \rightarrow LiF + H$ Reaction," LBL-10111.

Invited Talks

A. National and International Conferences

1. H. F. Schaefer, "The Sudden Polarization Effect," Université de Paris-Sud, Orsay, France, January 8-9, 1979.

2. H. F. Schaefer, International Symposium on Atomic, Molecular, and Solid State Theory, Collisional Phenomena, Quantum Statistics, and Computational Quantum Chemistry, Palm Coast, Florida, March 12-17, 1979.

3. H. F. Schaefer, ACS Pure Chemistry Award Symposium, American Chemical Society, Honolulu, Hawaii, April 1-6, 1979.

4. H. F. Schaefer, Nobel Symposium on Many Body Theory of Atomic Systems, Aspenäsgråden, Lerum, Sweden, June 11-16, 1979.

5. H. F. Schaefer, "The Relationship Between Cluster Compounds, Metal Surfaces and Catalysis," U. S. National Science Foundation, Pacific Grove, California, November 18-21, 1979.

6. H. F. Schaefer, Discussion Meeting on Polyatomic Photodissociation, Eindhoven University of Technology, Eindhoven, Holland, December 3-4, 1979.

B. University Colloquia

1. H. F. Schaefer, Institute of Physics, National University of Mexico, February 1979.

2. H. F. Schaefer, Petroleum Research Institute, Mexico City, February 1979.

3. H. F. Schaefer, University of Texas, Austin, March 1979.

4. H. F. Schaefer, Virginia Polytechnic Institute, May 1979.

5. H. F. Schaefer, University of Washington, Seattle, May 1979.

6. H. F. Schaefer, Stanford University, July 1979.

3. Atomic Physics

a. Low Energy Atomic Physics*

H. A. Shugart, Investigator

1. OBSERVATION OF PARITY NONCONSERVATION IN THE $6\ 2P_{1/2} - 7\ 2P_{1/2}$ TRANSITION IN ATOMIC THALLIUM[†]

E. D. Commins, P. Bucksbaum, L. Hunter and P. Drell

The results of our first successful observations of parity nonconservation were published in February 1979. In this work we investigated the transition $6\ 2P_{1/2} - 7\ 2P_{1/2}$ (292.7 nm) in atomic thallium, using a pulsed dye laser. The transition is forbidden M1 with a dipole amplitude $M = (-2.1 \pm 0.3) \times 10^{-5} |eh/2m_e c|$ measured by us earlier. Parity nonconservation causes the $6\ 2P_{1/2}$, $7\ 2P_{1/2}$ states to be admixed with $2S_{1/2}$ states. The transition amplitude then contains an additional E1 component ϵ_p and this gives rise to circular dichroism δ , defined by

$$\delta = \frac{\sigma_+ - \sigma_-}{\sigma_+ + \sigma_-} = \frac{2\text{Im}(\epsilon_p M^*)}{|\epsilon_p|^2 + |M|^2} \approx \frac{2\text{Im}(\epsilon_p)}{M}$$

where σ_{\pm} are the cross sections for absorption of 293 nm photons with \pm helicity, respectively. Theoretical estimates of δ based on the Weinberg-Salam model yield:

$$\delta_{\text{theo}} = (2.3 \pm 0.9) \times 10^{-3}$$

for $\sin^2\theta = 0.25$ where θ is the Weinberg angle. In order to measure δ we employ an external electric field E which causes Stark mixing of the $2P_{1/2}$ states with $2S_{1/2}$ and $2D_{3/2}$ states. The transition intensity, proportional to E^2 is thereby increased above background. Also, interference between the Stark transition amplitudes and the M and ϵ_p amplitudes polarizes the $7\ 2P_{1/2}$ state, permitting the measurement of M and δ . The polarization of the $7\ 2P_{1/2}$ state is itself measured by means of an optical pumping technique in which the (allowed) $7\ 2P_{1/2} - 8\ 2S_{1/2}$ transition (2.18 μ) is induced by means of a second laser, and decay-fluorescence of $8\ 2S_{1/2}$ is observed. Our preliminary experimental value $\delta_{\text{expt.}} = (5.2 \pm 2.4) \times 10^{-3}$ agrees in sign and magnitude with the Weinberg-Salam Model.

Since the preliminary results were obtained we have devoted our efforts to improvement in the stability, precision, and sensitivity of the apparatus, and have examined very carefully possi-

ble sources of systematic error. The following major steps were taken between January 1, 1979 and the present:

(a) An LSI-11 computer was installed to control the experiment and to analyze data on-line. It replaced the older, slower, and more cumbersome PDP-5. With the new computer we can analyze several correlation effects in the experiment that might lead to systematic errors. These effects were previously inaccessible to analysis. They have now been shown to be small.

(b) A new thallium cell of simplified design with external pulsed electrodes has been installed. It yields much better signal-to-background ratios than the older cell (which had internal electrodes), because light scattering in the new cell is considerably smaller.

(c) Production of ultraviolet light by frequency doubling has been stabilized by improved doubling crystal temperature control.

(d) Various changes in infrared beam optics have resulted in much more stable infrared excitation from the $7\ 2P_{1/2}$ to the $8\ 2S_{1/2}$ state.

(e) Improvements have been made in the vacuum system, to prevent deterioration of lenses and windows at the very high operating temperature we must employ.

(f) An attempt was made to analyze the $7\ 2P_{1/2}$ polarization by excitation to the $11\ 2S_{1/2}$ state. In spite of much effort lasting six months this attempt ultimately failed, and was abandoned.

The improved apparatus is now in use and extensive data have been obtained to examine possible sources of systematic error. We have satisfied ourselves that these are all within acceptable limits, and we are proceeding to obtain final parity data.

* * *

[†]Brief version of Phys. Rev. Lett. 42, 343 (1979) and Phys. Lett. 60A, 96 (1978).

2. NEW EXPERIMENTS IN PARITY NON-CONSERVATION

E. D. Commins, P. Bucksbaum, L. Hunter and P. Drell

The $6\ 2P_{1/2} - 7\ 2P_{3/2}$ transition in thallium, which occurs at 2844 Å and can readily be excited

* This work was supported by the Division of Chemical Sciences, Office of Basic Energy Sciences, U. S. Department of Energy.

by our pulsed UV laser oscillator-amplifier, is also a very interesting candidate for parity non-conservation studies. The component $6^2P_{1/2}$, $F=0 - 7^2P_{3/2}$, $F=1$ is an M1 transition (with a small E1 amplitude ϵ_p due to parity violation). In contrast to the case $6^2P_{1/2} - 7^2P_{1/2}$ where the M1 amplitude is very small, the $6^2P_{1/2} - 7^2P_{3/2}$ M1 amplitude is quite large (calculation predicts $M \approx 0.04 \mu_0$, where μ_0 is the Bohr magneton). Thus the M1 transition is much larger than background, and circular dichroism can be observed directly, without the necessity of using an external electric field. Theory predicts the circular dichroism δ to be

$$\delta = \frac{2 \operatorname{Im}(M^* \epsilon_p)}{|M|^2 + |\epsilon_p|^2} \approx 1.5 \times 10^{-6} .$$

A complication is that the transition $6^2P_{1/2}$, $F=0 - 7^2P_{3/2}$, $F=2$ cannot be resolved from the desired $F=0 - F=1$ transition, since these are separated by a frequency difference of only 600 MHz, considerably less than the Doppler width of either line. This is a serious difficulty, because the $F=0 - F=2$ line is pure E2 with a strength 100 times that of the $F=0 - F=1$ component. We have devised a method for separating these 2 components, however, which involves use of a second laser. The experiment has been designed and the apparatus is virtually complete. We expect to be able to observe the $6^2P_{1/2} - 7^2P_{3/2}$ transition for the first time before January 1980.

Experiments using external magnetic fields and linearly polarized light offer another approach for detecting weak interaction effects in atomic physics. We have devised an entirely new method for observing parity nonconservation in the $6^2P_{1/2} - 7^2P_{1/2}$ transition. This method utilizes an external magnetic field for state selection and linearly polarized light instead of circularly polarized light to excite the transition at 2927 Å. The advantages are as follows:

- i) Signal strengths should be enhanced by at least one order of magnitude.
- ii) Possible sources of systematic errors which are very serious in the present $6^2P_{1/2} - 7^2P_{1/2}$ experiment are largely eliminated in the new one.

In the present experiment parity nonconservation is observed by detecting the pseudoscalar term in the transition probability:

$$\hat{k} \times \underline{E} \cdot \underline{J} \hbar$$

where \hat{k} is a vector in the direction of the 2927 Å light beam, \underline{E} is the external electric field, \underline{J} is the polarization of the $7^2P_{1/2}$ atoms, and \hbar is the 2927 Å photon helicity. In the new experiment the pseudoscalar term is

$$\hat{e} \cdot \underline{B} \hat{e} \cdot \underline{E} \times \underline{B}$$

where \underline{B} is an external magnetic field, \underline{E} is as before, and \hat{e} is the linear polarization of the light beam.

We are extremely optimistic about this new experiment and eagerly await the time when the necessary equipment has been built. At present, design is completed and construction of the necessary components is getting underway.

Additional experiments have been conducted utilizing absorption of monochromatic laser light. We are now designing a novel but very simple experiment for studying the $6^2P_{1/2} - 6^2P_{3/2}$ and $6^2P_{1/2} - 7^2P_{3/2}$ transitions in thallium with our powerful pulsed laser amplifier. These rely simply on the difference in absorption of the atomic vapor for left- and right-circularly polarized light, which arises from parity violation.

3. FLUORESCENCE OF LASER EXCITED TRAPPED Li^+ METASTABLE IONS

M. H. Prior and R. D. Knight[†]

We have extended our studies of the fluorescence of laser excited trapped metastable Li^+ ions, by observing new transitions and making use of a computer scanned narrow bandwidth dye laser to collect fluorescent response spectra. The relevant energy levels of Li^+ are shown in Fig. 1. We observe the fluorescence from the $1s2p^3P_{1,2}$ states excited by the laser beam from the $1s2s^3S_1$ metastable level. An experiment to measure the radiative lifetime of this state was recently completed and utilized some of the techniques described here. The transition to the $3P_2$ state lies about 60 GHz higher in frequency than that to $3P_1$; the nominal wavelength for either transition is 5485 Å. E1

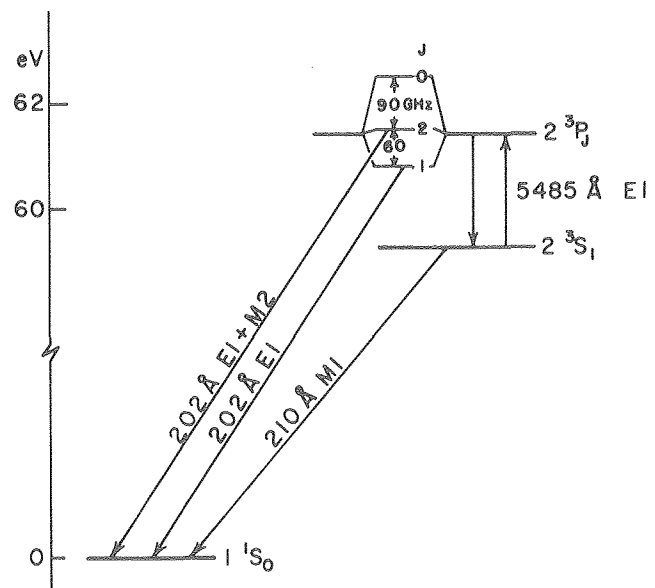


Fig. 1. Energies and decay modes of Li^+ levels relevant to this work. (XBL 7912-13571)

a) XUV Fluorescence from $1s2p\ ^3P_{1,2}$ in Decay to $1s^2\ ^1S_0$

Excitation of the $^3P_{1,2}$ states has been observed by detecting the weak XUV fluorescence at 202 Å produced when these states decay directly to the ground state ($1s^2\ ^1S_0$). In the case of 3P_1 , this occurs with a branching ratio of 1/1200 (versus decay back to 3S_1) via E1 intercombination radiation caused by a small mixture of 1P_1 character in the " 3P_1 " wavefunction. For 3P_2 , however, a combination of hyperfine induced E1 and pure M2 amplitudes result in a much smaller branching ratio ($\sim 1.5 \times 10^{-5}$) for decay to the ionic ground state. We also detect excitation of these states by observation of the scattered laser photons ("visible" fluorescence); because of the weak XUV decay of 3P_2 , this is the preferred method for this state, yielding a count rate some 10^4 times higher than the XUV rate.

The metastable Li^+ ions are confined inside a radio-frequency quadrupole trap with a collision dominated lifetime of about 5 seconds. The XUV photons are detected by windowless CuBe venetian blind electron multipliers which view the trap through 800 Å Al foils. The scattered 5485 Å laser photons are detected by a photomultiplier located outside the vacuum chamber containing the ion trap. A lens mounted inside the chamber focuses light from the trap volume out through a viewport onto an interference filter placed over the photocathode of the photomultiplier. Careful focusing and steering of the laser beam, together with a light baffle system in the entrance and exit arms of the chamber, reduced the scattered light from the entrance and exit windows to an acceptable level ($\sim 500\ \text{sec}^{-1}$ photomultiplier count rate at a laser power $\sim 10\ \text{mW}$). The frequency of the laser was scanned at variable rates over a range of 30 GHz under control of a computer based data collection system. The residual scattered light signal, collected when the trap was empty, was subtracted in alternate cycles from data collected with Li^+ ions stored.

The most striking result of these studies is the narrow fluorescence response curves produced (fluorescence signal versus laser frequency). These curves can be considerably narrower than the complex of blended Doppler broadened hyperfine lines one would expect from a normal absorption spectrum of a Li^+ "gas" at the equivalent temperature of the trapped ions. Consider the 3S_1 to 3P_1 transition complex in $^7\text{Li}^+$ (nuclear spin $I = 3/2$). There are three hyperfine levels with total angular momentum quantum numbers $F = 5/2, 3/2, 1/2$ in both the 3S_1 and 3P_1 states. This produces seven optical hyperfine transitions extending over a range of about 30 GHz. The trapped ions have a Maxwell-Boltzmann distribution of energies characterized by a temperature of several thousand degrees Kelvin, yielding a Doppler width of $\sim 10\ \text{GHz}$ for each hyperfine line (the natural width is $\sim 3.5\ \text{MHz}$). Thus one might expect a fluorescence response over a range of some $\sim 50\ \text{GHz}$ in laser frequency (the laser "linewidth" was $\sim 50\ \text{MHz}$). In fact we observe a single near-Gaussian shaped signal with a full width of 5 to 10 GHz depending on trap parameters). This effect is the result of optical pumping of the 3S_1 hyperfine states in an environ-

ment (the ion trap and residual background gas) where the relaxation rate among the hyperfine levels is weak in comparison to the pumping rate.

This behavior can be understood by considering a simpler system which would exhibit the same effect. Figure 2 shows the hypothetical spectrum appropriate to an ion with a single pair of hyperfine levels in the lower state and a single level in the excited state. Allowed optical transitions connect each lower level to the excited state. The rest spectrum would consist of two lines as shown in the left portion of the figure. An ion confined inside a trap will execute a complex periodic motion; this is a superposition of harmonic motions in the rf quadrupole trap, but the component of motion along the laser beam can be approximated as simple harmonic motion at a frequency and amplitude dependent upon the trap parameters, ion charge-to-mass ratio, and total energy. The resultant frequency modulation of the absorption spectrum for a particular ion energy is shown in the right half of Fig. 2.

For the rest ion, a laser beam tuned to either transition frequency would quickly empty the cor-

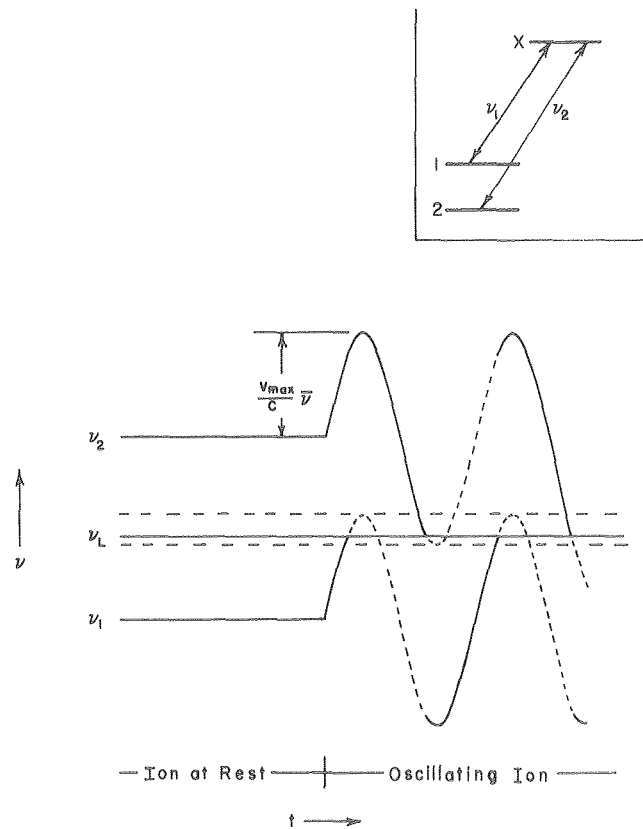


Fig. 2. Absorption spectrum for three level ions at rest and undergoing simple harmonic oscillation parallel to the laser beam with velocity amplitude v_{max} . The Doppler effect modulates the absorption spectrum and allows quasi-continuous interaction with the laser when its frequency ν_L lies between the horizontal dashed lines. The solid portion of the modulated absorption spectrum indicates the lower level populated by complete laser pumping at each coincidence with ν_L . (XBL 7912-13572)

responding lower level, transferring its population to its non-resonant companion. The system would be optically pumped and no more photons would be scattered unless the initial state were repopulated by some other mechanism or the laser were tuned to the opposite transition. Depending upon the relative strengths of the two transitions, only a few transient photons would be scattered during the pumping time.

For the oscillating trapped ions, the same brief pumping transient would occur over much of the range of laser frequencies between the two rest values, yielding near zero time-averaged scattering rate. It is clear, however, that there is a range between the two rest frequencies where the laser may cause sequential alternate pumping of each lower level, yielding a non-zero average scattered signal. This region is just the overlap region of the Doppler shifted resonant frequencies. The signal from a collection of such oscillators would be given by an average over the Maxwell-Boltzmann distribution of ion energies capable of interacting with the laser beam when in either lower level. This produces a fluorescence response curve centered between the rest frequencies with a width which can be narrower than the Doppler width of either transition and the separation of the two rest frequencies.

A more general treatment of the fluorescence from an ensemble of atomic absorbers can be made by solving a set of rate equations for the populations of the levels involved. We have found this useful for the case of the $\text{Li}^+ \ ^3\text{S}_1 - \ ^3\text{P}_J$ pumping cycle. The equations are

$$\dot{N}_i = \sum_j (A_{ji}X_j - I_\nu \delta_\nu B_{ij}(\nu)N_i) - \Gamma(N_i - w_i n)$$

$$\dot{X}_j = -AX_j + \sum_i I_\nu \delta_\nu B_{ij}(\nu)N_i$$

where the N_i and X_j are populations of the $\ ^3\text{S}_1$ and $\ ^3\text{P}_J$ levels, respectively. A_{ji} is the spontaneous emission rate for the $j \rightarrow i$ transition ($A = \sum_i A_{ji}$). $B_{ij}(\nu)$ is proportional to the absorption coefficient multiplied by the fraction of ions in the i^{th} state capable of absorbing a photon of frequency ν to make the $i \rightarrow j$ upward transition. I_ν is the laser spectral intensity (intensity per unit bandwidth) and δ_ν is the laser bandwidth. n is the total number of ions in the $\ ^3\text{S}_1$ levels and w_i is the statistical weight of the i^{th} level ($\sum_i w_i = 1$). Γ is a relaxation rate which forces the populations to statistical equilibrium in the absence of laser pumping. We have found that it is appropriate to use in the $B_{ij}(\nu)$, a Doppler profile to represent the fraction of ions resonant with the laser frequency for each $i \rightarrow j$ transition. This is equivalent to averaging the system of Fig. 2 over the Maxwell-Boltzmann distribution with the additional proviso that the thermal relaxation of the oscillation energy is rapid compared to the pumping rate. This insures that a thermal distribution of oscillator energies is maintained for the collection of ions in each lower level separately.

Once the $\ ^3\text{P}_J$ level populations are determined, the fluorescence signal is obtained by multiplying these by the appropriate spontaneous emission rates for the radiation observed. For $\ ^7\text{Li}^+$ pumped by the transition to $\ ^3\text{P}_1$ and observed via the 202 Å intercombination emission, the results of the steady state rate equation solution (all time derivatives set to zero) are shown in Fig. 3 for various values of Γ . The calculation was done for conditions (trap parameters, laser power) similar to a case experimentally studied, and plotted on the same figure are those results. Because an absolute measurement of the fluorescence rate and laser frequency are not made, the amplitude and line center of the data have been adjusted to best agree with the calculated shape; this occurs for small Γ . The frequency scale is known and no adjustment to it was made. The vertical lines indicate the locations and relative absorption strengths of the seven hyperfine lines. The normal absorption line shape would be that obtained in the limit $\Gamma \rightarrow \infty$; this curve would lie off the figure; however, one can see the marked narrowing

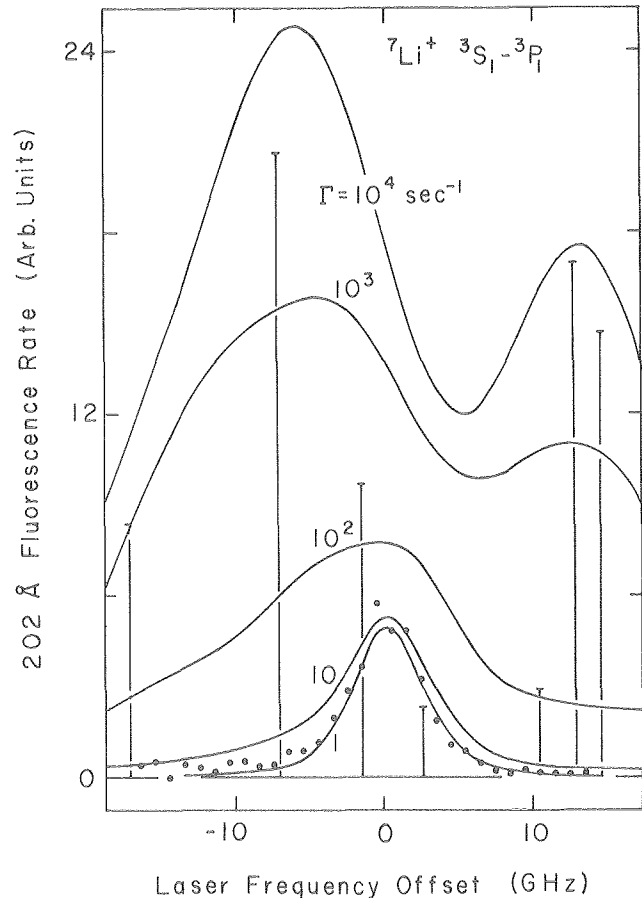


Fig. 3. Fluorescence response from observation of 202 Å intercombination decay of $\ ^3\text{P}_1 \ ^7\text{Li}^+$ ions. The curves are the steady state solutions for various hyperfine relaxation rates Γ . The spherical effective well depth for the ions was 20 eV, and the ion temperature used in the calculations was 6440 K. The vertical lines indicate the location and relative strengths of the $\ ^3\text{S}_1 \rightarrow \ ^3\text{P}_1$ hyperfine lines. (XBL 7912-13573)

of the fluorescence signal by comparing the shape of the observed response to the curve for $\Gamma = 10^4 \text{ sec}^{-1}$.

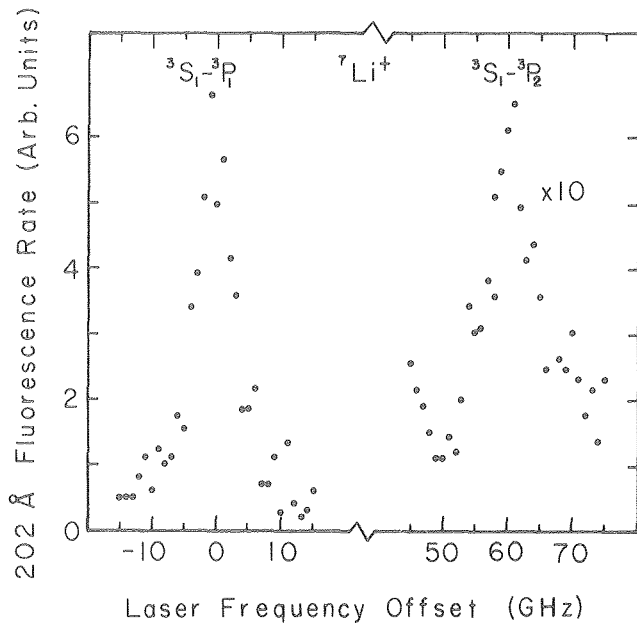
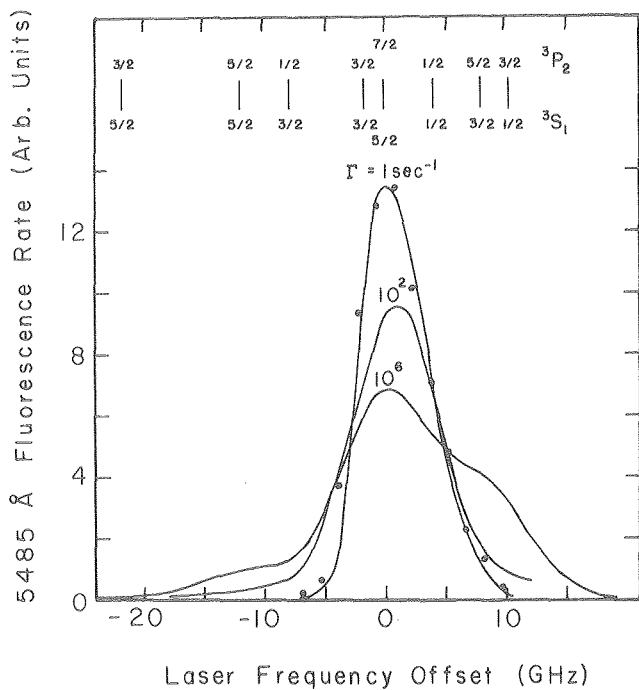


Fig. 4. Observation of the 202 Å fluorescence from ${}^7\text{Li}^+$ ions excited to the ${}^3\text{P}_2$ levels (right). The signal is located about 60 GHz above the considerably stronger 202 Å signal from ${}^3\text{P}_1$ fluorescence (left) in rough agreement with the ${}^3\text{P}_1$ to ${}^3\text{P}_2$ separation. (XBL 7912-13578)

In Fig. 4 is presented an observation of the very weak 202 Å fluorescence of the ${}^3\text{P}_2$ state in ${}^7\text{Li}^+$. The curve on the left is the fluorescence of ${}^3\text{P}_1$ similar to that shown in Fig. 3, after acquiring this signal (requiring about 10 minutes



of integration) the laser frequency was increased by 60 GHz and integration for about one hour produced the small resonance shape shown. The relative size of the two signals is in rough agreement with that expected.

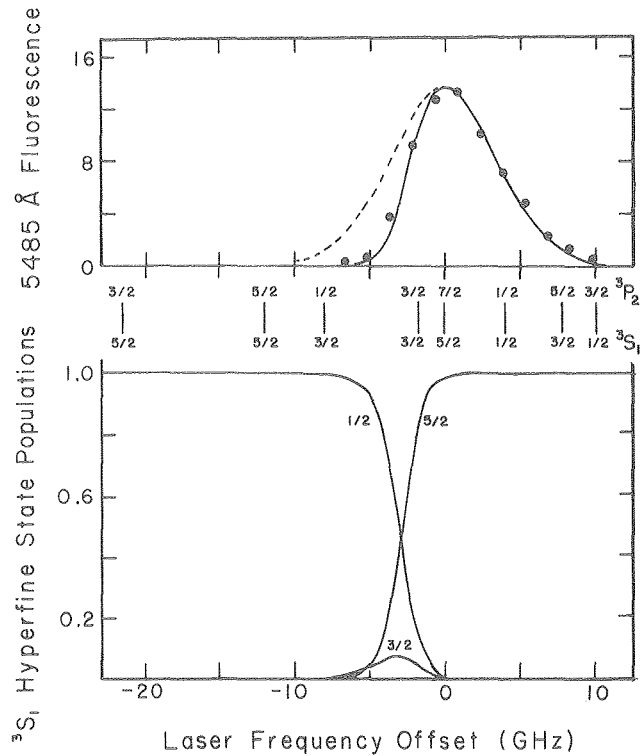


Fig. 6. The data of Fig. 5 and the $\Gamma = 1 \text{ sec}^{-1}$ curve replotted (upper) together with the corresponding ${}^3\text{S}_1$ hyperfine level populations (lower) predicted by the steady state solution. The location of the hyperfine lines is shown in between. A prominent role is played by the non-pumping $5/2 - 7/2$ transition which contributes nearly all the signal and whose Doppler profile (frequencies > 0) is eroded by the pumping process for frequencies < 0 . The dashed line indicates the Doppler profile matched to the high frequency side of the observed response. (XBL 7912-13574)

b) Visible Fluorescence from $1s2p \ {}^3\text{P}_2$ in Decay to $1s2p \ {}^3\text{S}_1$ (Scattered Laser Photons).

In Fig. 5 we present the 5485 Å fluorescence (scattered laser photons) from the ${}^3\text{P}_2$ state of

Fig. 5. Fluorescence response from observation of 5485 Å scattered laser photons following excitation of ${}^7\text{Li}^+$ ions to the ${}^3\text{P}_2$ hyperfine level in 10 eV spherical well. The curves are steady state rate equation solutions for various amounts of relaxation among the ${}^3\text{S}_1$ levels. The shape of the observed response (points) is in agreement with the smallest hyperfine relaxation rate. The location of the ${}^3\text{S}_1 \rightarrow {}^3\text{P}_2$ hyperfine lines are indicated at the top of the figure. (XBL 7912-13575)

${}^7\text{Li}^+$ when held in a 10 eV effective spherical potential well. The curves are the steady state rate equation solutions for three values of Γ . The curve for $\Gamma = 10^6 \text{ sec}^{-1}$ is essentially the normal absorption line shape. The data shown have been adjusted as was done for Fig. 3 and agree best with the lowest relaxation rate curve. In Fig. 6 the same data are shown in the upper portion with the curve for $\Gamma = 1$. The lower portion shows the corresponding variation of the ${}^3\text{S}_1$ hyperfine state populations. For this case a special role is played by the ${}^3\text{S}_1, F = 5/2$ to ${}^3\text{P}_2, F = 7/2$ transition. This transition does not contribute to the optical pumping since ${}^3\text{P}_2, F = 7/2$ can only decay back to ${}^3\text{S}_1, F = 5/2$. One notes that the peak of the fluorescence response curve (Fig. 6) is at the frequency of the $5/2 - 7/2$ transition and that for frequencies greater than this value, the ${}^3\text{S}_1, 5/2$ state is fully populated ($3/2, 1/2$ are empty). It follows that the high frequency half of the response curve is due only to the $5/2 - 7/2$ transition and should be that of the Doppler profile of this transition alone. In fact the high frequency half of the observed line shape is indistinguishable from a Doppler profile characterized by a temperature of 3100 K. This temperature is in agreement with results obtained previously from studies of the spatial density distribution of the Li^+ metastable ions. The fall off of the data and rate equation solution below the Doppler shape (dashed curve) on the low frequency side is due to the switching of the ${}^3\text{S}_1$ hyperfine populations as shown in the lower portion of Fig. 6.

* * *

[†]Brief version of LBL-9757, and J. Appl. Phys. 50, 3044 (1979).

4. HYSTERESIS IN SWEEPED FREQUENCY FLUORESCENT RESPONSE[†]

M. H. Prior and R. D. Knight

In article 3 above, the data and calculations of Figs. 3, 4, 5 and 6 have all been addressed to the case of steady state fluorescence. That is, the laser frequency is steady, and its beam has interacted with the trapped ions long enough to establish a static population distribution. Experimentally this is carried out by holding the laser frequency constant for a fixed number of trap cycles (fill, store, dump), collecting fluorescence counts and stepping to the next laser frequency. The storage time is long ($\sim 1 \text{ sec}$) compared to the pumping time ($\sim 1 \text{ msec}$) so the steady state solutions are appropriate. In Fig. 1 we show data collected from the 5485 Å fluorescence from ${}^3\text{P}_2$ ${}^7\text{Li}^+$ ions when the laser frequency is scanned rapidly up and down during the storage period. A marked hysteresis is observed in the fluorescence response curves which increases as the rate of scan is increased. This is a reflection of the inability of the ${}^3\text{S}_1$ level populations to reach the steady state distribution during the dwell time of the laser at each frequency. In this domain one cannot ignore the transient solu-

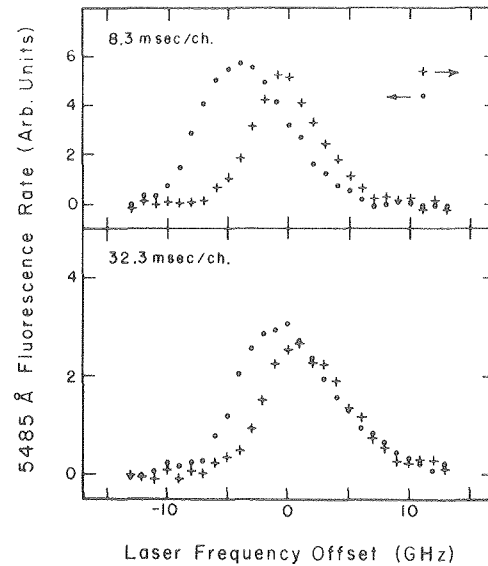


Fig. 1. Hysteresis in the 5485 Å fluorescence from ${}^7\text{Li}^+ {}^3\text{P}_2$ ions for two different laser frequency scan rates. The laser frequency was held at each point for the dwell time shown. The direction of sweep was down for the solid circles and up for the crosses. (XBL 7912-13577)

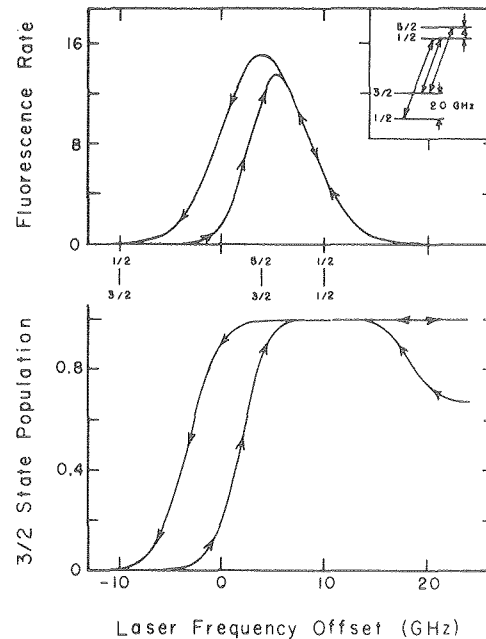


Fig. 2. Transient rate equation solution for the artificial system shown in the inset. The solution includes a non-pumping transient ($3/2 \leftrightarrow 5/2$) and the dwell time at each frequency was about twice the shortest pumping time. The upper curve shows the fluorescent response and the lower curve the $3/2$ state population. The system starts at high frequency with a population $2/3$ in the $3/2$ state, and the Doppler width used was 10 GHz. The arrows indicate the direction of the laser frequency scan. (XBL 7912-13576)

tion to the rate equations. We have not carried out the complete transient solution for the ${}^7\text{Li}^+ {}^3\text{S}_1 \rightarrow {}^3\text{P}_2$ transition complex, but a simpler calculation for an artificial but analogous problem is shown in Fig. 2. The system includes a non-pumping transition $3/2 \rightarrow 5/2$, analogous to the $5/2 \rightarrow 7/2$ transition in the ${}^7\text{Li}^+$ ion. The solution starts at high frequency with the statistical population (2/3) in the 3/2 level and moves down in frequency as shown by the arrows. The results bear a strong resemblance to the data shown in Fig. 1.

* * *

[†]Brief version of Bull. Am. Phys. Soc. 24, 1202 (1979).

RESEARCH PLANS FOR CALENDAR YEAR 1980

With the first successful measurement of parity nonconservation in atomic thallium published, our efforts will turn toward reducing the experimental uncertainty of the published result and toward newly devised methods which promise complementary verification of the observations. Although the 1979 Nobel Prize to S. Glashow, S. Weinberg and A. Salam for their theoretical unification of weak and electromagnetic interactions was based upon experimental evidence gained in high energy particle physics, it is extremely important to obtain supportive evidence in the low energy atomic physics region. Since thallium has thus far provided the best atomic physics test of the gauge theory predictions, further investigations are considered very important for advancing understanding of detailed atomic structure. A number of different experimental approaches are currently being pursued and hold promise of yielding results next year.

Recently during experiments on the radiative lifetime of metastable $2 {}^3\text{S}_1 \text{Li}^+$, a number of curious phenomena were observed when laser light interacted with trapped ions. These have now been shown to be related to both steady-state and transient optical pumping of the Doppler broadened ionic spectrum. With far reaching consequences in the fields of trapped ion diagnostics and ion spectroscopy via optical pumping, these effects are now being understood theoretically. Applications of these pumping methods to ion spectroscopy seem straightforward and are likely to receive wide attention in the future.

1979 PUBLICATIONS AND REPORTS

Refereed Journals

1. R. Conti, P. Bucksbaum, S. Chu, E. Commins, and L. Hunter, "Preliminary Observation of Parity Nonconservation in Atomic Thallium," Phys. Rev. Lett. 42, 343 (1979).

2. R. D. Knight and M. H. Prior, "Laser Scanning Measurement of the Density Distribution of Confined ${}^6\text{Li}^+$ Ions," J. Appl. Phys. 50, 3044 (1979), LBL-8093.

3. R. D. Kaul, "Measurement of Excitation Cross Section of the $6 {}^3\text{P}_1$ State of Mercury Using Self-Calibrating Apparatus," J. Opt. Soc. Am. 69, 150 (1979).

4. M. H. Prior and R. D. Knight, "Fluorescence of Optically Pumped Trapped Li^+ Ions," Bull. Am. Phys. Soc. 24, 1202 (1979).

5. A. J. Muray, "Measurement of the Lifetime of the $4d^9 5s 5p {}^4\text{F}_{9/2}$ State in Silver," senior thesis, University of California, Berkeley, November 1979.

6. E. D. Commins, "Parity Nonconservation in Atoms and the Weinberg-Salam Model," Bull. Am. Phys. Soc. 24, 673 (1979).

7. P. Bucksbaum, "Experimental Tests of Parity Nonconservation in Atomic Thallium," in Proceedings of the International Workshop on Neutral Current Interactions in Atoms, Cargese, September 10-14, 1979.

8. R. S. Conti, "A Search for Parity Violation in Atomic Thallium," Ph.D. thesis, University of California, Berkeley, June 1979.

9. R. D. Knight and M. H. Prior, "Radiative Decay Rate and Laser Diagnostics of Confined Metastable Li^+ Ions," Bull. Am. Phys. Soc. 24, 770 (1979). Also in Program and Abstracts of the Second Conference on Atomic Processes in High Temperature Plasmas, Joint Institute for Laboratory Astrophysics, Boulder Colorado, January 1979.

LBL Reports

1. R. D. Knight, "Lifetime of the Metastable $2 {}^3\text{S}_1$ State in Stored Li^+ Ions," Ph.D. thesis, University of California, Berkeley, April 1979, LBL-9082.

2. R. D. Knight and M. H. Prior, "Radiative Lifetime of Metastable $2 {}^3\text{S}_1 \text{Li}^+$," LBL-9757.

Invited Talks

1. P. Bucksbaum, "Parity Non-conservation in Thallium," Cargese Conference, Corsica, September 1979.

2. E. D. Commins, "Parity Violation in Atoms and the Weinberg-Salam Model," Department of Physics, University of California, Berkeley, January 17, 1979.

3. E. D. Commins, "Parity Violation in Atoms and the Weinberg-Salam Model," Department of Physics, University of California, San Diego, January 24, 1979.

4. E. D. Commins, "Parity Violation in Atoms and the Weinberg-Salam Model," Department of Physics, University of Chicago, February 22, 1979.

5. E. D. Commins, "Parity Violation in Atoms and the Weinberg-Salam Model," Department of Physics, Princeton University, February 23, 1979.
6. E. D. Commins, "Parity Violation in Atoms and the Weinberg-Salam Model," Department of Physics, Yale University, February 24, 1979.
7. E. D. Commins, "Parity Violation in Atoms and the Weinberg-Salam Model," Department of Physics, Harvard University, April 23, 1979.
8. E. D. Commins, "Parity Violation in Atoms and the Weinberg-Salam Model," American Physical Society, Washington D. C. meeting, April 26, 1979.
9. E. D. Commins, "Parity Violation in Atoms and the Weinberg-Salam Model," Department of Physics, University of Washington, Seattle, May 7, 1979.
10. E. D. Commins, "Parity Violation in Atoms and the Weinberg-Salam Model," Neutrino '79 Conference, Bergen, Norway, June 20, 1979.
11. E. D. Commins, "Parity Violation in Atoms and the Weinberg-Salam Model," Ecole Normale Supérieure, Paris, June 27, 1979.
12. E. D. Commins, "Parity Violation in Atoms and the Weinberg-Salam Model," Laboratoire Orsay, Paris, June 28, 1979.
13. E. D. Commins, "Parity Violation in Atoms and the Weinberg-Salam Model," CERN, Geneva, July 11, 1979.
14. E. D. Commins, "Parity Violation in Atoms and the Weinberg-Salam Model," Department of Physics, University of Rome, July 13, 1979.
15. E. D. Commins, "Parity Violation in Atoms and the Weinberg-Salam Model," Department of Physics, University of California, Santa Barbara, November 14, 1979.
16. E. D. Commins, "Parity Violation in Atoms and the Weinberg-Salam Model," Department of Physics, University of Minnesota, December 5, 1979.
17. E. D. Commins, "Parity Violation in Atoms and the Weinberg-Salam Model," Department of Physics, New York University, December 6, 1979.
18. H. A. Shugart, "Recent Berkeley Measurements on Atomic Beams and on Trapped Ions," Laser Physics Group, University of Munich, and Max Planck Institute, Garching, West Germany, December 18, 1978.
19. H. A. Shugart, "Precision Measurements on Atomic Beams and on Trapped Ions," Department of Physics, Middle East Technical University, Ankara, Turkey, January 11, 1979.
20. H. A. Shugart, "Contributions of Atomic Beams to the Fundamental Developments in Physics," Department of Physics, Middle East Technical University, Ankara, Turkey, January 22, 1979.
21. H. A. Shugart, "Laser Fluorescence Measurements in the Study of the Reaction $Cs_2 + O \rightarrow CsO + Cs^*$," Turkish Atomic Energy Commission, Ankara, Turkey, January 23, 1979.
22. H. A. Shugart, "Precision Measurements on Atomic Beams and Trapped Ions," Department of Physics, University of Petroleum and Minerals, Dhahran, Saudi Arabia, February 11, 1979.
23. H. A. Shugart, "The Unit of Time--Time and Frequency Standards," Department of Physics, University of Petroleum and Minerals, Dhahran, Saudi Arabia, February 20, 1979.
24. H. A. Shugart, "Precision Measurements on Atomic Beams and Trapped Ions," Department of Physics, University of Riyadh, Riyadh, Saudi Arabia, February 21, 1979.
25. H. A. Shugart, "Contributions of Atomic Beams to the Fundamental Developments in Physics," Department of Physics, University of Ife, Ille-Ife, Nigeria, March 16, 1979.
26. H. A. Shugart, "Precision Measurements on Atomic Beams and Trapped Ions," Department of Physics, University of Ife, Ille-Ife, Nigeria, March 19, 1979.
27. H. A. Shugart, "Laser Fluorescence in the Study of the Reaction $Cs_2 + O \rightarrow CsO + Cs^*$," Atomic Physics Seminar, Department of Physics, University of California, Berkeley, April 11, 1979.
28. H. A. Shugart, "High Precision Measurements in Atomic Beams: g_J Value of $^{55}S_2$ Oxygen," Department of Physics, University of California, Davis, May 22, 1979.
29. H. A. Shugart and S. P. Davis, "Highlights of the 1979 Symposium on Atomic Spectroscopy," Atomic Physics Seminar, Department of Physics, University of California, Berkeley, October 10, 1979.
30. P. Drell, "Yet Another Method for Detection of Weak Interactions in Atomic Thallium," Atomic Physics Seminar, Department of Physics, University of California, Berkeley, October 17, 1979.
31. P. Bucksbaum, "The Cargese Conference on Parity Non-conservation in Atoms," Atomic Physics Seminar, Department of Physics, University of California, Berkeley, November 7, 1979.
32. M. H. Prior, "Fluorescence from Optically Pumped Trapped Ions," Atomic Physics Seminar, Department of Physics, University of California, Berkeley, November 21, 1979.

b. Atomic Physics*

R. Marrus, Investigator

1. RADIATIVE DECAY OF THE $2\ 2^2P_{3/2,1/2}$ STATES IN LITHIUMLIKE KRYPTON ($Z=36$) AND THE $2s2p\ 2^3P_1$ STATE IN BERYLLIUMLIKE KRYPTON†

H. Gould and R. Marrus

The study of relativistic effects in three and four electron atoms has been a subject of considerable theoretical effort with the aim of developing a tractable framework for accurate calculation of transition energies and decay rates in high Z systems.¹⁻²² These techniques have been applied to the $\Delta n = 0$ transitions in lithiumlike and berylliumlike ions and have yielded discrepant results.

Measurements of wavelengths and lifetimes of transitions between low-lying states in which the principle quantum number does not change ($\Delta n = 0$) provide a sensitive test of relativistic calculations. The large but easily calculated Rydberg term is absent, while the relativistic corrections to the Coulomb interaction between electrons represent a significant fraction of the transition energy which rapidly increases at A . Radiative corrections also make a measurably large contribution to the binding energy of low-lying S states. In this paper we report measured values of the wavelengths and mean lives of the $\Delta n = 0$ transitions to the ground states $2^2P_{3/2,1/2} \rightarrow 2^2S_{1/2}$ in lithiumlike Kr^{+33} ($A=36$) and $2s2p\ 3P_1 \rightarrow 2s^2\ 1S_0$ intercombination transition in berylliumlike Kr^{+32} which clearly distinguish between the discrepant calculations. Krypton is the highest Z system for which measurements of these transitions have been made.

Mean lives of the $2^2P_{3/2,1/2} \rightarrow 2^2S_{1/2}$ and the $2^3P_1 \rightarrow 2^1S_0$ transitions have previously been measured in lower Z systems by the beam foil technique. However, wavelengths of these transitions have not previously been determined from beam foil measurements. (A critical compilation of wavelengths for these transitions can be found in Refs. 15 and 16.)

Our measurements of the wavelengths and lifetimes in lithiumlike and berylliumlike krypton were made by the beam-foil and beam-foil time-of-flight techniques. A 5×10^{11} particle/sec beam of Kr^{84} at a velocity of 4×10^9 cm/sec (8.5 MeV/amu) obtained from the Lawrence Berkeley Laboratory SuperHILAC was passed through a $600\ \mu\text{g}/\text{cm}^2$ carbon foil mounted on a moveable support. Photons from decays in flight of Kr ions emitted downstream from the foil were analyzed in a 2.2 meter grazing incidence monochrometer (McPherson model 247). Details of the analyzer, detector, and some of the measurement techniques can be found in Ref. 23. The monochrometer was calibrated against the

584.334 Å, 537.0296 Å, and 522.2128 Å lines of neutral helium, the 303.7822 Å and 256.3170 Å lines of He^+ and the 460.7284 Å line of Ne^+ from a static source containing He and Ne. Calibration of the instrumental line shape with a moving source and determination of the linear Doppler shift correction due to beam-monochrometer misalignment was accomplished using lithiumlike iron lines (Ref. 24) $2^2P_{3/2} \rightarrow 2^2S_{1/2}$ at 192.03 Å in first and second order and $2^2P_{1/2} \rightarrow 2^2S_{1/2}$ at 255.1 Å produced by the beam foil technique. The experimental setup, beam velocity, and accelerator tune for the iron ions were identical to the ones used in the Kr measurements.

The instrumental linewidth is approximately 7.5 Å/mm of slit width, and the Doppler width contribution is about 0.5 Å at 200 Å for slit widths up to 1 mm. For entrance slit widths of 0.1 mm to 0.4 mm used in wavelength determinations the lineshapes of the static and moving sources were essentially identical. Using the He and Ne standards and a linear Doppler shift correction obtained from either of the lithiumlike Fe lines, the second lithiumlike Fe line was found to agree with the previously measured value to within 0.1 Å.

Wavelengths were determined from at least five scans over the spectral line using .1 mm slits (1.0 Å F.W.H.M.) for the lithiumlike transitions and 0.2 mm and 0.4 mm slits for the weaker long lived berylliumlike transitions. The wavelength and lifetime of the $2^2P_{3/2} \rightarrow 2^2S_{1/2}$ transition was measured in both first and second order. Statistical errors in the wavelengths are the standard deviation of the mean of the multiple wavelength scans. Lifetimes of the lithiumlike $2^2P_{3/2}$ state was determined from three decay curves, the $2^2P_{1/2}$ lifetime from two decay curves and the weak berylliumlike $2s2p\ 2^3P_1$ lifetime from a single decay curve. To partially account for quasi-systematic effects such as drift in the beam position, changes in background and foil deterioration which would average out or show up as scatter if many decay curves were measured, we use as the "statistical error" of the lifetime measurement the fitting uncertainty or 1.2% whichever is greater.

In addition to statistical errors the final errors include uncertainty in the lithiumlike Fe wavelengths 0.05 Å, calibration spectra measurement errors 0.03 Å, beam velocity uncertainty (1%) 0.07 Å, and the systematic uncertainties associated with the measurement of the lithiumlike $2^2P_{1/2}$ decay. A correction of 0.04 Å is applied to the measurement of the $2^2P_{3/2} \rightarrow 2^2S_{1/2}$ wavelength because the rapid decay of the $2^2P_{3/2}$ state results in a larger contribution from photons Doppler shifted towards shorter wavelengths. The effect of cascading from higher states is assumed to be negligible at this level of accuracy because the lifetimes of the higher levels that have significant initial populations are much shorter than the $2^2P_{3/2}$ and $2s2p\ 2^3P_1$ states.

*This work was supported by the Division of Chemical Sciences, Office of Basic Energy Sciences, U. S. Department of Energy.

In Table 1 measured values of wavelengths and lifetimes are compared with the various theoretical calculations. All of the wavelengths calculated by ab initio methods have been adjusted by decreasing the binding energy of the 2s state by 13940 cm^{-1} to account for the one electron Lamb shift. This value is obtained by interpolation of values calculated by Mohr for hydrogenlike atoms.²⁵ Theoretical lifetimes are corrected for the change in transition energies by scaling the $1/\lambda^3$ dependence of the electric dipole decay rate. We neglect the effect of core electrons upon the Lamb shift (leading term of relative order $1/Z$) and radiative corrections to the electric dipole matrix elements. In berylliumlike Kr we also neglect the effect upon the Lamb shift of configuration mixing. Without the Lamb shift included, no calculated wavelength in Table 1 would agree with our experiment. We wish to emphasize in this paper that Lamb shift effects in the lithium and beryllium isoelectronic sequences are not confined to high Z, and the existence of these effects are not of recent discovery; a deviation from relativistic theory having been established in Edlén's 1934 measurement²⁶ of the neutral lithium fine structure.

Among the calculations, the relativistic HF calculations show consistent agreement with measured values of wavelengths and lifetimes. Deviations from experiment in calculated lifetimes by other methods are largely the result of wave-

length errors since the electric dipole matrix elements have only small relativistic corrections at $Z = 36$. The small differences in wavelengths among the different RHF calculations arise predominantly from the way in which the Breit interaction is treated. The lifetime in Table 1 calculated by the relativistic random phase approximation (RRPA) uses the experimental wavelength. The value obtained using the RRPA generated wavelength is shown in parentheses.

The Z expansion calculation for the Li sequence yields wavelengths and lifetimes in agreement with measurement at $Z = 36$. At lower Z the relativistic Z expansion wavelengths are of comparable accuracy to the RHF calculations, and are quite close to RHF values through $Z = 45$. At higher Z however large discrepancies result. This may well be due to the absence in the Z expansion of higher order relativistic corrections which are contained in the RHF theory via the Breit interaction. Z expansion results are less satisfactory in predicting the berylliumlike wavelengths.

The semi-empirical wavelength values for Li-like Kr were obtained as an extrapolation to Edlén's tables using the formulas in Ref. 15. The agreement of the semi-empirical theory with all measurements in the Li isoelectronic sequences speaks for itself; however, extrapolations to higher Z will require a different formula for the Lamb shift.

Table 1 Wavelengths (angstroms) of the $2^2P_{3/2,1/2} \rightarrow 2^2S_{1/2}$ transition in lithiumlike Kr^{+33} and the $2s2p \ 2^3P_1 \rightarrow 2s^2 \ 2^1S_0$ transition in berylliumlike Kr^{+32}

| Transition | Experiment (Å) | Theory | | | | | |
|---|----------------|--|---|--------------------|--|---------------|--------------------|
| | | ab-initio (with hydrogenic Lamb shift of 13940 cm^{-1}) | | | | | |
| | | relativistic Hartree Fock | Hartree Fock with relativistic corrections | | relativistic Z expansion ^c | semiempirical | |
| | | KD | AFL | Weiss ^a | Cowan | | Edlén ^d |
| $\text{Kr}^{+33} \ 2^2P_{3/2} \rightarrow 2^2S_{1/2}$ | $91.1 \pm .2$ | 91.1 | 91.2 | 93.6 | 93.2 | 91.1 | 91.0 |
| $2^2P_{1/2} \rightarrow 2^2S_{1/2}$ | $174.1 \pm .3$ | 174.0 | 173.6 | 182.7 | 184.6 | 173.6 | 173.7 |
| | | | AFL/CJ | Weiss ^b | NS | | Edlén ^e |
| $\text{Kr}^{+32} \ 2^3P_1 \rightarrow 2^1S_0$ | $170.0 \pm .5$ | 169.6 | 169.4 | 177.3 | 193.1 176.8 | 167.2 | 169.(est) |

KD - Ref. 1 and Y.K. Kim, private communication.

c - this work.

AFL - Ref. 2 and L. Armstrong, private communication.

Edlén^d - extrapolated from Ref. 15.

CJ - ref. 3 and W.R. Johnson, private communication.

Edlén^e - extrapolated from Ref. 16.

Weiss^a - Ref. 7.

Weiss^b - Ref. 8.

Cowan - Ref. 11.

NS - Ref. 9

* * *

[†]Brief version of LBL-10153.

1. Y.-K. Kim and J. P. Desclaux, Phys. Rev. Lett. 36, 139 (1976).
2. L. Armstrong, Jr., W. R. Fielder, and D. L. Lin, Phys. Rev. A 14, 1114 (1976).
3. K. T. Cheng and W. R. Johnson, Phys. Rev. A 15, 1326 (1977).
4. D. L. Lin, Phys. Rev. A 16, 600 (1977).
5. J. P. Desclaux, Comp. Phys. Comm. 9, 31 (1975).
6. J. P. Desclaux in "Fast Ion Spectroscopy," Proceedings of the Fifth International Conference on Beam Foil Spectroscopy. Published in J. de Physique, Vol. 40 colloque C1, p. 1-109; J. P. Desclaux, D. F. Mayers and F. O'Brien, J. Phys. B4, 631 (1974).
7. A. W. Weiss, J. Quant. Spectrosc. Radiat. Transfer 18, 481 (1977).
8. A. W. Weiss, in Beam Foil Spectroscopy, edited by I. A. Sellin and D. J. Pegg, (Plenum, New York, 1976), Vol. 1, p. 51.
9. H. Nussbaumer and P. J. Strong, J. Phys. B12, 531 (1979).
10. H. Nussbaumer, Astron. Astrophys. 16, 77 (1972).
11. R. D. Cowan, Los Alamos Scientific Laboratory report LA-6679-MS.
12. R. D. Cowan and D. C. Griffin, J. Opt. Soc. Am. 66, 1010 (1976).
13. R. Glass and A. Hibbert, J. Phys. B11, 2413 (1978).
14. R. Glass, J. Phys. B12, 689 (1979).
15. B. Edlen, Physica Scripta 19, 255 (1979).
16. B. Edlen, Physica Scripta 20, 129 (1979).
17. W. R. Johnson and K. T. Cheng, J. Phys. B12, 863 (1979).
18. C. D. Lin and W. R. Johnson, Phys. Rev. A 15, 1046 (1977).
19. H. T. Doyle in Advances in Atomic and Molecular Physics, edited by D. R. Bates and I. Esterman (Academic Press, New York, 1969), Vol. 5, 337.
20. V. I. Safronova and A. B. Rudzikas, J. Phys. B9, 1989 (1976); V. I. Safronova, J. Quant. Spectrosc. Radiat. Transfer 15, 231 (1975); V. I. Safronova and A. N. Ivanova, Optics and Spectroscopy 25, 103 (1969).
21. D. S. Victorov and V. I. Safronova, J. Quant. Spectrosc. Radiat. Transfer 17, 605 (1971).
22. S. Goldsmith, J. Phys. B7, 2315 (1974).
23. D. Dietrich, J. A. Leavitt, S. Bashkin, J. G. Conway, H. Gould, D. MacDonald, R. Marrus, B. M. Johnson, and D. J. Pegg, Phys. Rev. A 18, 208 (1978).
24. G. D. Sandlin, G. E. Brueckner, V. E. Scherrer, and R. Tousey, Astrophys. J. 205, L47 (1976); K. G. Widing and J. D. Purcell, Astrophys. J. 204, L151 (1976).
25. P. J. Mohr, Phys. Rev. Lett. 34, 1050 (1975), and Ann. Phys. (N.Y.) 88, 26 (1974), and in Beam-Foil Spectroscopy, ed. T. A. Sellin and D. J. Pegg, (Plenum, New York, 1976), p. 89.
26. In Ref. 17 the authors calculate the first order correction to the average energy of the configuration. A more exact treatment has recently been performed by Kim and results in small changes in the transition wavelengths.

2. CHARGE CHANGING CROSS SECTIONS FOR HEAVY IONS AT ENERGIES TO 8.5 MeV/AMU[†]

J. Alonso, D. Dietrich, and H. Gould

In order to obtain beams of very high mass and energy, heavy-ion accelerators must be capable of accelerating partially stripped heavy ions. A crucial factor in designing these accelerators is the vacuum required for beam survival; this depends upon the charge changing cross sections for collisions between beam ions and residual atoms. However, cross section data in the energy range of interest are largely nonexistent. To assist in determining the vacuum requirements for the Bevalac vacuum improvement project, we are measuring the cross sections of SuperHILAC-produced ions from neon ($Z=10$) to xenon ($Z=54$) at energies from 3.4 MeV/amu to 8.5 MeV/amu ($.085 \leq v/c \leq .134$) in nitrogen gas over a wide range of incident charge states.

This article reports our first preliminary values for single electron capture and loss cross sections for ions of argon, iron, krypton, and xenon at 8.5 MeV/amu and for argon ions at energies of 3.4 MeV/amu to 8.5 MeV/amu. A schematic diagram of the apparatus is shown in Fig. 1. Heavy ions obtained from the Lawrence Berkeley Laboratory SuperHILAC are stripped by a carbon foil and charge-state selected in the beam switch yard. Once collimated, they pass through a differentially pumped 24 cm long charge exchange chamber. The final states are analyzed in a homogeneous 18 kG dipole magnet with an effective radius of 22 cm and detected on a position sensitive gas-filled proportional counter. At 8.5 MeV/amu each of the charge states of argon is separated by approximately 2 cm.

Ion charge states of atoms through $Z=26$ can be unambiguously identified by calibrating against fully stripped ions (bare nuclei) of the same atom produced by stripping in a solid foil. A narrow slit driven by a precision screw measures the absolute displacement of the beam for each charge state, permitting identification of heavier ions by matching the magnetic rigidity to lighter ions or by simple ray tracing calculations.

Data are collected by observing the relative number of ions striking the counter at each location corresponding to an ion charge state, as a function of gas pressure in the charge exchange cell. The ratio of peak heights to background is about 50:1.

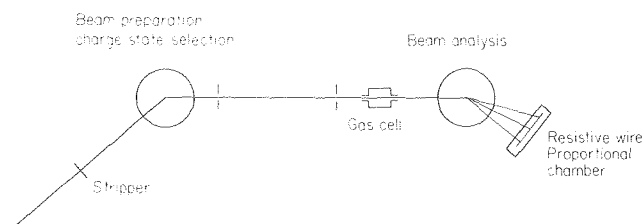


Fig. 1. Experimental layout at the SuperHILAC. (XBL 793-748)

The largest sources of error are due to uncertainties in the column densities of the gas in the charge exchange chamber, charge exchange due to slit scattering, and double electron capture and loss which is not as yet included in our data analysis. We estimate these uncertainties to be 20%. To test for gross errors we remeasured single electron pickup cross sections for Fe²⁵⁺ and Fe²⁶⁺ in argon gas (first measured by Berkner et al.¹). Our values of 5.0×10^{-18} and 5.5×10^{-18} cm²/atom for Fe²⁵⁺ and Fe²⁶⁺ respectively agree well with Berkner's values of 5.6 and 5.8×10^{-18} cm²/atom.

Figures 2 and 3 and Table 1 show the measured velocity dependence of the charge capture and loss cross sections in N₂ of argon ions with five or fewer electrons, and Table 2 lists the measured cross sections for highly stripped Fe, Kr, and Xe ions at 8.5 MeV/amu in N₂. A more extensive data analysis and measurements of charge changing cross sections for heavier ions is in progress.

* * *

[†]Brief version of LBL-8932, presented at the 1979 Particle Accelerator Conference, San Francisco, California, March 12-14, 1979.

1. K. H. Berkner, W. G. Graham, R. V. Pyle, A. S. Schlachter, and J. W. Stearns, LBL-5991 (1977); also, Proceedings of 10th Int. Conf. on Phys. of Electr. and At. Coll., Paris, July 1977, p. 542.

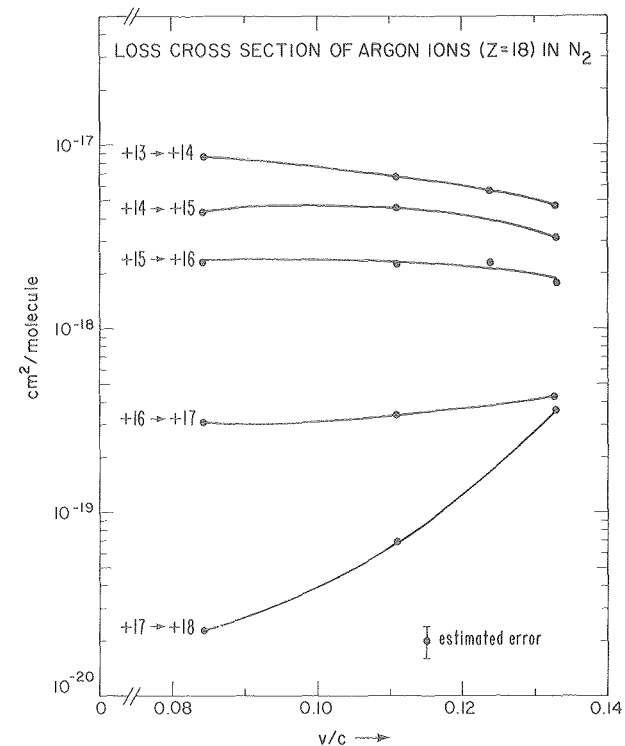


Fig. 2. Single electron loss cross sections as a function of ion velocity for argon ions in nitrogen gas. (XBL 793-900)

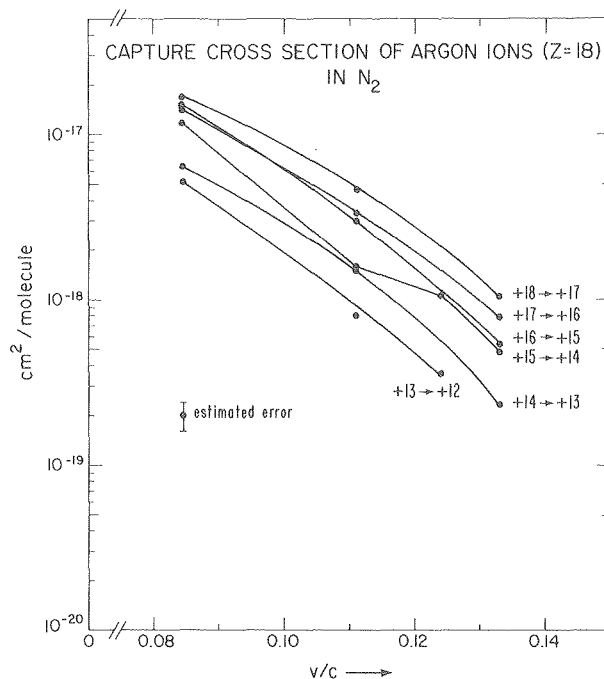


Fig. 3. Single electron pickup cross sections as a function of ion velocity for argon ions in nitrogen gas. (XBL 793-901)

Table 1. Argon charge changing cross sections in N₂.

| Velocity (v/c) | Ion | Cross Sections in Units of 10 ⁻¹⁹ cm ² /molecule | |
|-------------------------|-----|--|------|
| | | Capture | Loss |
| 1.342 (8.5 MeV/amu) | +18 | 10.3 | -- |
| | +17 | 8.0 | 3.7 |
| | +16 | 5.4 | 4.3 |
| | +15 | 4.8 | 18 |
| | +14 | 2.3 | 31 |
| | +13 | -- | 52 |
| .1236 (7.1 MeV/amu) | +15 | 11 | 23 |
| | +13 | 4.6 | 57 |
| .1113 (5.8 MeV/amu) | +18 | 48 | -- |
| | +17 | 33 | .69 |
| | +16 | 30 | 3.4 |
| | +15 | 16 | 21.7 |
| | +14 | 15 | 45.7 |
| | +13 | 8 | 66.3 |
| .0846 (3.35 MeV/amu) | +18 | 170 | -- |
| | +17 | 140 | .23 |
| | +16 | 150 | 3.1 |
| | +15 | 116 | 23. |
| | +14 | 63 | 43 |
| | +13 | 53 | 86 |

Table 2. Charge changing cross sections in N₂ at 8.5 MeV/amu.

| Atom | Ion | Cross Sections in Units of 10 ⁻¹⁹ cm ² /molecule | |
|-----------|-----|---|------|
| | | Capture | Loss |
| Fe (Z=26) | +26 | 34.3 | -- |
| | +25 | 27.4 | 3.2 |
| | +23 | 22.9 | 8.0 |
| | +20 | 11.4 | 41 |
| | +17 | 9.1 | 82 |
| Kr (Z=36) | +33 | 66 | 2.3 |
| | +27 | 21.7 | 18.3 |
| | +21 | 4.5 | 94 |
| Xe (Z=54) | +46 | 120 | 3.3 |
| | +41 | 77 | 16 |
| | +34 | 36.5 | 53 |
| | +28 | -- | 177 |

RESEARCH PLANS FOR CALENDAR YEAR 1980

Fine Structure in the n=2 State of the Helium-like Ions. New techniques of eliminating Doppler shifts will be explored and increasingly precise calibration lines will be investigated.

Electron Capture into the Continuum by Fast Projectiles. Fast, fully-stripped ions passing through a gas will give rise to ionization electrons with a continuous velocity distribution. These electrons exhibit a cusp at the velocity of the incident projectile. Precise measurements of the shape of this cusp will be made in order to test theoretical models based on the second Born approximation which predict an asymmetry.

Charge-Capture and Charge-Loss Cross Sections. Our previous measurements will be extended to lead projectiles. Targets will be the noble gases N₂ and O₂. A variety of beam energies will be studied.

Forbidden Transition in the L-Shell. An attempt will be made to observe M1 and E2 transitions of the type $\Delta n = 0$ in the L-shell vacancies of Ar⁺⁹, Ar⁺¹⁰ ... Ar⁺¹³. Wavelengths and lifetimes will be measured. This experiment involves the first attempt to capture these ions in a trap.

1979 PUBLICATIONS AND REPORTS

Other Publications

1. H. Gould, R. Marrus, D. Dietrich, and J. A. Leavitt, "Radiative Decay from Low-Lying Transitions in Li-like and Be-like Krypton," presented at the Second Topical Conference on Atomic Processes in High Temperature Plasmas, Boulder, Colorado, January 1979.

2. J. R. Alonso, H. Gould, and D. Dietrich, "Charge Changing Cross Section Measurements for Heavy Ions at Energies to 8.4 MeV/amu," presented at the Particle Accelerator Conference, San Francisco, March 1979 [Bull. Am. Phys. Soc., 24, 173 (1979)].

3. R. Marrus and P. J. Mohr, "Forbidden Transitions in One- and Two-Electron Atoms," in Advances in Atomic and Molecular Physics, Vol. 14, eds. D. R. Bates and B. Bederson (Academic Press, N.Y., 1979).

Invited Talks

1. R. Marrus, "Quenching of the Metastable State of Hydrogenlike Argon in an External Electric Field," Oxford University, Oxford, England, February 1979.

2. H. Gould, "Radiative Decay from Accelerator Produced Heliumlike High-Z Ions," A-division, Lawrence Livermore Laboratory, Livermore, California, February 1979.

3. D. Dietrich, "Wavelengths and Lifetime Measurements on Lithiumlike and Berylliumlike Iron and Krypton," E-division, Lawrence Livermore Laboratory, Livermore, California, February 1979.

B. PROCESSES AND TECHNIQUES

1. Chemical Energy

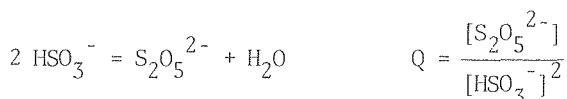
a. Formation of Oxyacids of Sulfur from SO₂*

Robert E. Connick, Investigator

1. THE DIMERIZATION OF HSO₃⁻

Thomas M. Tam and Marc Lipshutz

Values for the equilibrium quotient, Q, for the dimerization of bisulfite ion:



were earlier measured using a combination of Raman and ultraviolet spectroscopy. The data have been refined through careful correction for the presence of SO₃²⁻ and SO₂ in the solutions and "best" values obtained for Q and the molar absorptivity of S₂O₅²⁻. The results differ slightly from those reported earlier.

Measurements of Q made previously as a function of ionic strength, using sodium chloride as the principal electrolyte, have now been repeated for sodium perchlorate solutions. The overall variation with ionic strength is quite similar for the two electrolytes, although the Q values in the sodium perchlorate solutions are slightly higher. The close correspondence of the two results tends to confirm the conjecture made in the Raman and UV determination of Q that the dimerization equilibrium, involving as it does only anions, would not be strongly affected by the other anions in the solutions.

2. EXPERIMENTS TO DISTINGUISH BETWEEN H-SO₃⁻ AND SO₃-H⁻

Thomas M. Tam

In previous work evidence was found for the existence in aqueous solution of the bisulfite species with the proton attached to an oxygen. (The bisulfite species with proton attached to the sulfur is already well known.) The evidence came from the number of lines in the Raman spectrum of bisulfite solutions. It seemed desirable to check this finding by other observations.

One approach is to study the system under sufficiently different conditions that the ratio of

the two species would be changed significantly. Variation of the ratio with temperature was discarded because the ΔH for the equilibrium would be predicted to be quite small, and the presence of S₂O₅²⁻ in the solution complicates the Raman observations. Instead solvents other than water were investigated.

Salts of S₂O₅²⁻, the most convenient source of bisulfite ion, tend to be very insoluble in organic solvents, unless they contain a high concentration of OH groups, such as in glycerine or methanol. Unfortunately such hydroxylic solvents are rather similar to water -- that is why they dissolve the disulfites -- and therefore appear not to produce large changes in the ratio of the two bisulfite species. Attempts were made to increase the solubility in other solvents by using large cations, e.g. Cs⁺ and N(C₂H₅)₄⁺, but with no significant success.

A number of measurements were made on the ethylene glycol--water system, with various ratios of ethylene glycol to water. At low water content the S₂O₅²⁻ species appeared to be completely absent. Unfortunately, the Raman spectrum of the bisulfite was complicated by that of the glycol, and definitive results were not obtained.

RESEARCH PLANS FOR CALENDAR YEAR 1980

There will be a continuing interest in the basic chemistry of species formed from sulfur dioxide in aqueous solutions. Research is under way on the rate of exchange of oxygen atoms between water and HSO₃⁻, S₂O₅²⁻ and SO₂ in aqueous solution using the nuclear magnetic resonance of oxygen-17. The results should clarify the mechanism of the exchange as well as give information on the mechanism of dimerization of HSO₃⁻ and the reaction of SO₂ with water to form H⁺ and HSO₃⁻. Some further attempts will be made to confirm the existence of the two forms of HSO₃⁻ in solution. Measurements will be made of the first and second ionization constants of SO₂ in a variety of aqueous media in order to make available values of these important equilibrium quotients. The above chemistry is relevant to flue gas disulfurization by wet scrubbing methods, as well as to some of the reactions which sulfur dioxide undergoes as a pollutant in the atmosphere.

Computer modeling of a replacement reaction in the first coordination sphere of a metal ion is continuing, and some new data on water substitution will be obtained for comparison with theory.

* This work was supported by the Division of Chemical Sciences, Office of Basic Energy Sciences, U. S. Department of Energy.

1979 PUBLICATIONS AND REPORTS

Refereed Journals

1. B. Meyer, L. Peter and C. Shaskey-Rosenlund, "Raman Spectra of Isotopic Bisulfite and Disulfite Ions in Alkali Salts and Aqueous Solutions," *Spectrochim. Acta.* 35, 347 (1979).

Other Publications

1. R. E. Connick, T. M. Tam and E. von Deuster, "The Formation of $S_2O_5^{2-}$ in Solutions of HSO_3^- ," presented at American Chemical Society Meeting, Honolulu, Hawaii, April 5, 1979.
2. H. Weeks, B. Mulliken and B. Meyer, "The Reaction of Ammonia with Sulfur Dioxide," presented at ACS National Meeting, Washington, D.C., September 13, 1979.

LBL Reports

1. B. Meyer, H. Weeks, and B. Mulliken, "Reaction of Ammonia with Excess Sulfur Dioxide," LBL-8098, accepted for publication in *Phosphorus and Sulfur*.
2. B. Meyer, H. Weeks, and B. Mulliken, "Reaction of Sulfur Dioxide with Excess Ammonia," LBL-8098 A accepted for publication in *Phosphorus and Sulfur*.

Invited Talks

1. Robert E. Connick and Thomas M. Tam, "Species in Aqueous Solutions of Sulfur Dioxide," Gas Desulfurization Conference, Morgantown, West Virginia, June 7-8, 1979.

b. Conversion of Coal to Clean Liquid and Gaseous Fuels*

A. T. Bell, G. A. Somorjai, and K. P. C. Vollhardt,
Investigators

1. CARBON MONOXIDE HYDROGENATION OVER CLEAN AND OXIDIZED RHODIUM CRYSTAL SURFACE. CORRELATIONS OF STRUCTURE, COMPOSITION AND REACTIVITY[†]

D. G. Castner, R. Blackadar, and G. A. Somorjai

CO hydrogenation at 6 atm over Rh polycrystalline foil and single crystal (111) catalysts was investigated in a system where the surface structure and composition of the catalysts could be characterized both before and after the reaction. The reaction conditions ($H_2:CO$ ratio, reaction temperature, surface pretreatment and gas phase additives) were systematically varied to determine the conditions for the formation of oxygenated hydrocarbons. Initially clean Rh catalysts showed no structure sensitivity, primarily produced methane (90 wt %) at an initial rate of 0.15 molecules \cdot site $^{-1}\cdot$ sec $^{-1}$ at 300°C, and did not produce detectable amounts of oxygenated hydrocarbons. Preoxidation of the Rh (100 Torr O_2 , 600°C, 30 min.) resulted in dramatically increased initial rates, a larger fraction of higher molecular weight hydrocarbons in the product distribution, formation of methanol, ethanol and acetaldehyde, and some structure sensitivity. The different Arrhenius methanation preexponential factors and activation energies over the clean and preoxidized Rh foils indicate the methanation mechanism is different on these two surfaces. Decreasing the reaction temperature or $H_2:CO$ ratio increased the C_2H_4 to C_2H_6 ratio, and shifted the product distribution toward the higher molecular weight hydrocarbons. The addition of 1 mole % of CH_2OH , CH_3CH_2OH or C_2H_4 to the $H_2:CO$ reaction mixture caused only a small increase in the fraction of higher molecular weight hydrocarbons.

* * *

[†]Brief version of LBL-10018.

2. HIGH RESOLUTION ELECTRON ENERGY LOSS SPECTROSCOPY (HREELS) STUDY OF CO_2 DISSOCIATION ON RHODIUM SURFACES[†]

L. H. Dubois and G. A. Somorjai

In order to show that carbon dioxide dissociatively adsorbs on rhodium surfaces, high resolution ELS and thermal desorption mass spectrometry (TDS) were applied to a study of $^{12}CO_2$ and $^{13}CO_2$ chemisorption on the Rh (111) single crystal surface. This combination of techniques allowed us to determine the nature of the species while on the metal surface and after desorption into the gas phase. The chemisorption of CO_2 on Rh (111) at 300 K yielded vibrational spectra identical to those

found for adsorbed CO at the same temperature. We expect the weak Rh-O stretch from adsorbed oxygen to be hidden beneath the relatively intense metal-carbon stretching vibration. We noted that isotopically labelled $^{13}CO_2$ displayed the proper frequency shifts upon adsorption. The TDS spectra and LEED patterns of chemisorbed $^{12}CO_2$ and ^{12}CO were quite similar. Furthermore, $^{13}CO_2$ yielded only gaseous ^{13}CO desorbing from the surface. We therefore conclude that CO_2 dissociates on rhodium surfaces to form adsorbed CO and oxygen.

* * *

[†]Brief version of LBL-8976.

3. THE CATALYZED SURFACE REACTIONS OF CO AND NO ON RHODIUM CRYSTAL SURFACES, AND ELS STUDY

P. Hansma, L. H. Dubois, and G. A. Somorjai

Conclusive evidence for a surface oxygen intermediate in the reaction of NO and CO to form N_2 and CO_2 over rhodium surfaces was presented. High resolution ELS measurements indicated that both NO and CO associatively adsorb on the Rh (331) single crystal surface at 300 K. Chemisorbed NO readily dissociated on this surface upon heating to 450 K. At 700 K (the reaction temperature at which a typical automotive catalytic converter operates) high resolution ELS and Auger electron spectroscopy both indicated that only oxygen was present on the surface. N_2 desorption below this temperature was readily detected mass spectroscopically. The addition of CO to this surface oxygen at 700 K resulted in the formation of gaseous CO_2 and the removal of this surface oxygen species. Similar results were obtained when O_2 was substituted for NO as a control indicating that oxygen is indeed a surface intermediate under our experimental conditions.

4. SUPPORTED RUTHENIUM CLUSTER COMPLEXES AS CATALYSTS FOR FISCHER-TROPSCH SYNTHESIS^{††}

S. Kellner, V. L. Kuznetsov, and A. T. Bell

The preparation of supported metal catalysts through the use of cluster complexes offers the possibility of preparing high dispersion catalysts in which the metal is distributed in units of defined nuclearity. The present study was undertaken to characterize the structures formed by supporting $Ru_3(CO)_{12}$, $\alpha-H_4Ru_4(CO)_{12}$, and $Ru_6C(CO)_{17}$ on $\gamma-Al_2O_3$. The properties of these catalysts for Fischer-Tropsch synthesis were also examined and compared with those for Ru/Al_2O_3 catalysts prepared by reduction of $RuCl_3$.

The extent of $Ru_3(CO)_{12}$ adsorption on $\gamma-Al_2O_3$ is found to depend strongly on the temperature

* This work was supported by the Division of Chemical Sciences, Office of Basic Energy Sciences, U. S. Department of Energy.

at which the support has been dehydroxylated. Infrared spectra of alumina-supported $\text{Ru}_3(\text{CO})_{12}$ suggest that the cluster is adsorbed as a result of interactions of the carbonyl ligands with hydroxyl groups and Lewis acid sites present on the support surface. Similar interactions are proposed for alumina-supported $\alpha\text{-H}_4\text{Ru}_4(\text{CO})_{12}$ and $\text{Ru}_6\text{C}(\text{CO})_{17}$.

Decomposition of the supported clusters produces three surface structures, independent of the original cluster composition. The first structure is characterized by bands at 2045-2050 and 1965-1970/cm and is represented by $[\text{Ru}(\text{CO})_2\text{X}_2]_n$. The second and third structures are characterized by bands at 2130-2140, 2060-2070, and 1990-2000/cm and are represented by $[\text{Ru}(\text{CO})_3\text{X}_2]_n$ and $[\text{Ru}(\text{CO})_4\text{X}_2]_n$, respectively. In each of the three structures, X represents an oxygen atom of the alumina lattice. The nuclearity of the surface structures, n, cannot be defined from the present studies, since it is not known whether the metal lattice of the original cluster decomposes upon adsorption on the support or whether agglomeration of clusters occurs.

Complete decarbonylation of the Ru surface structures induces a stronger Ru-support interaction, which may lead to the entry of Ru ions into the support lattice and the formation of surface aluminates. The aluminates are not stable, however, and the initial three structures can be regained by heating in CO. Upon reduction of the supported clusters in H_2 at temperatures above 400°C , Ru microcrystallites appear to be formed. These particles are not stable and the Ru is redispersed into smaller units if the sample is heated in CO above 200°C .

An illustration of the distribution of hydrocarbons produced during Fischer-Tropsch synthesis over $\text{Ru}_3/\text{Al}_2\text{O}_3$ and $\text{Ru}_6/\text{Al}_2\text{O}_3$ is shown in Fig. 1. It is apparent that the product distributions for the two supported-cluster catalysts are nearly identical and that both distributions are practically indistinguishable from those for conventionally prepared $\text{Ru}/\text{Al}_2\text{O}_3$ catalysts. The ratio of olefin to paraffin for each carbon number is shown in Fig. 2. While each catalyst produces a somewhat different distribution of olefins to paraffins, it is again concluded that the supported-cluster catalysts are not significantly different.

A comparison of the turnover numbers for methane formation are presented in Table 1. This measure of catalyst activity is observed to decline with increasing ruthenium dispersion. A further correlation is observed with the ratio of CO to H_2 adsorbed. These data suggest that very highly dispersed ruthenium atoms or clusters do not contribute to Fischer-Tropsch synthesis and that it is only the larger clusters or microcrystallites, bearing a more metallic character, which are active. Further evidence supporting this conclusion was obtained from *in situ* infrared spectra, which showed that CO chemisorbed on the metal particles participates in reaction but that CO chemisorbed on Ru atoms strongly interacting with the support does not react.

* * *

† Brief version of LBL-9669.

‡ Supported in part by NSF.

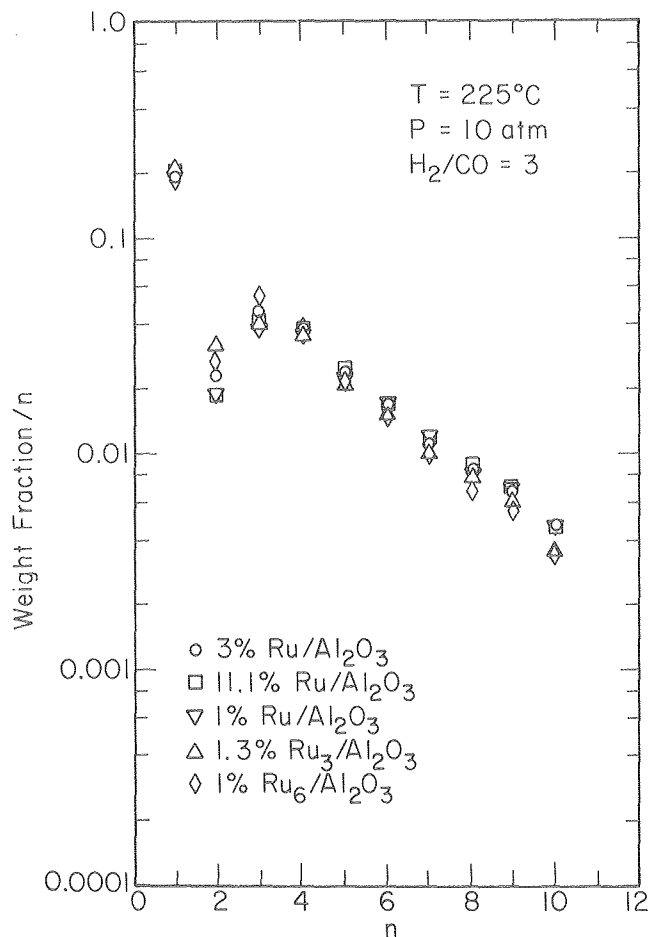


Fig. 1. Distribution of hydrocarbons produced during Fischer-Tropsch synthesis over $\text{Ru}/\text{Al}_2\text{O}_3$ catalysts. (XBL 7912-13722)

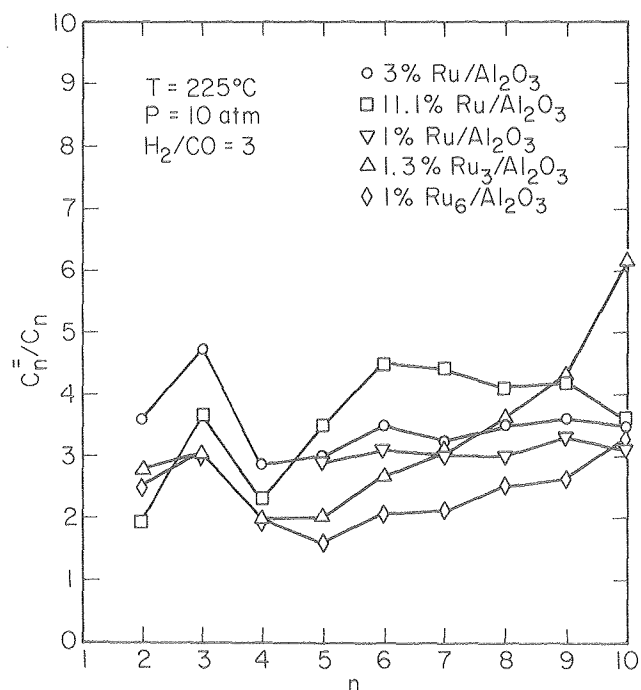


Fig. 2. Ratio of olefins to paraffins in products obtained during Fischer-Tropsch synthesis over $\text{Ru}/\text{Al}_2\text{O}_3$ catalysts. (XBL 7912-13723)

Table 1. Effect of Ru dispersion on methane activity.

| Catalyst | H/Ru | CO/Ru | CO/H | $N_{CH_4} (s^{-1})$ |
|--|------|-------|------|------------------------|
| 1.3% Ru ₃ /Al ₂ O ₃ | 0.92 | 1.94 | 2.10 | 1.26×10^{-3} |
| 1.0% Ru ₆ /Al ₂ O ₃ | 1.18 | 2.00 | 1.69 | 1.67×10^{-3} |
| 3.0% Ru/Al ₂ O ₃ | 0.54 | 0.81 | 1.50 | 7.13×10^{-3} |
| 11.1% Ru/Al ₂ O ₃ | 0.30 | 0.31 | 1.03 | 11.98×10^{-3} |

Reaction conditions: T = 225°C ; P = 10 atm H₂/CO = 3

5. HYDROGENOLYSIS OF ETHER LINKAGES IN COAL-RELATED MODEL COMPOUNDS CATALYZED BY NICKEL AND NICKEL SULFIDE IN THE PRESENCE AND ABSENCE OF ZINC CHLORIDE[†]

D. P. Mobley and A. T. Bell

The hydrogenolysis of ether linkages is an important process occurring during the liquefaction of coal by Lewis acid catalysts. As a model for these reactions we have investigated the hydrogenolysis of benzylic ethers in the presence of ZnCl₂.¹ The results of that effort have suggested that hydrogenolysis proceeds via an ionic mechanism and involves the release of benzylic carbonium ions during the early stages of reaction. These ions cannot be stabilized by hydride transfer from molecular H₂ and, instead, react with aromatic centers to form higher molecular weight products and tars. To preclude the formation of these latter products we have investigated the effects of using metallic Ni in conjunction with ZnCl₂.

Table 1 summarizes the products obtained from reactions of dibenzyl ether in cyclohexane solution using either ZnCl₂, Ni, or a ZnCl₂/Ni mixture as the catalyst. It is evident that while ZnCl₂ effects a complete conversion of the ether, an insoluble resin is the primary product. Nickel catalyzes the conversion of dibenzyl ether to toluene and benzyl alcohol but is not as active as ZnCl₂. By combining Ni and ZnCl₂, it is possible to obtain a very high conversion of ether to toluene and minimal tar formation. These results suggest that ZnCl₂ promotes cleavage of the ether while Ni facilitates the transfer of hydride ions to benzylic carbonium ions. By combining both catalysts a synergistic effect is achieved.

Under coal liquefaction conditions it is expected that Ni would be converted to NiS. As a result, an investigation was performed of the activity of NiS for ether hydrogenolysis both in the presence and absence of ZnCl₂. Selected results of these studies are shown in Table 1. It

Table 1. Products obtained from the catalytic hydrogenolysis of dibenzyl ether.

| Catalyst | Catalyst loading (mole) | | % Yield | % Ether Conversion |
|-------------------|-------------------------|---------------------------------------|---------|--------------------|
| None | - | Toluene | 1.4 | 3.8 |
| | | Bibenzyl + o,m and p-benzyl toluenes | 0.1 | |
| ZnCl ₂ | 5.0×10^{-3} | Toluene | 3.9 | 100 |
| | | Bibenzyl + o,m and p-benzyl toluenes | 2.5 | |
| | | Insoluble resin | 97 | |
| Ni ^(c) | 2.0×10^{-1} | Toluene | 19.5 | 38.2 |
| | | Benzyl alcohol | 5.7 | |
| | | Bibenzyl + o,m, and p-benzyl toluenes | 2.3 | |
| | | Insoluble resin | 2.5 | |

Table (continued)

Table 1. (continued)

| Catalyst | Catalyst loading (mole) | Products | % Yield | % Ether Conversion |
|-------------------|-------------------------|--------------------------------------|---------|--------------------|
| Ni ^(c) | 2.0×10^{-1} | Toluene | 39.6 | 100 |
| ZnCl ₂ | 5.0×10^{-3} | Bibzenyl + o,m and p-benzyl toluenes | 12.3 | |
| | | Insoluble resin | 35 | |
| Ni ^(c) | 2.0×10^{-1} | Toluene | 65.6 | 96.5 |
| ZnCl ₂ | 1.0×10^{-3} | Bibenzyl + o,m and p-benzyl toluenes | 8.2 | |
| | | Insoluble resin | 6.0 | |
| NiS | 6.1×10^2 | Toluene | 92.1 | 100 |
| | | Bibenzyl + o,m and p-benzyl toluenes | 0.5 | |
| NiS | 6.1×10^2 | Toluene | 89.3 | 100 |
| ZnCl ₂ | 1.0×10^{-3} | Bibenzyl + o,m and p-benzyl toluenes | 1.1 | |

Reaction conditions: 2.0×10^{-2} mole dibenzylether; 50 ml cyclohexane; 225°C; 13.8 MPa H₂ pressure; 60 min reaction time.

is noted that NiS is highly active for the conversion of bibenzyl ether to toluene, but in contrast to the behavior of metallic nickel, the addition of ZnCl₂ has a negative rather than a positive effect. Thus, it appears that NiS does not promote hydride transfer to benzylic carbonium ions.

The activity of NiS for the hydrogenolysis of benzylic ethers unprecedented and differs significantly from that of other common sulfides. For example, experiments performed with FeS, MoS₂, and ZnS showed very low conversions of dibenzyl ether to toluene.

* * *

[†]Brief version of LBL-9477 and LBL-9023.

1. D. P. Mobley and A. T. Bell, Fuel 58, 661 (1979).

6. COAL LIQUEFACTION USING A ZINC CHLORIDE CATALYST[†]

S. A. Gandhi and A. T. Bell

The effects of ZnCl₂ on the liquefaction of SRC-I, Wyodak subbituminous coal, and Illinois #6 bituminous coal were studied in a high pressure stirred autoclave at temperatures below 350°C to avoid the influence of pyrolytic reactions. Cyclohexane was used as the reaction solvent in order to extract oil-like products, which were then characterized by elemental analysis and ¹H-NMR.

At 300°C, 2000 psig, and catalyst to coal weight ratio of 1.0, the presence of zinc chloride in-

creased the cyclohexane solubility of SRC-I from 10.6% to 30.0%, Wyodak coal from 6.9% to 13.5%, and Illinois #6 coal from 1.8% to 8.0%. Data on catalyst loading showed that a catalyst to coal weight ratio of 0.6 was optimum for Wyodak coal and 1.0 for Illinois #6 coal. Studies on the effect of reaction time indicated that the solubility of SRC-I was mostly complete after about 1 hour. Increasing reaction temperature from 250°C to 400°C was found to linearly increase the yield of soluble products. Hydrogen pressure had a lesser effect on the yield, but the presence of gaseous hydrogen was necessary to produce a high cyclohexane solubility. For Wyodak coal and Illinois #6 coal, the H/C and H_{a1}/H_{ar} increased. For SRC-I, the H_{a1}/H_{ar} ratios increased as cyclohexane solubilities increased. The H/C ratios of all the extracts were always substantially higher than that of the parent coal. Soxhlet extractions with pyridine of the residues from Wyodak coal and Illinois #6 coal indicated that zinc chloride also increased the asphaltene and pre-asphaltene content of the coal.

Further studies with Wyodak coal demonstrated no difference in product yield or composition whether ZnCl₂ was added to the coal as a solid powder or impregnated into the coal pore structure from methanol solution. This suggests that once molten, ZnCl₂ effectively wets the particles of coal and penetrates the pore network. Experiments were also conducted to establish the influence of solvent to coal ratio. These investigations showed no influence of the solvent volume used for a given amount of coal, indicating that solvent saturation did not limit the extraction of cyclohexane soluble products.

In summary, the results of this investigation show that $ZnCl_2$ promotes the conversion of coal to oil-like (cyclohexane soluble) products at temperatures where pyrolytic reactions do not occur extensively. For a fixed catalyst to coal ratio, the extent of conversion increase with decreasing coal rank as well as with increasing severity of the reaction conditions.

* * *

[†]Brief version of LBL-10282.

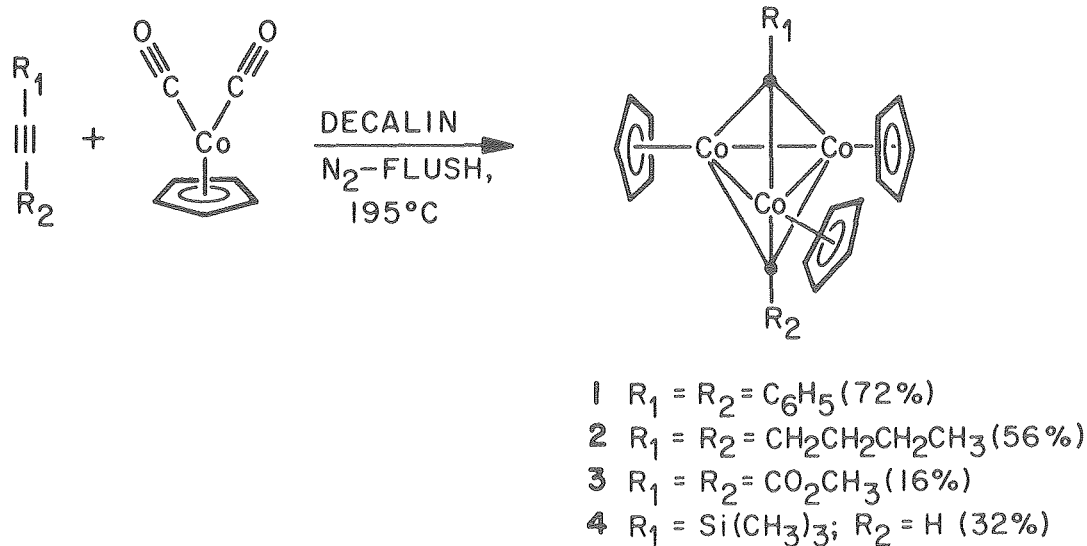
7. BISCARBYNE CLUSTERS OF COBALT AS POTENTIAL HOMOGENEOUS ANALOGS OF FISCHER-TROPSCH INTERMEDIATES[†]

J. R. Fritch and K. P. C. Vollhardt

Surface carbyne species have recently been implicated in the H-D exchange of polymethylcycloalkanes mediated by cobalt films, the isomerization

of saturated hydrocarbons on iridium catalysts, the interaction of acetylene and ethylene with platinum, nickel, and rhodium single crystals, and the hydrogenation of carbon monoxide (Fischer-Tropsch reaction) on heterogeneous systems. We have discovered a general synthesis of biscarbyne complexes by a conceptually most simple route, the cleave of alkynes, and we suggest that these clusters, particularly those derived from multiple cleavage of oligynes, apart from their novelty, have excellent potential to constitute suitable substrates on which to study surface-homogeneous cluster analogies.

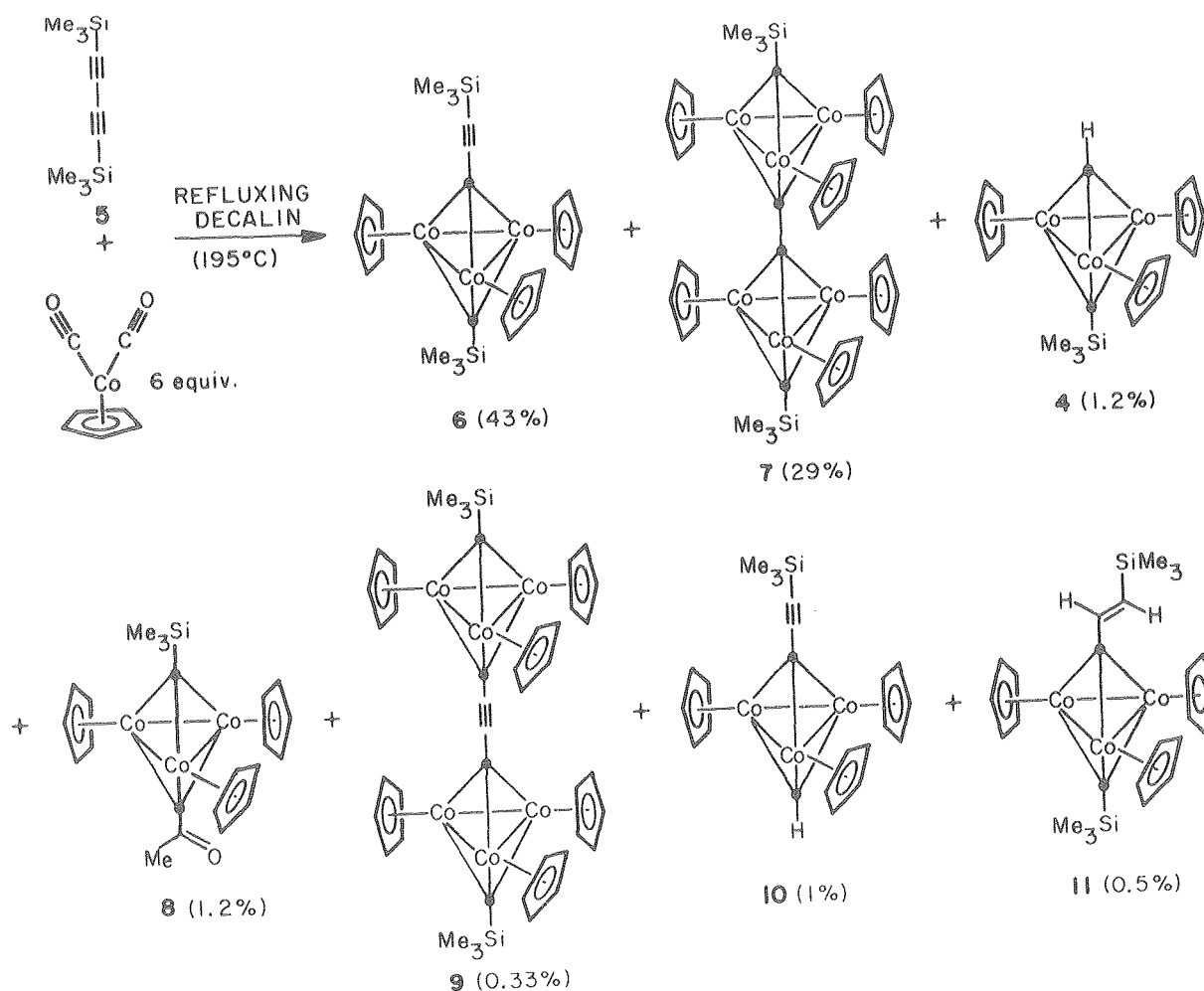
We have found that $(\eta^5-C_5H_5)Co(CO)_2$, which ordinarily functions as a mediator of alkyne oligomerizations to furnish catalytic and stoichiometric products (e.g., benzenes, complexed cyclopentadienones and cyclobutadienes) assembles a trinuclear $[(\eta^5-C_5H_5)Co]_3$ cluster which inserts into alkyne functions with remarkable ease, according to Scheme 1. Thus, when a solution of diphenylacetylene and the cobalt species (3 equiv.) in decalin is slowly added



Scheme 1

(syringe pump) to boiling and nitrogen flushed decalin over 24h only 9% of the ordinarily expected tetraphenylcyclobutadiene (and cyclopentadienyl) cyclopentadienyl cobalt is isolated on alumina chromatography. The major product (72%) is the biscarbyne cluster **1**. In similar fashion alkyl, proton bearing, silyl, and functionalized derivatives **2-4** may be prepared. In the reactions of trimethylsilylated alkynes, traces of other clusters are observed derived from silyl-acetylide metathesis, hydrolysis, and dimerization processes. For example, complete analysis of all chromatographable products from the conversion of

bis(trimethylsilyl)butadiyne **5** with six equivalents of $(\eta^5\text{-C}_5\text{H}_5)\text{Co}(\text{CO})_2$ reveals seven clusters **4** and **6-11**! It should be noted that the "triple decker" sandwich **7** is formed despite the considerable steric crowding in the system. Compounds **4** and **9** most likely arise via metathesis of **5** to trimethylsilylacetylene and bis(trimethylsilyl)butatriyne (**12**) (or their equivalents) in the coordination sphere of the metal. A control experiment (Scheme 2) showed that **7** is an unlikely source of **4** via cleavage of the carbidobridge under the reaction conditions.



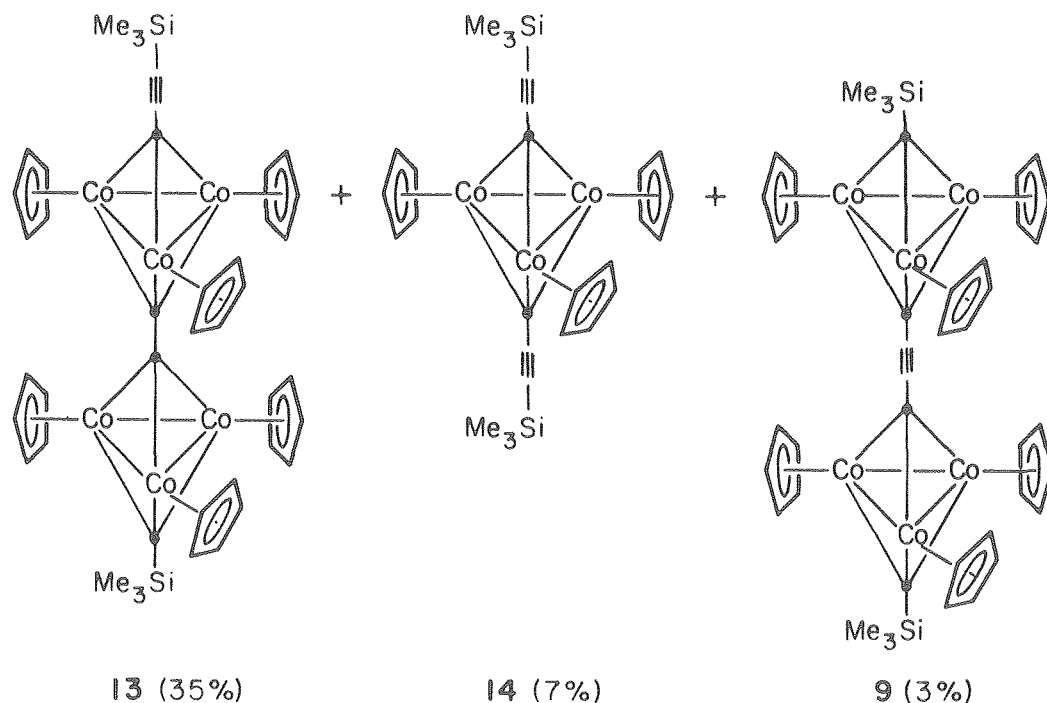
Scheme 2

Ketone **8** may be thought of as a hydrolysis product of **6**, cluster **10** is derived from **6** by proto-desilylation, and **11** from a dimer of trimethylsilylacetylene, 1,4-bis(trimethylsilyl)-1,3-butyne.

A similar array of products is obtained in the analogous reaction of bis(trimethylsilyl) hexatriyne (**17**), but again the major components of the reaction mixture are the singly inserted **14**, and the "triple deckers" **9** and **13** (see Scheme 3).

analysis, and spectral data indicate that in the reaction with acid, cluster **4** is protonated to a mixed carbenecarbyne cation, capable of desilylation and/or deprotonation. In contrast, cluster **1** is inert to $\text{CF}_3\text{CO}_2\text{H}$, but reacts with hot $\text{CF}_3\text{SO}_3\text{H}$ to furnish benzene and toluene. This suggests that after protonation at the apical carbon dephenylation may take place as well as complete hydrolysis.

Biscarbynes may act as, or be precursors of, catalytically active species. Heating **4** with



Scheme 3

Treatment of **6** with 1% KOH-EtOH gave quantitative monodesilylation to the unstable terminal acetylene, whereas the action of $(n\text{-Bu})_4\text{F}^-$ in hot THF led to complete desilylation and the formation of the unsilylated analog of **6**.

The parent biscarbyne $[\mu_3\eta^1\text{-HC}]_2[(\eta^5\text{-C}_5\text{H}_5)\text{Co}]_3$ is available from **4** by fluorodesilylation $[\text{C}_6\text{H}_5\text{CH}_2\text{N}(\text{CH}_2)_3\text{F}]^+$, DMSO, 105°C, 6h, 87%). Remarkably, instant H-D exchange at the carbyne carbon is observed when **4** is exposed to $\text{CF}_3\text{CO}_2\text{D}-\text{C}_6\text{D}_6$ (1:1, 25°C deep green solution) under conditions which lead to neither deuterodesilylation nor deuterium incorporation into the cyclopentadienyl ligands (1h). Moreover, treatment of **4** with stronger acid ($\text{CF}_3\text{-SO}_3\text{H}-\text{CH}_2\text{Cl}_2$) gave, on addition of hexane, green crystalline material, which on exposure to water furnished a mixture of desilylated **4** and recovered starting material. This result, elemental

1-heptene in a stainless steel bomb to 200°C in the presence of CO (400 psi) and H_2 (800 psi) gave 1-octanal, 1-octanol, 2-methylheptanal, and 2-methylheptanol with respective turnovers of 30, 6.8, 15.4, and 5.0 per equivalent of cobalt.

We foresee important applications of reaction (1) in organic and organometallic synthesis, the investigation of reactions analogous to surface catalyzed processes, and the construction of super-clusters in which to study novel bonding modes and the potential intramolecular mobility of attached ligands (for example **9** \rightleftharpoons **13**).

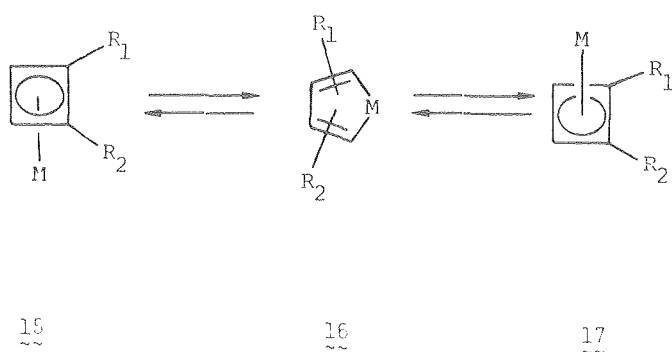
* * *

†Supported in part by NSF.

8. TRANSITION METAL ACTIVATION OF CARBON-CARBON BONDS†

M. J. Winter and K. P. C. Vollhardt

In an effort to determine the conditions under which sp^2 - sp^2 -carbon bonds may be cleaved, several complexes containing these linkages have been subjected to flash pyrolytical treatment. Thus, cleavage of one of the ligand bonds in complex 15 by oxidative insertion of the metal to give a metallacycle 16 should be readily detectable by making use of the chirality of the former, and achirality of the latter, respectively (Scheme 1). In this way a potentially observable equilibration of 15 with 17 might be postulated to proceed through 16.



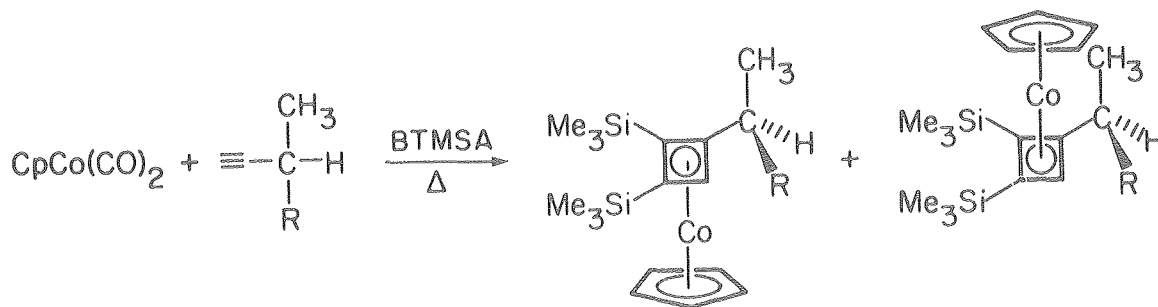
Scheme 1

For this purpose a series of diastereomeric η^5 -cyclopentadienyl cobalt cyclobutadiene complexes was constructed in good yield (2), and separated by column chromatography on alumina [R=OH, OCH₃, OSi(CH₃)₃] or high pressure liquid chromatography on a reverse phase column (R=C₆H₅). Sublimation through a hot silanized quartz tube (10⁻⁴ Torr, 540-650°C) revealed the gradual interconversion of both diastereoisomers until the establishment of thermodynamic equilibria. At higher temperatures, increasing retrocyclization of the four ring was observed furnishing all four possible component alkynes. The results provide for the first time an indication of the reversibility of the metalla-cyclopentadiene-cyclobutadiene metal rearrangement particularly hydrogenation and carbonylation (Scheme 2).

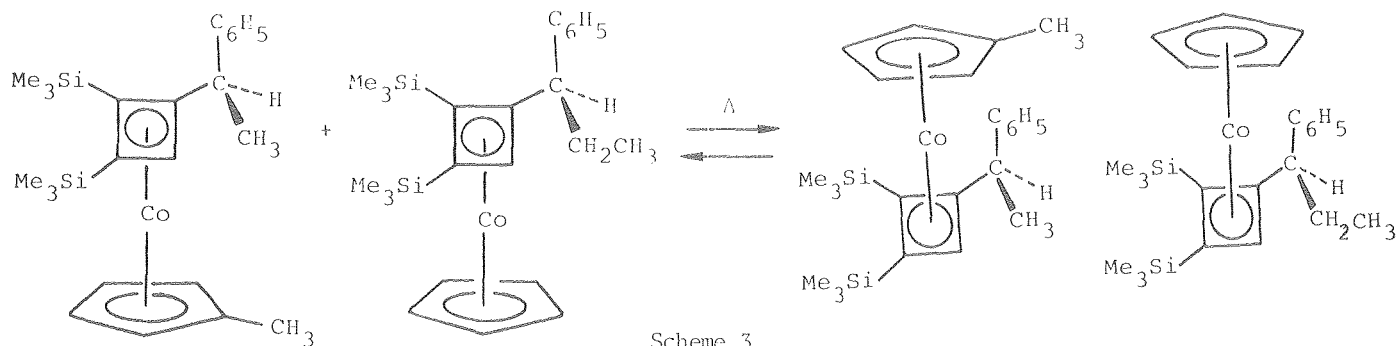
Although the flash vacuum conditions preclude the operation of intermolecular pathways, a control experiment confirmed the intramolecularity of the reaction (3), by revealing the absence of cross-over products derived from ligand exchange. Future work is directed at the synthesis of an optically active, simply substituted cyclobutadiene system on which racemization rates might be determined, and the execution of a labeling experiment designed to indicate whether alkyne formation in the decomposition pathway of cyclobutadiene cobalt complexes and racemization are mechanistically connected (Scheme 3).

* * *

†Supported in part by NSF.

R = OH, OCH₃, OSiMe₃, C₆H₅

Scheme 2



Scheme 3

9. POLYSTYRENE SUPPORTED HOMOGENEOUS CATALYSTS[†]

P. Perkins and K. P. C. Vollhardt

The attachment of soluble, homogeneous catalysts to polymer supports has been the subject of considerable recent research activity. Depending on bead and pore size, catalyst distribution, number and structure of pores, concentration and kind of attached ligands, degree of crosslinking, swelling properties of the polymer, and solvent, changes in rate and product distribution have been observed in catalytic processes effected by these catalysts when compared with their mobile counterparts. Never, however, has there been the observation of new catalytic activity on immobilization. As briefly outlined in a previous report (MMRD Annual Report 1978) we have discovered that polystyrene supported η^5 -cyclopentadienyl cobalt is catalytically active in the hydrogenation of carbon monoxide to give hydrocarbons, that this activity must be due to a defined attached homogeneous cobalt species and not to deposited metal crystallites, and that in contrast soluble $\text{CpCo}(\text{CO})_2$ is inactive and decomposed under hydrogenating conditions. The observed data characterize the title compound as the first catalyst activated to new activity on polymer attachment and the first immobilized homogeneous Fischer-Tropsch catalyst. Literature methods were used for the synthesis of two variants of polymer-supported cyclopentadiene. Treatment with $\text{Co}_2(\text{CO})_8$ gave species **18** and **19** characterized by elemental analysis and the characteristic infrared absorptions at 2012 and 1953 cm^{-1} (KBr). In a swelling solvent (CH_2Cl_2 , C_6H_6) both resins turned brown. Exposure to air led to slow oxidation (green color) although some resin-bound $\text{CpCo}(\text{CO})_2$ was left even after one month's exposure (28%).

Decarbonylation of **18** and **19** could be effected by irradiation (Pyrex, $\sim 20^\circ\text{C}$, toluene). In this reaction, resin **18** in contrast to resin **19**, revealed the formation of two bridged dicobalt-carbonyl species (ν_{CO} 1790, 1773 cm^{-1}) assigned to the polymer bound analogs of $\text{Cp}_2\text{Co}_2(\text{CO})_3$ and $(\text{CpCoCO})_2$, formed under similar conditions from $\text{CpCo}(\text{CO})_2$ in solution.

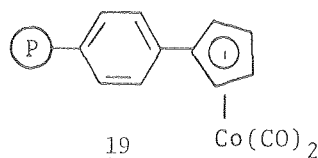
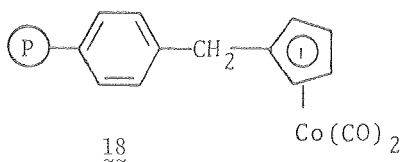
Analogously, vacuum pyrolysis of either resin (185°C, 10^{-3} Torr, 112h) led to complete decarbonylation. Microporous polymer **18** again revealed the formation of a bridged carbonyl during the course of CO removal. Significantly (vide infra), the original species could be completely regenerated on exposure to CO pressure (IR, analysis) (110 atm, 200°, benzene).

Limited hydroformylation and isomerization activity under mild conditions was noted with 1-pentene [resin **19** suspended in purified n-octane, 225 psi CO-H_2 (1:1), 140°C, ca. one turnover CO p.d.] resulting (90h) in a mixture of c,t-2-pentene (21%), pentane (3%), 2-methylpentanal (11%), and hexanal (13%), the mass balance being made up of recovered starting material.

However, exposure of macroporous **19** in suspension (purified n-octane) to CO/H_2 (3:1, 75 psi at RT) at 190-200°C in a static reactor revealed pronounced methanation and Fischer-Tropsch activity. After an initiation period, steady turnover of CO (ca. 0.01 mmoles/mmol Co/hr) was observed for many cycles without loss of catalytic activity. Moreover, when completely decarbonylated resin (vide supra) was employed, activity increased strongly (0.13 mmole CO/mmol Co/hr). Exposure to air eliminated catalytic activity. Under the same conditions, resin **18** was not active.

The products (CH_4 and higher hydrocarbons) were identified by gas chromatography and g.c. -mass spectroscopy. In addition, methane was ascertained by its infrared absorptions. The major oxygen-containing product was water, although mass spectral evidence pointed to the presence of small amounts of CO_2 . Deuterium gas led to CD_4 and deuterated hydrocarbons (g.c. and g.c. mass spectroscopy), in addition to D_2O . A small amount of CD_3H (10% in CD_4 after ca.10 turnovers) and the appearance of a weak C-D infrared stretch in the resin (2168 cm^{-1}) indicated some H-D exchange with the polymer backbone.

The following additional control experiments were run. (1) The resin (without bound cyclopentadiene) was subjected to the synthesis sequence



(P) = 1% divinylbenzene-crosslinked microporous polystyrene; 0.35 - 0.50 mmol Co/g; orange

(P) = 3% divinylbenzene-crosslinked macroporous polystyrene; 0.8 - 1.0 mmol Co/g; tan.

and then exposed to Fischer-Tropsch conditions: no activity was found. (2) The suspended resin in the presence of dissolved $\text{Co}_2(\text{CO})_8$ or $\text{CpCo}(\text{CO})_2$ showed no activity [but formation of a cobalt mirror with $\text{Co}_2(\text{CO})_8$]. (3) Soluble $\text{CpCo}(\text{CO})_2$ in *n*-octane gave on hydrogenation (75 psi, 190°C, 64h) cyclopentane and cyclopentene, CO, a cobalt mirror, and methane, but no Fischer-Tropsch products. (4) After completion of a catalytic run, the resin was filtered off, resuspended in fresh *n*-octane and exposed to CO/H₂: the catalysis resumed at an unchanged rate. Loss of cobalt from the resin was not evident (elemental analysis). The original octane solution was inactive. (5) On pressurization with CO the completely decarbonylated catalytically active resin quantitatively regenerated the starting catalyst 19.

The data indicate that methanation and Fischer-Tropsch activity of 19 is dependent on a defined and regenerable "homogeneous" cobalt species on the resin. The reproducibility of the results, product distribution, and regenerability of catalyst strongly argue against cobalt crystallites or heterogeneous clusters being responsible for catalytic action. This conclusion is reinforced by the lack of activity of the $\text{CpCo}(\text{CO})_2$ -resin and $\text{Co}_2(\text{CO})_8$ -resin mixtures, the latter generating cobalt metal on the resin and the walls of the vessel. Moreover, the deuterium labeling experiment and the matching mass balance between consumed CO and produced hydrocarbon rule out solvent or polystyrene as the sources of product.

The recent renaissance in research aimed at the conversion of CO to hydrocarbons has uncovered only a few homogeneous systems: some cluster based catalysts as well as a stoichiometric mononuclear system. Fischer-Tropsch activity of polymer supported catalysts in solvent suspension has never been demonstrated and could prove technologically useful in attempts to cope with the problem of heat transfer in this appreciably exothermic process. The discovery of a polymer activated, novel hydrogenation system should point the way to physical experiments aimed at further structural clarification and the construction of soluble models mimicking the unique structural environment around the metal.

* * *

†Brief version of LBL-8727.

RESEARCH PLANS FOR CALENDAR YEAR 1980

Iron carbides and nitrides will be tested for their activity and selectivity in Fischer-Tropsch synthesis.

The effects of alkali promoters on the Fischer-Tropsch activity and selectivity of iron catalysts will be examined using both polycrystalline foils and alumina-supported catalysts. Studies of hydrocarbon synthesis will be investigated over single crystal surfaces of ruthenium.

The influence of support composition and metal particle size will be investigated on the selectivity

of methanol versus methane synthesis over supported palladium catalysts.

The detection of Fischer-Tropsch intermediates by reactive scavenging with olefins will be utilized to explore the mechanism of Fischer-Tropsch synthesis over ruthenium and iron catalysts.

Biscarbyne clusters will be tested for Fischer-Tropsch and related activity. Super clusters will be constructed to determine the potential of ligand mobility.

Homogeneous models for the reported polymer supported Fischer-Tropsch catalysts are being designed and synthesized.

The activation of liganded benzene will be attempted to effect specific bond breaking processes.

A novel approach to coal liquefaction will utilize the concept of oxidative alkylation.

Catalytic and stoichiometric reactions will be sought, aimed at removing sulfur from coal and coal derived liquids and from model compounds.

1979 PUBLICATIONS AND REPORTS

Refereed Journals

1. I. Toyoshima and G. A. Somorjai, "Heats of Chemisorption of O₂, H₂, CO, CO₂ and N₂ on Polycrystalline and Single Crystal Transition Metal Surfaces," *Catal. Rev. Sci. Eng.* **19**, 150-159 (1979).
2. D. Dwyer and G. A. Somorjai, "The Role of Readsorption in Determining the Product Distribution During CO Hydrogenation Over Fe Single Crystals," *J. Catal.* **56**, 249 (1979).
3. G. A. Somorjai, "Catalysis on the Atomic Scale" (Emmett Lecture, 1977) *Catal. Rev.* **18**, 173 (1978).
4. D. J. Dwyer, K. Yoshida, and G. A. Somorjai, "Hydrogenation of CO and CO₂ on Clean Rhodium and Iron Foils. Correlations of Reactivities and Surface Composition," in *Adv. in Chemistry* No. 178, eds. E. Kulger and F. Steffgen, American Chemical Society, Washington, D.C. (1979).
5. J. G. Ekerdt and A. T. Bell, "Synthesis of Hydrocarbons from CO and H₂ Over Silica-Supported Ru: Reaction Rate Measurements and Infrared Spectra of Adsorbed Species," *J. Catal.* **58**, 170 (1979).
6. D. P. Mobley and A. T. Bell, "Effects of Zinc Chloride on the Cleavage of Ether Structures Present in Coal," *Fuel* **58**, 661 (1979).
7. J. R. Fritch and K. P. C. Vollhardt, "Cyclobutadiene Metal Complexes as Potential Intermediates in Alkyne Metathesis: Flash Pyrolysis of Substituted *n*⁴-Cyclobutadiene-*n*⁵-cyclopentadienyl Cobalt Complexes," *Angew. Chem.* **91**, 439 (1979); *Angew. Chem. Internat. Edn.* **18**, 409 (1979).

- [†]8. R. L. Funk and K. P. C. Vollhardt, "The Cobalt Way to dl-Estrone, A Highly Regiospecific Functionalization of 2,3-Bis(trimethylsilyl)-estratriene-17-one," *J. Am. Chem. Soc.* 101, 215 (1979).
- [†]9. R. I. Duclos, K. P. C. Vollhardt, and L. S. Yee, " η^4 -Benzocyclobutadiene- η^5 -cyclopentadienyl-cobalt, A New Aromatic Sandwich Complex," *J. Organometal. Chem.* 174, 109 (1979).^{††}
- [†]10. J. R. Fritch, K. P. C. Vollhardt, M. R. Thompson, and V. W. Day, "Apparent Concurrent Acetylene-Vinylidene Carbene Rearrangements, Silylacetylide Metathesis, and Alkyne Cleavage in the Interaction of Bis(trimethylsilyl)acetylene with Cobalt. The X-ray Structural Identification of a Biscarbene Complex: μ_3 -MeSiC- η^1 - μ_3 -Me₃SiC₃-Cp₃Co₃," *J. Am. Chem. Soc.* 101, 2768 (1979).[†]
- [†]11. C. Müller, A. Schweig, W. Grahn, K. P. C. Vollhardt, and R. G. Bergman, "The Photoelectron Spectra of 2,5-Dehydrotropylidene, 3,6-Dehydrooxepin, and Fulvenallene," *J. Am. Chem. Soc.* 101, 5579 (1979).[†]
- [†]12. W. G. L. Aalbersberg and K. P. C. Vollhardt, "Intramolecular Cycloadditions of Bis-*o*-Xylylenes. An Extremely Short Route to [2.2.2]Cyclophanes," *Tetrahedron Lett.* 1939 (1979).[†]
- [†]13. K. N. Houk, R. W. Strozier, C. Santiago, R. W. Gandour, and K. P. C. Vollhardt, "The Electronic Structure and Photoelectron Spectrum of 1,5,9-Cyclododecatriyne," *J. Am. Chem. Soc.* 101, 5183 (1979).[†]
- [†]14. A. Naiman and K. P. C. Vollhardt, "1,2:4,5-Tetrahydrodicyclobuta-[b,e]pyridine," *Angew. Chem.* 91, 440 (1979); *Angew. Chem., Internat. Edn.* 18, 411 (1979).[†]
15. P. Perkins and K. P. C. Vollhardt, "Polymer Supported η^5 -Cyclopentadienyl Cobalt: An Immobilized Homogeneous Fischer-Tropsch Catalyst," *J. Am. Chem. Soc.* 101, 3985 (1979).

Other Publications

1. A. T. Bell, "Research Profile," *MMRD-Newsletter* 3(5), 1 (1979).
2. K. P. C. Vollhardt, "The Place of Transition Metals in Organic Synthesis," *Synth. React. Inorg. Met.-Org. Chem.* 8, 505 (1978) (Book Review).
3. K. P. C. Vollhardt, "Transition Metal Mediated Transformations in the Synthesis of Complex Molecules," *MMRD Newsletter*, 3(1), 1 (1979).
4. K. P. C. Vollhardt, "The Cobalt Way to Estrone," Lecture published in the Proceedings of the 26th National Organic Symposium, Tucson, Arizona, 105 (1979).

LBL Reports

1. L. H. Dubois and G. A. Somorjai, "The Dissociative Chemisorption of CO₂ on Rhodium Surfaces," LBL-8976.

2. D. G. Castner, R. L. Blackadar, and G. A. Somorjai, "CO Hydrogenation Over Clean and Oxidized Rhodium Foil and Single Crystal Catalysts. Correlations of Catalyst Activity, Selectivity and Surface Composition," LBL-10018.
3. J. G. Ekerdt and A. T. Bell, "Evidence for Alkylidene Intermediates in Fischer-Tropsch Synthesis Over Ru," LBL-8716.
4. N. D. Taylor and A. T. Bell, "The Effects of Lewis Acid Catalysts on the Cleavage of Aliphatic and Aryl-Aryl Linkages in Coal-Related Structures," LBL-8880.
5. D. P. Mobley and A. T. Bell, "The Effects of Zinc Chloride on Sulfur Removal from Coal-Related Structures," LBL-9023.
6. J. G. Ekerdt, "Fischer-Tropsch Synthesis Over a Ruthenium Catalyst: Infrared and Kinetic Studies," (Ph.D. thesis) LBL-9108.
7. D. P. Mobley and A. T. Bell, "Hydrogenolysis of Dibenzyl Ether Using Zinc-Chloride Co-catalyst Systems," LBL-9477.
- [†]8. V. L. Kuznetsov, A. T. Bell, and Yu. I. Ermakov, "An Infrared Study of Alumina and Silica Supported Ruthenium Carbonyl Clusters," LBL-9669.

Invited Talks

1. G. A. Somorjai, "Active Sites for Hydrocarbon Catalysis on Metal Surfaces," Union Carbide, Tarrytown, New York, December 1978.
2. G. A. Somorjai, "Hydrogenation of CO Over Transition Metal Surfaces: Present Understanding of the Mechanism on the Atomic Scale," California Institute of Technology, Pasadena, CA, March 1979.
3. G. A. Somorjai, "The Molecular and Dissociative Chemisorption of CO and CO₂ on the Rh (111) Single Crystal Surface," California Catalysis Society Meeting, Stanford, California, March 1979.
4. G. A. Somorjai, "The Influence of Surface Composition on the Rate and Product Distribution of Rh and Fe Catalyzed Hydrogenation of CO," University of Pennsylvania, Chemistry Department, March 1979.
5. G. A. Somorjai, "The Hydrogenation of CO Over Fe and Rh Surfaces, Shell Laboratory," Amsterdam, March 1979.
6. G. A. Somorjai, "Catalysis and Surface Science," Mobil Research, Paulsboro, New Jersey, June 1979.
7. G. A. Somorjai, "The Application of High Resolution Electron Energy Loss Spectroscopy to the Characterization of Adsorbed Molecules on Rh Single Crystal Surfaces," ACS Fall Meeting, Washington, D.C., September 1979.

8. A. T. Bell, "Studies of the Kinetics and Mechanism of Fischer-Tropsch Synthesis Over Ruthenium Catalysts," Mobil Research & Development Corp., Central Res. Div., Princeton, New Jersey, February 1979.
9. A. T. Bell, "Studies of the Kinetics and Mechanism of Fischer-Tropsch Synthesis Over Ruthenium Catalysts," Department of Chemical Engineering, Princeton University, Princeton, New Jersey, February 1979.
10. A. T. Bell, "Chemical Changes Produced in Coal Through the Action of Lewis Acid Catalysts," Exxon Research & Engineering Co., Linden, New Jersey, February 1979.
11. A. T. Bell, "Studies of the Kinetics and Mechanism of Fischer-Tropsch Synthesis Over Ruthenium Catalysts," Dept. of Chemical Engineering, University of Florida, Gainesville, Florida, February 1979.
12. A. T. Bell, "Examples of Catalysis Over Ru: Fischer-Tropsch Synthesis and NO Reduction," Conference on Heterogeneous and Homogeneous Catalysis: Kinetic and Mechanistic Considerations, California Institute of Technology, Pasadena, California, March 1979.
13. A. T. Bell, "Studies of CO Desorption and Reaction with H₂ on Alumina-Supported Ru," Sixth North American Meeting of the Catalysis Society, Chicago, IL, March 1979.
14. A. T. Bell, "Hydrogenation and Cracking of Coal-Related Fused Ring Structures Catalyzed by Zinc Chloride," California Catalysis Society Meeting, Stanford University, Stanford, CA, March 1979.
15. A. T. Bell, "Reaction Intermediates in Fischer-Tropsch Synthesis Over Supported Ruthenium Catalysts," 177th National ACS Meeting, Honolulu, Hawaii, April 1979.
16. A. T. Bell, "A Step Toward Fuels from Carbon Monoxide and Hydrogen: Fischer-Tropsch Synthesis Over Ruthenium," Dept. Chemical Engineering, Stanford University, Stanford, CA, April 1979.
17. A. T. Bell, "Physical and Catalytic Behavior of Supported Ruthenium Clusters," Sixth US/USSR Symposium on Chemical Catalysis, Cherry Hill, New Jersey, June 1979.
18. A. T. Bell, "Fischer-Tropsch Synthesis Over Ruthenium Catalysts," Gordon Research Conference on Catalysis, Colby-Sawyer College, New London, New Hampshire, June 1979.
19. A. T. Bell, "Studies of Coal Liquefaction Using Lewis Acid Catalysts," Koninklijke/Shell Laboratorium, Amsterdam, The Netherlands, September 1979.
20. A. T. Bell, "The Mechanism and Kinetics of Fischer-Tropsch Synthesis Over Supported Ruthenium Catalysts," Department of Technology, Eindhoven, The Netherlands, September 1979.
21. A. T. Bell, "Applications of Fourier Transform Spectroscopy to the Study of Adsorbed Species," 178 National ACS Meeting, Washington, D.C., September 1979.
22. A. T. Bell, "Effects of Particle Size and Metal-Support Interactions on Fischer-Tropsch Synthesis Over Ru Catalysts," AIChE Meeting, San Francisco, CA, November 1979.
23. K. P. C. Vollhardt, "Grenzen der fassbaren Existenz elektronisch-und spannungsaktivierter Kohlenwasserstoffe," University of Zürich, Switzerland, January 1979.
24. K. P. C. Vollhardt, "Applications of Transition Metal Catalysts to Organic Synthesis," Stanford University, Stanford, California, January 1978.
25. K. P. C. Vollhardt, "Transition Metal Catalyzed Alkyne Cooligomerizations," The University of Akron, Akron, Ohio, February 1979.
26. K. P. C. Vollhardt, "The Cobalt Way to Estrone," Schering Corporation, East Orange, New Jersey, February 1979.
27. K. P. C. Vollhardt, "The Fascinating Chemistry of Extremely Strained Hydrocarbons," Florida State University, Tallahassee, Florida, February 1979.
28. K. P. C. Vollhardt, "Bizarre and Sometimes Useful Transformations in the Coordination Sphere of Cobalt," Florida State University, Mallinckrodt Lectureship, Tallahassee, Florida, February 1979.
29. K. P. C. Vollhardt, "Bizarre and Sometimes Useful Transformations in the Coordination Sphere of Cobalt," SUNY Stony Brook, New York, February 1979.
30. K. P. C. Vollhardt, "Bizarre Reactions in the Coordination Sphere of Cobalt," Cornell University, Ithaca, New York, February 1979.
31. K. P. C. Vollhardt, "The Cobalt Way to Estrone," Hoffmann-La Roche Inc., Nutley, New Jersey, February 1979.
32. K. P. C. Vollhardt, "The Cobalt Way to Estrone," Rohm and Haas Company, Philadelphia, Pennsylvania, February 1979.
33. K. P. C. Vollhardt, "The Cobalt Way to Estrone," University of Pennsylvania, Philadelphia, Pennsylvania, February 1979.
34. K. P. C. Vollhardt, "Excessively Unhappy Hydrocarbons," Philadelphia Organic Chemists' Club, Philadelphia, Pennsylvania, February 1979.
35. K. P. C. Vollhardt, "The Cobalt Way to Estrone," Smith, Kline, & French Laboratories, Philadelphia, Pennsylvania, February 1979.
36. K. P. C. Vollhardt, "Bizarre and Sometimes Useful Organic Transformations in the Coordination Sphere of Cobalt," University of Pittsburgh, Pittsburgh, Pennsylvania, March 1979.

37. K. P. C. Vollhardt, "The Cobalt Way to Estrone," Plenary Lecture, New York Academy of Sciences, Symposium on Transition Metal Mediated Organic Synthesis, New York, March 1979.
38. K. P. C. Vollhardt, "Bemerkenswerte Organische Reaktionen in der Koordinations-sphäre des Cobalts," Max Planck Institute for Coal Research, Mülheim, West Germany, May 1979.
39. K. P. C. Vollhardt, "Remarkable Alkyne Rearrangements, Rotation, and Ring-closures in the Pyrolysis of Diethynylcyclobutadiene Cobalt Complexes," Plenary Lecture, ACS-CSJ, Congress, Symposium on Synthesis and Chemistry of Acetylenic Compounds, Honolulu, Hawaii, April 1979.
40. K. P. C. Vollhardt, "The Cobalt Way to Estrone," Plenary Lecture, ACS-CSJ Congress, Symposium on Organic Synthesis Using Organometallic Compounds, Honolulu, Hawaii, April 1979.
41. K. P. C. Vollhardt, "Excessively Unhappy Hydrocarbons," Plenary Lecture, Conference on Physical Organic Chemistry, Holderness Academy, New Hampshire, June 1979.
42. K. P. C. Vollhardt, "The Cobalt Way to Estrone," Plenary Lecture, 26th National Organic Chemistry Symposium, Tucson, Arizona, June 1979.
43. K. P. C. Vollhardt, "Physical, Chemical, and Some Biological Properties of Strained Ring Activated Hydrocarbons," Plenary Lecture, International Symposium on Aromaticity, Dubrovnik, Yugoslavia, September 1979.
44. K. P. C. Vollhardt, "The Cobalt Way to Estrone," University of Paris at Orsay, France, September 1979.
45. K. P. C. Vollhardt, "Excessively Unhappy Hydrocarbons," CNRS Thiais, Paris, France, September 1979.
46. K. P. C. Vollhardt, "Cobalt-mediated Carbon-Carbon Bond Forming and Bond Breaking Reactions," École Normale Supérieure, Paris, France, September 1979.
47. K. P. C. Vollhardt, "Remarkable Organic Transformations in the Coordination Sphere of Cobalt," Washington University, St. Louis, Missouri, September 1979.
48. K. P. C. Vollhardt, "Cobalt Mediated Carbon-Carbon Bond Formation," Monsanto Corporation, St. Louis, Missouri, September 1979.

* * *

[†]Supported in part by NSF.

[‡]Supported in part by NIH.

c. Synthetic and Physical Chemistry*

William L. Jolly, Investigator

1. A STUDY OF THE BONDING IN TRANSITION METAL CARBONYL HYDRIDES**

H. W. Chen, W. L. Jolly, J. Kopf, and T. H. Lee

It has been well established that chemical shifts in core electron binding energies are related to changes in atomic charges. In general, an increase in core binding energy corresponds to an increase in the positive charge of the atom. However, it is recognized that changes in binding energy are not always entirely due to changes in atomic charge; sometimes they are at least partly caused by changes in the electronic relaxation energy associated with core ionization. Fortunately, this relaxation energy is essentially the same in compounds which have similar molecular structures in the vicinity of the core-ionizing atom. Hence core binding energies for a series of carefully chosen molecules with similar structures and similar electronic properties can be reliably interpreted in terms of atomic charges. In this study we have measured the gas-phase core electron binding energies of some first-row transition-metal carbonyls and carbonyl hydrides. The main object of this research was to determine the polarity of the metal-hydrogen bond in transition metal carbonyl hydrides.

The core binding energies determined in this study are listed in Table 1. On going from $\text{Co}_2(\text{CO})_8$ to $\text{HCo}(\text{CO})_4$ the cobalt $2p_{3/2}$ binding energy increases by 0.52 eV, corresponding to a significant increase in the positive charge on the cobalt atom. We may look upon $\text{Co}_2(\text{CO})_8$ as a dimer of an electroneutral $\text{Co}(\text{CO})_4$ group. Because the positive charge on the remaining cobalt atom increases when one of the $\text{Co}(\text{CO})_4$ groups is replaced by a hydrogen atom, we conclude that the hydrogen atom withdraws electron density from the $\text{Co}(\text{CO})_4$

Table 1. Core binding energies (in eV).

| Compound | Oxygen 1s | Carbon 1s | Metal $2p_{3/2}$ |
|------------------------------------|-----------|-----------|------------------|
| $\text{Co}_2(\text{CO})_8$ | 539.78 | 293.40 | 786.34 |
| $\text{HCo}(\text{CO})_4$ | 540.06 | 293.94 | 786.86 |
| $\text{Fe}(\text{CO})_5$ | 539.96 | 293.71 | 715.79 |
| $\text{H}_2\text{Fe}(\text{CO})_4$ | 540.17 | 294.15 | 715.97 |
| $\text{Mn}_2(\text{CO})_{10}$ | 539.57 | 293.28 | 647.01 |
| $\text{HMn}(\text{CO})_5$ | 539.95 | 293.80 | 647.46 |

* This work was supported by the Division of Chemical Sciences, Office of Basic Energy Sciences, U. S. Department of Energy.

group and hence is negatively charged. It should be noted that the carbon 1s and oxygen 1s binding energies of $\text{HCo}(\text{CO})_4$ are also higher than those of $\text{Co}_2(\text{CO})_8$, corresponding to more positively charged (less negatively charged) carbon and oxygen atoms in the hydride molecule. This change probably represents a reduction in the metal→CO back-bonding caused by the reduced electron density on the cobalt atom.

The increases in the manganese $2p_{3/2}$, carbon 1s, and oxygen 1s binding energies on going from $\text{Mn}_2(\text{CO})_{10}$ to $\text{HMn}(\text{CO})_5$ can be explained exactly as in the case of the cobalt compounds. In the case of $\text{H}_2\text{Fe}(\text{CO})_4$ we can make a comparison with $\text{Fe}(\text{CO})_5$. The replacement of one of the CO groups of $\text{Fe}(\text{CO})_5$ by two hydrogen atoms causes all the core binding energies to increase. If we accept the reasonable proposition that the iron atom in $\text{Fe}(\text{CO})_5$ is positively charged,¹ then these changes in binding energy indicate that the hydrogen atoms in $\text{H}_2\text{Fe}(\text{CO})_4$ are negatively charged.

The binding energy data may be used in conjunction with the potential model for binding energy shifts to calculate the actual atomic charges in the molecules under study. The change in binding energy of an iron, carbon, or oxygen atom on going from $\text{Fe}(\text{CO})_5$ to $\text{H}_2\text{Fe}(\text{CO})_4$ can be represented by an expression of the type

$$\Delta E_B = k(Q_2 - Q_1) + \Delta V$$

where k is a constant which is essentially the average r^{-1} value for the valence electrons of the atom, Q_1 and Q_2 are the atomic charges in $\text{Fe}(\text{CO})_5$ and $\text{H}_2\text{Fe}(\text{CO})_4$, respectively, and ΔV is the change in the potential energy at the atom due to the electrostatic charges of the other atoms in the molecules (essentially a linear combination of Q_i/r_i values). Thus we can write three such equations: one for iron, one for carbon, and one for oxygen. We can also write two more equations which are essentially statements of electroneutrality for the two molecules. To make it possible to solve for all seven charges, we add two more equations, $Q_1^{\text{Fe}} = 1.039$ and $Q_2^{\text{C}} = 0.174$, which simply specify that the atomic charges in $\text{Fe}(\text{CO})_5$ are those calculated in an ab initio study of Baerends and Ros.¹ In the cases of $\text{Mn}_2(\text{CO})_{10}$ and $\text{HMn}(\text{CO})_5$ and of $\text{Co}_2(\text{CO})_8$ and $\text{HCo}(\text{CO})_4$, our method of calculation was similar to that used for $\text{Fe}(\text{CO})_5$.

The results of the calculations are that hydrogen atom charges are -0.3, -0.8, and -0.75 for $\text{H}_2\text{Fe}(\text{CO})_4$, $\text{HMn}(\text{CO})_5$, and $\text{HCo}(\text{CO})_4$, respectively, with overall uncertainties of 30%. Hence the quantitative interpretation of the data confirms our qualitative conclusion that the hydrogen atoms in these compounds are negatively charged. The much smaller negative charge for the hydrogen atom in $\text{H}_2\text{Fe}(\text{CO})_4$ is probably significant. The smaller value may be due to the presence of two hydrogen atoms in the molecule as opposed to one; two

hydrogen atoms would not be expected to be able to withdraw twice as much electron density from a metal carbonyl group as one hydrogen atom.

* * *

[†]Brief version of J. Am. Chem. Soc. 101, 2607 (1979).
I. E. J. Baerends and P. Ros, J. Electron Spectrosc. Relat. Phenom. 7, 69 (1979).

2. AN XPS STUDY OF THE RELATIVE π -ACCEPTOR ABILITIES OF THE NITROSYL AND CARBONYL LIGANDS[†]

H. W. Chen and W. L. Jolly

Because of current interest in catalytic systems involving both NO and CO, the nature of the interaction of these ligands with transition metals is a subject of importance. In order to study the relative abilities of these ligands to withdraw electron density from transition-metal atoms, we have carried out an X-ray photoelectron spectroscopic (XPS) study of two sets of molecules: Ni(CO)₄, Co(CO)₃NO, Fe(CO)₂(NO)₂, Mn(NO)₃CO, and Cr(NO)₄, Fe(CO)₅ and Mn(CO)₄NO.

It has been shown that, for a wide variety of transition-metal carbonyls, both the carbon 1s and oxygen 1s binding energies are well correlated with the C-O stretching force constants: higher binding energies correspond to higher force constants. The binding energies essentially measure atomic charges; the force constants measure bond strengths. The fact that these entirely different quantities are correlated consistent with the concept of back-bonding (the more back-bonding, the more negative the CO group and the weaker the C-O bond) is strong evidence that both quantities are good measures of back-bonding. It seems reasonable to suppose that nitrogen 1s and oxygen 1s binding energies and N-O force constants can equally well be used to measure back-bonding in the isoelectronic NO⁺ ligand. Therefore we shall interpret increases in ligand atom binding energy

as evidence for decreased back-bonding and decreases in ligand atom binding energy as evidence for increased back-bonding. The core binding energies of the compounds we studied are listed in Table 1. In order to permit comparison with the binding energies, we have included the C-O and N-O force constants in Table 1.

The carbon 1s binding energies of Ni(CO)₄, Co(CO)₃NO, and Fe(CO)₂(NO)₂ are essentially identical, but that of Mn(NO)₃CO is significantly higher. The trend in these data is somewhat similar to the trend in the C-O force constant data. The nitrogen 1s binding energy decreases gradually on going from Co(CO)₃NO to Cr(NO)₄, paralleling the corresponding steady decrease in the N-O force constant.

We hoped to measure changes in the oxygen 1s binding energies of the CO and NO groups separately. Unfortunately we were unable to resolve the oxygen 1s spectra of Co(CO)₃NO and Fe(CO)₂(NO)₂ into two peaks. The O 1s spectrum of Co(CO)₃NO consists of a single, highly symmetric peak. Similarly, the spectrum of Fe(CO)₂(NO)₂ consists of a single, slightly broadened peak. Thus in these cases our measured O 1s binding energies are weighted averages of the binding energies of the CO and NO groups. These weighted averages can differ from the individual values for the CO and NO groups by as much as 0.25 eV. In the case of Mn(NO)₃CO, the O 1s spectrum is asymmetric and can be deconvoluted into two peaks with an intensity ratio of 1:3, as shown in Fig. 1. The deconvoluted peak binding energies are given in Table 1. It is clear that the oxygen 1s binding energy of the CO groups remains about constant (or decreases slightly) on going from Ni(CO)₄ to Fe(CO)₂(NO)₂ and then rises markedly at Mn(NO)₃CO, as in the case of the carbon 1s binding energy. The oxygen 1s binding energy of the NO groups decreases on going from Co(CO)₃NO to Mn(NO)₃CO and then rises at Cr(NO)₄.

On going from Fe(CO)₅ to Mn(CO)₄NO, both the average carbon 1s binding energy and the average oxygen 1s binding energy decrease, just as one

Table 1. Core binding energies (in eV) and force constants (mdyne/Å).

| Compound | Carbon 1s E _B | C-O Force Constants | Nitrogen 1s E _B | N-O Force Constants | Oxygen 1s E _B | Metal 2p _{3/2} |
|---------------------------------------|--------------------------|---------------------|----------------------------|---------------------|--------------------------|-------------------------|
| Ni(CO) ₄ | 293.78 | 17.23 | 407.83 | 14.44 | 540.11 | 861.15 |
| Co(CO) ₃ NO | 293.81 | 17.04 | 407.83 | 14.44 | 539.99 | 786.85 |
| Fe(CO) ₂ (NO) ₂ | 293.79 | 17.06 | 407.76 | 14.12 | 539.91 | 715.58 |
| Mn(NO) ₃ CO | 293.98 | 17.43 | 407.65 | 13.75 | 540.47 539.28 | 647.30 |
| Cr(NO) ₄ | | | 407.56 | 13.33 | 539.46 | 582.27 |
| Fe(CO) ₅ | 293.71 | 16.75 | | | 539.96 | 715.79 |
| Mn(CO) ₄ NO | 293.49 | 16.65 | 407.77 | 13.69 | 539.77 | 647.37 |

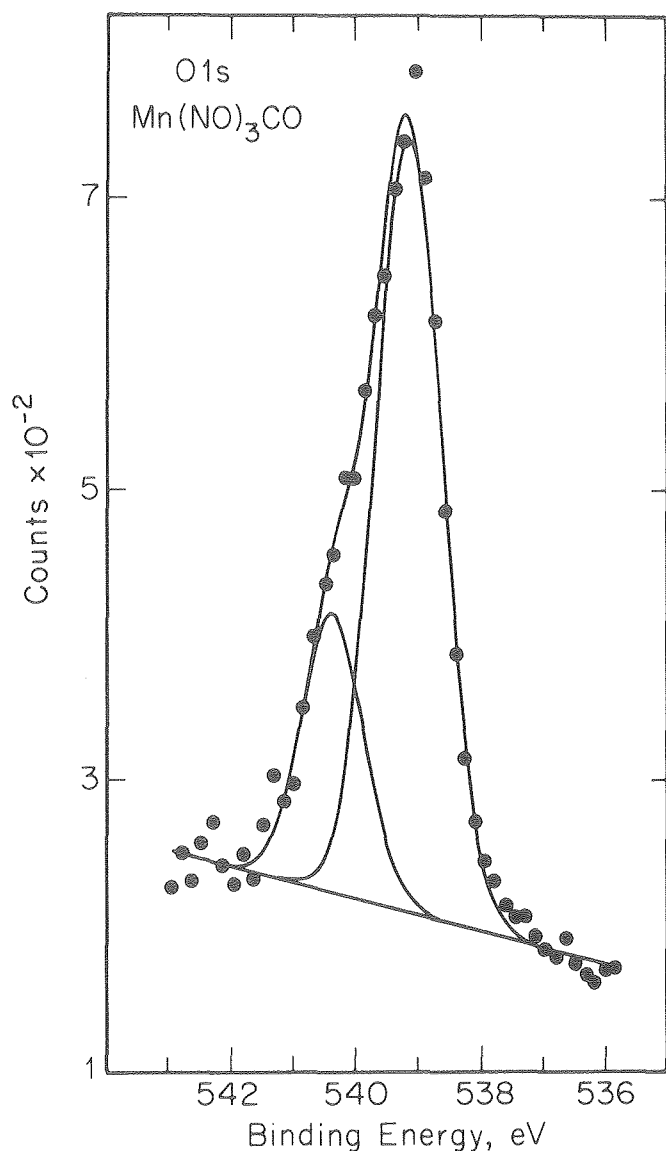


Fig. 1. Oxygen 1s spectrum of $\text{Mn}(\text{NO})_3\text{CO}$ vapor. The points have been fit to two Gaussian curves with intensity ratios of 1:3, corresponding to the CO and NO oxygen atoms, respectively.
(XBL 801-7816)

might expect from the decrease in the average C-O force constant.

The binding-energy shifts are, within experimental error, in the same directions as the corresponding shifts in the C-O or N-O force constant.

The total amount of negative charge transferred from the metal to the four ligands undoubtedly increases on going from $\text{Ni}(\text{CO})_4$ to $\text{Cr}(\text{NO})_4$ or from $\text{Fe}(\text{CO})_5$ to $\text{Mn}(\text{CO})_4\text{NO}$. The question is: does this shift of electron density occur principally by polarization of the metal-ligand σ bonds or by polarization of the metal-ligand $d\pi-\pi^*$ bonds? On going through the series from $\text{Ni}(\text{CO})_4$ to $\text{Cr}(\text{NO})_4$ or from $\text{Fe}(\text{CO})_5$ to $\text{Mn}(\text{CO})_4\text{NO}$, the changes in the oxygen 1s binding energy are at least of the same

approximate magnitude as the corresponding changes in either the carbon 1s or nitrogen 1s binding energies. This result is inconsistent with the expected attenuation by the inductive effort of σ -bond polarizations. The oxygen 1s binding energy of the NO ligand is considerably less than that of the CO ligand even when the ligands are attached to the same metal atom (in $\text{Mn}(\text{NO})_3\text{CO}$). This result is indicative of increased back-bonding to the NO ligand.

The data for $\text{Fe}(\text{CO})_5$ and $\text{Mn}(\text{CO})_4\text{NO}$ are clearly consistent with our general expectation regarding back-bonding; the carbon 1s and oxygen 1s binding energies and the C-O force constants indicate an increase in back-bonding on going from $\text{Fe}(\text{CO})_5$ to $\text{Mn}(\text{CO})_4\text{NO}$. The increase in back-bonding to the CO groups shows that these ligands are strongly affected by the decrease in the metal-atom nuclear charge but are not obviously affected by the competitive back-bonding to the NO group. However, the data for the $\text{Ni}(\text{CO})_4 \rightarrow \text{Cr}(\text{NO})_4$ series do show some effects of competition between the NO and CO groups. To rationalize the data, we must assume that the NO groups are much stronger π acceptors than the CO groups. Thus, on going from $\text{Ni}(\text{CO})_4$ to $\text{Fe}(\text{CO})_2(\text{NO})_2$, the back-bonding to the CO groups changes only slightly, because of the strong π -electron withdrawal by the NO groups. In the case of $\text{Fe}(\text{CO})_2(\text{NO})_2$, the metal π -electron density has been depleted so much that, on going another step to $\text{Mn}(\text{NO})_3\text{CO}$, the NO groups steal π -electron density from the single remaining CO group, and the back-bonding to CO actually decreases. The data are consistent with a steady increase in back-bonding to the NO groups on going from $\text{Co}(\text{CO})_3\text{NO}$ to $\text{Cr}(\text{NO})_4$. The back-bonding to the NO groups appears to be determined only by the nuclear charge on the metal atom and to be independent of the number of CO groups, which compete relatively weakly for π -electron density.

* * *

† Brief version of *Inorg. Chem.* **18**, 2548 (1979).

3. A STUDY OF CHARGE TRANSFER IN BACK-BONDING TO CARBONYL AND NITROSYL GROUPS†

S. C. Avanzino, A. A. Bakke, H. W. Chen, C. J. Donahue, W. L. Jolly, T. H. Lee, and A. J. Riccio

We have determined the carbon 1s and oxygen 1s binding energies for 55 metal carbonyl compounds in the gas phase. For those compounds for which the necessary vibrational spectroscopic data are available, we have calculated the degeneracy-weighted C-O stretching frequencies and the corresponding weighted C-O stretching force constants. In Fig. 1 the carbon 1s binding energies are plotted vs. the C-O force constants, and in Fig. 2 the oxygen 1s binding energies are plotted vs. the same force constants. The linear correlations shown by these plots confirm that transfer of electron density to the carbon and oxygen atoms of a CO group is accompanied by a weakening of the bond. The data strongly suggest that the carbon and oxygen core binding energies can be taken as measures of $d\pi \rightarrow \pi^*$ back-bonding in transition metal carbonyl compounds.

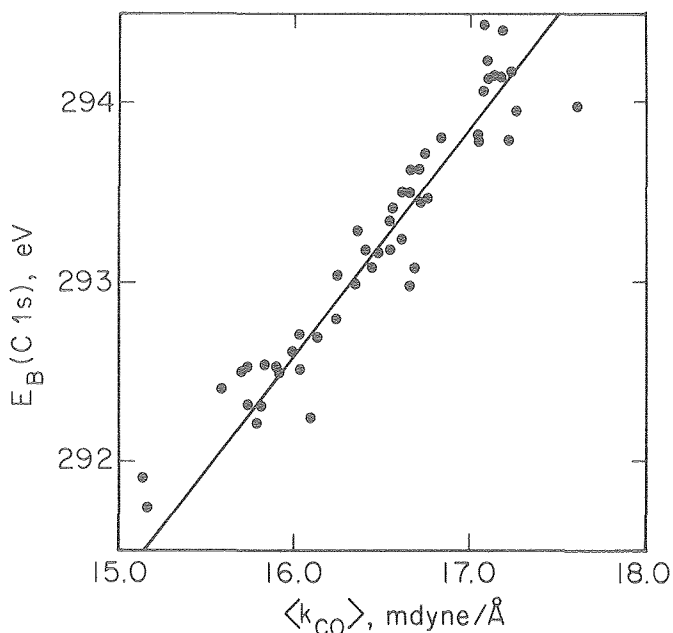


Fig. 1. Plot of carbon 1s binding energies for gas-phase metal carbonyl compounds vs. C-O stretching force constants. (XBL 801-7817)

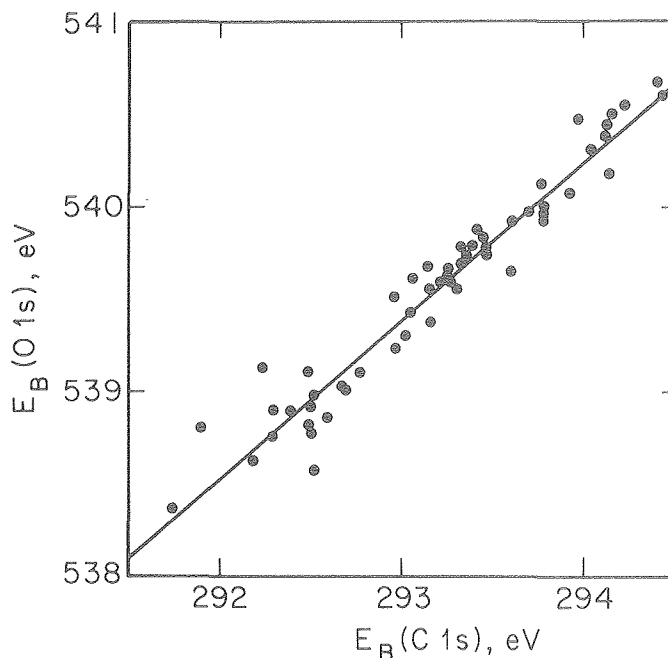


Fig. 3. Plot of oxygen 1s binding energies vs. carbon 1s binding energies for gas-phase metal carbonyl compounds. (XBL 801-7818)

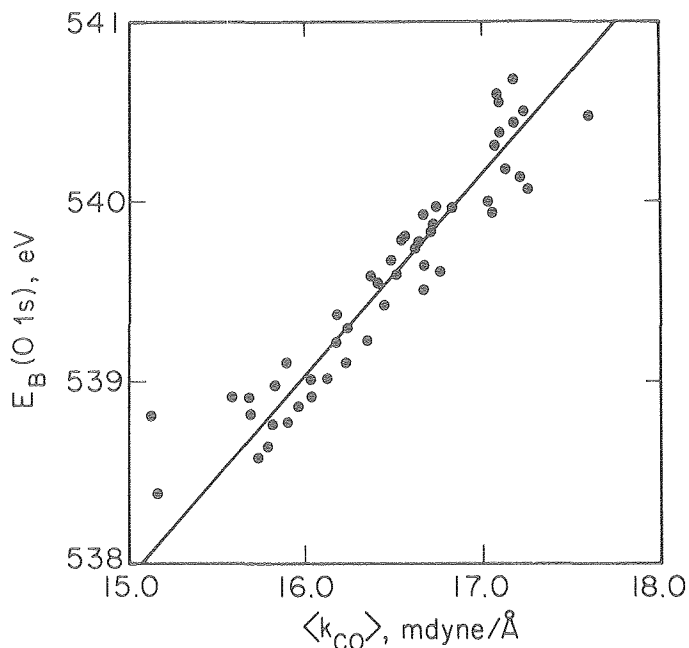


Fig. 2. Plot of oxygen 1s binding energies for gas-phase metal carbonyl compounds vs. C-O stretching force constants. (XBL 801-7814)

Figure 3 is a plot of the oxygen 1s binding energies vs the carbon 1s binding energies. The justifications for presenting this otherwise superfluous plot are that it includes points for five more compounds than are in Figs. 1 and 2 and

that it shows a significantly better linear correlation than shown in Figs. 1 and 2. From the slope of Fig. 3 we can calculate the average relative amounts of electronic charge transferred to or from the oxygen and carbon atoms of carbonyl groups on going from one carbonyl compound to another. If we ignore changes in relaxation energy and potential, we can write $\Delta Q = \Delta E/k$, where ΔQ and ΔE are the changes in atomic charge and core binding energy and k is a constant inversely proportional to the radial distance of the valence electrons. The ratio of the charge transferred to the oxygen and carbon atoms is calculated as follows.

$$\frac{\Delta Q_{\text{O}}}{\Delta Q_{\text{C}}} = \frac{\Delta E_{\text{B}}(\text{O } 1s)}{\Delta E_{\text{B}}(\text{C } 1s)} \cdot \frac{k_{\text{C}}}{k_{\text{O}}} = 0.849 \left(\frac{23.0}{32.5} \right) = 0.601$$

In other words, on going from one carbonyl compound to another, most of the change in charge of a CO group occurs at the carbon atom. There is little question that the π^* orbitals of a free CO molecule reside more on the carbon atom than on the oxygen atom. Our results indicate that the same is true for a coordinated CO: as the interaction of the metal $d\pi$ orbitals with the CO π^* orbitals increases, the shift of electron density to the carbon atoms is greater than that to the oxygen atoms.

We have also determined the nitrogen 1s and oxygen 1s binding energies for 15 metal nitrosyl compounds in the gas phase. Both the nitrogen 1s and oxygen 1s binding energies are linearly correlated with the N-O stretching force constants. As in the case of the carbonyl compounds, the plot of the binding energies against one another, shown in Fig. 4, also shows a linear correlation. From

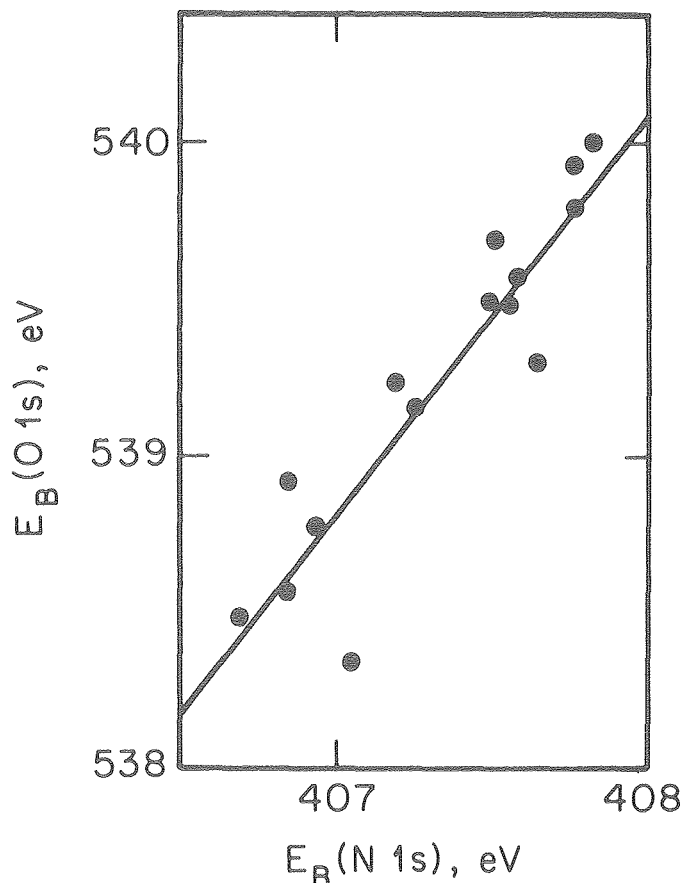


Fig. 4. Plot of oxygen 1s binding energies vs. nitrogen 1s binding energies for gas-phase metal nitrosyl compounds. (XBL 801-7815)

the slope of Fig. 4 we can calculate the average relative amounts of charge transferred to the oxygen and nitrogen atoms of nitrosyl groups on going from one nitrosyl compound to another:

$$\frac{\Delta Q_O}{\Delta Q_N} = \frac{\Delta E_B(O\ 1s)}{\Delta E_B(N\ 1s)} \cdot \frac{k_N}{k_O} = 1.257 \left(\frac{27.9}{32.5} \right) = 1.08$$

Apparently the oxygen and nitrogen atoms undergo comparable changes in charge, with perhaps slightly more change in charge occurring at the oxygen atom. To some extent this result is expected. An increase in the electronegativity of one atom in a diatomic molecule causes the contribution of that atom to the π^* MO to decrease. Thus, because nitrogen is more electronegative than carbon, one would expect that $d\pi \rightarrow \pi^*$ bonding would transfer relatively more charge to the oxygen atoms of NO groups than to the oxygen atoms of CO groups. Explanation for the fact that a greater (or at least comparable) amount of charge is transferred to the oxygen atom of a coordinated NO^+ group than to the nitrogen atom probably is to be found in the fact that the effective electronegativity of the nitrogen atom in a coordinated NO^+ group is much higher than it is in free NO^+ ; indeed it would not appear unreasonable if the nitrogen atom had

a greater electronegativity than that of the oxygen atom.

* * *

† Brief version of LBL-10121.

RESEARCH PLANS FOR CALENDAR YEAR 1980

We plan to study the bonding between various small organic molecules or molecular fragments (such as C, CH, CH_2 , CH_3 , C_2H_4 , C_3H_5 , etc.) and transition metals or transition metal clusters. This will be accomplished by XPS studies (at elevated temperatures, when necessary) on both mononuclear complexes, such as $\text{C}_3\text{H}_5\text{Mn}(\text{CO})_5$, and on polynuclear "clusters" such as $\text{Fe}_5(\text{CO})_{15}\text{C}$.

We shall continue our investigation of the relative π -acceptor and σ -donor abilities of various ligands L by studying the shifts in core binding energies in a series of molecules of the types $\text{LMn}(\text{CO})_5$ and $\text{LMo}(\text{CO})_5$.

We hope to study systematically the differences in bonding in terminal ligands and bridging ligands (i.e., ligands bound to one metal atom and ligands bound to more than one metal atom), for ligands such as CO and NO. We also plan to widen the scope of our work considerably, and will study ligands such as CS, NS, NH, NH_2 , etc.

1979 PUBLICATIONS AND REPORTS

Refereed Journals

1. H. W. Chen, W. L. Jolly, J. Kopf and T. H. Lee, "A Study of the Bonding in Transition Metal Carbonyl Hydrides," *J. Am. Chem. Soc.* **101**, 2607 (1979).
- †2. A. A. Bakke, W. L. Jolly, B. L. Pinsky and J. C. Smart, "Unusual Charge Distributions in Some Bis(fulvalene)dimetal Complexes as Revealed by X-ray Photoelectron Spectroscopy," *Inorg. Chem.* **18**, 1343 (1979).
3. A. Norman and W. L. Jolly, "Reaction of Silylphosphine with Ammonia," *Inorg. Chem.* **18**, 1594 (1979).
4. W. L. Jolly, Book Review: D. Nicholls, "Inorganic Chemistry in Liquid Ammonia," Elsevier, 1979, *J. Organomet. Chem.* **172**, C33 (1979).
5. H. W. Chen, W. L. Jolly, "An XPS Study of the Relative π -Acceptor Abilities of the Nitrosyl and Carbonyl Ligands," *Inorg. Chem.* **18**, 2548 (1979).

LBL Reports

- †1. T. H. Lee, W. L. Jolly, R. Weiss and J. G. Verkade, "On Correlating Phosphorus Core Binding Energies, Phosphorus Lone Pair Ionization Potentials, and Proton Affinities of Tervalent Phosphorus Compounds," LBL-9682.

2. S. C. Avanzino, A. A. Bakke, H. W. Chen, C. J. Donahue, W. L. Jolly, T. H. Lee and A. J. Ricco, "A Study of Charge Transfer in Back-Bonding to Carbonyl and Nitrosyl Groups," LBL-10121.

Symposium on Theoretical Chemistry, Southern University, New Orleans, La., Feb. 23, 1979.

2. W. L. Jolly, "Studies of Chemical Bonding by X-Ray Photoelectron Spectroscopy," University of California, Davis, Calif., May 22, 1979.

* * *

Invited Talks

1. W. L. Jolly, "Studies of Chemical Bonding by Gas-Phase X-Ray Photoelectron Spectroscopy,"

†Supported in part by the National Science Foundation.

d. Electrochemical Systems*

John Newman, Investigator

1. ANOMALOUS DIFFUSION COEFFICIENTS AND BIPOLAR ELECTRODES

Peter Pierini and John Newman

The ability of a highly polarized electrode to dominate a slightly polarized electrode, when the electrodes are near to each other, can be demonstrated with the rotating ring-disk electrode. Considering only mass transfer, diffusion coefficients measured on a ring electrode should be equal to those measured on the ring of a ring-disk electrode when the disk electrode is not polarized by any external voltage and has a zero net current. The ring diffusion coefficient should also be equal to a coefficient measured at a rotating disk. The ratio of the ring-limiting current, I_R^0 , to the disk-limiting current, I_D , can be found from the respective Levich expressions to be the following

$$\frac{I_R^0}{I_D} = \frac{(r_2^3 - r_1^3)^{2/3}}{r_0^2} \quad (1)$$

where r_0 is the radius of the disk, r_1 is the inner radius of the ring, and r_2 is the outer radius of the ring electrode. I_R^0 is the limiting current when all of the area enclosed in the disk defined

by r_1 is an insulator. Measured limiting currents on rings, disks, and ring-disk electrodes can then be compared. Smyrl¹ first noticed that ring-limiting currents measured on ring-disk electrodes with nonpolarized disks having zero net current were higher than would be predicted using Eq. (1). Data taken from Miller and Bellavance² confirm Smyrl's observation. Further experiments were undertaken in this laboratory using a commercial Pine rotator and a Pine DT6 platinum ring-disk electrode. The current measurements were made with a Pine potentiostat at 23°C. Table 1 gives the results of these three sources. These conclusions have been drawn from the data in Table 1:

- 1) All of the chemical systems have large exchange-current densities.
- 2) Each experiment had enough supporting electrolyte to minimize the effect of migration.
- 3) Each of the electrodes involved thin-gap and thin-ring electrodes designed for collection efficiency measurements. They are geometrically similar.
- 4) Laminar flow existed.
- 5) All show a positive deviation of measured ring current from the Levich theoretical ring current.

A possible explanation for this anomalously high ring current or measured diffusion coefficient

Table 1. Comparison of ring and disk limiting currents.

| Investigator | Chemical System and Supporting Electrolyte | r_0/r_2 | r_1/r_2 | Ω (rpm) | I_R/I_D Measured | I_R^0/I_D Eq. [1] | % Deviation from Eq. [1] | D_R/D_P |
|-----------------------|---|-----------|-----------|----------------|--------------------|---------------------|--------------------------|-----------|
| Smyrl | 0.05 M $K_3Fe(CN)_6$ | 0.716 | 0.808 | 1550 | 1.3606 | 1.1821 | 15% | 1.141 |
| | 0.05 M $K_4Fe(CN)_6$ | | | | | | | |
| | 1.0 M KNO_3 (Reduction) | | | | | | | |
| Miller and Bellavance | 0.0533 M Hg_2^{+2} 1.0 M $HClO_4$ (Reduction) | 0.738 | 0.812 | 1600 | 1.2711 | 1.1521 | 10% | |
| Pierini | 0.05 $K_3Fe(CN)_6$ | 0.908 | 0.945 | 396 | 0.400 | 0.3499 | 14% | 1.193 |
| | 0.05 $K_4Fe(CN)_6$ | 0.908 | 0.945 | 900 | 0.396 | 0.3499 | 14% | 1.193 |
| | 2 M KOH (Reduction) | 0.908 | 0.945 | 1600 | 0.399 | 0.3499 | 14% | 1.193 |
| | | 0.908 | 0.945 | 2440 | 0.397 | 0.3499 | 14% | 1.193 |
| | | 0.908 | 0.945 | 3590 | 0.405 | 0.3499 | 14% | 1.193 |

* This work was supported by the Division of Chemical Sciences, Office of Basic Energy Sciences, U. S. Department of Energy.

is that the potential distribution due to the ring limiting current drives the disk electrode as a bi-polar electrode with a zero net current. The concentration of the ring reactant would have to be driven above the bulk concentration. The insulating annulus between the ring and the disk would then have to be thin enough so that the surface concentration would not recover its bulk value. This mechanism would then yield a larger ring limiting current due to the enhanced reactant concentrations in the boundary layer near the ring electrode.

The simulation of Pierini and Newman³ can be used to model the systems of Table 1. Figure 1 shows the modeled current distribution obtained for the measurements taken by Smyrl.¹ The central disk electrode has a zero total current density while the outer portion of the disk has a negative density. The products generated at the outer edges of the disk would serve to enhance the limiting current on the ring. Similar cases can be found for the other two experiments. Qualitative agreement has been found between the postulated mechanism and the experimental data. The accuracy of the computer model must be refined to achieve quantitative agreement.

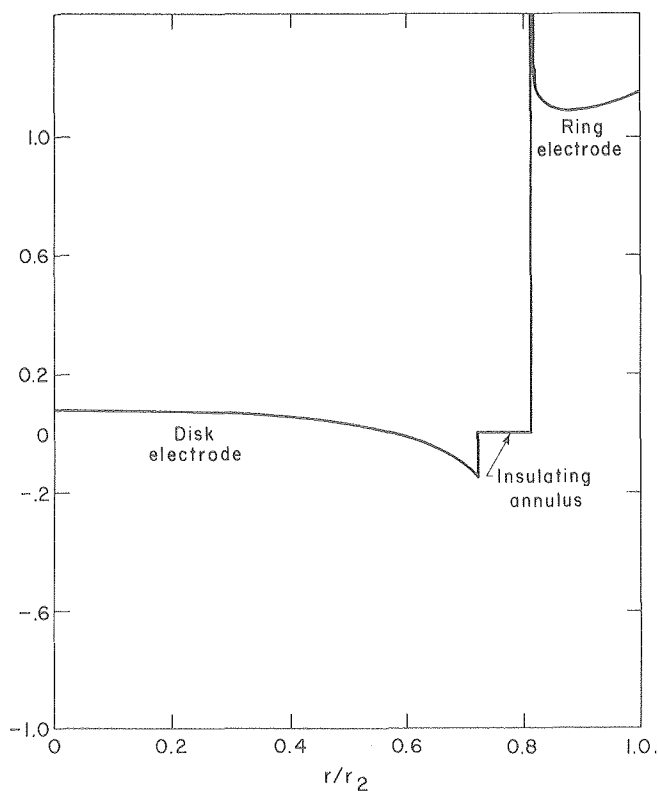


Fig. 1. Simulated current distribution for the rotating ring-disk experiments of Smyrl.
(XBL 802-273)

* * *

1. W. H. Smyrl, Private communication (1975).
2. B. Miller and M. S. Bellavance, *J. Electrochem. Soc.* **120**, 42 (1973).
3. P. Pierini and J. Newman, *J. Electrochem. Soc.* **124**, 701 (1977).

2. THE EFFECT OF COAL CHAR ON THE CORROSION OF 304 STAINLESS STEEL[†]

Thomas F. W. Foerster and John Newman

A layer of coal char covering a metal surface affects the sulfur and oxygen partial pressures at the metal surface and thus the rate and extent of corrosion. Experiments were conducted to determine the effect of char composition and depth and bulk gas composition and flow rate on the rate of sulfidation. A simple theoretical model was developed which predicts the concentration profiles and fluxes of the gaseous species in the char.

Since coal char contains carbon, the equilibrium oxygen partial pressure is less than 10^{-18} atm. This low oxygen partial pressure prevents the formation of protective oxide scales and, in some cases, leads to the formation of external sulfide scales.

The effect of the layer of char on the sulfur partial pressure at the metal surface depends on the composition of the char. If the char contains a large amount of sulfur-rich volatiles, the sulfur partial pressure of the gas in the char and the extent of sulfidation depend on the composition of the volatiles. If the char contains significant amounts of inorganic ash, the sulfur partial pressure of gas in contact with the char is determined by the equilibria of the various reactions between hydrogen sulfide and ash. For both types of char described above, the pattern and extent of corrosion of samples exposed for short times are essentially independent of the composition of the bulk gas and the thickness of the char layer. If the char does not contain large amounts of ash or if all of the ash has reacted, the sulfur partial pressure at the metal surface is determined by the diffusion of hydrogen sulfide through the char layer. In this case the rate of sulfidation is inversely proportional to the thickness of the char layer and roughly directly proportional to the concentration of hydrogen sulfide in the bulk gas.

* * *

[†]Brief version of LBL-9308.

3. CHARACTERISTICS OF THE DROPPING MERCURY ELECTRODE BELOW THE LIMITING CURRENT[†]

Clarence G. Law, Jr., Richard Pollard, and John Newman

A model has been developed to describe the combined effects of electrochemical kinetics, ohmic potential drop, and mass transfer for metal deposition reactions at a dropping mercury electrode. Below the limiting current, kinetic and ohmic factors influence the shape of the polarization curve. These effects are most noticeable for relatively short times during the life of a given drop and for small values of the applied potential. Results are obtained for the average and instantaneous current for a range of conditions that show

the relative importance of kinetic, ohmic, and mass transfer effects. Copper deposition from a dilute solution with an excess of supporting electrolyte has been treated as an example.

* * *

†Brief version of LBL-10079.

4. THE SHORT TIME SOLUTION FOR THE CONCENTRATION STEP AT THE SURFACE OF A ROTATING DISK

Daniel A. Scherson, Pier Filippo Marconi, and John Newman

Methods of following transient concentration changes are being developed in order to understand kinetic processes at interfaces, particularly with corrosion applications. A solution from the literature¹ for this concentration step is claimed to be convergent for all values of time. The first thirty coefficients of that series solution for this fundamental problem were evaluated in the present work. The results obtained tend to confirm our suspicion that this series actually diverges for all values of time, and they certainly show that practical applications of such a solution are limited to very short times where the first three terms have been obtained by another method. This short-time solution satisfactorily augments our earlier series solution,² which probably does converge for all nonzero values of time.

* * *

1. V. S. Krylov and V. N. Babak, Soviet Electrochem. 7, 626 (1971); Elektrokimiya 7, 649 (1971).
2. Kemal Nisancioglu and John Newman, J. Electroanal. Chem. 50, 23 (1974).

5. THE WARBURG IMPEDANCE IN THE PRESENCE OF CONVECTIVE FLOW[†]

Daniel A. Scherson and John Newman

The Warburg impedance deals with the concentration variations in a semi-infinite, stagnant region subjected to an alternating-current condition at the interface. In the presence of convective flow, such as that encountered near a rotating-disk electrode, these results need to be modified. Then alternating-current methods can be used more widely to elucidate interfacial processes in electrochemical and corroding systems, where the rotating disk is a commonly used research

tool. An inverse Laplace transformation method developed here allows the alternating-current problem to be reduced to another transient problem, that of a concentration step at the interface, for which solutions are known. The results obtained agree well with exact numerical values for a wide range of low and high frequencies.

* * *

†Brief version of J. Electrochem. Soc. 127, 110 (1980).

RESEARCH PLANS FOR CALENDAR YEAR 1980

Experiments will be conducted to determine the mass-transfer limiting reactant in the anodic dissolution of iron in H₂SO₄ solution, to identify the passive film that forms on the iron surface, and to clarify the importance of ohmic potential drop in the transition region. A model of corrosion on a rotating disk will be developed which includes the effect of chloride ion concentration on rate constants and the effect of mass transfer. The response of the supporting electrolyte under alternating current conditions will be developed along the lines already used for the reactant concentration and the a.c. impedance. Modeling of liquid-junction solar cells will be extended.

1979 PUBLICATIONS AND REPORTS

Refereed Journals

1. Peter Pierini and John Newman, "Potential Distribution for Disk Electrodes in Axisymmetric Cylindrical Cells," J. Electrochem. Soc. 126, 1348 (1979).
2. Bruce A. Gordon and John Newman, "Corrosion of Iron-Based Alloys by Coal Char at 871°C and 982°C," J. Electrochem. Soc. 126, 894 (1979).

LBL Reports

1. Thomas Friedrich-Wilhelm Foerster, "The Effect of Coal Char on the Corrosion of 304 SS," (M.S. thesis), June 1979, LBL-9308.
2. Clarence G. Law, Jr., Richard Pollard, and John Newman, "Characteristics of the Dropping Mercury Electrode Below the Limiting Current," LBL-10079, November 1979.

e. Metal Cluster—Metal Surface Analogy*

Earl L. Muetterties, Investigator

1. CHEMICAL AND STRUCTURAL FEATURES OF CHEMISORBED SPECIES ON METALLIC SURFACES

Cynthia Friend, Min-Chi Tsai, and Earl L. Muetterties

Essentially, two major advances have been achieved in this study of the coordination and catalytic chemistry of nickel and platinum surfaces. A technique has been developed for unambiguously defining whether chemistry observed for a metal crystal is that of the exposed crystal face or a composite of the exposed crystal face, the crystal sides and back, and other nearby metal surfaces. With such a technique, the chemical significance of crystallographic imperfections on a Pt(111) surface has been established. In addition, the molecular features of aromatic hydrocarbon chemisorption on Ni(111) have been defined in a definitive fashion.

Thermal desorption and chemical displacement reactions of chemisorbed molecules play a critical role in our studies of metal surface coordination chemistry. Hence it is essential that we know with certainty that all molecules that go into the gaseous phase through such reactions originated from the exposed metal crystal face under study--rather than from that face as well as from the sides and back and from adjacent metal surfaces. We have successfully devised an experimental blank procedure that fully removes uncertainties. For each metal surface reaction, a control experiment is performed with a blank metal crystal that has the exposed crystal face covered by a thin layer of gold (prepared by vapor deposition or by electroplating). By such control experiments, we have demonstrated that step-like imperfections on real Pt(111) surfaces give rise to an identifiable imperfection site chemistry for molecules like CO and C₆H₆ that is differentiable from the (111) terrace chemistry for the molecules. Thus the ubiquitous crystallographic imperfections on a real metal single crystal are chemically significant and can be probed by chemical and physical studies.

The chemisorption of benzene on Ni(111) has been shown to be fully associative between 20 and ~100°C. No C-H bonds are broken in either an irreversible or reversible fashion in this temperature range. This molecular feature of Ni(111)-C₆H₆ was unequivocally shown by the quantitative displacement of benzene molecules from Ni(111)-C₆H₆-C₆D₆ by trimethylphosphine. All desorbed benzene molecules were either C₆H₆ or C₆D₆. No isotopically labeled cross-product benzene molecules were detected, thus showing that no H-D exchange had occurred within 10-30 minute periods in the 20-100°C range. At ~130°C, there is rapid

C-H bond breaking for chemisorbed benzene. In sharp contrast to the benzene system, the toluene chemisorption process (20°C) on Ni(111) was shown to be fully irreversible. This irreversibility is ascribed to rapid C-H bond breaking at the methyl carbon site at 20°C on Ni(111).

RESEARCH PLANS FOR CALENDAR YEAR 1980

The molecular features of ethylene and of acetylene chemisorption on nickel and platinum surfaces will be established as a function of surface crystallography, carbon and sulfur surface contamination and temperature. Key to the experimental studies is the chemical displacement reaction whereby molecules, but no molecular fragments, can be displaced from a surface into the gas phase by a molecule that strongly binds to the surface and alters the electronic features of the surface. We have found trimethylphosphine, P(CH₃)₃, to be a very effective displacing molecule and have preliminary evidence that the phosphine displacement reaction will define the chemisorption states of ethylene and acetylene. After the ethylene and acetylene chemisorption states are rigorously defined for the nickel and platinum surfaces, the substituent effect will be defined from analogous studies of propylene and cis-2-butene in the olefin class and of propyne and 2-butyne in the acetylene class of reactions. Conformational and electronic effects will also be established for the olefin class by extending the analyses to *cis* and *trans* butadiene and to unconjugated dienes like 1,4-hexadiene.

1979 PUBLICATIONS AND REPORTS

Refereed Journals

- †1. E. Band and E. L. Muetterties, "Mechanistic Features of Metal Cluster Rearrangements," *Chem. Rev.* **78**, 639 (1978).
- †2. M. Y. Darensbourg and E. L. Muetterties, "Arene-Transition Metal Complexes. 1. Site Exchange and Chemical Characteristics of η^6 -C₆(CH₃)₆ Ru- η^4 -C₆(CH₃)₆," *J. Am. Chem. Soc.* **100**, 7425 (1978).
3. J. C. Hemminger, E. L. Muetterties and G. A. Somorjai, "A Coordination Chemistry Study of a Nickel Surface. The Chemistry of Ni(111) with Triply Bonded Molecules," *J. Am. Chem. Soc.* **101**, 62 (1979), LBL-7655.
- †4. L-Y. Goh, M. J. D'Aniello, Jr., S. Slater, E. L. Muetterties, I. Tavanaiepour, M. I. Chang, M. F. Fredrich and V. W. Day, "Metal Clusters in Catalysis. 20. The Chemistry of [η^5 -C₅H₅Cr(CO)₃]₂," *Inorg. Chem.* **18**, 192 (1979).
- †5. E. L. Muetterties, H. Schaffer, R. I. Mink, M. Y. Darensbourg, M. Millar, T. Groshens and

* This work was supported by the Division of Chemical Sciences, Office of Basic Energy Sciences, U. S. Department of Energy.

K. J. Klabunde, "Arene-Transition Metal Chemistry. 2. Hydrogenation of Metal-Arene and Allylmetal-Arene Complexes," *Inorg. Chem.* 18, 883 (1979).

6. E. L. Muetterties, "A Comment on Ligand Designators," *Inorg. Chem.* 18, 902 (1979).

[†]7. E. L. Muetterties, T. N. Rhodin, E. Band, C. F. Brucker and W. R. Pretzer, "Clusters and Surfaces," *Chem. Rev.* 79, 91 (1979).

[†]8. R. K. Brown, J. M. Williams, M. F. Fredrich, V. W. Day, A. J. Sivak and E. L. Muetterties, *Proc. Natl. Acad. Sci. (USA)* 76, 2099 (1979).

[†]9. A. J. Sivak and E. L. Muetterties, "Metal Clusters. 21. Synthesis of Rhodium Phosphite Clusters," *J. Am. Chem. Soc.* 101, 4878 (1979).

[†]10. E. L. Muetterties, J. R. Bleeke and A. C. Sievert, "Arene Transition Metal Chemistry III.

Arene Exchange Phenomena," *J. Organomet. Chem.* 178, 197 (1979).

[†]11. E. L. Muetterties and J. R. Bleeke, "Catalytic Hydrogenation of Aromatic Hydrocarbons," *Accts. Chem. Res.* 12, 324 (1979).

Papers Presented

[†]1. E. L. Muetterties, "Transition Metal Arene Chemistry," presented at ACS/CSJ Chemical Congress, Honolulu, Hawaii, April 1-6, 1979.

[†]2. E. L. Muetterties, "The Metal Surface-Metal Cluster Analogy," presented at ACS/CSJ Chemical Congress, Honolulu, Hawaii, April 1-6, 1979.

* * *

[†]Supported by NSF.

[‡]Partially supported by NSF.

f. High-Energy Oxidizers and Localized-Electron Solids*

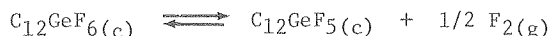
Neil Bartlett, Investigator

1. NOVEL GRAPHITE SALTS OF HIGH OXIDIZING POTENTIAL†

Eugene M. McCarron, Y. Jean Grannec‡ and Neil Bartlett

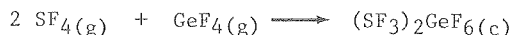
The intercalation of germanium tetrafluoride into graphite (HOPG) in the presence of fluorine (2 atmospheres pressure) yields a material which has a limiting composition of $C_{12}GeF_6$. X-ray diffraction data show that this is a first stage material with a gallery height of 7.80 Å. In a dynamic vacuum this material loses elemental fluorine but no GeF_4 , and the first stage character is maintained. The diffraction data show that this loss of fluorine is accompanied by an increase in the gallery spacing to 8.18 Å. On reintroduction of fluorine (at 2 atmos.) the gallery height again shortens. The fluorine uptake and removal are fully reversible.

The reversible equilibrium is:



and it is evident that ΔG for this process must approximate to zero. Since both $C_{12}GeF_6$ and $C_{12}GeF_5$ are at least as metallic as graphite, it is clear that $C_{12}GeF_6$ should be an effective oxidizing electrode, with a potential close to that of the F_2/F^- couple.

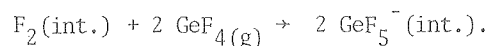
It is probable that the major guest species in $C_{12}GeF_6$ is GeF_6^{2-} and in $C_{12}GeF_5$ the monomeric ion, GeF_5^- . Each of these ions is known in salts. The similarity of the x-ray diffraction data of $C_{12}GeF_6$ to that of $C_{12}PtF_6$ (which is known to be a PtF_6^{2-} salt) and the shortening of the gallery height, with addition of fluorine, are consistent with these assignments. The conversion: $GeF_5^- + 1/2 F_2 + e^- \rightarrow GeF_6^{2-}$, doubles the positive charge in the graphite (for which there must be a very considerable increase in the work function) and also quadruples the repulsive interaction between the guests. All attempts to intercalate SiF_4 , in like fashion to GeF_4 , have failed. Although SiF_4 will form SiF_5^- and SiF_6^{2-} salts, it appears that the work required to oxidize the graphite is not compensated for by the fluoride ion affinities and the lattice energy (which should be slightly more favorable than the Ge cases because of the smaller size of the silicon species). Since SiF_4 will not form even the salt $SF_3^+ SiF_5^-$ with the fluoride-ion donor SF_4 , whereas GeF_4 , spontaneously generates $(SF_3)_2GeF_6^{2-}$:



* This work was supported by the Division of Chemical Sciences, Office of Basic Energy Sciences, U. S. Department of Energy under Contract Number W-7405-ENG-48.

it is clear that the enthalpies $\Delta H_{(1)} (GeF_4(g) + F(g) \rightarrow GeF_5(g))$ and $\Delta H_{(2)} (GeF_5(g) + F(g) \rightarrow GeF_6^{2-}(g))$ must be more exothermic (or less endothermic) than for SiF_4 .

With smaller concentrations of intercalant in the graphite, more GeF_4 or more F_2 is intercalated than required for the GeF_5^- or GeF_6^{2-} species respectively. The excess GeF_4 is readily removed and it seems likely that it is merely molecular GeF_4 occupying holes in a gallery formed by insertion of GeF_5^- into the graphite. However bridged species such as $F_4Ge-F-GeF_4^-$ cannot be ruled out. The excess fluorine, above that required to generate GeF_6^{2-} , may also be present simply as molecules residing in gallery holes. It has been observed in related studies that when graphite has been electron-oxidized by intercalation of transition metal hexafluorides (e.g., $8 C(c) + IrF_6(g) \rightarrow C_8 IrF_6$) the resultant salt will not interact with gaseous fluorine to 200°. Thus carbon-fluorine bonds, in the $C_xGeF_6 + F_2$ system, seem very unlikely, moreover such bonding is strong and elemental fluorine is not chemically recoverable from such bonds. The excess fluorine' can be titrated with GeF_4 (presumably to form GeF_5^-) such that both the fluorine and GeF_4 are retained in the graphite under vacuum:



Similarly, the GeF_4 in the $C_xGeF_5 + \delta GeF_4$ system can be titrated with F_2 , to fix the germanium as GeF_5^- .

A preliminary study of the graphite/ PF_5 / F_2 system shows that although PF_5 (even under pressure) will not enter graphite in the absence of fluorine, it does so in its presence, according to the equation $PF_5(g) + 1/2 F_2(g) + e^- \rightarrow PF_6^-(int.)$. This system is analogous to the C_xAsF_6 system which is discussed in the following section.

* * *

† Brief version of LBL-10228.

‡ Present address: Laboratoire de Chimie du Solide du C.N.R.S., Université de Bordeaux I, Talence, France.

2. COMPOSITION AND STAGING IN THE GRAPHITE/ AsF_6 SYSTEM AND ITS RELATIONSHIP TO GRAPHITE/ AsF_5 †

Eugene M. McCarron and Neil Bartlett

The intercalation of AsF_5 into graphite in the presence of fluorine yields material of composition C_xAsF_6 . More fluorine than that required for the formula can be intercalated, particularly at higher stages than the first, but this excess can be titrated with AsF_5 to yield the stoichiometry AsF_6^- .

X-ray diffraction data and the c -axis swelling t/t_0 (thickness, along c , of the intercalated graph-

ite to that of the original HOPG sample) have established that, for each stage higher than the first, the composition is $C_{12n}AsF_6$, n being the stage. Thus $C_{12}AsF_6$ is pure first stage, $C_{24}AsF_6$ is second stage, $C_{36}AsF_6$ third and so on. Each occupied gallery of the graphite up to the onset of first stage, has a composition $C_{12}AsF_6$. When x in C_xAsF_6 is not a simple multiple of twelve, an appropriate mixture of stages is obtained. Experimental data are given in Table 1. X-ray diffraction data provide the 'c' dimension for each stage. This is the gallery height in a first stage material, the height of one unoccupied gallery plus one occupied gallery in a second stage material and so on, as illustrated in Fig. 1. From the 'c' dimension and the gallery height of 3.35 Å in the parent graphite, the theoretical c-axis expansion, t/t_0 , may be calculated for any composition up to $C_{12}AsF_6$ by employing the $C_{12n}AsF_6$ formula (see Table 1). From composition $C_{12}AsF_6$ up to the intercalation limit of C_8AsF_6 the system is first stage, but the c spacing does diminish as the guest concentration increases; from a value of 8.04 Å for $C_{12}AsF_6$ to 7.86 Å for C_8AsF_6 . (See Fig. 2.)

These observations are in accord with the expectation that the guest species is AsF_6^- . Since single crystal studies had previously established¹ a simple unit cell, for C_8AsF_6 , with $a = 4.92$, $c = 7.86$ and $V = 169 \text{ Å}^3$, which volume is indicative of a close packed array of AsF_6^- within the gallery, it is appropriate to represent each anion as having six close-packed neighbors as represented in Fig. 2(a).

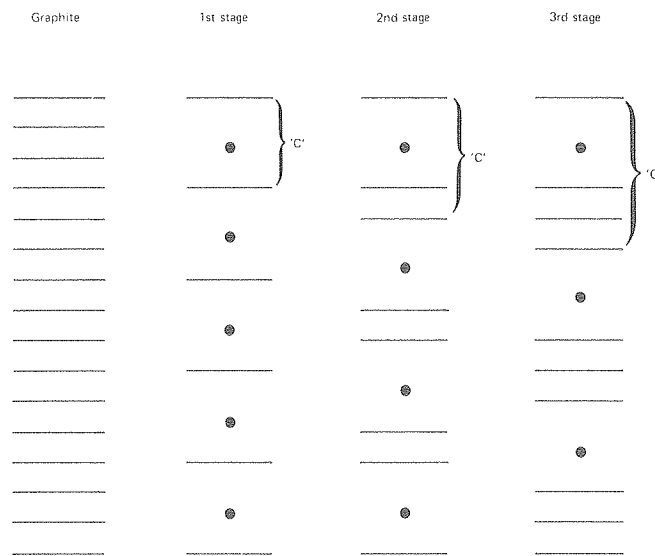


Fig. 1. The gallery occupancy for 1st, 2nd and 3rd stages in graphite intercalates. (XBL 802-266)

If one third of the anions of Fig. 2(a) are removed so as to reduce the number of nearest anion neighbors to three, (as shown in Fig. 2(b)), the stoichiometry which is represented is $C_{12}AsF_6$. Since this arrangement minimizes the repulsions for this stoichiometry it is a suitable model for the arrangement

Table 1. Composition--staging relationships for C_xAsF_6 .

| For $12 < x < 24$ | | | For $24 < x < 36$ | | |
|-------------------|------------------------------|---------|-------------------|------------------------------|---------|
| x | t/t_0 (ideal) ^a | t/t_0 | x | t/t_0 (ideal) ^b | t/t_0 |
| 11.6 | < 2.40(5) | 2.38 | 28.3 | 1.62(5) | 1.62 |
| 12 ideal | 2.40 | ---- | 30.9 | 1.57(5) | 1.59 |
| 13.1 | 2.34(5) | 2.28 | 36 ideal | 1.47 | ---- |
| 13.9 | 2.29(5) | 2.23 | | | |
| 14.6 | 2.25(5) | 2.20 | | | |
| 16.2 | 2.16(5) | 2.17 | | | |
| 16.6 | 2.13(5) | 2.15 | | | |
| 18.3 | 2.03(5) | 2.12 | | | |
| 19.7 | 1.95(5) | 2.11 | | | |
| 22.8 | 1.77(5) | 1.89 | | | |
| 24 ideal | 1.70 | ---- | | | |

$${}^a t/t_0 [C_xAsF_6] \equiv (1 - \frac{x-12}{12}) t/t_0 [C_{12}AsF_6] + (\frac{x-12}{12}) t/t_0 [C_{24}AsF_6].$$

$${}^b t/t_0 [C_xAsF_6] \equiv (1 - \frac{x-24}{12}) t/t_0 [C_{24}AsF_6] + (\frac{x-24}{12}) t/t_0 [C_{36}AsF_6];$$

t/t_0 for $C_{12}AsF_6$ calculated from x-ray diffraction data on HOPG:

$$\frac{c\text{-space } C_{12}AsF_6}{c\text{-space Graphite}} \equiv \frac{8.05 \text{ Å}}{3.35 \text{ Å}} = 2.40.$$

$$\text{For } C_{24}: \frac{8.05 + 3.35}{2 \times 3.35} = 1.70. \quad \text{For } C_{36}: \frac{8.05 + (3.35 \times 2)}{3.35 \times 3} = 1.47.$$

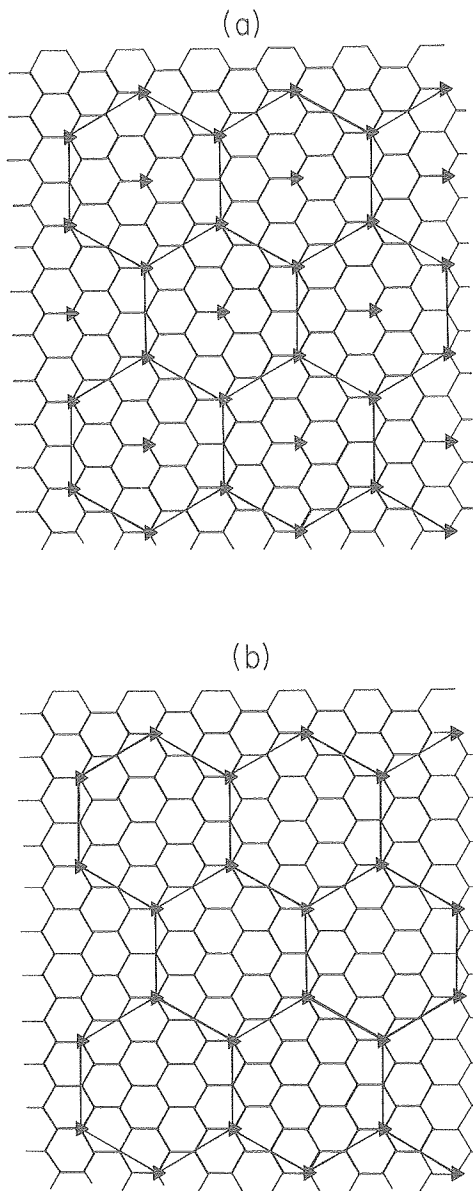
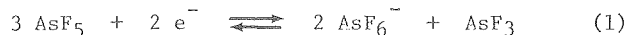


Fig. 2. Structural models for (a) C_8AsF_6 and (b) $C_{12}AsF_6$. (XBL 802-264)

of the contents of each gallery in $C_{12n}AsF_6$. The transition from second stage to first stage occurs at $C_{24}AsF_6$. A gallery occupancy richer in AsF_6^- than $C_{12}AsF_6$ can occur only when all galleries have attained that composition. Any introduction of AsF_6^- to a gallery of composition $C_{12}AsF_6$ will increase the repulsive interactions markedly. This readily accounts for $C_{24}AsF_6$ being a second stage material and not third stage. Similarly $C_{16}AsF_6$ is not a second stage material but is two thirds first stage ($C_{12}AsF_6$) and one third second stage ($C_{24}AsF_6$).

The staging-composition relationships of C_xAsF_6 throw light on the controversy surrounding the graphite/ AsF_5 system. Previous synchrotron radiation studies² had indicated that arsenic pentafluoride oxidizes graphite, as it is intercalated, according to the equation:



This has been contested,³ because of difficulties in matching the observed physical properties with the large electron transfer required, if the equilibrium is extensively to the right, as the As K_X preabsorption-edge findings² indicate.

Because of the reversibility of Eq. (1) it is possible to remove AsF_5 from the graphite/ AsF_5 intercalates but it is not possible to remove AsF_5 from C_xAsF_6 at least up to 200°. When C_xAsF_6 is treated with AsF_3 however the gas is consumed, without change in staging (i.e., t/t_0 remains essentially constant), and the stoichiometry satisfies the equation:



AsF_5 and some AsF_3 can be removed from these materials, as in the graphite/ AsF_5 product. Evidently graphite/ AsF_5 and the product of graphite/ $AsF_6^- + 1/2 AsF_3$ are one and the same. This establishes the existence of the equilibrium (1).

For graphite/ AsF_5 the composition for any stage is represented⁴ by $C_{8n}AsF_5$ where n is the stage. The comparison with the AsF_6^- system is made in Fig. 2, where it is seen that second stage graphite- AsF_5 is $C_{16}AsF_5$. If this is formulated assuming essentially complete conversion to AsF_6^- and AsF_3 according to Eq. (1) this becomes $C_{16}^{2/3+} 2/3 AsF_6^- \cdot 1/3 AsF_3$ or $C_{24}^+ AsF_6^- \cdot 1/2 AsF_3$. This compares with the second stage AsF_6^- salt, $C_{24}AsF_6^-$. If the holes in the occupied gallery (see Fig. 2(b)) of the latter, were each occupied by an AsF_3 molecule, the stoichiometry $C_{24}AsF_6^- \cdot 1/2 AsF_3$ would be attained. The similarity of the 'c' dimension for $C_{12}AsF_6$ (8.05(3)Å) with that for C_8AsF_5 (8.04(3)Å) is persuasive evidence for the equality of the charging in the two materials, i.e., $C_{12}AsF_6$ is $C_{12}AsF_6^-$ and C_8AsF_5 is $C_{12}F_6^- \cdot 1/2 AsF_3$.

All of these observations, together with the EXAFS findings (discussed below) and the preabsorption edge results, indicate that the intercalation of AsF_5 into graphite is associated with the nearly complete conversion of AsF_5 into AsF_6^- and AsF_3 according to Eq. (1). Any discussion of the physical properties of these materials ought to recognize that the intercalation of each AsF_5 molecule into graphite to form C_xAsF_6 requires the transfer of essentially 2/3 of an electron from the graphite to the guest.

* * *

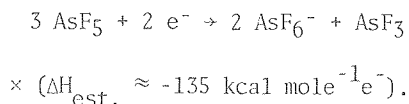
[†]Brief version of LBL-10190.

1. N. Bartlett, B. W. McQuillan and A. S. Robertson, *Mat. Res. Bull.* **13**, 1259 (1978).
2. N. Bartlett, R. N. Biagioni, B. W. McQuillan, A. S. Robertson and A. C. Thompson, *J. C. S. Chem. Comm.* 200 (1974) and Ref. 1.
3. J. E. Fischer, *J. C. S. Chem. Comm.* 544, (1978) and *Physica B* in press (1979).
4. E. R. Falardeau, L. R. Hanlon and T. E. Thompson, *Inorg. Chem.* **17**, 301 (1978).

3. EXAFS STUDIES OF ARSENIC FLUORIDES, AND GRAPHITE INTERCALATED BY AsF_5 AND AsF_6^-

Barry W. McQuillan, Alan S. Robertson, and Neil Bartlett

The final analysis of the EXAFS data of various arsenic fluoride compounds has been completed. The results provide further evidence that in the synthetic metal, graphite/ AsF_5 , the species present inside the graphite is not gaseous AsF_5 . The data are consistent with AsF_3 and AsF_6^- in approximately 1:2 molar ratio as expected for the known oxidation reaction:



As has been discussed in a previous report the pre-edge absorption white peaks are a very sensitive indication of arsenic oxidation state state (See Table 1.) Fits to the " C_8AsF_5 " pre-edge region with

Table 1. Arsenic preabsorption-edge (K_{α}) peak positions for several arsenic compounds.

| | As(III) | AsF_5 | AsF_6^- |
|---|----------|----------------|------------------|
| As_2O_3 | 11867.90 | | |
| | 67.54 | | |
| | 68.16 | | |
| | 67.64 | | |
| | 67.44 | | |
| | 68.09 | | |
| AsF_3 | 68.45 | | |
| AsF_5 | | 11874.25 | |
| | | 74.15 | |
| $\text{XeF}^+\text{AsF}_6^-$ | | | 11875.38 |
| $\text{Xe}_2\text{F}_3^+\text{AsF}_6^-$ | | | 75.12 |
| $\text{O}_2^+\text{AsF}_6^-$ | | | 75.82 |
| | | | 75.43 |
| $\text{Cs}^+\text{AsF}_6^-$ | | | 75.26 |
| $\text{Na}^+\text{AsF}_6^-$ | | | 75.24 |
| $\text{C}_{10}\text{F}_8^+\text{AsF}_6^-$ | | | 74.70 |
| $\text{C}_6\text{F}_6^+\text{AsF}_6^-$ | | | 75.21 |
| $\text{C}_n^+\text{AsF}_6^-$ | | | 11875.48 |
| | | | 75.37 |
| C_nAsF_5 | 11868.67 | | 11875.33 |
| | 68.24 | | 75.05 |
| | 68.80 | | 75.19 |
| | 68.96 | | 75.55 |
| $\text{C}_n\text{AsF}_5 + \text{F}_2$ | | | 75.55 |

standard files of $\text{AsF}_3(\text{g})$ and $\text{C}_8^+\text{AsF}_6^-$ give 40% AsF_3 60% C_8AsF_6^- (Fig. 1). Other " C_8AsF_5 " files yielded 25% AsF_3 and 75% C_8AsF_6^- (but recent work in these laboratories has shown that C_8AsF_5 will lose AsF_3 as well as AsF_5). The above half reaction would predict 33% AsF_3 . Adding in a standard $\text{AsF}_5(\text{g})$ file produced no improvement in fit, and never made more than a 5% contribution to the fit. Often the AsF_5 contribution was small and negative.

From the EXAFS data, the average As-F bond distance for a number of gaseous and solid compounds are given in Table 2. The excellent agreement with known structures encourages the view that the As-F bond distances in the " C_8AsF_5 " and $\text{C}_8^+\text{AsF}_6^-$ are sufficiently accurate to distinguish AsF_5 from AsF_3 plus AsF_6^- . Table 2 also shows the bond distances (plus error limits) for a series of graphite compounds. The reasonable number of nearest neighbors, N, encourages us that the compounds examined have not lost much AsF_3 . Figure 2 shows a summary of As-F bond distance (with 1 σ error ellipsoids) for a series of arsenic fluoride compounds. Figure 2 shows that the graphite compounds have As-F distances agreeing with AsF_3 and AsF_6^- , but not with AsF_5 .

* * *

† Brief version of LBL-10229 and LBL-10230.

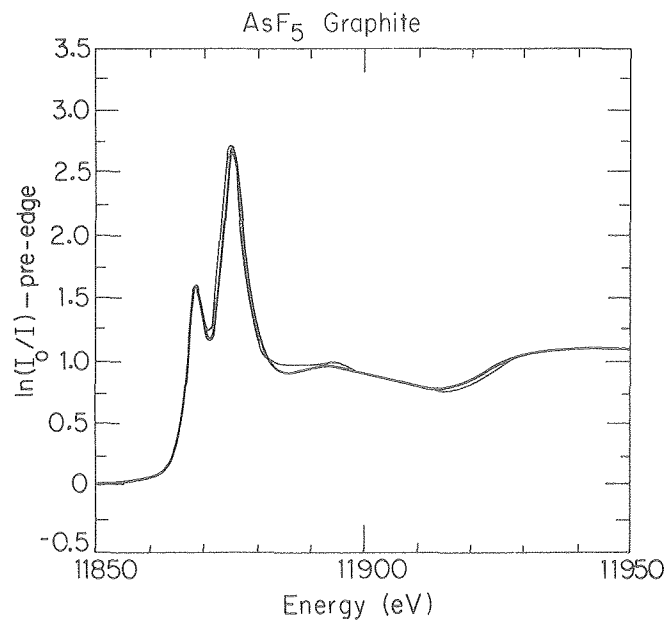


Fig. 1. Fit of $\text{C}_8\text{AsF}_5^{(-)}$ with $\text{AsF}_3(\text{g}) + \text{C}_8^+\text{AsF}_6^-$ (•••). (XBL 802-263)

Table 2. As-F distances from EXAFS studies compared with distances from other studies.

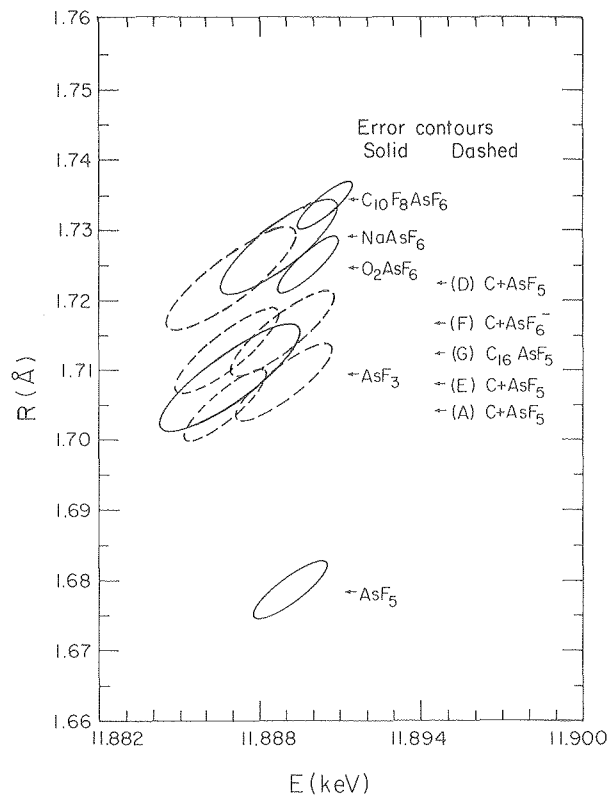
| | N* | EXAFS* (Amplitude Removed) | Other Techniques |
|---|-------------|-------------------------------|--|
| AsF ₃ (g) | 3 | 1.706(7) | 1.706(2) ^a |
| AsF ₅ (g) | 4.7 | 1.681(4) | 1.678(2) ^a 3 As-F 1.656(5) 2 As-F 1.711(4) |
| XeF ⁺ AsF ₆ ⁻ | | 1.732(11) | 1.750(10) ^b 5 As-F at 1.730(10) 1 As-F at 1.860(10) |
| Xe ₂ F ₃ ⁺ AsF ₆ ⁻ | 6.2 | 1.72(2) | 1.74(2) ^c 2 As-F at 1.67(3) 2 1.73(3) 6 1.76(3) 2 1.79(3) |
| O ₂ ⁺ AsF ₆ ⁻ | --- | 1.724(4) | |
| Cs ⁺ AsF ₆ ⁻ | 5.8 | 1.726(4) | |
| Na ⁺ AsF ₆ ⁻ | --- | 1.727(6) | |
| C _x ⁺ AsF ₆ ⁻ x ≈ 8 | {5.8 5.6 | 1.716(6) 1.714(5) | |
| C _x AsF ₅ x ≈ 10 | {5.2 4.9 | 1.706(3) 1.708(5) | |
| (-140°C) | 4.7 | 1.707(4) | |
| C ₁₆ AsF ₅ | 5.2 | 1.712(6) | |

^a F. B. Clippard Jr. and L. S. Bartell, *Inorg. Chem.*, **9**, 805 (1970).

^b A. Zalkin, D. Ward, R. Biagioni, D. H. Templeton and N. Bartlett, *Inorg. Chem.*, **17**, 1318 (1978).

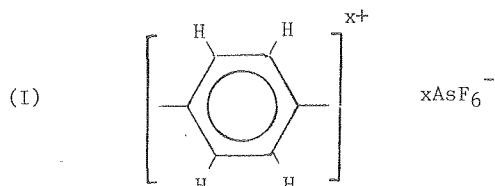
^c N. Bartlett, B. G. DeBoer, F. J. Hollander, F. O. Sladky, D. H. Templeton and A. Zalkin, *Inorg. Chem.*, **13**, 780 (1974).

* Values from $\chi(k) = \frac{N}{kR^2} A(k)e^{\sigma^2 k^2} \sin[2kR + \beta(k)]$

Fig. 2. Error limits ($\sim 1\sigma$) on As-F. (XBL 798-10976)4. ELECTRON OXIDATION OF BENZENE AND CORONENE[†]

Francis L. Tanzella and Neil Bartlett

Benzene. The oxidation of benzene by O₂⁺AsF₆⁻ or C₆F₆⁺AsF₆⁻ gives a green-brown polymeric, electrically conducting amorphous solid and the salt (C₆H₅)₂-AsF₂⁺AsF₆⁻. The preparation and characterization of the latter were described last year. A method has been devised for the purification of the former and analytical and spectroscopic work indicates that it is probably a hexafluoroarsenate salt derived from poly (para-phenylene) (I).

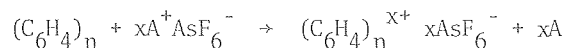
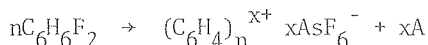
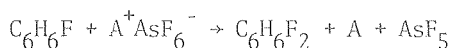
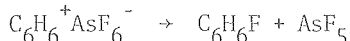
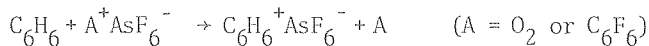


The poly-phenylene salt has been isolated, on a Teflon frit, by washing the reaction product several times with anhydrous HF to dissolve the $(C_6H_5)_2AsF_2^+AsF_6^-$. It has proved to be insoluble in all polar and nonpolar solvents which have been tried. The salt is evidently the same no matter which oxidant is used, although the AsF_6^- content does vary somewhat from preparation to preparation. Elemental analyses consistently show a C:H ratio of 6:4, but the arsenic content varies. The general formula is $(C_6H_4)_4(AsF_5O_16)^{4-x}$ with x having values between 2 and 3. The fluorine analyses are not decisive but the infrared data show the AsF_6^- ν_3 and ν_4 bands at their characteristic frequencies of 700 and 400 cm^{-1} respectively, as well as the bands characteristic of poly (para-phenylene).¹ Raman studies were prevented by strong fluorescence of the samples. Lack of monolithic samples has prevented a precise evaluation of the resistivity but measurements on the compacted powder indicate that the specific resistivity is less than 100 ohm/cm. The material is diamagnetic.

The observed properties are consistent with the poly (p-phenylene) salt formulation. The moderate electrical conductivity indicates that the cationic chain is metallic. Similar behavior has recently been noted by Baughman and his coworkers² for the product formed by direct interaction of poly(p-phenylene) with AsF_5 . These authors also suggest an AsF_6^- salt formulation for their product. This would be in harmony with the observation previously made in these laboratories³ that AsF_5 oxidizes graphite according to the equation:



Since AsF_5 reacts cleanly with C_6H_6 , under conditions similar to the O_2 and C_6F_6 oxidations, to give a 100% yield $(C_6H_5)_2AsF_2^+AsF_6^-$, it is probably that the first step, in the poly (p-phenylene) salt synthesis from benzene, involves C_6H_6 . A plausible mechanism is:



Coronene Hexafluoroarsenates(V). Although electron oxidation of coronene ($C_{24}H_{12}$) using C_6F_6 AsF_6^- yields two derivatives, $C_{24}H_{12}AsF_6$ and $(C_{24}H_{12})_2AsF_6$, depending upon the reactant stoichiometry, neither has been prepared in crystalline form. Rough resistivity measurements on the compacted powders have yielded upper limits on the resistivity of 5,000 and 10,000 ohm cm for the 1:1 and 1:2 salts respectively. This is in accord with the expectation that ring-ring overlap in such salts (with large flat cations and relatively small compact anion) would lead to extensive delocalization. Further progress will depend upon preparation of crystalline samples.

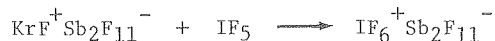
[†]Brief version of LBL-10478; Molecular Metals, edited by William E. Hatfield, Plenum Publishing, New York, 1979.

1. R. C. Doss and P. W. Solomon, J. Org. Chem. **29**, 1567 (1964).
2. R. H. Baughman, D. M. Ivory, G. G. Miller, L. W. Shacklette, and R. R. Chance, Organic Coatings and Plastic Chemistry **41**, 139 (1979).
3. N. Bartlett, B. W. McQuillan and A. S. Robertson, Mat. Res. Bull. **13**, 1256 (1978).

5. THE EXPLOITATION OF KrF_2 AND ITS SALTS IN THE PREPARATION OF FrF_6^+ AND ClF_6 SALTS

Klaus Züchner and Neil Bartlett

In early studies in these laboratories,¹ following characterization of the salt $KrF^+Sb_2F_{11}^-$ it was observed to oxidize IF_5 spontaneously below room temperature:



Attempts to prepare ClF_6^+ and BrF_6^+ salts in similar reactions failed. Subsequently ClF_6^+ was prepared by Christie² and Roberto³ in a photo-induced oxidation of ClF_5 using PtF_6 as the oxidizer, but a high yield synthesis of pure material has not been available hitherto. Gillespie and his coworkers⁴ were successful in oxidizing BrF_5 to BrF_6^+ using KrF_2 -rich fluoro-acid systems and the oxidation was attributed to KrF^+ and $Kr_2F_3^+$ species.

From a comparison of $Xe_2F_3^+$ and XeF^+ it is evident⁵ that the fluorine bonding to xenon in the former is much weaker than in the latter and it seemed likely that the same would be true of $Kr_2F_3^+$ and KrF^+ . It therefore appeared probable that the $Kr_2F_3^+$ would be a stronger and more facile oxidizer than KrF^+ . Indeed the failure of the earlier attempts to synthesize ClF_6^+ and BrF_6^+ using KrF^+ , taken with the success of Gillespie and his coworkers, pointed to the $Kr_2F_3^+$ being the effective oxidizer in the latter work.

Synthesis of both $ClF_6^+AuF_6^-$ and $BrF_6^+AuF_6^-$ was undertaken for two reasons. Firstly the vibrational frequencies for the AuF_6^- anion give a clearer separation from the frequencies anticipated for the cations, than is the case for other strong-acid anions. Secondly, the anion is, itself, a powerful oxidizer and thus would provide salts of remarkable total oxidizing capability, e.g., transformation of 1 mole of $ClF_6^+AuF_6^-$ to $AuCl$ yields six moles of fluorine.

Both syntheses have been achieved. Gold is oxidized by excess krypton difluoride in HF solution to yield $Kr_2F_3^+AuF_6^-$:



(It is essential to exclude oxygen or any other oxidizable species since this reduces the $Kr_2F_3^+$ salts: $Kr_2F_3^+ + O_2 \rightarrow O_2^+ + 2 Kr + 3/2 F_2$.) The HF is removed and excess bromine pentafluoride added,

to serve both as solvent and reactant. Brisk krypton evolution occurs on warming towards room temperature and the $\text{BrF}_6^+ \text{AuF}_6^-$ is formed in high yield: $\text{Kr}_2\text{F}_3^+ \text{AuF}_6^- + \text{BrF}_5 \rightarrow \text{BrF}_6^+ \text{AuF}_6^- + \text{KrF}_2 + \text{Kr}$. The yellow crystalline solid has a cubic unit cell with $a = 9.57(5) \text{ \AA}$, $V = 876 \text{ \AA}^3$, $z = 4$, with the $\text{IF}_6^+ \text{AsF}_6^-$ structure⁵ (Space Group Ia3). The Raman data are as expected and are given in the Table, where they are compared with data for $\text{ClF}_6^+ \text{AuF}_6^-$ and $\text{IF}_6^+ \text{AuF}_6^-$.

A parallel experiment using $\text{KrF}^+ \text{AuF}_6^-$ as oxidizer did not result in oxidation of the BrF_5 , the salt $\text{BrF}_4^+ \text{AuF}_6^-$ being the sole solid product:

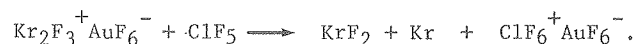


This confirms the superior oxidizing capability of Kr_2F_3^+ over KrF^+ .

The oxidation of chlorine pentafluoride proved to be unexpectedly difficult to accomplish until it was recognized that a small quantity of chloryl fluoride impurity, ClO_2F , present in the large excess of ClF_5 , used in the reaction (in which ClF_5 is also the solvent) was entirely consuming the acid anion:



This was overcome by making two batches of $\text{Kr}_2\text{F}_3^+ \text{AuF}_6^-$, the first of which consumed the ClO_2F . The ClF_5 distilled from that reaction was then treated with the second batch to give $\text{ClF}_6^+ \text{AuF}_6^-$ in quantitative yield:



The x-ray powder pattern of the yellow crystalline solid is unlike that for any other $\text{AF}_6^+ \text{BF}_6^-$ salt. It is curious that although $\text{IF}_6^+ \text{AuF}_6^-$ and $\text{BrF}_6^+ \text{AuF}_6^-$ have the same structure as $\text{IF}_6^+ \text{AsF}_6^-$, $\text{IF}_6^+ \text{AuF}_6^-$ is not isostructural with the set $\text{IF}_6^+ \text{MF}_6^-$ ($M = \text{Ru, Ir and Pt}$), all of which crystallize in space group C_2/m . Moreover $\text{IF}_6^+ \text{SbF}_6^-$ has a cubic, CsCl-like unit cell, whereas $\text{IF}_6^+ \text{AsF}_6^-$ is NaCl-like.

The Raman spectrum for $\text{ClF}_6^+ \text{AuF}_6^-$ is simple; as expected. The data given in Table 1 show that ν_1 , ν_2 and ν_5 frequencies for the cation are closer than for BrF_6^+ , which are closer than for IF_6^+ . This merging of the vibrational frequencies of ClF_6^+ is more extreme than for any other hexafluoro species. No doubt the small effective size of the heptavalent chlorine atom results in a very compact cation. The ligand crowding (and hence ligand-ligand repulsion) in ClF_6^+ is, presumably, more severe than in any

Table 1. Raman data for ClF_6^+ , BrF_6^+ and IF_6^+ in AuF_6^- salts.

| | ν_1 | ν_2 | ν_5 |
|------------------|---------|---------|---------|
| ClF_6^+ | 647 | --- | 525 |
| BrF_6^+ | 657 | 669* | 404 |
| IF_6^+ | 705 | 726 | 344 |

* Shoulder-of-uncertain frequency.

other case, but detailed understanding of these observations must await a full vibrational analysis.

* * *

1. N. Bartlett, D. E. McKee, C. J. Adams and Z. Zalkin, *J. Chem. Soc. Chem. Comm.* 27 (1973).
2. K. O. Christe, *Inorg. Nucl. Chem. Lett.* 8, 741 (1972).
3. F. O. Roberto, *Inorg. Nucl. Chem. Lett.* 8, 737 (1972).
4. R. J. Gillespie, G. J. Schrobilgen, *J. Chem. Soc. Chem. Comm.* 90 (1974).
5. N. Bartlett, B. G. Deboer, F. J. Hollander, F. O. Sladky, D. H. Templeton and A. Zalkin, *Inorg. Chem.* 13, 780 (1974); N. Bartlett, A. Zalkin, D. L. Ward, R. N. Biagioni and D. H. Templeton, *Inorg. Chem.* 17, 1318 (1978).

RESEARCH PLANS FOR CALENDAR YEAR 1980

Graphite and Related Salts. The structural characterization of the C_xGeF_5 and C_xGeF_6 will be undertaken, with emphasis on synchrotron radiation studies. Both pre-absorption edge and EXAFS data should be of value in settling whether the intercalated species are GeF_5^- and GeF_6^{2-} or some other. Synchrotron radiation data for oriented HOPG samples of C_8AsF_5 will also be obtained in order to determine the relative concentrations of AsF_6^- and AsF_3 at this composition. By exploiting the polarized nature of the radiation it may also be possible to determine the orientation of the polar AsF_3 molecules with respect to the graphite planes. Single crystal x-ray diffraction studies of C_8AsF_6 , in collaboration with Professor D. H. Templeton, will be continued, as will electron diffraction work in collaboration with Professor G. Thomas and his associates. The oxidizing potential and the reversibility of the oxidation and reduction of $\text{C}_x\text{GeF}_5/\text{C}_x\text{GeF}_6$ will be undertaken by incorporating this material as one electrode of an electrochemical cell. The electrode will be compared with the other graphite salts and with metals such as lead and antimony. These experiments will be undertaken in collaboration with the Laboratoire de Chimie du Solide of the Université de Bordeaux I, led by Professor Paul Hagenmuller. This is the foremost laboratory in the development of solid electrolytes (such as $\text{PbF}_2/\text{SbF}_3$ solid solutions) compatible with these graphite salt electrodes.

We will continue attempts to prepare graphite salts containing both an anion X^- (e.g., SO_3F^-) and its protic acid HX (e.g., HSO_3F), with X^-/HX ratios ranging from large to small numbers. These materials will be incorporated as electrodes in electrochemical cells so that the influence of the X^-/HX ratio on the potential can be traced. Simultaneously a search for a compatible solid electrolyte, which conducts primarily by proton transfer, will be undertaken.

Electrical conductivity studies of the graphite salts undertaken in collaboration with Dr. T. E. Thompson of SRI International will continue. We will be particularly concerned to determine the

factors which produce the best basal-plane conductivity in the graphite salts. Since the graphite/AsF₅/AsF₆ system is the one most open to chemical manipulation the emphasis will probably be placed on it.

Other Delocalized-Electron Solids. Synchrotron radiation studies are planned for the poly-paraphenylene AsF₆ salt (prepared by electron-oxidation of benzene) to support the vibrational spectroscopic data. Similar studies will be carried out on the coronene salts C₂₄H₁₂²⁺AsF₆⁻ and C₂₄H₁₂²⁺(AsF₆⁻)₂. Efforts will continue to find solvents for the production of more crystalline material from all of these polymeric materials.

The application of the oxidizers SO₃F, O₂⁺ and C₆F₆⁺ will be explored in the removal of electrons from polymeric materials such as long chain sulfur (plastic sulfur). Electron-oxidation of closocarboranes, e.g., 1,2, C₂B₁₀H₁₂ (which has a very stable 'aromatic' electron configuration) will also be attempted. Cations such as C₂B₁₀H₁₂⁺ would be large and paramagnetic and the unpaired spin an excellent bonding probe.

Complex Fluorides for Solid Electrolytes. The best fluoride ion conductors usually involve mixtures of fluorides of metal ions which retain a 'non-bonding' valence electron pair. Excellent examples are PbF₂ and SbF₃. It is likely that the facile transfer of F⁻ through a mixture of the salts is aided by the 'jelly-fish nature' of the coordination sphere about each ion. This depends on steric activity of the non-bonding electron pair and variable coordination number.

It is probable that some complex fluorides could be superior to PbF₂/SbF₃, and also more stable than are they to oxidation. We propose to attempt the synthesis of salts which contain "jelly-fish" cations or anions or both, which, in combination with alkali fluoride would yield a new salt which would dissolve in the first. A typical candidate is SF₃⁺GeF₅⁻ both ions of which exhibit 'jelly-fish' behavior. This is presently unknown, although (SF₃)₂GeF₆ is known. The possibility of salts like NaSF₃GeF₆ will be explored, as will the fundamental factors which determine the stability of one salt, e.g., SF₃⁺GeF₅⁻ relative to another e.g., (SF₃)₂GeF₆. The fluoride-ion conductor properties of each salt studied will be undertaken.

1979 PUBLICATIONS AND REPORTS

Other Publications

1. N. Bartlett, P. A. Cox, J. E. Fischer, W. B. Fox, A. J. Heeger, K. J. Klabunde and G. Shirane, "Metal-Rich Systems," in *Molecular Metals*, William E. Hatfield, Ed., Plenum Publishing Corp., New York, 1979.
2. N. Bartlett, R. N. Biagioni, E. M. McCarron, B. W. McQuillan and F. L. Tanzella, "Salts of Aromatic Cations and Related Graphite Salts," in *Molecular Metals*, William E. Hatfield Ed., Plenum Publishing Corp., New York, 1979.

3. N. Bartlett, E. M. McCarron, B. W. McQuillan and T. E. Thompson, "Novel Graphite Salts and Their Electrical Conductivities," *Synthetic Metals* **1**, in press.

LBL Reports

1. E. M. McCarron and N. Bartlett, "Composition and Staging in the Graphite-AsF₆ System and Its Relationship to Graphite-AsF₅," LBL-10190.
2. E. M. McCarron, V. J. Gramac and N. Bartlett, "Fluorogermanium(IV) Salts of Graphite - A System in Equilibrium with Elemental Fluorine," LBL-10228.
3. A. S. Robertson, B. W. McQuillan and N. Bartlett, "An Extended X-Ray Absorption Fine-Structure Study of Arsenic Trifluoride, Arsenic Pentafluoride and Some Hexafluoroarsenates(V)," LBL-10229.
4. B. W. McQuillan, A. S. Robertson and N. Bartlett, "EXAFS and Crystallographic Studies of Graphite Hexafluoroarsenates(V) and Graphite - Arsenic Pentafluoride Intercalates," LBL-10230.
5. J. Passmore, J. Trotter, F. Einstein, T. J. Richardson and N. Bartlett, "The Crystal Structure of ClO₂⁺IrF₆⁻ and Remarks on the Synthesis of Fluoro-chlorine Cation Salts," LBL-10231.
6. N. Bartlett, A. K. Cheetham, D. H. Templeton, A. Zalkin and B. Zemva, "The Crystal Structures of the 2:1, 1:1 and 1:2 Adducts which XeF₂ makes with XeF₅⁺AsF₆⁻ and the Pathway of XeF₂ towards XeF⁺F⁻," LBL-10232.

Invited Talks

1. N. Bartlett, "Unusual Oxidizers and their Application in the Synthesis of New Synthetic Metals" Inorganic Group of the North Jersey Section of the American Chemical Society, April 23, 1979.
2. N. Bartlett, "Noble-Gas Chemistry" Chemistry Department Lecture Series, Ithaca College, New York, April 24, 1979.
3. N. Bartlett, "The Synthesis of New Electron-Delocalized Solids" Symposium on Properties of Low Dimensional Solids, at the American Chemical Society Meeting, Honolulu, Hawaii, April 2-5, 1979.
4. N. Bartlett, "Salts of Aromatic Cations and Graphite and Boron Nitride Relatives" Symposium on Fluorine as a Probe for Structure and Mechanism Studies, American Chemical Society Meeting, Honolulu, Hawaii, April 2-5, 1979.
5. N. Bartlett, "New Graphite and Boron Nitride Salts and Related Delocalized Electron Systems" Stanford University Chemistry-Chemical Engineering Industrial Affiliates Symposium, Palo Alto, California, June 22, 1979.
6. N. Bartlett, "Novel Cations," Plenary Lecture, 9th International Symposium on Fluorine Chemistry, Avignon, France, September 3-7, 1979.
7. N. Bartlett, "Novel Graphite and Boron Nitride Salts" Symposium on the Structure and Properties of Highly Conducting Polymers and Graphite at IBM

Research Laboratories, San Jose, California, March 29-30, 1979.

8. N. Bartlett, "Noble-Gas Chemistry - What has it Taught Us?", Albert Einstein Centennial Lecture, Simon Fraser University, Burnaby, B. C. Canada, December 13, 1979.

9. N. Bartlett, "New Synthetic Metals", Chemistry Department Seminar, Simon Fraser University, December 14, 1979.

10. N. Bartlett, "Noble Gas Chemistry and Other Unusual Oxidations" Chemistry Department Seminar, San Jose State University, San Jose, California, May 1, 1979.

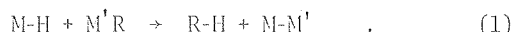
g. Transition Metal Catalyzed Conversion of CO, NO, H₂ and Organic Molecules to Fuels and Petrochemicals*

Robert G. Bergman, Investigator

1. MECHANISM OF THE REACTION BETWEEN ORGANO-TRANSITION METAL ALKYL AND HYDRIDES. A MODEL FOR THE ALDEHYDE-FORMING STEP IN THE OXO PROCESS[†]

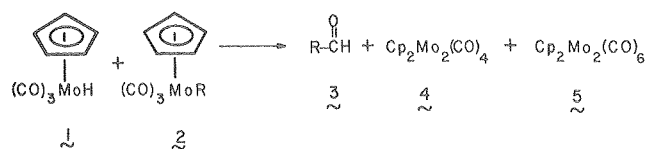
William D. Jones and Robert G. Bergman

The identification of primary reaction steps in organotransition metal chemistry (e.g., oxidative addition, reductive elimination, β -elimination, etc.) was an important advance in understanding organometallic reaction mechanisms.¹ These steps, characteristic of processes which occur at a single metal center, are now being augmented by the identification of steps which involve more than one metal.² One such process which has appeared repeatedly recently is the reaction of a metal hydride and a metal alkyl (or acyl) to give a product containing a new C-H bond:



The growing ubiquity and apparent facility of metal hydride-metal alkyl reactions makes it important to have good mechanistic information available on these processes. After briefly surveying the reactions of several well characterized hydrides and alkyls, we discovered that molybdenum hydride **1** and corresponding alkyls **2** undergo an especially clean and quantitative reaction which leads to aldehyde **3** and dimers **4** and **5** (Scheme 1). The

Scheme 1



- a** series: R=CH₃
b series: R=C₂H₅
c series: R=CH₂C₆H₅
d series: R=CD₃
e series: R=CD₂C₆D₅

methyl and ethyl complex **2a** and **2b** are converted into aldehydes **3a** and **3b** at temperatures between 25 and 50°C, **2b** reacting substantially more rapidly. Yields are quantitative and no trace of alkanes are observed. These reactions give clean second-order kinetics; rate constants are listed in Table 1.

It has been reported³ that **1** reacts with ethylene to give ethyl complex **2b**. Given that **1** and **2** are converted efficiently into aldehyde, it appeared that, if dimer **5** could be reconverted

Table 1. Rate constants for reaction between CpMo(CO)₃H and CpMo(CO)₃R in THF-d₈.^a

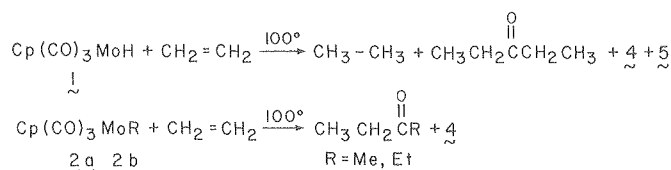
| alkyl | T, °C | k, M ⁻¹ s ⁻¹ |
|-------|-------|------------------------------------|
| 2a | 50 | 2.5 x 10 ⁻⁴ |
| 2b | 50 | 4.0 x 10 ⁻³ |
| 2b | 25 | 8.5 x 10 ⁻⁴ |
| 2c | 50 | 2.5 x 10 ⁻⁵ |
| 6a | 50 | 2.3 x 10 ⁻⁴ |

^aRates measured by monitoring disappearance of starting material resonances in the 180-MHz NMR spectrum.

into **1** with H₂, the reactions reported here could be used to design a catalytic hydroformylation system. We have found, however, that, contrary to the earlier report, **1** and ethylene do not give **2b**. At 100°C, **1** and ethylene do react, as reported earlier,³ to give a new material containing ethyl absorptions in the NMR, but these are very different from those associated with independently prepared **2b**. We have now found that the organic products are volatile and turn out to be a mixture of ethane (36%) and 3-pentanone (15%) (Scheme 2). To determine whether a molybdenum alkyl is an intermediate in this transformation, we examined the reaction between ethyl complex **2b** and ethylene. In this reaction diethyl ketone⁴ is formed in ~10% yield, even in the absence of added hydride **1**. Similarly, methyl complex **2a** reacts with C₂H₄ at 100°C to give 2-butanone in ~50% yield.

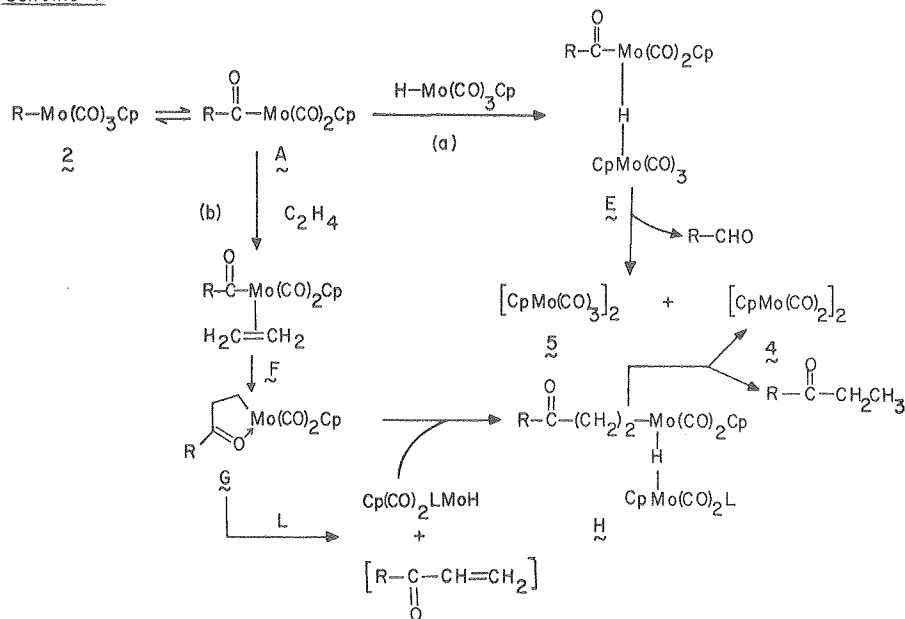
The chemistry of this molybdenum system mimics that observed in the oxo reaction very closely. The only major difference appears to be the difficulty of converting [CpMo(CO)₃]₂ into **1** by reaction with H₂; this prevents closure of the catalytic cycle. Even the formation of ketones from cobalt acyls and olefins has been observed when only small amounts of hydride are present.⁵ Concerning the mechanism of the molybdenum reac-

Scheme 2



*This work was supported by the Division of Chemical Sciences, Office of Basic Energy Sciences, U.S. Department of Energy.

Scheme 3



tions reported here, a radical pathway is ruled out, except as a minor component in the benzyl system. An alternative consistent with our data is illustrated in Scheme 3. This postulates initial isomerization of **2** to metal acyl **A**, followed by rapid entry of metal hydride into the unsaturated acyl coordination sphere and reductive elimination of aldehyde. The overall similarity of the molybdenum and cobalt systems reinforces the recent conclusions of others⁶ that the aldehyde-forming step in the oxo process also involves reaction between a cobalt hydride and cobalt acyl.

* * *

[†]Brief version of LBL-9050; *J. Amer. Chem. Soc.* **101**, 5447 (1979).

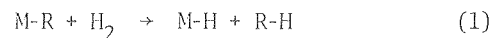
1. J. Halpern, *Chem. Eng. News* **44**(44), 68 (1966); J. P. Collman, *Acc. Chem. Res.* **1**, 136 (1968); J. Halpern, *ibid.* **3**, 386 (1970).
2. See, for example, M. H. Chisholm, D. A. Haitko, and C. A. Murillo, *J. Am. Chem. Soc.* **100**, 6262 (1978); J. P. Collman, R. G. Finke, P. L. Matlock, R. Wahren, and J. I. Brauman, *ibid.* **98**, 4685 (1976); M. P. Brown, R. J. Puddephatt, and C. E. E. Upton, *J. Chem. Soc., Dalton Trans.* 2490 (1976); J. E. Bulkowski, P. L. Burk, M. F. Ludmann, and J. A. Osborn, *J. Chem. Soc. Chem. Commun.* 498 (1977); C. P. Kubiak and R. Eisenberg, *J. Am. Chem. Soc.* **99**, 6129 (1977); M. M. Olmstead, H. Hope, L. S. Benner, and A. L. Balch, *ibid.* **99**, 5502 (1977); J. P. Collman, R. K. Rothrock, R. G. Finke, and F. Rosemunch, *ibid.* **99**, 7381 (1977); J. C. Smart and D. J. Curtis, *Inorg. Chem.* **17**, 3290 (1978); R. Poilblanc, *Nouv. J. Chim.* **2**, 145 (1978); S. A. R. Knox, R. F. D. Standfield, F. G. A. Stone, M. J. Winter, and P. Woodward, *J. Chem. Soc., Chem. Commun.* 221 (1978); J. Evans, S. J. Okrasinski, A. J. Pribula, and J. R. Norton, *J. Am. Chem. Soc.* **98**, 4000 (1976); N. E. Schore, C. Ilenda, and R. G. Bergman, *ibid.* **98**, 7436 (1976).
3. R. A. Schunn, *Inorg. Chem.* **9**, 2567 (1970).

4. Prepared according to the method of T. S. Piper and G. J. Wilkinson, *J. Inorg. Nucl. Chem.* **3**, 104 (1956).
5. R. F. Heck, *Acc. Chem. Res.* **2**, 10 (1969), and references cited therein.
6. N. H. Alemdaroglu, J. M. L. Penninger, and E. Oltay, *Monatsh. Chem.* **107**, 1043 (1976).

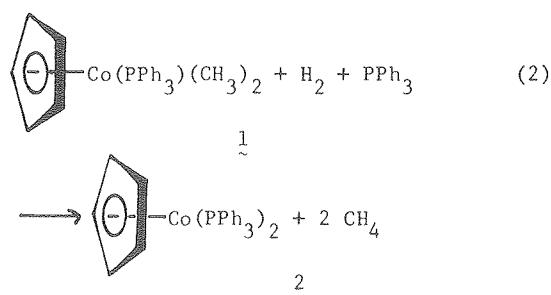
2. CONVERSION OF METAL ALKYL INTO ALKANES BY HYDROGENATION

Andrew H. Janowicz and Robert G. Bergman

We are studying the mechanism of metal alkyl hydrogenation (Eq. 1).



The mechanism can lead us to a better understanding of portions of significant industrial processes such as hydroformylation and homogeneous hydrogenation, where such a reaction is postulated to be the product-forming step in the process.¹ The specific system we are investigating is the reaction of $(\eta^5-C_5H_5)CoPPh_3(CH_3)_2$, **1**, with H_2 which yields two equivalents of methane and $(\eta^5-C_5H_5)Co(PPh_3)_2$, **2**, as the isolable organometallic product (Eq. 2).



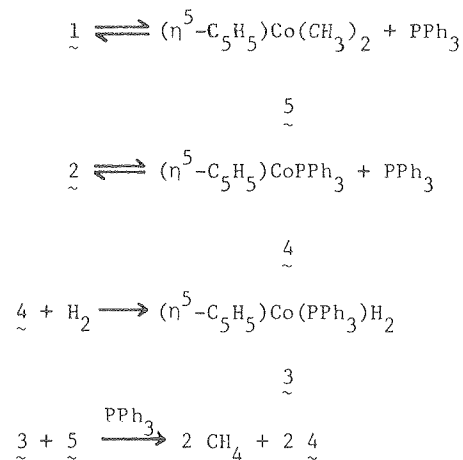
Adding ligand to the above reaction significantly retards the rate of hydrogenation. In fact, an added equivalent of PPh_3 leads to an induction period of almost 20 hours, while without added PPh_3 , the reaction is complete in two hours (Fig. 1). Since an induction period sometimes accompanies a radical chain mechanism, the hydrogenation of $\underline{1}$ was carried out with D_2 in the presence of a good radical trap,² 1,4-cyclohexadiene (CHD). In the absence of CHD, $\underline{1} + \text{D}_2$ yields two equivalents of $98 \pm 3\% \text{CH}_3\text{D}$. With CHD present, radicals should give considerable amounts of CH_4 . However, we find that the methane produced in this reaction is $>4:1 \text{CH}_3\text{D}:\text{CH}_4$, a result inconsistent with a major radical pathway. We believe the small amount of CH_4 formed in the reaction is linked to thermal decomposition or oxidation products of $\underline{1}$ due to the longer reaction times needed (13 hours at $50\text{--}55^\circ\text{C}$ for 50% reaction vs. complete reaction in two hours at 45°C without added trapping agent; the 1,4-cyclohexadiene seems to act as a ligand in slowing down the reaction).

As an alternative explanation for the induction period, we suggest an autocatalytic mechanism, involving catalysis by the product $\underline{2}$. In order to test this hypothesis, the hydrogenation of solutions of $\underline{1}$ containing added $\underline{2}$ was examined. When 15 mole % $\underline{2}$ was added to the hydrogenation mixture (containing one equivalent of PPh_3), the induction period disappeared completely. In fact, the hydrogenation of $\underline{1}$ in the presence of three equivalents of PPh_3 and one equivalent of $\underline{2}$ also proceeds without an induction period, albeit somewhat slower than in the presence of one equivalent of both PPh_3 and $\underline{2}$.

The above results suggest that a previously unknown dihydride species, $(\eta^5\text{-C}_5\text{H}_5)\text{Co}(\text{PPh}_3)_2\text{H}_2$, $\underline{3}$, is the actual hydrogenating agent formed continu-

ously in small amounts by the reaction $(\eta^5\text{-C}_5\text{H}_5)\text{CoPPh}_3$, $\underline{4}$, and hydrogen. A possible mechanism is shown in Scheme 1. This mechanism is also consistent with dissociation as an important step along the mechanistic pathway. We have also

Scheme 1



found that dihydrides such as $(\eta^5\text{-C}_5\text{H}_5)_2\text{MoH}_2$ react rapidly with $\underline{1}$ to yield methane. Work is presently in progress to try to obtain a stable Co(III) dihydride as well as to work out the specific kinetics of hydrogenation with other alkyl derivatives of $\underline{1}$.

* * *

1. M. Orchin and W. Rupilius, *Catal. Rev.* **6**, 85 (1972).
2. L. Kaplan, "Free Radicals," in *Reactive Intermediates*, Vol. 1, M. Jones, R. and R. A. Moss, eds., (John Wiley and Sons, New York, 1978).

3. REACTION OF A METAL ALKYL WITH ETHYLENE AS A MODEL FOR ZIEGLER-NATTA POLYMERIZATION. EVIDENCE FOR THE OLEFIN INSERTION MECHANISM^{††}

Eric R. Evitt and Robert G. Bergman

Dimerization, oligomerization, and Ziegler-Natta polymerization of ethylene and other olefins are among the most important homogeneous catalytic processes.¹ It has long been assumed that these reactions involve insertion of olefin into the metal-carbon bond of an intermediate metal alkyl.^{2,3} Green and his coworkers have pointed out recently, however, that there are no unambiguous examples--in either early or late transition metal complexes--in which a well-characterized metal-alkyl-olefin compound has been observed to undergo this insertion reaction.⁴ This has led them to suggest an alternative mechanism for apparent insertion reactions which involves α -elimination to form a transient carbene complex. In this article, we report that the well-characterized^{3e,5} cobalt

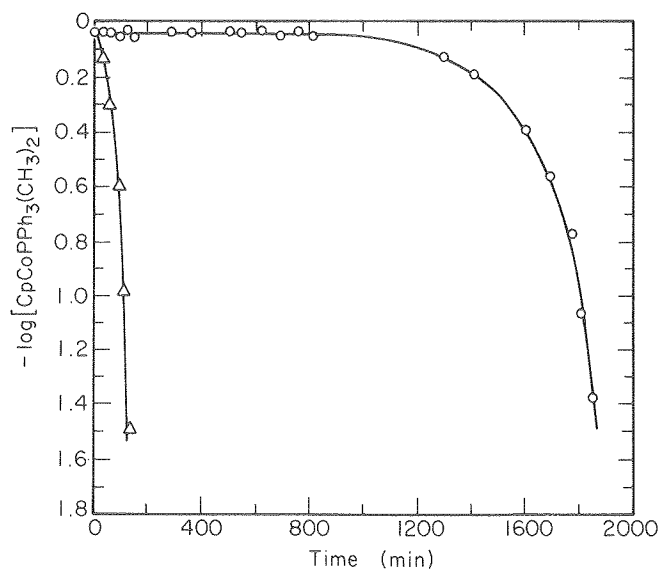
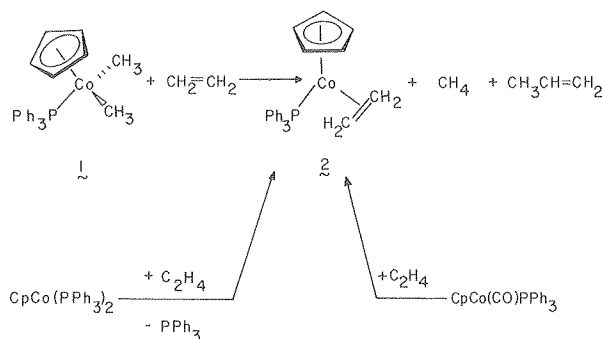


Fig. 1. Time dependence of the log of the concentration of starting complex $\underline{1}$ in benzene solution at 25° under approximately 3 atm H_2 . Legend: O, with no added complex $\underline{2}$; Δ , with 1.0 equivalent of added complex $\underline{2}$. (XBL 801-7811)

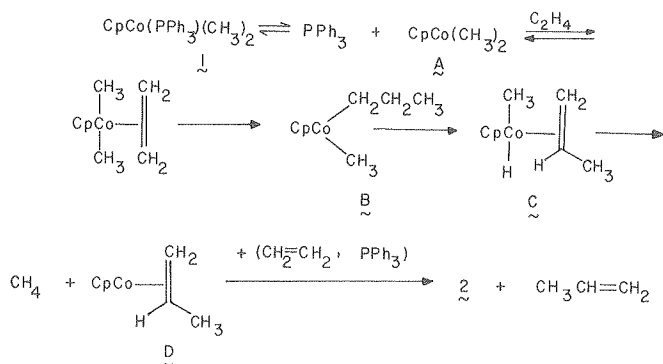
complex 1 (Scheme 1) reacts cleanly with ethylene, giving propylene and methane as products. We have carried out a labeling study which demonstrates (in agreement with the classical view) that insertion, rather than α -elimination, is the critical step in the mechanism of this reaction.

Scheme 1

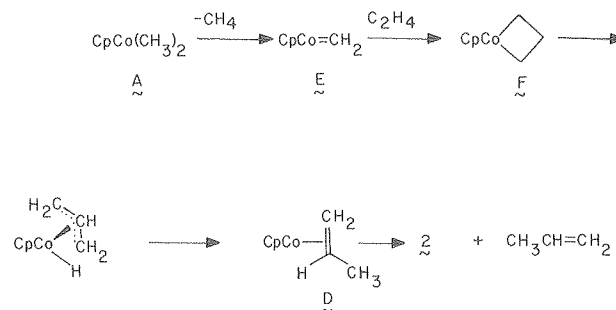


Reaction of 1 ethylene at 76° gave methane (91%), propene (84%), and complex 2 (100%). These products can be explained by either a classical mechanism involving insertion of ethylene into a metal-carbon bond (Scheme 2), or by the Green-Rooney alternative involving α -elimination (Scheme 3). Because our system involves characterizable complex 1, it is possible to carry out labeling experiments which clearly distinguish these two alternatives. This involves treatment of appropriately labeled 1 with labeled and unlabeled ethylene, and analysis of the isotropic distribution in the methane and propene produced. When 1-d₂₁ (completely deuterated phosphine and methyl groups) was treated with ethylene, mass spectral analysis of the product methane showed that it was identical with CD₃H synthesized by quenching a portion of the CD₃MgI, used to prepare 1-d₂₁, with H₂O. Similar analysis of the propene produced showed it to be $\geq 96\%$ propene-d₃. In a second experiment, reaction of 1-d₂₁ with ethylene-d₄ gave 95% CD₄. These results demonstrate that

Scheme 2



Scheme 3



(a) the new methane hydrogen is derived from the ethylene and from no other hydrogen source in the system (cyclopentadienyl ring, solvent, phosphine) and (b) a complete methyl group is transferred to the ethylene. This clearly establishes insertion, rather than α -elimination, as the mechanism responsible for ethylene methylation by complex 1.

It is still certainly possible that Ziegler-Natta polymerization and/or other apparent insertion reactions take place by the α -elimination route. However, in our opinion, those in favor of this mechanism must now shoulder the burden of proof for establishing it.

* * *

[†]Brief version of LBL-8471; *J. Am. Chem. Soc.* **101**, 3973 (1979).

[‡]Supported in part by the National Science Foundation.

1. L. S. Reich and A. Schindler, *Polymerizations by Organometallic Compounds* (Wiley-Interscience, New York, 1966); D. G. H. Ballard, *J. Polym. Sci.* **13**, 2191 (1975); M. M. Taqui Khan and A. E. Martell, *Homogeneous Catalysis by Metal Complexes*, Vol. II (Academic Press, New York, 1974), pp. 110-117.
2. See, for example, G. Henrici-Olivé and S. Olivé, *Fortschr. Chem. Forsch.* **67**, 107 (1976); D. L. Thorn, and R. Hoffman, *J. Am. Chem. Soc.* **100**, 2079 (1978); R. F. Heck, *ibid.* **90**, 5518 (1968); H. A. Dieck and R. F. Heck, *ibid.* **96**, 1133 (1974); M. P. Cooke, Jr. and R. M. Parlman, *ibid.* **99**, 5222 (1977) and **97**, 6863 (1975); B. L. Booth, M. Gardner, and R. N. Haszeldine, *J. Chem. Soc., Dalton Trans.* 1856 (1975); D. E. James and J. K. Stille, *J. Am. Chem. Soc.* **98**, 1810 (1976).
3. For some apparent examples of insertion of alkynes into metal-carbon σ -bonds, see (a) H. C. Clark and R. J. Puddephatt, *J. Chem. Soc., Chem. Commun.* 92 (1970); (b) M. H. Chisholm and H. C. Clark, *Acc. Chem. Res.* **6**, 202 (1973); (c) S. J. Tremont and R. G. Bergman, *J. Organomet. Chem.* **140**, C12 (1977); (d) H. G. Alt, *ibid.* **127**, 349 (1977); (e) E. R. Evitt and R. G. Bergman, *J. Am. Chem. Soc.* **100**, 3237 (1978).
4. K. J. Ivin, J. J. Rooney, C. D. Stewart, M. L. H. Green, and R. Mahtab, *J. Chem. Soc., Dalton Trans.* 262 (1979).
5. R. B. King, *Inorg. Chem.* **5**, 82 (1966); H. Yamazaki and N. Hagihara, *J. Organomet. Chem.* **21**, 431 (1970).

4. REACTION OF A BRIDGED BINUCLEAR DIALKYLCOBALT COMPLEX WITH CO AND PHOSPHINES. OBSERVATION OF COMPETING INTER- AND INTRAMOLECULAR METHYL TRANSFER †‡

Henry E. Bryndza and Robert G. Bergman

The binuclear dialkyl complex **1** reacts rapidly with carbon monoxide at 25°C, leading to a quantitative yield of **2** and acetone, a process in which a binuclear transition metal complex mediates the formation of two new carbon-carbon bonds (Chart 1). In a previous study,¹ we established that complex **3** is an intermediate in this reaction and that substantial amounts of d₃-acetone are produced in a carbonylation of equimolar mixtures of **1**-d₆ and **1**-d₀. This demonstrates that an intermolecular process occurs during the carbonylation of **1**.

In order to determine whether this intermolecular process is on the direct pathway leading from **1** to **3**, we have now prepared **7** (Chart 2), a complex analogous to **1**, but having its two cyclopentadienyl rings joined by a methylene bridge. We find this structural modification allows us to control the intramolecularity of the carbonylation reaction. In addition, **7** undergoes a remarkable reaction with phosphines which sharply restricts mechanistic possibilities for these reactions.

Complex **7** is less reactive than **1** and requires temperatures of 70°C to achieve carbonylation (to

a mixture of **5** and acetone, as shown in Chart 3) at a reasonable rate. Under these conditions, the carbonylation can be made to follow a predominantly intra- or intermolecular pathway by varying the concentration of starting complex **7** as shown in the crossover experiments listed in Table 1.

Treatment of **1** with PPh₃ gave a complicated reaction leading to some acetone as well as several carbonyl-phosphine complexes. We believe this is due, in part, to the rate of reaction of **1** with PPh₃ being comparable to the rate of thermal decomposition of **1**. In contrast, **7**, stable at room temperature, reacts rapidly with PPh₃ to give only **8** in quantitative yield (Chart 3). Despite the cleanliness of this reaction, crossover experiments indicate once again that inter- and intramolecular processes are occurring which are dependent upon the concentration of **7** (Table 1).

The production of only complex **8** strictly limits the mechanistic alternatives. In fact, the appearance of two CO ligands bound to one cobalt in a system where the mixed phosphine carbonyl complex is known to be more stable requires that one cobalt retain its bonding to both carbonyls throughout the entire reaction. This restriction leaves little reasonable alternative to path (b) on Chart 4 and rules out our initial hypothesis outlined in path (a).

Kinetic studies provide further details concern-

Chart 1

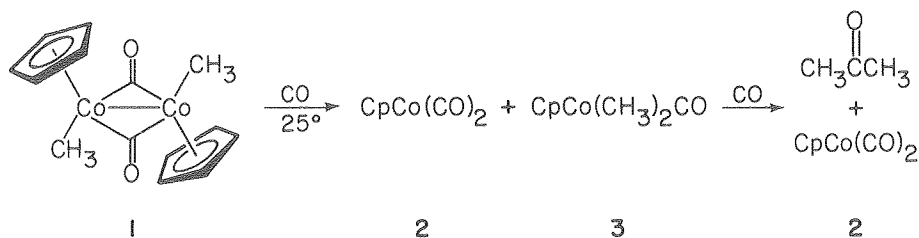


Chart 2

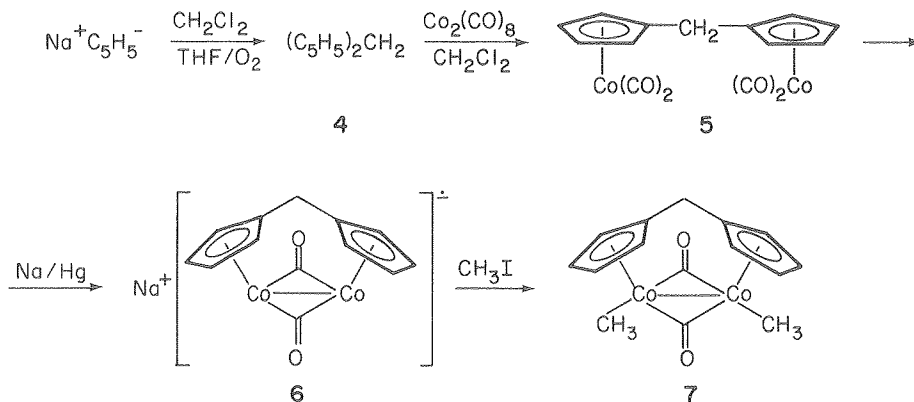
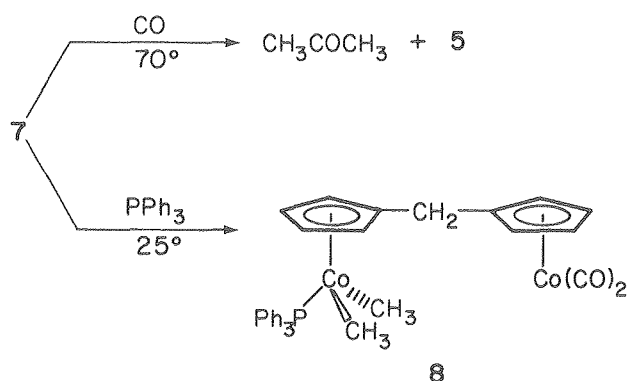


Chart 3



ing the intimate mechanism of the first step of this reaction. Two distinct possibilities exist for the generation of species C: either 7 and phosphine react in a direct associative process or reaction proceeds through an unsaturated unstable intermediate, such as E, which is then trapped by phosphine to yield C. The dependence of the reaction rate upon phosphine dramatically confirms the latter hypothesis. Reactions of 7 with excess PPh₃ show pseudo-first order kinetics in the conversion of 7 to 8. As (PPh₃) is raised from relatively low absolute concentrations the observed reaction rate becomes independent of phosphine as shown in Fig. 1. This is exactly the behavior predicted by the reaction scheme in Chart 5. Analysis of the kinetic data yields $k_1 = 1.28 \times 10^{-4} \text{ sec}^{-1}$ and $k_{-1}/k_2 = 4.3 \times 10^{-2} \text{ M}^{-1}$.

Chart 4

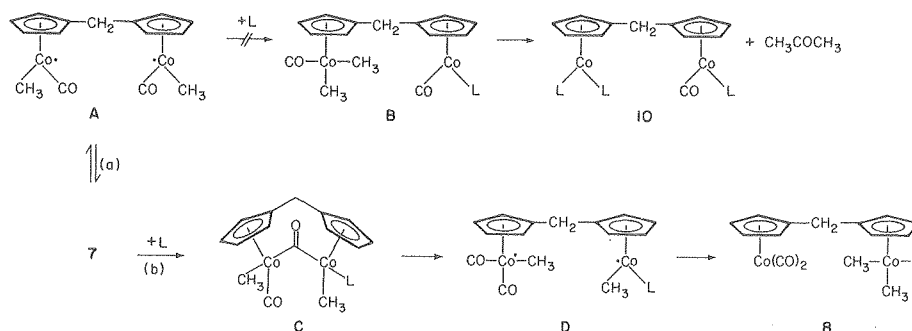


Table 1. Isotope labeling data obtained in crossover experiments on the reaction of mixtures 7-d₀ and 7-d₆ with CO and PPh₃.

| Starting Complex (%) Total Conc. (m) | 7-d ₀ | 7-d ₆ | Entering Ligand | T (°C) | Acetone Products ^c | | | Molecularity | |
|--|------------------|------------------|-------------------------------|--------|-------------------------------|----------------|----------------|--------------|---------|
| | | | | | d ₀ | d ₃ | d ₆ | %Intra- | %Inter- |
| 0.25 | 53 | 47 | CO ^a | 70 | 40 | 28 | 32 | 44 | 56 |
| 0.05 | 55 | 45 | CO ^a | 70 | 52 | 5 | 43 | 90 | 10 |
| 0.25 | 46 | 54 | PPh ₃ ^b | 25 | 38 | 16 | 46 | 67 | 33 |
| 0.05 | 49 | 51 | PPh ₃ ^b | 25 | 49 | 1 | 50 | 98 | 2 |
| 0.25 | 69 | 31 | PPh ₃ ^b | 70 | 69 | 3 | 28 | 93 | 7 |

^a Toluene solvent ^b Benzene solvent ^c Isotope Analysis was by GC/MS. Acetone was obtained as the direct product of the carbonylation reaction. In the PPh₃ reaction, product 8 was first diluted to a concentration $\leq 0.05 \text{ M}$ and then carbonylated to generate acetone for GC/MS analysis (the run at 0.05 M 7 precludes the possibility of significant label scrambling during the carbonylation of 8 at these concentrations).

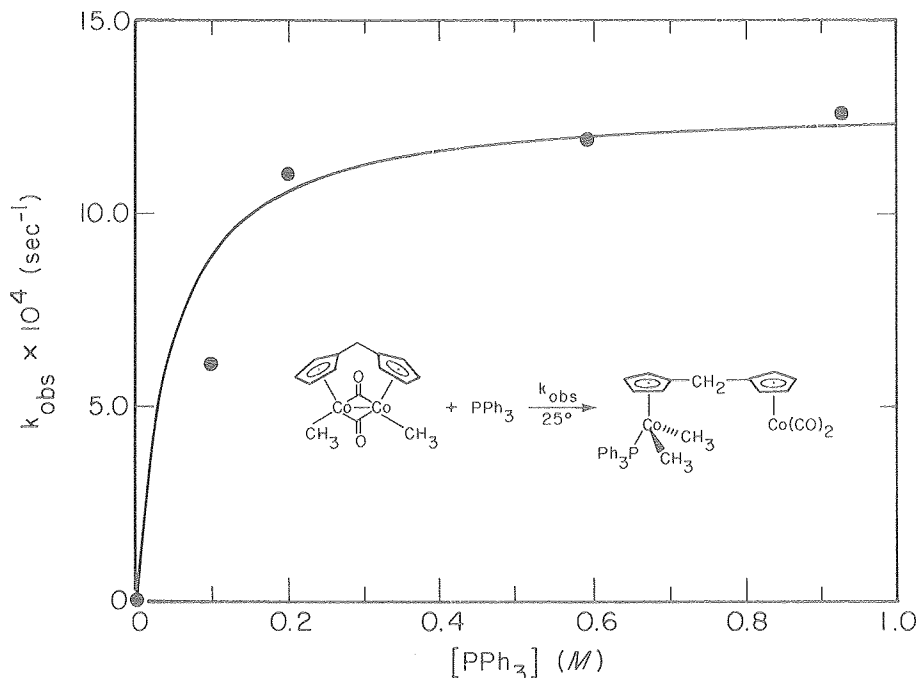
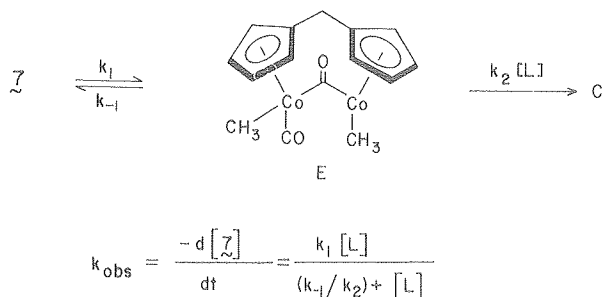


Fig. 1. Dependence of the pseudo-first-order rate constant for reaction of $\underline{7}$ with excess PPh_3 upon the concentration of PPh_3 . (XBL 802-8223)

Chart 5



This study emphasizes that even when organometallic reactions are kinetically well-behaved and give only one product in quantitative yield, it is critically important to carry out crossover experiments to test their intermolecularity. In this case such experiments, combined with the specific nature of the transformation involved, have allowed us to delineate especially sharply the mechanism of carbon-carbon bond formation mediated by this binuclear organotransition metal complex.

* * *

[†]Brief version of LBL-9027; J. Am. Chem. Soc. 101, 4766 (1979).

[‡]Supported in part by the National Science Foundation.

1. N. E. Schore, C. S. Ilenda, and R. G. Bergman, J. Am. Chem. Soc. 98, 7436 (1976).

5. REVERSIBLE METAL-TO-METAL METHYL TRANSFER IN η^5 -CYCLOPENTADIENYL(TRIMETHYLPHOSPHINE)DIMETHYL-COBALT(III)[†]

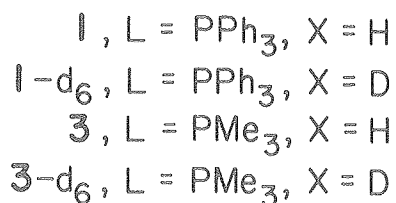
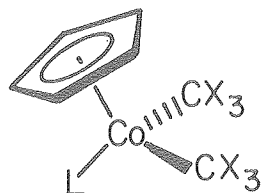
Henry R. Bryndza, Eric R. Evitt and Robert G. Bergman

Although hydride and halogen ligands which bridge two (or more) metals are ubiquitous in organotransition metal chemistry,¹ bridging alkyls are of interest with regard to the ease or difficulty of alkyl transfer between different types of atoms, and because they are species which can provide evidence about the structure of hypervalent carbon. Their occurrence as stable species in a few cases² suggests that they might be accessible as transition states or short-lived intermediates from many of the stable known unbridged metal alkyls.

Alkyl exchange involving the RCpCo(L)Me_2 moiety was implicated during an investigation of the intramolecularity of the carbonylation of $\underline{1}$ (Scheme 1). When a mixture of $\underline{1}$ and 1-d₆ was carbonylated at high (0.25M) concentrations, about 10% d₃-acetone was obtained, in addition to the expected d₀- and d₆-acetones arising from intramolecular reductive elimination. Heating a mixture of $\underline{1}$ and 1-d₆ at 60°C for 40 hrs in the absence of CO, followed by carbonylation at conditions where no d₃-acetone was formed from $\underline{1}$ and 1-d₆ directly, yielded a statistical (1:2:1) ratio of d₀-, d₃- and d₆-acetones. Clearly the scrambling reaction was taking place prior to and independent of carbonylation in the first experiment.

In order to study the alkyl transfer directly by ¹H NMR, we prepared and examined the reaction

Scheme 1



between **1-d₆** and its spectroscopically distinguishable unlabeled analog **2**. When equal amounts of **1-d₆** and **2** were allowed to react at 61.7°, the ¹H NMR spectrum of the mixture showed an increase, with time, in a signal arising from the methyl groups on **1** and a decrease in the analogous signal from **2**. Since addition of excess phosphine slowed the reaction, compounds **3-d₆** and **4-d₀** [in which the P(CH₃)₃ does not dissociate] were prepared. These showed no exchange. However, when **1-d₆** and **4** were heated together a slower, but nevertheless marked, methyl exchange was noted. These results indicate that exchange requires dissociation of one phosphine from a pair of reacting molecules.

By numerical integration using an interactive computer program,³ we were able to satisfactorily model this complex reaction system (Scheme 2) where many chemically distinct but spectroscopically identical species are present. Rate constants are calculated and listed in Table 1 with "methyl

Scheme 2

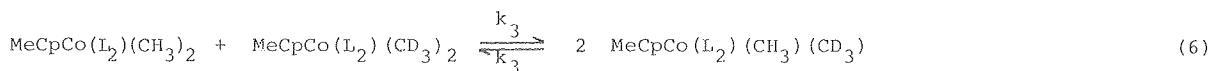
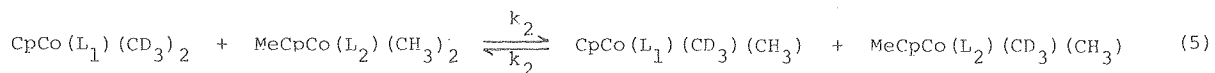
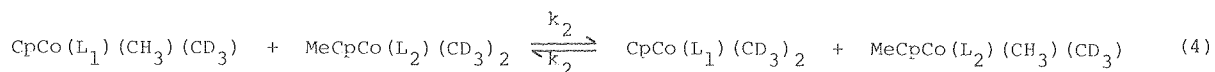
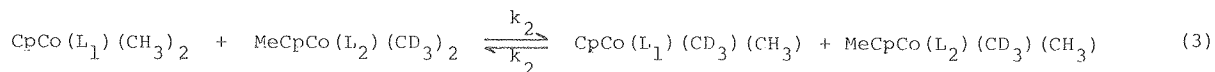
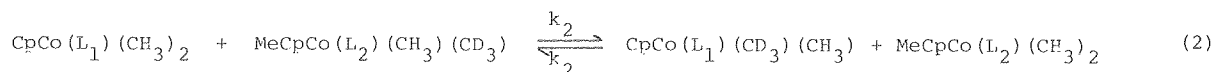
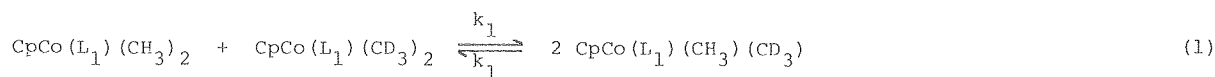


Table 1. Rate constants for methyl exchange reactions shown in Scheme 2 (Solvent: THF-d₈)

| System | Ligands | Rate constants ^a (M ⁻¹ sec ⁻¹) | | |
|--------|---|--|------------------------|------------------------|
| | | k ₁ | k ₂ | k ₃ |
| (a) | L ₁ = L ₂ = PPh ₃ | 3.6 × 10 ⁻³ | 2.2 × 10 ⁻⁴ | 8.3 × 10 ⁻⁶ |
| (b) | L ₁ = PPh ₃ , L ₂ = PMe ₃ | 3.6 × 10 ⁻³ | 8.6 × 10 ⁻⁵ | 0 |
| (c) | L ₁ = L ₂ = PMe ₃ | 0 | 0 | 0 |

^aStarting concentrations of cobalt complexes in each case are 0.175 M.

concentration" vs. time simulations plotted in Figs. 1 and 2.

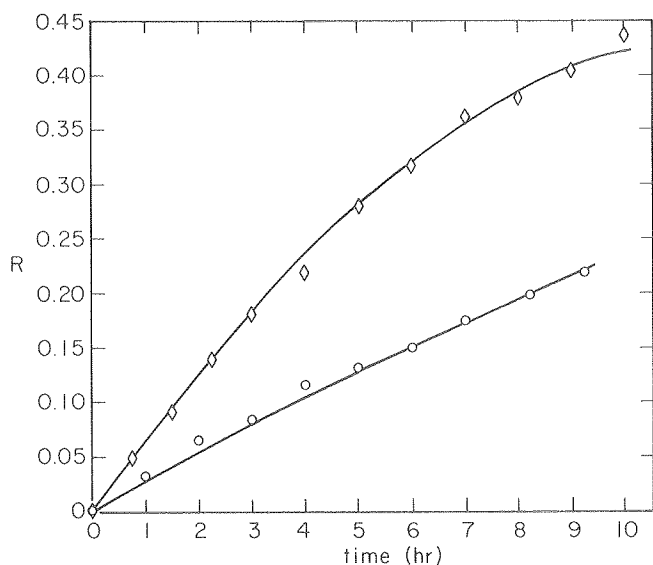


Fig. 1. Computer simulation of the rate of methyl exchange in the reaction between 1-d₆ and 2 (◇) and between 1-d₆ and 4 (○). Diamonds (◇) and circles (○) are experimental data; solid lines are calculated using the rate constants shown in Table 1. The function R plotted on the abscissa is the ratio of integrated metal-bound methyl absorption in the Cp-substituted complex in each reaction, divided by the total CH₃ integration (metal-bound methyls in Cp-substituted plus MeCp-substituted complexes). (XBL 802-8235)

The experimental data allow us to draw some conclusions about the mechanism of methyl exchange. We believe phosphine is first lost from a single reacting molecule in a rapid pre-equilibrium step, followed by reaction with a second, coordinatively saturated, molecule (as shown in Scheme 3). This gives a transition state such as B, which serves to exchange methyl groups reversibly.

Scheme 3

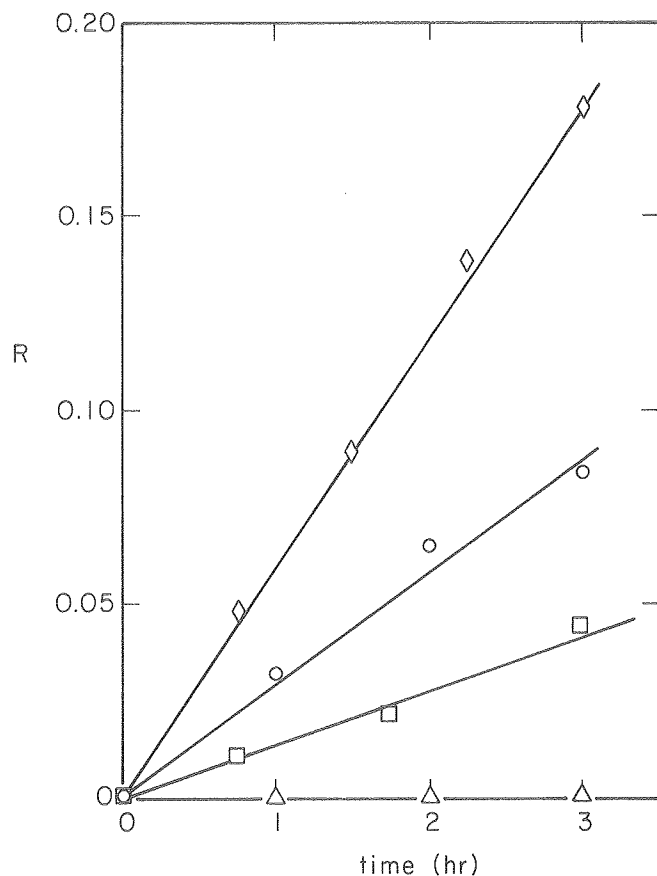
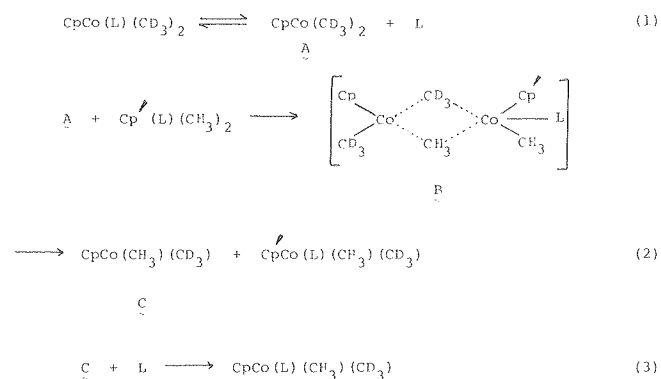


Fig. 2. Plots of the ratio R (see Fig. 1 for definition of this ratio) vs. time for the following reactions: ◇ = 1-d₆ with 2; ○ = 1-d₆ with 4; □ = 1-d₆ with 2 containing excess (1.75 M) PPh₃; △ = 3-d₆ + 4. (XBL 802-8234)

We have obtained preliminary results which indicate this exchange phenomenon may be more general than heretofore suggested. In related studies we have found that 1-d₀ and Cp₂ZrMe₂ show a similar exchange and that 2 and CpCo(PPh₃)(C₂H₄) show related access to the reaction manifold depicted in Scheme 2.

* * *

† Brief version of LBL-10213.

1. For leading references regarding the extensive body of literature dealing with bridging halogen and hydride ligands, see F. A. Cotton and G. Wilkinson, *Advanced Inorganic Chemistry*, 3rd edition, (Wiley-Interscience, New York, 1972), Chapter 22; E. L. Muetterties, ed., *Transition Metal Hydrides*, (M. Dekker, New York, 1971).
2. C. Krüeger, J. C. Sekutowski, H. Berke and R. Hoffman, *Z. Naturforsch.* 33b, 1110-S (1978); M. B. Hursthouse, R. A. Jones, K. M. Abdul Malik and G. Wilkinson, *J. Am. Chem. Soc.* 101, 4128 (1979); R. B. Calvert and J. R. Shapley, *J. Am. Chem. Soc.* 100, 6544 (1978); A. F. Masters, K. Mertis, J. F. Gibson and G. Wilkinson, *Nouv. J. Chim.* 1, 389 (1977); J. Holton, M. F. Tappert, D. G. H. Ballard, R. Pearce, J. L. Atwood and

W. E. Hunter, *J. Chem. Soc., Chem. Commun.* 480 (1976); R. B. Calvert and J. R. Shapley, *J. Am. Chem. Soc.* 100, 7726 (1978).

3. Program MSIM4 developed by D. L. Bunker and F. Houle, University of California, Irvine, CA, and available from the Quantum Chemistry Program Exchange (Program #293).

RESEARCH PLANS FOR CALENDAR YEAR 1980

One of the most important results uncovered in our work during the past year has been the discovery that interaction of transition metal hydrides and metal alkyls (M-H plus M-R reactions) can result in unusually rapid carbon-hydrogen bond formation. We will plan research that will help us understand the mechanism of this fundamental transformation, and examine known processes in which we now believe the process plays a critical role. We first plan to investigate the scope of M-H plus M-R reactions (e.g., how their rate is affected by changing metals, altering structure of the R group, and employing different ligands attached to the metal). We will examine further the reactions of metal alkyls with alkenes, to test our hypothesis that M-H plus M-R reactions are involved in certain of these processes. Many metal-catalyzed transformations of organic materials involve termination steps in which the organic product is released by cleavage of a metal-carbon bond and formation of a carbon-hydrogen bond (e.g., homogeneous hydrogenation, Fischer-Tropsch reactions, hydroformylation). Our recent results suggest that many of these processes also involve reaction between metal hydrides or dihydrides and metal alkyls, rather than direct reaction between the metal alkyl and H₂. A significant part of our effort will be devoted to determining which systems operate by this mechanism and which do not. These investigations should provide a deeper understanding of metal-catalyzed processes, and this understanding should provide more effective means of controlling and improving them.

1979 PUBLICATIONS AND REPORTS

Refereed Journals

- †1. P. L. Watson and R. G. Bergman, "Synthesis and Cyclization Reactions of Alkynyl(η^5 -cyclopentadienyl)tricarbonylmolybdenum and -tungsten Complexes," *J. Am. Chem. Soc.* 101, 2055 (1979).
- ‡2. G. C. Johnson and R. G. Bergman, "Synthesis and Thermal Rearrangement of a Potential Butalene-Anthracene Adduct," *Tetrahedron Lett.* 2093 (1979).
- ‡3. G. C. Johnson, J. J. Stofko, Jr. and R. G. Bergman, "Evidence for the Formation of 1,3-dehydrobenzene Diradicals by Silicon Shift in 1,4-dehydrobenzenes at High Temperature," *J. Org. Chem.*
- ‡4. E. R. Evitt and R. G. Bergman, "Reaction of a Metal Alkyl with Ethylene as a Model for Ziegler-Natta Polymerization. Evidence for the Olefin Insertion Mechanism," *J. Am. Chem. Soc.* 101, 3973 (1979), LBL-8471.
- †5. J. M. Juggins and R. G. Bergman, "Reaction of Alkynes with a Methylnickel Complex: Observation of

a *cis* Insertion Mechanism Capable of Giving Kinetically Controlled *trans* Products," *J. Am. Chem. Soc.* 101(15), 4410 (1979).

- †6. H. E. Bryndza and R. G. Bergman, "Reaction of a Bridged Binuclear Dialkylcobalt Complex with Carbon Monoxide and Phosphines. Observation of Competing Inter- and Intramolecular Metal to Metal Methyl Transfer," *J. Am. Chem. Soc.* 101(16), 4766 (1979), LBL-9027.
7. C. Muller, A. Schweig, W. Grahn, K. P. C. Vollhardt and R. G. Bergman, "The Photoelectron Spectra of 2,5-dehydrotropylidene, 3,6-dehydrooxepin and Fulvenallene," *J. Am. Chem. Soc.* 101, 5579 (1979).
8. W. D. Jones and R. G. Bergman, "Mechanism of the Reaction Between Organotransition Metal Alkyls and Hydrides. A Model for the Aldehyde-Forming Step in the Oxo Process," *J. Am. Chem. Soc.* 101, 5447 (1979), LBL-9050.

LBL Reports

1. Robert G. Bergman, "The Use of Isotope Cross-over Experiments in Investigating Carbon-Carbon Bond Forming Reactions of Binuclear Dialkyl Cobalt Complexes," LBL-10212.
2. Henry E. Bryndza and Robert G. Bergman, "Reversible Metal-to-Metal Methyl Transfer in η^5 -cyclopentadienyl(triphenylphosphine)dimethylcobalt(III)," LBL-10213.
3. William D. Jones, "Reactivity Patterns of Transition Metal Hydrides and Alkyls," LBL-10214 (Ph.D. thesis).

Invited Talks

1. Robert G. Bergman, "Transformations of Organic Compounds Mediated by Mono- and Binuclear Cobalt Complexes," Lawrence Berkeley Laboratory, January 10, 1979.
2. Robert G. Bergman, "Transformations of Organic Compounds Mediated by Binuclear Cobalt Complexes," IBM Research Laboratory, San Jose, California, February 26, 1979.
3. Robert G. Bergman, "Transformations of Organic Compounds Mediated by Binuclear Cobalt Complexes," Johns Hopkins University, Baltimore, Maryland, March 7, 1979.
4. Robert G. Bergman, "Carbon-carbon Bond Forming Reactions Induced by Organotransition Metal Complexes," Service to Inorganic Chemistry Award Symposium, American Chemical Society Meeting, Honolulu, Hawaii, April 2, 1979.
5. Robert G. Bergman, "Transformations of Organic Compounds Mediated by Binuclear Cobalt Complexes," Rice University, Houston, Texas, April 25, 1979.
6. Robert G. Bergman, "Transformations of Organic Compounds Mediated by Binuclear Cobalt Complexes," Harvard-MIT Inorganic Chemistry Colloquium, Cambridge, Massachusetts, April 27, 1979.
7. Robert G. Bergman, "Transformations of Organic Compounds Mediated by Binuclear Cobalt Complexes,"

Mobay Lecture, University of South Carolina,
April 27, 1979.

8. Robert G. Bergman, "Transformations of Organic Compounds Mediated by Binuclear Cobalt Complexes," Allied Chemical Corporation, June 11, 1979.

9. Robert G. Bergman, "Para-Benzyne," Union Carbide Corporation, Bound Brook, New Jersey, June 12, 1979.

10. Robert G. Bergman, "Carbon-Carbon Bond Forming Processes Mediated by Binuclear Transition Metal Complexes," Union Carbide Corporation, South Charleston, West Virginia, June 14, 1979.

11. Robert G. Bergman, "Carbon-Carbon Bond Forming Reactions Induced by Binuclear Cluster Complexes," Industrial Affiliates Conferences, University of Southern California Hydrocarbon Research Institute, August 20, 1979.

12. Robert G. Bergman, "Transformations of Organic Compounds Mediated by Binuclear Cobalt Complexes,"

University of Illinois, Urbana, Illinois,
September 5, 1979.

13. Robert G. Bergman, "Transformations of Organic Compounds Mediated by Binuclear Cobalt Complexes," University of Nebraska, Lincoln, Nebraska, September 7, 1979.

14. Robert G. Bergman, "Carbon-Carbon and Carbon-Hydrogen Bond Forming Reactions Mediated by Organotransition Metal Complexes," Pacific Conference on Chemistry and Spectroscopy, Pasadena, California, October 10, 1979.

* * *

†Supported in part by the National Institutes of Health.

‡Supported in part by the National Science Foundation.

2. Chemical Engineering Sciences

a. High-Pressure Phase Equilibria in Hydrocarbon-Water (Brine) Systems*

John M. Prausnitz, Investigator

1. HIGH-PRESSURE PHASE EQUILIBRIA FOR METHANE-WATER (BRINE)[†]

Wallace B. Whiting and John M. Prausnitz

Geological studies have indicated that there are very large deposits of natural gas in deep reservoirs in Louisiana and the Gulf of Mexico region. These reservoirs, or aquifers, contain natural gas (mostly methane) in contact with water or brine at pressures near 100 MPa. At present, it is not economical to mine these reservoirs, but, in view of the very large deposits, there is much incentive to make such mining attractive. This project is concerned with obtaining some of the fundamental physico-chemical information required to do so.

We seek a molecular-thermodynamic method for calculating the high-pressure phase equilibria of aqueous systems containing methane, small amounts of other light hydrocarbons, nitrogen, and carbon dioxide. Toward that end, we have initiated experimental and theoretical research. The latter is to supply a suitable model for interpreting and correlating previously published and new experimental data.

a. *Experimental.* We are using a high-pressure static-equilibrium apparatus similar in concept to those described by Schneider.¹

We have constructed a high-pressure cell of INCONEL (a nickel-chromium alloy) with a 2.5 cm inside diameter and an inside height of 33 cm. All surfaces within the system exposed to the methane-water (brine) mixture are of INCONEL or type 316 stainless steel. Our major tool for analyzing the samples is a gas chromatograph that we are now calibrating.

The cell is charged with a mixture of methane and water (brine). The temperature of the cell is raised by an external, electrical-resistance heating mantle, and the pressure is increased by a hand-operated piston pump. For various temperature-pressure conditions, small (less than 0.1 cm³ each) samples of both phases (vapor and liquid) are removed for chemical analysis. We determine the concentration of methane and water in the samples by gas chromatography and the concentration of salt by titration.

Our apparatus is designed for temperatures between ambient and 400°C and pressures to 200 MPa. Working within these ranges, we expect to observe the critical region of the methane-water and methane-brine systems. Very little reliable experimental information is available for the former system in this region; none is available for the latter.

To assure safety, we have pressure-tested our system at twice its rated working pressure and are arranging a schedule of periodic inspections by the LBL mechanical engineering department. In the event of equipment failure, operating personnel are protected by the strong barricade of steel, aluminum, and wood erected around the high-pressure portion of the apparatus.

b. *Molecular-Thermodynamic Model.* We have developed three models for the methane-water system. For each model, we have derived a partition function from which we can calculate the fluid-phase equilibria.

1. The perturbed-hard-chain theory of Beret, Donohoe, and Prausnitz^{2,3} for fluid mixtures of nonpolar compounds has been extended to include water by splitting the potential-energy parameter for water into a nonpolar part (from the spherically-symmetric portion of the potential) and a polar part (from the orientation-dependent portion of the potential). The latter is temperature-dependent, approximately proportional to the inverse of the absolute temperature.

2. By superimposing a chemical dimerization hypothesis on the perturbed-hard-chain theory, Gnebling et al.⁴ developed a model that is reasonably accurate for calculating the phase equilibria of polar fluids. In this model, the strong orientational forces between polar molecules are accounted for by postulating the existence of dimers in equilibrium with the monomers. Whiting and Prausnitz⁵ extended this idea to water by considering not only water dimers but trimers, tetramers, and all higher-order *j*-mers. We have extended the dimerization model to methane-water mixtures.

3. By considering the nonrandomness of polar fluids, we have developed a two-fluid theory, which we are applying to the methane-water system. This theory is more fully explained in article 2.c. below.

* This work was supported by the Division of Chemical Sciences, Office of Basic Energy Sciences, U.S. Department of Energy.

Methods 1 and 2 above show semi-quantitative agreement with the limited experimental data now available for methane-water. Method 3, the two-fluid theory, shows better quantitative agreement; we expect to develop it more fully.

Once we have a satisfactory model for methane-water, we expect to allow for salt effects by incorporating some of the work of Pitzer⁶ on aqueous salt solutions.

* * *

[†]Brief version of LBL-9571.

1. G. M. Schneider, Chapter 16, Part 2, in *Experimental Thermodynamics, Volume II*, edited by B. Le Neindre and B. Vodar, Butterworths, London, 1975.
2. S. Beret and J. M. Prausnitz, *AIChE J.* **21**, 1123 (1975).
3. M. D. Donohue and J. M. Prausnitz, *AIChE J.* **24**, 849 (1978).
4. J. Gmehling, D. D. Liu, and J. M. Prausnitz, *Chem. Eng. Sci.* **34**, 951 (1979).
5. W. B. Whiting and J. M. Prausnitz, in *Proc. Int. Conf. Prop. Steam*, 9th, 1979; LBL-9571.
6. K. S. Pitzer, *Accounts of Chem. Res.* **10**, 371 (1977).

2. MODIFICATIONS OF GENERALIZED VAN DER WAALS THEORY FOR MIXTURES

Wallace B. Whiting, Eldon R. Larsen, and John M. Prausnitz

The generalized van der Waals theory has been the most useful theory of fluids for engineering purposes. The simplicity of the resulting partition function far outweighs, in most cases, the inaccuracies caused by the assumption that the intermolecular potential can be separated into a hard-sphere-repulsive and a simple, attractive part. However, in three regions the generalized van der Waals theory, as presently used, becomes significantly inaccurate. We have focused our attention on these three regions.

a. Low-Density Region. In the low-density region, the common assumption of random mixing, or uniform density, is not valid. Because almost all equations of state are based on the random-mixing assumption, they predict second-virial coefficients that are consistently too positive. We have used this observation to develop an empirical correction^{1,2} to the partition function that enables reproduction of the experimental second-virial-coefficient data but does not affect properties far from the zero-density limit. This correction can be applied to any partition function for pure components and for mixtures.

b. Critical Region. No generalized van der Waals equation of state fits pure-component vapor-liquid-equilibria data near the critical point if the adjustable parameters are evaluated from data away from the critical region. We have examined this problem using the equation of state and accompanying parameters reported by Oellrich,

Knapp, and Prausnitz.³ By use of their equation and parameters, we obtain a good representation of the vapor-liquid equilibria of simple molecules away from the critical point, but the prediction is bad in the critical region. We are, therefore, trying to make semi-empirical corrections to this equation of state so as to improve the fit in the critical region yet not affect accuracy remote from the critical point. We are using error functions that are finite only in the critical region and essentially zero elsewhere.

c. Asymmetric Mixtures. The poor (although common) assumption of random mixing is particularly bad for asymmetric mixtures, where the molecules of the two (or more) components vary greatly in size and/or intermolecular potential. For such a mixture, homogeneity is not attained; local concentrations differ from overall concentrations. For a binary mixture, we propose a two-fluid theory in which the local compositions are related to the overall compositions with Boltzmann factors of the intermolecular energies of the local configurations. By using local surface fractions (rather than local mole fractions), we can take into account differences in molecular size, and, by using the Boltzmann factors, we can take into account differences in intermolecular potentials. Our initial success with the two-fluid theory (for the methane-water system) is promising.

* * *

1. W. B. Whiting and J. N. Prausnitz, in *Proc. Int. Conf. Prop. Steam*, 9th, 1979; LBL-9571.
2. A. I. El-Twaty, Ph.D. thesis, University of California, Berkeley, 1979.
3. L. R. Oellrich, H. Knapp, and J. M. Prausnitz, *Fluid Phase Equilib.* **2**, 163 (1978).

3. LIQUID-LIQUID PHASE EQUILIBRIA FOR HEAVY HYDROCARBON-WATER SYSTEMS

Frank E. Anderson and John M. Prausnitz

In coal gasification operations, a complex mixture of primarily aromatic compounds, called coal tar, is contained in the effluent gases. A large portion of the molecules in coal tar contain heteroatoms; these are primarily oxygen, but some sulfur and nitrogen are also present. Roughly 85% of the compounds in coal tar have normal boiling points in the range: 220 to 420°C.¹ In normal gasifier operation, the hot effluent gases are quenched with water. This quenching removes the high-boiling coal tar and results in clean, transportable gases plus a liquid water-coal tar mixture.

As many of the molecules in the coal tar are polar, it is unlikely that a simple ambient-temperature decantation scheme will provide effluent water of purity sufficient for legal discharge. Also, some compounds contained in these coal tars may be valuable and, hence, their recovery may be warranted. We must, therefore, perform some separation process on the water-coal tar mixture. Thus, it is necessary to predict both the liquid-liquid (LLE) and the vapor-liquid (VLE) phase

equilibria for these water-coal tar systems. Towards that end, we have initiated experimental and theoretical programs.

An apparatus is currently being designed for measurement of both binary and multicomponent LLE from ambient conditions to 250°C and 5 MPa. Correlation of the binary LLE data will be accomplished with the UNIFAC method for activity-coefficient estimation.² UNIFAC is a group-contribution method that requires group-interaction energy parameters. From our binary LLE data, we can evaluate these parameters for groups not previously studied. These new groups appear in aromatic compounds containing nitrogen, sulfur, or oxygen. The expanded parameter table will then be used to predict the water-coal tar phase equilibria of interest. From such a model whose parameters have been evaluated from LLE data only, one can predict both VLE and LLE. An alternate possible technique for data correlation is suggested by the scaled-particle theory.³

* * *

1. A. B. Macknick, Ph.D. thesis, University of California, Berkeley, 1979.
2. Aa. Fredenslund, R. L. Jones, and J. M. Prausnitz, *AIChE J.* 21, 1086 (1975).
3. R. A. Pierotti, *Chem. Rev.* 76, 717 (1976).

RESEARCH PLANS FOR CALENDAR YEAR 1980

During 1980, we expect, first, to obtain experimental data for methane-water phase equilibria using our high-pressure apparatus. Second, we plan to construct a new apparatus for measuring heavy hydrocarbon-water liquid-liquid equilibria. Finally, we expect to develop further our two-fluid theory for asymmetric mixtures, our critical-region and low-density-region corrections to the generalized van der Waals partition function, and the scaled-particle theory for correlating aqueous-hydrocarbon phase equilibria.

1979 PUBLICATIONS AND REPORTS

Refereed Journals

- †1. D. D. Liu and J. M. Prausnitz, "Molecular Thermodynamics of Polymer Compatibility: Effect of Contact Agility," *Macromolecules* 12, 454 (1979).
2. O. R. Rivas and J. M. Prausnitz, "Apparatus for Rapid Determination of Low-Pressure Solubilities of Gases in Liquids over a Wide Range of Temperatures. Application to Corrosive Systems," *Ind. Eng. Chem., Fundam.* 18, 289 (1979).
3. A. B. Macknick and J. M. Prausnitz, "Vapor Pressures of High-Molecular-Weight Hydrocarbons," *J. Chem. Eng. Data* 24, 175 (1979).
- ‡4. J. Gmehling, D. D. Liu, and J. M. Prausnitz, "High-Pressure Vapor-Liquid Equilibria for Mixtures Containing One or More Polar Components," *Chem. Eng. Sci.* 34, 951 (1979).

†5. D. D. Liu and J. M. Prausnitz, "Thermodynamics of Gas Solubilities in Molten Polymers," *J. Appl. Polym. Sci.* 24, 725 (1979).

‡6. J. M. Prausnitz, "Molecular Thermodynamics for Chemical Process Design," *Science* 205, 759 (1979).

7. J. A. Zarkarian, F. E. Anderson, J. A. Boyd, and J. M. Prausnitz, "UNIFAC Parameters from Gas-Liquid Chromatographic Data," *Ind. Eng. Chem., Process Des. Develop.* 18, 657 (1979).

8. G. Müller and J. M. Prausnitz, "Residual Enthalpies of High-Boiling Hydrocarbons," *Ind. Eng. Chem., Process Des. Develop.* 18, 679 (1979).

Other Publications

1. A. I. El-Twaty, "Molecular Thermodynamics of Dew-Point Calculations in Coal Gasification Processes," Ph.D. thesis, Dept. of Chemical Engineering, University of California, Berkeley, April 1979.

2. A. B. Macknick, "Heavy Hydrocarbons from Coal Gasification. Vapor Pressures and Dew Points," Ph.D. thesis, Dept. of Chemical Engineering, University of California, Berkeley, June 1979.

‡3. J. R. Wells, "Vapor-Liquid Equilibria of the Ammonia-Water System," M.S. thesis, Dept. of Chemical Engineering, University of California, Berkeley, June 1979.

‡§4. H. Lazalde-Crabtree, "Solvent Losses in Sweetening of Natural Gas by Absorption. Solubility of Methanol in Compressed Gases at Low Temperatures," M.S. thesis, Dept. of Chemical Engineering, University of California, Berkeley, June 1979.

5. W. B. Whiting and J. M. Prausnitz, "A New Equation of State for Fluid Water Based on Hard-Sphere Perturbation Theory and Dimerization Equilibria," in *Proc. Int. Conf. Prop. Steam*, 9th, 1979; LBL-9571.

‡§6. H. Lazalde-Crabtree, G. J. F. Breedveld, and J. M. Prausnitz, "Solvent Losses in Gas Absorption. Solubility of Methanol in Compressed Natural and Synthetic Gases," paper presented at the 72nd Annual Meeting of the American Institute of Chemical Engineers, San Francisco, November 1979.

Invited Talks

1. J. M. Prausnitz, Technical University of Berlin, May 1979.
2. J. M. Prausnitz, University of Pennsylvania, Philadelphia, November 1979.
3. J. M. Prausnitz, General Electric Laboratories, Louisville, Kentucky, November 1979.
4. J. M. Prausnitz, Degussa Research Laboratories, Hanau, West Germany, 1979.

5. J. M. Prausnitz, Chemische Werke Hüls, Marl,
West Germany, 1979.

* * *

†Supported in part by the Petroleum Research Fund
(administered by the American Chemical Society).

‡Supported in part by the National Science
Foundation.

§Supported in part by the Deutsche Forschungsge-
meinschaft (administered by the Technical Uni-
versity of Berlin).

III

Nuclear Sciences

A. LOW ENERGY NUCLEAR SCIENCES

1. Heavy Element Chemistry

a. Actinide Chemistry*

Norman M. Edelstein, Richard A. Andersen, Neil Bartlett, John G. Conway, Kenneth Raymond, Glenn T. Seaborg, Andrew Streitwieser, Jr., David H. Templeton, and Allan Zalkin, Investigators

Specific Sequestering Agents for the Actinides

1. REMOVAL OF $^{238}\text{Pu(IV)}$ FROM MICE BY SULFONATED TETRAMERIC CATECHOYL AMIDES[†]

P. W. Durbin, E. S. Jones, K. N. Raymond and F. L. Weitl

In response to the biological hazards associated with the nuclear fuel cycle and nuclear research sites, we have developed and are investigating a biomimetic design concept of sequestering agents for eight-coordinate actinide ions in general, and Pu(IV) in particular. Plutonium is a potent carcinogen¹ since once absorbed by body tissues, it exhibits long term retention in mammals. This is known for humans² as well as test animals such as dogs.³ Although plutonium commonly exists in aqueous solution in each of the oxidation states from III to VI, biological evidence indicates that most, if not all, exists in vivo as Pu(IV), where it is complexed by available bioorganic ligands.⁴

There are many similarities between Pu(IV) and Fe(III). These range from the similar charge/ionic-radius ratio for Fe(III), and Pu(IV) (4.6 and 4.2 e/Å, respectively) to their similar transport properties in mammals, where it is known that Pu(IV) is bound by the iron-transport protein, transferrin, at the site which normally binds Fe(III).⁴ Thus the design of Pu(IV) sequestering agents which are similar to naturally occurring Fe(III) sequestering agents suggests itself as a biomimetic approach. Since 2,3-dihydroxybenzoic acid (DHB) is a component of several siderophores and in particular is found in enterobactin [cyclotris(2,3-dihydroxybenzoyl)-N- β -serine], a powerful iron transport and sequestering agent of enteric bacteria,⁵ we anticipated that the macrocyclic tetra(DHB) chelates would prove to be highly specific and powerful sequestering agents for actinide ions. In fact they promise to be more effective than the agent in use today, CaNa₃ DTPA (diethylenetriaminepentaacetic acid).

The CAM (catechoylamide) ligands were subjected to a preliminary test of acute toxicity. Groups of five mice were each given five consecutive daily injections of a CAM ligand. Body weights

were recorded before the first injection and at the end of the test. One week after the first injection, the surviving mice were killed and the viscera inspected for gross pathological changes.

The nitrated CAM ligand, 3,2,3,2-CYCAM(NO₂) (cyclicCAM) (Fig. 1), was 100% lethal at seven days (after a total dose of 150 $\mu\text{mole/kg}$). Three separate toxicity tests were made of 4,4,4-LICAMS (linearCAMsulfonated) (Fig. 2), in which one of 15 mice died in seven days (after a total dose of 110 $\mu\text{mole/kg}$), and most of the mice showed oliguria and severe anorexia leading to 20% loss of body weight and fecal emaciation of viscera, particularly liver and kidneys. None of the other linear or cyclic sulfonated CAM ligands (Figs. 1 and 2) were acutely toxic in mice—there were no deaths, no significant weight losses, and no gross pathology of the viscera.

In summary, the initial premise proved correct—electron donor groups that preferentially bind Fe(III) (in this case the o-hydroxyls of catechol) also bind Pu(IV) efficiently. All of the tetrameric CAM ligands tested, even those that were toxic or too insoluble to be excreted, bound nearly all circulating $^{238}\text{Pu(IV)}$. Sulfonation of the benzene rings produced CAMS ligands, which were water soluble and could be filtered by the kidneys, thereby promoting significant $^{238}\text{Pu(IV)}$ excretion. The linear CAMS, with greater structural freedom, was somewhat more effective than the cyclic CAMS, (Table 1). Propylene bridges were originally selected for the prototype ligand, 3,3,3,3-CYCAM (Fig. 1), because the intergroup spacing would then be about the same as in the cyclic l-serine tri-ester backbone of enterobactin, for which the bridge structure is $-\text{CH}_2-\text{O}-\text{C}(\text{O})-$. However, in vivo testing indicated that 3,3,3-LICAMS (Fig. 2) bound $^{238}\text{Pu(IV)}$ only about as well as hexadentate DFOM, and pH titration verified that only six of the eight electron-donor groups of 3,3,3-LICAMS coordinated with Th(IV). Enlargement of the charge cavity (by lengthening all three connecting bridges to butylene units) produced a ligand, 4,4,4-LICAMS (Fig. 2), that completely coordinated with Th(IV) and significantly increased in vivo binding and elimination of $^{238}\text{Pu(IV)}$, compared to the other CAM ligands tested. The 4,4,4-LICAMS was moderately toxic. The introduction of a single butylene bridge at the midpoint of the backbone yielded a ligand, 3,4,3-LICAMS (Fig. 2), that was as efficient for in vivo $^{238}\text{Pu(IV)}$ binding as an equimolar amount of CaNa₃ DTPA or 4,4,4-LICAMS, and was not

* This work was supported by the Division of Nuclear Sciences, Office of Energy Sciences, U. S. Department of Energy.

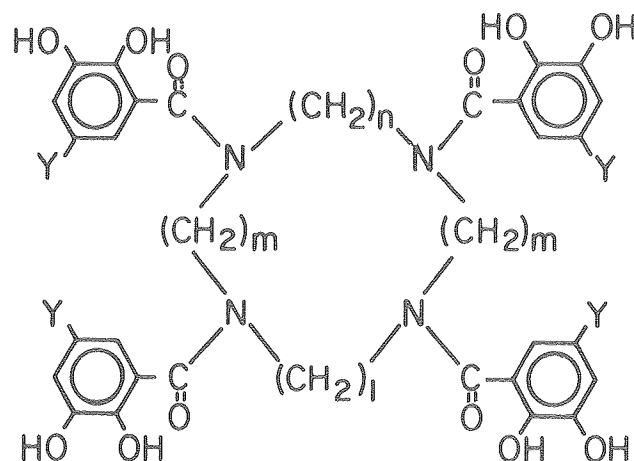


| Fig. 1. | Abbreviation(Y) | l, m, n | Molecular Formula | IUPAC Name |
|---------|-----------------------------------|-----------|--|--|
| | 3,3,3,3-CYCAM(H) | 3,3,3 | $C_{40}H_{44}N_4O_{12} \cdot 2H_2O$ | N^1, N^5, N^9, N^{13} -tetra(2,3-dihydroxybenzoyl)-tetraazacyclohexadecane |
| | 2,3,3,3-CYCAM(SO ₃ Na) | 2,3,3 | $C_{39}H_{38}N_4O_{24}S_4Na_4 \cdot 2H_2O$ | N^1, N^4, N^8, N^{12} -Tetra(2,3-hydroxy-5-sulfobenzoyl)-tetraazacyclopentadecane |
| | 3,3,3,3-CYCAM(SO ₃ Na) | 3,3,3 | $C_{40}H_{40}N_4O_{24}S_4Na \cdot 5H_2O$ | N^1, N^5, N^9, N^{13} -tetra(2,3-dihydroxy-5-sulfobenzoyl)-tetraazacyclohexadecane |
| | 3,2,3,2-CYCAM(NO ₂) | 3,2,3 | $C_{38}H_{36}N_4O_{20} \cdot 2H_2O$ | N^1, N^4, N^8, N^{11} -tetra(2,3-dihydroxy-5-nitrobenzoyl)-tetraazacyclotetradecane (XBL 794-3344) |

toxic in mice in the preliminary five-dose screening test.

All of the tetrameric CAM ligands, even those that could not be eliminated, bound $^{238}\text{Pu(IV)}$ in the body fluids and prevented further deposition in the skeleton (skeletons contained $\leq 18\%$ of the injected dose) and six of the nine CAM ligands prevented additional deposition of $^{238}\text{Pu(IV)}$ in liver (livers contained $\leq 30\%$) (Table 2).

None of the CAM ligands appeared capable of removing ^{238}Pu from the liver; by contrast some ^{238}Pu present in liver seems to be mobilized by CaNa_3DTPA . All of the linear CAM ligands removed as much or more $^{238}\text{Pu(IV)}$ from the skeleton as an equimolar amount of CaNa_3DTPA .

The CAMS ligands are specific for small highly charged cations; at pH 7 they do not complex

divalent Mg, Ca, Mn, or Co and react only weakly with Cu(II) and Zn(II).^{6,7} Thus, acute depletion of essential divalent metals, which is the toxic action of CaNa_3DTPA , would not be expected in the case of the CAMS compounds. However, catechol is moderately toxic; the lethal dose in rats and cats is about 500 $\mu\text{mole/kg}$.⁸ Two possible reasons for the toxicity of 4,4,4-LICAMS in mice and of 3,4,3-LICAMS in dogs (F. W. Bruenger, University of Utah, unpublished) are being investigated. First, new methods are being developed to synthesize and purify the CAMS compounds to eliminate any toxic oxidized or halogenated impurities remaining from the synthetic procedures,^{9,10} and second, experiments are in progress to determine whether the CAMS compounds¹¹ deplete essential cytochrome iron from liver and/or kidney cells. However, evidence of toxicity at a dosage of 30 $\mu\text{mole/kg}$ of 3,4,3-LICAMS or 4,4,4-LICAMS should not be a serious impediment to development of their use as potential

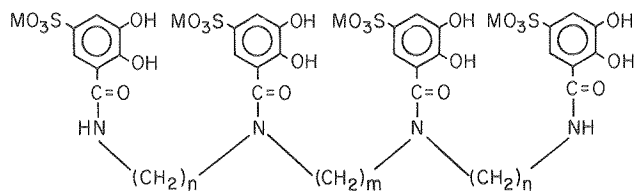


| Fig. 2. | Abbreviation(Y) | M n m | Molecular Formula | IUPAC Name |
|---------|-----------------|--------|--|---|
| | 2,3,2-LICAMS | K 2 3 | $C_{35}H_{32}N_4O_{24}S_4K_4 \cdot 3H_2O$ | N^1, N^5, N^9, N^{13} -tetra(2,3-dihydroxy-5-sulfo benzoyl)-tetraazaundecane |
| | 3,3,3-LICAMS | Na 3 3 | $C_{37}H_{36}N_4O_{24}S_4Na_4 \cdot 2H_2O \cdot 1/4Na_2SO_4$ | N^1, N^5, N^9, N^{13} -tetra(2,3-dihydroxy-5-sulfo benzoyl)-tetraazatridecane |
| | 4,4,4-LICAMS | Na 4 4 | $C_{40}H_{42}N_4O_{24}S_4Na_4 \cdot 4H_2O \cdot 1/2Na_2SO_4$ | N^1, N^6, N^{11}, N^{16} -tetra(2,3-dihydroxy-5-sulfo benzoyl)-tetraazahexadecane |
| | 4,3,4-LICAMS | K 4 3 | $C_{39}H_{40}N_4O_{24}S_4K_4 \cdot 6H_2O$ | N^1, N^6, N^{10}, N^{15} -tetra(2,3-dihydroxy-5-sulfo benzoyl)-tetraazapentadecane |
| | 3,4,3-LICAMS | Na 3 4 | $C_{38}H_{38}N_4O_{29}S_4Na_4 \cdot 6.5H_2O$ | N^1, N^5, N^{10}, N^{14} -tetra(2,3-dihydroxy-5-sulfo benzoyl)-tetraazatetradecane (XBL 794-3345) |

therapeutic agents, because dose-response studies now in progress show that both are nearly as effective for promoting Pu(IV) excretion as reported here (50 to 60%) when given at dosages less than one-tenth those used in the present studies (P. W. Durbin and E. S. Jones, unpublished results).

* * *

[†]Brief version of LBL-9016.

1. A. Catsch, Radioactive Metal Mobilization in Medicine, Thomas, Springfield, Illinois, 1964.
2. B. J. Stoves, D. R. Atherton, and D. S. Buster, Health Phys. **20**, 369 (1971).
3. H. Foreman, W. Moss, and W. Langham, Health Phys. **2**, 326 (1960).
4. P. W. Durbin, Health Phys. **29** 495 (1975), and

references therein.

5. J. B. Neilands, Ed., Microbial Iron Metabolism (Academic Press, New York, N.Y., 1974).
6. A. E. Martell and R. M. Smith, Critical Stability Constants (Plenum, New York, 1976) vol. 3, pp. 200, 205, 209.
7. L. G. Sillen and A. E. Martell, Stability Constants of Metal-Ion Complexes, Chemical Society of London (special Publication No. 25, Suppl. 1), pp. 400-402, 1971.
8. T. Sollman, A Manual of Pharmacology (Saunders, Philadelphia, 1957), 8th ed., p. 812.
9. F. L. Weitl, K. N. Raymond, W. L. Smith, and T. R. Howard, J. Am. Chem. Soc. **100**, 1170 (1978).
10. F. L. Weitl and K. N. Raymond, J. Am. Chem. Soc., in press.
11. F. L. Weitl, W. R. Harris, and K. N. Raymond, J. Med. Chem. **22**, 1281 (1979).

Table 1. Sequence of studies of in vivo chelation of $^{238}\text{Pu(IV)}$ by tetrameric catechoylamides.

| Experiment no. ^a | Compound ^b | Ligand dose ^c ($\mu\text{mole/kg}$) | ^{238}Pu injection | Data on mice | | ^{238}Pu excreted ^d (% absorbed dose) |
|-----------------------------|-------------------------------------|---|-----------------------------|--------------|------------|--|
| | | | | Age (wks) | Weight (g) | |
| 1 | 3,3,3,3-CYCAM | 33 | i.m. | 68 | 26 | 11 |
| 2 | 3,2,3,2-CYCAM(NO_2) | 30 | i.p. | 74 | 24 | 7.2 |
| 3 | 3,3,3,3-CYCAMS | 24 | i.p. ^e | 14 | 34 | 37 |
| 4 | 2,3,2-LICAMS | 23 | i.p. | 18 | 36 | 37 |
| 6 | DICAMS | 80 | i.p. | 22 | 40 | 6.4 |
| | DHBA | 78 | i.p. | 22 | 40 | 3.5 |
| 7 | 1-hr ^{238}Pu distribution | - | i.p. | 22 | 38 | - |
| 8 | 4,4,4-LICAMS | 19 | i.p. ^e | 23 | 38 | 59 |
| 9 | 3,3,3-LICAMS | 24 | i.v. | 9 | 32 | 44 |
| 10 | CaNa_3DTPA | 21 | i.p. | 14 | 35 | 63 |
| | DFOM | 21 | i.p. | 14 | 35 | 48 |
| 11 | 1-hr ^{238}Pu distribution | - | i.v. | 16 | 37 | - |
| 12 | 2,3,3,3-CYCAMS | 29 | i.v. | 17 | 36 | 39 |
| 13 | 3,3,3,3-CYCAMS | 30 | i.v. | 19 | 38 | 35 |
| 14 | 4,4,4-LICAMS | 22 | i.v. | 20 | 41 | 63 |
| | 4,4,4-LICAMS | 22 | i.p. | 20 | 41 | 68 |
| 20 | 4,4,4-LICAMS | 22 | i.v. | 20 | 40 | 56 |
| 21 | 3,4,3-LICAMS | 20 | i.v. | 20 | 40 | 65 |
| | 4,3,4-LICAMS | 20 | i.v. | 20 | 40 | 43 |

^aExperiments in the sequence not relevant to this report are omitted.

^b ^{238}Pu -injected controls accompanied all experiments except Nos. 6, 20 and 21.

^cSee Figs. 1-5 for formula names and structures.

^dLigands were injected intraperitoneally (in 0.5 ml of isotonic saline) 1 hr after the ^{238}Pu injection.

^eIn experiments 1 and 2, mice were killed at 48 hr; in all other experiments, at 24 hr.

^eRepeated with i.v. ^{238}Pu -injection, see experiments 13 and 14.

Table 2. Effect of tetrameric catechoylamides on the distribution of $^{238}\text{Pu(IV)}$ in the mouse. Ligands were administered at 1 hr, and mice were killed 24 hrs after injection of $^{238}\text{Pu(IV)}$ citrate.^{a,b,c}

| CAM Compounds, (mode of ^{238}Pu injection) | Per cent of absorbed dose \pm S.D. at 24 hrs after ^{238}Pu injection | | | | | |
|---|--|---------------|---------------|--------------------|---------|---------------|
| | Liver | Skeleton | Soft tissue | GI tract (full) | Kidneys | Whole body |
| 3,4,3-LICAMS (i.v.) | 22 \pm 8.9 | 6.6 \pm 1.2 | 1.8 \pm 0.3 | 3.3 | 1.2 | 35 \pm 8.1 |
| 4,4,4-LICAMS (i.v.) ^b | 25 \pm 5.7 | 8.0 \pm 1.2 | 3.0 \pm 0.8 | 3.0 | 1.5 | 41 \pm 7.7 |
| 4,4,4-LICAMS (i.p.) ^b | 27 \pm 3.9 | 4.8 \pm 0.4 | 5.6 \pm 0.5 | 6.7 | 2.4 | 37 \pm 4.3 |
| 3,3,3-LICAMS (i.v.) | 41 \pm 6.3 | 9.1 \pm 0.4 | 2.8 \pm 0.2 | 3.3 | 1.0 | 56 \pm 6.3 |
| 4,3,4-LICAMS (i.v.) | 30 \pm 6.1 | 11 \pm 1.6 | 3.7 \pm 0.6 | 4.3 | 7.5 | 57 \pm 6.6 |
| 2,3,3,3-CYCAMS (i.v.) | 28 \pm 6.6 | 18 \pm 2.1 | 7.0 \pm 1.4 | 4.7 | 4.0 | 61 \pm 6.1 |
| 2,3,2-LICAMS (i.p.) | 26 \pm 2.9 | 13 \pm 1.0 | 12 \pm 1.3 | 8.1 | 3.9 | 63 \pm 2.9 |
| 3,3,3,3-CYCAMS (i.v.) | 32 \pm 4.4 | 14 \pm 1.4 | 9.8 \pm 2.3 | 4.7 | 4.7 | 65 \pm 4.1 |
| 3,3,3,3-CYCAMS (i.p.) | 24 \pm 3.5 | 17 \pm 3.4 | 10 \pm 2.4 | 8.0 | 3.7 | 63 \pm 3.2 |
| 3,3,3,3-CYCAM (i.m.) ^c | 23 \pm 7.0 | 18 \pm 4.3 | 3.3 \pm 0.8 | 3.6 | 41 | 89 \pm 6.1 |
| 3,2,3,2-CYCAM(NO ₂)(i.p.) ^c | 37 \pm 8.2 | 7.9 \pm 0.8 | 26 \pm 4.0 | 16 | 6.0 | 93 \pm 13.8 |
| <u>Other Ligands</u> | | | | | | |
| CaNa ₃ DTPA (i.p.) | 17 \pm 4.4 | 10 \pm 1.4 | 3.3 \pm 1.4 | 5.2 | 0.5 | 37 \pm 6.8 |
| DFOM (i.p.) | 22 \pm 5.9 | 20 \pm 2.4 | 4.1 \pm 1.0 | 4.2 | 1.6 | 52 \pm 6.4 |
| DiMCAMS (i.p.) | 49 \pm 7.4 | 30 \pm 7.1 | 7.0 \pm 1.0 | 5.9 | 1.5 | 94 \pm 2.9 |
| DHBA (i.p.) | 50 \pm 5.6 | 31 \pm 5.7 | 7.8 \pm 1.7 | 6.7 | 1.5 | 96 \pm 5.1 |

^aLigand dose levels are shown in Table 1.

^bResults are means for five mice except those for 4,4,4-LICAMS, which represent ten mice each.

^cMice in experiments 1 and 2 were killed at 48 hr.

2. CRYSTAL AND MOLECULAR STRUCTURES OF TETRAKIS (CATECHOLATO)-HAFNATE(IV) AND -CERATE(IV). FURTHER EVIDENCE FOR A LIGAND FIELD EFFECT IN THE STRUCTURE OF TETRAKIS (CATECHOLATO)-URANATE(IV)[†]

S. R. Sofen, S. R. Cooper, and K. N. Raymond

Although the presence of ligand field effects has been suggested for actinide complexes, definitive recognition of such effects has been hampered by the complex interplay of 5f, 6d, and 7s orbitals for the actinides and the lack of a suitable isostructural series to preclude changes in crystal packing forces.

Previous investigations for actinide-specific chelators analogous to microbial iron transport chelates led us to examine the structures of the tetrakis(catecholato) complexes of U(IV) and Th(IV), in which a small structural distortion was observed for the uranium complex.¹ This distortion renders the two catechol oxygens of a given molecule inequivalent, in contrast to the thorium case, and was tentatively attributed to the presence of a ligand field effect induced by the two 5f electrons of U(IV). However, the importance of another possible cause of this distortion, the smaller ionic radius of uranium(IV) vs. thorium(IV), could not be evaluated. As an extension of our previous interest in catechol coordination chemistry and

for clarification of the structural effect of the 5f electrons, the corresponding Hf complex was prepared and examined crystallographically. However, the results were—by themselves—ambiguous as far as resolving the metal-oxygen bond distance distortion problem is concerned.

In the course of this work, it became apparent that, somewhat surprisingly, the analogous Ce(IV) chelate could be prepared; surprising because the strongly oxidizing Ce(IV) ion ($E_0 = +1.70 \text{ V}^2$) might have been expected to react with a facile reducing agent such as the catechol dianion.³ That the cerium complex exists is a reflection of the impressive coordinating ability of the catechol group, which coordinates and stabilizes, with respect to reduction, such oxidizing ions as Fe(III),⁴ V(V),⁵ and Mn(III).⁶ In an effort to understand the distortions of the dodecahedral skeleton observed for the $[\text{U}(\text{cat})_4]^{4-}$ complex, we have prepared and characterized structurally the analogous hafnium(IV) and cerium(IV) complexes and examined the optical, magnetic, and electrochemical properties of the cerium chelate.

A for the thorium and uranium complexes, the crystal structure consists of discrete, eight-coordinate $[\text{M}(\text{cat})_4]^{4-}$ dodecahedra, sodium ions, and waters of crystallization (Figs. 1-2). The 21 waters form a hydrogen-bonded network throughout

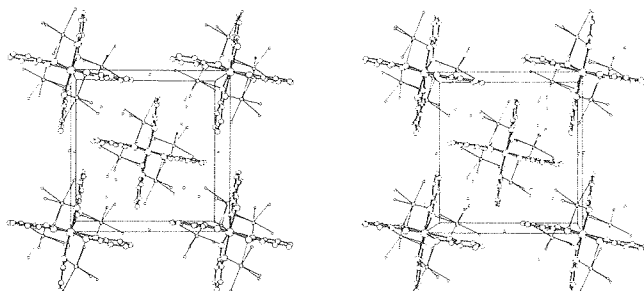


Fig. 1. A stereoscopic packing diagram of the $\text{Na}_4[\text{M}(\text{O}_2\text{C}_6\text{H}_4)_4] \cdot 21\text{H}_2\text{O}$ ($\text{M} = \text{Hf}, \text{Ce}$) structures viewed down the crystallographic c axis.

(XBL 781-6967)

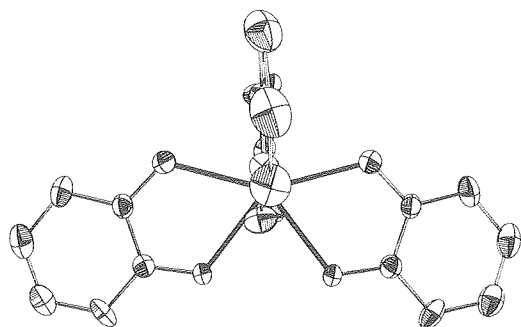


Fig. 2. The $[\text{M}(\text{O}_2\text{C}_6\text{H}_4)_4]^{4-}$ anion viewed along the molecular mirror plane with the 4 axis vertical. The atom labels used in the text as well as the dodecahedral A and B sites are shown.

(XBL 781-6965)

the crystal, with the sodium ion coordinated to two catecholate oxygens and four water oxygens.

Although a coordinated semiquinone formulation (with three catecholates) could not have been excluded a priori, the Ce complex is best considered as a simple cerium(IV) catechol complex. The diamagnetism of the Ce(IV) complex agrees with the crystallographic assignment of a simple catecholato formulation to this complex, rather than a semiquinone formulation. If the Ce complex existed as the cerium(III) semiquinone, the weak coupling expected between the Ce(III) 4f electron and the π electron of the ligand would be expected to yield an at least weakly paramagnetic complex.

The ratio of the formation constants of the cerium(IV) and -(III) tetrakis(catecholato) complexes, i.e., the equilibrium constants K_n for the reaction



can be calculated from the cyclic voltammetric data. From these potentials the formation constants of the tetrakis complexes differ by a factor of 10^{36} .

The experimentally determined differences in metal-oxygen distances for tetrakis(catecholato) complexes of hafnium, cerium, uranium, and thorium are given in Table 1 for the A and B sites of the Hoard and Silverton dodecahedron.⁷ As seen in Table 1, despite a significant difference in metal ionic radius, the metal-oxygen distances in the f^0 cerium and thorium structures are equal within experimental error. Since the ionic radius of uranium lies between those of cerium and thorium, it is unlikely that the metal size has any great effect on the structure. We stress that all four of these complexes have identical unit cell contents and are identical except for the metal ion and conclude that the distortion of the uranium structure by lengthening of the $\text{M}-\text{O}_A$ bond is attributable solely to the previously proposed¹ ligand field effect from the f electrons.

Table 1. Structural parameters for $\text{Na}_4[\text{M}(\text{O}_2\text{C}_6\text{H}_4)_4] \cdot 21\text{H}_2\text{O}$ complexes.

| Metal | Ionic radius, Å | $[(\text{M}-\text{O}_A)(\text{M}-\text{O}_B)], \text{Å}$ | $\text{O}_A-\text{O}_A, \text{Å}$ |
|-------|-----------------|--|-----------------------------------|
| Hf | 0.83 | 0.026(4) | 2.554(5) |
| Ce | 0.97 | 0.005(5) | 2.831(7) |
| U | 1.00 | 0.027(5) | 2.883(7) |
| Th | 1.05 | 0.004(5) | 2.972(6) |

* * *

[†]Brief version of *Inorg. Chem.* **18**, 1611 (1979).

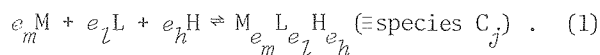
1. S. R. Sofen, K. Abu-Dari, D. P. Freyberg, and K. N. Raymond, *J. Am. Chem. Soc.* **100**, 7882 (1978).
2. W. M. Latimer, *Oxidation States of the Elements and Their Potentials in Aqueous Solution* (Prentice-Hall, Englewood Cliffs, New Jersey, 1952), 2nd ed., p. 294.
3. T.-L. Ho, T. W. Hall, C. M. Wong, *Chem. Ind. (London)*, 729 (1972).
4. K. N. Raymond, S. S. Isied, L. D. Brown, F. F. Fronczek, J. H. Nibert, *J. Am. Chem. Soc.* **98**, 1767 (1976).
5. S. R. Cooper, D. P. Freyberg, and K. N. Raymond, manuscript in preparation.
6. K. D. Magers, C. G. Smith, and D. T. Sawyer, *Inorg. Chem.* **17**, 515 (1978).
7. J. L. Hoard and J. V. Silverton, *Inorg. Chem.* **2**, 235 (1963).

3. FREE METAL AND FREE LIGAND CONCENTRATIONS DETERMINED FROM TITRATIONS USING ONLY A pH ELECTRODE. PARTIAL DERIVATIVES IN EQUILIBRIUM STUDIES

A. Avdeef and K. N. Raymond

Osterberg¹ and, later, Sarkar and Kruck² and McBryde³ introduced an extremely valuable technique for evaluating the free metal and free ligand concentrations in multicomponent equilibria by the use of pH titration data alone. That is, one could indirectly measure pM (-log [M], [M] = free metal concentration) and pL ([L] = free [unassociated] ligand concentration) values by using only a pH electrode. The technique is an extension of earlier work by Hedström⁴ and Sillén.⁵ It is based on partial differential relations arising from the mass balance equations and requires several titrations, per reactant, performed in a special way. Surprisingly, the method is not widely known, judging by the near absence of its reported use. Sarkar and co-workers⁶⁻⁹ have experimentally applied it to rather complicated equilibria, involving the determination of as many as three different nonhydrogen reactants. The technique has been very important in our studies of the equilibria involving Th⁴⁺, U⁴⁺, and Pu⁴⁺ complexes with catechol and hydroxamate ligands, where evidence for mixed-ligand and polynuclear species is abundant.¹⁰

For solutions containing one type of metal and one type of ligand as reactants, along with hydrogen and hydroxide ions, the species present in solution may be represented by equilibria of the sort



The stability constant of the j th associated species is given by

$$\beta_j = C_j / m^{e_{mj}} l^{e_{lj}} h^{e_{hj}} \quad (2)$$

where e_{kj} is the stoichiometric coefficient of the k th reagent, C_j is the concentration of the j th associated species, and m , l , and h are the free (unassociated) concentrations of metal, ligand, and hydrogen. Usually only h (in addition to the total concentrations) is known from a simple pH titration. In refinement programs such as SCOGS^{11a} and MINIQAD^{11b} unknown values of pM and pL are calculated only after a model is assumed along with the corresponding β values. Thus such values of pM and pL can be model-biased. Osterberg's¹ proposal is the model-independent "variation" relation

$$\Delta pL(M_0, L_0) = pL_2 - pL_1 = \left[\int_{pH_2}^{pH_1} \left(\frac{\partial H}{\partial L} \right)_{M_0, h} dpH \right]_{L_0} \quad (3)$$

where M , L , and H are the total metal, ligand,

and hydrogen concentrations. The relation states that for given values of M and L (M_0 , L_0) the change in pL corresponding to a change in pH is related to the extent the variation of L affects H . One thus needs at least two titrations where L is the only varied nonhydrogen total concentration.

One least-squares procedure¹² for the refinement of formation constants β_j calls for minimization of the differences between observed pHs and those calculated from an assumed set of constants. In the normal equations, partial derivatives ($\partial \text{pH} / \partial \log \beta_j$) are required. These can be calculated numerically but such a procedure requires a considerable computational effort. If one recognizes that pH is also a function of the total concentrations, one can state

$$\begin{aligned} \left(\frac{\partial \text{pH}}{\partial \log \beta_j} \right)_{\beta_k \neq j} &= \left(\frac{\partial \text{pH}}{\partial M} \right)_{L, H} \left(\frac{\partial M}{\partial \log \beta_j} \right)_{\beta_k \neq j, L, H} + \\ &\quad \left(\frac{\partial \text{pH}}{\partial L} \right)_{M, H} \left(\frac{\partial L}{\partial \log \beta_j} \right)_{\beta_k \neq j, M, H} + \\ &\quad \left(\frac{\partial \text{pH}}{\partial H} \right)_{M, L} \left(\frac{\partial H}{\partial \log \beta_j} \right)_{\beta_k \neq j, M, L} \end{aligned} \quad (4)$$

The partial derivatives of the explicit functions on the right side of Eq. (4) are easily evaluated. For example, $(\partial L / \partial \log \beta_j)_{\beta_k \neq j} = 2.303 e_{lj} C_j$. The evaluation of the implicit function derivatives ($\partial \text{pH} / \partial X$) is less direct.

One needs to set up the Jacobian matrix $J[(M, L, H) / (\ln m, \ln l, \ln h)]$ which linearly relates dX to $d \ln x$ (Eq. 5):

$$\begin{pmatrix} dM \\ dL \\ dH \end{pmatrix} = J \begin{pmatrix} d \ln m \\ d \ln l \\ d \ln h \end{pmatrix} \quad (5)$$

This matrix is symmetric and its elements are easily evaluated, as shown in Eq. (7). In fact, this matrix is used to calculate pM and pL values by the nonvariational methods.^{11,12} In the process, its inverse is computed.

It is a remarkable fact that the elements of the inverse matrix are precisely the partial derivatives of the implicit functions that we need to compute ($\partial \text{pH} / \partial \log \beta_j$) and are given by (6) - (8).

$$\begin{pmatrix} \left(\frac{\partial M}{\partial \ln m} \right)_{l, h} & \left(\frac{\partial M}{\partial \ln l} \right)_{m, h} & \left(\frac{\partial M}{\partial \ln h} \right)_{m, l} \\ \left(\frac{\partial L}{\partial \ln m} \right)_{l, h} & \left(\frac{\partial L}{\partial \ln l} \right)_{m, h} & \left(\frac{\partial L}{\partial \ln h} \right)_{m, l} \\ \left(\frac{\partial H}{\partial \ln m} \right)_{l, h} & \left(\frac{\partial H}{\partial \ln l} \right)_{m, h} & \left(\frac{\partial H}{\partial \ln h} \right)_{m, l} \end{pmatrix}^{-1} \quad (6)$$

$$= \begin{pmatrix} m + \sum_{j=1}^N e_{mj}^2 C_j & \sum e_{mj} e_{lj} C_j & \sum e_{mj} e_{hj} C_j \\ \sum e_{mj} e_{lj} C_j & l + \sum e_{lj}^2 C_j & \sum e_{lj} e_{hj} C_j \\ \sum e_{mj} e_{hj} C_j & \sum e_{lj} e_{hj} C_j & h + \frac{K_w}{h} + \sum e_{hj}^2 C_j \end{pmatrix}^{-1} \quad (7)$$

$$= \begin{pmatrix} \left(\frac{\partial \ln m}{\partial M} \right)_{L,H} & \left(\frac{\partial \ln m}{\partial l} \right)_{M,H} & \left(\frac{\partial \ln m}{\partial H} \right)_{M,L} \\ \left(\frac{\partial \ln l}{\partial M} \right)_{L,H} & \left(\frac{\partial \ln l}{\partial l} \right)_{M,H} & \left(\frac{\partial \ln l}{\partial H} \right)_{M,L} \\ \left(\frac{\partial \ln h}{\partial M} \right)_{L,H} & \left(\frac{\partial \ln h}{\partial l} \right)_{M,H} & \left(\frac{\partial \ln h}{\partial H} \right)_{M,L} \end{pmatrix} \quad (8)$$

That is, for $K = J^{-1}$

$$\begin{pmatrix} \frac{d \ln m}{d \ln l} \\ \frac{d \ln l}{d \ln h} \end{pmatrix} = K \begin{pmatrix} \frac{dM}{dl} \\ \frac{dH}{dH} \end{pmatrix}$$

A more general statement of Eq. (4) thus becomes

$$\left(\frac{\partial p X_i}{\partial \log \beta_j} \right)_{\beta_k \neq j} = - \sum_{l=1}^3 K_{il} e_{lj} C_j \quad (9)$$

This simple relationship proves to be extremely useful and is a substantial shortcut in the least-squares refinement of equilibrium data.

The variation techniques presented by Osterberg,¹ Sarkar and Kruck,² and McBryde³ are powerful extensions of the pH titration experiment, particularly for equilibria involving polymeric species. We have presented a completely general mathematical basis for these techniques to multi-component systems. Very useful relationships involving partial derivatives are used in the process. One of the relations derived allows for the first time the use of analytical derivatives in the refinement of equilibrium constants. However, the most important task remains the acquisition of data of sufficient accuracy so that these techniques can be successfully applied.¹³

* * *

[†]Brief version of LBL-8741.

1. R. Osterberg, *Acta Chem. Scand.* **14**, 471 (1960).
2. B. Sarkar and T. P. A. Kruck, *Can. J. Chem.* **51**, 3541 (1973).
3. W. A. E. McBryde, *Can. J. Chem.* **51**, 3572 (1973).
4. B. Hedström, *Acta Chem. Scand.* **9**, 613 (1955).
5. L. G. Sillén, *Acta Chem. Scand.* **15**, 1981 (1961).
6. T. P. A. Kruck and B. Sarkar, *Can. J. Chem.* **51**, 3549 (1973).
7. T. P. A. Kruck and B. Sarkar, *Can. J. Chem.* **51**, 3555 (1973).
8. S.-J. Lau, T. P. A. Kruck, and B. Sarkar, *J. Biol. Chem.* **249**, 5878 (1974).

9. T. P. A. Kruck, S.-J. Lau, and B. Sarkar, *Can. J. Chem.* **54**, 1300 (1976).
10. A. Avdeef, T. L. Bregante, and K. N. Raymond, paper in preparation.
11. I. G. Sayce, *Talanta* **15**, 1397 (1968); A. Sabatini, A. Vacca, and P. Gans, *ibid.* **21**, 53 (1974).
12. A. Avdeef, paper in preparation.
13. T. B. Field and W. A. E. McBryde, *Can. J. Chem.* **56**, 1202 (1978). These authors also considered the variation method with computer-generated data and presented an excellent critical evaluation of data handling.

4. STABILITY CONSTANTS FOR CATECHOL MODELS OF ENTEROBACTIN[†]

A. Avdeef, S. R. Sofen, T. L. Bregante, and K. N. Raymond

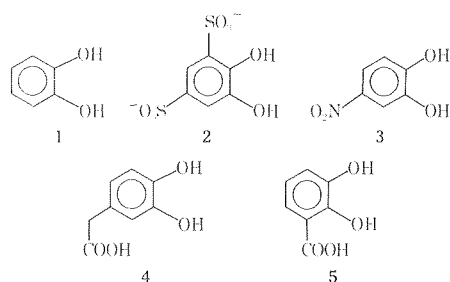
The siderophores (previously called siderochromes)¹ are a class of low molecular weight chelating agents that are manufactured by microorganisms suffering iron deficiency because these agents facilitate uptake of iron into the organisms. The profound insolubility of ferric hydroxide and the low equilibrium concentrations of ferric ion in biological environments are overcome by the enormous stability and ion selectivity of the ferric siderophore complexes. One important siderophore is enterobactin,² the iron sequestering agent for enteric bacteria such as *Escherichia coli*. Since iron is an essential nutrient for all pathogenic bacteria and since the availability of iron often limits the rate of bacterial growth, the siderophores have considerable medical importance.¹ Of particular interest are the formation constants of the ferric siderophore complexes, since these constants define the limits for conditions in which iron will be extracted from other biological ferric complexes in the host organism.

The chelating moieties in enterobactin are catechol (1,2-dihydroxybenzene) groups. It has been recognized for some time that ferric ions can form very stable complexes with catechol ligands.³ For example, adrenaline can extract iron from ferritin.⁴ Although there have been several studies of the stabilities of ferric complexes with catechol-containing ligands,⁵⁻¹³ no general correlation of the stability of these complexes with electronic and steric substituent effects of the ligands has been found. In acidic aqueous solutions (pH 1-2), Mentasti and co-workers^{12,13} studied the formation of 1:1 (metal to ligand) ferric complexes with a wide variety of catechols using stopped-flow and spectroscopic techniques.

Our interest in the coordination chemistry of enterobactin has led to the study of simpler catechol complexes as models for the more complicated biological molecules.¹⁴ The extensive hydrolysis of enterobactin in even mildly basic solutions (pH > 8), involving the cleavage of the ester linkages, precludes the direct determination of its proton dissociation constants. Moreover, its ferric complex appears to be oxidatively

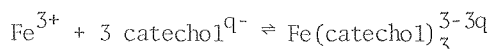
unstable in acidic medium. It was thus important to establish, by the use of readily available simple compounds, (1) a realistic lower bound for the formation constant of ferric enterobactin and related biological compounds, (2) the extent and nature of the oxidative instability, and (3) the effect of the substituent groups on the complex stability.

The present study extends and reexamines previous determinations of stability constants of ferric-catechol complexes to a wider range in hydrogen ion concentration (pH 2-11), using both potentiometric and spectroscopic techniques. The ligands chosen for the study exhibit a considerable range in proton dissociation constants and include catechol (cat, 1), 4,5-dihydroxy-*m*-benzenedisulfonate (Tiron, 2), 4-nitrocatechol (ncat, 3), 3,4-dihydroxyphenylacetic acid (dhpa, 4), and 2,3-dihydroxybenzoic acid (dhba, 5).



By examining the formation constants of ferric complexes with substituted catechol ligands, we have established a reasonable model with which to predict the lower limit for the constant in those ferric siderophore complexes where catechol moieties are the functional units.

The results of the present study and those from reliable past studies delimit the value for the equilibrium constant for the reaction



to the range 10^{40} - 10^{45} . This number is enormous by comparison to iron complexes with other oxygen-containing ligands. It predicts, for example, that catechol ligands should readily displace cyanide groups from ferricyanide and that Fe_2O_3 (rust) should easily dissolve in basic solutions of catechol. Both reactions occur.

With the exception of the dhba system, which was complicated by mixed-mode coordination, the ligands formed complexes of varying overall stabilities which parallel their ligand base strengths. For a group of similar ligands the plot of the first dissociation constants of the ligands ($\text{p}K_{\text{a}1}$) against the first formation constants of the corresponding metal-ligand complexes ($\log K_1$) is expected to produce a straight line. Such a plot for ferric catechol complexes (Fig. 1) shows linear behavior with sulfonated catechols giving the greatest deviation, to form complexes more stable than predicted. In general there is good correlation between proton and ferric ion

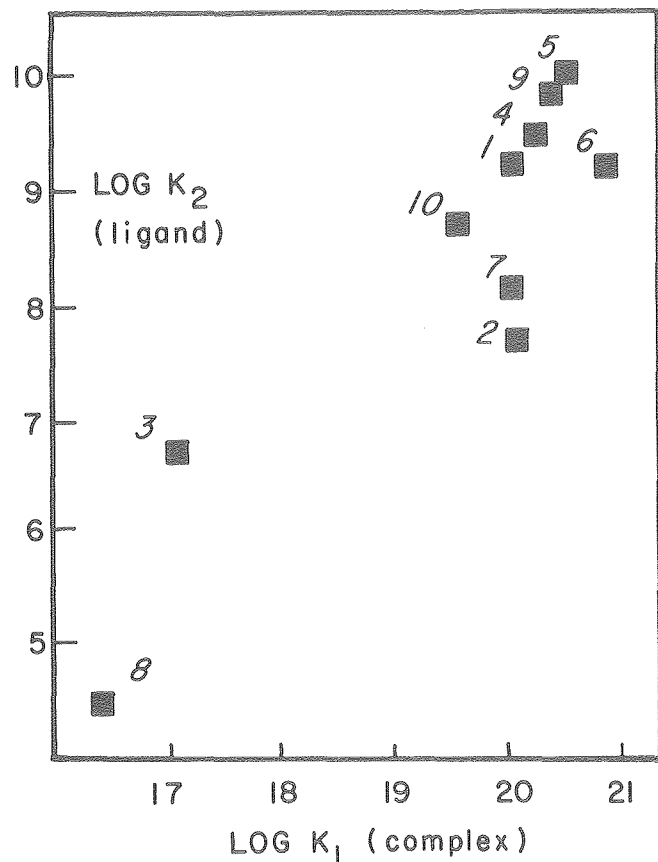


Fig. 1. Plot of $\text{p}K_{\text{a}1}$ (ligand) vs. $\log K_1$ (complex). Ferric complexes with ligands cat (1); Tiron (2), Ref. 6; ncat(3); dhpa (4); dhba (5); cat (6), Ref. 6; 2,3-dihydroxy-6-sulfonaphthalene (7); Ref. 5; 4-nitroso-5,6-dihydroxybenzene-1,3-disulfonate (8), Ref. 5; L-3,4-dihydroxyphenylalanine (9), Ref. 6; 3,4-dihydroxybenzoic acid (10), Ref. 6. (XBL 7610-4896)

affinity with neither steric factors nor the overall charge on the deprotonated ligand contributing greatly to the stability trends.

* * *

[†]Brief version of *J. Am. Chem. Soc.* **99**, 2003 (1977).

1. J. B. Neilands, Ed. *Microbial Iron Metabolism* (Academic Press, New York, N.Y., 1974); J. B. Neilands, in *Inorganic Biochemistry*, G. Eichhorn, Ed. (American Elsevier, New York, N. Y., 1973), p. 167 ff; K. N. Raymond, *Adv. Chem. Ser.* **162**, 1977.
2. J. R. Pollack and J. B. Neilands, *Biochem. Biophys. Res. Commun.* **38**, 989 (1970); I. G. O'Brien and F. Gibson, *Biochem. Biophys. Acta* **215**, 393 (1970).
3. G. Vogler, *Arch. Exp. Pathol. Pharmacol.* **194**, 281 (1940).
4. S. Green, A. Mazur, and E. Shorr, *J. Biol. Chem.* **220**, 237 (1956).
5. A. Willi and G. Schwarzenbach, *Helv. Chim. Acta* **34**, 528 (1951); G. Heller and G. Schwarzenbach, *ibid.* **35**, 812 (1952); L. Vareille, *Bull. Soc. Chim. Fr.*, 1496 (1955); R. Nasanen and J. Veivo, *Suom. Kemistil.* **29B**, 213 (1956).

6. W. A. E. McBryde, *Can. J. Chem.* **42**, 1917 (1964).
7. J. Tsin-Jao, L. Sommer, and A. Okac, *Collect. Czech. Chem. Commun.* **27**, 1171 (1962).
8. Y. Murakami and K. Nakamura, *Bull. Chem. Soc. Japan* **36**, 1408 (1963).
9. M. Beran and S. Havelka, *Collect. Czech. Chem. Commun.* **32**, 2944 (1967).
10. R. Abu-Eittah, Z. Mobarak, and S. El-Lathy, *J. Prakt. Chem.* **316**, 235 (1974).
11. J. H. Nibert, M. S. thesis, University of California, Berkeley, 1975.
12. E. Mentasti and E. Pelizzetti, *J. Chem. Soc., Dalton Trans*, 2605 (1973); E. Mentasti, E. Pelizzetti, and G. Saini, *ibid.*, 2609 (1973).
13. E. Mentasti, E. Pelizzetti, and G. Saini, *J. Inorg. Nucl. Chem.* **38**, 785 (1976).
14. S. S. Isied, G. Kuo, and K. N. Raymond, *J. Am. Chem. Soc.* **98**, 1763 (1976); K. N. Raymond, S. S. Isied, L. D. Brown, F. R. Fronczek, and J. H. Nibert, *ibid.* **98**, 1767 (1976).

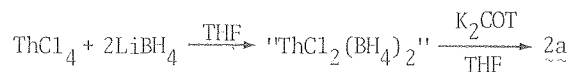
Synthetic and Structural Studies of Actinides and Other Compounds

1. CYCLOOCTATETRAENEACTINIDE (IV) BIS-BOROHYDRIDES[†]

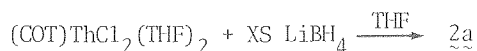
Jeffrey P. Solar, Andrew Streitwieser, Jr. and Norman Edelstein

Although bis(η^8 -cyclooctatetraene)actinide (IV) complexes have been extensively studied since the synthesis of uranocene in 1968,¹ mono-COT actinide "half-sandwiches" were unknown until the recent synthesis of (RCOT)ThCl₂(THF)₂ (1) by Streitwieser and LeVanda.² Based on the volatility of actinide borohydride complexes,³ we hoped that replacement of the chlorines by BH₄⁻ groups would result in more volatile complexes. Also of interest is the nature of the bonding of the BH₄ groups to the metal center; both bidentate and tridentate bonding to the BH₄ groups are known for actinide compounds.

The preparations of (C₈H₈)Th(BH₄)₂ (2a) and (η -C₄H₄C₈H₇)Th(BH₄)₂ (2b) have been achieved by several routes.⁴ Refluxing an equimolar mixture of Th(BH₄)₄(THF)₂ and di-n-butylthorocene in THF gave 2b in 90% yield. Because of the low solubility of thorocene, 2a is more easily prepared by the reaction of equimolar amounts of Th(BH₄)₄(THF)₂ and K₂COT in THF. We also prepared 2a by the sequence:



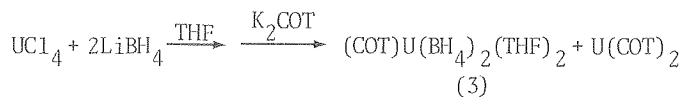
This route is made more complicated, however, by the necessity to remove the LiCl also formed. In addition, 2a is formed in the reaction of 1 with excess LiBH₄:



2a and 2b are white microcrystalline products soluble in THF and benzene but not volatile. The compounds are readily characterized by ¹H NMR and infrared spectroscopy. The room temperature pmr

spectrum of 2a in C₆D₆ shows 2 molecules of coordinated THF in addition to the COT and two equivalent BH₄ groups. The quartet from the borohydride protons collapses to a singlet at low temperature due to loss of B-H coupling and indicates fluxional behavior among these protons. The IR spectrum is in accord with tridentate bending to the borohydride. The B-H_{terminal} (2482 cm⁻¹) and B-H_{bridging} (2282, 2220, 2150 cm⁻¹) bonds are similar to those for Th(N(SiMe₃)₂)₃BH₄ for which tridentate geometry has been established by a crystal structure determination.⁵ The strong bond at about 715 cm⁻¹ appears to be characteristic of the mono-ring or "half-sandwich" structure.

The preparation of the uranium analog of 2 has also been achieved. Both uranocene and (COT)U(BH₄)₂ (3) are formed on addition of COT⁼ to a mixture of UCl₄ in THF; (3) is favored by the slow addition of a dilute solution of the dianion. The resultant brown product



is soluble in benzene and THF and has an IR spectrum nearly identical to 2a. The visible spectrum of 3 contains a strong band at 396 nm and tails off to longer wavelengths much like a uranocene.

* * *

[†]Brief version of LBL-10348.

1. A. Streitwieser, Jr., "Organometallic Compounds of the f-Elements," T. J. Marks and R. D. Fischer, Eds. (Reidel Publishing Co., Amsterdam, 1979), pp. 149-177.
2. C. LeVanda, Jeffrey P. Solar, and A. Streitwieser, Jr., submitted to *J. Am. Chem. Soc.*
3. H. I. Schlesinger and H. C. Brown, *J. Am. Chem. Soc.* **75**, 219-221 (1953).
4. J. P. Solar, A. Streitwieser, Jr., and N. M. Edelstein, submitted to *A.C.S. Symposium Series*.
5. H. W. Turner, R. A. Andersen, A. Zalkin, and D. H. Templeton, *Inorg. Chem.* **18**, 1221-1224 (1979).

2. STRUCTURE OF TWO CRYSTALLINE FORMS OF CYCLOOCTATETRAENETHORIUM(IV) DICHLORIDE BISTETRAHYDROFURAN[†]

Allan Zalkin, David H. Templeton, Carole LeVanda and Andrew Streitwieser, Jr.

White crystals of the title compound, because of their extreme sensitivity to the atmosphere, were sealed inside thin-walled quartz capillaries for the x-ray experiments.

Two chemically equivalent but crystallographically different crystalline materials were observed. A complete molecular structure determination was performed on each type of crystal by single-crystal x-ray diffraction techniques. The α -form crystallizes in the monoclinic space group P2₁/n with parameters a = 8.589(3) Å, b = 27.22(2) Å, c = 7.950(3) Å and β = 96.92(4)°; with 4 molecules

in the unit cell the x-ray density is 1.985 g cm^{-3} . The β -form crystallizes in the monoclinic space group $P2_1/c$ with parameters $a = 13.036(4) \text{ \AA}$, $b = 11.601(3) \text{ \AA}$, $c = 24.598(8) \text{ \AA}$ and $\beta = 102.90(4)^\circ$; with 8 molecules in the unit cell the x-ray density is 2.020 g cm^{-3} .

The Th atom is bonded to the cyclooctatetraene (COT) ring, to two chloride ions and to the oxygen atoms of the two tetrahydrofuran (THF) molecules (Figs. 1 and 2). The Th atom is 2.02 \AA from the plane of the COT ring. The chloride ions and THF molecules are alternately disposed on the opposite side, with Th-Cl and Th-O distances of $2.686 \pm 0.006 \text{ \AA}$ and $2.57 \pm 0.02 \text{ \AA}$ respectively. The Cl and the O atoms are very nearly equidistant from the COT plane. The comparable Th-to-ring distance in thoracene¹ is 2.00 \AA , and the Th-Cl distance in these structures are just slightly under the 2.72 \AA and 2.90 \AA reported for ThCl_4 .²

The three molecular structures determined in this study are chemically identical with essentially identical bond distances. About the only significant geometrical difference between the α and β forms is the larger Cl-Th-Cl and smaller O-Th-O angles that the α form exhibits and which is probably a packing effect. Nothing in the experiments reported here gives any information as to what fosters the crystallization of one form or another.

* * *

† Brief version of LBL-10537.

1. A. Avdeef, K. N. Raymond, K. O. Hodgson, and A. Zalkin, *Inorg. Chem.* **11**, 1083 (1972).
2. K. Mucker, G. S. Smith, Q. Johnson, and R. E. Elson, *Acta Crystallogr.* **B25**, 2362 (1969).

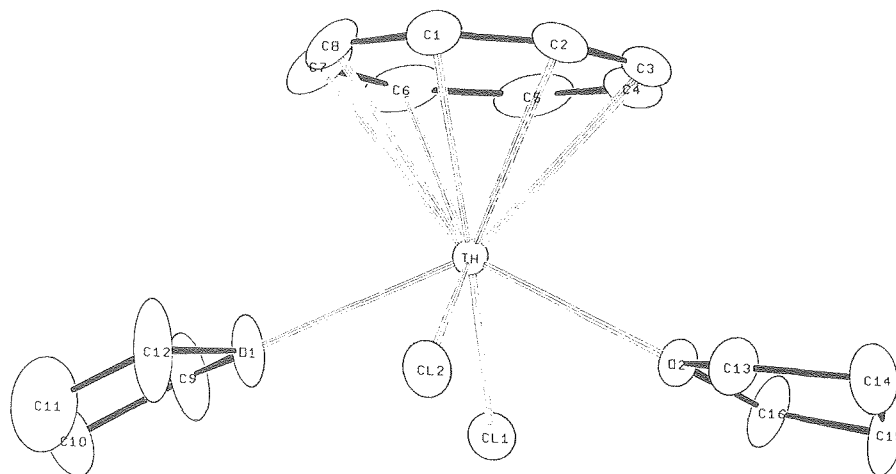


Fig. 1. ORTEP drawing of the $\text{C}_8\text{H}_8\text{ThCl}_2(\text{OC}_4\text{H}_8)_2$ molecules, α -form. (XBL 793-8720)

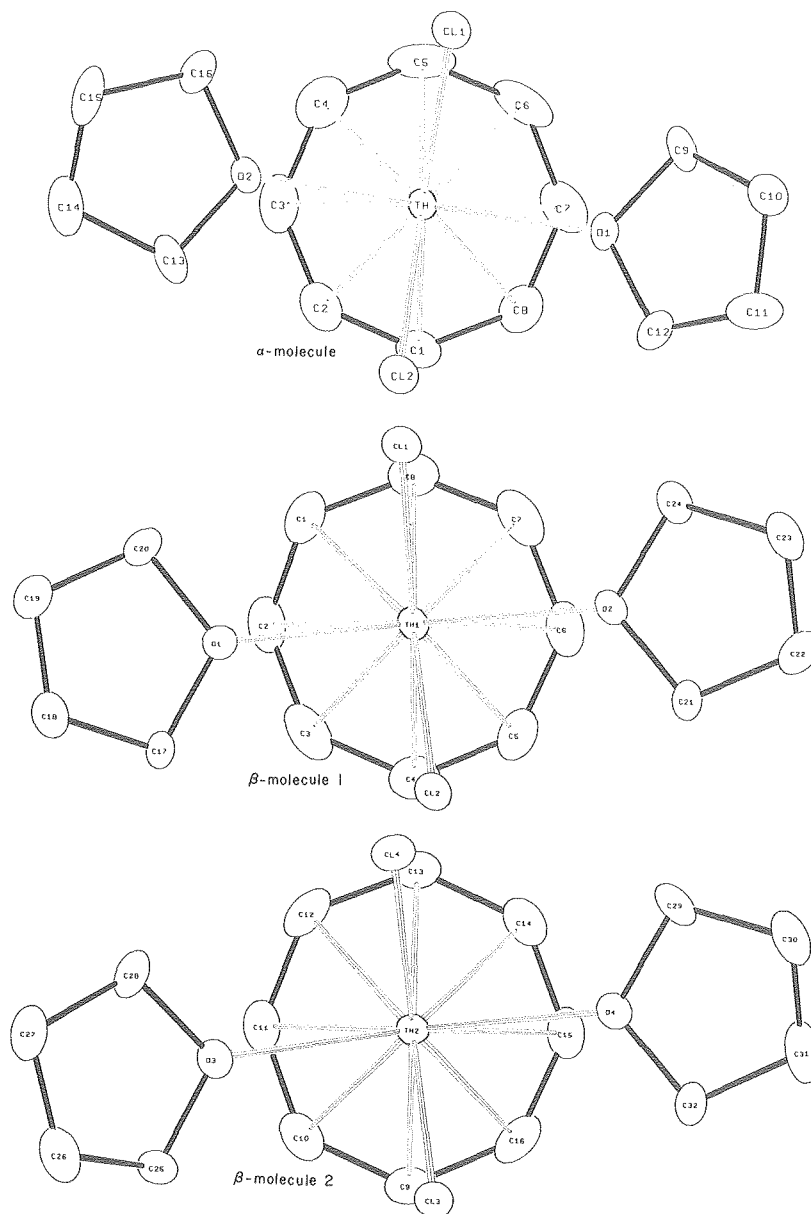


Fig. 2. ORTEP drawing perpendicular to the COT ring showing the orientation of the Cl atoms and THF molecules to the COT ring in the three independently determined molecular structures.

(XBL 792-9430)

3. HYDRIDO[TRIS(HEXAMETHYLDISILYLAMIDO)]-THORIUM(IV) AND -URANIUM(IV)⁺

Howard W. Turner, Stephen J. Simpson, and Richard A. Andersen

Reaction of chlorotris(hexamethyldisilylamido)thorium(IV)¹ with one molar equivalent of sodium hexamethyldisilylamide in refluxing tetrahydrofuran yields hydridotris(hexamethyldisilylamido)thorium as white needles from pentane,² mp 145-147°C, $\nu_{\text{ThF}} = 1480 \text{ cm}^{-1}$, $^1\text{HNMR}$ (PhH) δ 0.90 and 0.40 due to the hydride and trimethylsilyl resonances, respectively. The deuteride, $\text{DTh}[N(\text{SiMe}_3)_2]$,

$\nu_{\text{ThD}} = 1060 \text{ cm}^{-1}$ can be prepared by refluxing $\text{ClTh}[N(\text{SiMe}_3)_2]_3$ and $\text{NaN}(\text{SiMe}_3)_2$ in perdeuterio-tetrahydrofuran. The uranium hydride and deuteride were prepared similarly. Hydridotris(hexamethyldisilylamido)uranium was crystallized from pentane as brown-yellow needles,² mp 97-98°C, $\nu_{\text{UH}} = 1430 \text{ cm}^{-1}$, $\nu_{\text{UD}} = 1020 \text{ cm}^{-1}$. We have been unable to locate the hydride signal in the $^1\text{HNMR}$ spectrum of this paramagnetic ($\mu_B = 2.6 \text{ B.M.}$ in benzene solution) substance, though the trimethylsilyl groups resonate at δ -19.5. The hydrides can also be prepared from $\text{ClM}[N(\text{SiMe}_3)_2]_3$ and *tert*-butyllithium or lithium triethylhydridoborate in pentane.

The metal-bound hydrides were further characterized by their reaction chemistry, see Scheme 1. The hydrides react with carbon tetrachloride, yielding chloroform (identified by its NMR spectrum) and $\text{ClM}[\text{N}(\text{SiMe}_3)_2]_3$, M is thorium or uranium. The latter were identified by mp, mixed mp, ir, and NMR spectra. Further, addition of n-butyllithium to a pentane solution of the hydrides followed by methylbromide yields $\text{MeM}[\text{N}(\text{SiMe}_3)_2]_3$,¹ M = Th or U quantitatively. The product from reaction of n-butyllithium with the hydride derivatives affords $\text{HM}[\text{N}(\text{SiMe}_3)_2]_3$ or $\text{DM}[\text{N}(\text{SiMe}_3)_2]_3$ (M is Th or U) upon addition of trifluoroacetic acid or deuterio-trifluoroacetic acid, respectively.

* * *

[†]Brief version of J. Am. Chem. Soc. 101, 2782 (1979).

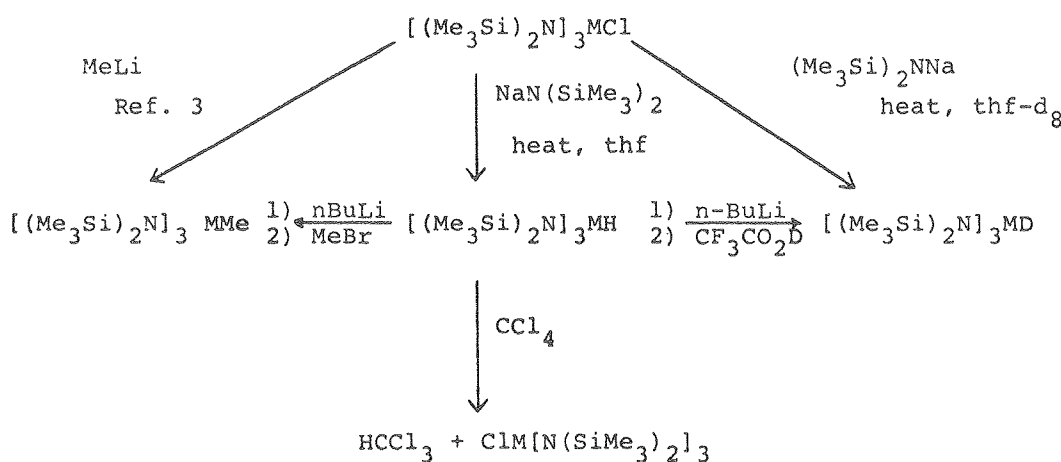
1. H. W. Turner, R. A. Andersen, D. H. Templeton, and A. Zalkin, Inorg. Chem. 18, 1221 (1979).

2. All new compounds gave satisfactory elemental analysis for C, H, and N and molecular ions (M-2) in the mass spectrometer.

methyl-, tetrahydroborato-, chloro-tris(hexamethyl-disilyl)amido uranium analogues⁷ nor the uranium (III) species, $\text{U}[\text{N}(\text{SiMe}_3)_2]_3$,⁸ exchange with deuterium under similar conditions.

The observation of H-D exchange in the uranium (IV) species might be explained by a series of oxidative-addition, reductive-elimination cycles since uranium (VI) is a well-known oxidation state. This mechanism might seem questionable, since no H-D exchange in the corresponding thorium derivative, $\text{HTh}[\text{N}(\text{SiMe}_3)_2]_3$, occurs, thorium(VI) being unknown. However, the thorium hydride undergoes complete exchange under similar conditions, yielding $\text{DTh}[\text{N}[\text{Si}(\text{CD}_3)_2]_3]_3$, $\nu_{\text{CD}} = 2207 \text{ cm}^{-1}$, $\nu_{\text{ThD}} = 1060 \text{ cm}^{-1}$, mp, 144-147°C.⁹ Elemental analysis,¹⁰ lack of a ¹H NMR spectrum, and mass spectroscopic analysis¹¹ confirm that the f⁰-hydride undergoes complete exchange.

Insight into the mechanism of exchange is assisted by isolation of the four-membered ring metallobutane, $[\text{Me}_3\text{Si}_2\text{N}]_2\text{-M}[\text{N}(\text{SiMe}_3)_2]_2$ (SiMe_2CH_2)



M = Th, U

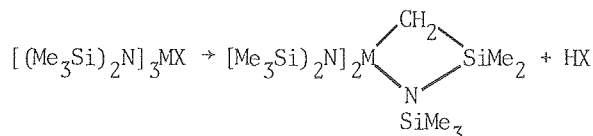
Scheme 1

4. HYDROGEN-DEUTERIUM EXCHANGE: PERDEUTERO-HYDRIDO-TRIS (HEXAMETHYLDISILYL)AMIDO-THORIUM(IV) AND -URANIUM(IV)[†]

Stephen J. Simpson, Howard W. Turner, and Richard A. Andersen

Stirring a pentane solution of $\text{HU}[\text{N}(\text{SiMe}_3)_2]_3$ ¹ under deuterium (1 atm, 40 equivalents/5 cycles, room temperature) results in complete exchange of all hydrogen atoms for deuterium yielding $\text{DU}[\text{N}[\text{Si}(\text{CD}_3)_2]_3]_3$, $\nu_{\text{CD}} = 2210 \text{ cm}^{-1}$, $\nu_{\text{UD}} = 1027 \text{ cm}^{-1}$, mp, 95-97°C.² Elemental analysis,³ absence of a ¹H NMR spectrum, and isolation of $[(\text{CD}_3)_3\text{Si}]_3\text{ND}$ after hydrolysis⁴ confirms that all fifty-five hydrogen atoms have been exchanged for deuterium. The exchange reaction is reversible since the perdeutero-compound exchanges with molecular hydrogen to give $\text{HU}[\text{N}(\text{SiMe}_3)_2]_3$. Neither the

where M is thorium or uranium by pyrolysis of the thorium or uranium hydrides (neat, 180-190°C, 1 atm) or methyls (neat, 150-160°C, 1 atm). The colorless diamagnetic thorium derivative¹² mp, 109-111°C, yields at 180 MHz a ¹H NMR spectrum



M = Th or U; X = H or Me

which is temperature independent to -85°C and which consists of four single resonances at δ 0.37, 0.38, 0.49, and 0.56 in area ratio 36:9:2:6 due to $(\text{Me}_3\text{Si})_2\text{N}$, Me_3Si , CH_2 , and Me_2Si , respectively. The ¹³C NMR spectrum proves the metallacycle formation, since it consists of three quartets centered

7. H. W. Turner, R. A. Andersen, D. H. Templeton, and A. Zalkin, *Inorg. Chem.* **18**, 1221-1224 (1979).
 8. R. A. Andersen, *Inorg. Chem.* **18**, 1507-1509 (1979).
 9. Melting point of the undeuterated hydride is 145-147°C.³
 10. Analysis of $C_{18}D_{55}N_3Si_6Th$ requires C, 28.1; D, 14.3; N, 5.49%. Found: C, 28.4; D, 13.6; N, 5.54%.
 11. The amine is $\geq 91\%$ deuterated.^{6,7,8}
 12. Satisfactory C, H and N analysis and a monomeric molecular ion by mass spectrometry were obtained.
 13. K. I. Geil and J. Schwartz, *J. Am. Chem. Soc.* **100**, 3246-3248 (1978).
 14. D. R. McAlister, D. K. Erwin and J. E. Bercaw, *J. Am. Chem. Soc.* **100**, 5966-5968 (1978).

5. STRUCTURE AND BONDING OF f- AND d- TRANSITION METAL ORGANOMETALLIC COMPOUNDS[†]

K. N. Raymond and C. W. Eigenbrot, Jr.

Before the structure analysis of uranocene,¹ $U(C_8H_8)_2$, almost nothing was known about the structure and bonding of organoactinides and lanthanides—a situation we have endeavored to change during the past ten years. A question that frequently occurs in discussions of this chemistry is: "How covalent is the bonding in these compounds?" Within a careful and limited structural definition of covalent and ionic bonding, this question can be examined in some detail.

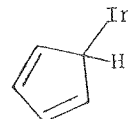
A Structural Definition of Covalent/Ionic Bonding

1. The geometries of ionic compounds tend to be irregular and depend on the steric bulk, number, and charge of the ligands. The coordination number observed is the result of a balance between ionic attractive forces and nonbonded repulsions. This is in marked contrast to the regular, directional bonds which typify covalent compounds.
2. Bond lengths for a series of structurally similar compounds will follow systematically from their "ion size" and coordination number—that is, ionic radii can be used to predict

bond lengths. In contrast, the structure of predominantly covalent compounds show pronounced departures from such predictions.

Structural Types and Coordination Numbers

Among MCp_3 compounds, the structure of tris(cyclopentadienyl)indium(III)² is composed of indium atoms which achieve a relatively regular four-coordinate tetrahedral environment of σ bonds by bonding to 2 η^1 Cp rings, with the third ring forming a η^1, η^1 bridge. The C-C bond lengths within the Cp rings show localized double bond character of the type



In short, $InCp_3$ provides a classic example of the structural effects of covalent bonding.

In stark contrast, the $LnCp_3$ compounds show structures whose coordination numbers and geometries change markedly with the metal ion radius. The small (0.87 Å) Sc^{3+} ion in $ScCp_3$ (Ref. 3) is eight-coordinate in a polymeric structure formed by 2 η^5 Cp rings and a third ring which forms an η^1, η^1 bridge. All of the Cp rings show undistorted pentagonal symmetry with no evidence of C-C double bond localization. The larger (1.13 Å) Sm^{3+} ion in $Sm(indenyl)_3$ ⁴ is nine-coordinate with three η^5 rings providing all of the coordination. In tris(methylcyclopentadienyl)-neodymium(III), $Nd(MeCp)_3$,⁵ the metal ion (1.17 Å) is 10-coordinate through formation of a tetramer in which all three Cp rings form η^5 bonds to Nd and one of the rings also bridges to form an η^1 ring bridge to the adjacent metal ion. It is clear from these examples that the principal determinant of coordination numbers and geometries is the metal size, indicating that an ionic mode of bonding best describes these MCp_3 compounds.

For the series MCp_4 (Fig. 1) there is again a pronounced change in coordination number and structure as the metal ion size increases. In $TiCp_4$ ⁶ the coordination number of the Ti^{4+} ion (0.74 Å) is eight, from two η^5 rings and two η^1 rings. For the larger Zr^{4+} ion (0.91 Å) in $ZrCp_4$ ⁷

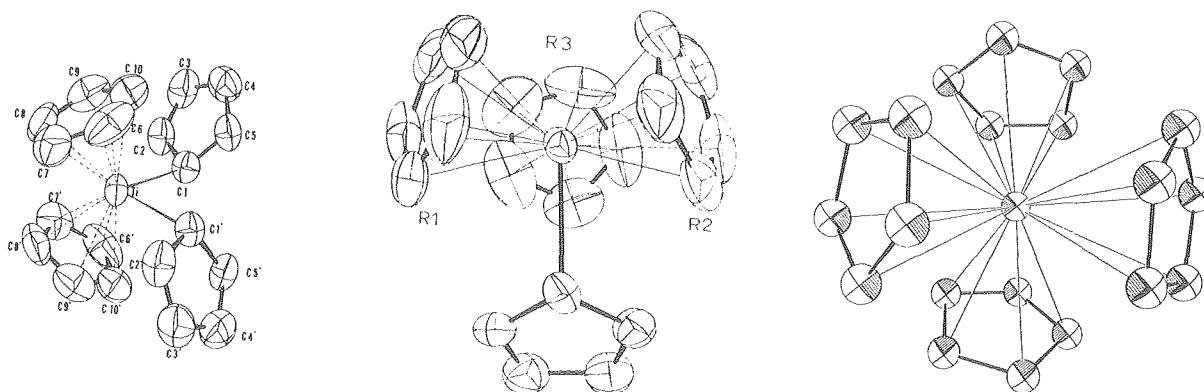


Fig. 1. Structures of tetrakis(cyclopentadienide) complexes: $TiCp_4$ (left), $ZrCp_4$ (center and UCp_4 (right)). (XBL 799-12049)

there are three η^5 rings and one η^1 ring to give a total coordination number of 10. In UCp_4 ⁸ all four Cp rings are η^5 bound in a tetrahedral array to give a total coordination number of 12 around the U^{4+} ion (1.17 Å). Thus, these MCp_4 compounds again demonstrate that metal-ion size plays the dominant role in determining the coordination number and geometry, indicating an ionic mode of bonding.

In the $M(COT)_2$ series, the compounds $Ti(C_8H_8)_2$ and $Ti_2(C_8H_8)_3$ exhibit similar structures,^{9,10} involving one symmetrical η^8 -coordinated COT ring and one nonplanar ring of lower hapticity per atom of titanium. In the analogous zirconium complex,¹¹ the metal's larger size is manifested in an additional coordination site being occupied by a THF molecule in the otherwise similar structure.

Cyclooctatetraene complexes of larger metal ions such as cerium,¹² thorium,¹ and uranium¹ all exhibit two symmetrical η^8 -coordinated COT rings.

Two possible explanations suggest themselves for the failure of the early metals to accept a uranocene-type structure. One is to note that the lanthanide and actinide ions are substantially larger, thereby requiring more ligands to saturate their coordination sphere. The early metals cannot accommodate so large a coordination number and so one COT ring slips to the side—providing a total coordination number of seven or eight. Alternatively, one may note that two η^8 -coordinated COT rings provide 20 π electrons to the metal center in violation of the effective atomic number rule. Thus the second COT ring slips to one side to reduce the number of valence electrons. Both arguments lead one to view the bonding in the actinide metals as largely ionic.

The Covalent/Ionic Structural Criterion of Bond Lengths

Having seen the conclusions drawn by considering the general structural features (i.e., metal coordination number and ligand hapticity) of carbocyclic complexes of the actinides and lanthanides, we now turn to another structural criterion of the mode of bonding—the metal-to-carbon bond distance $[R(M-C)]$. Structural data collected from x-ray and gas phase electron diffraction studies of first-row metallocenes are summarized in Fig. 2. If these compounds involved ionic bonding, the metal-to-carbon distances could be predicted as the sum of the ionic radii of the metal ion and the Cp anion. Another way of saying this is that the difference between the metal-to-carbon distance and the ionic radius of the metal (the effective ionic radius of the Cp ligand) should be constant. In the d-transition metal metallocenes, one cannot assign an effective ionic radius to the Cp anion. If we plot $R(M-C)$ vs. the metal ion radius (Fig. 2) we see that this is not a smooth function.

Figure 3 summarizes corresponding structural data for lanthanide and actinide Cp complexes. We can see that the effective ionic radius for the Cp ligand is essentially invariant in structures of 23 complexes, and is 1.64 ± 0.04 Å. This consistency is illustrated in Fig. 3, where the plot

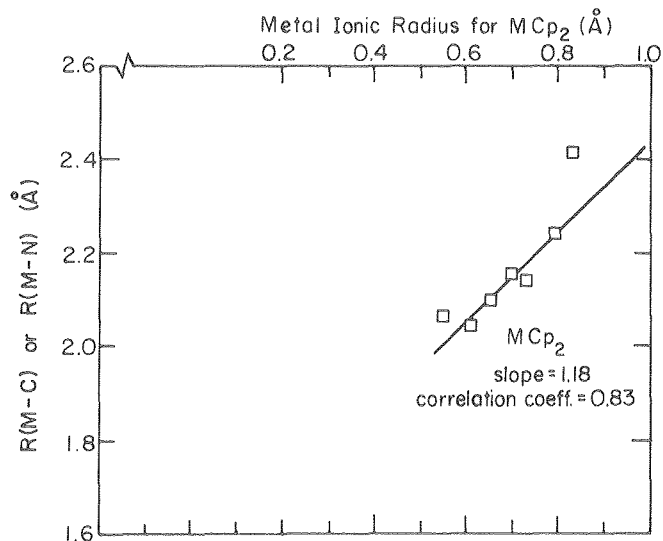


Fig. 2. Plots of average metal ligand distances for metallocenes and silylamide complexes. (XBL 7911-7287A)

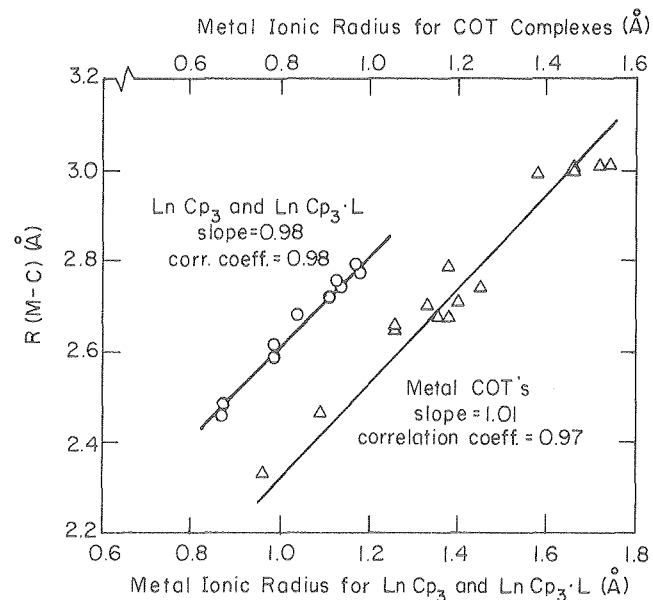


Fig. 3. Plots of average metal carbon distances for lanthanide Cp and metal COT complexes. (XBL 7911-7288)

of $R(M-C)$ vs. the metal ion radius is presented for the available lanthanide complexes. A linear least squares refinement of these data yields a line with slope equal to 0.98 and a correlation coefficient of 0.98 [Eq. (1)] requires that the slope, $dR(M-C)/dr_+$, = 1]. A similar treatment of the MCp_2 data produces a slope equal to 1.18 and a correlation coefficient of 0.83 (Fig. 3). The relatively high correlation coefficient and near unit slope in the former case shows metal-to-carbon bond length varies in direct proportion to metal ion size, a clear indication of predominantly ionic bonding.

A similar treatment of the data from x-ray structures of COT complexes reveals that an effective ionic radius for COT^- can be assigned equal to $1.56 \pm 0.04 \text{ \AA}$, and that the graph of metal ionic radius vs. $R(\text{M}-\text{C})$ (Fig. 3) is a smooth function, with slope = 1.01 and correlation coefficient 0.97.

We conclude that in the limits of our structural definition of covalent/ionic bonding, the bonding in organolanthanides and -actinides is predominantly ionic.¹³

* * *

Brief version of manuscript submitted to Accounts of Chemical Research.

1. A. Avdeef, K. N. Raymond, K. O. Hodgson, and A. Zalkin, *Inorg. Chem.* **11**, 1083 (1972).
2. F. W. B. Einstein, M. M. Gilbert, and D. G. Tuck, *Inorg. Chem.* **11**, 2832 (1972).
3. J. L. Atwood and K. D. Smith, *J. Am. Chem. Soc.* **95**, 1488 (1973).
4. J. L. Atwood, J. H. Burns, and P. G. Lauberau, *J. Am. Chem. Soc.* **95**, 1830 (1973).
5. J. H. Burns, W. H. Baldwin, and F. H. Fink, *Inorg. Chem.* **13**, 1916 (1974).
6. J. L. Calderon, F. A. Cotton, B. G. DeBoer, and J. Takats, *J. Am. Chem. Soc.* **93**, 3592 (1971).
7. R. D. Rogers, R. V. Bynum, and J. L. Atwood, *J. Am. Chem. Soc.* **100**, 5238 (1978).
8. J. H. Burns, *J. Organometal. Chem.* **69**, 225 (1974).
9. H. Dietrich and M. Soltwisch, *Angew. Chem. Intern. Ed. Engl.* **8**, 765 (1969).
10. H. Dierks and H. Dietrich, *Acta Cryst.* **B24**, 58 (1968).
11. D. J. Brauer and C. Kruger, *J. Organometal. Chem.* **42**, 129 (1972).
12. K. O. Hodgson and K. N. Raymond, *Inorg. Chem.* **11**, 3030 (1972).

13. References to the papers cited in Figs. 1 through 3 can be found in: K. N. Raymond, "The Structure and Bonding of 4f and 5f Series Organometallic Compounds," *Organometallics of the f-Elements*, T. J. Marks and R. D. Fischer, Eds. (D. Reidel Publishing Co., Dordrecht, Holland, 1979), pp. 249-280 or K. N. Raymond and C. W. Eigenbrot, Jr., *Acct. Chem. Res.*, submitted for publication.

6. TOWARDS THE SYNTHESIS OF HEPTAVALENT NEPTUNIUM FLUORIDES AND OXYFLUORIDES

Sam Yeh and Neil Bartlett

Model Syntheses for NpOF_5 and its Precursors.
Xenon hexafluoride has been explored as a fluorinator by oxygen-fluorine exchange, as an oxidizer and as a solvent, with potential application to the synthesis of high oxidation state neptunium compounds. Since this material is not only a powerful oxidizer but also yields the detonator xenon trioxide, on interaction with water or oxides, its chemistry has been explored initially with systems related to those anticipated in the neptunium chemistry, but without its radiation hazard.

UOF_4 , KUOF_5 , CsUOF_5 and the related compounds of the third row transition metals were treated with XeF_6 . The findings are summarized in Table 1. The AMOF_5 salts ($A = \text{K}$ or Cs , $M = \text{U}$ or W) were obtained by treating MOF_4 with the corresponding alkali fluoride in anhydrous HF. In the tungsten case, the HF solutions were refluxed at about 60° , whereas for uranium the reaction was carried out at ambient temperature. The XeF_6 reactions were carried out using Teflon FEP tubes sealed at one end and each fitted with a Whitey valve (1KS4). Excess XeF_6 was always used. The vacuum system was pre-treated with F_2 before transferring XeF_6 . The gas products were characterized using gas-phase infrared spectroscopy and solid products were subjected to Raman and X-ray powder diffraction spectroscopy.

The oxide scavenging ability of XeF_6 was demonstrated in the reactions with uranium and tungsten compounds, where the molecular or complex oxide fluorides lost all their oxide to XeF_6 . This is consistent with the report¹ that UO_2F_2 reacts with XeF_6 to form UF_6 .

The M-F stretching and M-O stretching frequencies from the Raman spectroscopic data, for related fluorides and oxyfluorides, are given in Table 2. They indicate the anticipated reduction in bond strength with decrease in oxidation state or increase in coordination number and provide a useful guide for what should be anticipated for NpOF_5^- , NpF_7^- and NpOF_5 .

On the basis that a comparison of the tungsten fluorides and oxyfluoride systems with those of rhenium and osmium could give hints of what to expect for neptunium in relationship to uranium, studies of related rhenium and osmium systems have

Table 1. Interaction of XeF_6 with various oxides and oxyfluorides.

| XeF_6 + reactants | XeOF_4 + products |
|---------------------------------|---|
| UOF_4 | UF_6 |
| KUOF_5 | KUF_7^a |
| CsUOF_5 | CsUF_7^a |
| WOF_4 | WF_6 |
| KWO_5 | KWF_7^a |
| $\text{CsF} \cdot \text{WOF}_4$ | CsWF_7^a |
| KReU_4 | $\text{K}^+ \text{ReO}_2\text{F}_4^{-b}$ |
| OsO_4 | $\text{XeF}_5^+ \text{OsO}_3\text{F}_3^-$ |

^aX-ray powder diffraction data for CsWF_7 and CsUF_7 are in agreement with previous reports.^{3,4} CsUOF_5 has a rhombohedral unit cell $a = 5.39 \text{ \AA}$, $\alpha = 95.54^\circ$ and is iso-structure with CsWOF_5 ³. Although KUF_7 , KWO_5 and KWF_7 show unique patterns, they have not been indexed.

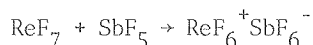
^bAlso prepared by the method of Peacock.⁵

Table 2. Some stretching frequencies for fluoro and oxyfluoro derivatives of uranium and tungsten.

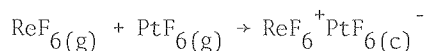
| Compounds | $\nu_{M=O}(\text{cm}^{-1})$ | $\nu_{M-F}(\text{cm}^{-1})$ |
|--------------------|-----------------------------|-----------------------------|
| UF ₆ | --- | 667 |
| KUF ₇ | --- | 626 |
| CsUF ₇ | --- | 619 |
| UOF ₄ | 895, 891, 885 | 667, 658, 647 |
| KUOF ₅ | 815 | 592 |
| CsUOF ₅ | 818 | 593 |
| WF ₆ | --- | 771 |
| KWF ₇ | --- | 714 |
| CsWF ₇ | --- | 707 |
| WOF ₄ | 1055 | 733 |
| KWOF ₅ | 1040 | 697 |

been undertaken. In contrast to the complete fluorination of the tungsten oxyfluorides by XeF₆, its interaction with rhenium and osmium oxy-systems was only partial, as may be seen from Table 1. The vibrational spectroscopic data for KReO₂F₄ and XeF₅OsO₃F₃ indicate pseudo-octahedral anions ReO₂F₄⁻ and OsO₃F₃⁻ respectively. The absence of ReOF₆⁻, ReO₃F₂⁻, or OsO₂F₅⁻ suggests that a six-coordinate mononegative anion is preferred. Certainly such anions as ReO₂F₄⁻ and OsO₃F₃⁻ must be compact. Perhaps this compactness contributes inertness to further interaction with XeF₆. The reactivity of the WOF₅⁻ and UOF₅⁻ may simply be a consequence of the larger size and coordinating ability of the central atoms in these ions.

Syntheses for NpF₆⁺ Salts. In 1976 Jacob reported² the preparation of ReF₆⁺ salts by employing SbF₅ as a fluoride ion acceptor for ReF₇:

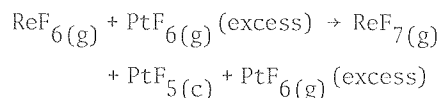


He also claimed that ReF₆ was oxidized by PtF₆ according to the equation:

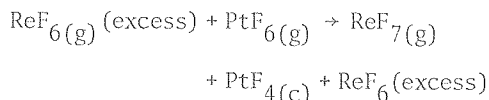


Since NpF₇ is unlikely to be a very stable entity (if it can be made at all), the latter synthesis has great appeal as an approach to NpF₆⁺. As a preliminary to the NpF₆/PtF₆ study the Jacob synthesis was repeated. The claim for ReF₆⁺PtF₆⁻ has not been sustained.

Treatment of ReF₆ with excess PtF₆ proceeded according to the equation:



With ReF₆ in excess the reaction was:



It is possible that the interaction to produce the ReF₆⁺PtF₆⁻ salt can occur at low temperatures, but not as Jacob described, at room temperature. Jacob's material was not characterized and his description of the solid product matches that for PtF₅. NpF₆ oxidation remains to be tried and since NpF₇ is not a thermodynamically favored entity it remains possible that PtF₆ can yield NpF₆⁺.

Jacob's claim for a complex between ReF₇ and SbF₅ appears to be valid since treatment of a molar excess of ReF₆ with Kr₂F₃⁺SbF₆⁻ yields a colorless solid which has the stoichiometry required for ReF₆⁺SbF₆⁻. The Raman spectrum agrees with that given by Jacob.² It appears however that the ReF₆⁺SbF₆⁻ loses ReF₇ in the laser beam (used in Raman spectroscopy) and it may be that ReF₆⁺Sb₂F₁₁⁻ is a more thermodynamically favorable salt.

It is evident that ReF₇ is a very poor fluoride ion donor, since attempts to prepare ReF₆⁺SbF₆⁻ from the components, in anhydrous HF, failed. This indicates that the solvent effectively competes with ReF₇ as a F⁻ donor. Clearly it is desirable to carry out a single crystal X-ray diffraction study to settle the structure of ReF₆⁺SbF₆⁻ decisively.

It is evident that the most promising approach to synthesis of NpF₆⁺ is via the interaction of NpF₆ with Kr₂F₃⁺SbF₆⁻ or KrF⁺Sb₂F₁₁⁻ but a study of the interaction of NpF₆ with PtF₆ (or better, AuF₆ if it can be prepared) will also be undertaken.

* * *

1. M. Bohinc and B. Frlec, *J. Inorg. Nucl. Chem.* 34 2942 (1972).
2. F. Jacob and M. Fahnle, *Angew. Chem. Int. Ed.* 15, 159 (1976).
3. R. D. Peacock, *J. Chem. Soc.*, 2170 (1958).
4. N. S. Nikolaev and V. F. Sukhovekhov, *Dokl. Akad. Nauk. SSSR* 136, 621 (1961).
5. R. D. Peacock, *J. Chem. Soc.*, 602 (1955).

7. STRUCTURE OF TRIS(UREA)DIOXOURANIUM(VI) SULFATE, UO₂(OC(NH₂)₂)₃ SO₄⁺

Helena Ruben, Brock Spencer, David H. Templeton, and Allan Zalkin

Slow evaporation of aqueous solutions of uranyl sulfate and urea yielded fluorescent, lime-green crystals similar in color to crystals of

$\text{UO}_2(\text{OC}(\text{NH}_2)_2)_5(\text{NO}_3)_2$.¹ The crystals were stable in air during the month of x-ray investigation. The crystals are monoclinic, space group $P2_1/n$ with parameters $a = 7.619(2) \text{ \AA}$, $b = 24.706(8) \text{ \AA}$, $c = 6.928(2) \text{ \AA}$, $\beta = 91.06(2)^\circ$, and $V = 1303.9 \text{ \AA}^3$; for $Z = 4$, the calculated density is 2.78 g cm^{-3} ; the density measured by flotation in a mixture of tetrachloromethane and tribromomethane was 2.79 g cm^{-3} .

The molecular structure was determined by single-crystal x-ray diffraction methods.

The structure (Fig. 1) consists of chains of alternate tris(urea) dioxouranium(IV) ions and sulfate ions, with the sulfate ions contributing two oxygen atoms to the pentagonal bipyramid of oxygen atoms coordinated to the uranium(VI) ion. Two urea oxygen atoms [O(4) and O(5)] are perpendicular to the uranyl ion axis; the third urea oxygen atom [O(7)] is 0.16 Å from the equatorial plane defined by U, O(4), and O(5) while the two sulfate oxygen atoms are 0.30 Å [O(3)] and 0.20 Å [O(6)] from the equatorial plane on the side opposite to O(7). The urea molecules are planar. One urea molecule is held approximately coplanar with the uranyl equatorial plane by hydrogen bonds to two of the sulfate oxygen atoms, [N(1)-H(1)---O(8) and N(2)-H(3)---O(8) in Fig. 1], while the other two urea molecules are approximately perpendicular to the uranyl equatorial plane. Bond distances and angles for urea and for the uranium(VI) coordination polyhedron are in close agreement with those in $[\text{UO}_2(\text{OC}(\text{NH}_2)_2)_5](\text{NO}_3)_2$ ¹ and

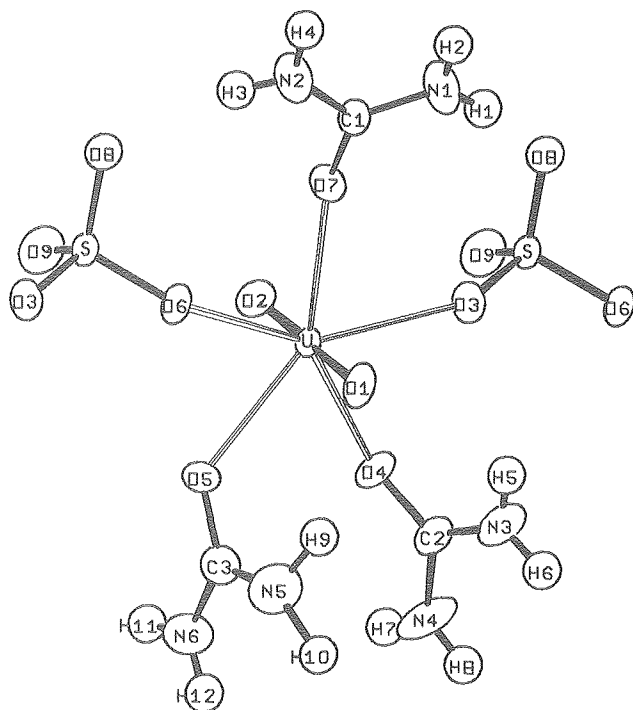


Fig. 1. ORTEP drawing of the tris(urea)dioxouranium(VI) sulfate structure. An additional sulfate group is included to show the bridging. The sulfate on the right is related to the one on the left by a translation along c of one unit cell length. (XBL 796-10086)

$[\text{UO}_2(\text{H}_2\text{O})(\text{OC}(\text{NH}_2)_2)_4](\text{NO}_3)_2$.² The present compound, with two sulfate oxygen atoms coordinated to the uranyl ion, is intermediate between the nitrate salts mentioned above, in which the nitrate ions are not coordinated to the uranyl ion so that anion bridging between cation complexes cannot occur, and the two forms of $2\text{UO}_2\text{SO}_4 \cdot 7\text{H}_2\text{O}$ ^{3,4} in which three sulfate oxygen atoms are coordinated to the uranyl ion, resulting in complex anion bridging between cation complexes.

* * *

⁺Brief version of LBL-9478.

1. A. Zalkin, H. Ruben, and D. H. Templeton, *Inorg. Chem.* **18**, 519 (1979).
2. N. K. Dalley, M. H. Mueller, and S. H. Simonsen, *Inorg. Chem.* **11**, 1840 (1972).
3. A. Zalkin, H. Ruben, and D. H. Templeton, *Inorg. Chem.* **11**, 3701 (1978).
4. N. P. Brandenberg and B. O. Loopstra, *Cryst. Struct. Commun.* **2**, 243 (1973).

8. A STRUCTURE OF DI- μ -AQUO-BIS(DIOXODINITRATO-URANIUM(VI))DIIMIDAZOLE, $[\text{UO}_2(\text{NO}_3)_2 \cdot \text{H}_2\text{O} \cdot \text{C}_3\text{H}_4\text{N}_2]_2$, A WATER-BRIDGED DIMER OF URANYL NITRATE[†]

Dale L. Perry, Helena Ruben, David H. Templeton, and Allan Zalkin

While a large number of uranium complexes have been postulated as dimers, trimers, or polymers, relatively few of them have been corroborated by x-ray crystallography. Several of these compounds are connected by oxygen-containing bridging units such as carboxylates or hydroxy groups; uranyl acetate dihydrate, for example, is a dimer with both bridging and terminal acetate groups.¹ Uranyl oxalate trihydrate² contains bridging, coordinated oxalate groups (with both coordinated and uncoordinated hydrogen bonded water molecules) that contribute to the formation of a pentagonal bipyramidal structure.

The title compound was prepared by very slowly evaporating (in one or two weeks) a 1:1 millimole ratio of uranyl nitrate hexahydrate and imidazole in 500 ml of water. The complex, which appeared as greenish yellow crystals, was then washed with diethyl ether and air dried for several hours. The rate of evaporation seems to be quite critical, with other products and mixtures of other products sometimes being formed. The infrared spectrum of the complex in the $2500\text{--}3500 \text{ cm}^{-1}$ region, however, is quite distinctive (see discussion below) and provides a good "fingerprint" identification.

The green-yellow fluorescent crystals are monoclinic, space group is $P2_1/c$, with cell parameters, $a = 9.314(4) \text{ \AA}$, $b = 16.230(16) \text{ \AA}$, $c = 7.053(3) \text{ \AA}$, $\beta = 100.72(4)^\circ$ and $V = 1047.6 \text{ \AA}^3$. For $Z = 4$ and a molecular weight of 480.13, the calculated density is 4.04 g/cm^3 .

The molecular structure was determined by single-crystal x-ray diffraction methods. Figure 1 shows an ORTEP view of two formula units that form the water-bridged dimer.

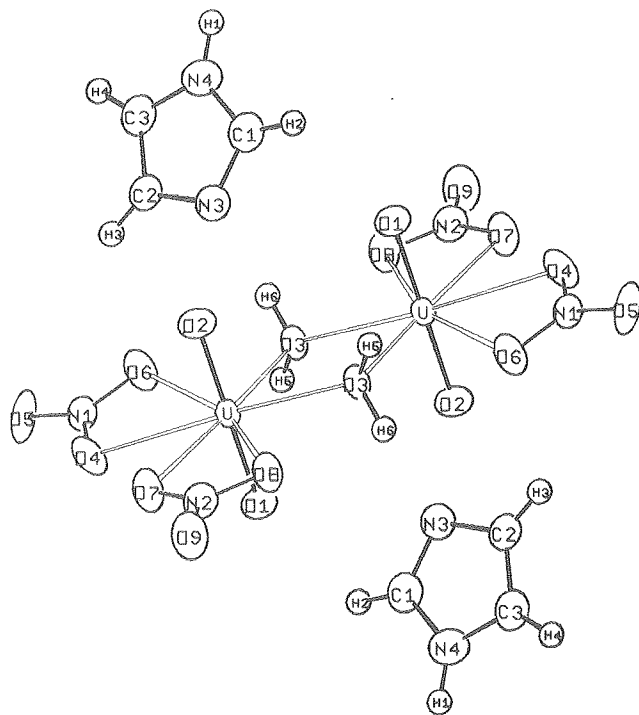


Fig. 1. An ORTEP drawing of two formula units in the dimer configuration. (XBL 7810-11953)

The structure is a dimer of two formula units related to each other by a center of symmetry. Two $\text{UO}_2(\text{NO}_3)_2$ units are bridge bonded via the oxygen atoms of two water molecules. The water molecule is hydrogen bonded to the nonprotonated nitrogen atom (N3) of the imidazole, and to a nitrate oxygen (O5) of an adjacent dimer. The nitrate-to-water bond links the dimers together into an infinite chain.

Uranium is eight-coordinate at the center of a distorted hexagonal bipyramid which has the uranyl oxygen atoms at the apices. The O-U-O axis is perpendicular to the distorted equatorial plane, while the largest deviation from orthogonality of the O-U-O axis to any U-O bond in the equatorial plane is 6° . A slight twist of the nitrate groups out of the equatorial plane indicates some crowding in the coordination environment about UO_2^{2+} . The geometry and bond distances of the water-bridged uranyl dimer in this structure are remarkably similar to the hydroxy-bridged uranyl dimer found in $[(\text{NO}_3)_2\text{UO}_2(\text{OH})_2\text{UO}_2(\text{H}_2\text{O})_3]\cdot\text{H}_2\text{O}$,⁵ in which hydroxide instead of H_2O is the bridging group, and three waters occupy one end of the dimer rather than two nitrate groups. Another similar type uranyl dimer is found in the $\text{Cl}(\text{H}_2\text{O})_3\text{UO}_2(\text{OH})_2\text{UO}_2(\text{H}_2\text{O})_3\text{Cl}$ structure,⁴ which has heptacoordinate rather than octacoordinate uranium. The U-U distances in the title compound is 3.927 Å and compares to 3.939 Å³ and 3.944 Å⁴ in the two other compounds mentioned above. The bridging U-O (water) distances are about 0.2 Å shorter than the U-O (nitrate) distances, and this is consistent with what is observed in the other compounds.^{3,4} The double oxygen bridging of the uranyl ion is somewhat rare, but several examples exist for thorium in which

the Th-Th distances vary from 3.97 to 4.09 Å in a series of double hydroxo-bridged thorium(IV) complexes.⁵ The imidazole molecules are associated by hydrogen bonds to the bridging water molecules and are not directly bonded to the uranyl cations.

The infrared spectrum of the complex is quite distinctive in the O-H and N-H stretching region and is shown in Fig. 2. Rather than the broad band in the 3500 cm^{-1} region which is customarily seen for metal ion complexes involving water, a single, considerably sharpened peak is found at 3500 cm^{-1} . An N-H stretching band, similar in contour to the O-H band, is found at 3328 cm^{-1} , while a second, sharper N-H frequency lies at 3132 cm^{-1} . These values compare quite favorably with those of transition metal-imidazole complexes.⁶

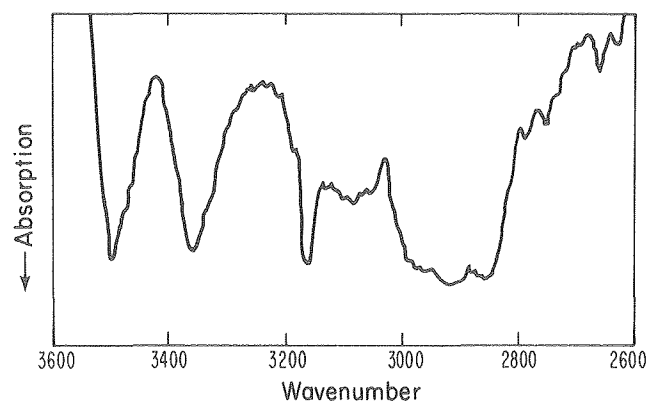


Fig. 2. Infrared spectrum of the title compound taken as a Nujol mull. (XBL 797-2322)

* * *

[†]Brief version of LBL-9973.

1. J. Howatson, D. M. Grev, and B. Morosin, *J. Inorg. Nuc. Chem.* **37**, 1933 (1975).
2. N. C. Jayadevan and D. M. Chackraburty, *Acta Crystallogr. (Sect. B)* **28**, 1933 (1972).
3. A. Perrin, *Acta Crystallogr. (Sect. B)* **32**, 1658 (1976).
4. M. Aberg, *Acta Chem. Scand.* **23**, 791 (1969).
5. G. Johansson, *Acta Chem. Scand.* **22**, 389 (1968) and references therein.
6. W. J. Davis and J. Smith, *J. Chem. Soc. A* 317 (1971).

9. IMIDAZOLIUM TETRACHLORODIOXOURANIUM(VI), $[\text{C}_3\text{N}_2\text{H}_5^+]_2 [\text{UO}_2\text{Cl}_4]^{-2}$

Dale L. Perry, Derek P. Freyberg, and Allan Zalkin

Imidazole forms complexes and salts with metallic atoms in a variety of ways. A novel example is a ruthenium complex with a carbon-ruthenium bond.¹ We studied the reaction of imidazole with uranyl chloride to see if a similar derivative could be made; instead, the resultant product was a hydrogen-bonded salt of the imidazolium cation with the uranyl chloride anion, $\text{UO}_2\text{Cl}_4^{-2}$.

The title compound was prepared by dissolving 2 mmoles of imidazole and 1 mmole of $\text{UO}_2\text{Cl}_2 \cdot 3\text{H}_2\text{O}$ in hydrochloric acid which was maintained at a pH of ~ 2.5 - 3.0 followed by a stirring for two hours. The reaction solution was allowed to evaporate slowly over a period of several days, yielding a batch of yellow, crystalline product.

The yellow crystals are monoclinic, space group $P2_1/n$, with cell parameters: $a = 9.838(5) \text{ \AA}$, $b = 10.891(5) \text{ \AA}$, $c = 6.966(4) \text{ \AA}$, $\beta = 104.56(5)^\circ$ and $V = 722.41 \text{ \AA}^3$. For $Z = 2$ the calculated density is 2.53 g/cm^3 .

The molecular structure was determined by single-crystal x-ray diffraction methods.

The compound is a salt consisting of discrete planar imidazolium cations and octahedral tetrachlorodioxouranate anions (Fig. 1). The closest non-hydrogen atom approaches between the two ions are 3.20 \AA between $\text{Cl}(1)$ and $\text{N}(1)$, and 3.26 \AA between $\text{Cl}(2)$ and $\text{N}(2)$. The $\text{H}(1)$ - $\text{Cl}(1)$ and $\text{H}(2)$ - $\text{Cl}(2)$ distances are 2.51 \AA and 2.46 \AA respectively, and the angles $\text{N}(1)$ - $\text{H}(1)$ - $\text{Cl}(1)$ and $\text{N}(2)$ - $\text{H}(2)$ - $\text{Cl}(2)$ are 144° and 140° respectively; these values are consistent with the criteria for N-H...Cl hydrogen bond.²

The imidazolium cation is a planar five-membered ring. The geometry reported here is in good agreement with other determinations,^{3,4} with bond angles and distances within 4σ of the literature values.

The tetrachlorodioxouranium(IV) anion is a tetragonally distorted octahedron, with four chlorine atoms in the equatorial positions and the two uranyl oxygen atoms at the apices. The U-O distance is $1.770(3) \text{ \AA}$, and the two U-Cl distances are $2.692(2)$ and $2.657(2) \text{ \AA}$.

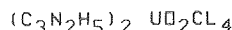
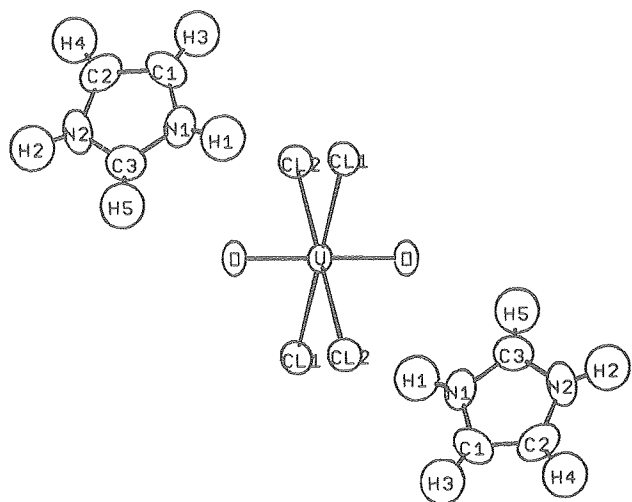


Fig. 1. ORTEP drawing of one formula unit.
(XBL 789-10683)

†Brief version of LBL-8687.

1. R. J. Sundberg, R. F. Bryan, I. F. Taylor, and H. Taube, *J. Am. Chem. Soc.* **96**, 381 (1974).
2. W. C. Hamilton and J. A. Ibers, *Hydrogen Bonding in Solids* (W. A. Benjamin Inc., New York, 1968), Chap. 1.
3. M. N. G. James and M. Matsushima, *Acta Crystallogr. (Sect. B)* **32**, 1708 (1976).
4. H. C. Freeman, F. Huq, J. M. Rosalky, and I. F. Taylor Jr., *Acta Crystallogr. (Sect. B)* **31**, 2833 (1975).

10. CRYSTAL AND MOLECULAR STRUCTURES OF DECAMETHYLMANGANOCENE AND DECAMETHYLFERROCENE. STATIC JAHN-TELLER DISTORTION IN A METALLOCENE†

D. P. Freyberg, J. L. Robbins, K. N. Raymond, and J. C. Smart

Previous structural investigations of metallocenes have demonstrated the dependence of the metal-to-(ring carbon) distance $[R(M-C)]$ on the spin state of the molecule. Manganocene $[(\eta\text{-C}_5\text{H}_5)_2\text{Mn}$ or $\text{Cp}_2\text{Mn}]$ possesses a high-spin ${}^6A_{1g}$ $[(e_2g^2 a_{1g}^1 e_{1g}^2)]$ electronic configuration in benzene solution¹ and in the vapor phase.² Bünder Weiss³ have determined the structure of solid Cp_2Mn , which is polymeric, while a gas-phase electron diffraction⁴ study yielded an $R(Mn-C)$ of $2.383(3) \text{ \AA}$. This is an exceptionally long metal to ring bond when compared to other metallocenes of the first transition series, where $R(M-C)$ ranges from $2.064(3) \text{ \AA}$ for Cp Fe to $2.280(5) \text{ \AA}$ for Cp_2V .⁵ Magnetic susceptibility, EPR,⁶ and UV photoelectron² studies of 1,1'-dimethylmanganocene $[(\text{MeCp})_2\text{Mn}]$ have demonstrated a thermal equilibrium between high-spin (${}^6A_{1g}$) and low-spin (${}^2E_{2g}$, $[e_2g^3 a_{1g}^2]$) electronic configurations, with the high-spin form predominating at elevated temperatures. A gas-phase electron diffraction investigation similarly revealed the presence of two isostructural species in the vapor at 100°C , with average $R(M-C)$ s of $2.433(8)$ and $2.144(12) \text{ \AA}$.⁵ Comparison of these bond lengths with the bond length observed in the high-spin Cp_2Mn led to the conclusion that the former distance represents high-spin and the latter low-spin $(\text{MeCp})_2\text{Mn}$. An unusually large Mn-C vibrational amplitude (0.160 \AA) was noted for low-spin $(\text{MeCp})_2\text{Mn}$, and it was concluded that this was a manifestation of a dynamic Jahn-Teller distortion involving ring-tilting modes. The ${}^2E_{2g}$ configuration is orbitally degenerate; thus in theory the low-spin manganocene is subject to Jahn-Teller distortion from pentagonal symmetry. Such a dynamic distortion has been inferred from EPR spectra of low-spin Cp_2Mn and $(\text{MeCp})_2\text{Mn}$ in diamagnetic host lattices.⁷

Two of us recently reported the synthesis and magnetic properties of decamethylmanganocene $[(\eta\text{-C}_5(\text{CH}_3)_5)_2\text{Mn}$ or $(\text{Me}_5\text{Cp})_2\text{Mn}]$.⁸ A temperature-independent magnetic moment of $2.18 \pm 0.1 \mu_B$ was found in the range $4.6 - 313 \text{ K}$, indicating a low-spin ($S = 1/2$) electronic configuration. Subsequent EPR investigations have shown that $(\text{Me}_5\text{Cp})_2\text{Mn}$, like low-spin $(\text{MeCp})_2\text{Mn}$, has a ${}^2E_{2g}$ ground state.⁹

As these molecules are isoelectronic, it might be expected that structural parameters, such as metal-to-ring distances and distortions from axial symmetry, should also be comparable. To test this hypothesis, the structure of $(\text{Me}_5\text{Cp})_2\text{Mn}$ was determined by single-crystal x-ray diffraction. The structure of the d^6 , closed-shell $(\text{Me}_5\text{Cp})_2\text{Fe}$ was also determined, to provide a "benchmark" compound.

Both $(\text{Me}_5\text{Cp})_2\text{Mn}$ and $(\text{Me}_5\text{Cp})_2\text{Fe}$ are planar metallocenes with staggered configurations of the rings. A representative view of the geometry is shown in Fig. 1. The crystal packing of both compounds is substantially the same and involves rows of metallocene molecules of one orientation alternating along the c direction with rows whose pentagonal axes are nearly perpendicular to the first. Along the b direction, the orientations of the pentagonal axes are constant, but there is alternation from x to $x + 1/2$ along the rows. For the iron structure there are mirror planes at $x = 0$ which pass through the molecule, whose crystallographic site symmetry is C_{2h} . For the manganese structure, although the packing is nearly the same, there are subtle changes in the methyl orientations that occur in going from the C_{mca} to the $C_{2/c}$ structure. The cell constants of the two structures are very similar. The high crystal quality and close relationship of these structures provide an unusually good opportunity for detailed comparisons of structural parameters.

A metallocene such as $(\text{Me}_5\text{Cp})_2\text{Mn}$ in the ${}^2E_{2g}$ state possesses an orbitally degenerate electronic configuration subject to Jahn-Teller distortion. Deviations from pure axial (D_{5d}) symmetry by either a static or dynamic mechanism would serve to lift

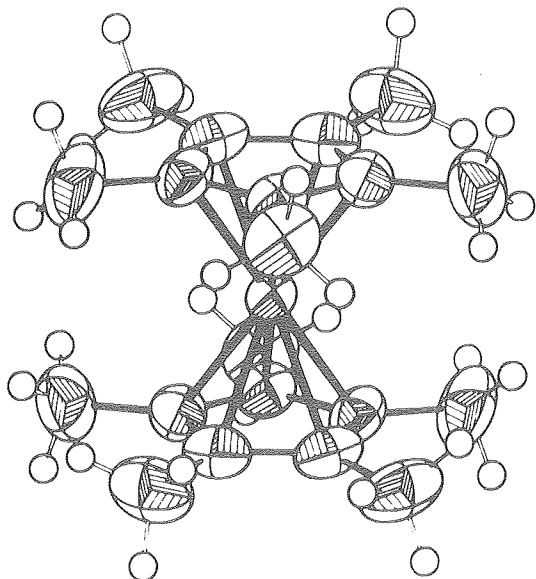


Fig. 1. ORTEP drawing of $(\text{Me}_5\text{Cp})_2\text{Mn}$. The non-hydrogen atoms are drawn at 50% probability contours of the thermal motion. The hydrogen atoms have an arbitrary size. (XBL 801-7813)

the degeneracy of the ${}^2E_{2g}$ ground state. While evidence for a dynamic distortion in low-spin $(\text{MeCp})_2\text{Mn}$ and Cp_2Mn has been presented,^{5,7} we find in the structure of $(\text{Me}_5\text{Cp})_2\text{Mn}$ indications of a static distortion which involves primarily distortion of the Cp ring through changes in the C-C bond lengths.

Examination of the bond lengths in Table 1 reveals two discrepancies between the structures of $(\text{Me}_5\text{Cp})_2\text{Mn}$ and $(\text{Me}_5\text{Cp})_2\text{Fe}$. First, the metal-(ring C) distances in $(\text{Me}_5\text{Cp})_2\text{Mn}$ vary from 2.105 to 2.118 Å, reflecting a difference of 0.013 Å (6σ) from closest to most distant ring carbon. By comparison, in $(\text{Me}_5\text{Cp})_2\text{Fe}$, the prototype metallocene not subject to Jahn-Teller distortion, these distances vary by only 0.008 Å ($<4\sigma$). This type of distortion, marginal in the manganese complex, is illustrated in Fig. 2. The distortion may be envisioned as a ring slippage with C_4 and C_5 (and C_4' , C_5') moving away from the metal while C_2 and C_3 move toward the metal. Alternatively, this may be viewed as a symmetric ring tilt, a recognized vibrational mode (E_{1g}) for metallocenes. While the metal-C distances vary significantly in $(\text{Me}_5\text{Cp})_2\text{Mn}$, the rings themselves remain essentially planar.

The second, and major, distortion of the metallocene structure occurs in the Cp ring itself. In the $(\text{Me}_5\text{Cp})_2\text{Fe}$ structure, the (ring C)-(ring C) distances do not deviate significantly from the mean of 1.419 Å. However, as seen in Table 1, these distances range from 1.409(2) to 1.434(2) Å in $(\text{Me}_5\text{Cp})_2\text{Mn}$. This distortion is exaggerated in Fig. 2. The C_3 - C_4 bond expands while the C_2 - C_3 and C_1 - C_5 bonds contract relative to the idealized bond distance of 1.419 Å. The net result of these two distortions is depicted in Fig. 2, in a projection view. To our knowledge, this is the first observation of such a Jahn-Teller distortion in an organometallic compound.

* * *

† Brief version of J. Am. Chem. Soc. 101, 892 (1979).

1. G. Wilkinson, F. A. Cotton, and J. M. Birmingham, J. Inorg. Nucl. Chem. 2, 95 (1956).
2. S. Evans, M. L. H. Green, B. Jewitt, G. H. King, and A. F. Orchard, J. Chem. Soc. Faraday Trans 2, 356 (1974). S. Evans, M. L. H. Green, B. Jewitt, A. F. Orchard, and C. F. Pygall, *ibid.*, 1847 (1972).
3. W. Bünder, Dissertation, Universität Hamburg, 1974. Cited, with figure, in Ref. 7, p. 308.
4. A. Almenningen, A. Haaland, and T. Motzfeldt, Selected Topics in Structure Chemistry, (Universitetsforlaget: Oslo, 1967), p. 105.
5. A. Almenningen, A. Haaland, and S. J. Samdal, J. Organomet. Chem. 149, 219 (1978).
6. M. E. Switzer, R. Wang, M. F. Rettig, and A. H. Maki, J. Am. Chem. Soc. 96, 7669 (1974). J. H. Ammeter, R. Bucher, and N. Oswald *ibid.*, 96, 7833 (1974).
7. J. H. Ammeter, J. Magn. Reson. 30, 299 (1978).
8. J. C. Smart and J. L. Robbins, J. Am. Chem. Soc. 100, 3936 (1978).
9. J. L. Robbins, J. C. Smart, and N. Edelstein, Manuscript in preparation.

Table 1. Bond distances in $(\text{Me}_5\text{Cp})_2\text{M}$, $\text{M} = \text{Mn}, \text{Fe}$.

| bond | dist, Å | bond | dist, Å | bond | dist, Å |
|--------------------------------|--------------------------|---------------------------------|-------------|----------------------------------|-------------|
| Mn-C ₁ | 2.118 (2) | | | Fe-C ₁ | 2.045 (3) |
| | [1.216 (3)] ^a | | | | [1.199 (4)] |
| Mn-C ₂ | 2.105 (2) | Mn-C ₅ | 2.118 (2) | Fe-C ₂ | 2.049 (2) |
| | [1.194 (3)] | | [1.217 (3)] | | [1.206 (3)] |
| Mn-C ₃ | 2.107 (2) | Mn-C ₄ | 2.112 (2) | Fe-C ₃ | 2.053 (2) |
| | [1.197 (3)] | | [1.206 (3)] | | [1.212 (3)] |
| | av ^b | 2.112 (3) | | av | 2.050 (2) |
| | | [1.206 (5)] | | | [1.207 (3)] |
| C ₁ -C ₂ | 1.414 (2) | C ₁ -C ₅ | 1.409 (2) | C ₁ -C ₂ | 1.419 (3) |
| C ₂ -C ₃ | 1.411 (2) | C ₄ -C ₅ | 1.421 (3) | C ₂ -C ₃ | 1.419 (3) |
| C ₃ -C ₄ | 1.434 (2) | | | C ₃ -C _{3''} | 1.418 (4) |
| | av | 1.418 (4) | | av | 1.419 (2) |
| C ₁ -C ₆ | 1.506 (3) | | | C ₁ -C ₄ | 1.495 (5) |
| C ₂ -C ₇ | 1.504 (3) | C ₅ -C ₁₀ | 1.498 (3) | C ₂ -C ₅ | 1.509 (3) |
| C ₃ -C ₈ | 1.497 (3) | C ₄ -C ₉ | 1.508 (3) | C ₃ -C ₆ | 1.497 (3) |
| | av | 1.504 (2) | | av | 1.502 (3) |

^a Distances in square brackets represent "in-plane" distances, the distances from the projection of the M atom on the ring plane to the ring carbons. ^b The end of the mean is the larger of the two given by (1) $\sigma^2(\bar{x}) = \Sigma(x_i - \bar{x})^2/[n(n-1)]$ or (2) $\sigma^2(\bar{x}) = 1/\Sigma(1/\sigma_i^2)$. The mean in each case is the weighted mean.

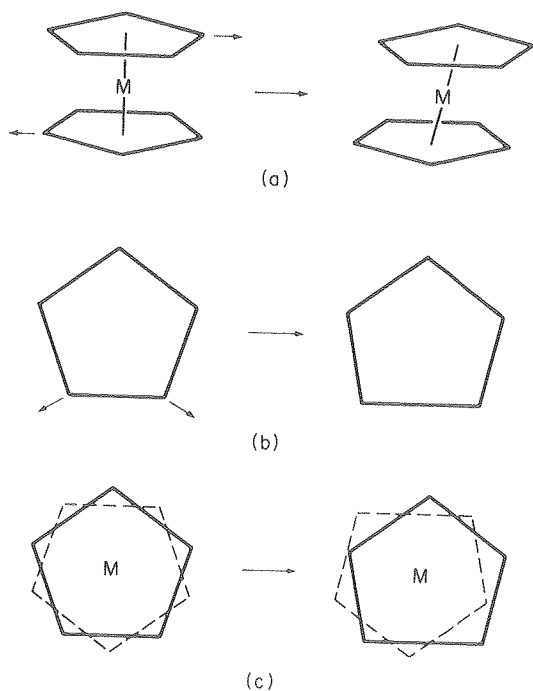


Fig. 2. The principal modes of Jahn-Teller distortion in $(\text{Me}_5\text{Cp})_2\text{Mn}$: (a) ring slippage (concerted rotation); (b) intra-ring distortion; and (c) the resulting distortion observed in $(\text{Me}_5\text{Cp})_2\text{Mn}$ in the solid state. (XBL 801-7812)

11. ANOMALOUS SCATTERING BY COBALT AND CHLORINE OF (+)-TRIS(ETHYLENEDIAMINE)COBALT(III) CHLORIDE (+)-TARTRATE PENTAHYDRATE AND ITS CRYSTAL STRUCTURE[†]

David H. Templeton, Allan Zalkin, Helena W. Ruben, and Lieselotte K. Templeton

Werner¹ demonstrated the optical activity and octahedral nature of complexes of cobalt and ethylenediamine by using the crystallization of (+)-tartrate salts to separate the enantiomers. One of the salts he isolated was (+)-tris(ethylenediamine)cobalt(III) chloride (+)-tartrate pentahydrate. We have determined the crystal structure of this salt and used it to measure anomalous scattering effects of cobalt and chlorine for $\text{MoK}\alpha$ and $\text{CuK}\alpha$ radiation. This study provides a foundation for some similar experiments with synchrotron radiation.

Crystals of $\text{Co}(\text{C}_2\text{H}_8\text{N}_2)_3\text{Cl}(\text{C}_4\text{H}_4\text{O}_6) \cdot 5\text{H}_2\text{O}$ are triclinic, space group $P1$; $a = 8.261(3)$ Å, $b = 8.507(3)$ Å, $c = 8.149(3)$ Å, $\alpha = 101.20(1)$, $\beta = 95.27(1)$, $\gamma = 102.31(1)^\circ$, $Z = 1$.

Anomalous scattering effects are not especially large for this crystal and $\text{MoK}\alpha$ radiation, but they are significant. We used the method of least squares to determine the values of f' and f'' listed in Table 1. There is a significant discrepancy with the value calculated by Cromer and Liberman² for f'' of Co at 1.54 Å; pending further investigation we ascribe it to the effect called extended x-ray absorption fine structure ("EXAFS"), which

Table 1. Anomalous scattering terms.

| | $\lambda, \text{\AA}$ | Experiment | Theory ² |
|------------------|-----------------------|------------|---------------------|
| $f''(\text{Co})$ | 0.711 | 0.962(10) | 0.973 |
| | 1.542 | 3.92(2) | 3.608 |
| $f'(\text{Co})$ | 1.542 | -2.36(2) | -2.464 |
| $f''(\text{Cl})$ | 0.711 | 0.155(10) | 0.159 |
| | 1.542 | 0.72(2) | 0.702 |
| $f'(\text{Cl})$ | 1.542 | 0.23(2) | 0.348 |

is expected to occur at this photon energy only about 300 eV from the cobalt K edge. The theoretical value is calculated for an isolated atom, which is free of this effect.

A calculation to test the variation of f'' with angle for Co and Cl yielded the values (for 1.542 \AA):

$$f''(\text{Co}) = (4.01 \pm 0.04) - (0.6 \pm 0.2)s^2,$$

$$f''(\text{Cl}) = (0.69 \pm 0.04) + (0.2 \pm 0.3)s^2,$$

where $s = \lambda^{-1} \sin \theta$. The variation of $f''(\text{Cl})$ with angle is not significant. The equation for $f''(\text{Co})$ gives $f'' = 3.8$ at $\theta = 63^\circ$, the upper limit of the experiment. This 5% reduction (relative to zero angle) is similar to the 3.3% reduction at this angle estimated by Hazell³ from orbital Fourier transforms, an approximate method which may be expected to give the order to magnitude of the change. A similar calculation at 0.711 \AA detected no significant variation with respect to scattering angle.

* * *

⁴Brief version of LBL-8421.

1. A. Werner, Ber. 45, 121 (1912).

2. D. T. Cromer and D. Liberman, J. Chem. Phys. 53, 1891 (1970).

3. A. C. Hazell, *Anomalous Scattering*, S. Ramaseshan and S. C. Abrahams, Eds., Munksgaard, Copenhagen, 1975, p. 41-51.

12. L₃-EDGE ANOMALOUS SCATTERING OF X-RAYS BY PRASEODYMIUM AND SAMARIUM^{††}

Lieselotte K. Templeton, David H. Templeton and R. Paul Phizackerley[§]

Anomalous scattering terms f' and f'' for Pr and Sm have been derived from diffraction experiments with synchrotron radiation at wavelengths near the L₃ absorption edges. Both components exhibit exceptionally large changes in a narrow interval of wavelength, changes which offer a powerful tool

for solving the phase problem in crystal structure analysis. Similar experiments with cesium hydrogen tartrate^{1,2} showed anomalous scattering effects large enough to be useful in solving macromolecular crystal structures, but cesium is not very convenient for this purpose because of strong absorption of x-rays by light atoms at the wavelength of the L₃ edge. The rare earth elements have L₃ edges (2.26 \AA for lanthanum to 1.34 \AA for lutetium) which span the wavelength range normally used to study large molecules. The present work demonstrates effects for these elements even larger than those for cesium.

The method is to use least-squares adjustment to derive f' , f'' and a scale factor from diffraction intensities measured at the wavelength of interest with a crystal whose structure is known from a conventional experiment at another wavelength. We used crystals of sodium praseodymium ethylenediaminetetraacetate octahydrate ($\text{NaPrC}_{10}\text{H}_{12}\text{N}_2\text{O}_8 \cdot 8\text{H}_2\text{O}$) and the isomorphous samarium salt. The atomic coordinates and thermal parameters were determined using MoK α radiation.³ The values found for the anomalous scattering terms are plotted in Fig. 1. For both elements, f'' exhibits the striking resonance line which is observed in absorption curves. The peak values are substantially larger than we observed for cesium, and in the praseodymium case more than double the values for any element near K or L edges calculated by Cromer and Liberman⁴ with a model which neglects fine structure lines.

The curves for f' show the characteristic shape demanded by the dispersion relation for a sharp absorption line. In Fig. 1 the broken lines show f' calculated from f'' by a Kramers-Kronig integration;² for this purpose the experimental f'' curve

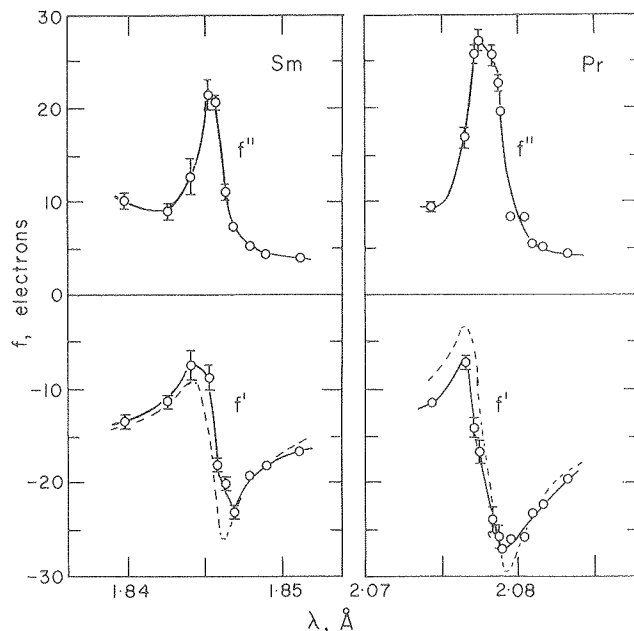


Fig. 1. Anomalous scattering terms f' and f'' near the L₃ edges for samarium (left) and praseodymium (right). The broken lines are calculated from f'' by a dispersion relation. (XBL 7912-13732)

was extended to higher and lower wavelengths by estimated values.

The use of f' to help solve the phase problem in x-ray crystallography, by means of the intensity difference it causes for reflections hkl and $\bar{h}\bar{k}\bar{l}$, is well established. The effect of a change in f' is similar to that of a change in atomic number. Thus, experiments at two or more wavelengths where f' is different can be analyzed like isomorphous replacement data. Large anomalous scattering terms also facilitate the determination of heavy atom positions. Once the positions are known for the anomalously scattering atoms, one can derive phase angles without ambiguity from diffraction data measured for one crystal at three or more wavelengths, or at two or more wavelengths if both members of each Bijvoet pair are measured. The phase angles are found by solving vector equations in the complex plane. If these equations are represented by a Harker diagram the centers of intersecting circles must be well separated and noncollinear for accuracy and uniqueness. These conditions are met if f'' is large enough for at least one wavelength and f' changes enough between two wavelengths. Hoppe and Jakubowski⁵ showed that phases could be determined with an accuracy of about 50° for many of the reflections of a protein (erythrocrucorin, M.W. ~16,000) using two wavelengths near the K edge of iron, where the anomalous scattering effects are about 7 times smaller than those reported here for praseodymium. An atom of praseodymium in a molecule of 800,000 daltons would be a somewhat similar case, since the percentage effects of anomalous scattering depend on the ratio of changes in f to the square root of the number of atoms.

The crystals for this experiment were prepared by Helena W. Ruben. We thank her and Dr. Allan Zalkin for cooperation in the determination of the structural parameters needed for this work.

* * *

[†]Brief version of LBL-9865.

[‡]Supported in part by the National Science Foundation.

[§]Stanford Synchrotron Radiation Laboratory and Department of Structural Biology, Stanford University, Stanford, California 94305.

1. J. C. Phillips, D. H. Templeton, L. K. Templeton, and K. O. Hodgson, *Science* **201**, 257 (1978).

2. D. H. Templeton, L. K. Templeton, J. C. Phillips, and K. O. Hodgson, submitted to *Acta Crystallogr.*, LBL-9880.

3. A. Zalkin, H. W. Ruben, and D. H. Templeton, unpublished.

4. D. T. Cromer, D. Liberman, *J. Chem. Phys.* **53**, 1891 (1970).

5. W. Hoppe and U. Jakubowski, *Anomalous Scattering*, S. Ramaseshan and S. C. Abrahams, Eds. (Munksgaard, Copenhagen, 1975), pp. 437-461.

13. POLARIZED X-RAY ABSORPTION AND DOUBLE REFRACTION IN VANADYL BISACETYLACETONATE^{†‡}

David H. Templeton and Lieselotte K. Templeton

We have observed a variation of x-ray absorption in crystals of vanadyl bisacetylacetonate according to the direction of the electric vector of the photon. This polarized absorption or dichroism is the result of two distinct phenomena which involve the symmetry of unoccupied molecular orbitals and the geometry of neighbor atoms. It may be used to study the geometry, orientation, and electronic structure of molecules. It gives rise to x-ray double refraction and anisotropy of anomalous scattering which introduce interesting complications into the x-ray optical and diffraction properties of the crystal.

The experiments made use of a Nonius CAD-4 diffractometer at the Stanford Synchrotron Radiation Laboratory. This apparatus is designed for recording single-crystal diffraction intensities with the horizontally-polarized synchrotron radiation. To permit calibration of the monochromator wavelength setting, the computer control system includes provision for scanning an absorption curve. An ion chamber measures the initial intensity, and the diffractometer scintillation counter, set at zero angle, records the transmitted intensity. In these experiments a crystal of vanadyl bisacetylacetonate, $\text{VO}(\text{C}_5\text{H}_7\text{O}_2)_2$, with dimensions $1.0 \times 1.2 \times 1.5$ mm, was the absorber. Its orientation with respect to the diffractometer coordinate system was determined using high-angle Bragg reflections. Absorption curves (Figs. 1 and 2) were recorded using a 0.4 mm collimator, which gave a small enough beam to be eclipsed by the crystal.

As shown in Fig. 1, the absorption line at 5466 eV nearly disappears when the electric vector is perpendicular to the molecular axis. Several spectra measured for other orientations of the crystal verify that the absorption depends on the direction of the electric vector and not on the path direction, with intermediate intensities at intermediate angles of polarization. The width of this line (about 5 eV at half height) is due to the finite wavelength spread of the radiation which results from the effect of the focusing mirror. This dichroism will not occur in highly symmetrical molecules such as permanganate ion, which has a similar resolved pre-edge line, but it may be commonplace in less symmetrical molecules. A search for other examples seems worthwhile. Several applications can be suggested. The polarization properties will help test theoretical models for the molecular electronic structure. The angular variation of the intensity of the absorption line is a probe which can be used to measure the molecular orientation of vanadyl ions, or distribution of orientations, in an anisotropic specimen, whether crystalline or not. This crystal may be used as a polarizing filter to modify or detect the state of polarization of an x-ray beam (but only at these limited wavelengths).

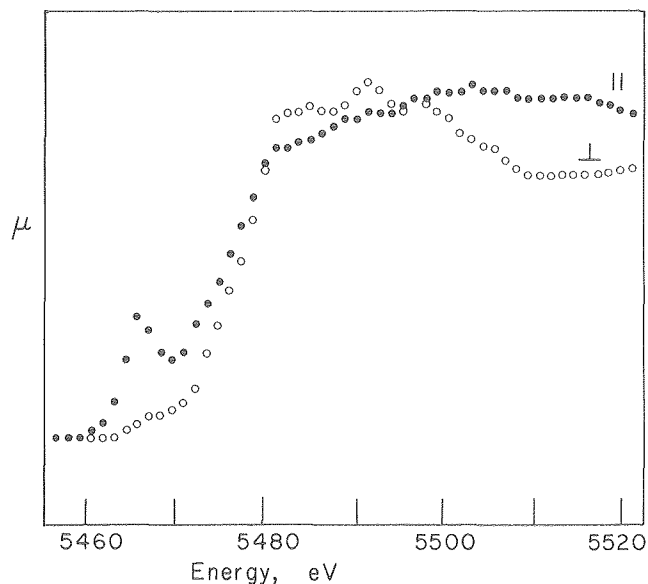


Fig. 1. Absorption coefficient (on an arbitrary scale) vs. photon energy for vanadyl bisacetylacetonate and linearly polarized x-ray with electric vector parallel (black circles) and perpendicular (open circles) to the short V-O bonds.

(XBL 797-10696)

Scattering of the photoelectrons from neighboring atoms, the oxygen atoms in this case, gives rise to the diffraction ripples in the EXAFS region (Fig. 2). The polarization effect arises out of a factor $\cos^2\theta$, where θ is the angle between the electric vector of the x-ray and the direction of the neighboring atom. In vanadyl bisacetylacetonate each vanadium atom has five oxygen neighbors at the corners of a nearly square pyramid.¹ The vanadyl oxygen atom, at a distance 1.581(2) Å, lies at the apex of this pyramid, and this axial V-O bond is the reference vector for our discussion of the polarization effects. The other four oxygen atoms of the acetylacetonate ligands, at the corners of the pyramid base, are at distances ranging from 1.963(2) to 1.971(2) Å. Using the phase-shift functions of Teo and Lee² for V and O, we calculated the energies at which maxima and minima occur in the EXAFS spectra due to V-O distances of 1.58 and 1.97 Å. These energies are marked by arrows in Fig. 2 on the parallel and perpendicular curves, respectively. Some of the peaks and valleys are quite different for the two polarizations, and the longer bond length fits the perpendicular curve, while the shorter one dominates the other.

Any polarization of the absorption cross section will cause f'' at the same wavelength and f' at neighboring wavelengths to have values which change according to the orientation of the electric vector. The index of refraction n is related to the scattering factor, and thus the index of refraction depends on the direction of the electric vector: in other words the crystal is birefringent for x-rays. An x-ray beam penetrating the crystal will be split into a parallel ray and a perpendicular ray, one being more strongly attenuated than

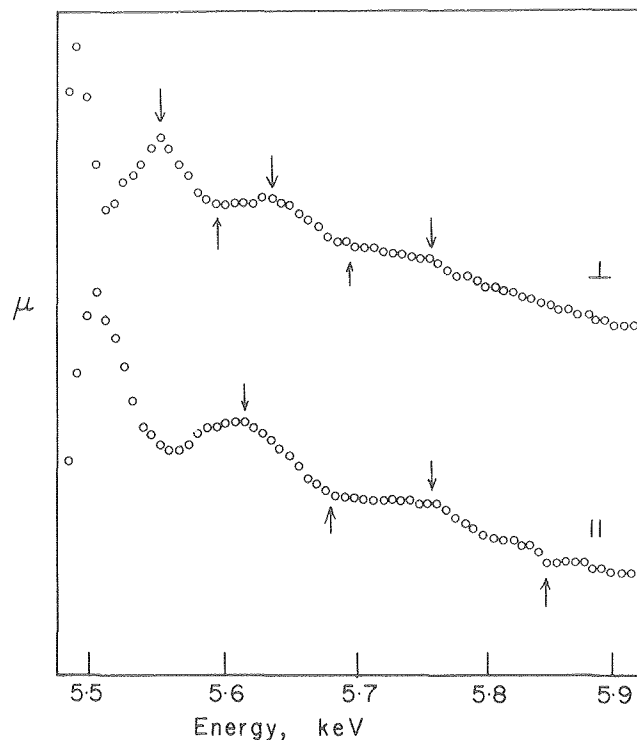


Fig. 2. Polarized EXAFS spectra for vanadyl bisacetylacetonate; electric vector perpendicular (top curve) and parallel (bottom curve) to the short V-O bond. The arbitrary absorbance scale is magnified about $2 \times$ that of Fig. 1 and is displaced for the two curves. The slope of the smooth background absorption is partly the result of instrumental effects. Arrows mark values for the positions of maxima and minima calculated as described in the text for V-O distances of 1.97 Å (top curve) and 1.58 Å (bottom curve).

(XBL 797-10697)

the other. To calculate a diffraction intensity one must use different values of f' , f'' , the absorption correction, and the polarization factor for each ray. The polarization factor becomes more complicated than in the usual case and depends on the state of polarization of the incident beam, the orientation of the optic axis (or axes), and the direction of the diffracted ray. These effects introduce formidable complications into diffraction experiments and the experimental determination of anomalous scattering.

We thank Helena W. Ruben for growing the crystal used in this experiment.

* * *

[†]Brief version of LBL-9530.

[‡]Supported in part by the National Science Foundation.

1. R. P. Dodge, D. H. Templeton, and A. Zalkin, *J. Chem. Phys.* **35**, 55 (1961).
2. B.-K. Teo and P. A. Lee, *J. Am. Chem. Soc.* **101**, 2815 (1979).

Physical and Spectroscopic Studies

1. NMR STUDIES OF URANOCENES[†]

Wayne D. Luke and Andrew Streitwieser, Jr.

Proton magnetic resonance spectra have been recorded as a function of temperature for over two dozen substituted uranocenes. Results for the chemical shifts at a single temperature are summarized in Table 1. Almost all of the ring protons show isotropic shifts that are linear in T^{-1} . The results for the four different ring protons in 1,1'-dimethyluranocene shown in Fig. 1 are typical.

1,1',4,4'-Tetra-*t*-butyluranocene shows a substantial barrier to ring rotation. At temperatures above -30°C the NMR spectrum consists of four singlets with an area ratio of 18:2:2:2 corresponding to the *t*-butyl protons and three sets of ring protons. In the low temperature spectrum below -80°C, the spectrum consists of eight singlets with an area ratio of 9:9:1:1:1:1:1:1, corresponding to a conformationally rigid structure with two kinds of *t*-butyl group and six distinct sets of ring protons. Coalescence behavior gives an average ΔG^\ddagger of rotation of 8.42 kcal mol⁻¹.

For comparison with the d-transition metallo-cenes, 1,1',3,3'-tetra-*t*-butylferrocene was prepared by alkylation of ferrocene with *t*-butyl

chloride and boron fluoride etherate. At 30°C the ¹H NMR spectrum consists of one *t*-butyl resonance at δ 1.22 ppm. Below -35°C, two distinct *t*-butyl resonances are observed at 1.231 and 1.206 ppm. The coalescence temperature of -27.5°C corresponds to ΔG^\ddagger for ring rotation of 13.1 kcal mol⁻¹, substantially higher than for the corresponding uranocene as expected for the shorter ring-ring distance in the ferrocene.

Detailed study of various alkyluranocenes shows that the predominant conformation of ethyluranocene is that in which the terminal methyl group is swung away from the rings. In neopentyl-uranocene this is the exclusive conformation.

The pattern of ring proton shifts is shown in Fig. 2 for several 1,1'-dialkyluranocenes. The variations in isotropic shift are due primarily to contact shift changes around the ring. Study of several uranocenes prepared from deuterated *n*-butyl- and methyl-COT's shows the progression of ring protons with increasing field to be 4,5,3,2. The pattern for *t*-butyl is greatly different. A tentative assignment based on comparison of mono- and di-*t*-butyluranocenes is 2,3,4,5 in order of increasing field. Most substituted uranocenes studied by x-ray structure techniques show the substituent bent several degrees towards uranium.^{2,3,4} The differing NMR pattern for ring protons in *t*-butyl-uranocenes suggests that this group is bent away from the central metal. Note

Table 1. ¹H NMR resonances of substituted uranocenes; δ ppm from TMS.

| Substituent ^a | Shift ^b at 30°C |
|---|---|
| H | -36.63 |
| 1,3,5,7-tetramethyl | -35.15, -4.21 (CH ₃) |
| CH ₃ | -31.70, -33.67 (H5), -36.10, -40.39 -7.20 (CH ₃) |
| CH ₂ CH ₃ | -32.89, -34.45 (H5), -36.33, -39.7 -17.47 (CH ₂), -1.20 (CH ₃) |
| <i>i</i> -C ₃ H ₇ | -35.50, -35.98, -36.00 (H5), -36.40 -14.47 (CH), -9.98 (CH ₂ , <i>d</i> , J=4.4Hz) |
| <i>n</i> -C ₄ H ₉ | -32.64, -34.10 (H5), -35.22, -39.74 -19.03 (α -CH ₂), 0.22 (β -CH ₂) 0.98 (η -CH ₂ , <i>m</i>), 0.36 (CH ₃ , <i>t</i> , J=6.3Hz) |
| <i>t</i> -C ₄ H ₉ | -33.43, -33.80, -37.30, -40.54 (H5) -11.49 (CH ₃) |
| <i>t</i> -C ₄ H ₉ ^c | -33.41, -34.74, -39.51, -43.37 (H5) -36.02 (8H, unsubstituted ring), -10.82 (CH ₃) |
| 1,4-di- <i>t</i> -butyl | -25.23, -39.66, -42.23 -10.25 (CH ₃) |
| neo-C ₅ H ₁₁ | -32.84, -33.42 (H5), -36.26, -41.07 -23.97 (CH ₂), 3.86 (CH ₃) |
| (CH ₂) ₃ N(CH ₃) ₂ ^d | -31.5, -32.9 (H5), -34.9, -38.1, -18.3 (α -CH ₂ , <i>t</i> , J=7.5Hz) 0.63 (β -CH ₂ , <i>m</i>), 113 (CH ₃) 2.80 (γ -CH ₂ , <i>t</i> , J=7.0Hz) |

Table 1 cont.

| Substituent ^a | Shift ^b |
|--|---|
| C ₆ H ₅ | =34.29, -36.15, -36.45, -37.13 (H5) 0.76 (p, d, J=7.2Hz) 0.85 (m, t, J=7.6Hz) -13.95 (o, d, J=7.3Hz) |
| p-(CH ₃) ₂ NC ₆ H ₄ | -34.29, -26.15, -26.46, -37.13 (H5) -14.10 (o, d, J=7.6Hz) 0.13 (m, d, J=7.6Hz), -0.04 (CH ₃) |
| cyclobuteno | -27.70, -35.90, -43.80 -26.75 (α _{endo}), 19.65 (α _{exo}), (J=9.64Hz) |
| cyclopenteno | -32.12, -34.20, -41.15 -32.58 (β _{endo} , m), -8.28 (β _{exo} , m) -18.78 (α _{endo} , m), 24.43 (α _{exo} , m) |
| dimethylcyclopenteno | -32.43, -33.26, -39.83 -12.91 (CH ₃ endo), 5.39 (CH ₃ exo) -22.90 (α _{endo}), 8.28 (α _{exo}) (J=14.5Hz) |
| cyclohexeno | -30.64, -32.53, -38.70 -22.35 (β _{endo} , m), -2.94 (β _{exo} , m) -16.42 (α _{endo} , m), 6.56 (α _{exo} , m) |
| C(C ₆ H ₅) ₃ ^e | -21.35, -34.87, -49.50, -52.01 (H5) 4.88 (o, d, J=6.8Hz) 4.95 (m, t, J=6.6Hz) 5.44 (p, t, J=6.6Hz) |
| OCH ₃ ^d | -27.5, -30.2 (H5), -35.6, -43.7 -3.73 (CH ₃) |
| O-t-C ₄ H ₉ ^d | -28.1, -28.7 (H5), -36.2, -45.7 2.08 (CH ₃) |
| OCH ₂ CH=CH ₂ ^d | -27.9, -30.5 (H5), -35.5, -43.5 -0.33 (α-CH ₂ , d, J=5.0Hz) 0.70 (trans-H, d, J=17.5Hz) 1.75 (β-CH, m), 2.60 (cis-H, d, J=10.5Hz) |
| CO ₂ -t-C ₄ H ₉ | -30.51, -32.65, -36.01 (H5), -42.45 -6.07 (CH ₃) |
| CO ₂ -t-C ₄ H ₉ ^c | -29.42, -33.69, -36.0 (H5), -40.06, -37.06 (8H, unsubstituted ring) -6.27 (CH ₃) |
| CO ₂ CH ₂ C ₆ H ₅ | -29.81, -32.08, -36.23 (H5), -43.16 -2.98 (CH ₂) -0.56 (o) 4.09 (m) 5.20 (p) |
| CO ₂ CH ₂ C ₆ H ₅ ^c | -28.51, -32.40, -32.98 (H5), -40.63 -2.99 (CH ₂) -36.06 (8H, unsubstituted ring) -1.16 (o) 3.94 (m) 5.30 (p) |

^aSubstituent on both 8-membered rings except where indicated. Some of these compounds were prepared by NSF-supported research.

^bIn monosubstituted cyclooctatetraene ligands the ring H5 could be identified by integration relation relative to the other ring proton resonances.

^cOnly one ligand ring substituted.

^dData from Ref. 1 at 39°C.

^eAt 26°C.

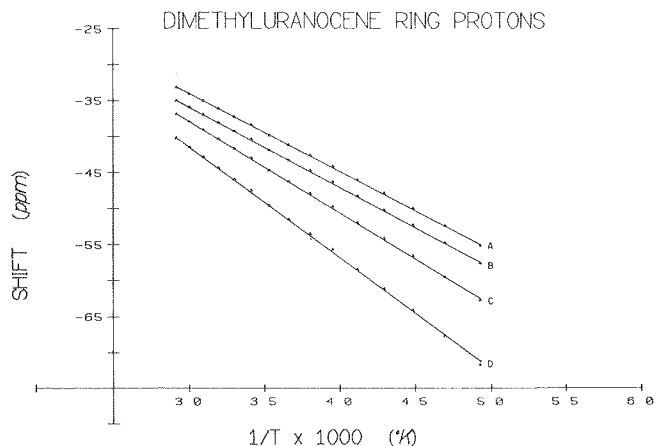


Fig. 1. Isotropic shifts of the 4 ring protons of 1,1-dimethyluranocene as a function of $1/T$ showing linear behavior. (XBL 7912-13544)

$1,1'$ -DIALKYLURANOCENE RING PROTONS at 30°C

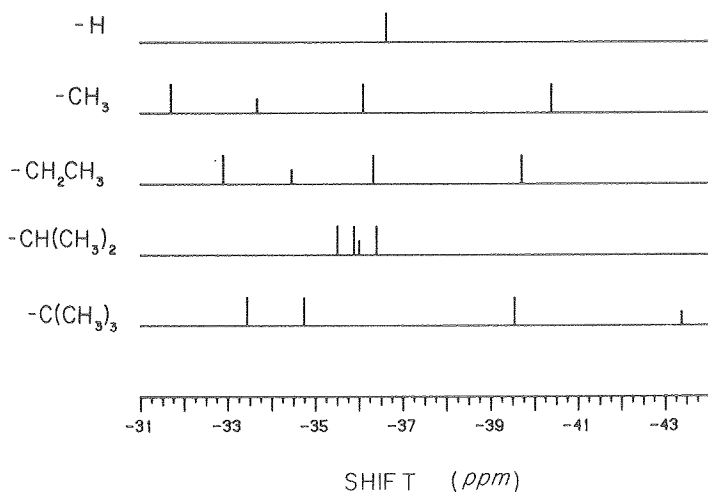


Fig. 2. Ring proton ^1H NMR shifts for $1,1'$ -dialkyluranocenes. H5 is identified by its reduced intensity. (XBL 7912-13545)

that for a coplanar ring-substituent bond, a *t*-butyl hydrogen approaches within Van der Waals contact of a ring hydrogen on the opposite ring.

The present results permit some important conclusions regarding the factoring of isotropic shifts in uranocenes into contact and pseudocontact components. Previous attempts at such factoring involved the assumption that these systems can be viewed as having axial symmetry. The temperature dependent ^1H NMR spectra of uranocene and a variety of substituted uranocenes clearly verify this assumption and show that Eq. (1) can be used to evaluate the pseudocontact contribution to the total isotropic shift in uranocenes. In this equation $\chi_x \approx \chi_y$ for substituted uranocenes and are replaced by χ_{\perp} .

$$\delta_{\text{PSEUDOCONTACT}} = \frac{\chi_{\parallel} - \chi_{\perp}}{3N} \frac{3\cos^2\theta - 1}{R^3} \quad (1)$$

These early attempts to factor the isotropic shifts in alkyluranocenes using Eq. (1) were not completely successful because of failure to correctly assess the conformation of the substituent in solution and overestimation of the value of the anisotropy term, $\chi_{\parallel} - \chi_{\perp}$.^{5,6,7}

Another important result of this study is the confirmation of Fischer's⁸ demonstration that χ_{\perp} is not equal to zero in uranocene. Early attempts to factor isotropic shifts in uranocene have generally assumed that $\chi_{\perp} = 0$, and lead to overestimation of the anisotropy term. A precise value of χ_{\perp} is difficult to determine rigorously from analysis of available NMR data. We have found that $\mu_{\parallel}^2 - \mu_{\perp}^2 = 12.5 \text{ B.M.}^2$ leads to the best internal consistency in factored isotropic shifts for a wide variety of $1,1'$ -dialkyluranocenes. assuming $\mu_{\text{av}}^2 = 5.76 \text{ B.M.}^2$ and $\mu_{\parallel}^2 - \mu_{\perp}^2 = 12.5 \text{ B.M.}^2$ at 30°C, the corresponding values of μ_{\parallel}^2 and μ_{\perp}^2 are 14.09 B.M.² and 1.59 B.M.², respectively. This implies that $\chi_{\parallel}/\chi_{\perp} \approx 8$ in uranocene, a value substantially larger than Fischer's ratio of $\chi_{\parallel}/\chi_{\perp} \approx 2.8$.⁸

As a result of $\chi_{\perp} \neq 0$, early work on factoring the isotropic shift of the ring protons in uranocene underestimated the magnitude of the contact shift. Using our value of $\mu_{\parallel}^2 - \mu_{\perp}^2 = 12.5 \text{ B.M.}^2$, the pseudocontact and contact shifts for uranocene ring protons are -8.30 ppm and -34.2 ppm, ($G_i = -2.34 \times 10^{21} \times 10^{21} \text{ cm}^{-3}$), respectively. Thus, this study confirms that both contact and pseudocontact interactions contribute to the observed isotropic shifts in uranocenes. The contact component is dominant for ring protons, but rapidly attenuates with increasing number of σ -bonds between the observed nucleus and the uranium such that the contact shift is effectively zero for β -protons.

The value of the contact shift for ring protons in uranocene is of the same sign but about 10 to 15 ppm larger in magnitude than the contact shift for ring protons in $\text{Cp}_2\text{U-X}$ compounds. If a linear correlation exists between the magnitude of the contact shift and the degree of covalency in ligand-metal bonding in these systems, then the NMR data suggest a higher degree of covalency in the ligand-metal bonds in uranocene.

* * *

[†]Brief version of LBL-10432.

1. C. A. Harmon, D. P. Bauer, S. R. Berryhill, K. Hagiwara, and A. Streitwieser, Jr., *Inorg. Chem.* **16**, 2143 (1977).
2. K. O. Hodgson and K. N. Raymond, *Inorg. Chem.* **12**, 458 (1973).
3. A. Zalkin, D. H. Templeton, S. R. Berryhill and W. D. Luke, *Inorg. Chem.* **18**, 2287 (1979).
4. A. Zalkin, D. H. Templeton, W. D. Luke and A. Streitwieser, Jr., in preparation.
5. N. Edelstein, G. N. La Mar, F. Mares and A. Streitwieser, Jr., *Chem. Phys. Lett.* **8**, 399 (1971).

6. A. Streitwieser, Jr., D. Dempf, G. N. La Mar, D. G. Karraker, and N. Edelstein, *J. Am. Chem. Soc.* 93, 7343 (1971).
 7. S. R. Berryhill, Ph.D. thesis, U. C. Berkeley (1978).
 8. R. D. Fischer, in *Organometallics of the f-Elements*, T. J. Marks and R. D. Fischer, eds. (Reidel, 1979) p. 337.

2. CYCLIC VOLTAMMETRY STUDIES OF SUBSTITUTED CYCLOOCTATETRAENES

Elizabeth S. Hillard and Andrew Streitwieser, Jr.

Uranocenes are prepared by the reaction of a substituted cyclooctatetraene dianion with UCl_4 .¹ Many substituted cyclooctatetraene dianions readily form stable uranocenes, but some do not. For example, 1,3,5,7-Tetra-*t*-butylcyclooctatetraene dianion reduced UCl_4 to uranium metal² and the uranocenes formed from cyclooctatetraene esters were unstable.³ A study of the electrochemistry of substituted cyclooctatetraene was undertaken in order to explore the relationship between the

electronic properties of the COT's and the stability of uranocenes. Several other ligands were also studied in hopes of further elaborating the electronic structure of uranocenes.

Reduction potentials were obtained by cyclic voltammetry in dry, air-free dimethylformamide (DMF) and are summarized in Table 1. In addition, the difference between the cathodic and anodic peak potentials is a measure of the reversibility of the reduction (and the stability of the dianion). The reversibility of the reduction of cyclooctatetraene was confirmed as was the formation of 1,3,5- and 1,3,6-cyclooctatetraenes at more cathodic potentials.⁴ Presumably, these compounds arose from the reaction of the dianion with trace amounts of water. Triene formation was also observed with substituted cyclooctatetraenes.

The first reduction potential appears to be dependent on the size as well as the polar effects of the substituent electron-donating groups and increasing size cause more negative potentials. This is demonstrated by the potentials for *n*-butyl and *t*-butyl cyclooctatetraenes; the *t*-butyl potential is 110 mV cathodic of *n*-butyl. The effect is undoubtedly due to steric constraints in the

Table 1. CV reduction potentials in DMF.

| Compound ^a | E1/2 | E2/2 |
|-----------------------------------|-------------|--------|
| COT | -1.65V | -1.09V |
| ethylCOT | -1.76V | -1.96V |
| <i>n</i> -butylCOT | -1.79V | -1.96V |
| <i>t</i> -butylCOT | -1.90V | -2.03V |
| neopentylCOT | -1.77V | -1.96V |
| methoxyCOT | -1.76V | -1.94V |
| phenylCOT | -1.64V | -1.74V |
| triphenylmethylCOT | -1.78V | -1.91V |
| naphthoCOT | -1.74V | -1.91V |
| benzyl ester of COT | -1.26V | -1.58V |
| <i>t</i> -butyl ester of COT | -1.34V | -1.65V |
| 1,2,3,4-tetramethylCOT | -2.43V (2e) | - |
| 1,3,5,7-tetramethylCOT | -2.11V (2e) | - |
| 1,4-di- <i>t</i> -butylCOT | -2.16V (2e) | - |
| 1,3,5,7-tetra- <i>t</i> -butylCOT | (b) | - |
| naphthalene | -2.46V | - |

^a Some of these compounds were prepared by NSF-supported research.

^b Reduction potential not observed.

flattening of the tub-shaped COT to the planar COT radical anion. In several of the more hindered compounds, the first reduction was sufficiently negative to overlap with the second and only a single, two-electron wave is observed. Evidently, the bulk of the *t*-butyl group in neopentylcyclooctatetraene is sufficiently far removed so that ring flattening is not hindered and the reduction potentials are similar to those of *n*-butyl-COT. In the case of phenylcyclooctatetraene, it appears that the inductive effect of the phenyl group is more pronounced than the steric effects since both reduction potentials are anodic of normal alkyl-COT's.

The electrochemistry of those COT's which do not form a uranocene are of particular interest. Although the dianion of naphthocyclooctatetraene does not react to give a uranocene,⁴ its reduction potentials are well within the range of COT's which do form uranocenes. The dianions of 1,3,5,7-tetra-*t*-butyl and 1,2,3,4-tetramethyl COT reduce UC1₄ to uranium metal rather than forming a uranocene. The reduction potential of 1,2,3,4-tetramethyl COT is -2.34 V as compared to -2.11 V for 1,3,5,7-tetramethyl COT which does give a uranocene. One would expect the reduction potential of 1,3,5,7-tetra-*t*-butyl COT to be even higher. We have been unable to observe a reduction potential for this compound.

In general, it appears that COT's with reduction potentials more negative than -2.3 V would not be expected to form uranocenes. The low stability of uranocenes formed from COT-esters may indicate a narrow range of reduction potentials of COT's which will give stable uranocenes.

* * *

1. A. Streitwieser, Jr., *Organometallic Compounds of the f-Elements*, T. J. Marks and R. D. Fischer, Eds. (Reidel Publishing Co., Amsterdam, 1979), pp. 149-177.
2. M. Miller, results to be published.
3. H. P. G. Burghard, D. G. Morrell, and A. Streitwieser, Jr., submitted to *Inorg. Chem.*
4. L. A. Paquette, et al., *J. Am. Chem. Soc.* **98**, 4936 (1976) and earlier papers.

3. SYNTHESIS AND CHARACTERIZATION OF Pa(IV), Np(IV), AND Pu(IV) BOROHYDRIDES[†]

Rodney H. Banks, Norman M. Edelstein, Brock Spencer, David H. Templeton, and Allan Zalkin

Four of the seven known metal tetrakis-borohydrides--Zr, Hf, Th, and U borohydrides^{1,2}--were first synthesized about 30 years ago during the Manhattan Project. They were found to be very volatile and reactive compounds. In recent years, much structural, spectroscopic, and chemical studies were done on these molecules. New tetrakis-borohydrides of the actinides Pa, Np, and Pu have recently been prepared by analogous reactions used in the syntheses of U and Th borohydrides.³ The Pa compound, Pa(BH₄)₄, is isomorphous to and behaves like U(BH₄)₄ and Th(BH₄)₄ while x-ray studies on Np(BH₄)₄ and the isostructural Pu(BH₄)₄ have shown that they resemble the highly volatile Zr and Hf compounds both in structure and properties. The physical properties of some of the metal borohydrides are shown in Table 1.

Table 1. Physical properties of metal tetrakis-borohydrides.

| Property | Th(BH ₄) ₄ ^a | U(BH ₄) ₄ ^b | Hf(BH ₄) ₄ ^a | Zr(BH ₄) ₄ ^a | Np(BH ₄) ₄ ^c |
|------------------------------------|--|---|--|--|--|
| Crystallographic space group | P4 ₃ 2 ₁ 2 (tetragonal) | P4 ₃ 2 ₁ 2 ^d (tetragonal) | P4 ₃ m ^e (cubic) | P4 ₃ m ^f (cubic) | P4 ₂ /nmc (tetragonal) |
| Solid-state structure | polymeric | polymeric | monomeric | monomeric | monomeric |
| Density in the solid state(gm/cc) | 2.53 | 2.69 | 1.85 | 1.13 | 2.23 |
| Melting point (°C) | 203 ^g | 126 ^g | 29.0 | 28.7 | 14.2 |
| Boiling point (°C) extrap. | - | - | 118 | 123 | 153 |
| Vapor pressure (mmHg/°C) | 0.05/130 | 0.19/30 | 14.9/25 | 15.0/25 | 10.0/25 |
| Liquid ^h A | - | - | 2097 | 2039 | 1858 |
| Liquid B | - | - | 8.247 | 8.032 | 7.24 |
| Solid ^h A | - | 4264.6 | 2844 | 2983 | 3168 |
| Solid B | - | 13.354 | 10.719 | 10.919 | 11.80 |
| Heat of sublimation (Kcal/mol) | 21 | 19.5 | 13.0 | 13.6 | 14.5 |
| Heat of vaporization (Kcal/mol) | - | - | 9.6 | 9.3 | 8.5 |
| Heat of fusion (Kcal/mol) | - | - | 3.4 | 4.3 | 6.0 |
| Entropy of sublimation (cal/mol°) | - | 61.1 | 49.0 | 50.0 | 54.0 |
| Entropy of vaporization (cal/mol°) | - | - | 37.7 | 36.8 | 33.1 |
| Entropy of fusion (cal/mol°) | - | - | 11.3 | 13.2 | 20.9 |
| Solubility in pentane | insol | slight | high | high | high |

^aRef. 1

^eRef. 7

^bRef. 2

^fRef. 6

^cRef. 5

^gWith decomposition

^dRef. 4

^hLog p(mmHg) = -A/T + B

* * *

All seven compounds contain triple hydrogen bridge bonds connecting the boron atom to the metal. The 14 coordinate Th, Pa, and U borohydrides,⁴ in addition, have double-bridged borohydride groups that are involved in linking metal atoms together in a low-symmetry, polymeric structure. The structures of the other four borohydride molecules are monomeric and much more symmetrical; the 12-coordinate metal is surrounded by a tetrahedral array of BH_4^- groups.⁵⁻⁷ Its structure is shown in Fig. 1.

In an effort to understand the energy level structures of actinide 4+ ions in borohydride environments, optical and magnetic measurements have been initiated. Spectra of $\text{Np}(\text{BH}_4)_4$ and $\text{Np}(\text{BD}_4)_4$, both pure and diluted in single-crystal host matrices of $\text{Zr}(\text{BH}_4)_4$ and $\text{Zr}(\text{BD}_4)_4$, respectively, have been obtained in the region 2500-300 nm at 2 K. The covalent actinide borohydrides display rich vibronic spectra,⁸ and assignment of the observed bands depends on a knowledge of the vibrational energy levels of $\text{M}(\text{BH}_4)_4$ molecules. A normal coordinate analysis derived from low-temperature infrared and Raman spectra of $\text{Np}(\text{BH}_4)_4$ and $\text{Np}(\text{BD}_4)_4$ was undertaken to elucidate the nature of their fundamental vibrations and overtones. Electron paramagnetic resonance (EPR) spectra of $\text{Np}(\text{BH}_4)_4$ and $\text{Np}(\text{BD}_4)_4$ that characterize the ground electronic state have been obtained in a number of host materials. Optical spectra of $\text{Pa}(\text{BH}_4)_4$ and $\text{Pa}(\text{BD}_4)_4$ isolated in an organic glass were obtained in the near infrared and visible regions at 2 K. Analyses of these spectra are being completed.

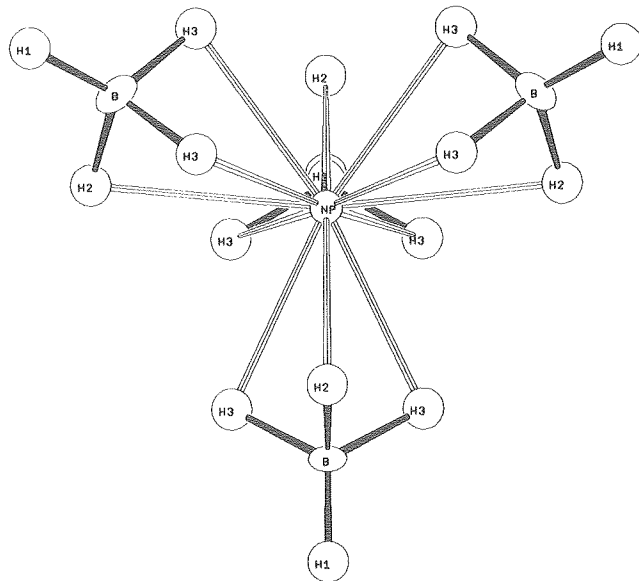


Fig. 1. Structure of $\text{Np}(\text{BH}_4)_4$. (XBL 795-9592)

† Brief version of LBL-9229 and LBL-9874.

1. H. R. Hoekstra and J. J. Katz, *J. Am. Chem. Soc.* **71**, 2488 (1949).
2. H. I. Schlesinger and H. C. Brown, *J. Am. Chem. Soc.* **75**, 219 (1953); J. J. Katz and E. Rabinowitch, *Chemistry of Uranium*, (McGraw-Hill, New York, 1951).
3. R. H. Banks, N. M. Edelstein, R. R. Rietz, D. H. Templeton, and A. Zaikin, *J. Am. Chem. Soc.* **100**, 1975 (1978).
4. E. R. Bernstein, W. C. Hamilton, T. A. Keiderling, S. J. LaPlaca, S. J. Lippard, and J. J. Mayerle, *Inorg. Chem.* **11**, 3009 (1972); E. R. Bernstein, T. A. Keiderling, S. J. Lippard, and J. J. Mayerle, *J. Am. Chem. Soc.* **94**, 2552 (1972).
5. R. H. Banks, N. M. Edelstein, B. Spencer, D. H. Templeton, and A. Zaikin, *J. Am. Chem. Soc.* **102**, 0000 (1980).
6. P. H. Bird and M. R. Churchill, *Chem. Comm.* **403** (1967).
7. R. S. Broach, I. S. Chuang, J. M. Williams, and T. J. Marks, private communication, 1979; T. A. Keiderling, Ph.D. thesis, Princeton University, 1974.
8. E. R. Bernstein and T. A. Keiderling, *J. Chem. Phys.* **59**, 2105 (1973).

4. ENERGY LEVEL ANALYSIS OF $\text{Np}^{3+}:\text{LaCl}_3$ AND $\text{Np}^{3+}:\text{LaBr}_3$ †

W. T. Carnall,† H. Crosswhite,† H. M. Crosswhite,† J. P. Hessler,† N. M. Edelstein, J. G. Conway,§ G. V. Shalimoff, and R. Sarup||

Previous investigations of the spectra of $\text{Np}^{3+}:\text{LaCl}_3$ ^{1,2} have included experimental data on the crystal-field components, but the theoretical treatment was limited to parametrization of the free-ion structure. Together with an analysis of the spectrum of $\text{U}^{3+}:\text{LaCl}_3$,³ the present investigation establishes for the first time the relative magnitudes of the crystal-field parameters characteristic of trivalent actinides in C_{3h} symmetry. A crystal-field analysis for $\text{Np}^{3+}:\text{LaBr}_3$ has been published,⁴ but some aspects require revision. Figure 1 shows qualitatively the energy level diagram for Np^{3+} diluted in LaCl_3 .

Previous analyses of the solid state spectra of Np^{3+} were carried out using theoretical models that varied in the degree of their sophistication, but attention was focused on parametrization of the free-ion or atomic interactions. The existing crystal-field analysis of $\text{Np}^{3+}:\text{LaBr}_3$ was based on a perturbation calculation.⁴ The foundation for the interpretation used here is identical to that used for $\text{Pm}^{3+}:\text{LaCl}_3$.⁵ The energy level structure within any f^N configuration, assuming a single-configuration model, can be written in terms of the matrix elements of atomic (E_f) and crystal-field (E_{cf}) interactions:

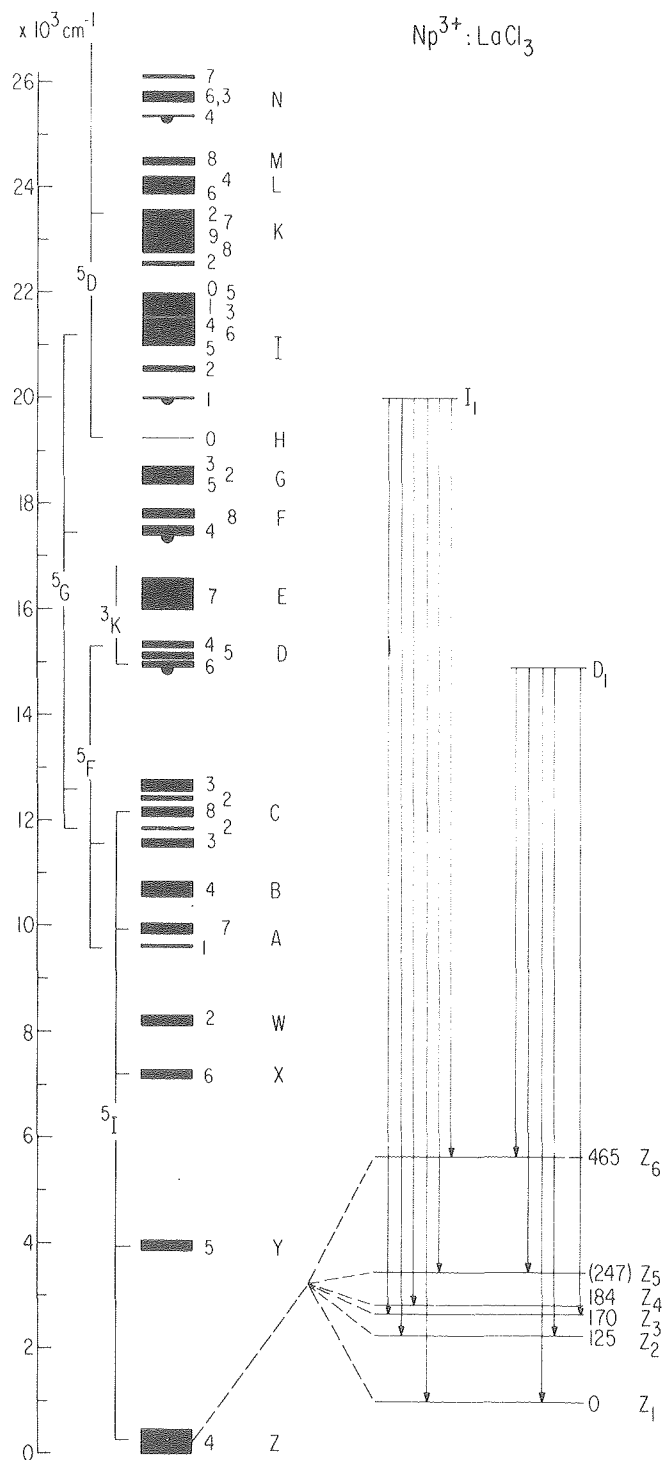


Fig. 1. Energy level diagram for $\text{Np}^{3+}:\text{LaCl}_3$. Principal fluorescing levels are indicated with a half circle. Levels that show spectroscopic multiplet character greater than 50% are indicated by brackets to the left. (XBL 7912-13546)

$$E = E_F + E_{CF}$$

where

$$E_F = \sum_{k=0}^6 F^k(nf,nf) f_k + \zeta_f A_{SO} + \alpha L(L+1) + \beta G(G_2) + \gamma G(R_7) + T^i t_i \quad (i = 2, 3, 4, 6, 7, 8) + E_M \quad (k \text{ even})$$

and

$$E_{CF} = \sum_{k,q,i} B_q^k (C_q^k)_i$$

$F^k(nf,nf)$ and ζ_f represent the radial parts of the electrostatic and spin-orbit interactions between f -electrons, respectively, while f_k and A_{SO} are the angular parts of the interactions, whose matrix elements can be calculated. α , β , and γ are the parameters of the two-body configuration-interaction operators;^{6,7} while the T^i are the corresponding parameters of the three-body configuration-interaction operators.⁸ E_M represents the magnetically correlated effects of configuration interaction in terms of the M^k and P^k parameters discussed by Judd, Crosswhite, and Crosswhite.⁹ The crystal-field interaction (E_{CF}) was assumed to be adequately described by the same single-particle model used to interpret the spectrum of $\text{Pm}^{3+}:\text{LaCl}_3$.⁵ The deviation between observed and computed crystal-field levels for $\text{Np}^{3+}:\text{LaCl}_3$ is about twice that for $\text{Pm}^{3+}:\text{LaCl}_3$. This suggests that corrections to the present model are needed.

At the outset of the energy-level parameter analysis it was apparent that the basic free-ion structure was satisfactorily represented by the previous analysis of NpCl_3 ,² so that with this as a starting point, only the principal free-ion parameters were allowed to vary as the crystal-field parameters were adjusted to the experimental data. As the parameter values became established, more of the free-ion interactions were allowed to freely vary. In the final computations involving diagonalization of the complete atomic and crystal-field matrices, a total of 150 levels extending to $\sim 26000 \text{ cm}^{-1}$ were satisfactorily fit with a mean error (σ) of 20 cm^{-1} . The parameter values, most of which were freely varied in the final stages of the fitting process, are given in Table 1. These results may be compared to the results for $\text{Pm}^{3+}:\text{LaCl}_3$ where a total of 106 levels were fit with a mean error of 9.0 cm^{-1} . Except for B_0^2 , the crystal-field parameters for $\text{Np}^{3+}:\text{LaCl}_3$ are essentially a factor of two larger than those for the lanthanide analog. Similar results have been obtained for $\text{U}^{3+}:\text{LaCl}_3$.³

The correlation between the energies and intensities of corresponding transitions observed in $\text{Np}^{3+}:\text{LaCl}_3$, NpCl_3 , and NpBr_3 (all three exhibit the same 9-coordinate UCl_3 -type lattice) was discussed earlier.² As a result of the present investigation, a much more extensive and exact comparison of chemical shifts was possible. However, even though there appeared to be a (small) clearly expressed red shift when comparing the centers of gravity of the crystal-field components observed in various states of $\text{Np}^{3+}:\text{LaCl}_3$ to those in NpCl_3 , calculation showed that the shifts were

too small to reflect any significant change in the atomic energy level parameters for the systems concerned. It was apparent that the same crystal-field parameters were equally appropriate in the two cases.

Based on these preliminary results, an extensive correlation existed between calculated and observed levels in $\text{Np}^{3+}:\text{LaBr}_3$. Additional assignments were made and many of the parameters allowed to vary freely. Final parameter adjustments were made with 147 assignments that included essentially the complete table of experimental results.⁴ Correlation with experiment was excellent. The parameters, as recorded in Table 1, are slightly smaller than those for $\text{Np}^{3+}:\text{LaCl}_3$, as expected, while the mean error (σ) of 19.8 cm^{-1} was the same.

Only 14 levels from Krupke's total set were inconsistent with the computed level scheme. Essentially all of these were "zero"-intensity transitions, possibly of vibronic origin.

We have shown that the existing crystal-field data for Np^{3+} in a hexagonal $\text{LaCl}_3(\text{LaBr}_3)$ single-crystal host has been accommodated in a successful attempt to parameterize the crystal-field, and that except for B_0^2 the parameters obtained are approximately a factor of 2 larger than in the lanthanide analog in the same host. Point-charge model approximations suggest that covalency effects are not apparent in the values obtained for the crystal-field parameters in Np^{3+} compared to those characteristic of a corresponding lanthanide. These results together with those for $\text{U}^{3+}:\text{LaCl}_3$

Table 1. Parameters for $\text{Np}^{3+}:\text{LaCl}_3$ (LaBr_3) energy levels.

| | $\text{Np}^{3+}:\text{LaCl}_3$ | | $\text{Np}^{3+}:\text{LaBr}_3$ | |
|-----------------------------|--------------------------------|-----------------------|--------------------------------|----------------------|
| E average | 29989 | (19) cm^{-1} | 29864 | (8) cm^{-1} |
| F ² | 44907 | (161) | 44659 | (59) |
| F ⁴ | 36918 | (245) | 36818 | (179) |
| F ⁶ | 25766 | (221) | 25589 | (163) |
| Alpha | 31.5 | (.32) | 31.9 | (.26) |
| Beta | -740 | (18) | -766 | (16) |
| Gamma | 899 | (70) | 954 | (50) |
| Zeta | 1938 | (2) | 1933 | (1) |
| T ² | 278 | (22) | 270 ^c | |
| T ³ | 44 | (7) | 45 ^c | |
| T ⁴ | 64 | (7) | 61 ^c | |
| T ⁶ | -361 | (18) | -360 ^c | |
| T ⁷ | 434 | (22) | 440 ^c | |
| T ⁸ | 353 | (17) | 355 ^c | |
| M ⁰ | 0.68 | (0.17) | 0.68 ^c | |
| M ² | 0.38 ^a | | 0.38 ^c | |
| M ⁴ | 0.26 ^a | | 0.26 ^c | |
| P ² | 894 | (44) | 905 ^c | |
| P ⁴ | 671 ^b | | 678 ^c | |
| P ⁶ | 447 ^b | | 452 ^c | |
| B ₀ ² | 163 | (26) | 101 | (28) |
| B ₀ ² | -632 | (48) | -661 | (42) |
| B ₀ ⁶ | -1625 | (52) | -1339 | (48) |
| B ₆ ⁶ | 1028 | (35) | 955 | (33) |
| σ^d | 20.0 | | 19.8 | |

^aM² and M⁴ constrained to vary as $M^2/M^0 = 0.56$, $M^4/M^0 = 0.38$.

^bP⁴ and P⁶ constrained to vary as $P^4/P^2 = 0.75$, $P^6/P^2 = 0.50$.

^cNot allowed to vary. Parameter values consistent with those

for $\text{Np}^{3+}:\text{LaCl}_3$ were assumed.

^dDeviation (σ) = $\sum(\Delta i^2/n-p)^{1/2}$ where Δi is the difference between observed and calculated energies, n is the number of levels used in the fitting procedure, and p is the number of parameters freely varied. For $\text{Np}^{3+}:\text{LaCl}_3$, $n = 150$; for $\text{Np}^{3+}:\text{LaBr}_3$, $n = 147$.

and $\text{Pu}^{3+}:\text{LaCl}_3$,³ provide an excellent basis for beginning the analysis of the heavier actinides.

* * *

‡ Brief version of manuscript submitted to J. Chem. Phys.

† Permanent address: Argonne National Laboratory, Argonne, IL 60439.

§ Current address: Institut de Physique Nucleaire, University of Paris, Orsay, France.

|| Permanent address: Physics Department, College of the Holy Cross, Worcester, MA 01610.

1. S. P. Cook, Ph.D. thesis, The John Hopkins University, Baltimore, MD (1959).

2. W. T. Carnall, H. M. Crosswhite, R. G. Pappalardo, D. Cohen, S. Fried, P. Lucas, F. Wagner, Jr., J. Chem. Phys. **61**, 4993 (1974).

3. H. M. Crosswhite, H. Crosswhite, W. T. Carnall, A. P. Paszek, submitted to J. Chem. Phys.

4. W. F. Krupke and J. B. Gruber, J. Chem. Phys. **46**, 542 (1967).

5. W. T. Carnall, H. Crosswhite, H. M. Crosswhite, J. G. Conway, J. Chem. Phys. **64**, 3582 (1976).

6. K. Rajnak and B. G. Wybourne, Phys. Rev. **132**, 280 (1963).

7. R. E. Trees, J. Opt. Soc. Am. **54**, 651 (1964).

8. B. R. Judd, Phys. Rev. **141**, 4 (1966).

9. B. R. Judd, H. M. Crosswhite, H. Crosswhite, Phys. Rev. **169**, 130 (1968).

5. A QUASI-RELATIVISTIC SCF X- α STUDY OF OCTAHEDRAL $5f^1$ COMPLEXES[†]

G. Thornton,[‡] Notker Rösch[§] and Norman Edelstein

Although ab-initio calculations of ML_N complexes have been carried out extensively for the situation in which M is a transition metal or main group element,¹ lanthanide and actinide complexes have been somewhat neglected. Such calculations are computationally difficult for traditional LCAO schemes, although the multiple scattering X- α (MSX α) method is capable of solving such a problem without undue cost, even when relativistic effects are included. The X- α method has been applied to the neutral species UF_5 ,² UF_6 ,²⁻⁶ UCl_6 ,⁷ NpF_6 ,^{4,5} and PuF_6 .^{4,5} Considerable success was obtained in their agreement with photoelectron and absorption spectra.

In the present study, quasi-relativistic SCF X- α calculations were carried out on a series of $5f^1$ complexes: PaX_6^{2-} , UX_6^- (X = F, Cl, Br, I) and NpF_6 . The study of such series has aided the interpretation of the electronic structure in terms of parameters commonly used in inorganic chemistry. In this case, the main object of study was the nature of the 5f ligand field splitting relative to the oxidation state of the metal ion and to the halide ion. Previously, only the relative extent of σ and π type ligand-f-orbital interactions has been discussed, in terms of the semi-empirical angular-overlap model.⁸ The X- α one-electron energies found in the calculations are shown in Fig. 1, and the electron charge within each muffin-tin sphere is presented in Table 1.

An appropriate test for the calculations presented here is to compare the calculated 5f - 5f excitation energies with corresponding absorption spectra.⁹⁻¹¹ Table 2 shows this comparison and it can be seen that the agreement between theory and experiment is remarkably good. The excitation energies were calculated using the transition-state procedure of Slater.¹²

The trend in the calculated ligand field splittings observed in Fig. 1 follows that found experimentally and that expected from the spectrochemical series, i.e., $\text{F}^- > \text{Cl}^- > \text{Br}^- > \text{I}^-$. Also, the order of $\text{Np}^{6+} > \text{U}^{5+} > \text{Pa}^{4+}$, expected on purely ionic grounds is observed. In the MS X- α scheme a charge fraction analysis of each of the orbitals can reveal the relative σ and π contributions in each of the spheres.

The following trends are apparent on comparing the relative ligand contribution to the bonding orbitals. The fluoride complexes are the most ionic in each of the various ionic groups, and the ligand contribution increases as the halide ion becomes heavier. Within a particular halide-complex series, the heavier the metal ion (and the lesser the total ionic charge) the greater the ligand contribution. In particular, NpF_6 appears to be the most covalent complex in the entire hexahalide series.

Considering only the t_{1u} antibonding orbitals, the percentage of ligand σ bonding increases from 17.4% (UF_6^-) and 7.8% (PaF_6^{2-}) to 26.6% (UI_6^-) and 12.7% (PaI_6^{2-}). The ligand π bonding component in the t_{1u} antibonding orbital increases from 2.3% and 2.6% in UF_6^- and PaF_6^{2-} to 5.5% and 3.9% in UI_6^- and PaI_6^{2-} . For the antibonding t_{2u} orbital (where only π bonding with the f orbitals can occur), the ligand π bonding increases from 8.5% and 4.8% for UF_6^- and PaF_6^{2-} to 11.6% and 6.2% for UI_6^- and PaI_6^{2-} .

The increase in both σ and π bonding as the halide becomes heavier is substantial. However, it is small when compared with the dramatic decrease in the f orbital splitting as the ligand is changed from F^- to I^- (see Table 2). These results suggest that the f orbital splittings of the hexahalide complexes are dominated by ionic effects with a lesser contribution from covalent bonding. It appears that the decrease in ionic effects due to changes in bond length outweighs the gain in covalent bonding on descending the halogen series.

Another measure of the covalent/ionic nature of the complexes can be found in the gross atomic charge assigned to the metal and ligand, as shown in Table 3. This is equivalent to a Mulliken population analysis in the LCAO scheme. The pattern obtained here is different from that discussed previously considering only the f orbitals. Clearly, NpF_6 is the most covalent but PaF_6^{2-} appears more covalent than UF_6^- . However, if the bonding is mainly ionic then these results are consistent, i.e., the greater the charge on the complex as a whole the smaller the charge on the central ion. Since the F^- ion is the smallest and least polarizable halide ion, an overall charge on the complex will result in more charge being

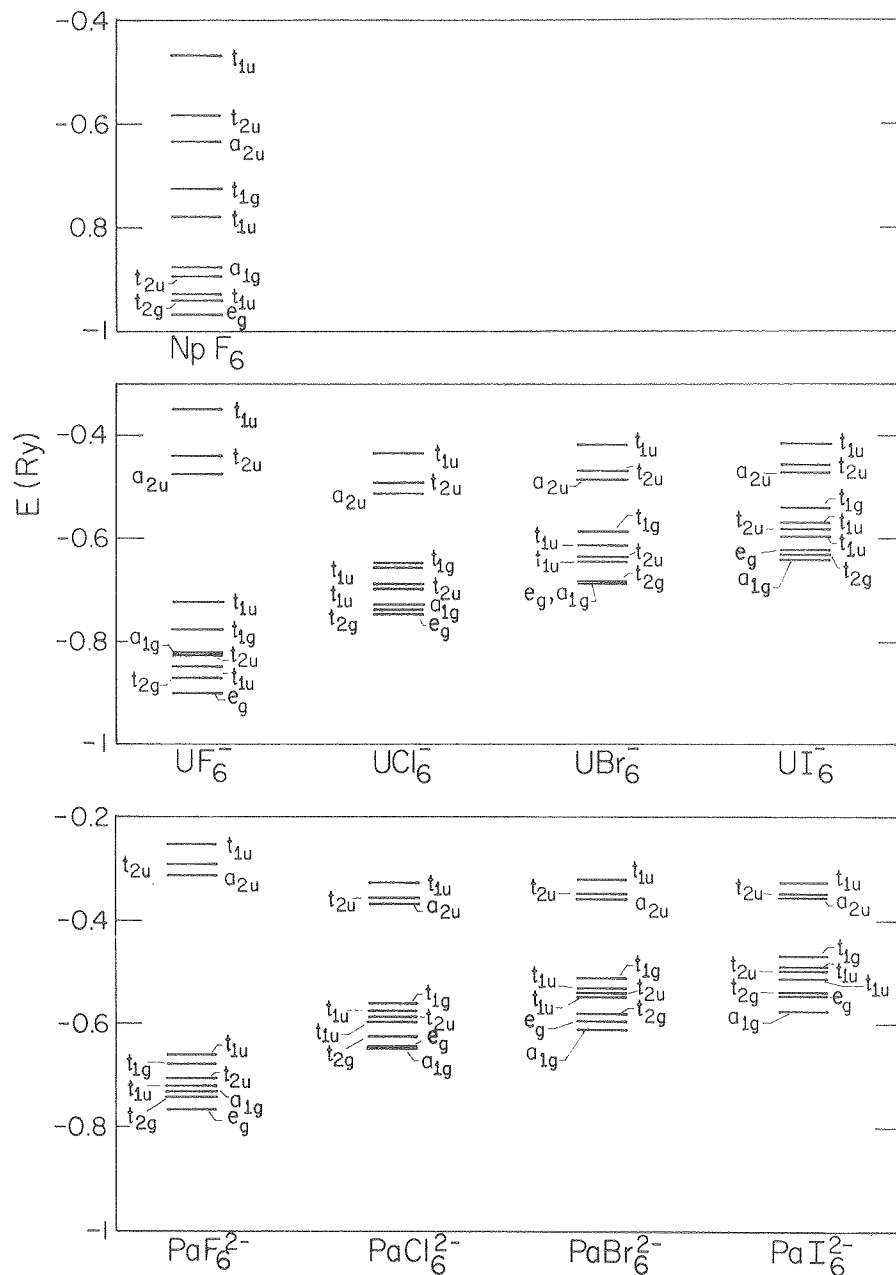


Fig. 1. Calculated one-electron energies for the $5f^1$ hexahalide complexes. (XBL 797-2171)

placed on the central metal ion. There appears to be little difference for the other halide ions.

* * *

† Brief version of LBL-9693; submitted to Inorg. Chem.

‡ Permanent address: Department of Chemistry, University of Manchester, Manchester M13 9PL, England.

§ Permanent address: Lehrstuhl für Theoretische Chemie, West Germany.

1. W. G. Richards, P. R. Scott, E. A. Calbourn, and A. S. Marchington, *Bibliography of ab initio molecular wavefunctions—supplement for 1976-1977*

(Oxford University Press, Oxford, 1978), and earlier publications in this series.

2. D. H. Maylotte, R. L. St. Peters, and R. P. Messmer, *Chem. Phys. Lett.* **38**, 181 (1976).

3. M. Boring and J. W. Moskowitz, *Chem. Phys. Lett.* **38**, 185 (1976).

4. D. D. Koelling, D. E. Ellis, and R. J. Bartlett, *J. Chem. Phys.* **65**, 3331 (1976).

5. M. Boring and H. G. Hecht, *J. Chem. Phys.* **69**, 112 (1978).

6. M. Boring and J. G. Wood, *J. Chem. Phys.* **71**, 32 (1979).

7. G. Thornton, N. Edelstein, N. Rösch, R. G. Egdell, and D. R. Woodward, *J. Chem. Phys.* **70**, 5218 (1979).

Table 1. Sphere radii and interatomic distances used in the MS X- α calculations (a.u.), and the charge found within each sphere for the ground state complexes.

| | R_M | R_L | R_{OUT} | D_{ML} | Q_M | Q_{HAL} | Q_{INT} | Q_{OUT} |
|---------------|-------|--------|-----------|----------|--------|-----------|-----------|-----------|
| PaF_6^{2-} | 3.212 | 1.3781 | 5.6767 | 2.274 | 89.582 | 7.843 | 9.148 | 1.208 |
| $PaCl_6^{2-}$ | 3.212 | 2.2856 | 7.4920 | 2.754 | 89.351 | 16.039 | 8.482 | 0.925 |
| $PaBr_6^{2-}$ | 3.212 | 2.5690 | 8.0586 | 2.904 | 89.414 | 34.031 | 8.480 | 0.891 |
| PaI_6^{2-} | 3.212 | 3.0280 | 8.9713 | 3.144 | 89.437 | 52.078 | 8.235 | 0.812 |
| UF_6^- | 2.789 | 1.3781 | 5.2666 | 3.888 | 90.879 | 7.803 | 8.927 | 1.197 |
| UCl_6^- | 2.789 | 2.2856 | 7.0816 | 4.796 | 89.879 | 16.018 | 8.147 | 0.859 |
| UBr_6^- | 2.789 | 2.5690 | 7.6484 | 5.079 | 89.982 | 34.014 | 8.093 | 0.815 |
| UI_6^- | 2.789 | 3.0280 | 8.5670 | 5.539 | 90.022 | 52.070 | 7.781 | 0.729 |
| NpF_6 | 2.763 | 1.2322 | 4.9765 | 3.744 | 91.457 | 7.294 | 10.359 | 1.412 |

Table 2. 5f \rightarrow 5f excitation energies; theoretical and experimental¹⁰⁻¹² (cm⁻¹).

| | $a_{2u} \rightarrow t_{2u}$ | | $a_{2u} \rightarrow t_{1u}$ | |
|---------------|-----------------------------|-------|-----------------------------|-------|
| | calc | exptl | calc | exptl |
| PaF_6^{2-} | 2381 | 3074 | 6979 | 7576 |
| $PaCl_6^{2-}$ | 1350 | 1634 | 4521 | 3507 |
| $PaBr_6^{2-}$ | 1218 | 1707 | 4104 | 2975 |
| PaI_6^{2-} | 944 | 1546 | 3424 | 2378 |
| UF_6^- | 4148 | 4479 | 17130 | 11361 |
| UCl_6^- | 2294 | 2936 | 8658 | 6307 |
| UBr_6^- | 2008 | 2935 | 7725 | 5310 |
| UI_6^- | 1525 | -- | 6277 | -- |
| NpF_6 | 5662 | 5619 | 18676 | 23117 |

Table 3. Gross atomic charges.

| | M | L |
|---------------|------|-------|
| PaF_6^{2-} | 0.11 | -0.35 |
| $PaCl_6^{2-}$ | 0.44 | -0.41 |
| $PaBr_6^{2-}$ | 0.38 | -0.39 |
| PaI_6^{2-} | 0.39 | -0.39 |
| UF_6^- | 0.68 | -0.28 |
| UCl_6^- | 0.96 | -0.33 |
| UBr_6^- | 0.86 | -0.31 |
| UI_6^- | 0.87 | -0.30 |
| NpF_6 | 0.06 | -0.01 |

8. K. D. Warren, Inorg. Chem. 16, 2008 (1977).

9. D. Brown, P. Lidster, B. Whittaker, and N. Edelstein, Inorg. Chem. 15, 511 (1976).

10. N. Edelstein, D. Brown, and B. Whittaker, Inorg. Chem. 13, 563 (1974).

11. W. Wagner, N. Edelstein, B. Whittaker, and D. Brown, Inorg. Chem. 16, 1021 (1977).

12. J. C. Slater, The Self-Consistent Molecular Field for Molecules and Solids (McGraw-Hill, New York, 1974).

6. IDENTIFICATION OF UIII AND UIV LINES[†]

J. O. Berg,[‡] T. E. Christensen, P. W. Kidd,[‡]
G. R. Neil,[‡] and J. G. Conway[§]

Although considerable progress has been made on identifying and assigning lines of UI and UII,^{1,2} very little is known about higher charge states of uranium. The only published experiments on higher charge states of uranium have two lines of UIII,³ 70 lines in the ultraviolet from 2800-3500 Å associated with charge states higher than UII,⁴ and eight lines of UVI in the vacuum ultraviolet.⁵ Calculations of the energies of the various possible configurations for UIII and UIV have been performed by Brewer.⁶ We report here on lines of UIII and UIV observed in the visible and near ultraviolet regions of the spectrum.

Three different experiments were performed to identify UIII and UIV lines and to assure proper assignments. Two involved spatial variations between the different species while the third used temporal dependences. In the first experiment, spectra were taken at different spatial positions in a steady state uranium/argon plasma, using a fiber optic probe with a spectrometer and photodetector at the TRW labs in Redondo Beach, CA. The second experiment was performed on the same machine, using a mass spectrometer probe. This probe is basically a curved slot perpendicular to the magnetic field (B). Only ions possessing a q/m (charge to mass ratio) given by

$$q/m = \frac{2V}{r^2 B^2} \quad (1)$$

will reach the collector, where V is the slot voltage relative to the plasma and r is the radius of curvature of the slot. Since B is a constant, different q/m can be sampled by varying the slot voltage. The third set of experiments were uranium spectra taken in a sliding spark discharge at Lawrence Berkeley Laboratory.⁷ With a sector wheel and a varying time delay, different portions of the light from the discharge were passed through a spectrograph.

The fiber optic experiments showed that the uranium lines could be divided into four groups on the basis of their relative intensity as a function of position from the uranium neutral source. The intensity of lines of UI fell off rapidly with distance from the neutral source due largely to geometric factors. UII lines fell off somewhat more slowly. The UI and UII lines were identified on the basis of uranium line lists.^{1,2} Lines that we assign as UIII rose further away from the neutral source and then fell off; those of UIV rose more slowly and fell off more slowly. These different spatial dependencies are due to the different formation, ionization, and transport rates for the various species.

Mass spectrometer collector current vs. slot voltage plots were taken at various distances from the neutral source and the results compared to a fiber optic scan of a line of a given species. Excellent agreement was found for a line of UIII

(U⁺⁺) as expected, since the electron density and temperature are spatially constant. The agreement for U⁺ was equally good while that for UIV was not as good.

For the spark spectra, the intensity distribution followed three general patterns: one in which there was very little change in intensity, second where the intensity of the rise and peak were stronger than the tail, and third where the tail was stronger than the rise and peak. The second pattern is characteristic of higher ionizations than those of the third type. An electrodeless discharge lamp and a low-energy oscillating spark were compared to the sliding spark source, and all lines in the sliding spark were new and did not appear in the other sources. The assignments of all lines on the basis of the spark spectra agreed with the fiber optic assignments. Tables 1 and 2 list the lines identified as UIII and UIV, respectively.

Only the strongest lines from the U/Ar plasma have been spatially mapped. More lines have been seen in the spark spectra. Work is in progress to identify more lines of UIII and UIV.

Table 1. Lines of double ionized uranium (UIII)

| Wavelength (Å) | Wavenumber (cm ⁻¹) |
|----------------|--------------------------------|
| 4286.83 | 23320.7 |
| 4414.65 | 22645.5 |
| 4838.74 | 20660.8 |
| 4873.71 | 20512.5 |
| 4989.88 | 20035.0 |

Table 2. Lines of triply ionized uranium (UIV)

| Wavelength (Å) | Wavenumber (cm ⁻¹) |
|----------------|--------------------------------|
| 4158.54 | 24040.1 |
| 4202.76 | 23787.2 |
| 4363.61 | 22910.4 |
| 4717.98 | 21189.6 |

* * *

[†]Brief version of manuscript submitted to J. Opt. Soc. Am.

[‡]Permanent address: TRW, One Space Park, Redondo Beach CA 90278.

[§]Current address: Institut de Physique Nucleaire, University of Paris, Orsay, France.

1. D. W. Steinhaus, L. J. Radziemski, Jr., R. D. Cowan, J. Blaise, G. Guelachvili, Z. B. Osman, and J. Verges, "Present Status of the Analyses of the First and Second Spectra of Uranium (UI and UII) as Derived from Measurements of Optical Spectra," Los Alamos Scientific Laboratory Report LA-4501 (October 1971).
2. D. W. Steinhaus, M. V. Phillips, J. B. Moody, L. J. Radziemski, Jr., K. J. Fisher, and D. R. Hahn, "The Emission Spectrum of Uranium Between 19,080 and 30,261 cm^{-1} ," Los Alamos Scientific Laboratory Report LA-4944 (August 1972).
3. P. Schuurmans, "On the Analysis of Some Complex Spectra (Th and U)," Atomic Energy Research Establishment Lib/Trans 513 (Harwell, Berkshire, England, 1955).
4. N. G. Morozova and G. P. Startev, Opt. I Spek. 2, 382-384 (1957).
5. V. Kaufman and L. J. Radziemski, Jr., J. Opt. Soc. Am. 66, 599-600 (1976).
6. L. Brewer, J. Opt. Soc. Am. 61, 1666-1682 (1971).
7. C. H. H. Van Deurzen and J. G. Conway, Appl. Spectrosc. 28, 223-234 (1974).

RESEARCH PLANS FOR CALENDAR YEAR 1980

The basic purpose of the project in heavy element chemistry is to study lanthanide and actinide materials in order to provide the basic knowledge necessary for their safe and economic utilization in present and future technology. This work encompasses related problems of an applied nature in actinide chemistry.

The program includes the preparation of new gaseous, liquid, and solid phases and studies of their physical and chemical properties. Techniques for characterization include x-ray diffraction, optical and vibrational spectroscopy, magnetic resonance, and magnetic susceptibility. Equilibrium and kinetic data for complex formation will be measured. From these complementary studies, new insights into the structural and chemical principles of actinide compounds will be obtained with which to design new synthetic schemes to produce new materials.

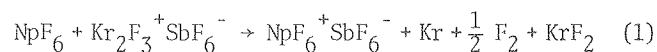
A major aspect of our program is the design of sequestering agents for actinide ions that can engulf the ion and generate neutral or negatively charged complexes. A biomimetic approach that notes the biological similarity between Pu^{4+} and Fe^{3+} suggested that catechol groups, which are in naturally occurring Fe^{3+} sequestering agents, should be useful ligands. Four such ligands have been incorporated in a series of macrocyclic chelating agents, two of which at low concentration show an efficiency for Pu^{4+} removal in mice and rats, more than an order of magnitude better than agents in present clinical use. Future plans involve the optimization of these ligands by modifying the cavity size and electronic structure of the catechol groups. In addition, new bidentate chelating groups will be studied for the feasibility of incorporating them into macrocyclic chelating agents.

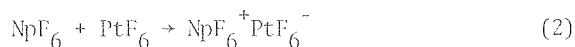
NMR studies of uranocene in the past year have been very successful in revealing many aspects of the uranocene system. Plans for this year include continuing this work with the preparation and study of tetramethyl and cyclohexyl-uranocenes, and confirming the assignment of ring protons in t-butyluranocenes by study of deuterated compounds. The suggestion that the t-butyl group is bent away from the uranium will also be tested by x-ray structure analysis of suitable compounds. Studies will continue on the preparation and chemistry of transuranium organoactinide compounds, including proton NMR spectra of plutonocene. In collaboration with Dr. N. Rösch of Munich and Dr. J. Green of Oxford, plans have been made to continue the $X\alpha$ -SW SCF calculations of cyclooctatetraene actinide and lanthanide sandwich compounds and to determine and evaluate the photoelectron spectra of substituted uranocenes. In NSF-supported research, biuranocenylenes, bis(bi-cyclooctatetraenyl)diuranium has been prepared. The corresponding neptunium compound and the potentially mixed valence anion and cation will be synthesized for Mössbauer isomer shift studies.

These studies are expected to provide additional understanding of the electronic structure and chemistry of organoactinide compounds. In addition, we will continue studies to follow-up our discovery of the air- and thermal-stability of octaphenyl-uranocene. These include preparing related structures in which bulky substituents shield the central uranium from attack by oxygen and other reagents. The preparation of 1,5-di-t-butylcyclooctatetraene is well underway. Cyclooctatetraene ligands with several trimethylsilyl and cyclohexyl substituents will be examined. Tetrakis (diphenylallyl) uranium(IV) should have a structure similar to octaphenyluranocene, and its preparation will be attempted. Volatile, air-stable organoactinide compounds may provide useful new routes for isotope separation. Finally, studies will continue of monocyclooctatetraeneactinide compounds by preparation of the alkylborohydride derivatives. These compounds are expected to have significant volatility and the potential for providing useful catalysts.

Studies on the preparation and physical properties of new actinide amides, alkoxides, alkyls, and borohydrides will continue. The reaction chemistry on compounds of the type $\text{XM}[\text{N}(\text{SiMe}_3)_2]_3$ where X is H, BH_4 , or Me and M is Th or U will be pursued. Reactions with unsaturated and other organic molecules with the intent of developing new chemistry is of particular interest. Studies will continue on the low-valent (i.e., divalent oxidation) state of Sm, Eu, and Yb with the bulky ligands $(\text{Me}_3\text{Si})_2\text{N}$ and C_5Me_5 . Our principal objective is to understand the chemistry and reactivity of these low-valent materials.

Attempts to prepare discrete Np^{7+} species such as NpOF_5 , NpF_7^- , and NpF_6^+ will continue. First priority will be given to the attempted synthesis of NpF_6^+ by the following routes:





The second study will be carried out at -196° or below by spraying the reactants onto a cold silver chloride window in a cell from which infrared and Raman studies can be made. Attempts will also be made to prepare NpOF_5 by oxidation of NpOF_5^- salts.

The spectroscopic program will emphasize the crystal spectra of lanthanide and actinide ions in a variety of host crystals. Included in this work will be further experiments and analysis of $\text{Np}(\text{BH}_4)_4$ as a pure single crystal and diluted in $\text{Zr}(\text{BH}_4)_4$. The deuterated analogs will also be studied. Work will continue on magnetic and optical studies of $\text{Pa}(\text{BH}_4)_4$ and $\text{Pu}(\text{BH}_4)_4$. Further optical data will be collected and analyzed on tris(hexamethyldisilylamido) $\text{Nd}(\text{III})$ and $\text{Pr}(\text{III})$ in solution and in the solid state. A major effort is underway to collect free-ion spectra of U in a spark source as a function of current and time after excitation. This type of systematic study should allow a classification of the spectra according to charge state, i.e., U^{2+} , U^{3+} , U^{4+} , and U^{5+} .

1979 PUBLICATIONS AND REPORTS

Refereed Journals

- D. H. Templeton, A. Zalkin, H. W. Ruben, and L. K. Templeton, "Anomalous Scattering of Cobalt and Chlorine and Crystal Structure of (+)-Tris(ethylenediammine) cobalt(III) Chloride (+)-Tartrate Pentahydrate," *Acta Crystallogr. Sect. B* **35**, 1608 (1979).
- H. W. Turner, R. A. Anderson, D. H. Templeton, and A. Zalkin, "Chloro-, Methyl-Tetrahydroborato-Tris(hexamethyl disilylamido) Thorium(IV) and Uranium(IV). Crystal Structure of Tetrahydroborato Tris(hexamethyldisilylamido)-Thorium(IV)," *Inorg. Chem.* **18**, 1221 (1979).
- A. Zalkin, D. H. Templeton, S. R. Berryhill, and W. D. Luke, "Crystal and Molecular Structure of Bis- π -(cyclobutenocyclooctatetraene)Uranium(IV)," *Inorg. Chem.* **18**, 2287 (1979).
- A. Zalkin, H. Ruben, and D. H. Templeton, "Structure of Pentakis(urea) dioxuranium(VI) Nitrate, $[\text{UO}_2(\text{OC}(\text{NH}_2)_2)_5](\text{NO}_3)_2$," *Inorg. Chem.* **18**, 519 (1979).
- D. L. Perry, D. H. Templeton, and A. Zalkin, "The Synthesis and Structure of Di-n-propylammonium Ethoxybis(di-n-propylmonothiocarbamate)dioxouranium(VI), A Mixed Chelate Alkoxide of Uranium," *Inorg. Chem.* **18**, 879 (1979).
- D. M. Rousch, E. M. Price, L. K. Templeton, D. H. Templeton, and C. H. Heathcock, "Synthesis, Stereostructure, Pyramidal Inversion, and Alkylation of 1-Thioniabicyclo(4.4.0)decane Salts," *J. Am. Chem. Soc.* **101**, 2971 (1979).
- R. A. Andersen, "Fluoroalkoxides of Uranium(IV)," *Inorg. Nucl. Chem. Lett.* **15**, 57 (1979).
- H. W. Turner, S. J. Simpson, and R. A. Andersen, "Hydrido[Tris(hexamethyldisilylamido)-Thorium and Uranium]," *J. Am. Chem. Soc.* **101**, 2782 (1979).
- R. A. Andersen, "Tris(hexamethyldisilylamido) Uranium(III), Preparation and Coordination Chemistry," *Inorg. Chem.* **18**, 1507 (1979).
- S. R. Sofen, S. R. Cooper, and K. N. Raymond, "The Crystal and Molecular Structure of Tetrakis(catecholato)-hafnate(IV) and -cerate(IV). Further Evidence of a Ligand Field Effect in the Structure of Tetrakis(catecholato) uranate(IV)," *Inorg. Chem.* **18**, 1611 (1979).
- A. Avdeef and K. N. Raymond, "Free Metal and Free Ligand Concentrations Determined from Titrations Using only a pH Electrode. Partial Derivatives in Equilibrium Studies," *Inorg. Chem.* **18**, 1605 (1979).
- A. Avdeef, S. R. Sofen, T. L. Bregante, and K. N. Raymond, "Stability Constants for Catechol Models of Enterobactin," *J. Am. Chem. Soc.* **100**, 5362 (1978).
- D. P. Freyberg, J. L. Robbins, and K. N. Raymond, "The Crystal and Molecular Structures of Decamethylmanganocene and Decamethylferrocene. Static Jahn-Teller Distortion in a Metallocene," *J. Am. Chem. Soc.* **101**, 892 (1979).
- J. L. Robbins, N. Edelstein, S. R. Cooper, and J. C. Smart, "Syntheses and Electronic Structures of Decamethylmanganocenes," *J. Am. Chem. Soc.* **101**, 3853 (1979).
- G. Thornton, N. Edelstein, N. Rösch, R. Egdeil, and D. R. Woodward, "The Electronic Structure of UCl_6 : Photoelectron Spectra and Scattered Wave $X\alpha$ Calculations," *J. Chem. Phys.* **70**, 5218 (1979).
- Earl F. Worden and John G. Conway, "Laser Spectroscopy of Neptunium; First Ionization Potential, Lifetimes, and New High-Lying Energy Levels of Np (I)," *J. Opt. Soc. Am.* **69**, 733 (1979).
- Earl F. Worden and John G. Conway, "The Emission Spectrum of Berkelium," *Atomic Data and Nuclear Data Tables* **22**, 329 (1978).
- W. L. Smith and K. N. Raymond, "The Oxidation of Uranium(IV) by N-Phenylbenzohydroxamic Acid and the Structure of the Reaction Product: Chloro dioxo-N-phenylbenzohydroxamate-bis(tetrahydrofuran) Uranium(VI)," *J. Inorg. Nucl. Chem.* **41**, 1431 (1979).
- G. T. Seaborg, W. Loveland, and D. J. Morrissey, "Superheavy Elements, A Crossroads," *Science* **203**, 7711, (1979).

Other Publications

- A. Streitwieser, Jr., "Preparation and Chemistry of Uranocenes," *Organometallics of the f-Elements*, T. J. Marks and R. D. Fischer, Eds., Amsterdam, 1979, pp. 149-177.

2. N. Edelstein, "Electronic Structure of the f-Block Compounds," Organometallics of the f-Elements, T. J. Marks and R. D. Fischer, Eds., Amsterdam, 1979, pp. 37-79.
3. K. N. Raymond, "The Structure and Bonding of 4f and 5f Series Organometallic Compounds," Organometallics of the f-Elements, T. J. Marks and R. D. Fischer, Eds., Amsterdam, 1979, pp. 249-280.
4. G. T. Seaborg, Ed., Transuranium Elements--Products of Modern Alchemy, (Benchmark Papers in Physical Chemistry and Chemical Physics), vol. 1., Dowden, Hutchinson & Ross, Inc., Stroudsburg, PA, 1978.
5. G. T. Seaborg, "Actinides and Transactinides," Encyclopedia of Chemical Technology, Kirk and Othmer, Eds., vol. 1, 3rd edition, John Wiley & Sons, 1978, pp. 456-488.
6. G. T. Seaborg, Transuranium and Superheavy Elements, Hauxue Tongbao 5, People's Republic of China, 1978, pp. 24-25.
9. N. Edelstein, W. Kolbe, and J. E. Bray, "The Electron Paramagnetic Resonance Spectrum of the f_8 Ground State of Np^{4+} Diluted in Cs_2ZrCl_6 ," LBL-8787, Phys. Rev. B., in press.
10. Jan P. Hessler, W. T. Carnall, H. M. Crosswhite, N. Edelstein, J. G. Conway, and R. Sarup, "Energy Level Analysis of $Np^{3+}:LaCl_3$ and $Np^{3+}:LaBr_3$," submitted to J. Chem. Phys.
11. G. Thornton, N. Rösch, and N. Edelstein, "A Quasi-Relativistic SCF X- α Study of Octahedral $5f^1$ Complexes," LBL-9693, submitted to Inorg. Chem.
12. W. Luke and A. Streitwieser, Jr., "NMR Spectra of Uranocenes," submitted for publication in the ACS Symposium Series, The Chemistry of the Lanthanides and Actinides, September 1979, N. Edelstein, Ed. American Chemical Society, Washington DC, 1980.
13. R. H. Banks and N. Edelstein, "Synthesis and Characterization of Pa(IV), Np(IV), and Pu(IV) Borohydrides," submitted for publication in the ACS Symposium Series, The Chemistry of the Lanthanides and Actinides, September 1979, N. Edelstein, Ed. American Chemical Society, Washington DC, 1980.

LBL Reports and Other Reports

1. R. H. Banks, N. M. Edelstein, B. Spencer, D. H. Templeton, and A. Zalkin, "Volatility and Molecular Structure of Neptunium(IV) Borohydride," LBL-9229, J. Am. Chem. Soc., in press.
2. H. Ruben, B. Spencer, D. H. Templeton, and A. Zalkin, "Structure of Tris(urea)dioxouranium(VI) Sulfate, $UO_2(OC(NH_2)_2)_3SO_4$," LBL-9478, submitted to Inorg. Chem.
3. D. L. Perry, H. Ruben, D. H. Templeton, and A. Zalkin, "Structure of Di- μ -aquo-bis[dioxodinitratouranium(VI)]Dimidazole, $[UO_2(NO_3)_2 \cdot H_2O \cdot C_3H_4N_2]_2$, a Water Bridged Dimer of Uranyl Nitrate," LBL-9973, submitted to Inorg. Chem.
- ‡4. D. H. Templeton, L. K. Templeton, J. C. Phillips, and K. O. Hodgson, "Anomalous Scattering of X-rays by Cesium and Cobalt Measured with Synchrotron Radiation," LBL-9880, submitted to Acta Crystallogr. Sect. A.
- ‡5. L. K. Templeton, D. H. Templeton, and R. P. Phizackereley, " L_{3-} Edge Anomalous Scattering of X-rays by Praseodymium and Samarium," LBL-9865, submitted to Acta Crystallogr. Sect. A.
- ‡6. D. H. Templeton and L. K. Templeton, "Polarized X-ray Absorption and Double Refraction in Vanadyl Bisacetylacetonate," LBL-9530, submitted to Acta Crystallogr. Sect. A.
7. S. J. Simpson, H. W. Turner, and R. A. Andersen, "Hydrogen-Deuterium Exchange; Perdentero-hydridotris (hexamethyldisilylamido)-Thorium(IV) and Uranium(IV)," LBL-9575, J. Am. Chem. Soc., in press.
8. W. L. Smith and K. N. Raymond, "The Synthesis of Aliphatic Dimeric-N-Isopropyl Hydroxamic Acids and the Crystal and Molecular Structure of N,N'-Diisopropylhexanediamide; a Hydroxamic Acid in the Trans Conformation," LBL-9954, J. Am. Chem. Soc., in press.
14. Jeffrey P. Solar, Andrew Streitwieser, Jr., and N. M. Edelstein, "Cyclooctatetraeneactinide(IV) Bis-borohydrides," submitted for publication in the ACS Symposium Series, The Chemistry of the Lanthanides and Actinides, September 1979, N. Edelstein, Ed. American Chemical Society, Washington DC, 1980.
15. Richard A. Andersen, "Alkyl, Hydride, and Related Bis(trimethylsilyl)-Amide Derivatives of the 4f- and 5f-Block Metals," submitted for publication in the ACS Symposium Series, The Chemistry of the Lanthanides and Actinides, September 1979, N. Edelstein, Ed. American Chemical Society, Washington DC, 1980.
16. K. N. Raymond, W. L. Smith, F. L. Weigl, P. W. Durbin, E. S. Jones, K. Abu-Dari, S. R. Sofen, and S. R. Cooper, "Specific Sequestering Agents for the Actinides," submitted for publication in the ACS Symposium Series, The Chemistry of the Lanthanides and Actinides, September 1979, N. Edelstein, Ed., American Chemical Society, Washington DC, 1980.
17. E. Worden and J. G. Conway, "Multistep Laser Photoionization of the Lanthanides and Neptunium," submitted for publication in the ACS Symposium Series, The Chemistry of the Lanthanides and Actinides, September 1979, N. Edelstein, Ed., American Chemical Society, Washington DC, 1980.
18. P. W. Durbin, E. S. Jones, K. N. Raymond, and F. L. Weigl, "Removal of $^{238}Pu(IV)$ from Mice by Sulfonated Tetrameric Catechoyl Amides," Radiation Research, in press.
19. K. N. Raymond and C. W. Eigenbrot, Jr., "Structural Criteria for the Mode of Bonding in Organolanthanides and -actinides," submitted to Accounts of Chemical Research.

20. Glenn T. Seaborg, "The Periodic Table: Tortuous Path to Man-Made Elements," *Chemical and Engineering News*, 57, 46 (1979), LBL-9074.

21. Glenn T. Seaborg, Ed., *Proceedings of the Symposium Commemorating the 25th Anniversary of Elements 99 and 100*, January 23, 1978 at Lawrence Berkeley Laboratory, prepared for the U. S. Department of Energy, LBL-7701, UC-34C, CONF-780134, April 1979.

Invited Talks

1. R. A. Andersen, "Alkyl and Hydride Derivatives of the f-Block Metals," University of Southern California, January 1979.

2. R. A. Andersen, "Alkyl and Hydride Derivatives of the f-Block Metals," University of Los Angeles, March 1979.

3. R. A. Andersen, "Alkyl, Hydride, and Related Bis(trimethylsilyl)-Amide Derivatives of the 4f- and 5f-Block Metals," Symposium on the Lanthanides and Actinides, Washington DC, September 1979.

4. R. H. Banks and N. Edelstein, "Synthesis and Characterization of Pa(IV), Np(IV), and Pu(IV) Borohydrides," Symposium on the Lanthanides and Actinides, Washington DC, September 1979.

5. W. Luke and A. Streitwieser, Jr., "NMR Spectra of Uranocenes," Symposium on the Lanthanides and Actinides, Washington DC, September 1979.

6. K. N. Raymond, W. L. Smith, F. L. Weigl, P. W. Durbin, E. S. Jones, K. Abu-Dari, S. R. Sofen, and S. R. Cooper, "Specific Sequestering Agents for the Actinides," Symposium on the Lanthanides and Actinides, Washington DC, September 1979.

7. E. Worden and J. G. Conway, "Multistep Laser Photoionization of the Lanthanides and Neptunium," Symposium on the Lanthanides and Actinides, Washington DC, September 1979.

8. A. Streitwieser, Jr., "The Chemistry of Uranocenes, An Organometallic Sandwich Compound," Exxon Corporation, Linden NJ, March 5, 1979.

9. A. Streitwieser, Jr., "The Chemistry of Uranocenes, An Organometallic Sandwich Compound," Chemistry Department, New York University, March 9, 1979.

10. G. T. Seaborg, "Transuranium Elements--Some Examples of Modern Alchemy," The Electric Club, Vasteras, Sweden, December 11, 1978.

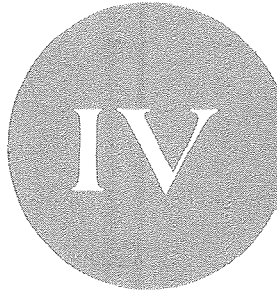
11. G. T. Seaborg, "Otto Hahn--Nuclear Fission and the Transuranium Elements," Memorial Lecture, 100th Birthday of Otto Hahn, Karlsruhe, Germany, March 22, 1979.

12. G. T. Seaborg, "The Actinide Elements," Plenary Lecture, Symposium on Actinide Separations, Ion Exchange Precipitation Methods, ACS/CSJ Chemical Congress, Honolulu, Hawaii, April 3, 1979.

* * *

† Partially supported by NIH.

‡ Partially supported by NSF.



Fossil Energy

Fossil Energy

a. Electrode Surface Chemistry*

Philip N. Ross, Investigator

Introduction. Commercialization of phosphoric acid fuel cell technology requires a capital cost reduction and an extension of power plant life compared to currently available technology. Significant capital cost reduction can be achieved if an oxygen reduction catalyst that is catalytically more active than platinum can be developed. The objective of the present research is to develop the physical and chemical understanding of the oxygen-platinum surface interactions necessary for the rational selection of alloying components or for the development of other means of modifying the basic properties of platinum. The approach used in this research is to study in parallel the kinetics of gas-phase adsorption of oxygen and the kinetics of anodic oxide formation-reduction on platinum surfaces modified by the substitution of selected ligands. The ligand modification of the surface is produced by either conventional alloying or ion implantation. The structure, composition, and chemical state of the modified surfaces are determined by a combination of surface analytical tools: low energy electron diffraction (LEED), Auger electron spectroscopy (AES), and photoemission spectroscopy (both XPS and UPS). The kinetics of oxygen chemisorption and oxide formation from the gas-phase are studied using a combination of AES and UPS. The kinetics of anodic layer formation and reduction are studied using a microcell directly coupled to the surface analysis chamber by a transfer and auxiliary pumping system developed especially for this application. Previous studies¹ have shown that the kinetics of oxygen reduction is correlated (via a volcano-type relation) to the metal-oxygen bond energy of the metal oxide. It is felt that the platinum-oxygen bond energy, which we can measure directly, will be changed when ligands are bonded to the surface platinum atoms and that by the use of appropriate ligands an optimal bond energy will result in enhanced catalytic activity related to the pure platinum surface.

1. STRUCTURE SENSITIVITY IN THE ELECTROSORPTION OF HYDROGEN ON PLATINUM.†

Philip N. Ross

Determining how the platinum-hydrogen bond energy is related to surface structure is an im-

portant preliminary step to determining how the platinum-oxygen bond energy is related to surface structure, since the latter is a much simpler (both experimentally and theoretically) reaction. Platinum surfaces of varying (ordered) structure were produced by using the three different low index faces (111), (100), and (110) and by cutting a (111) crystal at varying angles towards the [100] and [110] poles. The location of the crystal faces examined in the fcc stereographic triangle is shown in Fig. 1. LEED studies² have shown that cutting a Pt (111) crystal at increasingly larger angles towards the [100] pole introduces increasing numbers of (100) microfacets which, at certain

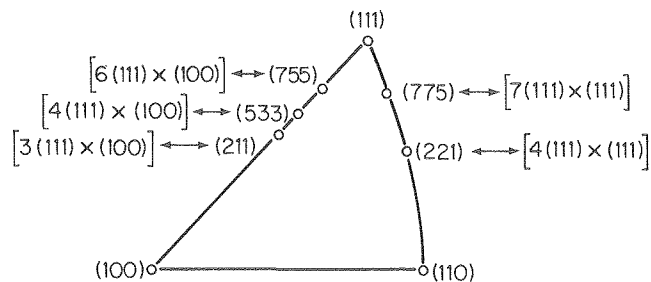


Fig. 1. Stereographic projection showing the crystallographic orientation of the single crystal faces studied. (XBL 801-6)

angles, have the form of highly ordered (periodic) monoatomic steps. Cutting towards the [110] pole introduces increasing numbers of (111) microfacets which as monoatomic steps form a ridge having the (110) "trough" geometry. Thus, the stepped surfaces introduce a regular progression of structure from one low index surface to another enabling the effect of microfacets of differing orientation in a polycrystalline surface to be clearly differentiated.

The voltammograms for the single crystal surfaces of Fig. 1 clearly indicated structure sensitivity in the platinum-hydrogen bond. The curves for the low index surfaces of orientation (111) and (100) (Figs. 2 and 3) showed single peaks separated by 0.14V, corresponding to a difference in adsorption enthalpy of 27.5 kJ/mol.

* This work was supported by the Division of Fossil Fuel Utilization, Office of Energy Technology, U.S. Department of Energy.

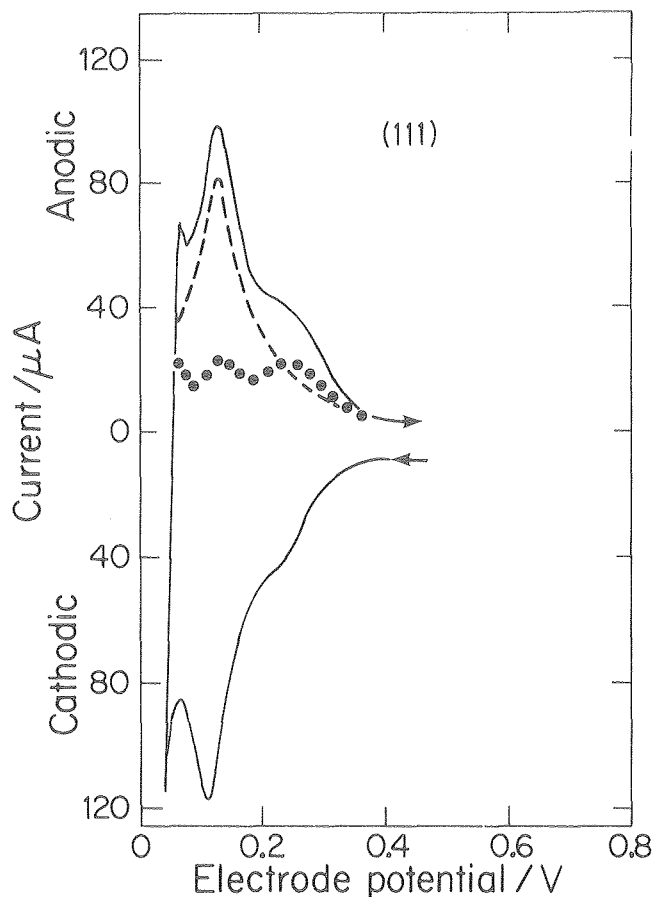


Fig. 2. Voltammogram for hydrogen adsorption-desorption on the (111) crystal. (...) Specific contribution due to the crystal edge. (---) Desorption curve corrected for edge effects. 50 mVs^{-1} . 0.1N HClO_4 . (XBL 801-9)

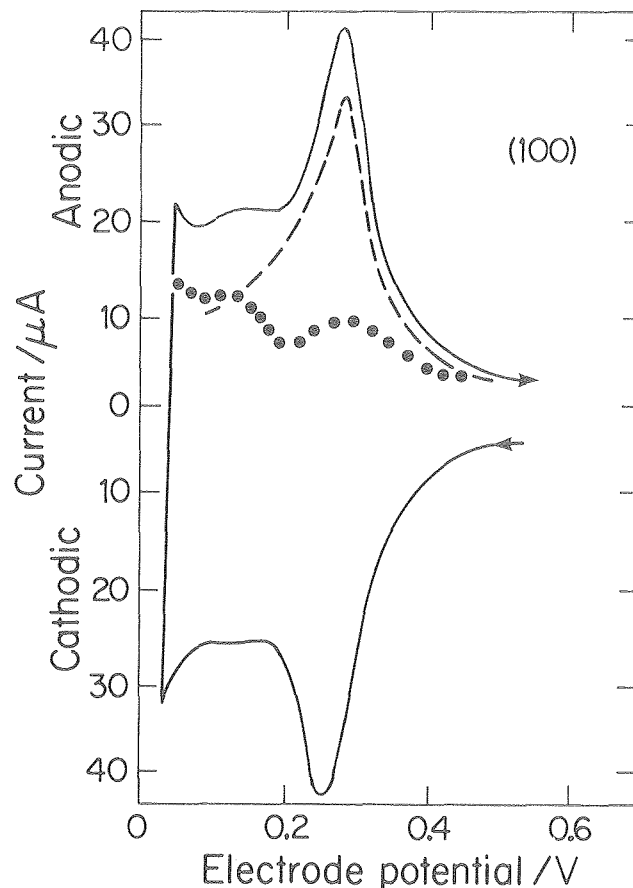


Fig. 3. Voltammogram for hydrogen adsorption-desorption on the (100) crystal. (...) Specific contribution due to the crystal edge. (---) Desorption curve corrected for edge effects. 50 mVs^{-1} . 0.1N HClO_4 . (XBL 801-7)

The n(111)-(111) series of crystals (Fig. 4) indicated a well defined peak (0.08V above the (111) peak) associated with the step, which has the (110) "trough" geometry, and with the (110) surface. LEED analysis of the (110) surface indicated a (2×1) reconstructed surface; the most probable structure for this surface is the "sawtooth" model³ (S) $[3(111) \times 2(111)]$ which is in perfect agreement with the results of Fig. 5. The n(111)-(100) series of crystals indicated two peaks associated with the step, and only one of these is related to the macroscopic (100) surface. We postulate that the high energy hydrogen peak [57.7 kJ/mol

greater than for the (111) surface] corresponds to adsorption at the five-fold sites formed by the acute intersection of (100) and (111) planes.

* * *

[†]Brief version of LBL-10444.

1. A. J. Appleby, *Catalysis Reviews* **4**, 221 (1970).
2. D. Blakely and G. Somorjai, *Surf. Sci.* **65**, 419 (1977).
3. R. Ducros and R. Merrill, *Surf. Sci.* **55**, 227 (1976).

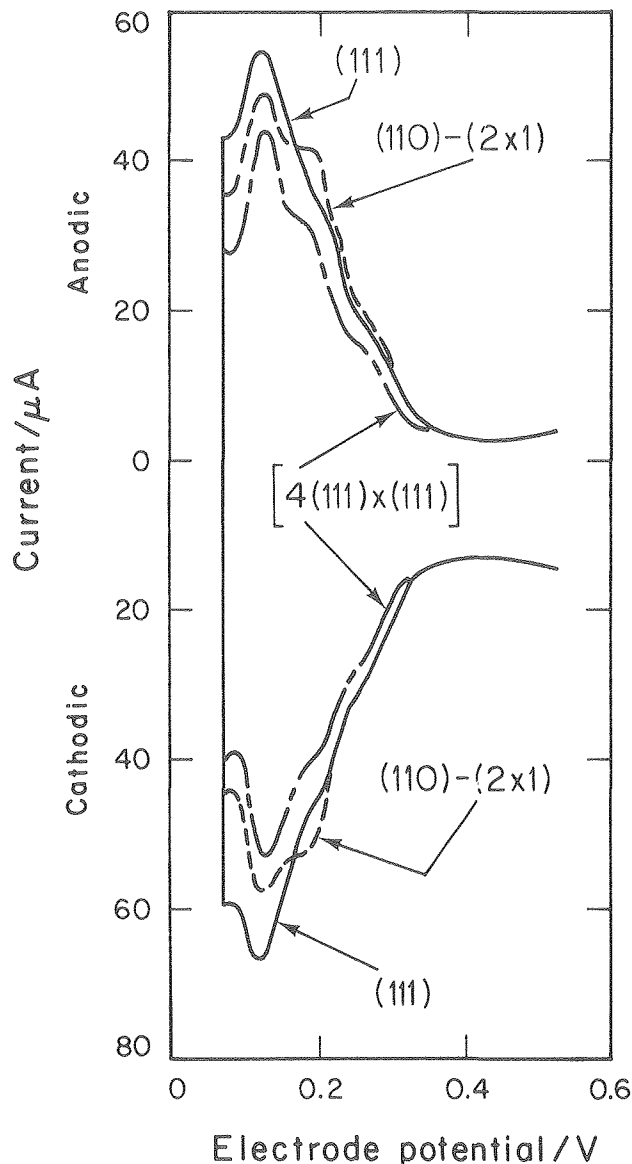


Fig. 4. Voltammograms for the $n(111) \times (111)$ series of crystal faces. 50 mVs^{-1} , 0.1N HClO_4 . (XBL (XBL 802-194))

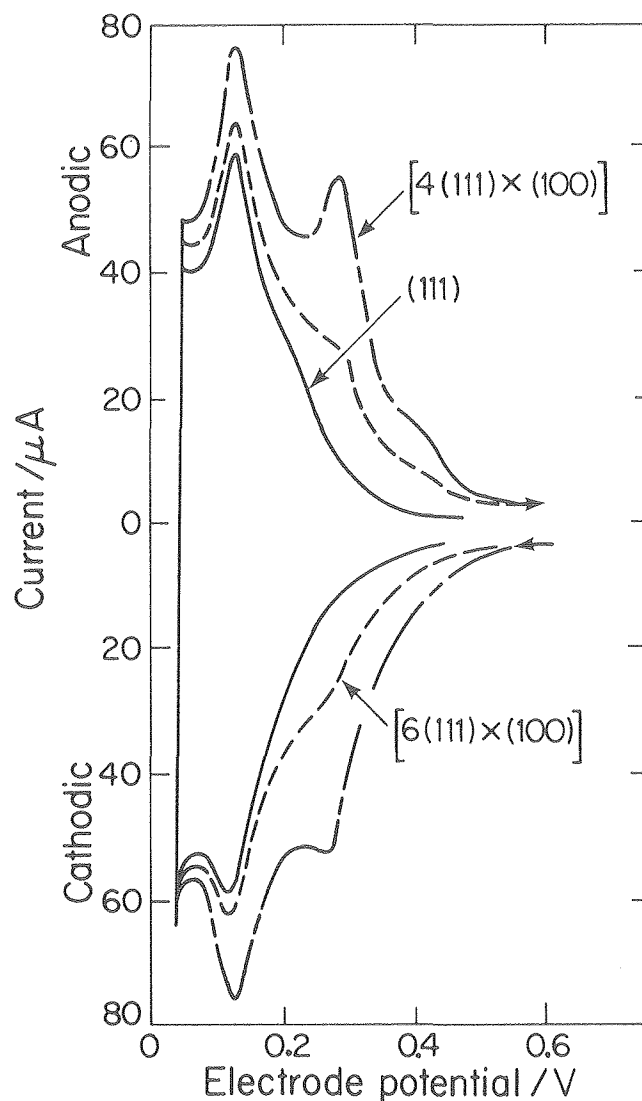


Fig. 5. Voltammograms for the $n(111) \times (1000)$ series of crystal faces. 50 mVs^{-1} , 0.1N HClO_4 . (XBL (XBL 801-8))

2. THE EFFECT OF PT STRUCTURE AND CARBON CHEMISTRY ON THE ELECTROCATALYTIC PROPERTIES OF PT SUPPORTED ON CARBON.[†]

Philip N. Ross

Previous studies of clean, well-ordered single crystal surfaces of Pt in dilute acids did not indicate any significant (factor of 3) difference in catalytic activity between the low index surfaces, e.g. (100), (111) or (211)¹. These studies do suggest that there are no large (order of magnitude) effects of structure on the activity of Pt for oxygen reduction in the limited temperature

range for aqueous acid electrolytes, 300-470 K. The recent study by Bregoli² indicated a small (factor of 2) but statistically valid difference in activity between Pt black and Pt on carbon in 99 w/o H_3PO_4 at 450 K. The present study was undertaken to determine what the physical basis for this 'weak' effect might be.

The electrochemical properties of smooth Pt were compared to those of Pt microparticles with varying structure. The structure of the microparticles was determined using the extended x-ray absorption fine structure (EXAFS) technique and transmission electron microscopy (TEM). Fourier

analysis of the absorption fine structure produces a structure function (XSF) that is analogous to the radial (electron) distribution function (RDF) produced by Fourier analysis of wide-angle x-ray scattering. The XSF for Pt microparticles produced by adsorption from colloidal suspensions onto carbon black (Vulcan XC72) and mild reduction (100.3 kPa H_2 at 370 K or lower) indicated (Fig. 1) only fcc nearest-neighbor ordering with vibrational mean-square displacements much larger than in bulk Pt. This type of structural characterization often occurs in the description of "amorphous" or "glassy" metals, generally metastable structures produced by rapid quenching from the melt³, and is often called the pseudo-liquid model for the "glassy" state of metals. TEM did show liquid-like shapes for these Pt microparticles, e.g. drop-like shapes with various degrees of "wetting" the carbon surface (varying contact angle), in agreement with the pseudo-liquid interpretation of the XSF. It was found that inert gas or vacuum heat treatment of the catalyst caused a critical change in structure, (Fig. 2) and that at intermediate temperatures (~ 800 -1000 K) structure transformation could be produced without drastic alteration of the mean particle size. The transformation shown by Fig. 2 is interpreted to be pseudo-liquid to microcrystalline, i.e. small particles with an XSF very close to that for bulk Pt.

The carbon structure was also found to have an effect on the Pt morphology. Deposition of Pt onto a graphitized carbon black produced by vacuum heat treatment of Vulcan XC72 to 3000 K and mild reduction in hydrogen resulted in a degree of crystalline ordering (Fig. 3) and the formation of particles having well-defined crystal planes observable by TEM.

The underpotential deposition of hydrogen on Pt microparticles in dilute H_2SO_4 revealed significant differences in Pt-H bond energy directly related to structure. The voltammetry (Fig. 4) for the pseudo-liquid structure of Pt was uniquely

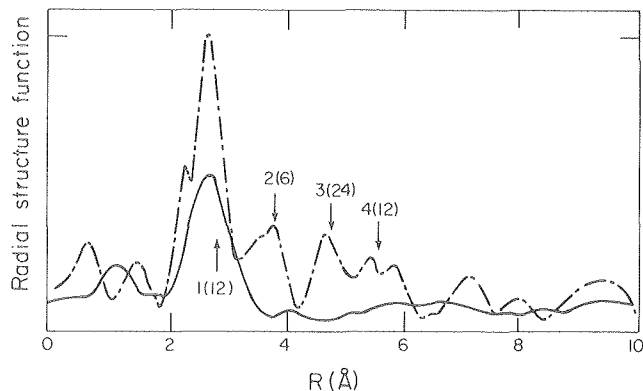


Fig. 1. Comparison of the EXAFS derived radial structure functions for Pt clusters on amorphous carbon black (—) to that for a polycrystalline Pt foil (---). The first four nearest neighbor distances and coordination numbers in crystalline Pt are indicated. (XBL 7910-12158)

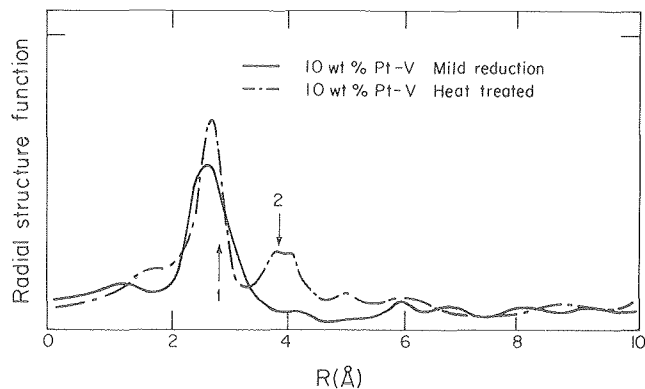


Fig. 2. The EXAFS derived radial structure functions for Pt clusters on amorphous carbon black pre-treated by mild hydrogen reduction (—) and by heat treatment in vacuum to 1073K (---). (XBL 7910-12168)

different from that for any of the low index faces but similar to that seen on some high Miller index faces that produce stepped surfaces. Microparticles with the crystalline structure exhibited voltammetric curves which could be directly related to underpotential deposition at ordered low index surfaces.

Oxygen reduction was studied on these catalysts in H_3PO_4 at 380-450 K. A "weak" effect of structure was observed that indicated a lower (by 10.5 kJ/mol) activation energy and lower pre-exponential (factor of 2) for the pseudo-liquid structure of Pt than for microcrystalline or bulk Pt. These differences can be attributed quantitatively to a measured difference (21 kJ/mol) in the heat adsorption of the oxygen reduction intermediates on the pseudo-liquid microparticles. Stronger bond-

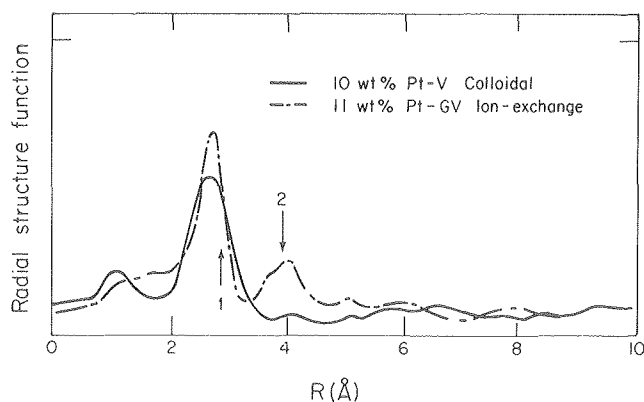


Fig. 3. Comparison of the radial structure functions for Pt clusters on an amorphous (—) and a graphitized (---) carbon black substrate after mild hydrogen reduction. (XBL 7910-3033)

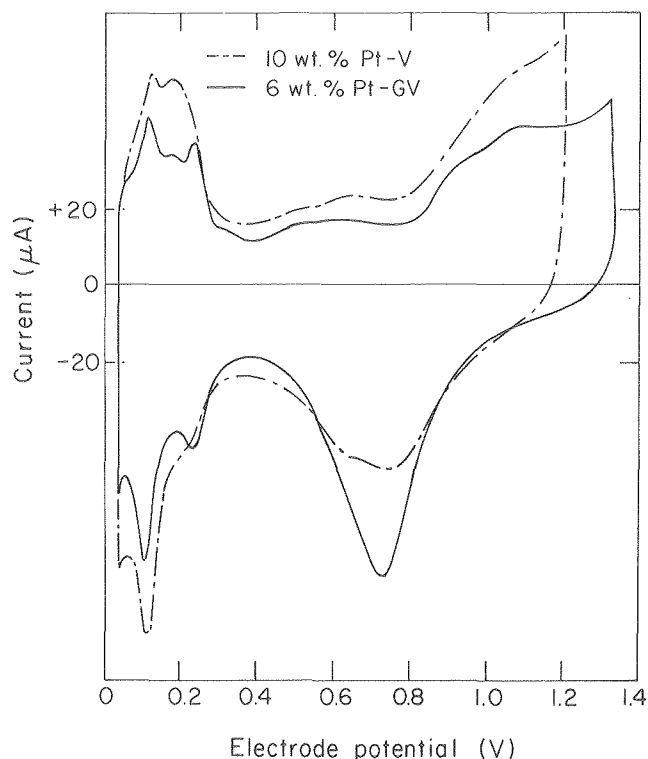


Fig. 4. Comparison of the underpotential curves for hydrogen on Pt clusters having the pseudo-liquid structure (---) and on Pt clusters having a microcrystalline structure (—). (XBL 799-2946)

ing of adsorbates on surfaces of low (<7) coordination appears to be a fundamental property of metal surfaces that will produce in any catalytic reaction at least a "weak" effect of structure on reactivity.

* * *

† Brief version of extended abstract, 156th Meeting of Electrochemical Society of Los Angeles, The Electrochemical Society Inc., Princeton, NJ 1979.

1. L. Bregoli, *Electrochim. Acta* **23**, 489 (1978).
2. P. Ross, *J. Electrochem. Soc.* **126**, 78 (1979).
3. P. Gaskell, *J. Non-Cryst. Solids* **32**, 207 (1979).

RESEARCH PLANS FOR CALENDAR YEAR 1980

The photoemission (XPS and UPS) module will be added to the existing LEED-Auger Spectroscopy system and will complete the construction of the apparatus. The study of oxygen chemisorption and oxide formation on Pt and on the Pt-Group IVb and Vb intermetallic compounds will be started. Further studies of the structure sensitivity of Pt are planned using surface structure modification by noble gas ion implantation.

1979 PUBLICATIONS AND REPORTS

Refereed Journals

1. P. N. Ross, Jr., "Structure Sensitivity in the Electrocatalytic Properties of Pt:I. Hydrogen Adsorption on Low Index Single Crystals and the Role of Steps," *J. Electrochem. Soc.* **126**, 67 (1979).
2. P. N. Ross, Jr., "Structure Sensitivity in the Electrocatalytic Properties of Pt:II. Oxygen Reduction on Low Index Single Crystals and the Role of Steps," *J. Electrochem. Soc.* **126**, 78 (1979).

Invited Talks

1. P. N. Ross, Jr., "Hydrogen Electrocatalysis," Workshop on Electrocatalysis, Institute for Physical Chemistry Theory and Application, La Plata, Argentina, Dec. 11-15, 1978.
2. P. N. Ross, Jr., "Ex. Situ Analysis of Electrodes by Electron Spectroscopy," Gordon Research Conference on Electrochemistry, Santa Barbara, Jan. 5-9, 1979.
3. P. N. Ross, Jr., "The Electrochemistry of Pt and Other Noble Metal Surfaces," Workshop on Oxygen Electrochemistry, Case Western Reserve University, May 2-4, 1979.
4. P. N. Ross, Jr., "The Effect of Structure and Carbon Chemistry on the Electrocatalytic Properties of Pt Supported on Carbon," the Electrochemical Society Meeting, Los Angeles, CA, Oct. 14-19, 1979, paper #190.

b. Deuterium Analysis of Coal by NMR*

A. Pines, Investigator

1. CARBON-13 ANALYSIS OF WHOLE AND PROCESSED COALS[†]

D. Wemmer, G. Drobny, and A. Pines

Together with the Central Research Division of Mobil Oil Company, we are continuing our characterization of materials used in fuel technology, in particular coal and oil shale. Using solid state NMR techniques, we can distinguish four types of carbon functional groups: condensed, aromatic, ether and aliphatic. These have been used to characterize coals by rank and to understand the changes which occur during processing of the coals. Figure 1 shows, as an example, that the H/C ratio, commonly used as a measure of aromaticity does not correlate well with aromatic content as determined by us. Catalytic products are found to contain more isolated aromatic rings than thermal products. Further experiments including double resonance with spinning have enhanced our resolution and work is in progress on other samples, correlation with contact times during liquefaction, and the use of our novel deuterium techniques for these studies. Model compounds have been designed by such deuterium labeling studies and are described in other sections. Together with Mobil, we are applying these model studies to hydrogen labeling during coal processing.

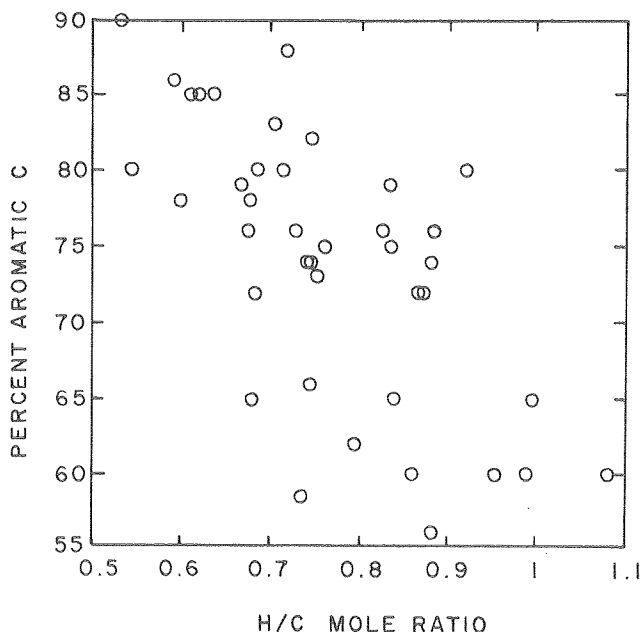


Fig. 1. Plot of percent aromatic carbon from solid state ^{13}C NMR versus H/C ratio showing lack of good correlation. (XBL 7812-14093)

* * *

[†]Brief version of EPRI Report of Mobil Research and Development.

2. DOUBLE QUANTUM POWDER LINESHAPES

J. Murdoch and A. Pines

The magnetic field experienced by a nucleus in a NMR experiment is modified by local electron densities. In solids the extent of shielding and hence the nuclear resonance frequency are functions of molecular orientation relative to the external magnetic field. One may determine the principal values of this chemical shielding tensor from the characteristic lineshape of a powder.

When the nucleus to be studied is hydrogen, spin-spin dipolar coupling is sufficiently strong to hopelessly broaden any chemical shielding anisotropy unless special techniques are employed. We have chosen to look at proton-decoupled, double-quantum deuterium lineshapes from samples with a few percent of the molecules selectively deuterated. This method allows the isolation of chemical shielding effects: the proton decoupling removes proton-deuterium dipolar interaction, deuterium-deuterium dipolar coupling is small since the average distance between the scarce ^2H nuclei is large, and the double-quantum spectral frequencies are unaffected (to first order) by the deuterium electric quadrupolar splitting.

The detailed lineshape for such an experiment depends not only on the principal values of the chemical shielding tensor but also on the preparation and detection pulse sequences, on the strength of the exciting rf radiation compared to other terms in the Hamiltonian, and on the relative orientation of the chemical shielding and quadrupolar tensor principal axes. This latter dependence is interesting; if the orientation of the quadrupolar tensor in the molecular axis system is known or can be estimated, we learn something about the alignment of the chemical shielding tensor relative to the molecule from just a powder experiment.

Several computer programs have been written and used to generate chemical shielding lineshapes for a wide variety of pulse sequences and tensor orientations. Experiments will be continuing on the measurement of actual shielding tensor lineshapes with the hope of improving resolution sufficiently to see more of the expected structure.

* This work was supported by the Division of Coal Research, Office of Fossil Energy, U. S. Department of Energy.

3. HIGH RESOLUTION DEUTERIUM NMR BY MAGIC ANGLE SAMPLE SPINNING[†]

R. Eckman and A. Pines

Measurement of isotropic high-resolution or liquid-like NMR spectra of deuterium in solids obtained by fast magic angle sample spinning is in progress. Stability of the sample turbine-optical tachometer system has been increased which allows accurate synchronization of the spectrometer data acquisition to the sample rotation, a critical requirement for spectral resolution. Highly resolved isotropic spectra have been recorded for several per-deuterated and partially-deuterated model compounds for coal analysis.

In Fig. 1 is shown the isotropic spectrum of per-deutero para-di-t-butylbenzene-d₂₂ at a rotation speed of 62,000 rpm. A splitting between crystallographically inequivalent aromatic deuterons is evident, illustrating the high resolution obtained. This allows more accurate measurement of deuterium chemical shifts in solids. Resolution can be increased dramatically by increased magnetic field strength. Construction of magic angle sample spinning probes for a new higher field spectrometer is under way.

* * *

[†]Brief version of LBL-8845, Chem. Phys. 42, 423 (1979).

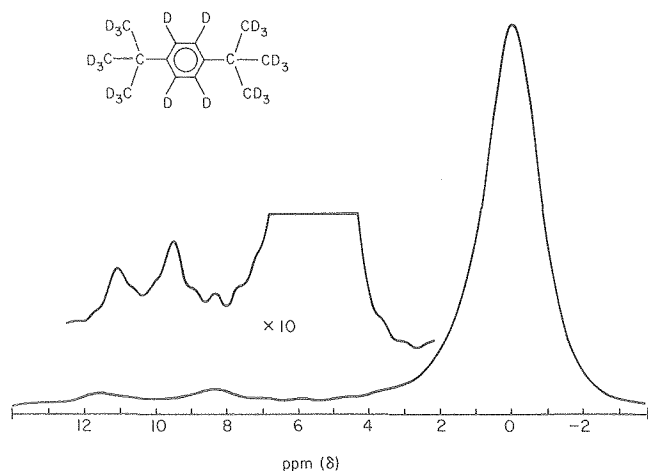


Fig. 1. Isotropic liquid-like spectrum of para-di-t-butylbenzene-d₂₂ rotating at 62,000 rpm. Single peak on right is due to methyl groups. Doublet at left arises from inequivalence in the solid state of opposing pairs of ring deuterons. (XBL 799-12058)

4. DOUBLE QUANTUM NMR IN ROTATING SAMPLES[†]

L. Mueller, D. Eckman, and A. Pines

High resolution deuterium NMR spectra have been obtained with the magic angle spinning technique. By using this method the deuterium resonance line-widths can be reduced by several orders of magnitude.

This requires, however, an extremely stable sample spinner (angular instabilities smaller than a few millidegrees). This proposed method circumvents this requirement.

For deuterium, as a spin one nuclei, forbidden double quantum transitions can be generated. These transitions are fortunately independent from first order quadrupolar broadening. Thus detection of double quantum transition in a magic angle spinning sample yields high resolution spectra which are fairly insensitive to spinner instability (Fig. 1).

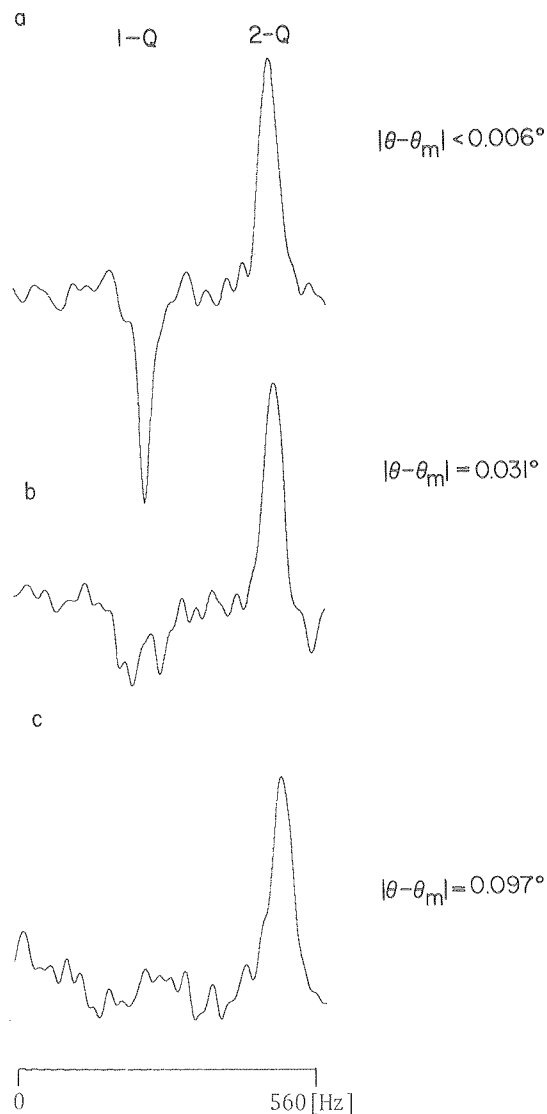


Fig. 1. A double quantum pulse sequence was applied to a sample of 28% deuterated ferrocene. Data were taken at 50 subsequent t_1 values (150 accumulations per t_1 value). For the selected experimental parameters the phase difference between single and double quantum peaks happens to be about 180°. (a) The angle of the rotor axis θ was optimally adjusted $|\theta - \theta_m| < 0.006^\circ$ ($\theta_m = \arctan \sqrt{2}$), sample rotation speed $\nu_r = 1125$ Hz. (b) Slightly misadjusted angle, $|\theta - \theta_m| = 0.031^\circ$ ($\nu_r = 1250$ Hz). (c) $|\theta - \theta_m| = 0.097^\circ$ ($\nu_r = 1090$ Hz). Here the single quantum peak is too broad to be detectable. (XBL 801-7819)

This novel method will be applied in the future to analyze chemical of practical interest.

* * *

† Brief version of LBL-10331.

5. NMR DEUTERIUM CROSS-POLARIZATION IN ROTATING SAMPLES†

L. Mueller, D. Eckman, and A. Pines

Cross polarization of magnetization from one spin species to another by a "Hartmann-Hahn" type matching of rf field amplitudes has become very useful since it permits a considerable increase of sensitivity of rare nuclei. The mechanism of this polarization transfer is based on a mixing of heteronuclear spin states due to static dipolar interactions in solids. In magic angle spinning solid [$\theta_m = \arctan(\sqrt{2})$], all dipolar interactions are modulated. However, it has been shown experimentally and theoretically by several workers in the field that an efficient cross polarization still takes place when the mechanical rotation frequency is smaller than the dipolar couplings (local field) in a solid.

Our goal was to apply this method to magic angle spinning deuterium spins. None act as spin labels and should allow the study of proton sites without multiple pulse experiments. Their quadrupolar interactions, however, pose a problem for a successful cross polarization, since they cause deuterium energy levels to be strongly modulated during the sample spinning. We found theoretically that magnetization transfer is possible if:

$$\omega_{ID}^2 \gg |\omega_r \cdot \omega_Q|$$

ω_r : rotation frequency

ω_Q : quadrupolar coupling constant

ω_{ID} : rf field amplitude

Figure 1 demonstrates that matching is possible over a very broad range--range of rf field values.

Thus the method increases the sensitivity of deuterium in spinning solids. In the future we shall further investigate the cross-polarization dynamics to gain more insight into the physics of the process and begin application to model compounds for full research.

* * *

† Brief version of LBL-10245.

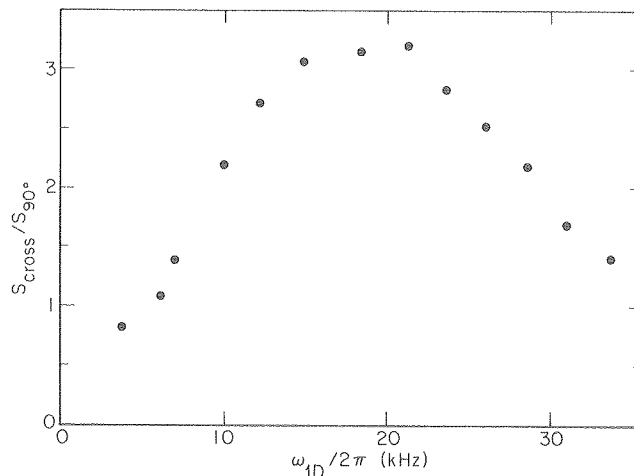


Fig. 1. Cross-polarized deuterium magnetization for a contact time of 25 rotor cycles (17.24 msec) has been measured as a function of the deuterium rf field amplitude whilst the proton rf field amplitude ω_{1H} remained constant at 18 kHz. Spinner rotation speed 1450 Hz. Sample: 25% randomly deuterated hexamethylbenzene (isotope exchanged over palladium). 50 of FID's were accumulated per experiment. The deuterium signal was detected under rotation synchronous sampling of the rotation echoes. The signal plotted is the signal gain by cross polarization relative to the signal obtained by deuterium 90° pulses. For lower values of ω_{1D} a substantial part of the transferred polarization goes into double quantum and quadrupolar polarization.

(XBL 7912-13692)

6. SPIN DIFFUSION AND RELAXATION IN MAGIC ANGLE NMR†

R. Eckman, L. Mueller and A. Pines

A crucial aspect of high resolution deuterium NMR in solids by magic angle sample spinning is the rate of spin-lattice relaxation. Spin-lattice relaxation times, T_1 , of deuterium in solids can be some minutes and longer making the observation of deuterium resonances almost useless. However, we have found that certain T_1 's were much shorter than expected in rotating samples and have shown that this is due to spin diffusion between crystallographically inequivalent deuterium nuclei.

Deuterium solid state T_1 's have been measured selectively from the isotropic magic angle spinning spectra by a saturation recovery sequence. Results shown in Table 1 indicate that the methyl deuterons relax quickly (~1 sec.). Aromatic deuterons relax quickly (5-30 sec.) when there is spin diffusion to $-CD_3$ groups, but slowly (~10 min.) when there is

Table 1. Deuterium solid state T_1 (second).

| Compound | $-CD_3$ | $-\phi D_4$ |
|---|----------------|----------------|
| terephthalic acid dimethylester- d_{10} ($D_3CO_2C\phi D_4CO_2CD_3$) | $0.86 \pm 7\%$ | $28 \pm 7\%$ |
| p-dimethoxybenzene- d_{10} ($D_cCO\phi D_4OCD_3$) | $0.26 \pm 4\%$ | $5 \pm 20\%$ |
| terephthalic acid dimethylester- d_4 ($H_3CO_2C\phi D_4CO_2CH_3$) | --- | $640 \pm 13\%$ |

no spin diffusion to $-CH_3$ groups. The magic angle sample rotation partially restores spin diffusion in the deuterium system and makes it possible to obtain high resolution spectra with good sensitivity. Further measurement of deuterium T_1 's and dependence of T_1 on frequency of rotation and temperature are in progress.

* * *

[†]Brief version of LBL-9948.

7. SYNTHESIS OF DEUTERIUM LABELED MATERIALS[†]

S. Wolfe and A. Pines

Deuterated compounds using magic angle spinning provide a means for observing chemical shifts in solids where the proton spectra would be obscured by dipolar interactions. Deuterated compounds are often prepared by: 1) catalytic exchange with D_2O or D_2 , 2) acid or base catalyzed exchange with D_2O , or 3) with the use of commercially available deuterated reagents. Compounds can be prepared in a perdeuterated fashion, selectively labeled manner, or in a manner where deuterium is randomly distributed throughout the molecules (or over a portion of it).

Various p-disubstituted benzene derivatives such as terephthalate esters, p-dimethoxybenzenes and p-tert-butylbenzenes have been prepared in a partially deuterated and perdeuterated manner. These compounds have provided model studies for understanding chemical shifts and relaxation mechanisms of deuterium in solids. Partially deuterated compounds such as hexamethylbenzene and durene have been prepared in a 10% randomly deuterated manner by catalytic exchange using 10% Pd/C and D_2 gas at 200°C. Compounds such as these have been used to study cross polarization between protons and deuteria. Recently, we have discovered that 10% Pt on carbon is a superior catalyst to Pt black in exchange reactions with D_2O since it is less susceptible to deactivation and provides more catalytic

activity for the amount of Pt used. Future synthesis will include such compounds as long chain aliphatic alcohol deuterated in the alpha and omega positions to be used in model studies of membrane. Other compounds which are solids at room temperature will also be synthesized to provide more information on chemical shifts of deuterium in solids.

* * *

[†]Brief version of LBL-8845.

8. HIGH FIELD NMR SPECTROMETER

G. Drobny, D. Wilkinson and A. Pines

A high field NMR spectrometer has been designed and its construction has been recently completed. The spectrometer uses a superconducting magnet operating at a field strength of 84 kilogauss. The Larmor frequency of protons in such a field is 360 MHz. The device has two rf channels for double resonance experiments, each channel generating four phases in quadrature at an intermediate frequency of 30 MHz. Spectrometer operation is controlled by a Data General Nova 820 minicomputer equipped with a 10 megabyte disk drive, and a floppy disk drive will soon be added for mass data storage. Novel components include a microprocessor-controlled pulse programmer, a home built completely solid state 300 watt, 360 MHz power amplifier, a microprocessor-controlled phase shifter for use in selective multiple quantum experiments, a high speed turbine rotor for magic angle spinning experiments, and a dual channel, manually controlled, high pressure espresso generator.

This device has been designed with solid state deuterium NMR in mind. At this frequency two advantages are expected. Firstly, the second order quadrupolar broadening should decrease by a factor of two since it is inversely proportional to the magnetic field strength. Secondly, the chemical shifts should increase by a factor of two, thus giving us an effective resolution enhancement of four. Specialized high frequency magic angle probes are being constructed to capitalize on these advantages.

RESEARCH PLANS FOR CALENDAR YEAR 1980

1. Synthesis of model compounds for coal processing intermediates. These will include both perdeuterated and selectively deuterated materials.
2. Completion of high frequency magic angle spinning probe. This will be used to obtain a factor of 4 increase in resolution.
3. Application of 2D techniques developed in the last year, including double quantum, double resonance and high stability spinning methods.
4. Application to coal liquefaction intermediates.
5. Development of techniques to observe deuterium in natural abundance.

1979 PUBLICATIONS AND REPORTS

Refereed Journals

1. D. Suwelack, M. Mehring, and A. Pines, "Quantitative Aspects of Deuteron (Spin 1) Spin-Decoupling in Solids," *Phys. Rev. B* 19, 238 (1979).
2. G. Drobny, A. Pines, S. Sinton, D. Weitekamp, and D. Wemmer, "Fourier Transform Multiple Quantum NMR," *Faraday Symposia of the Chemical Society* 13, 49 (1979), LBL-8565.
3. S. Emid, A. Bax, J. Konijnendijk, J. Smidt, and A. Pines, "Multiple Quantum Coherence in Dipolar Relaxation Measurements," *Physica* 96B, 333-336 (1979).
4. W. Warren, D. P. Weitekamp, S. Sinton, and A. Pines, "Selective Excitation of Multiple Quantum Coherence in Nuclear Magnetic Resonance," *Phys. Rev. Lett.* 43, 1791 (1979).
5. J. L. Ackerman, R. Eckman, and A. Pines, "Experimental Results on Deuterium NMR in the Solid State by Magic Angle Sample Spinning," *Chem. Phys.* 42, 423 (1979).
2. A. Pines, Chemistry Department, University of California, Irvine, California, February 1979, Seminar.
3. J. Ackerman, M. Alla, R. Eckman, and A. Pines, "High Resolution Deuterium NMR in Solids," 20th Experimental NMR Conference, Asilomar, California, February 1979.
4. A. Pines, New Developments in Solid State NMR, Pittsburgh Conference on Chemistry and Spectroscopy," Symposium on New Techniques, Cleveland, Ohio, March 1979.
5. A. Pines, Chemistry Department, Colorado State University, Fort Collins, Colorado, April 1979, Seminar.
6. A. Pines, Chemistry Department, University of Colorado, Boulder, Colorado, April 1979, Seminar.
7. A. Pines, Harvard-M.I.T. Seminar, Harvard University, Cambridge, Massachusetts, April 1979, Seminar.
8. A. Pines, Chemistry Department, University of California, Los Angeles, California, May 1979, Seminar.

LBL Reports

1. M. Alla, R. Eckman, and A. Pines, "Enhanced Resolution in Deuterium Chemical Shift Spectra of Powders," LBL-9537.
2. S. Emid, S. Konijnendijk, J. Smidt, and A. Pines, "On the Short Time Behavior of Dipolar Relaxation," LBL-9261.
3. M. Alla, R. Eckman, and A. Pines, "Dipolar Spin Diffusion and Spin-Lattice Relaxation of Deuterium in Rotating Powders," LBL-9852.
4. J. Tang and A. Pines, "Multiple-Quantum NMR and Relaxation of an Oriented CH₃ Group," *J. Chem. Phys.* (in press), LBL-9853.
5. L. Müller, R. Eckman, and A. Pines, "Proton-Deuterium Cross Polarization in Magic Angle Spinning Solids," LBL-10245.
6. J. Tang, A. Pines, and S. Emid, "Spin-Lattice Relaxation of Reorienting or Tunneling Deuterated Methyl Groups," *Chem. Phys.* 43, 1791 (1979), LBL-10162.
7. R. Eckman, L. Müller, and A. Pines, "High Resolution Deuterium NMR in Polycrystalline Solids," LBL-10281.
8. L. Müller, R. Eckman, and A. Pines, "Deuterium Double Quantum NMR Magic Angle Spinning," LBL-10331.
9. A. Pines, "Nuclear Magnetic Resonance with Lots of Photons," IBM, San Jose, California, May 1979.
10. A. Pines, Chemistry Department, University of Texas, Austin, Texas, May 1979, 5 Invited Lectures in Distinguished Visiting Lectures Series.
11. A. Pines, International Symposium on Magnetic Resonance in Chemistry, Biology and Physics, Argonne National Laboratory, June 1979.
12. A. Pines, "The Analogy of Multiple Quantum Spectroscopy to Isotopic Labeling and Supersonic Beams," Fourth European Experimental Nuclear Magnetic Resonance Conference, Grenoble, France, June 1979.
13. A. Pines, "Magnetic Resonance," Gordon Research Conferences, Wolfeboro, New Hampshire, June 1979.
14. A. Pines, University of Witwatersrand, Johannesburg, South Africa, presented 10 Invited Lectures, August 1979.
15. A. Pines, "Multiple Quantum Spectroscopy," Bat-Sheva Workshop on Magnetic Resonance, Israel, presented 6 Invited Lectures, September 1979.
16. A. Pines, University of California, Berkeley, California, September 1979, Seminar.
17. A. Pines, Chemistry Department, Purdue University, West Lafayette, Indiana, November 1979, Seminar.
18. A. Pines, Chemistry Department, University of Pennsylvania, Philadelphia, Pennsylvania, November 1979, Seminar.

Invited Talks

1. G. Drobny, A. Pines, S. Sinton, D. Weitekamp, J. Tang, and W. Warren, "Multiple Quantum Fourier Transform NMR in Liquid Crystals," 20th Experimental NMR Conference, Asilomar, California, February 1979.

19. A. Pines, "Nuclear Magnetic Resonance with Lots of Photons," Symposium on Magnetic Resonance in Biology, Stanford University, November 1979.

20. A. Pines, "Recent Developments in High Resolution Deuterium NMR Solids by Magic Angle Spinning," 21st Annual Mountain Conference, Denver, Colorado, August 1979.

c. Coal Liquefaction Alloys Test Program*

Alan V. Levy, Investigator

Introduction. The behavior of ductile metals in both cast and wrought forms in the erosion-corrosion environments that occur in coal liquefaction process components from the actions of elevated temperature coal-solvent slurries are being studied. New information is being developed on the role of such variables in the slurry as solids content, velocity, entrained moisture and gas content, viscosity, temperature and particle comminution in promoting or retarding erosion behavior of metal alloys. Different alloys have opposite rankings of erosion resistance in different slurries with relatively small differences in the slurry. Distinct geometry effects on erosion of pipe elbows have been found that vary with slurry velocity and solids loading. Non-dimensional correlation analyses of erosion data have related slurry and target material properties with respect to erosion behavior.

1. EROSION BEHAVIOR OF METALS IN COAL SLURRIES[†]

W. Tsai

The use of the small, two liter capacity slurry pot tester has developed knowledge of the effect of several variables on the erosion of structural metals exposed to non-aqueous coal slurries.¹ Both test conditions and sample composition have been varied. It has been determined that small modifications in test conditions can have major effects on the erosion behavior of different materials.² Comparative erosion rates of A-53 mild steel and 304SS have been reversed by small changes in particle size distribution and initial water content of the coal. Figure 1a shows the erosion of the two steels as a function of drying the coal prior to mixing the slurry. It is probable that a thin film of water formed on at least the larger coal particles, providing an encapsulating energy absorber that markedly decreased the amount of erosion that occurred.

Figure 1b shows that the coal particle solids loading in the slurry has a relatively small effect on the erosion of an A-53 mild steel over the range of coal concentrations typically used in coal liquefaction systems 30-50 wt.%. The effect of velocity difference is significant and can be seen in the curves. Based on the type of data obtained by varying several different test parameters, plots have been prepared giving erosion at known conditions as a function of time. The tangent at time zero to an erosive wear curve is taken as the characteristic rate of erosion in an experiment. This value is correlated, through dimensional analysis consideration with the dimensionless groups characterizing the experiment.

* This work was supported by the Division of Planning and Systems Engineering, Office of Fossil Energy, U. S. Department of Energy.

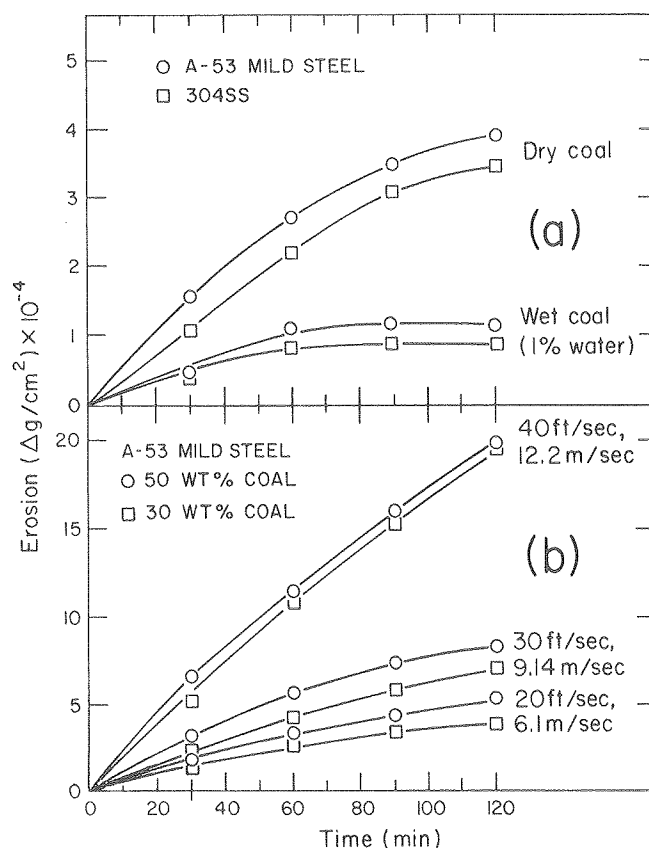


Fig. 1. (a) Effect of water content in 30 wt.% coal on erosion of A-53 mild steel (o) and 304SS (\square) in kerosene at 25°C at $V = \text{fps}$. (b) Effect of particle concentration and velocity on erosion of A-53 mild steel in kerosene at 25°C using 50 wt.% coal (o) and 30 wt.% coal (\square) slurries.

(XBL 801-49A)

Erosive wear of the metal specimens tested (A-53 mild steel, 304SS and 316SS) with coal and silicon carbide particles in kerosene was found to increase with increasing particle density, concentration, velocity and hardness and with decreasing target metal yield strength or hardness. Figure 2 shows the fit of the regressed equation. Data clustered about 9.5 (for coal) has an average error of 19.4% while that clustered about 7.25 (for SiC) has an average error of 14.3%.

[†]Brief version of LBL-10044.

1. R. Gardi, B. Ricks, and T. Audl, "Control of Erosion-Corrosion in Slurry Pipelines," 1st International Conference on the Internal and External Protection of Pipes, Sect. G-4, pp. 39-52, Sept. 1979.

2. B. Ellison, "Corrosion-Erosion in Multi-Phase Systems," presented at 70th Annual Meeting AiChE, Nov. 1977.

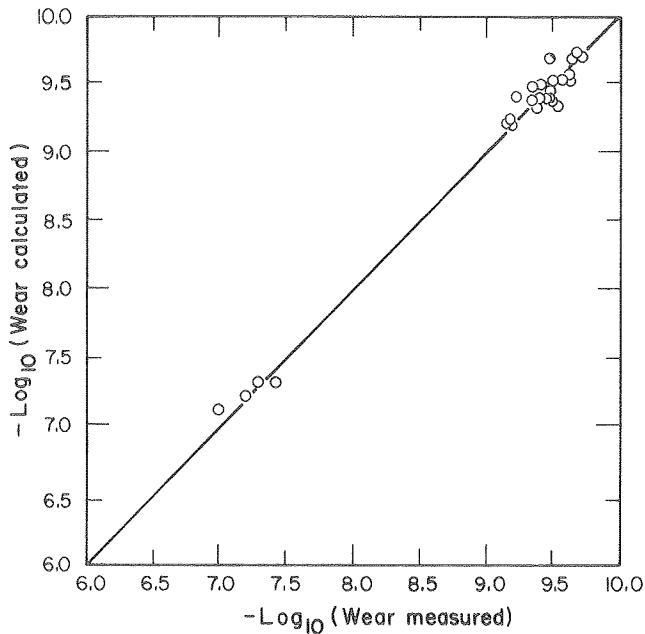


Fig. 2. Comparison of measured and calculated erosive wear. (XBL 801-48)

2. EROSION OF PIPING IN A SLURRY LOOP

A. Shaw and A. Levy

The slurry loop system using a recirculating slurry of 30 and 50 wt% coal in kerosene has been operated in excess of 2000 hrs in a series of tests to determine the erosion behavior of mild steel and stainless steel elbow components at ambient temperature. Figure 1 shows the reduction in piping wall thickness of a side loop to the primary 2" diam. pipe loop. The smaller diameter pipe sections of A-53 mild steel were used to increase the velocity and, hence, the amount of erosion to be able to obtain measurable wall thickness reductions in a reasonable test duration of 250 hours. The numbers opposite each measurement location are the number of thousandths of thickness reduction as measured by an ultrasonic thickness gage. It can be seen that the erosiveness of the slurry flow increased with velocity and as a function of geometry. For example, the erosion in the entry 2" diam elbow of the side loop where the flow velocity was 8-10 fps (points 1, 2, 3) was considerably less than that of the 2" dia elbow at the exit section (points 31, 32, 33) where the flow from the 1" diam pipe (velocity = 35-40 fps) impinged on the 2" diam elbow as from a nozzle.

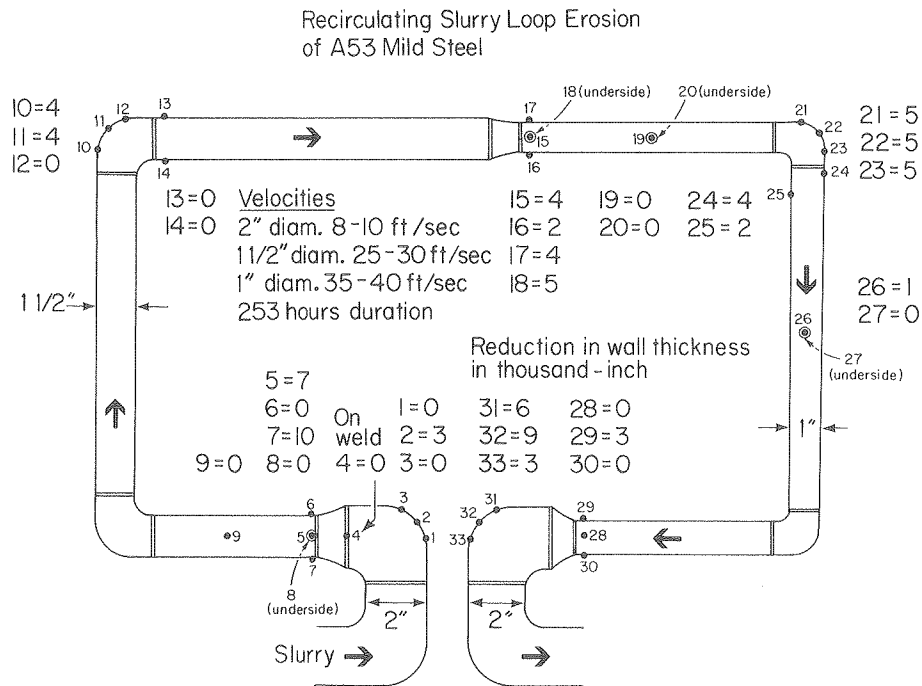


Fig. 1. Erosion thickness loss measurements in a recirculating slurry loop testing A-53 mild steel elbows in a 30 wt.% coal-kerosene slurry. (XBL 7910-4249)

In both elbows maximum erosion occurred at the middle point where the impingement angle was the greatest.

In a subsequent test, 304 and 316SS had comparable thickness reductions. When the slurry viscosity was increased by increasing the wt.% of coal in the kerosene from 30 to 50 wt.%, the amount of erosion for 304 and 316SS was reduced by approximately half.

RESEARCH PLANS FOR CALENDAR YEAR 1980

The erosion behavior of additional materials, including some coatings on mild steel substrates will be determined at several temperatures using a range of slurry variables. The data will be used to further develop the erosion rate prediction model. Extensive use will be made of the jet impingement tester to direct slurries at flat surface specimens of several materials in a once-through mode for the eroding particles. The unit's slurry capacity has been increased by several times to permit longer runs to be made. The slurry loop will continue to operate at ambient and elevated temperatures in a new flow passage design and

using specimens which can be disassembled readily to obtain mechanical thickness measurements of the amount of erosive wear.

1979 PUBLICATIONS AND REPORTS

Other Publications

1. A. V. Levy, I. Cornet, and D. Abdollahian, (Quarterly Report) January 1979, LBID-020.

LBL Reports

1. W. Tsai, J. A. C. Humphrey, I. Cornet, and A. V. Levy, "Experimental Measurement of Accelerated Erosion in a Slurry Pot Tester," LBL-10044.

Invited Talks

1. A. V. Levy, "Erosion-Corrosion in Coal Liquefaction Systems," Golden Gate Metals and Welding Conference, San Francisco, Calif., Feb. 1979.
2. A. V. Levy, "Coal Liquefaction Alloy Test Program," 3rd Annual Coal Conversion Materials Conference, Gaithersburg, MD, Oct. 1979.

d. Oil Shale Retort Components*

A. Levy and D. Whittle, Investigators

Introduction. The corrosion of alloy and stainless steels and aluminized type coatings exposed in in-situ oil shale retorting environments is being investigated. To date 11 simulated in-situ retorts and 2 underground retorts have been utilized to test 12 different steel alloy compositions and one steel coating material. The alloys have been exposed in these retorts to temperatures up to 1000°C for time periods up to 80 hours. Both Antrim and Green River type shales were being retorted at the time of the metal sample tests. The specimens were exposed directly in the shale beds near the location of monitoring thermocouple wells. To date, 160 specimens have been tested.

1. CORROSION IN SIMULATED IN-SITU OIL SHALE RETORTS

A. Levy and E. Elliott

It has been determined that different alloys corrode in different manners and to different degrees in high sulfur (3.2%) antrim shale and in low sulfur (0.8%) Green River Shale. In tests with antrim shale in the LETC 10 ton retort, 18% reduction in metal thickness occurred in 347 stainless steel exposed to temperatures above 1500°F for exposure times of only 40 hours. In general, the corrosion of 300 series stainless steels observed in Green River shale exposures is markedly less than that which occurs when antrim shale is retorted. Figure 1 shows this difference on 310SS. Note the magnification difference in the two photos. However, the lower chromium content 410 stainless steel corroded more than 347SS in the low sulfur Green River shale. It corroded less than 347SS in antrim shale. The morphology of the scale products and their chemical composition differed from alloy to alloy in antrim shale.

The higher chromium content alloys formed some Cr_2O_3 as well as considerable iron and chromium sulfides and iron-chrome sulfide spinels in layers while the lower chromium content alloys only formed sulfides. Non-chromium containing alloys underwent extensive sulfidation. In Green River shale, the 300 series stainless steels only formed a protective Cr_2O_3 scale layer and no sulfides. Generally, the Green River shale retort specimens were exposed to lower temperatures and times than the antrim shale retort specimens as well as to a lower sulfur content shale.

A marked difference in the corrosive attack also occurred as the result of exposures to large and smaller oil content shales. Figure 2 shows

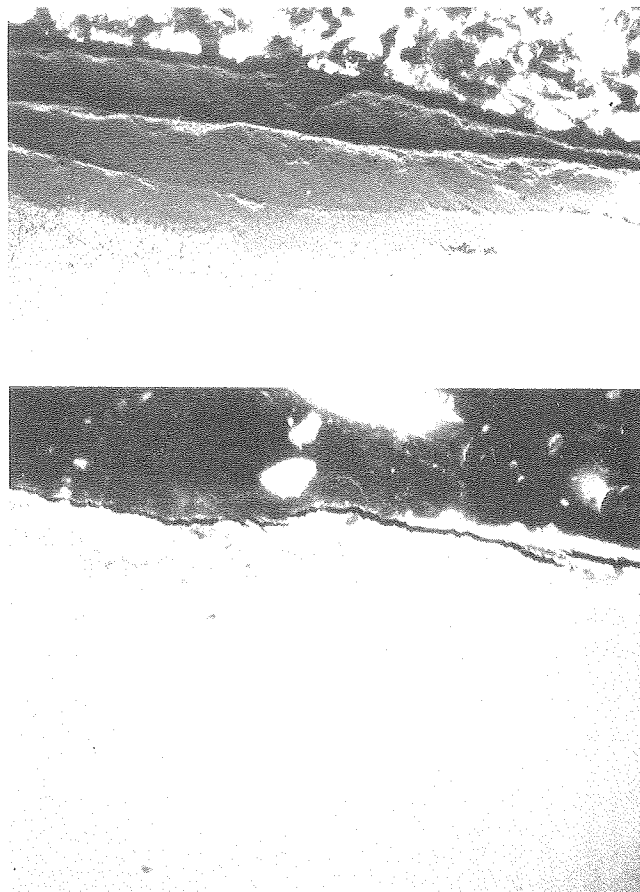


Fig. 1. Scales formed on 310SS exposed in simulated antrim (above, 200X) and Green River (below, 3000X) shale retorting operations. (XBB 7912-16283)

specimens of 410SS exposed to a high (36 gal/ton) Green River shale (upper photo) and a lower (18 gal/ton) shale in the same simulated in-situ retort run at LLL. The samples exposed to the richer shale were more heavily attacked and had a porous, single phase scale. A thinner, dense, two phase scale formed on the specimens in the leaner shale.

Aluminide coatings formed a protective Al_2O_3 scale on both stainless and low alloy steels and protected them from attack under all of the retort conditions and types of shale tested. See Fig. 3 for 1018 mild steel. The underground tests conducted were not productive in establishing corrosion behavior patterns because of lack of control in their placement and difficulty in their recovery.

* * *

* This work was supported by the Division of Planning and Systems Engineering, Office of Fossil Energy, U. S. Department of Energy.

† Brief version of LBL-9906; to be presented at NACE Corrosion 80, Chicago, IL, March 1980.

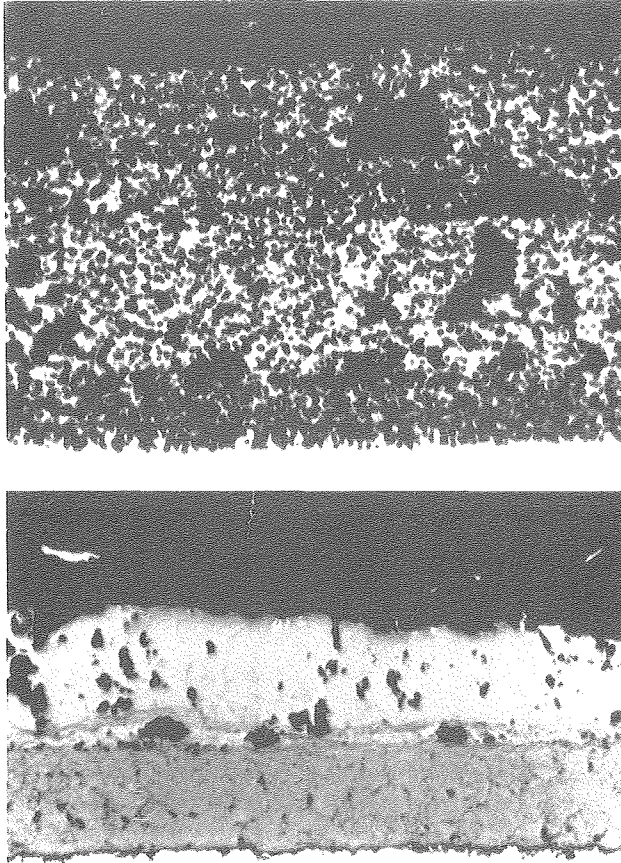


Fig. 2. Scales formed on 410SS exposed in rich Green River Shale (above, 200X) and lean Green River Shale (below, 400X). (XBB 7912-16284)

RESEARCH PLANS FOR CALENDAR YEAR 1980

Sufficient knowledge has been obtained from specimen exposures in simulated in-situ retorts to develop a test program where specimens will primarily be exposed in laboratory crucible tests using Green River and antrim shales with bulk gas compositions over the shales that simulate retort conditions. More controlled temperatures and times representative of the higher temperature, longer time exposures that will occur in underground retorting operations can be achieved in the crucible tests.

Additional coating tests will be conducted on low alloy and stainless steels with the objective of finding the lowest possible cost combination of coating and alloy that can withstand underground retorting environments. Specimens, coated and

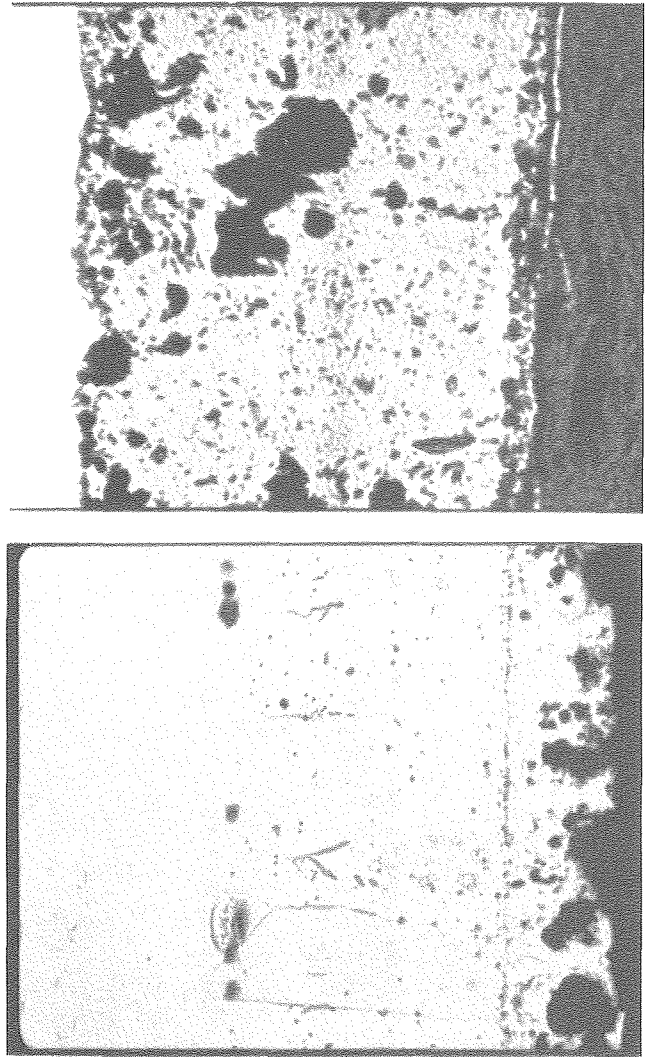


Fig. 3. Scales formed on 1018 mild steel without coating (above, 320X) and with coating (below, 320X). (XBB 7912-16285)

uncoated, will be placed in underground retort tests as they become available. Tests will also be conducted in shale oil product material.

1979 PUBLICATIONS AND REPORTS

Invited Talk

1. A. V. Levy, "Corrosion of Metals in Oil Shale Retorts," ASM WESTEC '79, Los Angeles, Calif., March, 1979.

e. Chemistry and Morphology of Coal Liquefaction*

H. Heinemann, Investigator

Introduction. This project was funded only in July 1979, and in its early months time and effort were concentrated on equipment procurement, staffing, and detailed planning.

1. GENERATION AND CHEMISTRY OF 1,4-DEHYDROBENZENE: HYDROGEN TRANSFER TO REACTIVE AROMATIC FREE RADICAL SITES†

Thomas P. Lockhart and Robert G. Bergman

An important focus in present fossil fuel research pertains to the processes of hydrogen transfer. The occurrence of hydrogen transfer in coal liquification processes is usually envisioned as taking place between a partially unsaturated species and a reactive molecule (particularly organic radicals). In this process, hydrogen atom transfer from the unsaturated species is most important when aromatization of the unsaturated species results.¹

As a model for such hydrogen transfer processes, we have been examining both intra- and intermolecular hydrogen atom transfer reactions in p-benzyne (1,4-dehydrobenzene), a very reactive aromatic biradical.² Scheme 1 outlines our mechanistic proposal for the reactions of a dipropyl substituted p-benzyne intermediate (2). The biradical is generated from the pyrolysis of a diethynyl olefin, compound 1. In gas phase flow pyrolysis experiments, three products (3, 6, and 7) are isolated in quantitative yield. The same products are obtained in high mass balance when compound 1 is pyrolyzed in solution at 190°C in a solvent inert toward free radical H-atom abstraction [(1) = 0.01M in diphenyl ether, chlorobenzene or benzene]. In addition, several products are observed which appear to be derived from the combination of radical intermediates with the aromatic

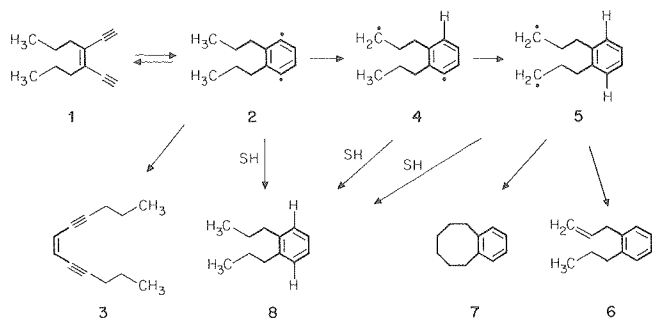
solvent (ca. 5% total yield, identified by vpc/ms). Pyrolysis of 1 in alkyl-H containing solvents such as toluene, cumene or alkanes produces a new product, ortho-dipropyl benzene (8), but the overall yield of 3, 6, and 7, and 8 is poor (ca. 40%). In this case the pyrolyzed solutions are badly discolored, which is suggestive of competing polymerization reactions. We have found that a high yield of 8 can be obtained by performing the pyrolysis in an inert solvent to which has been added a good H-atom donor (1,4-cyclohexadiene or 9,10-dihydroanthracene). In addition to product 8, several other products are observed which presumably arise from combination between radical intermediates and cyclohexadienyl radicals (caged pairs produced by H-atom transfer to the reactive biradical intermediates). These compounds have been identified by vpc/ms analysis, and are present in ca. 1/3 the yield of product 8. By increasing the percent of trapping agent in the pyrolysis solution it is possible to increase the yield of 8 at the expense of the three unimolecular products. These results are summarized in Table 1.

By our proposed mechanism, p-benzyne 2 is formed in a unimolecular cyclization step. In the absence of trapping agent, this intermediate undergoes ring opening to diyne 8, which is stable under these conditions, or suffers H atom transfer from the alkyl side chains to produce rearranged biradicals 4 and then 5. Biradical 5 has two low energy unimolecular pathways available to it: radical-radical combination to give 7 or disproportionation to give 6. In the presence of 1,4-cyclohexadiene, H-atom transfer occurs from the diene to the radical intermediates, 2, 4, and 5. At moderate concentrations of trapping agent (greater than 5%), 2 appears to be trapped appreciably before it can proceed to either 4 or 3.

Present work is directed toward elucidating the details of the proposed mechanism. We are using a deuterated trapping agent to determine unambiguously the point of trapping of the intermediates in this reaction. Combining these results with a kinetic analysis may allow us to determine the relative rates of the various reaction pathways. The results of these studies will be of use in understanding the behavior of the reactive species present in coal pyrolyses, since aromatic and alkyl radicals are believed to play a significant role, and "prearomatic" compounds (such as tetralin) serve as hydrogen donors in a way that is analogous to that of 1,5-cyclohexadiene in our studies.³

* * *

Scheme 1.



* This was supported jointly by the Division of Chemical Sciences, Office of Basic Energy Sciences and the Division of Advanced Research and Technology Development, Office of Fossil Energy, U. S. Department of Energy.

† Supported in part by the National Science Foundation.

1. B. M. Benjamin, E. W. Hagaman, V. F. Raaen and C. J. Collins, *Fuel* **58**, 386 (1979).
 2. R. G. Bergman, *Accts. Chem. Res.* **6**, 25 (1973).
 3. R. J. Hooper, H. A. J. Battard and D. G. Evans, *Fuel* **58**, 132 (1979); T. Gangwer, D. MacKenzie and S. Casano, *J. Phys. Chem.* **83**, 2013 (1979); P. Bredael and T. H. Vinh, *Fuel* **58**, 211 (1979).

Table 1. Pyrolysis of 1

| Pyrolysis Conditions | % Cyclohexadiene in solution | Products (%) | | | | |
|--|------------------------------|--------------|------|------|----|--------------|
| | | 8 | 9 | 10 | 11 | Total (8-11) |
| Gas phase ^a | -- | 32 | 19 | 25 | -- | 76 |
| C ₆ H ₅ Cl Solution ^b | 0% | 21 | 40 | 22 | -- | 83 |
| " | 5% | 9.6 | 8.3 | 5.3 | 48 | 71 |
| " | 10% | 7.5 | 3.8 | 3.2 | 65 | 80 |
| 1,4-Cyclohexadiene solution ^b | 100% | ~1.0 | <1.0 | <1.0 | 76 | ≤79 |

^aN₂ flow, contact time ca. 2.2 min.

^b[1] = 0.01 M, 190°C.

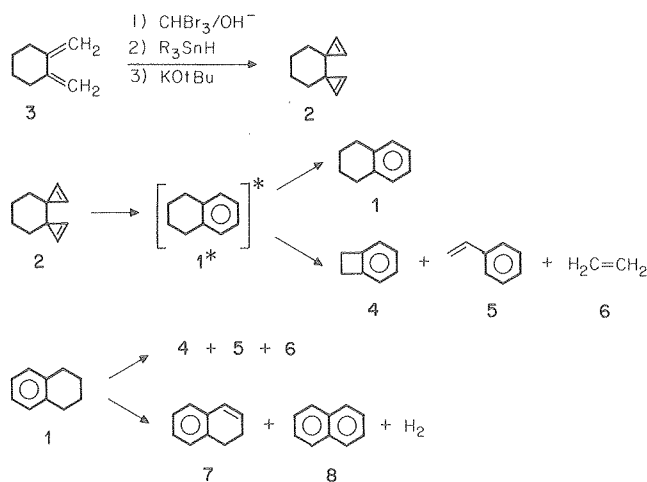
2. THERMAL REACTIONS OF TETRALIN: A MODEL FOR HYDROGEN TRANSFER PROCESSES OCCURRING DURING COAL PYROLYSIS AND LIQUEFACTION[†]

Paul B. Comita and Robert G. Bergman

Tetralin (1), a "partially hydrogenated" aromatic molecule, is an important model for molecules which act as both hydrogen donors and receptors in coal. However, the thermal chemistry of tetralin is only poorly understood.¹ In an effort to improve this situation, we are studying the reactivity of tetralin (1) using several different methods of energization. The purpose of this investigation is to determine what differences, if any, arise in the chemical reactivity of an organic molecule when subject to chemical activation, collisional activation, and infrared laser photochemical activation.

Chemical Activation. The highly strained molecule 1,1'-tetramethylene bicyclopropenyl (2) was synthesized in three steps from 1,2-bismethylene-cyclohexane (3). We have studied the pyrolysis of this molecule and have obtained evidence for the intermediacy of a chemically activated tetralin. The products of this rearrangement (see Scheme 1) are tetralin (1), benzocyclobutene (4), styrene (5) and ethylene (6); the ratio of these products is dependent upon the pressure at which the pyrolysis is run. This pressure dependence shows that at high pressure (1 atm. N₂) where collisional deactivation is competitive with chemical reaction,² 75% of the product is tetralin. At low pressure, the major products are benzocyclobutene and styrene (see Fig. 1). These studies were carried out in a quartz flow pyrolysis reactor over a span of five decades in pressure. Analysis of the products was by glass capillary gas chromatography (see Fig. 2)

Scheme 1.



Collisional Activation. The chemistry of thermally activated tetralin has been widely studied, due to interest in its fate as a hydrogen donor in coal liquefaction processes.¹ Interestingly, most investigators report that the major thermal reaction of tetralin is loss of hydrogen, yielding 1,2-dihydronaphthalene (7) and naphthalene (8). We have repeated these studies in our quartz flow pyrolysis reactor and get largely the same results. The product distribution varies somewhat with pressure, but at all pressures studied, the major products are dihydronaphthalene and naphthalene. Under vacuum flash conditions, the product distribution appears not to be dependent on the surface

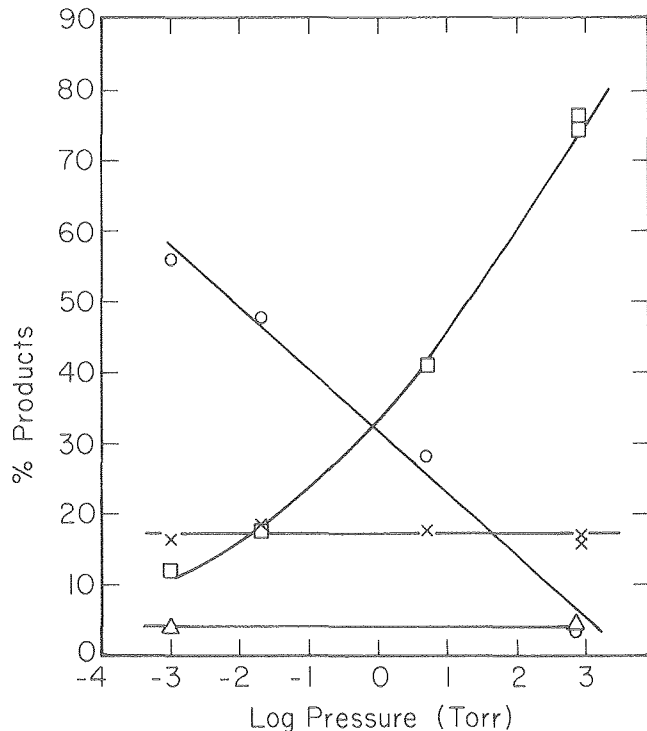


Fig. 1. Pressure dependence of the products of pyrolysis of strained hydrocarbon 2 at 375°C.
(XBL 802-8035)

to volume ratio. However, we believe the dehydrogenation reaction is not a homogeneous thermal reaction, but is in fact a surface-catalyzed process.³ We will be carrying out surface/volume studies in a quartz static pyrolysis reactor in order to monitor the kinetics of the decomposition. We are also attempting to carry out the collisional activation experiments without surface effects by performing laser induced pyrolysis of tetralin. In these experiments, CO₂ laser light is absorbed by a sensitizing gas (SiF₄) which then collisionally transfers its energy to tetralin.⁴

Infrared Laser Photochemical Activation. We have used infrared multiphoton excitation as an alternate method of producing highly excited tetralin. In this method, initial excitation is vibrational rather than collisional. Experiments consist of irradiating tetralin in the gas phase with a focused CO₂ laser and analyzing the products by gas chromatography. Photolyses were performed as a function of laser fluence to judge the effect of the up-pumping rate on competing ethylene-loss and hydrogen-loss reaction channels. At high fluences, 30% of the dissociated tetralin forms dehydrogenation products. As fluence is decreased, the benzocyclobutene-styrene yield steadily increases to 85%. These experiments provide evidence for our hypothesis that the low energy homogeneous channel for tetralin decomposition is loss of ethylene, and not dehydrogenation.

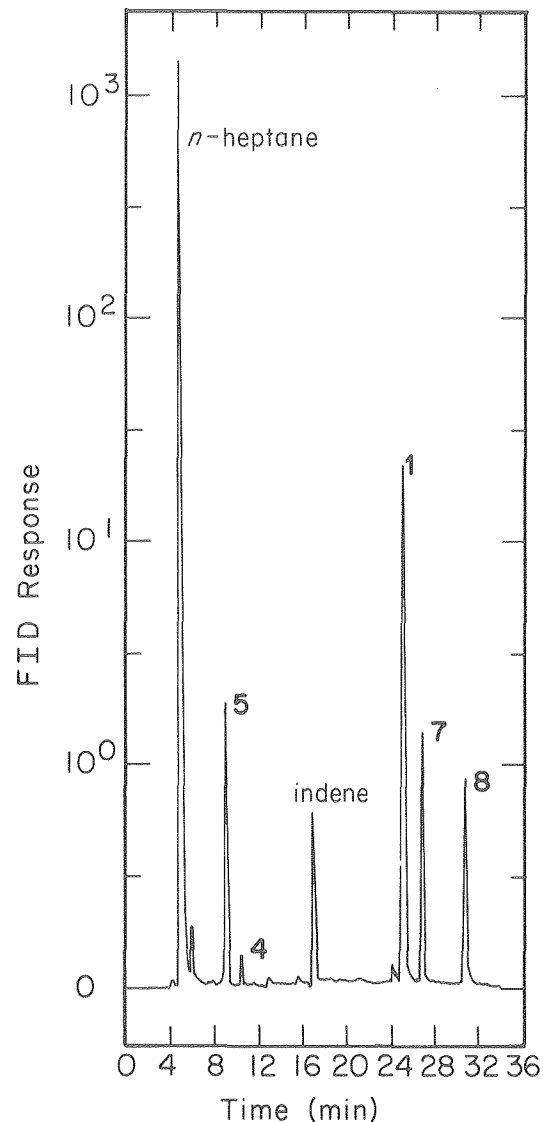


Fig. 2. Vapor phase chromatogram showing peaks due to each of the products of vacuum flash pyrolysis of tetralin (1) at 763°C (analysis conditions: 250 ft x 1/16" open tubular column packed with OV-17, temperature programmed from 100-120 C; 0.05 microliter sample size).
(XBL 802-8034)

* * *

[†]Supported in part by the National Science Foundation.

1. B. M. Benjamin, E. W. Hagaman, V. F. Raaen, and C. J. Collins, *Fuel* 58, 386 (1979); P. Bredael and T. M. Vinh, *Fuel* 58, 211 (1979); A. G. Loudon, A. Maccoll, and S. K. Wong, *J. Chem. Soc. (B)* 1733 (1970).
2. At 760 Torr, the collision frequency is $\sim 1 \times 10^{10} \text{ sec}^{-1}$ based on a collision diameter of 9 Å for tetralin.
3. T. Gangwer, D. Mackenzie, and S. Casano, *J. Phys. Chem.* 83, 2013 (1979).
4. K. J. Olszyna, E. Grunwald, P. M. Keehn, and S. P. Anderson, *Tet. Lett.* 1609 (1977).

RESEARCH PLANS FOR CALENDAR YEAR 1980

1. SELECTIVE SYNTHESIS OF GASOLINE RANGE COMPONENTS FROM SYNTHESIS GAS

A. T. Bell and Heinz Heinemann

Preparation of a series of iron catalysts supported on Al_2O_3 and promoted with potassium in different ratios. Surface and compositional analysis of the catalysts and testing of them for the conversion of $CO+H_2$ in a slurry reactor. Investigation of the effect of shape selective catalyst components on product distribution.

2. ELECTRON MICROSCOPE STUDIES OF COAL DURING HYDROGENATION

J. W. Evans and Heinz Heinemann

Reaction of single crystal graphite with pre-determined gas mixtures in the environmental cell of a 65 kV electron microscope. Morphological changes of the graphite at different temperatures and pressures will be observed while chemical products will be identified in a mass spectrometer attached to the cell. Reactions will be studied in the presence and absence of catalysts and will be extended to coals of high crystalline character.

3. CATALYZED LOW TEMPERATURE HYDROGENATION OF COAL

G. A. Somorjai and H. Heinemann

Transition metal catalysts will be deposited on a coal surface. Hydrogenation or steam-carbon reactions will be carried out on these samples at low temperatures (150-400°C). Catalyst-coal surface changes will be observed at various stages of reaction by means of a low pressure-high pressure apparatus, permitting the analysis of the

surface structure and surface composition of reactants and catalysts. Surface science techniques such as Auger and photoelectron spectroscopy will be applied.

4. SELECTIVE HYDROGENATION, HYDROGENOLYSIS AND ALKYLATION OF COAL AND COAL LIQUIDS BY ORGANO-METALLIC SYSTEMS

K. P. C. Vollhardt and Heinz Heinemann

Study of novel transition metal catalysts, capable of cleavage of carbon-carbon and carbon-heteroatom bonds with concomitant reduction. Application of findings to selective coal depolymerization, hydrogenation and liquefaction under mild conditions.

5. CHEMISTRY OF COAL SOLUBILIZATION AND LIQUEFACTION

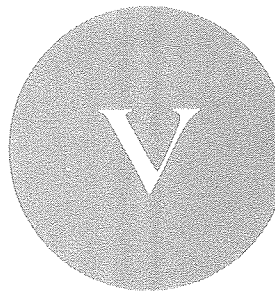
R. G. Bergman and Heinz Heinemann

This study will concentrate on the hydrogen transfer from donor molecules such as tetralin to condensed aromatic coal-like molecules. Both thermal and catalytic mechanisms will be investigated with the ultimate objective of a catalytic donor mechanism at lower temperatures than are used in current practice.

6. COAL CONVERSION CATALYSTS-DEACTIVATION STUDIES

A. V. Levy, E. E. Petersen, and Heinz Heinemann

Cobalt-molybdena-alumina catalysts will be aged by metal deposition under controlled conditions and a mechanism for scale formation on spent catalysts will be defined. Porosity and diffusion measurements will determine whether the scales form a diffusion barrier.



**Advanced Isotope
Separation Technology**

Advanced Isotope Separation Technology

a. Laser Isotope Separation*

C. Bradley Moore, Investigator

Introduction. There have been two significant advances made in projects supported by this program. The use of a continuously tunable IR source has made it possible to study multiphoton dissociation yield spectroscopy. This yields valuable information on the MPD excitation mechanism and allows the prediction of dissociation yields and isotopic enrichment factors based on linear spectroscopy data. The effect of electric field on single rotational level lifetimes in S_1 formaldehyde has been studied. Important information on density and distribution of levels in the high lying vibrational states of the ground electronic level is obtained. These two pieces of work are described succinctly in the following sections. Work on multiphoton excitation of d_2 -formaldehyde has been progressing. The lack of spectroscopic data on highly excited vibrational levels prevents a detailed quantitative analysis of this system at present. Use of IR MPD to probe competing reaction pathways of moderately sized organic compounds is also being demonstrated.

1. 3.3 μm MULTIPHOTON DISSOCIATION

Hai-Lung Dai and A. H. Kung

Isotope separation has been one of the most important applications of IR multiphoton dissociation (MPD). Enrichments of about a dozen elements have been achieved. The most impressive one is the separation of deuterium where the enrichment factor is as large as 10^4 . A pilot plant is in operation for ^{13}C separation by CF_3X ($\text{X} = \text{Br}, \text{I}$) MPD. Very recently, enrichment of U isotopes was reported.¹

To achieve more efficient separation as well as to improve the theoretical understanding of MPD, the process needs to be explored in detail. What is the multiphoton excitation mechanism? How does one decide what type or types of molecules will undergo MPD? Will different excitation mechanisms result from different molecular properties? What are the dynamics of unimolecular dissociation during and after excitation? What is the role of collisions in excitation and in dissociation? With a tunable 3.3 μm laser source, MPD of ethyl chloride by exciting the CH stretching modes is studied to provide answers to some of these questions.

The MPD spectrum in the C-H fundamental region² exhibited strikingly different features from 10 μm MPD, Fig. 1. Resonances in MPD yields match the position and shape of peaks in the fundamental, as narrow as 0.4 cm^{-1} , and in the first- and second-overtone spectra. These facts strongly indicate that transitions within the discrete region and thereafter to the quasicontinuum are resonant in nature. Since CH stretching anharmonicities, usually about 50 cm^{-1} , are larger than vibration-rotation widths and much larger than power broadening at MPD intensities, the mechanisms established for anharmonic compensation in SF_6 cannot operate for ethyl chloride. However, the existence of five CH stretching modes with similar frequencies provides a resonant pathway for excitation.

The resonant nature of the excitation enables us to extend the rate equations description for transitions in the quasicontinuous and continuous regions to include the discrete levels. Coherence effects should be relatively unimportant. A computer program used by Grant et al.³ based on the rate equation model was modified for this calculation. Absorption parameters used in the calculation are estimated from linear spectra obtained by ordinary ir spectroscopy. MPD yields and other characteristics can then be calculated. When a set of constant or slowly decreasing cross

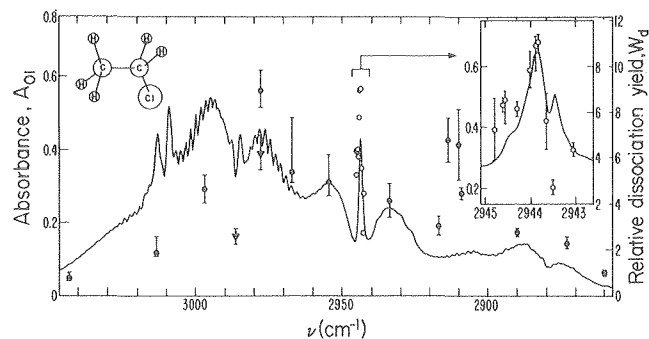


Fig. 1. Relative dissociation yield, W_d , and linear absorption spectrum, A_{01} [Nicolet 7199 Fourier-transform infrared (FTIR) spectrometer with 1 cm^{-1} resolution, 22 Torr $\text{C}_2\text{H}_5\text{Cl}$, 10 cm path length] vs. frequency. Points denoted by filled circles were measured at the peaks of absorption lines. Two points, filled triangles, were taken in valleys. A sharp resonance, open circles, is shown enlarged with an absorption spectrum at 0.24 cm^{-1} resolution. Two points near 2977 cm^{-1} show sharp structure in a P-branch. (XBL 791-173)

*This work was supported by the Division of Advanced Nuclear Systems and Projects, Office of Advanced Isotope Separation, U. S. Department of Energy.

sections for sequential absorptions in the quasi-continuum is used dissociation yields are obtained which are in excellent agreement with experimental data, Table 1.

The experimental fluence dependence of absorption (measured by the optoacoustic method) and yield can be reasonably reproduced by the calculation. One of the most interesting results is the pressure dependence of yield. The yield decreases by nearly a factor of two between 0.25 and 2 Torr and only about 10% decrease from 2 to 6 Torr, Fig. 2. By using the strong collision assumption for the molecules excited above the dissociation limit and by assuming RRKM rates for dissociation, the pressure dependence curve is calculated and is shown to match semi-quantitatively with the measurements.

Table 1. Calculated and measured ethyl chloride MPD yields at selected frequencies. Laser fluence at 1.1 J/cm^2 .

| ν_{laser} (cm^{-1}) | 2976.6 | 2943.8 | 2913 |
|--|---------------|---------------|---------------|
| $\sigma_{01}^{\text{abs.}}$ | 30 | 13 | 11 |
| $\sigma_{12}^{\text{abs.}}$ | 5 | 5 | 5 |
| $\sigma_{\ell, \ell+1}^{\text{abs.}}$ ($\ell \geq 2$) | 2.5 | 2.5 | 2.5 |
| $W_d, \text{ cal.}(\%)$ | 1.7 | 2.1 | 1.2 |
| $W_d, \text{ expt.}(\%)$ | 1.8 ± 0.2 | 1.8 ± 0.2 | 1.3 ± 0.2 |

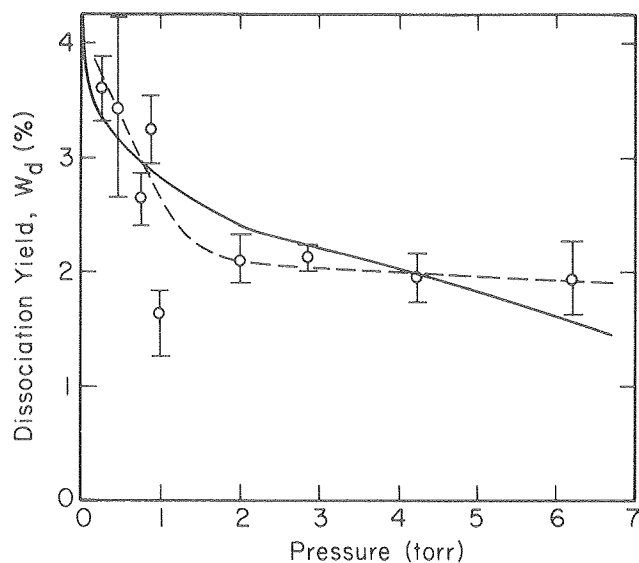


Fig. 2. Ethyl chloride pressure dependence of MPD yield at 1.1 J/cm^2 fluence. Points (ϕ) show experimental results. Solid line is from rate equation calculation with RRKM dissociation rate and strong collision assumption. (XBL 802-8022)

The ethyl chloride example demonstrates clearly the importance of detailed structural and spectroscopic properties of molecules for IRMPD. While it is probable that the dynamics are quite similar for all molecules in the quasicontinuum and the continuum, it should be expected that the great variety of molecular properties in the discrete region will yield a correspondingly great variety of MPD phenomena. These experiments on ethyl chloride and experiments under way on d_2 -formaldehyde probe the small molecule limit of multiphoton dissociation dynamics.

* * *

1. S. S. Miller, D. D. Deford, T. J. Marks, and E. Weitz, *J. Am. Chem. Soc.* **101**, 1036 (1979); D. M. Cox, R. B. Hall, J. A. Horsley, G. M. Kramer, P. Rabinowitz, and A. Kaldor, *Science* **205**, 390 (1979).
2. H. L. Dai, A. H. Kung, and C. B. Moore, *Phys. Rev. Lett.* **43**, 761 (1979), LBL-8767.
3. E. R. Grant, P. A. Schulz, A. S. Sudbo, Y. R. Shen, and Y. T. Lee, *Phys. Rev. Lett.* **40**, 115 (1978).

2. SINGLE ROTATIONAL LEVEL LIFETIME OF S_1 FORMALDEHYDE: ELECTRIC FIELD EFFECTS[†]

J. C. Weisshaar

The collision-free fluorescence lifetimes of S_1 H_2CO have been shown to vary from 66 nsec to 4.2 μsec with rotational state within the 4^0 vibrational level.¹ Further single rotational (SRL) lifetime measurements on 4^1 H_2CO show even larger fluctuations from 20 nsec to 3.1 μsec .² All but the longest lifetimes are dominated by a fast, collision-free non-radiative process which is apparently $S_1 \rightarrow S_0 \rightarrow \text{H}_2 + \text{CO}$ predissociation. Each S_1 SRL interacts with a sparse manifold of broadened S_0 levels. The unusual fluctuations of decay rate with J' and K' are due to variations in S_1 - S_0 couplings $V_{S_1 \ell}$, S_0 widths Γ_ℓ , and S_1 - S_0 energy spacings $\delta_{S_1 \ell}$.

Confirmation of these ideas has come from the new technique^{2,3} of measuring the S_1 SRL fluorescence decay in the presence of small, uniform electric fields of 0-4.6 kV/cm. The field has a completely negligible effect on the couplings $V_{S_1 \ell}$. Since the S_1 and S_0 dipole moments are different (1.56 D and 2.33 D, respectively), the field can smoothly vary the relative spacings of the S_1 level excited and the S_0 levels to which it is coupled. Changes of at least a factor of four have been observed in fluorescence decay rates in the presence of the electric field. For a first-order Stark effect in both S_1 and S_0 , the quantity $(\mu_{S_0} - \mu_{S_1})E$ is $1.3 \times 10^{-5} \text{ cm}^{-1}$ per (V/cm), so that the relative shift $\Delta \mu_{\text{EKM}}/J(J+1)$ is at most 0.06 cm^{-1} for the fields employed.

Figure 1 shows the lengthening of the average fluorescence lifetime of the $J'=4, K'=4$ level of 4^1 H_2CO with increasing applied voltage. (Field

strength can be obtained by dividing each voltage by 1.29 cm, the electrode gap.) The longest decay component lifetime increases from 25 nsec to ~100 nsec. In other examples the average lifetime decreases or remains constant, apparently depending on the local S_0 level structure near each S_1 level. Figure 2 shows plots of the reciprocal of the M-averaged fluorescence lifetime obtained for the same $J'=4, K'=4$ case and for the $J'=13, K'=2$ case by integrating fluorescence intensity vs. time curves. In the former case, the decrease in average lifetime is clear. In the latter case, a very narrow resonance shape is observed, perhaps indicative of a single S_0 level sweeping into and then out of resonance with the S_1 level. There exists S_0 levels widely spaced compared with their widths.

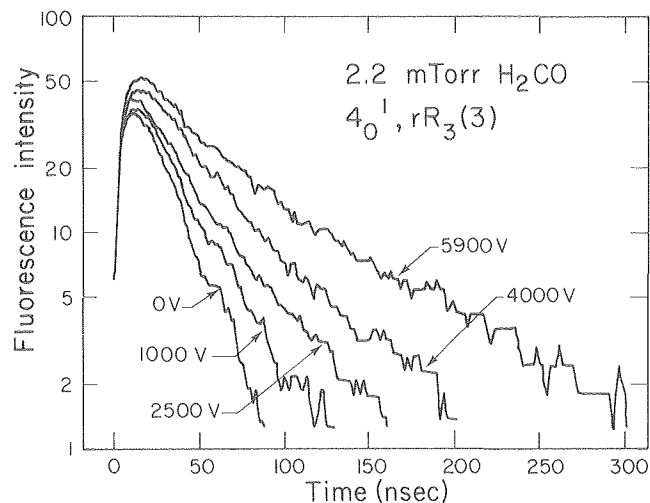


Fig. 1. Decay of total fluorescence intensity after $rR_3(3)$ excitation of 4_0^1 H_2CO for various applied Stark voltages. Note the lengthening of the mean decay time as the field increases. Voltages can be converted to field strengths by dividing by 1.29 cm. (XBL 798-2715)

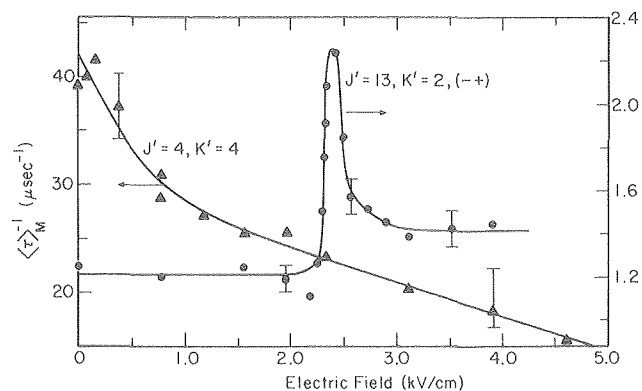


Fig. 2. Plots of the reciprocal of the M-weighted average lifetime vs. applied electric field for two different H_2CO 4_0^1 SRL's. (XBL 802-8023)

In favorable cases, quantitative information about the couplings V_{S_0} and the S_0 widths Γ_0 can be derived from these experiments. No other experimental estimates of V_{S_0} and Γ_0 have been available to date. These parameters are crucial for theoretical calculations of the non-radiative decay rate of S_1 . Preliminary estimates yield V_{S_0} 's of $\sim 10^{-3}$ cm^{-1} and Γ_0 's of $\sim 5 \times 10^{-4}$ cm^{-1} (corresponding to $\tau_{S_0} \sim 10$ nsec). These are in good agreement with recent theoretical estimates of V_{S_0} (Ref. 4) and the $S_0 \rightarrow H_2 + CO$ tunneling rate Γ_0 .⁵ Further experiments at higher energy in S_1 and on other isotopes will yield detailed information about the shape of the continuum of broadened S_0 levels.

* * *

† Brief version of LBL-10182 and LBL-10183.

1. J. C. Weisshaar and C. B. Moore, J. Chem. Phys. 70, 5135 (1979), LBL-8766.
2. J. C. Weisshaar and C. B. Moore, J. Chem. Phys., to be published, LBL-10182.
3. J. C. Weisshaar and C. B. Moore, J. Chem. Phys., to be published, LBL-10183.
4. M. L. Elert, Ph.D. dissertation, U.C. Berkeley, 1978.
5. W. H. Miller, J. Am. Chem. Soc., November 1979, LBL-8649.

RESEARCH PLANS FOR CALENDAR YEAR 1980

The fundamental mechanism of IR multiphoton dissociation and the relations among structure, spectra and MPD dynamics will continue to be studied. Experiments on D_2CO are helping to define the small molecule limit for MPD. The role of collisions in excitation through the discrete levels is probed by the pressure dependence of IR fluorescence and dissociation yield. Competition between dissociation channels $D_2 + CO$ and $D + DCO$ is monitored. Ultraviolet excitation of the excited singlet state followed by internal conversion will allow the IR absorption cross section in the quasicontinuum at a specific total energy to be measured. Detailed dynamic calculations can then be made using the *a priori* potential surface from H. F. Schaefer's group and the tunneling rates from Miller's group. Spectral studies of the type carried out for C_2H_5Cl will define the transition from discrete to quasicontinuous levels for medium size molecules. These results will tie together with those from high overtone spectroscopy (see Selective Photochemistry of this Annual Report). The comparison of thermal pyrolysis in a reactor, to homogeneous gas phase laser-induced pyrolysis (no walls), to collision-free MPD will be studied for larger organic systems such as tetralin.

Chemical reactions of single-photon selectively excited molecules are also of interest for laser isotope separation. Iodine monochloride is being excited into specific vibronic states. Its chemical reactivity in collision with hydrogen, deuterium, acetylene, and other reagents is being studied. The kinetics of the reactions will be determined.

The $\text{ICl} + \text{H}_2$ system has been shown to be a bimolecular reaction in which no radicals are involved. It is an ideal system for studying the chemical reactivity of electronically excited molecules with potential application for chemical purification and isotope separation.

1979 PUBLICATIONS AND REPORTS

Refereed Journals

†1. J. C. Weisshaar, A. P. Baronavski, A. Cabello, and C. B. Moore, "Collisionless Decay, Vibrational Relaxation, and Intermediate Case Quenching of S_1 Formaldehyde," *J. Chem. Phys.* **69**, 4720 (1978), LBL-7607.

†2. D. J. Douglas and C. B. Moore, "Vibrational Relaxation of $\text{HV}(v=3,4)$ by H_2 , D_2 , and CO_2 ," *J. Chem. Phys.* **70**, 1769 (1979), LBL-8213.

†3. C.-C. Mei and C. B. Moore, "Thermal Rate Constants, Energy Dependence, and Isotope Effect for Halogen-Hydrogen Halide Reactions," *J. Chem. Phys.* **70**, 1759 (1979), LBL-8209.

†4. S. J. Harris, W. C. Natzle, and C. B. Moore, "Zero Pressure Lifetimes and Fluorescence Quenching of $\text{ICl}(A^3\Pi_1)$," *J. Chem. Phys.* **70**, 4215 (1979), LBL-8475.

†5. J. C. Weisshaar and C. B. Moore, "Collisionless Non-Radiative Decay Rates of Single Rotational Levels of S_1 Formaldehyde," *J. Chem. Phys.* **70**, 5135 (1979), LBL-8766.

†6. H.-L. Dai, A. H. Kung, and C. B. Moore, "Resonant Multiphoton Dissociation and Mechanism of Excitation for Ethyl Chloride," *Phys. Rev. Lett.* **43**, 761 (1979), LBL-8767.

Other Publications

1. A. H. Kung, H.-L. Dai, M. R. Berman, and C. B. Moore, "Resonant Multiphoton Dissociation of Small Molecules," in Proceedings of the Fourth International Conference on Laser Spectroscopy, Rottach-Egern, West Germany, June 1979, LBL-9782.

2. A. H. Kung and H.-L. Dai, "Resonant Multiphoton Dissociation of Ethyl Chloride at $3.3 \mu\text{m}$," in Proceedings of the Electro-Optic Conference, Anaheim, CA., October 23-25, 1979, LBL-9988.

LBL Reports

†1. J. C. Weisshaar and C. B. Moore, "Electric Field Dependence of Collisionless, Single Rotational Level Lifetimes of S_1 H_2CO ," submitted to *J. Chem. Phys.*, LBL-10182.

†2. J. C. Weisshaar and C. B. Moore, "Isotope, Electric Field, and Vibrational State Dependence of Single Rotational Level Lifetimes of S_1 Formaldehyde," submitted to *J. Chem. Phys.*, LBL-10183.

†3. J. C. Weisshaar, "Non-Radiative Decay of Single Rotational States of S_1 Formaldehyde," LBL-10233.

* * *

†Partially sponsored by the National Science Foundation

†Partially sponsored by the U. S. Army Research Office, Triangle Park, NC.

Invited Talks

1. C. Bradley Moore, "High Resolution Multiphoton Dissociation and Photophysics of Formaldehyde," University of Colorado, Joint Institute for Laboratory Astrophysics, Boulder, CO.

2. C. Bradley Moore, "Formaldehyde Photophysics," Allied Chemical Materials Research Center, Morristown, NJ.

3. C. Bradley Moore, "High Resolution Multiphoton Dissociation," Exxon Research and Engineering Co., Linden, NJ.

4. C. Bradley Moore, "Laser Isotope Separation," Physical Science Society of Shanghai, Shanghai, China.

5. C. Bradley Moore, "Multiphoton Dissociation" and "Laser Photochemistry Research at Berkeley," Institute for Molecular Science, Okazaki, Japan.

6. C. Bradley Moore, "Vibrational Photochemistry" and "Formaldehyde Photochemistry," Symposium on Applications of Lasers to Chemical Reactions, Okazaki, Japan.

7. C. Bradley Moore, "Laser Isotope Separation," Institute for Physical and Chemical Research, Tokyo, Japan.

8. C. Bradley Moore, "Photophysics and Photochemistry of Formaldehyde," Tohoku University, Sendai, Japan.

9. C. Bradley Moore, "Laser Isotope Separation," Osaka University, Toyonaka Campus, Osaka, Japan.

10. C. Bradley Moore, "High Resolution Lifetime Measurements and Photophysics of Formaldehyde," Photodissociation of Polyatomic Molecules Meeting, Veldhoven, Holland

11. A. H. Kung, Fourth International Conference on Laser Spectroscopy, Tegernsee, West Germany – Talk.

12. A. H. Kung, CNRS, Orsay, France – Seminar.

13. A. H. Kung, Electro-Optics/Laser 79 Conference, Anaheim, CA – Talk.

14. A. H. Kung, Sandia Laboratories, Livermore, CA – Seminar.

b. Molecular Beam Laser Isotope Separation*

Y. T. Lee and Y. R. Shen, Investigators

1. IDENTIFICATION OF PRIMARY PRODUCTS IN MULTI-PHOTON DISSOCIATION OF CF_3CDCl_2

D. J. Krajnovich, F. Huisken, Z. Zhang,
Y. R. Shen, and Y. T. Lee

Recent studies¹ have shown the compound CF_3CHCl_2 to be a promising candidate for laser separation of deuterium. Highly selective absorption occurs in CF_3CDCl_2 near 10.2 μ and 10.6 μ , and a single-step deuterium enrichment factor of 1400 has been obtained in gas cell experiments where the dominant photoproduct is trifluoroethene (CF_2CFD). CF_2CFCl and CF_3CCl_3 are also produced to a lesser extent. These products are evidently the result of a Cl atom chain reaction initiated by the collisionless multiphoton dissociation of CF_3CDCl_2 to form $\text{CF}_3\text{CDCl} + \text{Cl}$. However, it is difficult to identify unambiguously the primary products in a high-pressure gas cell experiment.

We have collaborated with Marling and Herman of Lawrence Livermore Laboratory to study the multiphoton dissociation of CF_3CDCl_2 in a crossed laser-molecular beam experiment. We had hoped to measure the relative importance of the two lowest dissociation channels: C-Cl bond rupture, and three-center elimination of D-Cl. Sekhar et al.² deduced an activation energy of 63.1 ± 3.8 kcal/mole for the three-center elimination process, although their analysis was complicated by chain reactions initiated by the parallel Cl atom elimination channel. The C-Cl bond strength in CF_3CDCl_2 is not accurately known, but is probably between 70 and 80 kcal/mole.

In our experiment, CF_3CDCl_2 held at a temperature of -33°C was seeded in helium to a total pressure of 150 Torr, and expanded through a 0.004" diameter quartz nozzle. A Gentec DD-250 CO_2 TEA laser was tuned to 944 cm^{-1} and focused to an energy fluence of $\sim 9\text{ J/cm}^2$ at the interaction region. Products were detected by a rotatable mass spectrometer detector as previously described.³ Under these conditions, essentially no D^{37}Cl^+ signal could be detected. Signal was observed at masses 35 and 37. Since HCl fragments to form 80-90% HCl^+ in the ionizer, it appears that the mass 37 product comes solely from the atomic elimination of chlorine and not from D^{35}Cl . At $\theta = 10^\circ$ from the molecular beam, the ratio of mass 39 to mass 37 signal was

$$r\left(\frac{39}{37}\right) = 0.061 \pm 0.058$$

where the listed uncertainty is two standard deviations. From this we conclude that less than 10% of the CF_3CDCl_2 molecules which dissociate yield $\text{C}_2\text{F}_3\text{Cl} + \text{DCl}$. The angular distributions of the

dominant products, CF_3CDCl^+ and Cl^+ , are shown in Fig. 1. Why do we observe only the Cl elimination channel even though the DCl elimination is significantly lower (or at best comparable) in energy?

In general, the irradiated molecules continue to absorb IR photons until the dissociation rate becomes comparable to the excitation rate due to the laser field. For small molecules and molecules with very low dissociation energies, the dissociation rate increases very rapidly with excess energy and the molecules can only absorb one or a few photons beyond the dissociation level before they fall apart. In such cases only the lowest dissociation channel is actually observed.³ For large molecules, however, the dissociation rate increases only gradually with excess energy and the molecules may be excited well above the thresholds of two (or more) dissociation channels. Then, competition between the various open channels is possible.

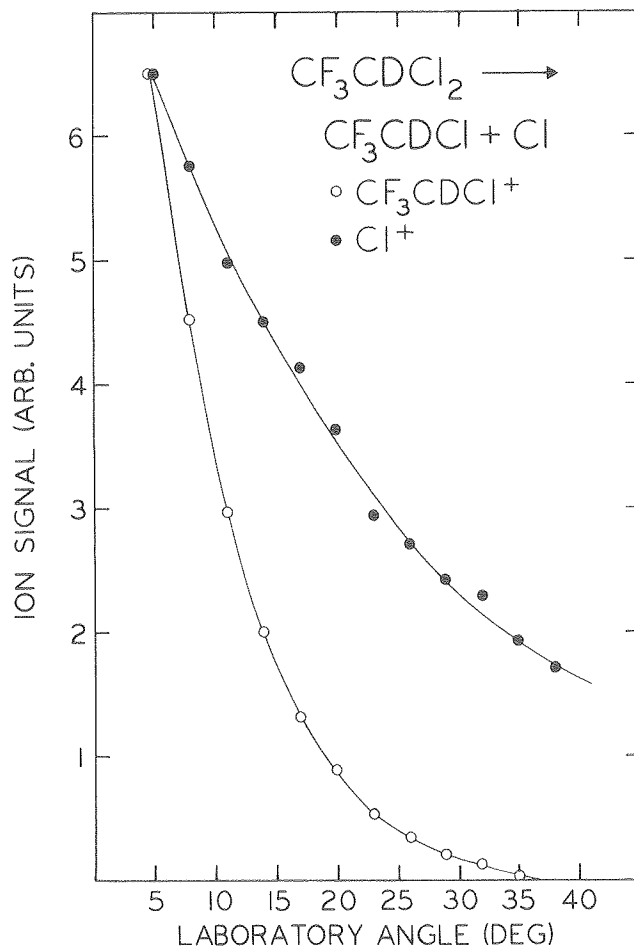


Fig. 1. Angular distributions of the products of the reaction $\text{CF}_3\text{CDCl}_2 \rightarrow \text{CF}_3\text{CDCl} + \text{Cl}$.
(XBL 7911-12914)

*This work was supported by the Division of Advanced Nuclear Systems and Projects, Office of Nuclear Energy, U. S. Department of Energy.

Since the pre-exponential factor is much larger for an atomic elimination compared to a three-center elimination, the rate of Cl elimination from CF_3CDCl_2 will grow faster with excess energy than the rate of DCl elimination. Assuming energy thresholds of 63 and 75 kcal/mole for the DCl and Cl eliminations, respectively, RRKM calculations indicate that the rate of Cl elimination does in fact "catch up" with the rate of DCl elimination at excitation energies around 120 kcal/mole. From the observed angular and time-of-flight distributions of the CF_2CDCl and Cl products, we conclude that the molecules absorb, on average, around 10 photons beyond the C-Cl threshold, corresponding to excitation energies of only 100 kcal/mole. At this level of excitation, the DCl elimination rate is calculated to be four times the Cl elimination rate, which is inconsistent with the experimental results.

However, if the energy thresholds of the two channels are assumed to be equal (70 kcal/mole), the RRKM calculation predicts that the Cl elimination is 25 times faster than the DCl elimination for excitation energies around 100 kcal/mole. It therefore seems likely that the activation energy for DCl elimination determined by Sekhar et al. is too low and/or that the C-Cl bond is unusually weak in CF_3CDCl_2 .

Acknowledgment. We thank Jack Marling and Irving Herman at Lawrence Livermore Laboratory for providing the sample of CF_3CDCl_2 .

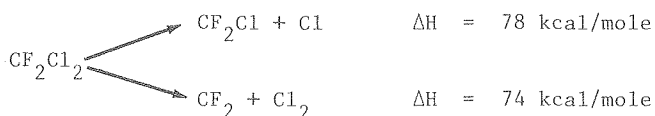
* * *

1. J. B. Marling, I. P. Herman, *Appl. Phys. Lett.* **34**, 439 (1979).
2. M. V. C. Sekhar, G. E. Millward, E. Tschuikow-Roux, *Int. J. Chem. Kin.* **5**, 363 (1973).
3. Aa. S. Sudbø, P. A. Schulz, E. R. Grant, Y. R. Shen and Y. T. Lee, *J. Chem. Phys.* **70**, 912 (1979).

2. MOLECULAR ELIMINATION OF Cl_2 IN MULTIPHOTON DISSOCIATION OF CF_2Cl_2

D. J. Krajnovich, F. Huisken, Z. Zhang, Y. R. Shen, and Y. T. Lee

Infrared multiphoton dissociation of CF_2Cl_2 has received a lot of attention in recent years. This molecule has two dissociation channels with nearly the same endoergicity:



The energy threshold for the molecular elimination is expected to be somewhat larger than its endoergicity, since a barrier probably exists for the reverse reaction.

In a previous crossed laser-molecular beam experiment,¹ only the atomic elimination was

observed, and an upper limit of 10% was placed on the fraction of molecules dissociating via the molecular elimination channel. An energy fluence of 3-5 J/cm² was used in this experiment. However, King and Stephenson² have estimated that about 15% of the CF_2Cl_2 molecules which dissociate yield $\text{CF}_2 + \text{Cl}_2$ for energy fluences in the range 1.5 J/cm². They used the laser induced fluorescence technique to measure the initial internal energy distribution of the ground electronic state CF_2 fragments produced in multiphoton dissociation of CF_2Cl_2 . In addition, an optical time-of-flight technique was used to estimate the average kinetic energy of the nascent CF_2 photofragments at 1.5 ± 0.5 kcal/mole. The Cl_2 product was not monitored in this experiment.

There is additional support for the Cl_2 elimination mechanism. Using a beam sampling mass spectrometer and energy fluences between 10 and 140 J/cm², Hudgens³ has measured the branching ratio of Cl vs. Cl_2 formation to be greater than 33:1. Morrison and Grant⁴ measured the $\text{CF}_2\text{Cl}:\text{CF}_2$ branching ratio over a fluence range of 0.5 - 5 J/cm² in a gas cell scavenger experiment. They found that the $\text{CF}_2 + \text{Cl}_2$ channel comprised only 4% of the total dissociation yield at 6 J/cm² and that this percentage increased as the energy fluence was lowered. This is not surprising, since the rate constant for the concerted molecular elimination is expected to increase less steeply with excess energy than that for the atomic elimination. Thus, harder laser pumping will tend to favor the Cl elimination channel. As the fluence was lowered further, the CF_2 yield passed through a maximum (around 7% of the total yield) and then decreased. At the maximum, the fractional conversion per shot was less than 1%. From this behavior at low fluence, Morrison and Grant concluded that the threshold for Cl_2 elimination (endoergicity plus barrier) must be slightly higher than that for C-Cl bond rupture. This implies an exit barrier of at least 4 kcal/mole.

Equipped with a high repetition rate CO_2 laser, we decided to reinvestigate the multiphoton dissociation of CF_2Cl_2 by the crossed laser-molecular beam technique. We hoped to obtain the following information: 1) The amount of translational energy released in the molecular elimination reaction and, therefore, a lower bound on the height of the exit barrier. 2) An accurate branching ratio. 3) The dependence of the branching ratio on laser energy fluence.

Pure CF_2Cl_2 was run through a 0.004" diameter quartz nozzle heated to 180°C at a stagnation pressure of 200 torr. A Genfec DD-250 CO_2 TEA laser was turned to 1083 cm^{-1} and focussed to an energy fluence of ~ 4 J/cm² at the interaction region. Products were detected by a rotatable mass spectrometer detector as described previously.¹

The angular distributions of the products of the atomic elimination channel are shown in Fig. 1. The angular distributions of CFCl^+ and CF_2^+ were found to accurately coincide with CF_2Cl^+ . The observed Cl_2^+ signal was 100 times lower than the Cl^+ signal at $\theta = 5^\circ$ from the molecular beam (only ~ 0.04 counts/shot). This explains why the CF_2^+ angular distribution deviates negligibly from those

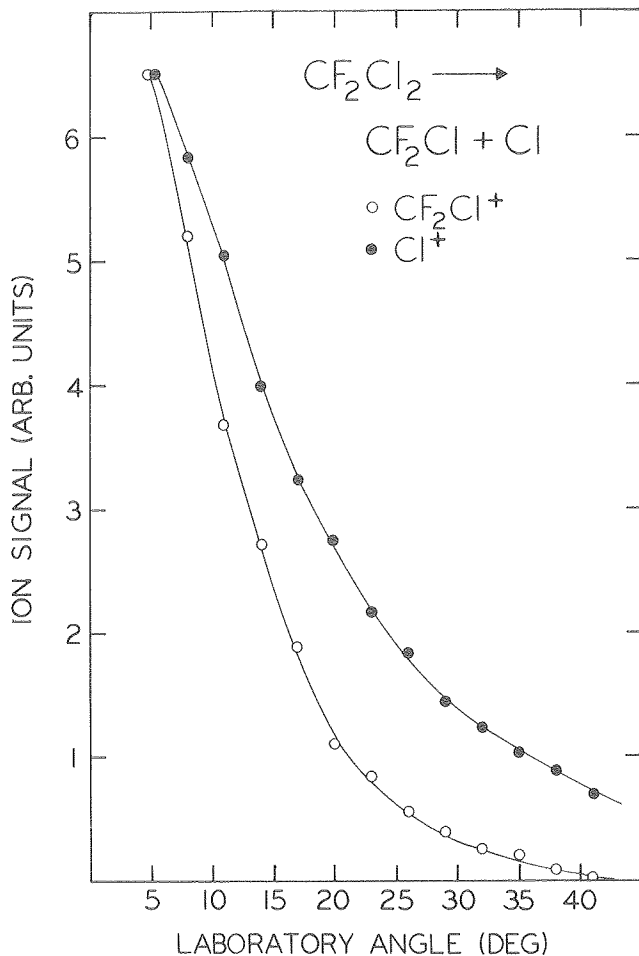


Fig. 1. Angular distributions of the products of the Cl atom elimination channel. (XBL 7911-12912)

of CF_2Cl^+ and CFCl^+ . The time-of-flight spectra of CF_2Cl^+ , Cl^+ , and Cl_2^+ obtained at $\theta = 5^\circ$ are compared in Fig. 2. The CF_2Cl and Cl products are peaked around the center-of-mass beam velocity, which is a characteristic result of statistical translational energy distributions in the absence of exit channel effects. The Cl_2 product, on the other hand, has a peak velocity nearly twice that of the CF_2Cl_2 beam, confirming the presence of an exit channel barrier. A rough preliminary calculation indicates that Cl_2 is formed with an average of ~ 2.1 kcal/mole translational energy, which by momentum conservation leaves the CF_2 partner with ~ 2.9 kcal/mole. This is nearly twice King and Stephenson's result. This also indicates that the height of the potential barrier in the exit channel is at least 5 kcal/mole (and possibly quite a bit more), which is already sufficient to raise the $\text{CF}_2 + \text{Cl}_2$ threshold above that for $\text{CF}_2\text{Cl} + \text{Cl}$.

With some reasonable assumptions concerning the relative ionization cross sections of Cl_2 and Cl and the fragmentation of Cl_2 in the ionizer, it should be possible to calculate the total relative yields of the Cl_2 and Cl products (and hence the branching ratio) from the laboratory angular

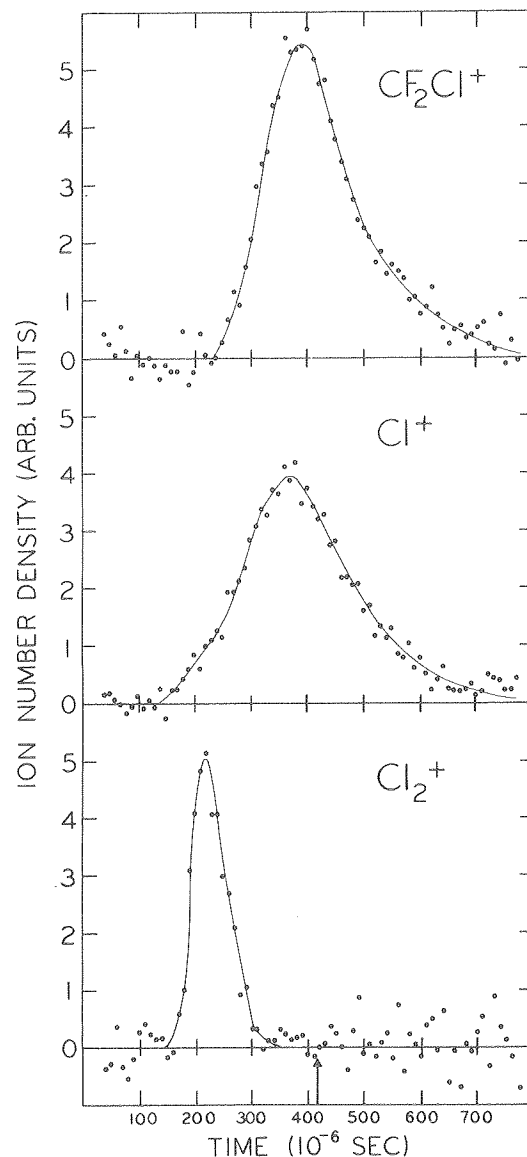


Fig. 2. Time-of-flight spectra of CF_2Cl^+ , Cl^+ and Cl_2^+ obtained at $\theta = 5^\circ$ in the laboratory. The arrow marks the flight time corresponding to the peak molecular beam velocity. The flight path was 22 cm. (XBL 7911-12913)

distributions and time-of-flight spectra. While this has not yet been carried out, the $\text{Cl}_2:\text{Cl}$ branching ratio will certainly be substantially larger than the measured 1% laboratory $\text{Cl}_2^+:\text{Cl}^+$ product ratio because the Cl_2 is scattered into a much wider angular range (in the lab) and the ionization efficiency is smaller for the faster Cl_2 product.

Finally, we investigated the dependence of the $\text{Cl}_2^+:\text{Cl}^+$ ratio on laser energy fluence. As expected, this ratio increased slightly as the energy fluence was lowered. However, we could not go to low enough fluence to observe the subsequent decrease in the $\text{Cl}_2:\text{Cl}$ ratio reported by Morrison and Grant.

* * *

† Brief version of LBL-10534.

1. Aa. S. Sudbø, P. A. Schulz, E. R. Grant, Y. R. Shen, and Y. T. Lee, *J. Chem. Phys.* **70**, 912 (1979).
2. D. S. King, J. C. Stephenson, *Chem. Phys. Lett.* **51**, 48 (1977); J. C. Stephenson, D. S. King, *J. Chem. Phys.* **69**, 1485 (1978).
3. J. W. Hudgens, *J. Chem. Phys.* **68**, 777 (1978).
4. R. J. S. Morrison, E. R. Grant, *J. Chem. Phys.* **71**, 3537 (1979).

3. COMPETING DISSOCIATION CHANNELS IN MULTIPHOTON DISSOCIATION OF ETHYL VINYL ETHER†

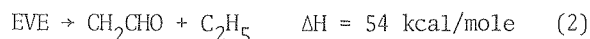
D. J. Krajnovich, F. Huisken, Z. Zhang, Y. R. Shen, and Y. T. Lee

Infrared multiphoton excitation is an elegant means of preparing vibrationally excited molecules for studies of unimolecular reaction dynamics. Most of the reactions which have been studied by this method fall into one of three categories: (1) Simple bond rupture reactions, in which the weakest chemical bond is broken; (2) isomerization reactions; (3) three- and four-center elimination reactions, in which a diatomic molecule is released. For larger, more complex molecules, other possibilities arise. The thermal decomposition of many unsaturated aliphatic ethers proceeds through a concerted transition state to produce an aldehyde and an alkene. Here we will focus on ethyl vinyl ether (EVE).

Wang and Winkler¹ found that EVE decomposes around 400°C to give acetaldehyde plus ethylene



at a rate given by $k = 4 \cdot 10^{11} e^{-44000/RT}$. They also found evidence for a minor free radical pathway, which is probably given by



The activation energy for channel (2) is estimated to be 60 kcal/mole, although this number has large uncertainty. Using radioactive tracers, Molera et al.² proved that reaction (1) involves a hexagonal transition state.

Rosenfeld et al.³ studied multiphoton dissociation of EVE at pressures between 5 and 440 Torr where the reaction is mainly collisional in nature. With an unfocused laser beam only acetaldehyde and ethylene were observed, but with a focused beam comparable amounts of ketene, ethane and butane were formed, indicating competition from reaction (2). Brenner⁴ also studied multiphoton dissociation of EVE and found a different branching ratio when laser pulses of different durations (0.2 and 2 μs) but constant energy fluence were used. With the 2 μs pulses only the lower energy dissociation channel was observed. With the 0.2

μs pulses, reaction (2) was found to dominate over reaction (1). These observations were interpreted as evidence of mode selective decomposition due to slow intramolecular energy transfer.

These reports of competition between reactions (1) and (2) prompted us to study multiphoton dissociation of EVE by the crossed laser-molecular beam technique. We were also interested in finding out the amount of excess energy released as product translational energy in both the concerted rearrangement reaction and the simple C-O bond rupture reaction. The experimental conditions were as follows. EVE held at -33°C was seeded in helium to a total pressure of 320 Torr and expanded through a 0.004" diameter quartz nozzle which was heated to 300°C to enhance multiphoton absorption. A gentec-DD-250 CO₂ TEA laser was turned to 1041 cm⁻¹ and focused to an energy fluence of $\sim 1.5 \text{ J/cm}^2$ at the molecular beam. Products were detected by a rotatable quadrupole mass spectrometer as described previously.⁵

Serious problems arise in the identification of the dissociation products due to fragmentation in the ionizer. Significant signal was observed at masses 43, 42, 41, 29, 27, 26, 25, 15 and 14. By observing the ion signal as a function of time after the laser pulse it is possible to gain a partial understanding of the reactions occurring. Time-of-flight spectra of masses 43, 42 and 26 are shown in Fig. 1. The different time-of-flight spectra of $m=43$ and 42 suggest that these arise from two different dissociation channels. Since the potential energy barrier is much larger for reaction (1), it seems likely that the faster $m=43$ signal is from production of acetaldehyde. This is our tentative assumption. However, no acetaldehyde parent ion ($m=44$) could be detected. The $m=42$ signal probably comes from CH₂CHO produced in reaction (2), although the fast shoulder indicates some contribution from acetaldehyde. (Again, no CH₂CHO parent was detected.) The lighter fragments produced in reactions (1) and (2) (C₂H₄ and C₂H₅) should be moving faster than their heavier partners (CH₃CHO and CH₂CHO) because of momentum conservation. The $m=26$ spectrum shows contributions from both of these light fragments--the fast peak due to C₂H₄, and the slow peak due to C₂H₅. The positions of the $m=43$ peak and the fast $m=26$ peak are in fact correctly related by momentum conservation, and similarly for the $m=42$ and slow $m=26$ peaks. A rough analysis indicates that the translational energy distribution for the products of reaction (1) peaks at ~ 30 kcal/mole (roughly 80% of the potential barrier). If the EVE molecules absorb, on the average, 30-40 kcal/mole beyond the energy threshold for reaction (1), this leaves 40-50 kcal/mole in the internal degrees of freedom of the acetaldehyde and ethylene products. This high level of internal excitation might cause acetaldehyde to fragment more extensively in the ionizer, possibly explaining the absence of acetaldehyde parent ion in this experiment. Secondary dissociation of acetaldehyde to CH₂CHO + H, caused by multiphoton absorption of acetaldehyde during the laser pulse, cannot be ruled out, either. In the case of reaction (2), the product translational energy distribution peaks at ~ 6 kcal/mole.

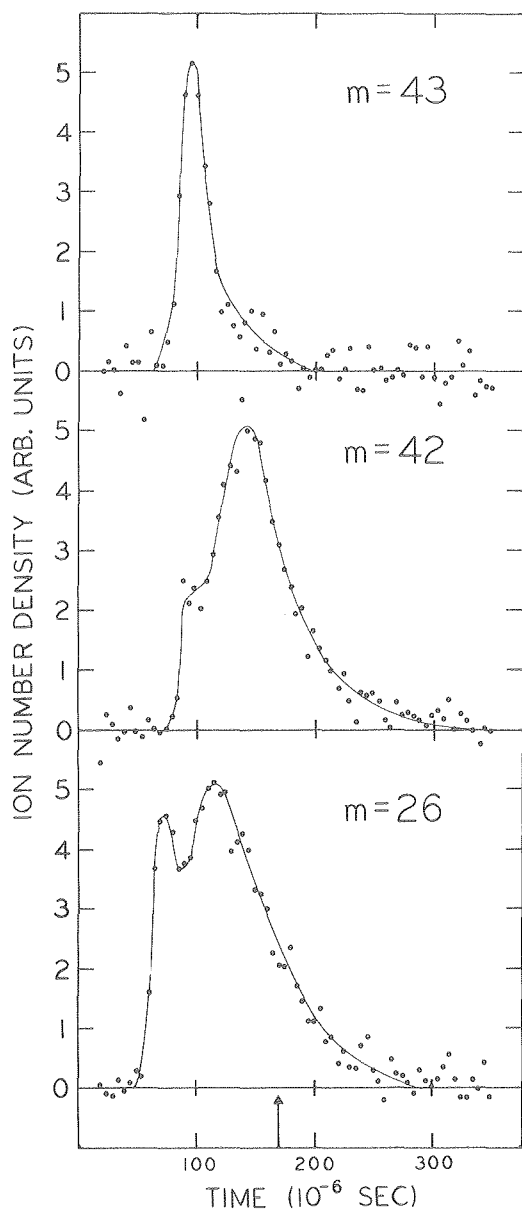


Fig. 1. Time-of-flight spectra of mass 43, 42, and 26 ions obtained at $\theta = 20^\circ$ in the laboratory. The arrow marks the flight time corresponding to the peak molecular beam velocity. The flight path was 22 cm. (XBL 7911-12911)

We also measured the relative 43:42 product ratio at three different laser energy fluences. The results, shown in Table 1, especially the dependence on energy fluence and intensity of the laser pulses, are in qualitative agreement with those of Brenner. (While Brenner varied the pulse length at constant energy fluence, we used a fixed pulse length and varied the energy fluence and intensity simultaneously.) Since the pre-exponential factor for the concerted reaction (1) is certainly much smaller than that for reaction (2), it is expected that the branching ratio will shift in favor of (2) as the level of excitation is increased. Although the absorption in the quasi-continuum seems to

Table 1. The ratio of mass 43 to mass 42 product at $\theta = 10^\circ$ in the laboratory for three values of the energy fluence. The listed errors are one standard deviation.

| Energy Fluence (J/cm^2) | $r = \frac{43}{42}$ |
|---|---------------------|
| 0.6 | 0.64 ± 0.10 |
| 1.5 | 0.23 ± 0.02 |
| 8.8 | 0.14 ± 0.02 |

depend only on energy fluence, the level of excitation above the dissociation threshold does depend on laser intensity. This interdependence of branching ratio, excitation level and laser intensity satisfactorily explains the observed results. The variation in the branching ratio in Brenner's experiments thus appears to be entirely due to the differences in the level of excitation rather than slow intramolecular energy migration.

* * *

[†]Brief version of LBL-10535.

1. S.-N. Wang, C. A. Winkler, *Can. J. Res.* **21**, 97 (1943).
2. M. J. Molera, J. M. Gamboa, J. A. Garcia Dominguez, A. Couto, *J. Gas Chromatography* **6**, 594 (1968).
3. R. N. Rosenfeld, J. I. Brauman, J. R. Barker, D. M. Golden, *J. Am. Chem. Soc.* **99**, 8063 (1977).
4. D. M. Brenner, *Chem. Phys. Lett.* **57**, 357 (1978).
5. Aa. S. Sudbø, P. A. Schulz, Y. R. Shen, Y. T. Lee, *J. Chem. Phys.* **69**, 2312 (1978).

4. VIBRATIONAL PREDISSOCIATION SPECTRA OF HF AND MIXED HF-DF CLUSTERS

D. J. Krajnovich, H. S. Kwok, M. R. Vernon, Y. R. Shen, and Y. T. Lee

We have used a tunable infrared optical parametric oscillator to obtain the vibrational predissociation spectra of small hydrogen bonded clusters of HF. At a nozzle stagnation pressure of 300 Torr the dominant polymeric species in the molecular beam is the trimer. The trimer absorbs an infrared photon and predissociates to give a monomer and a dimer. The yield spectrum of the dimer product (detected as $(\text{HF})\text{H}^+$ in the ionizer) is shown in Fig. 1a. At a stagnation pressure of 800 Torr, the dissociation of tetramers into trimers plus monomers also becomes significant, and the yield spectrum of the trimer product (detected as $(\text{HF})_2\text{H}^+$) is shown in Fig. 1b.

The most striking feature of these spectra is the enormous red-shift from the HF monomer frequency of 3958 cm^{-1} . We found that this red-shift occurs

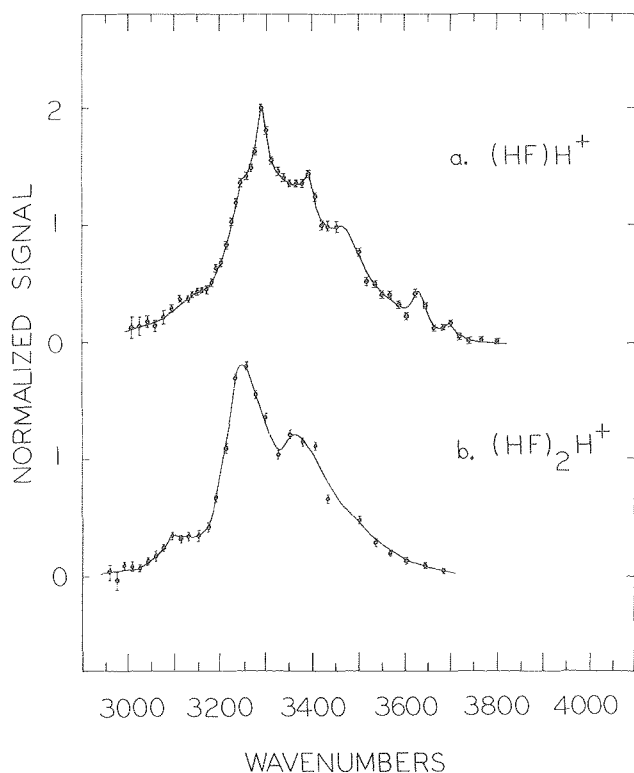


Fig. 1. Vibrational predissociation spectra of HF clusters. (XBL 7911-12655)

in all polymeric complexes and the amount of shifting is directly proportional to the strength of the hydrogen bonding. Despite extensive searching, no $(\text{HF})\text{H}^+$ or $(\text{HF})_2\text{H}^+$ signal could be detected between 3600 and 4000 cm^{-1} . This suggests that the trimers and higher polymers have cyclic structures, since all of the hydrogens appear to be involved in direct intermolecular bonding. This conclusion is also supported by the results of molecular beam electric resonance experiments.¹

Although some structure is evident, especially in the trimer spectrum, assignments are uncertain. The tetramer spectrum appears to have a smoother envelope which must be due to the existence of additional combination bands coming from the extra monomer.

In addition to studying pure HF clusters, we also investigated mixed HF-DF clusters. Using a 65% DF - 35% HF mixture, trimers were produced in the ratio $(\text{HF})_3 : (\text{HF})_2\text{DF} : \text{HF}(\text{DF})_2 : (\text{DF})_3 = 1 : 5.3 : 9.4 : 5.5$. By exciting around 3200 cm^{-1} , all the trimer species except $(\text{DF})_3$ could be dissociated. Since the mixed trimers are expected to dissociate by losing an HF monomer (due to the fact that deuterium is energetically favored in hydrogen-bonding), the $(\text{HF})_2\text{DF}$ and $\text{HF}(\text{DF})_2$ dissociations were monitored as HDF^+ and D_2F^+ , respectively. The yield spectra of HDF^+ and D_2F^+ are shown in Fig. 2. They were very similar to each other, although significantly narrower than the H_2F^+ spectrum, particularly on the low-frequency side. At 3275 cm^{-1} , the ratio of $\text{H}_2\text{F}^+ : \text{HDF}^+ : \text{D}_2\text{F}^+$ signal was 1 : 2.4 : 1.7. The net

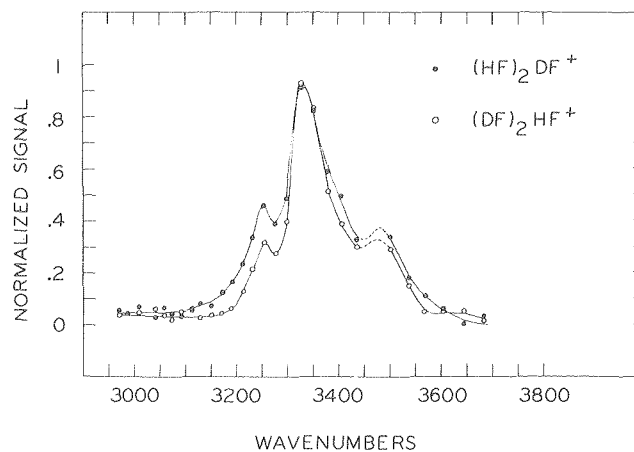


Fig. 2. Vibrational predissociation spectra of $\text{HF}(\text{DF})_2$, $(\text{HF})_2\text{DF}$ mixed clusters. The dissociation yields have been normalized to unity. (XBL 7912-13565)

D:H ratio in the total dissociated product was 40:60, compared to the initial ratio of 65:35. Therefore the trimers which remain in the beam are significantly enriched in deuterium. This enrichment is largely due to the simple fact that the pure DF trimers do not dissociate at all at this frequency. However, our data indicate that the absorption coefficient per hydrogen is slightly greater for $(\text{HF})_2\text{DF}$ than for $\text{HF}(\text{DF})_2$, so that dissociation of mixed trimers may also contribute to the isotope enrichment. Of course, the net enrichment is diluted by the presence of monomers and dimers in the beam. It is probably not possible to get more than 30% of the beam in the form of trimers.

* * *

1. T. R. Dyke, G. R. Tomasevich, W. Klemperer, W. E. Falconer, *J. Chem. Phys.* **57**, 2277 (1972).

RESEARCH PLANS FOR CALENDAR YEAR 1980

Vibrational predissociation of van der Waals molecules by a tunable IR laser has been shown to be quite successful in molecular beam experiments for many molecules. Preliminary studies on deuterium separation in DF-HF systems will be extended to other systems, especially HF-rare gas complexes. The implication of these studies to practical isotope separation will be examined.

Chemical and physical properties of highly vibrationally excited molecules will be investigated in crossed molecular beam experiments using the infrared multiphoton excitation process to energize the molecules.

With the new optical parametric oscillator, the IR multiphoton dissociation process will be studied in the beam by exciting either CH or OH stretching frequencies. Comparison will be made on the dissociation of the same molecules using the CO_2 laser.

Chemical reactions of electronically excited molecules will be studied in crossed beam experiments using a single frequency dye laser excitation of specific vibrational rotational states of isotopic species.

1979 PUBLICATIONS AND REPORTS

Refereed Journals

1. Aa. S. Sudbø, P. A. Schulz, E. R. Grant, Y. R. Shen, and Y. T. Lee, "Simple Bond Rupture Reactions in Multiphoton Dissociation of Molecules," *J. Chem. Phys.* 70, 912 (1979), LBL-7684.
2. P. A. Schulz, Aa. S. Sudbø, D. J. Krajnovich, H. S. Kwok, Y. R. Shen, and Y. T. Lee, "Multiphoton Dissociation of Polyatomic Molecules," *Ann. Rev. Phys. Chem.* 30, 379 (1979), LBL-8751.
3. Aa. S. Sudbø, P. A. Schulz, D. J. Krajnovich, Y. T. Lee, and Y. R. Shen, "Photoionization Study of Multiphoton Excited SF₆ in a Molecular Beam," *Opt. Lett.* 4, 219 (1979), LBL-8765.

LBL Reports

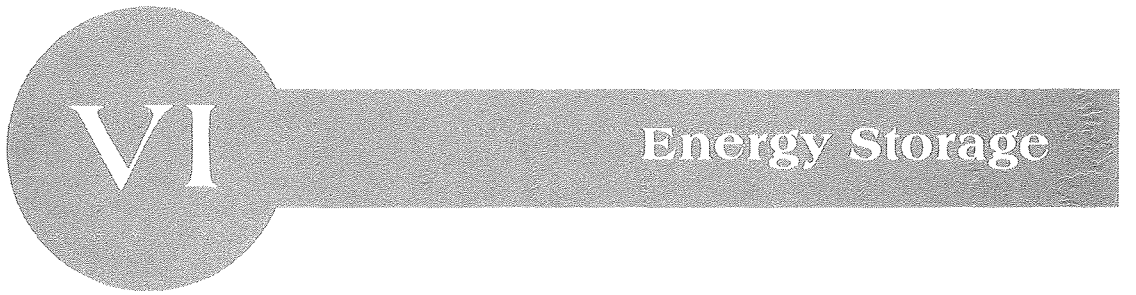
1. Aa. S. Sudbø, D. J. Krajnovich, P. A. Schulz, Y. R. Shen, and Y. T. Lee, "Molecular Beam Studies of Laser Induced Multiphoton Dissociation," in *Topics in Current Physics*, Vol. on "Multiple-Photon Excitation and Dissociation of Polyatomic Molecules" Springer-Verlag, New York, 1979, LBL-8993.
2. P. A. Schulz, Aa. S. Sudbø, E. R. Grant, Y. R. Shen, and Y. T. Lee, "Multiphoton Dissociation of SF₆ by a Molecular Beam Method," submitted to *J. Chem. Phys.* September 1979, LBL-9202.

3. Aasmund Sveinung Sudbø, "Multiphoton Processes in Isolated Atoms and Molecules," Ph.D. thesis, LBL-9796.

4. Peter A. Schulz, "Multiphoton Dissociation of Polyatomic Molecules," (Ph. D. thesis), LBL-10009.

Invited Talks

1. Y. T. Lee, "Dynamics of Infrared Multiphoton Dissociation of Polyatomic Molecules," Department of Chemistry, Rice University, Houston, Texas, March 7, 1979.
2. Y. T. Lee, "Dynamics of Multiphoton Dissociation in Molecular Beams," ACS/CSJ Chemical Congress, 1979, Laser Chemistry Symposium, Honolulu, Hawaii, April 2-6, 1979.
3. Y. T. Lee, "Molecular Beam Studies of Infrared Dissociation of Polyatomic Molecules," Department of Chemistry, University of California, Los Angeles, California, April 24, 1979.
4. Y. T. Lee, "Infrared Multiphoton Dissociation of Polyatomic Molecules," CNEN, Centro di Frascati (Roma), June 7, 1979.
5. Y. T. Lee, "Infrared Multiphoton Excitation and Dissociation of Molecules," Europhysics Study Conference on Multiphoton Processes, Benodet, France, June 18-22, 1979.
6. Y. T. Lee, "Dynamics of IR Multiphoton Processes," Summer School on Chemical Photophysics, Les Houches, France, June 26, 1979.
7. Y. T. Lee, "Photoionization and Vibrational Predissociation of van der Waals Molecules," Herzberg International Conference on van der Waals Molecules, Quebec, Canada, August 1-3, 1979.



VI

Energy Storage

Energy Storage

a. Development of Electrochemical Synthesis and Energy Storage*

James W. Evans, Rolf H. Muller, John Newman,
Phillip N. Ross, and Charles W. Tobias, Investigators

Introduction. The overall aim of this program is to improve the energy efficiency, lower the capital cost, and increase the materials yield of electrochemical processes employed in the direct conversion of chemical to electrical energy in galvanic cells and in the production of materials by electrolysis.

Surface Morphology of Metals in Electrodeposition

The objective of this project is to develop a pragmatic understanding of the detail-processes and their interactions in the macrocrystallization of metals, necessary for the design and optimization of metal deposition processes, including those in rechargeable galvanic cells. Current projects include a) the effect of hydrodynamic flow on the surface morphology of copper and of zinc, and b) dynamic modeling of surface profiles in electrodeposition and dissolution.

In work that is still ongoing, the morphology of copper electrodeposited from well supported acid sulfate is being studied using scanning electron microscopy (SEM). Current density (as a fraction of i_0), flow rate, and smoothness of substrate are varied. The nature of deposits is evaluated by SEM and roughness measurements. Results so far indicate that there are two competing processes involved in the development of roughness: primary protrusion growth of faceted pyramids, and covering these, amorphous-appearing layers. How these protrusions interfere with the mass transfer boundary layer and thereby contribute to the propagation of surface roughness is not yet understood. A 3 cm wide, 0.5 cm high, and 30 cm long flow channel has been completed for the study of flow-generated striations (grooves) in Zn deposits. Frequency of nucleation as a function of zinc ion concentration is being evaluated on polycrystalline and single crystal Zn substrates.

1. DYNAMIC MODELING OF SURFACE PROFILES IN ELECTRODEPOSITION AND DISSOLUTION†

Geoffrey A. Prentice and Charles W. Tobias

The method developed earlier in this laboratory for the modeling of time dependent surface

* This work was supported by the Division of Energy Storage Systems, Office of Conservation and Solar Energy, U. S. Department of Energy.

profiles^{1,2} has been employed in a systematic study of deposition of copper on a sine-wave profile. Calculated profiles are compared to experimental deposits obtained on rotating cylindrical cathodes. The stainless steel spindles have sine waves of various amplitudes and wavelength machined into them, maintaining axial symmetry. The rotating cylinder has uniform accessibility both in respect to electric field and ionic mass transfer. Deposits of thicknesses comparable to the initial sine wave amplitudes were obtained in runs of up to 48 hours (Fig. 1). Kinetic parameters (apparent i_0 and α) were obtained from measurements on smooth rotating cylinders. Calculated and experimental profiles are shown to agree closely (Fig. 2), with the exception of the peak, where an experimentally reproducible small depression is observed.

The other test geometry, a two-dimensional electrode corner, was employed for the study of the effects of geometric ratios and overpotential on the tendency of deposits to form thick nodules at free edges and corners.² The smoothing effect of increasing Wagner number on the developing geometry of the deposit is shown in Fig. 3. Further simulation studies were made on the well known empirical technique of employing current shields or auxiliary electrodes to lower or to increase deposit thickness on complex shaped objects. The smoothing effect of these devices is also shown in Fig. 3.

Improvements in our ability to efficiently simulate developing metal surfaces upon anodic or cathodic charge transfer processes allow taking into account mass transport effects (tertiary distribution) as well. This extension of our capabilities is expected to provide a needed underpinning to our efforts toward understanding how macroscopic surface textures develop in electrodeposition and dissolution.

* * *

† Brief version of Abstract No. 458, Electrochem. Soc. Meeting, Los Angeles, October 14-19, 1979.

1. G. A. Prentice and C. W. Tobias, MMRD Annual Report 1978, LBL-8580, p. 490.

2. G. A. Prentice and C. W. Tobias, "Simulation of Electrode Profiles Undergoing Deposition or Dissolution," Abstract No. 458, p. 1146, Extended Abstract, Vol. 79-2, The Electrochemical Society, October 1979.

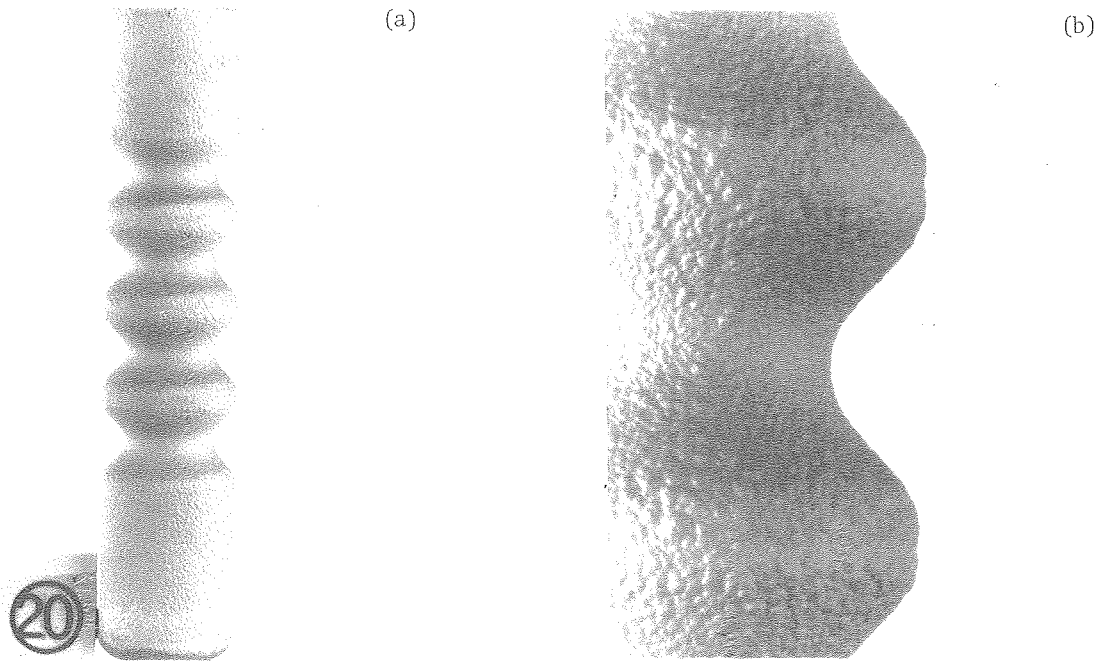


Fig. 1. (a) Copper deposited on a rotating cylinder with sinusoidal initial contour. 0.8 M CuSO_4 , 1.0 M H_2SO_4 , 80 mA/cm^2 , 800 rpm, 25 hours. (b) Detail of contour after 25 hours. [(a) CBB 798-10523; (b) CBB 798-10521]

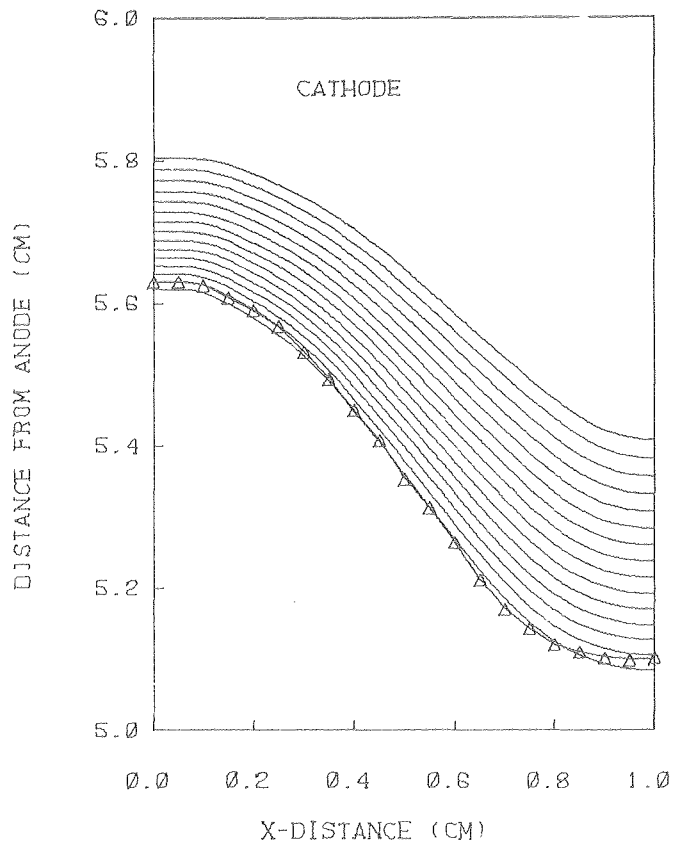


Fig. 2. Comparison of experimental (Δ) and calculated surface profiles: 80 mA/cm^2 , 800 rpm, 25 hours. (XBL 7910-12232)

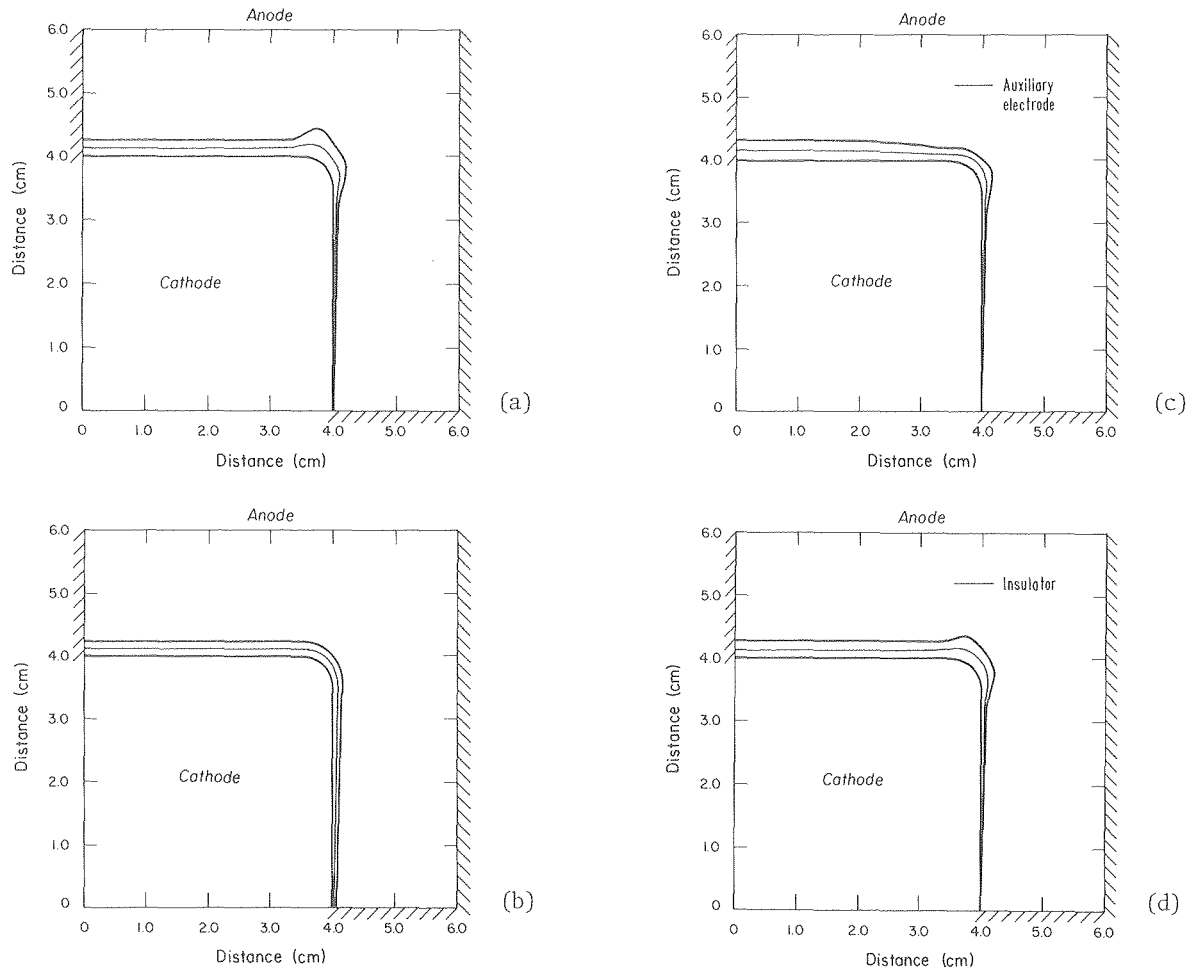


Fig. 3. Simulation of deposition on an electrode corner in successive time steps. All figures depict an equivalent deposition under each curve. (a) Primary current distribution. (b) Deposition under Tafel polarization, Wagner number = 1.0. (c) Deposition in the presence of an auxiliary cathode ("thief") at the same potential as the corner electrode. Primary distribution. (d) Deposition in the presence of an insulating shield. Primary distribution.

[(a) XBL 794-1024; (b) XBL 794-1026; (c) XBL 704-1027; (d) XBL 794-1028]

Anodic Surface Layers on Battery Materials

The purpose of this work is to provide direct experimental information about processes involved in the formation of anodic surface layers during reactions of interest for battery applications. Physically meaningful mechanistic parameters for the prediction of electrode behavior under different operating conditions are derived from the observations and related to the electrochemical behavior of battery electrodes. A more broadly-based, fundamental research program, supported by the Division of Materials Sciences, Office of Basic Energy Sciences, is described under "Electrochemical Phase Boundaries," R. H. Muller, Investigator.

1. ELLIPSOMETRY OF SULFATE FILMS ON LEAD⁺

Rolf H. Muller and Richard D. Peters

The growth of PbSO_4 films has been studied using fast in situ automatic ellipsometry. Parameters describing film structure and mechanism of growth have been obtained from measurements. Films have been followed from initial nucleation on clean planar electrodes until they are about 0.5 μm thick. Constant anodic current (0.1 A/m^2 to 13 A/m^2) and open circuit conditions have been used in H_2SO_4 solutions (1.3 to 5.0 M). Experiments were performed under free convection and laminar flow conditions.

Ellipsometer data have been analyzed using a multiparameter fit in which the surface film is represented by plano-parallel layers of porous material. Film porosity represents the overall void space between crystals. Thickness of layers is established from porosity and a material balance; refractive index is derived from volume averaging solid anodic product and electrolyte within the pores.

Film porosity, as derived from ellipsometer measurements, is influenced by three experimental variables: applied current density, H_2SO_4 concentration, and flow conditions over the electrode. Conditions which lead to a higher supersaturation of anodic species at the interface lead to a greater number density of crystals which, in turn, results in a reduced porosity. This observation is consistent with a solution-precipitation mechanism, of film formation.

Current efficiency for solid film formation ranges from 75 to 90%. The balance of current forms material which apparently remains in solution. Supersaturated ionic species cannot account for the required flux away from the surface, and the necessary Pb^{+2} concentrations are precluded by potential measurements. The formation of a colloidal species during anodic oxidation of Pb in H_2SO_4 that had been postulated before^{1,2}, is also indicated in the present work. Scattering of light from large crystals must be considered when discussing ellipsometer-derived film current efficiency. Crystals having dimensions near the wavelength of light act as scattering centers, with only a small fraction of the incident beam being emitted in the specular direction. Thus, such crystals may optically disappear.

Formation of new anodic products at the Pb/PbSO₄ electrode is signaled by a sudden rise in potential during constant current oxidation and a simultaneous change in the slopes of optical parameters ψ and Δ (relative amplitude and relative phase difference) as seen in Fig. 1, point a. At point b, the current is interrupted (open circuit) and slopes of optical parameters ψ and Δ are momentarily zero, indicating transient passivation of the electrode. The potential falls to values associated with basic lead sulfates (-0.56 to -0.63V vs. Hg/Hg₂SO₄ corresponding to 4PbO·PbSO₄ and 3PbO·PbSO₄·H₂O). At point c, ψ and Δ resume changing due to film formation from corrosion of lead at open circuit. These findings are consistent with the theory that basic sulfates are produced anodically in small amounts and can passivate the lead electrode.³ Depassivation occurs when basic sulfates dissolve.

Open circuit corrosion rates were evaluated from ellipsometer measurements at different acid concentrations for periods of up to five minutes. A square dependence on water concentration has been found. This agrees with Lander's data which were obtained from gravimetric measurements over many hours.⁴

The cathodic reduction of sulfate films can be observed as a reversal of ψ vs. Δ obtained during the previous anodic cycle. Reduction apparently terminates with the onset of H₂ evolution as ψ and Δ no longer change even though they are far from the starting point corresponding to clean Pb. A large fraction of PbSO₄ therefore remains on the

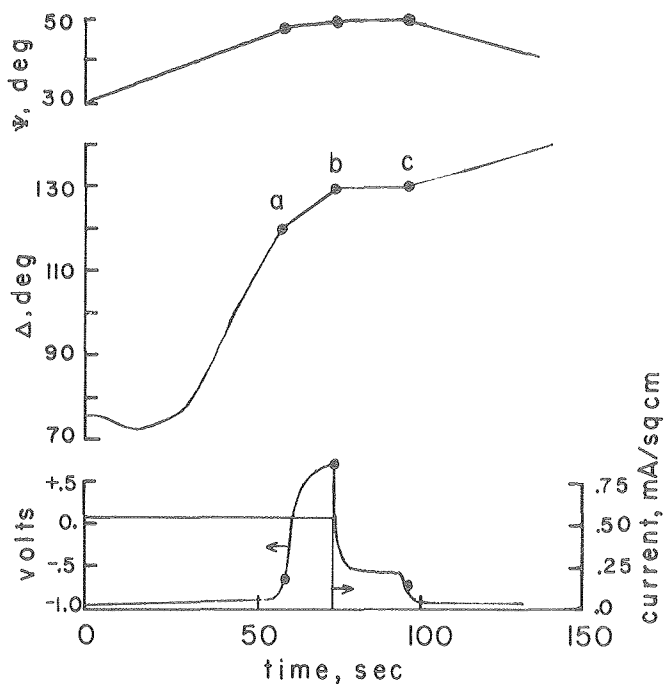


Fig. 1. Potential and optical transients observed during high potential oxidation (a to b) and passivation (b to c) of Pb in H_2SO_4 . Potentials vs. Hg/Hg₂SO₄ in the same solution (3.1 M H_2SO_4). Depassivation occurs at c. (XBL 789-11320)

surface, apparently unavailable for reduction. Loss of rechargeability is usually attributed to sulfation, a formation of "hard" lead sulfate by recrystallization after many cycles, over periods of weeks or months, and does not explain the loss of reduction capability observed here. The present findings suggest that reduced material utilization may also be caused by changes on the lead surface (instead of in the sulfate layer) which result in preferred H₂ evolution.

* * *

[†]Brief version of LBL-9265.

1. G. Archdale and J. A. Harrison, *J. Electroanal. Chem. and Interfacial Electrochem.* **34**, 21 (1972).
2. N. Y. Lyzlov, V. I. Pshenitsyn, and I. A. Aguf, *Sov. Electrochem.* **13**, 1201 (1978).
3. D. Pavlov and N. Iordanov, *J. Electrochem. Soc.* **117**, 1103 (1970).
4. J. J. Lander, *J. Electrochem. Soc.* **98**, 213 (1951).

Metal Couples in Non-Aqueous Solvents

The objective of this project is to develop practical alternatives to aqueous, or high temperature molten salt systems for the efficient electrochemical reduction and oxidation of reactive metals. Current emphasis is placed on the study of electrochemical behavior of potassium in propylene carbonate electrolytes.

1. STUDIES ON THE ELECTROCHEMICAL BEHAVIOR OF POTASSIUM IN PROPYLENE CARBONATE^{††}

Henry H. Law and Charles W. Tobias

Our studies on the electrodeposition of potassium from 0.5 molar solutions of KAlCl_4 in propylene carbonate have led to the following conclusions:

(a) Large amounts of good quality KAlCl_4/PC electrolyte (less than 1 ppm water) can be prepared in a straightforward manner: the solvent is purified by using alumina and molecular sieves or treated charcoal, and then by vacuum distillation; the electrolyte is prepared by dissolving KAlCl_4 , instead of AlCl_3 and KCl separately, in PC.

(b) A surface layer is formed on a potassium electrode in KAlCl_4 solution; this layer affects the electrochemical behavior of potassium only slightly. The use of a potassium reference electrode is meaningful, provided high input impedance instruments are used.

(c) For all practical purposes potassium is stable in the electrolyte prepared (Figs. 1 and 2). The reaction of the solvent with potassium proceeds at a rate less than that corresponding to 20 microampere/cm².

(d) The deposition of potassium proceeds with near 100% current efficiency. Aluminum is not co-deposited.

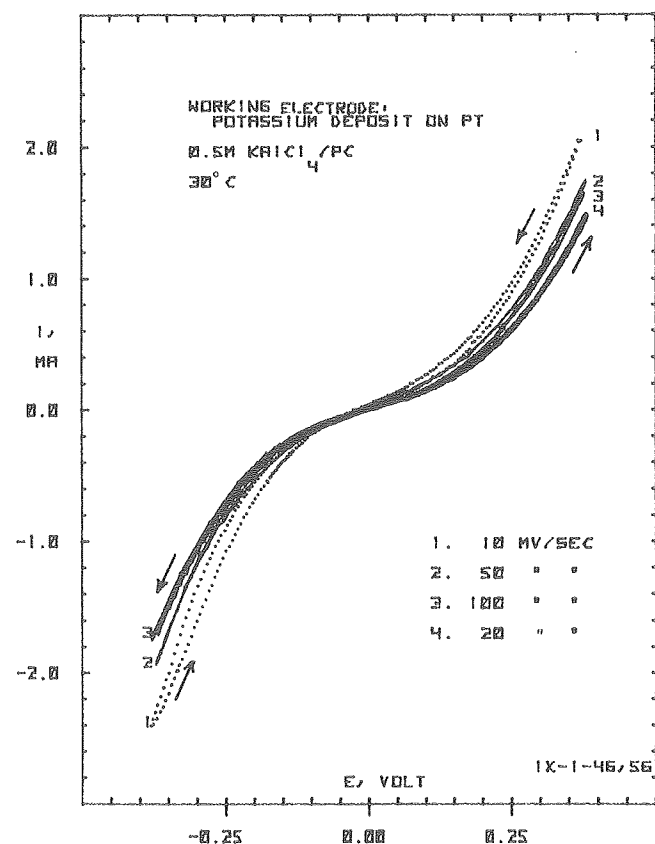


Fig. 1. Cyclic voltammogram of potassium deposit on Pt in 0.5 M KAlCl_4/PC solution at 30°C. reference electrode K/K^+ . IR included. (XBL 792-8459)

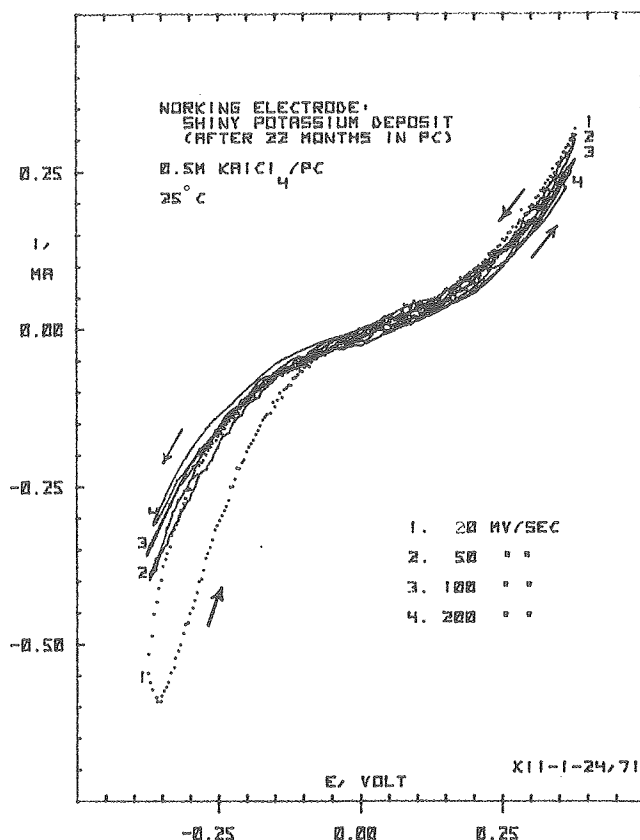


Fig. 2. Cyclic voltammogram of a potassium deposit (after immersion in propylene carbonate for 22 months) in 0.5 M KAlCl_4/PC solution at 25°C, K/K^+ reference electrode. IR included. (XBL 792-8461)

(e) The deposit morphology is strongly affected by temperature. Deposits obtained on different electrode substrates show no significant differences, ranging from loose powders at 25°C, fine needles at 50°C (Fig. 2), and liquid globules at 70°C. Presence of a fluorinated surfactant yields large liquid globules at temperatures above the melting point of potassium.

(f) The steady state galvanostatic technique yielded kinetic parameters with reasonable reproducibility; i_0 was found to be in the range of 1×10^{-4} to 5×10^{-4} amp/cm². The current-pulse technique and the potentiostatic steady-state method were found to be not ideally suited for the purpose of overpotential measurements.

(g) Cathodic overpotentials are influenced by the electrolyte concentration, temperature, concentration of cationic surfactant, and by the nature of the electrode substrate.

(h) Good deposits of potassium up to gram quantities have been obtained under practical conditions. When coupled with an appropriate anodic reaction, potassium could be electrowon or refined in PC electrolyte.

(i) Assuming aluminum dissolution as the anodic reaction, the energy requirement per kg of potassium in a plausible cell configuration is estimated

at 2.4 kw-hr/kg or at \$0.05/kw-hr, \$0.12/kg. Including the cost of Al at \$0.53/lb and KCl (99.9%) at \$40 per ton and not crediting the value of the side product AlCl_3 , the total energy and material cost would amount to \$0.45/kg of potassium produced. (Fig. 3). The attractive energy and material cost, however, would be offset by the probable need for cumbersome reprocessing of the electrolyte, including removal of the product, AlCl_3 .

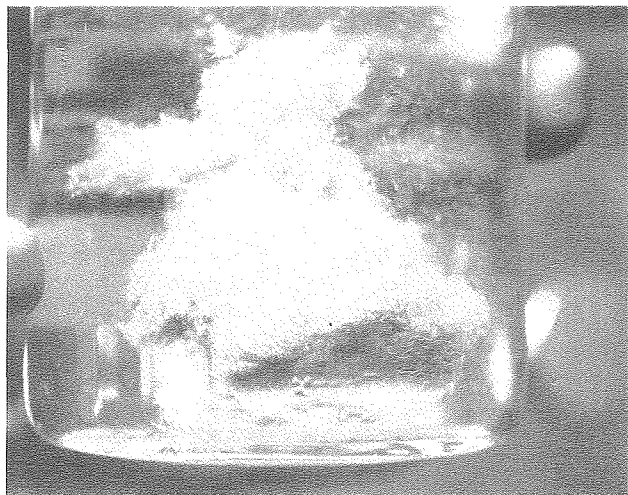


Fig. 3. Potassium deposit from 0.5 M KAlCl_4/PC on a platinum substrate, 50°C , 2 ma/cm^2 , electrode area 1.68 cm^2 . (XBB 793-4547, bottom portion)

* * *

† From its inception until FY 1976, this project was supported by the Division of Materials Science, Office of Basic Energy Sciences, U. S. Department of Energy.

‡ Brief version of LBL-9207.

1. Henry H. Law and Charles W. Tobias, Process Evaluation for the Electrowinning and Refining of Potassium, Fig. 2, p. 497 MMRD Annual Report 1978, LBL-8580.

Analysis and Simulation of Electrochemical Systems

This work supports the development of energy storage systems by means of mathematical models and by experiments designed to test the accuracy and completeness of the models. A one-dimensional model has been developed for the Li(Al)-FeS_x battery in conjunction with a major experimental program at Argonne National Laboratory. This model can be used to identify system limitations and to describe the physical phenomena associated with the Li(Al)-FeS_x battery. A one-dimensional model has been developed which describes the interactions between hydrodynamics, multi-component heat and mass transfer, and reaction kinetics for the rotating disk system. This model has been applied to the chemical vapor deposition of silicon from silicon tetrachloride in excess hydrogen. An economic comparison was made between flow-through and flow-by porous electrodes for redox energy storage.

This comparison incorporated one-dimensional steady state models for each electrode system, and the results show that the flow-by electrode configuration is superior.

In on-going work, a high-pressure electrochemical reactor has been designed to remove aqueous lead ions from dilute feed streams. The competing side reaction (decomposition of water to hydrogen) is suppressed by increases in system pressure. Ten-fold increases in pressure can lead to a ten-fold decrease in lead ion effluent concentrations with no loss of current efficiency. Experimental data have been taken that indicate the feasibility of removing lead ions by this process. The performance of the system is a complex function of the mass transfer, charge transfer, and ohmic potential drop through the reactor. Efforts are being made to quantify experimental data in a form suitable for comparison to theoretical models¹ and to provide a basis for reactor design and scale-up. Modeling work has also begun on the $\text{Fe(0)/Fe(II)/Fe(III)}$ energy storage system.

1. MATHEMATICAL MODELING OF THE LITHIUM/IRON SULFIDE BATTERY[†]

Richard Pollard and John Newman

A one-dimensional model has been developed which considers a whole prismatic cell consisting of negative electrode, separator, electrolyte reservoir, and positive electrode. Physical phenomena described are ohmic potential drop and diffusion potential within the electrolyte, changes in porosity and electrolyte composition due to electrochemical reactions, local reaction rates in their dependence on local composition and potential, and diffusion, convection, and migration of electrolyte. Variations in total cell potential and overall cell temperature are also calculated. Several additional features are included in the analysis: variable physical properties, the dependence of local matrix conductivity on state of charge, and the possibility of precipitation of electrolyte. Furthermore, the model can simulate the effects of current interruption and charging, as well as cell discharge behavior.

This model, in conjunction with a separate analysis of current-collector design and matched with experimental results, can be used to identify system limitations and to improve our understanding of the lithium-iron sulfide battery.

Figure 1 shows the composition profile at several times during constant current discharge. The initial composition (67 mole percent LiCl) is Li rich compared with the eutectic composition. Consequently, precipitation of KCl in the positive is delayed until about 3 hr of discharge. However, LiCl would have had a tendency to precipitate in the negative if the temperature of the cell had not risen (from 450°C to 477°C after 2.5 hours of discharge). The dashed horizontal line indicates the solubility limit for LiCl at the initial temperature of 450°C .

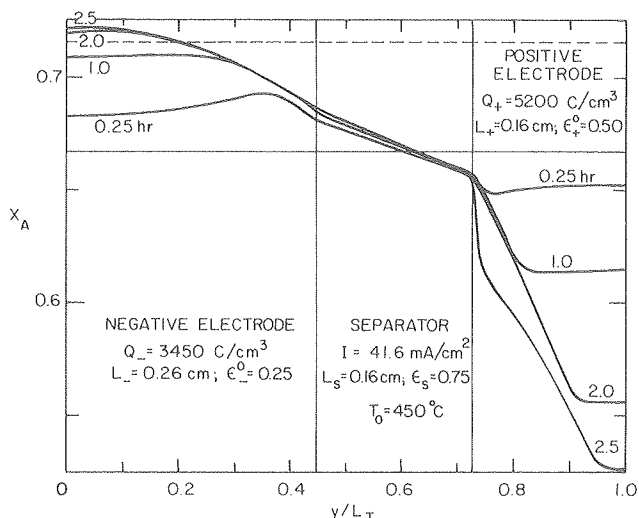
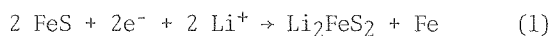
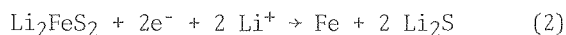


Fig. 1. Composition profile at constant current discharge in the lithium/iron sulfide battery. (XBL 7910-7169A)

Generally speaking, the nonuniform concentration profile results because Li ions are removed from the electrolyte at the positive according to one of the reactions



or



and introduced into the electrolyte at the negative according to the reaction



Since the transference number of Li^+ is not unity, the concentration profile develops, and diffusion aids migration in the transport of lithium ions.

The negative starts with a small initial porosity (0.25) and opens up as the reaction proceeds. The reaction zone also penetrates somewhat into the negative as lithium is partially consumed and the potential required for reaction 3 becomes more positive. At the positive, reaction 1 proceeds first, and a reaction front has proceeded about two-thirds of the way through the positive after 2 hours, as shown in Fig. 1. The FeS is fully converted to Li_2FeS_2 behind this reaction front, which is itself relatively narrow. Subsequently, a reaction front for reaction 2 begins to move through the positive, and its affect on the composition can be seen in Fig. 1 at 2.5 hr. The porosity becomes smaller in the positive as reactions 1 and 2 proceed, and this results in steeper concentration gradients in the positive. Any precipitation of KCl (or LiCl in the negative) which might occur further aggravates the problem of ohmic potential drop in electrolyte.

Figure 2 shows the microstructure in the positive shortly after the second reaction has begun to occur. Here the initial composition is that of the eutectic, 58 mole percent LiCl , and precipitation of KCl can occur. This is responsible for the extremely small value of the porosity ϵ at a distance of about 0.075 cm. This effectively blocks the back portion of the electrode. In the depth of the electrode, reaction 1 has occurred to some extent, producing a certain volume fraction ϵ_X of Li_2FeS_2 and decreasing the porosity somewhat from its initial value of 0.5. Near the front for reaction 1, KCl has precipitated, as mentioned already. Towards the separator from this front there is a plateau for the values of ϵ_X , ϵ , and ϵ_{Fe} corresponding to completion of reaction 1. At distances less than 0.01 cm the consequence of reaction 2 can be seen. $\text{Li}_2\text{FeS}_2(\epsilon_X)$ is consumed, Li_2S is produced, and the porosity ϵ drops to a small value. (This effect may be compensated for in the real system by appreciable swelling of the positive.)

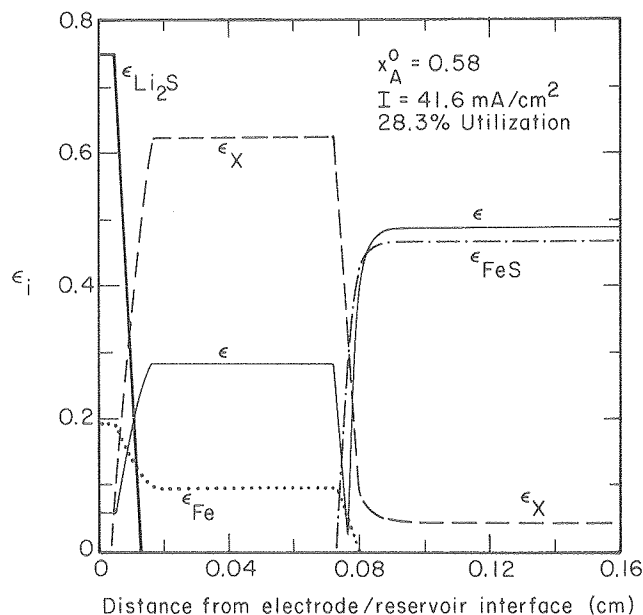


Fig. 2. Composition microstructure in the positive electrode shortly after reaction 2 begins. (XBL 7910-12434A)

The detailed modeling described here can be used to develop local discharge curves for use in the current-collector scale-up studies, to clarify our understanding of the actual mechanism of the reactions, and to elucidate basic causes of failure or capacity fading--which might include precipitation of KCl or LiCl .

* * *

† Brief version of Abstract No. 182, Electrochem. Soc. Meeting, Los Angeles, October 14-19, 1979.

2. SILICON DEPOSITION ON A ROTATING DISK[†]

Richard Pollard and John Newman

A one-dimensional model has been developed which describes the interactions between hydrodynamics, multicomponent heat and mass transfer, and reaction kinetics for the rotating disk system. The analysis includes variable physical properties and finite interfacial velocity and has provision for an arbitrary number of simultaneous homogeneous and heterogeneous reactions. The model has been applied to the chemical vapor deposition of silicon from silicon tetrachloride in excess hydrogen. Predictions for the dependence of silicon production rate on disk temperature and rotation rate are compared with available experimental data.

* * *

[†]Brief version of LBL-9154.3. A COMPARISON BETWEEN FLOW-THROUGH AND FLOW-BY POROUS ELECTRODES FOR REDOX ENERGY STORAGE[†]

James A. Trainham and John Newman

An a priori economic comparison was made between the two electrode configurations for flow redox battery applications: (i) the flow-through configuration (current parallel to the fluid flow) and (ii) the flow-by configuration (current perpendicular to the fluid flow). Steady-state computer models were developed for each electrode system. These models were used to produce current density, cell voltage, and power density over a complete cycle (charge and discharge). The economic comparison was made by optimizing each configuration with respect to an objective function appropriate for this application. In this case, only the variable costs were considered. The results of the optimization show that the flow-by configuration is superior. The flow-through configuration not only yields a lower return on investment, but it is impractical due to a requirement of extremely low flow rates ($Re < 0.001$). Its failure is due to current flow (and ohmic potential drop) in the same direction as the fluid flow.

* * *

[†]Brief version of LBL-9221.4. EXPERIMENTAL DETERMINATION OF CUPRIC ION DIFFUSIVITIES IN $CuSO_4/H_2SO_4/C_3H_5(OH)_3$ SOLUTIONS

Cecilia Mak and John Newman

Copper sulfate and sulfuric acid solutions are frequently used in electrochemical studies and applications. In many of these cases, special interest is placed on the viscosities and diffusivities of these solutions. To examine the effect of the solution viscosity on the system behavior, investigations were made with glycerol addition. Glycerol was used to increase solution viscosity

because it forms Newtonian solutions with water and was found to be electrochemically inert.

Densities, viscosities and limiting currents were measured on a rotating disk electrode for varying concentrations of copper sulfate, sulfuric acid and glycerol. With the use of the Levich equation, experimental diffusion coefficients were computed. A further attempt was made to correlate the Stokes-Einstein constant ($D\mu/T$) as a function of the concentrations of the component species in the solutions.

Improvements in Efficiency of Aluminum Reduction Cells

The research project has the objective of reducing the electrical energy consumed in the electrolytic production of aluminum by increasing the current efficiency of the cells in which this operation is carried out. The current efficiency falls short of 100% in such cells because of the turbulent transport of aluminum product, dissolved in the molten salt electrolyte, to the anode region where it is reoxidized. The predominant driving force for this transport is the electromagnetic force caused by the interaction of the current within the electrolyte and the magnetic fields generated by this current and currents in surrounding cell components.

1. CALCULATED CURRENT EFFICIENCIES FOR 185kA ALUMINUM CELLS WITH ALTERNATIVE BUS-BAR ARRANGEMENTS

Y. Zundelevich and J. W. Evans

A finite element procedure has been employed to solve the equation




$$\nabla^2 E = 0$$

for the electric potential distribution within a 185kA aluminum cell approximating a commercial design. The current density field within the electrolyte, molten metal and carbon cell lining was then found by application of the differential form of Ohm's law. Magnetic fields within electrolyte and metal were then calculated from the Biot-Savart law enabling the calculation of the electromagnetic stirring forces as the cross product of the current density and magnetic induction vectors. In such calculations, magnetic fields due to currents in conductors external to the cell were allowed for. Magnetic fields due to currents in some of these conductors are attenuated by the steel shell of the cell and this was allowed for by means of a shielding factor.

The electromagnetic force distribution was then substituted in the time averaged turbulent Navier-Stokes equations describing the motion of the electrolyte and metal. In conjunction with the time averaged continuity equation and the k- ϵ model for

the turbulent viscosity, these equations were then solved iteratively by a finite difference procedure to obtain the distribution of velocities within the two liquids as well as the distribution of the turbulence kinetic energy. Finally the mass flux of aluminum from the aluminum-electrolyte interface (and consequently the current efficiency) was calculated by an equation developed by Levich for mass transport from an interface where turbulence is damped by surface tension.¹

Figure 1 shows schematically three possible bus-bar arrangements whereby current passes from the cell on the right via a "riser" to that in the center and thence to that on the left. The shell and lining of the cell, as well as the electrolyte and metal pools, have been left out of the figure, and only four of the eighteen anodes in each cell are shown, in order to emphasize the bus-bar arrangement. Heavy lines represent conductors which are not shielded by the shell while the lighter lines represent shielded conductors. Broken lines are conductors in adjacent cells. Computed current efficiencies for the three possible arrangements are:

| | | | | | | |
|------------------------|---|------|---|------|---|------|
| |  | |  | |  | |
| Shielding factor | 0.1 | 0.4 | 0.1 | 0.4 | 0.1 | 0.4 |
| Current efficiency (%) | 88.4 | 88.7 | 89.3 | 89.4 | 87.9 | 88.0 |

The results reveal that there is little to choose between the three riser arrangements (which are common in industrial cells), at least as far as current efficiency is concerned. The calculated efficiencies lie in the range 80-95% commonly reported for industrial cells. The shielding factor is seen to have little influence on the current efficiency which is a valuable result since there is some question concerning an approximate value in the range 0.1-0.4.

The proximity of the bus-bar returning the current from the end of the line of cells is calculated to have a significant influence on current efficiency:

Distance of return bus from end of cell
(meters): 0.5 2.5 5.5

Current efficiency (%): 78.2 88.5 88.7

In many instances, current would return to the rectifier via another line of cells, rather than via a return bus-bar, and it is inferred from these calculations that the separation between the lines may have a significant influence on current efficiency.

* * *

1. Proceedings of the seminar "Heat and Mass Transfer in Metallurgical Systems," Dubrovnik, Yugoslavia, September, 1979, LBL-8519.

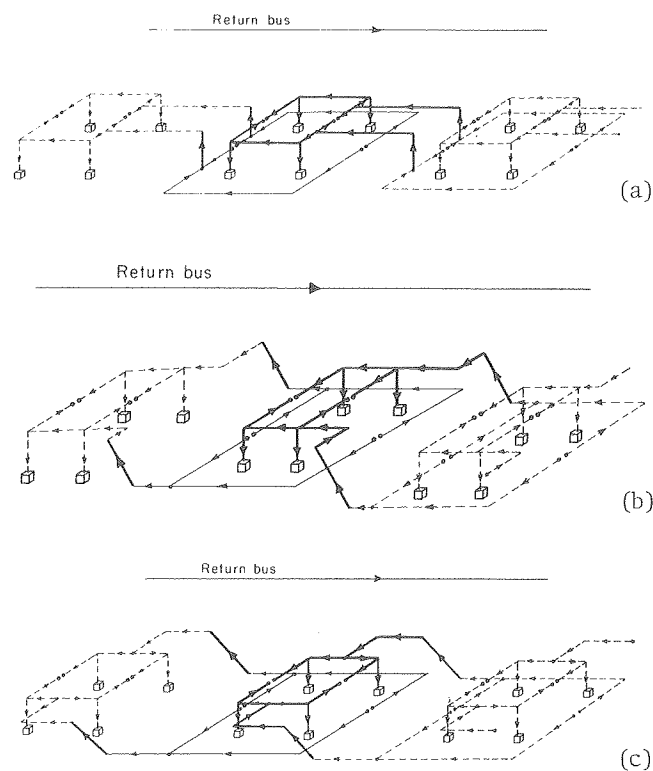


Fig. 1. Three possible bus-bar arrangements for aluminum reduction cells. [(a) XBL 7911-14526; (b) XBL 7911-14527; (c) XBL 7911-14525]

Engineering Analysis of Gas Evolution in Electrolysis

Gas evolution by electrolysis is one of the most common reaction types in electrosynthesis. As of late, electrically rechargeable batteries are under development which also develop gases on charge. This project is directed toward the physical description and correlation of the behavior of electrochemically-generated gas-electrolyte emulsions, including the effect bubble streams have on mass transport at electrode surfaces. Liberation of hydrogen or oxygen from various metallic surfaces, situated in a flow channel, is observed under intense illumination, over broad ranges of current densities and flow rates. The ohmic component of overpotential is measured and correlated to process conditions. Understanding the behavior of bubble streams should lead to improvements in the energy efficiency of gas generating processes.

1. GAS EVOLUTION IN FORCED FLOW[†]

Wing Hui and Charles W. Tobias

The channel flow apparatus developed earlier in this laboratory has been employed for measuring the effect of flow (0-135 cm/sec in 6x10 mm cross section) on the effective overpotential of hydrogen evolving in nickel in 5 M KOH at current densities up to 2.0 amperes/cm². The capillary junction connecting to an Hg/HgO,OH⁻ reference electrode was

situated directly in line with the leading edge of the 5x5 mm Ni cathode; a 125 μm diameter hole was drilled in the transparent plexiglass wall for this purpose. A Bolex H 16 camera was used to take magnified observations of gas bubbles evolved at low current densities ($< 10 \text{ ma/cm}^2$) in stagnant electrolyte. At higher current densities, and in flowing electrolyte, a Hycam movie camera, capable of up to 10,000 frames per second, was employed.

Surfaces of the nickel cathodes were either (a) polished with 1 μm diamond paste, (b) sanded with 100 grit sandpaper at 90° to the direction of the flow, or (c) sanded parallel to the flow. The IR components were measured by an interruptor technique. Figure 1 illustrates the effect of flow on the incremental ohmic resistance, $(\Delta IR)_B$, caused by bubbles in the immediate vicinity of the cathode. The high values of $\Delta (IR)_B$ on the smooth surface may be explained by relatively lower number of nucleation sites and longer residence times, both of which were demonstrated in the motion pictures taken. At low current densities the effect of flow on reducing the ohmic drop is much less important.

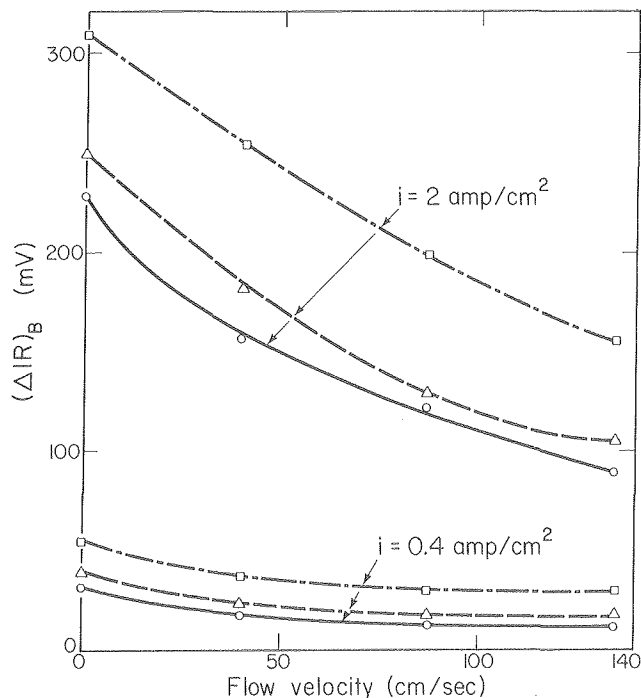
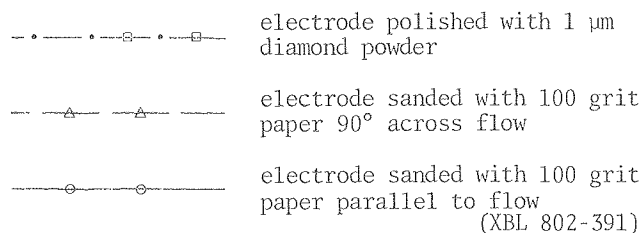


Fig. 1. The effect of flow on the incremental ohmic resistance caused by gas bubbles at the electrode surface. Hydrogen evolution is 5 M KOH, 5x5 mm electrode coplanar with 10 mm wide channel of 6x10 mm cross section.



The effect of flow on the concentration overpotential associated with the discharge of water to hydrogen shows an interesting pattern: due to the stirring effect of bubbles in free convection, only concentration overpotentials observed at current densities below about 40 ma/cm^2 are reduced by forced flow. At higher current densities, although the ohmic drop due to bubbles is reduced by flow, the concentration overpotential is not. It is a well known fact that the free convection generated by gas evolution is one of the most effective stirring mechanisms to enhance mass transport to and from electrode surfaces.

* * *

†Supported by the Division of Industrial Energy Conservation, Office of Conservation and Solar Energy, U.S. Department of Energy.

RESEARCH PLANS FOR CALENDAR YEAR 1980

1. SURFACE MORPHOLOGY OF METALS IN ELECTRO-DEPOSITION

C. W. Tobias, Investigator

The mechanism responsible for the initiation and propagation of grooved, striated deposits will be evaluated by artificially induced secondary flows. The deposition of copper and zinc from acid solutions will receive continued emphasis. A planar electrode, up to 30 cm long, imbedded into the walls of a flow channel, will serve as test geometry. To identify the initial step in the formation of deposits which contain imprints of hydrodynamic events, the dependence of frequency of nucleation on concentration and on small variations of surface potential will be studied on rotating disk electrodes. The purpose of this investigation is to understand in a quantitative sense the steps involved in the evolution of surface morphology in thick metallic deposits and to establish regimes of operational conditions in which deposits of acceptable character may be obtained.

2. ANODIC SURFACE LAYERS ON BATTERY MATERIALS

R. Muller, Investigator

Surface layers on lithium in non-aqueous solvents of interest in battery technology will be investigated. Techniques for the preparation of polished metal surfaces and anhydrous solutions have been developed. Of particular interest is a characterization of the effect of solvents and solutes on the properties of the layers in order to predict and control the electrochemical behavior of the films, and to find means to cycle electrodes.

Installation of a digital data acquisition system for the efficient evaluation of transient and spectroscopic measurements will be completed.

3. ANALYSIS AND SIMULATION OF ELECTROCHEMICAL SYSTEMS

J. Newman, Investigator

Experimental work on the removal of lead ions with a high pressure electrochemical reactor will continue with the goal of providing a firm basis for design and scale-up. A mathematical model will be developed for the Fe(0)/Fe(II)/Fe(III) energy storage system. Experimental work will continue on the characterization of cupric ion diffusivities in $\text{CuSO}_4/\text{H}_2\text{SO}_4/\text{C}_3\text{H}_5(\text{OH})_3$ solutions.

4. METAL COUPLES IN NON-AQUEOUS SOLVENTS

C. W. Tobias, Investigator

Further refinements are to be introduced in the (propylene carbonate) solvent purification steps, and simple practical methods will be evaluated for the routine characterization of the treated solvent. The thin protective layers detected on potassium in propylene carbonate by the chronopotentiometric technique will be studied using parallel electrochemical and ellipsometric measurements. As a first step in this investigation lithium metal will be employed instead of potassium, because of the relative ease of obtaining smooth, bright surfaces on lithium as against on potassium. Propylene carbonate is one of the more interesting organic ionizing media for potential use in galvanic cell and electrosynthesis applications.

5. CURRENT INEFFICIENCIES IN ALUMINUM REDUCTION CELLS

J. Evans, Investigator

The calculations of the type described will be extended to cells of the end-to-end configuration and the effect of other changes in cell design on current efficiency will be computed. It is planned to do preliminary work on the electromagnetically driven oscillation of the electrolyte-metal interface. Energy consumption in the cells could be reduced by reducing the separation of the anodes from this interface. The lower limit on this separation is imposed by the oscillation since a short circuit exists when the anode contacts the metal. Development of cell designs where such oscillation is minimized should therefore enable reductions in energy consumption.

6. ENGINEERING ANALYSIS OF GAS EVOLUTION

C. W. Tobias, Investigator

Effect of low, current density and electrode surface texture on the ohmic- and mass transfer-component of overpotential will be measured, and high-speed motion picture records will be taken of the gas evolving electrode surface in our flow channel apparatus. A mosaic-electrode, composed of $100 \times 100 \mu\text{m}$ surface elements, separated by $1 \mu\text{m}$ insulating strips, will be developed to study in detail the effect of bubble separation and coalescence on the mass transport boundary layer over the surrounding surface regime. For each electrode element of the mosaic, we will be able to measure and control the current and/or the potential. It is expected that the precise location of a nucleation event, and the rate of growth of bubbles at any and all mosaic elements, will be predetermined. Certain mosaic elements will be used only for reference electrode purposes, or for measuring limiting current of indicating ions. This detailed mechanistic evaluation of the behavior of gas bubble assemblages, and their effect on mass transfer boundary layers, is expected to open up novel approaches for electrode design, and, through this, for the optimization of gas evolving electrolysis processes.

7. ELECTRODE PROPERTIES, ELECTRIC BEHAVIOR AND MICROSTRUCTURE OF NASICON

L. C. De Jonghe, Investigator

Electrochemical storage systems continue to be viable and potentially economical devices for load leveling or for vehicle propulsion. One of the more attractive systems is based on the sodium/sulfur electrochemical couple with a ceramic electrolyte. To date, sodium-beta" alumina is the most developed ceramic electrolyte, and construction is now underway of modules to be tested in the next few years in the Battery Energy Storage Test Facility. The search for fast ion conductors is continuing to provide alternatives to the sodium-beta" alumina ceramic electrolytes. One of these is the three-dimensional sodium ion conductor Nasicon, $(\text{Na}_{1+x}\text{Zr}_2\text{Si}_x\text{P}_{3-x}\text{O}_{12})$. Nasicon possesses some advantage, especially in the fabrication stage, over beta" alumina. Its resistivity is potentially lower at 300°C than that of sodium-beta" alumina polycrystalline electrolyte. The research intends to examine the properties of Nasicon so that they can be critically compared with sodium-beta" alumina solid electrolytes. The nature of microstructural transformations, and of microstructural

inhomogeneities that occurred as a result of preparation will be examined by transmission electron microscopy. Further, the tolerance of this solid electrolyte to impurities will be compared to that of sodium-beta alumina. In the near future, this research intends to clarify the microstructure-properties relationship of Nasion and to characterize the ionic conduction processes by means of dispersive measurements, as well as to examine the electrode polarization phenomena that occur at clean electrodes.

8. REVERSIBLE AIR ELECTRODES FOR METAL-AIR BATTERIES

P. Ross, Investigator

The objective of this program is to examine in detail the oxygen reduction and oxygen evolution reactions in alkaline electrolyte on selected electrocatalyst surfaces. More than a decade of hydrogen-air fuel cell research and development has led to the general conclusion that the most cost-effective electrocatalyst is a highly active metal dispersed on a high surface area, stable, conducting substrate. In the reversible oxygen electrode, the substrate must be structurally stable over the entire potential range for both oxygen reduction and oxygen evolution, typically 0.8-1.6 V (RHE). Graphitic carbon blacks appear to be the best support for dispersing metal electrocatalysts and meet this stability requirement. As an example of this concept, state-of-the-art phosphoric acid fuel cell electrodes with only 0.1 mg Pt/cm² when used as an electrode in KOH discharge oxygen at better than 50 ASF at 0.85 V (RHE), an effective catalyst cost of only \$2/kW capacity. Even lower cost should be possible since other metals or combinations of metals may be more cost effective than Pt in alkaline electrolyte. It is anticipated that multi-metallic clusters dispersed on carbon will be the most active and cost-effective type of electrocatalyst.

Detailed kinetic studies will be conducted of the oxygen reduction and oxygen evolution reactions on clean, well-characterized Group VIII and IB metals in KOH using rotating ring-disk electrode techniques. The most active metals in both the charge and discharge mode will be used to catalyze a pyrolytic graphite rotating disk electrode in binary and ternary combinations by electrodeposition. The charge and discharge polarization behavior using these supported multi-metallic clusters will be determined and the stability of the performance over repeated cycling will also be examined. If the initial, proof of concept phase is successful, practical reversible air electrodes using high surface area carbons will be tested employing hydrophobic, PTFE bonded structures.

1979 PUBLICATIONS AND REPORTS

Refereed Journals

- [†]1. Frank R. McLarnon, Rolf H. Muller, and Charles W. Tobias, "Interferometric Study of Forced Convection Mass Transfer Boundary Layers in Laminar Channel Flow," *I&EC Fundamentals* 18, 97 (1979).
2. John Newman, "Optimization of Potential and Hydrogen Utilization in an Acid Fuel Cell," *Electrochem. Acta* 24, 223 (1979).
3. Richard Pollard and John Newman, "Transport Equations for a Mixture of Two Binary Molten Salts in a Porous Electrode," *J. Electrochem. Soc.*, 126, 1713-1717 (1979).
- [†]4. J. W. Evans and C-H. Koo, "Structural and Reduction Characteristics of Some Venezuelan Iron Ores," *Trans. Iron Steel Inst. Japan*, 19, 95 (1979).
- [§]5. J. W. Evans and B. J. Sabacky, "Electrodeposition of Metals in Fluidized Bed Electrodes; Part I, Mathematical Models," *J. of the Electrochem. Soc.* 126, 1176 (1979).
- [§]6. J. W. Evans and B. J. Sabacky, "Electrodeposition of Metals in Fluidized Bed Electrodes; Part II, An Experimental Study of Copper Electrodeposition at High Current Densities," *J. of the Electrochem. Soc.* 126, 1180 (1979).
- ^{||}7. J. W. Evans and C. A. Natalie, "The Influence of Lime Properties on the Rate of Dissolution in CaO-FeO-SiO₂ Slags," *Ironmaking and Steelmaking*, 6, No. 5, 101 (1979).
- [†]8. J. W. Evans and M. Ranade, "The Grain Model for Gas-Solid Reactions: A Refined Approximate Solution to the Equations," *Chem. Eng. Sci.*, in press (1979).
- [†]9. J. W. Evans and M. Ranade, "The Reaction Between a Gas and a Solid in a Non-Isothermal Packed Bed: Simulation and Experiments, I. and E. C. Process Design and Development," in press (1979).
- [†]10. J. W. Evans and A. Malazgirt, "Production of Aluminum and Aluminum Coatings by Thermal Decomposition of Aluminum Alkyls, Metallurgical Transactions," in press (1979).
11. J. W. Evans, A. Sarin, and M. Abbasi, "A Monte Carlo Simulation of the Diffusion of Gases in Porous Solids," *J. of Chem. Phys.*, in press (1979).

Other Publications

1. William H. Tiedemann and John Newman, "Mathematical Modeling of the Lead-Acid Cell," Sidney Gross, ed., *Proceedings of the Symposium on Battery Design and Optimization*, pp. 23-38, The Electrochemical Society, Inc., Princeton, (1979).

2. William H. Tiedemann and John Newman, "Current and Potential Distribution in Lead-Acid Battery Plates," Sidney Gross ed., Proceedings of the Symposium on Battery Design and Optimization, pp. 39-49, The Electrochemical Society, Inc., Princeton, (1979).

†3. J. W. Evans and C-H. Koo, "The Reduction of Metal Oxides," in Rate Processes of Extractive Metallurgy, edited by Sohn and Wadsworth, Plenum, New York, (1979).

LBL Reports

†1. J. B. Riggs, R. H. Muller, and C. W. Tobias, "A Model for Prediction of Work Piece Geometry for Electrochemical Hole Sinking," submitted for publication to *Electrochimica Acta*, LBL-6282 Rev., December 1979.

†2. Paul J. Sides and Charles W. Tobias, "Primary Potential and Current Distribution Around a Bubble on an Electrode," accepted for publication in the *J. Electrochem. Soc.*, LBL-8745, March 1979.

†3. Karrie Jo Hanson, "Interferometric Study of Mass Transfer Enhancement by Turbulence Promoters," M.S. thesis, (co-directed with R. H. Muller), LBL-9038, April 1979.

4. Henry H. Law, "Studies on the Electrochemical Behavior of Potassium in Propylene Carbonate," Ph.D. thesis, LBL-9207, May 1979.

†5. John F. Cooper, Rolf H. Muller, and Charles W. Tobias, "Periodic Phenomena During Anodic Dissolution of Copper at High Current Densities," submitted for publication to the *J. Electrochem. Soc.*, LBL-9404 Rev., December 1979.

†6. Suen-Man G. Yu, Philip N. Ross, and Charles W. Tobias, "An Investigation of the Degradation of Propylene Carbonate by Chlorine," LBL-10069, November 1979.

7. James Arthur Trainham, III, "Flow-Through Porous Electrodes," Ph.D. thesis, LBL-9565, August 1979.

8. James A Trainham and John Newman, "A Comparison between Flow-Through and Flow-by Porous Electrodes for Redox Energy Storage," LBL-9331, June 1979.

9. R. Pollard and J. Newman, "Silicon Deposition on a Rotating Disk," LBL-9154, May 1979.

10. J. W. Evans, J. A. Little, and K. Westmacott, "Early Stages of Reduction of Nickel and Oxide Single Crystals: An Investigation by Transmission Electron Microscope," LBL-10176.

Invited Talks

1. C. W. Tobias, "A Close Look at Electrolyte Gas Evolution," Symposium on Electrochemical Reaction Engineering, sponsored by the Society of Chemical Industry and the Institution of Chemical Engineers, University of Southampton, England, April 18-20, 1979.

†2. C. W. Tobias, "Gas Evolution at Electrodes," Bell Laboratories, Murray Hill, New Jersey, May 4, 1979.

3. M. Jaksic and C. W. Tobias, "Hydrodynamic Flow Visualization by the Electrochemical Method," Sixth Yugoslav Symposium on Electrochemistry, Dubrovnik, Yugoslavia, June 1979.

†4. P. J. Sides and C. W. Tobias, "Primary Potential and Current Distribution Around a Bubble on an Electrode," 156th Meeting of the Electrochemical Society, Los Angeles, October 14-19, 1979.

5. G. A. Prentice and C. W. Tobias, "Simulation of Electrode Profiles Undergoing Deposition or Dissolution," 156th Meeting of the Electrochemical Society, Los Angeles, October 14-19, 1979.

6. W. H. Tiedemann and J. Newman, "Nonuniform Current and Potential Distribution in Composite Sheet Type Battery Electrodes," Los Angeles Meeting of the Electrochemical Society, October 18, 1979.

7. R. Pollard and J. Newman, "Mathematical Modeling of the Lithium/Iron Sulfide Battery," Los Angeles Meeting of the Electrochemical Society, October 19, 1979.

8. R. H. Muller and R. D. Peters, "Ellipsometry of Sulfate Films on Lead," Electrochemical Society Meeting, Los Angeles, October 14-19, 1979, Abstract No. 93 (LBL-9265).

9. J. W. Evans, "Magnetic Fields, Current Densities, Melt Velocities and Current Efficiencies in Hall-Heroult Cells--Computations and Comparisons with Measurements," Seminar on Heat and Mass Transfer in Metallurgical Systems, Dubrovnik, Yugoslavia, September 1979.

10. J. W. Evans, "Computation of Melt Velocities and Current Efficiency in Hall-Heroult Cells," The Electrochemistry Society Meeting, Boston, May 1979.

11. J. W. Evans, "Computation of Mass Transport and Current Efficiencies in Hall-Heroult Cells," International Society of Electrochemistry Meeting, Trondheim, Norway, August 1979.

12. J. A. Little, "The Physical and Chemical Properties of Copper β -alumina," The International Conference on Fast Ionic Conduction in Solid Electrolytes and Electrodes, Lake Geneva, Wisconsin, May 1979.

13. R. H. Muller, "Development of Electrochemical Synthesis and Energy Storage," program review, Division of Energy Storage Systems, Office of Conservation and Solar Energy, DOE, Washington, DC, September 20, 1979.

14. R. H. Muller, "Aqueous Battery Studies at Lawrence Berkeley Laboratory," DOE Battery and Electrochemical Contractors Conference, Arlington, Virginia, December 10-12, 1979.

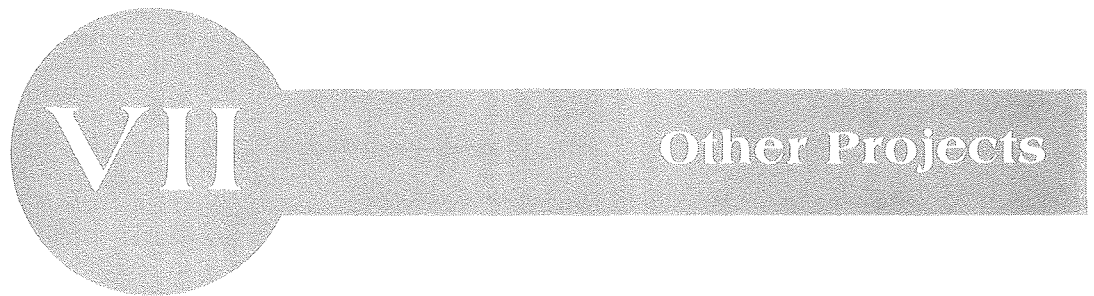
* * *

†This work was supported by the Division of Materials Sciences, Office of Basic Energy Sciences, U. S. Department of Energy.

‡This work was supported by the National Science Foundation.

§This work was supported by the U. S. Bureau of Mines.

||This work was supported by the American Iron and Steel Institute.



VII Other Projects

Other Projects

a. Solution Thermodynamics of Sulfites and Sulfite Oxidation Mechanisms*

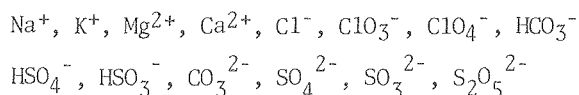
Leo Brewer and Robert Connick, Investigators

1. THERMODYNAMIC PROPERTIES OF MULTICOMPONENT AQUEOUS SOLUTIONS OF ALKALI AND ALKALINE EARTH SULFITES, SULFATES, AND HALIDES†

G. Rosenblatt

One of the critical problems of the operation of limestone flue gas desulfurization systems is the control of precipitation of calcium sulfite and sulfate so as to avoid coating of the limestone that would interfere with its efficient utilization. Because of changing salt concentrations due to accumulation of various halogen and nitrogen anions together with sodium and potassium cations and varying pH and bisulfite concentration due to variations in the sulfur content of the coal, it is necessary to know the thermodynamic properties of these complex salt mixtures to be able to control the behavior of the process to maintain optimum performance.

The extended Debye-Hückel theory of Pitzer and coworkers¹ was used to estimate activity coefficients in complex electrolyte solutions at 25-55°C. A computer program was developed to calculate the activity coefficients up to high ionic strength in aqueous mixtures containing any combination of the following ions:



* * *

†Brief version of LBL-9671.

1. L. F. Silvester and K. S. Pitzer, *J. Soln. Chem.* **7**, 327 (1978) and earlier papers of the series.

2. THERMODYNAMIC PROPERTIES OF SOLID PHASES OF THE CaSO_3 - CaSO_4 - H_2O SYSTEM†

B.-J. Lin and Leo Brewer

A review of the literature for the Ca-S-O-H system indicated many contradictions which could possibly be reconciled if one recognized the existence of solid solutions of calcium sulfite and calcium sulfate. Subsequently confirmations^{1,2} were found of the existence of such solid solutions. A program is underway to determine the thermodynamic

properties of these solid solutions for the hydrate and for the anhydrous phases. The partial pressure of water in equilibrium with the hydrate and anhydrous phases is being determined through use of a thermal balance in a controlled water vapor atmosphere.

In preparation for the treatment of the equilibria between the hydrated solid solutions of calcium sulfite and calcium sulfate and various aqueous salt solutions and the equilibria between the anhydrous solid solutions and the vapor phase, thermodynamic data have been compiled for the various species of the Ca-O-S-H system that might play a role.

* * *

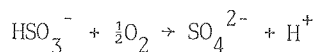
1. R. H. Borgwardt, Pilot Support at Research Triangle Park, N. C., Summary of Research Related to Process Improvement of Lime/Limestone Scrubbing Process, November 1973.

2. K. Setoyama and S. Takahashi, *Yogyo-Kyokai-Shi* **88**, 244 (1978).

3. THE KINETICS OF OXIDATION OF BISULFITE ION BY OXYGEN

Thomas G. Braga

The oxidation of bisulfite ion to sulfate ion by oxygen



is of importance in flue gas desulfurization processes as well as in pollution arising from sulfur dioxide. Although many studies have been made of its rate, the rate law and mechanism are still not established. The difficulty arises from the reaction being a chain reaction and therefore subject to catalysis and/or inhibition by many substances. It is our aim in the present study to produce initiation and termination by substances deliberately added, and thus to investigate the reaction under controlled conditions.

In beginning the study, the method of measurement adopted was to follow the rate of absorption of oxygen gas as the solution was violently agitated, the method used by most previous investigators. Results were obtained for the rate when sulfite ion was the starting species for comparison with the work of others who have generally worked with

*This work was supported by the Morgantown Energy Technology Center, U. S. Department of Energy.

this species. In addition, the rate of uptake of oxygen by de-gassed water was measured. Comparison of the two showed that oxygen was absorbed by water considerably more slowly than by the sulfite solutions, a result which leads to the conclusion that in the sulfite experiments the aqueous solution is not saturated with oxygen. Therefore, in the sulfite experiments the rate of absorption of oxygen is in part mass-transfer controlled, rather than kinetically controlled. The result throws into doubt many earlier conclusions reached about rates and rate laws for the rate of oxidation of sulfite ion by oxygen. It may be noted that chemical engineers working with this reaction were aware of the problem, unlike chemists who did not seem to know about it.

RESEARCH PLANS FOR CALENDAR YEAR 1980

Studies will be made of the rate of oxidation of bisulfite ion by oxygen in aqueous solutions in order to determine rate laws and mechanisms. Attempts will be made to control both the initiation and termination steps of this chain reaction in order to eliminate extraneous effects from impurities. Once controlled conditions are established, catalytic effects of a variety of substances --particularly certain transition metal ions--will be investigated.

The computer program for calculation of thermodynamic properties of aqueous salt solutions will be extended to include weak acid interactions. The thermodynamic measurements on solid solutions of sulfites and sulfate will be extended to higher temperatures and combined with the complete tabulation of thermodynamic values of related compounds.

1979 PUBLICATIONS AND REPORTS

Other Publications

[†]1. R. E. Connick and T. G. Braga, "Solution Thermodynamics of Sulfites and Sulfite Oxidation Mech-

anisms," Quarterly Report - July, August, September 1979.

[†]2. L. Brewer, "Thermodynamic Properties of the Ca-S-O-H System," Quarterly Report - July, August, September 1979.

LBL Reports

1. G. Rosenblatt, "Estimation of Activity Coefficients in Concentrated Sulfite-Sulfate Solutions," submitted to AIChE, LBL-9671.

2. B. Meyer, M. Ospina, and L. Peter, "Raman Spectrometric Determination of Oxysulfur Anions in Aqueous Systems," submitted to Anal. Chem. Acta, LBL-9974.

Invited Talks

1. Robert E. Connick and Thomas M. Tam, "Species in Aqueous Solutions of Sulfur Dioxide," Gas Desulfurization Conference, Morgantown, West Virginia, June 7-8 1979.

2. Leo Brewer, "CaO/SO₂/H₂O System," Gas Desulfurization Conference, Morgantown, West Virginia, June 7-8 1979.

3. Leo Brewer, "Present and Future Energy Demands on Thermodynamics," High-Temperature Symposium, Richland, Washington, June 13-15 1979.

* * *

[†]Supported by Morgantown Energy Technology Center, U. S. Department of Energy.

b. Process Chemical Parameters in Aqueous Sulfur Dioxide Removal by Lime/Limestone Scrubbers*

Beat Meyer and Robert E. Connick, Investigators

1. THE REACTION OF AMMONIA WITH SULFUR DIOXIDE[†]

H. Weeks,[‡] B. Mulliken,[§] and B. Meyer

IR and Raman spectroscopy were used to follow the reaction of sulfur dioxide and ammonia in rare gas matrices, liquid ammonia, liquid sulfur dioxide and aqueous solution. We have now reached a milestone in this five year study. We know, for example, that HNSO appears as an intermediate in matrices. In liquid ammonia the reaction consists of auto-redox disproportionation of sulfur dioxide yielding sulfate, thiosulfate, polythionates, elemental sulfur, and eventually deeply colored purple S_x^- radicals. Ammonia serves as a catalyst without entering products. In liquid sulfur dioxide the reaction yields a series of sulfur-nitrogen bonded compounds comprising various oxidation states.

* * *

[†]Brief version of LBL-8098 and LBL-8098 Rev.

[‡]Permanent address: Physics Department, University of California, Berkeley.

[§]Permanent address: Chemistry Department, University of Washington, Seattle.

2. RAMAN SPECTROMETRIC DETERMINATIONS OF AQUEOUS SULFUR OXYANION[†]

M. Ospina, L. Peter,[‡] and B. Meyer

Relative intensities were measured and absolute Raman scattering intensities were estimated for sulfate, bisulfate, dithionate, sulfite, sulfur dioxide, bisulfite, disulfite, thiosulfate, dithionite, trithionate, polythionates, and polysulfides. The purpose of this work is to make it possible to identify and determine species in situ in complex mixtures during reactions involving different sulfur species. The results of this work are being applied in work dealing with sulfur dioxide abatement reactions and kinetics, in a study of the Wackenroder reaction and in the decomposition study of thiosulfate and similar systems. Figure 1 (see article 3) shows the power of this method for thermal disproportionation of bisulfite-disulfite mixtures, containing sulfur dioxide and yielding sulfate. All species can be clearly identified in the mixture, and their concentration can be derived by comparing the scattering intensities of their peaks with the water serving as an internal standard.

* * *

[†]Brief version of LBL-9974.

[‡]Permanent address: Seattle Pacific University.

3. CHEMISTRY OF AQUEOUS OXYACIDS OF SULFUR

L. Peter,[†] M. Ospina,[‡] M. Hinnawi,[‡] T. Burner,[‡] M. Rigdon,[‡] L. Ugham,[‡] A. Tini,[‡] and B. Meyer

Several milestones were reached in these studies: Raman spectra show that dithionite ion, which has C_2 structure in all its known salts, changes reversibly to the C_{2h} structure in aqueous solution. The latter symmetry corresponds to the structure of isoelectronic P_2F_4 and other similar ions, and explains much of the unusual chemistry of dithionite.

Isotopic work with ^{15}N , ^{18}O , D and ^{34}S has helped assign several vibrational bands in the disulfite ion ($S_2O_5^{2-}$) and this has ultimately helped to analyze disulfite, bisulfite (HSO_3^-), and sulfite (SO_3^{2-}).

Mixed thiosulfato-cyano complexes of copper, silver and gold were analyzed in solution. Raman spectra indicate that these systems contain at least three different kinds of species. This means that a terminal sulfur serves as ligand contact.

It was also found that the thermal auto-redox disproportionation of sulfite and disulfite occurred at lower temperature and with greater speed than formerly proven, evidenced by the Raman spectroscopy of Fig. 1. Furthermore, ammonia and traces of vanadium or other catalysts are sufficient to cause 90% decomposition of the 1M disulfite solution at 90°C within 24 hours.

As shown in Fig. 1, the first spectrum was taken after 1 hour at 160°C. The water band at 1650 cm^{-1} was used to calibrate the spectrum. The spectrum shows mainly HSO_3^- with some $S_2O_5^{2-}$ and some SO_2 . The sulfate peak appears as a very weak shoulder. After 4 hours the second spectrum is unchanged, except for the sulfate peak which is about 4 times stronger. The third spectrum taken after 8 hours shows an increase in the sulfate spectrum as well as the sulfur dioxide spectrum. The water peak shows that the spectrum was recorded at lower sensitivity. Yellow sulfur, the reduced product, separates as a second liquid phase. Its spectrum is not shown, as it does not appear in the aqueous phase. After 23 hours the fourth spectrum is dominated by the sulfate and sulfur dioxide. The fifth spectrum shows that the thermal decomposition of sulfite [sulfur(IV)] is almost completed. The sulfate concentration is close to saturation. When solid sodium sulfate precipitates, the intensity of the sulfate ion in solution is no longer representative of the total sulfate formed.

* * *

[†]Permanent address: Seattle Pacific University.

[‡]Permanent address: Chemistry Department, University of Washington, Seattle.

*This work was supported by the Morgantown Energy Center, U. S. Department of Energy.

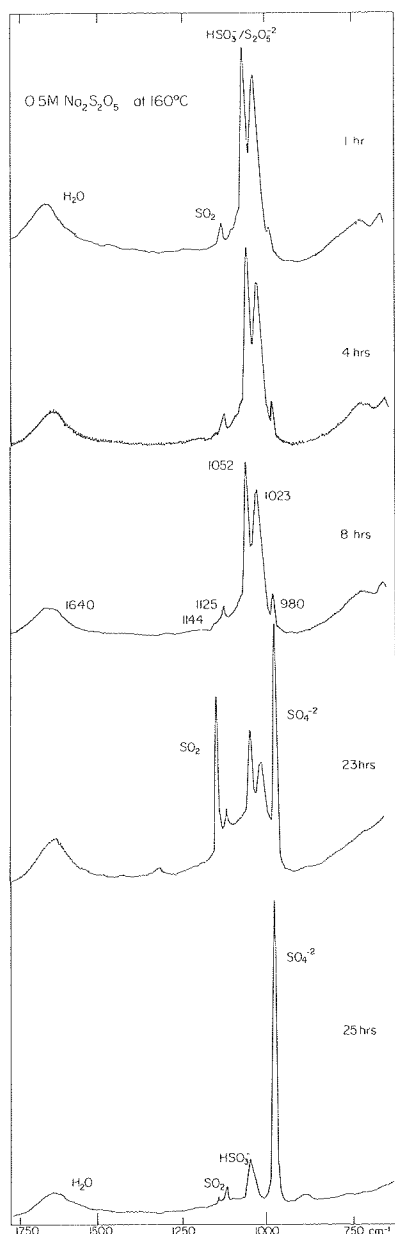


Fig. 1. Raman spectrum of a 1M $\text{Na}_2\text{S}_2\text{O}_5$ solution in a sealed pyrex tube. (XBL 7912-13657)

4. CHEMISTRY OF WASTE SULFUR UTILIZATION[†]

K. Woo,[‡] W. Johns,[§] M. Rigdon,^{||} and B. Meyer

Interdisciplinary work continues to help correlate some of our basic research findings with work of scientists in other fields. Chemical reasoning was used to assist the Federal Highway Administration and its contractors to identify polysulfides, vinyl and aromatic species as sulfur polymer stabilizers in non-petroleum base highway pavement mixtures containing 85% elemental waste sulfur. Highway test sections have been built in Texas, Washington, Canada, and France.

The chemical interaction of sulfur oxyacids with wood and urea-formaldehyde resin adhesives and insulating foams was studied in cooperation with the forest products departments at U.C. Berkeley and Washington State University. The chemical bonding properties have been related to mechanical and environmental (i.e., odor) properties of products. This work has led to the development of a new model for the formaldehyde release mechanism for home foam insulation and particle board. This work has been partially covered in the book listed under references (see this report).

* * *

[†]Brief version of LBL-9396.

[‡]Permanent address: Physics Department, University of California, Berkeley.

[§]Permanent address: Forest Products Laboratory, University of California, Berkeley.

^{||}Permanent address: Chemistry Department, University of Washington, Seattle.

RESEARCH PLANS FOR CALENDAR YEAR 1980

A systematic study of the effect of concentration, temperature, and catalysts will be made of the auto-redox decomposition of sulfur(IV) to establish the kinetics and identify the reaction mechanism. Other systems relevant to the determination of process parameters for sulfur dioxide scrubbing by lime/limestone will be studied for DOE Morgantown. Among the factors considered in this continuing study will be the kinetics and mechanism of bisulfite, sulfite, and sulfate complexation; the kinetics of calcium sulfate and sulfite precipitation; sulfur(IV) and sulfur(VI) metal ligand reactions; and sulfur(IV) oxidation. This work will remain in close contact with complementary work conducted by L. Brewer and R. E. Connick.

Research on metal-sulfur oxyacid ligand systems, especially silver thiosulfato complexes, will be continued to determine the influence of the metal-ligand interaction on redox processes within the molecules, and between complex and solution, in order to identify the mechanism of catalysis.

Interdisciplinary research will center on reactions of sulfur(IV) as recovered from sulfur dioxide abatement systems, to establish possible utilization paths which are environmentally more acceptable than their precursors.

1979 PUBLICATIONS AND REPORTS

Refereed Journals

1. B. Meyer, L. Peter and C. Shaskey-Rosenlund, "Raman Spectra of Isotopic Bisulfite and Disulfite Ions in Alkali Salts and Aqueous Solutions," *Spectrochim. Acta.* **35**, 347 (1979).
2. B. Meyer, "Geochemical and Cosmochemical Cycles Involving Sulfur, Sulfide, Sulfite and Sulfate," *Geochim. Cosmochim. Acta* **43**, 1579 (1979).

Other Publications

1. L. Peter, "Oxyacids of Sulfur," Ph.D. thesis, University of Washington, Seattle, WA (August 1979).
2. B. Meyer, "Urea-Formaldehyde Resins," (Addison Wesley, Reading, Massachusetts, 1979).
3. B. Meyer, "Formaldehyde Release from Urea-Formaldehyde Systems," in Proceedings of 13th Int. Conference on Particleboard; Washington State University, Pullman, WA, T. Maloney, ed., p.239, (1979).
3. B. Meyer, "Energy and Environmental Chemistry," Federal Institute for Reactor Research, Wuhrenlingen, Switzerland, May 28, 1979.
4. B. Meyer, "Aqueous Chemistry of Sulfur Dioxide," Clemson University, May 8, 1979.
5. B. Meyer, "Redox Disproportionation of Sulfur (IV)," Gas Desulfurization Conference, Morgantown, West Virginia, June 7-8, 1979.

LBL Reports

1. B. Meyer, H. Weeks and B. Mulliken, "Reaction of Ammonia with Excess Sulfur Dioxide," LBL-8098, accepted for publication in Phosphorus and Sulfur.
2. B. Meyer, H. Weeks and B. Mulliken, "Reaction of Sulfur Dioxide with Excess Ammonia," LBL-8098 A, accepted for publication in Phosphorus and Sulfur.
3. M. Ospina, L. Peter and B. Meyer, "Raman Spectroscopic Determination of Sulfur Oxyacids," LBL-9974.
4. B. Meyer, K. Woo and W. Johns, "Formaldehyde Release from Sulfur Modified Urea-Formaldehyde Resin Systems," LBL-9396, accepted for publication in Forest Products Journal.
5. B. Meyer, "Elemental Sulfur and Sulfuric Acid," LBL-9875, entries in the World Encyclopedia, 1980.
6. B. Meyer, "Consultation on Sulfur Utilization," Conference and Field Demonstration of Sulfur Utilization in Highway Construction. (Sponsored by FHWA), Southwest Research Institute, San Antonio, Texas, July 9-10, 1979.
7. M. Hinnawi and B. Meyer, "Sulfato Complexes of Copper, Silver and Gold," ACS National Meeting, Washington, D.C., September 11, 1979.
8. L. Peter and B. Meyer, "Structure of Aqueous Dithionite and Dithionite Salts," ACS National Meeting, Washington, D.C., September 12, 1979.
9. M. Ospina and B. Meyer, "Raman Spectroscopic Determination of Sulfur Oxyions," ACS National Meeting, Washington, D.C., September 13, 1979.
10. H. Weeks, B. Mulliken and B. Meyer, "The Reaction of Ammonia with Sulfur Dioxide," ACS National Meeting, Washington, D.C., September 13, 1979.
11. B. Meyer, "Redox Reactions of Sulfur Oxyacids," Monsanto Chemical Co., St. Louis, Missouri, September 27, 1979.

Invited Talks

1. B. Meyer, "Formaldehyde Release from UF Systems," 13th Int. Conference on Particleboard, College of Engineering, Washington State University, April 5, 1979.
2. B. Meyer, "Sulfur Dioxide Abatement," U. S. Environmental Protection Agency, Cincinnati, Ohio, April 9, 1979.
12. B. Meyer, "Chemistry of UF Resins and F Release," Hearing: State of California, Joint Legislative Audit Committee, Sacramento, CA, November 8, 1979.
13. B. Meyer, "Chemistry of Formaldehyde," Hearing: U.S. Consumer Product Safety Commission, Portland, Oregon, December 13, 1979.

c. Coal Liquefaction Research

Heinz Heinemann, Investigator

1. CATALYTIC CRACKING OF n-HEXADECANE

W. McKee, A. T. Bell, and Heinz Heinemann

A study was undertaken to determine the effect of liquid water on the rate and product distribution obtained in the catalytic cracking of n-hexadecane over silica-alumina type catalysts. The hypothesis that an increase in Brönstedt acid sites might enhance cracking was not supported. In fact, the rate of cracking was less in the presence than in the absence of water. Two interesting observations were made: (1) Cracking occurred, though at very low conversions, at temperatures as low as 250°C. This has not been observed previously, probably due to lack of analytical tools to identify very small amounts of products. (2) While all of four catalysts tested gave more conversion in the absence of water and while conversion was,

as expected, a function of acid strength of the catalyst, one catalyst (Catalyst A: 75% silica, 25% alumina) gave a very different product distribution in the presence of water. All other catalysts in the presence or absence of water (and the catalyst A in the absence of water) showed product paraffin/olefin and straight chain/branched chain ratios consistent with a carbonium ion mechanism. Catalyst A in the presence of water gave product characteristics indicative of free radical cracking. Figure 1 shows the differences in product distribution. The gas chromatogram in (A) is for use of catalyst A in the absence and in (B) in the presence of water. The phenomenon observed has not yet been explained. Addition of a trace of an olefin to n-hexadecane in the presence of water to initiate carbonium ion formation did not change the appearance of a free radical type product distribution.

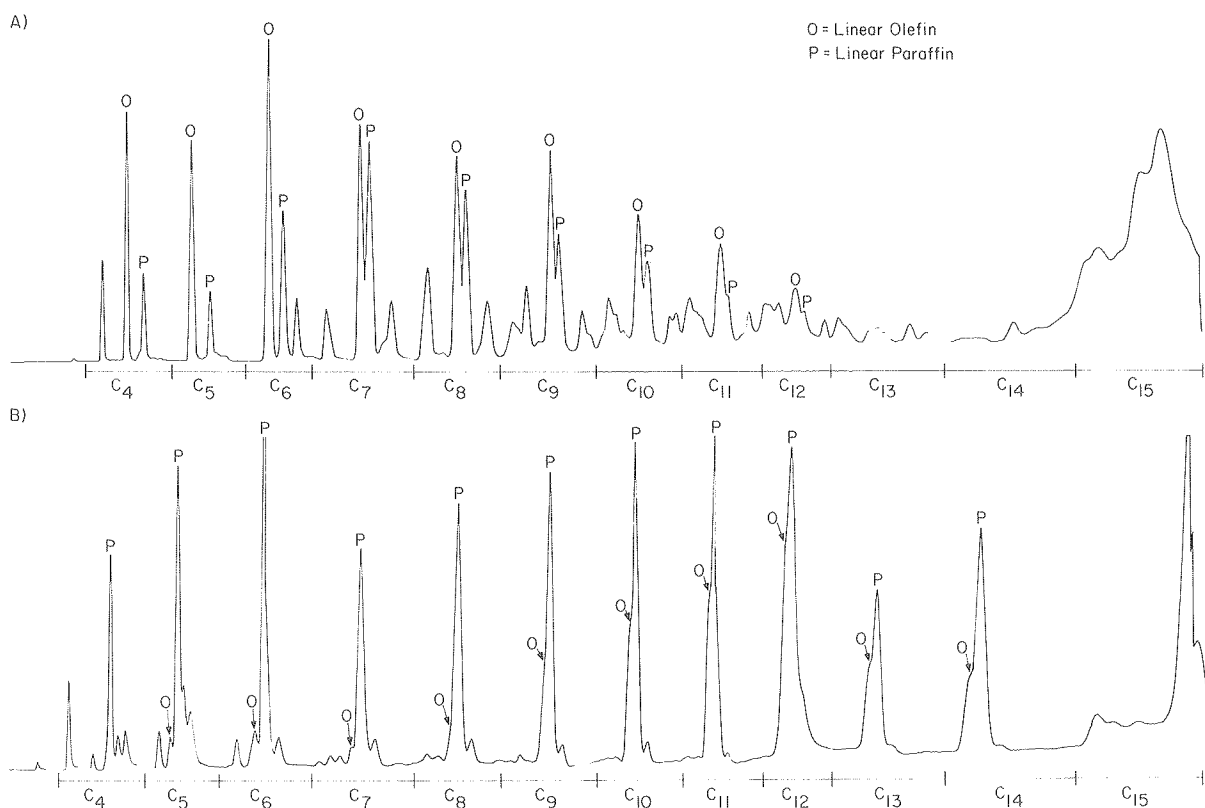


Fig. 1. Gas chromatogram of liquid products from n-hexadecane over Catalyst A. (A) Absence of water. (B) Presence of water. (XBL 798-10837)

* This work was supported by the Office of Fossil Energy through the Pittsburgh Energy Technology Center, U. S. Department of Energy.

2. FIXED BED AND SUSPENSION BED FISCHER-TROPSCH REACTION

W. McKee, A. T. Bell, and Heinz Heinemann

An isothermal reactor has been built, consisting of a very small diameter reactor tube connected to a high pressure flow system and maintained in a fluidized sand bath. Because of the high surface/volume ratio, exothermic reactions can be carried out without appreciable temperature rise in the reactor. This equipment will be used for research planned for 1980.

RESEARCH PLANS FOR CALENDAR YEAR 1980

The major emphasis will be directed toward determining causes for the different behavior of a gas-solid reaction compared to a gas-solid entrained liquid reaction in the Fischer-Tropsch reaction. It is known that the so-called "Kölbel" reactor can tolerate much higher CO/H₂ ratios than a gas-solid reactor. This is of major industrial importance, but the reasons for this behavior are not understood. They may rest in close temperature control; in dissolving coke or wax precursors in the liquid; or in different

diffusion rates of CO and H₂ from the liquid to the catalyst. Once causes of reactor behavior have been explained, better reactor design and use of more active catalysts may become possible.

1979 PUBLICATIONS AND REPORTS

Invited Talks

1. Heinz Heinemann, "Conversion of Methanol to Gasoline," Chemical Engineering Seminar, University of California, Berkeley.
2. Heinz Heinemann, "Shape Selective Catalysis," Catholic University of Louvain, Belgium.
3. Heinz Heinemann, "Major Industrial Catalytic Breakthroughs During the Last 40 years," Catholic University of Louvain.
4. Heinz Heinemann, "Chemistry of the Conversion of Methanol to Hydrocarbons," Riks University, Gent, Belgium.
5. Heinz Heinemann, "Chemicals Production From Coal," University of Liege, Belgium.

d. Thermodynamic Properties of Chemical Species in Nuclear Waste*

N. Edelstein, S. D. Brown, and R. J. Silva, Investigators

1. THEORETICAL STUDIES OF METAL COMPLEXATION AT STATIONARY ELECTRODES

R. M. Corn and S. D. Brown

The desire for a better understanding of the transport and adsorption properties of trace metals has led to attempts at identifying chemical species in dilute solution and defining their complexation thermodynamics. This is particularly true for the actinides involved in nuclear fuels, in view of their long lives and potential toxicity.

During the last six months, we have begun a study of the solution species of the actinides, concentrating our efforts on geologically significant ligands. At the start of this work it was observed that, despite numerous other studies of metal complexation using stationary electrodes, no theoretical basis existed. In fact, all previous work relied on theories suited to polarographic boundary conditions^{1,2} and these are not suited to stationary electrodes, where diffusion complicates the electrochemical response and produces asymmetric peaks.

To provide a sound theoretical basis for the analysis of our data, we have obtained equations that predict the response of the system as a function of metal-ligand thermodynamics and substitutional kinetics.

The theory involves an adaptation of the work of Saveant³ and Oldham,⁴ who convolute the linear scan waveform with $t^{-1/2}$, which removes the effects of semi-infinite diffusion and allows the solution of the Fick equations, with appropriate boundary conditions, to give:

$$E = E_{1/2}^R + \frac{RT}{nF} \ln \left(\frac{m^* - m(E)}{m(E)} \right)$$

where E is the potential, $E_{1/2}^R$ is the reversible half-wave potential, m^* is a constant, and $m(E)$ is given by:

$$m(E) = \pi^{1/2} \int_{E_i}^E \frac{i(\gamma)}{\sqrt{E-\gamma}} d\gamma$$

the convolution integral. Equation 1 describes a wave called the semi-integral analogous to a polarographic wave. The derivation of this equation produces a peak centered at $E_{1/2}^R$, namely:

$$e(E) = \frac{dm}{dE} = \frac{n^2 F^2 A v^{1/2} D_0^{1/2}}{4RT} \operatorname{sech}^2 \frac{nF}{RT} (E - E_{1/2}^R)$$

Figure 1a shows a typical linear scan voltammogram, and Fig. 1b the plot of the semiderivative $e(E)$.

In a similar fashion to the derivation of Eqs. 1 and 3, equations considering complexation can be derived, as these may be considered as cases where

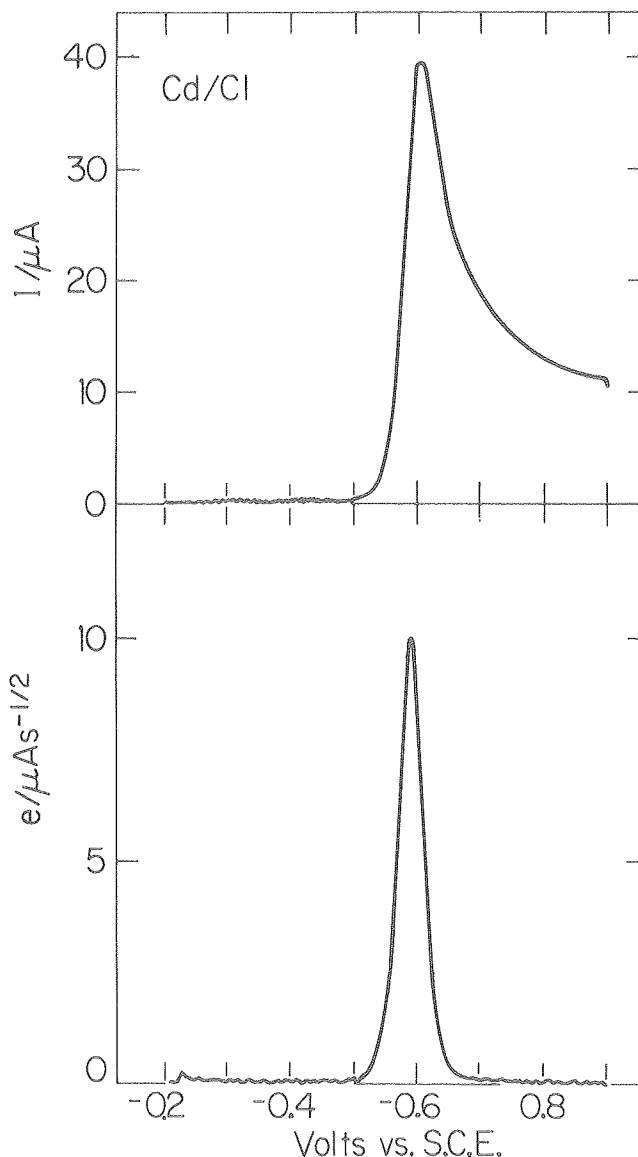


Fig. 1. (a) Typical linear scan voltammogram for cadmium. (b) Result of convolution of (a) with $t^{-1/2}$ and subsequent differentiation.

(XBL 7910-4540)

the chemical reaction precedes the electrochemical change transfer. For cases where the rate of ligand substitution is high, and only one complex exists, the following is observed:

$$\Delta E_{1/2}^R = \frac{RT}{nF} \ln(1 + \beta_p a_L^P)$$

which is analogous to the Lingane equation in classical polarography.¹ For slower rates of ligand substitution, the equation predicts an asymmetry in $e(E)$ that is related to the exchange kinetics for the metal complex. For substitutionally inert ligands (on the electrochemical timescale), no signal is expected.

* This work was supported by the Battelle Project Management Division, Office of Nuclear Waste Isolation, U. S. Department of Energy.

For many labile complexes, the DeFord-Hume relationship² is obtained:

$$\Delta E_{1/2}^r = \frac{RT}{nF} \ln F_0(L)$$

where F_0 is defined by:

$$F_0 = 1 + \beta_1 a_L + \beta_2 a_L^2 + \beta_3 a_L^3 + \cdots + \beta_p a_L^p$$

Similar expressions were derived for electrochemically irreversible complexes.

* * *

1. J. J. Lingane, Chem. Rev. 29, 1 (1941).
2. D. D. DeFord and D. N. Hume, J. Am. Chem. Soc. 73, 5321 (1951).
3. C. P. Andrieux, L. Nadjio, and J. M. Saveant, J. Electroanal. Chem. 26, 147 (1970).
4. M. Grenners and K. B. Oldham, Anal. Chem. 44, 1121 (1972).

2. EVALUATION OF METAL COMPLEXATION KINETICS AND THERMODYNAMICS AT THE HANGING MERCURY DROP ELECTRODE[†]

J. J. Toman, R. M. Corn, and S. D. Brown

To test the theoretical predictions of our theory of metal complex analysis using convolution potential voltammetry, we studied two model systems.

The first of these systems, the $\text{Cd}^{+2}/\text{Cl}^-$ system, is a reversible system with fairly well-known formation constants. This system is interesting because all three of the constants for the CdCl^+ , CdCl_2 , and CdCl_3^- species are of approximately the same magnitude. Previous work¹ has shown that the usual analyses of polarographic half-wave potential vs. ligand activity plots are especially sensitive to the precision in determining $E_{1/2}^r$ values. For determinations of sequential stability constants of similar magnitude, at least 0.4 mV precision is required. The $\text{Cd}^{+2}/\text{Cl}^-$ system thus critically tests our measured reproducibility for electrochemically reversible systems.

The second system studied was the $\text{Eu}^{+3}/\text{SO}_4^{2-}$ system. Although this system is poorly understood, a fair amount is known on the Eu^{+3} ion. This system was chosen as a good model of a typical actinide (III) solution as it was expected to be quite irreversible electrochemically.

Both studies were carried out using a PAR 173 potentiostat interfaced to an LSI 11/2 laboratory microcomputer. Usually, the scans were collected, averaged, and a 256 or 512 point convolution taken. From the experimental half-wave potentials obtained, the species present and their respective stability constants were determined by polynomial regression techniques.

The $\text{Cd}^{+2}/\text{Cl}^-$ system was observed to fit a three-species model for 10^{-3} M Cd^{+2} in 1.0 M ionic strength (KNO_3) solution, over ligand concentrations ranging from 0.1 M Cl^- to 10 M Cl^- . Table 1

Table 1. Stability constants for Cd-Cl complexes.

| Run | Supporting electrolyte | Stability constants | Regression constant |
|---------------|------------------------|---------------------|---------------------|
| 1 | IM KNO ₃ | 19.0, 30, 16 | 0.987 |
| 2 | IM KNO ₃ | 17.1, 27, 15 | 0.985 |
| Literature(2) | IM NaClO ₄ | 18.3, 49, 34 | - |

reports the stability constants observed for two consecutive runs, and compares them with the literature results.

A typical plot of the experimental data is shown in Fig. 1. Considering the difference in supporting electrolytes, the data agree very well, thus indicating that our computer-controlled convolution voltammetry technique is well-suited to accurate determination of stability constants.

For the $\text{Eu}^{+3}/\text{SO}_4^{2-}$ system, a one-species model fits the data best, as shown in Fig. 2. Runs were made on 10^{-4} M Eu^{+3} in 1.2 M NaClO_4 containing SO_4^{2-} concentrations ranging from 0.5 to 1.2 M. The single species observed was $\text{Eu}(\text{SO}_4)_2^-$ with a stability constant, β_2 , of 1.01×10^5 . Similar values are observed in the literature, indicating the suitability of our approach to irreversible system.

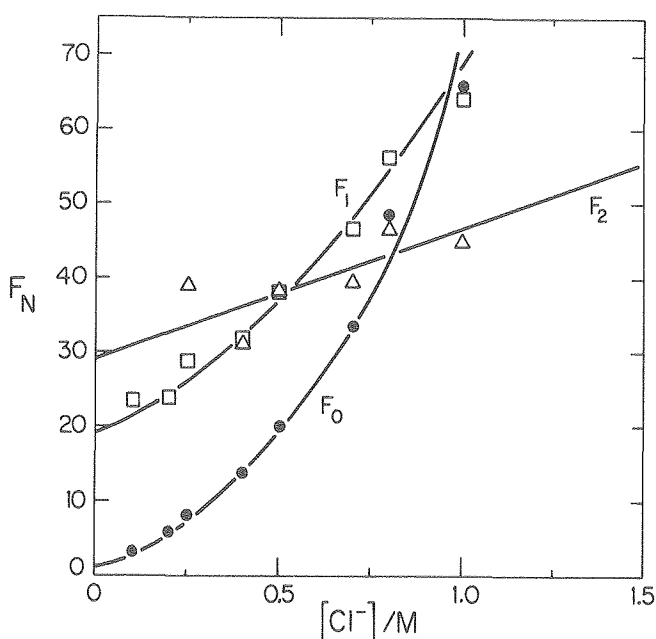


Fig. 1. DeFord-Hume plot of $\text{Cd}^{+2}-\text{Cl}^-$ complexation. Ionic strength was controlled at 100 M with KNO_3 , pH = 5.00. Graphic evaluation of the stability constants is shown. (XBL 7910-4513)

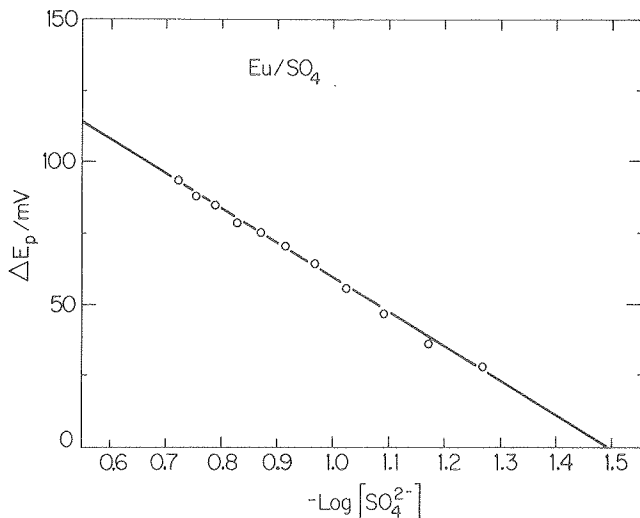


Fig. 2. Lingane plot of $\text{Eu}^{+3}\text{-SO}_4^{2-}$ complexation. Ionic strength was controlled at 1.25 M with KNO_3 , pH = 5.00. (XBL 7910-4538)

* * *

[†]Brief version of Topical Report, submitted to ONWI, October 1979.

1. L. N. Klatt and R. L. Rouseff, *Anal. Chem.* **42**, 1234 (1970).
2. G. A. Heath and G. Hefter, *J. Electroanal. Chem.* **84**, 295 (1977).
3. L. G. Sillen and A. E. Martell, *Spec. Pub. No. 17*, Chem. Society, London, 1964.

RESEARCH PLANS FOR CALENDAR YEAR 1980

The purpose of this program is to investigate the thermodynamic properties of anticipated actinide and fission product ions and the compounds they may form in geologic environments so that their chemical behavior, and potential migration, in a nuclear waste setting can be assessed with improved capability.

A number of laboratory studies will be undertaken to obtain data concerning species, oxidation states, effect of complexing ligands, and other related information. Such data will contribute to a better understanding of the chemical systems that may be involved in various geologic media and will furnish more reliable input parameters for radionuclide migration modeling studies.

Among the problems to be addressed are:

(1) Identification of the principle monomeric and polynuclear chemical species formed in aqueous solution as a function of pH, temperature, ionic strength, concentration of radionuclides, and concentration of environmentally important complexing ligands.

(2) Measurement of the formation constants for the above species.

(3) Determination of the oxidation states of the various radionuclide ions as a function of pH, Eh, and the composition of the solution.

(4) Determination of the conditions for colloidal polymer formation and the nature of the colloids. This work would include studies of the effects of pH, composition of solution, and other important parameters of the system on polymer formations.

Electrochemical techniques are being widely used in these studies. For CY 1980 the following activities are planned:

(1) Extend studies on the effects of complexation to other waveforms and to anodic stripping analysis.

(2) Investigate the trace electrochemical analyses of actinide species on various electrode surfaces.

(3) Initiate studies on the Pu(IV) system with hydroxide, carbonate, and phosphate ligands.

In addition, studies are being initiated on the solubilities of americium hydroxide and americium carbonate by radiochemical tracer techniques.

1979 PUBLICATIONS AND REPORTS

Refereed Journals

- [†]1. S. D. Brown and B. R. Kowalski, "Minicomputer-Controlled, Background-Subtracted Anodic Stripping Voltammetry," *Anal. Chim. Acta.* **107**, 13 (1979).
2. S. D. Brown and B. R. Kowalski, "Pseudopolarographic Determination of Metal-Complex Stability Constants," *Anal. Chem.* (in press).

Invited Talks

1. S. D. Brown, "Voltammetric determination of metal stability constants," Department of Environmental Sciences, University of California-Riverside, February 1979.
2. S. D. Brown, "Kinetic limitations to determination of stability constants by voltammetry," Department of Civil Engineering, University of Washington, April 1979.
3. S. D. Brown, "Actinide speciation studies," Department of Nuclear Engineering, University of California-Berkeley, October 1979.

* * *

[†]Supported by the Office of Naval Research and by the American Chemical Society.

e. High Strength Austenitic Alloys for Generator Retaining Rings*

J. W. Morris, Jr. and G. Thomas, Investigators

Introduction. The purpose of this project is to provide fundamental research support to a companion alloy development effort (also sponsored by the Electric Power Research Institute) for the design of ultra-high strength austenitic steels for use in the retaining rings of two-pole (fossil fuel) electrical generators. Research in the companion project has led to the invention of Fe-based superalloys which combine high room temperature strength (>200 ksi yield) with good toughness and hydrogen resistance. The present project addresses the fundamental metallurgy of these alloys and metallurgical devices for improving them. Research during the past year particularly addressed relevant precipitation reactions.

1. PRECIPITATIONS HARDENING IN Fe-Ni BASE AUSTENITIC ALLOYS†

K. M. Chang

The precipitation of metastable Ni_3X phases in the austenitic Fe-Ni-base alloys has been investigated by using various combinations of hardening elements, including Ti, Ta, Al, and Nb. The theoretical background on the formation of the $L1_2$ type, γ' , and DO_{22} type, γ'' , transition precipitates has been summarized based on three controlling factors: atomic size, compressibility, and electron/atom ratio. A model for their appearance is proposed from an analysis of static concentration waves ordering the fcc lattice. It is established experimentally that the ordered structure of metastable precipitates will change from the triangularly ordered γ' , to the rectangularly ordered γ'' , as the atomic ratio $(Ti+Al)/(Ta+Nb)$ decreases. The concurrent precipitation of γ' and γ'' occurs at 750°C when the ratio is between 1.5 and 1.9.

The aging behavior of these alloys was studied over the temperature range of 500°C to 900°C. Typical hardness curves show a substantial hardening effect due to precipitation. An excellent combination of strength and fracture toughness can be developed by employing double aging techniques. It is found by transmission electron microscopy (TEM) that the growth of these coherent intermediate precipitates follows the power law with the aging time: $t^{1/3}$ for the spherical γ' particles; and $t^{1/2}$ for the disc-shaped γ'' . The equilibrium phase is observed to be able to nucleate on the surface of imbedded carbides (Fig. 1).

The addition of 5 wt.% Cr to the age-hardened alloys provides a non-magnetic austenite which is stable against the formation of mechanically induced martensite. It has been shown that the Cr

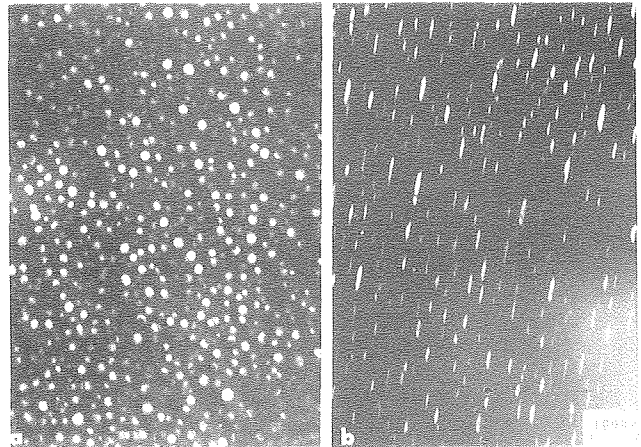


Fig. 1. Dark field electron micrographs showing (a) spherical γ' precipitates and (b) disc-shaped γ'' precipitates in an Fe-based superalloy.

(XBB 793-3351)

addition retards the aging kinetics of the precipitation reactions, and also suppresses intergranular embrittlement caused by the high temperature solution anneal. The aging kinetics are also found to be influenced by solution annealing treatments.

* * *

†Brief version of LBL-9208.

RESEARCH PLANS FOR CALENDAR YEAR 1980

The present project is scheduled to be completed by July, 1980. In the interim three items of work will be undertaken:

- (1) A continuation of present investigations on the fundamentals of precipitation reactions in these Fe-based superalloys.
- (2) Testing and characterization of a scaled-up ingot of new superalloy now being cast.
- (3) Collaboration with EPRI in the implementation of an application program to manufacture a prototype retaining ring.

1979 PUBLICATIONS AND REPORTS

Other Publications

1. K. M. Chang, J. Y. Koo, J. W. Morris, Jr., and G. Thomas, 37th Ann. Electron Microscopy Soc. Am., San Antonio, Texas, August, 1979, LBL-10127.

* This work was supported by the Electric Power Research Institute (EPRI), through the Lawrence Berkeley Laboratory.

LBL Reports

1. Keh-Mim Chang, Ph.D. thesis, "Precipitation Hardening in Fe-Ni Base Austenitic Alloys," LBL-9208.

2. K. M. Chang, D. H. Klahn, S. Jin, G. Thomas, and J. W. Morris, Jr., "Heat Treatment and Mechanical Properties of a Ta-Modified Fe-Base Superalloy," to be published in Met. Trans., LBL-9799.

f. Oxygen Reduction in Concentrated Phosphoric Acid by Carbon-Supported Pt Alloy Electrocatalysts*

Philip N. Ross, Investigator

1. OXYGEN REDUCTION IN CONCENTRATED PHOSPHORIC ACID BY CARBON-SUPPORTED PT ALLOY CATALYSTS

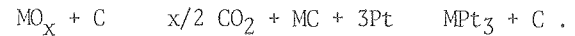
Philip N. Ross

First generation electric utility fuel cell power plants are limited by the performance and life capabilities of the phosphoric acid cathode. The cathodes are basically carbon structures with very small quantities of highly dispersed platinum deposited on the surface. In such structures the carbon is required to have high electronic conductivity, high surface area, and corrosion (oxidation) resistance. Simultaneously, it is desired that the (carbon) substrate inhibit the coalescence of platinum crystallites. This coalescence causes a reduction in surface area with a resulting loss in performance. In general, it is difficult to maximize platinum surface area and minimize carbon corrosion simultaneously. It would be desirable to use a metallic catalyst which is more strongly bonded to the carbon substrate than pure platinum, so that its tendency to migrate on the surface is less. An increase in metal-metal bonding may imply an increase in surface energy (hardness), giving less tendency to sinter if migration does occur. Simultaneously, this increase in metallic bonding may have an advantageous effect on catalytic properties. Equally, if one metallic catalyst is a platinum alloy, its method of preparation may be such that in alloying the second metal, the carbon support is oxidized and the chemical pre-corrosion of the carbon may remove weaker areas of the surface before immersion in the fuel cell electrolyte. Hence, an enhanced corrosion resistance would be expected, especially if initially resistant carbon precursors are used.

It is the purpose of this study to investigate alloys of platinum of an intermetallic type, whose metallic bonding is enhanced compared with the parent metal, as fuel cell electrocatalysts.

The Preparation of Carbon Supported Alloys. Alloying constituents were chosen that are known to form intermetallic compounds with Pt of the type $M\text{Pt}_3$, whose structure type is generally either AuCu_3 (fcc) or TiNi_3 (hcp). The Pt-Group IVb and Vb binary systems form intermetallic compounds of this type at 70-80 a/o Pt with free energies of formation (-200 to -420 kJ/mol)¹ that indicate strong platinum-base metal bonding. Other alloying constituents of interest that result in weaker (bonding) interactions are Al, W and Re. These were examined to provide a comparison with the strongly interacting elements. A procedure was developed for preparing these binary systems as small (3-5 nm) metallic clusters dispersed on a conductive carbon substrate. Vulcan

XC-72 R (Cabot Corp.) carbon black was impregnated with platinum to 10 w/o by use of a colloidal method.² The alloy metal of interest was deposited (as hydrated oxide) onto the carbon by precipitation from chloride solution with ammonium hydroxide. The binary alloy was formed by heat treating; the most probably reaction sequence is



Characterization of the Alloy Catalysts. That small alloy (intermetallic) clusters were indeed formed on the carbon surface was confirmed by detailed structure analysis using x-ray diffraction (XRD) and transmission electron microscopy (TEM). Lattice imaging by TEM confirmed the existence of metallic clusters, of mean diameter 3-5 nm, of a single phase. Lattice parameters were measured using standard x-ray powder diffraction methods. The structure and composition of the alloys (intermetallics) studied so far are summarized in Tables 1 and 2.

Determination of Catalytic Activity. For the purposes of initial screening of catalytic activity, the catalysts were fabricated into polytetrafluorinated ethylene (PTFE)--bonded gas diffusion electrodes of the type used in commercial phosphoric acid fuel cells. Steady-state current-potential curves for oxygen reduction were measured in a conventional three electrode half-cell using a galvanostatic method. Pt-Al,

Table 1. Characterization of supported Pt-Group IVb and Group Vb alloys and intermetallics by x-ray diffraction.

| Alloy | Phases | Lattice Parameter | Est. Composition | Crystallite Size |
|-------|------------------------------|-------------------|------------------|------------------|
| Pt-Ti | fcc Ti Pt ₃ | 3.906Å | 25 a/o Ti | 6 nm |
| Pt-Zr | fcc "Zr Pt ₄ " | 3.958 | 20 a/o Zr | 4 |
| Pt-Hf | fcc "Hf Pt ₄ " | 3.955 | 20 a/o Hf | 4 |
| Pt-V | fcc sol. solu. | 3.888 | 20 a/o V | 3.5 |
| Pt-Nb | fcc sol. solu. | 3.963 | 20 a/o Nb | 5 |
| Pt-Ta | fcc sol. solu. | 3.965 | 20 a/o Ta | 5 |

*This work was supported by the Electric Power Research Institute (EPRI), through the Lawrence Berkeley Laboratory.

Table 2. Characterization of other supported Pt alloys by x-ray diffraction.

| Alloy | Phases | Lattice Parameter | Est. Composition | Crystallite Size |
|-------|-------------------|-------------------|------------------|------------------|
| Pt-Al | fcc sol. solu. | 3.896 | 10-15 a/o Al | 3.0 nm |
| Pt-W | fcc sol. solu. | 3.914 | ca. 40 a/o W | 5.5 |
| Pt-Re | fcc sol. solu. | 3.905 | ca. 40 a/o Re | 6.0 |

Pt-W and Pt-Re alloys did not produce stable polarization curves in H_3PO_4 at 430-460 K. Pt-Ti, Pt-Zr and Pt-Hf produced current-potential curves close to those for the standard pure Pt catalyst. Pt-V and Pt-Ta had a significantly higher catalytic activity for oxygen reduction than the standard pure Pt catalyst, as the curve in Fig. 1 clearly shows. The activation energy for the Pt-Group Vb alloys is 9.7 kJ/mol lower than that for pure Pt. We postulate that the lower activation energy on these alloys is due to a change in the energy of adsorption of intermediates on the bimetallic surface brought about by an electronic structure altered (from pure Pt) by strong intermetallic bonding.

* * *

1. P. Meschter and W. Worrell, *Met. Trans. A* **7**, 299 (1976); *ibid.*, **8**, 503 (1977).
2. Proprietary material provided by and used with permission of the Prototech Corporation.

RESEARCH PLANS FOR CALENDAR YEAR 1980.

The three most catalytically active alloys (Zr, V, Ta) have been selected for further development. Preparation methods and the electrode structures need to be optimized. Long term testing as cathodes in subscale fuel cells is required to determine changes in the rates of surface area loss and platinum dissolution due to alloying. It is anticipated that further development of these

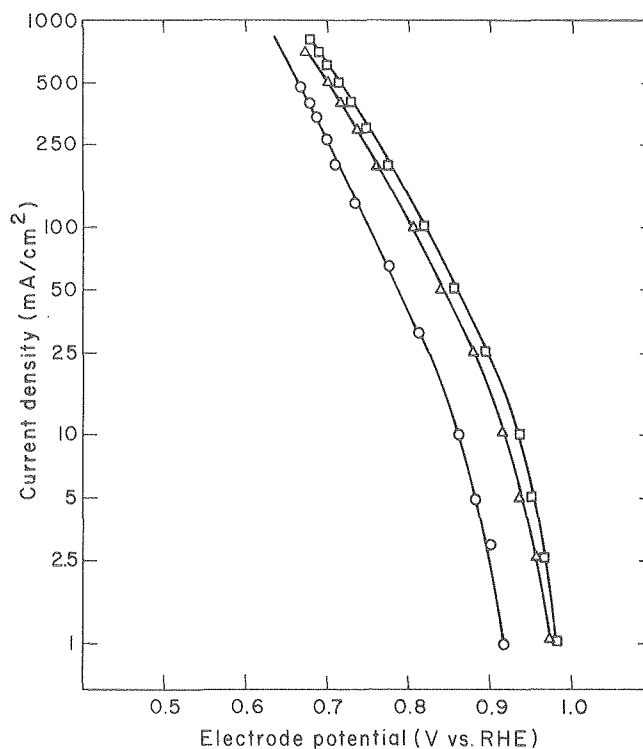


Fig. 1. Current-potential curves for oxygen reduction on a standard Pt catalyst and on catalytically more active Pt intermetallic catalysts. 443 K, 95 w/o H_3PO_4 , pure oxygen, 0.2 mg/cm² loading of Pt. (XBL 802-258)

alloys will be done in cooperation with a commercial subcontractor.

Extensive fundamental studies will be necessary in order to determine more clearly why these platinum alloys are better electrocatalysts. These fundamental studies will be conducted in 1980 as part of the research program funded by the Division of Fossil Fuel Utilization of DOE.

New work on the kinetics of oxygen reduction on platinum and selected platinum intermetallics in strong polymeric acid electrolytes (e.g., tetrafluoroethane disulfonic acid) will be initiated in 1980.

g. Substructure and Properties of Sodium Beta Alumina Solid Electrolytes*

L. C. De Jonghe, Investigator

Introduction. About 12 years ago, a high energy density battery was conceived at Ford Motor Company using molten sodium and sodium polysulfides as an electrochemical couple and sodium beta alumina as a solid electrolyte separator. This battery has now evolved to a stage where large-scale commercial application may be expected in a few years. The importance of high energy density electrochemical storage systems is derived from their potential use as load leveling systems for the electric utilities. The key ingredient in a sodium sulfur battery is the solid electrolyte separator, sodium beta alumina. The ionic conductivity, mechanical strength, and the lifetime of the electrolyte in operating cells depends to a significant degree on a number of factors. These factors include impurities and microstructures of the electrolytes. The present work is aimed at clarifying the role of impurities and microstructure in determining the in-cell lifetime of the solid electrolyte sodium beta alumina.

1. BREAKDOWN STUDIES[†]

A. Buechele, L. Feldman, and L. C. De Jonghe

It has been established that under certain conditions of ionic current, temperature and electrolyte composition a breakdown can occur in sodium beta aluminas involving the penetration of metallic sodium into the bulk of the electrolyte.¹ This metal penetration, and the crack-like features thought to be associated with it, has been modeled by several workers.² To examine the validity of the models, a number of experiments were performed in which breakdown was induced, both at 300°C and at room temperature, with blocking and with non-blocking electrodes.

Electrolytes were subjected to a high Na^+ current with Na^+ electrodes (NaNO_3 - NaNO_2 eutectic) at 300°C. The electrolytes were constricted in the center so as to give a high bulk current density, but a low electrode current density.

Increasing currents were passed through samples until a blackening, accompanying the DC breakdown, was seen to emerge rapidly from the negative electrode. Sectioning of the sample revealed that the blackening had started at a point where the Kovar electrode reservoir was welded directly to the electrolyte, providing a Na^+ blocking site with electron injection. The geometry of the breakdown shown in Fig. 1 strongly suggests that the Na metal penetration is not readily described in terms of a single, metal filled crack propagating through the sample. The material appearing

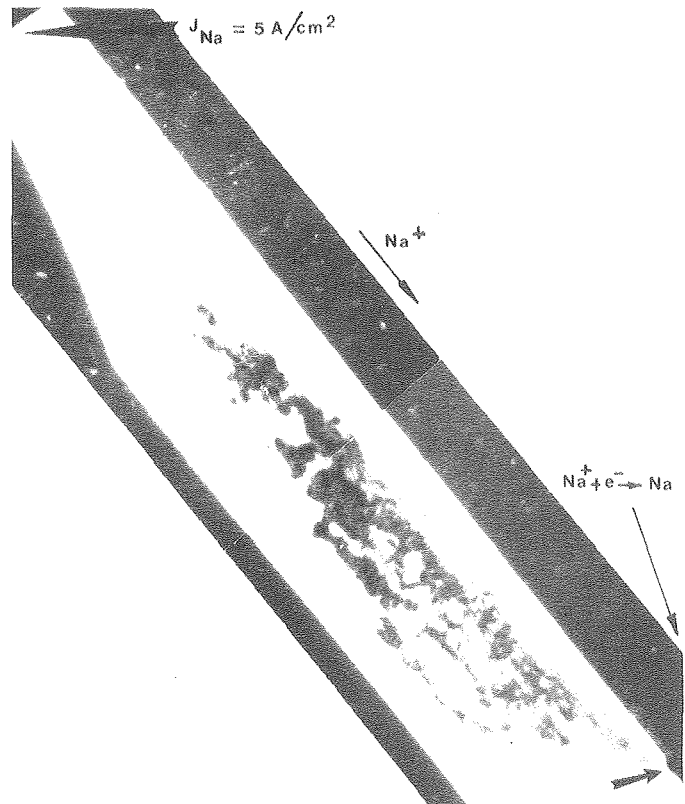


Fig. 1. Geometry of the 300°C, DC breakdown after partial propagation of degradation. The degradation apparently initiated at the place where the Kovar reservoir welded to the electrolyte (arrow at lower right corner). (XBB 7812-15575)

dark and rather shapeless in these electron micrographs was identified as sodium carbonate. It can be attributed to the reaction of the metallic sodium with the atmosphere upon thin foil preparation. The sodium carbonates can thus be conceived of as "relics" of the metallic sodium that formed in the degradation process. Interestingly, both transgranular and intergranular degradation is observed. The transmission electron microscopy thus strongly suggests that the sodium filled crack morphology is a highly branched one in which the crack is deflected, as one would expect, by microstructural features. No other compounds, such as sodium aluminates or alumina were found to be associated with this degradation.

The center of the samples was also studied by means of transmission electron microscopy. No traces of breakdown were found, even for electrolytes that had withstood a local ion current density of about 10 A/cm^2 for 1 hour. We conclude that intrinsic degradation, i.e., decomposition away from electrodes when electron injection is absent, does not occur in beta aluminas.

*This work was supported by the Electric Power Research Institute (EPRI), through the Lawrence Berkeley Laboratory.

Small single crystals, 0.1 cm x 0.1 cm x 1 cm were cleaved from a larger crystal. The cleavage plane is the conduction plane. Na metal formation was initiated and the Na filled crack geometry was studied directly with optical interference microscopy, as shown in Fig. 2. The examinations



Fig. 2. Optical interferometry revealing the structure of a sodium filled cleavage crack induced by direct current passage through a single crystal of sodium beta alumina. (XBB 7811-14127)

indicated that the crack must be filled with metallic sodium from its steps, or crack rivermarks that intersect many conduction planes. The observations indicate that in modeling beta alumina breakdown progression, one cannot simply assume that the crack is only tip fed, as is necessary in stress corrosion models.²

* * *

[†]Brief version of Mat. Res. Bull. 14, 589 (1979).

1. R. D. Armstrong, T. Dickinson, and J. Turner, *Electrochim. Acta* 19, 187 (1974).

2. R. Richman, G. J. Tennenhouse, *J. Am. Ceram. Soc.* 58, 63 (1975).

2. LOCAL ELECTRODE CURRENT DENSITIES

L. C. De Jonghe and L. Feldman

The initiation of DC breakdown in beta alumina has been found to occur above a critical electrode current density level. While the actual value of this current density threshold is not well established, it can be reasonably postulated that local current excursions above the macroscopic average current at the sodium/beta alumina electrolyte interface will enhance the probability of failure initiation. In an effort to bring the microinhomogeneity of the electrode/electrolyte current distribution to light, a decoration method was devised revealing the local ionic current densities qualitatively. In this method, Ag^+ is electrolyzed for a few seconds at an electrode potential of 16 volts, into a polished beta alumina polycrystalline sample. The electrodes are silver nitrate solutions. Where Ag^+ is supposed to enter the beta-alumina, to replace the Na^+ ions, silver metal deposits instead. While the details of the deposition mechanism have not been fully clarified, it appears that H_3O^+ rather than Ag^+ enters the beta alumina lattice thereby permitting the generated OH^- at the electrolyte/electrode interface to donate an electron to the Ag^+ ions. For the initial stages of this reaction the rate of the H_3O^+ injection is expected to be approximately proportional to the local current density that would occur at a reversible sodium/beta alumina interface with identical microstructure. When the decorated sample is examined with a reflection optical microscope, the areas of high silver deposition appear bright. This is shown in Fig. 1.

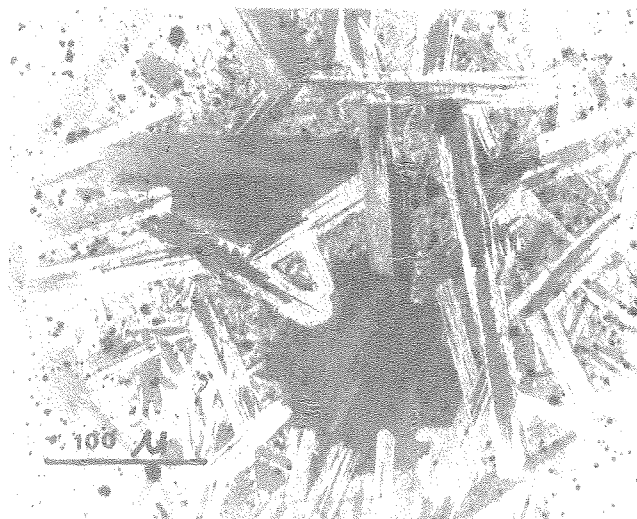


Fig. 1. Beta alumina solid electrolyte sample decorated by silver electrolysis. The large grain, appearing dark in this micrograph corresponds to an area of low local electrode current density.

(XBB 794-4263)

Note the large, circular grain, appearing dark in the center of the micrograph. A low local electrode current density is indeed to be expected for this grain, since beta alumina is a layer compound that is highly anisotropic and does not permit ionic conduction in a direction normal to the basal planes. For the dark grain, the ion conducting basal planes are indeed approximately parallel to the interface, thus confirming that the dark contrast in the decoration method is related to low local current density. It is interesting to note that in the large grains regions of high and low local current density can be discerned. Such inhomogeneous current flows would indeed be expected based on the detailed microstructural observations of De Jonghe.

RESEARCH PLANS FOR CALENDAR YEAR 1980

In the coming program year, experiments will be carried out on sodium-beta alumina solid electrolyte tubes in Na/Na cells at 300°C, and on bars above and below the melting point of sodium. The degree to which factors, such as surface perfection and electrolyte microstructure, can affect initiation of failure degradation will be studied.

1979 PUBLICATIONS AND REPORTS

Refereed Journals

1. L. C. De Jonghe, L. Feldman, and P. Millett, "Some Geometrical Aspects of Breakdown in Sodium Beta Alumina," *Mat. Res. Bull.*, 14, 589 (1979).

2. L. C. De Jonghe, "Grain Boundaries and Ionic Conduction in Sodium Beta Alumina," *J. Mat. Sci.*, 14, 33 (1979).

3. L. C. De Jonghe, "Fast Ion Conductors," *J. Am. Ceram. Soc.* 62, 289 (1979).

Other Publications

1. A. Buechele, L. Feldman, and L. C. De Jonghe, "Breakdown of β'' -Al₂O₃ by DC," Abstract 18-E-79, *Ceram. Bull.* 3, 364 (1979).

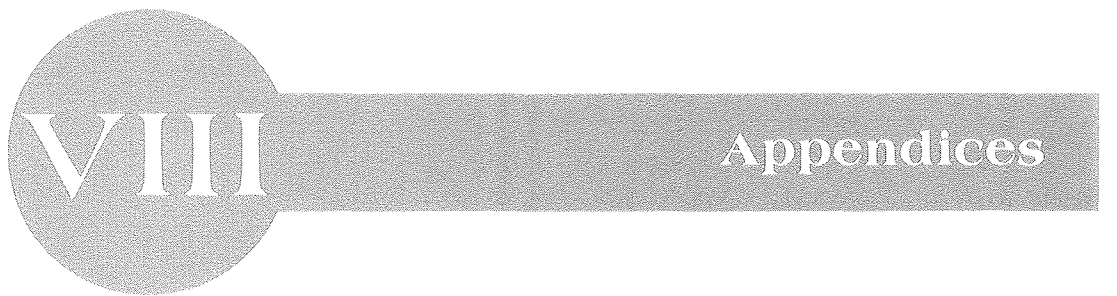
2. L. C. De Jonghe and Edward Goo, "Transient Eutectics in Sintering of Sodium Beta Alumina," in "Processing of Crystalline Ceramics," H. Palmour, III, R. F. Davis, and T. M. Hare, Ed., Plenum Press, 1978, pp 433-441.

LBL Reports

1. L. C. De Jonghe, "Microstructures, Defects, and Sodium Transport in Sodium Beta Alumina Solid Electrolytes," LBL-9802, September 1979.

Invited Talks

1. L. C. De Jonghe, "D. C. Breakdown of Sodium β -Alumina," University of Utah, Salt Lake City, Utah, April 1979.

A decorative graphic consisting of a grey circle on the left and a grey horizontal bar extending to the right. The Roman numeral 'VIII' is printed in white inside the circle, and the word 'Appendices' is printed in white on the bar.

VIII Appendices

APPENDIX A

MATERIALS AND MOLECULAR RESEARCH DIVISION STAFF - 1979

| <u>Investigators</u> | <u>Postdoctoral and Other Scientists</u> | <u>Graduate Students</u> |
|--|---|--|
| Neil Bartlett | G. Beindorf J. Gramnc H. Hollfelder H. Zuchner | R. Biagioni T. Mallouk E. McCarron B. McQuillan F. Tanzella S. Yeh |
| Robert Bergman | L. Stuhl | P. Becker M. Berger H. Bryndza P. Comita E. Evitt J. Frommer J. Huggins A. Janowitz W. Jones T. Lockhart K. Theopold M. Wax |
| Robert Bragg | O. Adewoye S. Rao | D. Baker L. Henry B. Mehrotra |
| Leo Brewer | R. Lamoreaux C-B. Meyer | D. Davis D. Goodman B. Lin M. Ospino |
| John Clarke | C. Chi B. Gregory T. Lemberger D. Van Harlingen | R. Koch R. Lee R. Miracky D. Seligson |
| Marvin Cohen | J. Chelikowsky | K. Ho J. Ihm P. Lam J. Northrup M. Yin |
| Robert Connick | T. Braga G. Rosenblatt T. Tam | D. Horner E. Livingston |
| Lutgard DeJonghe | J. Porter | A. Buechele C. Cameron M. Chang L. Feldman S-C. Hu |
| Norman Edelstein | R. Andersen J. Bucher C. Carrano S. Davis W. Harris F. Hollander S. Jones E. Juaristi C. LeVanda R. McLaughlin D. Perry H. Ruben | K. Abu-Dari R. Banks S. Barclay C. Berke R. Corn C. Eigenbrot B. Gilbert G. Girolami M. Halpern T. Hayhurst E. Hillard D. Kagan |
| N. Bartlett J. Conway K. Raymond G. Seaborg A. Streitwieser D. Templeton Z. Zalkin | | |

| <u>Investigators</u> | <u>Postdoctoral and Other Scientists</u> | <u>Graduate Students</u> |
|---------------------------|---|---|
| Norman Edelstein (Cont'd) | B. Schilling G. Shalimoff S. Simpson J. Solar E. Soulie B. Spencer L. Templeton C-H. Van Deurzen H-K. Wang F. Weitzl G. Wong Y-T. Wu | W. Luke B. Lulu M. Lyttle V. Mainz V. Pecoraro G. Phillips R. Planalp J. Robbins R. Shinomoto K. Smith W. Smith R. Sofen E. Strauss R. Tatz T. Tilley J. Toman |
| Anthony Evans | W. Kriven D. Marshall J. Porter | W. Blumenthal W. Burlingame K. Faber Y. Fu C-H. Hsueh M. Huang A. Rana M. Spears |
| James Evans | J. Little Y. Zundlevich | M. Abbasi B. Tracy |
| Ron Gronsky | D. Cockayne P. Rez | J. Briceno-Valero S. Cheruvu E. Kamenetzky J. Rose |
| Charles Harris | H. Auweter A. Champion | M. Berg C. Berman J. Chao P. Cornelius A. Gallo S. George G. Goncher A. Harris S. Marks H. Robota P. Whitmore |
| Heinz Heinemann | J. Sinclair | W. McKee |
| Dennis Hess | | C. Blair A. Wakita L. William D. Wroge |
| Carson Jefferies | J. Furneaux P. Westervelt | B. Black J. Culbertson S. Kelso E. Pakulis J. Perez J. Weiner |
| William Jolly | H. Chen C. Donahue T. Lee | M. Ajmani A. Bakke T. Briggs |

| <u>Investigators</u> | <u>Postdoctoral and Other Scientists</u> | <u>Graduate Students</u> |
|----------------------|---|--|
| Harold Johnston | | P. Connell J. Girman M. Kowalczyk D. Littlejohn K. Lubic F. Magnotta W. Marinelli H. Nelson J. Podolske G. Selwyn S. Solomon C. Truesdale |
| Yuan Lee | R. Buss P. Casavecchia J. Delgado D. Gerlich H. Guozhong G. He T. Hirooka F. Houle F. Huiskens J. Lizy K. Shobatake R. Sparks P. Tiedemann Z-J. Zhang | S. Anderson R. Baseman R. Buss S. Bustamente L. Carlson C. Hayden C. Kahler D. Neumark S. Sibener D. Trevor M. Vernon |
| Alan Levy | D. Abdollahian D. Boone W. Coons I. Cornet I. Finnie R. Glardon M. Holt J. Humphrey T. Jacob S. Johanmir J. Laitone M. Landkof A. Modavi D. Rao F. Ravitz J. Stringer W. Worrell M. Yeung G. Zambelli | P-K. Chen M. DesJardin T. Foerster B. Gordon R. Jagaraman M. Khatibloo J. Kim S. Li P. Liang R. Mayville F. Pourahmadi J. Raju A. Sallman A. Shaw W. Tsai R-J. Yang M. Yeung W. Yeung |
| Bruce Mahan | | R. Davis F. Grieman S. Hansen A. O'Keefe T. Turner |
| Richard Marrus | D. Dietrich H. Gould J. Leavitt J. Silver C. Vane | |
| William Miller | C. Cerjan G. Herling H-D. Meyer | J. Adams S. Gray A. Orei R. Stratt B. Waite |

| <u>Investigators</u> | <u>Postdoctoral and Other Scientists</u> | <u>Graduate Students</u> |
|----------------------|--|---|
| C. Bradley Moore | D. Goodall A. Kung Z. Sabet Imani | A. Abbate D. Bamford M. Berman H. Dai P. Ho F. Hovis A. Langford W. Natzle E. Specht J. Weisshaar J. Wong L. Young |
| John W. Morris, Jr. | K-M. Chang K. Hanson A. Khachatryan J. Kim D. Klahn M. Niikura C. Syn H. Yamanchi | K. Chang S. Chen D. Dietderich G. Fior Zurlo B. Fultz T. Herh M. Hong H. Kim H-J. Kim J. Kim H. Lee H-L. Lin P. Ling K. Mahin T. Mohri B. Neilson E. Pundarika K. Sakai J. Sanchez Y-C. Shih H. K. Shin M. Strum L. Summers D. Wedge D. Williams I-W. Wu |
| Earl Muettertities | R. Gavin J. Kouba D. Mohajer G. Nelson J. Stein M. Tachikawa R. Tau | J. Bleeke R. Burch H. Choi W. Cwirla C. Friend G. Schmidt K. Shanahan A. Sievert S. Slater M. Tsai R. Wexler |
| Rolf Muller | F. Schwager J. Winnick | C. Coughanowr J. Farmer K. Hanson G. Neumann |
| John Newman | | C. Law M. Matlosz M. Orazem P. Pollard G. Trost D. Ullman |

| <u>Investigators</u> | <u>Postdoctoral and Other Scientists</u> | <u>Graduate Students</u> |
|----------------------|--|---|
| Donald Olander | M. Balooch S. Kokhtev A. Machiels E. Muchowski | D. Dooley M. Farnaam K. Kim S. Shann D. Sherman F. Tehranian C. Tsai S. Yagnik R. Yang |
| Joseph Pask | J. Bakken P. Dokko W. Kriven R. Langston J. Moya S. Shiosaki P. Spencer A. Tomsia F. Zhang | N. Aiko N. Cassens S. Chandratreya S. Chiang P. Flaitz S. Johnson D. Miller V. Nagesh A. Rana M. Sacks S. Tso |
| John Prausnitz | | F. Anderson E. Larsen W. Whiting |
| Norman Phillips | G. Brodale E. Hornung | J. Boyer W. Fogle M. Mayberry J. Van Curen |
| Alexander Pines | L. Mueller U. Nitsan S. Wolfe | G. Drobney R. Eckman J. Garbow J. Murdoch S. Sinton L. Sterna J. Tang W. Warren D. Weitekamp Y-S. Yen |
| Kenneth Pitzer | P. Christiansen Y. Lee | J. Simonson |
| Paul Richards | R. Bailey T. Iri E. Kreysa T. Timusk J. Tucker D. Woody | R. Bailey J. Bonomo R. Britt W. Challener S. Chiang C. Collins M. Hueschen D. Lambert P. Latham S. McBride W. McGrath D. Murphy T. Shen |
| Moshe Rosen | M. Pickus J. Wang | |
| Philip Ross | G. Derry D. Scherson | |

| <u>Investigators</u> | <u>Postdoctoral and Other Scientists</u> | <u>Graduate Students</u> |
|------------------------------|---|---|
| Alan Searcy | R. Berger D. Beruto A. Buchler D. Meschi Z. Munir G. Spinolo | T. Dai J. Ewing M. Huang N. Jacobson G. Knutsen T. Reis S. Roche R. Shukla |
| Y. Ron Shen | K-C. Chu A. DeCastro P. Motisuke J-L. Oudar M. Sigrist | G. Boyd C. Chen S. Durbin P. Hislop R. Hsu A. Jacobson R. Pecyner R. Smith A. Sudbo |
| David A. Shirley | W. Brewer B. Garrison W. Heppler Z. Hussain B. Lu G. Mason E. Matthias P. Perfectti V. Rehn R. Rosenberg J. Stohr G. Thornton R. Watson S. Williams N. Winograd | A. Baca J. Barton R. Davis D. Denley S. Kevan L. Klebanoff P. Kobrin D. Lindle K. Mills C. Parks E. Poliakoff J. Pollard R. Rosenberg D. Rosenblatt S. Southworth J. Tobin C. Truesdale M. White |
| Howard Shugart E. Commins | M. Prior R. Knight | P. Bucksbaum W. DeHeer P. Drell L. Hunter R. Knight P. Latham |
| Henry Schaefer | J. Goddard R. Pitzer S. So | B. Brooks D. Fox J. Hutchinson K. Kim W. Laidig G. Pittman P. Saxe W. Swope |

Investigators

Gabor Somorjai
 A. Bell
 P. Vollhardt

Postdoctoral
and Other Scientists

H. Arakawa
 J. Biberian
 W. Brennen
 A. Daneshrad
 D. Danielson
 P. Davies
 S. Ferrer
 J. Frost
 P. Hansma
 M. Langell
 W. McLean
 H. Nozoye
 S. Sachtler
 W. Tam
 M. Van Hove
 P. Watson
 M. Winter

Graduate Students

W. Aalbersberg
 J. Baker
 R. Blackadar
 W. Canella
 R. Carr
 D. Castner
 S. Ceyer
 R. Colborn
 J. Crowell
 S. Davis
 R. Dictor
 L. Dubois
 T. Frederick
 J. Fritch
 C. Galik
 S. Gandhi
 E. Garfunkel
 W. Gillespie
 W. Guthrie
 R. Hicks
 S. Kellner
 R. Koestner
 T-H. Lin
 D. Mobley
 P. Perkins
 A. Salhi
 S. Salim
 J. Sokol
 D. Stern
 F. Wagner

Gareth Thomas

A. Baker
 K. Easterling
 P. Furrier
 R. Hoel
 O. Krivanek
 C. Kung
 R. Mishra
 M. Mychliaev
 B. Narasimha Rao
 P. Rez
 R. Sinclair

C. Ahn
 J. Ahn
 Y. Belli
 P. Costello
 U. Dahmen
 J-S. Gau
 E. Goo
 A. Jhingan
 N. Kim
 K. Kubarych
 I-N. Lin
 J. Mazur
 A. Nakagawa
 T. O'Neill
 S. Ong
 A. Pelton
 T. Rabe
 L. Rabenberg
 W. Salesky
 M. Sarikaya
 T. Shaw
 M. Sung
 B. Steinberg
 H. Tokushige
 J. Wasynczuk
 P. Williams
 C. Wu

| <u>Investigators</u> | <u>Postdoctoral and Other Scientists</u> | <u>Graduate Students</u> |
|----------------------|--|--|
| Charles Tobias | Y. Geronov V. Kommeric | C. Coughanowr D. Dees J. Faltemier K. Hanson W. Hui A. Kindler G. Prentice D. Roha P. Sides T. Tsuda S. Yu |
| Jack Washburn | U. Dahmen C. Lampert D. Sadana | B. Chin R. Drosd A. Forouhi T. Huo C. Jou C. Lampert H. Ling T. Mowles N-R. Wu |
| David Whittle | I. Allam M. El Dahshan F. Gesmundo O. Goncel H. Hindam F. Viani | H. Akuezue L. Kingsley L. McConnell A. Misra P. Risse S. Shaffer F. Yang |
| John Winn | | J. Goble B. Hale D. Hartman W. Hollingsworth D. Horak H. Luftman S. Sherrow |

MMRD SUPPORT STAFF

C. Peterson - Division Administrator
 K. McArthur - Assistant Division Administrator

Administrative Staff

M. Janzen - Staff Assistant - Administration
 +L. Lizama - Technical Editor
 +C. Webb - Technical Editor
 E. Skrydlinski - Staff Assistant - Personnel
 S. Stewart - Staff Assistant - Purchasing

Clerical and Secretarial Staff

| | | |
|---------------|---------------|---------------|
| J. Amoroso | S. Harris | L. McGuire |
| M. Barsony | J. Hayes | V. Narasimhan |
| M. Bowman | L. Irvin | M. Norton |
| G. Brazil | K. Janes | C. Payne |
| B. Burt | D. Jeffery | S. Quarello |
| B. Carter | S. Jennings | J. Smith |
| M. Chin | R. Jones | M. Stefonetti |
| J. Denney | T. Judson | C. Sterling |
| R. Fletcher | K. Krushwitz | N. Taylor |
| P. Gassler | S. Lasarte | A. Weightman |
| S. Gooden | P. Maher | K. Wilkinson |
| C. Hacker | E. McClelland | C. Yoder |
| A. Harrington | R. McCollough | |

Technical Staff

W. Toutolmin - Technical Coordinator

| | | | |
|---------------|--------------|------------------|---------------|
| +G. Baum | W. Goward | +B. McAllister | +J. Severns |
| J. Barrett | H. Harrell | L. McCoy | D. N. Shirley |
| D. Bazell | G. Hirsch | L. McCullough | L. Sindelar |
| R. Bellman | J. Holthuis | M. Mulvehill | B. Snyder |
| J. Bregante | J. Jacobsen | +D. Newhart | H. Sokol |
| T. Britt | M. Jayko | Q. Nguyen | R. Stanley |
| +M. Brown | +L. Johnson | A. Noman | B. Steakley |
| T. Burner | M. Johnson | J. Pan | P. Tevor |
| C. Carvalho | D. Jurica | G. Papan | C. Thom |
| M. Clement | K. Kostlan | G. Papapolymerou | A. Tobias |
| C. Coulman | +D. Krieger | +B. Pope | M. Trenary |
| J. Cox | C. Lam | J. Posthill | P. Trevor |
| D. Dietderich | L. Lapidés | C. Ramsay | K. Wada |
| S. Edwards | D. Levitsky | J. Randall | M. Wainger |
| M. Elleman | J. Lince | M. Rasor | J. Wallace |
| E. Elliott | +R. Lindberg | W. Reid | H. Weeks |
| J. Fattaruso | M. Lindley | A. Ricco | P. Westdal |
| +K. Frank | M. Lipshutz | +H. Riebe | +J. Wodei |
| R. Friedman | J. Maasberg | M. Rigdon | W. Wong |
| L. Galovich | D. MacDonald | D. Rosenberg | P. Yarnold |
| K. Gaugler | R. Mackey | K. Sakai | +M. Zbinden |
| W. Giba | C. Markley | H. Sawhill | |
| C. Gosnell | S. Masuo | J. Sender | |

+LBL Support Staff

APPENDIX B

LIST OF SEMINARS

Surface and Catalysis Science

| <u>Date</u> | <u>Speaker and Affiliation</u> | <u>Seminar Title</u> |
|-------------|--|---|
| 1-10-79 | Prof. R. Bergman UC-Berkeley MMRD/Lawrence Berkeley Laboratory | Transformation of Organic Compounds Mediated by Mono- and Bi-Nuclear Cobalt Complexes |
| 1-12-79 | Prof. M. Wrighton Massachusetts Institute of Technology | Semi-Conductor Photoelectrochemistry: Chemically Derivatized Photoelectrodes |
| 1-17-79 | Dr. P. B. Vernuto Mobil Research and Development Corp. | Underground in situ Energy Recovery Schemes and Catalytic Processes: Some Interfaces |
| 1-24-79 | Dr. Farid F. Abrahan IBM Research Laboratory | Computer Simulation and Theory of Interfaces: I. Structure of the Solid-Liquid and Solid- Amorphous Interface II. Bond and Strain Energy Effects in Surface Segregation |
| 1-31-79 | Prof. David A. Shirley UC-Berkeley MMRD/Lawrence Berkeley Laboratory | Surface Structural Studies of Angle-Resolved Photoemission: 1. Electronic Structure of Steps; 2. Atomic Configuration from Photoelectron Diffraction |
| 2-7-79 | Dr. C. D. Prater Mobil Research and Development | Automation of Catalytic Pilot Plants and Computer Assisted Data Interpretation of Results |
| 2-9-79 | Prof. Thor N. Rhodin Cornell University | Angle-Resolved Photoemission Studies of Chalcogen and Chemisorption on Ni(111) |
| 2-14-79 | Dr. R. Fischer DOE, Washington | Catalysis in Advanced Development in Coal Liquefaction |
| 2-21-79 | Dr. Carol Amberg Carleton University Ottawa, Ontario, Canada | Inhibition of Hydrodesulfurization Over Unsupported Sulfide Catalysis |
| 2-28-79 | Dr. R. Maddix Stanford University | Oxygen Activated Adsorption on Silver Single Crystals |
| 3-7-79 | Dr. John Sinfelt Exxon Research and Development | Catalysis by Metals |
| 3-14-79 | Dr. N. Smith Bell Telephone Labs | Photoelectron Diffraction Effects from Na, Se and Te Atoms Adsorbed on Nickel |
| 3-15-79 | Prof. H. Knozinger University of Munich | Hydrogenation Catalysts from Molecular Metal Carbonyl Clusters Attached to Chemically Modified Silicas |
| 3-26-79 | Dr. R. Feder Julich, West Germany | Determination of the Si(111) (2xL) Surface Reconstruction via Dynamical LEED |
| 4-4-79 | Dr. R. T. Lewis Chevron Research | Surface Studies of Catalysis by ESCA |
| 4-6-79 | Dr. J. Wei Massachusetts Institute of Technology | CO Oxidation Over Platinum |
| 4-9-79 | Dr. M. Sheleff Ford Motor Company | Catalyst-Support Interaction, Some New Perspectives |
| 4-18-79 | Dr. R. Banks Phillips Petroleum | Olefin Disproportionation |

| <u>Date</u> | <u>Speaker and Affiliation</u> | <u>Seminar Title</u> |
|-------------|--|---|
| 4-20-79 | Dr. Garcia de la Banda Spanish Research Council | Science and Technology in Spain: Present and Future Trends |
| 4-25-79 | Prof. J. B. Butt Northwestern University | Modification of Structure Sensitivity of Supported Platinum for Some Hydrocarbon Reactions |
| 4-30-79 | Dr. P. B. Weisz Mobil Research and Development | Shape Selectivity in Catalysis |
| 5-2-79 | Dr. A. Frennet Stanford - Chemical Engineering | Effect of Multiple Sites and Competition with Hydrogen on the Kinetic Factors of the Adsorption Rate of Light Alkanes on Metals |
| 5-9-79 | Prof. Earl Muetterties UC - Berkeley MMRD/Lawrence Berkeley Laboratory | Chemistry of Transition Metal-Aromatic Hydrocarbon Complexes--The Catalytic Hydrogenation of Aromatic Hydrocarbons |
| 5-16-79 | Dr. Leon B. Levy Celanese Corporation | Heterogeneous Catalysis at Celanese |
| 5-23-79 | Prof. W. Keith Hall University of Wisconsin | Relationship Between the Surface Chemistry of Molybdena-Alumina Catalysts and Their Catalytic Function |
| 5-30-79 | Mr. Steven Sibener Lawrence Berkeley Laboratory | The Internal Energy Dependence of Molecular Condensation Coefficients |
| 8-24-79 | Prof. Kenzi Tamaru University of Tokyo | Carbon Monoxide Hydrogenation Over Ruthenium Surfaces |
| 8-29-79 | Prof. Kenzi Tamaru University of Tokyo | Ammonia Decomposition on Tungsten |
| 10-3-79 | Dr. S. W. Wang Stanford University | Surface Penning Ionization: Theory and Application as a New Technique for the Analysis of Chemisorbed Systems |
| 10-10-79 | Prof. G. A. Somorjai UC - Berkeley MMRD/Lawrence Berkeley Laboratory | Photocatalytic Dissociation of Water |
| 10-12-79 | Dr. Roger Parsons Laboratoires Bellevue CNRS France | Structure of the Solid-Electrolyte Interface |
| 10-17-79 | Prof. M. P. Rosynek Texas A & M University | Catalytic and Surface Properties of Activated Lanthanum Sesquioxide |
| 10-24-79 | Dr. W. O. Haag Mobil Research and Development Corporation | Acid Catalyzed Reactions on Zeolites |
| 10-31-79 | Dr. A. J. Nozik Solar Energy Research Institute | Hot Carrier Effects at Illuminated Semi-Conductor Electrolyte Interfaces |
| 11-7-79 | Dr. John Gland General Motors Research Center | The Interactions of Oxygen with the Platinum (III) Surface |
| 11-14-79 | Dr. O. R. Hughes Celanese Corporation | Hydroformylation with Rh Complexes and Diphosphines |
| 11-16-79 | Prof. W. O. Milligan Welsh Foundation | Structure and Morphology of the Complex Metal Cyanides |
| 11-28-79 | Prof. S. W. Weller University of New York at Buffalo | Studies in Catalytic Coal Liquefaction |
| 11-30-79 | Prof. A. G. Oblad University of Utah | Catalytic Steam Reforming of Aromatics |

| <u>Date</u> | <u>Speaker and Affiliation</u> | <u>Seminar Title</u> |
|--------------------------|--|---|
| 12-4-79 | Prof. M. Simonetta University of Milan | Interactions Between Organic Molecules and Metal Surfaces |
| 12-5-79 | Dr. R. Chianelli Exxon Research and Engineering Company | Structure and Properties of Molybdenum Sulfide Catalytic Materials |
| <u>Reaction Dynamics</u> | | |
| 1-10-79 | Mr. James Weisshaar Dept. of Chemistry UC - Berkeley MNRD/Lawrence Berkeley Laboratory | Non-Radiative Decay of Single Rotational Level of S ₁ Formaldehyde |
| 1-22-79 | Prof. Dudley Herschbach Dept. of Chemistry Harvard University | Multivector Properties of Reaction Dynamics |
| 2-9-79 | Dr. G. S. Hurst Oak Ridge National Laboratory | Recent Development in One-Atom Detection |
| 2-14-79 | Prof. P. Pechukas Dept. of Chemistry Columbia University | Transition State Theory, Trapped Trajectories, and Classical Bound States Embedded in the Continuum |
| 3-19-79 | Prof. Peter Ortoleva Dept. of Chemistry Indiana University | Non-Equilibrium Order in Physical Chemical Systems |
| 3-23-79 | Prof. Kozo Kuchitsu Dept. of Chemistry University of Tokyo | Chemical Reactions of Highly Excited Rydberg States |
| 4-9-79 | Prof. J. J. Turner Dept. of Chemistry University of Nottingham England | Infrared Laser Induced Chemical Reactions in Matrices |
| 4-10-79 | Dr. Michael V. Berry University of Bristol England | Regular and Irregular Semi-Classical Quantum States |
| 4-25-79 | Dr. Sheldon Green Institute for Space Studies NASA Goddard Space Flight Center | Exotic Molecules in Space |
| 5-21-79 | Prof. John Wiesenfeld Dept. of Chemistry Cornell University | Laser Spectroscopy for Photochemists |
| 6-6-79 | Prof. E. I. Yablonovitch Division of Applied Sciences Harvard University | Infrared Laser Induced Unimolecular Reactions |
| 7-12-79 | Dr. Phillip Bunker Herzberg Institute of Astrophysics Ottawa, Canada | Molecular Symmetries |
| 10-31-79 | Dr. Alan Luntz IBM Research Laboratory San Jose | Reaction Dynamics of Oxygen Atoms with Hydrocarbons |
| 11-19-79 | Dr. J. Vigue Lab. de Spectroscopie Hertzienne de L'Ecole Normale Superieure Paris, France | Optical Pumping of Molecules |

Miscellaneous

| <u>Date</u> | <u>Speaker and Affiliation</u> | <u>Seminar Title</u> |
|-------------|--|--|
| 2-22-79 | Dr. Kirk W. Beach School of Medicine University of Washington | Non-Invasive Techniques in the Diagnosis of Carotid Artery Disease, or Examining the Fluid Dynamics of an Inaccessible Hydrodynamic System |
| 4-23-79 | Prof. Sigrid Peyerimhoff Department of Chemistry University of Bonn, Germany | Theoretical Predictions of Electronic Spectra for Small Polyatomic Molecules Including Vibrational Structure and Radiation Lifetime |
| 8-21-79 | Dr. Herb S. Bennett Division Director National Science Foundation | Concerns and Activities of the Division of Materials Research at the National Science Foundation |
| 9-5-79 | Dr. O. O. Adewoye Department of Physics University of Ife, Nigeria | Some Aspects of the Indentation Deformation and Fracture Behavior of SiC |
| 9-10-79 | J. Winnick, P. Ross Lawrence Berkeley Laboratory | Molten Carbonate Fuel Cell Kinetics |
| 10-2-79 | Prof. W. Plieth Institute of Physical Chemistry Free University, Berlin | Reflection Spectroscopic Studies of Electrode Surfaces |

